PROGRESS IN BIOMEDICAL OPTICS AND IMAGING

Vol. 1, No. 8
ISSN 1605-7422

# *Laser-Tissue Interaction XI: Photochemical, Photothermal, and Photomechanical*

**Donald D. Duncan**
**Jeffrey O. Hollinger**
**Steven L. Jacques**
*Chairs/Editors*

**22–27 January 2000**
**San Jose, USA**

*Sponsored by*
AFOSR—U.S. Air Force Office of Scientific Research
SPIE—The International Society for Optical Engineering
IBOS—International Biomedical Optics Society





**Proceedings of SPIE**
**Volume 3914**

# REPORT DOCUMENTATION PAGE

*Form Approved*
*OMB No. 0704-0188*



| 1. REPORT DATE (DD-MM-YYYY) | 2. REPORT DATE | 3. DATES COVERED (From - To) |
|---|---|---|
| 16-06-00 | Final Technical Report | 15-01-2000 to 14-07-2000 |

**4. TITLE AND SUBTITLE**
Laser-Tissue Interaction XI: Photochemical, Photothermal and Photomechanical

**5a. CONTRACT NUMBER**

**5b. GRANT NUMBER**
F49620-00-1-0135

**5c. PROGRAM ELEMENT NUMBER**

**6. AUTHOR(S)**
Duncan,Donald
Hollinger, Jeffrey
Jacques, Steven

**5d. PROJECT NUMBER**

**5e. TASK NUMBER**

**5f. WORK UNIT NUMBER**

**7. PERFORMING ORGANIZATION NAME(S) AND ADDRESS(ES)**
Society of Photo-optical Instrumentation Engineers (SPIE)
PO Box 10
Bellingham, WA 98227-0010

**8. PERFORMING ORGANIZATION REPORT NUMBER**
Volume 3914

**9. SPONSORING/MONITORING AGENCY NAME(S) AND ADDRESS(ES)**
Air Force Office of Scientific Research
801 N. Randolph St. Room 732
Arlington, VA 22203-1977

**10. SPONSOR/MONITOR'S ACRONYM(S)**
AFOSR/NE

**11. SPONSORING/MONITORING AGENCY REPORT NUMBER**

**12. DISTRIBUTION AVAILABILITY STATEMENT**
Approved for public release

**13. SUPPLEMENTARY NOTES**
ISBN 0-8194-3530-9

**14. ABSTRACT**
This proceedings contains papers on the following topics: PDT and Immunotherapy, Photothermal Interactions,Laser Ablation, Photoacoustics, Tissue Optics, Beam Propagation in Random Media, Bone Engineering, Ultrastructure, and Tissue Mechanics.

**15. SUBJECT TERMS**
Laser, Photochemical, Photothermal, Photomechanical

| 16. SECURITY CLASSIFICATION OF: | | | 17. LIMITATION OF ABSTRACT | 18. NUMBER OF PAGES | 19a. NAME OF RESPONSIBLE PERSON |
|---|---|---|---|---|---|
| a. REPORT | b. ABSTRACT | c. THIS PAGE | | | Marshall Weathersby |
| Non-Classified | | | SAR | 652 | 19b. TELEPONE NUMBER (Include area code) (360)676-3290 |

PROGRESS IN BIOMEDICAL OPTICS AND IMAGING
Vol. 1, No. 8

# *Laser-Tissue Interaction XI: Photochemical, Photothermal, and Photomechanical*

**Donald D. Duncan**
**Jeffrey O. Hollinger**
**Steven L. Jacques**
*Chairs/Editors*

**22–27 January 2000**
**San Jose, USA**

*Sponsored by*
AFOSR—U.S. Air Force Office of Scientific Research
SPIE—The International Society for Optical Engineering
IBOS—International Biomedical Optics Society

*Published by*
SPIE—The International Society for Optical Engineering

**Proceedings of SPIE**
**Volume 3914**

The papers appearing in this book compose the proceedings of the technical conference cited on the cover and title page of this volume. They reflect the authors' opinions and are published as presented, in the interests of timely dissemination. Their inclusion in this publication does not necessarily constitute endorsement by the editors or by SPIE. Papers were selected by the conference program committee to be presented in oral or poster format, and were subject to review by volume editors or program committees.

Please use the following format to cite material from this book:

Author(s), "Title of paper," in *Laser-Tissue Interaction XI: Photochemical, Photothermal, and Photomechanical*, Donald D. Duncan, Jeffrey O. Hollinger, Steven L. Jacques, Editors, Proceedings of SPIE Vol. 3914, page numbers (2000).

ISSN 1605-7422
ISBN 0-8194-3530-9

Published by
**SPIE—The International Society for Optical Engineering**
P.O. Box 10, Bellingham, Washington 98227-0010 USA
Telephone 1 360/676-3290 (Pacific Time) • 1 Fax 360/647-1445
http://www.spie.org/



Printed in the United States of America.

# Contents

# Conference Committee

## Part A Laser-Tissue Interaction XI: Photochemical, Photothermal, and Photomechanical

*Conference Chair*

**Steven L. Jacques,** Oregon Medical Laser Center (USA)

*Program Committee*

**Wei R. Chen,** University of Central Oklahoma (USA) and University of Oklahoma (USA)
**Bernard S. Gerstman,** Florida International University (USA)
**Randolph D. Glickman,** University of Texas Health Science Center at San Antonio (USA)
**Tayyaba Hasan,** Wellman Laboratories of Photomedicine (USA), Massachusetts General Hospital (USA), and Harvard Medical School (USA)
**E. Duco Jansen,** Vanderbilt University (USA)
**Sean J. Kirkpatrick,** Oregon Health Sciences University (USA)
**Richard A. London,** Lawrence Livermore National Laboratory (USA)
**Steen J. Madsen,** University of Nevada/Las Vegas (USA)
**William P. Roach,** Uniformed Services University of the Health Sciences (USA)
**Alfred Vogel,** Medical Laser Center Lübeck GmbH (Germany)
**Lihong V. Wang,** Texas A&M University (USA)

*Session Chairs*

PDT and Immunotherapy
**Wei R. Chen,** University of Central Oklahoma (USA) and University of Oklahoma (USA)

PDT, Immunotherapy, and Other Photochemistry
**Tayyaba Hasan,** Wellman Laboratories of Photomedicine (USA), Massachusetts General Hospital (USA), and Harvard Medical School

Photothermal Interactions I
**Richard A. London,** Lawrence Livermore National Laboratory (USA)

Photothermal Interactions II
**E. Duco Jansen,** Vanderbilt University (USA)

Laser Ablation
**William P. Roach,** Uniformed Services University of the Health Sciences (USA)

Laser Ablation and Disruption
**Randolph D. Glickman,** University of Texas Health Science Center at San Antonio (USA)

Photoacoustics
**Alfred Vogel,** Medical Laser Center Lübeck GmbH (Germany)

Photoacoustics and Bubbles
**Bernard S. Gerstman,** Florida International University (USA)

Laser Ablation
**Richard A. London,** Lawrence Livermore National Laboratory (USA)

Laser-Tissue Interaction
**Steven L. Jacques,** Oregon Medical Laser Center (USA)

Tissue Optics I
**Lihong V. Wang,** Texas A&M University (USA)

Tissue Optics II
**Lihong V. Wang,** Texas A&M University (USA)

Beam Propagation in Random Media I
**Norman S. Kopeika,** Ben-Gurion University of the Negev (Israel)

Beam Propagation in Random Media II
**Steven L. Jacques,** Oregon Medical Laser Center (USA)

Beam Propagation in Random Media III
**Steven L. Jacques,** Oregon Medical Laser Center (USA)

Beam Propagation in Random Media IV
**Norman S. Kopeika,** Ben-Gurion University of the Negev (Israel)

## Part B Optical Technologies to Solve Problems in Tissue Engineering

*Conference Chairs*

**Jeffrey O. Hollinger, D.D.S.,** Oregon Health Sciences University (USA)
**Donald D. Duncan,** Johns Hopkins University (USA)

*Program Committee*

**Steven L. Jacques,** Oregon Medical Laser Center (USA)
**Sean J. Kirkpatrick,** Oregon Health Sciences University (USA)

*Session Chairs*

Bone Engineering
**John Schmitz,** University of Texas Health Sciences Center at San Antonio (USA)

Ultrastructure
**Sean J. Kirkpatrick,** Oregon Health Sciences University (USA)

Tissue Mechanics
**Donald Dean Duncan,** Johns Hopkins University (USA)

Part A

# LASER-TISSUE INTERACTION: PHOTOCHEMICAL, PHOTOTHERMAL, AND PHOTOMECHANICAL

## SESSION 1

# PDT and Immunotherapy

Invited Paper

# Photosensitizers for Photodynamic Immune Modulation

John R. North, Ron Boch, David W.C. Hunt, Leslie G. Ratkay, Guillermo O. Simkin, Jing-Song Tao, Anna M. Richter, and Julia G. Levy.

QLT PhotoTherapeutics, Inc.
887 Great Northern Way
Vancouver, British Columbia
Canada V5T 4T5

## ABSTRACT

PDT may be an effective treatment for certain immune-mediated disorders. The immunomodulatory action of PDT is likely a consequence of effects exerted at a number of levels including stimulation of specific cell signaling pathways, selective depletion of activated immune cells, alteration of receptor expression by immune and non-immune cells, and the modulation of cytokine availability. QLT0074, a potent photosensitizer that exhibits rapid clearance kinetics *in vivo*, is in development for the treatment of immune disorders. In comparison to the well-characterized and structurally related photosensitizer verteporfin, lower concentrations of QLT0074 were required to induce apoptosis in human blood T cells and keratinocytes using blue light for photoactivation. Both photosensitizers triggered the stress activated protein kinase (SAPK) and p38 (HOG1) pathways but not extracellularly regulated kinase (ERK) activity in mouse Pam212 keratinocytes. In cell signaling responses, QLT0074 was active at lower concentrations than verteporfin. For all *in vitro* test systems, the stronger photodynamic activity of QLT0074 was associated with a greater cell uptake of this photosensitizer than verteporfin. In mouse immune models, sub-erythemogenic doses of QLT0074 in combination with whole body blue light irradiation inhibited the contact hypersensitivity response and limited the development of adjuvant-induced arthritis. QLT0074 exhibits activities that indicate it may be a favorable agent for the photodynamic treatment of human immune disease.

**Keywords:** apoptosis, contact hypersensitivity, immunomodulation, keratinocytes, photodynamic therapy, photosensitizers, psoriasis, signal transduction, T cells, verteporfin.

## 1. INTRODUCTION

The chlorin-like photosensitizer, benzoporphyrin derivative monoacid ring A, BPD-MA[1,2] (its formulated product is termed Verteporfin for Injection, VFI) has been extensively characterized for its mode of action and for assessing the influence of photodynamic therapy (PDT) upon different immune parameters[3-9]. Of significance, VFI has been tested in clinical trials for its activity against the human immune-mediated condition of psoriasis[10]. In combination with activating light, VFI is photo-cytotoxic at relatively low concentrations *in vitro*. VFI combined with light irradiation can induce the apoptotic death of different tumor[11-15] and normal immune[8,9] cell types. The marked capacity of PDT to induce apoptosis is believed related to the localization of certain photosensitizers to the mitochondrion[15-17], a key site for the regulation of apoptosis-related stimuli[18,19]. A gradient in cell responses to PDT is evident. At high photosensitizer/light doses, cells may rapidly lose membrane integrity and viability without undergoing apoptosis (necrosis). Necrotic cell death may promote the development of an inflammatory state at the treatment site. At lower, yet still cytotoxic PDT doses, cells may undergo programmed cell death (apoptosis). Phagocytic cells efficiently take up and dispose of cells dying by apoptosis without producing inflammation in the tissue[19]. At sub-lethal levels, PDT may trigger cell signaling events that may influence cell surface receptor expression, cytokine formation and/or growth kinetics. Mobilization of stress activated protein kinase (SAPK) and p38/high osmolarity glycerol protein kinase (HOG1), but not extra-cellularly regulated kinases (ERK) 1 or 2 was demonstrated for mouse Pam212 keratinocytes (KC) treated with VFI and red light[20]. The full significance of these signaling events is still unclear. However, the relative levels of activation and overlap with other signaling pathways may influence the function and/or survival of cells treated at an intensity of PDT less than that required to induce rapid cell death.

Activated T lymphocytes are highly sensitive to photodynamic killing with VFI. Mitogen-stimulated murine splenocytes accumulated greater amounts of verteporfin and the activated cell populations were more vulnerable to photodynamic killing than their non-activated counterparts[5]. Anti-CD3 activated mouse spleen T cells exhibited greater verteporfin uptake and were more susceptible to PDT-induced apoptosis than resting T cells[8]. A tissue-specific depletion of activated T cells may be a therapeutic goal for the treatment of immune-mediated disease with PDT.

The photosensitizer dose, as well as the dose and timing of light irradiation, can be adjusted so that immune-modulating effects can be achieved without producing skin erythema or influencing the general immune status[21]. This form of PDT, in which a large body surface area is illuminated to generate a disseminated low-intensity PDT effect, inhibited the



In *Laser-Tissue Interaction XI: Photochemical, Photothermal, and Photomechanical*, Donald D. Duncan, Jeffrey O. Hollinger, Steven L. Jacques, Editors, Proceedings of SPIE Vol. 3914 (2000)
1605-7422/00/$15.00

immunologically mediated contact hypersensitivity (CHS) response to the hapten dinitrofluorobenzene (DNFB) in mice[7]. PDT with VFI was also tested upon the development of autoimmune adjuvant-induced arthritis of MRL/*lpr* strain mice[4]. Mice given a series of three low-intensity, whole body photodynamic treatments at 10-day intervals exhibited joint histologic and clinical profiles similar to the untreated control mice[3]. The therapeutic effect achieved with PDT was comparable to that produced by different agents with immunomodulatory activity[4]. Importantly, hematopoietic progenitor activity and spleen cell mitogenic responses were preserved in PDT-treated mice[3]. PDT with VFI can dampen the immune response to a topically applied hapten[7] and reduce disease severity in mouse autoimmune models[3,4,6].

The human immune-mediated condition of psoriasis is manifested in the skin. Patients with psoriasis exhibit dramatically heightened KC proliferation leading to elevated plaque formation at various body sites. Psoriatic plaques contain large infiltrates of activated T cells within the epidermal and dermal regions of the skin. The instigating factors for psoriasis are not fully defined, although it is now evident that it is a T cell-mediated condition. Cytokines released by activated T cells drive the altered proliferation and differentiation behavior of KC within the plaque. Treatments that deplete or impair the activity of skin-infiltrating T cells can produce a beneficial clinical effect on psoriasis[22-24]. Patients with psoriatic arthritis (PsA) exhibit degenerative joint changes in association with psoriasis. In a recent clinical trial, PsA patients were administered VFI systemically and treated with half or whole body-UVA light irradiation 3 hours later[10]. The drug and light dose combinations did not cause skin erythema. Four PDT treatments given one week apart produced a greater than 35% improvement in total psoriasis area and severity index (PASI) scores in 5 of the 17 patients by the completion of the study[10]. Importantly, few side effects were reported. Earlier studies indicated that PDT might be an effective psoriasis treatment[25].

To achieve a beneficial clinical effect against psoriasis, PDT may imperil pathogenic T cell survival, modify APC function and directly or indirectly alter KC proliferation within the psoriatic plaque. A photosensitizer, presently designated QLT0074, has been synthesized and formulated for possible use in the treatment of human immune-mediated conditions with PDT. A series of characterization studies has now been performed with this photodynamic agent to reveal whether it has the potential to serve as an anti-psoriasis drug.

## 2. MATERIALS AND METHODS

### 2.1. Photosensitizers

The A-ring of benzoporphyrin derivative (BPD) diethylene-glycol ester (QLT0074), a chlorin–type photosensitizer, was used in a lipid formulation. Like verteporfin, QLT0074 is derived from protoporphyrin IX. Lyophilized QLT0074 and VFI (QLT PhotoTherapeutics, Inc., Vancouver, B.C.) were reconstituted in sterile, distilled water. For *in vivo* use, photosensitizers were diluted with 5% dextrose while for *in vitro* studies, these preparations were diluted with culture medium. The molecular structure of QLT0074 is provided below (Fig. 1).

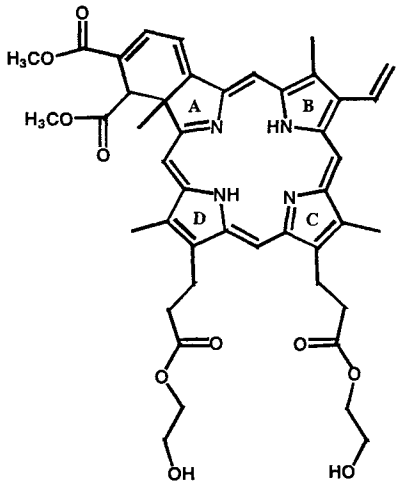


Fig. 1. Molecular structure of QLT0074 (molecular weight = 792).

### 2.2. Isolation and activation of human blood T lymphocytes

Heparinized blood obtained from healthy laboratory personnel was diluted with RPMI 1640 medium with 5% fetal calf serum (FCS) and antibiotics and fractionated by Ficoll Paque density gradient centrifugation. The mononuclear cell fraction was passed over T cell immuno-affinity columns (R&D Systems, Minneapolis, MN). The eluted T cell fraction comprised >98% T cells as indicated by their expression of CD3, determined by flow cytometric analysis (Fig.

2A). Of the isolated cells, approximately 2/3 were $CD4^+$ (helper T cells) and the remainder were $CD8^+$ (cytotoxic T cells) (data not shown). Few of the purified cells expressed the T cell activation marker CD25 (interleukin-2 receptor, IL-2R). Activation was elicited by culturing the cells at 0.5-1 x $10^6$/mL in RPMI 1640 medium, 5% FCS in plastic microtiter plates pre-coated with immobilized mouse monoclonal anti-CD3 (clone UCHT1, PharMingen, San Diego CA) and anti-CD28 (clone CD28.2, PharMingen) antibodies. Plates were initially treated with antibodies at 5 μg/mL in phosphate-buffered saline (PBS) for 3 h and then washed several times with PBS. Co-ligation of CD3 and CD28 surface structures triggers signaling events that stimulate T cell activation and proliferation in the absence of antigen presenting cells (APC)[26]. Recombinant IL-2 (rIL-2, Amgen Biologicals, Thousand Oaks CA) at 100 U/mL was added to sustain T cell proliferation.

### 2.3. Photosensitization and determination of cell viability

All cell work with photosensitizer was carried out under light-attenuated conditions. Cells were incubated with photosensitizer at 37°C in the dark for 1 h. The blue light source was a light panel of 8 fluorescent tubes with an emission spectrum of 420 - 490 nm. Panel intensity was checked with a light meter before each experiment. Cell viability was assessed 24 h later with the MTT (3-[4-,5-dimethylthiazol-2-yl]-2,4-diphenyl tetrazolium bromide, Sigma) colorimetric assay[27]. Replicates of 3-6 were performed at each photosensitizer concentration. Color development was terminated after 4 h at 37°C in the presence of MTT and read with an automated microtiter plate reader (Dynatech, Hamilton VA) at a wavelength of 590 nm. Absorbance values for wells containing medium alone were subtracted from the result obtained for wells containing cells. Results are given as a percentage of the absorbance obtained for cells treated with light alone.

### 2.4. Detection of T cell apoptosis

During apoptosis, phosphatidylserine (PS) molecules migrate to the outer portion of the cell membrane. Apoptotic cells are detectable by the binding of an Annexin-V-fluorescein isothiocyanate (FITC) conjugated probe (PharMingen) to PS[15]. Cell membrane integrity was assessed in parallel by propidium iodide (PI) uptake studies. Cells were evaluated with an Epics XL flow cytometer using two-color analysis and appropriate color compensation techniques. Cells with an intact plasma membrane exclude PI. Annexin-V+/PI- cells are considered to be in the early stages of apoptosis while Annexin-V+/PI+ cells may be in late stage apoptosis or are undergoing necrotic cell death.

### 2.5. PDT effects on normal human KC

Human neonatal foreskin KC (Clonetics, San Diego, CA) were maintained in serum-free keratinocyte growth medium (Clonetics). These cells have a limited proliferative potential *in vitro* and were used in experiments at culture passages 2 or 3. KC at 50-60% confluency were incubated with photosensitizer for 60 min at 37°C in medium containing 2% FCS and then irradiated with blue fluorescent light. Whole cell lysates were prepared 3 h post-PDT[11]. These preparations were separated by sodium dodecyl sulfate polyacrylamide gel electrophoresis (SDS-PAGE) in 10% gels, transferred to nitrocellulose and stained for apoptosis-related changes using antibodies to caspase-3, caspase-8, caspase-9 or the DNA repair enzyme poly(ADP-ribose)polymerase (PARP) as described[11-15]. Blots were developed using chemiluminescence and autoradiography techniques. For cell viability determinations, KC were maintained for a further 24 h after PDT and MTT assays were then performed.

### 2.6. Imapct of PDT on cell signaling activity

The spontaneously transformed mouse Pam212 KC line was provided by Dr. Stephen E. Ullrich (University of Texas, Houston TX). The cell line was initially established by culturing KC isolated from newborn Balb/c mice. Cells were maintained in 22 ml of Dulbecco's minimum essential medium (DMEM, Gibco) supplemented with heat-inactivated 5% FCS, penicillin (100 U/mL) and streptomycin (100 μg/mL) in 100 x 20 mm Falcon 3003 polystyrene tissue culture dishes[20]. Following PDT, cells were maintained at 37 °C in the dark for 45 min. The medium was aspirated, and the cells were washed twice with ice-cold PBS containing 1 mM $Na_3VO_4$. The cells were lysed by scraping in 800 μl of ice-cold homogenizing buffer (20 mM MOPS, pH 7.2, 5 mM EGTA, 1% (W/V) Nonidet P-40 (NP40), 1 mM dithiothreitol, 75 mM β-glycerol phosphate, 1 mM $Na_3VO_4$ and 1 mM phenylmethylsulfonyl fluoride). The mixture was transferred into a 1.7 mL micro-centrifuge tube and sonicated at 4°C for 30 sec. Insoluble material was pelleted by centrifugation (10,000 x *g*) for 15 min at 4°C. The supernatant removed, divided into aliquots, quickly frozen in liquid nitrogen and stored at -70°C.

Immunoprecipitation of ERK1/2 was performed with 500 μg Pam 212 cell lysate by addition of 30 μL of protein A Sepharose (1:1 slurry) and 5 μl (0.5 μg) of a 1:1 mixture of anti-ERK1 (C-16, rabbit IgG against C-terminal residues 352-367; cat # sc-93 Santa Cruz, Biotechnology, Inc., Santa Cruz CA) and anti-ERK2 (C-14, rabbit IgG against C-terminal residues 345-358; Santa Cruz cat # sc-154) antibody. Mixtures were rotated at 4°C for 3 h. Protein A-Sepharose beads were pelleted by microfuge centrifugation at 4°C for 2 min and the supernatant discarded. Protein A-Sepharose beads were washed

with twice with 3% NP40 and NP40-free NETF buffer (100 mM NaCl, 5 mM EDTA, 50 mM Tris-HCl, pH 7.4, and 50 mM NaF).

Suspensions of ERK1/2 immune complexes were incubated in a 60 μL reaction mixture containing 20 mM $MgCl_2$, 25 mM β-glycerophosphate, 20 mM MOPS, 5 mM EGTA, 2 mM EDTA, 0.25 mM DTT, 5 mM β-methyl aspartic acid, 1 μM of the cAMP-dependent kinase inhibitor (PKI), 50 μM [$\gamma$-$^{32}$P]ATP (2000 cpm/pmol) and 5 μg MBP. The reaction was performed in 1.7 mL microcentrifuge tubes for 5 min and the reaction was terminated by the addition of 20 μl SDS sample buffer. Full-length myelin basic protein (MBP, Sigma) was used for *in vitro* kinase assay of ERK1 and ERK2 activity. A fusion protein consisting of GST and N-terminal residues 1-79 of c-Jun (Stressgen, Victoria, B.C.) was used to assay SAPK/JNK kinase activity. Full-length heat shock protein (HSP27) (Stressgen) was used to indirectly assess p38 HOG activity[20]. For the SAPK/JNK and p38 assays, 50 μg of cell lysate was incubated as above in a 75 μL reaction mixture with 2.5 μg of either GST-c-Jun [1-79] or HSP27, respectively. The reaction was terminated after 15 min by the addition of 20 μl SDS sample buffer. After boiling for 5 min, the samples were separated by SDS-PAGE. After electrophoresis, the proteins were transferred to nitrocellulose membrane in 25 mM Tris, 192 mM glycine and 20% methanol) for 3 h at 4°C at 300 mA with a TE Series Transphor Electrophoresis Unit (Hoefer Scientific Instruments). The membrane was stained for protein with Ponceau S (Sigma), rinsed with distilled water and dried prior to exposing to autoradiography film (Kodak BioMax MR, VWR). Following autoradiography, substrate bands on the nitrocellulose membrane were excised and counted by liquid scintillation counting[20].

### 2.7. Contact hypersensitivity (CHS) response

Female Balb/c mice were pre-treated with whole body PDT consisting of intravenous (i.v.) photosensitizer injection, followed by whole body blue fluorescent light (15 J/cm$^2$) irradiation 1 h later. Twenty-four h later, CHS to dinitrofluorobenzene (DNFB, Sigma Chemicals, St. Louis, MO) was initiated by applying a DNFB solution to a shaved flank region[7]. Control animals were administered PBS and exposed to the light source. Five days later, the hapten was applied to the dorsal surface of the right ear. To gauge its irritant effect, the delivery solvent alone was applied to the left ear. Non-sensitized mice were evaluated in parallel to determine the effect of the DNFB challenge solution. The CHS response was gauged immediately before and 24 h after DNFB application by measuring ear thickness with a dial caliper. Measurements were carried out in a blinded manner.

### 2.8. Adjuvant-induced arthritis

To induce arthritis, MRL/lpr strain mice were immunized intra-dermally with complete Freund's adjuvant (CFA)[3]. The photodynamic treatment consisted of an i.v. injection of photosensitizer followed 1 h later by whole body blue light irradiation. PDT was given 3 times at 10-day intervals. Arthritis was evaluated every 5 days by measuring ankle width with a micrometer.

## 3. RESULTS

### 3.1. PDT with QLT0074 or VFI induces apoptosis in T lymphocytes

The majority of purified human blood T cells incubated with immobilized anti-CD3 and anti-CD28 monoclonal antibodies and rIL-2 for 5 days, exhibited a blast-like appearance and 50-60% expressed the CD25 activation antigen (Fig 2A). Treatment with increasing amounts of QLT0074 or VFI and a constant level (2 J/cm$^2$) of blue light lead to decreased cell viability at nanomolar photosensitizer concentrations as determined by MTT assays (Fig. 2B). QLT0074 was phototoxic at lower concentrations than VFI. Annexin-V-FITC binding assays indicated that QLT0074 produced apoptosis by 3 h post-light irradiation in a larger proportion of T cells than VFI, when equimolar amounts of the photosensitizers were compared (Fig. 2C).

### 3.2. Sensitivity of normal human KC to PDT

In the absence of light, neither VFI nor QLT0074 affected KC viability (Fig. 3A). For blue-light-irradiated (1 J/cm$^2$) cells. QLT0074 was marginally more potent against KC viability than VFI. As anticipated, increasing the amount of blue light delivered to the cells lowered the concentration of photosensitizer required to elicit photodynamic killing of KC (data not shown). Biochemical changes representative of apoptosis were evident in whole cell lysates prepared from KC 3 h after treatment treated with VFI or QLT0074 and irradiation with blue light (Fig. 3B). At 100 nM, but not at 10 nM, both photosensitzers produced evidence in light-irradiated KC of caspase-3, -8 and –9 processing and the degradation of the caspase-3 substrate PARP. At 200 nM, caspase processing and PARP degradation was evident for light-irradiated KC treated with VFI but not with QLT0074. Neither photosensitizer produced evidence of caspase processing or PARP degradation in light-protected KC.

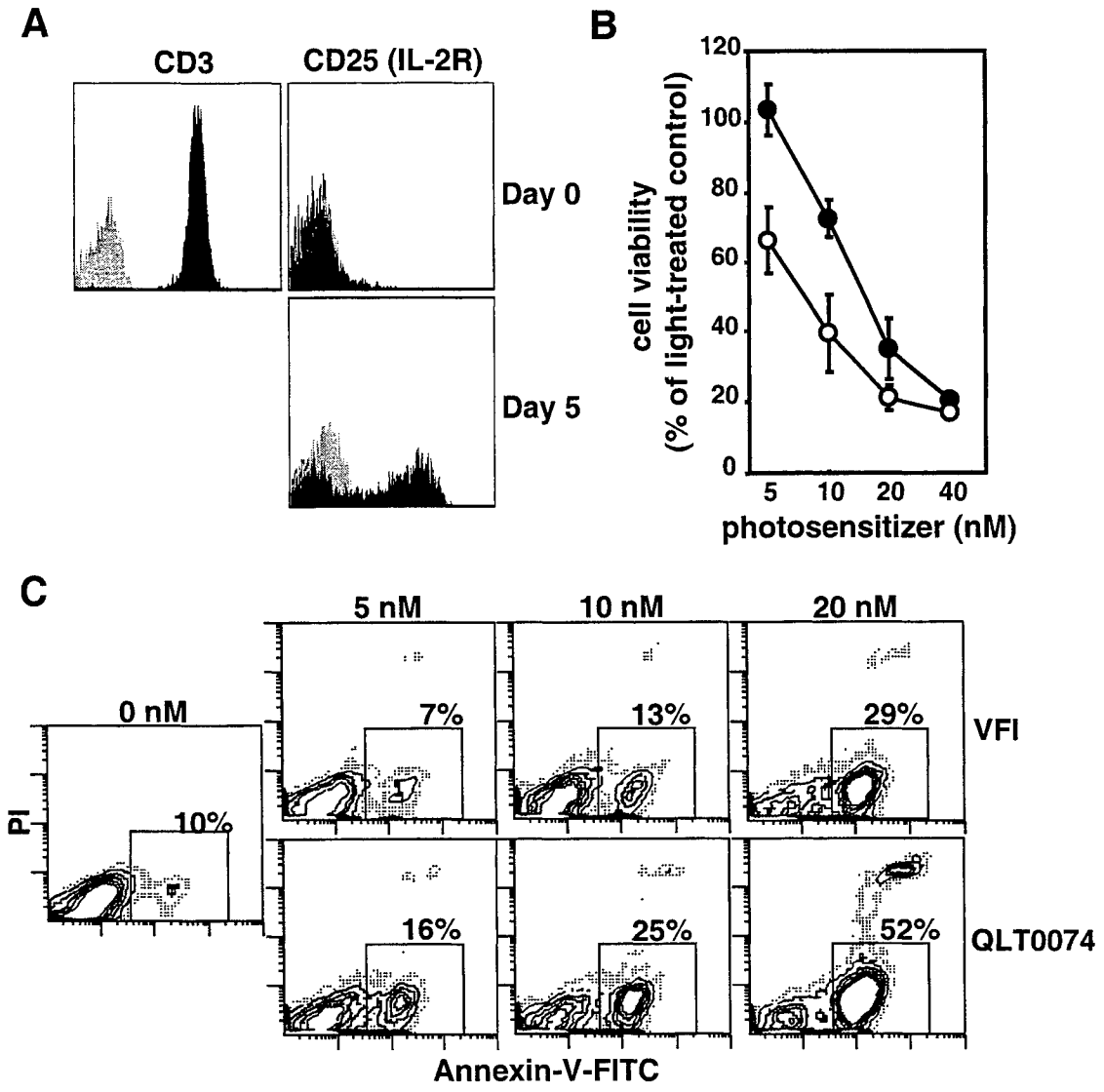


Fig. 2. Activated human blood T cells are sensitive to photodynamic killing with VFI or QLT0074. (A) T cell purity was assessed by staining the preparation with an FITC-conjugated monoclonal antibody against the pan-T cell marker CD3 (filled area) or an IgG1 isotype control reagent (gray area) and flow cytometric analysis. Staining with anti-CD25 monoclonal antibody was performed to assess T cell activation status on day 0 and after 5 days in microtiter plate wells containing immobilized anti-CD3 and anti-CD28 monoclonal antibodies and rIL-2. Staining with an FITC-conjugated IgG1 isotype control monoclonal antibody was performed in parallel. (B) Day 5 activated T cells were treated with increasing amounts of VFI (●) or QLT0074 (○) and then exposed to blue light (2 J/cm$^2$). Cell survival was determined 24 later by the MTT assay. Results are given as a percentage of the MTT result (absorbance value at 590 nm) obtained for cells exposed to light alone (5 independent experiments). (C) Photodynamic induction of apoptosis with blue light irradiation occurs in activated T cells with lower concentrations of QLT0074 than VFI. Annexin-V binding and PI uptake studies were performed 3 h post-PDT. Early apoptotic cells (Annexin-V+, PI negative) are demarcated and this percentage is given.

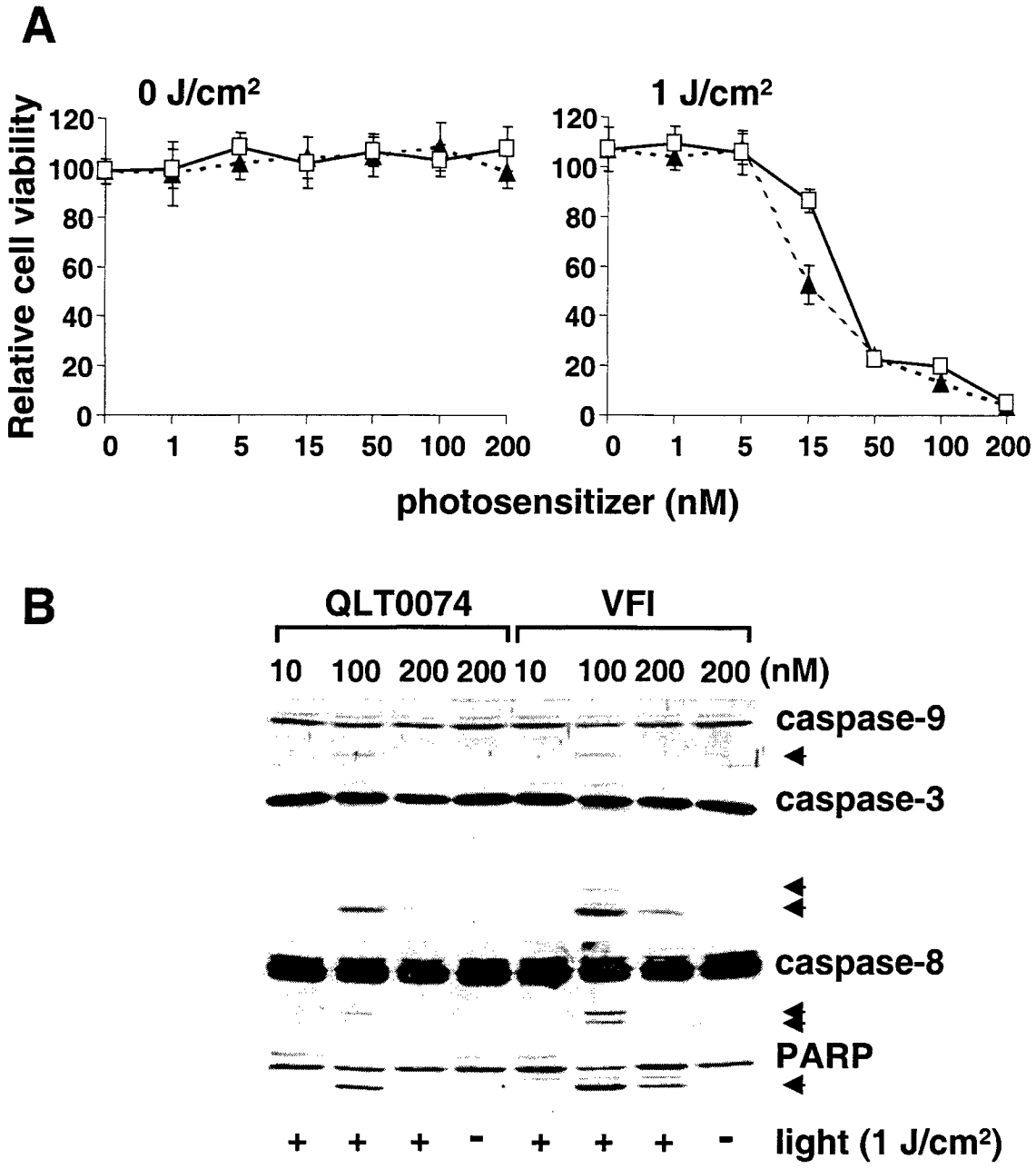


Fig. 3. PDT with QLT0074 or VFI and blue light irradiation reduces the viability of normal human KC and induces apoptosis-related changes. Cells were incubated for 60 min with increasing amounts of photosensitizer and either light-protected or irradiated with blue light. (A) Cell survival was determined 24 h later by the MTT colorimetric assay. For KC treated with VFI (□) or QLT0074 (▲) and light, results are presented as a percentage of the mean absorbance value obtained for cells not incubated with photosensitizer. (B) Apoptosis-associated events were assessed for cell lysates prepared 3 h post-PDT. These extracts were separated by SDS-PAGE, transferred to nitrocellulose and immunoblotted with antibodies against caspase-3, -8, -9 and the caspase substrate PARP. Arrows indicate the electrophoretic position of active caspase fragments and the PARP degradation product.

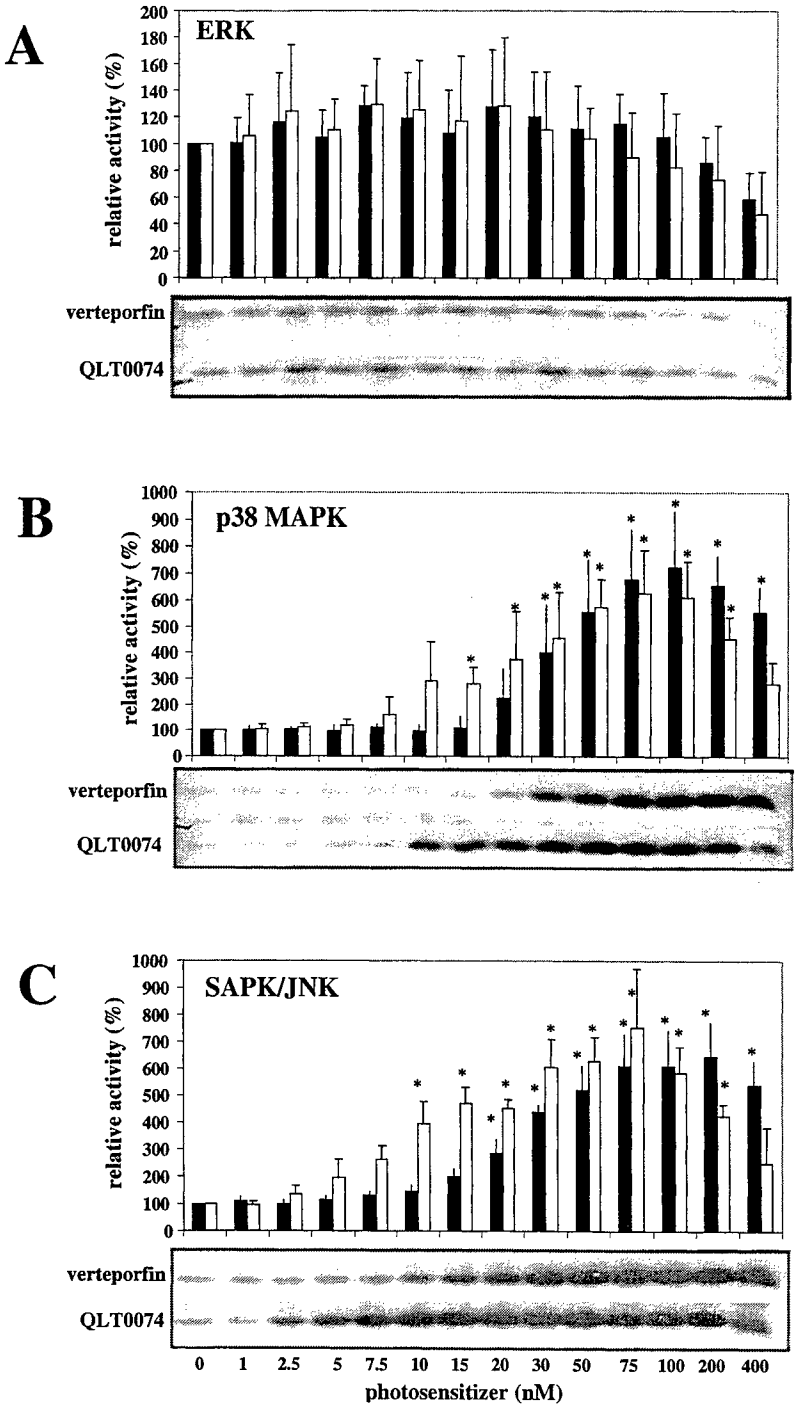


Fig. 4. Influence of PDT on (A) ERK, (B) p38 (HOG1) and (C) SAPK/JNK activity of PAM212 KC. Cells were incubated with VFI or QLT0074 for 1 h prior to exposure to 2 J/cm$^2$ of blue light (420-490 nm). Cells were lysed at 45 min post-light exposure and kinase activity within these lysates was assessed. Samples were run on SDS-PAGE, followed by transfer to nitrocellulose and autoradiography. Data is presented as a percentage (mean ± SD) of the $^{32}$P counts obtained for cells treated with light alone activity (4-5 independent experiments). Lower panels show representative autoradiograms. Significant differences ($P<0.05$, ANOVA) from control are indicated by asterisks (*) above each bar.

### 3.3. Impact of PDT on signaling pathways in mouse KC

Pam212 cells were treated with PDT with either QLT0074 or VFI combined with blue light irradiation. Forty-five min later, cell lysates were prepared and were tested for their ability to phosphorylate defined kinase substrates *in vitro*. Neither QLT0074 nor VFI increased ERK signaling activity in light-irradiated KC (Fig. 4A). ERK activity declined below control values at higher photosensitizer levels. Both photosensitizers produced a concentration-dependent increase of SAPK and (Fig. 4B) and p38/HOG1 kinase (Fig. 4C) activity in light-irradiated KC. Lower amounts of QLT0074 than VFI were required to stimulate these biochemical activities. In contrast, blue light alone or either photosensitizer in the absence of light irradiation did not affect these biochemical pathways (data not shown).

### 3.4. Influence of PDT on the CHS response

QLT0074 or VFI in combination with whole body blue light irradiation produced significant (~40%) reductions in the ear swelling response of Balb/c mice painted with DNFB (Fig. 5). Blue light alone did not affect the magnitude of the CHS response.

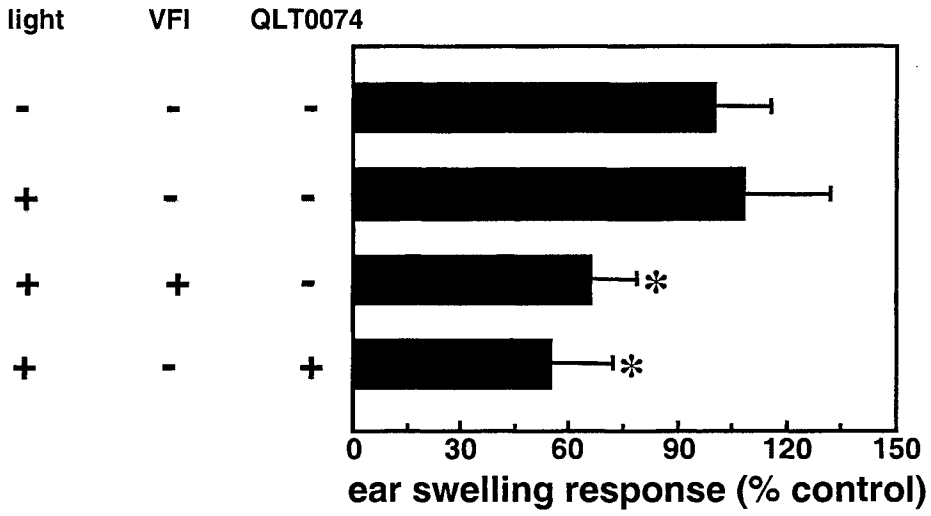


Fig. 5. PDT with VFI or QLT0074 combined with whole body and blue light irradiation inhibits the CHS response to a topically applied hapten DNFB. Balb/c mice were treated with photosensitizer (1.4 μmol/kg) 1 h prior to blue light irradiation (15 J/cm$^2$) and 24 h prior to the initial DNFB application. The hapten was applied to an ear 5 days after PDT and ear-swelling responses were determined 24 h later. Each group consisted of 10-15 mice. Results are presented as a percentage of the response generated by DNFB-sensitized animals not exposed to light or given PDT. For mice not given an initial exposure to DNFN the ear swelling irritant reaction produced an increase in ear swelling thickness of 1.7 ± 0.6 mm x $10^{-2}$.

* $P < 0.05$: Difference from the control result as determined by the Bonferoni multiple comparison t-test.

### 3.5. Inhibition of adjuvant-induced arthritis with PDT

MRL/*lpr* mice exhibited frank arthritic changes within 10 days following the administration of CFA. Animals given a series of 3 PDT treatments 10 days apart, with QLT0074 combined with blue light irradiation, exhibited less ankle swelling than the CFA-injected control mice over the final 15 days of the experiment (Fig. 6). Untreated MLR/*lpr* mice display joint swelling as a component of their underlying autoimmune disease (3), accounting for the modest increase in ankle thickness within the control group.

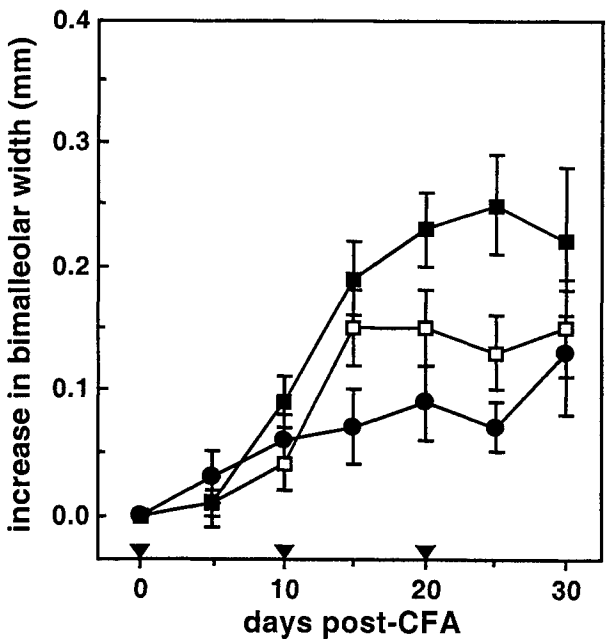


Fig. 6. PDT with QLT0074 and blue light irradiation inhibits the development of adjuvant-induced arthritis in MRL/*lpr* mice. CFA-injected, PDT-treated mice ( ) were given QLT0074 (1.4 μmol/kg) and fluorescent blue light (14.5 J/cm$^2$) irradiation on days 0, 10 and 20 as indicated (▼). CFA-injected (■) and untreated (●) animals served as controls. Ankle width determinations were performed every 5 days. Means ± the standard error values for 8-13 mice per group are shown.

## 4. DISCUSSION

Verteporfin was developed to meet a need for an effective photodynamic agent that did not produce extended skin photosensitivity. Extensive laboratory work with VFI demonstrated its potent capacity to produce the photodynamic killing of a wide variety of cell types. This capacity was likely due to the localization of the photosensitizer to intracellular regions that influence cell death/viability[15,18,19]. The quest for photosensitizers with high specific activity against target cell populations and limited retention *in vivo* has continued. We present evidence that QLT0074 exhibits characteristics that indicate it may be a suitable candidate for the photodynamic treatment of immune disease. First, normal human T cells and KC as well as mouse Pam212 KC are sensitive to the effects of this photosensitizer at low concentrations *in vitro* using blue light for photo-activation. Secondly, the photodynamic induction of cell death with QLT0074 is rapid, a property this photosensitizer shares with verteporfin. For KC, frank apoptosis-related changes (caspase-3, -8 and –9 activation, PARP degradation) were observed by 3 h post-PDT with both photosensitizers. This rapid induction of apoptosis suggests that the cellular sites of interaction include those (*e.g.* mitochondria) that are directly linked to the cell death machinery. The mobilization of caspase-3 in PDT-treated KC corresponds to events elicited in different tumor cell types (11-15) and normal human endothelial cells[28] treated with VFI and red light. Activated caspase-3 is associated with apoptosis instigated by a wide variety of cell death initiators[19]. Although caspase-8 activation is typically associated with apoptosis-regulating receptor (*e.g.* Fas, TNF-α) signaling, it may also be activated by other caspases in cells treated with chemotherapeutic agents[29] as well as PDT[12,15]. Pro-caspase-9 requires the release of cytochrome c from the mitochondrion to the cytsolic fraction and the formation of a pro-caspase-9/cytochrome c/APAF-1 complex in the presence of ATP for its activation[30,31]. The early involvement of caspase-9 in PDT-induced apoptosis using either QLT0074 or VFI is suggestive that mitochondrial events likely initiate the death cascade in these cells with these photosensitizers.

The capacity of VFI and QLT0074 to activate SAPK and HOG1 kinase, but not ERK, activity in mouse Pam212 cells indicates that these two photosensitizers impart a similar biochemical signature on these cells. Lower amounts of QLT0074 than VFI were required to trigger Pam212 cell SAPK and HOG1 activation. Experiments performed with human T cells and mouse Pam212 cells indicate that these cell types take up QLT0074 to higher levels than verteporfin (data not shown), likely accounting for the greater photodynamic activity observed with QLT0074. The significance of these signaling events triggered by PDT remains unresolved. Blockade of p38/HOG1 kinase activity with specific pyridinyl imidazole compounds inhibited PDT-induced apoptosis with the photosensitizer Pc4 in mouse lymphoma cells[32]. In contrast, inhibition of SAPK and p38/HOG1 kinase exaggerated the extent of apoptosis produced in HeLa cells treated with hypericin and red light[33]. Different cell types may differ in their utilization of biochemical signaling pathways in their response to photodynamic stress. The interaction of

a number of signaling pathways likely influences the functional behavior or survival of cells treated at PDT intensities lower than those that induce rapid cell death.

Inhibition of the immunologically mediated CHS response to topically applied haptens has been previously described for mice treated with different photosensitizers and light[7,34,35]. In the present work, treatment with VFI or QLT0074 combined with whole body blue light irradiation caused a 40-60% reduction in ear swelling responses upon DNFB challenge. Under the treatment conditions utilized, no significant difference in the magnitude of the inhibitory effect of these two photosensitizers on the CHS response was evident. Although the mechanisms that account for the inhibitory action of PDT on the CHS response have not been fully defined, it is clear that both photodynamic agents have a comparable inhibitory impact in this murine model. It is possible that PDT may inhibit the CHS response by effects on skin APC, since the sensitization phase but not the elicitation stage of the response is most sensitive to PDT[7].

PDT with VFI and red light irradiation was shown to impair the development of adjuvant-induced arthritis in Fas-deficient MRL/*lpr* strain mice (3,4). Autoreactive T cells are believed responsible for orchestrating the degenerative joint changes associated with this immune condition (3). It was suggested that PDT might target activated arthritogenic T lymphocytes to protect against arthritis development in this model[3,4]. A series of PDT treatments, consisting of QLT0074 combined with blue light irradiation, inhibited arthritis induction as indicated by the degree of ankle swelling that normally develops following the administration of adjuvant. PDT with QLT0074 and blue light was as effective as VFI and red light irradiation [3,4] in preventing adjuvant arthritis in this model.

QLT0074 is a highly potent photosensitizer and exhibits a similar biological activity to VFI for the induction of human KC and T cell apoptosis as well as in the triggering of Pam212 KC signaling events. QLT0074 was generally effective at lower concentrations than VFI. The stronger photodynamic activity of QLT0074 than VFI appears related to its greater uptake by cells. QLT0074 and VFI had comparable inhibitory impact upon two murine immune models revealing the immunomodulatory attributes of these photosensitizers in combination with blue light irradiation.

For the treatment of psoriasis with PDT, it is unclear whether an effective therapy should target plaque T cells or also directly influence the growth rate and/or survival of the hyper-proliferative KC within these regions. It has been indicated that KC within psoriatic plaques express high levels of the anti-apoptosis protein Bcl-xl and are more resistant to apoptosis than normal KC[36]. Clearly, PDT can induce apoptosis in normal human KC. PDT with VFI can effectively kill tumor cell types that over-express the pro-survival Bcl-2[14,15] or Bcl-xl[13,15] proteins. To further understand its anti-psoriasis potential, it will be important to determine the impact of PDT with QLT0074 on the growth characteristics, cytokine secretion, surface immuno-regulatory receptor expression and survival of cytokine-activated KC and to define the relative sensitivity of T cells and KC to photodynamic killing.

## 5. ACKNOWLEDGMENTS

The authors thank Chris Carthy, Corina Dyck, Diane King, Huijun Jiang, Mohammed Hasham, Carla White and Randi Yang for their technical expertise during these studies.

## 6. REFERENCES

1. A.M. Richter, B. Kelly, J. Chow, D.J. Liu, G.H.N. Towers, D. Dolphin, and J.G. Levy "Preliminary studies on a more effective phototoxic agent than hematoporphyrin", *J. Natl. Cancer Inst.* 79, pp 1327-1332, 1987.

2. E. Sternberg, and D. Dolphin, "Pyrrolic photosensitizers", *Curr. Med. Chem.* 3, pp 239-272, 1996.

3. R.K. Chowdhary, L.G. Ratkay, H.C. Neyndorff, A. Richter, M. Obochi, D.J. Waterfield, and J.G. Levy, "The use of transcutaneous photodynamic therapy in the prevention of adjuvant-enhanced arthritis in MRL/lpr mice", *Clin. Immunol. Immunopathol.* 72, pp 255-263, 1994.

4. L.G. Ratkay, R.K. Chowdhary, H.C. Neyndorff, J. Tonzetich, J.D. Waterfield, and J.G. Levy, "Photodynamic therapy: a comparison with other immunomodulatory treatments of adjuvant-enhanced arthritis in MRL/lpr mice", *Clin. Exp. Immunol.* 95, 373-377, 1994.

5. M.O.K. Obochi, A.J. Canaan, A.K. Jain, A.M. Richter, and J.G. Levy, "Targeting activated lymphocytes with photodynamic therapy: susceptibility of mitogen-stimulated splenic lymphocytes to benzoporphyrin derivative (BPD) photosensitization", *Photochem. Photobiol.* 62, pp 169-175, 1995.

6. S. Leong, A.H. Chan, J.G. Levy, D.W.C. Hunt, "Transcutaneous photodynamic therapy alters the development of an adoptively transferred form of murine experimental autoimmune encephalomyelitis", *Photochem. Photobiol.* 64: pp 751-757, 1996.

7. G.O. Simkin, D.E. King, A.H. Chan, and D.W.C. Hunt, "Inhibition of contact hypersensitivity with different analogs of benzoporphyrin derivative", *Immunopharmacology* 37, pp 221-230, 1997.

8. D.W.C. Hunt, H. Jiang, D.J. Granville, A.H. Chan, S, Leong, and J.G. Levy, "Consequences of the photodynamic treatment of resting and activated peripheral T lymphocytes", *Immunopharmacology* 41, pp 31-44, 1999.

9. H. Jiang, D.J. Granville, B.M. McManus, J.G. Levy, and D.W.C. Hunt, "Selective depletion of a thymocyte sub-population in vitro with an immunomodulatory porphyrin photosensitizer", *Clin. Immunol.* 91, pp 178-187, 1999.

10. R. Bissonnette, D.I. McLean, G. Reid, J. Kelsall, and H. Lui, "Photodynamic therapy of psoriasis and psoriatic arthritis with BPD verteporfin", Abstract RC87. 7th Biennial Congress of the International Photodynamic Association. Nantes France, July 7-9, 1998.

11. D.J. Granville, J.G. Levy, and D.W.C. Hunt, "Photodynamic therapy induces caspase-3 activation in HL-60 cells", *Cell Death Differ.* 4, pp 623-628, 1997.

12. D.J. Granville, C.M. Carthy, H. Jiang, G.C. Shore, B.M. McManus, and D.W.C. Hunt, "Rapid cytochrome c release, activation of caspases 3, 6, 7 and 8 followed by Bap31 cleavage in HeLa cells treated with photodynamic therapy", *FEBS Lett.* 437, pp 5-10, 1998.

13. D.J. Granville, H. Jiang, M.T. An, J.G. Levy, B.M. McManus, and D.W.C. Hunt, "Overexpression of Bcl-XL prevents caspase-3-mediated activation of DNA fragmentation factor (DFF) produced by treatment with the photochemotherapeutic agent BPD-MA", *FEBS Lett.* 422, pp 151-154, 1998.

14. D.J. Granville, H. Jiang, M.T. An, J.G. Levy, B.M. McManus, and D.W. Hunt, "Bcl-2 overexpression blocks caspase activation and downstream apoptotic events instigated by photodynamic therapy", *Br. J. Cancer* 79, pp 95-100, 1999.

15. C.M. Carthy, D.J. Granville, H. Jiang, J.G. Levy, C.M. Rudin, C.B. Thompson, B.M. McManus, and D.W.Hunt, "Early release of mitochondrial cytochrome c and expression of mitochondrial epitope 7A6 with a porphyrin-derived photosensitizer: Bcl-2 and Bcl-xL overexpression do not prevent early mitochondrial events but still depress caspase activity", *Lab. Invest.* 79, pp 953-965, 1999.

16. C.J. Gomer, A. Ferrario, N. Hayashi, N. Rucker, B.C. Szirth, and A.L. Murphree, "Molecular, cellular and tissue responses following photodynamic therapy", *Lasers Surg. Med.* 8, pp 450-463, 1988.

17. C.J. Gomer, N. Rucker, A. Ferrario, and S. Wong, "Properties and applications of photodynamic therapy", *Radiat. Res.* 120, pp 1-18, 1989.

18. G. Kroemer, N. Zamzami, and S.A. Susin, "Mitochondrial control of apoptosis", *Immunol. Today* 18, pp 44-51, 1997.

19. D.J. Granville, C.M. Carthy, D.W. Hunt, and BM McManus, "Apoptosis: molecular aspects of cell death and disease", *Lab Invest.* 78, pp 893-913, 1998.

20. J. Tao, J.S. Sanghera, S.L. Pelech, G. Wong, and J.G. Levy, "Stimulation of stress-activated protein kinase and p38 HOG1 kinase in murine keratinocytes following photodynamic therapy with benzoporphyrin derivative", *J. Biol. Chem.* 271, pp 27107-27115, 1996.

21. A.M. Richter, A.K. Jain, M. Obochi, H. Meadows, A.J. Canaan, and J.G. Levy, "Activation of benzoporphyrin derivative in the circulation of mice without skin photosensitivity", *Photochem. Photobiol.* 59, pp 350-355, 1994.

22. S.L. Gottlieb, P. Gilleaudeau, R. Johnson, L. Estes, T.G. Woodworth and A.B. Gottlieb, and J.G. Krueger, "Response of psoriasis to a lymphocyte-selective toxin ($DAB_{389}$IL-2) suggests a primary immune, but not keratinocyte, pathogenic basis", *Nature Med.* 1, pp 442-447.

23. V.P. Vallat, P. Gilleaudeau, L. Battat, J. Wolfe, R. Nabeya, N. Heftler, E. Hodak, A.B. Gottlieb, and J.G. Krueger, "PUVA bath therapy strongly suppresses immunological and epidermal activation in psoriasis: a possible cellular basis for remittive therapy", *J. Exp. Med.* 180: pp 283-296, 1996.

24. M. Ozawa, K. Ferenczi, T. Kikuchi, I. Cardinale, L.M. Austin, T.R. Coven, L.H. Burack, J.G. Krueger, "312-nanometer ultraviolet B light (narrow-band UVB) induces apoptosis of T cells within psoriatic lesions", *J. Exp. Med.* 189, pp 711-718, 1999.

25. P.G. Calzavara-Pinton, R.-M. Szeimies, B. Ortel and C. Zane, "Photodynamic therapy with systemic administration of photosensitizers in dermatology", *J. Photochem. Photobiol. B* 35, pp 225-231, 1996.

26. T. Mosmann, "Rapid colorimetric assay for cellular growth and survival: application to proliferation and cytotoxicity assays", *J. Immunol. Methods* 65, pp 55-63, 1983.

27. B.L. Levine, W.B. Bernstein, M. Connors, N. Craighead, T. Lindsten, C.B. Thompson, and C.H. June, "Effects of CD28 costimulation on long-term proliferation of CD4+ T cells in the absence of exogenous feeder cells", *J. Immunol.* 159, pp 5921-5930, 1997.

28. D.J. Granville, J.R. Shaw, S. Leong, C.M. Carthy, P. Margaron, D.W. Hunt, and B.M. McManus, "Release of cytochrome c, Bax migration, Bid cleavage, and activation of caspases 2, 3, 6, 7, 8, and 9 during endothelial cell apoptosis", *Amer. J. Pathol.* (1999) 55, pp 1021-1025.

29. X.M. Sun, M. MacFarlane, J. Zhuang, B.B. Wolf, D.R. Green DR, and G.M. Cohen GM, "Distinct caspase cascades are initiated in receptor-mediated and chemical-induced apoptosis", *J. Biol. Chem.* 274, pp 5053-5060, 1999.

30. P. Li, D. Nijhawan, I. Budihardjo, S.M. Srinivasula, M. Ahmad, E.S. Alnemri, and X. Wang X, "Cytochrome c and dATP-dependent formation of Apaf-1/caspase-9 complex initiates an apoptotic protease cascade", *Cell* 91, pp 479-489, 1997.

31. H. Zou, Y. Li X. Liu, and X. Wang X, "An APAF-1.cytochrome c multimeric complex is a functional apoptosome that activates procaspase-9", *J. Biol. Chem.* 274, pp 11549-1156, 1999.

32. L.-Y. Xue, J. He, and N.L. Oleinick, "Promotion of photodynamic therapy-induced apoptosis by stress kinases", *Cell Death Different.* 6, pp 855-864, 1999.

33. Z. Assefa, A. Vantieghem, W. Declercq, P. vandenabeele, J.R. Vandenheede, W. Merlevede, P. de Witte, and P. Agostinis, "The activation of the c-Jun terminal kinase and p38 mitogen-activated protein kinase signaling pathways protects HeLa cells from apoptosis following photodynamic therapy with hypericin", *J. Biol. Chem.* 274, pp 8788-8796, 1999.

34. C.A. Elmets, and K.D. Bowen, "Immunological suppression in mice treated with hematoporphyrin derivative photoradiation", *Cancer Res.* 46, pp 1608-1611, 1986.

35. D.H. Lynch, S. Haddad, V.J. King, M.J. Ott, R.C. Straight, and C.J. Jolles, "Systemic immunosuppression induced by photodynamic therapy (PDT) is adoptively transferred by macrophages," *Photochem. Photobiol.* 49, pp 453-458, 1989.

36. T. Wrone-Smith, T. Johnson, B. Nelson, L.H. Boise, C.B. Thompson, G. Nunez, and B.J. Nickoloff, "Discordant expression of Bcl-x and Bcl-2 by keratinocytes in vitro and psoriatic keratinocytes in vivo", *Am. J. Pathol.* 146, pp 1079-1088, 1995.

Invited Paper

# Immunotherapy regimens for combination with photodynamic therapy aimed at eradication of solid cancers

Mladen Korbelik*

British Columbia Cancer Agency, Vancouver, B.C., Canada V5Z 1L3

## ABSTRACT

Due to inflammatory/immune responses elicited by photodynamic therapy (PDT), this modality is particularly suitable in combination with various forms of immunotherapy for an improved therapeutic gain. A wide variety of approaches that may be applicable in this context include those focusing on amplifying the activity of particular immune cell types (neutrophils, macrophages, dendritic cells, natural killer cells, helper or cytotoxic T lymphocytes). Another type of approach is to focus on a specific phase of immune response development, which comprises the activation of non-specific inflammatory immune effectors, immune recognition, immune memory, immune rejection, or blocking of immune suppression. These different strategies call for a variety of immunotherapeutic protocols to be employed in combination with PDT. These include treatments such as: i) non-specific immunoactivators (e.g. bacterial vaccines), ii) specific immune agents (cytokines, or other activating factors), iii) adoptive immunotherapy treatments (transfer of dendritic cells, tumor-sensitized T lymphocytes or natural killer cells), or iv) their combinations. Techniques of gene therapy employed in some of these protocols offer novel opportunities for securing a potent and persistent immune activity. Using PDT and immunotherapy represents an attractive combination for cancer therapy that is capable of eradicating both localized and disseminated malignant lesions.

**Keywords:** photodynamic therapy, solid cancers, inflammatory response, immunotherapy, cytokines

## 1. INTRODUCTION

Photodynamic therapy (PDT) exploits the capacity of drugs called photosensitizers to absorb the energy of light and transfer it to molecular oxygen, which results in the formation of highly reactive oxygen radicals (predominantly singlet oxygen) responsible for initiating the destruction of targeted tissue[1-3]. Regulatory approval for the PDT treatment of several types of early and advanced stage cancers has been obtained in various countries, while additional clinical trials, including a number of new generation photosensitizers, are in progress[1]. The application of PDT is also being extended to a variety of non-malignant diseases.

Direct killing of tumor cells by the phototoxic action is only one element participating in a combined action of several cancer tissue destroying mechanisms responsible for tumor regression following PDT[1,2,4]. Tumor cells spared from the direct killing effect can be inactivated by: i) the ischemia developing after the vascular occlusion due to the damage inflicted by PDT in the vasculature of treated tumors; ii) deleterious effects of the induced damage to tumor extracellular matrix; iii) activated inflammatory cells sequestered in large numbers to the treated site; or iv) immune cells recognizing cancer epitopes that are generated and activated in the context of PDT-induced tumor immunity.

Strong immune reaction elicited against PDT-treated solid cancers was suggested to originate from the basic character of the insult inflicted by this therapy and to be subsequently propagated by the PDT-induced inflammatory process[1,4,5]. The initial impact comes from singlet oxygen-mediated oxidative stress that triggers early events associated with physiological signaling cascades, as well as the activation of membrane-localized phospholipases responsible for the liberation of pro-inflammatory mediators from damaged cellular membranes. Another profound pro-inflammatory impact comes from the events triggered by phototoxic lesions inflicted directly in tumor vasculature. Damage induced by PDT directly in the extracellular matrix was also implicated to have a major influence on tumor response, which includes inciting the release of powerful inflammatory mediators[5,6]. The engaged signal transduction pathways are responsible for the activation of transcription factors for multiple genes involved in the development of inflammatory/immune responses[1,7,8]. These events create conditions for the generation and propelling of a robust immune response dominated by the Th1-type and cellular arm of the immune system that is capable of developing and maintaining a protective immunity against PDT-treated cancer. A factor of crucial importance is

* Correspondence: E-mail: mkorbeli@bccancer.bc.ca; Telephone: 604 877 6098 ext.3044; Fax: 604 877 6077



In *Laser-Tissue Interaction XI: Photochemical, Photothermal, and Photomechanical*, Donald D. Duncan, Jeffrey O. Hollinger, Steven L. Jacques, Editors, Proceedings of SPIE Vol. 3914 (2000)
1605-7422/00/$15.00

the uniquely rapid disintegration of tumor tissue following photodynamic light exposure. Within several hours, large amounts of debris are produced from many dead cancer cells, which provides the abundance of peptide antigens that antigen-presenting cells can ingest and present for the generation of major histocompatibility complex-restricted immune responses[5].

The induction of tumor immunity by PDT was directly demonstrated using techniques of bone marrow transplantation or adoptive splenocyte/T cell transfer between immunocompetent and immunodeficient mice[9,10], as well as specific depletion of helper and cytotoxic T lymphocytes[10,11]. Recovery of immune memory cells from distant lymphoid sites confirmed the induction of systemic immunity raised even against poorly immunogenic tumors[10,12,13].

Effectiveness of modern clinical cancer protocols is in many cases based on successful combinations of several treatment modalities. It is, therefore, reasonable to expect that further improvements in the exploitation of PDT in clinical cancer therapy will largely depend on the development of protocols in which this therapy will be used in conjunction with other anti-cancer treatments. The absence of systemic (organ) toxicity or other serious side effects makes PDT suitable to be combined with a variety of other tumor therapies without inducing additional damage to normal tissues. On the other hand, the complexity of the antitumor effect by PDT opens a variety of approaches for intervention with second types of treatment at different levels of interaction[14]. In addition to immunotherapy, encouraging prospects for the application in conjunction with PDT were reported for various treatments, including surgery[15,16], hyperthermia[17], chemotherapy[18], hyperbaric oxygen[19], ionizing radiation[20], and hypoxic cytotoxins[21,22].

A growing list of publications is being accumulated, which demonstrate that the response of tumors to PDT can be enhanced (in some cases dramatically) by combining this modality with various types of immunotherapy[4]. In these pre-clinical studies, encouraging results were documented with different rodent tumor models, and it was shown that the therapeutic benefit is achievable even with poorly immunogenic cancers. These findings clearly demonstrate that PDT response is exceptionally receptive to modulation with largely diverse types of immunotherapy protocols. The present report attempts to outline various strategies that have been employed or are contemplated for using immunotherapy in conjunction with PDT.

## 2. BASIC CONCEPTS FOR IMMUNE TARGETING WITH PDT

Various immunotherapy regimens have been examined for their efficacy to improve the therapeutic outcome of PDT in treatment of solid cancers. They encompass different classes of immune agents that have previously been established in preclinical and/or clinical studies, and they are listed in Table 1. Each of these classes will be examined in more detail below.

**Table 1: Classes of immune agents for use in conjunction with PDT**

| |
|---|
| Non-specific immunoactivating agents |
| Cytokines |
| Other specific immunoactivating agents |
| Modulators of immune cell adhesion |
| Adoptively transferred immune cells |
| Modulators of PDT-induced immunosuppression |

Another way of designing immunotherapy protocols for use with PDT is to target a specific phase of immune response development, as outlined in Table 2. Remarkably, the accumulated experimental evidence suggests that all of these different approaches can be successful and none of these has as yet emerged as a clear favorite by proving to be superior to the others. The choice is most likely to depend on the specific type of cancerous lesion treated with PDT and immunotherapy. It remains also to be determined whether certain classes of photosensitizers used for PDT require specific types of

immunotherapy. For instance, it should be determined whether immunotherapy that potentiates early stages of immune development process interacts equally well with PDT based on photosensitizers inducing primarily vascular damage as with photosensitizers not targeting tumor vasculature.

**Table 2: Approaches for immune response enhancement in PDT-treated tumors**

| |
|---|
| Accentuation of inflammatory reaction responsible for the development of immune response |
| Facilitating the immune recognition of tumor antigens |
| Enhancing the accumulation of tumor-sensitized immune memory cells |
| Augmenting the immune rejection of treated tumors |
| Blocking the development of PDT-induced immunosuppression |

Since the antitumor immune response induced by PDT is primed and driven by the inflammatory process, it was warranted to examine how effective is the use of agents that amplify the induced inflammatory response. Interestingly, no benefit to the therapeutic outcome of PDT treatment of mouse mammary EMT6 sarcoma was obtained by tumor-localized injection of incomplete Freund's adjuvant immediately after PDT, despite the greatly increased tumor edema[13]. Hence, not any additional non-specific inflammatory impact can influence the mechanism of antitumor action of PDT. However, agents such as pro-inflammatory cytokines were shown to be effective in enhancing PDT-mediated tumor cures[23]. It should be noted, though, that in most cases even specific agents like cytokines are not exclusively affecting one type of immune cells or a single phase of immune response. Consequently, the observed therapeutic benefit (increased cure rate of PDT-treated tumors) may result from an integrated effect of multiple actions boosted by a single immunomodulating agent.

The enhancement of immune recognition in PDT-treated tumors likely underlies the beneficial effects obtained when cytokines interleukin (IL)-3[24], granulocyte macrophage-colony stimulating factor (GM-CSF)[25] and adoptively transferred dendritic cells[26] were combined with this therapy. Expanded engagement of later phases in the antitumor immune response is presumably responsible for increased tumor cures when PDT was combined with adoptive transfer of tumor-sensitized lymph node cells[27,28], BCG[13] or cytokine IL-7[29].

**Table 3: Immune cell types targeted by immunotherapy used with PDT**

| |
|---|
| Neutrophils |
| Macrophages |
| Dendritic cells |
| Helper T lymphocytes |
| Cytotoxic T lymphocytes |
| NK cells |

Some immunotherapy regimens that were examined in conjunction with PDT are acting primarily on certain type of immune effector cells (Table 3), as will be elaborated below. Again, it is remarkable that boosting the activity of divergent immune cell types was shown suitable for elevating the PDT-based tumor cures.

## 3. NON-SPECIFIC IMMUNOACTIVATING AGENTS

Non-specific immunoactivating agents are generally inducing an immune reaction indirectly through innate immune mechanisms, in most cases by elaborating inflammatory responses and/or activating phagocytes. Most of these agents are attenuated microbes or components of their membranes. Two types of bacterial vaccines, *Bacillus Calmette-Guérin* (BCG) and *Corynebacterium parvum*, were reported to enhance the PDT response of various mouse tumor models[13,30-32]. Agents of bacterial origin, mycobacterium cell-wall extract and endotoxin have also shown similar beneficial results[31,33]. Another non-specific immunoactivator demonstrated to improve the curative effect of PDT was SPG (glucan of fungal origin)[34]. Increased accumulation of activated Mac-1 positive myeloid cells into treated tumors induced by SPG was suggested to play a role in the enhancement of tumor regression following PDT. This benefit was observed with SPG only when administered before, and not after, PDT (9 daily doses i.m.), in contrast to BCG that was shown to be most effective when given after PDT as tumor-localized injection[13].

Among the above agents, the most detailed study was done with BCG plus PDT combination using murine EMT6 mammary sarcoma[13]. Six different photosensitizers (Photofrin, BPD, mTHPC, NPe6, Lu-Tex and ZnPC) were used for PDT in this study. It was shown that BCG (single injection) improved the therapy outcome irrespective of the type of photosensitizer used. Compared to PDT only, PDT plus BCG treatment resulted in markedly greater incidence of immune memory T cells found in tumor-draining lymph nodes analyzed 6 days post treatment. This finding suggests that the mechanism of BCG interaction with PDT involves the amplification of T-lymphocyte-mediated immune response against PDT-treated tumors.

## 4. CYTOKINES

Cytokines are increasingly coming into focus of PDT plus immunotherapy studies. These agents are either administered as pure (recombinant) proteins, or are delivered using gene therapy techniques. With respect to the latter, retroviral and adenoviral vectors were used in our laboratory for the transfection of tumor cells with genes encoding particular cytokines. In protocols with retroviral vectors, single of multiple tumor-localized injections are used of about 10 million lethal (x-ray) irradiated cells originating from the same tumor that have been transfected *in vitro* with a cytokine gene[25]. The transfection of tumors *in situ* with cytokine genes can be achieved with adenoviral vectors, and this is usually done several days before PDT[24].

In our PDT studies, retroviral vectors were employed for tumor-localized delivery of cytokines GM-CSF and IL-7[25,29]. The results demonstrated that the immunotherapy with both these cytokines enhances the response of subcutaneous mouse tumors to PDT. While interluekin-7 primarily stimulates the antitumor activity of T-lymphocytes[35], the action of GM-CSF is more complex as it stimulates the maturation and function of granulocytes and monocytes/macrophages, induces release of other cytokines, and stimulates the antigen presentation activity[36].

The use of adenoviral vector-based cytokine gene transfer in conjunction with PDT is investigated in our laboratory in collaboration with Dr. G. Dougherty (UCLA, Los Angeles). The results we obtained with adenoviral constructs containing the gene encoding interleukin-3 (AdvIL3) are particularly encouraging. High titre AdvIL3 were injected subtumorally in mice bearing subcutaneous Lewis lung carcinomas four days before these poorly immunogenic tumors were treated with mTHPC-based PDT. This produced high tumor cure rates, in contrast to PDT only treatment that was not curative[24]. The observed effect of interleukin-3 appears to involve the mobilization of neutrophils, enhanced immune recognition of tumor, and participation of helper T lymphocytes in immune rejection of PDT-treated tumors.

The cytokines that have been used successfully as recombinant proteins in PDT studies are IL-1β, IL-6, IL-8, IL-18, TNF-α and IFN-γ[23,37]. They are commonly regarded as inflammatory cytokines and known as potent activators of neutrophils, which draws the attention to considerable potential that these cells appear to have in the eradication of PDT-treated cancers[23,38]. Their effect on PDT tumor response is critically dependent on the administration site and timing relative to PDT light exposure. Tumor-localized injection appears optimal with most of these agents, which also helps avoiding harmful systemic toxicity known to be a serious problem with some cytokines.

## 5. OTHER SPECIFIC IMMUNOACTIVATING AGENTS

Very effective potentiation of the curative effect of PDT was achieved with vitamin $D_3$-binding protein-derived macrophage-activating factor (DBPMAF)[39]. This highly potent specific activator of macrophages is also known as GcMAF, since vitamin $D_3$ binding protein in human serum is called group-specific component or Gc protein[40,41]. The most effective DBPMAF therapy consisted of a combination of intraperitoneal and peritumoral injections (50 and 0.5 ng/kg respectively) administered on days 0, 4, 8 and 12 after Photofrin-PDT. Used with a PDT treatment that was curative to 25% of the treated subcutaneous mouse SCCVII squamous cell carcinomas, this DBPMAF regimen boosted the cures to 100%. The results of this study suggest that the activation of macrophages in PDT-treated mice by adjuvant immunotherapy has a synergistic effect on tumor cures.

## 6. MODULATORS OF IMMUNE CELL ADHESION

Adhesion molecules on immune cells and their counterparts in the endothelium and extracellular matrix play a crucial role in inflammatory/immune responses, since they regulate the trafficking of leukocytes and their activation. Modulators of immune cell adhesion, such as antibodies to specific adhesion molecules established as agents that can dramatically affect various inflammatory and immune responses, have a pronounced influence on the PDT tumor response[42,43]. We have shown that the treatment with monoclonal antibody against mouse CD18 (common chain of $\beta_2$ integrin receptors) dramatically changes the outcome of PDT treatment of mouse tumors and this effect appears to be largely influenced by the type of treated tumor[42]. Interestingly, the outcome of Photofrin-PDT treatment of mouse SCCVII tumors was markedly improved by the anti-CD18 antibody administered not only before, but also after photodynamic light exposure. The inhibited leukocyte-endothelium interaction, which diminishes the occlusion of blood vessels and consequently improves oxygenation of tumors during photodynamic light delivery, is one possible explanation for this result. However, this cannot account for the enhancement of PDT-mediated tumor cures by anti-CD18 injected after light treatment. Evidently, the underlying mechanism of the effect of this antibody is more complex. This is not surprising since integrins are involved in a number of important physiological functions. This includes complement activation, phagocytosis, oxidative burst, degranulation and antigen-dependent cell cytotoxicity in neutrophils, as well as mediation of cellular transduction pathways (control of apoptosis), while it is also known that blocking integrins inhibits the induction of immunosuppression[44-46]. Further studies aimed to elucidate the effects of blocking adhesion molecules in conjunction with PDT are in progress in our laboratory.

## 7. ADOPTIVE IMMUNOTHERAPY

Adoptive immunotherapy protocols involving the transfer of lymphoid killer cells, tumor-sensitized T lymphocytes, or dendritic cells to tumor-bearing recipients are in the focus of numerous ongoing cancer immunotherapy studies[47-49]. Protocols for adoptive transfer of these three immune cell types in conjunction with PDT are under investigation in our laboratory[26,27].

The NK-92MI variant of NK-92 cell line originally established from a patient with non-Hodgkin's lymphoma[50] that was stably transfected with IL-2 gene[51] (obtained from Dr. H.-G. Klingemann) was used in our studies as a source of large numbers of *in vitro* expanded activated NK cells. Typically, 50 million of these cells are injected peritumorally after PDT treatment in our studies with human tumors xenografted subcutaneously in scid/NOD mice. This protocol proved beneficial for the outcome of mTHPC-PDT with two different human tumor models, since markedly higher cure rates were observed with this combined protocol compared to PDT alone.

The source of tumor-sensitized T lymphocytes in our experiments are the inguinal lymph nodes draining tumors implanted in the lower back of syngeneic donor mice. These cells are injected intravenously (typically also 50 million/mouse) into recipients bearing the same tumor after it was PDT treated. In addition to this basic protocol, a variety of procedures could be used to enhance the activity of adoptively transferred T cells. They either aim at increasing the incidence of tumor-sensitized T-lymphocytes in the lymph nodes of future donors, or focus on expanding and activating T-cells *in vitro* before their injection into recipients, or target the activity of these cells after the adoptive transfer. Hence, a great deal of work can be done on the optimization of protocols involving PDT and adoptive T cell transfer. Nonetheless, the results obtained so far demonstrate that this type of immunotherapy can potentiate curative effects of PDT[27,28].

Dendritic cells for the adoptive transfer combined with PDT were obtained from mouse bone marrow cultured *ex vivo* with GM-CSF and IL-4[52]. Either naïve or tumor lysate-pulsed dendritic cells are included in our studies. While single tumor-

localized injection of 1 million dendritic cells showed no significant effect on tumor growth, the same treatment combined with PDT resulted in cures of poorly immunogenic Lewis lung and SCCVII carcinomas that were markedly higher compared to PDT only treatment[26]. Importantly, even adoptively transferred naïve dendritic cells were effective in these protocols, which indicates that PDT treatment results in liberation of tumor antigenic peptides that dendritic cells can effectively process and present to T lymphocytes.

## 8. INHIBITORS OF PDT-INDUCED IMMUNOSUPPRESSION

The PDT treatment of solid cancers elicits not only an immune response against these lesions, but is also accompanied by an immunosuppressive reaction[39,53,54]. The latter is known to develop after some types of inflammatory challenge[55], presumably as a natural feedback mechanism to prevent the excessive inflammatory damage of the affected tissue. For the outcome of tumor therapy with PDT, it is important that the induced immunoactivation dominates over immunosuppression[4]. This reasoning led to formulation of approaches designed to "de-couple" the PDT induced immunosuppression by inhibiting or preventing events critical for its development, and thus secure an un-hindered action of PDT-activated immune cells and hence more pervasive tumor eradication.

Several of the immune agents mentioned above may have produced positive interaction with PDT not only by stimulating immune responses, but also by diminishing the PDT-induced immunosuppression. For DBPMAF, it was shown that its action includes the reduction of PDT-induced immunosuppression assessed by the evaluation of delayed-type contact hypersensitivity response in tumor-bearing mice[39]. Other immune agents shown to enhance the response of tumors to PDT that are also known to exhibit an inhibitory effect on immunosuppression are GM-CSF and antibodies against integrins[56,57].

A more specific target for blocking the PDT-induced immunosuppression is the neutralization of IL-10. This cytokine, whose expression was reported to be elevated following PDT[58], is known as a key mediator in the attenuation of a wide range of inflammatory and immune responses and is instrumental in the development of immunosuppression[59,60]. Although Reddan and co-workers reported that the PDT-induced immunosuppression was not reversed by pre-treatment of mice with antibodies to IL-10 in their experimental model[61], we have recently been successful in improving the response of Lewis lung carcinomas to mTHPC-PDT and adoptive T-cell immunotherapy by additional treatment with anti-IL-10 (Korbelik, unpublished results).

## 9. CONCLUSIONS

The development of protocols in which PDT is used in conjunction with advanced immunotherapy regimens appears to have potential for further advancing the exploitation of this modality for treatment of solid cancers. Hopefully, some of such combined protocols will be clinically tested in a near future.

Successful application of cancer immunotherapy is frequently impeded by its inefficiency against larger tumor burden. Thus the immunotherapy treatments investigated in the above-discussed pre-clinical studies were generally not successful when used alone to cure the treated subcutaneous tumors. De-bulking the tumor mass can be effectively achieved by PDT, even with relatively large lesions provided the light dosimetry is adequately planned. Other characteristics of PDT-induced response that facilitate the effect of adjuvant immunotherapy include: i) the stimulation of leukocyte sequestration/homing to the treated cancerous lesion; ii) elaboration of various inflammatory/immune mediators that are necessary for the development and propagation of the antitumor immune response; and iii) generation of large amounts of debris containing antigenic tumor peptides.

## ACKNOWLEDGMENTS

The author's research is supported by grants from the Medical Research Council of Canada and National Cancer Institute of Canada.

## 1. REFERENCES

1. T. J. Dougherty, C. J. Gomer, B. W. Henderson, G. Jori, D. Kessel, M. Korbelik, J. Moan, Q. Peng, "Photodynamic therapy," *J. Natl. Cancer Inst.* **90**, pp. 889-905, 1998.

2. B. W. Henderson, and T. J. Dougherty, "How does photodynamic therapy work?," *Photochem. Photobiol.* **55**, pp. 145-157, 1992.
3. A. M. R. Fisher, A. L. Murphree, and C. J. Gomer, "Clinical and preclinical photodynamic therapy," *Lasers Surg. Med.* **17**, pp. 2-31, 1995.
4. M. Korbelik, "Induction of tumor immunity by photodynamic therapy," *J. Clin. Med. Lasers Surg.* **17**, pp. 329-334, 1996.
5. M. Korbelik, "Antitumor immune reaction elicited by photodynamic therapy," *Proc. SPIE* **3601**, pp. 68-74, 1999.
6. G. M. LaMuraglia, F. Adili, S. J. Karp, R. G. S. van Eps, and M. T. Watkins, "Photodynamic therapy inactivates extracellular matrix – basic fibroblast growth factor: Insights to its effect on the vascular wall," *J. Vasc. Surg.* **26**, pp. 294-301, 1997.
7. C. J. Gomer, M. Luna, A. Ferrario, S. Wong, A. M. R. Fisher, and N. Rucker, "Cellular targets and molecular responses associated with photodynamic therapy," *J. Clin. Med. Lasers Surg.* **17**, pp. 315-321, 1996.
8. M. Grilli, J.-S. Chiu, and M. Leonardo, "NF-κB and Rel: participants in a multiform transcriptional regulatory system," *Int. Rev. Cytol.* **143**, pp. 1-62, 1993.
9. M. Korbelik, G. Krosl, J. Krosl, and G. J. Dougherty, "The role of host lymphoid populations in the response of mouse EMT6 tumor to photodynamic therapy," *Cancer Res.* **56**, pp. 5647-5652, 1996.
10. M. Korbelik, and G.J. Dougherty, "Photodynamic therapy-mediated immune response against subcutaneous mouse tumors," *Cancer Res.* **59**, pp. 1941-1946, 1999.
11. M. Korbelik, and I. Cecic, "Contribution of myeloid and lymphoid host cells to the curative outcome of mouse sarcoma treatment by photodynamic therapy," *Cancer Lett.* **137**, pp. 91-98, 1999.
12. S. O. Gollnick, D. A. Musser, and B.W. Henderson, "Photodynamic therapy affects the expression of IL-6 and IL-10 *in vivo*," Conference on Laser-Tissue Interaction IX, International Biomedical Optics Symposium BiOS '98, San Jose, CA, January 24-30, 1998.
13. M. Korbelik, J. Sun, and J. J. Posakony, "Myeloid and lymphoid cell activity following photodynamic therapy of mouse EMT6 tumors: the effect of BCG and the associated therapeutic gain," *Cancer Res.* (submitted).
14. M. Korbelik, I. Cecic, J. Sun, and D. J. Chaplin, "Examples of adjuvant treatment enhancing the antitumor effect of photodynamic therapy", *Proc. SPIE* **3592**, pp. 65-72, 1999.
15. T. F. DeLaney, W. F. Sindelar, Z. Tochner, P. D. Smith, W. S. Friauf, G. Thomas, L. Dachowski, J. W. Cole, S. M. Steinberg, and E. Glatstein, "Phase I study of debulking surgery and photodynamic therapy for disseminated intraperitoneal tumors," *Int. J. Radiat. Oncol. Biol. Phys.* **25**, pp. 445-457, 1993.
16. H. Takita, and T. J. Dougherty, "Intracavitary photodynamic therapy for malignant pleural mesothelioma," *Semin. Surg. Oncol.* **11**, pp. 368-371, 1995.
17. Q. Chen, H. Chen, H. Shapiro, and F. W. Hetzel, "Sequencing of combined hyperthermia and photodynamic therapy," *Radiat. Res.* **146**, pp. 293-297, 1996.
18. M. Y. Nahabedian, R. A. Cohen, M. F. Contino, T. M. Terem, W. H. Wright, M. W. Berns, and A. G. Wile, "Combination cytotoxic chemotherapy with cisplatin or doxorubicin and photodynamic therapy in murine tumors, " *J. Natl. Cancer Inst.* **80**, pp. 739-743, 1988.
19. Q. Chen, J. Beckers, and F. W. Hetzel, "Modification of tumor response by manipulation of tumor oxygenation," *Proc. SPIE* **3592**, pp. 60-64, 1999.
20. J. Winther, J. Overgaard, and N. Ehlers, "The effect of photodynamic therapy alone and in combination with misonidasole or x-rays for management of a retinoblastoma-like tumour," *Photochem. Photobiol.* **47**, pp. 419-423, 1998.
21. J. C. M. Bremner, G. E. Adams, J. K. Pearson, J. Sansom, I. J. Stratford, J. Bedwell, , S. G. Brown, and D. Philips, "Increasing the effect of photodynamic therapy on the RIF1 murine sarcoma using the bioreductive drugs RSU1069 and RB6145," *Br. J. Cancer* **66**, pp. 1070-1076, 1992.
22. I. P. J. van Geel, H. Oppelaar, Y. G. Oussoren, J. J. Schuitmaker, and F. A. Stewart, "Mechanisms for optimising photodynamic therapy: second-generation photosensitizers in combination with mitomycin C," *Br. J. Cancer* **72**, pp. 344-350, 1995.
23. M. Korbelik, and I. Cecic, "Role of neutrophils in the destruction of PDT-targeted lesions," Conference on Optical Methods for Tumor Treatment and Detection: Mechanisms and Techniques in Photodynamic Therapy IX, International Biomedical Optics Symposium BiOS 2000, San Jose, CA, January 22-28, 2000.
24. M. Korbelik, and G. J. Dougherty, "Interleukin-3 immunotherapy potentiates the curative effect of photodynamic therapy in treatment of cancerous lesions," Cancer Res. Proc. **41**, (in press).
25. G. Krosl, M. Korbelik, J. Krosl, and G. J. Dougherty, "Potentiation of photodynamic therapy-elicited antitumor response by localized treatment with granulocyte-macrophage colony-stimulating factor," Cancer Res. 56, pp. 3281-3286, 1996.
26. M. Korbelik, J. Sun, V. R. Naraparaju, and N. Yamamoto, "Eradication of solid cancers by photodynamic therapy combined with dendritic cell-based adoptive immunotherapy," *Cancer Res. Proc.* **40**, pp. 86, 1999.

27. M. Korbelik, and J. Sun, "Cancer treatment by photodynamic therapy combined with NK cell line based adoptive immunotherapy," *Proc. SPIE* 3254A, pp. 4-11, 1998.
28. G. Canti, R. Cubeddu, P. Taroni, and G. Valentini, "Photodynamic therapy and immune response in tumor bearing mice," *Proc. SPIE* **3601**, pp. 82-88, 1999.
29. G. J. Dougherty, J. D. Thacker, W. H. McBride, G. Krosl, and M. Korbelik, "Effect of immunization with genetically-modified tumor cells on tumor recurrence following photodynamic therapy," *Lasers Med. Sci.* **7**, pp. 226, 1992.
30. Y.-H. Cho, R. C. Straight, and J. A. Smith Jr., "Effects of photodynamic therapy in combination with intravesical drugs in a murine bladder tumor model," *J. Urol.* **147**, pp. 743-746, 1992.
31. M. Korbelik, and I. Cecic, "Enhancement of tumour response to photodynamic therapy by adjuvant mycobacterium cell-wall treatment," *J. Photochem. Photobiol. B: Biol.* **44**, pp. 151-158, 1998.
32. R. C. Myers, B. H. S. Lau, D. Y. Kunihira, R. R. Torrey, J. L. Wooley, and J. Tosk, "Modulation of hematoporphyrin derivative-sensitized phototherapy with *Corynebacterium parvum* in murine transitional cell carcinoma," *Urology* **33**, pp. 230-235, 1989.
33. V. F. Dima, V. Vasiliu, D. Laky, M. D. Ionescu, and S. V. Dima, "Treatment of rat Walker-256 carcinosarcoma with photodynamic therapy and nedotoxin irradiated with high energy electrons," *Proc. SPIE* **2078**, pp. 547-557, 1994.
34. G. Krosl, and M. Korbelik, "Potentiation of photodynamic therapy by immunotherapy: The effect of schizophyllan (SPG)," *Cancer Lett.* **84**, pp. 43-49, 1994.
35. W. H. McBride, J. D. Thacker, S. Comora, J. S. Economou, D. Kelley, D. Hogge, S. M. Dubinett, and G. J. Dougherty, "Genetic modification of a murine fibrosarcoma to produce interleukin 7 stimulates host cell infiltration and tumor immunity," *Cancer Res.* **52**, pp. 3931-3937, 1992.
36. G. Dranoff, E. Jaffee, A. Lazenby, P. Golumbek, H. Levitsky, K. Brose, V. Jackson, H. Hamada, D. Pardoll, and R. C. Mulligan, "Vaccination with irradiated tumor cells engineered to secrete murine granulocyte-macrophage colony-stimulating factor stimulates potent, specific, and long-lasting anti-tumor immunity," *Proc. Natl. Acad. Sci. USA* **90**, pp. 3539-3543, 1993.
37. D. A. Bellnier, "Potentiation of photodynamic therapy in mice with recombinant human tumor necrosis factor-α," *J. Photochem. Photobiol. B: Biol.* **8**, pp. 303-210, 1991.
38. I. Cecic, and M. Korbelik, "Neutrophil-associated events in the inflammation of cancerous tissue following treatment with photodynamic therapy," *Trends Photochem. Photobiol.* **6**, pp. 53-61, 1999.
39. M. Korbelik, V. R. Naraparaju, and N. Yamamoto, "Macrophage-directed immunotherapy as adjuvant to photodynamic therapy of cancer," *Br. J. Cancer* **75**, pp. 202-206, 1997.
40. N. Yamamoto, and V. R. Naraparaju, "Role of mouse vitamin $D_3$-binding protein in activation of macrophages," *J. Immunol.* **157**, pp. 1744-1751, 1996.
41. N. E. Cooke, and J. G. Haddad, "Vitamin D binding protein (Gc-globulin)," *Endocrine Rev.* **10**, pp. 294-307, 1986.
42. M. Korbelik, and G. Krosl, "Photosensitizer distribution and photosensitized damage of tumor tissues," *The Fundamental Bases of Phototherapy*, H. Hönigsman, G. Jori, and A. Young editors, pp. 229-245, OEMF spa, Milan, 1996.
43. K. L. Freye, C. Y. Anderson, K. A. Tubesing, and C. A. Elmets, "*In vivo* effects of adhesion molecule antibodies on PDT-induced tumor regression." *Photochem. Photobiol.* **65**, pp. 17S, 1997.
44. S. M. Albelda, C. W. Smith, and P. A. Ward, "Adhesion molecules and inflammatiory injury," *FASEB J.* **8**, pp. 504-512, 1994.
45. M. A. Arnaout, "Leukocyte adhesion molecules deficiency: Its structural basis, pathophysiology and implications for modulating the inflammatory response," *Immunological Reviews (Copenhagen)* **114**, pp. 145-180, 1990.
46. F. G. Giancotti, and E. Ruoslahti, "Integrin signaling," *Science* **285**, pp. 1028-1032, 1999.
47. S. A. Rosenberg, J. R. Yannelli, J. C. Yang, S. L. Topalian, D. J. Schwartzentruber, J. S. Weber, D. R. Parkinson, C. A. Seipp, J.H. Einhorn and D.E. White, "Treatment of patients with metastatic melanoma with autologous tumor-infiltrating lymphocytes and interleukin 2", *J. Natl. Cancer Inst.* **86**, pp. 1159-1166, 1994.
48. B. D. Curti, D. L. Longo, A. C. Ochoa, K. C. Conlon, J. W. Smith, II, W. G. Alvord, S. P. Creekmore, R. G. Fenton, B. L. Gause, J. Holmlund, J. E. Janik, J. Ochoa, P. A. Rice, W. H. Sharfman, M. Sznol and W. J. Urba, "Treatment of cancer patients with *ex vivo* anti-CD3-activated killer cells and interleukin-2", *J. Clin. Oncol.* **11**, pp. 652-660, 1993.
49. G. P. Murphy, B. A. Tjoa, S. J. Simmons, H. Ragde, M. Rogers, A. Elgamal, G. M. Kenny, M. J. Troychak, M.J. Salgaller, and A. L. Boynton, "Phase II prostate cancer vaccine trial: report of a study involving 37 patients with disease recurrence following primary treatment," Prostate 39, pp. 54-59, 1999.
50. J.-H. Gong, G. Maki and H.-G. Klingemann, "Characterization of a human cell line (NK-92) with phenotypical and functional characteristics of activated natural killer cells", *Leukemia* **8**, pp. 652-658, 1994.

51. Y. K. Tam, G. Maki, B. Miyagawa, B. Hennemann, T. Tonn, and H.G. Klingemann, "Characterization of genetically altered, interleukin 2-dependent natural killer cell lines suitable for adoptive cellular immunotherapy," Hum. Gene Ther. 10, pp. 1359-1373, 1999.
52. D. I. Gabrilovich, S. Nadaf, J. Corak, J. A. Berzofsky, and D. P. Carbone, "Dendritic cells in antitumor immune responses II. Dendritic cells grown from bone marrow precursors, but not mature DC from tumor-bearing mice, are effective antigen carriers in the therapy of established tumors," *Cellular Immunol.* **170**, pp. 111-119, 1996.
53. C. A. Elmets, and K. D. Bowen, "Immunological suppression in mice treated hematoporphyrin derivative photoradiation," *Cancer Res.* **46**, pp. 1608-1611, 1986.
54. D. H. Lynch, S. Haddad, K. J. Vernon, M. J. Ott, R. C. Straight, and C. J. Jolles, "Systemic immunosuppression induced by photodynamic therapy (PDT) is adoptively transferred by macrophages," Photochem. Photobiol. 49, pp. 453-458, 1989.
55. Z. Metzger, J. T. Hoffeld, and J. J. Oppenheim, "Macrophage mediated suppression: I. Evidence for participation of both hydrogen peroxide and prostaglandins in suppression of murine lymphocyte proliferation," *J. Immunol.* **124**, pp. 983-988, 1980.
56. N. Bilyk, and P. G. Holt, "Inhibition of the immunosuppressive activity of resident pulmonary macrophages by granulocyte/macrophage colony-stimulating factor," J. Exp. Med. 177, pp. 1773-1777, 1993.
57. H. Rosen, G. Milon, and S. Gordon, "Antibody to the murine type 3 complement receptor inhibits T lymphocyte-dependent recruitment of myelomonocytic cells *in vivo*," *J. Exp. Med.* **169**, pp. 535-548, 1989.
58. S. O. Gollnick, X. Liu, B. Owczarczak, D. A. Musser, and B. W. Henderson, "Altered expression of interleukin 6 and interleukin 10 as a result of photodynamic therapy *in vivo*," *Cancer Res.* **57**, pp. 3904-3909, 1997.
59. K. W. Moore, A. O'Garra, R. de Waal Malefijit, P. Veira, and T. R. Mosmann, "Interleukin-10," *Annu. Rev. Immunol.* **11**, pp. 165-190, 1993.
60. L. Li, J. F. Elliott, and T. R. Mosmann, "IL-10 inhibits cytokine production, vascular leakage, and swelling during T helper 1 cell-induced delayed-type hypersensitivity," *J. Immunol.* **153**, pp. 3967-3978, 1994.
61. J. C. Reddan, C. Y. Anderson, H. Xu, S. Hrabovsky, K. Freye, R. Fairchild, K. A. Tubesing, and C.A. Elmets, "Immunosuppressive effects of silicon phthalocyanine photodynamic therapy," Photochem. Photobiol. 70, 72-77, 1999.

## SESSION 2

# PDT, Immunotherapy, and Other Photochemistry

Invited Paper

# Passive adoptive transfer of antitumor immunity induced by laser-dye-immunoadjuvant treatment in a rat metastatic breast cancer model

Wei R. Chen [*a, b] Hong Liu [c], Anil K. Singhal [d], and Robert E. Nordquist [e, f]

[a] Department of Physics, University of Central Oklahoma, Edmond, OK 73034

[b] Department of Physics and Astronomy, University of Oklahoma, Norman, Oklahoma 73109

[c] Department of Radiology and Biomedical Engineering, Johns Hopkins University, Baltimore, MD 21205

[d] Light Sciences, 1065 12 TH Avenue, NW E-5, Issaquah, WA 98027

[e] Department of Ophthalmology, University of Oklahoma, Oklahoma City, OK 73104

[f] Wound Healing of Oklahoma, 3945 N. Walnut Street, Oklahoma City, OK 73105

## ABSTRACT

The ideal cancer treatment modalities should not only cause tumor regression and eradication but also induce a systemic anti-tumor immunity. This is essential for control of metastatic tumors and for long-term tumor resistance. Laser immunotherapy using a laser, a laser-absorbing dye and an immunoadjuvant has induced such a long-term immunity in treatment of a mammary metastatic tumor. The successfully treated rats established total resistance to multiple subsequent tumor challenges. For further mechanistic studies of the antitumor immunity induced by this novel treatment modality, passive adoptive transfer was performed using splenocytes as immune cells. The spleen cells harvested from successfully treated tumor-bearing rats provided 100% immunity in the naive recipients. The passively protected first cohort rats were immune to tumor challenge with an increased tumor dose; their splenocytes also prevented the establishment of tumor in the second cohort of naïve recipient rats. This immunity transfer was accomplished without the usually required T-cell suppression in recipients.

**Keywords**: laser immunotherapy, adoptive immunity, indocyanine green, glycated chitosan

## 1. INTRODUCTION

The most effective cancer treatment modality should target the host immune system so that it can not only eradicate the treated primary tumors, but also cause regression and eradication of metastases. Furthermore,

* Correspondence: Email: wchen@ucok.edu; Telephone: 405/974-5198; Fax: 405/974-3812



In *Laser-Tissue Interaction XI: Photochemical, Photothermal, and Photomechanical*, Donald D. Duncan, Jeffrey O. Hollinger, Steven L. Jacques, Editors, Proceedings of SPIE Vol. 3914 (2000) 1605-7422/00/$15.00

such a modality should produce in treated hosts a long-term resistance to tumors to which they were originally exposed. Tumor immunity has been achieved by immunotherapy [1-7], or by a combination of chemotherapy and immunotherapy [8-9]. Antitumor immunity resulted from using immunoadjuvant has been shown to reject subsequent tumor challenges, and to be adoptively transferred using immune lymphoid [1] or spleen cells [2-9] in animal experiments. However, in most cases such immunity transfer requires T-cell suppression in recipients, [1, 3-5, 10-11] and sequential passively transferred immunity often loses the tumor resistance [8]. Immune enhancement was also observed after Photodynamic Therapy (PDT), using light activated photosensitizers [12-15]. However, the real mechanism of immune responses induced by PDT is unclear and the adoptive transferability has not been investigated.

To induce a long-term tumor-specific immunity, a novel treatment modality, laser immunotherapy, was developed. It utilizes a novel immunoadjuvant administered together with a laser-absorbing dye, followed by non-invasive irradiation by a near-infrared laser. This novel therapy caused regression of both treated primary tumors and untreated metastases in animal studies. It also induced a long-term resistance to subsequent tumor challenges. Histochemical and immunological studies showed that the laser immunotherapy treatment has induced a tumor-specific host immune response. [16-18]

To test the protection ability of the induced immunity, several groups of successfully treated rats were challenged repeatedly with increased inoculation dose of the tumor cells to which they were originally exposed. To study the mechanism of the induced antitumor immunity, adoptive transfer using immune spleen cells was performed. The resistance to tumor challenges after laser immunotherapy treatment, and the inhibition of tumor growth in naïve recipients and the protection again subsequent tumor challenge after immunity transfer were studied. Also tested was the ability of the passively transferred immunity to protect subsequent cohorts of naïve recipient rats.

## 2. MATERIALS AND METHODS

### 2.1. Tumor Model

DMBA-4 transplantable, metastatic mammary tumor model [19-20] in female Wistar Furth rats (Harlan Sprague-Dawley, Indianapolis, Indiana) was used in the experiments. The tumor cells were harvested from live tumor-bearing rats and naïve rats were inoculated subcutaneously in one of the inguinal fat pads, seven to ten days before laser immunotherapy treatment. The usual inoculation dose is $10^5$ viable tumor cells per rat. Without treatment, the tumor bearing rats usually survive an average of 30 days after tumor inoculation.

### 2.2. Laser Immunotherapy

This novel treatment method consists three components: a near-infrared diode laser, Indocyanine Green (ICG), and Glycated Chitosan (GC). The solution of ICG, serving as the laser absorbing dye, and GC, serving as the immune stimulant, was directly injected to the tumor before the non-invasive laser irradiation. The injection dose was 200 μl solution containing 0.25% ICG and 1% GC. The tumor was irradiated with the 805-nm laser at 2 watts (CW) for 10 minutes. The successfully treated usually experienced a gradual regression in both treated primary tumor and untreated metastases. (For detailed laser immunotherapy procedure, see Refs. 16-18).

### 2.3. Adoptive Immunization

Viable tumor tissue was harvested from live rats bearing the DMBA-4 tumor and was dispersed to a single cell suspension by grinding in a loose-fitting ground glass homogenizer. The successfully treated rats by laser immunotherapy were challenged with an increased tumor dose of $10^6$ cells per rat. At the same time, control rats were inoculated with a dose of $10^5$ cells per rat. Twenty-eight days after the tumor inoculation,

the control and long-surviving rats were sacrificed by cervical dislocation and their spleens were dissected free of fat and cell suspensions were prepared by mechanical disruption into medium with 10% calf fetal serum. Also collected was the spleen cells from a naïve rat without prior exposure to the tumor cells. Spleen cells and viable tumor cells were counted on a haemocytometer before admixed. The admixture had a 400:1 spleen to tumor cell ratio. Naïve rats were inoculated with the admixture containing $4x10^7$ spleen cells and $10^5$ tumor cells in a volume of 200 μl.

# 3. RESULTS

## 3.1. Rechallenge of Cured Rats

Following successful treatment by laser immunotherapy, fifteen cured rats were challenged with $10^6$ viable tumor cells 120 days after the treatment. To compare with the tumor growth in control rats of the same age, eighteen naïve rats of age 25 weeks (the same age as the successfully treated rats) were also challenged with a dose of $10^6$ viable tumor cells per rat. As shown in Table 1, all the cured rats showed total resistance to the challenge; neither primary tumors nor metastases were observed. On the contrary, the control rats all developed primary and metastatic tumors and died around 30 days after the inoculation. The survival time appeared to be dependent on the tumor dose. The control rats with the inoculation of $10^5$ cells survived on average 33 days, while the control rats with inoculation of $10^6$ cells survived only 28 days.

After the first rechallenge, the rats from several different experimental groups were followed by two subsequent challenges in a time interval from one month to five months, again with the increased tumor dose. As shown in Table 1, all the cured rats were totally refractory to three tumor challenges after the successful treatment by laser immunotherapy.

**TABLE 1**

**Tumor rechallenge of rats previously cured by laser immunotherapy treatment**

| Group | Number of rats | Number of Tumor Cells | Tumor Occurrence | Survival (days) |
|---|---|---|---|---|
| Young Control Rats [1] | 20 | $10^5$ | 100% | 32.7±3.5 |
| Age-Matched Control Rats [2] | 18 | $10^6$ | 100% | 28.2±2.8 |
| Cured Rats (1st challenge) [3] | 15 | $10^6$ | 0% | >120 |
| Cured Rats (2nd challenge) [4] | 15 | $10^6$ | 0% | >120 |
| Cured Rats (3rd challenge) [5] | 15 | $10^6$ | 0% | >120 |

[1] Young female Wistar Furth rats with tumor inoculation at the age of 8 weeks, with the normal tumor dose of $10^5$ viable tumor cells.
[2] Untreated rats of the same age as the cured rats at the time of inoculation, without previous exposure to tumor.
[3] Tumor-bearing rats cured by laser-ICG-GC treatment. These tumor-free rats were challenged with $10^6$ viable tumor cells 120 days after the initial inoculation.
[4] Successfully treated rats from different experiments were challenged the second time one to five months after the first challenge.
[5] Successfully treated rats from different experiments were challenged the third time one to five months after the second challenge.

## 3.2. Adoptive Immunity

Naïve rats were divided into four different groups for the adoptive immunity transfer experiments and then inoculated with tumor cells. Group A contains the tumor-bearing control rats, inoculated by $10^5$ viable

tumor cells without any treatment. Group B contains the rats inoculated with tumor cells admixed with spleen cells from a control tumor-bearing rat. Group C contains rats inoculated with tumor cells admixed with immune spleen cells from a laser immunotherapy cured rat, 28 days after tumor rechallenge. Group D contains the rats inoculated with viable tumor cells admixed with spleen cells harvested from a naïve rat without prior exposure to tumor. Figure 1 displays the survival curves for all four groups from two separate experiments. The spleen cells from a laser immunotherapy cured rat provided 100% protection to the recipients; neither primary nor metastatic tumors were observed among the rats in Group C. The control rats in Group A all died with multiple metastases within 35 days of tumor inoculation. The spleen cells from a healthy rat did not provide any protection to the recipients in Group D, as shown by the thin solid curve in Figure 1. Only one in ten rats in Group B survived, as shown by the dotted curve in Figure 1; however, this rat developed both primary and metastases.

Sixty days after the adoptive immunity transfer, all the rats in Group C were challenged again and all the rats withstood the challenge. To test of the ability of their splenocytes in protecting a subsequent cohort of normal Wistar Furth recipient rats, the spleen cells of the rats in Group C were collected. These immune spleen cells were admixed with tumor cells in the same ratio as in the first adoptive transfer. Six naïve rats were inoculated with this admixture. The results are shown in Figure 2. For comparison, the data of the first protected cohort (Group C in Figure 1, the thick solid line), and that of control rats (Group A in Figure 1, the gray line), are also presented in Figure 2. As shown in Figure 2, the immune cells from the rats in Group C protected five out of six rats (the thin solid curve); neither primary tumor nor metastases were observed in the five protected rats. One rat in this group died with a prolonged survival time, in comparison with the control group (60 days versus 30 days), and with a delayed emergence of tumors, 37 days after tumor inoculation, compared with 7 to 10 days in control rats.

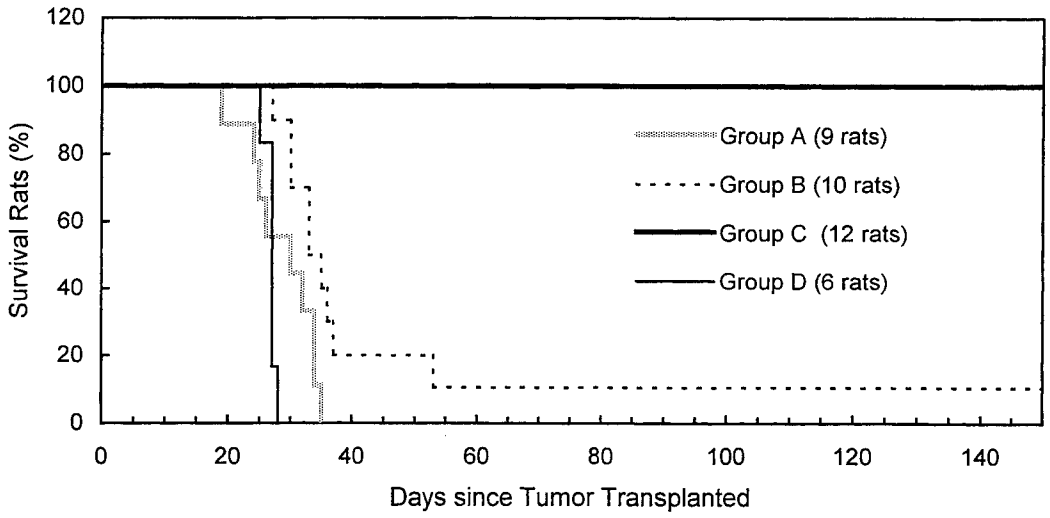


**Figure 1.** Rat survival curves in the adoptive immunity experiments using rat splenocytes as immune cells. Data were collected from two separate experiments. Viable tumor cells were admixed with spleen cells from different rats, then injected to naive rats. The ratio is 40 million spleen cells to 100,000 tumor cells per rat. The thick gray line represents the rats in Group A, the tumor control rats. The dotted line represents the rats in Group B, injected with tumor cells admixed with spleen cells from an untreated tumor-bearing rat. The thick solid line represents the rats in Group C, injected with tumor cells admixed with spleen cells from a laser immunotherapy cured rat. The thin solid line represents the result using spleen cells from a naive rat (Group D). The spleen cells from laser immunotherapy treated rat totally inhibited the tumor growth; all the rats survived and none developed tumors. In comparison, only the spleen cells from tumor-bearing rats had certain impact on rat survival with a 10% survival (see the dotted line). Rats in all three groups except for rats in Group C developed metastases.

# 4. DISCUSSION

Our previous animal experiments showed the efficacy of laser immunotherapy in treating metastatic tumors through a local application [16-18]. This novel treatment modality utilizes the combined effect of a selective photothermal effect and an immunological effect. The former is achieved through direct application of a near-infrared laser coupled with an absorbing dye with a corresponding absorption spectrum. [21-22] The latter is achieved by introducing a novel immunoadjuvant, Glycated Chitosan, to the treatment site. The selective photothermal reaction reduces the tumor burden and at the same time exposes the tumor antigens; the immunoadjuvant *in situ* first stimulates the host immune system and then directs the immune system against the residue tumor and metastases. In fact, an *in situ* autovaccine is resulted in each individual treated host. It is the tandem effect that not only resulted in total tumor eradication but also led to a long-term tumor-specific immunity. This method, therefore, provides a systemic immunotherapy in each individual host without the usually required immune cross-reactivity.

The rats successfully treated by laser immunotherapy can withstand several times of subsequent challenges with the increased tumor dose, as shown in Table I. The tumor challenges were performed on cured rats from four different experimental groups and at different time intervals. These results show that the induced immunity has a long-lasting effect.

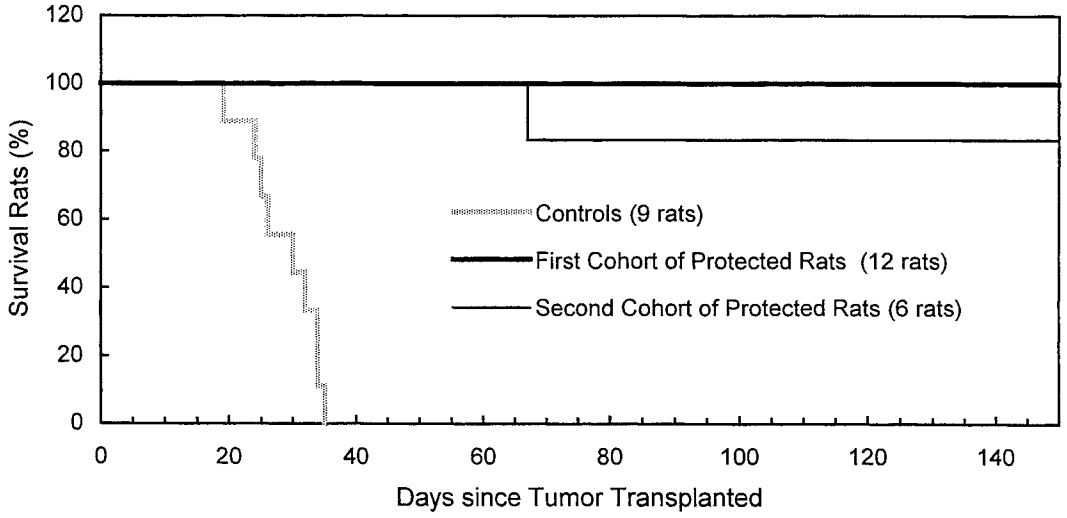


**Figure 2**. Rat survival rate for the second cohort of recipient rats using passive adoptive transfer. Immune cells were collected from rats protected by the first immunity transfer and admixed with tumor cells in a ratio of 400:1. The admixture was injected to a second cohort of naïve recipient rats. The thin solid curve represents six rats in this group. In comparison, the thick gray line represents the tumor control rats (Group A in Figure 1) and the thick solid line represents the results of the first adoptive immunity transfer (Group C in Figure 1). 5 out of 6 rats (83%) in the second cohort of rats showed total tumor resistance; only one rat in this group died, but with a longer survival time and delayed emergence of primary and metastatic tumors.

Our experiments also show that the immunity can be passively transferred using immune spleen cells. After the laser immunotherapy, the immune splenocytes from cured rats when admixed with tumor cells can provide 100% protection to the normal recipient rats, as shown in Figure 1. Apparently, the spleen cells from laser immunotherapy treated rat totally inhibited the tumor growth; all the rats survived and none developed tumors. These passively protected first cohort rats are immune to tumor rechallenge, and their spleen cells can provide strong protection to second cohort of normal recipients, as shown in Figure 2. The

protection to the second cohort of recipients reached 83%. The only non-survival rat in this second cohort had a long survival time (sixty days versus 30 days of controls) and a delayed emergence of primary tumors (37 days versus 7 to 10 days of controls). This definitely showed the strong immunity induced by the laser immunotherapy. In comparison, the spleen cells from a naïve donor not exposed to the tumor cells did not show any impact on rat survival or on tumor growth in normal recipient rats, as show by the data in Figure 1.

The spleen cells from the donor bearing the same tumor provided a limited protective effect to the recipients (one in ten rats in two separate experiments survived after the inoculation), as shown in Figure 2. This could be attribute to the natural immune development in the host after the exposure to the tumor. However, the protection by the tumor-bearing rat spleen cells was not enough to inhibit the tumor growth. Even the survived rat developed primary and metastatic tumors then later regressed.

Although passive transfer of tumor immunity has been reported after immunotherapy [1-9], most successful adoptive immunity transfers required T-cell depletion in the recipients [1, 3-5, 10-11]. Furthermore, large amount of the immune cells is often needed in the transfer (an effective ratio of 1000:1 was reported in Ref. 8), and the subsequent protection of the passive transfer can be diminished significantly. For instance, immune cells from the passively protected rats in the first cohorts could only protect 30% rats in the second cohort of naïve recipients [8].

Laser immunotherapy produced a much stronger immunity based on the following findings. (1). The successfully treated rats can withstand repeated challenge with increased tumor dose. (2). The passive adoptive immunity transfer in our experiments does not require the T-cell suppression in recipients. (3). A ratio of 400:1 immune to tumor cells can provide 100% passive protection to the first cohort of naïve recipients. (4). The spleen cells from the protected rats in first cohort can strongly protect the second cohort of normal recipients (at an 83% level). These results may be related to proliferation of donor cells in syngeneic hosts or immunological recruitment and expansion of recipient responses. Our current experiments are not able to determine which is the true cause of these phenomena.

The dose of immune cell may be an important factor in the adoptive immunity transfer, as indicated by the results in Ref. 8. As the first step in determining the protective ability, only one spleen cell to tumor cell ratio (400:1) was used in our experiments. Future studies with different ratios will yield important information on this protection ability of the immune spleen cells. Furthermore, it is important to learn which subset(s) of splenocytes is (are) responsible for the observed results. These studies are currently in progress.

## 5. ACKNOWLEDGMENTS

We thank Scottye Davis for animal preparation. This research was supported in part by grants from Pacific Pharmaceuticals, Inc., and from the Mazie Wilkonson Fund.

## 6. REFERENCES

1. Boyer, C.M., Kreider, J.W. and Bartlett, G.L. Systemic Adoptive Transfer of Immunity to 13762A Rat Mammary Adenocarcinoma. Cancer Res., **41**: 2394-2400, 1981.
2. Galton, J.E., Palladino, M.A., Xue, B., Edelman, A.S. and Thorbecke, G.J. Immunity to Carcinogen-Induced Transplantable Fibrosarcoma in B2/B2 Chickens. Cellular Immunology, **73**: 247-263, 1982.
3. Mills, C.D., North R.J. Expression of Passively Transferred Immunity against an Established Tumor Depends on Generation of Cytolytic T Cells in Recipient. J. Exp. Med., **157**: 1448-1460, 1983.
4. North, R.J. γ-Irradiation Facilitates the Expression of Adoptive Immunity against Established Tumors by Eliminating Suppressor T Cells. Cancer Immunol. Immunother., **16**: 175-181, 1984.

5. Reichert, C.M., Rosenstein, M., von Glatz, J., Hsu, S.-M. and Rosenberg, S.A. Curative Intravenous Adoptive Immunotherapy of Meth A Murine Sarcoma. Laboratory Investigation, **52**: 304-313, 1985.
6. Nigam, S.K., Venkatakrishna-Bhatt, H. Adoptive Transfer of Immunity in Sensitized Spleen Cells Collected from Experimentally Produced Sarcomas in Mice. Discovery and Innovation, **6**: 72-76, 1994.
7. Chen, K., Braun, S., Lyman, S., Fan, Y., Traycoff, C.M., Wiebke, E.A., Gaddy, J., Sledge, G., Broxmeyer, H.E. and Cornetta, K. Antitumor Activity and Immunotherapeutic Properties of Flt3-Ligand in a Murine Breast Cancer Model. Cancer Res., **57**: 3511-3516, 1997.
8. Slater, L.M., Wetzel, M., Cho, J. and Sweet, P. Development of Cyclosporin A Mediated Immunity in L1210 Leukaemia. Br. J. Cancer, **64**: 1098-1102, 1991.
9. Shu, S., Fonseca, L.S., Hunter, J.T. and Rapp, H.J. Mechanisms of Immunological Eradication of a Syngeneic Guinea Pig Tumor. Transplantation, **35**: 56-61, 1983.
10. Awwad M. and North, R.J. Radiosensitive Barrier to T-Cell-Mediated Adoptive Immunotherapy of Established Tumors. Cancer Res., **50**: 2228-2233, 1990.
11. North, R.J. The Therapeutic Significance of Concomitant Antitumor Immunity II. Passive Transfer of Concomitant Immunity with Ly-$1^{+}2^{-}$ T Cells Primes Established Tumors in T Cell-Deficient Recipients for Endotoxin-Induced Regression. Cancer Immunol. Immunother., **18**: 75-79, 1984.
12. Canti, G., Marelli, O., Ricci, L. and Nicolin, A. Hematoporphyrin Treated Murine Lmphocytes: in vitro Inhibition of DNA Synthesis and Light-Mediated Inactivation of Cells Responsible for GVHR. Photochemistry and Photobiology **34**, 589-594, 1981.
13. Krosl, G. and Korbelik, M. Potentiation of Photodynamic Therapy by Immunotherapy: the Effect of Schizophyllan (SPG). Cancer Letters **84**: 43-49, 1994.
14. Krosl, G., Korbelik, M. and Dougherty, G. J. Induction of Immune Cell Infiltration into Murine SCCVII Tumor by Photofrin Based Photodynamic Therapy. British Journal of Cancer **71**: 549-555, 1995.
15. Canti, G., Lattuada, D., Nicolin, A., Taroni, P., Valentini, G. and Cubeddu, R. Antitumor Immunity Induced by Photodynamic Therapy with Aluminum Disulfonated Phthalocyanines and Laser Light. Anticancer Drugs **5**: 443-447, 1994.
16. Chen, W.R., Adams, R.L., Carubelli, R. and Nordquist, R.E. Laser-Photosensitizer Assisted Immunotherapy: A Novel Modality for Cancer Treatment. Cancer Letters **115**: 25-30, 1997.
17. Chen, W.R., Zhu, W.-G., Dynlacht, J.R., Liu, H. and Nordquist, R.E. Long-Term Tumor Resistance Induced by Laser Photoimmunotherapy. International Journal of Cancer **81**: 808-812, 1999.
18. Chen, W.R., Liu, H., Nordquist, J.A. and Nordquist, R.E. Tumor Cell Damage and Leukocyte Infiltration after Laser Immunotherapy Treatment", Lasers in Medical Science, 15, 43-48, 2000.
19. Kim, U. Metastasizing Mammary Carcinomas in Rats: Induction and Study of Their Immunogenicity. Science, **167**: 72-74, 1970.
20. Kim, U. Pathogenesis of Spontaneously Metastasizing Mammary Carcinomas in Rats. Gann Monograph on Cancer Research, **20**: 73-81, 1977.
21. Chen, W.R., Adams, R.L., Heaton, S., Dickey, D.T., Bartels, K.E. and Nordquist, R.E. Chromophore-Enhanced Laser-Tumor Tissue Photothermal Interaction Using an 808-nm Diode Laser. Cancer Letters **88**: 15-19, 1995.
22. Chen, W.R., Adams, R.L., Bartels, K.E. and Nordquist, R.E. Chromophore-Enhanced in vivo Tumor Cell Destruction Using an 808-nm Diode Laser. Cancer Letters **94**: 125-131, 1995.

Invited Paper

# Photosensitizer Quantitation in Vivo by Fluorescence Micro-sampling

**Brian W. Pogue[*], Gregory Burke[+], Claudia Lee[*,**] and P. Jack Hoopes[*,**]**

[*]Thayer School of Engineering, Dartmouth College, Hanover, New Hampshire 03755
[**]Department of Surgery, Dartmouth Medical School,
Hanover, New Hampshire 03755

[+]Aurora Optics, Inc., Hanover, New Hampshire 03755

## ABSTRACT

Photodynamic therapy can provide a reliable method of tumor destruction when the appropriate dosimetry is applied. Current dosimetry practice involves quantification of the drug and light doses applied to the tumor, but it would be desirable to monitor in vivo light and drug levels to provide the most accurate determination of dosimetry. In vivo measurements can be used to minimize variations in treatment response due to inter-animal variability, by providing animal-specific or patient-specific treatment planning. This study reports on the development of a micro-sampling method to measure fluorescence from tissue, which is not significantly affected by the tissue optical properties. The system measures fluorescence from the surface of a tissue, using a fiber bundle composed of individual 100 micron fibers which are all spaced apart by 700 microns from one another at the tissue contact end. This design provides sampling of the fluorescence at multiple sites to increase the signal intensity, while maintaining a micro-sampling of the tissue volume just below the surface. The calibration studies here indicate that the 1/e sampling depth is near 60 microns when measured in optical phantoms, which are similar to typical tissue properties. The probe fluorescence signal is independent of blood concentration up to a maximum of 10% blood by volume, which is similar to most tumor tissue. Animal tests indicate that the sensitivity to drug concentration is essentially the same in when measured in murine liver and muscle tissues, both in vivo and ex vivo. These preliminary calibration results suggest that the probe can be used to measure photosensitizer uptake in vivo non-invasively and rapidly via conversion of fluorescence intensity to photosensitizer concentration.

## 1. INTRODUCTION

The overall goal of this study was to develop a prototype system for fluorescence based measurement of photosensitizer uptake in tissue and to test its ability for improved photodynamic therapy dosimetry. The fiber optic bundle is designed to quantify photosensitizer concentration by detecting a fluorescence intensity signal, which is not significantly affected by the tissue optical properties from which the signal is measured [1]. This system provides a convenient means to measure photosensitizer uptake non-invasively in vivo, and has been tested and calibrated in this study to characterize its performance.

While laser induced fluorescence has been utilized for a number of years in photodynamic therapy dosimetry[2-4], there are some well recognized problems with this method which have limited the utility from routine dosimetry use. Principally, the main problem areas are (i) that the fluorescence signal is affected by the tissue optical properties[2, 5], (ii) that calibration of the signal to absolute concentration is confounded by changes in spectra and fluorescence yields due to binding or aggregation in vivo [6-8]. While the latter issue is complicated, and can perhaps be solved with some detailed in vivo calibration, the first problem is addressed in this study. Thus it would be desirable to find a method of detecting the fluorescence which reduces the variation in signal due to different tissue properties. There have been many elegant attempts to model the effects of tissue optical properties upon the fluorescence signal[5, 9], yet incorporation of model-based analysis of fluorescence signals is always hindered by inaccuracies in the assumed boundary conditions or the radiative transport approximation. In this study we have investigated a simple method to limit the influence that tissue optical properties can have on the detected signal by reducing the fiber diameter to below the average scattering length of tumor tissue. This method eliminates the need for model-data matching, and can be calibrated with some detailed animal experimentation.

In *Laser-Tissue Interaction XI: Photochemical, Photothermal, and Photomechanical*, Donald D. Duncan, Jeffrey O. Hollinger, Steven L. Jacques, Editors, Proceedings of SPIE Vol. 3914 (2000)
1605-7422/00/$15.00

Monte Carlo simulations suggested that minimizing the diameter of the fibers used to sample tissue would reduce the scattering of the fluorescence signal and thus minimize the effects of intrinsic tissue scattering and absorption parameters of the tissue being interrogated [1, 10]. However, since small fiber diameters will lead to lower signal to noise ratio, the fiber bundle was designed with several individual 100 micron fibers with a spatial separation of 700 to 1000 microns from one another on the tissue surface. This spatial separation allows distinct micro-sampling of independent regions on the tissue surface, while still maintaining a high signal intensity and hence high signal to noise ratio. This paper examines the depth sensitivity, absorption coefficient sensitivity in vitro, as well as the in vivo accuracy of the micro-sampling bundle in two distinct and different tissue types.

## 2. THEORY

The details of our modeling have been described in previous papers[1, 10, 11], so that only the salient features will be explained here. When photons are launched into tissue, they are both scattered and absorbed, and some fraction of the absorbed photons are re-emitted as fluorescent photons (see Figure 1, left). These photon tracks can be predicted well by Monte Carlo simulation, and images of the total fluence within the tissue can be calculated for both fluorescence and excitation light. In Figure 1, the resulting fluence distributions are shown from two separate simulations, where the first was done with a 2 mm diameter fiber simulation, and the second was completed with a 100 micron fiber simulation. The first row of images in Figure 1 (left), show that the depth of excitation fluence is not affected by the fiber diameter significantly, but the bottom row of images show that the fluorescence fluence is constrained closer to the surface by using the smaller fiber diameter. Thus, by using smaller fiber diameters, the detected fluorescence is constrained both laterally as well as in the depth direction. Our previous results indicate that when 100 micron fibers are used, that the signal detected is composed of photons which have not been scattered on average, and have simply been converted to fluorescent light near the surface of the tissue. Thus the attenuation of the signal due to Beer's law is actually less than 5% on average for most types of tumor tissue[1].

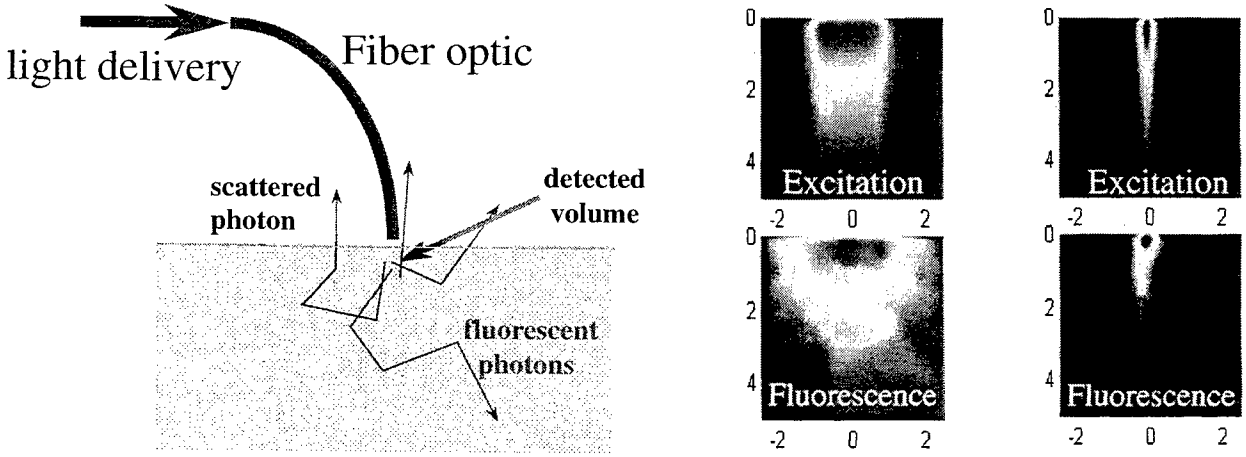


**Figure 1.** **(left)** Diagram depiction of the geometry used for Monte Carlo simulation of excitation light and fluorescence emission light in tissue. The images **(right)** of excitation light fluence **(top row)** for a 2 mm fiber and a 0.1 mm fiber are shown, respectively, along with images of the resulting fluorescence emission fluence pattern **(bottom row)** in the same simulated tissue volume. Assumed optical properties for these simulations were absorption coefficient of 0.01 $mm^{-1}$ and scattering coefficient of 10.0 $mm^{-1}$ and scattering anisotropy parameter of 0.9.

## 3. EXPERIMENT

This prototype system was developed using a compact breadboard setup (see Figure 2). The input light is provided by a Helium-Cadmium laser producing nearly 30 mW of light at either 325 nm or 442 nm, which correspond to the major Soret-band peaks of phthalocyanines and porphyrins, respectively. A chopper wheel is used to modulate the input signal at 200 Hz, to provide lock-in detection at this frequency. An LED-photodiode combination is fixed into the chopper wheel to provide the trigger frequency. A dichroic mirror is used to reflect the excitation light into the fiber bundle, and measurements of the input light intensity can be directly measured from the bundle through one of the fibers which is separate, and can be coupled

to a photodiode. Similarly, the reflected excitation light can be detected through a bifurcated fiber which has been incorporated into the bundle, so that changes in the light reflectance from the surface can be detected to normalized the fluorescence signal. The signal is coupled to an analog to digital data acquisition board in a laptop computer, with LABVIEW data acquisition software for instrument control and data processing. The light detector is an H6354 Hamamatsu photomultiplier, which provides high red-light sensitivity, in a compact space providing more than $10^6$ gain in the dynode chain. In most of the following studies, 325 nm excitation was used to excite the photosensitizer aluminum phthalocynanine disulphonated ($AlS_2Pc$).

The current bundle design incorporates 37 fibers into a single bundle, and at the tissue contact end, the fibers are all spaced apart by 700 microns through the use of hollow capillary fiberoptics, which permit the 100 micron fiber inside each, and have an outer diameter of 700 microns. These capillaries are added to space the individual fibers apart at the tissue contact end, so that inter-fiber cross talk through the tissue is minimized. The concept of the fiber bundle is specifically designed to confine the region of tissue, which is sampled by each fiber to within 100-200 micron depth, allowing minimal scattered fluorescent light to be captured. The small diameter of the individual fibers (100 microns) confines the signal laterally, and the tissue confines the detected signal in the z-direction, so that the captured fluorescent photons have scattered an average of less than once [1]. The following sections are devoted to exploring the spatial confinement and fluorescence quantitation characteristics of the fiber bundle in tissue and tissue-simulating media.

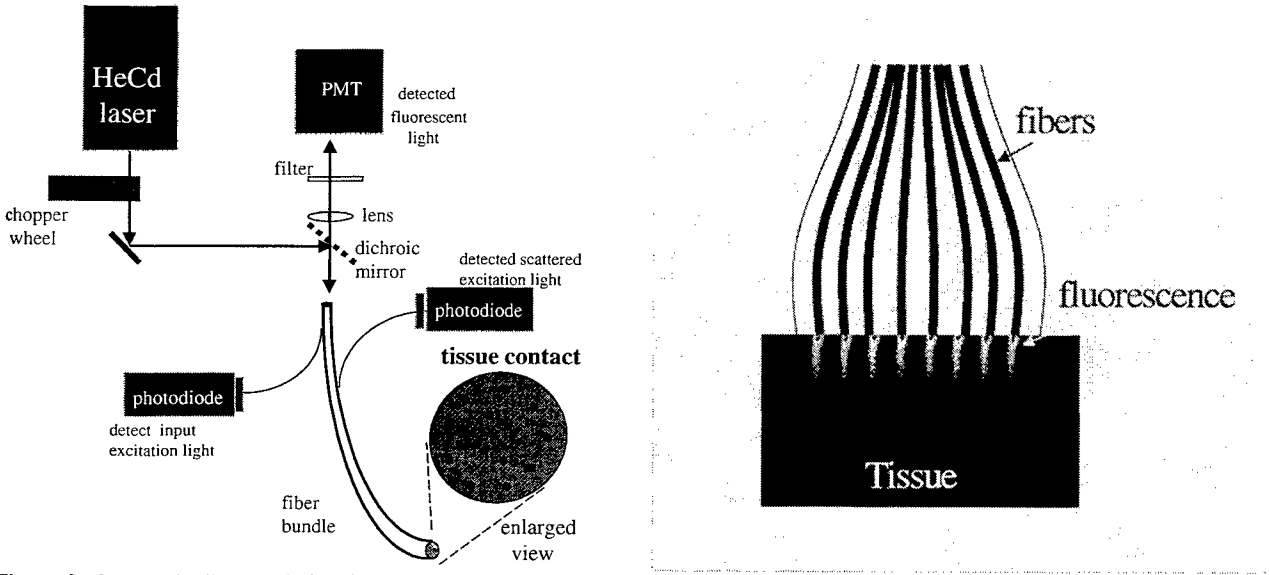


**Figure 2.** Schematic diagram **(left)** of the optical arrangement use with the fiberoptic bundle. Fiberoptic bundle arrangement **(right)** depicting the microsampling of each fiber in the bundle by separating the fibers out at the tissue-contact surface. Note that while only a few fibers are shown in this schematic, there are 37 individual fibers in the actual bundle.

## 3. RESULTS

### 3.1 Depth sensitivity testing

The design of the fiber bundle is such that it should limit the penetration of the light in tissue. This is a difficult thing to measure in practice, but in tissue simulating solutions, this can be measured quite easily. Initial experiments were completed to compare the detected signal from the new fiber bundle to measurements taken with a standard silica fiber optic bundle, where all fibers are kept close together. The initial test to measure the depth of penetration estimate in the solution was set up as shown in the following figure, where a 1 mm layer of aluminum disulphonated phthalocynanine ($AlS_2Pc$) was fixed into a container, and the remainder of the container was filled with 1% Intralipid (a lipid emulsion which has similar scattering properties to tissue) and 1% whole blood, by volume. The fiber bundle was translated away from the fluorescent layer in 10 micron increments, and the fluorescence intensity was recorded at each depth.

The measurements shown in Figure 4 demonstrate that for a standard incoherent silica fiber bundle of 3 mm diameter, the detected signal is higher than from the micro-sampling bundle, and that the slope of the intensity versus distance from the

fluorophore has two distinct slopes. The terminal slope for both fiber bundles is dominated by the attenuation of light in the medium, and governed by the effective attenuation coefficient, $\mu_{eff} = (3\mu_a \mu_s')^{1/2}$. However the standard fiber bundle demonstrates an initial slope of fluorescence versus depth which is low, due to interactions between the fibers as the fluorescent light is multiply scattered, and is collected by neighboring fibers. The micro-sampling fiber bundle does not demonstrate this regime of light collection, and the signal decays by one order of magnitude in 60 microns. While this test is not definitive proof of the microsampling of the bundle, it provides a good indication that the light collection is behaving as we expect.

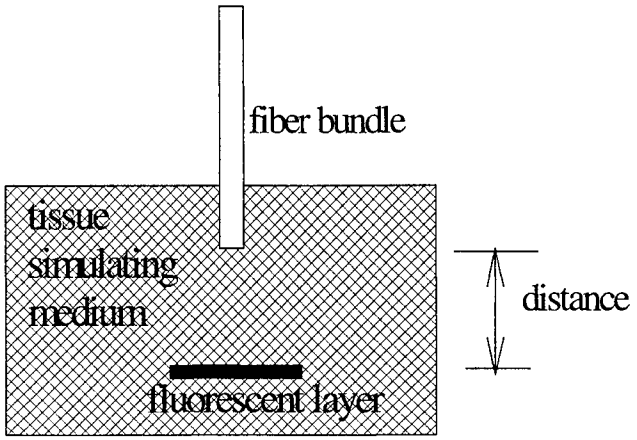


**Figure 3.** The fiber bundle was translated vertically through the solution towards a fluorescent layer of photosensitizer contained in a thin plastic sheet. The fluorescence versus recovery distance was measured for a standard fiber bundle, and for the new micro-sampling fiber bundle.

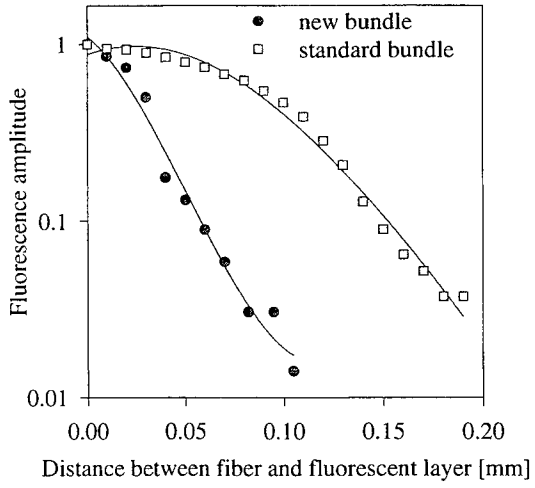


**Figure 4.** Measured fluorescence versus distance between the fiber bundle and the fluorescent layer, with a tissue-simulating fluid between consisting of 1% Intralipid and 1% whole blood, with geometry as shown in the previous figure. A standard 3 mm fiber bundle and the new micro-sampling fiber bundle are shown for comparison.

### 3.2 Sensitivity to intrinsic absorption coefficient

In the next test, a solution of Intralipid in water was mixed with 10 μg/ml $AlS_2Pc$, and a series of solutions with increasing ink added to them was created. The fiber bundles (standard and the new design) were used to measure the fluorescence by placing the bundle on the surface of the solution. The results are plotted in figure 5, where the standard silica fiber bundle shows a decreasing detected signal from the more absorbing solutions. The new micro-sampling fiber bundle design produces a fluorescence signal, which is not attenuated significantly over this range of absorption coefficients. The highest absorption coefficient used here was 0.16 $mm^{-1}$, which is typical of the darkest pigmented tissues, such as liver, while most red muscle is closer to 0.01 to 0.1 $mm^{-1}$, at the emission wavelength of 675 nm.

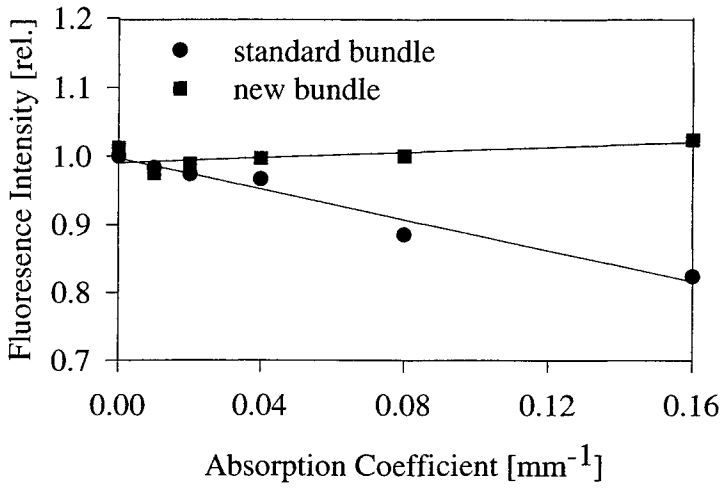


**Figure 5.** Measured fluorescence versus increasing ink concentration for a fixed solution of Intralipid and $AlS_2Pc$ photosensitizer. The photosensitizer was at 10 mg/ml concentration, and the ink concentration was varied to cover the range of physiologically relevant absorption coefficient values. The solution simulates the scattering typical within tissue ($\mu_s' = 2.0$ $mm^{-1}$).

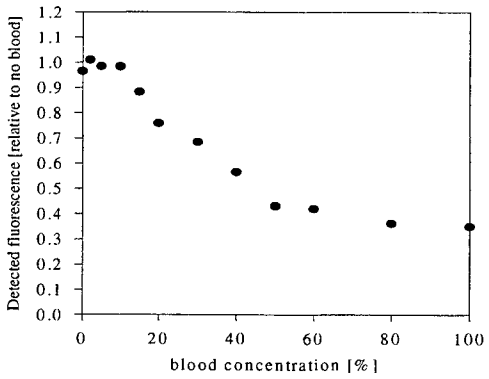


**Figure 6.** Measured fluorescence from tissue simulating solutions with a fixed photosensitizer concentration of 20 μg/ml in 1% Intralipid, with the fraction of blood in the solution varied between 0 and 100 %. The absorption coefficient of blood at 325 nm wavelength is near 0.3 $mm^{-1}$ per % of volume, so that above 10% blood concentration is a very high absorption coefficient. Most mammalian tissues have less than 10% blood concentration by volume.

While the detected fluorescent light was linear with fluorophore concentration, and presented little attenuation in highly pigmented tissue-simulating solutions, we found there to be considerable attenuation when measuring from within 100% whole blood. Figure 6 shows a plot of detected signal for a constant concentration of photosensitizer in solution, but with the

fraction of blood in solution varied between 0 and 100 % by volume, mixed into an aqueous solution of 1% Intralipid. At concentrations above 15% blood, there was more than a 10 % attenuation of the detected light, and in whole blood, the detected light was only 38% of that observed in bloodless solution. These measurements indicate that for measurements taken in whole blood, a secondary set of calibrations must be performed. Also since most tissues have less than a 15% blood volume, we can expect that attenuation by blood within any tissue should not be a significant factor in the detected signal. However it is important to be aware that certain tumors and bloody cyst areas can have high blood volume fractions, which may decrease the signal intensity accordingly.

### 3.3 In vivo testing versus extraction methods

The most accurate method for quantifying photosensitizer uptake in tissue is to biopsy the tissue and extract the chemical from the tissue using a solubolizing solution. Once extracted, the monomerized fluorophore can be directly quantified in a luminescence spectrophotometer by detecting the fluorescence intensity of the solution. The biopsied tissues were solubolized by digestion in 0.1 N NaOH with 1% SDS. After 4 hours of heating at 50°C with shaking, the solutions were measured for fluorescence in a Perkin-Elmer luminescence spectrophotometer. The excitation was set to 610 nm, and emission between 640 and 740 nm. The longer wavelength excitation was needed to transmit sufficient light through the turbid solutions of solubolized tissue without significant attenuation. These measurements in the spectrophotometer were viewed as representing of the absolute concentration in the tissue and used to compare with the fiber bundle measurements of fluorescence. The following figure presents the direct correlation of the two measurements, and demonstrates that the detected signal from the fiber bundle is independent of the tissue type. Note also that while the uptake of the muscle is generally much less than the liver, there is also a parallel decrease in fluorescence measured. Here liver and muscle were used for two reasons, they represent significantly different tissue types with respect to vascular morphology and drug uptake, but practically they are two of the few organs that can be measured in a mouse without potential artifacts due to the small size, compared to the 1 cm fiber bundle probe. In the next phase of this work, the fiber bundles will be tested in larger animals to provide a more uniform and stable probe positioning.

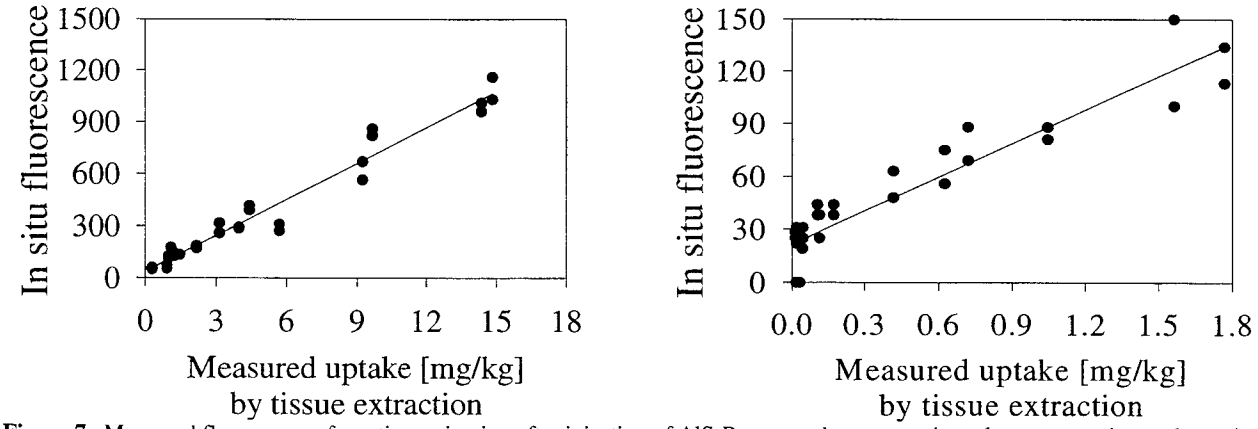


**Figure 7.** Measured fluorescence from tissues in vivo after injection of $AlS_2Pc$ versus the measured uptake concentration as determined by chemical extraction from the tissue biopsy and spectrofluorimeter detection. Both liver (left) and muscle (right) tissues were measured in the same manner, and the slopes of these graphs are similar, indicating that the response of the probes is roughly independent of tissue type.

## 4. DISCUSSION

The fiber bundle fluorescence monitor tested here appears to provide a fluorescence sampling from tissue volumes which are constrained both laterally and vertically below the tissue surface. The depth sensitivity measurements, shown in Figure 4, indicate that the depth response is at least a factor of 3 lower than that of a standard 3 mm diameter fiber bundle, and the sensitivity 1/e penetration depth is near 60 microns in typical tissue phantoms. Thus the attenuation of the fluorescence signal in most tumor tissues should be no more than a few percent of the total signal, as calculated by Beer's law attenuation.

Based on the data in Figures 5 and 6, the signal is not significantly attenuated in phantoms with absorption coefficients up to 0.16 mm-1, and in blood solutions up to 10% total blood volume. These two parameters are near the maximal values expected in tumor tissues, suggesting that the signal should not be altered by blood volume differences in different animals and tumors, except in regions of high blood pooling or large vascularity.

Finally, testing in murine liver and muscle tissue indicate that response of fluorescence per unit concentration is the same to within 11%, as shown in Figure 7. These measurements can be directly compared to those of Panjehpour et al. [2], who showed that when measuring the uptake of AlSPc in liver and muscle with a standard fiberoptic fluorescence system, there was a factor of 5 different in the response of fluorescence per unit concentration of drug. Thus the results in Figure 7 provide significant evidence that our measurement system will be independent of tissue optical properties. The next phase of system testing will be to measure uptake in murine tumors, and to provide animal/tumor specific dosimetry measurements to reduce the inter-patient or inter-animal variability in response to treatment.

## 5. ACKNOWLEDGEMENTS

This work has been partially funded by NCI grants RO1CA78734 and R44CA76913.

## 6. REFERENCES

1. Pogue, B.W. and G.C. Burke, *Fiber optic bundle design for quantitative fluorescence measurement from tissue.* Appl. Opt., 1998. **37**(31): p. 7429-36.
2. Panjehpour, M., *et al.*, *Quantification of phthalocyanine concentration in rat tissue using laser-induced fluorescence spectroscopy.* Lasers in Surgery & Medicine, 1993. **13**(1): p. 23-30.
3. Sinaasappel, M. and H.J.C.M. Sterenborg, *Quantification of the hematoporphyrin derivative by fluorescence measurement using dual-wavelength excitation and dual-wavelength detection.* Appl. Opt., 1993. **32**(4): p. 541-548.
4. Konig, K., *et al.*, *Photodynamic Tumor-Therapy and Online Fluorescence Spectroscopy After ALA Administration Using 633-nm Light as Therapeutic and Fluorescence Excitation Radiation.* Opt Eng, 1994. **33**(9): p. 2945-2952.
5. Durkin, A.J., *et al.*, *Relation between fluorescence spectra of dilute and turbid samples.* Appl. Opt., 1994. **33**(3): p. 414-423.
6. Smith, G.J., *The effects of aggregation on the fluorescence and the triplet state yield of hematoporphyrin.* Photochem. Photobiol., 1985. **41**: p. 123-126.
7. van Lier, J.E. and J.D. Spikes, *The chemistry, photophysics and photosensitizing properties of phthalocyanines. [Review].* Ciba Foundation Symposium, 1989. **146**: p. 17-26; discussion 26-32.
8. Star, W.M., *In vivo action spectra, absorption and fluorescence excitation spectra of photosensitizers for photodynamic therapy.* Journal of Photochemistry & Photobiology, 1995. **B - Biology. 28**(1): p. 101-2.
9. Patterson, M.S. and B.W. Pogue, *Mathimatical model for time-resolved and frequency-domain fluorescence spectroscopy in biological tissues.* Appl. Opt., 1994. **33**(10): p. 1963-1974.
10. Pogue, B.W., Hasan, T., *Fluorophore quantitation in tissue-simulating media with confocal detection.* IEEE J. Quan. Electr., 1997. **2**(4): p. 959-964.
11. Pogue, B.W., Hasan, T., *Quantitative fluorescence measurements from tissue using confocal detection.* Proceedings of SPIE, 1997. **2975**: p. 202-207.

# Photodynamic effect produced by HeNe radiation in Harderian glands of Wistar rats: an experimental model for PDT studies

Edmyr R. dos Reis, Ester M. D. Nicola*, Konradin Metze and Jorge H. Nicola

Lab. Laser – Núcleo de Medicina e Cirurgia Experimental, Universidade Estadual de Campinas,

UNICAMP, Campinas, SP, Brazil

## ABSTRACT

In rats, the Harderian Gland secret Protoporphirin IX which is retained at acinar lumina. Since this photosensitizer is important for PDT of malignant tumors, we propose to study this gland as a model to help understanding PDT with endogenous photosensitizers. Twenty Wistar SPF adult rats were submitted to surgical exposure of both Harderian glands, revealing red fluorescence upon UV, characterizing the protoporphirin IX presence. After that, one gland of each pair (one kept as control) was irradiated with an 8mW HeNe (6328 angstron) for 45 minutes, delivering about 2.7 joules/mm$^2$. After 24 hours a group of 10 animals were sacrificed and the glands removed for histological analysis. The remaining animals were subjected to the same procedure but the glands were removed immediately after laser treatment. Histological and fluorescence analysis immediately after laser irradiation showed cell fragmentation with loss of acinar architecture with diffusion of protoporphirin in the cytoplasm of damaged cells, as well as interstitial edema. After 24 hours these alterations were more pronounced with accentuated loss of intraluminal protoporphirin and beginning of leukocytic demarcation of necrotic areas. The innate Harderian glands of rats, exposed to HeNe laser, showed a similar behavior as tumor tissue under PDT.

**Keywords:** Harderian gland; protoporphyrin IX; PDT; endogenous

## 1. INTRODUCTION

Optical absorption, reflection and fluorescence are physical methods capable to characterize different matters, in special biologic tissue[1]. Particularly Photodynamic Therapy of malignant tumors (PDT) is an optical process either for diagnostic procedure[2] or for therapy[3]. PDT is well described in the literature (see for example Dougherty, 1993)[4]. Photosensitizers like protoporfirin IX, among others structurally related compounds, is a substance that can be injected in the subject allowing the diagnostic or treatment of malignant tissue[5, 6]. A more recent approach to PDT involves endogenous photosensitization by administration of 5-aminolevulinic acid (ALA)[7, 8], which is converted by the heme biosynthesis pathway to protoporphyrin IX[5], an efficient photosensitizer.

Some biologic tissues present endogenous substances that may fluoresce or absorb optical radiation in a similar way to PDT process. Harderian gland, named after the Swiss physician Johann Jakob Harder,[9, 10] of rats can sintetize high concentration of protoporfirin IX[11]. This substance is retained at the lumen of the acinos[12] and is easily identified by UV fluorescence, readily differentiated from blood.

Various physiological functions have been attributed to the rat Harderian gland. It appears to serve, like the pineal gland, as an extraretinal photoreceptor[10, 13, 14, 15, 16, 17, 18]. Harderian porphyrin may have a photoprotective role, as it is increasingly secreted in response to light exposure and as other porphyrins show an intense absorption of light[5].

The Harderian gland acinus cell secrets protoporfirin IX in a considerable quantity, this photosensitiser is abundant found in the acinar luminae as well as in the acinar cells, which can be identified by fluorescence or by the frozen cuts under fluorescence microscopy.

Many attempts are doing to explain the PDT mechanism[19, 20] and, based on the facts described above we hope the study of photodynamic response of Harderian gland secretion, may contribute to this development.

* Correspondence: Email: nicolaemd@nmce.unicamp.br



In *Laser-Tissue Interaction XI: Photochemical, Photothermal, and Photomechanical*, Donald D. Duncan, Jeffrey O. Hollinger, Steven L. Jacques, Editors, Proceedings of SPIE Vol. 3914 (2000)
1605-7422/00/$15.00

## 2. MATERIAL AND METHODS

For this work we have used 20 SPF (Specific Pathogen Free) Wistar rats of both sex, 7 weeks old and body mass from 150 to 200 g. The animals was maintained in polypropylene cages and had access to standard rodent chow and water *ad libitum*. The anesthetic procedure were according to ethical international protocols, with intravenous sodium hypinol. The glands was exposed by means of microsurgery (Figure 01).

Fig. 01 - Harderian gland of Wistar rat, surgically exposed and prepared for the present work.

The fluorescence of Harderian gland was produced using a 20 Watts UV lamp with maximum output at 365 nm, positioned 5 cm away from the gland and, the intense red fluorescence was compared with the protoporfirin IX fluorescence and registered photographically. Figure 02 (a)a show the Harderian gland photographed with regular light and, (b), the same gland when illuminated with UV light, showing the red fluorescence (seen in white at the photo).

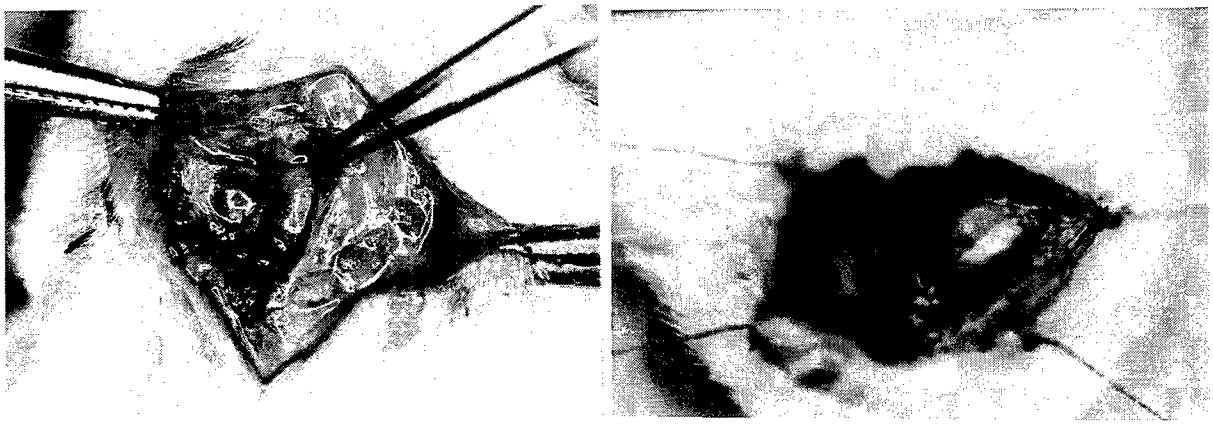

(a) (b)

Fig. 02 –Harderian gland: (a) as seeing when illuminated by white light and, (b) fluorescence of the same gland obtained with 365 nm light source.

An HeNe, 8 mW, was the light source used for the absorption process. The red, 6328 angstrom light, emitted by this laser, is in good agreement with the absorption energy level of the protoporfirin founded in the glands. Left and right side glands of each animal were exposed, allowing to keep one gland of each pair as a non irradiate control to be compared with the irradiated one.

We irradiated the glands under study for 45 minutes, providing a fluence of 21.6 J/mm$^2$. Four groups of five animals were sorted. The rats of first group were sacrificed and the glands were excised 72 hours after laser irradiation; the second group at 48 hours; the third group at 24 hours and the fourth group of rats, immediately after laser irradiation.

For regular microscopy we have fixed the material in buffered 4 % formaldehyde for 24 h and embedded in paraffin. Step sections perpendicular to the surface were cut, mounted on glass slides and stained with hematoxylin and eosin for examination by light microscopy. For fluorescence microscopy studies the tissue was frozen, hematoxilin and eosin-stained as well as unstained, and cut to 5 microns and mounted in glass slides. The photos presented in this work were all taken from frozen cuts.

## 3. RESULTS AND DISCUSSION

Before proceeding with the photodynamic experiments we have identified the occurrence of protoporfirin IX by fluorescence experiment, using an UV lamp (365 nm line output). The Harderian gland displays the characteristic protoporfirin IX red fluorescence as registered photographically (Fig. 2a). The full spectrum of this fluorescence will be registered and published in the near future. The microscopic analysis of the material identify the tubules of the normal rat Harderian gland, composed of a single layer of columnar epithelial cells surrounded by myoepithelial cells (figure 3a, b). In the lumina there are deposits of yellow brown amorphous masses (3a), which show the red fluorescence of porphyrin and are composed of porphyrin-lipid complexes (3b).

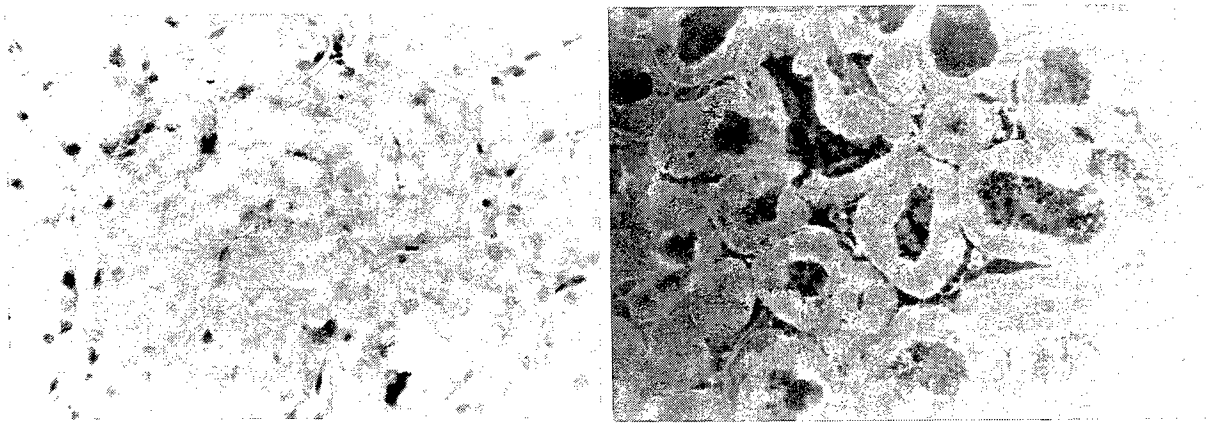

(a) (b)

Fig. 03 - Normal (control) Harderian gland epithelial cells of the tubuli composed of epithelial cells (3a) which shows yellow - green autoflourescence of the cytoplasm under fluorescence light examination (b). Amorphous porphyrinlipid complexes are found inside the lumina (3a) with red autofluorescence (3b).

Immediately after exposure to laser light, necrosis of the tubular cells characterized by fragments of the epithelial cells (Fig. 4a and 4b – next page) admixed with porphyrinlipid complexes, can be observed (figure 4 b). The basement membrane of the tubuli may still be intact.

After 24 hours a marked interstitial edema with granulocytic infiltration in the previously irradiated area is found. The fragmentation of the necrotic epithelial cells is more advanced. (Fig. 5a) Remnants of the porphyrin-lipid complexes can only rarely be detected by fluorescence microscopy in the area of necrosis (figure 5b).

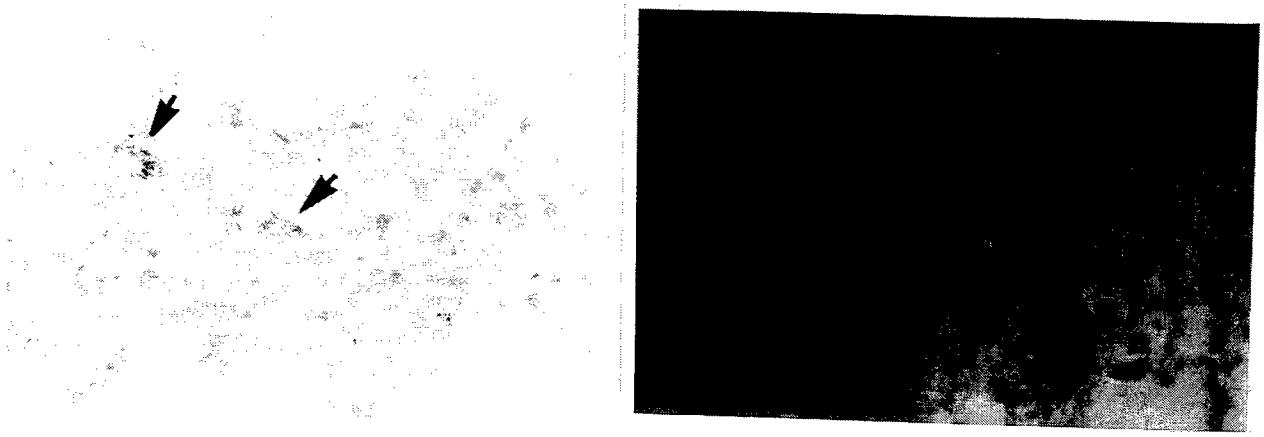

(a) (b)

Fig. 04 - Harderian gland removed immediately after exposure to laser light: necrosis with fragmentation of the tubular epithelial cells is the predominant feature. (4a) Examination with UV light shows that the protophyrin-lipid complexes (red fluorescence) are mixed together with necrotic cell fragments. Absence of inflammatory infiltrate (4b).

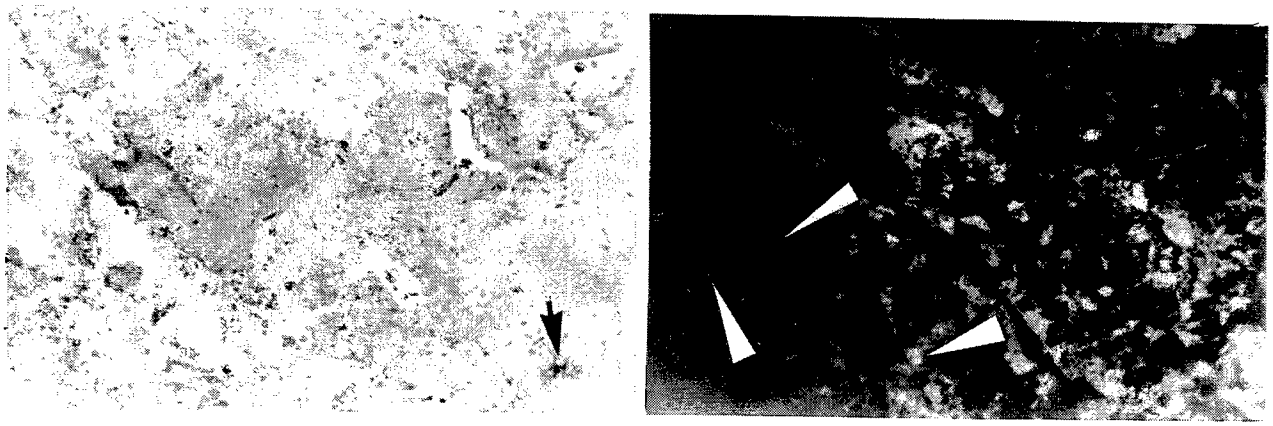

(a) (b)

Fig. 05 – Harderian gland tissue 24 hours after laser irradiation: marked cellular fragmentation of the necrotic epithelial cells Porphyrinlipid complexes are nearly totally absent (5a). Marked edema and presence of granulocytes was observed. With the help of UV light remnants of protoporphyrin-lipid-complexes can only be rarely detected (arrows) (5b).

The contralateral sham-operated Harderian glands, kept as control, showed neither necrosis nor inflammatory infiltrate (figure not presented).

Previously studies demonstrated[21] that exposure to intensive sun light for one day may cause severe necrosis of the glandular cells, with edema and cellular infiltration of the Harderian gland adjacent to the retina. The red fluorescence was faint in areas injured by exposure to light for 4 and 8 days, and porphyrin content of the gland decreased after 4 and 8 days. Thus exposure to high-intensity light induced necrosis of the glandular cells in the Harderian glands, probably as a result of photodynamic action on the porphyrins in the gland.
In order to contribute to the knowledge of the photodynamic mechanism we have studied the effect of HeNe laser on endogenous protoporphyrin IX of Harderian gland. The process of necrosis has to be interpreted as due to a photodynamic effect. Damage caused by porphyrins causes essentially necrosis not apoptosis, as seen in our study, in contrast to the photodynamic therapy of the Walker tumour[22].

## 4. CONCLUSIONS

The Harderian glands of rats present an intense red fluorescence which can be easily perceived by stimulation with ultra violet lamp, or in frozen cuts under fluorescence microscopy. This fluorescence is due to a photosensible substance with a red emission (630 – 635 nm) which has been identified as protoporphirin IX.
When irradiated with an HeNe laser source (6328 angstrons), the gland presented a photodestruction effect very similar to the one found in tumor tissue treated with ALA, which leads to protoporphirin IX formation and retention in tumor cells.
Thus the Harderian gland, through its intense production and retention of protoporphirin IX represents a very good and easy to handle model for the study of photodynamic effects that result in tumor cell destrution.

## 5. ACKNOWLEDGEMENT

Special thanks to Dr. Valdir C. Colussi for helping in early stages of this work.

## 6. REFERENCES

1. A. P. Payne, J .Mc Gadey, and H. S. Johnston. "The structure of the Harderian glan of the golden hamster. In Harderian gland effects", (Ed. Weeb S. M., Hoffman R. A., Puig-Domingo & R. J. Reiter) pp 53-67, Berlin Springer, 1992
2. O. Raab, "Ueber die wirkung fluorescierender stoffe auf infusoria". *J. Biol.*, **39**: pp 524, 1900
3. H. Tappenier. & A. Jesionek, "Therapeutishe versuche mit fluoreszierenden stoffe". *Muench. Med. Woshschr.*, **1**: pp 2042-2044, 1903
4. T. J. Dougherty, "Photodynamic therapy: Yearly Review", *Photochem. Photobiol.*, **58** (6), pp 895-900, (1993)
5. C. J. Bayne, L. V. Marshallsay, and , A. D. Ward, "The composition of Photophrin II", *J. Photochem. Photobiol.*, **6**, pp 13-27, 1990
6. V. C. Colussi, E. D. Nicola, and J. H. Nicola, "Fototerapia, Fotoquimioterapia e alguns fotossensibilizadores", *Rev. Ass. Med. Brasil*, **42** (4), pp 229-236, 1996
7. E. E. Gallegos, I. De Leon Rodrigues, G. L. Martinez, and Z. A J. Perez, "In vitro study of protoporphyrin IX induced by delta-aminolevulinic acid in normal and cancerous cells of the human cervix". *Arch. Med. Res.*, **30** (3), pp 163-170, 1999.
8. S. L Gibson, , M. L Nguyen., J. J. Havens, Barbarin,.and R. Hilf, "Relationship of delta-aminolevulinic acid-induced protoporphyrin IX levels to mitochondrial content in neoplastic cells in vitro", *Biochem. Biophys Res. Commun.*, nov. **19,** 265(2), pp 315-321, 1999.
9. T Sakai; T. Yohro, "A histological study of the Harderian gland of Mongolian gerbils", Sakai and R. B.Burns (1992), "The Harderian gland in birds: histology and immunology. In the Harderian glands: Porphirin Metabolism, Behavioral and Endocrine Effects", (Ed. S. M. Webb, R. A. Hoffman, M. L. Puig-Domindo & R. J. Reiter), pp 155-163, Berlin Springer, 1981
10. G. Chieffi, B. G. Chieffi, L Di Matteo, M D'Istria, S Minucci, and B Varriale, "Cell Biology of the Harderian Glasnd", *International Review of Citology*, **168**, pp 1-80, 1997
11. R. C. Spike, S. L. Stewart., K Murray,. F. M. Kelly, J. A. Maharaj, P. A. Payne, and M. R Moore, "Porphirin sinthesis in the Harderian gland and other tissues of golden hamster during pregnaney and lactation", *Mol. Aspects. Med.* **11** pp 151-152, 1990

12. J. Hugo, J. Krijt, M. Vokurka, and V. Janousek,. "Secretory response to light in rat Harderian gland: Possible photoprotective role of Harderian porphyrin", *Gen. Physiol. Biophys.* **6**, pp 401-404,1987
13. T. R Scott, M. L. Savage. and I. Oláh, "Plasma cells of the chicken Harderian gland", *Poult. Sci.*, **72**, pp 1273-1279, 1993
14. S Minucci., B. G Chieffi, I. Di Mateo, and G. Chieffi, "A sexual dimorphism of the Harderian gland of the toad, Bufo viridis", *Basic. Appl. Histochem.*, **33,** 299-310, 1989
15. B. G. Chieffi, S Minucci, L. Di Mateo, "The orbital glands of the terrapin Pseudemys seripta in response in osmotic stress: a light and electron microscope study", *J. of Anatomy*, **18**, pp 21-33, 1993
16. B. Chieffi "Organogenisis of the Harderian Gland. A comparative survey", *Microsc. Res. Tech.*, **34**, 6-15, 1996
17. P. Pevet, G. Heth, A. Hiamand, E. Nevo, "Photoperiod perception in the blind male rat (Sphalex Chenbergi, Mehring): Involvement of the Harderian gland atrophied eyes and melatonin", *J. Exp. Zool.*, **232**, 41-50, 1984
18. D. D. Thiessen, The function of the Harderian gland in the Mongolian gerbil Meriones unguiculatus. In Harderian glands: Porphirin metabolism. Behavioral and endocrine effects. (S. M. Webb, R. A. Hoffman, M. L. Perig-Domingo and R. J. Reiter, eds), pp 127-140. *Springer-Verlag, Berlin*, 1992
19. K.R. Weishaupt, C.J. Gomer and T.J. Dougherty, "Identification of singlet oxygen as the cyotoxic agent in cancer photoinactivation of a murine tumor", *Cancer Res* **36,** pp 2326-2329, 1976
20. B.W. Henderson and T.J. Dougherty, "How does photodynamic therapy work?", *Photochem Photobiol* **55**, pp 145-157, 1992
21. K. Kurisu, O. Sawamoto, .H Watanabe and A. Ito, "Sequential changes in the Harderian gland of rats exposed to high intensity light" .*Lab Anim Sci* **46** (1):71-6, 1996
22. J. H. Nicola, V. C. Colussi, E. M. D. Nicola, and K. Metze, "Enhancement of Photodynamic Therapy due to Hyperbaric Hyperoxia: an experimental study of Walker 256 tumors in rats". - Optical Methods for Tumor Treatment and Detection Mechanisms and Techniques in Photodynamic Therapy VI, Thomas J. Dougherty; Ed. Vol. **2972**, pp 88 - 94 1997.

## SESSION 3

# Photothermal Interactions I

# Modeling Infrared Temperature Measurements: Comparison of Experimental Results with Simulations

Bernard Choi, John A. Pearce, Ashley J. Welch

The University of Texas at Austin Biomedical Engineering Program,
Austin, TX 78712-1084

## ABSTRACT

Infrared cameras have been used to monitor the thermal response of tissue to pulsed and continuous wave laser irradiation. A computer model has been developed previously to predict radiometric temperature estimations and demonstrate potential discrepancies between surface and radiometric temperatures. To quantitatively verify the modeling, experiments were performed in which gelatin phantoms (~98% water) were irradiated with low-radiant-exposure (e.g. subablative) $CO_2$ laser pulses. Radiometric temperatures were estimated using a 3-5 μm band-limited thermal camera and compared to computer model predictions of the measured temperatures. By fitting model calculations to measured data, theoretical surface temperatures were determined as a function of time and the onset of nonlinear changes in the thermal response of tissue identified.

**Keywords:** IR detector, numerical modeling, finite difference, $CO_2$ laser, dynamic optical and thermal properties

## 1. INTRODUCTION

Infrared (IR) temperature measurements during laser irradiation of biological media have been performed in a number of recent studies [1-7]. However, one characteristic of IR detection that is oftentimes not taken into account is that superficial thermal gradients may result in a discrepancy between the measured radiometric temperature and the actual surface temperature [1].

For typical IR imaging bands (3-5 μm and 8-12 μm), if thermal gradients are not significant within approximately the first 100 μm of the surface, then the radiometric temperature will approximate the actual surface temperature. However, for laser irradiation studies involving highly absorbed laser light (e.g., the tissue absorption coefficient $\mu_a$ [$cm^{-1}$] at the laser wavelength is equal to or larger than the average absorption coefficient over the IR detection bandwidth), there will be a discrepancy between the estimated and actual temperatures. If transient temperatures are important, then it may be necessary to correct radiometric temperatures. For example, if radiometric temperature measurements are used 1) to identify threshold temperatures of an event (i.e. photocoagulation of blood [2]), or 2) to determine optical and/or thermal properties of an object using pulsed photothermal radiometric techniques [8]; then any errors associated with the temperature values obtained from an IR detection scheme will result in an inaccurate property calculation.

We developed a finite difference model that incorporates 1) heat transfer during and after a laser pulse to heat tissue or a cryogen spurt to cool the surface, 2) any type of temperature distribution (e.g. surface or subsurface temperature peak, etc.), and 3) any bandwidth limit for the IR detector (e.g. 3-5 μm, 8-12 μm) [9]. This paper deals with experimental verification of this model.



In *Laser-Tissue Interaction XI: Photochemical, Photothermal, and Photomechanical*, Donald D. Duncan, Jeffrey O. Hollinger, Steven L. Jacques, Editors, Proceedings of SPIE Vol. 3914 (2000)
1605-7422/00/$15.00

## 2. NUMERICAL MODEL

The method of finite differences (Incropera and DeWitt 1996) was applied to the modeling of 1) the thermal response of tissue to laser irradiation and 2) radiometric temperature measurements with an IR detector. Following is a brief description of the basic features and structure of the model; for more detailed information, the reader is directed to Ref. [9].

The program was developed in the MATLAB 5.2 coding environment (The MathWorks, Inc., Natick, MA). Optical and thermal properties were assumed to be constant values. The optical properties included the absorption coefficient of the tissue at the wavelength of the incident laser light ($\mu_a$, in $cm^{-1}$) and an average absorption coefficient of the tissue to the IR radiation that comprised the signal reaching the IR detector ($\mu_{IR}$, in $cm^{-1}$). For the latter value, we chose to use a constant value of $\mu_{IR}$ = 300 $cm^{-1}$ [1]. The thermal properties included: density ($\rho$, in $g/cm^3$), specific heat ($c$, in J/g/°C), thermal conductivity ($k$, in W/cm/°C), and thermal diffusivity ($\alpha = k/\rho c$, in $cm^2/s$).

The optical distribution of the laser light as a function of depth was described using Beer's law (potential scattering events were not considered). The fluence distribution was converted to temperature values. The contribution of each node to the overall infrared signal reaching the IR detector was calculated under the assumption that emission from a given node was attenuated in a Beer's law fashion as it traveled to the tissue surface. The total emissive power reaching the detector was converted to a radiometric temperature using band-limited blackbody curves [10, 11].

## 3. MATERIALS AND METHODS

**Experimental Study.** The experimental setup is shown in Figure 1. Gelatin tissue phantoms (98% water by mass) were created in petri dishes. A petri dish was mounted on an XYZ-translation stage to allow for accurate positioning. Thermal imaging was performed using a HgCdTe flying spot scanner (Model 600L, Inframetrics, Billerica, MA) in fast line scan mode (acquisition rate = 8 kHz) and equipped with a 24.13-cm focal length zoom lens. Images were recorded using a Super VHS video recorder (Diamond Pro, Mitsubishi) with a video counter providing a time stamp on each recorded frame. A short-pulsed (pulsewidth = 110 μs) $CO_2$ laser (TruPulse, Tissue Medical Lasers) was used to irradiate the gelatin samples. The handpiece was mounted at a 45° angle with respect to the surface plane of the sample. Infrared windows of various materials were used as necessary to attenuate the incident laser radiation. The spot size was estimated using burn paper (Zap-It!, Kentek) and pulse energy measured with a calibrated energy meter (EPM 2000, Molectron). Software written in LabVIEW 5.1 (National Instruments, Austin, TX) was used to aid in synchronization of the laser with the thermal camera.

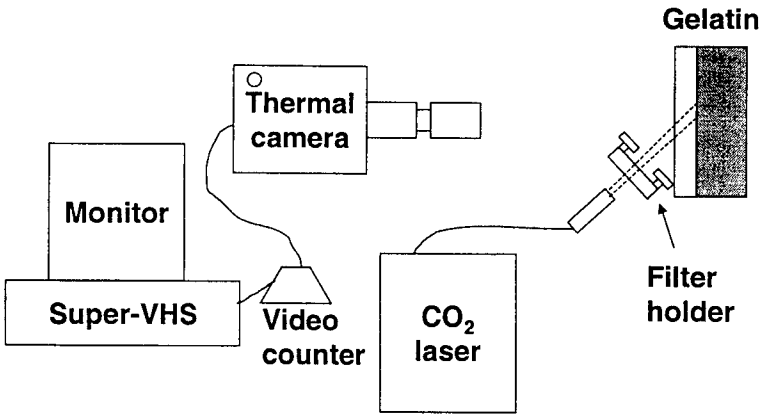


**Figure 1. Diagram of experimental setup.**

Incident radiant exposures were chosen by using the following equation:

$$\Delta T = \frac{H_o \mu_a}{\rho c} \tag{1}$$

where $\Delta T$ is the predicted temperature rise [°C] in the absence of heat conduction, $H_o$ is the radiant exposure [J/cm$^2$], $\mu_a$ is the absorption coefficient [cm$^{-1}$], $\rho$ is the density [g/cm$^3$], and $c$ is the specific heat [J/g/°C]. Subablative ($T_{max}$ < 100°C) radiant exposures were desired, so appropriate values (with one exception) were chosen so that the maximum temperature predicted by Eq. 1 was less than 100°C. Values for $\mu_a$, $\rho$, and $c$ were taken from water data [10, 12].

Blackbody calibration was performed using a resistively-heated aluminum block painted with high-emissivity black paint. Algorithms written in MATLAB were used to process the grayscale thermal images and calculate calibrated radiometric temperatures as a function of time.

**Numerical Modeling.** Simulations were run to calculate temporal histories of the predicted surface temperature and predicted radiometric temperature estimation for the radiant exposures used in the experimental study. Pertinent model parameters are listed in Table 1. Model results were analyzed in the LabVIEW 5.1 programming environment.

**Table 1. Input parameters to computer simulations.**

| | |
|---|---|
| **OPTICAL** | |
| Absorption coefficient, $\mu_a$ | 792 cm$^{-1}$ |
| Pulsewidth | 110 μs |
| **THERMAL** | |
| Initial temperature | 25°C |
| Thermal diffusivity | 1.01x10$^{-3}$ cm$^2$/s |
| Thermal conductivity | 4.28x10$^{-3}$ W/cm/°C |
| **SPATIAL** | |
| Tissue thickness | 1 mm |
| Spatial resolution | 1 μm |

**Assumptions and Limitations of Model.** 1) Although the 1-D geometry was a reasonable approach to model the tissue (since $\delta$ << laser spot size), heat conduction occurred to a minor extent in the radial direction; only axial heat transfer was considered in these simulations. 2) The entire IR signal generated from the tissue volume was assumed to reach the detector. Absorption of the emitted radiation by the environment was not considered. 3) The responsivity of the IR detector was assumed to be uniform across its bandwidth. For photon detectors, the responsivity is not constant as a function of wavelength, and so wavelength-dependent emission would need to be considered during conversion from emissive power to radiometric temperature. 4) $\mu_{IR}$ was assumed to be a constant value. The IR regions typically used for detection are 3-5 μm and 8-12 μm. Assuming that water is the primary absorbing chromophore of the target object for the generated IR signal, $\mu_{IR}$ is approximately the value for water. However, the absorption spectrum of water in these wavelength ranges varies over several orders of magnitude [12]. Also, the absorption coefficient of water has been shown experimentally to have a temperature dependence [13-15]. Thus, determination of the IR signal reaching the detector should include the wavelength- and temperature-dependence of the absorption coefficient; modeling $\mu_{IR}$ as a constant was performed as a first approximation to the solution of the problem.

## 4. RESULTS

A total of 45 irradiations was performed. A representative comparison between experimental results and model predictions is shown in Figure 2. The predicted surface temperature rise for a 0.292 J/cm$^2$ $CO_2$ laser pulse was approximately 43°C. Note the relatively good agreement between the predicted and measured thermal camera temperature estimations.

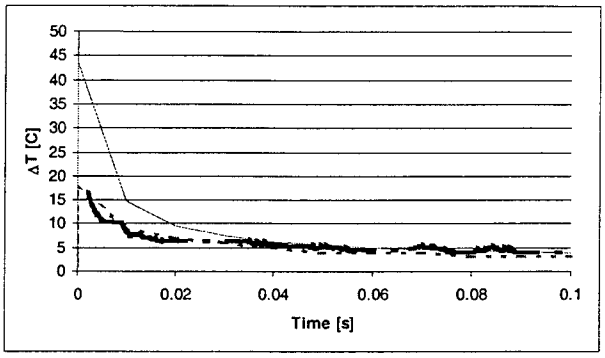


**Figure 2. Temperature-time history of predicted surface temperature (thin solid line), predicted thermal camera temperature estimation (dashed line), and measured radiometric temperature estimation (thick solid line). Radiant exposure = 0.292 J/cm$^2$. Note that the line representing the measured radiometric temperature values is actually a best-fit line to the raw data.**

A summary of the results obtained with different radiant exposures is provided in Table 2. Relatively good agreement between measured and predicted radiometric temperature estimations was obtained for $H_o$ values less than or equal to 0.414 J/cm$^2$. For the three samples at higher radiant exposures, the measured radiometric temperature rises were considerably larger than the corresponding predicted values. For all radiant exposures, the measured and predicted radiometric temperature estimations were comparable in magnitude at points in time well after the end of the laser pulse.

Table 2. Compiled model and average measured temperature rises for various radiant exposures.

| $H_o$ [J/cm$^2$] | Predicted $\Delta T_s$ [C] | Predicted $\Delta T_{rad}$ [C] | Measured $\Delta T_{rad}$ [C] |
|---|---|---|---|
| 0.122 | 18 | 5 | 5 |
| 0.170 | 25 | 8 | 5 |
| 0.191 | 28 | 8 | 5 |
| 0.205 | 31 | 10 | 5 |
| 0.219 | 33 | 11 | 16 |
| 0.292 | 44 | 17 | 20 |
| 0.325 | 48 | 20 | 23 |
| 0.371 | 55 | 23 | 26 |
| 0.414 | 62 | 26 | 29 |
| 0.441 | 66 | 27 | 38 |
| 0.461 | 68 | 29 | 40 |
| 0.574 | 85 | 37 | 49 |

## 5. DISCUSSION

Laser light that is highly absorbed in a medium will induce a steep temperature gradient within the superficial layers. Since IR radiometers receive thermal emission from a finite "viewing depth" within an object, surface temperature estimations will be erroneous if the thermal gradient is significant within this region.

In this study, an instantaneous, sharp decrease in temperature existed superficially immediately after $CO_2$ laser irradiation, resulting in radiometric temperature estimations that were significantly less than the actual surface temperatures. The simple experiment performed in this study demonstrated the gross underestimation of the surface temperature by the thermal camera measurement (Table 2). Heat conduction from the surface to the cooler internal regions of the tissue phantom led to a gradual decrease in the slope of the thermal gradient, resulting in better agreement between the surface and radiometric temperatures.

Good agreement between model and experimental results were obtained for all but the three highest radiant exposures. For those exceptions, the measured radiometric temperature values were considerably greater than the predicted values. The large temperature rises (>66°C) associated with these radiant exposures may have induced changes in tissue ultrastructure, such as collagen denaturation or focal pockets of water vaporization. The latter would result in a decrease in the local absorption coefficient, which may explain the increased radiometric temperature measurements. A decrease in the absorption coefficient would lead to an increased penetration depth of the laser light. Within the approximate "viewing depth" of the IR detector (~100 μm) in soft tissue, the peak temperature would be lower, but the average temperature within this region may actually be greater. If this were to occur, the measured radiometric temperature values would be larger than the values predicted by the numerical model.

## 6. CONCLUSIONS

A simple experiment was performed to test the accuracy of a numerical model. Experimental data fit model results fairly well and demonstrated the potential discrepancy between measured radiometric temperatures and actual surface temperature. For larger radiant exposures, the measured radiometric temperatures deviated considerably from model predictions during initial points in time; this may be due to the onset of nonlinear changes in tissue optical and/or thermal properties.

## 7. ACKNOWLEDGMENTS

The authors thank Tissue Medical Lasers for providing the TruPulse laser system. The research was supported by the Office of Naval Research Medical Free Electron Laser Biomedical Science Program (N0014-91-J1564), the Albert W. and Clemmie A. Caster Foundation, and the Air Force Office of Scientific Research through MURI from DDR&E (F49620-98-1-0480).

## 8. REFERENCES

1. Pearce JA, Welch AJ, Motamedi M, and Agah R. Thermographic measurement of tissue temperature during laser angioplasty. Heat and Mass Transfer in the Microcirculation of Thermally Significant Vessels 1986; pp. 49-54.

2. Pfefer TJ, Choi B, Vargas G, McNally KM, and Welch AJ. Mechanisms of laser-induced thermal coagulation of whole blood *in vitro*. Proceedings SPIE 1999; 3590:20-31.

3. Small W, Celliers PM, Da Silva LB, Matthews DL, and Soltz BA. Two-color infrared thermometer for low-temperature measurement using a hollow glass optical fiber. Proceedings SPIE 1997; 2977:115-120.

4. Torres JH, Ghaffari S, and Welch AJ. Laser probe temperature control by measuring the returning infra-red radiation. Med & Biol Eng & Comput 1990; 28:1-7.

5. Torres JH, Motamedi M, and Welch AJ. Disparate absorption of argon laser radiation by fibrous versus fatty plaque: Implications for laser angioplasty. Lasers Surg Med 1990; 10:149-157.

6. Welch AJ, Bradley AB, Torres JH, Motamedi M, Ghidoni JJ, Pearce JA, Hussein H, and O'Rourke RA. Laser probe ablation of normal and atherosclerotic human aorta in vitro: A first thermographic and histologic analysis. Circulation 1987; 76:1353-1363.

7. Anvari B, Milner TE, Tanenbaum BS, and Nelson JS. A comparative study of human skin thermal response to sapphire contact and cryogen spray cooling. IEEE Trans Biomed Eng 1998; 45:934-941.

8. Prahl SA, Vitkin IA, Bruggemann U, Wilson BC, and Anderson RR. Determination of optical properties of turbid media using pulsed photothermal radiometry. Phys Med Biol 1992; 37:1203-1217.

9. Choi B, Pearce JA, and Welch AJ. Modeling infrared temperature measurements: Implications for laser irradiation and cryogen cooling studies. Phys Med Biol 2000 (in press).

10. Incropera FP and DeWitt DP. Fundamentals of Heat and Mass Transfer. New York: John Wiley & Sons. 1996.

11. Valvano JW and Pearce J. Temperature measurements. In: Welch AJ, van Gemert MJC, eds. "Optical-Thermal Response of Laser-Irradiated Tissue". New York: Plenum Press, 1995.

12. Hale GM and Querry MR. Optical constants of water in the 200-nm to 200-μm region. Appl Opt 1973; 12:555-563.

13. Jansen ED, van Leeuwen TG, Motamedi M, Borst C, and Welch AJ. Temperature dependence of the absorption coefficient of water for midinfrared laser radiation. Lasers Surg Med 1994; 14:258-268.

14. Marechal Y. Infrared spectra of water. I. Effect of temperature and of H/D isotopic dilution. J Chem Phys 1991; 95:5565-5573.

15. Walsh JT and Cummings JP. Effect of the dynamic optical properties of water on midinfrared laser ablation. Lasers Surg Med 1994; 15:295-305.

# Determination of the temperature distribution in skin using a finite element model

Thim Nørgaard Andersen* [a], Niels Christian Jessen[b], Lars Arendt-Nielsen[a]
[a]Center for Sensory Motor Interaction, Aalborg University, Frederik Bajers Vej 7/D3, DK-9220 Aalborg, Denmark
[b]Optics and Fluid Dynamic Department, Risø National Laboratory, Frederiksborgvej 399, P.O. Box 49, DK-4000 Roskilde, Denmark

## ABSTRACT

When applying noxious heat stimuli to human skin in the study of the pain system, one of the main problems is not to cause permanent damage. A better understanding of the temperature distribution and the propagation of heat, i.e. heat flux, in human skin is thus needed. In order to investigate these problems thoroughly, we have developed a 3-dimensional finite element model (FEM) 4-layer of human skin. The model is kept simple for better understanding of the boundary problems. The water content in each layer is used for determining the thermal properties. It is therefore not a homogenous structure. In this model the stratum corneum has been included with lower water content than in the epidermis. Simulations shows that the surface temperature reaches high levels whereas the temperature in the deeper structure is much lower. Thermal and optical constants found in the literature was applied. Heat propagation downwards and outwards from the source has been investigated to understand of the accumulation of energy in the boundary between two layers. Prediction of the heat flux at boundary between the epidermis and dermis shows that for repetitive stimulation there is a risk of exceeding the threshold temperature of 65°C for irreversible damage.

**Keywords:** Temperature distribution, heat, FEM

## 1. INTRODUCTION

Within the research of the human pain system it is important that the use of lasers for studies of the thermal pain sensory system can be conducted without causing irreversible damage to the skin of the subject. The skin absorbs at different depths at different wavelengths[1] therefore the use of broadband radiance sources is not optimal for the studies of the thermal pain sensation. The laser and other radiant heat sources have the advantage compared to conductive heating sources that the temperature increase of the source is immediate. Typical rise time for conductive sources, e.g. a thermofoil, is 30-50°C/s [2] which is slower that the response time of the pain receptors[3]. Hardy *et al.*[4] were the first to use radiant sources for inducing thermal pain and study the pain system. They used a broadband infrared radiant source. In 1975 Mor and Carmon[5] were the first to introduce a $CO_2$ laser as an infrared radiant heat source, followed only one year later by Meyer *et al*[6].

Pain receptors are found by Stoll and Greene[7] to be evoked at 52°C. It is not possible to measure the temperature of the skin non-invasively. Evaluating this threshold temperature can therefore not be conducted presently. One way of assessing the temperature in the skin is to construct a model of the skin. This has been done to predict the level of burn injury in several studies, starting with the work by Henriques and Moritz in 1947[8]. Later others have developed models that also predict the propagation of heat in skin[9,10,11,12]. Some are based on Pennes' bioheat equation[13] for heat conduction others are finite element models. These models are based on the assumption that the skin is homogenous with respect to the thermal parameter values and they have given an understanding of the occurrence of irreversible damage to, e.g. burn injury. In order to understand the heat propagation in skin which is not assumed to be homogeneous we have examined a finite element model which is a 4 layer model of the skin. The model is considered to be circular symmetric which is done in order to ease the computational task.

In this paper a finite element model is presented and the temperature and heat flux is examined for a single pulse to estimate the complex heat propagation when the layers have different thermal properties. The thermal properties are based on the

* Correspondence: Email: thim.andersen@risoe.dk; WWW: http://www.smi.auc.dk/~tna; Telephone: +45 4677 4519; Fax: +45 4677 4565



In *Laser-Tissue Interaction XI: Photochemical, Photothermal, and Photomechanical*, Donald D. Duncan, Jeffrey O. Hollinger, Steven L. Jacques, Editors, Proceedings of SPIE Vol. 3914 (2000)
1605-7422/00/$15.00

water, fat and protein content of the layer, and the inclusion of a top layer (the stratum corneum) with a water mass fraction much lower then that of the rest of the epidermis, shows a high surface temperature compared to the deeper structures of the skin, even though the stratum corneum is 1/4 the thickness of the epidermis. Water is assumed to determine the thermal parameters, mass density, specific heat and thermal conductivity. The model is also used to look at repetitive heat stimulation to examine the accumulation of heat in the boundary between the epidermis and dermis. The pain receptors are believed to be located at the boundary and the accumulation can cause the temperature to exceeds the limit of permanent/irreversible damage in the dermis. Whereas the epidermis is capable of sustaining temperatures above damage threshold and repair itself.

The water mass fraction in the epidermis and dermis is almost equal, but the water is tight more closely to the cells in the dermis than in the epidermis. This is the assumption we are using to differentiate between the thermal properties in the epidermis and the dermis.

## 2. METHODS AND MATERIAL

The skin has a complex structure as seen in figure 1, with a complicated vascular morphology and an irregular, almost wavelike structure, boundary between the epidermis and dermis. In order to understand some of the fundamental processes that takes place during heat propagation the proposed model was chosen to be as simple as possible. The model is an idealised representation of the physical structure of the human skin.

The vessels in the skin are of importance for the thermal regulation and as nutritive flow to the cells in the epidermis and dermis. Since the vessels in the upper half of the dermis are so small that the blood in them are at thermal equilibrium with the surrounding tissue[14], it was assumed that the vessels are a part of dermis and have the same physical and thermal properties as dermis.

Another assumption that was made is that the boundary between each of the different component layer is smooth. Incorporating an irregular structure between the layers would give a higher degree of complexity to the system and thus complicate the interpretation of the fundamental physics involved in the heat propagation further.

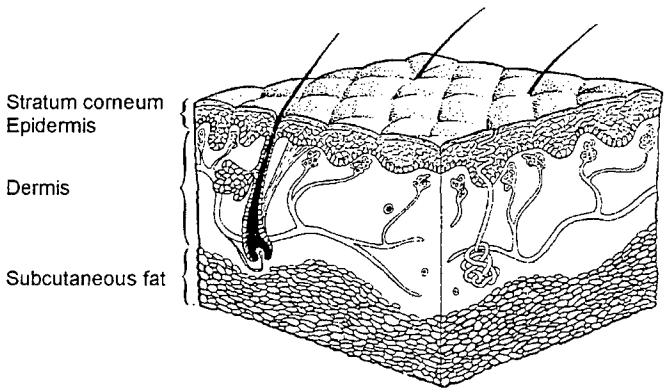


Figure 1. Illustration showing the skin[11]. The stratum corneum is the upper layer of the epidermis. Only part of the subcutaneous fat is present.

### 2.1 Finite element model

The model of the human skin was build as a 3 dimensional Finite Element Model (FEM). The software used was MSC/NASTRAN™ from MSC.Software Corporation, running on a PC with a 400 MHz Intel Pentium II processor.

In order to ease the computational task of the calculation the model was constructed as a circular symmetric slice as seen in figure 2. The model consists of a thin top layers, stratum corneum, a slightly thicker epidermis, followed by dermis and subcutaneous fat. Dimension of the model is listed in table 1.

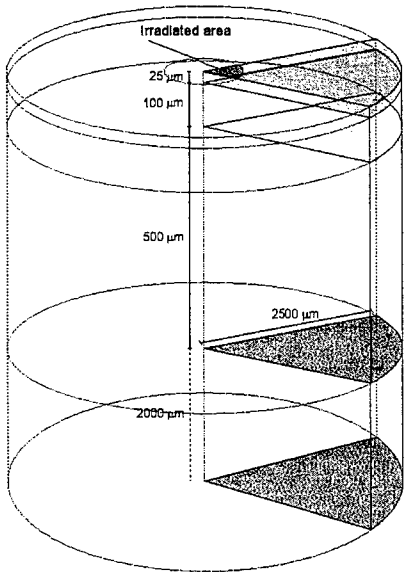


Figure 2. Schematic drawing of circular symmetric model of the skin. The irradiated point is 1 mm in diameter, and the total diameter is 5 mm. The scale on the axes is not proportional.

| Component | Size |
|---|---|
| Stratum corneum | 25 µm |
| Epidermis | 100 µm |
| Dermis | 500 µm |
| Subcutaneous fat | 2000 µm |
| Stimulation source | 1000 µm |
| Model | 5000 µm |

Table 1. Physical properties of the component layers in the model. The values for the stimulation source and model size is the diameter.

A copy of the model can be seen in figure 3. The angle of the slice is 5°. The grid divides the model into elements. In each corner there is a node which is used for calculating the heat propagation. The MSC/NASTRAN has the option of using either 8 nodes per element or 20 nodes per element. The precision of the calculations were not increased significantly using 20 nodes per element. Calculation time was increased with more than a factor of 20.

In table 2 the numbers of elements layer for each is listed.

In total the model consists of 14124 elements and 17470 nodes.

| Component | Number of element layers |
|---|---|
| Stratum corneum | 2 |
| Epidermis | 4 |
| Dermis | 11 |
| Subcutaneous tissue | 20 |

Table 2. Number of element layers for the components.

The temperature of the subcutaneous layer was set to 37°C and the surface temperature was set to 33°C. Evaporation of water on the surface originating from the deeper structure of the body will create a thin (1-3 µm) layer of water moisture on the surface. This moisture layer was excluded from the model, again to keep the model simple.

Free convection from the surface was included. Free convection is described as

where $h$ is the heat transfer coefficient, $A$ is the area of

$$q = h \times A \times (T - T_{amb})^{m}(T - T_{amb}) \qquad (1)$$

the element, $T$ is the temperature of the deep structure and $T_{amb}$ is the temperature of the air. The surrounding air temperature is set to 20°C. $m$ is a factor which is dependent on the geometry of the structure. In the case of a horizontal plate facing upward, $m$ = 1/3 [15,16]. Forced convection was not used.

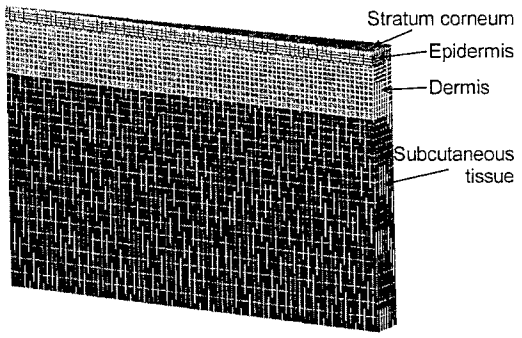


Figure 3. Model of skin. The gridlines indicate the division of the slice into elements and at each corner there is a node used in calculating the heat propagation and temperature distribution.

### 2.2 Thermal properties

In order for MSC/NASTRAN to run the simulations correctly the thermal properties of each component is needed. These properties are the density, the specific heat and the thermal conductivity of the material.

It is assumed that the heat source is a $CO_2$ laser radiating at 10.6 μm. This is a part of the spectrum where water is highly absorbing[17] with an absorption coefficient of 0.0784 $\mu m^{-1}$. The mass fraction of water is determining the thermal properties of the component. Cooper and Trezek[18] found an empirical relationship between density, specific heat and thermal conductivity and mass fractions of water, protein and fat. The density of tissue can be estimated as

$$\rho\left(g/cm^3\right) = \frac{1}{\sum_n \frac{m_n}{\rho_n}} = \frac{1}{m_{water} + 0.649\, m_{protein} + 1.227\, m_{fat}} \qquad (2)$$

The specific heat can be estimated as

$$c(J/g\cdot^\circ C) = \sum_n c_n\, m_n = 4.2\, m_{water} + 1.09\, m_{protein} + 2.3\, m_{fat} \qquad (3)$$

And finally the thermal conductivity can be estimated as

$$k\,(mW/cm\cdot^\circ C) = \rho \sum_n \frac{k_n m_n}{\rho_n} = \rho\left(6.28\, m_{water} + 1.17\, m_{protein} + 2.31 m_{fat}\right) \qquad (4)$$

The mass fraction of protein and fat it is chosen to be in equal proportional. This assumption is based on Cooper and Trezek[3]. It could be argued that in the stratum corneum the lipid cells mostly consists of keratin, which it nearly all protein. Changing the relation between protein and fat in stratum corneum would increase the complexity of the model and further complicate the understanding of the physical processes in the heat propagation.

The mass fraction of water was taken from Rothman[19] and the approximate values are listed in table 2. The water mass of dermis depends on where it is taken. The dermis is divided into 3 layers, but on average the water content was 61%. According to investigations using NMR scanning by Richard[20] the water in the dermis is tied stronger to the cells than in epidermis. When the water is tied closer to the cells the density of the material increase which can seen as a decrease in water mass fraction. From figure 4 it is seen that an increase in density relates to a decrease in water content. Therefore the water mass fraction for dermis is set lower than for epidermis.

| Component | Water mass fraction |
|---|---|
| Stratum corneum | 10-15% |
| Epidermis | 60-80% |
| Dermis | 60-80% |
| Subcutaneous tissue | 60-80% |

Table 3. Water mass fraction in skin

Using equation (2) - (4) with the mass fraction of water and calculating the thermal constants it is seen that the differentiation of the mass fraction have a high impact on the thermal properties. See figure 4.

A reduction of the mass fraction of water by a factor of 2 will increase the specific heat and the thermal conductivity by a factor of 2. Because of this relation it was decided to include the stratum corneum as a separate component in the model.

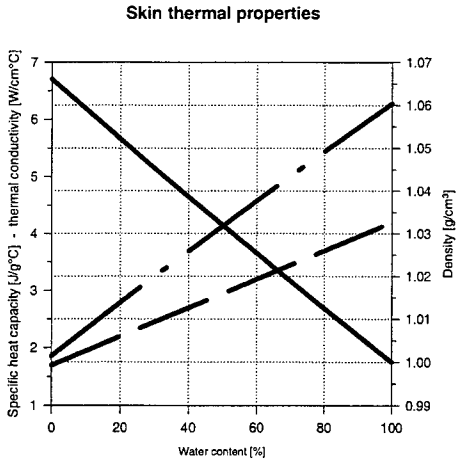


Figure 4. Thermal properties. Density, specific heat and thermal conductivity as a function of water mass fraction. Solid line (—) is density. Dotted line (- -) is specific heat. Dash-dotted line (-·-) is thermal conductivity. Mass fraction of protein and fat are in equal proportion.

### 2.3 Simulation

The heating of the skin is done as a radiant heat source on the surface of the stratum corneum. Two types of simulation was investigated: single stimulation type as used in pain research and repetitive stimulation as used in clinical treatment sessions were chosen. The power was set to 10 W, which gives a power density of 127324 W/m$^2$, on a circle of 1 mm in diameter. For the single stimulation the pulse duration, $\tau$, is 200 ms and the course of the temperature and heat flux was followed for 5 seconds. The water content was varied from being homogeneous (all component have the same mass fraction of water) to large deviation as listed in table 3.

A "standard skin" was introduced. The water mass fraction in the layers was chosen to be the following: stratum corneum: 15%, epidermis: 80%, dermis: 60% and subcutaneous tissue: 80%

For the repetitive stimulation study the standard skin and a variant where the water content in dermis was 2 orders of magnitude less than in epidermis. For these simulations the power density was 127324 W/m$^2$ and the pulse duration was 150 ms with an inter-pulse interval of 500 ms.

The peak temperature for some of the nodes were fitted using regression.

Table 4. Water mass fraction in the simulations run for single stimulation [%].

| Stratum corneum | Epidermis | Dermis | Subcutaneous tissue |
|---|---|---|---|
| 10 | 10 | 10 | 10 |
| 70 | 70 | 70 | 70 |
| 15 | 80 | 60 | 80 |
| 10 | 80 | 60 | 80 |
| 15 | 60 | 80 | 60 |
| 10 | 60 | 80 | 60 |
| 10 | 80 | 30 | 80 |

### 2.4 Laser scanning

The simulations were compared with stimulation using a set-up consisting of a 100 W $CO_2$ laser (Synrad ) and a scanning head (GSI Lumonics Inc.) controlled by a PC. The scanning pattern was a spiral with variable diameter of 2, 3, 5cm. Thermographic pictures was acquired using a infrared camera (Raytheon Amber Radiance). The distance to the target was 25 cm, which gave a spot size of 2.65 mm.

## 3. RESULTS

### 3.1 Single stimulation

The first simulation was done on a homogeneous material with a water mass fraction of 70% and of 10% in the four components (figure 1a and 1b). In figure 1 the temperature versus time is seen for the nodes at the center axis of the stimulation area. Figure 1a is with water mass fraction at 70%, and figure 1b is with water mass fraction at 10%. In table 1 the peak temperatures of the center nodes and the nodes at the midpoint of the stimulation (half the radius of stimulation) are listed.

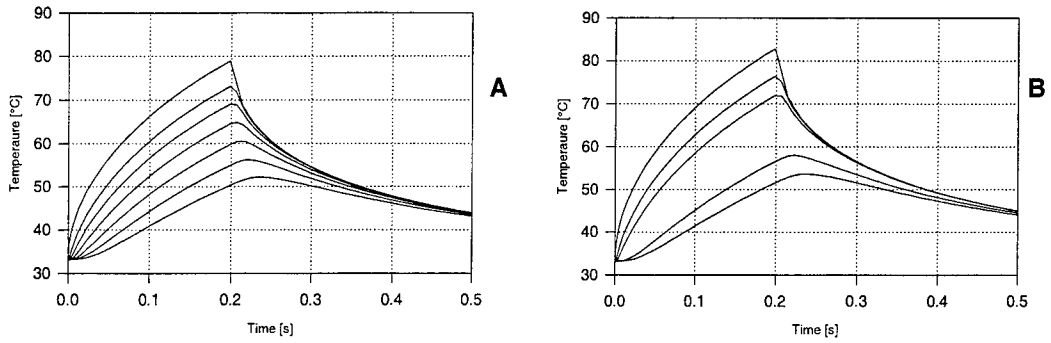


Figure 5. Homogeneous skin. The water mass fraction is 70% for all the components in **A** and 10% in **B**. The lines represents the temperature for the nodes at the centre axis of the stimulation point. Top line is the nodes at the surface, button line is the node at the top level of the dermis. The values for two nodes in epidermis are not included in **B**.

| Node position | 70% water Temperature [°C] | 10% water Temperature [°C] |
|---|---|---|
| Surface (SC) | 78.92 | 82.77 |
| SC | 73.12 | 76.43 |
| Epidermis | 69.06 | 71.98 |
| Epidermis | 64.95 | |
| Epidermis | 60.54 | |
| Epidermis | 56.24 | 58.02 |
| Dermis | 52.22 | 53.65 |

Table 5. Peak temperature for homogeneous model. SC = Stratum corneum.

As explained in section 2.3 a "standard skin" was defined. This definition is not an absolute since there are variations. The water content is 15% in stratum corneum, 80% in epidermis, 60% in dermis and 80% in subcutaneous tissue. The center and mid-stimulation nodes are seen in figure 2a and 2b.

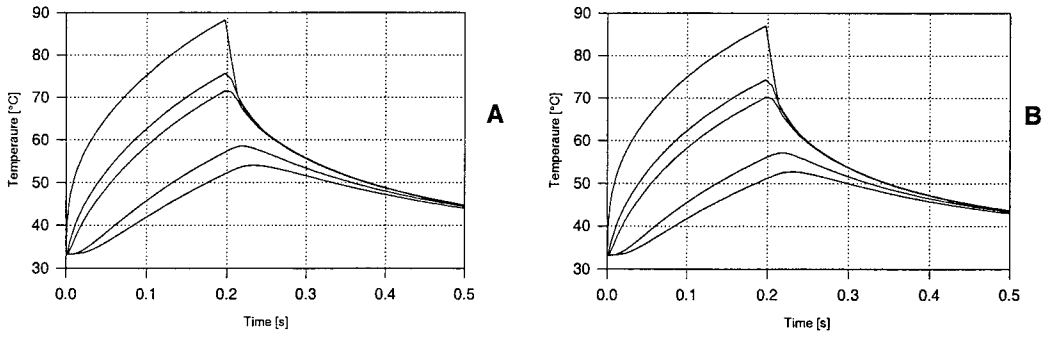


Figure 6. "Standard skin". Water mass fraction is 15% in SC, 80% in epidermis, 60% in dermis and 80% in subcutaneous tissue. **A** is the centre axis, **B** is at mid-stimulation.

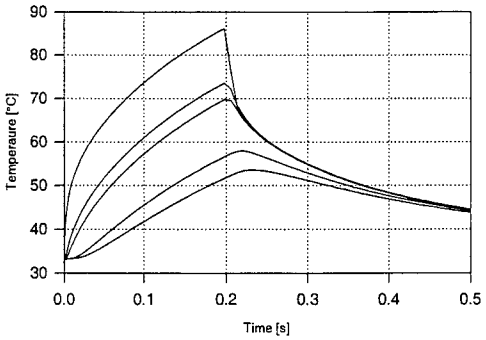


Figure 7. Temperature course for 10% water mass fraction in stratum corneum. Peak temperature are listed in table 2.

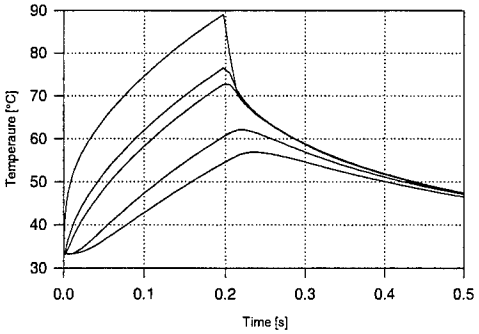


Figure 8. Temperature at centre axis for water mass fraction in dermis lowered to 30%.

The influence of small variations of the water content in stratum corneum is of interest. In figure 7 the temperature development is seen with water mass fraction at 10% in stratum corneum. The water content in the epidermis, dermis and subcutaneous musclefat is 80%, 60% and 80% respectively.

The water content in the dermis is different depending on the depth. Part of is has a water content of 30% (Rothman). A simulation with a water mass fraction of 80% in muscle/fat tissue , 30% in dermis, 80% in epidermis and 10% in stratum corneum is seen in figure 8, with peak temperatures listed in table 6.

| Node position | Standard skin Temperature [°C] | Low water fraction in SC Temperature [°C] | Low water fraction in dermis Temperature [°C] |
|---|---|---|---|
| Surface (SC) | 88.31 | 86.19 | 89.09 |
| SC | 75.70 | 73.59 | 76.53 |
| Epidermis | 71.53 | 69.75 | 72.75 |
| Epidermis | 58.52 | 57.96 | 62.16 |
| Dermis | 54.06 | 53.60 | 56.86 |

Table 6. Peak temperature for nodes at centre axis.

### 3.2 Repetitive stimulation

In figure 5 the temperature development of 10 stimulations on "standard skin" is seen. Figure 5a shows the temperature at the mid axis nodes, and figure 5b shows the temperature at mid stimulation nodes. Peak temperature fit for the centre axis for the layers are shown in figure 5c. The peak temperature of each layer are marked and fitted using regression. The best fit for all repetitive stimulation peak temperature was a Wiebull model:

$$f(x) = a - b\, e^{-c\, x^{d}} \qquad (5)$$

The asymptotic value, $a$, for each of the layers and the time needed to reach the asymptotic temperature is listed in table 7a.

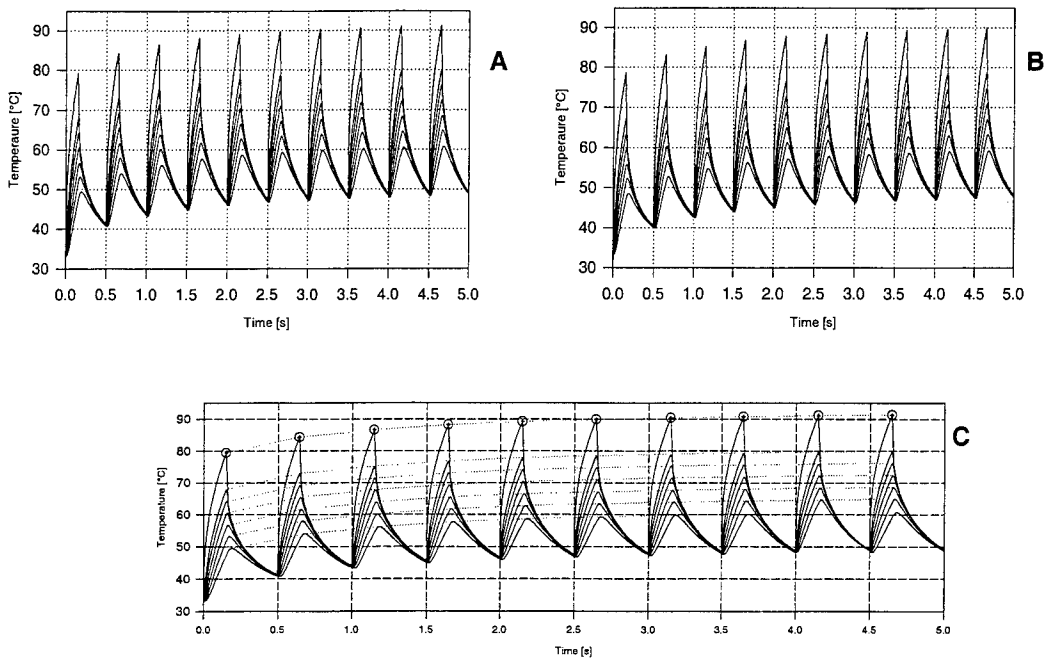


Figure 9. Repetitive stimulation with "standard skin". Water mass fraction is 15%, 80%, 60% and 80% respectively in the 4 layers. **A** shows the temperature for nodes at the centre axis, **B** shows the temperature at mid-stimulation nodes. In **C** the peak temperature is fitted. The best representation is a Weibull model. The circles at the peak temperatures indicate the points used for the regression.

Next the water mass fraction of the dermis was lowered to 40% and set to 10% in the stratum corneum. For the epidermis and muscle/fat tissue the water mass fraction was kept at 80%. The course of the temperature versus time is seen in figure 6 with center axis node temperature in figure 6a and mid stimulation node temperature in figure 6b. Table 3b lists the asymptotic values of the $a$ parameter. The time for reaching 99% of this value is

$$\tau = \sqrt[d]{\frac{1}{c}\ln\left(100\frac{b}{a}\right)} \qquad (6)$$

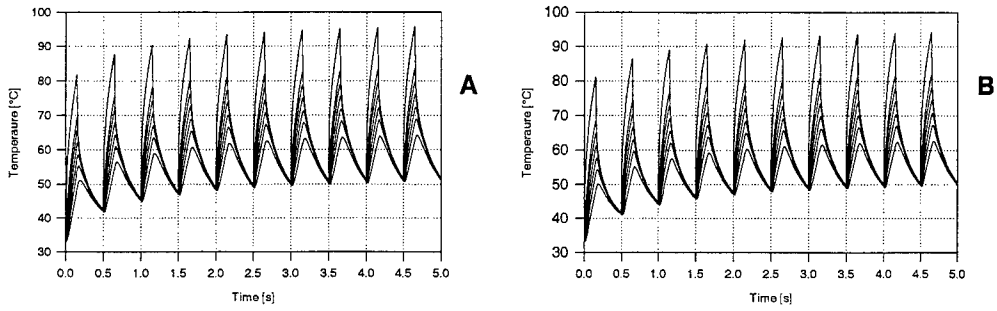


Figure 10. Repetitive stimulation with 10% water mass fraction in stratum corneum and 40% in dermis. **A** represents the nodes at the centre axis, **B** shows the nodes at mid-stimulation.

| Node postition | Centre axis nodes | | Mid-stimulation nodes | |
|---|---|---|---|---|
| | Asymptotic value, $a$ | Time, $\tau$, for 0.99$a$ | Asymptotic value, $a$ | Time, $\tau$, for 0.99$a$ |
| Surface (SC) | 92.32 | 4.86 | 90.85 | 4.84 |
| SC | 81.00 | 5.24 | 79.52 | 5.22 |
| Epidermis | 77.29 | 5.55 | 75.76 | 5.37 |
| Epidermis | 73.58 | 5.62 | 72.06 | 5.61 |
| Epidermis | 69.71 | 5.88 | 68.16 | 5.88 |
| Epidermis/Dermis | 66.03 | 6.18 | 64.48 | 6.19 |
| Dermis | 61.89 | 6.37 | 60.54 | 6.83 |

Table 7a. Repetitive stimulation on "standard skin". $a$ is in °C, $\tau$ is in seconds.

| Node postition | Centre axis nodes | | Mid-stimulation nodes | |
|---|---|---|---|---|
| | Asymptotic value, $a$ | Time, $\tau$, for 0.99$a$ | Asymptotic value, $a$ | Time, $\tau$, for 0.99$a$ |
| Surface (SC) | 96.83 | 4.86 | 95.19 | 4.84 |
| SC | 84.42 | 5.24 | 82.75 | 5.22 |
| Epidermis | 80.65 | 5.55 | 79.07 | 5.37 |
| Epidermis | 77.18 | 5.62 | 75.46 | 5.61 |
| Epidermis | 73.53 | 5.88 | 71.77 | 5.88 |
| Epidermis/Dermis | 70.10 | 6.18 | 68.35 | 6.19 |
| Dermis | 65.40 | 6.37 | 63.80 | 6.83 |

Table 7b. Repetitive stimulation with 40% water mass in dermis. $a$ is in °C, $\tau$ is in seconds.

## 4. DISCUSSION

### 4.1 Single stimulation

The homogeneous model with a water mass fraction of 70% has been the used in the finite element models by Diller *et al*[11] and by Choi *et al*[21] in the theoretical part of the evaluation of skin resurfacing. Others[22,23,24,25] have concentrated on predicting damage to the skin mainly using Pennes' bioheat transfer equation[13] and in these the thermal properties have been varied but stratum corneum has been seen as a part of the epidermis thus having the same thermal properties as the epidermis. In figure 5 the temperature development is shown with a equal water mass fraction in all layers of the skin. The temperature has an even decay with linear decrease down through the skin. With 10% water mass fraction in the layers the course of the temperature is a little different as seen in figure 5b. The difference occurs in the temperature that is reached which is higher when the water content is low. The lower water mass fraction causes the thermal conductivity and the specific heat to decrease, as seen in figure 4 therefore the heat propagates slower and the energy needed for heating the material is lower.

When the "standard skin" was used the temperature showed a somewhat different course of development as can be seen in figure 6 and table 2. The maximum surface temperature increased from 78.92°C to 88.31°C. Due to the increased thermal conductivity and high specific heat more energy is needed for heating the epidermis which causes the relatively low temperature in the deeper layer. The lower maximum temperature at the mid-stimulation axis, seen in figure 6b, is most likely caused by the possibility for the heat to propagate in the longitudinal direction of the skin. The area outside the stimulated area function as a heat sink, where the heat from the stimulated area can be deposited, but due to the higher thermal conductivity in epidermis the heat propagate deeper into the skin rather than in the longitudinal direction. This can be seen by the sharp slope of the temperature course at the surface node in both figure 6a and 6b.

An interesting effect is that if the assumption about a pain threshold of 52°C for the pain receptors is correct as found by Stroll *et al* and it is assumed that these receptors are located in and around the boundary between the epidermis and dermis, then the pain receptors will surely start firing using the "standard skin" as a predictive tool whereas it is not for certain that this will happen when using the 70% water content model.

Reducing the water content in the stratum corneum from 15% to 10% will give a further reduction in thermal conductivity and specific heat. As seen in table 2 the result is that the surface temperature is reduced by 2°C, but the effect is not instrumental for the epidermis-dermis boundary. The reason is that the relative reduction in specific heat is lower than the

relative reduction in thermal conductivity. This causes the heat to propagate slower in the stratum corneum, but the energy needed for heating the tissue is still high. Therefore the heat is not absorbed in the stratum corneum.

When the water mass fraction of the dermis is reduced by a factor of 2 to 30% the consequences are a little more drastic. The peak surface temperature is increased by 3°C and the temperature of the epidermis-dermis boundary is raised 3 to 4 degrees. This change can be explained by looking at figure 4. The thermal conductivity is decreased by 30% and specific heat is reduced by 23% in dermis forcing less heat propagating from the epidermis into dermis. Thereby accumulating energy in epidermis affecting the surface temperature up when the stratum layer is as thin as it is.

In figure 11 a thermographic picture has been acquired immediately after a scan with a $CO_2$ laser has been completed on the dorsal side of the left underarm. The power of the laser is 5 W and the scanning speed is 1000 mm/s. The heated area is 7.07 $cm^2$. The maximum temperature is 84°C. The temperature of the surroundings is 23°C.

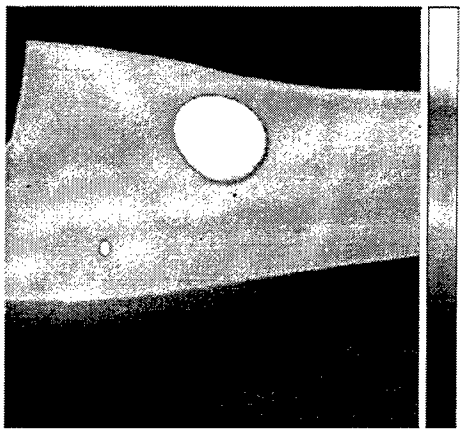

Figure 11. Thermographic picture of the dorsal side of the left underarm. Maximum temperature is approximately 84°C. The stimulation was done with a $CO_2$ laser . Ther power was 3 W and the scanning speed was 1000 mm/s.

The energy density in the stimulation using the $CO_2$ laser is 4.8 J/$cm^2$ and 6.37 J/$cm^2$ for the model. The stimulation with the $CO_2$ laser did not cause any damage to the skin. The subject reported slight pain sensation, but the sensation was dominated by a warmth sensation. The reaction of the skin after the stimulation was a light reddening which is a typical response after irritation of the skin. Whether from thermal or mechanical stimulation. The reddening started after 15 minutes to 1 hour and was present for a 2-3 hours. The skin was sensitive to tactile stimulation at the stimulated area for 1-2 hours after the stimulation.

Evaluating the damage the temperature reached in the model will cause, the cells in dermis and epidermis will be destroyed by temperatures above 45°C[26] so the tissue should at this point be destroyed, but the skin has an ability to withstand heat and excessive temperatures in a short amount of time[8]. It is therefore not unlikely that the temperature seen in the model with "standard skin" is close to what an experiment would show. From Michael Spicer *et al*[27] and Wolbarsht[28] the thermal relaxation time for skin is 700 μs which is so short compared to the stimulation time of 200 ms that the skin does not have the possibility of reaching its original temperature with the 200 ms stimulation time. The stimulation time with $CO_2$ laser is 5.3 ms at a single point during the scan.

We have defined the threshold temperature for permanent damage to be 65°C. This is based on the listing by Arndt *et al*[26] where proteins will surely will be unstable and have unfolded. This starts at 50°C. Membranes become permeable at 50°C, but since pain receptors are not evoked before the temperature reaches 52°C we set the limit for damage at 65°C.

It is not possible to compare the parameters used in this model with the stimulation, but it is possible to get an estimate of the temperature in the area which is the aim of this study. The model does leave the option of chancing the parameters regarding the stimulation in order for the experiments to be compared with the model. One other thing that can be seen is that in order to get an estimate of the temperature course in the skin it is necessary to include the stratum corneum as a separate layer since the low mass fraction of water has an influence on the temperature of the surface.

### 4.2 Repetitive stimulation

In many clinical application of the $CO_2$ laser more than one pulse is used, either for skin resurfacing purposes or for treatment of skin diseases. This can give rise to accumulation of heat the layers thus causing permanent damage. With a pulse duration of 150 ms and a pulse frequency of 2 Hz as seen in figure 9 and table 3a the peak temperature of the nodes are fitted and the best fit was a Wiebull model as described in the previous section. Looking a the epidermis/dermis boundary the asymptotic temperature value is 66°C. Using (5) the threshold temperature is exceeded and irreversible damage will be induce induced after 5.2 seconds, or 11 pulses. For the mid-stimulation the damage is just below the threshold.

With a water content of 40% in dermis and 10% in stratum corneum the temperature level is increased so much that damage will occur at an earlier point in time. Again using (5) to find the time at which the temperature exceeds 65°C gives $\tau_{65°C}$ =

1.52 second or at the fourth stimulation. Looking at the mid-stimulation axis gives a time of $\tau_{65°C}$ = 2.23 second for the epidermis/dermis boundary to reach 65°C. This time difference corresponds to one additional stimulation. It can be concluded that one should be aware of the water content in the different layers of the skin before applying laser stimulation to the skin. From (6) the time, $\tau$, for getting infinitely close to the asymptotic temperature is found and listed in table 7.

### 4.3 Model overview

The model constructed here is an idealised representation of the skin, but it shows that by introducing the stratum corneum with thermal properties different from the underlying tissue it is possible to reach high temperatures on the surface and still have relatively low temperatures in the epidermis and dermis. The depth of the different layers, e.g. dermis may be too thin, but the in this model the aim was to look at the area of the boundary between the epidermis and dermis in order to get a better understanding of what levels the temperature will reach. The believe is that the pain receptors are located in this region and that the temperature needed for evoking these receptors is 52°C. Using this model is will possible to estimate the temperature and the possibility of damage before starting a experiment. It is difficult are to obtain absolute values for thermal conductivity and specific heat of the layers. One way to obtain useable estimates could be to use ultrasound scanning or nuclear magnetic resonance for determining the water mass fraction, and the fat and protein content[29,17], and apply the empirical equations (2) - (4) for determining the thermal properties. The repetitive stimulation simulations shows that the level of damage to the deeper structures of the skin can occur after few stimulation on the same spot. Using the model will give an estimate of the maximum number of stimulation a patient could sustain before a damage would occur.

This model is simple and more work is needed before the estimates can be used in clinical settings, but it is shown that it is important to include the stratum corneum in models of the heat propagation. The thermal properties are based on the water content in the layers because water has a high absorption coefficient at 10.6 μm, or at 2.9μm (HF laser) which has a penetration depth of less that 1 μm[30]. The penetration depth of 10.6 μm is approximately 13 μm and a future model will have the heat source located at this depth instead of at the surface.

## CONCLUSION

In summery a finite element model of skin was constructed. It is a simple model consisting of 4 layers: stratum corneum, epidermis, dermis and subcutaneous muscle/fat tissue. The thermal properties of each layer is governed by the water mass fraction using a set of empirical equations established by Cooper and Trezek. The protein and fat are in equal proportion. The simulation of the temperature shows that it is of importance to include the stratum corneum since the surface temperature can reach temperatures which normally would induce damage to the skin. In a model with equal water mass fraction the temperatures do not reach these temperatures as seen in experiments and in clinical settings. The model can be used for evaluating the temperature in the epidermis/dermis boundary area for determination of the whether or not the pain receptors are evoked or not.

Repetitive stimulation was simulated and these simulations show that there is accumulation of heat in the deeper layers of the skin which can cause permanent damage.

Further investigation is needed for fine tuning of the model; also more experimental work is needed for evaluating the model and the thermal parameter values.

## ACKNOWLEDGEMENTS

The authors would like to thank Peter E. Anderson and Steen G. Hanson for their insightful discussions, comments and suggestions. Thanks are also due to Monica Gniadecka for comments and suggestions. This project was surported by the Danish National Research Foundation.

## REFERENCES

1 A.J. Welch, M.J.C. van Gemert (Eds.), *Optical-thermal Response of Laser Irradiated Tissue*, Plenum Press, NewYork, 1995.

2 L. Arendt-Nielsen, J.Nielsen, s. Petersen-Felix, T.W. Schnider, A.M. Zbinden, "Effect of racemic mixture and the (S+)-isomer of ketamine on temporal and spatial summation of pain", *Brit J Anaesthesia*, **77**, pp. 625-631, 1996.

3 P.D. Wall, R. Melzack (Eds.), *Textbook of Pain 3rd ed.*, Edinburgh, Churchill Livingstone, 1994.
4 J.D. Hardy, T.W. Oppel, "Studies in temperature sensation. III The sensitivity of the boy to heat and the spatial summation of the end organ responses", *J Clin Invest*, **16**, pp. 533-540, 1937.
5 J. Mor, A. Carmon, "Laser emitted radiant heat for pain research", *Pain*, **1**, pp. 233-237, 1975.
6 R.A. Meyer, R.E. Walker, V.B. Mountcastle, "A laser stimulator for the study of cutaneous thermal and pain sensations", *IEEE Trans Biomed. Eng.*, **23**, pp.54-60, 1976.
7 A.M. Stoll, L.C. Greene, "Relationship between pain and tissue damage due to thermal radiation", *J. Appl. Physiol.*, **14**, pp. 373-382, 1959.
8 F.C. Henriques, A.R. Moritz, "Studies of thermal injury, 1. The conduction of heat to and through skin and the temperatures attained therein. A theoretical and an experimental investigation", *Am J. Pathol.*, **23**, pp. 531-549, 1947.
9 S. Weinbaum, L.M. Jiji, D.E. Lemons, "Theory and Experiment for the Effect of Vascular Microstructure on Surface Tissue Heat Transfer - Part I: Anatomical Foundation and Model Conceptualization", *J. Biomech Eng.*, **106**, pp. 321-330, 1984.
10 A.J. Welch, "The Thermal Response of Laser Irradiated Tissue", *IEEE J. Quan Elec*, **QE-20**, pp. 1471-1481, 1984.
11 K.R. Diller, L.J. Hayes, "Analysis of tissue injury by burning: comparison of *in situ* and skin flap models", *J. Heat Mass Transfer*, **34** pp. 1393-1406, 1991.
12 T.N. Glenn, S. Rastegar, S.L. Jacques, "Finite Element Analysis of Temperature Controlled Coagulation in Laser Irradiated Tissue", *IEEE Trans. Biomed. Eng.*, **43**, pp 79-87, 1996.
13 H.H. Pennes, "Analysis of Tissue and Artierial Blood Temperatures in the Resting Human Forearm", *J. Appl Physiol*, **1**, pp. 93-122, 1948.
14 J.C. Chato, "Heat transfer to blood vessels", *Trans ASME, J. Biomech. Eng.* **102**, pp. 110-118, 1980.
15 J.P. Holman, *Heat Transfer, Seventh Edition*, McGraw-Hill, New York, 1990.
16 E.-U. Schlünder (ed), V. Gnielinski (ed), *VDI-Wärmeatlas, Berechnungsblätter für den Wärmeübergang*, VDI-Verlag GmbH, Düsseldorf 1991.
17 G.M. Hale, M. R. Querry, "Optical Constants of Water in the 200-nm to 200-μm Wavelength Region", *Appl Optics*, **12**, pp. 555-563, 1973.
18 T.E. Cooper, G.J. Trezek, "Correlation of thermal properties of some human tissue with water content", *Aerosp. Med.*, **42**, pp. 24-27, 1971.
19 S. Rothman, *Physiology and Biochemistry of the Skin*, The University of Chicago Press, Chicago, 1954.
20 S. Richard, "In vivo proton relaxation times analysis of the skin layers by magnetic resonance imaging", *Brit J. Dermatol*, **97**, pp. 120-125, 1991.
21 B. Choi, E.K. Chan, J.K. Barton, S.L. Thomsen, A.J. Welch, "Thermographic and Histological Evaluation of Laser Skin Resurfacing Scans", *IEEE J. Sel Top Quan Elec*, **5**, pp. 1116-1126, 1999.
22 D.A. Torvi, J.D. Dale, "A Finite Element Model of Skin Subjected to a Flash Fire", *J. Biomech Eng*, **116**, pp. 250-255, 1984.
23 M. Gerstmann, A. Sagi, A.Avidor-Zehavi, A. Ketzir, S. Akselrod, "Model simulation of biological damage in tissue exposed to $CO_2$ laser irradiation", *Optical Eng.*, **32**, pp. 291-297, 1993.
24 E.v. Ross, Y. Domankevitz, M. Skrobal, R.R. Anderson, "Effects of $CO_2$ Laser Pulse Duration in Ablation and Residual Thermal Damage, Implications for Skin Resurfacing", *Lasers in Surgery and Medicine*, **19**, 123-129, 1996.
25 F.H. Loesel, M.H. Niemz, J.F. Bille, T. Juhasz, "Laser-Induced Optical Breakdown on Hard and Soft Tissues and Its Dependence on the Pulse Duration: Experiment and Model", *IEEE J. Quan Elec*, **32**, pp. 1717-1722, 1996.
26 K.A. Arndt, J.M. Noe, S. Rosen, *Cutaneous LaserTherapy - Principles and Methods*, John Wiley & Sons, Chichestor, 1983.
27 M.S. Spicer, D.J. Goldberg, "Lasers in dermatology", *J of Am Ac of Dermatol*, **34**, pp. 1-25, 1996.
28 M.L. Wolbarsht, "Laser Surgery: CO2 or HF", *IEEE J. Quan Elec*, **QE-20**, pp. 1427-1432, 1984.
29 M. Gniadecka, B. Quistorff, "Assessment of dermal water by high-frequency ultrasound: comparative studies with nuclear magnetic resonance", *Brit J. Dermatol*, **135**, pp. 218-224, 1996.
30 G.M. Hale, M.R. Querry, "Optical Constants of Water in the 200-nm to 200-μm Wavelength Region", *Appl Optics*, **12**, pp. 555-563, 1973.

# Laser induced heat diffusion limited tissue coagulation as a laser therapy mode

Ihor A. Lubashevsky[a], Alexander V. Priezzhev[b], and Vasyl V. Gafiychuk[c]

[a]Theory Department, General Physics Institute, Russian Academy of Sciences
Vavilov str. 38, Moscow 117942, Russia
[b]Physics Department, Moscow State University, Vorobievy Gory, Moscow 119899, Russia
[c]IAPMM, National Academy of Sciences of Ukraine, 3b Naukova str. Lviv, 290601, Ukraine

## ABSTRACT

Previously we have developed a free boundary model for local thermal coagulation induced by laser light absorption when the tissue region affected directly by laser light is sufficiently small and heat diffusion into the surrounding tissue governs the necrosis growth. In the present paper keeping in mind the obtained results we state the point of view on the necrosis formation under these conditions as the basis of an individual laser therapy mode exhibiting specific properties. In particular, roughly speaking, the size of the resulting necrosis domain is determined by the physical characteristics of the tissue and its response to local heating, and by the applicator form rather than the treatment duration and the irradiation power.

**Keywords:** Thermal coagulation, heat diffusion, necrosis growth, interface dynamics, tissue response, applicator form

## 1. WHAT THE LASER INDUCED HEAT DIFFUSION LIMITED TISSUE COAGULATION IS

Thermal coagulation caused by local heating due to laser light absorption is used to obtain a necrosis domain of desired form for the removal of malignant tissue. However, particular details of the necrosis formation depend substantially on the specific conditions (see, e.g., Ref. 1), which necessitates studying different modes of the thermal treatment individually. The present paper discusses one of them singled out by the dominant role of heat diffusion in the necrosis growth.

### 1.1. Physical Process

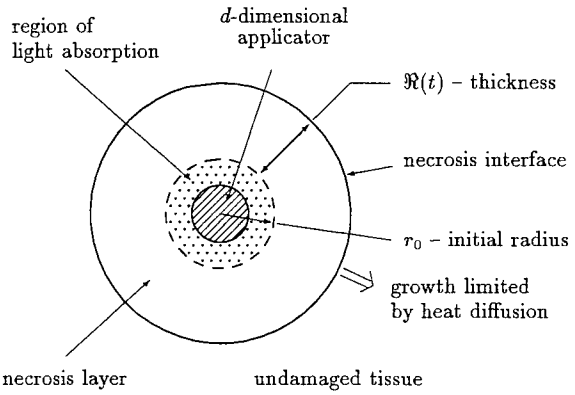


**Figure 1.** Physical process under consideration. (The values of $d = 1, 2, 3$ describe the necrosis formation in cases when ($d = 1$) the applicator radiating part is large in size (in comparison with $\Re$) and when its two ($d = 2$) or three ($d = 3$) spatial dimensions are small.)

We deal with the following physical process (Fig. 1). Through an applicator shown by the dashed circle laser light is delivered into a thin layer of living tissue. Its absorption causes the temperature to attain such high values (above

Correspondence (e-mail): I.A.L.: ialub@fpl.gpi.ru; A.V.P.: avp@lbp.ilc.msu.su; V.V.G.: gaf@viva.lviv.ua



In *Laser-Tissue Interaction XI: Photochemical, Photothermal, and Photomechanical*, Donald D. Duncan, Jeffrey O. Hollinger, Steven L. Jacques, Editors, Proceedings of SPIE Vol. 3914 (2000)
1605-7422/00/$15.00

70 °C) that lead practically to immediate tissue coagulation in this region. Heat diffusion into the surrounding live tissue causes its further thermal coagulation, giving rise to the growth of the necrosis layer. In this case heat diffusion plays a significant role in the necrosis growth because the thickness $\Re$ of the necrosis layer exceeds the depth of laser light penetration into the tissue. Therefore, the temperature distribution inevitably has to be substantially nonuniform and for the tissue to coagulate at the peripheral points heat diffusion should cause the temperature to grow at these points. The latter property singles out the particular case of thermal coagulation discussed in the present paper from other possible modes of thermotherapy treatment and that is why we refer to the necrosis growth under these conditions as to thermal coagulation limited by heat diffusion.

Considering the one-, two-, and three-dimensional models ($d = 1, 2, 3$) we actually simulate the necrosis formation when, correspondingly, the radiating part of the applicator is sufficiently large in size (in comparison with $\Re$), and the cases when its two or three spatial dimensions are small.

Heat diffusion in the live tissue is affected substantially by blood perfusion causing the heat sink.[2,3] Thus, the characteristics of the spatial distribution and the dynamics of the blood perfusion rate should have a substantial effect on the necrosis growth limited by heat diffusion. So, one dealing with this process has to take into account the tissue response to the temperature variations which can locally cause a tenfold increase in the blood perfusion rate.[4] The latter, in particular, gives rise to a substantially nonuniform distribution of the blood perfusion rate and visually manifests itself in a red ring ("hyperemic ring") appearing around the necrosis region during the thermotherapy treatment.

The aforementioned characteristics leads us to the following mathematical model for the laser induced heat diffusion limited tissue coagulation.

## 1.2. Mathematical Description

Below we will leave aside the detailed description of laser light propagation in the tissue and assume that the heat generation rate $q(\mathbf{r}, t)$ due to laser light absorption is given beforehand. Therefore, we model the thermal coagulation by the evolution of the temperature field $T(\mathbf{r}, t)$, the fraction of undamaged tissue $\zeta(\mathbf{r}, t)$, and the blood perfusion rate $j(\mathbf{r}, t)$. Namely, for the tissue temperature we write:[2,3,5–10]

$$c\rho\frac{\partial T}{\partial t} = \nabla\big(\kappa_{\text{eff}}(j)\nabla T\big) - f c_b \rho_b j (T - T_a)\,. \tag{1}$$

Here $c$, $\rho$, $c_b$, and $\rho_b$ are the heat capacity and density of the tissue and blood, respectively, $\kappa_{\text{eff}}$ is the effective tissue heat conductivity taking into account the effect of blood perfusion on heat propagation,[5] $T_a$ is the blood temperature in systemic circulation, $j$ is the blood perfusion rate, $f \sim 1/\ln(l/a) \sim 0.5$ [7,9,10] is practically a constant, where[11] $l/a \sim 10$ is the mean ratio of the individual length to radius of blood vessels forming peripheral circulation. The blood flow effect manifests itself in the appearance of the heat sink term on the right-hand side of equation (1) and the renormalization of the heat conductivity $\kappa$ of the cellular tissue, $\kappa \to \kappa_{\text{eff}}(j)$.

Thermal coagulation is governed by the equation:[1,12–14]

$$\frac{\partial \zeta}{\partial t} = -\zeta\omega(T)\,, \tag{2}$$

where the Arrhenius dependence $\omega(T)$ can be approximated by the expression:

$$\omega(T) = \omega_0 \exp\Big(\frac{T - T_0}{\Delta}\Big)\,. \tag{3}$$

In particular, for pig liver $\omega_0 = 0.2\,\text{min}^{-1}$, $T_0 = 60\,^\circ\text{C}$, and $\Delta = 3.6\,^\circ\text{C}$ as follows from the experimental data[1] for the threshold time of tissue coagulation under fixed temperature.

At the first approximation the tissue response to local heating obeys the equation:[10,7,8,15–17]

$$\tau\frac{\partial j}{\partial t} + j\Phi(T) = j_0\,, \tag{4}$$

where the function $\Phi(T)$ is specified as:

$$\Phi(T) = \begin{cases} \alpha + (1-\alpha)\dfrac{T_{\text{vr}} - T}{T_{\text{vr}} - T_a} & \text{for} \quad T < T_{\text{vr}}\,, \\ \alpha & \text{for} \quad T > T_{\text{vr}}\,, \end{cases} \tag{5}$$

$\tau \sim 1$ min is the delay time, the vessel response temperature $T_{\rm vr} \approx 45$–$46\,^{\circ}$C is the temperature at which the blood vessels exhaust their ability to expand and, so, the blood flow rate cannot increase under further heating, and the ratio $\alpha = j_0/j_{\max}$ of the blood flow rate $j_0$ under the normal conditions to its maximum $j_{\max}$ attained in living tissue due to the vessel widening is estimated as $\alpha \approx 0.05$ to 0.1.[4] The system of equations (1), (2) will be referred below as to the distributed model of local thermal coagulation.

To describe the necrosis growth limited by heat diffusion in the framework of the distributed model one has to consider in detail the temperature distribution inside the layer of partially damaged tissue, which, on one hand, is sufficiently thin[18,19] (of thickness about 1 to 2 mm) and, on the other hand, directly governs the necrosis growth. However, rigorously speaking, equation (1) does not hold in the layer of partially damaged tissue.[7,8,18,19] To overcome this problem we have developed[18,19] a free boundary model that treats the given layer as an infinitely thin interface $\mathcal{J}$ separating the totally damaged necrosis region and the undamaged tissue. Formally we define the interface $\mathcal{J}(t)$ as the locus where $\zeta(\mathbf{r}, t) = 0.5$. The motion of the interface $\mathcal{J}$ is governed by its normal velocity $\vartheta_n$ depending on the tissue temperature $T_i$ at $\mathcal{J}$ and the normal temperature gradient $|\nabla_n T|_{\mathcal{J}-0}$ taken also at $\mathcal{J}$, for example, on the necrosis side. Namely,

$$\vartheta_n = \Im_0 \frac{\Delta}{|\nabla_n T|_{\mathcal{J}-0}} \omega(T_i)\,, \tag{6}$$

where $\Im \sim 1$ is a constant. In addition, due to the layer of partially damaged tissue being thin the heat flux cannot vary substantially inside this layer. So in the free boundary model we impose the continuity condition on the heat flux through the interface $\mathcal{J}$:

$$\kappa\,|\nabla_n T|_{\mathcal{J}-0} = \kappa_{\rm eff}\,|\nabla_n T|_{\mathcal{J}+0}\,. \tag{7}$$

In the region of the undamaged tissue directly adjacent to the interface $\mathcal{J}$ (i.e. at the boundary $\mathcal{J}+0$) the heat conductivity is taken equal to its effective value $\kappa_{\rm eff}(j)$ in the bulk of the live tissue depending on the local blood perfusion rate.

In this way the mathematical description of laser induced heat diffusion limited tissue coagulation is reduced to the bioheat equation (1) written for the undamaged tissue and converting into the standard heat equation for the necrosis region ($\kappa_{\rm eff} \to \kappa$, $j = 0$), to equation (4) governing the response of the undamaged tissue to heating, and to the boundary conditions (6), (7) at the necrosis interface $\mathcal{J}$. This approach is self-consistent because the free boundary model deals with only smooth spatial variations of the temperature. Figure 2 compares the two models presenting their prediction on the necrosis growth in the one-, two-, and three-dimensional tissue phantoms (figures ($a$, $b$), ($c$, $d$)), and ($e$, $f$), respectively). The matching of these curves demonstrates that the particular details of the tissue distribution inside the layer of partially damaged tissue are not significant.

### Fixed coagulation temperature approximation

To single out different stages of the necrosis growth it is convenient to use a simplifying assumption[7,8] regarding the tissue temperature at the interface $\mathcal{J}$ as a fixed value about $T_{\rm cg} \approx 65\,^{\circ}$C:

$$T_i = T_{\rm cg}\,. \tag{8}$$

To justify the given approximation we present in Fig. 3 the time dependence of tissue temperature inside the layer of partially damaged tissue (actually at the point where $\zeta = 0.5$) obtained in the distributed model for the one-dimensional tissue phantom. As seen in it the smaller the parameter $\Delta$ of the tissue damaged rate $\omega(T, \Delta)$, the more the time variations in the interface temperature are smothered, except for a short initial period of the necrosis growth. So approximation (8) can be adopted at least in a qualitative analysis.

## 2. CHARACTERISTIC PROPERTIES OF THE NECROSIS FORMATION

As stated in Sec. 1 the necrosis formation under consideration is due to heat diffusion into the surrounding tissue causing the temperature at the peripheral points to grow and, so, inducing the further thermal coagulation. However, heat diffusion is not the only factor governing the temperature evolution, the latter is also affected by blood perfusion giving rise to the heat sink, and by the applicator form. Their integral effect is the subject of the following sections.

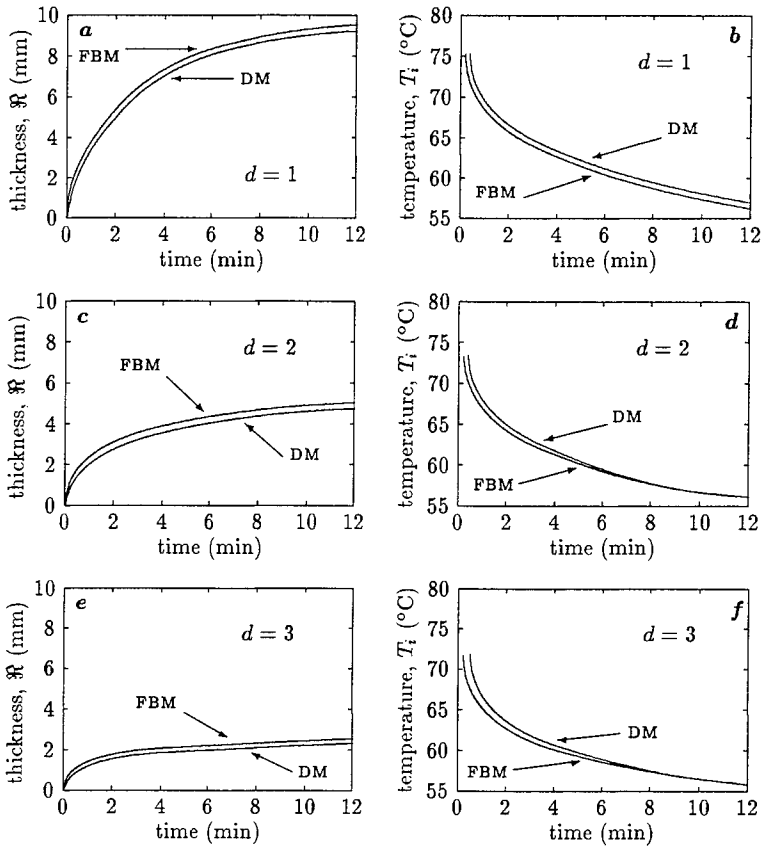


**Figure 2.** Comparison of the necrosis growth predicted by the distributed model (DM) and the free boundary model (FBM). The thickness $\Re(t)$ of the necrosis layer and the temperature $T_i(t)$ at the necrosis interface are plotted against time $t$ for heat sources of (a,b) the plane, (c,d) cylindrical, and (e,f) spherical forms. (In numerical calculations we set $\tau = 2\,\text{min}$, $j_{\max} = 10 j_0$. For the distributed model the value $T_i$ is specified as $T(r_i)$ at the point $r_i$ at which $\zeta(r_i) = 0.5$.) After [21].

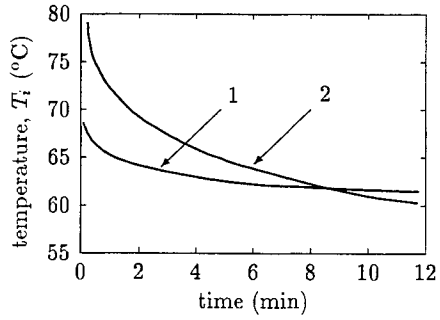


**Figure 3.** The time dependence of the tissue temperature $T_i$ at the point where $\zeta = 0.5$ for different values of the parameter $\Delta$ [18,19]. (Curve 1 and 2 correspond to $\Delta = 1.5\,°\text{C}$ and $\Delta = 5.0\,°\text{C}$. In obtaining the curves we considered an one-dimensional phantom of the tissue without response to heating.) After [18,19].

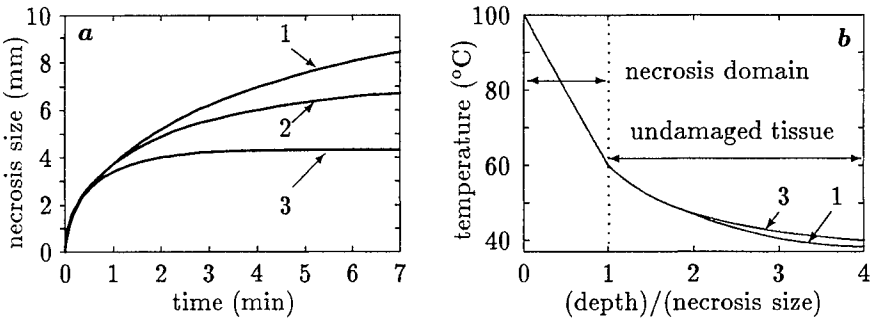


**Figure 4.** The thickness $\Re$ of the necrosis layer *vs* time (*a*) and the temperature distribution (*b*) for different values of $\alpha$. Curves 1, 2, 3 correspond to $\alpha = 1$, 0.3, 0.1, respectively ($\tau = 0$, one-dimensional tissue phantom, fixed coagulation temperature approximation). After [7,8].

## 2.1. Effect of Blood Perfusion and the Tissue Response

We consider the growth of the necrosis layer shown in Fig. 1 assuming that the tissue temperature $T_b$ at the boundary of the light absorption region is kept up at 100 °C due to the heat generation caused by laser light absorption. In this case all the tissue characteristics, such as the heat conductivity $\kappa$ and density $\rho$ of the cellular tissue, the ratio $\alpha = j_0/j_{\max}$, *etc.* can be combined into two quantities, a spatial scale and a temporal one:[7,8]

$$\Re_{\lim} \sim \sqrt{\frac{\kappa_{\text{eff}}}{c\rho f j_{\max}}} \sim 10\,\text{mm}, \quad t_{\text{cg}} \sim \frac{1}{f j_{\max}} \sim 2\,\text{min} \tag{9}$$

in order to characterize the necrosis formation. In obtaining these estimates we have used the following typical values of the tissue parameters: $\kappa \sim 7 \times 10^{-3}$ W/cm·K, $c \sim 3.5$ J/g·K, and $\rho \sim 1$ g/cm$^3$; set the blood perfusion rate $j \sim 0.3\,\text{min}^{-1}$ (for stomach[20]), the ratio $\alpha = 0.3$, and $\kappa_{\text{eff}} = 2\kappa$. If the tissue response to local heating is delayed substantially, i.e. $\tau > t_{\text{cg}}$, then $j_{\max}$ should be replaced in (9) by the value of the blood perfusion rate attained near the necrosis boundary during a time of order $t_{\text{cg}}$. Fig. 4 explains this feasibility presenting the results obtained in the free boundary model under the fixed coagulation temperature approximation.[7,8] Namely, the part (*a*) exhibits the necrosis growth in the one-dimensional tissue phantom without response to local heating, $\alpha = 1$, and with the immediate ($\tau = 0$) response of different vigor. It is seen that the blood perfusion rate affects the necrosis growth substantially. In contrast, the form of the temperature field (part (*b*)) is practically insensitive to the variations of the blood perfusion rate. Therefore, only the integral characteristics of the temperature field $T(\mathbf{r}, t)$ and, so, of the blood perfusion field $j(\mathbf{r}, t)$ are essential for the necrosis growth.

The temporal scale $t_{\text{cg}}$ divides the course of the necrosis formation into two stages,[7,8] the fast growth stage and slow one. Within the time interval $t < t_{\text{cg}}$ the effect of the heat dissipation caused by blood perfusion is not substantial and the necrosis growth is governed by the heat diffusion only. So at this stage the rate of the necrosis growth must be maximal. After the time $t_{\text{cg}}$ has elapsed and the thickness $\Re$ of the necrosis layer has attained the value $\Re_{\lim}$ the heat dissipation begins to depress the further temperature increase and the necrosis growth decelerates. To make this feature clearer we present in Fig. 5 (by thick lines) the necrosis growth in the one-dimensional tissue phantom predicted by the free boundary model using the fixed coagulation temperature approximation. In the given case the slow stage of the necrosis formation is characterized by the growth rate equal to zero. To compare with more rigorous description of this necrosis growth Fig. 5 exhibits also the motion of the points $r_{0.2}(t)$, $r_{0.5}(t)$, and $r_{0.8}(t)$ at which the fraction of undamaged tissue is $\zeta = 0.2$, 0.5, and 0.8, respectively. As seen in Fig. 5 the position of the necrosis interface predicted by the given sufficiently rough approximation is, nevertheless, inside the layer of partially damaged tissue within the time interval under consideration. The latter justifies our inference on the existence of the fast and slow stages. So, in spite of continuing to grow at the slow stage the necrosis layer forms mainly during the fast stage for the time $t_{\text{cg}}$.

## 2.2. Effect of the Applicator Form

In the previous section we have considered the necrosis growth when the applicator, or, more rigorously, its radiating part is large in all the dimensions. This assumption enabled us to regard the necrosis region as a plane layer. If

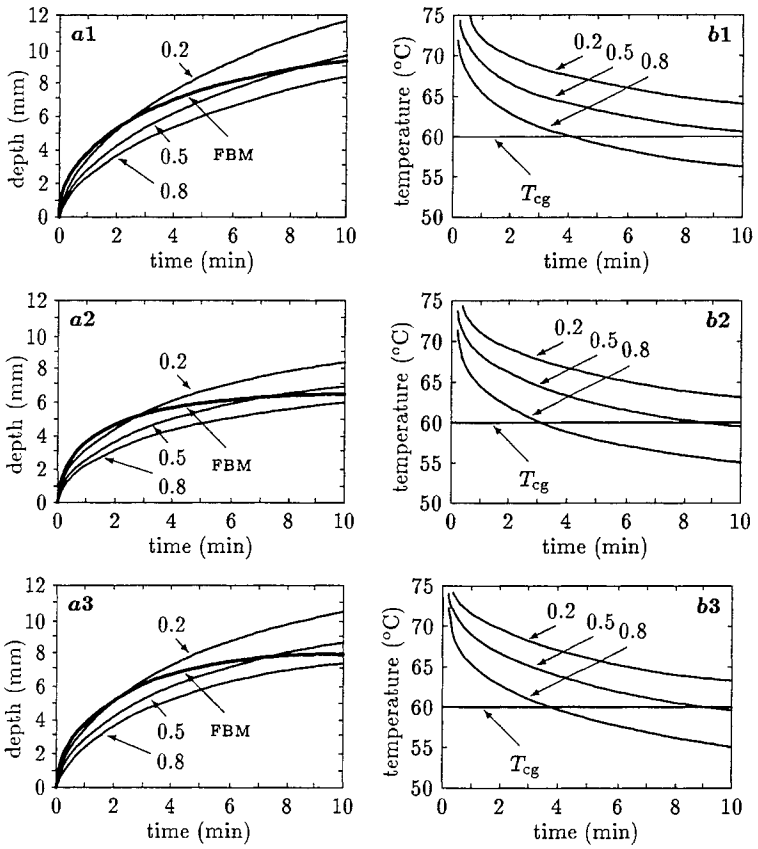


**Figure 5.** The coordinates $r_{0.2}$, $r_{0.5}$, $r_{0.8}$ of the points at which the undamaged tissue fraction $\zeta = 0.2, 0.5, 0.8$ ($a1$–$a3$) and the corresponding temperatures $T_{0.2}$, $T_{0.5}$, $T_{0.8}$ ($b1$–$b3$) as functions of time for different value of the parameters $\alpha$ and $\tau$. In fig. ($a1$–$a3$) the thick lines labeled with FBM are the position $\Re$ of the necrosis interface in the free boundary model using the fixed temperature coagulation approximation, $T_{cg}$ shown in fig. ($b1$–$b3$). (For fig. $a1$, $b1$ – $\{\alpha = 1\}$; for fig. $a2$, $b2$ – $\{\alpha = 0.3, \tau = 0\}$; for fig. $a3$, $b3$ – $\{\alpha = 0.3, \tau = 3$ min$\}$.) After [7,8].

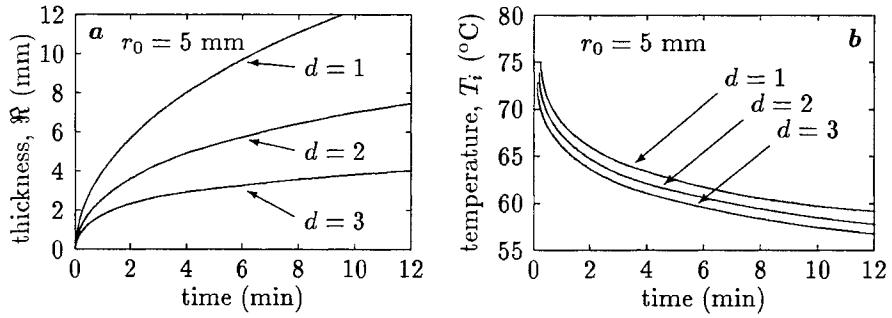


**Figure 6.** Thickness $\Re$ of the necrosis layer ($a$) and temperature $T_i(t)$ at the necrosis interface ($b$) *vs* time for the applicator of the plane ($d = 1$), cylindrical ($d = 2$), and spherical ($d = 3$) geometry (no tissue response, $r_0 = 5$ mm). After [21].

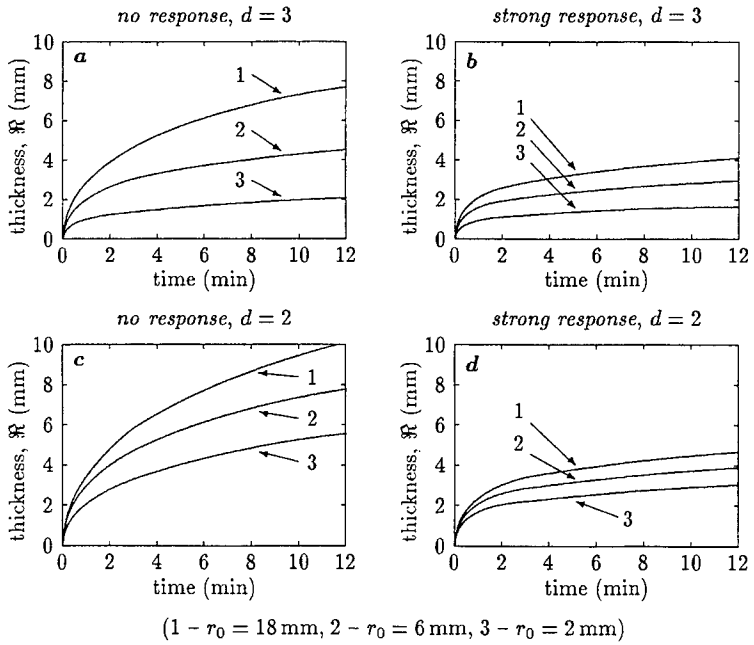


**Figure 7.** Thickness $\Re$ of the spherical ($a$, $b$) and cylindrical ($c$, $d$) necrosis layers *vs* time for different values of the initial necrosis radius $r_0 = 18$ mm (curve 1), $r_0 = 6$ mm (curve 2), and $r_0 = 2$ mm (curve 3) ($a$, $c$ – tissue without response, $b$, $d$ – tissue with strong, $j_{\max} = 10j_0$, immediate response). After [21].

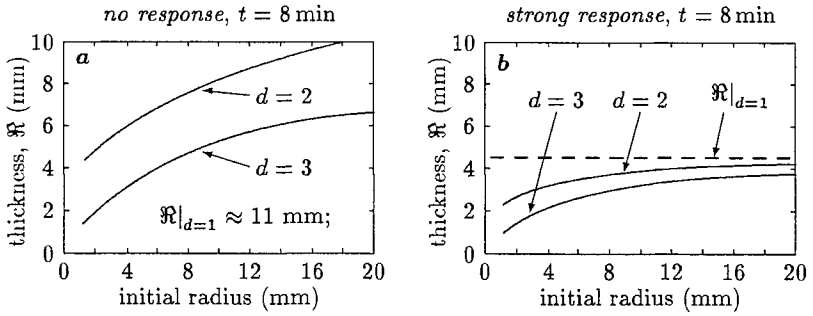


**Figure 8.** Thickness $\Re$ of the necrosis layer at the fixed moment of time $t = 8$ min for different values of the initial necrosis radius $r_0$ for the two- and three-dimensional tissue phantoms ($a$ – tissue without response, $b$ – tissue with a strong, $j_{\max} = 10j_0$, immediate response). After [21].

at least one dimension of the applicator is about or even less than the thickness $\Re$ of the necrosis layer then heat diffusion into the surrounding tissue gives rise to the temperature distribution depending on the applicator form. The latter in turn affects the necrosis formation.[21]

The dependence of the necrosis growth on the applicator geometry is demonstrated in Figs 6–8. Figure 6*a* shows how the time dependences of the necrosis layer thickness $\Re(t)$ differ for the applicators of plane ($d = 1$), cylindrical ($d = 2$), and spherical ($d = 3$) forms for the tissue phantom with the same properties. Here is exhibited the necrosis growth in the tissue phantom without response to temperature variations for $r_0 = 5$ mm. In particular, we see that for the one-dimensional tissue phantom the difference between the fast and slow stages is not well distinctive. For the three-dimensional tissue phantom we meet the opposite situation, the necrosis growth exhibits the clearly evident tendency to saturation after a lapse of several minutes. In particular, after 12 minutes the thickness $\Re|_{d=3}$ of the necrosis layer can attain only the value about its initial radius $r_0$. At the same time in the one-dimensional tissue phantom the necrosis radius exceeds this value by several times. In the two-dimensional case the necrosis growth is characterized by the intermediate behavior. It should be noted that, in contrast, the time dependence of the interface

temperature $T_i(t)$ (figure *b*) is practically of the same form for the three cases.

These results prompt us that for the spherical applicator the rate of the necrosis growth should depend substantially on the initial necrosis radius $r_0$ at least for $r_0 \ll \Re|_{d=1}$, where $\Re|_{d=1}$ is the thickness that the necrosis layer would attain for the plane applicator. This fact is directly demonstrated in Fig. 7 showing the dynamics of the necrosis growth in the tissue phantom without response to temperature variations (figure *a*) as well as with an immediate strong response (figure *b*). At a fixed moment of time the necrosis layers can differ in thickness by a factor of three to four as the initial radius $r_0$ changes from 2 to 18 mm. As should be expected for the two-dimensional tissue phantom this dependence is smoothed and under the same conditions the necrosis thickness can increase not more than twofold.

Figure 8 illustrates the dependence of the necrosis growth on the initial necrosis radius in the most clear form. These curves are obtained by fixing the time $t = 8$ min and interpolating the point collection $\{\Re|_{t=8\ \mathrm{min}}, r_0\}$ for different values of $r_0$ as the partition points of certain continuous curves. In other words, this figure shows the thickness $\Re(t, r_0)|_{t=8\ \mathrm{min}}$ of the necrosis layer as a function of its initial radius $r_0$ for the fixed moment of time under various physical conditions. We see that for the three-dimensional tissue phantom the curve $\Re|_{d=3}(r_0)$ practically goes into the origin of the plane $\{\Re, r_0\}$ as formally $r_0 \to 0$. When the initial radius $r_0$ becomes large enough ($r_0 > \Re|_{d=1}$) the curve $\Re|_{d=3}(r_0)$ (as it must) tends to the value $\Re|_{d=1}$ (figure *b*). In other words, until $r_0 < \Re|_{d=1}$ it is the initial radius of the necrosis domain that directly controls the size of the necrosis layer which can be attained during a typical course of thermotherapy.

The present properties of the necrosis growth are due to the fact that in the three-dimensional space the temperature field governed by heat diffusion from a local source would remain substantially nonuniform ($T(r) \propto 1/r$ as $r \to \infty$) even though we ignored the heat sink effect caused by blood perfusion. Therefore, for the spherical necrosis region the temperature at the necrosis interface $T_i$ inevitably has to decrease substantially as the necrosis layer grows. So, due to the strong temperature dependence of the coagulation rate $\omega(T_i)$ the necrosis growth will be practically suppressed after a lapse of time it takes for the value of $\Re|_{d=1}(t)$ to exceed the initial necrosis radius $r_0$.

## 3. LASER INDUCED HEAT DIFFUSION LIMITED TISSUE COAGULATION AS A SPECIFIC THERAPY MODE

One of the main parameters controlling a thermotherapy treatment is the power of irradiation delivered into the tissue and the treatment duration. These parameters as well as a specific therapy mode should be chosen in such a way that gives rise to the necrosis of desired form. Different modes, in principle, can give rise to a necrosis region of the same form and, in this case, a specific mode may be chosen keeping in mind, for example, its optimality and stability. Various thermotherapy modes are singled out by those physical mechanisms that play the leading role and endow them with individual properties.[1] The presented results enable us to regard the laser induced heat diffusion limited tissue coagulation as an individual therapy mode where heat diffusion into the live tissue, i.e. the tissue with active blood perfusion, plays the governing role.

To justify the latter statement let us briefly summarize the aforesaid. Namely, we have considered thermal tissue coagulation induced by local heating due to laser light absorption and limited by heat diffusion into the surrounding live tissue. The irradiation power is assumed to be enough high for the temperature inside the region affected directly by laser light to grow up to values about 100 °C. Then this process is characterized by the following.

- When all the dimensions of the laser light applicator (or, more rigorously, of its radiating part) are less than several millimeters the thickness $\Re$ of the necrosis layer forming under such conditions is mainly specified by the applicator size and, may be, by the depth of laser light penetration into the tissue after a lapse of time about several minutes.

- Otherwise, the thickness $\Re$ of the necrosis layer is mainly determined by the characteristics of the tissue and blood perfusion rather than the treatment duration and the irradiation power, in particular, $\Re \sim \Re_{\mathrm{lim}}$ provided the treatment duration exceeds the value $t_{\mathrm{cg}}$ (see expression (9)).

In other words, the laser induced heat diffusion limited tissue coagulation can be regarded as a self organization phenomenon because the corresponding formation of the necrosis domain is, roughly speaking, governed by the internal physical characteristics of the system rather than the external control parameters.

## ACKNOWLEDGMENTS

This study was made possible, in part, due to the STCU Grant 1675 and the Russian Foundation of Basic Research, Support of Leading Scientific Schools, Grant 96-15-97782.

## REFERENCES

1. S. L. Jacques, "Laser–tissue interactions: Photochemical, photothermal, and photomechanical", *Surgical Clinics of North America* **72**(3), pp. 531–558, 1992.
2. H. H. Pennes, "Analysis of tissue and arterial blood temperatures in the resting human forearm", *J. Appl. Phys.* **1**, pp. 93–122, 1948.
3. M. M. Chen and K. R. Holmes, "Microvascular contributions in tissue heat transfer", *Ann. N. Y. Acad. Sci.* **335**, pp. 137–154, 1980.
4. C. W. Song, A. Lokshina, I. G. Rhee, M. Patten, and S. H. Levitt, "Implication of blood flow in hyperthermia treatment of tumors", *IEEE Trans. Biom. Eng.* **BME-31** (1), pp. 9–15, 1984.
5. S. Weinbaum and L. M. Jiji, "A new simplified bioheat equation for the effect of blood flow on local average tissue temperature", *ASME J. Biomech. Eng.* **107**, pp. 131–139, 1985.
6. COMAC–BME workshop on Modelling and Treatment Planning in Hyperthermia (Iagonissi 1990), Conclusions subgroup Thermal Modelling. Reported by J. J. W. Lagendijk, *COMAC - BME Hyperthermia Bulletin* **4**, pp. 47–49, 1990.
7. I. A. Lubashevsky, A. V. Priezzhev, V. V. Gafiychuk, and M. G. Cadjan, "Free-boundary model for local thermal coagulation", in: *Laser-Tissue Interaction VII*, S. L. Jacques, ed., *Proc. SPIE* **2681**, pp. 81–91, 1996.
8. I. A. Lubashevsky, A. V. Priezzhev, V. V. Gafiychuk, and M. G. Cadjan, "Local thermal coagulation due to laser–tissue interaction as irreversible phase transition", *J. Biomed. Opt.* **2**(1), pp. 95–105, 1997.
9. S. Weinbaum, L. X. Xu, L. Zhu, and A. Ekpene, "A new fundamental bioheat equation for muscle tissue: Part I–Blood perfusion term", *ASME J. Biomech. Eng.* **119**, pp. 278–288, 1997.
10. I. A. Lubashevsky and V. V. Gafiychuk, "Mathematical description of the heat transfer in living tissue (Part I, II)", *e-print: adap-org/9911001, 9911002*; *Mathematical description of the heat transfer in living tissue*, VNTL Publishers, Lviv, 1999.
11. G. I. Mchedlishvili, *Microcirculation of Blood. General Principles of Control and Disturbances*, Nauka Publishers, Leningrad, 1989 (in Russian).
12. L. O. Svaasand, T. Boerslid, and M. Oeveraasen, "Thermal and optical properties of living tissue: Application to laser-induced hyperthermia", *Laser in Surgery and Medicine* **5**, pp. 589–602, 1985.
13. B. M. Kim, S. L. Jacques, S. Rastegar, S. Thomson, and M. Motamedi, "The role of dynamic changes in blood perfusion and optical properties in thermal coagulation of the prostate", in *Laser–Tissue Interaction VI*, S. L. Jacques, ed., *Proc. SPIE* **2391**, pp. 443–450, 1995.
14. A. Roggan and G. Müller. "Dosimetry and computer-based irradiation planning for laser-induced interstitial thermotherapy (LITT)", in *Laser-Induced Interstitial Thermotherapy*. G. Müller and A. Roggan, ed., SPIE Optical Engineering Press, Bellingham, Washington, 1995, pp. 114–156.
15. I. A. Lubashevsky and V. V. Gafiychuk, "A simple model of self-regulation in large natural hierarchical systems", *J. Env. Syst.* **23**(3), pp. 281-289, 1995.
16. I. A. Lubashevsky and V. V. Gafiychuk, "Mathematical model for a perfect hierarchically organized system of life-support of distributed living media", *Proc. Russ. Acad. Sci.*, **351**(5), pp. 611–613, 1996.
17. I. A. Lubashevsky and V. V. Gafiychuk, "Cooperative mechanism of self-regulation in hierarchical living systems", *e-print: adap-org/9808003.*
18. I. A. Lubashevsky, A. V. Priezzhev, V. V. Gafiychuk, and M. G. Cadjan, "Dynamic free boundary model for laser thermal tissue coagulation", in *Laser-Tissue Interaction and Tissue Optics II*, H. J. Albrecht, G. Delacrétaz, T. H. Meier, R. W. Steiner, and L. O. Svaasand, ed., *Proc. SPIE* **2923**, pp. 48–57, 1996.
19. I. A. Lubashevsky, A. V. Priezzhev, and V. V. Gafiychuk, "Effective interface dynamics of heat diffusion limited by thermal coagulation", *J. Biomed. Opt.* **3**(1), pp. 102–111, 1998.
20. E. B. Babsky, A. A. Zubkov, and G. I. Kositsky. "Circulation", in *Human Physiology*, G. I. Kositsky, ed., Mir Publishers, Moscow, 1990, Vol. 2, Chap. 10, pp. 50–127.
21. I. A. Lubashevsky, A. V. Priezzhev, and V. V. Gafiychuk, "Free boundary model for local thermal coagulation. Growth of a spherical and cylindrical necrosis domain", in *Laser–Tissue Interaction VIII*, S. L. Jacques, ed., *Proc. SPIE* **2975**, pp. 43–53, 1997.

# The effect of partial denaturation on Nd:YAG laser mediated stress relaxation of porcine septal cartilage

Timothy C. Kuo[a,b], Hong K. Kim[b], Thomas E. Milner[c], J. Stuart Nelson[b], Emil N. Sobol[d], and Brian J.F. Wong[a,b]

[a]University of California, Irvine Medical Center, Department of Otolaryngology/Head and Neck Surgery, 101 City Drive, Bdg 25, Rte 81, Rm 191, Orange, CA 92868

[b]Beckman Laser Institute and Medical Clinic, University of California, Irvine, 1002 Health Sciences Road East, Irvine, CA 92715

[c]Biomedical Engineering Program, University of Texas at Austin, Austin, TX 78712

[d]Department of Advanced Laser Technologies, Center for Technological Lasers, Russian Academy of Sciences, 2 Pionerskaya, Troitsk, Moscow Region 142092

## ABSTRACT

In this study, we examined 1) the effect of partial denaturation and 2) repetitive irradiation on porcine septal cartilage during Nd:YAG laser ($\lambda$= 1.32 μm,25 W/cm$^2$, 5 mm spot size) exposure. Diffuse reflectance from a HeNe probe laser and internal stress were measured in mechanically deformed cartilage specimens (2 x 10 x 25 mm) during Nd:YAG laser irradiation. Specimens were first partially denaturation in heated saline water baths at selected temperatures (50° C, 70° C, and 100° C all for 30 minutes). Native and water bath heated specimens were sequentially irradiated three times (pulse duration varying from 5-12 seconds, determined by noting the onset of accelerated stress relaxation) with a 5 minute cooling interval between pulses. After the first laser pulse, diffuse reflectance and internal stress changes occurred synchronously (*coupled*); the peak in internal stress occurred within less than 1 second following observation of the peak in diffuse reflectance. With repeated laser irradiation, this time interval lengthens with eventual *decoupling* of the diffuse reflectance and internal stress. With decoupling, internal stress increases during laser heating, and abruptly decreases when irradiation is terminated. Decoupling occurs with greater frequency in specimens pre-heated in the water bath. With the first laser exposure, only 15% of control, 8% of 50° C heated, 0% of 70° C heated, and 8% of 100° C specimens exhibited decoupling. However, after two laser exposures, decoupling was observed in 83% and 60% of specimens heated in water baths at 70° C (N=12) and 100° C (N=12), respectively; in contrast, decoupling was observed in less than 20% of the native (N=24) and 50° C (N=12) water bath pre-heated specimens with two laser irradiations. The effect of partial denaturation using water bath immersion mimics findings observed with sequential laser irradiation. Hence cartilage likely undergoes partial denaturation during laser reshaping, and that sustained laser irradiation may result in irreversible changes in the tissue matrix.

Keywords: Cartilage reshaping, Nd:YAG laser, denaturation, stress relaxation, optical scattering, proteoglycan, aesthetic surgery, reconstructive surgery

In *Laser-Tissue Interaction XI: Photochemical, Photothermal, and Photomechanical*, Donald D. Duncan, Jeffrey O. Hollinger, Steven L. Jacques, Editors, Proceedings of SPIE Vol. 3914 (2000)
1605-7422/00/$15.00

# INTRODUCTION

## 1.1 Cartilage Biology

Cartilage is a viscoelastic solid composed of 80% water, 13% Type II collagen, and 7% proteoglycans. The proteinaceous components (collagen and proteoglycan) are produced by chondrocytes, the constituitive cell of cartilage, which is predominantly acellular. The type II collagen is arranged into a three-dimensional lattice, which enmeshes proteoglycan moieties of strong negative charge (chondroitin and keratan sulfate). The strong negative charge is partially balanced by cations and hydrogen bonding of water. As a result of this hydrogen bonding of water, a natural tissue turgor is imparted to the cartilage. Any external force causing deformation of the natural shape of cartilage causes an imbalance of internal forces with areas of high negative charge coming in close proximity to each other. The imbalance of forces contributes to the underlying resiliency of cartilage; when the external force is removed, cartilage tends to return to its native shape as the bulk flow of water and counter ions act to restore balance to the internal forces.

## 1.2 Clinical Use of Cartilage

Because of its viscoelastic properties, cartilage is intrinsic to areas of the body requiring support that is pliable. These include the ear, nose, airway, joints, and ribcage. Congenital malformations, degenerative changes, traumatic destruction, and oncologic ablation of cartilaginous tissues often require reconstruction with cartilage harvested from the ear, nasal septum, or rib cage for the best outcome. Using autologous cartilage poses challenges to the reconstructive and plastic surgeon because of the limited quantities of cartilage at the donor sites. Often, the quantity of harvested cartilage exceeds the size of the original defect to be reconstructed because it is fashioned into the desired shape and as a consequence excess cartilage tissue is unusable and discarded. When cartilage is unavailable for the reconstructive process, bone is used sometimes but it has the disadvantage of leaving an unnatural appearance or texture. Allografts have the attendant risks of disease transmission (e.g., HIV), rejection and delayed resorption; alloplasts (synthetic material) tend to extrude or cause infection.

## 1.3 Cartilage Irradiation

Cartilage undergoes mechanical stress relaxation in response to prolonged deformation or contact heating. However, these methods are impractical for clinical application due to the long time intervals or excessive heating needed to effectively reshape cartilage. Sobol and colleagues demonstrated that laser irradiation of cartilage tissue held in mechanical deformation resulted in accelerated stress relaxation in cartilage with subsequent shape change(1, 2). Later investigations determined characteristic changes in cartilage biophysical properties during laser mediated cartilage reshaping(3-5). In particular, stress relaxation occurs when tissue temperature reaches approximately 65-75 C. These changes in tissue mechanical properties are also accompanied by changes in tissue optical and thermal properties.

In previous investigations, radiometric surface temperature [$S_c(t)$], diffuse reflectance or integrated backscattered light intensity [I(t)], and internal stress [$\sigma(t)$] were recorded during laser heating (**Figure 1**)(4). $S_c(t)$ is measured by thermopiles or solid-state detectors. As $S_c(t)$ approaches about 65-75° C (see

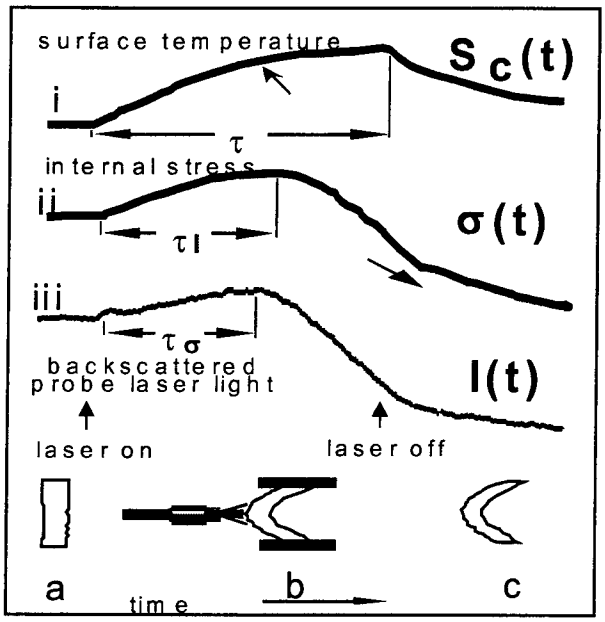


Figure 1. Radiometric surface temperature [$S_c(t)$], internal stress [$\sigma(t)$], and back-scattered light intensity [I(t)] during laser mediated cartilage reshaping.

arrow, curve i, **Figure 1**), a change in the heating rate is observed which suggests a change in the thermal properties of the specimen. At this same time, $\sigma(t)$ (measured using a tensiometric load cell device) begins to decrease rapidly, following an initial increase likely due to thermo-elastic expansion (see curve ii, **Figure 1**). This acceleration in stress relaxation occurs at about 65-75° C (as indicate by the large arrow in curve ii), but is dependent on laser fluence and heating rate. I(t) is measured by collecting back-scattered light from a visible wavelength probe laser ($\lambda$=632.8 nm) with an integrating sphere or fiber and a photoreceiver. With the onset of laser irradiation, I(t) increases monotonically until the surface temperature reaches 65-75 C; at this point, I(t) plateaus, and then decreases rapidly (see curve iii, **Figure 1**). These observed changes in I(t) mirror changes in $\sigma(t)$. The peak value for I(t) occurs at $t=\tau_I$, which in general is shorter than $\tau$ (the laser pulse duration). The peak value for $\sigma(t)$ occurs at $t=\tau_\sigma$. In previous investigations in native cartilage tissue, $\tau_I$ and $\tau_\sigma$ were similar(6).

### 1.4 Clinical Applicability of Laser Mediated Cartilage Reshaping

The interest in laser-mediated cartilage reshaping stems from its relative potential to spare or preserve cartilage during the reconstructive process. Several studies have demonstrated that cartilage maintains viability when subjected to irradiation at subablation thresholds(6-14). Observations on the thermal, optical, and mechanical responses of cartilage will assist in the development of devices for the feedback control of the reshaping process(15). Hence, determining the physical and biological basis of temperature dependent accelerated stress relaxation is critical. Proposed mechanisms of action include: a) denaturation of collagen and proteoglycan components of cartilage, b) the transition of water from bound to free states, and c) redistribution of the charged proteoglycan side chains. This study measured the effects of partial denaturation and repetitive laser irradiation on optical and mechanical properties in cartilage during laser reshaping.

## MATERIALS AND METHODS

### 2.1 Specimen Preparation

Porcine heads were obtained from a local abattoir (Clougherty Packing Company, Vernon, CA). Septal cartilage was harvested from the porcine heads as previously described. The cartilage was cut into slabs of approximate uniform thickness measuring 2 x 10 x 25 mm and immersed into normal saline. The cartilage specimens were divided into four groups: Group A) native tissue (N=24), Group B) 50 ° C (N=12), Group C) 70 ° C (N=12), and Group D) 100 ° C (N=12). Cartilage specimens were sealed in Nalgene bottles ( Nalge Nunc International, Naperville, IL) containing normal saline, which were then immersed into a controlled, preheated water bath (Magniwhirl Constant Temperature Bath, Blue M Electric Company, Blue Island, IL) for 30 minutes at the specified temperature for each group. After heating, the specimens were allowed to cool to room temperature (25 ° C) while immersed in saline.

## 2.2 Measurement of Diffuse Reflectance and Internal Stress

Cartilage specimens were held in compression between an aluminum plate attached to a calibrated one-dimensional micropositioner (Model M-461, Newport Corporation, Irvine, CA) and a thin beam load cell (0.25% full scale combined error, Model LCL-113G, Omega Engineering Inc., Stamford, CT) coupled to an aluminum mounting plate (**Figure 2**). The internal stress [$\sigma(t)$] (a.u.) across the cartilage specimen was adjusted by translating the micropositioner. Voltage output from the load cell was amplified (Stanford Research Systems, SRS 650, Sunnyvale, CA), and recorded on a digital storage oscilloscope (Textronix DSA 601, Beaverton, OR) during laser irradiation.

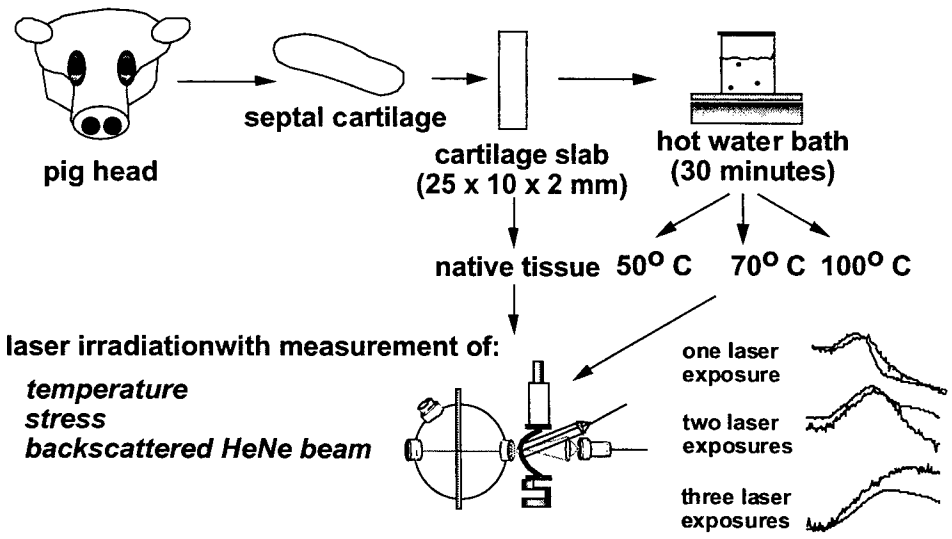


Figure 2. Experimental protocol.

Backscattered HeNe laser light ($\lambda_o$=632.8 nm, 15 mW, Melles Griot, Irvine, CA) incident on the non-Nd:YAG laser irradiated surface of the cartilage specimen was collected in an integrating sphere (6", Labsphere, North Sutton, NH) and measured using a silicon photodetector (Model 2001, New Focus, Mountain View, CA) to yield diffuse reflectance I(t). The HeNe beam was aimed at the center of the Nd:YAG laser spot on the specimen. HeNe laser light intensity was amplitude modulated (10 kHz) with a mechanical chopper (Ithaco, Ithaca, NY) and synchronously detected by a lock-in amplifier (Model SR 850, $\tau$=30 ms, Stanford Research Systems, Sunnyvale, CA). The change in diffuse reflectance from pre-irradiation levels was recorded on the oscilloscope.

Cartilage specimens were irradiated with light from a Nd:YAG laser ($\lambda$=1.32 μm, 50 Hz PRR, NewStar Lasers, Auburn, CA) delivered by a 600 μm core-diameter silica multimode optical fiber. Laser spot

size was estimated to be 5 mm by measuring the burn diameter of irradiated thermal paper (Zap-It, Kentek, Pittsfield, NH). Laser power (6.94 W, 38.45 W/cm2) was measured using a pyroelectric meter (Model 10A-P, Ophir, Jerusalem, Israel).

### 2.3 Cartilage Irradiation

Laser irradiation of each specimen was performed using the protocol illustrated in **Figure 3**. The specimen was irradiated with light from the Nd:YAG laser until a peak in I(t) was observed on the monitor of the lock-in amplifier. At this point, irradiation was terminated, the specimen was allowed to cool for 3-5 minutes before the next laser irradiation. This process ware repeated three times for each specimen. Because our experimental setup at the time allowed for measurement of only 2 parameters, $S_c(t)$ was not recorded. Native tissue (Group A), 50 ° C heated cartilage (Group B), 70 ° C heated cartilage (Group C), and 100 ° C heated cartilage (Group D) specimens were irradiated using the above protocol.

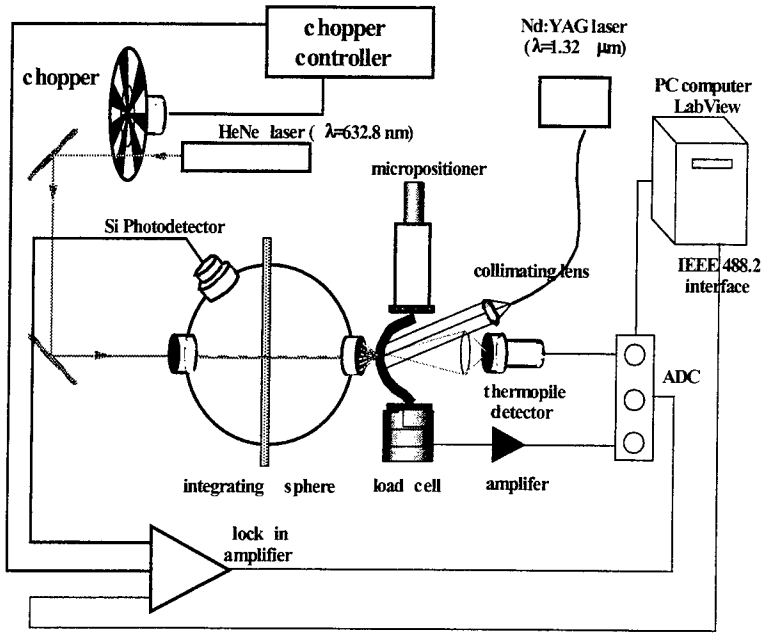


Figure 3. Experimental setup for measuring $S_c(t)$, $\sigma(t)$, and I(t).

In general, $\tau_I$ ranged from 4 to 8 seconds; however, identification of $\tau_I$ requires observation of a downturn in I(t) on the amplifier, clear identification of this trend results in exposure times ($\tau$) longer than $\tau_I$ by 2-3 seconds. In some specimens, particularly those which were heated in water baths or had undergone at least one prior laser irradiation, the peak in I(t) could not be clearly identified on the lock-in amplifier readout in real time, even with prolonged laser exposure in excess of 20 seconds. In these specimens, laser irradiation was terminated after 12 seconds, as the peak in I(t) is generally observed within 10 seconds following the onset of laser irradiation, and the radiometric surface temperature after 10 seconds is in excess of 80° C.

## RESULTS

### 3.1 Optical Response to Irradiation

Diffuse reflectance in native cartilage increases, plateaus, and then decreases following the first laser exposure as illustrated in **Figure 4**. After a cooling interval of 3-5 minutes between successive laser exposures, a second laser pulse results in similar behavior albeit with prolongation in $\tau_I$; a third laser

exposure results in further lengthening of this time interval. The prolongation of $\tau_I$ is also observed during sequential irradiation in specimens pre-heated in water baths (Groups B, C, and D). When compared within each irradiation, however, $\tau_I$ shows an increasing trend associated with the degree of denaturation; the average $\tau_I$ is shortest in Group A (native) and longest in Group D (100 ° C) (**Figure 5**).

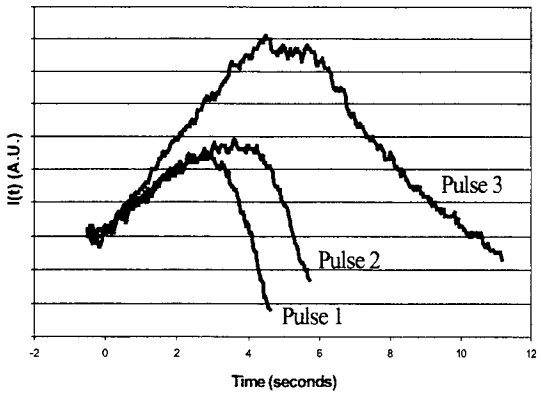


Figure 4. Response of I(t) and $\tau_I$ to repetitive irradiation in native cartilage.

$\tau_I$ (seconds)

| Group | Pulse 1 | Pulse 2 | Pulse 3 |
|---|---|---|---|
| A (native) | 2.9 | 4.4 | 10.1 |
| B (50 C) | 4.7 | 8.1 | 10.1 |
| C (70 C) | 4.8 | 7.7 | 8.3 |
| D (100 C) | 7.5 | 9.4 | 9.8 |

Figure 5. Effects of heating and repetitive irradiation on diffuse reflectance peaks ($\tau_I$).

### 3.2 Mechanical Response to Irradiation

In native cartilage tissue, $\sigma(t)$ exhibits similar features to I(t) with a characteristic increase, peak, and decay following a multiple laser exposures (**Figure 6**). With successive irradiation, $\tau_\sigma$ similarly lengthens. However, $\sigma(t)$ is occasionally observed to exhibit a sharp transition from its rise to its decline

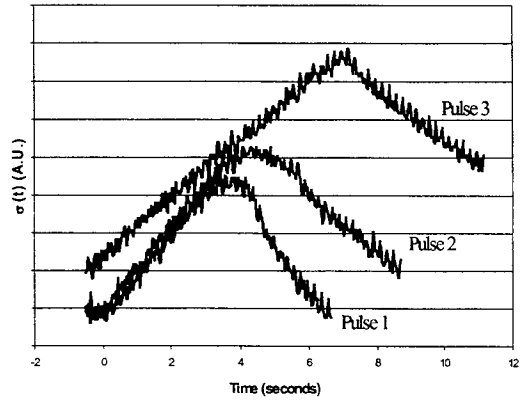


Figure 6. Response of $\sigma(t)$ and $\tau_\sigma$ to repetitive irradiation in native cartilage.

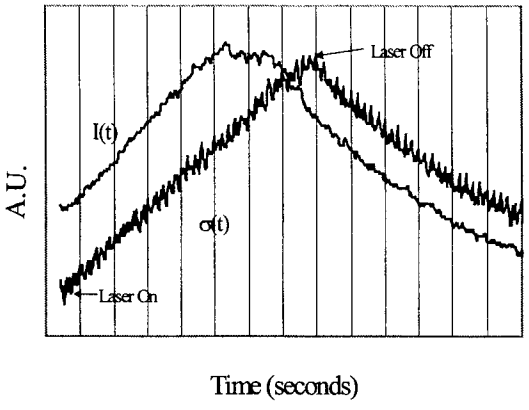


Figure 7. "Tenting" of $\sigma(t)$ and decoupling between I(t) and $\sigma(t)$.

resulting in a "tented" shape of its plot; this sharp transition occurs at the time when laser irradiation is terminated (**Figure 7**). In native cartilage tissue, this "tenting" is most often observed after the third laser exposure where nearly half of the specimens exhibiting this pattern (**Figure 8**).

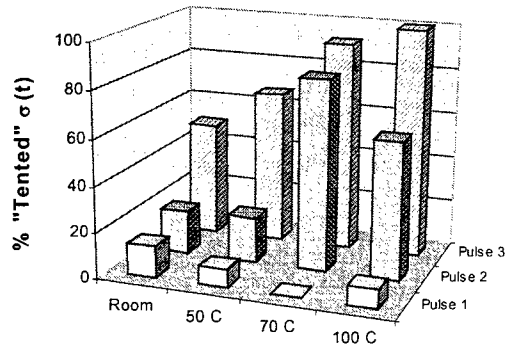


Figure 8. Percentage of specimens in which "tenting" was observed among experimental groups.

**Figure 9** represents all $\tau_\sigma$ data without "tenting"; when "tenting" did not occur, $\tau_\sigma$ increased with repeated laser irradiation in all experimental groups including water bath heated specimens. Compared with native specimens (for the corresponding laser pulse, i.e. first, second, or third), $\tau_\sigma$ generally increased in direct correlation with the degree of specimen pre-heating (and presumably denaturation). Following the third irradiation, 65 % of Group B exhibited "tenting" in $\sigma(t)$; in contrast, only two irradiation were required for the majority of Group C (85%) and Group D (60%) specimens to demonstrate "tenting" of $\sigma(t)$ (**Figure 8**).

$\tau_\sigma$ (seconds)

| Group | Pulse 1 | Pulse 2 | Pulse 3 |
|---|---|---|---|
| A (native) | 3.5 | 5.0 | 7.0 |
| B (50 C) | 5.6 | 6.9 | 9.5 |
| C (70 C) | 4.4 | 7.8 | 10.0 |
| D (100 C) | 6.5 | 10.0 | -* |

Figure 9. Effects of heating and repetitive irradiation on internal stress peaks ($\tau_\sigma$). *All $\sigma(t)$ were tented in Group D for the third laser irradiation.

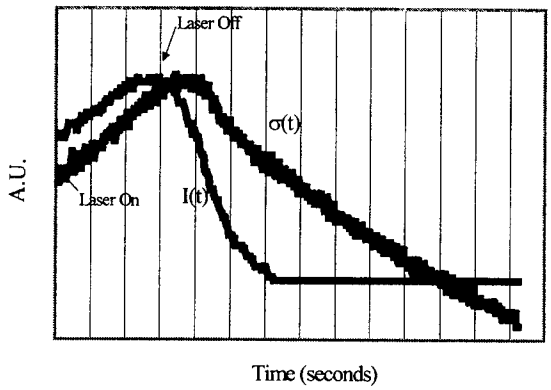


Figure 10. Coupling of I(t) and $\sigma(t)$.

### 3.3 Correlation between Optical and Mechanical Response Curves

Examination of both I(t) and $\sigma(t)$ curves shows that when $\sigma(t)$ is smooth (no tenting), both $\tau_I$ and $\tau_\sigma$ are approximately the same length (approximately 1-2 second difference (**Figure 10**). In contrast, when "tenting" is observed, I(t) and $\sigma(t)$ are decoupled, $\sigma(t)$ increases during laser irradiation and decreases at the termination of irradiation (**Figure 7**).

## 4. DISCUSSION

Cartilage can be reshaped using methods both mechanical and thermal in nature. When prolonged external force is applied to deform cartilage (such as with sutures), stress relaxation and creep occur, followed much later by true tissue matrix remodeling which is a slow, time-dependent process. Heating cartilage results in modification of matrix proteins resulting in a release of internal forces that maintain the native cartilage shape with resultant acceleration of stress relaxation. Contact heating with conventional thermal sources (e.g., heated iron, cautery, ultrasound) results in chondrocyte death due to the long time intervals needed to establish thermal equilibrium in relatively thick specimens. In contrast, photothermal heating results in rapid temperature changes with precise control over the time and space dependent temperature profile.

Previous studies which measured I(t) and $\sigma(t)$ suggest that cartilage undergoes a phase transformation when heated to 65-75. These observations provided the motivation for the present study where cartilage specimens were heated in water baths at 50° C and 70° C, representing different degrees of partial thermal denaturation. In order to demonstrate the effect of complete thermal denaturation, specimens were also heated in a 100° C water bath.

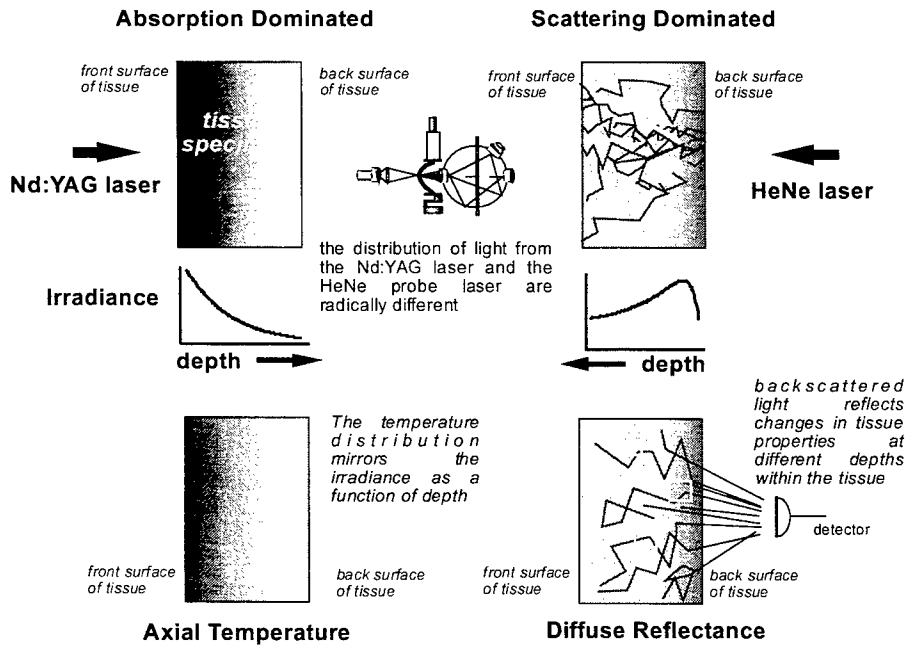


Figure 11. Schematic of the roles of Nd:YAG and HeNe lasers during cartilage irradiation.

Cartilage was irradiated with light from two lasers with the corresponding tissue effects schematically illustrated in **Figure 11**. Inasmuch as the low power HeNe laser light is highly scattered in cartilage (ref Madsen and Wong), diffusely reflected light is useful for monitoring changes in tissue optical properties throughout the entire thickness of the cartilage specimen. The Nd:YAG laser light is predominantly absorbed by water, and the high fluence rate used in this study results in heating accompanied by alterations in the tissue biophysical properties. With absorption dominance, irradiance decreases exponentially with tissue

depth. Effective temperature changes (resulting in shape change) deep within the tissue thus require longer irradiation times to reach a fluence threshold for conformational changes to occur. As the superficial tissues presumably have undergone a conformational change from earlier irradiations, changes in diffuse reflectance [I(t)] with successive irradiations presumably would represent conformational changes of successively deeper layers of cartilage. This partially explains why $\tau_I$ increases with each successive laser irradiation. In contrast, the light distribution from the HeNe probe laser results in a more uniform light distribution. Diffusely backscattered light collected by the integrating sphere reflects alterations in tissue optical properties along the axial orientation of the specimen. The measurement of diffuse reflectance alone does not provide any spatial information on the changes in tissue optical properties, though optical coherence tomography or photon migration techniques might provide more information.

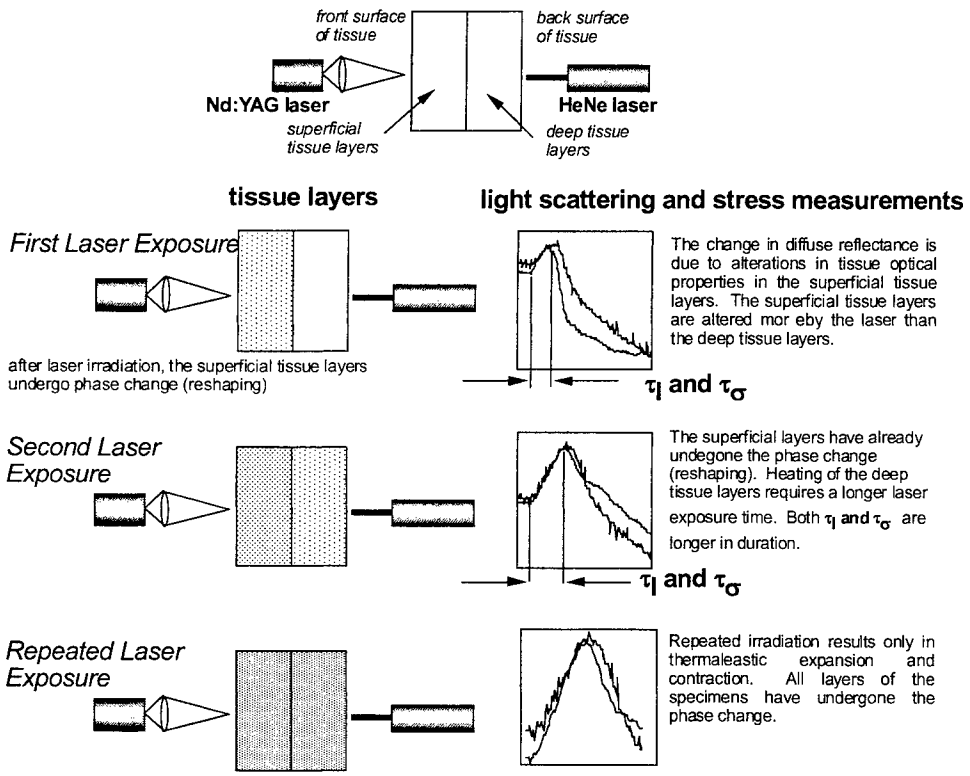


Figure 12. Schematic of two layer model for laser-mediated cartilage irradiation.

The prolongation in $\tau_I$ and $\tau_\sigma$ observed in these experiments may be partially explained by the differences in light distribution of the two lasers which we illustrate using a simple two-layer tissue model (**Figure 12**). During the first laser exposure, $\sigma(t)$ and I(t) are coupled. The first laser pulse heats the most superficial layers of tissue which undergo a phase transformation resulting in mechanical stress relaxation. In this simplified model, only the superficial layer undergoes change and the deep layer is largely unmodified. |In reality, a continuum of modified to unmodified tissue would exist in the axial direction, and the temperature change would be proportional to the underlying exponential light distribution. With a second laser pulse, Nd:YAG laser light would still be predominantly absorbed in the superficial layer. However, the phase change (and stress relaxation) has already occurred in this layer. The deep layer of tissue must be heated to the critical temperature, and as a consequence, the characteristic changes in diffuse reflectance and internal stress require a longer laser exposure time. With the second laser pulse, both $\tau_I$ and $\tau_\sigma$ lengthen which was observed in this study. Often, with a third

laser pulse, $\sigma(t)$ and I(t) are decoupled (**Figure 7**) as evidenced by observation of the "tenting" phenomenon. With "tenting", $\sigma(t)$ increases during the laser pulse, and decreases sharply with termination of laser irradiation. After extensive heating (e.g. three laser pulses or water bath pre-heating) in the two layer model, both superficial and deep layers have been adequately heated to the critical temperature required to accelerate stress relaxation. No further stress relaxation occurs. The increase in internal stress $\sigma(t)$ during laser heating is likely due entirely to thermo-elastic expansion. "Tenting" occurs with increasing frequency in specimens which have been preheated in water baths (**Figure 8**).

An alternative explanation for this observation is that thermal modification of the entire tissue specimen is not required to achieve adequate stress relaxation. As the cartilage is irradiated on its convex surface, irradiation of the superficial layers of cartilage may be enough to release interlocking forces (16-18); in essence creating a tissue effect analogous to scoring of the cartilage on one surface which has been observed to cause warping of the cartilage towards the opposite surface(19, 20).

An important observation from our experiments is that laser mediated stress relaxation of cartilage does not occur through protein denaturation alone. In other words, slow heating of cartilage produces changes in cartilage matrix that is different from that produced by photothermal modification alone. If protein denaturation alone is the mechanism for stress relaxation of cartilage, then we would expect Group D specimens, which are completely denatured, to exhibit decoupling at the first irradiation. This was not observed. However, slow heating does appear to facilitate the changes induced by photothermal modification as evidenced by the majority of Groups C and D specimens showing decoupling by the second irradiation in contrast to Groups A and B specimens which required three irradiations for the majority of specimens to become decoupled.

We speculate that bound to free water transitions, hydrogen bonding ,or selective dehydration of cartilage may also contribute to stress relaxation of cartilage. Further investigation will be necessary to determine whether these mechanisms play a role in laser mediated cartilage reshaping.

## 5. CONCLUSION

Inducing permanent shape change in cartilage using laser irradiation while maintaining tissue viability will minimize the need to harvest autologous cartilage and reduce donor site morbidity. We believe that in the long term this will lead to improved techniques to correct functional and aesthetic deformities of the cartilagenous structures in the head and neck. To optimize the process of laser-mediated cartilage reshaping, the underlying molecular mechanism must be characterized. This study focused on determining whether protein denaturation in cartilage matrix contributes to the reshaping process using specimens heated in a water bath. Characteristic parameters of diffuse reflectance and internal stress during laser exposure were measured in these denatured specimens and compared to native cartilage which had not been denatured. Our findings suggest that the denaturation of the framework of cartilaginous tissue only partially explains the phenomenon of laser mediated cartilage reshaping and that stress relaxation likely occurs through more than one mechanism. Further investigation will be needed to further elucidate the molecular mechanisms of accelerated stress relaxation of laser irradiated cartilage.

## 6. REFERENCES

1. Helidonis E, Sobol EN, Kavvalos G, et al. Laser Shaping of Composite Cartilage Grafts. American Journal of Otolaryngology 1993;14:410-412.

2. Sobol EN, Bagratashvili VV, Omel'chenko A, et al. Laser Shaping of Cartilage. Proceedings SPIE 1994;2128:43-49.

3. Wong BJF, Milner TE, Anvari B, et al. Measurement of radiometric surface temperature and integrated back-scattered light intensity during feedback controlled laser-assisted cartilage reshaping. Lasers in Medical Science 1998;13:66-72.

4. Wong BJF, Milner TE, Kim HK, Nelson JS, Sobol EN. Stress relaxation of porcine septal cartilage during Nd:YAG ($\lambda$ = 1.32 mm) laser irradiation: mechanical, optical, and thermal responses. Journal of Biomedical Optics 1998;3:409-14.

5. Wong BJF, Milner TE, Kim HK, et al. Characterization of Temperature Dependent Biophysical Properties During Laser Mediated Cartilage Reshaping. IEEE J Selected Topics Quantum Electronics 1999;5:1095-1102.

6. Wong BJF, Milner TE, Kim HK, et al. Proteoglycan Synthesis in Porcine Nasal Cartilage Grafts Following Nd:YAG ($\lambda$=1.32 $\mu$m) Laser Mediated Reshaping. Photochemistry and Photobiology 2000;in Press.

7. Pullin JG, Collier MA, Das P, et al. Effects of Holmium:YAG Laser Energy on Cartilage Metabolism, Healing, and Biochemical Properties of Lesional and Perilesional Tissue in a Weight-Bearing Model. Arthroscopy 1996;12:15-25.

8. Karamzadeh A, Wong BJF, Milner TE, Wilson M, Liaw L-H, Nelson JS. Angiogenic Response in the Chick Chorioallantoic Membrane Model to Laser-Irradiated Cartilage. Proceedings SPIE 1999;in Press.

9. Sviridov A, Sobol EN, Jones NS, Lowe J. Effect of Holmium laser radiation on stress, temperature and structure alterations in cartilage. Lasers in Medical Science 1998;13:73-77.

10. Ovchinnikov YM, Nikiforova GN, Svistushkin VM, et al. Arbitrary modification of cartilage shape under laser radiation. Russian Annals Otorhinolaryngology, 1995;3:5-10.

11. Helidonis E, Volitakis M, Naumidi I, Velegrakis G, Bizakis J, Christodoulou P. The histology of laser thermo-chondro-plasty. American Journal of Otolaryngology 1994;15:423-428.

12. Herman JH, Khosla RC. In vitro effects of Nd:YAG laser radiation on cartilage metabolism. Journal of Rheumatology 1988;15:1818-1826.

13. Smith RL, Montgomery L, Fanton G, Dillingham M, Schurman DJ. Holmium:YAG Laser Effects on Articular Cartilage Metabolism In Vitro. Proceedings SPIE 1994;2128:149-153.

14. Spivak JM, Grande DA, Ben-Yishay A, Menche DS, Pitman MI. The effect of low-level Nd:YAG laser energy on adult articular cartilage in vitro. Arthroscopy 1992;8:36-43.

15. Wong BJF, Milner TE, Harrington A, et al. Feedback Controlled Laser Mediated Cartilage Reshaping. Archives of Facial Plastic Surgery 1999;1:282-287.

16. Fry H. Interlocked stresses in human nasal septal cartilage. British Journal of Plastic Surgery 1966;19:276-278.

17. Fry H, Robertson W. Interlocked Stresses in cartilage. Nature 1967;251:53-54.

18. Fry H. Cartilage and cartilage grafts: the basic properties of the tissue and the components responsible for them. Plastic and Reconstructive Surgery 1967;40:426-439.

19. Gibson T, Davis W. The distortion of autogenous cartilage grafts: its cause and prevention. British Journal of Plastic Surgery 1958;10:257-74.

20. Gillies H. Plastic Surgery of the Face.London: Oxford University Press, 1920

## SESSION 4

# Photothermal Interactions II

# Hydrodynamic study of the behavior of chondroitin sulphate under nondestructive laser irradiation of cartilage

Emil N. Sobol*[a], Alexander I. Omel'chenko[a], Alexander P. Sviridov[a], Stephen E. Harding[b], Kornelia Jumel[b], Nickolas Jones[c]

[a]Institute of Laser and Information technologies, Russian Academy of Sciences
Pionerskaya 2, Troitsk, Moscow reg, 142092, Russia

[b]University of Nottingham, LE12 5RD, UK

[c]Queen's Medical Center, Nottingham, NG 2UH, UK

## ABSTRACT

The effects of laser irradiation on molecular mass and conformation of pure chondroitin sulphate dissolved in phosphate buffered saline were investigated using size exclusion chromatography/multi-angle light scattering (SEC/MALS) and sedimentation velocity in the analytical ultracentrifuge. In addition, cartilage pieces immersed in buffer were irradiated with a laser in order to study whether cartilage components may diffuse away from the matrix and into the surrounding aqueous medium as a result of laser treatment. Size exclusion chromatography/multi-angle light scattering and sedimentation velocity measurements showed that (a) laser irradiation decreases the molecular mass of chondroitin sulphate and (b) laser irradiation of cartilage induces diffusion of macromolecules into the medium. The results obtained allow us to understand the mechanism of stress relaxation and structural alterations in cartilage under non-destructive laser radiation.

**Keywords:** Laser, cartilage, molecular mass determination, sedimentation coefficient.

## 1. INTRODUCTION

The extracellular matrix in cartilage accounts for more than 90% of the volume of the tissue. It is composed of a dense network of fine collagen fibres which are embedded in a highly concentrated solution of aggregates in which proteoglycan molecules are attached to hyaluronic acid chains. The proteoglycans bind by a specific site at one end of the protein backbone which has a high affinity for a decasaccharide unit of hyaluronate[1]. In addition, link-protein molecules form an integral part of the aggregate structure and are supposed to increase the stability of the aggregate structure by bridging the proteoglycan molecule and the hyaluronate.

Stress relaxation and reshaping of cartilaginous tissue under non-destructive laser radiation is one of the novel applications of lasers in medicine[2-10]. It allows the potential treatment of deformed cartilage without any dramatic alterations in the structure of the extracellular matrix (ECM). A number of studies have been performed *in vitro* as well as *in vivo*, but the exact mechanism of laser induced stress relaxation in cartilage is not yet fully understood. Examination of the fine structure of ECM irradiated with atomic force microscopy has shown additional pores of tens of nms in size arising as a result of laser irradiation[11]. A phenomenological theoretical model of laser-induced alteration of cartilage structure has been presented which considers both the heating of the tissue and the diffusion of some components of ECM which are freed when tissue temperature was raised to some critical point (approx. 70° C)[12]. However, these components have as yet not been identified, and their molecular masses and diffusion properties have not been studied as far as we are aware. This paper describes a study on the effect of laser irradiation on pure chondroitin sulphate in solution and the effect of laser irradiation on the diffusivity of macromolecules through the cartilage matrix.

## 2.MATERIALS AND METHODS

Chondroitin sulphate was obtained from Sigma (No. 27042) and dissolved at a concentration of 10mg/ml in phosphate

* Correspondence: Email: sobol@laser.ru; Telephone/Fax: 007(095) 334 03 42



In *Laser-Tissue Interaction XI: Photochemical, Photothermal, and Photomechanical*, Donald D. Duncan, Jeffrey O. Hollinger, Steven L. Jacques, Editors, Proceedings of SPIE Vol. 3914 (2000)
1605-7422/00/$15.00

buffered saline (PBS, 0.01M phosphate/ 0.15M chloride, adjusted to pH 7.4). One aliquot of the solution (of 1.9 or 4 ml in volume) was irradiated using a Holmium:YAG laser (Verso Pulse 3000 Coherent) at an energy density of 0.55J/cm$^2$ at a pulse repetition rate of 5 Hz for 18 to 30 s to reach local temperatures of 70° C or 90° C. The temperature was measured with an accurately calibrated thermocouple.
In a second experiment, pieces of fresh porcine auricular cartilage (ten samples of a disk shape of 7 mm in diameter and 0.5 mm in thickness) were placed on the surface of 5ml of PBS (pH 7.4) in a syringe and held in that position during laser irradiation, the control samples (5g in total) was held in a similar syringe for the same length of time.
100µl of the pure chondroitin sulphate samples (treated and untreated) and the PBS (pH 7.4) from the irradiated and non-irradiated cartilage samples were injected into a SEC/MALS system in order to determine their absolute molecular masses[13] and aliquots of the pure chondroitin sulphate samples were used for sedimentation velocity studies[14].

### 2.1 SEC/MALS

The eluent (PBS as described above) was pumped at a flow rate of 0.8ml/min through the column system consiting of TSK G6000PW, TSK G5000PW, TSK G4000PW analytical columns protected by a guard column. The eluting fractions were monitored by a Dawn DSP multi-angle light scattering photometer (Wyatt Technology, Santa Barbara, USA) fitted with a 5mW He-Ne laser, and a Differential interferometric refractometer (Optilab 903, Wyatt Technology, Santa Barbara, USA). The injection volume was 100µl and the system was run at ambient temperature. Weight average molecular masses were obtained using the Zimm plot method in the dedicated ASTRA™ software using a value of 0.16ml/g for the specific refractive index increment (dn/dc)[15].

### 2.2 Sedimentation velocity in the analytical ultracentrifuge

400µl of sample and 400µl of solvent were loaded into respective solution and solvent channels of 12mm pathlength double sector ultracentrifuge cells. Samples were run in a Beckman Optima XL-I analytical ultracentrifuge (Beckman, Palo Alto, USA) fitted with a Rayleigh interference optical system at a temperature of 20° C and a speed of 50000rpm. Data acquisition was performed using the manufacturers software and sedimentation coefficients were determined using the DCDT routine developed by Stafford[15] which also gives the sedimentation coefficient distributions.

### 2.3 Chemical analysis

Toluidine Blue has been used to detect Proteoglycans of macromolecules diffused out of the cartilage matrix into the in phosphate buffered saline. $BaCl_2$ has been used to manifest sulphas groups in the solution.

## 3.RESULTS

Molecular masses and sedimentation coefficients obtained for the pure chondroitin sulphate sample are shown in table 1 and the elution profiles obtained from the pure chondroitin sulphate (irradiated and non-irradiated) and the aqueous medium ('diffusate') surrounding the irradiated and non-irradiated cartilage samples are shown in figures 1 and 2.
The molecular mass of the pure chondroitin sulphate decreased with laser irradiation and this decrease was greater at higher irradiation temperatures. The sedimentation coefficient however, remained fairly constant: this is typical for an elongated molecule, where loss of mass is compensated by loss in asymmetry ( and hence frictional resistance).
The diffusates from the irradiated and non-irradiated cartilage samples showed significant differences. Whilst there is no indication of any material present in the diffusate from the non-irradiated cartilage, two peaks are visible on the light scattering trace from the irradiated cartilage. Peak 1 of figure 2(b) is indicative of large molecular weight material and the second peak to which a concentration peak can be assigned (see figure 2(b) peak 2) elutes at an elution volume slightly higher than that of the pure chondroitin sulphate leading to the conclusion, that the majority of molecules which have diffused out of the cartilage matrix are slightly smaller in size than would be expected for chondroitin sulphate. Unfortunately, these 'diffusate' peaks are not sufficiently large to give sensible molecular mass values, but they qualitatively indicate that a macromolecular component has diffused from the cartilage into the buffer. Macromolecular concentrations of the diffusate were also too low for sedimentation velocity experiments.
Chemical analysis for the determination of sulphate groups and proteoglycan gave positive results for the PBS from the irradiated cartilage but were found to give negative results for the non-irradiated cartilage.

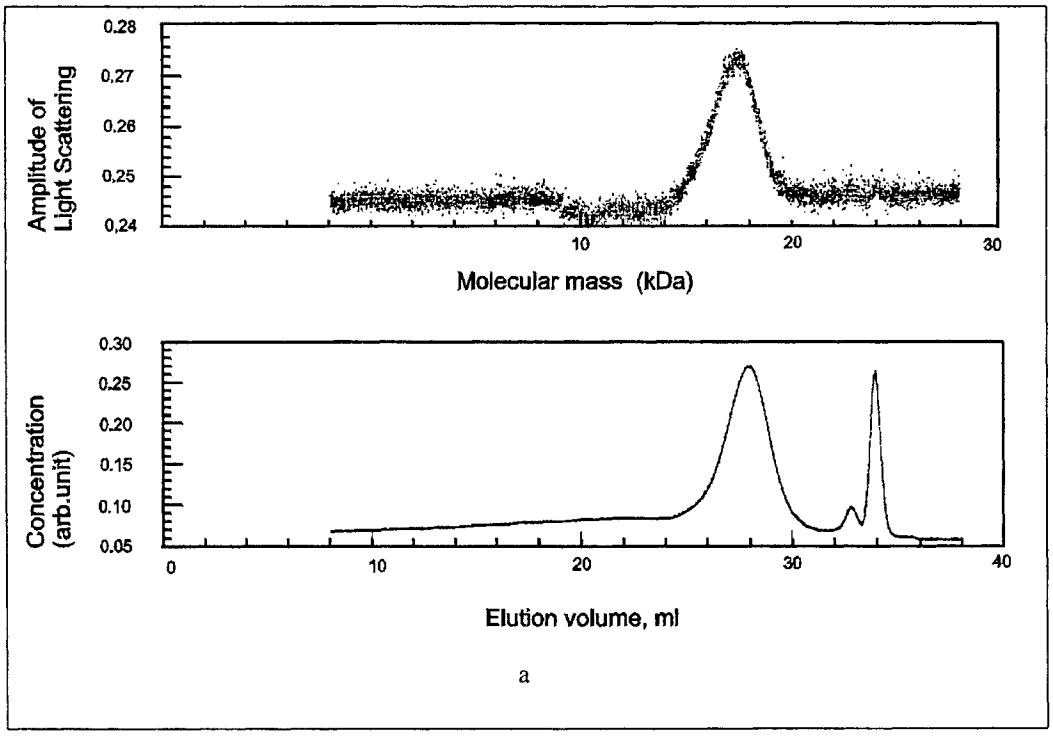


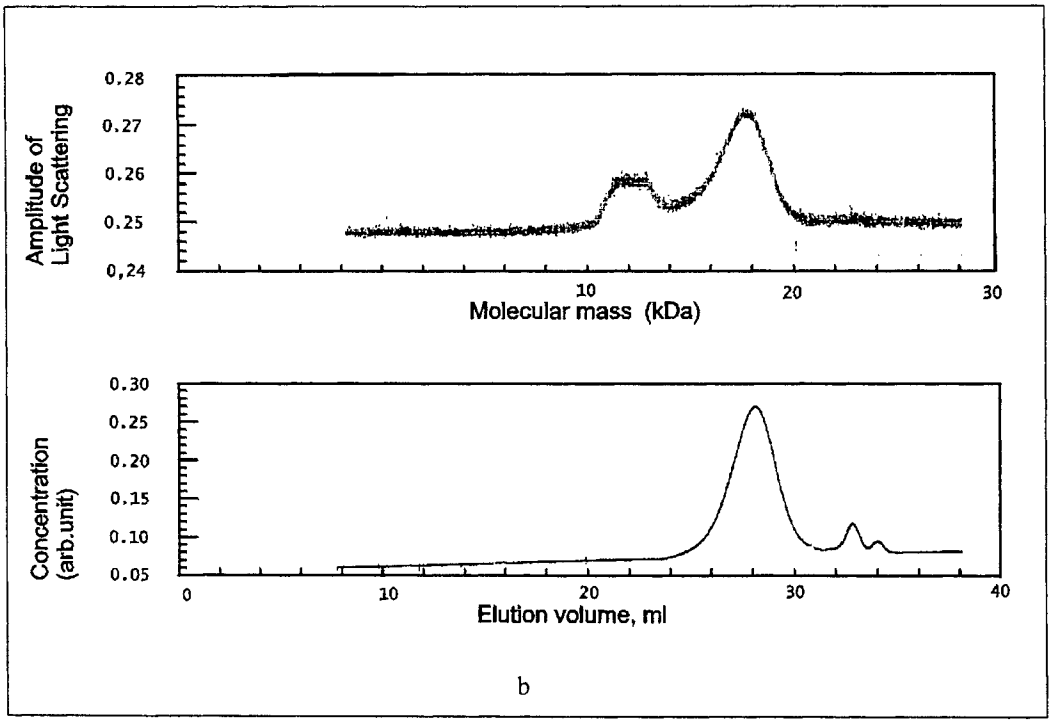


Fig. 1(a),(b). Molecular mass distribution and light scattering in the chondroitin sulphate solution
(a) - non-irradiated; (b) - irradiated.

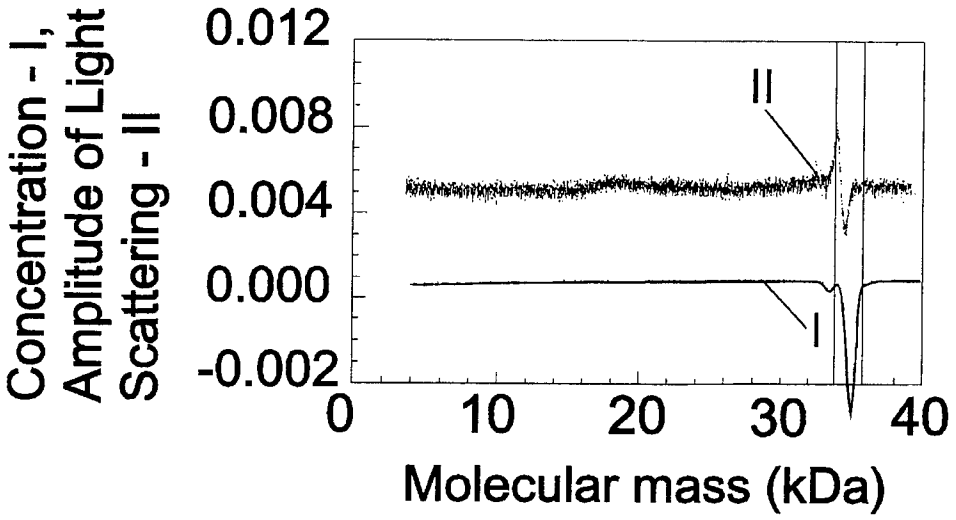


a

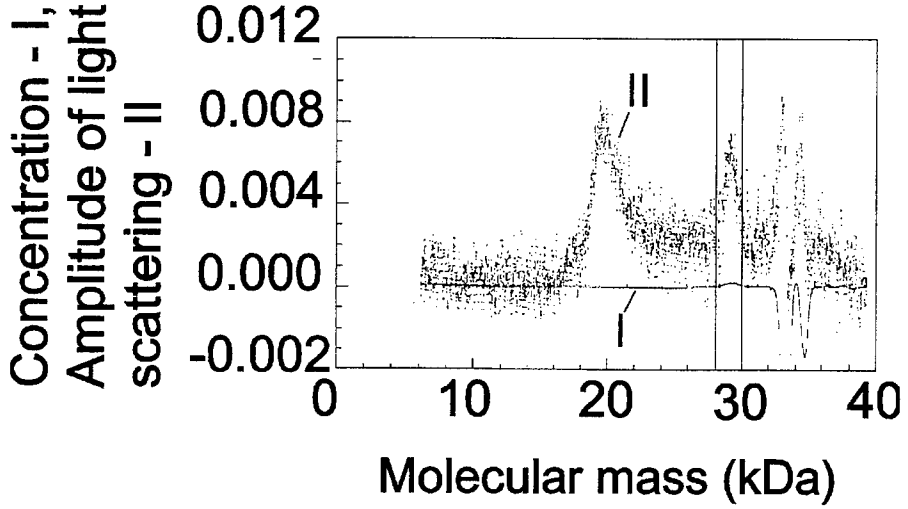


b

Fig.2 (a),(b) Molecular mass distribution and light scattering in the aqueous medium surrounding cartilage sample. (a) - non-irradiated; (b) - irradiated.

Table 1: Results from SEC/MALS and sedimentation velocity experiments for pure chondroitin sulphate

| Sample | Solution temperature as a result of irradiation | $M_w$, Da | $S \times 10^{13}$, $s^{-1}$ |
|---|---|---|---|
| Chondroitin sulphate, non-irradiated | | 21200±4800 | 1.351±0.001 |
| Chondroitin sulphate, irradiated | 90° C | 15500±2500 | 1.357±0.001 |
| Chondroitin sulphate, irradiated | 70° C | 17400±2400 | 1.354±0.001 |

## 4.DISCUSSION

The question central to this study was how laser treatment would effect components of cartilage - either the pure components or those within the cartilage itself, although we restricted ourselves initially to the investigation of chondroitin sulphate. The molecular mass obtained by SEC/MALS for the non-irradiated pure chondroitin sulphate agreed very well with literature values[1], whereas a decrease in molecular mass was detected after laser treatment, i.e., there is some disruption of the polymer chain. The SEC/MALS traces also revealed some aggregated material in the control sample which was no longer present after irradiation, a clear indication of disruption of the aggregates.

The more interesting finding was that of the diffusivity of material from cartilage into the buffer following laser treatment. Besides providing the structural framework for the cartilage, the extracellular matrix which contains the proteoglycans also forms a fluid compartment in which channels allow the flow of nutrients, ions, hormones etc. It is, therefore, very important the health of the cartilage tissue that these flow properties are maintained at the correct level. Previous experiments have shown[11] that laser treatment of cartilage induces channel formation and it was suggested that proteoglycan units detaching themselves from the hyaluronic acid backbone would be responsible for this channel formation. Our study has supported this hypothesis by clearly indicating that proteoglycans diffuse away from the cartilage matrix after laser irradiation. This finding consists with the theory of laser-induced alterations in cartilage structure[12] and allows to understand the molecular mechanism of the diffusion limitation of structural alterations. Moreover, it appears that these proteoglycans contain sulphate groups which suggests that it could be either keratan sulphate or chondroitin sulphate which diffuse out of the matrix. Comparison of chromatograms from the pure chondroitin sulphate and the 'diffusate' indicates a slightly higher elution volume for the latter, suggestive of lower molecular masses (even when compared to the irradiated chondroitin sulphate). However, according to Newman[17] the length of the chondroitin sulphate attachment region may vary depending on the age of the cartilage. Keratan sulphate would also fulfill the criteria of a sulphate bearing proteoglycan, however the molecular mass of this material has been quoted as approx.5500 Da which would suggest that the elution volume of this material would be higher than that measured, especially, when some degradation of the material must be expected due to laser irradiation. Obviously, full chemical analysis is required to determine the true nature of the diffusing component.

## 5.CONCLUSIONS

We have shown that (a) laser irradiation decreases the molecular mass of chondroitin sulphate and (b) laser irradiaton of cartilage induces diffusion of macromolecules into the medium. The results obtained allow us to understand the mechanism of stress relaxation and structural alterations in cartilage under non-destructive laser radiation.


## ACKNOWLEDGEMENTS

We are grateful to Professor V.N. Bagratashvili for helpful discussion. The authors thank INTAS (grant 97-1430) and the Russian Foundation of Basic Research (grants 97-02-17465 and 99-02-16906) for financial support.

## REFERENCES


1. T. Hardingham, "Proteoglycans: Their structure, interactions, and molecular organization in cartilage." *Biochem. Soc. Trans.* **9**, pp. 489-497, 1981.
2. J.M. Spivak, D.A. Grande, A. Ben-Yishay, D.S. Menche and M.I. Pitman, "The effect of low-level Nd:YAG laser energy on adult articular cartilage in vitro." *Arthroscopy* **8**(1), pp. 36-43, 1992.
3. Z. Wang, M.M. Pankratov, D.F. Perrault and S.M. Shapshay, "Laser-assisted cartilage reshaping: in vitro and in vivo animal studies." *Proc. SPIE* **2395**, pp. 296-302, 1995.
4. Z. Wang, D.F. Perrault, M.M. Pankratov and S.M. Shapshay, "Endoscopic laser-assisted reshaping of collapsed tracheal cartilage." *Ann. Otol Rhinol Laryngol* **105**, pp. 176-181, 1996.
5. J.G. Pullin, M.A. Collierr, D.V.M. Prajnan, R.L.Smith, L.E.DeBault, L.L.Johnson, R.C. Walls, "Effects of Holmium:YAG laser energy on cartilage metabolism, healing, and biochemical properties of lesional and perilesional tissue in a weight-bearing model." *Arthroscopy* **12**(1), pp. 15-25, 1996.
6. M.A. Collier, L.M. Haugland, J. Bellamy, L.L. Johnson, M.D. Rohrer, R.C. Walls, K.E. Bartels, "Effects of Holmium:YAG laser on equine articular cartilage and subchondral bone adjacent to traumatic lesions: a histopathological assessment." *Arthroscopy* **9**(5), pp. 536-545.
7. E. Helidonis, E. Sobol, G. Kavvalos, J. Bizakis, P. Christodoulou, G. Velegrakis, J. Segas, V.N. Bagratashvili "Laser shaping of composite cartilage grafts." *Amer. J. Otolaryngol.* **14**, pp. 410-412, 1993.
8. E.N. Sobol, *Phase Transformations and Ablation in Laser-treated solids*. Wiley, New York, 1995.
9. V.N. Bagratashvili, E.N. Sobol, A.P. Sviridov, A.I. Omelchenko and V.K. Popov, "Thermal and diffusion processes in laser-induced stress relaxation and reshaping of cartilage." *J. Biomech.* **30**(8), pp. 813-817, 1997.
10. A. Sviridov, E. Sobol, N. Jones and J. Lowe, "Effect of Holmium laser radiation on stress temperature and structure alterations in cartilage." *Lasers in Med. Sci.* **13**, pp. 73-77, 1998.
11. E. Sobol, M. Mertig, W. Pompe, and A. Omel'chenko, "Scanning force microscopy of the fine structure of cartilage irradiated with $CO_2$ laser." *Lasers in Med. Sci.* **15**(6), 1999. (accepted for publication)
12. E.N. Sobol, M.S. Kitai, N. Jones, A.P. Sviridov, T.E. Milner and B.J.Wong, "Heating and structural alterations in cartilage under laser radiation," *IEEE Journal of Quantum Electronics*, **35**(4), pp. 532-539, 1999.
13. P.J. Wyatt, "Light scattering and the absolute characterization of macromolecules." *Anal. Chim. Acta* **272**,pp.1-40, 1993.
14. G. Ralston, *Introduction to analytical ultracentrifugation.* Beckman Instruments Inc., Fullerton, 1993.
15. R.G. Kitchen and R.L. Cleland, "Dilute solution properties of proteoglycan fractions from bovine nasal cartilage." *Biopolymers* **17**, pp. 759-783, 1978.
16. W.F. Stafford, "Boundary analysis in sedimentation transport experiments: A procedure for obtaining sedimentation coefficient distributions using the time derivative of the concentration profile." *Anal. Biochem.* **203**, pp. 295-301, 1992.

# Laser-tissue photothermal interaction and tissue temperature change

Andrea K. Ives [a], Wei R. Chen [*a, b], Baha Jassemnejad [a], Kenneth E. Bartels [c], Hong Liu [d], John A. Nordquist [e] and Robert E. Nordquist [e, f]

[a] Department of Physics, University of Central Oklahoma, Edmond, OK 73034

[b] Department of Physics and Astronomy, University of Oklahoma, Norman, Oklahoma 73109

[c] Department of Medicine and Surgery, College of Veterinary Medicine, Oklahoma State University, Stillwater, OK 74078

[d] Department of Radiology and Biomedical Engineering, Johns Hopkins University, Baltimore, MD 21205

[e] Wound Healing of Oklahoma, 3945 N. Walnut Street, Oklahoma City, OK 73105

[f] Department of Ophthalmology, University of Oklahoma, Oklahoma City, OK 73104

## ABSTRACT

Responses of tissue to laser stimulation are crucial in both disease diagnostics and treatment. In general, when tissue absorbs laser energy photothermal interaction occurs. The most important signature of the photothermal reaction is the tissue temperature change during and after the laser irradiation. Experimentally, the tissue reaction to laser irradiation can be measured by numerous methods including direct temperature measurement and measurement of perfusion change. In this study, a multiple-channel temperature probe was used to measure tissue temperature change during irradiation of lasers with different wavelengths at different power settings. Tissue temperature in chicken breast tissue as well as skin and breast tumor of rats was measured during irradiation of an 805-nm diode laser. The vertical profiles of temperature were obtained using simultaneous measurement at several different locations. The absorption of laser energy by tissue was enhanced by injecting laser-absorbing dye into the tissue. A Nd:YAG laser of 1064-nm wavelength was also used to irradiate turkey breast tissue. Our results showed that both laser penetration ability and photothermal reaction depended on the wavelength of lasers. In the case of 805-nm laser, the temperature increased rapidly only in the region close to the laser source and the thermal equilibrium could be reached within a short time period. The laser absorbing dye drastically enhanced the thermal reaction, resulting in approximately 4-fold temperature increase. On the contrary, the laser beam with 1064-nm wavelength penetrated deeply into tissue and the tissue temperature continued increasing even after a 10-minute laser irradiation.

**Keywords**: 805-nm diode laser; 1064-nm Nd:YAG laser; Photothermal-tissue interaction; Indocyanine green; Temperature distribution

* Correspondence: Email: wchen@ucok.edu; Telephone: 405/974-5198; Fax: 405/974-3812



In *Laser-Tissue Interaction XI: Photochemical, Photothermal, and Photomechanical*, Donald D. Duncan, Jeffrey O. Hollinger, Steven L. Jacques, Editors, Proceedings of SPIE Vol. 3914 (2000)
1605-7422/00/$15.00

# 1. INTRODUCTION

Responses of tissue to laser stimulation are crucial in both disease diagnostics and treatment. Tissue absorption of laser energy in general produces three major photophysical reactions: photomechanical, photochemical and photothermal. [1-4] Among the three interactions, photothermal is the most common and is an important phenomenon. The photothermal reaction manifests itself in terms of tissue temperature change and tissue thermal damage. The photothermal reactions can cause tissue structure change at different levels, ranging from recoverable disruption to moribund damage. [5-7] The temperature distribution inside tissue is crucial in the laser treatment of lesions. When treating diseases, strong photothermal interaction is required. However, to treat deep lesions, a laser beam should be able to penetrate deeply into tissue. Lasers in the near infrared can penetrate organized tissue more readily than other lasers due to low light absorption of water. Therefore, near-infrared lasers can penetrate tissue without causing much damage in the path of the laser beam. Laser-tissue interaction with lasers in this wavelength region can be enhanced selectively using localized laser-absorbing dye to achieve the selective tissue destruction.

One laser-absorbing dye, Indocyanine green (ICG), is particular interesting because of its non-toxic nature and its absorption spectrum. It has an absorption peak around 800 nm, matching perfectly the 805-nm diode laser. When ICG is injected into a target tissue, the 805-nm laser causes the temperature of the target tissue to dramatically increase while leaving surrounding tissue unaffected. [8-12] This can be specifically important in the treatment of cancer where the temperature within a tumor should be above 60°C for hyperthermia treatment. A clear temperature profile during laser treatment, with or without absorbing dye can provide optimal treatment parameters.

In order to control the photothermal treatment procedure, it is crucial to understand quantitatively the tissue reactions, particularly the temperature distribution during the laser treatment, the thermal equilibrium of tissue, the maximum temperature increase, and relaxation of tissue after treatment.

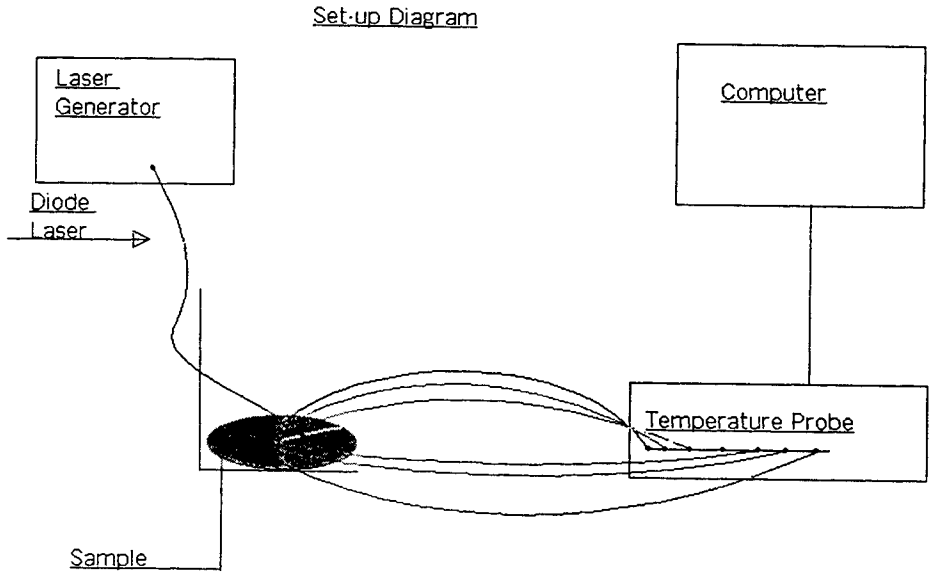


**Figure 1.** Set up of temperature measurement during laser irradiation of tissue.

## 2. MATERIALS AND METHODS

### 2.1 Tumor model

The animal model used in our experiments was the metastatic, rat mammary tumor in Wistar Furth female rats. Approximately $10^5$ live cancer cells were injected into the inguinal fat pad of the rats. For detailed information on the tumor model, see Refs. 13-15.

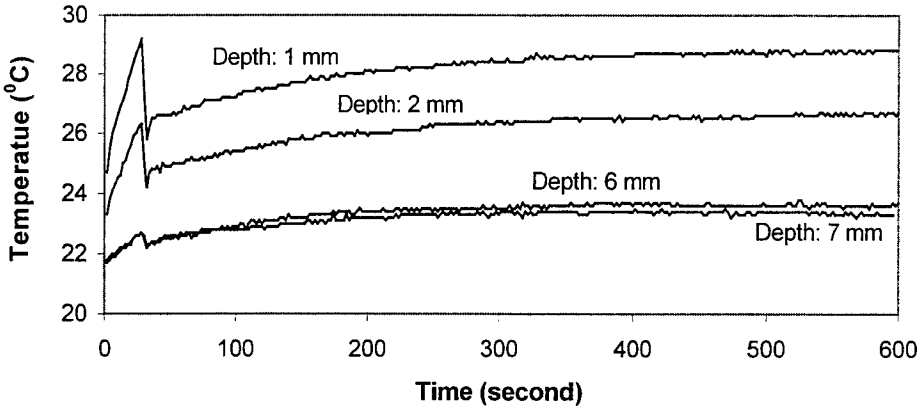


**Figure 2.** The chicken breast tissue temperature during irradiation of the 805-nm laser. The power setting was 2 watts for 10 minutes. The range of tissue depth for the measurement is 1 to 7 mm below the laser beam.

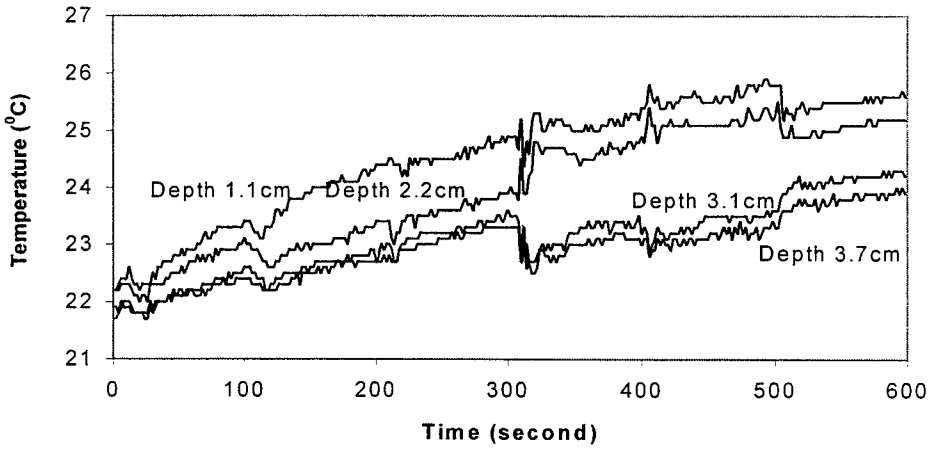


**Figure 3.** The turkey breast tissue temperature during irradiation of the 1064-nm laser. The power setting was 2 watts for 10 minutes. The range of tissue depth for the measurement is 1.1 cm to 3.7 mm below the laser beam.

## 2.2 Non-tumor model

Chicken and turkey breast tissue was used in laser irradiation. The tissue was cut into square sections and various irradiation tests were performed on them, including tests involving the injection of laser-absorbing dye.

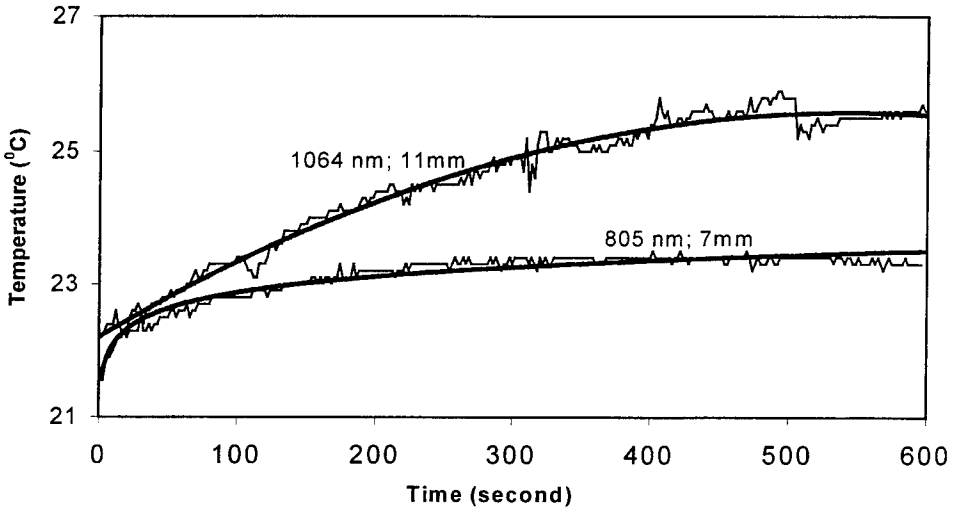


**Figure 4.** Temperature profile of turkey breast tissue under irradiation of two different lasers (2 watts for 10 minutes). At 11-mm depth, the 1064 nm laser caused the temperature to increase continuously throughout the 10-minute treatment. On the contrary, the temperature of the tissue under irradiation by 805 nm only increased during the first three minutes of the irradiation and quickly reached the thermal equilibrium. The thick solid line is a data-fitted curve to aid the eye.

## 2.3 Laser irradiation and temperature measurement

One laser used in this experiment was an 805-nm diode laser. The energy of the laser was delivered through an optic fiber to the treatment surface, and the tip of the fiber was maintained at a fixed distance (4 mm) from the treatment surface for the duration of the tests. The laser beam on the treatment surface is 3 mm in diameter. The secondary laser that was used for the purpose of comparison in this experiment was a Nd:YAG 1064-nm laser. The diameter of Nd:YAG laser beam is 2.5 cm. Data was collected using an OM-700 Omega Engineering Data Acquisition and Control Unit temperature probe, along with seven Omega copper constantine probes. The experimental set-up is given in Figure 1. The laser-absorbing dye used was indocyanine green (0.25%) which has a strong absorption peak around 800 nm.

## 2.4 Vertical temperature distribution in tissue

The vertical profiles of temperature distribution were obtained using simultaneous measurement at several different locations in chicken and turkey breast tissue. The breast tumors in rats were also treated by the 805-nm laser with different settings. The temperature of the tumor tissue at different depths during the treatment was recorded. Probes were placed under the skin (above the tumor), directly below the surface of the tumor, and deep in the tumor. One probe was inserted into the hind leg as a base line to record normal body temperatures away from the laser.

### 2.5 Dye enhancement of laser irradiation

To enhance the absorption of laser energy, a 0.3cc solution of ICG at 0.25% concentration was injected into the target tissue at a centered position of the rat tumor and an elapse time of five minutes was observed to ensure even distribution.

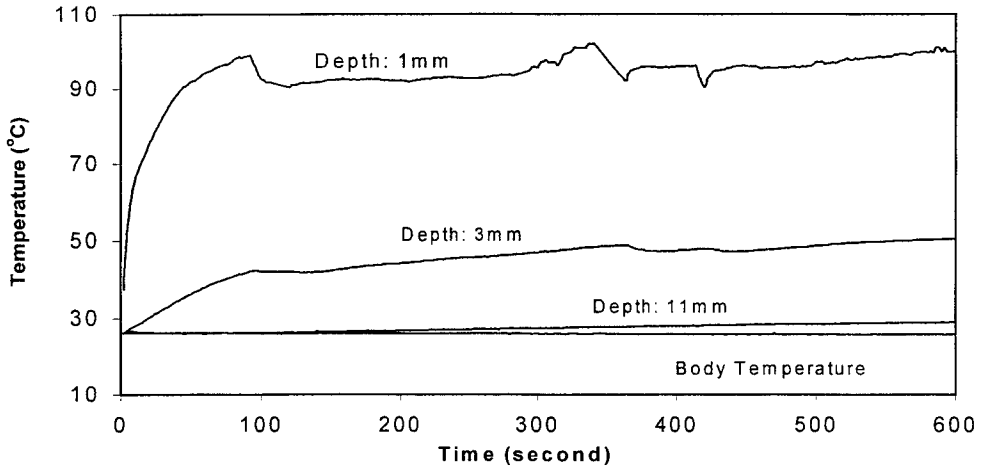


**Figure 5.** Temperature of tissue irradiated by the 805-nm laser with the aid of ICG solution in tissue. The surface of the tumor (1 mm beneath the surface of the skin) reached a temperature close to $100^0$C. This is partly due to strong coupling of the laser and the dye and partly due to the accumulation of ICG under the skin. At the depth of 3 mm, the ICG aided laser energy absorption caused the temperature increase to about $50^0$C. Comparing to the body base temperature, even tissue at a depth of 11 mm experienced a temperature increase.

## 3. RESULTS

### 3.1 Laser depth penetration

Using the 805-nm laser at a power of 2 watts, probes were placed vertically ranging from 1 to7-mm in chicken breast tissue, and the laser depth penetration was investigated. It was found that the temperature of surface tissue increased quickly at the beginning of the irradiation. Temperature change in deep tissue (depth > 6 mm) was not significant (Figure 2). The maximum temperature at all depths was reached and saturation occurred after approximately five minutes of irradiation.

In comparison, the 1064-nm laser was found to be able to cause temperature increase over a long period and in a wide range of depth (Figure 3). Using the 1064-nm laser at a power of 2 watts, probes were placed beneath the laser fiber ranging from 11 to 37 mm in turkey breast tissue, and the laser depth penetration and absorption were examined. The temperature of the tissue at all depths continued to increase even at the end of the ten-minute test period.

The temperature increase using the two different lasers were compared at a depth of 7 mm (for 805-nm laser) and 11 mm (for 1064-nm laser). The results are given in Figure 4.

### 3.2 Effects of laser absorbing dye in tissue

Indocyanine green solution of 0.3cc (0.25%) was injected to the center of a rat breast tumor (2 cm diameter). Five minutes later, the tumor was irradiated by the 805-nm laser at a power of 2 watts for ten minutes. The

probes were placed vertically ranging from 1 to 11 mm. The result was a significant temperature increase at depths of 1 mm and 3 mm. Even at the depth of 11 mm, the temperature increase was noticeable (Figure 5). Under the same condition, the temperature of the tumor without ICG only increased slightly during the course of the 10-minute irradiation (Figure 6).

### 3.3 Tissue Thermal Relaxation

Using the 805-nm laser, it was found that it takes approximately 10 minutes for the tissue sample to return to within a few degrees of its original temperature, as shown in Figure 7, after laser irradiation of a rat tumor for 10 minutes at 1.2 watts. Other experimental measurement showed that the longer a sample is irradiated, the higher the power it is irradiated at, or if a sample receives multiple treatments, the less likely it is that the tissue sample will return to its original temperature.

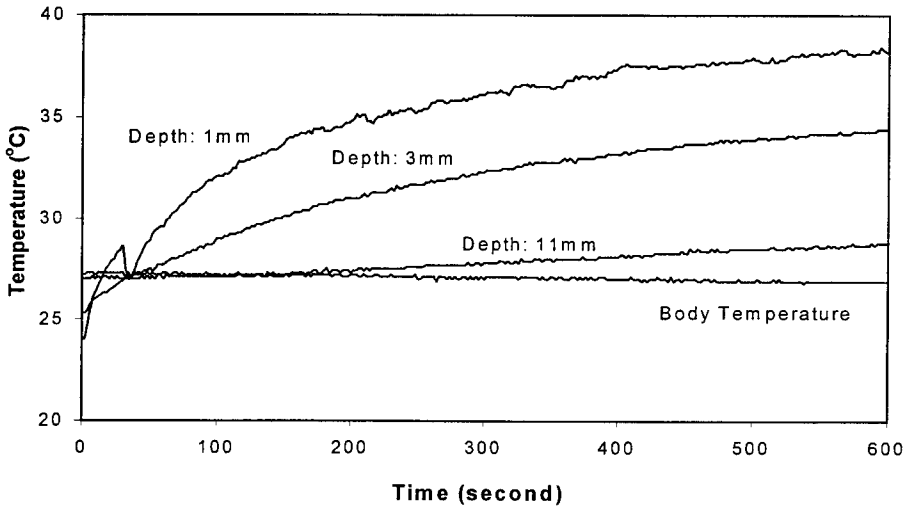


**Figure 6.** Temperature of tissue irradiated by the 805-nm laser without the injection of ICG solution. The surface of the tumor (1 mm beneath the surface of the skin) only experienced a mild temperature increase, reaching a maximum of 38°C.

## 4. DISCUSSION

The objectives for this experiment were to study the response of tissue to laser irradiation. The temperature profiles in chicken and turkey breast as well as tumor tissue in rats were directly measured using a multi-channel temperature probe during laser irradiation. The temperature changes in tissue samples due to the laser-enhancing dye Indocyanine Green were also examined, as well as the effects on tissue samples due to lasers of different wavelengths.

Using the 805-nm laser, a distinct trend was observed between tissue temperature and the duration of laser treatment. During the first five minutes a significant temperature rise on the surface of tumor was observed, and from five to ten minutes the thermal equilibrium was reached, as shown in Figure 2. In comparison, the 1064-nm laser caused a continued temperature increase in tissue over the entire experiment period (a ten-minute time span), as shown in Figure 3. The difference of temperature change using the two different lasers was given in Figure 4. It should be noted, however, that the beam spots of the two lasers were not identical. The beam spot of the 805-nm laser is 3 mm in diameter compared to 25-mm in diameter for the 1064-nm laser.

The laser-absorbing dye in situ makes significant difference in temperature change in tissue. With appropriate dye concentration and accumulation in tissue, the temperature could reach $100^0$C in the tissue close to the laser source, as shown in Figure 5. Even at certain depth, the increase of temperature was significant. Without ICG, the absorption of 805-nm laser energy by tissue only caused a limited temperature increase even in the tissue close to the source of the laser, as shown in Figure 6.

It took approximately 10 minutes for the tissue irradiated by the 805-nm laser to return to its original temperature during the relaxation time provided that no moribund damage had occurred to the surface, as shown in figure 4. The similar results were also obtained using the 1064 nm laser in chicken and turkey breast tissue.

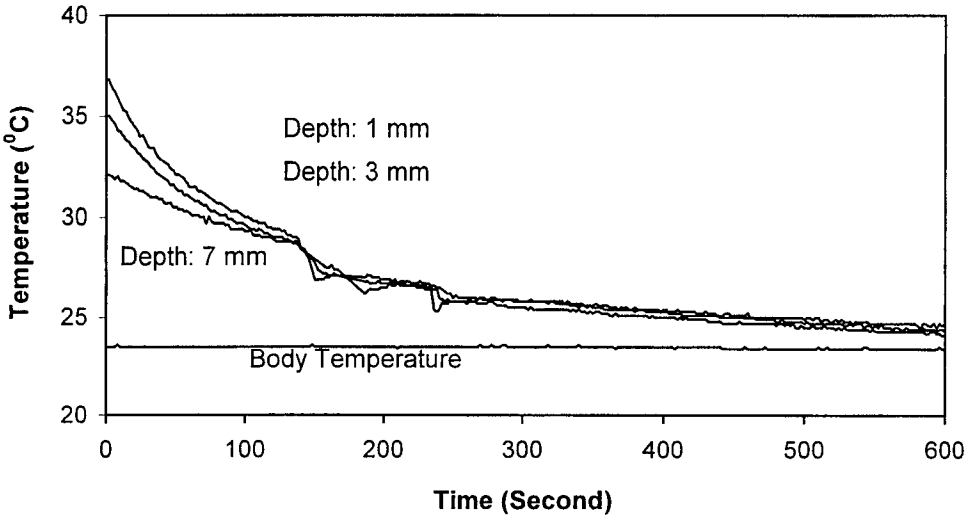


**Figure 7.** Thermal relaxation of a rat tumor after 10-minute irradiation by the 805-nm laser irradiation at 1.2 watts, without dye enhancement. The depths of placed temperature probe were 1 mm to 7 mm.

In summery, the results showed that tissue temperature profiles under laser irradiation are effected by the power and wavelength of the laser. These results obtained in our current experiments showed that the outcome of laser treatment, such as temperature increases and thermal equilibrium in tissue, can be controlled by laser settings and by dye enhancement. These data are useful in laser treatment and detection of lesions, where laser and dye parameters are crucial.

## 5. ACKNOWLEDGMENTS

This research was supported in part by a grant from the University of Central Oklahoma Office of Sponsored Research & Grants.

## 6. REFERENCES

1. J.-L. Boulnois, "Photophysical processes in recent medical laser developments: a review," Lasers Med Sci, Vol. 1, pp. 47-66, 1986.
2. S. L. Jacques, "Laser-tissue interactions," The Cancer Bulletin, Vol. 41, pp. 211-218, 1989.
3. S. Thomsen, "Pathologic analysis of photothermal and photomechanical effects of laser-tissue interactions," Photochemistry and Photobiology, Vol. 53, pp. 825-835, 1991.

4. S. L. Jacques, "Laser-tissue interactions. Photochemical, photothermal, and photomechanical," Surg Clin North Am, Vol. 72, pp. 531-558, 1992.
5. A. L. McKenzie, "A three-zone model of soft-tissue damage by a $CO_2$ laser," Phys Med Biol, 31:967-983, 1986.
6. A. L. McKenzie, "An extension of the three-zone model to predict depth of tissue damage beneath Er:YAG and Ho:YAG laser excisions," Phys. Med. Biol. Vol. 34(1):107-114, 1989.
7. A. L. McKenzie, "Theoretical limits to soft-tissue damage by Er:YAG and Ho:YAG lasers," Lasers in Medical Science, (March) 25-30, 1989.
8. W. R. Chen, R. L. Adams, S. Heaton, D. T. Dickey, K. E. Bartels, and R. E. Nordquist, "Chromophore-enhanced laser-tumor tissue photothermal interaction using an 808-nm diode laser," Cancer Letters, Vol. 88, pp. 15-19, 1995.
9. W. R. Chen, R. L. Adams, K. E. Bartels, and R. E. Nordquist, "Chromophore-enhanced in vivo tumor cell destruction using an 808-nm diode laser," Cancer Letters, Vol. 94, pp. 125-131, 1995.
10. W. R. Chen, R. L. Adams, A. K. Higgins K. E. Bartels, and R. E. Nordquist, "Photothermal effects on murine mammary tumors using indocyanine green and an 808-nm diode laser: an in vivo efficacy study," Cancer Letters, Vol. 98, pp. 169-173, 1995.
11. W. R. Chen, R. L. Adams, C. L. Phillips and R. E. Nordquist, "Indocyanine green in situ administration and photothermal destruction of tumor tissue using an 808 nm diode laser", SPIE Vol. 2681, pp. 94-101 1996
12. W. R. Chen, R. L. Adams, A. K. Higgins and R. E. Nordquist, "Effects of indocyanine green in treatment of murine mammary tumor by an 808 nm diode laser: an in vivo study", SPIE Vol. 2675, pp. 114-121, 1996.
13. U. Kim, "Metastasizing mammary carcinomas in rats: Induction and study of their immunogenicity," Science, 167, 72-74, 1970.
14. U. Kim, "Pathogenesis of spontaneously metastasizing mammary carcinomas in rats," Gann Monogr, 20, 73-81, 1977
15. U. Kim, "Characteristics of metastasizing and nonmetastasizing tumors and their interactions with the host immune system in the development of metastasis," Proc. European Organization for Research on Treatment of Cancer Metastasis Group international Conference on Clinical and Experimental Aspects of Metastasis, Editors: Hellman, K., Hilgard, P., and Eccles, S. Nijhoff, The Hague, The Netherlands, pp210-214, 1981.

# Kinetics of water transfer and stress relaxation in cartilage heated with 1.56 μm fiber laser

Victor Bagratashvili*[a], Nodar Bagratashvili[a], Alexander Sviridov[a], Emil Sobol[a], Alexander Omel'chenko[a], Svetlana Tsypina[a], Valentin Gapontsev[b], Igor Samartsev[b], Felix Feldchtein[c], and Roman Kuranov[c]

[a]Institute of Laser and Information Technologies, Russian Academy of Sciences, Troitsk, Moscow Region, Pionerskaya 2, Russia, 142092
[b]IRE Polus, Fryazino, Moscow Region, Russia
[c]Institute of Applied Physics, Russian Academy of Sciences, Nizhny Novgorod, Russia

## ABSTRACT

In this work we have used for the first time 1.56 μm fiber laser to study mechanisms of IR laser induced stress relaxation in cartilage. We have applied several *in-situ* monitoring techniques: local temperature measurements (IR radiometry and thermocouple), IR-light absorption, direct stress measurements, micro-balancing, visible light scattering and optical coherent tomography. We have measured temporal behavior of 1.56 μm laser light transmission through the cartilage sample at different intensities with synchronous temperature and stress monitoring. The observed bleaching effect (self-induced transparency) is caused by water release from irradiating zone, water evaporation from the cartilage surface and, also, by temperature shift and decrease of intensity of water absorption bands.

## 1. INTRODUCTION

The phenomenon of IR laser induced stress relaxation in cartilage tissue, established and studied in works [1-14](see, also the program of this conference), provides the basis for new types of laser medical operations (procedures) in otolaryngology, cosmetology and spinal surgery - laser reshaping of cartilage. Some of these approaches (for example, reshaping of deformed human nasal septum [7,8]) are already very close to wide clinical use. To study the process of laser induced stress relaxation in cartilage, different physical (thermal, optical, mechanical and photo-acoustic) effects accompanied this process have been applied [9,10]. Laser induced alterations in cartilage structure have also been studied [9,11].

Kinetics of stress relaxation in a heated cartilage, as well, as post-treatment stability of new shape, is controlled by both microscopic, and macroscopic processes. The microscopic processes involve, in particular, "bound -to- free" transition of water in a cartilage heated up to about $70^0$C (the proportion of "bound" water in cartilage is about 4%), and liberation of proteoglycans. The macroscopic processes involve, water transport from a heated zone of cartilage, heat transfer, and diffusion of proteoglycans. Different lasers have been applied so far in cartilage laser reshaping experiments. In attempting to reshape cartilage of about 1mm in thickness, the use of $CO_2$ laser ($\lambda$=10.6 μm) leads to serious overheating of the surface with consequent damage to the cartilage[12]. This is caused by strong ($\alpha=10^3$ $cm^{-1}$) absorption in cartilage at this wavelength. As it was shown previously[11], there is some "gap" in the diagram of cartilage temperature/irradiation time which allows laser shaping, but avoids damage to cartilage The use of pulsed Ho laser ($\lambda$=2.09 μm ) [4,8,11], and Nd:YAG laser at $\lambda$=1.32 μm [13] and 1.44 μm [14] allows to provide much more homogeneous heating of cartilage. However, the question of the most efficient laser for this approach is still currently central point, especially in the context of its wide clinical application. When analyzing the applicability of different lasers, our attention was attracted by diode pumped Er fiber laser emitting at wide near IR spectral range.($\lambda$=1.45-1.75 μm). These compact, reliable and powerful (up to tens of watts) lasers (developed, first of all, for telecommunication purposes) are extremely perspective for various laser medical applications. The aim of this work is to

* Correspondence: Email: bagrat@omega.laser.ru: Telephone/Fax: +7 095 3340342



In *Laser-Tissue Interaction XI: Photochemical, Photothermal, and Photomechanical*, Donald D. Duncan, Jeffrey O. Hollinger, Steven L. Jacques, Editors, Proceedings of SPIE Vol. 3914 (2000) 1605-7422/00/$15.00

study in-vitro the optical and mechanical properties of cartilage irradiated with λ=1.56 μm fiber laser, to reveal optimal conditions of cartilage reshaping.

## 2. EXPERIMENTAL

Figure 1 shows the schematics of our experimental setup used for the investigation of optical and mechanical properties of laser irradiated cartilage. Samples of porcine (4 month old) nasal septum cartilage were cut into sections 0.5-2.0 mm in thickness, 3-5 mm in width and 10-12 mm in length.

The universal single mode cw erbium fiber laser ( model ELD-5, IPG Laser GmbH [15], wavelength λ=1.56 μm and maximal output power P=5W) has been used. Spot diameter was measured by conventional beam profiling method and varied from 3mm to 10 mm by changing the distance between the fiber and the cartilage surface.

The tissue temperature was detected with a needle-shaped thermocouple of 30 μm in diameter inserted 0.5 mm into a small incision made by a scalpel with marking in the posterior side of the cartilage.

The effect of laser radiation on mechanical stress was monitored with a calibrated tensiometer which measured the force made by the deformed cartilage without any movement of the sample. (see Fig.1b). The internal stress across the cartilage sample was adjusted by translating the tensiometer [9].

The IR laser transmission by cartilage sample and its temporal behavior at various levels of IR light intensity was performed with IR detector located just next to a cartilage sample. To avoid deformation of cartilage during its laser irradiation and drying, cartilage samples have been fixed in special holder (two metal plates with holes for laser beam transmission). Temporal behavior of signals from tensiometer, thermocouple and IR detector were visualized with an oscilloscope and a computer.

To monitor a spatial distribution of visible light (λ=0.633 μm) back-scattered from a cartilage sample, we have used the multi-fiber optical system (see Fig.1a). This system allows to deliver light scattered by cartilage sample to the optical multi-channel analyzer (OMA). Optical coherent tomography technique[16,17] has been used to monitor laser induced alterations of cartilage structure. Laser shaping of cartilage samples *in vitro* was performed as was described previously [9].

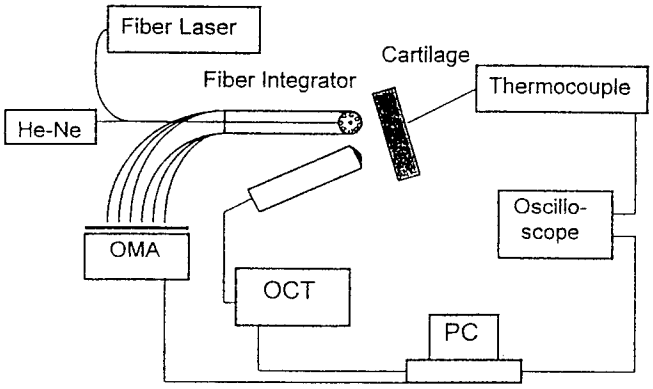


Fig.1a. Experimental setup for scattering and OCT measurements.

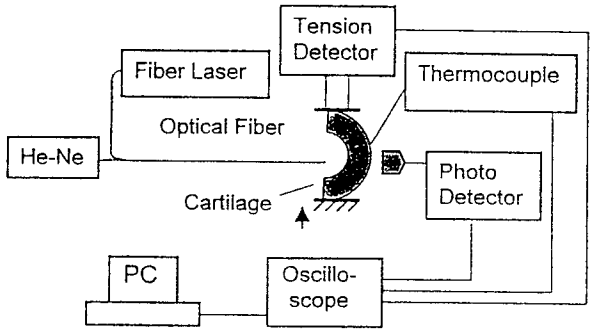


Fig.1b. Experimental setup for temperature, stress relaxation and IR transmission measurements.

## 3. RESULTS AND DISCUSSIONS

### 3.1. Kinetics of IR transmission.

To provide the optimal conditions for cartilage reshaping, one should have the depth of penetration of about the same value, as the thickness of treated tissue. Water in cartilage makes basic contribution to their IR absorption value in near IR spectral range. As it follows from IR absorption spectrum of liquid water[18], the absorption coefficient at λ=1.56 μm

is about 10 $cm^{-1}$. Since water concentration in fresh cartilage is about 70-80%, one can estimate the penetration depth in cartilage at this wavelength as about 1.2-1.3 mm. Our direct measurements of $\lambda$=1.56 μm fiber laser light transmission through slices of cartilage at a very low intensity (P=0.1W) gives slightly lower value of penetration depth – 1.0 mm. This can be explained by some contribution of scattering to transmission value.

Fig.2a demonstrates kinetics of $\lambda$=1.56 μm fiber l aser light transmission through the cartilage slice at different parameters of output laser power. As one can see, this kinetics is depends on laser light intensity. At low laser intensity the value of IR transmission is not dependent on irradiation time. At the same time, at higher laser intensities, the value of transmission becomes time dependent. The higher is laser intensity, the faster is the rate of tissue bleaching. At highest laser intensity given on Fig.2a the value of transmission after 7s of irradiation becomes more, 2.5 times higher then that before the beginning of irradiation.

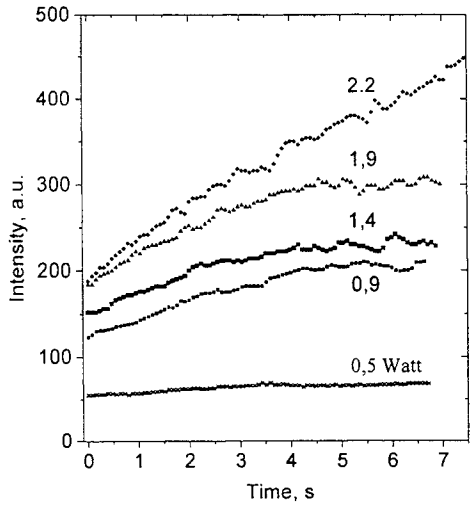


Fig.2a. Kinetics of transmission of 1.56μm laser light through cartilage sample (thickness-1.7mm) at different laser intensities (spot size on the sample-3mm).

In our view, the observed effect of self-induced transparency of IR laser irradiated cartilage is caused by heating of water. We consider several effects of water heating in cartilage. Firstly, heating of water causes de-aggregation of water molecules. This results in the decrease of oscillator strength for water IR absorption, and, also, in some shift of absorption band [19]. Secondly, temperature gradient in cartilage stimulates water transport across the sample from irradiated zone to non-irradiated one. Besides, heating increases the rate of water evaporation from a sample surface. One should, also, take into account, the contribution of scattering and its temperature dependence in irradiated cartilage. Notice, however, that cartilage heating increases intensity of scattered light and, thus, decreases transmission (see section 3.3). Besides, contribution of scattering to the transmission value in cartilage at $\lambda$=1.56 μm is much lower than that of absorption. This means that scattering doesn't contribute significantly to observed thermal bleaching effect at $\lambda$=1.56 μm

As it follows from Fig.2b, thermal bleaching effect in cartilage is partially reversible. Restoration of IR transmission in a cartilage after switching off the laser, is caused by a restoration of water concentration in the irradiated zone and increase of oscillator strength because of water cooling and aggregation. Some gradual rise of transmission observed in Fig.2b can be explained by water evaporation from the surface of heated cartilage sample.

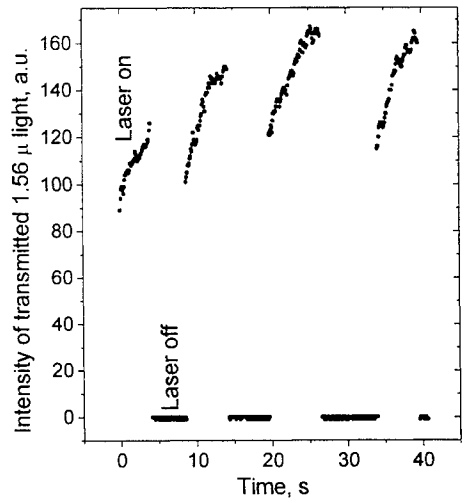


Fig.2b. Kinetics of transmission of 1.56μm laser light through cartilage sample (t=1.7mm) at step- by-step irradiation (spot size on the sample-3mm, P=1.9W).

### 3.2. Laser heating and stress relaxation.

The process of internal stress relaxation in laser irradiated cartilage tissue is controlled, first and foremost, by tissue temperature and, also, by its spatial and temporal evolution. For given cartilage sample this is governed, firstly, by laser irradiation parameters (wavelength, intensity, doze), secondly, by its optical properties (IR absorption and scattering), and, finally, by heat transport rate from irradiation zone. In our experiments we have measured the temperature of cartilage tissue by thin thermocouple placed in two different positions: at the center of laser spot, and at its periphery (see Fig.3). It should be noted, firstly, that despite the fact that IR laser light directly irradiates thermocouple, it is not overheated with respect to tissue. This follows directly from the analysis of temperature traces at the center of laser spot, and at its periphery.

From Fig.3 one can see that the temperature of cartilage sample in the center of laser spot (trace1) rises linearly with time at the first stage of irradiation, (t=0-3s), than almost stabilizes (at about 70$^0$C), and decreases rapidly when the laser is switched off. Deviation from a linear temperature relationship observed at t>3s, is due, firstly, to spatial spreading of heat, and, secondly, to temperature-induced decrease of IR absorption (see.Fig.2a and 2b).

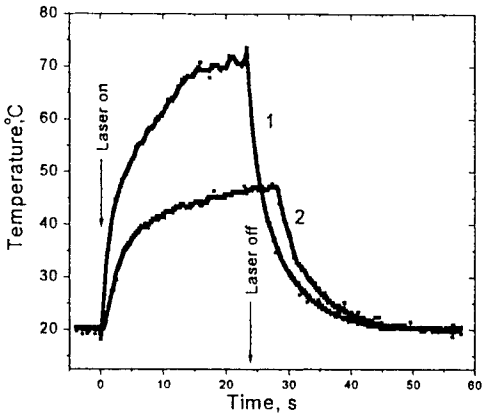


Fig.3. Kinetic of temperature change of cartilage sample (t=1.2mm) irradiated with 1.56μm laser light ( spot size on the sample-5mm; P=2.7W): 1- in the center of laser spot; 2 - at 3 mm distance from laser spot center.

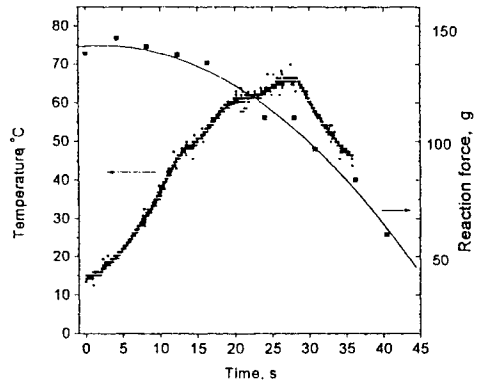


Fig.4. Kinetics of stress relaxation and temperature of cartilage sample (l=1.7mm) irradiated with 1.56μm laser light . Spot size on the sample-5mm; P=1.7W, sample width - 4mm.

The relationship between laser irradiation time, stress and temperature in cartilage are shown in Fig.4. At the very first step of IR laser irradiation reaction force slightly increases due to thermal expansion of cartilage. Further irradiation results in gradual decrease of reaction force. Our experiments show that the higher is laser intensity, the faster is the drop of the reaction force. The long-term stability of new shape is achieved only in the case of tissue heating up to 70°C, or higher. When cartilage heating is stopped at lower temperature, cartilage in 0.9% NaCl saline restores its initial shape completely after a lapse of time (from several minutes to several hours).

### 3.3. Light scattering and structural modification.

In order to prevent overheating of laser irradiated cartilage, a method is required to determine the laser doze which is sufficient for stable effect of stress relaxation (but avoids damage of tissue) to terminate irradiation. Since alterations in internal structure and mechanical properties of tissue are accompanied by changes of their optical properties (for example, light scattering), optimal conditions of laser reshaping may be selected using backscattered light from a probe laser, as a feedback control system [20]. The experiments on light scattering from laser irradiated cartilage produced with integrated sphere, demonstrate direct correlation of stress relaxation (and reshaping of cartilage) and character of backscattering behavior[9,20]. However, it is quite difficult to apply integrated sphere in practical medical procedure. This is why we have applied a simple multi-fiber optical system (see Fig.1a) to collect backscattered light from a laser irradiated cartilage.

Fig.5 demonstrates the kinetic curves of backscattered signal from cartilage irradiated with fiber laser. These signals are collected from different angles (points A, B and C) with respect to center of laser spot. They behave in different ways, and maximums of signals at different points take place at different irradiation times. Also, there is no correlation of these maximums with cartilage temperature. At the same time, the backscattering signal integrated over all fibers, reaches its maximum at about 70°C, that corresponds to irreversible stress relaxation temperature. It is quite naturally to explain such an irregular

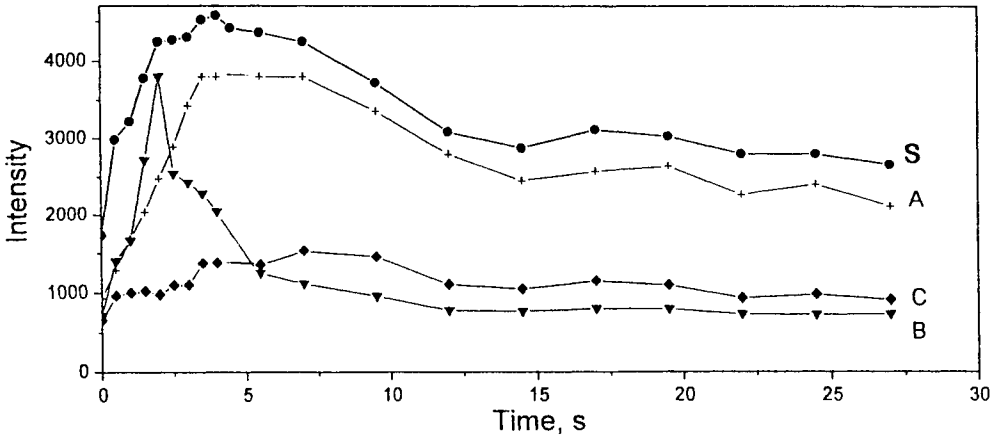


Fig.5. Kinetic curves of backscattered signal from cartilage irradiated with fiber laser.
A, B, C – collected from different angles ( wth different fibers), S – integrated over all fibers.

behavior of backscattering signals collected from different point (angles), by deformation of cartilage surface during its irradiation. This directly follows from OCT images from laser irradiated cartilage given at Fig.6. The signal recorded by our fiber system is composed of signal both scattered from a cartilage volume and reflected from a cartilage surface (surface reflectance is clearly seen at OCT images). It is clear that change in surface curvature affects angular distribution of reflected signal, and the signal recorded at some specific angle. Spatial integrating of light avoids this effect, and kinetics of integral signal (curve S at Fig.5 ) can give useful information about temporal behavior of backscattered light. The observed rise of scattered signal from cartilage at initial stage of its irradiation is caused by removal of water. Since water and cartilage matrix have different refractive indices, removal of mobile water from irradiated zone (see section 3.1) must increase the value of scattering signal. Further decrease of scattering at T>70$^0$C is caused, in our view, by liberation of "bound" water [6,9]. This leads to the lowering of matrix rigidity, its shrinking, and, as a result, to decrease of size of scattered centers and intensity of scattered light.

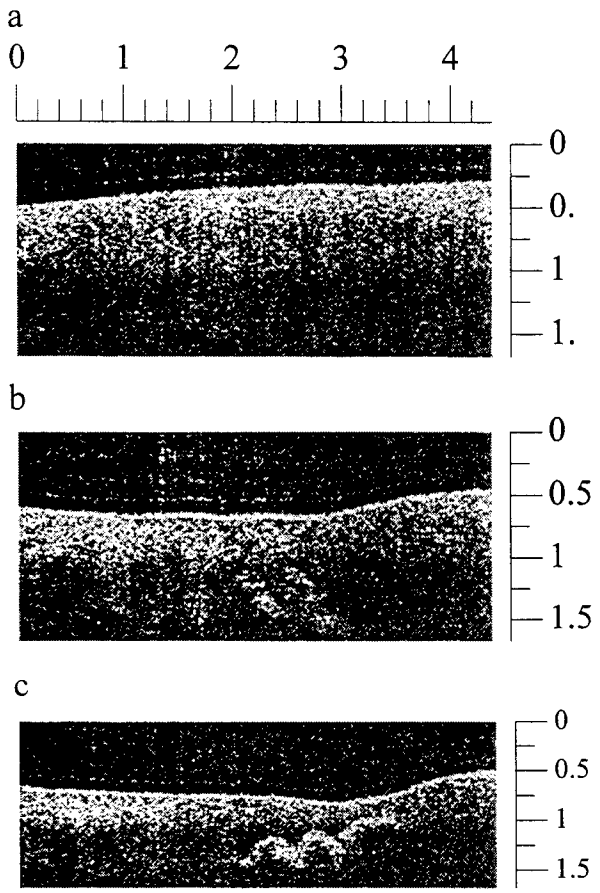


Fig.6. Optical coherent tomograph images of cartilage sample heated with 1.56μm fiber laser (P=2.2W, Spot size on the sample-9mm) at different irradiation times. a-initial; b-34 s; c-52s. Scales in mm.

## 4.CONCLUSIONS

Compact, reliable and powerful Er fiber lasers are extremely perspective for laser reshaping of cartilage, as well, as for other laser medical applications. Our studies of 1.56 μm fiber laser interaction with cartilage *in-vitro* demonstrate the effect of cartilage bleaching (self-induced transparency). This effect is caused by water release from irradiating zone, water evaporation from cartilage sample and, also, by temperature shift and decrease of intensity of water absorption bands. Light scattering and optical coherent tomography techniques have been used to reveal structural alterations in laser irradiated cartilage. The *in vivo* studies of λ=1.56 μm fiber laser reshaping of nasal septum are currently in progress.

## 5.ACKNOVLEDGEMENTS

We thank Russian Foundation for Basic Research (grants 99-02-16855, 00-02-16263), Foundation for Support of Leading Scientific Schools of Russia and INTAS (grant. 97-1430).

## 6. REFERENCES.

1. E.Helidonis, E.Sobol, G.Kavvalos, J.Bizakis, P.Christodoulou, G.Velegrakis, J.Segas, V.Bagratashvili, "Laser shaping of composite cartilage grafts", *Am. J. Otolaryngology*,. **14**, N6, pp. 410-412., 1993.
2. E.Helidonis, E.Sobol, G.Velegrakis, J.Bizakis, "Shaping of nasal septum cartilage with the carbon dioxide laser. Preliminary report of an experimental study", *Laser Med. Sci*, **9**, pp. 51-54, 1994.
3. Z.Wang, M. Pankratov, D.F. Perrault, S.M. Shapshay, "Laser assisted cartilage reshaping: in vitro and in vivo animal studies", *Proc. SPIE*, **2395**, pp. 296-302, 1995.
4. E.N.Sobol, V.N.Bagratashvili, A.P.Sviridov, A.I.Omel'chenko, A.B.Shechter "Study of cartilage reshaping with a Holmium laser", *Proc SPIE*, **2623**, pp. 544-547.,1996.
5. Y.M.Ovchinnikov , V.P. Gamov, E.N. Sobol, V.N. Bagratashvili, A.I.Omelchenko, A.P. Sviridov, I.Naumidi, E.Helidonis, "An arbitrary change of cartilage shape under the action of laser radiation", *Vestnik otolaryngology*, N3, p.5-11,1995.

6. V.N.Bagratashvili, E.N, Sobol, A.P. Sviridov, V.K. Popov, A.I.Omel'chenko, S.M.. Howdle, "Thermal and diffusion processes in laser-induced stress relaxation and reshaping of cartilage", *J.Biomechanics* **30**, N8, pp. 813-817, 1997.
7. Y.M.Ovchinnikov, V.P.Gamov, A.B.Shechter, V.M. Svistushkin, G.N.Nikiforova, E.N.Sobol, V.N.Bagratashvili, A.I.. Omelchenko, A.P.Sviridov, "The possibilities of application the surgical lasers for cartilage shape formation in ENT surgery", *Vestnik otolaryngology*, N3, pp.21-22, 1996 (in Russian).
8. E. Sobol, A. Sviridov, V. Bagratashvili, A. Omelchenko,Y. M. Ovchinnikov, A. Shekhter, V. Svistushkin, A. Shinaev. "Laser reshaping of nasal septum cartilage: clinical results for 43 patients", *Proc. SPIE,* **3907**, 2000.
9. E. Sobol, V.Bagratashvili, A. Sviridov, A.Omel'chenko, A.Shechter, S.Howdle, E.Helidonis, "Phenomenon of cartilage shaping using moderate laser heating", *Proc. SPIE*, **2623**, pp.548-553,1996.
10. B.Wong, T. Milner, H. Kim, S.Telenkov, C.Chew, E. Sobol, J.Nelson, "Characterization of temperature-dependent biophysical properties during laser mediated cartilage reshaping", *IEEE, J. of SELECTED TOPICS in QUANTUM ELECTRONICS* **5**, pp.1095-1102,1999.
11. A.Sviridov, E.Sobol, N.Jones, J.Lowe. 'Effect of Holmium laser radiation on stress, temperature and structure alterations in cartilage", *Lasers in Medical Science* **13,** pp.73-77,1998.
12. E.Helidonis, I.Volitakis, E.Naumidi, G.Velegrakis, J.Bizakis, P.Christodoulou,. "The histology of laser thermo-chondroplasty", *Amer J. Otolaryngology*,.**15**, pp.423- 428,1995.
13. B.Wong, T.Milner, H.Kim, J. Nelson,. E.Sobol . "Stress Relaxation of Porcine Septal Cartilage During Nd:YAG Laser Irradiation: Mechanical", Optical, and Thermal Responses. *Journal of Biomedical Optics*, **3**, pp.409-41, 1998.
14. Z.Wang, M.M.Pankratov, D.F.Perrault, and S.M.Shapshay. "Endoscopic laser-assisted reshaping of collapsed tracheal cartilage: a laboratory study", *Ann. Otol., Rhinol., and Laryngol.*, **105**, pp.176-181. 1996.
15. See Web site WWW.IRE-POLUSGROUP.COM
16. A.F.Fercher, C.K.Hitzenberger, W.Drexler, G.Kamp, H.Sattmann, "In vivo optical coherence tomography", Amer.Journ.Ophtlm.,**116**, pp.113-114, 1993
17. A.M.Sergeev, V.M.Gelikonov et al, "In vivo optical coherence tomography for human skin microstrukture", *Proc.SPIE*, **2328**, pp.144-150, 1994
18. K.F.Palmer and D.Williams, "Optical properties of water in the near infrared", *J.Opt.Soc. Am.,* **64**, 1107-1110,1974.
19. K.L.Vodopyanov, *Journ. Chem.Phys*, **94**, pp.5389-5394, 1991.
20. B.Wong et al, "Measurements of radiometric surface temperature and integrated back-scattered light intensity during feedback controlled laser associated cartilage reshaping", *Lasers. Med. Sci.*, **13**, pp.66-72, 1998.

## SESSION 5

# Laser Ablation

# Ablation of Skin Tissue by Nanosecond Laser Pulses at 1064, 532, 266 and 213nm

X.H. Hu [*a], Q. Fang[a], M. Cariveau[b], X. Pan[a], G.W. Kalmus[b]

[a]Department of Physics, [b]Department of Biology, East Carolina University, Greenville, NC 27858

## ABSTRACT

The ablation of porcine skin tissue has been investigated using nanosecond (ns) laser pulses at the wavelengths of 1064, 532 and 266nm. The ablation probability has been measured near the threshold through detection of the secondary radiation from the tissue sample surface at different wavelengths. Experimental results have indicated that the ablation of the skin tissue in the wide range of ablating wavelength is caused by optical breakdown induced by the strong electromagnetic field of the nanosecond pulses. Furthermore, we conclude that the initial seed electrons acquire ionization energy from the incident optical field mainly through a momentum-relaxing drift mechanism.

**Keywords:** tissue ablation, nanosecond laser pulses, skin tissue

## 1. INTRODUCTION

Ablation-based laser surgery using visible or near-infrared nanosecond laser pulses has gained significant recognition owing to the potential of achieving precise ablation and reducing collateral tissue damage. These capacities are especially desired in dermatology and cosmetic surgery. Indeed, the ablation of skin tissue and pigments has been investigated extensively in the last decade. Results of these studies have led to the wide acceptance of clinical procedures using the nanosecond laser pulses to treat disorders of cutaneous pigmentation.[1-6] A selective photothermolysis model [7] has been used almost exclusively to explain the experimental results obtained with the nanosecond laser pulses.[1-6] Assuming a photothermal mechanism, the selective photothermolysis model has been successful in the elucidation of tissue ablation by long pulses of hundreds of microseconds in duration.[8] However, we note that a fundamental difference may exist between tissue ablation by long laser pulses and by nanosecond pulses which exhibit strong electromagnetic fields. This strong field has not been widely appreciated in the literature on skin tissue ablation, while numerous studies have been published on the role of plasma in breakdown of water or ocular tissue by visible or near-infrared nanosecond pulses.[9-15] Given a 10 ns pulse delivered with a laser fluence of 10 J /cm$^2$, the electric field strength rises up to $8\times10^7$ V/m in the air. Such a strong electromagnetic field can cause ionization leading to a breakdown in condensed materials including biological tissue. The lack of an accurate model to understand tissue ablation by nanosecond pulses in a wide range of wavelengths has motivated us to pursue the current research project. The other important aspect of the present research is to find a new approach to treat pigmented lesions in the dermis with near-infrared nanosecond laser pulses and much smaller pulse energy than current practice (a few hundred mJ or larger). Thus, collateral tissue damage may be reduced and compact laser systems may be employed.[16,17]

In this paper we report recent experimental results on the ablation probability and depth measurements from fresh porcine skin samples ablated by 10 ns pulses at wavelengths of 1064, 532, 266 and 213nm. The dependence of the ablation probability was determined as a function of the rms electric field and ablation depth per pulse was measured as a function of laser fluence. With different laser wavelengths, we have studied the dependence of the ablation threshold on tissue absorption. The significance of these results will be discussed to demonstrate the needs and requirements to clearly understand the possible mechanisms underlying skin tissue ablation with nanosecond laser pulses.

## 2. EXPERIMENTAL METHODS

The experimental setup is displayed in Fig.1 for both ablation depth and spectral measurements which were carried out separately. A Q-switched Nd:YAG laser (Surelite I, Continuum) was used with a lowered flash lamp voltage to generate 14 ns pulses at 1064 nm wavelength and 10Hz repetition rate. The end mirror of the laser cavity was aligned before experiments to ensure symmetric energy distribution in the spatial profile of the beam which was monitored with a CCD laser beam profiling system (PC300, Spiricon). The pulse energy was adjusted in a range from 0.1 to 100 mJ by a combination of a half-waveplate and a polarizer cube at 1064nm and with the half-waveplate at other wavelengths. The pulse-to-pulse

*Correspondence: Email: hux@mail.ecu.edu; WWW: http://bmlaser.physics.ecu.edu; Tel: 252 328 1864; Fax: 252 328 6314



In *Laser-Tissue Interaction XI: Photochemical, Photothermal, and Photomechanical*, Donald D. Duncan, Jeffrey O. Hollinger, Steven L. Jacques, Editors, Proceedings of SPIE Vol. 3914 (2000)
1605-7422/00/$15.00

fluctuation was estimated to be ±5%. For experiments requiring pulse energies less than 5mJ at 1064nm, an uncoated optical wedge was inserted to fold the beam with an additional mirror (not shown in Fig.1). This step was taken to avoid excessive distortion of the beam profile which occurred when the laser beam transmission through the polarization cube is close to zero. The laser beam of 7mm diameter was focused at the surface of the skin sample by a plano-convex lens with 75mm focal length (nominal) at 1064nm. Quantitative measurements of tissue ablation require a detailed knowledge of the laser beam profile at the focal point or the ablation site. To accurately determine the focal spot size, the laser beam profiling system was used to obtain the transverse diameters $2w_x$ and $2w_y$, at $e^{-2}$ peak irradiance, of the beam along the beam axis, or the z-axis. The z-dependence of the diameter was used to determine the full divergence angles $\theta_x$ and $\theta_y$ after the focusing lens. Using the $M^2$ factor,[18] the focal spot radius were calculated from the divergence angle through, $w_{0x,y} = \frac{2\lambda M_{x,y}^{\ 2}}{\pi\theta_{x,y}}$, where λ = 1064nm. A knife-edge method with 0.5μm in stepping precision was used to verify the focal spot diameter. Results from the two measurements agree with each other within ±5%. To obtain nanosecond pulses at other wavelengths, we used a harmonic generator assembly consisting of a beam reducer and three type I BBO nonlinear crystals of $7mm^3$ size to obtain the second, fourth and fifth harmonics from the fundamental at 1064nm. The beam reducer was used to collimate and decrease the diameter of the laser beam to 5mm before entering the nonlinear crystals. The pulse durations at 532, 266 and 213nm were measured to be about 12ns. The same 75mm lens was used to focus the harmonic beam at the sample surface. Similar beam profile were measured for the harmonic beams and confirmed by the knife-edge measurements. The focal spot diameters used to calculate laser fluence and rms electric field are listed in Table 1.

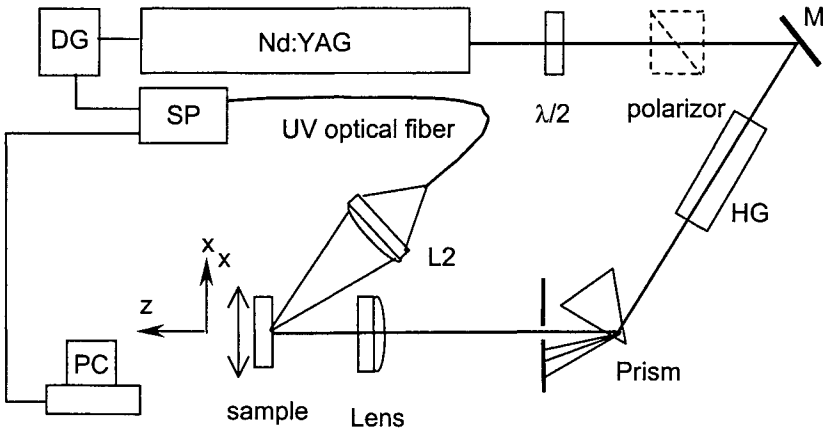


Fig. 1 The schematics of the experimental setup: DG: digital delay generator; M: mirror; SP: multichannel spectrometer; PC: personal computer for stepping motor control and data acquisition from the spectrometer; HG: the harmonic generator assembly. The polarizer was used to control the pulse energy at 1064nm without the nonlinear crystals and the sample was translated along the x-axis.

Measurements of secondary radiation spectrum were conducted with the optical setup shown in Fig. 1. Secondary radiation was collected by an ultraviolet fused silica lens of 100 mm focal length and coupled through an ultraviolet/visible fiber into a multi-channel spectrometer (S2000, Ocean Optics). The spectrometer, with a 2048-element linear CCD-array detector, was chosen to be equipped with a 100μm slit and a 600 lines/mm for high sensitivity and wide spectral range from 300 to 700 nm with a spectral resolution (FWHM) of 5 nm. The relative response of the spectrometer and fiber system between 350 nm and 800 nm was calibrated by the blackbody radiation from a tungsten-halogen lamp with a color temperature of 3100K (AS220, CVI Instruments). A digital delay generator was used to synchronize the spectrum acquisition with the pulse train from the Nd:YAG laser. The repetition rate of the laser pulses was lowered down to 1 pulse in 15 seconds to allow acquisition of the spectral data. The sample was translated so that each laser pulse ablated a fresh area with a distance of 0.5 mm away from the last ablation site.

Small patches of fair porcine skin were harvested from the back neck area of euthanized young (three months old) pigs weighing about 60 kg and stored inside crushed ice in a closed ice cup until use. The temperature of tissue samples during storage was measured to be about 4°C. All measurements were performed within 30 hours of animal euthanasia at the School of Medicine, East Carolina University. Samples were prepared by cutting the skin into strips of about 1×5 $cm^2$. The hair and subcutaneous tissue was removed. The sample was then kept in 0.9% saline solution at room temperature of about 25°C before ablation. The sample holder progressed in the x-axis at a constant speed resulting in a 3mm linear cut in the tissue for ablation depth measurements. For ablation depth measurements, the pulse repetition rate was set at 10 Hz. During the ablation process, the sample was treated every 5 minutes with saline solution to keep it from dehydrating. On each sample, a

series of 6 lines was ablated at different pulse energy with 1 mm distance between them. The speed of the translator was determined by the laser pulse repetition rate and spot size so that the pulse number per spot was kept at either 45 or 90 in order to increase the sensitivity of the ablation depth measurement. Ablated samples were immediately fixed in Bouin's fixative for 12 hours after ablation. Tissue cross sections were obtained by routine histological procedures. Ablation lines were observed under an optical microscope at a resolution of 5 μm. An average of 40-60 ablation depth measurements were made for each sample. One ablation curve was obtained for each sample at respective wavelengths in which the ablation depth per pulse is plotted as a function of laser fluence.

## 3. RESULTS

We first noted that a threshold clearly existed in skin tissue ablation under which no visible spark can be observed. Below this threshold, microscopic examination showed no sign of tissue removal. Measurements recorded a continuous spectrum equivalent to the baseline recorded in the absence of a laser pulse. We named this threshold to be the threshold of 0% probability. Beyond this threshold, the probability of observing the secondary radiation spectrum increases with the pulse energy to 100%. A typical spectrum is shown in Fig. 2 for a tissue sample ablated at 1064nm. Two lines within the 300 – 700nm window of the acquired secondary radiation spectrum were identified as the signature of tissue ablation near the threshold, as shown in Fig. 2. Using a Czerny-Turner monochrometer of 0.05nm resolution (270MX, McPherson), the position of the lines were determined at 589.04±0.08nm and 656.32±0.5nm which can be respectively associated with the electronic transitions in the excited Na and H atoms.[19,20] These two spectral lines appear also in the secondary radiation spectra for samples ablated at the 532, 266 and 213nm in which strong fluorescence from the illuminated tissue sample coexists.

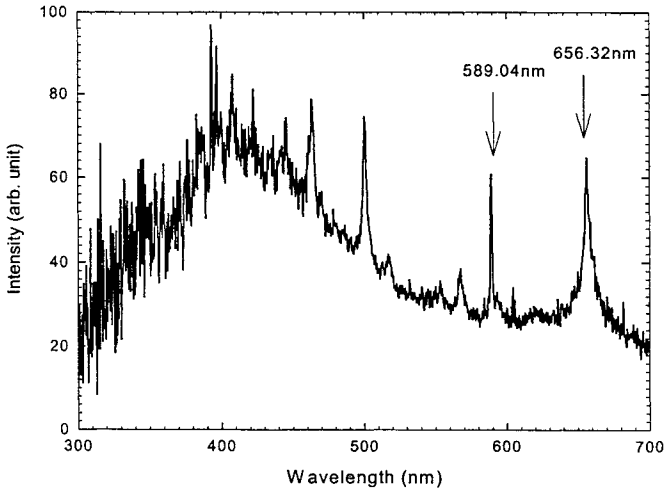


Fig. 2 A typical secondary radiation spectrum above the threshold of 100% probability from a skin tissue sample ablated at 1064nm.

We identified the two spectral lines as the signature of optical breakdown in skin tissue. From the ablation depth measurements, we further verified that the two spectral lines are concurrent with the tissue ablation. Therefore, the two spectral lines at 589 and 656nm can be used as a reliable signature of tissue ablation. The probability of optical breakdown or tissue ablation near the threshold at the skin surface was measured by calculating the ratio of the observed spectral lines observation to the total laser pulses delivered to the skin sample. At each pulse energy of different wavelengths, 100 pulses were used for the probability measurement with 2 seconds between the pulses. The ablation probabilities at the four different ablating wavelengths are plotted in Fig. 3 as a function of the inverse of the rms optical electric field E. The electric field E is calculated by averaging over the focal spot, i.e., $E = \sqrt{\frac{F}{\tau c n \varepsilon_0}}$, where $F = \varepsilon/(\pi w_{0x} w_{0y})$ is the laser fluence at the focal spot, $\varepsilon$ is the pulse energy, $\tau$ is the pulse duration, $n = 1.4$ is the refraction index of the skin tissue, c and $\varepsilon_0$ are the light speed and permittivity in vacuum. Furthermore, the ablation probability P is fitted to the electric field E by $P = P_0 \exp(-K_2^2/E^2)$, where

$P_0$ and $K_2$ are fitting constants. By extrapolating the fitting curves in Fig. 3, we determined the thresholds in the rms electric field of different wavelengths for which the fitted ablation probability are between 0% and 100%. The results are listed in Table 1.

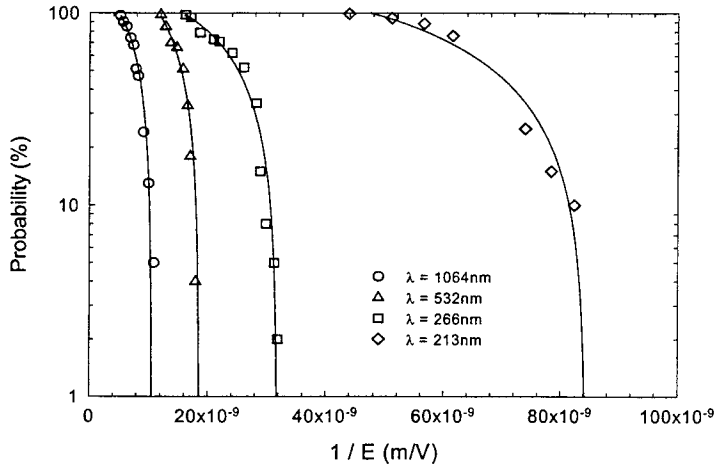


Fig.3 The ablation probability vs the inverse of the rms electric field of the laser pulses at different wavelengths. One hundred pulses were used to measure the probability at each wavelength. The solid lines are fitted curves for each set of data following an equation $P = P_0 \exp(-K_2^2/E^2)$, where P is the probability.

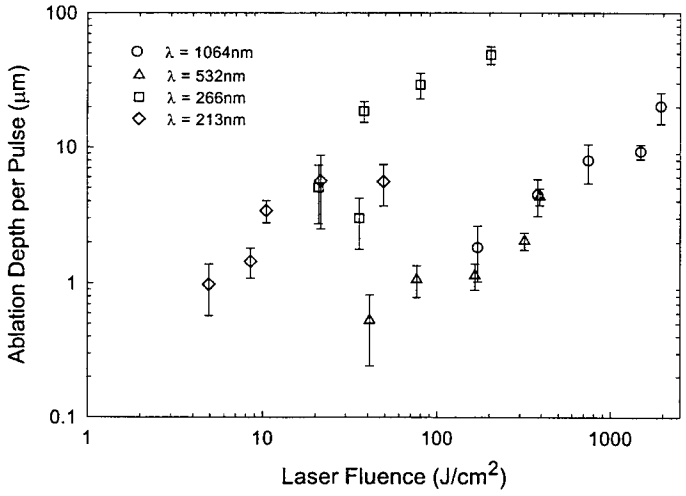


Fig.4 The ablation depth per pulse vs laser fluence. The number of pulses per spot N = 90 were used for pulses at wavelengths of 1064nm and 532nm and N= 45 for pulses at 266nm and 213nm.

The results of the ablation depth measurements for each respective wavelength are shown in Fig. 4. To investigate the ablation process above the threshold, the ablation depth per pulse were measured as a function of laser fluence, F. The skin sample progressed in the x-axis at a speed to allow multiple pulses per spot in order to increase the sensitivity of depth measurement at a pulse repetition rate of 10Hz. The pulse number per spot was set at N = 90 for ablation at 1064 and 532nm and reduced to N = 45 for 266 and 213nm so that the ablation depth would not exceed the thickness of the dermis at maximum laser fluence. For each set of data obtained at different wavelength, the smallest fluence was chose to be in the range of threshold values $F_{th}$ from 0-100% probability as determined from the ablation probability measurements. The average and standard deviation of the ablation depth data were determined for each wavelength.

Table 1. Focal Spot Diameters and Ablation Thresholds

| Ablation Wavelength λ (nm) | 1064nm | 532nm | 266nm | 213nm |
|---|---|---|---|---|
| Diameter (μm) | 14 | 25 | 20 | 20 |
| $2w_{0y}$ (μm) | 18 | 25 | 20 | 20 |
| $W_{th}$ (mJ) @ P=100% | 0.400 | 0.183 | 0.057 | 0.042 |
| $F_{th}$ (J/cm$^2$) @ P =100% | 202 | 36.7 | 18.5 | 13.6 |
| $F_{th}$ (J/cm$^2$) @ P =0% {1} | 45.6 | 12.9 | 4.40 | 0.618 |
| $E_{th}$ (V/m) @ P =100% | $2.04\times10^8$ | $9.38\times10^7$ | $6.51\times10^7$ | $2.35\times10^7$ |
| $K_2$ (V/m) | $1.06\times10^9$ | $6.58\times10^8$ | $3.88\times10^8$ | $1.43\times10^8$ |
| α (cm$^{-1}$) {2} | 5 | 1 | ~ 600 | N/A |

{1} obtained by extrapolation from the fitting curves shown in Fig. 3.
{2} skin epidermis tissue absorption coefficient data from ref. 21

## 4. DISCUSSION

This study was designed to correlate the secondary radiation with the ablation depth measurements of skin tissue near the ablation threshold. By using laser pulses from the near-infrared to ultraviolet with similar laser beam profiles and optical setup, we can investigate the dependence of laser ablation on tissue absorption in the nanosecond region. To minimize the effect of scattering, [21] the ablation was carried out at the surface of the porcine skin samples. For comparison with published results from other groups, we used laser fluence instead of irradiance for 12 or 14ns pulses. Our results demonstrated that the second radiation at 589 and 656nm can be used for identifying tissue ablation. We further confirmed that the probabilistic nature of the tissue breakdown near the ablation threshold exists in a wide spectral range from 1064nm to 213nm. This may provide the key information to the understanding of tissue ablation as a result of optical breakdown. When focused into a very small spot size as reported here, a strong electromagnetic field on the orders of $10^8$V/m is produced in the skin tissue by 12 or 14ns pulses. Irrespective of the large variation in the skin tissue absorption coefficient,[13-15, 21] we concluded that in all cases of wavelength studied, optical breakdown of the skin tissue and the formation of localized plasma cause tissue ablation.

From the secondary radiation measurements, we observed significant differences between data from skin tissue and water. First, the radiation spectra from the ablated skin tissue contain multiple spectral lines, as shown in Fig. 2. Consequently, recombination of the ionized atoms and subsequent relaxation dominate the secondary radiation from tissue while the blackbody radiation of the plasma dominates that from water.[9] Secondly, the probability of tissue ablation near the threshold, determined from the observation of the spectral lines at 589 and 656nm, display an exponential dependence on the inverse of the square of the electric field which can be described by $P = P_0 \exp(-K_2^2 / E^2)$. This is different from that measured from the optical breakdown in water by nanosecond pulses at 1064nm which exhibits an exponential dependence on the inverse of the electric field.[11] For condensed materials in a strong optical electric field, two mechanisms have been proposed for electrons to absorb energy from the incident field, thus becoming seed electrons for avalanche ionization.[22] The first mechanism postulates that some electrons travel for a time without momentum-relaxing collisions and can be accelerated under the influence of the optical field, leading to a breakdown probability given by $P_1 \propto \exp(-K_1/E)$. The second mechanism, however, assumes that electrons may suffer momentum-relaxing collisions during their drifting but maintain their energies. The corresponding probability has been shown to be given by $P_2 \propto \exp(-K_2^2/E^2)$. Both $K_1$ and $K_2$ are material parameters inversely proportional to the momentum-relaxing mean free path. The logarithm of the ablation probability, shown in Fig.3, have displayed a parabolic dependence on the inverse of the optical field and thus is fitted by $P = P_2 = P_0\exp(-K_2^2/E^2)$, where $P_0$ is a proportional constant. This behavior suggests that the initial stages of the optical breakdown in skin tissue differs significantly from those in pure water under similar experimental conditions which have been observed to be dominated by the first mechanism.[11] The difference is consistent with our expectation that the seed electrons in skin tissue gained energy from the nanosecond laser pulses. The seed electrons experience significantly more momentum-relaxing collisions before their energies reaching ionization threshold than those in pure water. This can be attributed to the presence of large molecules such as collagen and glycolipids in skin tissue in comparison to pure water. The $K_2$ constants (see Table 1) decrease with the ablating wavelength, which indicates an inverse relationship between ablation threshold and tissue absorption.

In recent years several reports have been published on investigations of the apparent paradox of tissue ablation in which the measured energy density deposited by a short laser pulse is an order of magnitude smaller than calculated values based on the

photothermal-mechanical model.[23,24] This has been attributed to the confined-stress condition because of the small intervals of short laser pulses. However, we would like to point out that for short laser pulses, with duration of 100ns or less, the effects of the strong electromagnetic fields by the laser pulses must be carefully examined to consider optical breakdown and the formation of plasma. Further investigations of the optical breakdown in porcine skin tissue are in progress.

## ACKNOWLEDGEMENT

X.H. Hu would like to acknowledge the partial support through a research grant from the National Institute of Health (R15GM/OD55940-01).

## REFERENCES

1. Anderson RR, Margolis MJ, Watanable S, Flotte T, Hruza GJ, Dover JS. "Selective photothermolysis of cutaneous pigmentation by Q-switched Nd:YAG laser pulses at 1064, 532, and 355nm", *J. Invest. Dermotol.*, **93**, pp.28-32 (1989)
2. Reid WH, Miller ID, Murphy MJ, Paul JP, Evans JH. "Q-switched ruby laser treatment of tattoos; a 9-year experience", *Brit. J. Plas. Surg.*, **43**, pp. 663-669 (1990)
3. Hruza GJ, Dover JS, Flotte TJ, Goetschkes M, Watanabe S, Anderson RR. "Q-switched ruby laser irradiation of normal human skin", *Arch. Dermatol.* **127**, pp.1799-1805 (1991)
4. Kilmer SL, Anderson RR. "Clinical use of the Q-switched ruby and the Q-switched Nd:YAG (1064nm and 532nm) lasers for treatment of tattoos", *Dermotol. Surg. Oncol.*, **19**, pp.330-338 (1993)
5. Watanabe S, Takahashi H. "Treatment of nevus of Ota with the Q-switched ruby laser", *The New England J. of Med.*, **331**, pp.1745-1750 (1994)
6. Stafford TJ, Lizek R, Boll J, Tan OT. "Removal of colored tattoos with the Q-switched Alexandrite laser", *Plas. Reconstroc. Surg.*, **95**, pp.313-320 (1995)
7. Anderson RR, Parrish JA. "Selective photothermolysis: precise microsurgery by selective absorption of pulsed radiation", *Science*, **220**, pp.524-527 (1983)
8. Wheeland RG. "Clinical uses of lasers in dermatology", *Laser.s Surg. Med* . **16**, pp.2-23 (1995)
9. Barnes PA, Rieckhoff KE. "Laser induced underwater sparks", *Appl. Phys. Lett.*, **13**, pp.282-284 (1968)
10. Bloembergen N. "Laser-induced electric breakdown in solid", *IEEE. J. Quan. Electron.*, **10**, pp.375-386 (1974)
11. Sacchi CA. "Laser induced electric breakdown in water", *J. Opt. Soc. Am. B*, **8**, pp.337-345 (1990)
12. Vogel A, Nahen K, Theisen D, Noack J. "Plasma formation in water by picosecond and nanosecond Nd:YAC laser pulses. 1. Optical breakdown at threshold and superthreshold irradiance", *IEEE J. Selected Topics Quan. Electron.*, **2**, pp.847-860 (1996)
13. Stern D, Schoenlein RW, Puliafito CA, Dobi ET, Biringruber R, Fujimoto JG. "Corneal ablation by nanosecond, picosecond, and femtosecond lasers at 532 and 625nm", *Arch. Ophthalmol.*, **107**, 587-592 (1989)
14. Niemz MH, Klancnik EG, Bille JF. "Plasma-mediated ablation of cornea tissue at 1053nm using Nd:YLF oscillator/regenerative amplifier laser", *Lasers Surg. Med.* , **11**, pp.426-431 (1991)
15. Kennedy PK. "A first-order model for computation of laser-induced breakdown thresholds in ocular and aqueous media. 1. Theory", *IEEE J. Quan. Electron.*, **31**, pp.2241-2249 (1995)
16. Hu XH. "Efficient use of Q-switched lasers in the treatment of cutaneous lesions", *SPIE Proceedings*, **2395**, pp.586-591 (1995)
17. Song Z, Dong K, Hu XH, Lu JQ, "Monte Carlo Simulation of Converging Laser Beams Propagating in Biological Tissue", *Applied Optics*, **37**, pp.2944-2949 (1999)
18. Siegman AE, "New developments in laser resonator", *SPIE Proceedings*, **1224**, pp. 2-14 (1990)
19. Harrison GR, *The M.I.T. Wavelngth Tables*, vol. 1, pp. 90-99 (MIT Press, Cambridge, Massachusetts, 1969)
20. Lubatschowski H, Kermani O, Otten C, Haller A, Schmiedt KC, Ertmer W. ArF-excimer laser-induced secondary radiation in photoablation of biological tissue. Lasers Surg. Med. **14**, pp.168-177 (1994)
21. van Gemert MJC, Jacque SL, Sterenborg HJCM, W.M. Star, "Skin optics",, *IEEE Trans. Biomed. Eng.*, **36**, 1146 (1989)
22. Ridley BK, "Lucky-drift mechanism for impact ionization in semiconductors", *J. Phys. C*, **16**, 3373 (1983)
23. Itzkan I, Albagli D, Dark ML, Perelman LT, von Rosenberg C, Feld MS. "The thermoelastic basis of short pulsed laser ablation of biological tissue", *Proc. Natl. Acad. Sci. USA*, **92**, 960-1964 (1995)
24. Oraevsky AA, Jacques SL, Esenaliev RO, Tittle FK. "Pulsed laser ablation of soft tissue, gels, and aqueous solutions at temperatures below 100°C", *Lasers Surg. Med.* , **18,** 231-240 (1996)

# Myocardium tissue ablation with nanosecond, ultraviolet pulses: *In-vitro* study with porcine myocardium tissues

Tomoaki Shimada*, Shunichi Sato[a], Miya Ishihara[b], Tsunenori Arai[b], Takemi Matsui[c], Akira Kurita[c], Makoto Kikuchi[b], Hitoshi Wakisaka[a], Hiroshi Ashida[a], and Minoru Obara

Department of Electronics and Electrical Engineering, Keio University, 3-14-1, Hiyoshi, Kouhoku-ku, Yokohama, Kanagawa 223-8522, Japan

[a]Division of Biomedical Information Sciences, National Defense Medical College Research Institute, 3-2, Namiki, Tokorozawa, Saitama 359-8513, Japan

[b]Department of Medical Engineering, National Defense Medical College, 3-2, Namiki, Tokorozawa, Saitama 359-8513, Japan

[c]Division of Biomedical Engineering, National Defense Medical College Research Institute, 3-2, Namiki, Tokorozawa, Saitama 359-8513, Japan

## ABSTRACT

**To investigate the optimum irradiation conditions for the transmyocardial laser revascularization (TMLR), ablation characteristics have been explored *in vitro* with porcine myocardium tissues. With a nanosecond optical parametric oscillator (OPO), the ablation depth and the thickness of thermally damaged tissue were measured at a constant peak intensity or fluence in the ultraviolet spectral region of 230 - 400 nm. It was found that at a peak intensity of 80 MW/cm$^2$, the ablation depth steeply increased for < 300 nm, while the thickness of thermally damaged tissue decreased with decreasing the wavelength. To understand the wavelength dependence of the ablation characteristics, we measured the optical properties of the tissue. This showed that the total attenuation coefficient largely increased with decreasing the wavelength for < 300 nm. Therefore, it is considered that at the shorter wavelengths the optical energy density deposited in the tissue would be high enough to ablate the whole region of the light-penetrated tisuue. However, the wavelength dependence might be changed at some higher intensities or fluences. But our experiment using the 3rd and 4th of a Q-switched Nd:YAG laser, the shorter wavelength (266 nm) still gave the deeper ablation for up to 2-5 J/cm$^2$. The influence of photomechanical effects on the ablation mechanism is also discussed.**

**Keywords:** transmyocardial laser revascularization (TMLR), myocardium tissue ablation, optical parametric oscillator, nanosecond, ultraviolet, wavelength dependence, photomechanical effects .

## 1. INTRODUCTION

Transmyocardial laser revascularization (TMLR) has been introduced to treat severe coronary artery diseases that cannot be treated by conventional treatments such as percutaneous transluminal coronary angioplasty (PTCA) or coronary artery bypass grafting (CABG). TMLR is a laser-ablation-based surgery, in which a laser beam irradiates the ischemic (oxygen-starved) myocardium and creates the channels through the myocardium. By this, the flow of blood in the ischemic myocardium can be increased and this relieves the functions of heart. For this treatment, various types of lasers whose output wavelengths range from the infrared to the ultraviolet have been used. For example, 10.6 μm $CO_2$ lasers, 2.1 μm Ho:YAG lasers and 308 nm XeCl excimer lasers are clinically applied[1-7]. However, the optimum irradiation conditions incruding wavelength, fluences, etc., have not yet been revealed for this treatment. It is reported that the XeCl excimer lasers that are clinically applied cause less thermal damage in the tissue than the infrared lasers do[6]. And the nanosecond

*Correspondence: Email:shimada@obara.elec.keio.ac.jp



In *Laser-Tissue Interaction XI: Photochemical, Photothermal, and Photomechanical,* Donald D. Duncan, Jeffrey O. Hollinger, Steven L. Jacques, Editors, Proceedings of SPIE Vol. 3914 (2000) 1605-7422/00/$15.00

pulsed lasers can further reduce the thermal damage because the pulse width is much shorter than the thermal relaxation time in the tissue. Therefore, we intensively investigated the characteristics of the myocardium tissue ablation with the ultraviolet nanosecond pulses.

## 2. MATERIALS AND METHODS

As light sources for ablation, we used an optical parametric oscillator (OPO) and the third and fourth harmonics of a Q-switched Nd:YAG laser. The OPO could generate the signal waves of 410-690 nm and the idler waves of 730-2000 nm. And a frequency doubler option with BBO crystals could generate the signal waves of 220-345 nm and the idler waves of 365-400 nm. We used the output beams in the wavelength range of 230-400 nm. Because the maximum output energy of the OPO was about 6 mJ at 250 nm, we used the Q-switched Nd:YAG laser to collect ablation data at higher fluences. The maximum output energies of the third and forth harmonics of the Q-switched Nd:YAG laser were both about 60 mJ. The repetition rate of the OPO and the Nd:YAG laser were 30Hz and 10 Hz respectively.

As sample, extracted fresh porcine hearts were obtained from a local slaughterhouse. After the epicardium was excised, myocardium tissue blocks of 7 mm×7 mm×5-10 mm in thickness were taken from the left ventricular free wall. The samples were put in saline and kept at ~5℃ until the ablation experiment.

The output beams from the light sources were focused with a lens and irradiated the sample with a constant spot diameter of 1.0 mm. After the irradiation, the samples were fixed with a 4% glutaraldehyde phosphate buffer solution or a 10% formalin solution. The glutaraldehyde-fixed samples were cut at the center of the ablation hole and the ablation depth was measured. The formalin-fixed samples were sliced and stained with hematoxylin and eosin, which we observed with a transmission polarizing microscope. We measured the thickness of the dark region on the microscope photographs as the thermal damage thickness, where the birefringence of the tissue was lost due to the thermal effect.

To measure the total attenuation coefficient of the tissue, a sliced fresh sample was clamped between two 10 mm×40 mm × 2 mm quartz plates. To detect only the straight transmitted light, 1-mm-in-diameter apertures were placed at both sides of the holder. The transmitted light was detected with a polychromator (Hamamatsu Photonics, PMA-11). The thickness of the sliced sample was measured with a micrometer. The total attenuation coefficient, $\mu_t$, is given by

$$\mu_t = -\frac{1}{t}\ln\frac{I(t)}{I_0}, \tag{1}$$

where $t$ is the thickness of the sample, $I(t)$ is the transmitted light intensity through the sample, and $I_0$ is the transmitted light intensity without sample.

## 3. RESULTS

We first investigated the wavelength dependence of the myocardial ablation characteristics using the OPO. Figure 1 shows the ablation depth by 900-pulse irradiation as a function of the OPO output wavelength at a constant intensity of 80 MW/cm$^2$ (which corresponds to a fluence of about 0.5 J/cm$^2$)[8,9]. At 400 nm, ablated hole was not formed. In the wavelength region shorter than 300 nm, the ablation depth steeply increased with decreasing the wavelength. A maximum ablation depth was about 3 mm at 230 nm. Figure 2 shows the dependence of the longitudinal and lateral thermal damage thicknesses on the OPO output wavelength. It is clear that the thermal damage thickness decreased with decreasing the wavelength. The thermal damage thickness was as small as 20 μm at 230 nm.

Figure3 shows the ablation depth as a function of the OPO fluence at 247 and 308 nm. The ablation depth linearly increased with increasing the fluence at both wavelengths. At 247 nm, the ablation efficiency (the ablation depth per fluence) was higher and the ablation threshold was lower when compared with each of those at 308 nm. The ablation thresholds were 0.076 J/cm$^2$ at 247 nm and 0.18 J/cm$^2$ at 308 nm.

As described above, it was considered that at some higher fluence the wavelength dependence might be changed. Figure 4 shows the ablation depth as a function of the fluence of the Q-switched Nd:YAG laser at 266 nm and 355 nm for up to 2-5 J/cm$^2$. At both wavelengths the ablation depth increased with increasing the fluence, and at 266 nm the ablation efficiency was higher and the ablation threshold was lower than each of those at 355 nm. The ablation thresholds were 0.11 J/cm$^2$ at 266 nm and 0.59 J/cm$^2$ at 355 nm. Figures 5 and 6 show the transmission polarizing microscope photograph of the ablation hole formed by 266-nm and 355-nm irradiation respectively. The fluences were 1.9 J/cm$^2$ at 266 nm and 5.0 J/cm$^2$ at 355 nm. The number of pulses was 300 in both cases. Although the flueneces were different, the thermal damage thickness at 266 nm was smaller than that at 355 nm.

To understand the wavelength dependence of the ablation characteristics described above, we measured the total attenuation coefficient of the myocardium tissue using the OPO. Figure 6 shows the measured total attenuation coefficients of the myocardium tissue as a function of the OPO output wavelength. The total attenuation coefficient increased in the wavelength region shorter than 350 nm.

## 4. DISCUSSION

The photothermal effects on the tissue ablation have been explained as follows. The absorption of laser energy by the tissue causes the rapid temperature rise in the tissue. In the temperature range of 43-60℃ the tissue starts to be denatured and then coagulated in the temperature range of 60-100℃. In the tissue where the denaturation of collagen starts, the birefringence of the tissue is lost. Therefore, we can observe the denatured tissue region using a transmission polarizing microscope[10]. The temperature at which the carbonization and the vaporization of water occur is in the range of 100-300℃. When the temperature of tissue reaches over 300℃, the solid tissue matrix is ablated[11]. It is considered that in our experiments the effect of the thermal relaxation is little because the pulse width is much shorter than the thermal relaxation time in the tissue. When the deposited energy density in the tissue is lower than the ablation threshold, the light-penetrated tissue is coagulated due to the temperature rise.

Assuming that the absorption coefficient is much larger than the scattering coefficient, i.e., the total attenuation coefficient is nearly equal to the absorption coefficient. The results shown in Figures 1 and 2 are explained as follows. In the shorter wavelength region, the energy density deposited in the tissue is high enough to ablate the almost all region of the light-penetrated tissue because of the high absorption. Therefore, a deep ablation with less thermal damage can be obtained. On the other hand, in the longer wavelength region the absorption of the myocardium is so low that only a part of the light-penetrated tissue can be ablated and the energy that does not contribute to the ablation heats the surrounding tissue and causes the thermal damage as described above. However, at some higher fluence the longer wavelength light might give deeper ablation because of the deeper light penetration in the tissue.

Figure 3 shows that the ablation depth linearly increased with increasing the fluence. It is considered, however, that at some higher fluences the ablation depth might be saturated. Figure 4 shows the ablation characteristics at higher fluences up to 2-5 J/cm$^2$, but it is shown that the ablation depth still linearly increases to the fluence. It should be noted that all the data shown in Figures 3 and 4 are of the multiple-pulse ablation and we confirmed in another experiment that the depth nonlinearly increased to the number of pulses. Data of single-pulse ablation are needed for further discussion on the fluence dependence of the ablation efficiency.

The histological sections (Figures 5 and 6) show the tissue fragments on the walls of the ablated holes, which might be caused by the photomechanical effects. At 355 nm, the plasma formation was clearly observed at fluences >3 J/cm$^2$ during the ablation. And in our previous study on the 1064-nm laser ablation, extraordinary deep ablation was obtained at fluences >5 J/cm$^2$ in spite of the low absorption coefficient being expected at this wavelength[9]. Therefore, the laser-induced plasma is considered to cause the photomechanical effects in the tissue.

As far as the present *in-vitro* study is concerned, the short wavelength UV light is advantageous to be used for the myocardium tissue ablation because of the high ablation efficiency and the less thermal damage in the tissue. But for clinical application further improvement in ablation rate is required to shorten the ablation time. This may be achievable by increasing the fluence and/or the repetition rate of the laser. In addition, for clinical applications of UV light, the cytotoxity and mutagenicity[12] should be carefully investigated in an *in-vivo* study.

## 5. CONCLUSION

To investigate the optimum irradiation conditions for TMLR, the characteristics of the myocardium tissue were revealed using an OPO and the third and forth harmonics of a Q-switched Nd:YAG laser. In the wavelength region shorter than 300 nm the ablation efficiency increased and the thermal damage decreased with decreasing the wavelength. The results can be explained based on the absorption spectrum of the myocardium tissue. The deepest ablation and the minimum thermal damage were obtained at 230 nm. It was also revealed that the ablation depth was linearly increased with increasing the fluence for up to 2-5 J/cm$^2$. The short-wavelength UV light is advantageous to be used for the myocardium tissue ablation. For clinical application, however, an *in-vivo* study should be performed.

## REFERENCES


1. E.D. Jansen, et al., "Laser-Tissue Interaction During Transmyocardial Laser Revascularization", *Ann. Thorac. Surg.* **63**, pp.640-647, 1997.
2. A. Milano, et al., "Early Results of Transmyocardial Revascularization With a Holmium Laser", *Ann. Thorac. Surg.* **65**, pp.700-704, 1998.
3. C. A. Mack et al., "Channel patency and neovascularization after transmyocardial revascularization using an excimer laser: results and comparisons to nonlased channels", *Circulation* **96**, pp. II 65-69, 1997.
4. R. Brinkmann, D. Theisen, and R. Birngruber, "Single-Pulse 30-J Holmium Laser for Myocardial Revascularization-A Study on Ablation Dynamics in Comparison to $CO_2$ Laser-TMR.", *IEEE J. Selected Topics in Quantum Electronics*, **5-4**, pp. 969-980, 1999.
5. P. E. Fisher, et al., "Histologic Analysis of Transmyocardial Channels: Comparison of $CO_2$ and Holmium:YAG Lasers.", *Ann. Thorac. Surg.* **64**, pp. 466-472, 1997.
6. G. Müller and B. Schaldach, "Laser tissue interaction in regard to transmyocardial revascularization.", *SPIE* **3681** (Advance in Laser Medicine 17), pp.80-97, 1998.
7. M. Okada and M. Nakamura, "Experimental and clinical studies on transmyocardial laser revascularization (TMLR).", *SPIE* **3681** (Advance in Laser Medicine 17), pp.67-76, 1998.
8. S. Sato, et al., "Influence of wavelength on laser ablation characteristics of myocardium tissue: *In-vitro* study with porcine myocardium tissue in the UV spectral region." to be published in *J. Jap. Soc. Laser Surg. Med.*(in Japanese).
9. S. Sato, et al., "Characteristics and Mechanism of Myocardium Tissue Laser Ablation: *In-vitro* study for Transmyocardial Laser Revascularization." to be published in *Proc. SPIE.*
10. G. Müller, K. Dörschel and H. Kar, "The Tissue Photoablation Process with short pulsed Lasers", *SPIE* **1524** (Bioptics), pp.150-177, 1991.
11. S. Thomsen, J. A. Pearce and W. Cheong, "Changes in Birefringence as Markers of Thermal Damage in Tissues.", *IEEE Trans. Biomed. Eng.* **36-12**, pp. 1174-1179, 1989.
12. H. Green, et al., "Cytotoxicity and Mutagenicity of Low Intensity, 248 and 193 nm Excimer Laser Radiation in Mammalian Cells.", *Cancer Research* **47**, pp.410-413, 1987.

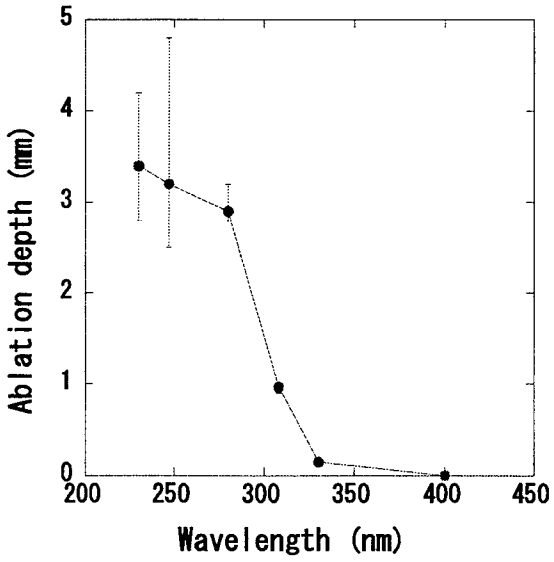


Fig.1 The wavelength dependence of the ablation depth of the myocardium tissue using the OPO. The intensity was 80 MW/cm$^2$ and the number of pulses was 900[8,9].

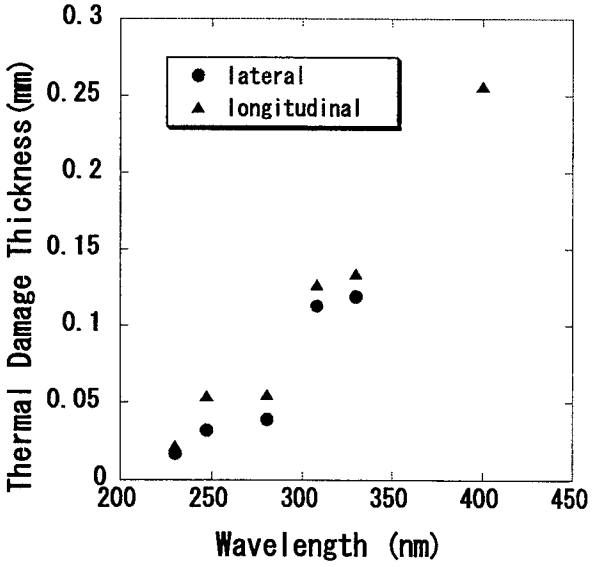


Fig.2 The wavelength dependence of the thermal damage thickness of the myocardium tissue using the OPO. The intensity was 80 MW/cm$^2$ and the number of pulses was 900.

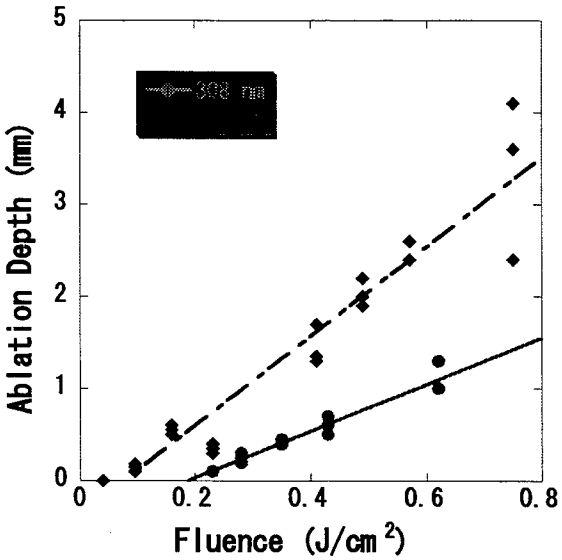


Fig.3 The ablation depth of the myocardium tissue as a function of the OPO output fluence at 247 nm and 308 nm. The number of pulses was 900.

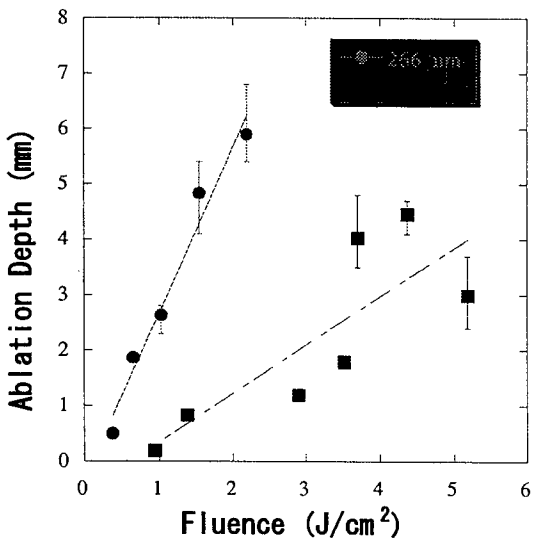


Fig.4 The ablation depth of the myocardium tissue as a function of the Q-switched Nd:YAG laser fluence at 266 nm and 355 nm. The number of pulses was 300.

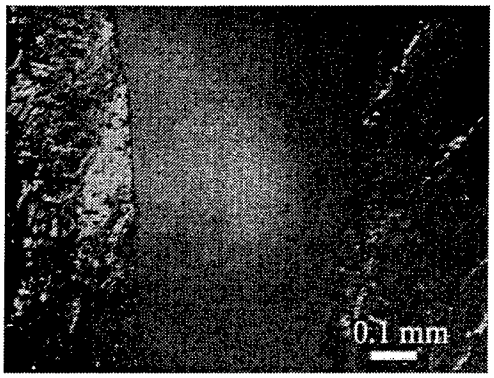


Fig. 5 The transmission polarizing microscope photograph of the ablated myocardium tissue by forth harmonics of Q-switched Nd:YAG laser. The irradiation fluence was 1.9 J/cm$^2$ and the number of pulses was 300.

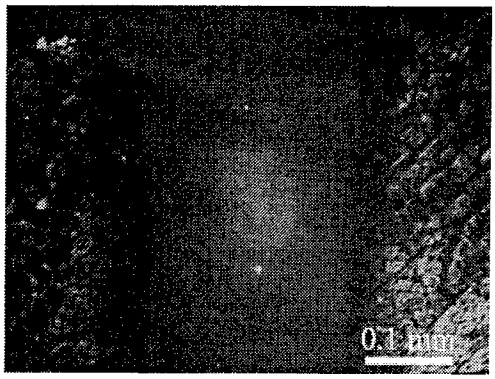


Fig. 6 The transmission polarizing microscope photograph of the ablated myocardium tissue by third harmonics of Q-switched Nd:YAG laser. The irradiation fluence was 5.0 J/cm$^2$ and the number of pulses was 300.

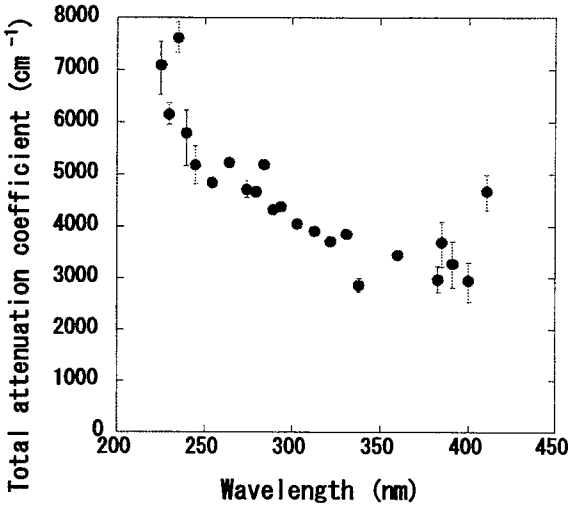


Fig.7 The total attenuation coefficient of the myocardium tissue at the OPO output wavelengths.

# 65MHz bandwidth measurement of thermal emission induced by ArF eximer laser ablation of cornea

Miya Ishihara*[a], Shunichi Sato[b], Tsunenori Arai[a], Minoru Obara[c], Makoto Kikuchi[a]

[a]Department of Medical Engineering, National Defense Medical College
[b] Division of Biomedical Information Sciences, National Defense Medical College Research Institute
[c]Department of Electrical Engineering, Faculty of Science and Technology, Keio University

## ABSTRACT

We measured thermal emission from cornea surface during and just after ArF excimer laser pulse with 65MHz bandwidth, corresponding to 15ns rise-time. The rise-time of the thermal emission measurement should be the same order of the heating pulse duration (ArF excimer laser pulse duration of 25ns) to obtain the rapid temperature change of cornea surface. To acquire the available rise-time, we employed a 150MHz cut off frequency photovoltaic HgCdTe detector with 100MHz preamplifiers. We measured the peak temperature of 175℃ at the fluence of 160mJ/cm$^2$. The irradiated cornea temperature decreased rapidly with 280ns in time constant. We measured the highest temperature elevation during the ArF excimer laser ablation of the cornea comparing with previous reports using our high speed temperature measurement system.

Keywords: ArF excimer laser, cornea ablation, photorefractive keratectomy (PRK), thermal emission, temperature, time-resolution,

## 1. INTRODUCTION

ArF excimer laser ablation of cornea has been applied for photorefractive keratectomy (PRK), which is able to perform with around 1μm accuracy without thermal damage to the ablation area and its surroundings[1]. Because of invasive therapy, PRK required precise real-time evaluation of ablation quantity (etch depth) and quality (surface smoothness and surrounding tissue damage) to achieve intended correction[2]. We employed the physical quantity measurement which directly relates to ablation kinetics in order to evaluate the ablation.

Since the ablation kinetics may be governed by photothermal ablation mechanism[3],[4], the photothermal mechanism might directly relate to ablation efficiency and thermal and/or acoustic complication. Therefore, temperature transient measurement of the cornea surface seems to be useful to evaluate the ablation quantity and quality[5]. To measure available temperature to our purpose, the rise-time of the temperature measurement should be fast enough to the heat input time duration, that is, the ArF excimer laser pulse duration (25ns). We measured the thermal emission from porcine cornea during and just after the ArF excimer laser pulse. We employed a photovoltaic HgCdTe detector with 150MHz cutoff

*Correspondence: Email: kobako@ndmc.ac.jp; Telephone: +81-429-95-1596; Fax: +81-429-96-5199



In *Laser-Tissue Interaction XI: Photochemical, Photothermal, and Photomechanical*, Donald D. Duncan, Jeffrey O. Hollinger, Steven L. Jacques, Editors, Proceedings of SPIE Vol. 3914 (2000)
1605-7422/00/$15.00

frequency, a series connection of low-noise preamplifiers, and high collection efficiency optics to achieve fast and sensitive transient measurement of the thermal emission.

## 2. MATERIALS AND METHODS

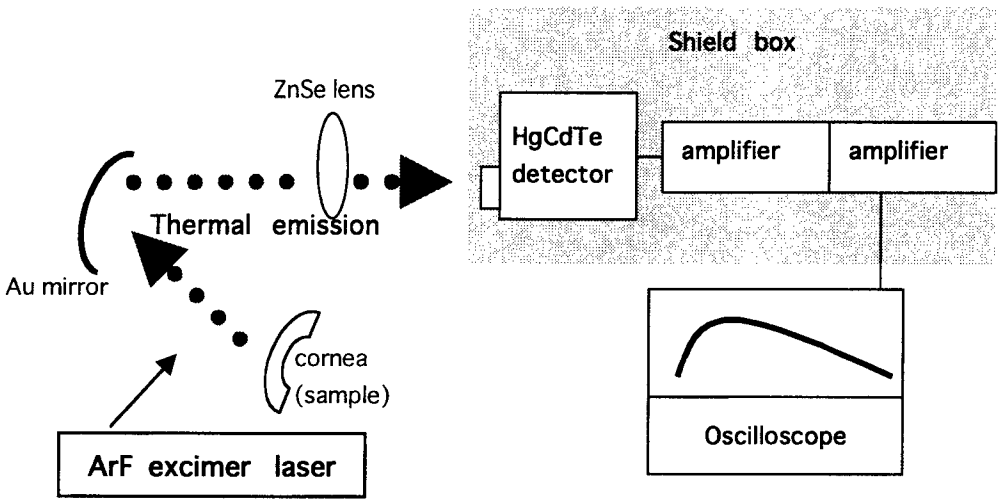


Fig.1 Experimental setup

Fresh porcine corneas were used as samples within 12 hours of the extraction. The experimental setup for thermal emission measurement is illustrated in Fig.1. A pulsed ArF excimer laser (wavelength; 193 nm, pulse duration; 25 ns , L4500, Hamamatsu Photonics Co., Ltd., Shizuoka, Japan) was used. The thermal emission from the cornea surface was collected by a Au coated concave mirror (radius of curvature; 120 mm, diameter; 100 mm) and detected by a photovoltaic HgCdTe detector (PV1596, SAGEM SA, Paris, France) with a ZnSe focusing lens (focal length; 127 mm, diameter; 40mm, II-VI, PA, USA). The response frequency of the HgCdTe detector was up to 150 MHz. The output of the HgCdTe detector was amplified by a series connection of two low noise amplifiers (Bandwidth; 400Hz-100MHz, Gain; 46dB, SA-230F5, NF Electronic Instruments, Yokohama, Japan). The amplified signal was recorded by a multi-channel digital oscilloscope (analog bandwidth; 1GHz, TDS680B, Textronics, OR, USA). The HgCdTe detector and amplifiers were enclosed by a electromagnetic (EM) shield box for EM noise reduction.

In order to determine collection efficiency of the thermal emission and detective sensitivity ( $\gamma$ ) of our experimental setup, a silicon rubber heater was placed at the sampling location in the experimental system shown in Fig.1. The thermal emission area of the heater was the same as the irradiation area of the cornea, that is, the ArF excimer laser beam area (0.65mm$^2$). The temperature of the heater was measured by a T-type thermocouple. The relation between the detected signal (V) from the heater and the temperature (T) of the heater could be described in Eq.(1). We could obtain ( $\delta * \gamma$ ) and used Eq.(1) for calculation of the cornea surface temperature.

$$\varepsilon * T^4 = V/(\delta * \gamma * \sigma * S) \qquad \text{Eq.(1)}$$

where, $\varepsilon$ is emissivity of the sample, T is temperature(K), V is observed detector output(V), $\sigma$ is Boltzmann constant and S is radiation area($mm^2$).

## 3. RESULTS

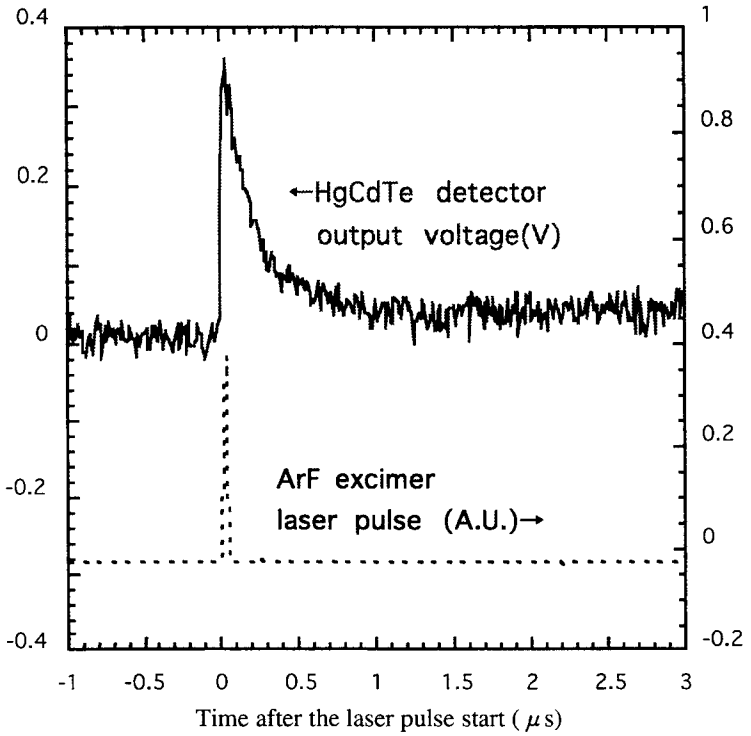


Fig.2 Time course of the amplified HgCdTe detector output and the ArF excimer laser pulse.

The measured time course of the amplified HgCdTe detector output voltage is shown in Fig.2. In Fig.2, the ArF excimer laser pulse is also indicated to compare with the waveform of the amplified HgCdTe detector output. These waveforms were obtained at the laser fluence of 160 $mJ/cm^2$.

The thermal emission signal increases sharply just after the laser pulse starts in Fig.2. This signal shows significant decrease after the peak following the long tail. As the part of the decrease waveform was fitted by exp(-At)+exp(-Bt), we obtained A=280ns and B=15 $\mu$s which were corresponding to the time constants of sharp fall and long tail of the waveform.

Measured peak temperatures with various fluences of the ArF excimer laser are summarized in Table 1. The initial temperature of the cornea was 23℃.

Table 1 Peak temperatures versus fluences

| Peak temperature | Fluence |
|---|---|
| 99±20℃ | 80mJ/cm$^2$ |
| 133±11℃ | 110 mJ/cm$^2$ |
| 157±15℃ | 130 mJ/cm$^2$ |
| 172±12℃ | 150 mJ/cm$^2$ |
| 221±11℃ | 170 mJ/cm$^2$ |

## 4. DISCUSSION

### 1. TIME COURSE OF MEASURED WAVEFORM

The rise of the waveform in Fig.2 was governed by the heat-input, that is, the ArF excimer laser irradiation. In fact, the rise-time of 22ns was approximately corresponded to the duration of the ArF excimer laser (25ns).

We found that the time constant of the sharp fall was roughly agreed with the thermal relaxation time of the laser heated region. If the volume which absorbed the laser irradiation is assumed to be a flat disc, the thermal relaxation time (t) is expressed by as follows[6],

$$t=1/(4*\alpha^2*D) \qquad \text{Eq.(2)}$$

where, $\alpha$ is absorption coefficient of cornea for the laser wavelength (193nm), and D is thermal diffusivity. We used 20000cm$^{-1}$ - 39900cm$^{-1}$ for cornea absorption coefficient in this calculation because this value has been reasonable considering the peptide-bond density in corneal tissue. We obtained the thermal relaxation time of 120 - 480ns, which agreed with the time constant of 280ns in Fig.2.

### 2. MEASURED TEMPERATURE OF CORNEA

The measured cornea temperature was over 100℃ which corresponded to the boiling point of water at 1atm. There has been no study which reported such a high temperature during the ArF excimer laser ablation of cornea. The reported temperature rises which were measured by various measurement methods were wide scattered[7][8][9]. Bende et al. reported the 8℃ temperature rise at fluence of 150 mJ/cm$^2$. The time constant of their thermocouple method was 200ms. In the case of 16.6 ms of the time constant, Kitai et al. measured up to 20℃ temperature rise at the same fluence described above. Our measured peak temperature at the same fluence indicated 175℃, corresponding to 152℃ temperature rise. Our time-resolution, 65MHz bandwidth equivalent to 15ns rise-time, acquired the highest temperature rise. We confirmed that we could obtain the feasible sharp temperature rise of the cornea surface because the rise-time of ours was sufficient for heat input time duration (25ns).

## 5. CONCLUSION

We measured the thermal emission of the cornea surface for temperature estimation with 15ns rise-time during the ArF excimer laser ablation. We measured the peak temperature of 175℃ at the fluence of 160mJ/cm$^2$. We obtained the highest temperature elevation during the ArF excimer laser ablation of the cornea comparing with previous reports using our temperature measurement system. It may improve the quality of the ablation performance and be useful to study the ablation dynamics.

## REFERENCE


(1) G.H.Pettit, M.N.Ediger, R.P.Weiblinger, "Excimer laser ablation of the cornea.", Optical Engineering, vol.34, no.3, pp661-667, 1995

(2) M.N.Ediger, G.H.Pettit, R.P.Weiblinger, "Noninvasive monitoring of excimer laser ablation by time-resolved reflectometry.", Refractive & Corneal Surgery, vol.9, pp268-275, 1993

(3) Z.Bor, B.Hopp, B.Racz, et al., "Physical problem of excimer laser cornea ablation.", Optical Engineering, vol.32, no.10, pp2481-2486, 1993

(4) G.H.Pettit, M.N.Ediger, "Corneal-tissue absorption coefficients for 193-and 213nm ultraviolet radiation.", Applied Optics, vol.35, no.19, pp3386-3391, 1996

(5) M.Ishihara, T.Arai, S.Sato, et al., "Temperature monitoring by infrared radiation measurements during ArF excimer laser ablation with cornea.", SPIE Proc., vol.3601, pp335-339, 1999

(6)A.A.Oraevsky, S.L.Jacques, R.O.Esenaliev, et al., "Pulsed laser ablation of soft tissues, gels, and aqueous solutions at temperature below 100℃.", Lasers in Surgery and Medicine, vol.18, pp231-240, 1996

(7) T.Bende, T.Seiler, J.Wollensak, "Side effects in excimer corneal surgery.", Graefe's Archive Ophthalmology, vol.226, pp277-280, 1988

(8) M.S. Kitai, V.L.Popkov, V.A.Semchishen, et al., "The Physics of UV laser cornea ablation.", IEEE J.of Q.E., vol.27, no.2, 1991

(9) S.Betney, P.B.Morgan, S.J.Doyle, et al., "Corneal temperature changes during photorefractive keratectomy.", vol.16, no.3, pp158-161, 1997

## SESSION 6

# Laser Ablation and Disruption

# Laser Ablation of Skull Tissue using Transverse Excited 9.6-μm $CO_2$ Lasers with Pulse Durations of 1-100 μs

Nathaniel M. Fried[a] and Daniel Fried[b]

[a] Biomedical Engineering Department, Johns Hopkins University, Baltimore, MD 21205
[b] Department of Restorative Dentistry, University of California, San Francisco, CA 94143-0758.

## ABSTRACT

Craniotomy using a drill and saw frequently results in fragmentation of the skull plate. Lasers have the potential to remove the skull plate intact. TE $CO_2$ lasers operating at the peak absorption wavelength of bone (λ=9.6 μm) and with pulse durations of 5-10 μs, approximately the thermal relaxation time in hard tissue, produced high ablation rates and minimal peripheral thermal damage. Both thick (2 mm) and thin (250 μm) bovine skull samples were perforated and the ablation rates calculated. Results were compared with Q-switched and free-running Er:YAG lasers (λ=2.94 μm, $\tau_p$= 150 ns and 150 μs). The $CO_2$ laser perforated thick sections at ablation rates of 10-15 μm per pulse and fluences of ~ 6 J/cm$^2$. There was no discernible thermal damage and no need for water irrigation during ablation. Pulse durations ≥ 20 μs resulted in significant tissue charring which increased with the pulse duration. Although the Er:YAG laser produced ablation rates of ~ 100 μm per pulse, fluences > 30 J/cm$^2$ were required to perforate thick samples, and thermal damage measured 25-40 μm. In summary, the novel 5-10 μs pulse length of the TE $CO_2$ laser is long enough to avoid a marked reduction in the ablation rate due to plasma formation and short enough to avoid peripheral thermal damage through thermal diffusion during the laser pulse. Further studies with the TE $CO_2$ laser are warranted for potential clinical application in craniotomy procedures.

**Key words**: craniotomy, skull, laser ablation, $CO_2$ laser irradiation, Er:YAG laser irradiation

## 1. INTRODUCTION

Prior to neurosurgical procedures, it is necessary to remove a portion of the skull to expose the underlying brain tissue. Currently a standard drill is used to create several holes through the skull, the holes are then connected using a saw, and the skull plate is removed. The drill and saw frequently cause fragmentation of the skull plate into numerous small bone chips, requiring constant water irrigation during the procedure to remove the bone chips and minimize thermal damage due to heating from the drill. Bone cement is used to recontruct the skull plate, and either bone cement or titanium plates are then used to reattach the skull plate to the rest of the skull once the neurosurgical procedure is completed.

Lasers have the potential to remove the skull plate intact, without fragmentation or the need for water irrigation. A clinical laser system designed for craniotomy procedures will require high ablation rates and high pulse repetition rates to efficiently remove large tissue volumes, as well as the minimization of peripheral thermal damage to prevent delayed wound healing after the skull plate is reattached. This study examines the effect of laser wavelength, pulse structure, and pulse duration on the ablation rates and peripheral thermal damage at the ablation site.

## 2. MATERIALS AND METHODS

### 2.1 Sample Preparation

Adult bovine skulls (Maurer & Maurer, Manchester, MD) were sectioned using a cryogenic blade and hard tissue microtome into thin (250 ± 20 μm) and thick (2.0 ± 0.1 mm) tissue samples, with an 8 x 8 mm area. The samples were sanded down to the desired thicknesses under water cooling, polished, and then frozen until use. Prior to irradiation, the samples were thawed and then kept hydrated with a swab.

Correspondence: Nathaniel M. Fried, Biomedical Engineering Department, Johns Hopkins University, 720 Rutland Avenue, Traylor 903, Baltimore, MD 21205. Email: nfried@bme.jhu.edu; TEL: (410) 614-6013; FAX: (410) 614-1980.



In *Laser-Tissue Interaction XI: Photochemical, Photothermal, and Photomechanical*, Donald D. Duncan, Jeffrey O. Hollinger, Steven L. Jacques, Editors, Proceedings of SPIE Vol. 3914 (2000) 1605-7422/00/$15.00

### 2.2 Laser Parameters

Three pulsed laser systems were used for this study. A transverse excited $CO_2$ laser (Argus Photonics Group, Jupiter, FL) with single-mode, Gaussian beam profile was operated at a wavelength of 9.6 μm and pulse durations of from 1-10 μs. A second TE $CO_2$ laser (Pulse Systems, Los Alamos, NM) was also used with a single-mode, Gaussian beam profile, a wavelength of 9.6 μm, and a variable pulse duration of 1-100 μs. The third laser system was an Er:YAG laser (Schwartz Electro-Optics, Orlando, FL) with a single-mode, Gaussian beam profile and a wavelength of 2.94 μm. The Er:YAG laser was operated in free-running mode with a pulse duration of 150 μs and in Q-switched mode with a pulse duration of 150 ns. The free-running Er:YAG laser is commonly used for ablation of both soft and hard tissue, and was therefore studied for comparison with the $CO_2$ laser. The Q-switched Er:YAG laser was used as a gold standard for ablation due to its short pulse duration which provides high ablation rates and minimal peripheral thermal damage.

Figure 1 shows the pulse structures for the $CO_2$ and Er:YAG lasers. For the conventional TE $CO_2$ laser, the majority of energy is contained within the initial gain-switched spike, which is on the order of 100-200 ns long, followed by a long tail of about 1-4 μs. This spike limits ablation rates by causing plasma formation to occur at low fluences. By slightly stretching the pulse to reduce the energy distributed in the initial 100-200 ns of the laser pulse, the plasma threshold can be raised sufficiently to increase the ablation rate. This results in more efficient ablation, making the TE $CO_2$ laser practical for clinical applications. In this study, the Argus TE $CO_2$ laser pulse duration was stretched out to 5-10 μs, and the amount of energy contained within the gain switched spike minimized. The ideal pulse structure was achieved with the 8 μs pulse, which most closely resembled a tophat with the energy most uniformly distributed.

The laser energy was measured using an energy meter, and the laser spot size was measured by both scanning a razor blade across the beam and by directly imaging the beam with a pyroelectric laser beam profilometer (Spirocon Model Pyrocam). The beam profile was single mode and fluences were defined using a Gaussian beam with a $1/e^2$ beam diameter. The laser spot diameters varied between 150-300 μm. All lasers were operated at pulse repetition rates of 1-2 Hz, low enough to avoid thermal buildup between pulses, and high enough to achieve pulse-to-pulse energy stability. For the $CO_2$ lasers, fluences between 1-35 J/cm$^2$ and energies of 1-25 mJ were studied. For the Er:YAG laser, fluences between 1-100 J/cm$^2$ and energies of 0.5-35 mJ were used.

Tissue samples were mounted in front of a pyroelectric detector and the number of pulses required to perforate each sample was measured. No saline irrigation was used during ablation. After ablation, a micrometer was used to measure the sample thickness, and a microscope interfaced to a digital CCD camera was used to determine the diameter of the entrance hole and measure the extent of thermal damage. Troughs were also created in the skull samples by scanning the laser beam across the tissue. Thick samples were fractured and sanded down to provide cross-sectional views of the craters and troughs.

### 2.3 Data Analysis

A minimum of five perforations was made for each set of laser parameters. At energies below the perforation threshold, only 3 measurements were made. Ablation rates were defined as the sample thickness divided by the average number of pulses required to perforate the sample, and recorded as the mean $\pm$ the standard deviation (S.D.). Irradiation was stopped if perforation was not achieved before 100 pulses for the thin samples and 500 pulses for the thick samples.

## 3. RESULTS

### 3.1 Ablation Rates

The ablation rates of the $CO_2$ laser are shown in Figure 2 for perforation of thin sections with pulse durations of 5, 20, 50, and 100 μs. For 5 μs pulse durations, ablation rates plateaued at ~ 20 μm per pulse at fluences of 5-10 J/cm$^2$ due to plasma formation. Samples were perforated at fluences of only ~ 2 J/cm$^2$, demonstrating efficient ablation. As the pulse duration was increased, the ablation rates and the threshold for plasma formation increased correspondingly. The perforation threshold also increased, but more slowly.

Although there was no significant difference in fluences required to perforate thin skull sections, perforation thresholds increased dramatically for thick sections as the pulse duration increased (Figure 3). $CO_2$ pulse durations of 5 μs were the most efficient, perforating 2-mm-thick skull sections at fluences as low as ~ 6 J/cm$^2$. Perforation thresholds increased with pulse duration, making ablation less efficient, because thermal diffusion during the laser pulse required more energy to be delivered into a fixed volume to achieve ablation temperatures in the tissue. Residual thermal energy left in the tissue during the laser pulse results in increased peripheral thermal damage, as will be shown in the next section.

Ablation rates using the Er:YAG laser operated in both free-running and Q-switched mode were also measured (Figure 4). The Q-switched Er:YAG removed up to 40 μm per pulse before plasma formation reduced the ablation efficiency. The perforation threshold was not detected, but occurred at fluences well below 2 J/cm$^2$, due to the short pulse duration. The free-running Er:YAG laser produced very high ablation rates, on the order of 100 μm per pulse, but was unable to perforate samples at fluences below 30 J/cm$^2$.

### 3.2 Thermal Damage

Both surface and cross-sectional images of the tissue were used to determine the extent of thermal damage after ablation. No discernible thermal damage was seen in samples ablated with $CO_2$ pulse durations of 4 and 8 μs (Figure 5). The holes and troughs appeared to be cleanly cut without evidence of charring. Although it was difficult to quantify the amount of thermal damage, it was estimated to be less than 10 μm. Considerable charring was noticeable, however, at longer pulse durations, as shown in Figure 7. The intensity of the char layer increased as the pulse duration increased from 20-100 μs.

A definitive layer of peripheral thermal damage and charring measuring 25-40 μm was also seen in the troughs and holes created with the Er:YAG laser operated in free-running mode (Figure 6ab). The Q-switched Er:YAG laser, however, produced very clean cuts with no evidence of peripheral thermal damage (Figure 6cd).

## 4. DISCUSSION

$CO_2$ laser ablation of hard tissues such as bone and dental hard tissues has been well explored.[1-13] The goal of this study was to determine the optimal laser parameters, including wavelength, pulse structure, pulse duration, and fluence for craniotomy procedures. The ideal laser for craniotomy would be capable of high ablation and pulse repetition rates to remove large tissue volumes in a short period of time, and also would be capable of minimizing peripheral thermal damage around the cuts to prevent delayed wound healing after reattachment of the skull plate. Previous studies have demonstrated that the peak absorption of bone occurs at the $CO_2$ laser wavelength of 9.6 μm.[4,7] To minimize thermal damage caused by thermal diffusion during the laser pulse, the laser pulse duration should roughly match the thermal relaxation time in hard tissue which is on the order of 2-3 μs. TE $CO_2$ lasers operate with pulse durations of approximately 1-4 μs, making them the ideal choice of laser for ablation of hard tissues. Unfortunately, the pulse structure of the laser is not well suited for producing high ablation rates. Typically, the majority of the energy is contained within the initial gain-switched spike, resulting in an effective pulse duration much shorter than 1 μs, on the order of 100-200 ns. This shorter effective pulse duration results plasma formation at lower fluences, in turn resulting in lower ablation rates. The major contribution of this study was to have the laser pulse duration stretched to approximately 5-10 μs, and the amount of energy contained within the initial gain-switched spike minimized, thus allowing higher ablation rates without plasma formation, thus making the TE $CO_2$ laser more efficient and practical for clinical use.

The optimal pulse duration was between 5-10 μs with definite evidence of charring found at pulse durations $\geq$ 20 μs. This optimal range of pulse durations is consistent with that predicted earlier by Krapchev et al.[7] Ablation rates were ~ 20 μm per pulse at fluences of 5-10 J/cm$^2$ with no evidence of charring. The thermal damage zone was less than 10 μm which is much smaller than that measured during previous $CO_2$ laser ablation studies. Conventional long-pulse and continuous-wave $CO_2$ lasers operated at a wavelength of 10.6 μm produce thermal damage zones on the order of 40-135 μm with significant charring.[1,2,11]

The ablation rates measured in this study would be practical for clinical craniotomy procedures if the laser could be operated with a high pulse repetition rate. Although all of these studies were performed with pulse repetition rates of only 1-2 Hz, TE $CO_2$ lasers are available with pulse repetition rates of over 1 kHz. Thermal buildup in the tissue due to multiple pulse irradiation would result in increased thermal damage, however, unless the laser was either scanned across the tissue and/or water was sprayed onto the tissue surface. Although these issues have yet to be explored for craniotomy applications, Ivanenko et al.[12] previously reported that Q-switched $CO_2$ laser ablation of bone at pulse repetition rates of 300 Hz using a water spray resulted in high ablation rates without any evidence of tissue charring. It is important to emphasize that all experiments performed during our study did not use a water spray to cool the tissue and reduce thermal damage. Previous studies have demonstrated, however, that water may reduce the thermal damage zone caused during ablation.[14,15]

The results of this study have demonstrated that the Er:YAG laser is not suitable for ablation of hard tissue when used without a water spray. When operated in free-running mode, the Er:YAG laser removes large amounts of tissue on the order of 100 μm per pulse, but produces peripheral thermal damage and charring measuring 25-40 μm which may result in delayed

wound healing. It should be noted that previous Er:YAG laser ablation studies have reported smaller thermal damage zones in bone, on the order of 5-15 μm.[1-3,16] This difference in thermal damage zones is most likely due to tissue preparation and the role of water cooling in reducing thermal damage during ablation. The Q-switched Er:YAG laser is capable of efficient ablation without thermal damage due to its short pulse duration, but is impractical for clinical application due to acoustic damage caused by the short pulse duration.[17,18] Finally, the Er:YAG laser is unsuitable for craniotomy procedures because it cannot be operated at pulse repetition rates > 10 Hz, making rapid removal of large tissue volumes impractical.

## 5. CONCLUSION

TE $CO_2$ lasers operated at the peak absorption wavelength of bone (9.6 μm) with pulse durations on the order of 5-10 μs, long enough to achieve high ablation rates (~ 20 μm per pulse) without plasma formation while short enough to avoid thermal diffusion during the laser pulse, are capable of perforating thick skull tissue samples at low fluences without evidence of thermal damage and without the need for water cooling. Er:YAG lasers operated without water cooling are impractical for clinical application due to the presence of peripheral thermal damage (25-40 μm) which may delay wound healing, and their limitation to low pulse repetition rates ≤ 10 Hz. Further studies with the TE $CO_2$ laser are warranted for possible clinical application in craniotomy procedures.

## ACKNOWLEDGMENTS

The authors thank Jerome Regadio and Christian Lee of the Department of Restorative Dentistry, University of California, San Francisco for their help in preparing the histology, and Kevin Dickenson and Michael Murray of the Argus Photonics Group (Jupiter, FL) for providing the TE $CO_2$ laser. We also thank Leonard J. Cerullo, MD, Director of the Chicago Institute of Neurosurgery and Neuroscience, Columbus Hospital, Chicago, IL and Larry C. Fried, MD, retired Chief of Neurosurgery, Riverside Hospital, Toledo, OH, for their clinical advice.

## REFERENCES

1. R. C. Nuss, R. L. Fabian, R. Sarkar, and C. A. Puliafito, "Infrared laser bone ablation," *Lasers Surg. Med.* **8**, pp. 381-391, 1988.
2. C. Gonzalez, W. P. van de Merwe, M. Smith, and L. Reinisch, "Comparison of the Er:YAG and $CO_2$ laser for in vitro bone and cartilage ablation," *Laryngoscope* **100**, pp. 14-17, 1990.
3. Z. Z. Li, L. Reinisch, and W. P. van de Merwe, "Bone ablation with Er:YAG and $CO_2$ laser: study of thermal and acoustic effects," *Lasers Surg. Med.* **12**, pp. 79-85, 1992.
4. M. Forrer, M. Frenz, V. Romano, H. J. Altermatt, H. P. Weber, A. Silenok, M. Istomyn, and V. I. Konov, "Bone-ablation mechanism using $CO_2$ lasers of different pulse duration and wavelength," *Appl. Phys. B* **56**, pp. 104-112, 1993.
5. T. Ertl and G. Muller, "Hard tissue ablation with pulsed $CO_2$ lasers," *Proc. SPIE* **1880**, 176-181, 1993.
6. L. Reinisch and R. H. Ossoff, "Acoustic effects during bone ablation," *Proc. SPIE* **1882**, pp. 112-121, 1993.
7. V. B. Krapchev, C. D. Rabii, J. A. Harrington, "Novel $CO_2$ laser system for hard tissue ablation," *Proc. SPIE* **2128**, 341-348, 1994.
8. D. Fried, R. E. Glena, and J. D. B. Featherstone, "Multiple pulse irradiation of dental hard tissues at $CO_2$ laser wavelengths," *Proc. SPIE* **2394**, 41-50, 1995.
9. D. Fried, W. Seka, R. E. Glena, and J. D. B. Featherstone, "Thermal response of hard dental tissues to 9- through 11-μm $CO_2$-laser irradiation," *Opt. Eng.* **35**, 1976-1984, 1996.
10. D. Fried, R. E. Glena, J. D. B. Featherstone, W. Seka, "Permanent and transient changes in the reflectance of $CO_2$ laser-irradiated dental hard tissues at $\lambda$ = 9.3, 9.6,10.3,10.6 μm and at fluences of 1-20 J/cm$^2$," *Lasers Surg. Med.* **20**, 22-31, 1997.
11. L. S. Krause, C. M. Cobb, J. W. Rapley, W. J. Killoy, and P. Spencer, "Laser irradiation of bone. I. An in vitro study concerning the effects of the $CO_2$ laser on oral mucosa and subjacent bone," *J. Periodontol.* **68**, pp. 872-880, 1997.
12. M. M. Ivanenko and P. Hering, "Wet bone ablation with mechanically Q-switched high-repetition-rate $CO_2$ laser," *Appl. Phys. B* **67**, 395-397, 1998.
13. D. Fried, M. W. Murray, J. D. B. Featherstone, M. Akrivou, K. M. Dickenson, C. Duhn, O. P. Ojeda, "Dental hard tissue modification and removal using sealed TEA lasers operating at $\lambda$ = 9.6 and 10.6 μm," *Proc. SPIE* **3593**, 196-203, 1999.
14. S. R. Visuri, J. T. Walsh, and H. A. Wigdor, "Erbium laser ablation of dental hard tissue: Effect of water cooling," *Lasers Surg. Med.* **18**, 294-300, 1996.
15. A. Shalhav, R. Wallach-Kapon, S. Akselrod, and A. Katzir, "Laser irradiation of biological tissue through water as a means of reducing thermal damage," *Lasers Surg. Med.* **19**, 407-412, 1996.
16. J. T. Walsh, T. J. Flotte, and T. F. Deutsch, "Er:YAG laser ablation of tissue: Effect of pulse duration and tissue type on thermal damage," *Lasers Surg. Med.* **9**, 314-326, 1989.
17. R. Hibst, "Mechanical effects of Er:YAG laser bone ablation," *Lasers Surg. Med.* **12**, pp. 124-130, 1992.
18. D. Fried, R. Shori, and C. Duhn, "Backspallation due to ablative recoil generated during Q-switched Er:YAG ablation of dental hard tissue," *Proc. SPIE*, 1999.

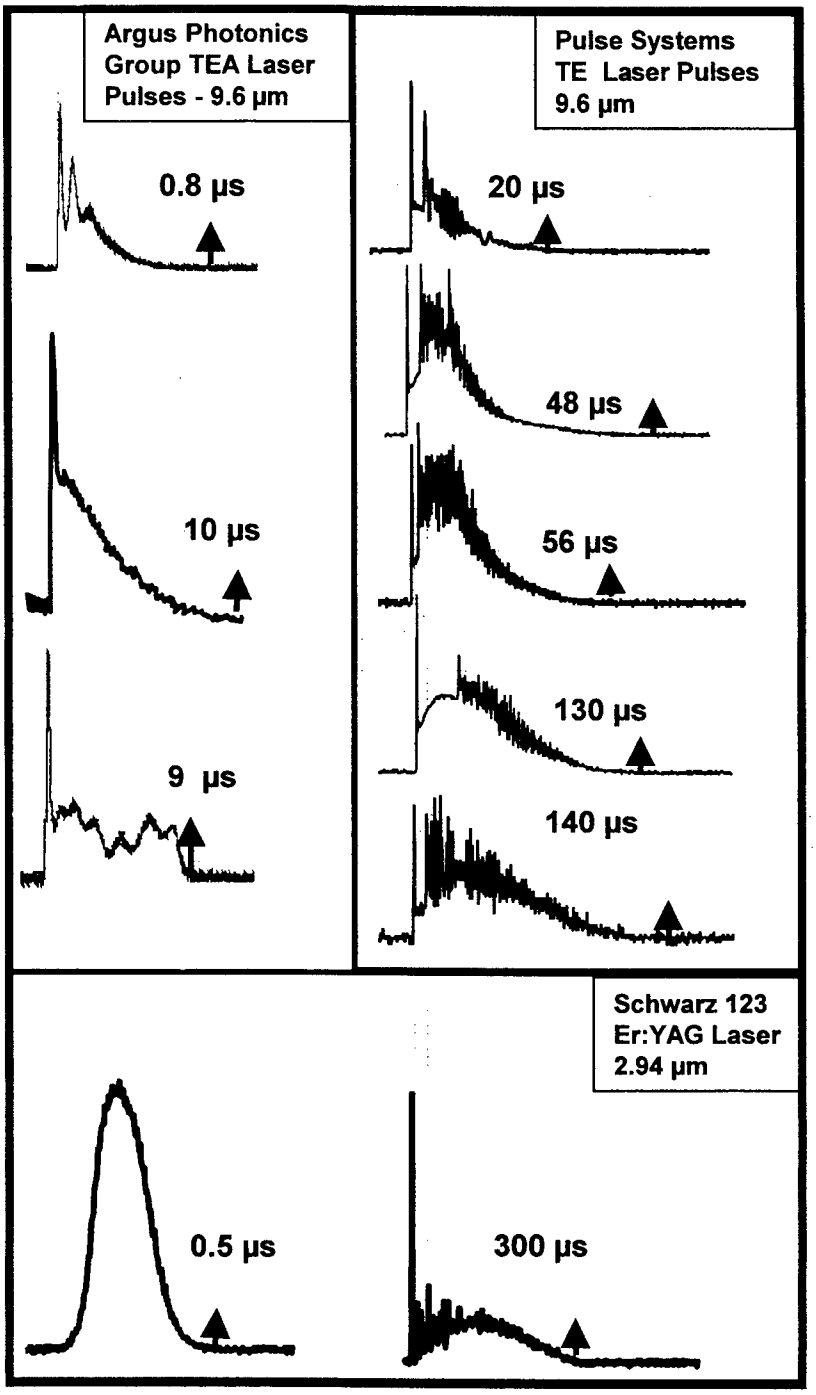


**Fig. 1.** *Temporal profiles of the IR laser pulses used in this study. The end of the laser pulse is indicated by the position of the arrows.*

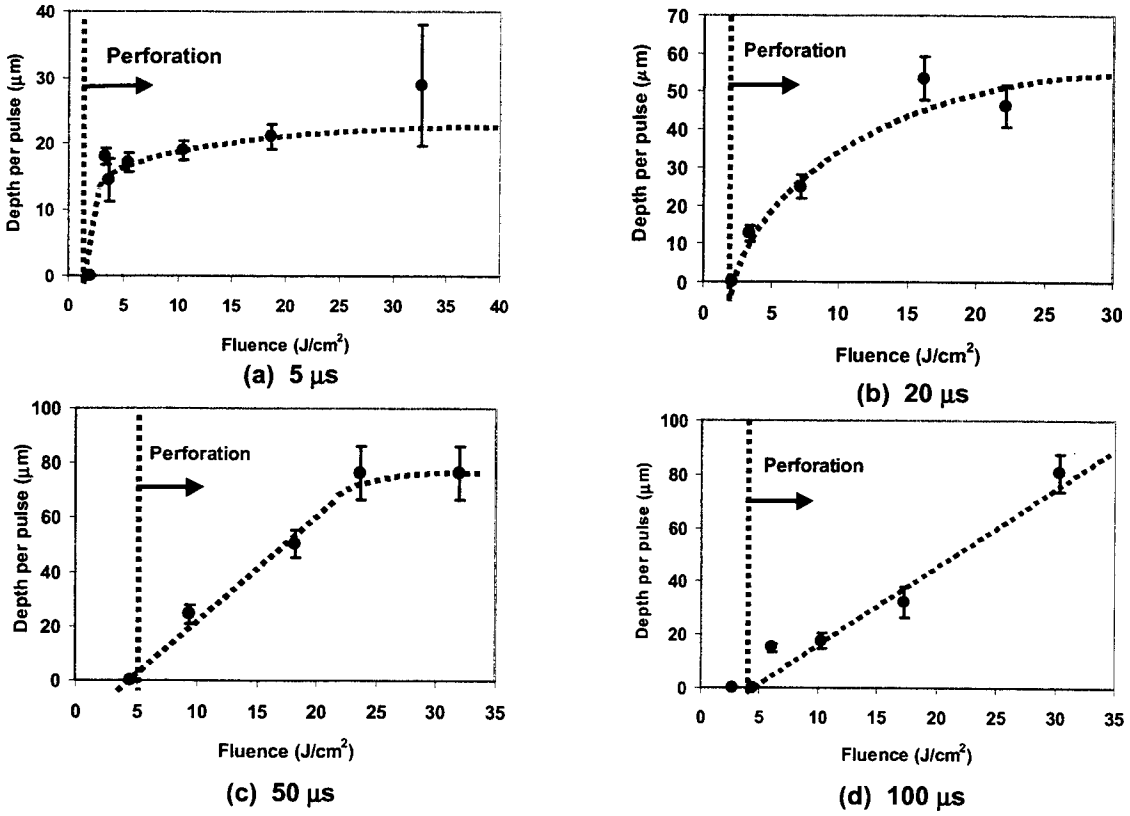


**Figure 2.** $CO_2$ ablation rates for pulse durations of from 1-100 μs.

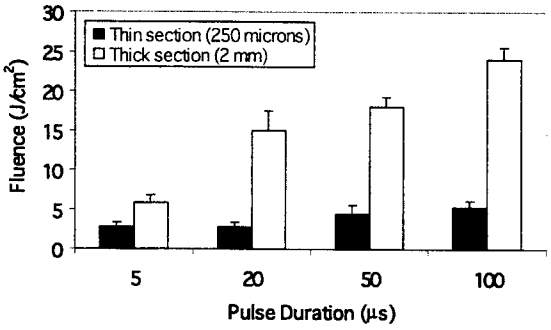


**Figure 3.** Perforation Thresholds for $CO_2$ laser pulse durations of from 1-100 μs

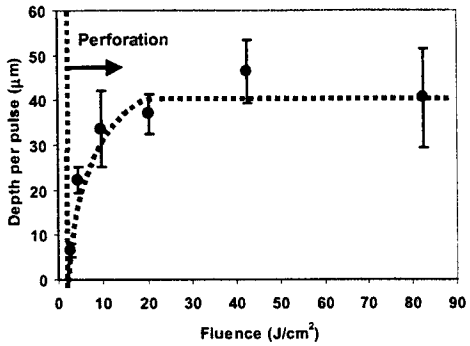


(a) Q-switched Er:YAG laser

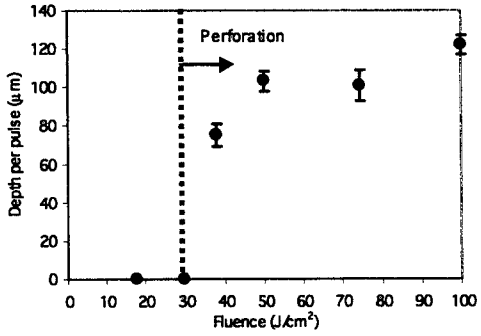


(b) Free-running Er:YAG laser (thick sample)

**Figure 4**. Er:YAG ablation rates.


(a) 4 μs, Surface View

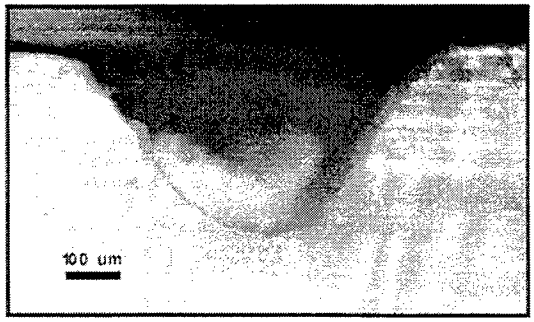


(b) 4 μs, Cross-Sectional View

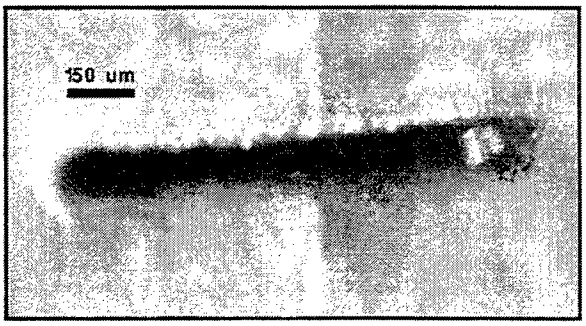


(c) 8 μs, Surface View

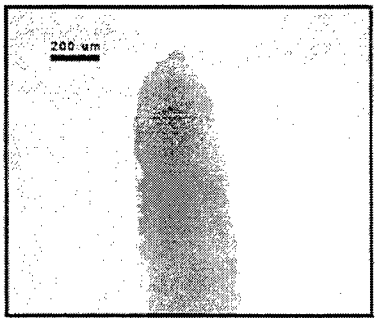


(d) 8 μs, Cross-Sectional View

**Figure 5**. Troughs created with $CO_2$ lasers having 4 μs and 8 μs pulse durations.

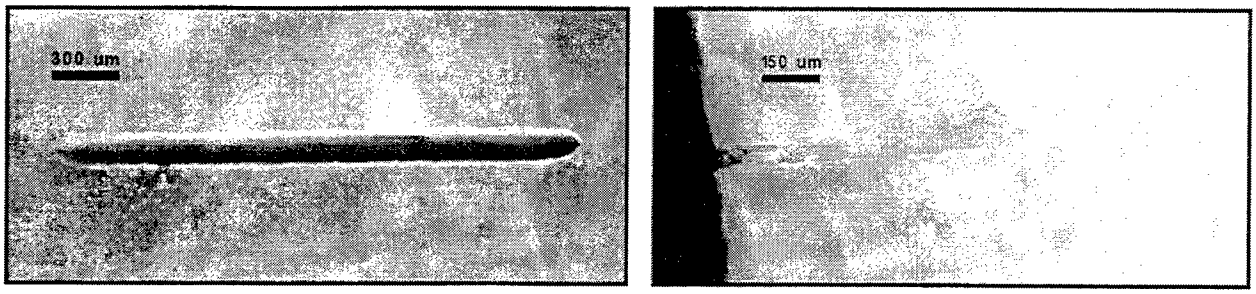


(a) Surface View (b) Cross-Sectional View

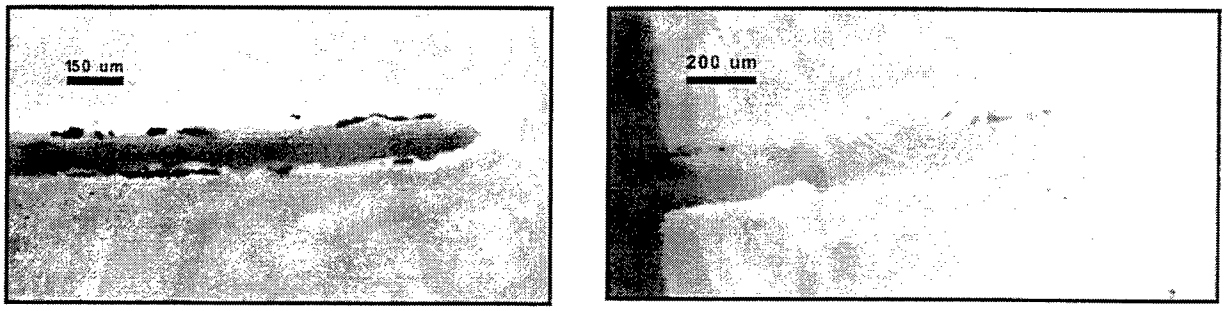


(c) Surface View (d) Cross-Sectional View

**Figure 6**. Troughs created with Q-switched (a,b) and free-running (c,d) Er:YAG laser. A char layer measuring 25-40 μm was observed using the free-running Er:YAG laser (c).

**Figure 7.** Thick fractures showing char layers for pulse durations of 20-100 microseconds.

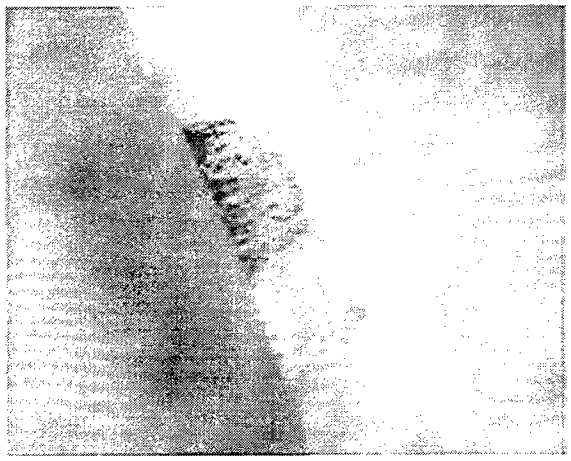

**20 μs pulse duration 5x**

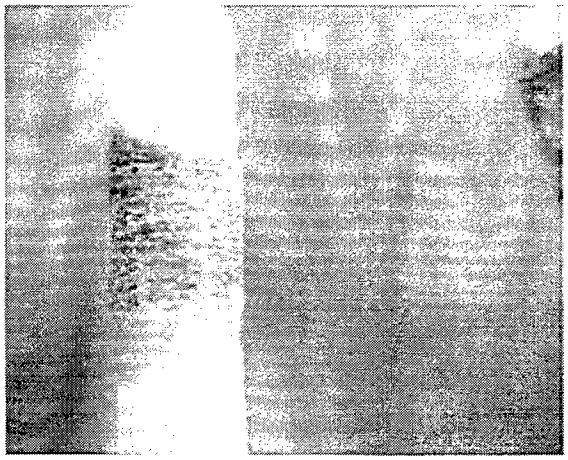

**40 μs pulse duration 5x**

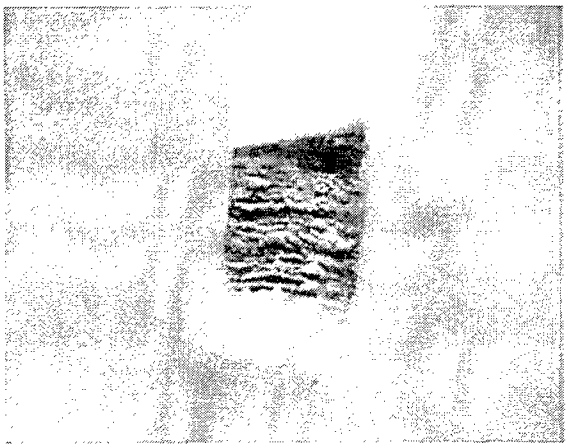

**60 μs pulse duration 5x**

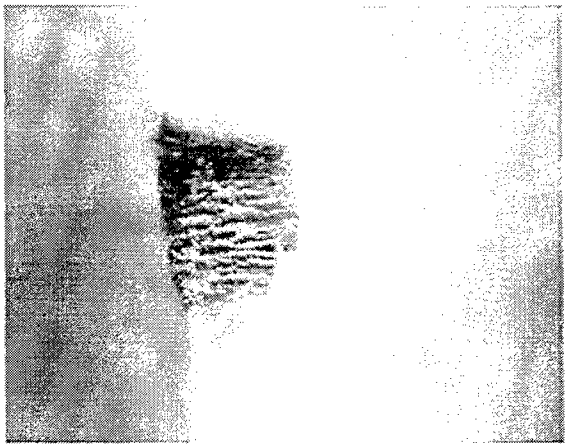

**80 μs pulse duration 5x**

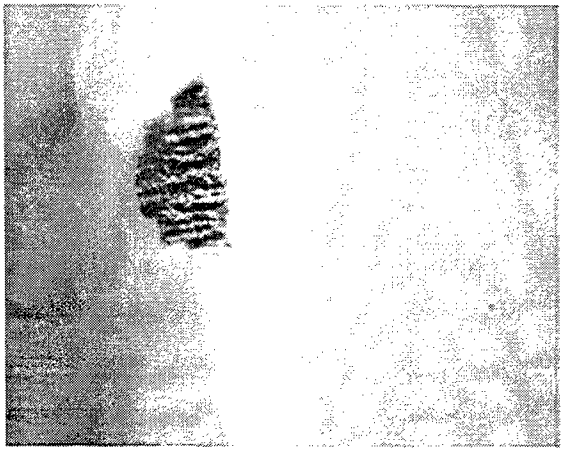

**100 μs pulse duration 5x**

# An investigation into the interaction of a XeCl excimer laser with hard tissue

Andrea K. Murray* and Mark R. Dickinson

Laser Photonics Group, University of Manchester, M13 9PL, U. K.

## ABSTRACT

An investigation into the interaction of a fibre deliverable, long pulse, xenon chloride (308 nm) excimer laser with hard biotissue has been carried out. The laser produces pulses of 200+ ns as opposed to around 10-20 ns for most of the previously reported data[1,2]. The threshold of ablation and the maximum ablation depth (AD) in human molar dentine were found to be 0.30± 0.05 J/cm$^2$ and 1.57± 0.04 μm/pulse respectively. The threshold for enamel was found to be above the achievable fluence with the available optics. The ablation process was investigated as a function of fluence (~ 0.1- 6 J/cm$^2$), pulse repetition rate (PRR) (5- 25 Hz) and number of pulses (500- 4000). Each variable was altered independently of the other two. At a constant number of pulses, ablation depth per pulse was found to increase linearly as a function of fluence, up to a saturation fluence of ~4 J/cm$^2$ . Variation of the PRR alone was found to affect both the ablation threshold and the AD. For constant fluence and PRR, AD decreases non-linearly with an increasing number of pulses . This could be because at high pulse numbers the craters are deep, the walls of the crater absorb more energy and as it is increasingly difficult for the debris to escape, shielding of the tissue occurs. Shielding may also be due to absorption in a luminescent plume. At high fluence and PRR, sharp holes were formed in the dentine although charring was sometimes found around the edges. High PRR also induced considerable mechanical damage.

**Keywords:** Ablation, dentine, laser-tissue interaction, UV, 308 nm.

## 1. INTRODUCTION

Over the past forty years lasers, have grown to span many medical applications. Most wavelengths have an application to which they are better suited than another, be it a laser scalpel or a replacement for the dentist's drill. For many years, excimer lasers have been used in industrial materials processing where the ability to produce clean, precise cuts is well documented[3] . More recently, these properties have been applied to medical applications where little thermal damage reduces necrosis and improved healing has been observed. Applications of the XeCl excimer have included treatment of athersclerosis[4], orthopaedic surgery[5], several opthalmological procedures such as cataract removal, myopia correction and glaucoma treatment[6-8] and many dental applications[9].

In hard tissue treatments erbium:YAG lasers (λ=2.94 μm) are ubiquitous, giving good ablation rates with relatively little thermal damage (~10 μm). Consequently, excimer ablation, in the UV spectral region, has not been studied very thoroughly. In hard dental tissues, 308 nm is weakly absorbed by hydroxyapatite and strongly scattered by enamel leading to a high ablation threshold. In dentine, however, there is strong absorption with little heating of the sensitive pulp. Unlike erbium lasers, water can be used to cool the tissue without appreciable absorption of incident radiation. This is the limiting factor of the ablation depth at 2.94 μm where water eventually absorbs all the incident energy. Excimer wavelengths have been found to be highly caries selective; the threshold limit for healthy dentine is four times as high as for carious dentine implying low energies, incapable of ablating healthy dentine could be used for cavity treatment.

The UV laser-tissue interaction is not well understood and there are several opposing views for mechanisms of tissue removal. More detailed work needs to be carried out to understand the mechanism behind XeCl ablation.

For medical treatments it is essential to understand the relationships between ablation depth and the parameters of the laser for total control of the procedure. The linear relationship between the ablation depth and irradiation time is important for non-feedback medical procedures, to ensure correct monitoring of the ablation depth.

*Correspondence: Tel. +44 (0)161 275 4292, Fax. +44 (0)161 275 4293, E-mail andi@fs4.ph.man.ac.uk

In *Laser-Tissue Interaction XI: Photochemical, Photothermal, and Photomechanical,* Donald D. Duncan, Jeffrey O. Hollinger, Steven L. Jacques, Editors, Proceedings of SPIE Vol. 3914 (2000)
1605-7422/00/$15.00

## 2. MATERIALS AND METHODS

The excimer (LAIS Dymer 200+) lases at 308 nm and was produced commercially for angioplasty. It produces 200 ns pulses, a factor of ten longer than most other excimers. This gives it the advantage of being fibre deliverable, with no damage to the fibre or optics. The maximum available energy is 200 mJ and this is deliverable in PRRs of 5 Hz - 30 Hz.
The laser is operable via an external trigger allowing individual pulses to be produced as desired. Alternatively it can be operated by a footswitch which when depressed runs the laser at the predetermined PRR. The cumulative number of pulses is displayed in a digital panel and the energy of the laser can be monitored by means of an in built energy meter.

The XeCl gas is replaced regularly after a few thousand pulses when the output energy falls to an unusable level due to degradation of the mixture. For this reason the energy of the laser was monitored throughout the experiment.

The samples, healthy, extracted human molars, were stored in 10% neutral buffered formalin. They were removed from the formalin just before the experiment and cut by a diamond saw into approximately 1 mm thick, parallel slices.

During ablation the samples were placed on an X-Y-Z translation stage with the beam normal to the surface of the tooth. The beam was attenuated by glass microscope slides and focused by a silica lens of focal length ~12 cm (figure 2.1). The teeth were placed in the focal plane, found using burn paper to locate the smallest spot size.
A calibrated, reverse-biased, silicon photodiode (RS OSD5.8-7Q) monitored pulse energy continuously via a beam splitter. This was connected to a Gould (DSO 4096) oscilloscope with nanosecond response. The data was collected from the oscilloscope by a PC and analysed.

Since the ablation depth of the crater was much smaller than the depth of focus of the system the dentine sample remained fixed in the Z direction during ablation. The tooth was assumed to be in the focal plane of the lens throughout the experiment. Hole areas were ~ 0.7 $mm^2$

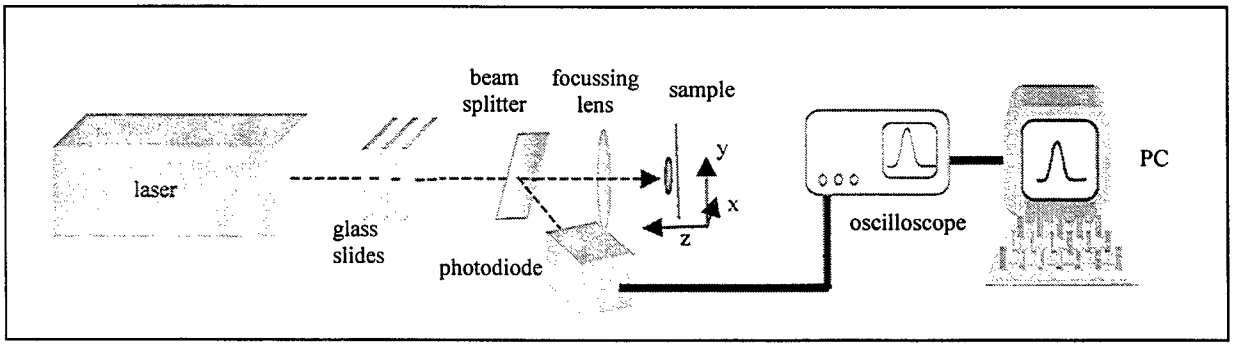


Figure 2.1. Experimental configuration

Initially the beam was attenuated to alter the fluence and craters were produced with 1000 pulses at 5 Hz. This was repeated for 500 and 2000 pulses. The maximum fluence achievable was ~6 $J/cm^2$. The number of pulses was then varied from 500 to 4000. This was carried out at set fluences and constant PRR but for PRRs of 5 Hz - 25 Hz in steps of 5 Hz. Finally the number of pulses per second (PRR) was varied, keeping the total number at 1000 and fluence at a steady value.

The holes were studied under a calibrated optical microscope; their depths were measured by focusing on the top edge and base of the hole. At threshold fluence the holes are particularly shallow and their depth is of the order of natural depressions in the dentine or those caused by the cutting with the saw. Away from threshold, holes are distinct and their depth is easily measurable.

# 3. RESULTS

## 3.1. Enamel

The ablation threshold fluence of enamel could not be overcome with the optics available, spot sizes were not small enough; consequently all ablation measurements taken are for dentine. Darkening and an alteration in the surface texture of enamel were observed after irradiance with the laser, possibly due to the removal of some organic constituents of the enamel.

## 3.2. Dentine

### 3.2.1. Effect of fluence on the ablation depth

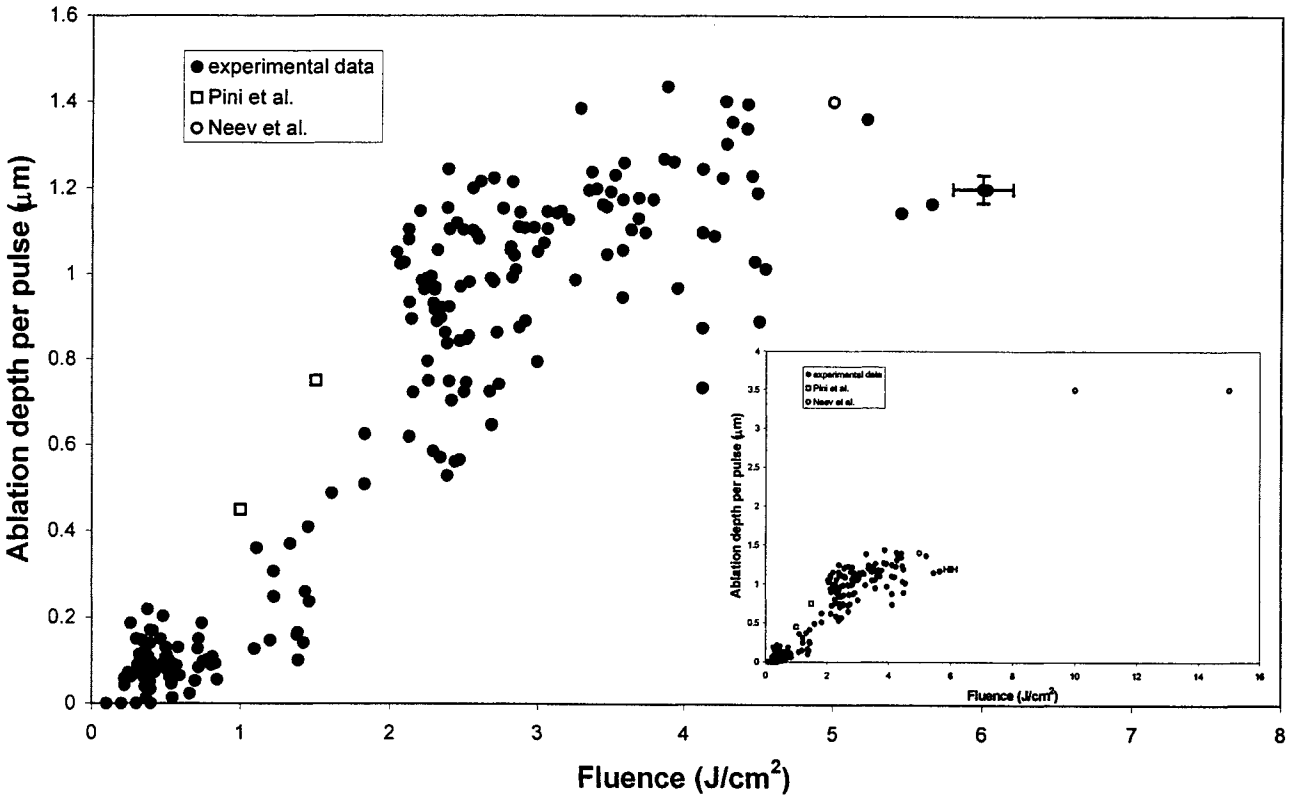


Figure 3.1 Ablation depth (μm/pulse) of dentine as a function of fluence (J/cm$^2$) for 1000 pulses at 5 Hz. Neev et al.[1] and Pini et al.[2] data are included, inset to show all Neev data points.

The ablation depth was studied at 5 Hz for 1000 pulses over a fluence range of ~ 0.1-6 J/cm$^2$. The relationship between fluence and the ablation depth per pulse is shown in Figure 3.1. The scatter of the points is due to the natural difference in composition of each sample and is a consequence of the different response to irradiation.

Initially, the ablation depth is linearly dependent on fluence, the ablation threshold of dentine lying at ~0.30 ± 0.05 J/cm$^2$. As the fluence reaches ~4 J/cm$^2$ the linear relationship is replaced with a logarithmic one, representing the saturation of the pulse. The escaping particles could block the beam in one of two ways, a dense plume ejected from the hole or, as the hole increases in depth, the ablated material experiencing difficulty escaping, blocks the beam incident on the base of the crater. The ablation efficiency is further reduced by the walls of the hole absorbing energy.

During the linear phase of ablation, the mean AD/pulse is 0.28± 0.03 μm/(J/cm$^2$). The maximum ablation depth per pulse of 1.44 ± 0.03 μm occurs just before saturation at 3.88 J/cm$^2$.

Above threshold fluence, a distinct, loud cracking noise was heard upon ablation and a blue/yellow plume was observed. Since the plume was observed for both high and low fluences but saturation did not occur until higher fluences it can be assumed that the plume has a low density and that saturation is caused by particles trapped in the crater.

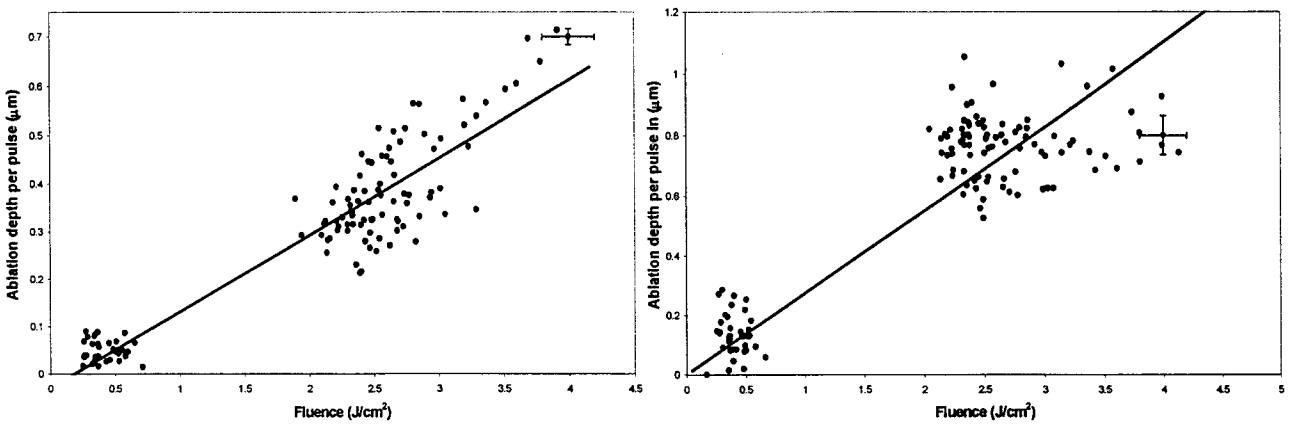


Figure 3.2 Ablation depth (μm/pulse) of dentine as a function of fluence (J/cm$^2$) at 5 Hz for 2000 (left) and 500 pulses (right).

At high fluence, sharp edged, rectangular holes with straight sides were observed under the microscope. Slight charring is also seen around the edges of the crater. As the fluence is reduced, the holes become more irregular with decreasing diameters.

The fluence-ablation depth relationship was also investigated for 500 and 2000 pulses, displayed in figure 3.2. Corresponding values for average ablation depth per pulse were 0.28± 0.06 μm/(J/cm$^2$) and 0.16± 0.02 μm/(J/cm$^2$) respectively. Maximum ablation was calculated as 1.00± 0.06 mm and 1.43± 0.02 mm respectively.

For comparison two sets of previously published data have been included on figure 3.1. The first data from Neev et al.[1] was taken with a constant number of 15 ns pulses at a PRR of 5 Hz, the second, from Pini et al.[2] is for 100, 20 ns pulses at 25 Hz. Neev's results lie out of the energy range of the Dymer 200+ but extrapolation of the results should give ablation rates in a similar range. Pini's results should give a higher ablation depth per pulse due to the increased heating caused by the higher PRR. The results correspond with both Pini and Neev. Pini's results do as expected lie on a steeper slope implying a PRR effect. Since the pulse lengths used by Pini and Neev are both an order of magnitude smaller than the Dymer 200+ this implies that it is fluence, not the peak pulse power, that is crucial for ablation.

### 3.2.2. Effect of the number of pulses on ablation depth

As ablation occurs and the crater produced by the laser deepens, the walls absorb more energy. The latter pulses are partially blocked by debris unable to escape from the deepening hole and so cannot ablate as efficiently as earlier pulses. As a consequence of this, the ablation depth per pulse decreases with an increasing number of pulses.

This is a trait that is independent of the fluence, as shown in figure 3.3 and was also found to be independent of the PRR. The relationship between number of pulses and ablation depth per pulse is logarithmic but AD is still strongly dependent on the fluence as expected. The trend follows that of data taken by Hame et al.[10], a rapid rise in ablation depth just after threshold, to a maximum value and then a slow, non-linear decrease as the number of pulses increases. The fact that a lower number of pulses removes more tissue could also explain Pini's ablation per pulse being higher in figure 3.1.

At 5 Hz, the energy input occurs slightly faster than the relaxation time of the tissue. At low numbers of pulses the effect is negligible but as the number of pulses is increased, the build-up of heat in the tissue begins to cause damage and melting around the crater edge. At a high number of pulses, mechanical damage in the form of fractures in the dentine occurred and char begins to build up around the edges.

For the highest fluence in figure 3.3 it can be seen that within approximately 1000 pulses, 0.5 mm in ablation depth, the depth per pulse falls by a factor of 2. By the time the hole has reached just over half its width in depth, the ablation has decreased in efficiency by half. Absorption of laser energy in the crater is constantly changing, due to the energy of the beam being absorbed elsewhere.

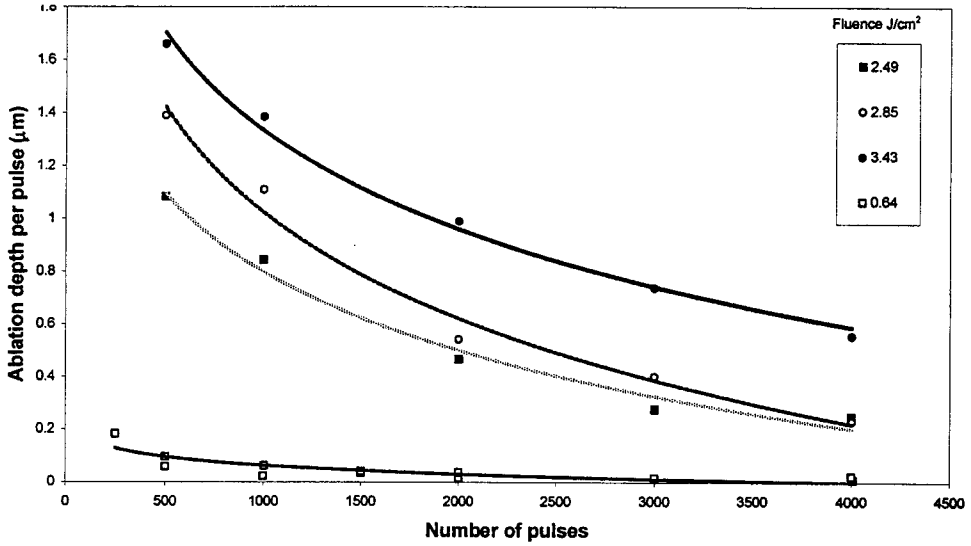


Figure 3.3 Ablation depth per pulse in µm for increasing numbers of pulses at 5 Hz and several fluences.

### 3.2.3. Effect of varying the PRR on the ablation depth

The expected effect of increasing the PRR whilst keeping the fluence and number of pulses constant, is to increase the ablation depth per pulse and decrease the ablation threshold. An increase in AD is indeed the result that was obtained, the individual fluence-AD shown in figure 3.4. Lines of best fit are also plotted for comparison. Since all threshold values lie within ~0.2 J/cm$^2$ of each other and the data is so scattered, it is unclear whether the PRR has a definite effect on the values.

The maximum ablation depths per pulse and average ablation depths per pulse and unit fluence for changing PRRs were calculated to be as shown in table 3.1.

| PRR Hz | Maximum ablation per pulse (μm) | Average ablation per pulse per unit fluence (μm/(J/cm$^2$)) | Ablation threshold J/cm$^2$ |
|---|---|---|---|
| 5 | 1.44± 0.03 | 0.28± 0.03 | 0.13± 0.05 |
| 10 | 1.41± 0.03 | 0.30± 0.03 | 0.09± 0.05 |
| 15 | 1.57± 0.04 | 0.32± 0.04 | 0.22± 0.05 |
| 20 | 1.55± 0.04 | 0.33± 0.04 | 0.23± 0.05 |
| 25 | 1.56± 0.04 | 0.39± 0.04 | 0.25± 0.05 |

Table 3.1 Maximum ablation depths per pulse and average ablation depths per pulse and unit fluence for changing PRRs.

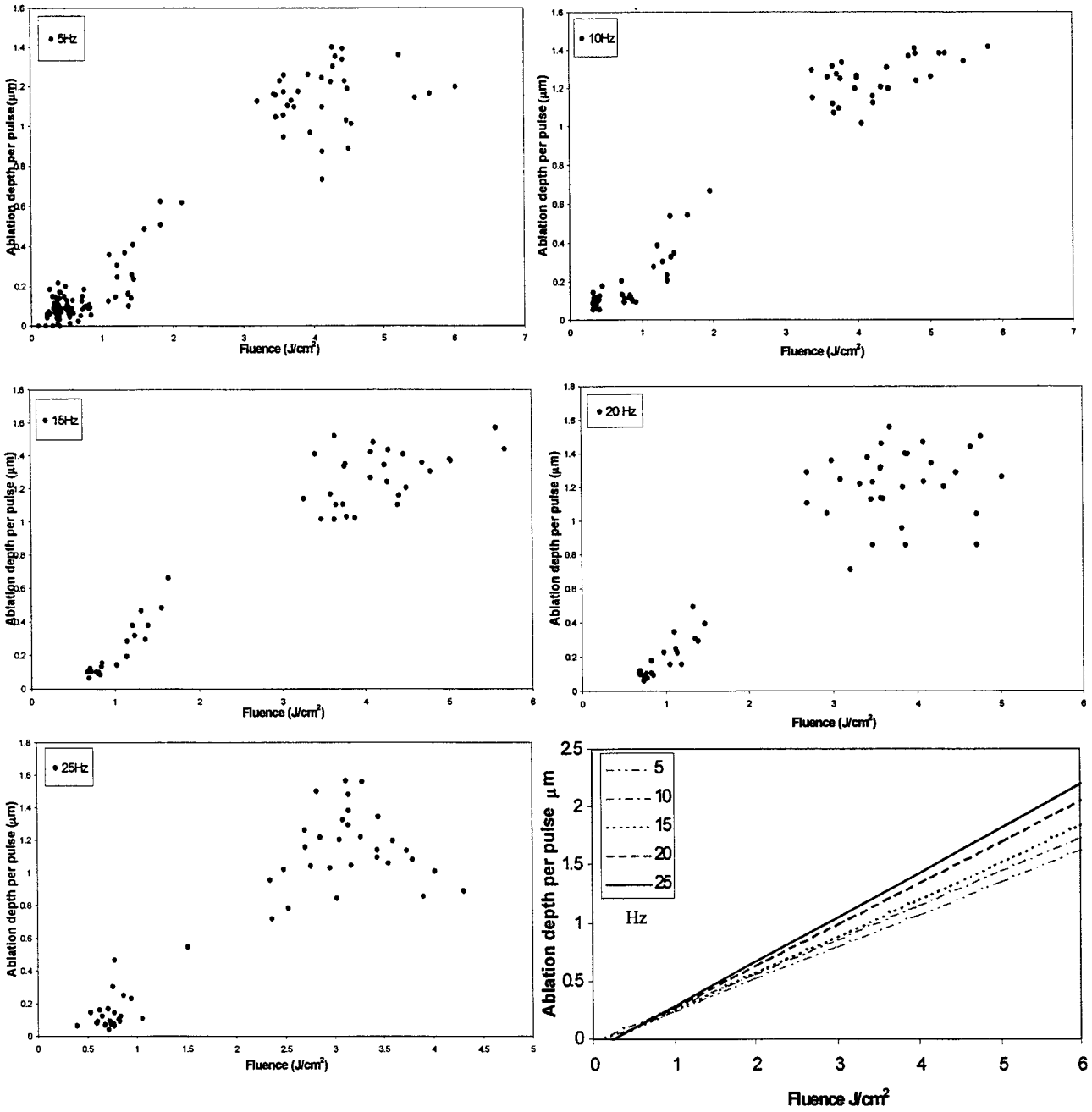


Figure 3.4 Ablation depth per pulse for PRRs between 5 Hz and 25 Hz. A graph of best fit for each set of data is also plotted for comparison of Ablation rates and thresholds.

As the PRR was increased there was obvious charring and fracturing around the crater edges. Holes are sharper but at the expense of weakened dentine. The affected dentine does not increase in area as the PRR is increased, instead the damage becomes concentrated. The thermal damage is due to the increased rate of energy into the tissue increasingly exceeding the thermal relaxation time rising with PRRs. At the lowest PRR of 5 Hz, the tissue gets a chance to cool down between pulses, at higher PRR the heat builds up in the tissue before it can dissipate, causing damage. The only way to avoid heat accumulation in the tissue would be to operate the laser manually one pulse at a time.

## CONCLUSIONS

The ablation threshold of enamel exceeded the achievable fluence (~30 J/cm$^2$) with the available optics.

Ablation per pulse for healthy, human, molar dentine has been found to depend linearly on fluence up to a saturation value of ~4 J/cm$^2$ where the relationship becomes logarithmic. A threshold fluence of 0.30± 0.05 J/cm$^2$ was calculated and a maximum ablation depth per pulse of 1.57± 0.04 μm was observed.

The effect of increasing the number of pulses led to a logarithmic decrease in the ablation depth per pulse implying a constantly changing absorption coefficient due to absorption of the beam by the walls of the hole, escaping particles that have been ablated but are trapped in the hole or possibly by a luminescent plume. This result suggests that it is not possible to fit the ablation mechanism with a simple Beer's law theory. This pulse number-AD relationship is reproducable for differing PRRs and energies.

PRR affects the ablation depth per pulse due to the escalating heat experienced by the tissue. Increasing the PRR increases the ablation depth per pulse (μm). The threshold of the ablation should decrease with increasing PRR, however, the thresholds are close together and the data points are scattered at low fluence, thus making threshold comparisons difficult.

At high fluence, pulse number or PRR there is a noticeable increase in thermal damage. High PRRs also cause considerable mechanical damage.

Fluence is the most influential factor in the ablation depth per pulse, outweighing the effects of both PRR and number of pulses.

## ACKNOWLEDGEMENTS

I would like to thank EPSRC and Spectranetics, CO.

## REFERENCES

1. J. Neev, D. V. Raney, W. E. Whalen, J. T. Fujishige, P. D. Ho, J. V. McGrann & M. W. Berns, "Dentin Ablation with Two Excimer Lasers: A Comparative Study of Physical Characteristics," Lasers in Life Sciences **5**, pp. 129-153, 1992.
2. R. Pini, R. Salimbeni, M. Vannini, R. Barone & C. Clauser, "Laser Dentistry: A New Application of Excimer in Root Canal Therapy," Lasers in Surgery and Medicine **9**, pp. 352-357, 1989.
3. U. Rebhan, H. Endert & G. Zaal, "Micromanufacturing benefits from excimer-laser development,"Laser Focus World, **November**, 91-96, 1994.
4. T. K. Bohley, F. Aparicio, G. S. Derrickson, R. A. Golobic, K. P. Grace, I. Trefil, G. A. Murray, "An excimer laser system for cornary angioplasty," *Laser Surgery: Advanced Characterisation, Therapeutics, and Systems II*, 1200, pp. 480-486, 1990.
5. L. Yow, J. S. Nelson, M. W. Berns, "Ablation of Bone and Polymethylmethacrylate by an XeCl (308 nm) Excimer Laser," Lasers in Surgery and Medicine **9**, pp. 141-147, 1989.
6. T. M. Nanevicz, M. R. Prince, A. A. Gawande, C. A. Puliafito, "Excimer Laser Ablation of the Lens," Arch. Opthalmol., **104**, pp. 1825-1829, 1986.
7. D. Muller, "Excimer Lasers in Medicine," Lasers & Applications, **May**, pp. 85-89, 1986.
8. D. Muller & R. Svrulga, "Excimer Lasers Offer Promise in Surgical Applications," Laser Focus, **July**, 70-81, 1985.
9. H. A. Wigdor, J. T. Walsh, J. D. B. Featherstone, S. R. Visuri, D. Fried & J. L. Waldvogel, "Lasers in Dentistry," Lasers in Surgery and Medicine **16**, pp. 103-133, 1995.
10. H. Hame, R. Voss, T. Papioannou, W. Grundfest, R. Johnson, "The effect of the 308nm excimer laser on tooth dentin," *Laser Surgery: Advanced Characterisation, Therapeutics, and Systems II*, 1200, pp. 452-458, 1990.

# Further Characterization of Photothermal Breakdown Products of Uric Acid Stones Following Holmium:YAG Laser Lithotripsy

Randolph D. Glickman[1a], Susan E. Weintraub[2], Neeru Kumar[1], Nicol S. Corbin[3], Omid Lesani[3], Joel M. H. Teichman[3]

[1]Dept. of Ophthalmology; [2]Dept. of Biochemistry, [3]Div. of Urology, Univ. of Texas Health Science Center, San Antonio, Texas 78229

## ABSTRACT

Previously we found that Ho:YAG laser (2120 nm) lithotripsy of uric acid stones produced cyanide, a known thermal breakdown product of uric acid. We now report that alloxan, another thermal breakdown product, is also likely produced. Uric acid stones (~98% pure) of human origin were placed in distilled water and subjected to one of the following experimental treatments: unexposed control, exposed to Ho:YAG laser, Nd:YAG laser, or mechanically crushed. Samples were then processed for HPLC analysis with UV detection. Peaks were identified by comparison to authentic standards. All samples contained uric acid, with retention time (RT) about 6 min. All of the laser-exposed samples contained a peak that eluted at 2.5 min, identical to the RT of authentic alloxan. Ho:YAG laser irradiation, however, produced a larger presumed alloxan peak than did the Nd:YAG laser. The peak at 2.5 min, as well as unidentified later-eluting peaks, were present in the laser-exposed, but not the unexposed or mechanically crushed, samples. These results confirm the thermal nature of lithotripsy performed with long-pulse IR lasers.

**Keywords**: holmium YAG lithotripsy, uric acid, ablation, thermal, cyanide, alloxan, HPLC, mass spectroscopy

## 1. INTRODUCTION

The earlier reports from this research group have documented that the ablation of urinary calculi by Ho:YAG laser irradiation proceeds primarily by a photothermal mechanism.[1-3] Based on measurements of mechanical forces produced during Ho:YAG irradiation[3], only weak forces were generated by the elongated cavitation bubbles produced during Ho:YAG laser irradiation. High speed photography also revealed that stone ablation commenced prior to the onset of the cavitation bubble[3]. Chemical analysis of the stone samples further revealed the presence of thermal decomposition products of stone materials following Ho:YAG irradiation[1,3-5]. Taken together, these findings are inconsistent with a photomechanical disruptive effect of the laser on the stone material, but rather support a thermal breakdown process.

### 1.1. Nature of uric acid stone breakdown

Most of the thermal breakdown products produced by Ho:YAG laser irradiation of the common types of urinary stones were identified as carbonates, oxides, and pyrophosphates[1,4,5]. The production of these compounds were readily predicted as the result of pyrolytic and oxidation reactions that occur at high temperatures. Somewhat unexpected, however, was the finding of cyanide resulting from laser irradiation of uric acid stones[6]. This finding is highly consistent with a thermal mechanism of Ho:YAG lithotripsy, because cyanide is a known thermal breakdown product of uric acid[7,8], but has been shown not to result from simple mechanical disruption of uric acid stones[6]. A proposed reaction pathway for laser-induced, thermal breakdown of uric acid was presented at last year's Laser-Tissue Interaction session[4], and some preliminary evidence for the production of at least one additional breakdown product, alloxan, has been reported elsewhere[5].

### 1.2 Proposed mechanism of uric acid thermal decomposition

The chemical reactions shown in Figure 1 summarize three possible reaction pathways for the thermal decomposition of uric acid.

[a]Corresponding author: E-mail: glickman@uthscsa.edu; Telephone: 210-567-8420; Fax: 210-567-8413



In *Laser-Tissue Interaction XI: Photochemical, Photothermal, and Photomechanical*, Donald D. Duncan, Jeffrey O. Hollinger, Steven L. Jacques, Editors, Proceedings of SPIE Vol. 3914 (2000)
1605-7422/00/$15.00

The relative yield of each pathway is probably a function of temperature and other local variables such as pH. Therefore, the results obtained with an *in vitro* experiment may not be identical to the *in vivo* situation. Nevertheless, the purpose of this study was to determine, in a laboratory setting, which of the indicated derivative compounds were produced during Ho:YAG ablation of uric acid stones. Identifications were based on standard physical chemical techniques, such as optical absorption and mass spectroscopy.

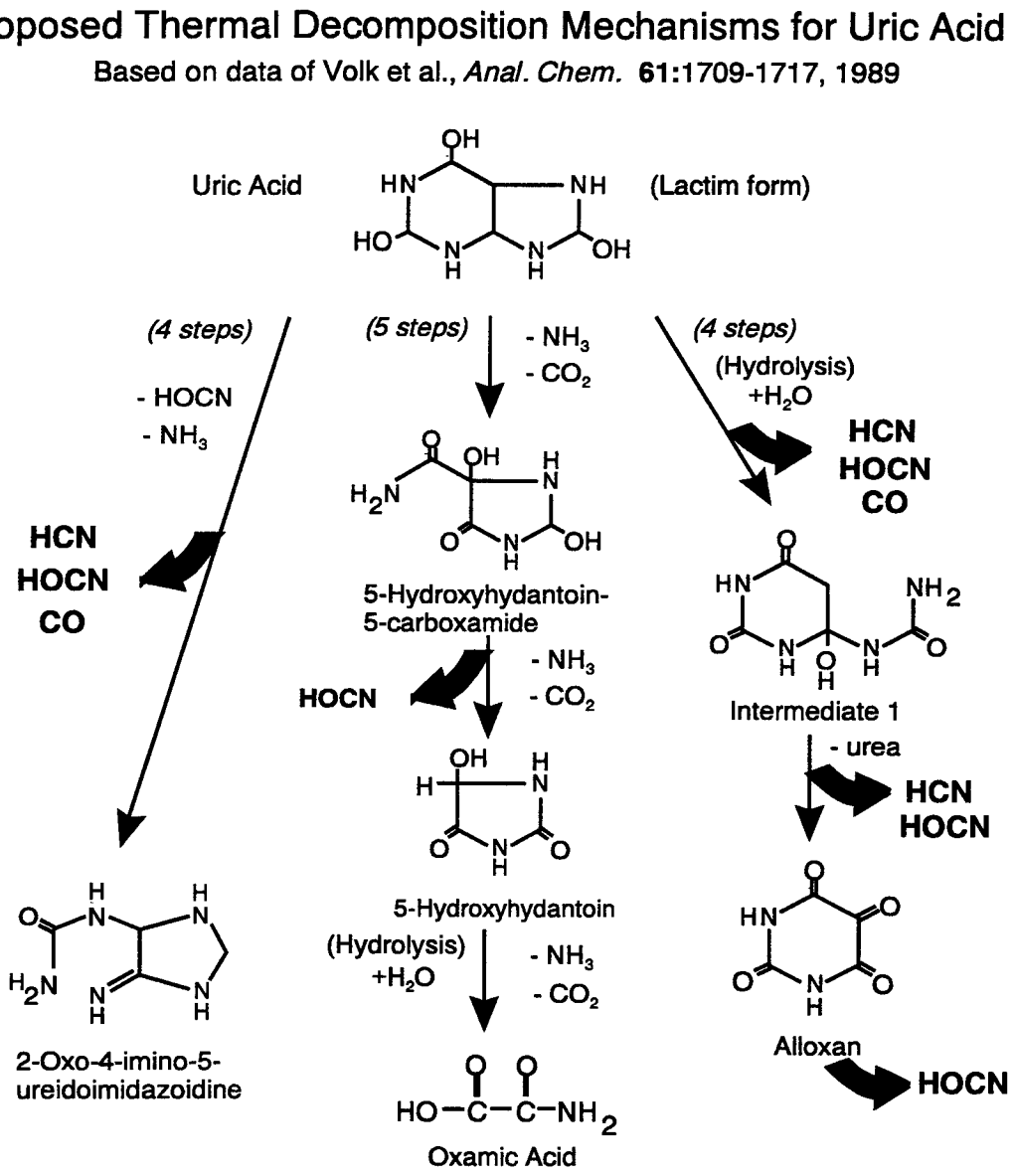


**Figure 1**. Alternative reaction pathways proposed for the thermal decomposition of uric acid. Chemical symbols: HCN: cyanide, HOCN: cyanic acid, CO: carbon monoxide. Heavy black arrows indicate loss of small molecular fragments during decomposition. Chemical reactions based, in part, on studies of uric acid oxidation by Volk et al.,1989[13].

## 2. METHODS

### 2.1. Urinary calculi

The urinary calculi used in this study were of human origin and were obtained from a stone analysis laboratory (L.C. Herring Co., Orlando, FL). They were analyzed as 98% pure uric acid. The stones were stored in capped, 50-ml plastic, conical centrifuge tubes until use.

### 2.2. Laser exposure

The experimental apparatus was arranged so that the stones were irradiated while submerged in distilled water. The stones were separated into two control groups (one unexposed sample, and one mechanically-crushed sample), and several laser-exposed groups. The laser source used was a VersaPulse Select clinical Ho:YAG lithotripter (Coherent Medical Group) emitting at 2120 nm, pulsewidth = 250 μs, that could also be operated in a non Q-switched Nd:YAG mode, emitting at 1064 nm in a pulsewidth of 1.8 msec. Laser emissions were delivered to uric acid stones through a low $OH^-$ optical fiber. The diameter of the optical fibers used for the laser irradiation was 365 μm. Sample exposures were accomplished by placing individual stones in plastic centrifuge tubes containing 50 ml of sterile distilled water. While stabilizing the stone with a pair of forceps, the laser delivery fiber optic was introduced into the water and positioned against the stone. A train of laser pulses was then delivered until the desired total amount of energy was deposited into the stone. With the Ho:YAG laser, a total of 10 kJ was delivered, and with the Nd:YAG laser, a total of 10 and 20 kJ total energy was delivered in different samples. The laser energy output was measured with an EPM-1000 power/energy meter fitted with a J25 pyroelectric joulemeter probe (Molectron Detector, Portland, OR).

### 2.3. Analysis of uric acid thermal breakdown products

At the conclusion of the laser exposure, the centrifuge tubes were capped and kept frozen at -20 °C until the water containing the stone was chemically analyzed. Control samples consisted of stones unexposed to laser or mechanically crushed in 50 ml of distilled water. Samples were analyzed by HPLC with UV absorption detection, as well as by absorbance spectroscopy, and mass spectroscopy (MS). MS was performed in the UTHSC Mass Spectroscopy Laboratory.

### 2.4. High performance liquid chromatography (HPLC) analysis of stone samples

HPLC was used to detect the presence of additional breakdown products in laser-exposed stones, to separate these components from each other, and also to purify them partially prior to analysis by mass spectroscopy. However, different HPLC methods had to be used for these various applications.

#### 2.4.1. HPLC method optimized for resolving peaks corresponding to uric acid breakdown products

Alloxan and other organic compounds formed by thermal decomposition of uric acid were detected by reversed phase HPLC analysis, using a 4.6 x 150 mm Waters Spherisorb ODS2 analytical column. The mobile phase was 25 mM potassium phosphate, pH 3, with a flow rate of 1 ml/min. UV absorbance detection was performed with a Waters 490 multiwavelength detector set to measure absorbance at 230 nm, 265 nm, and 285 nm. The samples were prepared for HPLC by first centrifuging them at 5,000 rpm for 10 min to precipitate heavier sediment. The supernatant was then passed through a 0.45 μm pore syringe filter to remove fine particles. Twenty μl aliquots of the filtered supernatant were injected onto the column. Chromatographic data was collected and analyzed with a Waters Millennium system. When possible, peaks were identified by comparing retention times to those of authentic standards.

#### 2.4.2. HPLC for sample clean-up prior to mass spectroscopy

In order to prepare samples for mass spectroscopy, the HPLC methods had to be modified to eliminate the use of inorganic salt buffers in the mobile phase. Switching to a pure organic solvent, however, decreased the retention time and resolution of the analytes of interest on the Spherisorb ODS2 column. Somewhat better resolution was obtained by using $NH_2$-based column chemistry. A Bondclone-$NH_2$ column (Phenomenex) was selected for use, and eluted with 60% acetonitrile in water, at a flow rate of 1 ml/min. This method separated the uric acid derivatives from the parent molecule (i.e. uric acid), but did not resolve the

individual derivatives themselves. This medium, however, was suitable for subsequent mass spectroscopy, because there was no interference from salt buffers, and the samples could be evaporated to any desired degree of dryness by lyophilization.

### 2.5. Mass spectroscopy

Mass spectroscopy using electron ionization was performed using a Finnigan MAT 4615 quadrupole spectrometer (Finnigan Corp., Palo Alto, CA). Electron energy was set to 70 eV, and the ion source temperature was set to 160 °C, depending on the

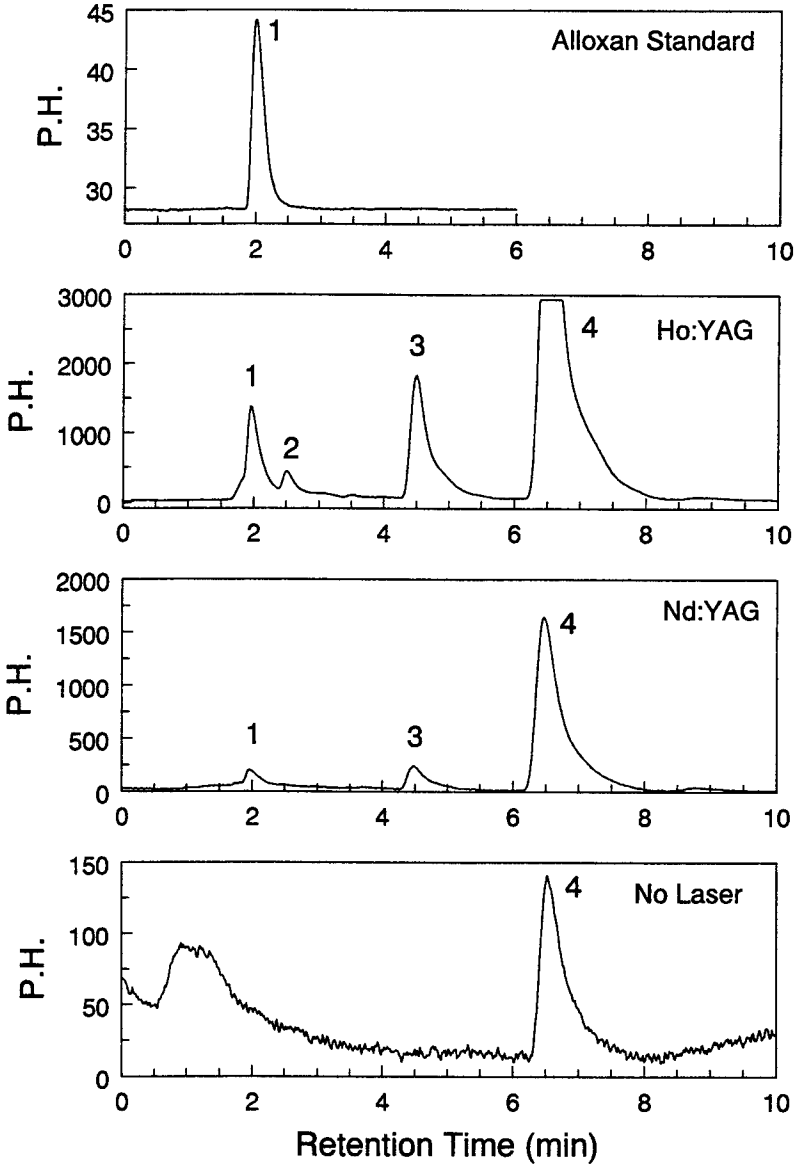


**Figure 2.** HPLC chromatograms obtained from uric acid stones either unexposed, exposed to Ho:YAG, or Nd:YAG laser. Top chromatogram is of alloxan standard. Experimental and HPLC conditions given in text. Numbers refer to analyte peaks in the chromatogram. Detection wavelength = 230 nm. P.H. = Peak Height.

sample. The samples were introduced into the instrument by direct insertion probe, which was then heated until the sample was completely vaporized. Identification of MS/MS peaks in the spectra were made by comparison to authentic reference standards.

## 3. RESULTS

### 3.1 Detection of derivatives after Ho:YAG lithotripsy of uric acid stones

In order to demonstrate that organic compounds other than cyanide were produced by the laser-induced uric acid decomposition, aliquots of the laser-exposed stones were subjected to HPLC analysis as described in section **2.4.1.** The stones were irradiated under water, either with the Ho:YAG or Nd:YAG laser, through a fiber optic placed in contact mode against the stones. Stones exposed to Ho:YAG laser received a total of 10 kJ energy delivered with the the laser set to 10W output and a repetition rate of 10 Hz. Stones exposed to the Nd:YAG laser received a total of 20 kJ energy delivered with the laser set to 20W and a repetition rate of 10 Hz. HPLC analysis of the resulting samples yielded the chromatograms shown in Figure 2. The only organic compound detected by HPLC in non-irradiated or mechanically crushed control samples was uric acid, i.e the parent compound (bottom trace in Figure 2, peak with retention time of ~6.5 min). In laser irradiated samples, several additional peaks appeared, with three major peaks noted with retention times of 2, 2.5, and 4.5 min (see middle two traces in Figure 2, peaks labeled #1, 2, and 3). Based on the expected formation of the compound, alloxan, as proposed in the reaction mechanism shown in Figure 1, the retention times of these unknown peaks were compared with the retention time of an authentic alloxan standard. Peak #1 found in both the Ho:YAG- and the Nd:YAG-exposed samples has the same retention time as that of alloxan. In Figure 2, compare peak #1 in the top trace (the alloxan standard), to peak #1 in the middle two traces (laser-exposed stones). The peaks labelled #2 and 3, detected in the laser-exposed stones, have not yet been identified.

It should also be noted that although the same breakdown products are produced during Ho:YAG or Nd:YAG laser exposure, the quantity of these compounds is much greater after Ho:YAG laser than after Nd:YAG laser. This may be appreciated by the relative heights of the chromatogram peaks (compare the ordinates of the two middle traces in Figure 2). Note that this difference occurred despite twice as much energy being delivered by the Nd:YAG laser than by the Ho:YAG laser, and probably reflects

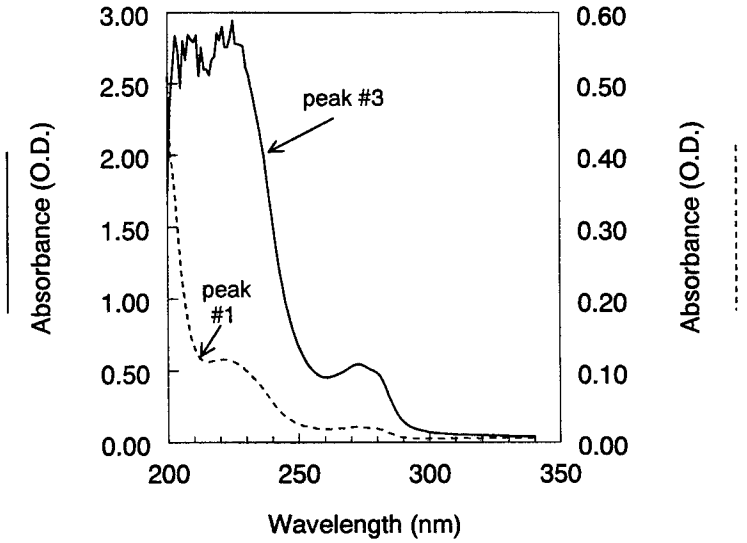


**Figure 3.** UV absorption spectrum taken of isolated fractions from HPLC analysis of Ho:YAG exposed stones. Peak numbers correspond to peaks in Figure 2.

wavelength-dependent absorption differences of the laser radiation in the stone matrix.

The peaks from these HPLC analyses were individually collected in order to obtain their UV absorption spectra to assist in identifying them. Although an attempt was made to fractionate peaks 1 and 2, their chromatographic separation was rather incomplete, and it is likely that the fractions were cross-contaminated. In contrast, peak 3 was well separated from the other peaks and could be isolated completely. Fractions from several successive runs were pooled and the UV absorption spectrum from 200 to 340 nm was obtained (Figure 3). The dotted curve in Figure 3 shows the absorption spectrum of peak 1, while the solid curve shows the absorption spectrum of peak 3. The other fractions collected had insignificant absorption in this region. Note that the extinction coefficient of the material in peak 3 was high enough below about 220 nm so that the spectrophotometer detector was saturated. Although the spectra obtained in these two fractions was clearly distinguishable from each other, they were not sufficiently diagnostic to make a clear identification of the compounds.

### 3.2. UV absorption spectra of isolated HPLC peaks

In an attempt to identify the peaks observed in the HPLC chromatograms shown in Figure 2, laser-exposed stone samples were processed with the HPLC method modified as described in section **2.4.2** to prepare them for mass spectroscopy. This method did not resolve the derivative compounds from each other, but did separate the derivatives (Figure 4, early peak with retention time of 12 min) from uric acid (Figure 4, later peak with retention time of 15 min). Fractions were pooled from ten HPLC runs on the Bondclone-$NH_2$ column so that the early and late peaks were collected separately. Absorption spectra were obtained for these two fractions in a spectrophotometer over the range of 200 nm to 400 nm (Figure 5). This HPLC method allowed more material to be collected in each fraction, and clear absorption spectra were measured. It is clear that the later peak (Figure 4, RT=15 min) is uric acid, as the sample spectrum (Figure 5A) is nearly identical to the uric acid standard (the small shift in RT in the sample spectrum is probably due to a slight difference in pH). The earlier peak (Figure 4, RT=12 min) in the sample is very interesting in that its absorption spectrum (Figure 5B) in the region below 250 nm closely resembles that of alloxan (note the slight shoulder between 220 and 230 nm). The relative peak in the sample at 270-280 nm is not seen in the alloxan standard, and indicates the presence of at least one additional component. This may be the derivative responsible for peak #3 visible in the chromatogram shown in Figure 2, because that material had also had an absorbance peak at about 275 nm as shown in Figure 3.

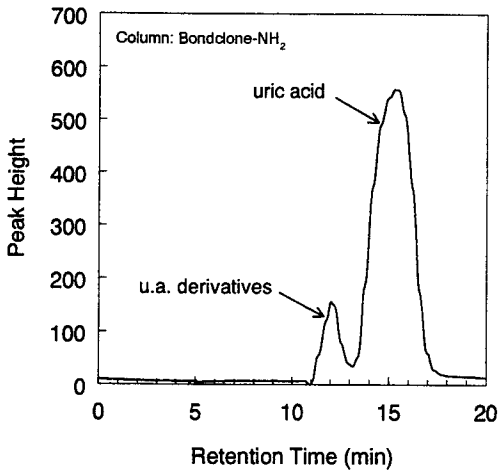


**Figure 4.** HPLC chromatogram of Ho:YAG laser exposed uric acid stones, using the Bondclone-NH2 column eluted with 60% acetonitrile. This method separated the derivative products as a group from the uric acid parent, but did not resolve the individual components.

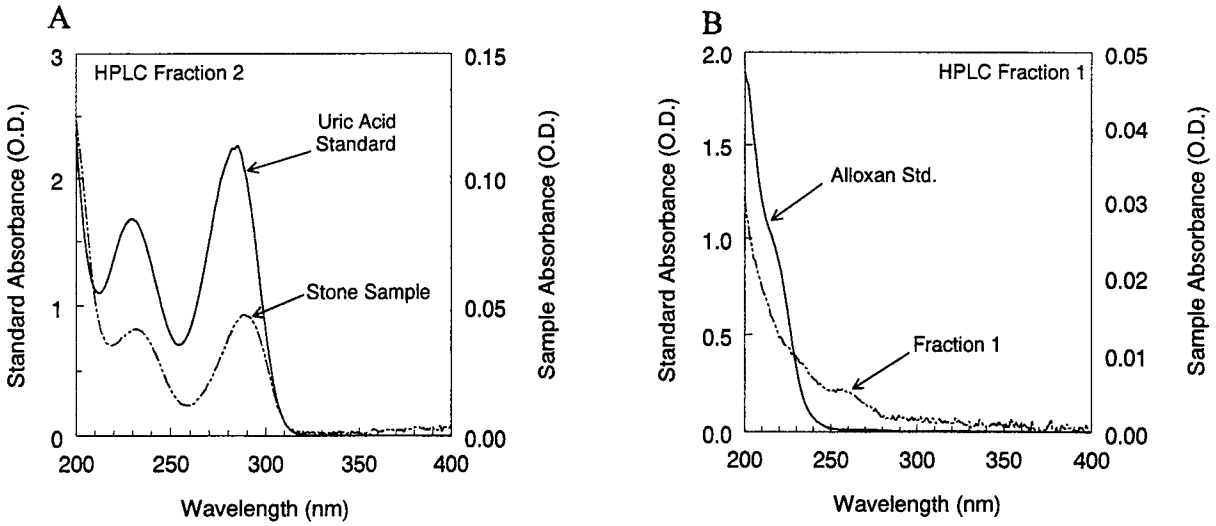


**Figure 5.** UV absorption spectra obtained from the uric acid peak (A, left) and the derivative peak (B, right) isolated from the HPLC separation shown in Figure 4. The solid lines are the spectra of authentic reference standards (uric acid in A, and alloxan in B, left-hand ordinates), while the dotted lines are the sample spectra (right-hand ordinates).

### 3.3. Mass spectroscopy of stone samples

While the identification of alloxan in the laser-exposed stone samples may be made with a high degree of confidence, the nature of the other derivatives could not be made on the basis of the HPLC analysis. Identification of these products may be possible by mass spectroscopy. In order to interpret mass spectroscopic data, the molecular weights of anticipated products must be known. Based on the proposed reaction pathways for uric acid decomposition, the molecular weights (in atomic mass units) of the principal products were calculated from their empirical formulas, and are shown in Table I.

**Table I. Molecular weights of predicted uric acid breakdown products**

| Compound | Empirical Formula | Mol. Wt. |
|---|---|---|
| Uric Acid | $C_5H_4N_4O_3$ | 168.13 |
| Intermediate I | $C_5H_6N_4O_4$ | 186.15 |
| Alloxan | $C_4H_2N_2O_4$ | 142.08 |
| 5-Hydroxyhydantoin-5-carboxamide | $C_4H_6N_3O_4$ | 160.13 |
| 5-Hydroxyhydantoin | $C_3H_4N_2O_3$ | 116.09 |
| Oxamic Acid | $C_2H_3NO_3$ | 89.06 |
| 2-Oxo-4-imino-5-ureidoimidazolidine | $C_4H_6N_5O$ | 140.15 |

Several samples of the uric acid stones were submitted for mass spectroscopy, but to date, insufficient material has been found in the samples to give a strong enough signal on which to make a positive identification of the unknowns. We are continuing to work on refining the sample preparation to improve the yield and make this analysis possible.

## 4. DISCUSSION

### 4.1. Ho:YAG ablation of uric acid stones

There seems little question, in view of the reported investigations on the mechanisms of Ho:YAG ablation of both biliary[9] and urinary stones[1-5] that the primary mechanism of stone removal involves thermal decomposition of the stone material itself. The present study, while not shedding much additional light on the ablative process itself, is completely consistent with the earlier findings because the only plausible mechanism for the formation of the uric acid derivatives found here is by thermal decomposition of the parent molecule. Such a mechanism is also in accordance with a model proposed for the laser ablation of calcified tissue that invokes a two-stage process starting with evaporation of tissue water (if any is present), followed by heating of the tissue components themselves[10,11]. Although this model proposed that explosive vaporization of interstitial water could carry off tissue components in the vapor plume, it is likely that in a structure will little interstitial water, such as urinary calculi, the action of the laser energy is primarily to heat the stone matter itself. Direct heating has been reported in dental enamel and dentin during Ho:YAG irradiation[12]. If critical temperatures required for thermal breakdown of any of the tissue components are reached, then the formation of breakdown products is to be expected. Indeed, this has been documented for uric acid and other urinary calculi.

### 4.2. Identification of thermal breakdown products

Although the mass spectroscopic identification of the derivatives is still a work in progress, the presence of alloxan has been inferred by UV spectroscopic analysis of laser-exposed stone fractions isolated by HPLC. This finding indicates that at least one of the three reaction pathways shown in Figure 1 is, in fact, initiated by Ho:YAG irradiation. The HPLC analysis also indicated other breakdown species are present, but their identification will have to await the completion of the MS analysis. Therefore, whether the other reaction pathways also occur is not yet known. The other notable finding of this study is that uric acid stone irradiation by the long-pulse Nd:YAG laser produced breakdown products identical to those found after Ho:YAG irradiation, but to a much lesser extent. This difference is probably due to the decreased efficiency of absorption at 1064 nm than at 2120 nm, and suggests that longer IR wavelengths may be even more efficient in stone ablation.

## ACKNOWLEDGMENTS

This research was partly supported by a grant from the Air Force Office of Scientific Research, as well as an unrestricted grant from Research to Prevent Blindness to the Department of Ophthalmology at the University of Texas Health Science Center at San Antonio.

## REFERENCES

1. G. J. Vassar, J. M. H. Teichman, R. D. Glickman, S. E. Weintraub, K. F. Chan, T. J. Pfefer, and A. J. Welch, "Holmium:YAG lithotripsy: Photothermal mechanism," *J. Endourol.* **13**, pp. 181-190, 1999.
2. K. F. Chan, G. J. Vassar, T. J. Pfefer, J. M. H. Teichman, R. D. Glickman, S. E. Weintraub, and A. J. Welch, "Chemical decomposition of urinary stones during holmium laser lithotripsy. Part I: Lack of a photomechanical effect," in *Laser-Tissue Interaction X: Photochemical,Photothermal,and Photomechanical*, S. L. Jacques, G. J. Müller, A. Roggan, and D. H. Sliney, Editors, Proceedings of the SPIE Vol. **3601**, pp. 377-386, 1999.
3. K. F. Chan, G. J. Vassar, T. J. Pfefer, J. M. H. Teichman, R. D. Glickman, S. T. Weintraub, and A. J. Welch, "Holmium:YAG laser lithtripsy: A dominant photothermal ablative mechanism with chemical decomposition of urinary calculi," *Las. Surg. Med.* **25**, pp. 22-37, 1999.
4. R. D. Glickman, J. M. H. Teichman, G. J. Vassar, S.E.Weintraub, K. F. Chan, T. J. Pfefer, and A. J. Welch, "Chemical decomposition of urinary stones during Holmium-laser lithotripsy. Part II: evidence for photothermal breakdown," in *Laser-Tissue Interaction X: Photochemical, Photothermal, and Photomechanical*, S. J. Jacques, G. J. Müller, A. Roggan, and D. H. Sliney,Editors, Proceedings of the SPIE Vol. **3601**, pp. 369-376, 1999.
5. R. D. Glickman, J. M. H. Teichman, N. S. Corbin, G. J. Vassar, S. E. Weintraub, K. F. Chan, and A. J. Welch, "Photothermal ablation is the primary mechanism in Holmium:YAG laser lithotripsy of urinary calculi," in *International Conference on Biomedical Optics (BMO '99)*, Q. Luo, B. Chance, L. Wang, and S. L. Jacques, Editors,Proceedings of the SPIE Vol. **3863**, pp. 376-384, 1999.
6. J. M. H. Teichman, G. J. Vassar, R. D. Glickman, C. M. Beserra, S. J. Cina, and I. M. Thompson, "Holmium:YAG

lithotripsy: Photothermal mechanism converts uric acid calculi to cyanide," *J. Urol.* **160**, pp. 320-324, 1998.
7. J. H. Lister, *Purines*, Wiley-Interscience, New York-London-Sydney-Toronto, 1971.
8. A. Bendich, "Chemistry of purines and pyrimidines," in *The Nucleic Acids*, E. Chargaff and J. N. Davidson, Editors, Vol. **1**, pp. 81-136, Academic Press, Inc., New York, NY, 1955.
9. S. A. Schafer, F. M. Durville, B. Jassemnejad, K. E. Bartels, and R. C. Powell, "Mechanisms of biliary stone fragmentation using the Ho:YAG laser," *IEEE Trans. Biomed. Engin.* **41**, pp. 276-283, 1994.
10. F. Partovi, J. A. Izatt, R. M. Cothren, C. Kittrell, J. E. Thomas, S. Strikwerda, J. R. Kramer, and M. S. Feld, "A model for thermal ablation of biological tissue using laser radiation," *Las. Surg. Med.* **7**, pp. 141-154, 1987.
11. J. A. Izatt, D. Albagli, I. Itzkan, and M. S. Feld, "Pulsed laser ablation of calcified tissue: physical mechanisms and fundamental parameters," in *Laser-Tissue Interaction,* S. L. Jacques, Editor, Proceedings of the SPIE Vol **1202**, pp. 133-140, 1990.
12. I. Cernavin, "A comparison of the effects of Nd:YAG and Ho:YAG laser irradiation on dentine and enamel," *Aus. Dent. J.* **40**, pp. 79-84, 1995.
13. K. J. Volk, R.A. Yost, and A. Brajter-Toth, "On-line electrochemistry/thermospray/tandem mass spectroscopy as a new approach to the study of redox reactions: the oxidation of uric acid," Anal. Chem. **61**, pp. 1709-1717, 1989.

# SESSION 7

# Photoacoustics

# Shock Wave Generation And Bubble Formation In The Retina By Lasers

Jinming Sun, Bernard S. Gerstman, Bin Li
(gerstman@biophys.fiu.edu)
Department of Physics, Florida International University, Miami, FL 33199

## ABSTRACT

The generation of shock waves and bubbles has been experimentally observed due to absorption of sub-nanosecond laser pulses by melanosomes, which are found in retinal pigment epithelium cells. Both the shock waves and bubbles may be the cause of retinal damage at threshold fluence levels. The theoretical modeling of shock wave parameters such as amplitude, and bubble size, is a complicated problem due to the non-linearity of the phenomena. We have used two different approaches for treating pressure variations in water: the Tait Equation and a full Equation Of State (EOS). The Tait Equation has the advantage of being developed specifically to model pressure variations in water and is therefore simpler, quicker computationally, and allows the liquid to sustain negative pressures. Its disadvantage is that it does not allow for a change of phase, which prevents modeling of bubbles and leads to non-physical behavior such as the sustaining of ridiculously large negative pressures. The full EOS treatment includes more of the true thermodynamic behavior, such as phase changes that produce bubbles and avoids the generation of large negative pressures. Its disadvantage is that the usual stable equilibrium EOS allows for no negative pressures at all, since tensile stress is unstable with respect to a transition to the vapor phase. In addition, the EOS treatment requires longer computational times. In this paper, we compare shock wave generation for various laser pulses using the two different mathematical approaches and determine the laser pulse regime for which the simpler Tait Equation can be used with confidence. We also present results of our full EOS treatment in which both shock waves and bubbles are simultaneously modeled.

Key Words: Laser, retina, shock, melanosome, damage

## 1. INTRODUCTION

The strongest absorbers in the retina are melanosomes. These micron size particles have an absorption coefficient of at least 1000 $cm^{-1}$, and possibly several times higher. The strength of their absorption makes them the likely site for the generation of light induced retinal damage at threshold levels of illumination. In addition to the potential danger, the same biophysical mechanisms can be used for a variety of beneficial medical applications.

Much research has been carried out, both experimental and theoretical, investigating the interaction of laser light with the visual system.[1] The biophysical mechanisms that transmute the laser energy into biological energy include temperature rise (thermal)[2-4], pressure (acousto-mechanical)[5-9], and vaporization (phase transitions)[9,10]. In this paper we present results for the last two mechanisms utilizing a theoretical treatment that incorporates a full Equation of State. This is the most realistic treatment we have seen and should allow us to model all possible effects, including non-linear shock waves and phase transitions that produce bubbles. Ultimately, this treatment will allow us to determine mechanical and thermal properties of the absorbing



In *Laser-Tissue Interaction XI: Photochemical, Photothermal, and Photomechanical*, Donald D. Duncan, Jeffrey O. Hollinger, Steven L. Jacques, Editors, Proceedings of SPIE Vol. 3914 (2000)
1605-7422/00/$15.00

melanosomes, and predict threshold levels for laser fluences that will cause damage at new and shorter pulse durations.

## 2. MODEL

### 2.1 Governing Equations for Absorbing Melanosome

Our model[7] consists of an uniform spherical absorber surrounded by a transparent medium. The rate of energy input per unit mass is given by[9]

$$\dot{I}_e = \frac{3I_o}{4a\tau_o\rho_o}\left[1 - \frac{1}{2\alpha_L^2 a^2}\left(1 - e^{-2a\alpha_L}(1+2\alpha_L a)\right)\right] \tag{1}$$

where $I_0$ is the incident laser fluence in *Joule/cm*$^2$, 'a' is the radius of the absorbing sphere, $\tau_0$ is the laser pulse duration, $\rho_0$ is the static density of the sphere, and $\alpha_L$ is the absorption coefficient of the sphere.

We use the Lagrangian coordinate *r* to denote the initial position of an element of mass and the Eulerian coordinate **u**(r,t) to denote its position at some later time, e.g. **u**(r,t=0)=r. The mathematical dot operation $\dot{f}(t)$ means a total time derivative, the spatial derivative $\nabla$ is taken with respect to *r*, while the spatial derivative with respect to **u** is denoted by $\nabla_u$. With this notation, the equation of motion of a point inside the absorbing sphere is

$$\rho\ddot{\boldsymbol{u}} = -\nabla_u P \tag{2}$$

where P is the pressure and $\rho(t)$ is the time varying density which is related to the static density by mass conservation

$$\rho_o r^2 = u^2 \rho \frac{\partial u}{\partial r} \tag{3}$$

where u is the radial component of the vector **u**. In spherical geometry, the equation of motion can be expressed as

$$\rho_o r^2 \ddot{\boldsymbol{u}} = -u^2 \nabla P \tag{4}$$

If we assume that the absorbing melanosome has a constant bulk modulus B and constant thermal expansion coefficient $\alpha$, the equation of state (EOS) of the absorber can be written as

$$\frac{\dot{v}}{v} = -\frac{\dot{P}}{B} + \alpha\dot{T} \tag{5}$$

where $v=1/\rho$ is the specific volume and is related to **u** by

$$\dot{v} = \frac{\partial v}{\partial t} + \dot{\boldsymbol{u}} \cdot \nabla_u v \tag{6}$$

This allows us to write Eq. (5) as

$$\frac{\dot{v}}{v} = \nabla_u \cdot \dot{\boldsymbol{u}} = -\frac{\dot{P}}{B} + \alpha \dot{T} \tag{7}$$

Energy conservation of the absorber relates the rate of absorption to temperature rise, volume change, and heat lost through conduction to the surrounding medium:

$$\dot{I}_e = T\dot{s} - \frac{\lambda}{\rho}\nabla_u^2 T = c_v \dot{T} + B\alpha T\dot{v} - \frac{\lambda}{\rho}\nabla_u^2 T \tag{8}$$

where $c_v$ is the specific heat, $\lambda$ is the thermal conductivity of the absorber and s is the specific entropy.

**2.2 Governing Equations for Surrounding Aqueous Medium**

The equation of motion, Eq. (4), the equation of state, Eq. (7), and the conservation of energy, Eq. (8), constitute the governing equations for the absorbing melanosome. Analogous, but not necessarily similar, equations must be obtained for the surrounding medium which is treated as water. For the medium, $\dot{I}_e$ is zero because there is no absorption.

Implementation of numerical algorithms require two additional considerations. First, we must set boundary conditions, and we use the following:
1)$\delta\mathbf{u}$ is always zero at r= 0 and $\infty$
2)$\dot{\boldsymbol{u}}$ is zero at t=0 for all r
3)$\mathbf{u}$ and P are continuous at r=a.

Second, we must use an appropriate equation of state for the aqueous medium. The equation of motion, Eq. (4) is the same for the absorber and the medium but we are especially interested in shock waves and phase transitions (bubbles) in the medium. This requires a more realistic EOS than that of Eq. (7) which is used only for the solid absorbing melanosome.

## 3. SHOCK WAVE GENERATION: TAIT EQUATION vs. EQUATION OF STATE

Non-linear phenomena such as shock wave generation are notoriously difficult to calculate because of numerical instabilities. In order to calculate the dependence of shock waves and bubble formation as a function of laser pulse parameters, we used two different equation of state formulations. The use of two different approaches allows us to feel confident of the predictions in the regimes in which the predictions for the shock fronts are in agreement.

The two different approaches for the thermodynamic state of the water used were the Tait Equation[12,13], and a numerical table based upon the NBS/NRC Steam Tables[14]. The Tait Equation is a relationship between only the pressure and density of liquid water and expresses the near

incompressibility of water:

$$P = P_a\left(\frac{\rho_m}{\rho_{mo}}\right)^{\gamma} - P_b \qquad (9)$$

where $\rho_{mo}$ is the static density of the medium and $\rho$ is the density of the medium at any specific time during the simulation. The other parameters in the equation have been determined by other researchers by numerical fitting to data for water and the values we adopted[6] were $P_a$=3141 Atm., $P_b$=3140 Atm. and $\gamma$=7 which gives v(sound)=$\sqrt{\partial P/\partial \rho}$ =1480 m/s.

The full EOS from the steam stables relates P,V,T,S such that a numerical value of any two of these thermodynamic parameters allows you to calculate values for the other two. The full EOS is valid for both liquid water and vapor, as well as the fluid phase above the critical temperature and pressure of 647 K and 218 Atm.

Our overall goal in this research is to be able to predict the temperature, pressure and bubble size created by a laser of any pulse duration and fluence. We now discuss results using each of the two approaches.

### 3.1 Tait Equation Results

The Tait Equation, Eq. (9), has the obvious disadvantage that it does not include the possibility of phase changes and therefore cannot be used to predict bubble generation. However, it was developed specifically to deal with pressure changes in liquid water, and therefore should be well suited for shock wave calculations. In addition to using the Tait Equation as a confirmation of shock wave calculations using the full EOS, the Tait Equation has some advantages over the full EOS. The Tait Equation allows for the system to take on negative (tensile) pressures whereas the EOS does not have a straightforward way of incorporating this possibility since tensile stress is unstable with respect to a transition to the vapor phase. Since water is known to be able to sustain negative pressures of at least 10 atmospheres, and much higher as the water becomes purer, excursions into negative pressures is likely and the Tait Equation is more realistic for calculating purely pressure effects. The inability to model phase transitions does not decrease the usefulness of the Tait Equation for shock front calculations because pressure waves and shock fronts moving at greater than 1500 m/s through water occur on nanosecond time scales, which is much shorter than the time for bubble growth. Thus, the shock waves are temporally and therefore experimentally distinct from the bubble growth, and calculations of just the shock fronts using the Tait Equation can be tested experimentally. The Tait Equation also has the advantage of being fairly quick in terms of computer time. The evolution of the history of a shock front which travels a few micrometers from the surface of a melanosome and takes a few nanoseconds requires only five minutes of CPU time using an R10000, 200 MHz RISC cpu from Silicon Graphics Inc.

In addition to an inability to include phase transitions, the Tait Equation does have another disadvantage. Its ability to handle negative pressures can create a problem because the Tait Equation allows the water to sustain unrealistically, huge negative pressures. The aqueous fluid in a cell is certainly not pure water, and therefore negative pressures stronger than -10 Atm. are likely to cause the liquid to rupture and lead to vapor pockets which the Tait Equation cannot

simulate. Therefore, negative pressures predicted by the Tait Equation to be greater than 10 Atm. must be viewed with suspicion.

Because of the numerical problems with algorithms that simulate non-linear systems, we employed several different numerical approaches for calculating shock fronts using the Tait Equation, as displayed in Figure 1. In all the figures, we used the following parameters for the melanosome: absorption coefficient $\alpha_L$ =1000 $cm^{-1}$, a= 1 μm, $\rho_o$=1.35 $g/cm^3$, and $c_v$=2.51 J/g·K. Reliable numbers for the bulk modulus B and bulk thermal coefficient of expansion α are not yet available, which we will see later is a major problem. In order to continue with the calculations, we adopt graphite as a substitute because of a chemical similarity to melanin[14] and use graphite's B=39.4 Gpa and $\alpha=2.98\times10^{-5}K^{-1}$. The surrounding medium is treated as having the thermal and mechanical properties of water. The laser pulse duration used is 0.1 nanosecond, and in some figures the fluence is varied.

We do not include the pressure spikes that are behind the leading one because the tail of the leading front dips to large negative pressures in our calculations which is physically unrealistic. The calculation of pressures at later times depends upon the earlier results, and once the pressure reaches unphysically large negative values at a given location, we cannot trust any later results at that location. Since the leading edge is the first pressure spike experienced at any location, it can be trusted because it is not influenced by the negative pressures that come later.

In Figure 1a, we plot the leading edge pressure profile at a time of 1 nanosecond after the start of a laser pulse of duration of 0.1 nanoseconds. The laser fluence is 20 $J/cm^2$. We use three different numerical methods and can see that all three numerical approaches give similar speeds and amplitudes. However, on the expanded scale of Fig. 1b, we see that the numerical approaches are not equally good in simulating a discontinuous shock front. The first numerical approach that we used was a low order Lax method.[15] Numerical diffusion is unavoidable with this method and Fig. 1b shows that the shock front is smeared out and not sharp. In order to simulate sharp shock fronts, we switched to the higher order "Leap Frog" numerical method.[15] Though this approach sharpens the shock front, inherent numerical instabilities in the method produce artificial oscillations that can become quite large. These oscillations make it difficult to determine where the shock front peak is located and how big it is. The addition of numerical viscosity[16] to the Leap Frog method can dampen out the oscillations but also tends to smear out the shock front, though not as bad as the Lax method. Fig. 1b shows the oscillations that can result from the Leap Frog method with a small coefficient of artificial viscosity (0.75). Finally, instead of artificial viscosity, we incorporated the fairly recently developed[17] Flux Corrected Transport (FCT) procedure with the Leap Frog approach and found that the simulation now gives a sharp shock front with no discernible oscillations. This is also shown in Fig. 1b and it can be seen that Leap Frog with FCT is clearly the superior approach and is also used with the full EOS.

### 3.2 Full Equation of State

In Figure 2, we compare the results for the pressure profile that is calculated using the Tait Equation with the FCT Leap Frog approach and the results using the full EOS from the Steam Tables. From the standpoint of biological damage, the shock front is the most important part of the profile, and we can see they are in excellent agreement in terms of amplitude and sharpness. The amplitude calculated from the full EOS is a few percent higher, and therefore it travels marginally faster. This excellent agreement using two very different thermodynamic expressions for the state of the system gives us confidence in the accuracy of both techniques.

## 4. SHOCK WAVE RESULTS

In the following figures we present results showing various features that are predicted by our model using the Tait Equation for water.

### 4.1 Shock Front Strength Dependence on Fluence and Radial Distance from the Absorber

In Figure 3a, we plot the decreasing strength of the shock front as a function of radial distance from the melanosome. This graph includes plots for three different fluences; 5 J/cm$^2$ , 20 J/cm$^2$, and 90 J/cm$^2$. All three plots show a rapid decrease in the strength of the shock front. In the near field region (u<3a), the shock front can be substantial. For the impractically large fluence of 90 J/cm$^2$, the temperature rise in the melanosome is $\Delta T$=24,680 K, and a shock front is created in the medium on the order of 50 Kbar, which corresponds to a shock front speed of $U_s$=3880 m/s. For a more reasonable fluence of 5 J/cm$^2$, producing a melanosome $\Delta T$=1,370 K, the shock front in the near field can be as large as 2 Kbar, corresponding to a shock front speed of $U_s$=1720 m/s (~15% above acoustic speed in water). Once the shock front leaves the near field region, it quickly decays to an acoustic type disturbance. Though not as dangerous as a shock front, a strong acoustic disturbance may cause biological damage, and this possibility remains to be investigated.

In Fig. 3b we scale the shock front pressures of Fig. 3a by their respective fluences merely to exhibit the non-linearity of the system. If the system behaved linearly, all three scaled curves would be identical, which is not seen. Close to the absorbing melanosome where the shock fronts are strongest, the behavior is supra-linear; the shock front pressure scales with a ratio larger than the ratio of the fluences. Farther away in the acoustic regime, the behavior is just the opposite, or sub-linear, possibly due to more rapid dissipation of larger shock fronts.

### 4.2 Stress-Confinement for Shock Fronts

Confinement is the concept that when an impulse is applied in a time shorter than the response time of the system, the response of the system will be independent of the actual duration of the impulse. This concept of confinement can be applied to a variety of mechanisms. The time for heat to travel across a melanosome is approximately 1 microsecond, so temperature rises due to thermal conduction alone should be the same for laser pulses of the same fluence no matter how short their duration is below a microsecond.

The time for pressure waves to travel across a melanosome is approximately 1 nsec, and confinement would imply that the pressure effects generated should be the same for all pulses shorter than a nanosecond if they have the same fluence. We showed in a previous paper[7] that confinement does NOT hold for tensile pressures generated at the core of the absorbing melanosome. As the pulse duration is shortened well below a nanosecond, the size of the tensile pressure continues to increase, possibly rupturing the melanosome. However, we find that the concept of stress confinement is valid for the generation of shock waves in the aqueous medium outside the melanosome. Figure 4 shows the size of the shock front as a function of the duration of the laser pulse. Each pulse has the same fluence of 30 J/cm$^2$. As the pulse is shortened from 1.0 ns to 0.5ns, the shock front increases almost in the inverse ratio. This trend continues down to a pulse length of 0.1 ns. However, when the pulse duration is shortened from 0.1 to 0.01 ns, the size of the shock front does not change. Clearly, confinement holds for shock fronts for pulse durations shorter than 0.1 nsec.

### 4.3 Shock Front Strength Dependence on Absorber's Thermo-Mechanical Characteristics

Figure 3 shows that substantial shock front strength requires fluences that are much larger than used in experiments on melanosomes. For the calculations leading to Fig. 3, the unknown physical characteristics of the melanosome are set equal to those of graphite. Equation (7) shows that pressures generated in the melanosome, which are transferred to the surrounding medium, depend on the values used for these parameters. We systematically varied the bulk thermal coefficient of expansion $\alpha$ of the melanosome and found that it had a noticeable effect on the size of the shock wave generated in the surrounding medium. Figure 5 displays these results. As the thermal coefficient of expansion is increased, the melanosome would like to expand to a greater size. Its inability to do so rapidly enough causes larger pressure build up inside. This increased internal pressure buildup results in smaller fluences producing larger shock fronts outside. The plots in Fig. 5 used the full EOS, which we had now incorporated, rather than the Tait Eq.

## 5. FULL E.O.S. RESULTS FOR SHOCK FRONTS AND BUBBLE FORMATION

As discussed earlier, our overall goal in this research is to be able to predict the temperature, pressure and bubble size created by a laser of any pulse duration and fluence. To do this, we must use a full EOS for water that includes the possibility of phase changes in which the specific volume increases dramatically and the density decreases dramatically. We have run some simulations utilizing the full EOS and in Figure 6 we present preliminary results using a 0.1nsec pulse with a fluence of 20 J/cm$^2$. Fig. 6a shows the shock wave decaying over period of a few nsec as it travels out several microns. Fig. 6b shows, for the same pulse, the expansion of the bubble (sharp drop in density) occurring on much longer time scales.

## 6. SUMMARY

We have shown that it is possible to predict shock fronts generated by laser absorption by melanosomes. The non-linearity of the process requires careful attention to the numerical algorithm employed. We have shown that the Tait Equation and the full Equation of State give similar predictions for the expected shock front, which assumedly confirms the correctness of both treatments. The strength of the shock front drops rapidly as it expands outward, and decreases to acoustic strength and speed within five microns of the absorbing melanosome. Whether or not these strong acoustic waves can still cause damage has not been investigated. We have shown that stress confinement is valid for shock waves in the surrounding medium when pulse durations are shortened below 0.1 nanosecond, even though confinement is not a valid concept for tensile stresses generated at the absorbing melanosome core. We have also shown that the size of the shock front that is generated depends on the thermal coefficient of expansion of the melanosome, and therefore this is a crucial parameter that must be measured independently.

Finally, we have shown that the full EOS can be used to predict both shock front generation and bubble formation. Future work will be the systematic investigation of shock front and bubble generation as a function of laser fluence and duration in the ultrashort regime.

The authors would like to thank the AFOSR for funding through Grant F49620-96-1-0438.

Laser Pulse Duration $\tau$=0.1nsec, Fluence $I_o$=20 J/cm$^2$

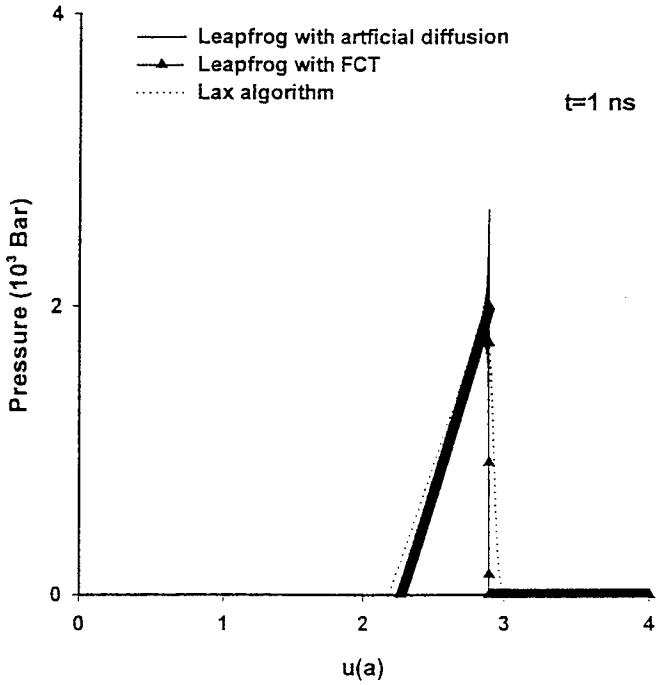


Figure 1a: Three different numerical methods for computing the evolution of the non-linear shock front. All three give approximately the same strength (pressure change) and speed.

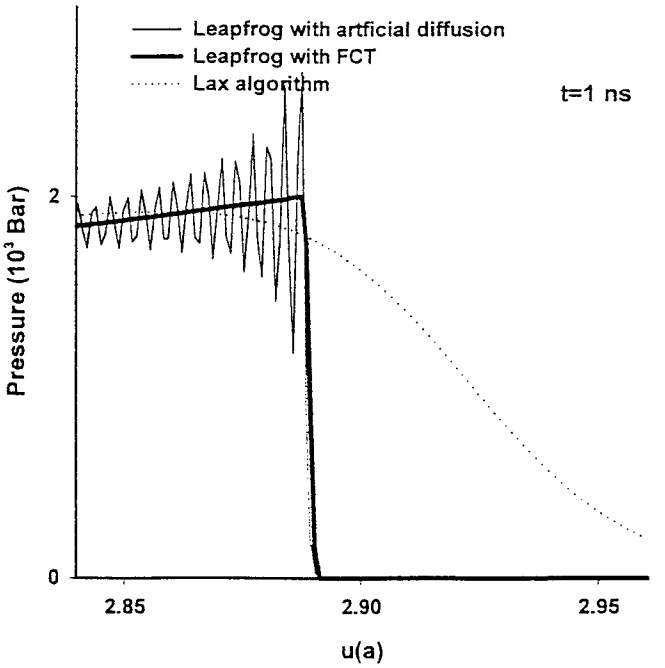


Figure 1b: Expanded scale for Fig. 1a showing the superiority of the FCT approach for modeling sharp shock fronts.

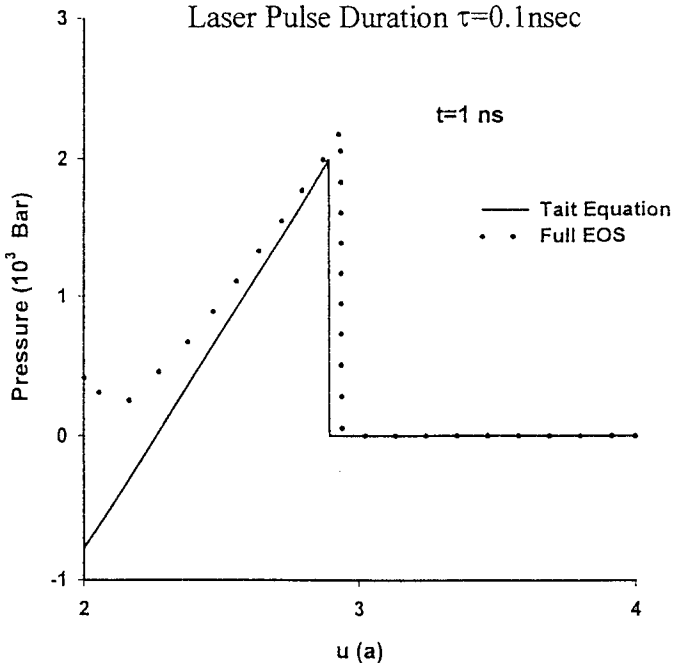


Figure 2. Comparison of shock front calculation using two different approaches for determining the thermodynamic state of the aqueous medium. The excellent agreement helps to confirm the validity of both approaches.

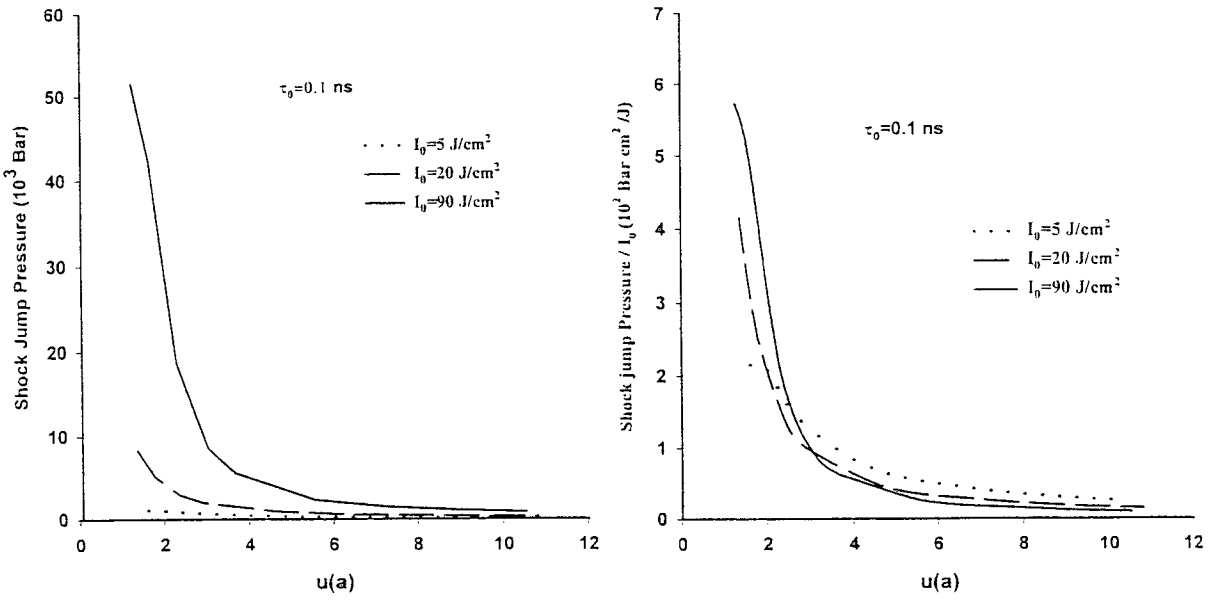


(a) (b)

Figure 3a. Calculations showing the decay of the shock front for different fluences.
Figure 3b. Same as Fig. 3a, but each curve is normalized by its own fluence. The differences in the curves exhibit the non-linearity of the system. If the shock front had a linear dependence on fluence, the curves would be identical. Near the absorber, the dependence is supra-linear; far from the absorber the dependence becomes sub-linear, perhaps due to stronger dissipation of larger shock fronts.

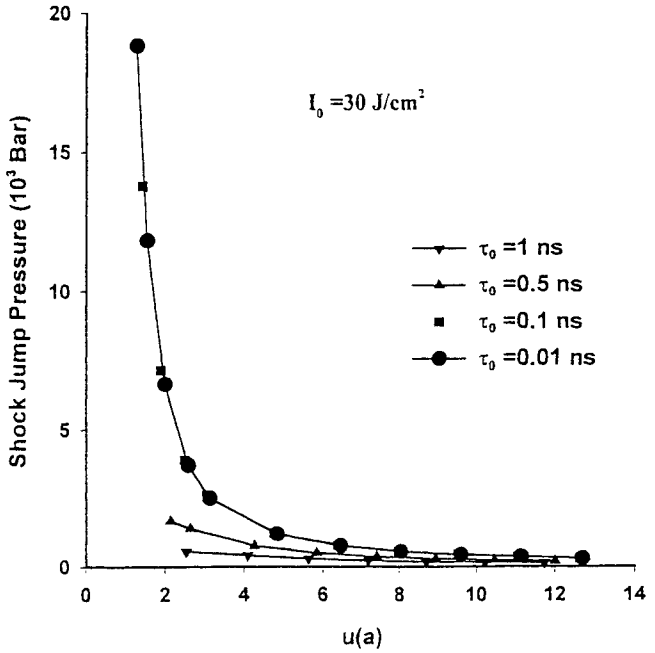


Figure 4. $I_0$=30 J/cm$^2$ for all pulses. The curves for $\tau$=0.1ns and $\tau$=0.01ns show that stress confinement is valid for shock fronts for pulse durations shorter than 0.1 nsec.

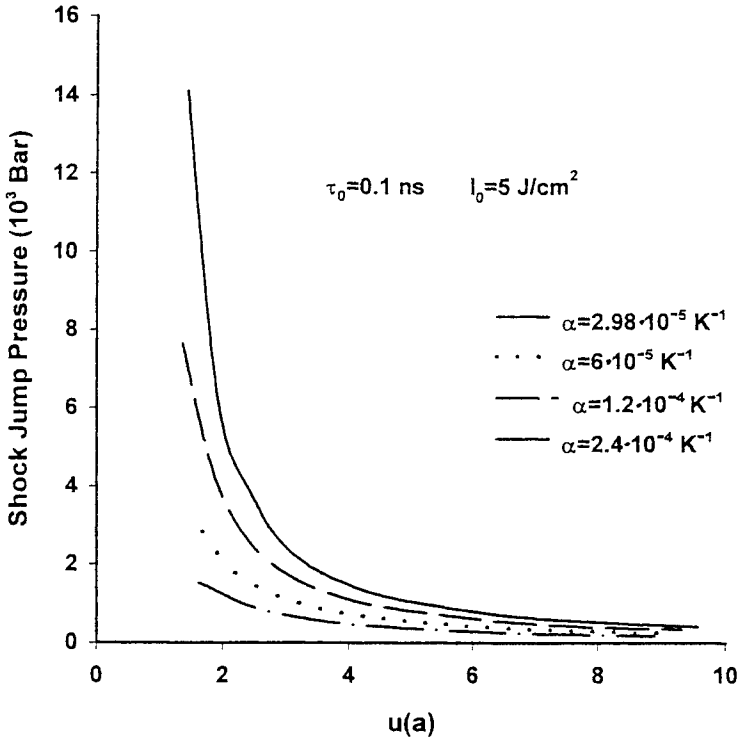


Figure 5. Different values of the thermal expansion coefficient of the melanosome will cause different strength shock fronts to be generated. Therefore, an independent measurement of the thermal expansion coefficient is crucial. All curves have the same laser pulse duration and fluence.

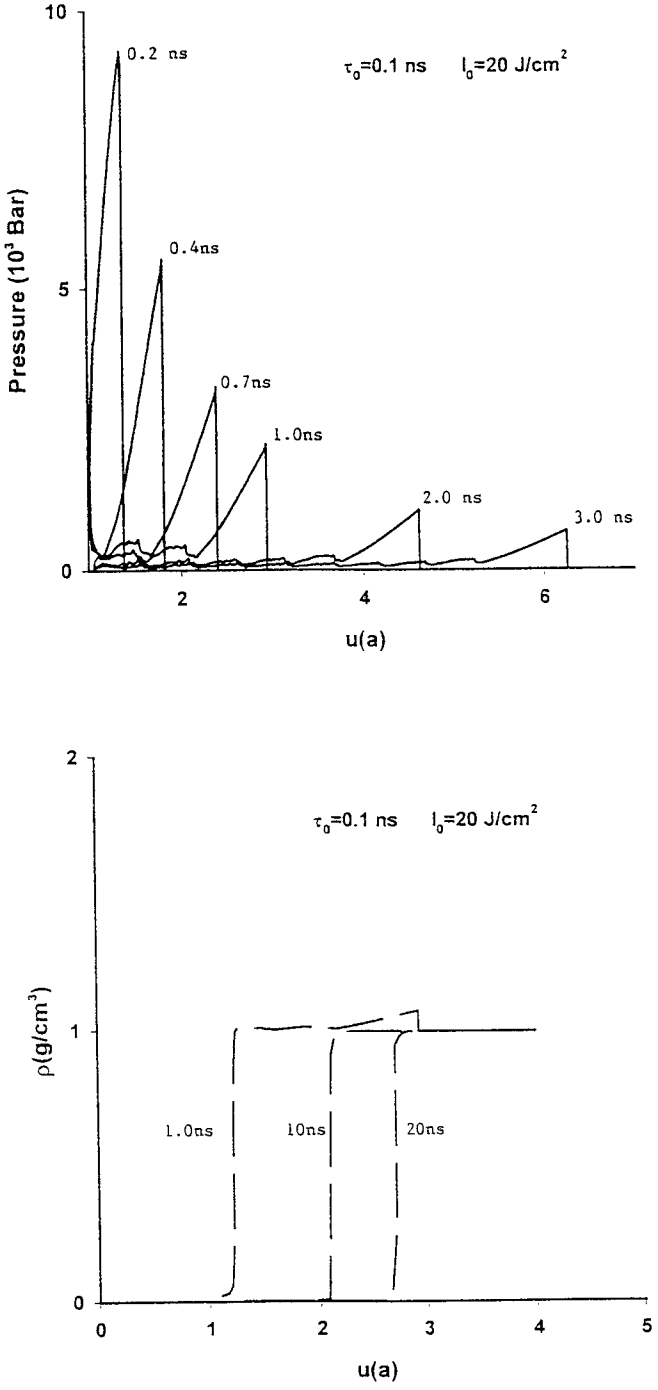


Figure 6. Calculation of both the shock front propagation and bubble expansion with a single model using the full EOS. (a) Shock front propagation. (b) Bubble expansion (drop in density). Note that expansion of the bubble occurs on a much longer time scale than the propagation of the shock wave, allowing the use of the Tait Equation, if desired, for modeling the initial shock front.

## REFERENCES


1. D. H. Sliney, Nonlinear Optics, **21**, 1, 1999.

2. B. S. Gerstman and R. D. Glickman, Journal of Biomedical Optics, **4(3),** 345, 1999.

3. C. R. Thompson, B. S. Gerstman, S. L. Jacques, and M. E. Rogers, Bulletin of Mathematical Biology, **58**, 513, 1996.

4. D. E. Freund and D. H. Sliney, Lasers in the Life Sciences, **8**, 228, 1999.

5. L. V. Zhiligei and B. J. Garrison, Appl. Surf. Sci., **142**, 127-129, 1998 ; Laser -Tissue Interaction IX, SPIE, 135, 1998.

6. A. Vogel, S. Busch, and U. Parlitz, J. Acoust. Soc. Am., **100**, 148, 1996.

7. J. M. Sun and B. S. Gerstman, Phys. Rev. E, **59(5),** 5772, 1999.

8. G. Paltauf, H. Schmidt-Kloiber, Laser-Tissue Interaction IX, SPIE **112**, 1998.

9. C. P. Lin and M. W. Kelly, Appl. Phys. Lett., **72**, 2800, 1998.

10. B.S. Gerstman, C.R. Thompson, S.L. Jacques and M. E. Rogers, Lasers in Surgery and Medicine, **18**, 10, 1996.

11. M. Strauss, et. al., Laser-Tissue Interaction VIII, ed: S. L. Jacques, Proc. SPIE **2975**, 261, 1997.

12. J. O. Hirshfelder, C. F. Curtiss, and R. Byron Bird, *Molecular Theory of Gases and Liquids,* Wiley, New York, 1964.

13. S. Ridah, J. Appl. Phys., **64(1)**, 152, 1988.

14. L. Haar, J. S. Gallagher and G. S. Kell, *NBS/NRC Steam Tables*, McGraw-Hill, New York, 1984.

14. W. N. Reynolds, Physical Properties of Graphite, Elsevier Pub. Co., 1968.

15. W. H. Press, *Numerical Recipes*, Cambridge University Press, Cambridge, 1986.

16. J. VonNeumann and R. D. Richtmyer, J. Appl. Phys., **21**, 232, 1950.

17. J. P. Boris and D. L. Book, J. Computational Phys., **11**, 38, 1973.

# Acoustic signal characteristics during IR laser ablation, and their consequences for acoustic tissue discrimination

Kester Nahen and Alfred Vogel

Medical Laser Center Lübeck, Peter-Monnik-Weg 4, D-23562 Lübeck, Germany

## ABSTRACT

IR laser ablation of skin is accompanied by acoustic signals the characteristics of which are closely linked to the ablation dynamics. A discrimination between different tissue layers, for example necrotic and vital tissue during laser burn debridement, is therefore possible by an analysis of the acoustic signal. We were able to discriminate tissue layers by evaluating the acoustic energy. To get a better understanding of the tissue specificity of the ablation noise, we investigated the correlation between sample water content, ablation dynamics, and characteristics of the acoustic signal. A free running Er:YAG laser with a maximum pulse energy of 2 J and a spot diameter of 5 mm was used to ablate gelatin samples with different water content. The ablation noise in air was detected using a piezoelectric transducer with a bandwidth of 1 MHz, and the acoustic signal generated inside the ablated sample was measured simultaneously by a piezoelectric transducer in contact with the sample. Laser flash Schlieren photography was used to investigate the expansion velocity of the vapor plume and the velocity of the ejected material. We observed large differences between the ablation dynamics and material ejection velocity for gelatin samples with 70% and 90% water content. These differences cannot be explained by the small change of the gelatin absorption coefficient, but are largely related to differences of the mechanical properties of the sample. The different ablation dynamics are responsible for an increase of the acoustic energy by a factor of 10 for the sample with the higher water content.

**Keywords:** Infrared photoablation, ablation dynamic, ablation noise generation

## 1. INTRODUCTION

The interaction of Er:YAG or $CO_2$ laser radiation with biological tissue is characterized by a small optical penetration depth of the laser wavelength into the tissue. This leads to a high energy density in a superficial tissue layer causing tissue ablation by an explosive vaporization of the tissue water. The ablation process generates an acoustic signal in air. It is the aim of our study to correlate characteristic features of this signal with the underlying ablation process, and to investigate the consequences for acoustic tissue discrimination. The insights gained shall be applied to monitor and control laser burn debridement.

Laser burn debridement is a clinical procedure where Er:YAG and $CO_2$ laser pulses can be used for the precise removal of necrotic tissue. To achieve the goal of a fast and selective ablation of the necrotic tissue that preserves the underlying vital tissue, an online control of the ablation process is needed. We want to use characteristic features of the ablation noise to discriminate between necrotic and vital tissue.

In our previous investigations using a free running Er:YAG laser we showed that the energy of the ablation noise is a suitable parameter for the discrimination between gelatin samples of different water content and between necrotic and vital tissue.[1,2] The acoustic energy differed by a factor of 2.9 between gelatin samples with 70% and 90% water content which were used as models for necrotic and vital tissue.[1,2] Even though water is the main absorber for the Er:YAG laser radiation, the large difference of the acoustic energy cannot be explained merely by the small difference in the sample water content.

To find the reason for the strong dependence of the acoustic energy on the water content of the gelatin samples we investigated the ablation dynamics by laser flash photography using a dark field Schlieren arrangement. The Schlieren photography allows to visualize the vaporization process at the sample surface and to distinguish between vapor and liquid or particle ejecta. The vapor front velocity and particle velocity were evaluated as a function of the sample water content.

Send correspondence to
nahen@mll.mu-luebeck.de, or vogel@mll.mu-luebeck.de
Phone: +49-451-5006513; Fax: +49-451-505486



In *Laser-Tissue Interaction XI: Photochemical, Photothermal, and Photomechanical*, Donald D. Duncan, Jeffrey O. Hollinger, Steven L. Jacques, Editors, Proceedings of SPIE Vol. 3914 (2000)
1605-7422/00/$15.00

## 2. METHODS

We used a free running Er:YAG laser with a pulse duration of 200 $\mu$s and a maximum pulse energy of 2 J (MCL29 Dermablate, AESCULAP MEDITEC, Jena, Germany). Gelatin samples with 70% and 90% water content (by weight) were irradiated with a spot diameter of 5 mm. In previous experiments, we were limited to a spot diameter of 500 $\mu$m because the maximum laser pulse energy was only 400 mJ.[1-3] All ablation experiments presented in this paper were performed with a radiant exposure of 4.6 J/cm$^2$. The ablation noise in air was detected using a piezoelectric transducer with a bandwidth of 5 kHz – 1 MHz placed at a distance of 30 mm from the sample surface (PCB, 132A42). The acoustic signal inside the irradiated sample was measured using a piezoelectric PVDF-slab transducer in contact with the sample placed below the irradiated spot (LBAT-18, Science Brothers Incorporated, Houston (TX), USA).

Laser flash photography of the ablation dynamics was performed using a dark field Schlieren arrangement described in detail in Ref..[1,3] This arrangement enables to observe the stress wave emission and the vaporization process at the sample surface, and makes it possible to distinguish between vapor and liquid or particle ejecta. Wire and slit used for spatial frequency filtering were oriented perpendicular to the sample surface with exception of the photographs taken of stress wave emission, where wire and slit were oriented parallel to the sample surface. The setup used for stress wave visualization has its maximum sensitivity to refractive index variations perpendicular to the sample surface as and is insensitive to variations parallel to the surface. A frequency doubled Nd:YAG laser emitting pulses at 532 nm wavelength and 6 ns pulse duration was used to take pictures with different delays relative to the ablation laser pulse.

## 3. RESULTS

### 3.1. Acoustic signals

Figure 1 shows the Er:YAG laser pulse (a) and the ablation noise in air (b) measured simultaneously during the ablation of a gelatin sample of 90% water content. The ablation noise is mainly generated during the initial 80 $\mu$s of the laser pulse. The acoustic signal shows high frequency oscillations during the initial 25$\mu$s of the laser pulse followed by a strong bipolar transient starting 30$\mu$s after the beginning of the laser pulse.

The acoustic signal in the sample depicted in figure 1 (d) starts with a short acoustic transient with a large positive and a small negative amplitude. Afterwards we observe a strong bipolar signal which coincides with the strong bipolar signal measured simultaneously in air as shown in figure 1 (c).

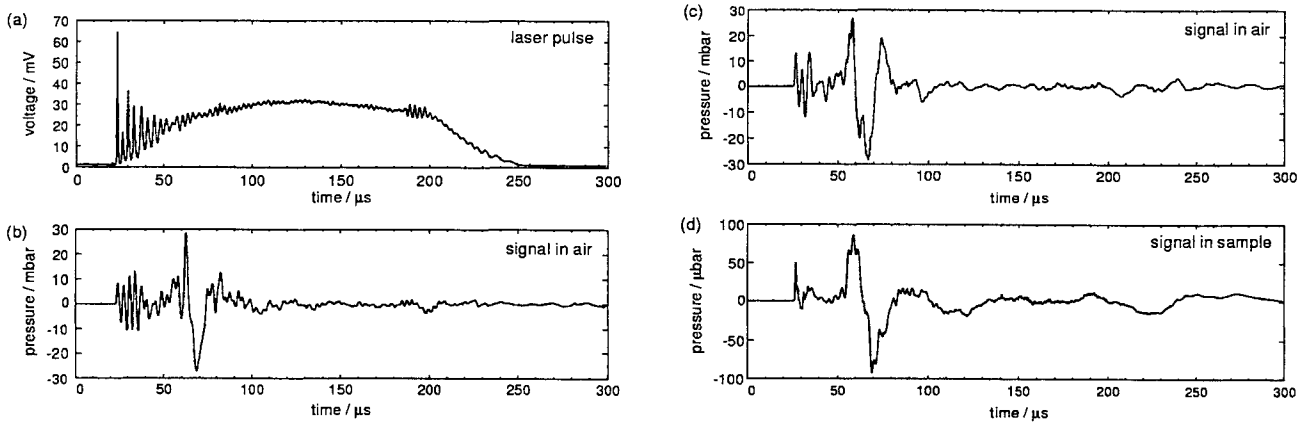


**Figure 1.** Er:YAG laser ablation of a gelatin sample with 90% water content. (a) laser pulse, (b) acoustic signal in air (signals (a) and (b) were measured simultaneously), (c) acoustic signal in air, (d) acoustic signal in the sample (signals (c) and (d) were measured simultaneously).

### 3.2. Acoustic energy

The acoustic energy of the ablation noise measured for gelatin samples of 70% and 90% water content differed by a factor of 10.0. The energy ratio obtained in the experiments with 5 mm beam diameter and a radiant exposure of 4.6 J/cm$^2$ is thus even larger than the ratio of 2.9 measured in earlier experiments with a beam diameter of only 500 $\mu$m and a radiant exposure of 15 J/cm$^2$. This result emphasizes the need for an explanation for the strong dependence of the acoustic energy on the sample water content.

### 3.3. Laser flash photography of the ablation dynamics

The pictures in figure 2 were taken 2.5 $\mu$s and 5.0 $\mu$s after the beginning of the laser pulse, with the laser beam incident from the top. They show the propagation of a stress wave generated by the first spike of the free running Er:YAG laser pulse.

The ablation dynamics for gelatin samples with 70% is shown in figures 3 to 5. Figures 6 and 7 show the ablation of gelatin samples with 90% water content.

Figure 8 and 9 shows the time interval of 20 $\mu$s – 40 $\mu$s for the 70% sample and the interval of 30 $\mu$s – 40 $\mu$s for the 90% water content sample with higher temporal resolution. During this time interval most of the ablation noise is generated (see Figs. 1 (a) and (b)).

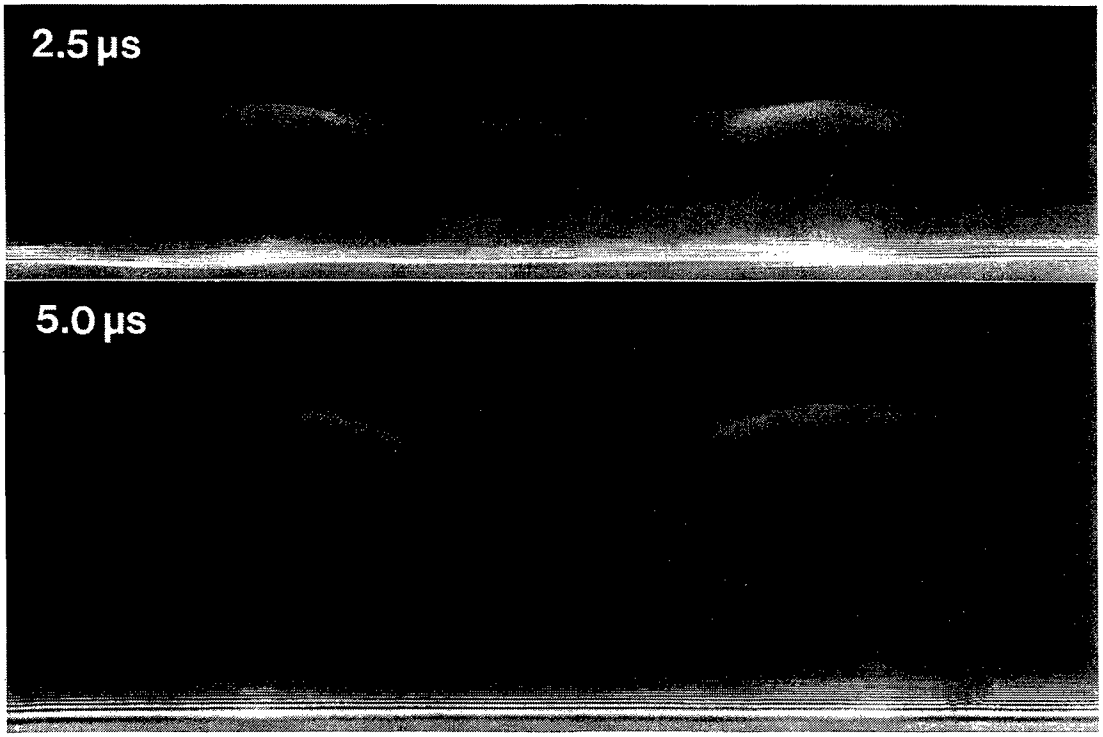


**Figure 2.** Stress waves emitted during the initial phase of Er:YAG laser ablation of gelatin with 90% water content. The pictures were taken 2.5 $\mu$s and 5.0 $\mu$s after the beginning of the laser pulse (|——| = 1 mm). The stress wave consists of a plane wave part with the same width as the laser beam diameter and a half toroidal diffraction wave that is irradiated by the edges of the laser spot.

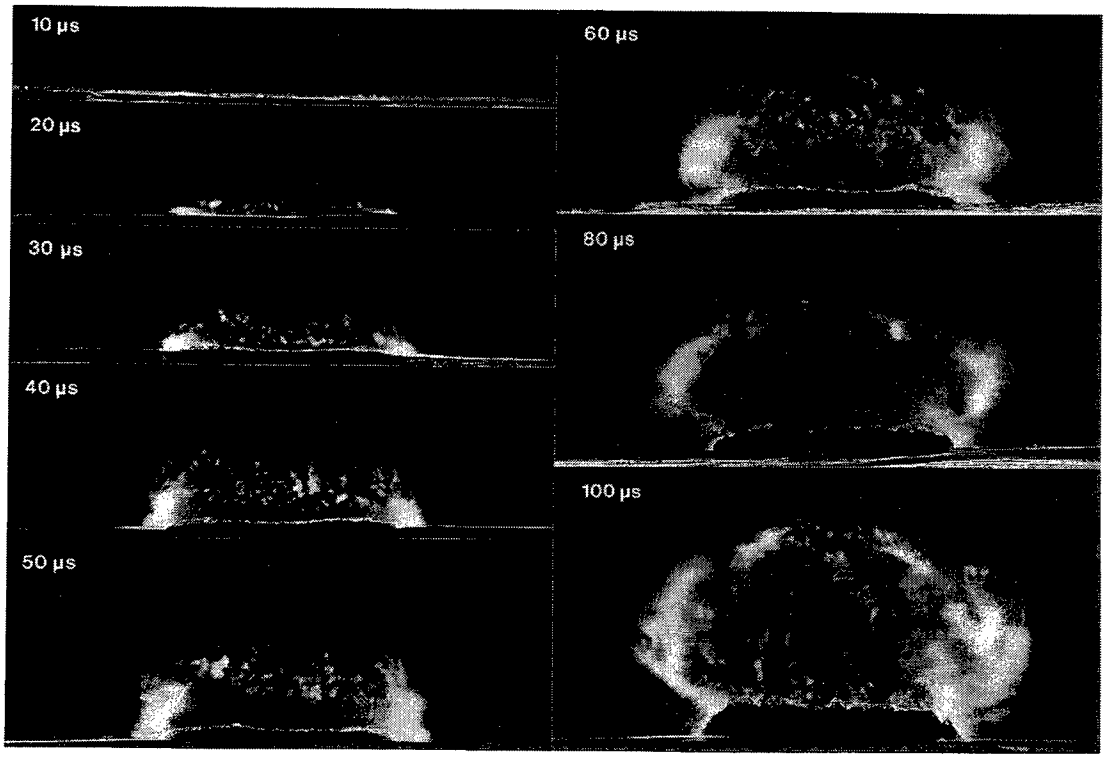


**Figure 3.** Overview of Er:YAG laser ablation of gelatin with 70% water content. The pictures were taken 10 $\mu$s – 100 $\mu$s after the beginning of the laser pulse (⊢—⊣ = 1 mm). The ablation starts with the formation of a vapor plume. The water vapor becomes visible by the dark field Schlieren technique because its refractive index differs from the surrounding air. After 30 $\mu$s the sample surface starts to rise because of partial vaporization of the water inside of the sample. The surface is still intact after 100 $\mu$s because the tensile strength of the gelatin counteracts the vapor pressure.

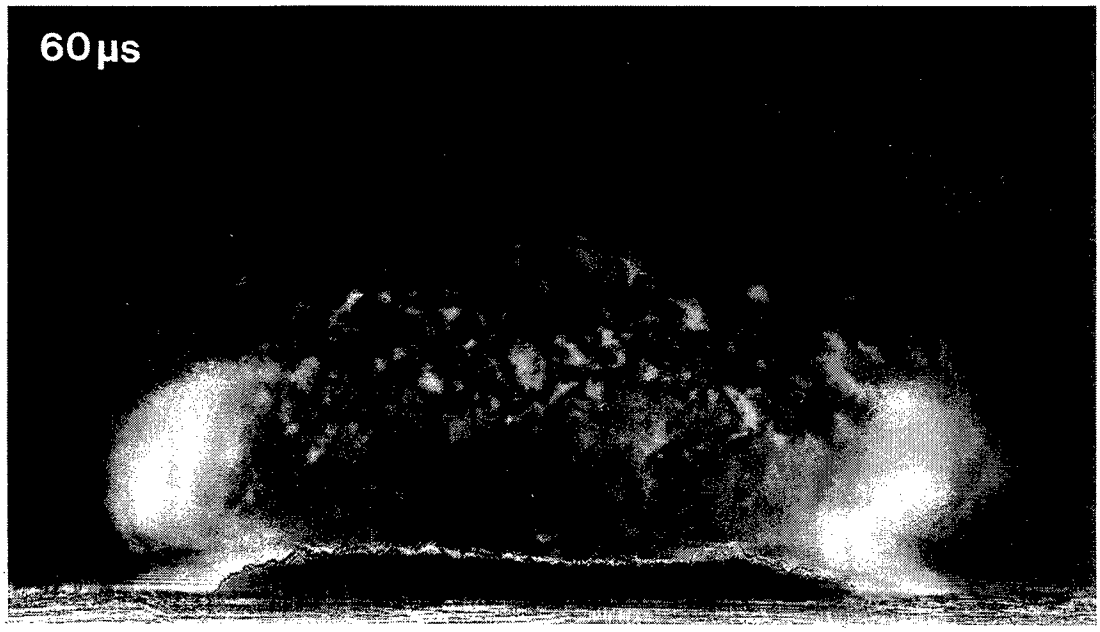


**Figure 4.** Enlarged view of the Er:YAG laser ablation of gelatin with 70% water content. The picture was taken 60 $\mu$s after the beginning of the laser pulse (⊢——⊣ = 1 mm).

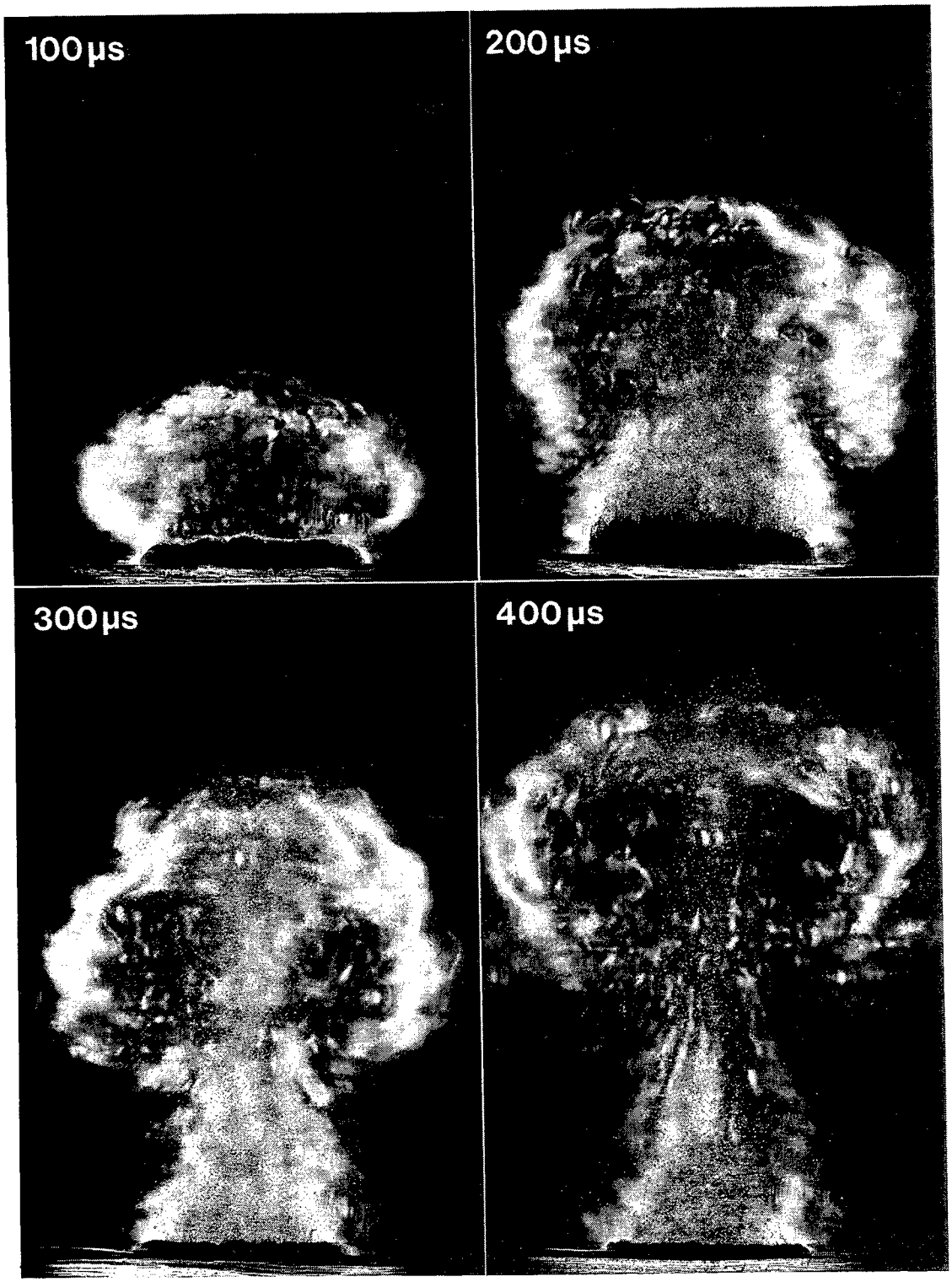


**Figure 5.** Ablation dynamics during and after Er:YAG laser irradiation of gelatin with 70% water content. The pictures were taken 100 $\mu$s, 200 $\mu$s, 300 $\mu$s, and 400 $\mu$s after the beginning of the laser pulse (|—| = 1 mm). At t = 200 $\mu$s, the sample surface is torn open and particles have been ejected into the vapor plume. Particles partly overtake the vapor front after 300 $\mu$s. The expansion of the ablation plume in vertical direction leads to the formation of a vortex ring and to a lateral constriction of the flow above the sample surface (see section 4.1).

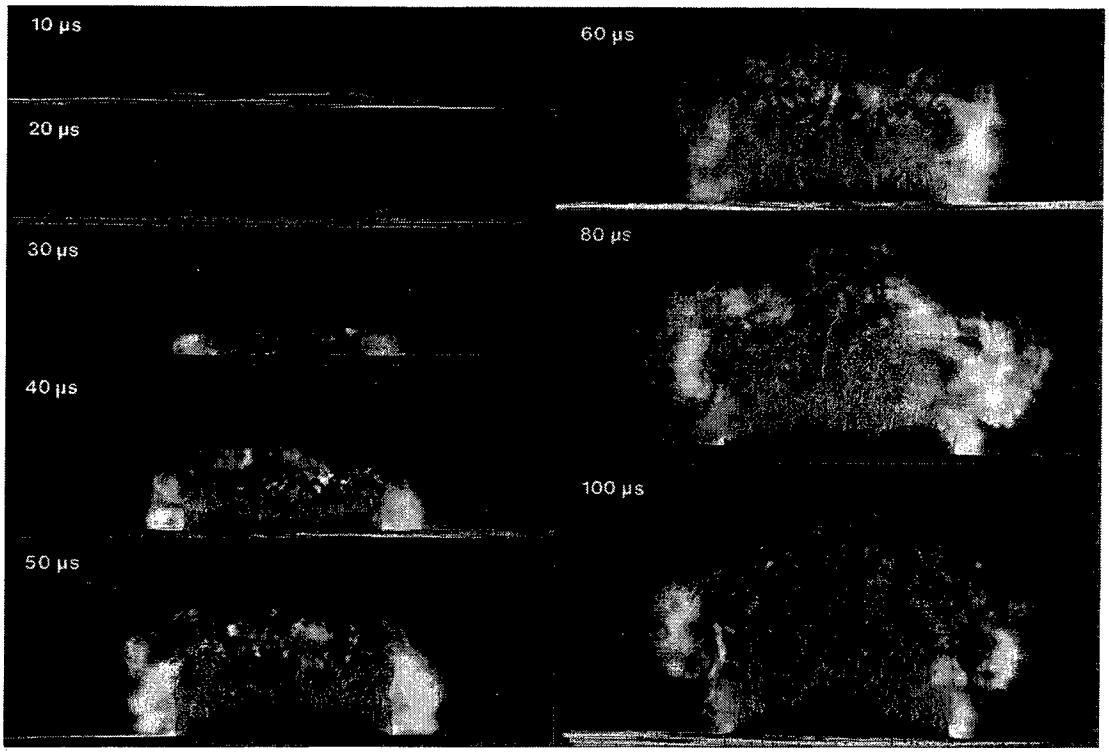


**Figure 6.** Overview of Er:YAG laser ablation of gelatin with 90% water content. The pictures were taken 10 $\mu$s - 100 $\mu$s after the beginning of the laser pulse (|—| = 1 mm). After 30 - 40 $\mu$s the surface tears apart, and string-shaped gelatin droplets are ejected. This is in contrast to the dynamics of 70 % water content samples where first the whole surface is lifted and particle ejection occurs only after 200 $\mu$s.


**Figure 7.** Enlarged view of the Er:YAG laser ablation of gelatin with 90% water content. The pictures were taken 60 $\mu$s after the beginning of the laser pulse (|—| = 1 mm). Strings of liquefied gelatin are ejected in the direction perpendicular to the sample surface.

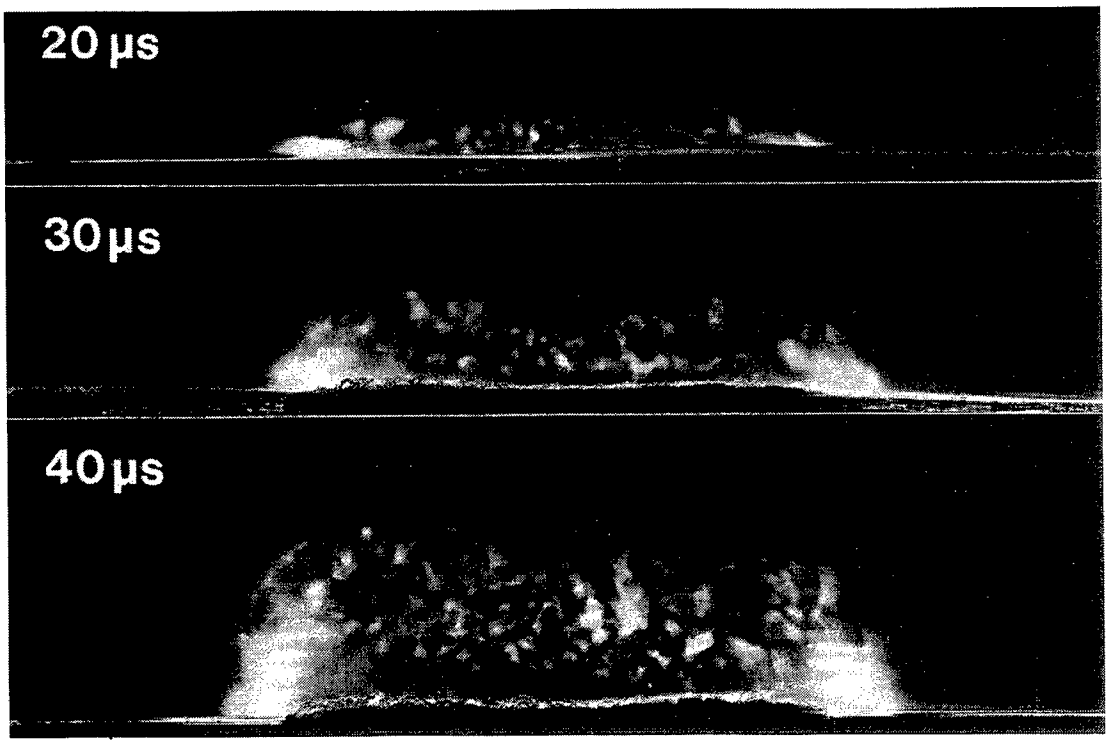


**Figure 8.** Enlarged view of the ablation dynamics of gelatin with 70% water content for the phase where most of the ablation noise is generated. The pictures were taken 20 $\mu$s, 30 $\mu$s, and 40 $\mu$s after the beginning of the laser pulse (|——| = 1 mm).

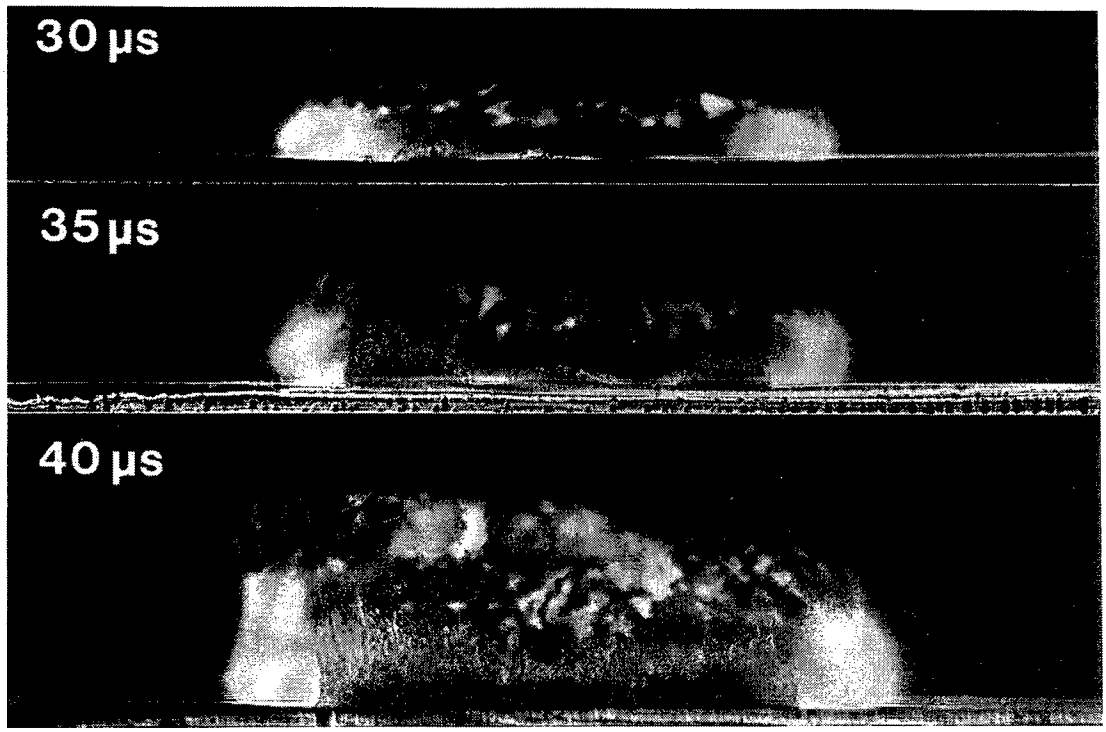


**Figure 9.** Enlarged view of the Er:YAG laser ablation of gelatin with 90% water content for the ablation phase where most of the acoustic signal is generated. The pictures were taken 30 $\mu$s, 35 $\mu$s, and 40 $\mu$s after the beginning of the laser pulse (|——| = 1 mm).

### 3.4. Velocity of vapor front and material ejecta

The photographic series were evaluated to obtain the position of the vapor front and of the ejected material as a function of time (Fig. 10). For the plots in figure 10 (a), we measured the distance of the vapor front from the sample surface at the center of the laser beam. For each sample water content and time delay, 12 pictures were analyzed. Figure 10 (b) shows the position versus time plots for the lifting of the sample surface for the 70% sample and for the ejection of the molten gelatin for the sample with 90% water content.

The data of figure 10 (b) were used to obtain the velocity and acceleration of the ejected material versus time data shown in figure 11.

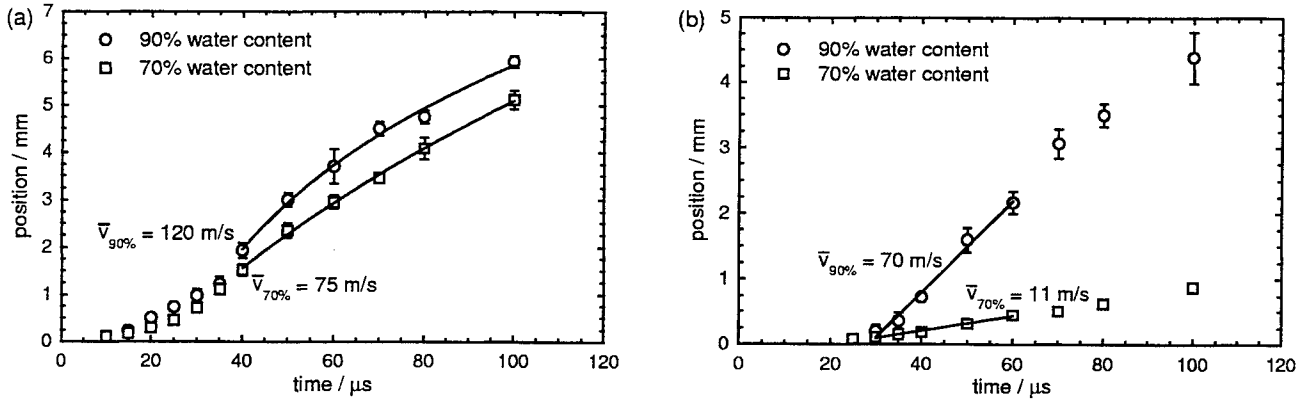


**Figure 10.** Er:YAG laser ablation of gelatin samples with 70% and 90% water content. (a) Position of the vapor front versus time, (b) position of the sample surface / particle front versus time. The functions fitted to the data points in (a) and (b) are described in the sections 4.2 and 4.3, respectively.

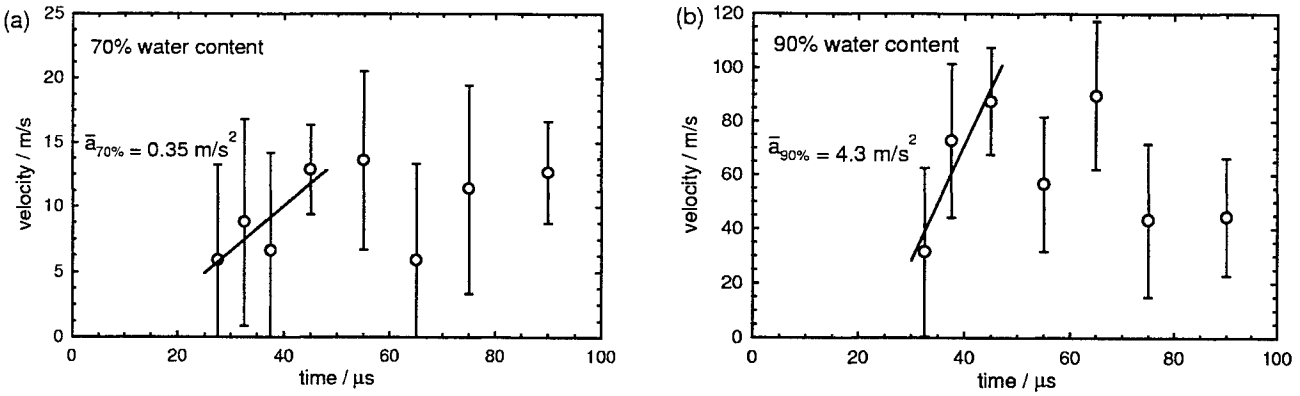


**Figure 11.** Velocity of the ejected material versus time (a) for the gelatin sample with 70% water content (b) for the sample with 90% water content. The velocity values refer to the average velocity between the measured points in the position versus time plots of figure 10 (b). The mean acceleration of the ejected material during the acceleration phase was obtained from a linear fit over the 25 – 45 $\mu$s time interval.

## 4. DISCUSSION

We shall first discuss the ablation dynamics for the gelatin samples with different water content and than relate the dynamics to characteristic features of the acoustic signals in air and in the samples. On that basis we can finally explain the high tissue specificity of the acoustic energy and its connection to optical and mechanical sample properties.

### 4.1. Ablation dynamics

The ablation dynamics can be subdivided into several phases. During the initial phase of the laser pulse we observe the emission of stress waves from the irradiated sample surface. The stress wave shown in figure 2 consists of a plane wave part with the same width as the laser beam diameter and a half toroidal diffraction wave that is radiated by the edges of the laser spot. The first laser spikes of the free running Er:YAG laser pulse cause a rapid heating of a superficial sample layer. The air in front of the sample is therefore rapidly heated by heat conduction. This causes a fast expansion of the air volume and the emission of stress waves correlated to each laser spike. The correlation between individual stress waves and laser spikes was already shown in.[3,1]

The initial phase described above is not yet accompanied by an ablation of the target material. Ablation starts after a delay of about 10 $\mu$s and is characterized first by the formation of a vapor plume and afterwards by material ejection. The sequence of events for gelatin with 70% water content is shown in figure 3. We first see the formation and expansion of a vapor plume which is caused by the superficial vaporization of the sample water content. The vapor is made visible by means of the dark field Schlieren arrangement because it has a different refractive index from that of the surrounding air. After 30 $\mu$s, the sample surface starts to rise. On the magnified picture shown in figure 4 we see that the elevation of the sample surface occurs simultaneously across the whole beam diameter. The sample surface is probably pushed upwards by partial vaporization of the water beneath the sample surface. The tensile strength of the material counteracts the expansion of the water vapor and leads to a pressure rise inside the sample. The elevated sample surface finally tears open when the pressure exceeds the ultimate tensile strength of the material.

Surface tearing happens more than 100 $\mu$s after the beginning of the laser pulse as shown in figure 5. Small gelatin droplets are ejected with high speed. After 300 $\mu$s they reach the top of the ablation plume, and after 400 $\mu$s they have partly overtaken the vapor front. The mushroom-like shape of the vapor plume shown in figure 5 can be explained by the laws of fluid dynamics. The fast flow of the gaseous ablation products away from the sample surface results in a lower pressure region at the periphery of the ablation plume (Bernoulli's law's), causing an inflow of the surrounding air parallel to the surface of the sample. The radial inflow produces a constriction of the ablation plume above the center of the ablation zone. Further above the surface, recirculation of ablation products back into the low pressure region causes a ring vortex to appear. The ablation particles partly follow the gas flow into the ring vortex.

For gelatin with 90% water content, the formation of the vapor plume occurs also 10 $\mu$s after the beginning of the laser pulse, but it is after 30 – 40 $\mu$s, directly followed by tearing of the surface and ejection of droplet- and string-like material in liquid phase (Figs. 6 and 7). An intermediate phase with uplifting of the sample surface is not observed, probably because the material is weaker than in the case of 70% water content.

The sequence of superficial vaporization and material ejection observed for both gelatin types shows that Er:YAG laser ablation of a heterogeneous biological material cannot be adequately described by a "steady state" theory considering only superficial vaporization.[4,5]

For both types of gelatin samples, material ejection occurred only in the direction perpendicular to the sample surface. This indicates that the material ejection is not driven by the pressure in the vapor plume as suggested previously by Zweig et al..[6] It seems more likely that it is driven by high pressure developing below the sample surface. One model describing the material ejection during IR laser ablation of tissue is based on the assumption of a phase explosion of the tissue water.[7] Another model describing the development of a high pressure zone below the sample surface was recently published by Majaron et al..[8] It combines the thermodynamic behavior of partially vaporized, pressurized water with the elastic response of the solid components within the biological material. Ablation occurs when the pressure inside the material exceeds its ultimate tensile strength. The pronounced differences which we observe in the ablation dynamics of 70% and 90% gelatin samples suggest that the mechanical properties of the samples play a very important role, but a detailed comparison with model predictions still deeds to be done. Majarons model describes, unfortunately, only the onset of ablation, but not the ablation process itself.

## 4.2. Relation between acoustic signal and ablation dynamics

With respect to the acoustic signal generation we can separate three time intervals. The initial energy deposition leads to a superficial heating of the sample which causes a thermoelastic expansion generating the initial pressure in the sample shown in figure 1 (d). The air in front of the sample is rapidly heated by heat conduction and the expansion of the heated gas causes stress waves as observed in the acoustic signal in air after the first laser spikes (Fig. 1 (b)).

After $10 - 20$ $\mu$s, vaporization at the sample surface starts. Figure 10 (a) shows that the vapor front is continuously accelerated during the first 30 $\mu$s of its propagation. This acceleration indicates that the vapor production rate exceeds the vapor expansion rate which can be explained by the increasing laser power during this time interval (Fig. 1 (a)). At the onset of vapor generation, a pressure peak is caused by the compression of the air in front of the phase front. The following laser spikes cause individual vaporization events at the sample surface which lead to a compression of the vapor next to the newly formed vapor layer and thus to further pressure peaks.

For times later than 40 $\mu$s, the vapor front is decelerated by the lateral expansion of the vapor plume and the resistance of the turbulent layer between plume and air. The function fitted to the data points shown in figure 10 (b) was derived from the flow resistance of a turbulent flow which is proportional to the flow velocity squared. It is given by $z(t) = (v_0/k)\, ln[(k(t - t_0) + 1)]$ where $v_0$ is the vapor front velocity at time $t_0$, and $k = \text{const.}$.[9]

Material ejection starts for both gelatin types about 30 $\mu$s after the beginning of the laser pulse (Fig. 8, 9, and 10 (b)). It generates the strong bipolar signal in air and the strong recoil signal in the sample. The high pressure amplitude in air is caused by the fast acceleration of a large surface area which acts like a piston compressing the air in front of the sample. This is particularly clearly seen in the case of gelatin with 70% water content where the rise of the sample surface occurs simultaneously across the whole beam diameter. It applies, however, in a similar way also to gelatin with 90% water content where the material ejection is nonisotropic. The acceleration of the ejected surface mass creates also the large recoil pressure amplitude inside the sample. It should be noted that it is the acceleration of the ejected material and not its propagation with a constant velocity which creates the signal in air and the recoil signal.

For the sample with 70% water content, the piston-like movement of the sample surface is at $t > 100\,\mu$s followed by a tearing of the sample surface and the ejection of very fast particles (Fig. 5). This event does, however, not generate a significant contribution to the acoustic signal in air and inside the sample, probably because the mass of the ejected particles is too small.

We can conclude that the largest contribution to the acoustic signal and, hence, to the acoustic energy, originates from the material ejection in the third phase of the ablation process.

## 4.3. Tissue specificity of the acoustic energy

To explain the large difference of the acoustic energy created during the ablation of the two gelatin types, we have to compare the respective processes of the acoustic signal generation.

The stress wave emission during the initial phase of the laser pulse is similar in both cases, but the pressure amplitudes are slightly larger for the case of 90% water content.

The dynamics of the vapor plume is also similar in both cases, but its expansion velocity is slightly larger for the sample with higher water content. The maximum vapor front velocity calculated as the slope of the curve fit shown in figure 10 for $t = 40\mu$s is 75 m/s for the sample with 70% water content and 120 m/s for 90% water content. This relatively small difference of the propagation velocities does not explain the large difference of the acoustic energy for both gelatin types. One should further keep in mind that the vapor plume expansion does not seem to contribute very much to the acoustic signal.

The largest differences in the ablation dynamics are observed during the phase of material ejection which also yields the largest contribution to the acoustic signal generation. Material ejection in the 70% case consists of a relatively slow uplifting of the whole sample surface, whereas liquid gelatin strings and droplets are rapidly ejected in the 90% case. The values for the mean ejection velocity over the 30 $\mu$s to 60 $\mu$s time interval are $\bar{v}_{70\%} = 11$ m/s and $\bar{v}_{90\%} = 70$ m/s, respectively (Fig. 10 (a)). The large ratio of the ejection velocity which differs by a factor of 6.4 explains the large difference of the acoustic energy in both cases.

As mentioned above, the pressure signal is mainly generated in the acceleration phase of the material ejection. The pressure depends on the acceleration of the ejected material compressing the air in front of the sample. To get

an estimation for the material acceleration we calculated the velocity versus time plot of the material ejection. The velocities plotted in figure 11 refer to the average velocity between the measured points in the position versus time plots of figure 10 (b). The mean acceleration during the time interval from 25 – 45 $\mu$s is $\bar{a}_{70\%} = 0.35$ m/s$^2$ for the sample with 70% water content, but $\bar{a}_{90\%} = 4.3$ m/s$^2$, i.e. it is 12 times larger for the sample with 90% water content (Fig. 11).

These differences give rise to the different values of the acoustic energy for the two gelatin types. We separately calculated the acoustic energy for the first 20 $\mu$s characterized by stress wave emission and vaporization of the surface layer, and for the subsequent time interval of 80 $\mu$s which is the phase of material ejection. The analysis showed that 88% of the acoustic energy is contained in the later part of the acoustic signal. The ratio of the acoustic energy for the two gelatin types is 3.5 during the first part of the signal and 16.2 during material ejection. These results prove the importance of the material ejection process for the material specificity of the acoustic energy.

The differences in the material ejection process are, in turn, probably more strongly related to differences of the mechanical properties of the gelatin samples than to differences of the optical properties. The absorption coefficient and optical penetration depth differ by only 20% whereas the difference of the ultimate tensile strength is certainly much larger. For 70% water content, the material strength is high enough to prevent surface tearing for more than 100 $\mu$s, whereas for 90% gelatin the surface disintegrates already after 30 $\mu$s.

## 5. CONCLUSIONS

Our investigations showed that the correlation between the acoustic energy of the ablation noise and the water content of the ablated gelatin samples is mainly caused by the different mechanical properties of the samples. The difference of the acoustic energy is much larger than expected from the optical properties. The acoustic energy is well suited for the discrimination of tissues with different optical and mechanical properties. The clinical relevance of the acoustic tissue discrimination for online monitored laser necrectomy is shown in Ref.[10]

## 6. ACKNOWLEDGMENTS

This work was funded by the German Ministry for Education and Research (Grant BMBF No. 13N7240). The authors thank AESCULAP MEDITEC, Jena, Germany, for providing the Er:YAG laser system.

## REFERENCES

1. K. Nahen and A. Vogel, "Investigations on acoustic on-line monitoring of IR laser ablation of burned skin," *Lasers Surg. Med.* **25**, pp. 69–78, 1999.
2. K. Nahen and A. Vogel, "Acoustic on-line monitoring of IR laser ablation of burnt skin," in *Laser-Tissue Interaction X*, vol. 3601, pp. 392–397, SPIE, 1999.
3. K. Nahen and A. Vogel, "Acoustic spectroscopy of Er:YAG laser ablation of skin – first results," in *Laser-Tissue Interaction IX*, vol. 3254, pp. 218–229, SPIE, 1998.
4. F. W. Dabby and U.-C. Paek, "High-intensity laser-induced vaporization and explosion of solid material," *IEEE Journal of Quantum Electronics* **QE-8**, pp. 106–111, 1972.
5. V. Venugopalan, N. S. Nishioka, and B. B. Mikic, "The effect of laser parameters on the zone of thermal injury produced by laser ablation of biological tissue," *Transactions of the ASME* **116**, pp. 62–70, 1994.
6. A. D. Zweig, M. Frenz, V. Romano, and H. P. Weber, "A comparative study of laser tissue interaction at 2.94 $\mu$m and 10.6 $\mu$m," *Appl. Phys. B* **47**, pp. 259–265, 1988.
7. V. Venogopalan, N. S. Nishioka, and B. B. Mikic, "Thermodynamic response of soft biological tissue to pulsed infrared-laser irradiation," *Biophysical Journal* **70**, pp. 2981–2993, 1996.
8. B. Majaron, P. Plestenjak, and M. Lukac, "Thermo-mechanical laser ablation of soft biological tissue: modeling the micro-explosions," *Appl. Phys. B* **69**, pp. 71–80, 1999.
9. R. Hibst, *Technik, Wirkungsweise und medizinische Anwendungen von Holmium- und Erbium-Lasern*, pp. 1–58. Fortschritte in der Lasermedizin; 15, ecomed, Landsberg, Germany, 1996.
10. K. Nahen, W. Eisenbeiß, and A. Vogel, "Acoustic online monitoring of IR laser ablation of burnt skin," in *Biomedical Optoacousctics*, vol. 3916, SPIE, 2000. in print.

# Analysis of stress waves generated in water using ultrashort laser pulses

Beop-Min Kim[1], Michael. D. Feit[1], Alexander M. Rubenchik[1], Aleksey M. Komashko[1], Steffen Reidt[2], Jürgen Eichler[2], Luiz B. Da Silva[1]

[1]Medical Technology Program, Lawrence Livermore National Laboratory, Livermore,

[2]Technische Fachhochschule-Berlin, Berlin Germany

## Abstract

A Mach-Zehnder interferometer was used for analysis of pressure waves generated by ultrashort laser pulse ablation of water. It was found that the shock wave generated by plasma formation rapidly decays to an acoustic wave. Both experimental and theoretical studies demonstrated that the energy transfer to the mechanical shock was less than 1%.

## Results and Discussion

Fig. 1 shows the schematic of the Mach-Zehnder interferometer. The Nitrogen-pumped dye laser was used as a probing light source. The green beam from the dye laser was split in a 50:50 beam splitter. One of the beams passes through a water-filled cuvette on which the ultrashort laser pulse (USLP) is incident and generates surface ablation. Another water cuvette was placed in the other beam path to match the path difference between the two beams. The pressure waves generated by the surface ablation caused the fringe shift, which can be correlated to the pressure. The fringe shift was recorded on a CCD camera with a resolution as high as 1 μm per pixel.

Fig. 2 shows the typical interferogram with fringe shift due to the spherical wave generated from the small surface area. Assuming axial symmetry and triangular pulse shape, the peak pressure can be calculated. The maximum fringe shift is

$$\Delta\varphi_{\max} = \frac{2\pi a}{b}$$

The peak change of refractive index is calculated using

$$n_{peak} = \frac{\lambda\Delta\varphi_{max}}{2\pi s} f(s/2R)$$

$$f(\alpha = s/2R) = \frac{\alpha^3}{\alpha + (1-\alpha)ln\left(\sqrt{\frac{1-\alpha}{1+\alpha}}\right)} \approx 1.5\ (s << R)$$

In *Laser-Tissue Interaction XI: Photochemical, Photothermal, and Photomechanical*, Donald D. Duncan, Jeffrey O. Hollinger, Steven L. Jacques, Editors, Proceedings of SPIE Vol. 3914 (2000)
1605-7422/00/$15.00

using a triangle-like pulse shape function. The ablation threshold for water ablation is shown in Fig. 3. The threshold was defined as beam fluence ($J/cm^2$) that causes formation of the spherical waves. As expected the threshold increases with increasing pulse width and the slope of the threshold follows typical ablation threshold patterns for other dielectric ablation.

The estimated peak pressure was calculated for various pulse widths and at multiples of the threshold intensity; the results are presented in Fig. 4. The pressure is several kbars at 50 μm for most cases and rapidly decays to 200 – 300 bars after traveling 200 – 300 μm. The solid lines are the curve fit to the data. It seems that the peak pressure is inversely proportional to the travel distance, which is expected in normal acoustic waves.

Fig. 5 shows the radius of the spherical waves as a function of time. We used various pulse widths and beam intensities. It was found that the speed of the waves is dependent on the ratio of the intensity to the threshold but not on the pulse width. The speed of the pressure waves was approximately 1.53 km/sec for all cases. The typical speed of sound in water is 1.48 km/sec. It was also found that the waves initiated by more intense pulses were more advanced due to the fast initial propagation.

The total energy in the pressure waves was estimated using the following expression (See Fig. 6):

$$E = \int \frac{p(t)^2}{c_0 \rho_0} 2\pi R^2 \, dt = \frac{2\pi R^2 p_{peak}{}^2 \tau}{3 c_0 \rho_0}$$

$$= \frac{2\pi R^2 p_{peak}{}^2 \Delta x}{3 c_0{}^2 \rho_0}$$

The energy conversion rate for various pulse widths and beam intensities was calculated and presented in Fig. 7. An important observation in this study is that the conversion efficiency is less than 1% for all cases. This result was confirmed by a theoretical calculation. We used the one dimensional hydrodynamics code "HYADES" to calculate the conversion efficiency and this result also shows that the efficiency is less than 1% [1]. This result supports the small collateral mechanical damages induced by USLP as reported in many other publications [2-3].

**Acknowledgments**

This work was performed at Lawrence Livermore National Laboratory under the auspices of the U.S. department of Energy under contract No. W-7405-ENG-48.

## References


1. J. T. Larsen, HYADES – a radiation hydrodynamics code for dense plasma studies, in: W. Goldstein, C. Hooper, J. Gauthier, J. Seely, R. Lee (Eds.), Radiative Properties of Hot Dense Matter, World Scientific, Singapore, 1991.
2. B. C. Stuart, M. D. Feit, S. Herman, A. M. Rubenchik, B. W. Shore and M. D. Perry, "Nanosecond-to-femtosecond laser-induced breakdown in dielectrics," *Phys. Rev. B* **53**(4), 1749-1761 (1996).
3. A. A. Oraevsky, L. B. Da Silva, A. M. Rubenchik, M. D. Feit, M. E. Glinsky, M. D. Perry, B. M. Mammini, W. Small IV and B. C. Stuart, "Plasma mediated ablation of biological tissues with nanosecond-to-femtosecond laser pulses: relative role of linear and nonlinear absorption," *IEEE J. of Selected Topics in Quantum Electronics*, **2**(4), 801-809 (1996).


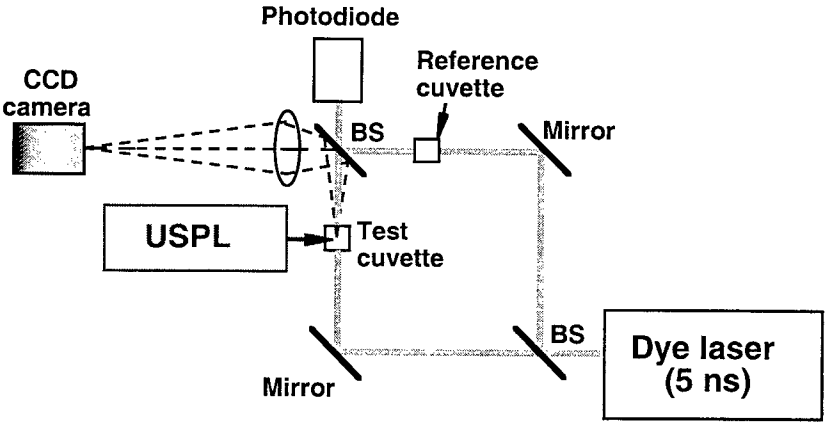


Fig. 1. Schematic of Mach-Zehnder interferometer

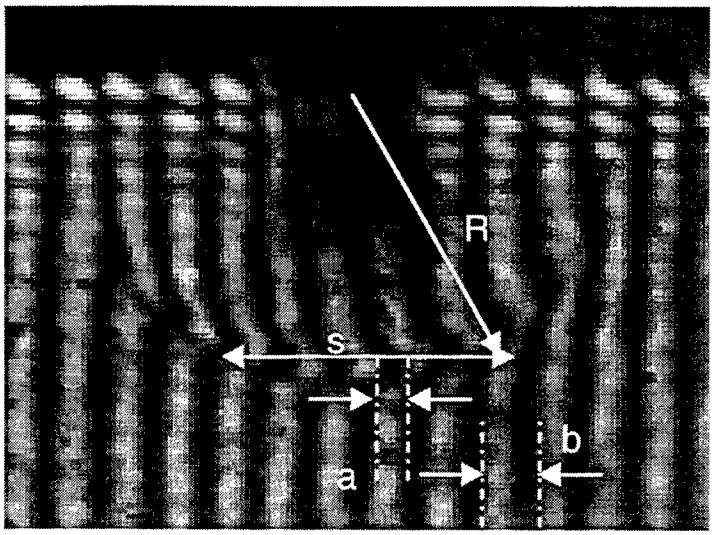


Fig. 2. Typical interferogram obtained using Mach-Zehnder interferometer. Spherical wave generates the symmetric fringe shift.

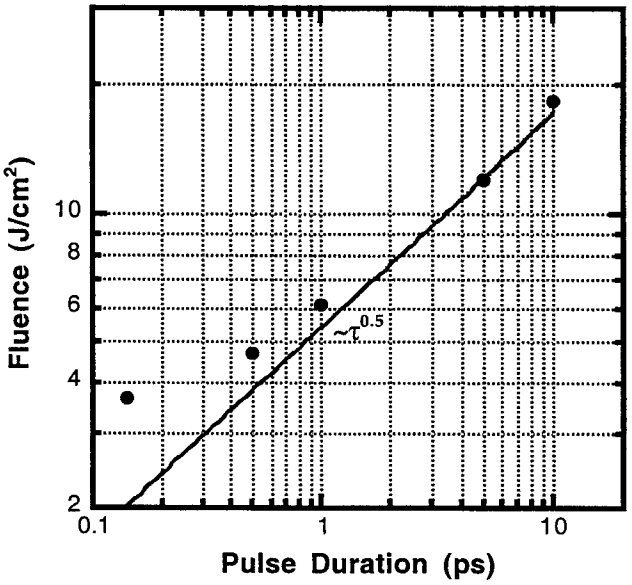


Fig. 3. Thresholds for spherical wave formation for various pulse durations.

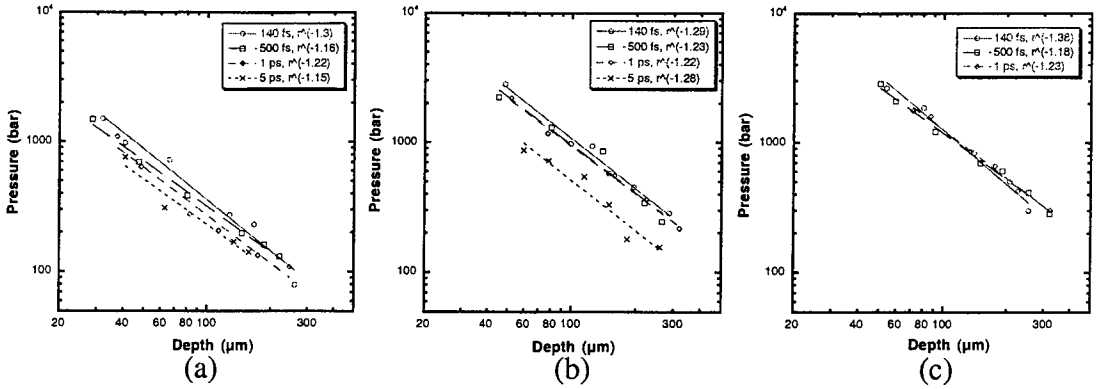


Fig. 4. Peak pressures calculated using the fringe shift of interferograms at (a) threshold, (b) 2 x threshold, and (c) 3 x threshold.

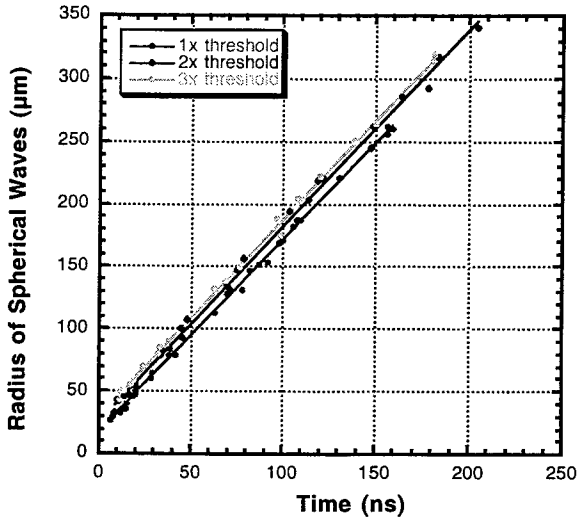


Fig. 5. Propagation of pressure wave front with time. Speed of waves are calculated using the curve-fit procedure.

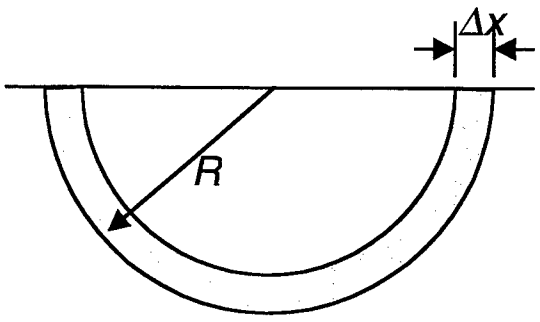


Fig. 6. Typical wave shape.

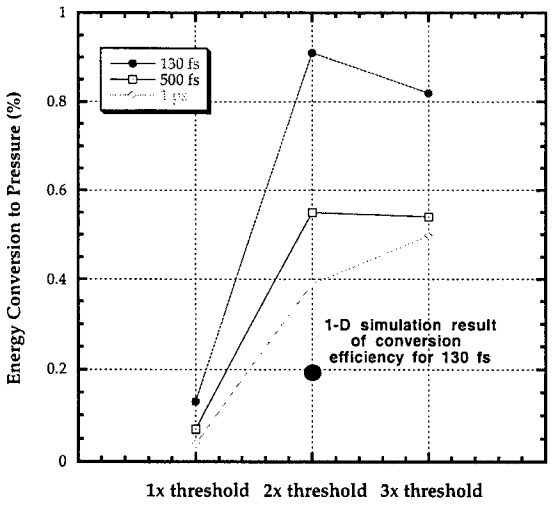


Fig. 7. Energy transfer to the pressure waves estimated at various pulse widths and beam intensities. Results of HYADES calculation is also shown.

# Opto-Acoustic Cell Permeation

Steven R. Visuri, Nicholas Heredia

Lawrence Livermore National Laboratory
P.O. Box 808, L-399
Livermore, CA 94551

## ABSTRACT

Optically generated acoustic waves have been used to temporarily permeate biological cells. This technique may be useful for enhancing transfection of DNA into cells or enhancing the absorption of locally delivered drugs. A diode-pumped frequency-doubled Nd:YAG laser operating at kHz repetition rates was used to produce a series of acoustic pulses. An acoustic wave was formed via thermoelastic expansion by depositing laser radiation into an absorbing dye. Generated pressures were measured with a PVDF hydrophone.

The acoustic waves were transmitted to cultured and plated cells. The cell media contained a selection of normally-impermeable fluorescent-labeled dextran dyes. Following treatment with the opto-acoustic technique, cellular incorporation of dyes, up to 40,000 Molecular Weight, was noted. Control cells that did not receive opto-acoustic treatment had unremarkable dye incorporation. Uptake of dye was quantified via fluorescent microscopic analysis. Trypan Blue membrane exclusion assays and fluorescent labeling assays confirmed the vitality of cells following treatment. This method of enhanced drug delivery has the potential to dramatically reduce required drug dosages and associated side effects and enable revolutionary therapies.

Keywords: acoustic, ultrasound, drug delivery

## 1. INTRODUCTION

In recent years, significant attention has focused on enhancing the delivery of drugs and genes across cell barriers. We have developed the concept of optically generated ultrasound that could greatly improve drug efficiency, with the potential to decrease dosages and side effects and enable revolutionary new drug therapies. This technique enables ultrasound production at remote sites in the body and offers a new regime of stress wave characteristics. Initial studies of this novel technology are encouraging, warranting further development.

Many other techniques have been used to permeate cell barriers and have shown limited or no success for in vivo applications. One method that shows promise for limited applications is therapeutic transdermal ultrasound. This established method has been shown to increase the efficiency, up to 5000 times, of drug transfer across the stratum corneum[1]. This technique has virtually been confined to dermal applications due to poor localization of ultrasound in deep tissues and associated collateral thermal damage[2]. Mounting piezo-electric transducers on the end of catheters is an option but the required size of the transducers would limit applications to large vessels. A recently developed alternative that has shown initial success is laser-induced stress waves that use high energy shock waves to temporarily increase membrane permeability[3,4]. The technique appears to be highly sensitive to dosimetry and thus far drug concentrations have only been increased by 10 times that obtained using simple diffusion.

We have combined aspects of these two mechanisms by using high-frequency optically-produced low-energy stress waves, a technology recently developed at LLNL. Our minimally-invasive optical method of locally generating ultrasound facilitates the delivery of required intensities into remote locations with the potential to significantly increase drug concentration rates. There are many potential applications including: intra-arterial delivery of thrombolytics or restenosis preventing drugs, and localized delivery of photosensitive and cytotoxic drugs for cancer therapy. This procedure could also facilitate the delivery of gene-vectors into target cells for gene therapy.

Optical ultrasound employs a laser coupled to an optical fiber with the distal end of the fiber delivered through a guiding catheter or introducer needle to the target tissue (Figure 1). The laser radiation that emerges from the fiber may be absorbed either by native fluids such as blood, or by an exogenous absorber. Blood has acceptable absorption ($\alpha = 250\ cm^{-1}$) near

In *Laser-Tissue Interaction XI: Photochemical, Photothermal, and Photomechanical*, Donald D. Duncan, Jeffrey O. Hollinger, Steven L. Jacques, Editors, Proceedings of SPIE Vol. 3914 (2000)
1605-7422/00/$15.00

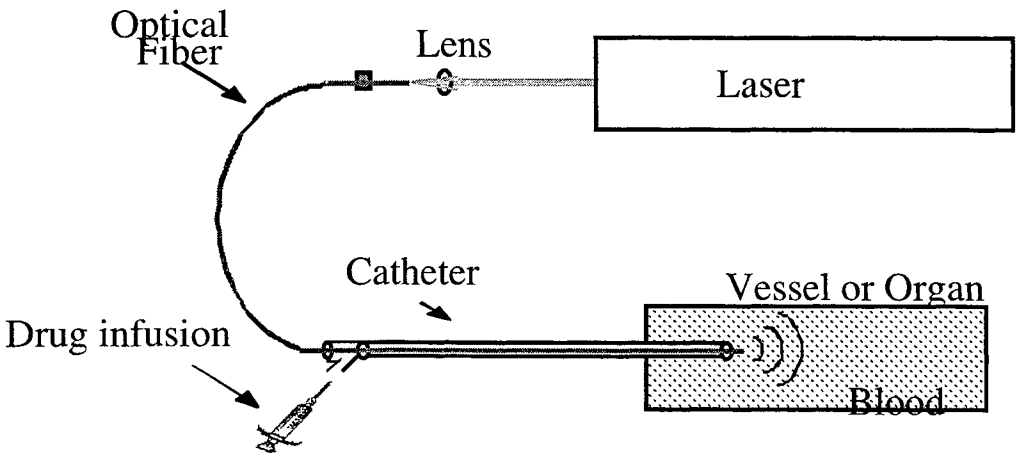


**Figure 1.** Opto-acoustic ultrasound is created by delivering laser radiation via an optical fiber to an absorber. Acoustic waves are formed in the absorbing material and enhance the uptake of a simultaneously applied drug in surrounding tissues.

532 nm as do many biocompatable dyes, making standard frequency-doubled Nd:YAG lasers a convenient laser source. These lasers, operating at kHz pulse repetition frequencies are commercially available and fairly robust. If the laser pulse duration is sufficiently short, the absorbed optical energy creates a stress wave in the material through a thermoelastic expansion. There are differences in this method of ultrasound production compared to traditional piezoelectric-produced ultrasound. The opto-acoustic ultrasound produces high frequency (10-200 MHz) acoustic waves with very low duty cycle (< 0.1%). Therapeutic piezoelectic ultrasound typically produces sinusoidally varying ultrasound with 50-100% duty cycling.

Acoustic energy interacts with cells such that passive diffusion of compounds into cells is enhanced. Acoustic waves are postulated to transiently and non-destructively disrupt or disorder the lipid bilayer membrane of cells, causing channels to form, through which compounds can enter the cell[1]. Ultrasound-enhanced drug delivery can increase intracellular concentrations of compounds which normally are impermeable or have low diffusion rates. The required drug dosage can be decreased, resulting in fewer potential side effects. Local drug delivery also decreases drug loss due to liver metabolism and systemic absorption further improving dose efficiency. We have used optically-generated ultrasound to permeate cells in monolayers and allow infusion of a fluorescent dye.

## 2. MATERIALS AND METHODS

Optically-generated ultrasound was delivered to monolayers of cells. An amount of "impermeant" fluorescent dextran conjugated dye was added to the cell media prior to ultrasound treatment. These dyes have a number of characteristics that make them attractive for study, namely, ease of imaging, low toxicity and availability of different sized molecular complexes. Using fluorescent dextran conjugates of varying weights and sizes, we were be able to probe the limitations of our technique. Dyes were applied at discrete post-irradiation time-points to determine the transient nature of the permeability. Results were observed under a fluorescent microscope and captured on a CCD camera.

Cell cultures (ATCC Manassas, VA) were grown under standard conditions: 37°C, 10% $CO_2$. Multiple cell types were investigated including: MES-SA (human uterine sarcoma), 769P (human renal carcinoma), NCTC (mouse fibroblast), and NIH3T3 (mouse fibroblast) Cells were allowed to reach near confluency in culture flasks, trypsinized, and subcultured onto glass cover slips coated with poly-L-lysine within culture dishes. Cells were again allowed to grow to near confluency. Immediately prior to experimentation, cell media was removed and replaced with approximately 3 ml of PBS containing fluorescent dye (50 mg/l). Dyes consisted of fluorescently labeled dextran conjugates (Molecular Probes, Eugene, OR), Texas-red or Fluorescein, with molecular weights ranging from 4,000 to 40,000 Da.

Acoustic pressure waves were produced by thermoelastic expansion and vaporization resulting from deposition of laser radiation. The laser used was a diode-pumped frequency-doubled Q-switched Nd:YAG laser (Spectra-Physics T40-Y70, Mountain View, CA) emitting pulses of 532 nm radiation with pulse duration of approximately 90 ns (FWHM). The

repetition rate of the laser, producing required pulse energies, was variable up to 5 kHz. The laser emission was coupled to a 50 μm diameter silica optical fiber and delivered to an absorbing media. Pulse energy exiting the optical fiber ranged from 100 to 350 μJ. The resulting optical power delivered varied up to 500 mW but typically was in the range of 150-300 mW.

Laser radiation exiting the optical fiber was absorbed into a 1% solution (wt/vol) of Amaranth red dye (Sigma Chemical Co., St. Louis, MO) solubilized in distilled water. This dye concentration resulted in an optical absorption coefficient at 532 nm of approximately 900 $cm^{-1}$. The dye was contained in a segment of Tygon tubing with the distal end sealed with 1 mil thick plastic film (PVC resin). This transducer tip allowed for efficient transmission of acoustic energy from the dye solution through the plastic, and into the surrounding aqueous media. Two small diameter tubes led into the transducer: one tube allowed for passage of the optical fiber and inflow of absorbing dye, the other tube allowed for outflow of dye. Dye was continually pumped during experiments at a rate of 1 ml/min to mitigate thermal effects.

Opto-acoustic treatment was applied to a confined area of cells. The optical-to-acoustic transducer tip was submerged in the cell media. The height above the plated cells was maintained at approximately 1 mm. Treatment was applied for periods of 1, 2, 5, 10, 20, or 30 minutes. Appropriate control groups were run in which samples were prepared identically but received no opto-acoustic treatment.

Acoustic pressure was measured with a PVDF hydrophone (#TNU001A NTR Systems, Seattle, WA) connected to a 1 GHz digital oscilloscope (Tektronix, Beaverton, OR). The hydrophone was submerged in a water bath and translated with a micrometer for positionally precise measurements along an axis.

*Permeability*

Determination of opto-acoustic cell permeability was made via fluorescent light microscopy. Following treatment, cells were washed three times with PBS to remove background fluorescence in the media. Cover slips containing the cells were removed from the culture dishes and mounted on glass microscope slides. Cells were observed under an epifluorescent microscope using appropriate excitation and emission filters for each dye. Cells were analyzed within 4 hours of treatment. Fluorescence activity was quantified by capturing an image with a CCD camera and integrating fluorescence intensity over a defined area. Comparisons between treated and non-treated areas were made.

*Cell Viability*

In separate experiments cell viability following optical or piezoelectric ultrasound was analyzed via two methods relying primarily on membrane integrity as a determination of viability. One method used was the Trypan Blue exclusion assay that is well known in the field. The method that we preferred was a two-color fluorescence cell assay (Live/Dead kit, Molecular Probes). Post-ultrasound treatment, the cells were incubated with calcein-AM, which is a 'non-fluorescent' molecule easily taken up into viable cells. Live cells enzymatically cleave the complex into an extremely fluorescent (green), membrane-impermeable calcein molecule. This is done in conjunction with ethidium homodimer-1, a membrane-impermeant dye that only enters cells with compromised membranes, a defining characteristic of dead cells. Once inside the cell, ethidium homodimer-1 binds to the nucleic acids and its fluorescent (red) intensity increases significantly.

## 3. RESULTS

Successful transient permeation of cells was demonstrated with opto-acoustic ultrasound. Figure 2 shows incorporation of 10 kDa Fluorescein-Dextran dye into MES-SA cells using 100 μJ laser pulses at 5 kHz repetition rate. Compared to control cells, a 14-fold improvement in fluorescence (dye uptake) was achieved. Approximately 50% of opto-acoustic treated cells incorporated dye vs. 6% of control cells. Measurements made with the hydrophone showed that cells experienced pressure magnitudes of approximately 10 bar compressive and nearly equal magnitude in tension. When cells experienced less than these pressures, little cell permeation was seen.

*Cell Viability*

Cell viability assays demonstrated minimal effect of opto-acoustic ultrasound on short-term viability. Figure 3 shows a representative result 2 hours after treatment with opto-acoustic ultrasound. A small fraction (<4%) of cells are considered dead.

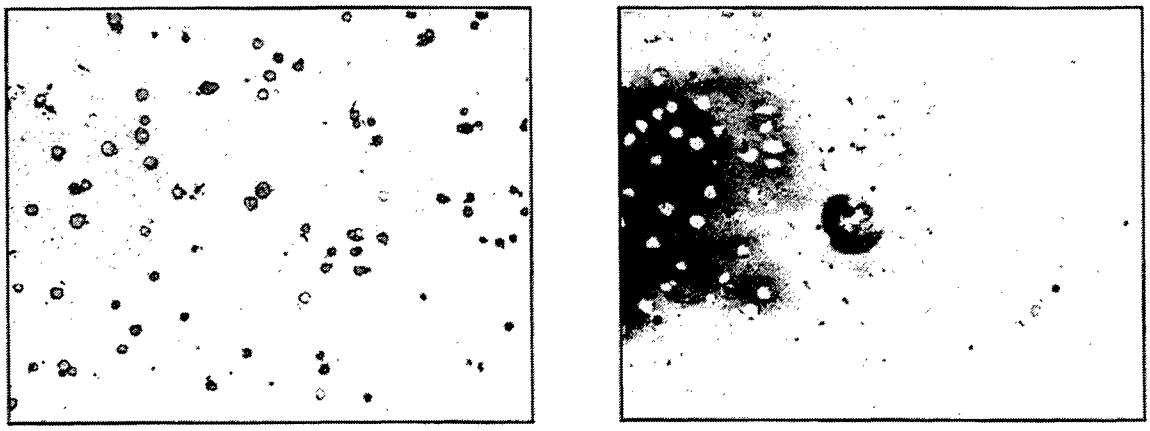

(a) (b)

**Figure 2.** Incorporation of 40 kDa dye into a) opto-acoustic treated cells and b) control cells. Both figures represent similar numbers of cells.

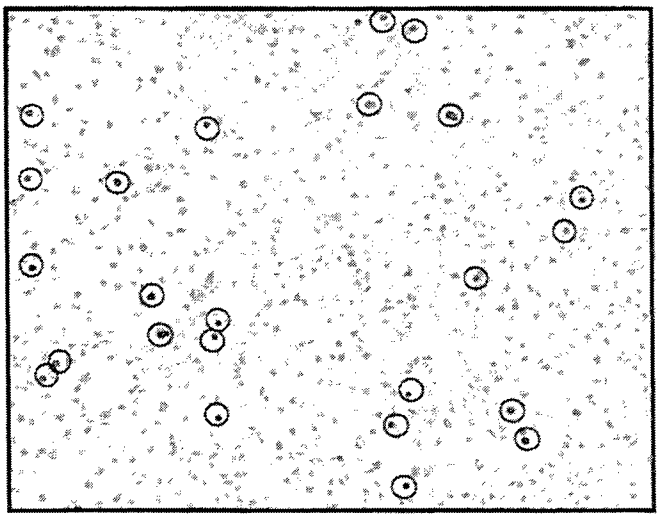

**Figure 3.** Cell viability assay showing live (green) and dead (red-highlighted with circles) cells 2 hours post-opto-acoustic treatment. Dead cells account for approximately 3.4%.

## 4. DISCUSSION

We have proven that cells can be transiently permeated with the use of acoustic energy. Others have shown that low frequency continuous wave ultrasound can permeate membrane barriers such as the skin. However, we are the first to use optically generated "ultrasound" to accomplish the same goals. This technique offers the important advantage of remote generation of ultrasound for site specific enhanced drug delivery. There are schemes for delivering therapeutic levels of ultrasound internally, but none have proven practical for remote sites. Opto-acoustic ultrasound has the potential to make this a reality. Further, the waveform characteristics of opto-acoustic ultrasound differ from those of piezoelectric ultrasound and may offer additional advantages.

There are several mechanisms that could be responsible for the transient permeability. Although cavitation with the opto-acoustic technique was not confirmed, the pressures produced are likely capable of water cavitation. Cavitation is thought to disorder the normally highly ordered lipid bilayer comprising the cell membrane, thus forming pores for the infusion of

molecules. Other means for permeation include mechanical stresses and large pressure gradients associated with microjets and microstreaming. The mechanism of action remains to be proven.

Viability assays have demonstrated low levels of cell death, in some instances not much above cell plating efficiency. Acceptable limits of cell death need to be established for particular applications. Likely, one would desire to operate just below this threshold to achieve maximal permeability. Further long term evaluation on cell viability and cell function remain to be performed.

We have explored a range of laser parameters for opto-acoustic enhanced drug delivery and have determined optimal settings within constraints of available lasers. The conversion of optical to mechanical (acoustic) energy is inefficient. It would be advantageous to increase the pressures that the cells are exposed to and there are several ways to exploit this. The easiest method is to increase the laser energy but this can only be accomplished by decreasing the pulse repetition rate as there is limited power available. Further, higher pulse energy beyond that used here may result in optical fiber damage. Another solution is to improve the efficiency of the optical to mechanical conversion which we continue to explore. Factors that affect the conversion at the distal end of the optical fiber include: pulse duration, fiber size, optical penetration depth, thermal and mechanical properties of the absorbing material. Due to the inefficiency of the current configuration, heat accumulated at the fiber tip. We have implemented a system of flowing the absorber past the optical fiber. A flow rate of 1 ml/min was sufficient to alleviate thermal energy and also prevent bleaching of the absorber.

The success of these techniques for transient permeation of cells is encouraging and work in this field will continue. The mechanism of action will be further explored and once elucidated, will be exploited for maximum permeation effect. The use of opto-acoustic ultrasound offers a novel range of acoustic parameters and also enables remote generation of ultrasound. This will make possible the use of drugs that were previously prohibited due to their poor selective uptake and enable exciting new pharmacologic and gene therapies.

## ACKNOWLEDGEMENTS

This work was performed under the auspices of the U.S. Department of Energy by the Lawrence Livermore National Laboratory under Contract W-7405-ENG-48.

## REFERENCES

1. Mitragotri S, Blankschtein D, Langer R. Transdermal drug delivery using low-frequency sonophoresis. Pharmaceutical Research 1996; 13(3): 411-420.
2. Nishioka T, et al. In vivo clot disruption by combination of Dodecafluoropentane and transcutaneous ultrasound. Circulation 1996; 94: 499.
3. Doukas AG, McAuliffe DJ, Flotte TJ. Biological effects of laser-induced shock waves: structural and functional cell damage in vitro. Ultrasound in Med & Bio 1993; 19: 137-146.
4. McAuliffe DJ, Lee S, Flotte TJ, Doukas AG. Stress-wave –assisted transport through the plasma membrane in vitro. Laser in Surgery and Medicine 1997; 20: 216-222.

# Mechanism of Laser-induced Drug Delivery in Tumors

Rinat O. Esenaliev[1,2], Irina V. Larina[1], Kirill V. Larin[1,2], Massoud Motamedi[1], B. Mark Evers[3]

[1]Center for Biomedical Engineering, [2]Department of Physiology and Biophysics,
[3]Department of Surgery

University of Texas Medical Branch, Galveston, TX 77555

Penetration of anti-cancer drugs (especially macromolecular agents) from blood in tumor cells is limited due to the presence of physiological barriers: tumor capillary wall, slow diffusion in the interstitium, and cancer cell membrane. Interaction of exogenous nano- or microparticles with laser or ultrasonic radiation may enhance drug delivery in tumor cells due to laser- or ultrasound-induced cavitation. Our previous studies demonstrated enhanced delivery of model macromolecular anti-cancer drugs in tissues in vitro when laser or ultrasonic radiation is applied. In this paper, we studied laser-induced cavitation in suspension of strongly absorbing particles and laser-enhanced drug delivery in human colon tumors of nude mice in vivo. Cavitation kinetics and thresholds were measured for carbon and colored polystyrene particle suspensions. Histological examination of control and irradiated tumors with fluorescent microscopy demonstrated that Q-switched Nd:YAG laser irradiation enhances delivery of a model macromolecular drug (FITC-dextran) in tumor blood vessel and interstitium. Enhanced delivery of an anti-cancer drug (5-FU) that is currently used in clinics resulted in tumor necrosis and inhibited tumor growth. Results of our studies suggest that the drug delivery enhancement is due to cavitation produced by local heating of particles with pulsed laser radiation.

**Keywords:** Cancer therapy, interstitium, cavitation, colon tumor, laser radiation

## 1. INTRODUCTION

Limited success has been achieved in therapy of solid tumors despite the progress in the development of anti-cancer therapeutic agents for the past two decades. The presence of physiological barriers to drug delivery in tumors (blood vessel wall, interstitial space, and cancer cell membrane) results in poor penetration of anti-cancer drugs (especially macromolecular) from blood into cancer cells [1-4]. A technique was proposed to enhance penetration of the anti-cancer drugs through these barriers based on interaction of exogenous micro-and nanoparticles with laser or ultrasonic radiation [5]. The interaction of the particles with laser or ultrasonic radiation may result in formation of localized cavitation that may mediate selective treatment of tumor. The laser-induced cavitation can be achieved by local heating of strongly absorbing particles by pulsed laser radiation [6, 7]. The ultrasound-induced cavitation is produced by interaction of ultrasonic radiation with particles that exhibit lower cavitation threshold. The laser- or ultrasound-induced cavitation can perforate tumor blood vessel walls and cancer cell membranes and produce microconvection in the interstitial space.

*Correspondence: Email: rinat.esenaliev@utmb.edu; Telephone: (409)-772-8144; Fax: (409)-772-0751



In *Laser-Tissue Interaction XI: Photochemical, Photothermal, and Photomechanical*, Donald D. Duncan, Jeffrey O. Hollinger, Steven L. Jacques, Editors, Proceedings of SPIE Vol. 3914 (2000)
1605-7422/00/$15.00

Experimental studies performed with various types of tissues *in vitro* demonstrated enhanced penetration and migration of particles and a model macromolecular anti-cancer drug (FITC-dextran) in the interstitium when laser or ultrasonic radiation is applied [5]. In this paper, we studied laser-induced cavitation in suspension of strongly absorbing nanoparticles and performed *in vivo* experiments to study laser-enhanced drug delivery in human colon tumors of nude mice.

## 2. MATERIALS AND METHODS

We used a Q-switched Nd:YAG laser operating at the wavelength of 1064 nm as a source of pulsed laser radiation in the near infra-red spectral range (Fig. 1). The duration of laser pulses was 10 ns. Laser fluence was up to 0.75 J/cm$^2$ in the experiments with particle suspensions. The diameter of laser spot was 2 mm.

In the experiments with mice, Nd:YAG laser pulses had incident energy of 45 mJ and repetition rate of 2 Hz. The diameter of laser spot was 3 mm yielding incident fluence of 0.64 J/cm$^2$. This laser fluence is substantially below the threshold of tissue damage and ablation by pulsed laser radiation [8]. Duration of laser irradiation per tumor was 10 min. Tumor heating and irreversible damage is not expected at these irradiation conditions because of heat dissipation due to blood perfusion and thermal conductivity [8].

Strongly absorbing carbon particles (dia. = 130 nm, 0.02% v/v in water) and colored polystyrene spheres (dia. = 240 nm, 0.03% v/v in water) were used to induce local heating and cavitation in water upon laser irradiation. Cavitation was studied by detecting backward scattering of probing He-Ne laser beam (wavelength = 633 nm, diameter of laser spot = 1.5 mm) from cavitation bubbles (Fig. 1). This technique was used to study laser-induced cavitation in tissue-like structures [9]. Laser light scattered from cavitation bubbles was delivered through an optical fiber (dia. = 1 mm) and an interferometric filter to a photomiltiplier tube (PMT). The signals from PMT were recorded by a fast scope (TDS-520).

Athymic nude male mice (10 animals, average weight of 30 g) were used in this study. The mice were housed in the Nude Mouse Facility of the Animal Research Center of UTMB. The animal protocol for these studies was approved by the Institutional Animal Care and Use Committee of UTMB. Suspension of human colon cancer cells KM 20 (2 x $10^6$ per site) was injected sc. in the dorso-scapular area on the left and right sides of each mouse. Experiments were initiated when tumors reached the size of 5 to 10 mm (usually two weeks after the injection). One tumor was irradiated by laser pulses, while the other tumor served as control. Since KM 20 colon tumors grow quickly and are capable of producing metastases, they are often used in colon cancer studies [10, 11]. Moreover, they are highly resistant to chemotherapy and serve as a good tumor model in our studies.

Suspension of carbon particles (dia. = 130 nm, 2% v/v in saline) was injected in the tail vein of nude mice three hours prior to irradiation to allow extravasation of the particles in tumor capillaries. Fluorescein isothiocyanate-dextran (FITC-dextran) (Sigma, St. Louis, MO), a macromolecular fluorescent dye (M.W. = 4,000), was used as a model macromolecular anti-cancer drug. This macromolecular fluorescent dye is widely used in perfusion studies in animals. FITC-dextran solution (2.5% in saline) was injected in the tail vein before irradiation.

Anti-cancer drug 5-Fluorouracil (5-FU) (Pharmacia, Inc.) was used in our experiments. 5-FU is not a macromolecular drug (M.W. = 130). However, it is currently used for colon cancer chemotherapy. The drug was injected i.p. prior to irradiation at the dose of 90 mg/kg which is the optimal dose for colon cancer therapy in nude mice [12-17]. Tumor necrosis was examined using standard H&E staining.

Animals were euthanized 72 hours after irradiation to assess necrosis induced by 5-FU. Irradiated and control tumors were harvested and fixed in formalin. Thin slices of the tumors were analyzed histologically after standard staining with hematoxylin and eosin (H&E).

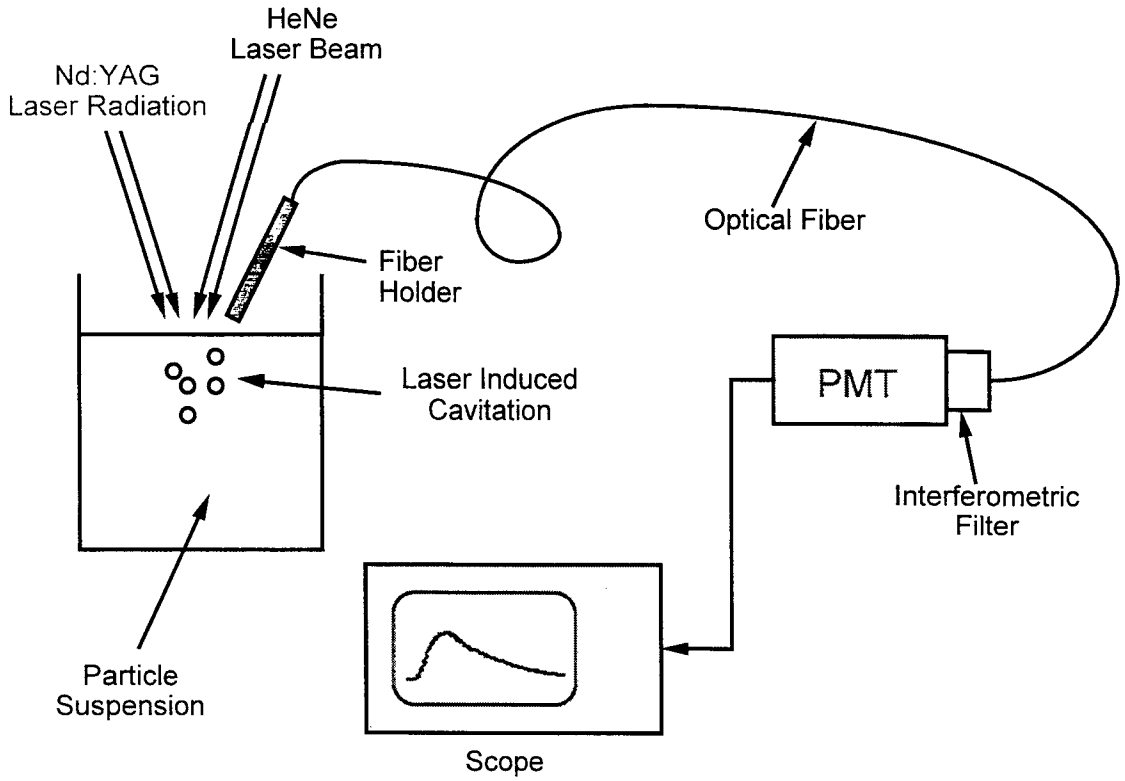


**Figure 1.** Experimental setup for detection of laser-induced cavitation in particle suspensions.

Length and width of each tumor were measured with a caliper. Tumor volume, V, was calculated by the formula: $V = L \times W^2 / 2$, where L and W are the length and the width of the tumor, respectively. This formula is commonly used for the calculation of tumor volume in cancer therapy studies. The tumor volume was plotted as a function of time (in days) after the first treatment (irradiation).

## 3. RESULTS AND DISCUSSION

Typical PMT signal recorded upon laser-induced cavitation in absorbing particle suspension is presented in Fig. 2. The first sharp peak is induced by scattered Nd:YAG laser radiation partially transmitted through the filter. Signal from laser-induced microbubbles was delayed and lasted for the time in the order of 1 μs. The delay was due to the formation and growth of the cavitation bubbles after rapid laser heating. This kinetics is typical for the formation, growth, and collapse of cavitation bubbles inside tissue phantoms [9]. The use of short (nanosecond) laser pulses allowed effective and local

heating of the particles because the rate of heat diffusion from the particles is much less that the rate of heat deposition during the course of the nanosecond laser pulse.

To measure threshold of laser-induced cavitation, the amplitude of the signal from cavitation bubbles was plotted as a function of fluence (Fig. 3 and 4). The threshold was 0.02 and 0.1 J/cm$^2$ for the carbon and polystyrene particles, respectively. The differences in the threshold values are due to higher absorption coefficient of carbon compared with that of colored polystyrene. Strong cavitation was detected at the fluence above 0.1 and 0.4 J/cm$^2$ in carbon and polystyrene particle suspensions, respectively. These data indicate that irradiation of the particles in tissues with the fluence above 0.1 J/cm$^2$ will result in cavitation.

Figure 5 shows regular (top) and fluorescent (bottom) microscopy of a control tumor. The tissue slice was not stained with H&E to avoid artifacts for fluorescent microscopy. A tumor blood vessel with well-defined walls is visible in the central part of the top picture with regular microscopy. Fluorescent microscopy of the same site of the tumor revealed moderate fluorescence from some parts of the vessel. No fluorescence was observed in the interstitium. This indicates that the macromolecules can not penetrate in the interstitium and cancer cells and can accumulate only in some areas of tumor vessel walls. Regular (top) and fluorescent (bottom) microscopy of a laser-irradiated tumor is presented in Fig. 6. Tumor blood vessels had damage that was easily observed using light microscopy. Fluorescence from the laser-irradiated tumors was substantially brighter and was detected not only from the vessels, but also from the interstitium and cancer cells.

Histopathological examination of tumor slices stained with H&E revealed slight necrosis in control tumors. Fig. 7 shows viable tumor tissue with local necrosis in small areas produced by 5-FU. Viable tumor cells with well-defined nuclei are visible in the figure. No necrosis was obtained in the tumors, if 5-FU was not injected in mice (Fig. 8). Irradiation of tumors by laser pulses resulted in tissue necrosis in large areas (Fig. 9). Examination of this figure demonstrates killing of cancer cells in the irradiated tumor where pronounced shrinkage of nuclei was observed while no viable cells were present.

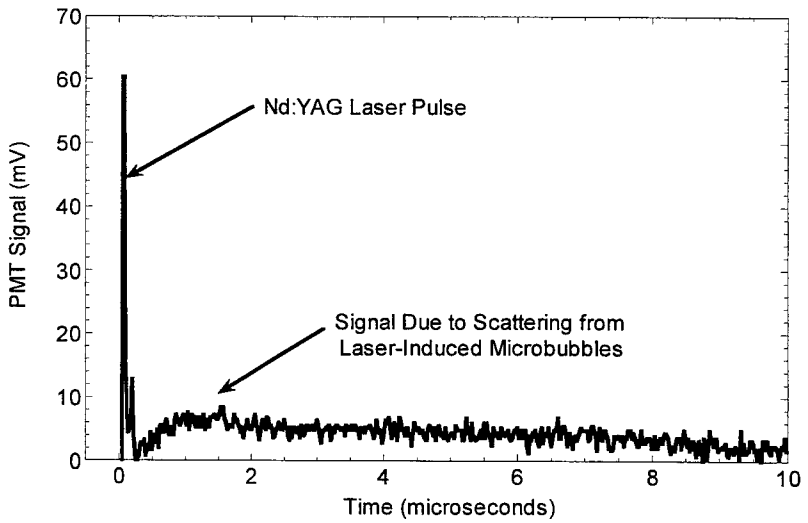


**Figure 2.** Typical signal recorded upon laser-induced cavitation in particle suspension.

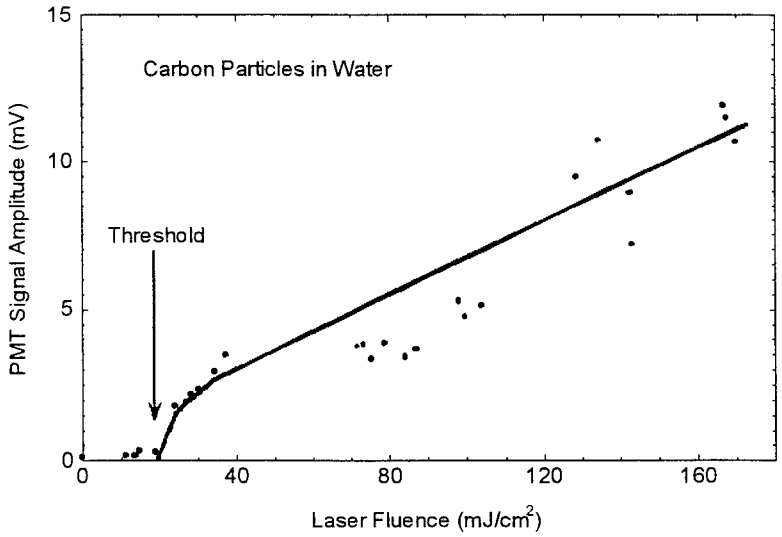


**Figure 3.** Amplitude of PMT signal from cavitation bubbles in carbon particle suspension as a function of laser fluence.

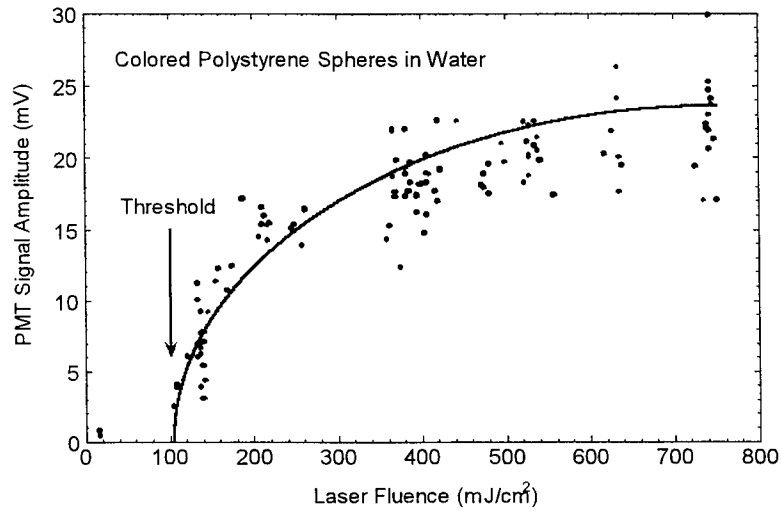


**Figure 4.** Amplitude of PMT signal from cavitation bubbles in polystyrene particle suspension as a function of laser fluence.

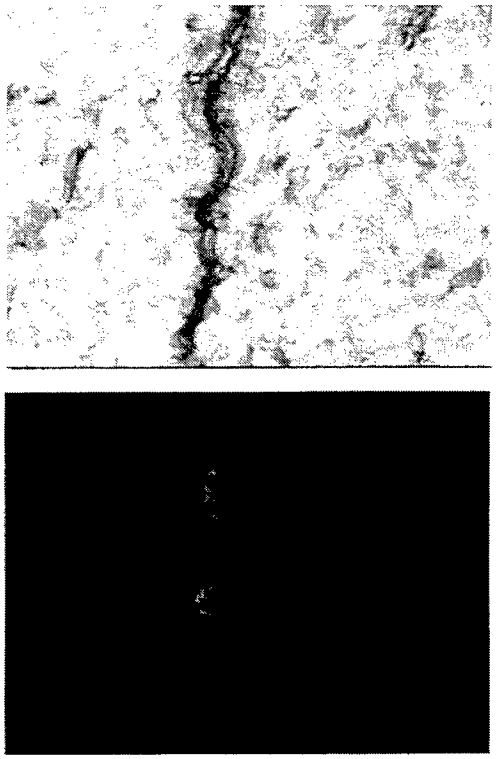

**Figure 5.** Regular and fluorescence microscopy of control (non-irradiated) tumor.

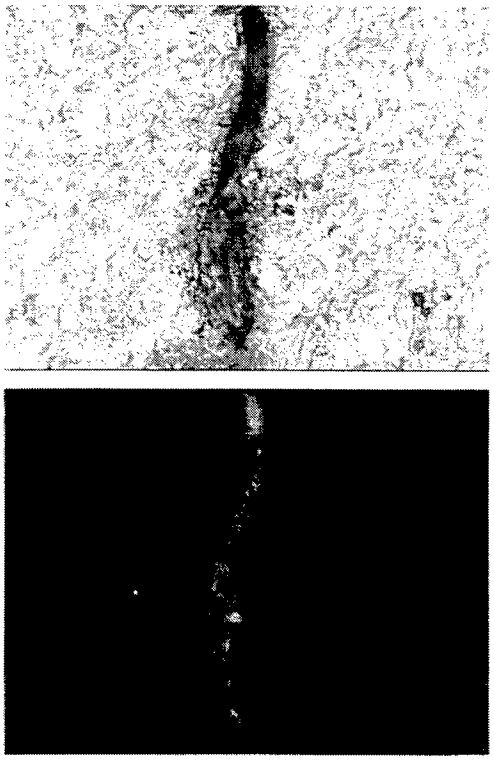

**Figure 6.** Regular and fluorescence microscopy of laser-irradiated tumor.

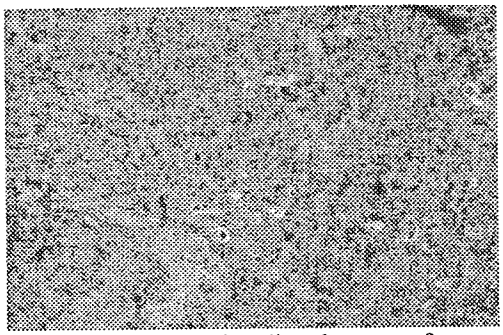

**Figure 7.** Non-irradiated tumor after treatment with 5-FU.

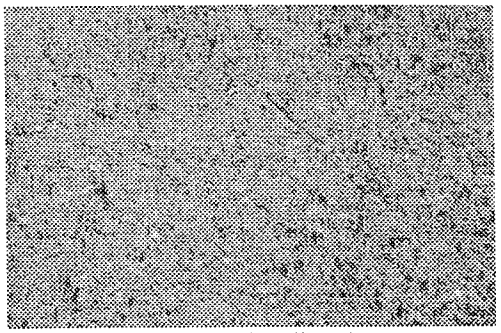

**Figure 8.** Non-irradiated tumor (no treatment with 5-FU).

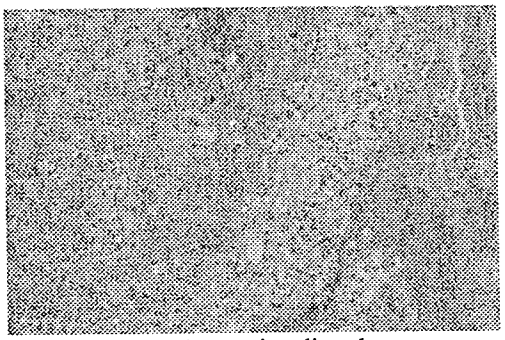

**Figure 9.** Laser-irradiated tumor (with treatment with 5-FU).

Figure 10 shows tumor volume as a function of time after first treatment with laser radiation. Volume of the control tumor increased despite injections of 5-FU, while volume of the irradiated tumor was stable. Scattering of the data points for the control tumor is caused by an error of tumor dimension measurements due to irregular shape of the tumor. The volume of the control tumor increased more than 3 times during the total duration of the treatment. No thermal damage in the tumors was observed during laser irradiation.

The KM 20 tumors (as well as other colon tumors) are highly resistant to chemotherapy. Only decreased growth can be achieved with the use of 5-FU [12-17]. These results indicate that the laser-enhanced drug delivery has the potential to improve efficacy of cancer therapy.

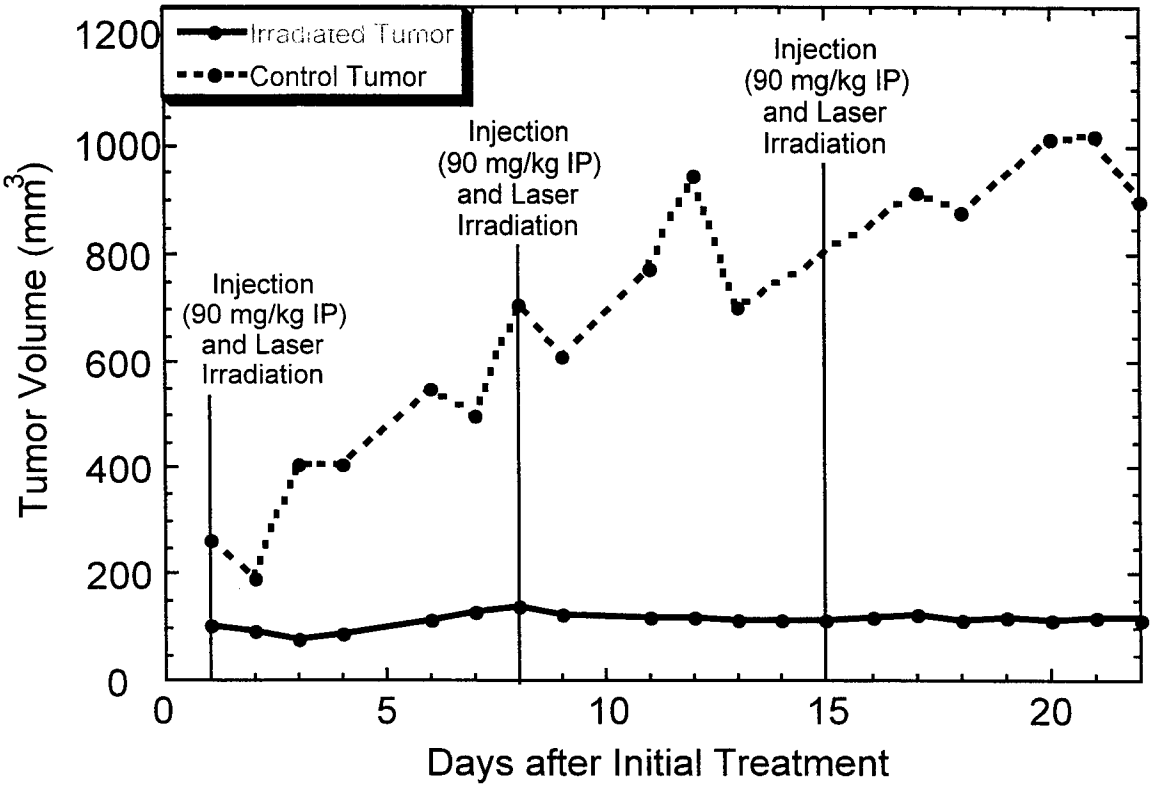


**Figure 10.** Efficacy of tumor therapy with laser-enhanced drug delivery.

## 4. CONCLUSION

Our pilot preliminary studies reveal promising results further encouraging the development of a novel approach for selective treatment of malignant tumors. Our progress can be summarized as:

1. Cavitation in water can be achieved by irradiating strongly absorbing carbon and colored polystyrene nanoparticles by short (nanosecond) laser pulses with the fluence above 0.02 - 0.1 J/cm$^2$;

2. Laser-induced cavitation enhances delivery of model macromolecular anti-cancer drugs in tumors;

3. Laser-enhanced delivery of real anti-cancer drug 5-FU results in pronounced tumor necrosis;

4. Laser-enhanced drug delivery can improve efficacy of cancer chemotherapy in nude mice.

## ACKNOWLEDGMENT

The authors would like to thank the John Sealy Memorial Endowment Fund for support of this research and Kelly M. Lightfoot for assistance in nude mouse studies.

## REFERENCES

1. Jain R.K. Delivery of Novel Therapeutic Agents in Tumors: Physiological Barriers and Strategies. Journal of the National Cancer Institute, v.81(8), pp. 571-576, 1989.
2. Jain R.K. Delivery of Molecular Medicine to Solid Tumors. Science, v. 271, pp. 1079-1080, 1996.
3. Curti B.D. Physical Barriers to Drug Delivery in Tumors. In: Chabner B. A. and Longo D. L., eds. "Cancer Chemotherapy and Biotherapy", pp. 709-719, 1996.
4. Gerlowski L.E., Jain R.K. Microvascular permeability of Normal and Neoplastic Tissues. Microvasc. Res., v. 31, pp. 288-305, 1986.
5. Esenaliev R.O. Interaction of radiation with microparticles for enhancement of drug delivery in tumors. In "Laser-Tissue Interaction", ed. S.L. Jacques, SPIE Publishing, Bellingham, WA., v. 3601, 1999, pp. 166-176.
6. Hopper R.W., Uhlmann D.R. Mechanism of Inclusion Damage in Laser Glass. J. Appl. Phys., v. 41 (10), pp. 4023-4037, 1970.
7. Esenaliev R.O., Karabutov A.A., Podymova N.V., Letokhov V.S. Laser Ablation of Aqueous Solutions with Spatially Homogeneous and Heterogeneous Absorption. Appl. Phys. B, v. 59, pp. 73-81, 1994.
8. Optical and Thermal Response of Laser Irradiated Tissue, eds. Welch A.J. and van Gemert M.J., Premium Press, New York, 1995.
9. Esenaliev R.O., Jacques S.L. Transient and permanent cavitation in collagen gels by laser-induced thermoelastic pressure waves. In "Laser-Tissue Interaction", ed. S.L.Jacques, SPIE Publishing, Bellingham, WA. , v. 2681, pp.185-193, 1996.
10. Evers BM, Zhou Z, Dohlen V, Rajaraman S, Thompson JC, Townsend CM. Fetal and neoplastic expression of the neurotensin gene in the human colon. *Annals of Surgery. 223(5):464-70; discussion 470-1, 1996.*
11. Yoshinaga K, Evers BM, Izukura M, Parekh D, Uchida T, Townsend CM Jr, Thompson JC. Neurotensin stimulates growth of colon cancer. *Surgical Oncology. 1(2):127-34, 1992.*
12. Pratesi G. Manzotti C. Tortoreto M. Prosperi E. Zunino F. Effects of 5-FU and cis-DDP combination on human colorectal tumor xenografts. Tumori. 75(1):60-5, 1989.
13. Van Ginckel R. Distelmans W. De Brabander M. Callens M. Janssens B. Jagers E. Wouters L. De Coster R. Janssen PA. Levamisole plus 5-fluorouracil inhibits the growth of human colorectal xenografts in nude mice. European Journal of Cancer. 28A(6-7):1137-9, 1992.

14. Britten CD. Hilsenbeck SG. Eckhardt SG. Marty J. Mangold G. MacDonald JR. Rowinsky EK. Von Hoff DD. Weitman S. Enhanced antitumor activity of 6-hydroxymethylacylfulvene in combination with irinotecan and 5-fluorouracil in the HT29 human colon tumor xenograft model. Cancer Research. 59(5):1049-53, 1999.
15. Inada T. Ichikawa A. Kubota T. Ogata Y. Moossa AR. Hoffman RM. 5-FU-induced apoptosis correlates with efficacy against human gastric and colon cancer xenografts in nude mice. Anticancer Research. 17(3C):1965-71, 1997.
16. Kase S. Kubota T. Watanabe M. Furukawa T. Tanino H. Kuo TH. Saikawa Y. Teramoto T. Kitajima M. Recombinant human interferon alpha-2a increases the antitumor activity of 5-fluorouracil on human colon carcinoma xenograft Co-4 without any change in 5-FU pharmacokinetics. Anticancer Research. 15(1):153-5, 1995.
17. Laurent PL. Tevaearai HT. Eliason JF. Givel JC. Odartchenko N. Interferon alpha and 5'-deoxy-5-fluorouridine in colon cancer: effects as single agents and in combination on growth of xenograft tumours. European Journal of Cancer. 30A(12):1859-65, 1994.

# SESSION 8

# Photoacoustics and Bubbles

# *In Vitro* Erbium:YAG Laser Lithotripsy

Kin Foong Chan[a], Gracie Vargas[a], Patricia J. Parker[b],
Joel M. H. Teichman[b], Randolph D. Glickman[b], H. Stan McGuff[b], A. J. Welch[a]

[a]University of Texas at Austin, Austin, TX 78712
[b]University of Texas Health Science Center, San Antonio, TX 78284

## ABSTRACT

The potential application of an Erbium:YAG (Er:YAG) laser ($Q_o$ = 50 mJ/pulse; $\tau_p$ = 275 μs; rep. rate = 2, 10 Hz) with a sapphire delivery fiber for intracorporeal laser lithotripsy was explored. Preliminary measurements on calculus mass-loss and fragmentation efficiency were conducted and results were compared with that of Ho:YAG laser lithotripsy. Laser induced bubble and lithotripsy dynamics were investigated to assess the mechanism(s) involved in the fragmentation process. Results showed that the fragmentation efficiency (mass-loss/$H_o$ - g.μm$^2$/J) in Er:YAG laser lithotripsy was about 2.4 times that of Ho:YAG laser lithotripsy (used: $Q_o$ = 500 mJ/pulse; $\tau_p$ = 250 μs; rep. rate = 10 Hz). Acoustic transients were found to have minimal effect during Er:YAG laser lithotripsy. Schlieren flash images suggested a predominantly photothermal mechanism due to direct laser energy absorption, which resulted in recrystallization and plume formation. These events indicated melting and chemical decomposition of the calculus composition. Another observation led to the possibility of a plasma-mediated photothermal mechanism. The 'Moses effect' facilitating pulsed mid-infrared laser delivery appeared more efficient for the Er:YAG laser than for the Ho:YAG laser. With the sapphire fiber, experimental results suggested the potential of an improved treatment modality by the Er:YAG laser for intracorporeal laser lithotripsy.

**Keywords**: ablation, chemical decomposition, erbium laser, fragmentation, hard tissue, kidney stone, lithotripsy, photothermal, plasma formation

## 1. INTRODUCTION

Clinical applications of the Er:YAG laser include dentistry [1, 2], stapedotomy [3, 4], and ophthalmology [5]. However, its potential in urology and lithotripsy has not been explored. One major obstacle has been the lack of an efficient delivery system for minimally invasive surgeries such as intracorporeal laser lithotripsy.

D'yakonov *et al.* [6] and Bloch *et al.* [7] performed preliminary studies on *in vitro* Er:YSGG laser fragmentation of urinary calculi in the early 1990's. Unfortunately, the progress was hampered by the lack of an efficient and flexible optical fiber. Hollow waveguides [8, 9] were not suitable for applications in a saline environment, while fluoride fibers were brittle and hygroscopic [10]. At mid-infrared wavelengths > 2.5 μm, optical loss in low $OH^-$ quartz fibers was too high for practical applications [7, 10].

Recent advances in infrared fiber technologies have produced single crystal sapphire fibers with low loss (< 1.73 dB/m) and relatively good flexibility (bending radius < 80 mm) [11, 12] that are suitable for delivery of the 2.94 μm Er:YAG laser beam. The solid core optical fibers increase the potential of mid-infrared laser applications in minimally invasive to invasive surgeries. Here, we explored the feasibility of the Er:YAG laser in lithotripsy using

[a]Author contact information:
Kin Foong Chan, kfchan@ccwf.cc.utexas.edu, Tel: (512)471-9497, Fax: (512)475-8854
Department of Electrical and Computer Engineering, University of Texas at Austin, ENS 610; Austin, TX 78712, U.S.A.



In *Laser-Tissue Interaction XI: Photochemical, Photothermal, and Photomechanical*, Donald D. Duncan, Jeffrey O. Hollinger, Steven L. Jacques, Editors, Proceedings of SPIE Vol. 3914 (2000)
1605-7422/00/$15.00

a sapphire fiber. A preliminary study was performed comparing the fragmentation efficiencies of the Er:YAG laser and the Ho:YAG laser. The fragmentation mechanism(s) during Er:YAG laser lithotripsy was investigated.

## 2. METHODS

### 2.1 Urinary Calculi and Water

Deionized water was used in the experiments. Cut calculi, composed of > 95% calcium oxalate monohydrate (COM), were obtained from a calculus analysis laboratory (Louis C. Herring Co., Orlando, FL).

### 2.2 Experiments

The initial experiment was an assessment of the sapphire fiber to deliver Er:YAG laser energy to a COM calculus submerged in deionized water. It was found that for a 425-μm core diameter fiber, plasma formation occurred consistently when more than 50 mJ/pulse energy was delivered with the fiber in contact with the calculus (firing the Er:YAG laser in water alone did not produce plasma or optical breakdown). Consistent plasma formation damaged the sapphire fiber tip. Therefore, it was decided that subsequent experiments would be performed around the threshold pulse energy for plasma formation to prevent fiber damage as well as to maximize the energy delivered to the COM calculus. At 50 mJ/pulse, the pulse duration of the Er:YAG laser was measured to be approximately 275 μs, providing a fiber output fluence of about 35 J/cm$^2$.

*Mass-loss measurements*

The COM calculi were desiccated and their initial mass measured. They were left submerged in water for one day and randomly sorted into two groups. Each group of COM calculi was irradiated with the Er:YAG laser and the Ho:YAG laser at 10 Hz. An SEO-1-2-3 Er:YAG laser was set to 50 mJ per pulse at 275-μs pulse duration. A sapphire fiber with 425-μm core diameter was used with the Er:YAG laser. A Coherent VersaPulse Ho:YAG laser was tuned to an output of 500 mJ per pulse at 250-μs pulse duration. A low $OH^-$ 365-μm core diameter fiber was used with the Ho:YAG laser. After laser irradiation, the COM calculi were desiccated and the final mass of the parent COM calculi were measured. The difference between the initial mass and the final mass designated the mass-loss (g) for an individual calculus. The mass-loss (g) results were normalized to the output fluence, $H_o$ (J/μm$^2$) of the Er:YAG laser and the Ho:YAG laser, and the fragmentation efficiency (g.μm$^2$/J) for each group was calculated. These fragmentation efficiency results between Er:YAG laser lithotripsy and Ho:YAG laser lithotripsy were compared and a student t-test was performed to determine if the differences in values were statistically significance. The fragment sizes in Er:YAG and Ho:YAG laser lithotripsies were also examined and compared.

*Bubble dynamics and fragmentation mechanism(s)*

The bubble and lithotripsy dynamics were studied with Schlieren flash photography and measurements of acoustic transients. Schlieren flash images provided visualization of the fragmentation process, which was correlated to acoustic emission due to Er:YAG laser irradiation or bubble dynamics.

The Schlieren flash photography system consisted of a computer-based data acquisition and instrumentation control software module. The software communicated with a pulse generator, which in turn synchronized the firing of the Er:YAG laser and the flashlamp (nitrogen-dye laser), as shown in Figure 1. For each measurement, nine warm-up pulses and one delivery pulse were fired (rep. rate = 2 Hz). The shutter opened before and closed after the tenth laser pulse to allow Er:YAG laser delivery to the water cuvette. The time between the onset of the Er:YAG laser irradiation and the activation of the flashlamp was altered to capture dynamic events at different time delays. A series of images at different time delay allowed analyses of Er:YAG laser induced bubble dynamics and fragmentation process. The laser energy delivered to the water cuvette via the sapphire fiber was monitored real-time using an energy probe and a Molectron EPM 2000 to ensure stability of the laser pulse. Pressure or acoustic transients were acquired and recorded simultaneously through the oscilloscope using a PVDF needle-hydrophone.

Three sets of experiments were performed. The Er:YAG laser induced bubble dynamics were studied to assess the behavior of the bubble and the 'Moses effect [13]' that contributed to laser energy delivery. The second experiment examined the possible contribution of acoustic transients or shockwaves to fragmentation by positioning the sapphire fiber in contact and parallel to the calculus surface. The last experiment recorded the lithotripsy dynamics by placing the sapphire fiber in contact and perpendicular to the calculus surface. Combinations of these studies provided clues to the contribution of photothermal and photomechanical/photoacoustical mechanisms to calculus fragmentation.

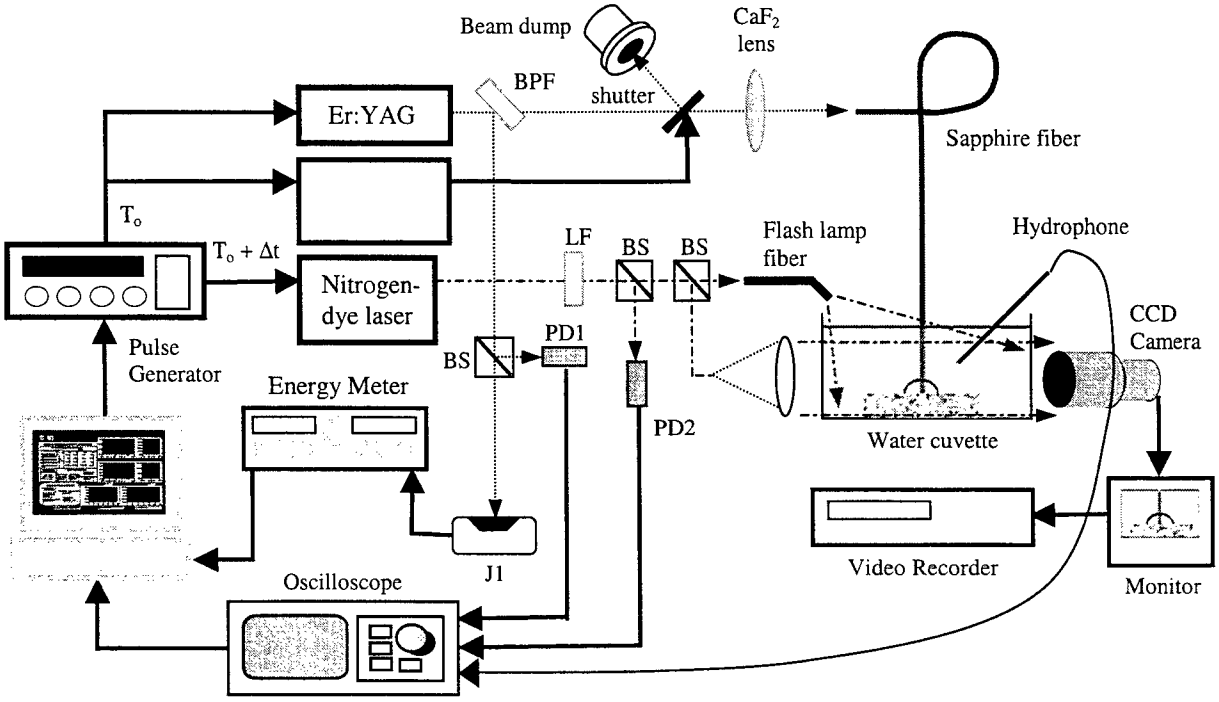


**Figure 1.** Experimental setup for Schlieren flash photography with simultaneous measurement of acoustic transients. BS: beam splitter; LF: line filter; PD1, PD2: photodiodes; BPF: band-pass filter; J1: energy probe.

## 3. RESULTS

### 3.1 Mass-loss Measurements

Fragmentation efficiency values (mass-loss/$H_o$) were 53.6 g.$\mu m^2$/J for the Er:YAG laser and 22.6 g.$\mu m^2$/J for the Ho:YAG laser. Statistical analysis using student t-test revealed a p-value of 0.04 for these results. The sizes of fragments in Er:YAG laser lithotripsy were not statistically different from those in Ho:YAG laser lithotripsy.

### 3.2 Bubble Dynamics and Fragmentation Mechanism(s)

Figure 2 illustrates the bubble dynamics induced by the Er:YAG laser, and Figure 3a shows the acoustic transient induced by Er:YAG laser irradiation and collapses of the vapor bubble. Note that all acoustic signals in Figure 3 were corrected to approximately 1-mm distance from the vapor bubble. A rapidly expanding vapor bubble was visible at 5 $\mu s$. By 20 $\mu s$, a bubble shape characteristic of a Ho:YAG laser induced bubble was formed. This was due to an extremely small penetration depth at 2.94 $\mu m$ for the Er:YAG laser (compared to about 400 $\mu m$ for the Ho:YAG laser). Therefore, the pear-shaped bubble formation appeared much earlier in the expansion phase of the Er:YAG laser induced vapor bubble. However, of interest was the continuous axial deposition of Er:YAG laser energy through the vapor channel, and expansion of the bubble axially rather than radially by 100 $\mu s$.

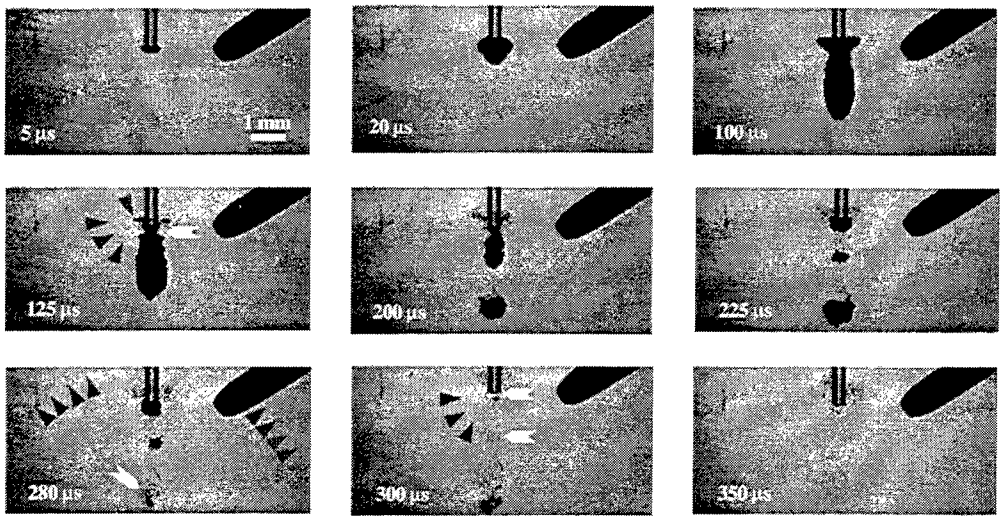


**Figure 2.** Er:YAG laser induced vapor bubble formation. Notice the bubble dynamics differs from that of the Ho:YAG laser. At maximum size, the Er:YAG laser induced bubble appeared torpedo-shaped; the 'Moses effect' at 2.94 µm facilitated a more axial penetration of Er:YAG laser energy and a less radial expanding vapor bubble than at 2.12 µm, mainly due to a difference in the optical absorption coefficients.

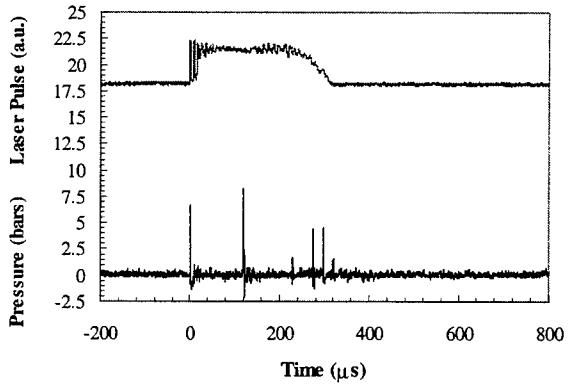


(a)

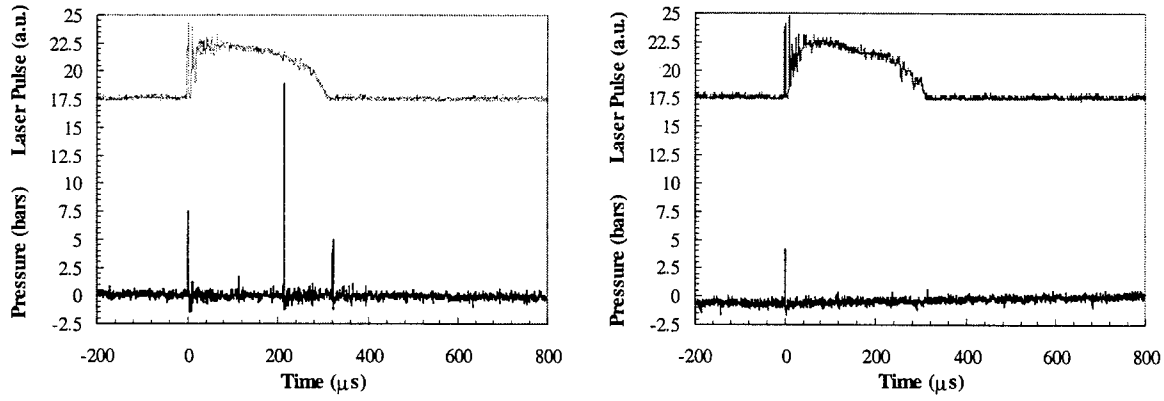


(b) (c)

**Figure 3.** Acoustic response to Er:YAG laser irradiation (a) in clear water, (b) with sapphire fiber in contact and parallel to the calculus surface, and (c) with sapphire fiber in contact and perpendicular to the calculus surface.

Because of the narrow vapor channel, there were multiple vapor bubble collapses and separations of vapor bubbles from the fiber tip. These multiple collapses distributed the acoustic energy along the fiber axis, thus weakening the acoustic or mechanical effects by Er:YAG laser irradiation. As shown in Figure 2 and Figure 3a, the first collapse occurred at about 125 μs, generating an acoustic pressure front and separating the original vapor bubble from the fiber tip. Since the Er:YAG laser pulse has not ended, continuous energy deposition created another bubble while the original bubble was collapsing. This process continued along the fiber axis, with multiple bubble collapses resulting in multiple small amplitude acoustic emissions (collapse loci shown by arrows, acoustic wavefronts shown by triangular pointers in Figure 2; small amplitude acoustic transients shown between 250 μs and 350 μs in Figure 3a). Rebound of collapsed bubble was minimal, and no re-collapsed acoustic emission was observed.

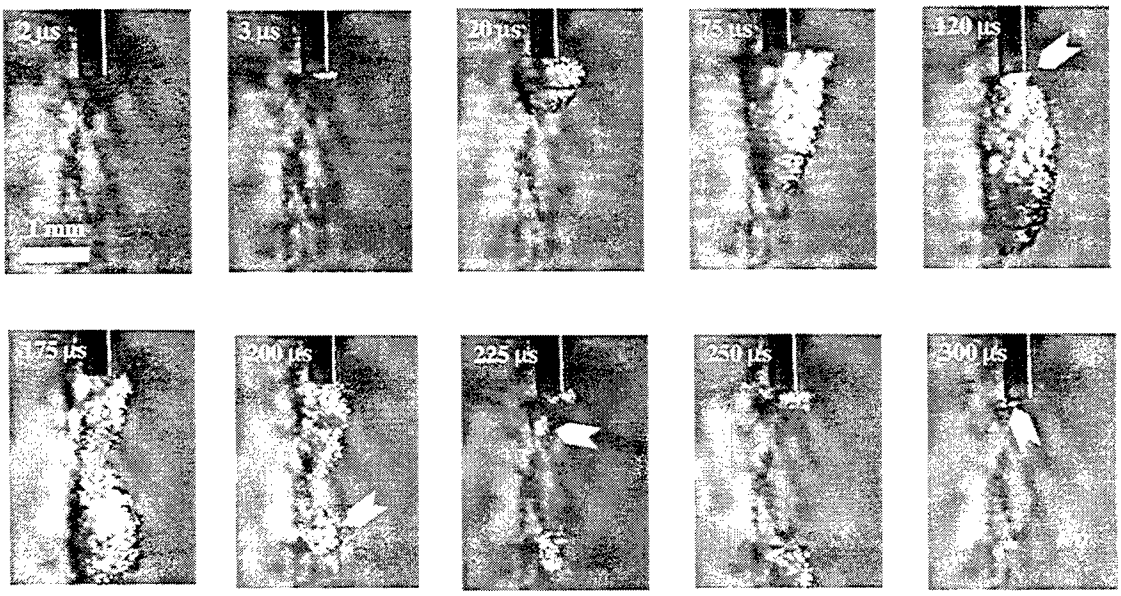


**Figure 4.** The sapphire fiber was placed in contact and parallel to the calculus surface to investigate the contribution of acoustic emission to the fragmentation process. In this case, no fragmentation occurred.

When the sapphire fiber was placed in contact and parallel to the calculus surface, a similar acoustic signal with multiple bubble collapses was recorded. Figure 4 shows the bubble dynamics involving multiple bubble collapses and bubble generations and separations similar to Figure 2. In Figure 4, the collapse loci were indicated at about 120 μs, 200 μs, 225 μs, and 300 μs, respectively. The corresponding acoustic signal is shown in Figure 3b. The acoustic transients recorded in clear water and in parallel fiber orientation were always below 20 bars. No fragmentation occurred.

Figure 5 illustrates the fragmentation dynamics induced by the Er:YAG laser when the sapphire fiber was placed in contact and perpendicular to the calculus surface. Since the Er:YAG laser fluence (or pulse energy) was set around the threshold for plasma formation, two modes of fragmentation processes occurred: without plasma formation (Figure 5a) and with plasma formation (Figure 5b). In both cases, ablation seemed to occur shortly after laser onset (5 – 7 μs), and a plume consisted of fine and emulsified material was ejected slowly to the surrounding water. In the case without plasma formation, recrystallization process at the fiber periphery was noted. Plume formation continued to expand in both ablation modes, and by 50 ms, the slowly dispersing ablation products appeared similar in both cases. We also noticed that plasma formation lasted longer than the Er:YAG laser pulse duration, up to at least 1ms. The corresponding acoustic signal (with or without plasma formation) is shown in Figure 3c. Only a small pressure transient occurred at the onset of Er:YAG laser irradiation due to rapid expansion of the evaporated water layer underneath the fiber tip. The amplitude of this acoustic transient was always below 10 bars. No further acoustic emission was identified.

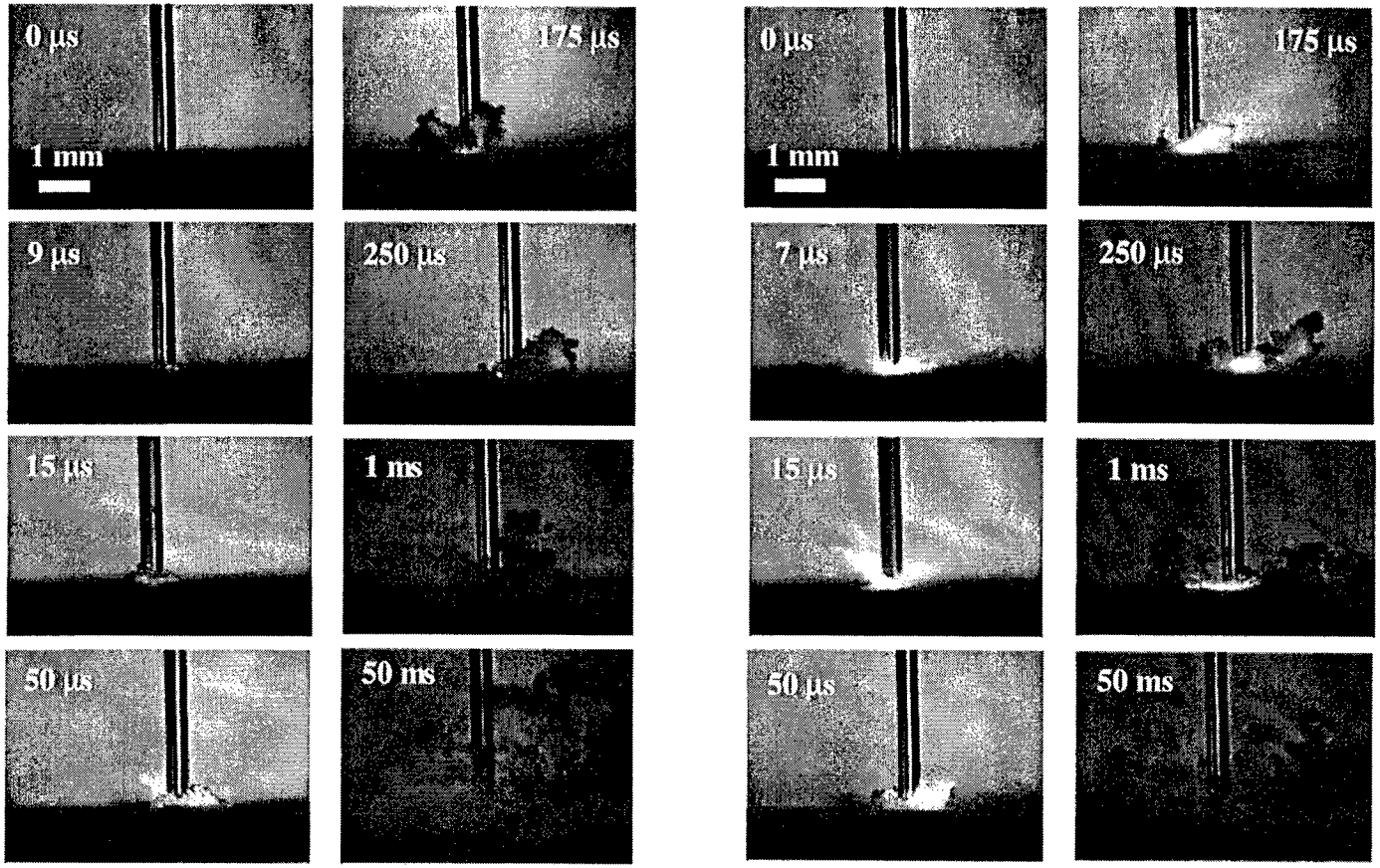


(a) (b)

**Figure 5.** Er:YAG laser lithotripsy with a pulse energy of 50 mJ ($H_o$ = 35 J/cm$^2$, $\tau_p$ = 275 µs) occurred in two modes: (a) without plasma formation, and (b) with plasma formation. Note that the plasma did not expand rapidly but was sustained up to at least 1 ms, long after the end of the laser pulse.

## 4. DISCUSSIONS

The Er:YAG laser induced vapor bubble differed markedly from that of the Ho:YAG laser. In this case, the absorption coefficient of water at 2.94 μm was much larger ($\mu_a$ = 12,000 $cm^{-1}$) compared to 2.12 μm ($\mu_a$ = 25 $cm^{-1}$). The spiking Er:YAG laser pulse structure at the onset deposited optical energy within a thin layer of water of 1-μm penetration depth (as opposed to 400 μm at 2.12-μm wavelength). This resulted in superheating within the small volume of water. The rapid expansion of water vapor produced the initial acoustic transient in Figure 3. Upon removal of this layer of water, a vapor channel (the 'Moses effect[13]') was formed, allowing further energy deposition at the distal end of the bubble. In the case of Er:YAG laser irradiation, rapid expansion of water caused the pressure within the bubble to decline rapidly, resulting in condensation of water molecules at the bubble wall and at the sapphire fiber periphery, as suggested by Ith et al. [14]. A decline in vapor pressure and condensation slowed and reversed the radial bubble growth, but axial growth resumed due to continuous water vaporization at the distal end by direct Er:YAG laser energy absorption. Water vapor from the distal end filled the void left over by condensation, and compensated a rapid bubble collapse. This helped damp the magnitudes of acoustic emissions due to subsequent bubble collapses. The axial growth of the vapor bubble was also a consequence of the dynamic optical property of water, as proposed by Walsh et al. As temperature increased at the distal end of the vapor bubble due to laser deposition, the absorption coefficients of water rapidly reduced, allowing longer penetration depth of the Er:YAG laser energy and producing an elongated torpedo-shaped vapor bubble. This Er:YAG laser induced bubble behavior indicated a more directional energy delivery. Most of the Er:YAG laser energy was propagated forward axially, and less radially as in the case of the Ho:YAG laser (pear-shaped bubble). Hence, one would expect more efficient energy delivery to the target tissue for the Er:YAG laser than for the Ho:YAG laser.

Figure 4 shows that despite close proximity of the urinary calculus from the location of acoustic emissions (from multiple bubble collapses), no fragmentation occurred. This was due to the distribution of mechanical energy within the vapor bubbles over multiple collapses at different locations and different delay times, hence reducing the effects of an otherwise strong single bubble collapse. Therefore, acoustic transients have little or no contribution to fragmentation in Er:YAG laser lithotripsy. The significance of other photomechanical mechanisms such as interstitial water expansion remained unknown. A mass-loss experiment involving Er:YAG laser irradiation of dry calculus, wet calculus, and calculus submerged in water should clarify the role of this mechanism.

Two modes of fragmentation processes – with and without plasma formation – occurred when the sapphire fiber was placed in perpendicular to the calculus surface as shown in Figure 5. The dynamics of both processes seemed to be predominantly photothermal. As stated earlier, by 50 ms after laser onset, the dynamics of both processes appeared indistinguishable. The prolonged plasma, which lasted beyond the Er:YAG laser pulse duration, probably initiated chemical decomposition of the urinary calculus. The exothermic chemical reactions in turn might have provided enough energy to sustain the plasma after the laser pulse ended. However, the difference in fragmentation efficiency between the two modes of ablation – with and without plasma formation – is unclear. Walsh et al. have found that plasma formation may reduce the amount of available laser energy for fragmentation [15].

Our results showed that the fragment sizes between Er:YAG laser lithotripsy and Ho:YAG laser lithotripsy were not statistically different. This suggested that a photothermal fragmentation process similar to that of the Ho:YAG laser has taken place [16, 17]. In addition, visualization of Schlieren flash images revealed recrystallization of calculus composition at the periphery of the sapphire fiber, indicating a melting process during laser irradiation [18]. Except for an initial acoustic emission (< 10 bars), no further acoustic transients were recorded, implying the absence of bubble dynamics and the minimal role of acoustics in the fragmentation process. In Ho:YAG laser lithotripsy, bubble dynamics were responsible for swift dispersion of the plume formation [18]. Thus in general, a photothermal ablative process is associated with Er:YAG laser lithotripsy.

Unlike laser induced shockwave lithotripsy (LISL) [19, 20] using pulsed-dye and Q-switched Nd:YAG lasers, Er:YAG laser lithotripsy occurred through direct laser energy absorption [17, 18]. In contrast to large fragments usually associated with a shockwave action, the fragments in Er:YAG laser lithotripsy appeared fine and emulsified, thus facilitating passage. In comparison to the Ho:YAG laser, our results indicated that the Er:YAG laser was more efficient in laser energy delivery. Moreover, the fragmentation efficiency of Er:YAG laser lithotripsy was found to be approximately 2.4 times better than that of Ho:YAG laser lithotripsy. If the sapphire fiber tip was not placed in

contact with the calculus during lithotripsy, Er:YAG laser minimized the risks of ureteral dilation because the bubble induced did not expand radially as much as in the case of Ho:YAG laser (pear-shaped bubble) [21].

## 5. CONCLUSION

The Er:YAG laser induced vapor channel allowed direct deposition of laser energy on the urinary calculus. Calculus melting, chemical decomposition, and plasma-mediated photothermal ablation seemed to be the predominant mechanisms during Er:YAG laser lithotripsy. Acoustic pressure, shockwave, and bubble dynamics had minimal or no direct contribution to the fragmentation process. The role of other photomechanical effects such as interstitial water expansion has not been evaluated. The Er:YAG laser appeared to outperform the Ho:YAG laser in lithotripsy. Experimental results suggested that the Er:YAG laser was more efficient than the Ho:YAG laser, and showed potential in further minimizing mechanical damage to adjacent tissue. Our studies indicated an improved treatment modality for intracorporeal laser lithotripsy using sapphire fiber-delivery Er:YAG laser irradiation.

## 6. ACKNOWLEDGEMENTS

Funding for this research was provided in part by grants from the Air Force Office of Scientific Research through MURI from DDR&E (F49620-98-1-0480), the Texas Higher Education Coordinating Board (BER-ATP-253), the Office of Naval Research Free Electron Laser Biomedical Science Program (N00014-91-J-1564), the Albert W. and Clemmie A. Caster Foundation, and the SPIE Educational Scholarship in Optical Science and Engineering.

*Paper # 3914A-30*

## 7. REFERENCES

1. B. E. Hoke JA, Gomes ED, Wolbarsht ML,, "Erbium:YAG (2.94-um) laser effects on dental tissues," *J Laser Applications,* Summer/Fall: 1990.
2. Visuri SR, Walsh JT and Wigdor HA, "Erbium laser ablation of dentin hard tissue: effect of water cooling," *Lasers Surg Med,* 18: 294-300, 1996.
3. Schlenk E, Profeta G, Nelson JS, Andrews JJ and Berns MW, "Laser assisted fixation of ear prostheses after stapedectomy," *Lasers Surg Med,* 10: 444-447, 1990.
4. Pratisto H, Frenz M, Ith M, Romano V, Felix D, Grossenbacher R, Altermitt HJ and Weber HP, "Temperature and pressure effects during erbium stapedotomy," *Lasers Surg Med,* 18: 100-108, 1996.
5. Dietlein TS, Jacobi PC and Krieglstein GK, "Erbium:YAG laser trabecular ablation (LTA) in the surgical treatment of glaucoma," *Lasers Surg Med,* 23: 104-110, 1998.
6. D'yakonov GI, Konov VI, Mikhailov VA and Nikolaev DA, "Comparative performance of infra-red solid-state lasers in laser lithotripsy," *Proc SPIE,* 1421: 156-162, 1991.
7. Bloch MA, Fedorovskii SL, Suslov AM, Mikhailov BA, Pak SK and Shcherbakov IA, "In-vitro lithotripsy with Er:Cr:YSGG lasers through fiber," *Proc SPIE,* 1879: 182-185, 1993.
8. Kozodoy RL, Pagkalinawan AT and Harrington JA, "Small-bore hollow waveguides for delivery of 3-um laser radiation," *Appl Optics,* 35: 1077-1082, 1996.
9. Matsuura Y, Rabii CD, Matsuura K and Harrington JA, "Low order multimode generation in hollow glass waveguides," *Electronic Letters,* 32: 1096-1098, 1996.
10. Pratisto H, Ith M, Frenz M and Weber HP, "Infrared multiwavelength laser system for establishing a surgical delivery path through water," *Appl Phys Lett,* 67: 1963-1965, 1995.
11. Fitzgibbon JJ, Bates HE, Pryshlak AP and Dugan JR, "Sapphire optical fibers for the delivery of Erbium:YAG laser energy," *Proc SPIE,* 2396: 60-70, 1995.
12. Pryshlak AP, Dugan JR and Fitzgibbon JJ, "Advancements in sapphire optical fibers for the delivery of Erbium laser energy and IR sensor applications," *Proc SPIE,* 2677: 35-42, 1996.
13. Isner JM, "Blood," in:*Cardiovascular laser therapy,* Isner JM and Clarke R (eds.), New York: Raven Press, pp. 39-62, 1989 .

14. Ith M, Pratisto H, Altermatt HJ, Frenz M and Weber HP, "Dynamics of laser-induced channel formation in water and influence of pulse duration on the ablation of biotissue under water with pulsed erbium-laser radiation," *Appl Phys B,* 59: 621-629, 1994.
15. Walsh JT and Deutsch TF, "Er:YAG laser ablation of tissue: measurement of ablation rates," *Lasers Surg Med,* 9: 327-337, 1989.
16. Teichman JMH, Vassar GJ, Bishoff JT and Bellman GC, "Holmium:YAG lithotripsy yields smaller fragments than lithoclast, pulsed dye laser or electrohydraulic lithotripsy," *J Urol,* 159: 17-23, 1998.
17. Chan KF, Vassar GJ, Pfefer TJ, Teichman JMH, Glickman RD, Weintraub SE and Welch AJ, "Holmium:YAG laser lithotripsy: A dominant photothermal ablative mechanism with chemical decomposition of urinary calculi," *Lasers Surg Med,* 25: 22-37, 1999.
18. Schafer SA, Durville FM, Jassemnejad B, Bartels KE and Powell RC, "Mechanisms of biliary stone fragmentation using the Ho:YAG laser," *IEEE Trans Biomed Eng,* 41: 276-283, 1994.
19. Rink K, Delacretaz G and Salathe RP, "Fragmentation process of current laser lithotriptors," *Lasers Surg Med,* 16: 134-146, 1995.
20. Rink K, Delacretaz G and Salathe RP, "Influence of the pulse duration on laser-induced mechanical effects," *Proc SPIE,* 2077: 181-194, 1994.
21. van Leeuwen TG, Jansen ED, Motamedi M, Borst C and Welch AJ, "Pulsed laser ablation of soft tissue," in: *Optical-thermal response of laser-irradiated tissue,* Welch AJ and van Gemert MJC (eds.), New York: Plenum Press, pp. 709-763, 1995.

# Optimization of Parameters for Photodisruptively Nucleated Ultrasonic Cavitation in Water and Tissue Models

G.J.R. Spooner[a], Gabrielle Marre[a], Doug L. Miller[b], A. Roy Williams[c],

[a]Center for Ultrafast Optical Science, University of Michigan,
2200 Bonisteel Blvd., Ann Arbor, MI 48109-2099 USA

[b]Department of Radiology, University of Michigan, Ann Arbor, MI 48105 USA

[c]Department of Medical Biophysics, University of Manchester, Manchester, England, UK

## ABSTRACT

Laser induced optical breakdown (LIOB) in fluids produces a localized plasma, an expanding radial shock wave front, heat transfer from the plasma to the fluid, and the formation of cavitation bubbles. Collectively these phenomena are referred to as photodisruption. Subjecting photodisruptively produced cavitation bubble nuclei to an ultrasonic field can result in strong cavitation and local cellular destruction. The ability of ultrafast lasers to produce spatially localized photodisruptions with microJoule pulse energies in combination with the possibility of larger scale tissue destruction using ultrasound presents an attractive and novel technique for selective and non-invasive tissue modification, referred to as photodisruptively nucleated ultrasonic cavitation (PNUC)[1]. Optimization of PNUC parameters in a confocal laser and ultrasound geometry is presented. The cavitation signal as measured with an ultrasound receiver was maximized to determine optimal laser and ultrasound spatial overlap in water. A flow chamber was used to evaluate the effect of the laser and ultrasound parameters on the lysis of whole canine red blood cells in saline. Parameters evaluated included laser pulse energy and ultrasound pressure amplitude.

**Key words**: cataract, cavitation, femtosecond, laser, lens, nuclei, ophthalmology photodisruption, ultrafast, ultrasound

## 1. INTRODUCTION

The World Health Organization[2] reports that in 1997 16 of the 38 million cases of bilateral blindness world wide are a result of cataracts, by far the largest single cause of blindness on Earth. The American Academy of Ophthalmology[3] reports that 1.3 million cataract surgeries are performed in the United States annually, accompanied by Medicare reimbursements that exceed $3 billion per year. The treatment of cataracts will have ever more importance as the world population average age rises over the next few decades. Treatment options for cataracts are limited to the improvement of refractive aids such as spectacles, or surgical removal of the lens (current standard of care.) While existing in cataract removal surgical techniques are very successful, less invasive approaches could reduce complications and potentially leave intact the capsular bag which surrounds the natural lens. Preservation of the lens capsule better supports intra-ocular lens (IOL) implants, while fully intact capsular bags may someday permit restoration of accommodation in aphakic eyes with advanced IOLs or ersatz-phaco materials.

Most cataract surgeries in the US are now performed by the phacoemulsification technique. An incision varying between 3 and 5.5mm is made in the cornea, limbus or sclera, with the size dependent upon the phacoemulsification probe size and whether the planned IOL implant is the foldable type. Next, the top of capsule is removed (capsulorhexis) to allow access to the lens, and the probe is introduced through the incision. The phacoemulsification probe housing contains an ultrasonic transducer and two lumens for irrigation and aspiration. The irrigant carries microbubbles that serve as cavitation nuclei for the ultrasound field to act upon (tissues *in vivo* are generally free of cavitation nuclei and, in the absence of these nuclei, cavitation by the direct application of ultrasonic fields does not occur before the onset of thermal or other effects[4].) The lens material is irrigated, emulsified through both ultrasonically driven cavitation as well as direct mechanical destruction by the vibrating probe[5], and the emulsified material is aspirated. These processes occur simultaneously until the lens is completely removed.

In *Laser-Tissue Interaction XI: Photochemical, Photothermal, and Photomechanical*, Donald D. Duncan, Jeffrey O. Hollinger, Steven L. Jacques, Editors, Proceedings of SPIE Vol. 3914 (2000)
1605-7422/00/$15.00

If emulsification could be performed non-invasively, the entire procedure might be performed less invasively since aspiration-only probes could be made smaller than multi-lumen phacoemulsification probes.

We propose a new method for the localized destruction of lens tissue, which uses an ultrasonic field to cavitate nuclei produced through LIOB. A short pulse laser beam is tightly focused into the target tissue, inducing LIOB and resulting in the creation of a micro-bubble with each LIOB producing pulse. These bubbles serve as nuclei for a non-invasively applied ultrasonic field. Tissue destruction proceeds from the excitation and growth of these seeded cavitation nuclei. The application of both the laser and ultrasound fields may be performed non-invasively to selectively destroy any tissue which is sufficiently optically and acoustically transparent and supports bubble formation and growth. We refer to this effect as photodisruptively nucleated ultrasonic cavitation (PNUC.)

We report on the maximization of canine whole blood cell hemolysis as a means of optimizing the PNUC effect for NIR picosecond laser pulses. Determination of the dependence of PNUC-driven hemolysis on the laser and ultrasound parameters is a step towards the optimal parameters for *in vivo* tissue destruction.

## 2. PHYSICAL MECHANISM OF TISSUE INTERACTION

### 2.1 Cavitation

Cavitation refers to a range of phenomena associated with the motion of micro-bubbles in fluids, and includes a wide range of processes, such as stable bubble oscillation, equilibrium and non-equilibrium bubble expansion, re-radiation of acoustic energy, pressure and temperature transient catalyzed chemical reactions, and acoustic streaming. Interplay between the bubble surface tension and the flow of vapor in and out of the bubble under a dynamic pressure field determines the behavior, size, and life of the cavitating bubble. The strong forces associated with transient or collapse-type cavitation can by used to mechanical disrupt or emulsify tissue.

Cavitation requires the production or introduction of nucleation sites, particles or bubbles. The introduction of nuclei, beyond being simply difficult to perform *in vivo*, can be difficult to control spatially and temporally. Production of nuclei by the ultrasound field itself occurs above the intensity thresholds for other ultrasound mediated effects, rendering ultrasonic nucleated cavitation impractical as a surgical tool.

### 2.2 Photodisruption

Photodisruption describes a sequence of processes associated with optical breakdown in a material. Optical breakdown occurs when the local electric field intensity is high enough to produce nonlinear absorption. Optical breakdown is initiated by multiphoton ionization, tunneling ionization or simply free carrier absorption, and is followed by catastrophic "avalanche" or cascade ionization which produces a strongly absorbing plasma[6]. The breakdown plasma produces associated phenomena, including shock wave generation and propagation, and in fluids or tissues, the creation, expansion and oscillation of a cavitation bubble[7]. Photodisruption is commonly produced at the focus a laser beam of sufficient intensity to produce optical breakdown.

Suitable target tissues or materials must not absorb heavily or scatter strongly at the laser wavelength. The anterior of the eye is ideal in this regard, allowing NIR laser light to be transmitted without appreciable absorption or scattering. This fact has enabled photodisruption with nanosecond Nd:YAG lasers to become a standard surgical tool in ophthalmology[8,9,10]. Recently lasers operating in the picosecond and femtosecond regimes have been developed for new ophthalmic refractive surgical procedures[11-24]. These ultrashort lasers are associated with significantly lower breakdown thresholds, reduced photodisruption pulse energies, and increased localization of tissue destruction. The general approach for these procedures has been to use sub-picosecond pulses of the appropriate wavelength in a tight focusing geometry to create sub-surface photodisruptions in the target tissue. The breakdown threshold in the NIR for cornea is on the order of $1 J/cm^2$, requiring only microJoules of pulse energy to produce tissue destruction. A further advantage of sub-picosecond pulses is the deterministic nature of the observed LIOB threshold[11]. Offsetting these advantages is the difficulty of producing NIR sub-picosecond pulses of sufficient energy to overcome optical losses to reach breakdown threshold in the target tissue.

### 2.3 Photodisruptively nucleated ultrasonic cavitation

The existence of both laser- and ultrasound-induced cavitation presents the possibility of their combination. This work tests the idea that photodisruptive laser nucleation and subsequent (or immediate) cavitation under an applied ultrasound field together could produce spatially and temporally controllable cell destruction in sufficiently transparent tissue.

The sequence of events in PNUC is shown schematically in Figure 1. A short pulse laser beam is focused below the surface of a target tissue of sufficient transparency that LIOB may occur. The photodisruption processes referred to in section 2.2

follow. The time scales of these processes depend on the breakdown laser pulse width and energy[25]. The photodisruption-produced microbubble is then subjected to a focused ultrasound excitation beam, which induces cavitation and bubble growth, disrupting tissue in some volume.

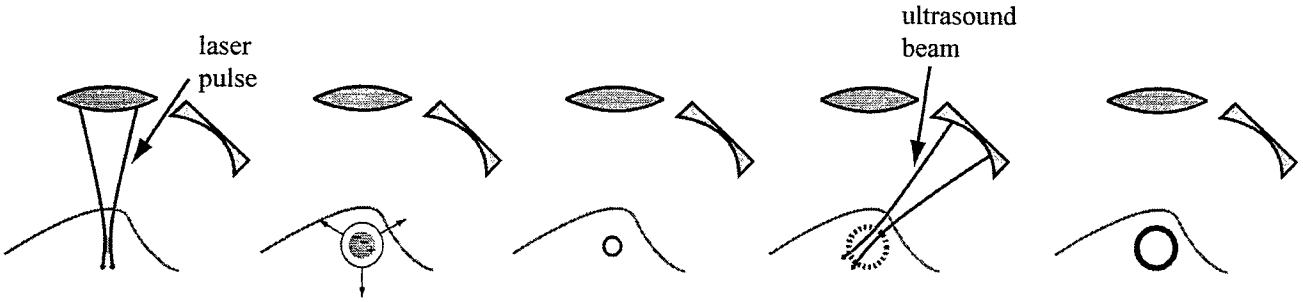


**Figure 1**: Schematic illustration of PNUC. a) tightly focused high intensity laser pulse initiates optical breakdown below the surface of a target tissue. b) electron-ion plasma expands, transfers energy to surrounding tissue and propagates shock wave c) local vaporization of tissue produces a nucleating bubble d) excitation by externally applied ultrasound field e) resulting volume of cavitated tissue.

The nuclei size scales with the absorbed laser pulse energy[25-28]. The threshold fluence for LIOB depends inversely on the square root of the laser pulse width, becoming independent of pulse width below 100fs[14]. The optimal laser pulse width for PNUC will depend on the optical properties of the target tissue and on the desired size of the cavitation nuclei. In this work we use picosecond pulses to explore other PNUC parameters.

## 2.4 Demonstration of tissue destruction

Complete destruction of enucleated human and porcine lenses using PNUC has been observed[1]. In these demonstration experiments, lenses were sealed and supported in an acoustically and optically transparent gelatin block and placed in a degassed water bath in order to isolate them from any potential cavitation nuclei present in the water. . Cavitation nuclei were photodisruptively generated at kHz PRFs using a 500fs, 5μJ, 1.05μ laser system (IntraLase Corp.) focused sharply into the bath and lens specimen to a small spot (6μ diameter measured in air). Ultrasound was generated from a signal originating with Hewlett Packard (HP3314A) oscillator and amplified by an Electronic Navigation Industries (A-300) amplifier. A custom ultrasound transducer was constructed with an initial wavefront diameter of 3.75cm and a 3.75cm radius of curvature to produce a focused beam. The driving acoustic signal consisted of 2.5ms duration pulses at the transducer fundamental (770kHz), repeated every 25ms. The pressure amplitude was variable up to approximately 5MPa. The focused ultrasound beam was directed at the target tissue mounted in the gelatin block, coincident with the laser focus. The laser and ultrasound pulse trains were asynchronous.

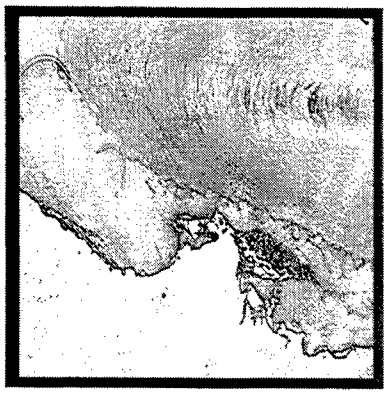

**Figure 2:** Histologic section of human lens following PNUC demonstration. The frame shown is approximately 2mm across.

After cavitation was initiated, destruction of lens tissue was rapid and easily apparent to an observer. Destruction of both human and pig eye lenses was accomplished. In one human lens, we allowed cavitation to produce complete destruction of the lens cortex and near destruction of the lens nucleus. In another human lens, we initiated cavitation and proceeded until

large amplitudes of acoustic signal were observed. Laser and ultrasound exposures were stopped and the lens fixed for histologic evaluation using standard hematoxylin eosin preparations (see Figure 2.)

Femtosecond cavitation nuclei stabilize at diameters on the order of 10μ for energies within an order of magnitude of LIOB threshold[26,27]. The histologic section shows damage from the ultrasound on a scale much larger than the nuclei, demonstrating cavitation nuclei growth and tissue destruction. The gelatin blocks containing the treated lenses were unaffected by the laser or ultrasound.

## 3. EXPERIMENTAL METHODS

### 3.1 Flow chamber

The apparatus constructed to accommodate both laser and ultrasound exposure is illustrated in Figure. 3. A flow-through chamber was placed in an 8 liter water bath, with vertical flow upward through the chamber provided by a syringe pump. The room temperature bath water was degassed to minimize bubble formation in the bath. The chamber consisted of an 8x12x12mm transparent plastic block having three perpendicular axes: a 6mm diameter cylindrical bore oriented horizontally

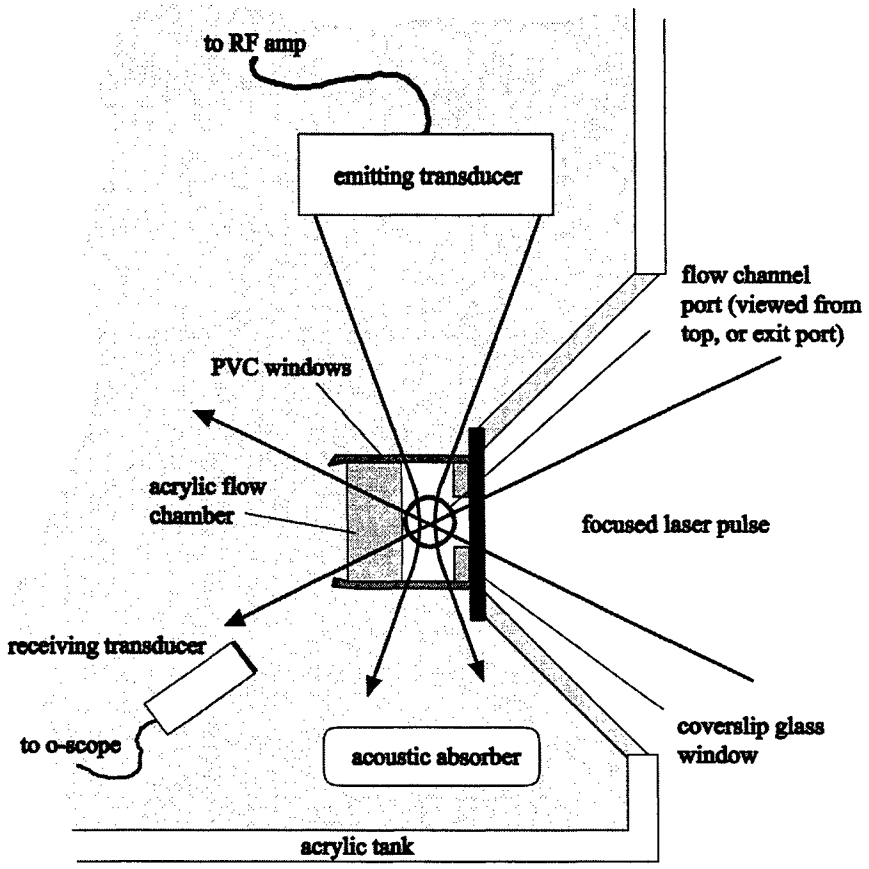


**Figure 3:** Exposure chamber for PNUC parameter optimization. A focused short pulse laser enters the flow chamber through a window at page right, coincident with the focused ultrasound incident from page top. Fluid flows upward through the page plane, past the beam foci, and is collected for hemolysis measurements.

for transmission of the ultrasound beam; a 1cm diameter bore for transmission of the laser beam oriented horizontally and perpendicular to the ultrasound bore; and vertically oriented 1.3mm ID surgical tubing entering the top and exiting the bottom of the chamber to allow target fluid flow. The syringe pump was operated at a constant rate of 2.1ml/min flow (25mm/s) and cleared the chamber within a few seconds.

A focused ultrasound beam was directed along the axis of the ultrasound bore, with the beam focus at the chamber center. To facilitate transmission of the ultrasound under near-free-field conditions, acoustically transparent windows made of 12μ thick polyvinyl chloride were used on the ends of the cylindrical chamber. The ultrasound beam passed through the chamber, defocused in the bath and was terminated at a block of ultrasound absorbing material (SOAB rubber, BF Goodrich).

The laser delivery system focused the beam through No.1 cover glass window through the bath wall and into the chamber, at a depth of approximately 2-3mm, coincident with and at right angles to the bore center.

### 3.2 Laser system

The laser used was a complete clinical system developed for corneal refractive surgery (Model QC2000, Intelligent Surgical Lasers). The console consists of a laser source, power supply and control electronics, a PC with a menu-driven software interface, and an integrated slit lamp delivery system. The laser source begins with a diode-pumped, actively mode-locked Nd:YLF oscillator. A MHz train of picosecond pulses from the oscillator is injected into a Nd:YLF regenerative amplifier using a Pockels cell, and after amplification, a kHz pulse train is gated out of the amplifier by the Pockels cell. The result is a 1.05μ wavelength, multimode, 30 picosecond pulse duration, kHz pulse train with energies up to a few hundred microJoules[29]. Polarization optics attenuate and control the pulse energy, which is monitored by two energy detectors. A mechanically decoupled delivery system focuses the beam to a small spot (f/# = 0.9) producing a focused spot size in air of approximately 10μ. The delivery system also allows the beam focus to be steered by a user, with the focal region observable through a slit lamp operating microscope. Pre-pulsing of the amplifier was observed with a photodetector at amplitudes approximately 100x below the output pulse amplitude. No attempt was made to determine the pulse contrast. It was assumed that variation in the apparent breakdown threshold due to pre-pulsing was unimportant, as the goal of the laser breakdown was simply to produce cavitation nuclei rather than determine the true threshold energy.

### 3.3 Ultrasound system

A sealed, air-backed ultrasound transducer of diameter 3.75cm with radius of curvature 3.75cm was used to produce the ultrasound beam. The piezoelectric ceramic element had a fundamental thickness resonance at 770kHz, but was operated at 2.5MHz. The wavelength in water at 2.5MHz is about 0.6mm, which allowed tight focusing into the flow chamber. The transducer was electrically driven by a signal generator (Model 3314A, Hewlett-Packard Co., Santa Clara, CA) and amplifier (Model 350L, Electronic Navigation Industries, Rochester, NY). The ultrasound field was measured with a calibrated hydrophone with 0.4mm sensitive spot (model 805, Sonic Technologies, Hatboro PA). The half power focal diameter and length were 1.3mm and 8.6mm, respectively.

An ultrasound receiving transducer (6mm diameter, 1MHz Gamma series, KB-Aerotech, Lewiston PA) was aimed at the position of the laser and ultrasound beam intersecting foci. This receiver was oriented with its axis in the plane of the intersecting beams, and placed about 3cm away. The finite bandwidth of the sensor and reverberation of the acoustic emissions within the flow chamber distorted this signal considerably. Signals emitted by the laser photodisruption were received by this sensor, were useful in providing a triggering signal and serving as a diagnostic on the consistency of the optical breakdown. The receiver, placed just outside the ultrasound beam at a position of minimal pickup, was also utilized for alignment of the laser and ultrasonic foci. Acoustic emissions with both the laser and ultrasound beams operating were due to photodisruptively nucleated ultrasonic cavitation, allowing the optimization of the relative positions of the beams by maximizing the acoustic signal strength.

### 3.4 Blood cell preparation

Canine whole blood was collected by sterile venipuncture into collection tubes with EDTA anti-coagulant (Vacutainer no. 6457, Becton-Dickinson and Co., Franklin Lakes, NJ). Several tubes were pooled with a hematocrit of about 54%. The whole blood cells were washed once in phosphate buffered saline (PBS), and diluted in degassed PBS to a final cell concentration of 0.11% (~500:1 dilution). In some experiments, 5% bovine serum albumin was added to the medium. All cell suspensions were briefly degassed by vacuum to reduce extraneous bubble formation and the population of naturally occurring nuclei. During exposure, approximately 1ml specimens were collected after passage of the tubing dead volume.

### 3.5 Hemolysis measurements

Samples were centrifuged and the absorbance of the supernatants measured using a spectrophotometer at 414nm to determine the free hemoglobin concentration. This instrument was zeroed with PBS, and calibrated using a blood sample 100% hemolyzed in water. Four repeated experimental measurements for each data point were made, and the two-sided T-test was used for statistical comparisons between data means.

## 4. RESULTS

### 4.1 Photodisruption and cavitation acoustic detection

Firing the laser in the absence of an applied ultrasound field produces variable strength acoustic signals at the receiving transducer, ringing twice typically, and lasting a few tens of microseconds. The duration and variability of the acoustic

signature are consistent with the observed behavior of bubbles produced through near-threshold picosecond photodisruptions [28]. Variability is explained by the non-deterministic nature of LIOB above 1ps pulse duration, while the life span of a near-threshold bubble is 10-100μs, depending on the amount by which the pulse energy exceeds LIOB threshold. The transducer reports photodisruptions reliably when laser is present, and none when the laser is blocked.

Firing the laser in the presence of continuous ultrasound exposure at laser focus produces distinct ultrasonic cavitation emissions (UCE) in addition to the photodisruption emissions, with a superposition of the excitation field present as well. The UCE were strongly dependent on ultrasonic amplitude, beginning to be appear intermittently in the case of a photodisrupting pulse energy of 75μJ above a pressure amplitude of 3-4MPa. Both the amplitude and duration of the UCE increased with the ultrasound pressure amplitude.

Switching off either the laser or the ultrasonic excitation field switches off the UCE.

## 4.2 Pressure amplitude

The percentage of cells lysed under simultaneous ultrasound and laser exposure increases strongly with ultrasound amplitude. Figure 4 displays the results of a 500Hz, 75μJ laser pulse train and continuous ultrasound exposures as the ultrasound pressure amplitude was increased. For these parameters a threshold for the effect occurs at about 4.3MPa. Hemolysis approaches 100% at the highest pressure amplitudes, presumably occurring when the cavitation volume per laser shot multiplied by the laser PRF approaches the fluid flow rate. The size of the PNUC effect is apparent in the hemolysis seen at an ultrasound field amplitude of 7.4MPa, where the combined exposure gave 62% hemolysis, compared to the background hemolysis of 1.4% (obtained with the laser switched off.)

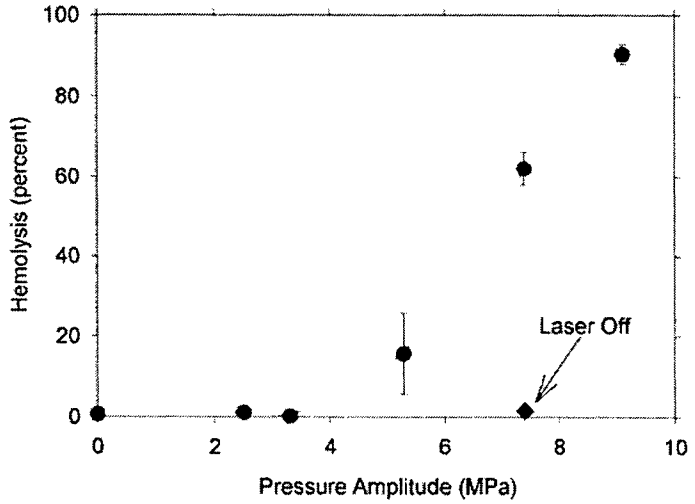


**Figure 4:** Effect of ultrasound pressure amplitude on PNUC hemolysis. The laser operating point was 75μJ, 500Hz and 30ps. Note the cessation of hemolysis when the laser is switched off.

Continuing the ultrasound exposure at this amplitude with the laser beam blocked produces hemolysis at background levels, demonstrating conclusively photodisruptive laser nucleation of ultrasonic cavitation. Measurements made with 1) ultrasound exposure with no laser and 2) laser exposure with no ultrasound were not statistically distinguishable from 3) background-level hemolysis with no ultrasound and no laser exposure (i.e. sham exposure).

## 4.3 Laser energy and nuclei lifetime

The dependence of hemolysis on laser energy was investigated using burst mode ultrasound exposure to produce a delay between photodisruption nucleation and subsequent ultrasonic cavitation. Figure 5 shows results for laser-triggered and random burst mode ultrasound at 7.4MPa with 0.8ms bursts and 1kHz laser PRF. In laser-triggered burst mode (circles), the optical detection of the laser pulse initiated the ultrasound burst. In random burst mode (squares), the triggering of the ultrasound and laser were asynchronous.

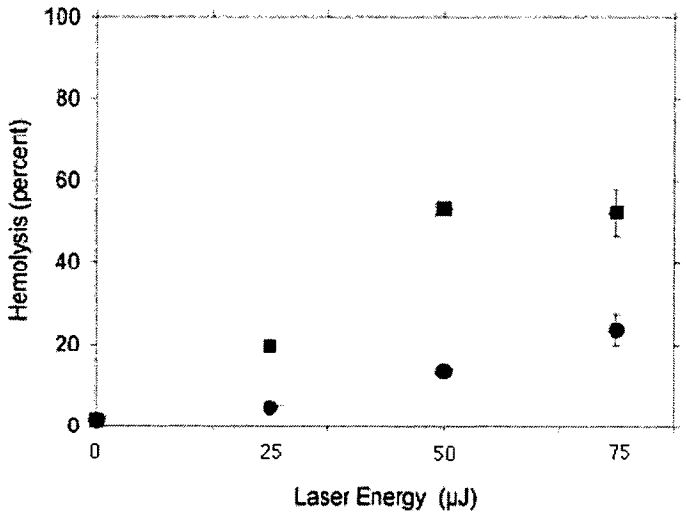


**Figure 5:** Effect of laser pulse energy on PNUC-driven hemolysis. Squares show randomly triggered ultrasound bursts, while circles show laser-triggered ultrasound bursts. Random triggering always produces more hemolysis than laser triggered as the ultrasound transit delay time is on the order of the photodisruptively produced nuclei lifetime.

Photodisruption bubble size and bubble lifetime should be important factors in PNUC. If a nucleating bubble is too small or vanishes before it can be cavitated, the resulting level of hemolysis will be decreased. Nucleating bubble lifetime and duration depend on the absorbed laser pulse energy (the minimum energy depending in turn on the laser pulse width.) A rough determination of the LIOB threshold in PBS by observing the breakdown plasma yields for our arrangement approximately 18μJ. The photodisrupting laser pulse energy is then only several times above threshold, for which the lifetime of picosecond bubbles falls between 10-100μs. Since the laser and ultrasound foci were ~3.75cm from the ultrasound transducer, a laser-triggered ultrasound burst arrives about 25μs after the photodisrupting pulse (assuming 1500m/s for the speed of sound). Since this delay is on the order of the nuclei lifetime, we expect a reduction in the amount of nuclei present during the laser-triggered case than in the random case (in which the photodisrupting pulse arrives during the ultrasound burst 80% of the time for 0.8ms bursts and 1kHz PRF). It follows that laser-triggered bursts produce much less hemolysis than random-triggered bursts, consistent with the results of Figure 5.

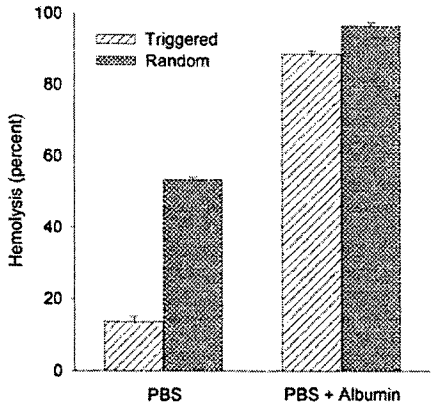


**Figure 6:** Stabilizing effect of albumen on nuclei. 5% Serum albumen added to the blood/PSA medium increased the amount of hemolysis in both the laser-triggered and the random triggered ultrasound bursts.

Addition of the protein albumin to the medium produced more consistent photodisruptive acoustic emissions. A test was conducted to determine the influence this factor might have on PNUC-driven hemolysis. The results for random and .laser-triggered burst mode ultrasound with and without added 5% serum albumin is shown in Figure 6 for the intermediate 50μJ laser energy. The increase in hemolysis with added protein is particularly large for the triggered bursts, presumably indicating that the albumin-stabilized bubbles were stabilized for times at least as long as the 25μs ultrasound transit delay. Nuclei stabilization by the addition of albumen should have a smaller effect in the randomly triggered case, since for the parameters used, 80% of the total amount of nuclei generated appear during the ultrasound burst on-time.

## 5. DISCUSSION

Our hemolysis experiment suggests that temporally and spatially selective and non-invasive destruction of optically transparent soft tissue is possible using photodisruptive lasers to seed nuclei for ultrasonically-driven cavitation. PNUC represents both a novel surgical technique as well as a new tool to study cavitation phenomena. As applied in the lens, PNUC is distinct from the standard phacoemulsification technique, which is a combination of direct mechanical disruption by the probe and ultrasonic cavitation using irrigant introduced nuclei[5], while PNUC is a purely cavitation-mediated effect and does not require the invasive introduction a probe to produce tissue emulsification.

Optimal PNUC conditions would permit switchable, strong, and highly localized destruction or emulsification at arbitrary locations in tissue.

We first consider optimal laser source parameters. Localization of the effect requires small nuclei. Small nuclei require small pulse energies and short pulse widths. The shortest pulse widths at which practical NIR sources operate are in the hundreds of femtoseconds. LIOB thresholds in tissue[14] at these pulse widths are on the order of 1J/cm$^2$. At the laser focus, perhaps as much as 10μJ of laser pulse energy is needed, producing bubbles from a few to a few tens of microns in diameter. However, attenuation by optical losses in lens tissue may be 10dB or higher, making the utility of longer pulse, higher energy lasers such as our 30ps laser apparent (in spite of the larger LIOB threshold associated with longer pulses.) Ideally, scattering losses would be reduced by employing a long wavelength source operating in the NIR between 1000 and 1350nm, avoiding the strong water absorption peak at ~1450nm. Optical losses would be less important with a short pulse, low LIOB threshold source. These strategies for defeating optical losses are important in cataractus lenses, in which optical absorption and scattering can be strong. An optimal laser source might have the following pulse parameters: 1000-1350nm wavelength, ~100fs pulsewidth, and 100μJ pulse energy. An investigational source comprised of a Ti:sapphire femtosecond laser and a tunable NIR optical parametric amplifier is under construction in our laboratory for these and other studies involving photodisruption in scattering tissues. The ideal parameters described here will be achievable with this system.

We now consider optimal ultrasound parameters. For nuclei measuring a few microns in diameter, the driving frequency for resonance in water will be in the range used here, 2-5MHz[30,31]. The cavitation volume should be as small as possible. A simple estimation of the cavitation volume can be made from the results shown in Figure 4. As the hemolysis level saturates with increased pressure amplitude, the effective cavitation volume per laser nucleation multiplied by the laser PRF of 500Hz approaches the fluid flow rate of 2.1ml/min. This gives a sphere of diameter ~5μ, which is reasonably small. Since the cavitating bubbles presumably grow throughout their life, this estimate represents the average extent of the cavitation effects, rather than the maximum. In order to keep the cavitation volumes small, the ultrasound pressure amplitudes should be near the hemolysis threshold (in the several MPa range.) The efficiency of tissue emulsification will decrease, necessitating a compensating increase in the PRF of the laser and ultrasound bursts, perhaps operating in a mode in which several to many nuclei are placed, and subsequently ultrasonically cavitated for a short period before bubble growth becomes large. Laser PRFs in the 10kHz range may be required for this type of scheme, while the ultrasound burst rate could still be in the kHz range.

Agents such as albumen clearly stabilize the nuclei, however it may not be necessary to add them to target tissues since other proteins present may act in the same manner.

## ACKNOWLEDGEMENTS

This research received grant support from National Science Foundation (STCPHY 8920108), National Institute of Health (N.E.I. Core Grant EY-00703, 1R43EY12340-01 ), as well as intramural support from the Center for Biomedical Engineering Research and the School of Medicine at the University of Michigan.

## REFERENCES


1 Kurtz R. Spooner GJR, Sletten K, Yen K, Sayegh S, Loesel F, Horvath C, Liu H, Elner V, Cabrera D, Meunier MH, Sacks Z, Juhasz T, Miller DL, Williams AR. "Ophthalmic Applications of Femtosecond Lasers," 1999; SPIE Vol. **3616**, pp 51-65.

2 World Health Organization Fact Sheet N 146, February 1997

3 American Academy of Ophthalmology, 1997

4 Williams, A. Roy, *Ultrasound: Biological Effects and Potential Hazards*. Academic Press 1983: 132-137.

5 Bond LJ, Cimino WW. "Physics of ultrasonic surgery using tissue fragmentation: part II. Ultrasound in Medicine and Biology," Vol. **22**, No. 1, pp. 101-117, 1996

6 Bloembergen N. "Laser-induced breakdown in solids," IEEE J. Quantum Electron., 1976;Vol **10**, pp 375-386.

7 Vogel A, Noack J, Nahen K, Theisen D, Birngruber R, Hammer DX, Noojin GD, Rockwell BA. "Laser-induced breakdown in the eye at pulse durations from 80ns to 100fs," 1999; SPIE Vol. **3255**, pp 34-49.

8 Aron RD, Aron JJ, Griesemann J, Thyzel R. "Use of the neodymium YAG laser to open the posterior capsule afte lens implant surgery: a preliminary report," J. Am. Intraocul. Implant Soc. 1980; **6**:352-324.

9 Fankhauser F, Roussel P, Steffen J, Van der Zypen E, Chererkova A. "Clinical studies on the efficacy of high power laser irradiation upon some structures of the anterior segment of the eye," Int. Ophthalmol. 1981;**3**:129-139.

10 Steinert RF, Puliafito CA. *The Nd:YAG Laser in Ophthalmology*. Philadelphia, PA: WB Saunders; 1985.

11 Du D, Squier J, Kurtz R, Elner V, Liu X, Gutmann G, Mourou G. "Damage threshold as a function of pulse duration in biological tissue," *Ultrafast Phenomena IX*, ed. by P.F. Barbara et al. New York, Springer, 1995, pp 254-256.

12 Zysset B, Fujimoto JG, Puliafito CA, Birngruber R, Deutsch TF. "Picosecond optical breakdown: Tissue effects and reduction of collateral damage," Lasers Surg Med **9**: 193-204, 1989.

13 Stern D, Schoenlein RW, Puliafito CA, Dobi ET, Birngruber R, Fujimoto JG. "Corneal ablation by nanosecond, picosecond and femtosecond lasers at 532 and 625nm," Arch Ophthalmol. 1989; **107**: 587-92.

14 Loesel FH, Niemz MH, Bille JF, Juhasz T. "Laser-induced optical breakdown on hard and soft tissue and its dependence of the pulse duration: Experiment and Model," IEEE J Quant Elect. 1996; **32**: 1717-22.

15 Kurtz RM, Liu X, Elner VM, Squier JA, Due D, Mourou GA. "Plasma-mediated ablation in human cornea as a function of laser pulsewidth. Journal of Refractive Surgery," 1997; **13**: 653-658.

16 Juhasz T, Kastis GA, Suarez C, Bor Z, Bron WE. "Time-resolved observations of shock waves and cavitation bubbles generated by femtosecond laser pulses in corneal tissue and water," Lasers Surg Med. 1996; **19**: 23-29.

17 Brown DB, O'Brien WJ, Schultz RO. "Corneal ablations produced by the neodynium doped yttrium-lithium-fluoride picosecond laser," Cornea. 1994; **13**: 471-478.

18 Brown DB, O'Brien WJ, Schultz RO. "The mechanism of ablation of corneal tissue by the neodynium doped yttrium-lithium-fluoride picosecond laser," Cornea. 1994; **13**: 479-486.

19 Vogel A, Gunther T, Asiyo-Vogel M, Birngruber R. "Factors determining the refractive effects of intrastromal photorefractive keratectomy with the picosecond laser," J Cataract Refract Surg. 1997; **23**: 1301-1310.

20 Kurtz RM, Horvath C, Liu H-H, Krueger RR, Juhasz T. "Lamellar refractive surgery with scanned intrastromal picosecond and femtosecond laser pulses," 1998; J Refract Surg.

21 K. Sletten, K. Yen, S. Sayegh, F. Loesel, C. Eckhoff, C. Horvath, H. Liu, T. Juhasz, and R. Kurtz, "An In Vivo Model of Femtosecond Laser Intrastromal Refractive Surgery," submitted, 1998; J. Ophthalmic Lasers and Surgery.

22 H. Meunier, G. Spooner, S. Sayegh, K. Sletten, D. Cabrera, F. Loesel, C. Eckhoff, T. Juhasz, and R. Kurtz, "Further Developments in an In Vivo Model of Femtosecond Laser Intrastromal Refractive Surgery," submitted, 1999; J. Refractive Surgery.

23 R. M. Kurtz, C. Horvath, T. Juhasz, "Optimal laser parameters for intrastromal corneal surgery," Proceedings of SPIE, 1998; vol. **3255**, no. 11.

24 T. Juhasz, C. Horvath, H. Liu, R.M. Kurtz, "Refractive surgical application with ultrashort pulsed lasers," Proceedings of SPIE, 1998; vol. **3255**, no. 12.

25 Noack J, Hammer DX, Noojin GD, Rockwell BA, Vogel A. "Influence of pulse duration on mechanical effects after laser-induced breakdown in water," Journal of Applied Physics, 1998, **Vol**. 83, No. 12, pp 7488-7495.

26 Juhasz T, Hu XH, Turi L, Bor Z. "Dynamics of shock waves and cavitations generated by picosecond laser pulses in corneal tissue and water," Lasers Surg. Med. 1994; vol **15**, pp 91-96.

27 Juhasz T, Kastis GA, Suarez C, Bor Z, Bron WE. "Time-resolved observations of shock waves and cavitation bubbles generated by femtosecond laser pulses," Lasers in Surgery and Medicine 1996; vol **19**, pp 23-31.

28 Juhasz T, Fischer JP, Bille JF, Kurtz RM. "Time-resolved studies of plasma-mediated surface ablation of soft biological tissue with near-infrared picosecond laser pulses," SPIE Proceedings, 1997; Vol. **2975**, pp 271-281.

29 Niemz MH, Klancnik EG, Bille JF. "Plasma-mediated ablation of corneal tissue at 1053nm using a Nd:YLF oscillator/regenerative amplifier laser," Lasers in Surgery and Medicine, 1991, **11**:426-431.

30 Coakley WT, Nyborg WL. "Cavitation; dynamics of gas bubbles: applications," *Ultrasound: its applications in medicine and biology, part I: Methods and Phenomena 3*, 1978, ed. Fry FJ. Elsevier, pp 86.

31 Miller DL, J. Acoust. Soc. Amer., 1977; vol. **47**.

# A study for the Ho:YAG laser - intervertebral disc cell interaction using three-dimensional cell culture system

Masato SATO*[a], Miya ISHIHARA[b], Tsunenori ARAI[b], Takashi ASAZUMA[a], Toshiyuki KIKUCHI[a], Makoto KIKUCHI[b], Kyosuke FUJIKAWA[a]

[a] Department of Orthopaedic Surgery, National Defense Medical College, Japan
[b] Department of Medical Engineering, National Defense Medical College, Japan

**Keywords:** Ho:YAG laser, PLDD, intervertebral disc, cultured cell, cell reaction, proteoglycan synthesis

## ABSTRACT

The purpose of this study is to evaluate the influence on the intervertebral disc cells after laser irradiation using three- dimensional culture system and to clarify the optimum Ho:YAG laser irradiation condition on percutaneous laser disc decompression (PLDD) for lumbar disc herniation. Since the Ho:YAG laser ablation is characterized by water-vapor bubble dynamics, not only thermal effect but also acoustic effect on cell metabolism might occur in the intervertebral disc. We studied the disc cell reaction from the metabolic point of view to investigate photothermal and photoacoustic effects on three-dimensional cultured disc cell. Intervertebral discs were obtained from female 30 Japanese white rabbits weighing about 1 kg. A pulsed Ho:YAG laser (wavelength : 2.1μm, pulse width : about 200μs) was delivered through a 200μm-core diameter single silica glass fiber. We used the Ho:YAG laser irradiation fluence ranging from 60 ~ 800 J/cm$^2$ at the fiber end. To investigate acoustic effect, the acoustic transducer constructed with polyvinylidene fluoride (PVdF) film and acoustic absorber was used to detect the stress wave. Thermocouple and thermography were used to investigate thermal effect. Concerning damage of plasma membrane and ability of matrix synthesis, thermal effect might mainly affect cell reaction in total energy of 54J (closed to practically used condition), but in 27J, acoustic effect might contribute to it. We found that total energy was key parameter among the optimum condition, so that temperature and/or stress wave may influence Ho:YAG laser - disc cell interactions.

## 1. INTRODUCTION

Percutaneous laser disc decompression (PLDD) (1) for lumbar disc herniation is considered to be a therapeutic mean to be performed as a minimally invasive therapy. Various lasers have been applied to PLDD, and practical ones of them are Nd:YAG and Ho:YAG lasers. Even for widely used Ho:YAG laser, the irradiation parameters, i.e., laser energy per pulse, energy density (fluence), repetition rate, etc. have not been definitely determined. Recently several side-effects caused by laser therapy have been reported (2 - 4). Although endoscopic PLDD by Ho:YAG laser was considered to be a safe system, the necrosis of catilage endplate was sometimes generated after this method. Meanwhile, laser - intervertebral disc cell interaction has been little studied. The purpose of this study is to analyze the response of disc cells to laser irradiation and to clarify the photoacoustic and photothrmal effects on the cells using three-dimensional (3-D) culture system (5, 6).

* Correspondence : Email: ma-sato@md-phd.com, Telephone: +81-42-995-1596, Fax: +81-42-996-5199



In *Laser-Tissue Interaction XI: Photochemical, Photothermal, and Photomechanical*, Donald D. Duncan, Jeffrey O. Hollinger, Steven L. Jacques, Editors, Proceedings of SPIE Vol. 3914 (2000) 1605-7422/00/$15.00

## 2. MATERIALS AND METHODS

### 2.1 Preparation and three-dimensional culture condition

Intervertebral discs of lumbar spine were obtained from 30 female Japanese white rabbits weighing about 1 kg. Intervertebral discs were shredded with scissors and digested in Dulbecco's Modified Eagle's Medium (DMEM, Nissui Pharmaceutical, Tokyo, Japan) containing 0.2% (w/v) pronase E (Kaken Co., Tokyo, Japan) for an hour and then in DMEM containing 0.025% (w/v) bacterial collagenase P (Boehringer Mannheim GmbH, Mannheim, Germany) for 4 hours. The digested tissue was passed through the cell strainer (Becton Dickinson Labware, Franklin Lakes, NJ, USA) with a pore size of 40 μm. The filtrate was centrifuged at 1500 rpm for 5 minutes. The isolated cells were washed three times with DMEM. The cells were seeded in 96-well culture plates at cell densities of 1 x $10^6$ /ml and incubated within 1% agarose gel containing DMEM supplemented with 10% fetal bovine serum (FBS, Gibco BRL, Grand Island, NY, U.S.A.). An equal amount of the medium was added onto the gel at 37°C in an atmosphere of 5% $CO_2$ and 95% air.

### 2.2 Experimental Setup

A pulsed Ho:YAG laser (Model LASER1-2-3HO2100, SEO Inc., CA, USA, Wave length:2.1μm, Pulse width:250μs) device was used for the 3-D cultured disc cells irradiation. (Fig.1). Total energy ( = laser energy / pulse x number of shots ; 27J, 54J) with 5Hz repetition rate was used. Irradiation energy at the fiber end (40~180mJ/pulse) and number of shot (150~1350) were varied. Total laser energy per a unit sample volume (dose density) was arranged to clinical irradiation condition. Total energy of 54J was close to clinical laser dose density (7).

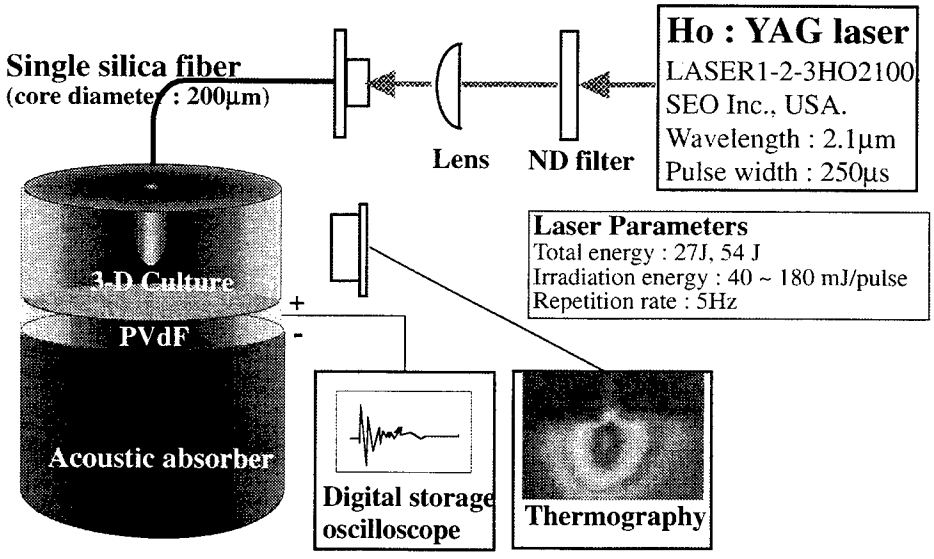


**Fig.1 Experimental Setup**

### 2.3 Monitoring of Photoacoustic Effect

The stress wave was measured using an acoustic transducer according to the method reported by Ishihara et al. (8), and was monitoring at the bottom of 3-D cultured system. The transducer was consisted of polyvinylidine fluoride (PVdF) piezoelectric film (Imotec Germaney) and acoustic absorber, which thicknesses were 40μm and 7mm, respectively. The electorical output waveform from this transducer was documented by the digital storage oscilloscope. The stress amplitude was given by Eq.(1) and (2) using measured output voltage (Fig.2) (9).

$$F(t) = V(t) * (Cd+Cp)/dt \quad (1)$$

$$P(t) = 54.2 * V(t) \quad (2)$$

Where, F(t) is detected stress at transducer, V(t) is output voltage of the transducer, Cd is loading capacitance of oscilloscope, Cp is capacitance of the transducer, and dt is strain constant for PVdF.

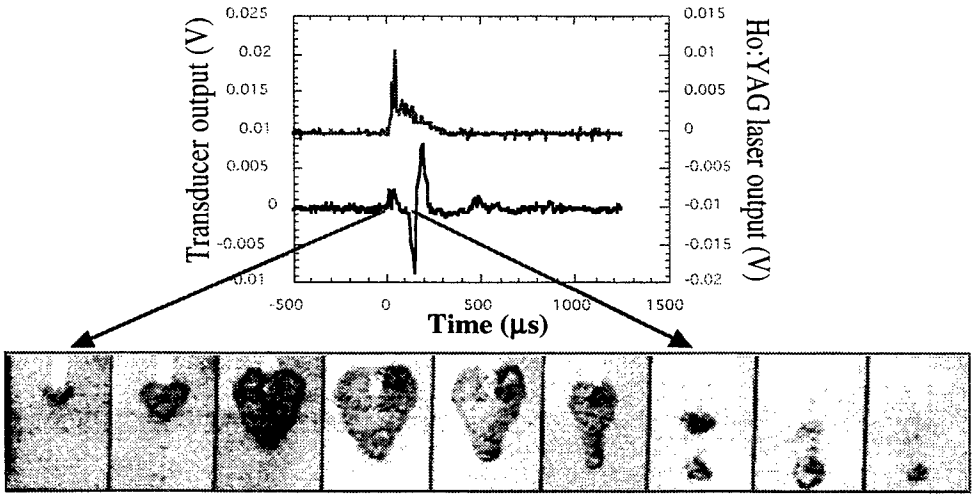


**Fig.2 Waveform of Stress Wave**

### 2.4 Analysis of Photothermal Effect

The volumes of which temperature were over 50°C in the 3-D culture system were measured by thermography for 3 types of irradiation energy. These volumes of 100 and 180 mJ/pulse were normalized by the volume of 40mJ/pulse. The ratios of them were 3.33 and 7.32, respectively. These normalized over 50°C volume ratios varied with the levels of irradiation energy. We defined the thermal load as Eq. (3), and used it as an index of thermal effect.

$$\Omega = \int (\text{more than } 50°C \text{ volume ratio})\, dt \quad (3)$$

### 2.5 Evaluation of damage of plasma membrane and ability of matrix synthesis

Lactate dehydrogenase (LDH) was a stable cytoplasmic enzyme present in all cells. It was rapidly released into the cell culture supernatant upon damage of the plasma membrane. It indicated loss of membrane integrity and was an indicator of cell death. With the use of the Cytotoxicity Detection Kit (Boehringer Mannheim GmbH, Mannheim, Germany), LDH release could be measured in culture supernatants by ELISA(10, 11). LDH rate was calculated as formula (4).

LDH rate (%) = [exp. value - low cont. value] / [high cont. value - low cont. value] x 100 (4)

Proteoglycan synthesis was used as an index of matrix synthesis. It was measured by rapid filtration assay of $^{35}S$ incorporation (12). The 3-D cultured cells and DMEM containing $^{35}S$-sulfate at 10μCi/ml were incubated for every 12 hours (12 hours pulse labeling) from 0 to 48 hours after the laser irradiations, and quantified by scintillation counting. This assay was applied to measure the ability of matrix sinthesis of damaged target cells.

## 3. RESULTS

### 3.1 Pressure of stress wave

The measured stress waveform was shown in Fig 2. These time-resolved photographs indicated the dynamics of bubble formation and collapse. The initial stress wave corresponded to the compression wave generated by bubble expansion phase, and the spiky wave corresponded to the bubble collapse. The pressure levels calculated from the stress amplitude were changed by irradiation energy, and wave indicated increasing tendency with increasing irradiation energy (Table 1).

**Table 1. Pressure of Stress Wave**

| Irradiation energy (mJ/pulse) | Pressure of stress wave (bar) |
|---|---|
| 40 | 15 ± 5.1 |
| 100 | 31 ± 5.9 |
| 180 | 78 ± 3.5 |

### 3.2 Plasma membrane damage

The levels of LDH rate with the pressure of stress wave and the thermal load were shown in Fig.3. Concerning the pressure, the levels of LDH rate in total energy of 54J remained highly stable, and those in 27J remained at low level. On the other hand, concerning the thermal load, the levels of LDH rate were divided into 2 groups.

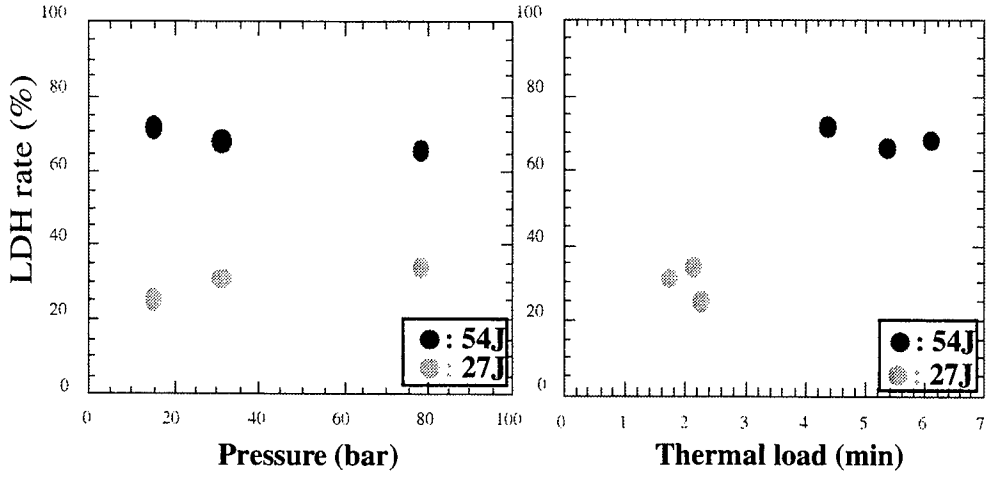


**Fig.4 LDH Rate**

### 3.3 Ability of matrix synthesis

The levels of proteoglycan synthesis with the pressure of stress wave and the thermal load were shown in Fig.4. Concerning the thermal load, the levels of proteoglycan synthesis in total energy of 54J remained at low level, but the levels of 27J varied greatly within the narrow range.

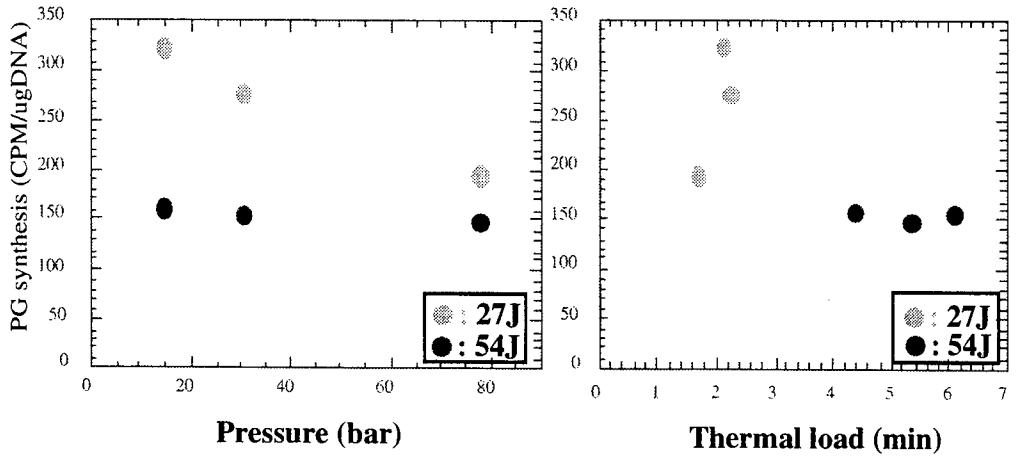


**Fig.5 Proteoglycan Synthesis**

## 4. DISCUSSION

Ho:YAG laser irradiation provides photothermal and photoacoustic effects to irradiated tissue. Cell reaction might depend on these effects modified by laser parameters, as total energy, irradiation energy, irradiation time, repetition rate, and so on. Various types of cell reaction have been considered to be induced by laser irradiation. Therefore, concerning cell reaction, laser tissue interaction should be further discussed. We used 3-D cell culture system and analyzed laser- disc cell interaction quantitatively. We could monitor and measure both photoacoustic and photothermal effects simultaneously using this culture system

Concerning the pressure, the levels of LDH rate in total energy of 54J remained highly stable, and those in 27J remained at low level. LDH rate was not related to the pressure. Concerning the thermal load, the levels of LDH rate were divided into 2 groups. These results indicated that LDH rate was more influenced by photothermal effect than photoacoustic one. On the other hand, concerning the thermal load, the levels of proteoglycan synthesis in total energy of 54J remained at low level, but the levels of 27J varied greatly within the narrow range. We considered two reasons for this drastic change, the one was the influence of the pressure because the levels of proteoglycan synthesis also varied with the pressure, and the other was the possibility of the threshold in the thermal load. In summary, major effect on disc cell might vary with the types of cell reaction and total energy. Membrane damage highly depended on photothermal effect, but different major effects on matrix synthesis were observed by each total energy. These effects might affect the disc cells, and the different types of cell reaction might be influenced by each effect. Regulation of these effects could transform the cell reaction.

## 5. CONCLUSIONS

Laser - intervertebral disc cell interaction was investigated in terms of cell metabolism and physical agents as the thermal load and the pressure of the stress wave. Photothermal and photoacoustic effects might contribute to different types of the cell reaction. Regulation of these effects could transform the cell reaction.

## ACKNOWLEDGEMENTS

The authors wish to express their gratitude to Prof. Nishijima, Kanazawa Medical University, who provided the clinical information.

## REFERENCES

1. Choy, D. S., Case, R. B., Fielding, W., Hughes, J., Liebler, W., and Ascher, P. (1987) *N Engl J Med* **317,** 771-772.
2. Garino, J.P., Lotke, P.A., Sapega, A.A., Reilly, P.J., and Esterhai, J.L.,Jr. (1995) *Arthroscopy* **11,** 467-474.
3. Fink, B., Scneider, T., Baunsttein, S., Schmielau, G., and Rother, W. (1996) *Arthroscopy* **12,** 217-223.
4. Rozbruch, S.R., Wickiewict, T.L., DiCarlo, E.F., and Potter, H.G. *Arthroscopy* **12,** 245-250.
5. Sato, M., Asazuma, T., Kikuchi, T.,Yamada, H., Yamagishi, M., and Fujikawa, K. (1998) *J Jpn Orthop Assoc* **72,** S1346.
6. Sato, M., Ishihara, M., Arai, T., Asazuma, T., Kikuchi, T., Kikuchi, M., and Fujikawa, K. (1999) *SPIE* **3601**, 387-391.
7. Quigley, M. R., and Maroon, J. C. (1994) *Spine* **19,** 53-6.
8. Ishihara, M., Arai, T., Kikuchi, T., Nakano, H., Kawauchi, S., and Obara, M.(1998) *SPIE* **3254**, 319-324.
9. Srinivasan, R., Dyer, P.E., and Braren, B. (1987) *Laser Surg Med* **6**, 514-519.
10. de Luca, A., Weller, M., and Fontana, A. (1996) *J Neurosci* **16,** 4174-85.
11. Dimmeler, S., Haendeler, J., Nehls, M., and Zeiher, A. M. (1997) *J Exp Med* **185,** 601-7.
12. Masuda, K., Shirota, H., and Thonar, E. J. (1994) *Anal Biochem* **217,** 167-75.

# Corneal and Skin Laser Exposures from 1540 nm Laser Pulses

Thomas E. Johnson[a], Michael A. Mitchell[b], Pedro J. Rico[a], David J. Fletcher[a], Thomas E. Eurell[c], W.P. Roach[a]

Departments of Preventive Medicine and Biometrics[a], and Laboratory Animal Medicine[b], Uniformed Services University, 4301 Jones Bridge Road, Bethesda MD, 20814

Department of Veterinary Biosciences[c], University of Illinois at Urbana-Champaign, Urbana, IL, 61802

## ABSTRACT

Mechanisms of tissue damage are investigated for skin and cornea exposures from 1540 nm ("eye safe") laser single pulses of 0.8 milli-seconds. New skin model data point out the advantages of using the Yucatan mini-pig versus the Yorkshire pig for in-vivo skin laser exposures. Major advantages found include similarities in thickness and melanin content when compared with human skin. Histology from Yucatan mini-pig skin exposures and the calculation of an initial $ED_{50}$ threshold indicate that the main photon tissue interaction may not be solely due to water absorption. In-vitro corneal equivalents compared well with in-vivo rabbit cornea exposure under similar laser conditions. In-vivo and in-vitro histology show that initial energy deposition leading to damage occurs intrastromally, while epithelial cells show no direct injury due to laser light absorption.

**Keywords:** Cornea, skin, $ED_{50}$, 1540 nm, "eye safe", Yucatan mini-pig, Yorkshire pig, rabbit

## 1. INTRODUCTION

Our overall research efforts are to investigate laser tissue interaction mechanisms that explain threshold damage from 1540 nm lasers in cornea and skin. The mechanisms of laser tissue interaction at this wavelength for skin and cornea is not agreed upon by researchers[1,2]. This is an important wavelength in laser technology since a number of commercial and military lasers are in use that operate at this wavelength. Further, several commercial manufacturers market the 1540 nm laser as an "eye-safe" system. Previous studies and textbooks show remarkable disparity in reporting where 1540 nm laser energy is deposited and the quantity of energy or power required to cause tissue damage[1-6].

We have found that 1540 nm light is absorbed in the corneal stroma, rather than epithelium or other corneal tissue, prior to reaching the retina. This finding is clearly inconsistent with the use of the term "eye-safe." Also, in some cases it has been suggested that skin threshold data may be used for corneal end points[7]. Our work includes researching skin damage thresholds and mechanisms to investigate the differences between skin and cornea exposure to 1540 nm laser pulses. While non-human primate models for corneal exposure have been used in the past, current recommended models use Dutch Belted rabbit for corneal exposures[8]. In this work we examine not only the rabbit model but also an in-vitro corneal model as a possible replacement for in-vivo exposures. The in-vitro model under consideration is commonly known as a corneal equivalent (CE) and are produced by the University of Illinois[9]. CE's are a live, in-vitro cell culture developed to mimic certain properties of human cornea. The CE's are produced from rabbit corneal origin using specialized techniques. They are



In *Laser-Tissue Interaction XI: Photochemical, Photothermal, and Photomechanical*, Donald D. Duncan, Jeffrey O. Hollinger, Steven L. Jacques, Editors, Proceedings of SPIE Vol. 3914 (2000) 1605-7422/00/$15.00

grown in transwell containers such that they match the anatomy and physiology of normal corneal tissue. The layered structure consists of a single endothelial bed, overlaid with multiple beds of stromal collagen, fibroblasts, keratocytes, and topped with epithelial cells.

Studies have been performed for many years utilizing the Yorkshire pig flank as a model for laser-human skin interaction. Our group has recently competed the first comparative anatomy study specifically addressing tissue thickness and pigmentation on both pig skin and human skin[10,11]. The Yorkshire pig is a lightly pigmented skin model when compared to the Yucatan mini-pig. We report on our investigation into a more highly pigmented model, the Yucatan mini-pig, and the differences in absorption of 1540 nm light due to the increased presence of melanin.

Threshold damage at 50% probability, $ED_{50}$, histology and theoretical analysis of energy deposition are presented as part of a larger study investigating several aspects of infrared laser exposures to both skin and cornea[12,13]. The scope of the overall work includes determining the appropriate corneal and skin models, along with replacement models for skin and corneal laser exposure. Our investigation is not simply concerned with threshold endpoints, but the microscopic mechanisms of damage which present as gross laser tissue interaction. In this discussion we will present histological images that aid in elucidating the mechanism of damage to tissue.

## 2. MATERIALS AND METHODS

### 2.1 Laser System

The laser utilized for exposures is manufactured by Laser Sight Technologies Inc. (3300 University Blvd. Suite 140, Winter Park FL 32792). It utilizes an Er:Glass rod to produce 0.8 ms pulses at 1540 nm. The pulse duration is measured utilizing a Germanium detector (Thor Labs PDA 255) connected to a Tektronix TDS 644B digitizing oscilloscope. Energy measurements are made with a Molectron EPM 2000 connected to a J 25 energy probe. Components are arranged as shown in Rico et al[14]. All spot sizes in this paper were measured with the technique described by Cain et al[15].

### 2.2 Cornea

A total of five Dutch Belted rabbits have been used thus far in our study. A spot size of 0.0013 $cm^2$ was employed for this portion of the study. The animals were maintained under general anesthesia during laser exposure procedures. Each cornea is exposed in three locations in addition to a marker lesion. Marker lesions are utilized to identify the orientation of the cornea during histological preparation. Corneas were examined both pre- and post exposure opthalmoscopically and using slit lamp biomicroscopy. The rabbits were euthanized at 24 hours and enucleated. Histological examination of the cornea was accomplished by sectioning and staining with hematoxylin and eosin (H&E). Measurements of the depth and width of the damage sites is also performed. Lesion determination is accomplished as described in Fletcher et al[16].

### 2.3 Corneal Equivalents

A total of 83 CE's have been utilized for laser exposures in this study. Spot sizes of 0.0013 and 0.0025 $cm^2$ have been employed. CE's are shipped in from the University of Illinois, exposed the same day, examined ophthalmoscopicaly and using confocal microscopy, then returned for histological evaluation. A single equivalent is not exposed from each batch so that it may serve as a control. An assessment of possible laser induced damage to the equivalent is made immediately following exposure. Grading is performed acutely and evaluation is accomplished as described in Fletcher, et al[16].

### 2.4 Skin Thickness

Skin thickness for humans, Yorkshire pigs and Yucatan mini-pigs were determined as described in Eggleston et al[10, 11, 17]. Pig skin samples were collected from seven sites: the face; the top of the head; the dorsal neck; the ventral neck; the left flank; the ventral abdomen; and the inguinal region. No animals were used solely for the collection of skin samples.

Human skin samples were collected from patients who were receiving surgical excisions, biopsies or other procedures. No human samples were obtained solely for this study. The samples of normal skin were from the periphery of surgical incisions, or extraneous tissue removed during surgical closure.

The epidermal thickness was measured using a light microscope (American Optical, Buffalo, NY) with a calibrated intra-ocular micrometer at 450×. Measurements were made from the base of the sloughing stratum corneum to the base of the stratum basal. Melanin content was assessed with an Olympus BX40 light microscope (Olympus Optical Co. Ltd., Tokyo, Japan). Samples were evaluated at 1000× using a 10 by 10 grid reticle in the eyepiece.

### 2.5 Skin

A total of two female Yucatan mini-pigs (30-75 kgs.) and two female Yorkshire pigs (35-80 kgs.) have so far been used for $ED_{50}$ determination. The animals are maintained and evaluated as described by Rico et al[14]. A spot size of 0.0025 $cm^2$ was employed for this study. Histological samples were evaluated using light microscopy to determine epidermal lesion extent and to characterize the type of tissue and cellular damage produced by the laser exposure. The histological sample is measured in random locations throughout the injury site to characterize the size of the lesion using an intra ocular micrometer. No animals were euthanized after skin sample collection as they are part of an animal sharing program.

### 2.6 Statistical Analysis

Probit analysis is the statistical method used to determine the estimated dose for 50% probability of laser induced damage, $ED_{50}$, of both corneal equivalents and in-vivo corneal models[12]. For the in-vivo models, readings of sites were performed acute, one-hour, and 24 hours post exposure. Each site is counted as either an injury or no injury, as described elsewhere[14, 16]. All data points were entered into a Probit statistical analysis package and the $ED_{50}$ was calculated. An advantage in using this statistical methodology is the ability to reduce the amount of data points necessary for statistical significance and thus reduce the number of animals used.

## 3. RESULTS

### 3.1 Cornea

Our $ED_{50}$ value for in-vivo corneal exposures is not yet statistically significant, but has been preliminarily determined to be 33 J/cm$^2$ at acute, 1 hour and 24 hours post exposure with a 0.0013 cm$^2$ spot size[16]. Slit lamp examination of the corneas did not identify any lesions which were not seen ophthalmoscopically. The lesions were clearly seen to be limited to the stroma, with none penetrating to the endothelium. Lesions presented immediately following exposure, and no additional lesions appeared to develop or disappear over the following 24 hour period. Acute histological examination of the cornea reveals that energy is absorbed in the stroma, with damage to the epithelial cells apparently distended by the underlying stromal injury. The lesion appears to be well demarcated with little damage outside the diameter of the beam intersection with the tissue[16].

### 3.2 Corneal Equivalents

Preliminary results indicate the acute $ED_{50}$ value for laser tissue damage to the CE's is approximately 70 J/cm$^2$ with a spot size of 0.0025 cm$^2$ and 50 J/cm$^2$ with a spot size of 0.0013 cm$^2$. Visible damage consistently occurred at and above these energy levels. Histological examination of the CE's may yield a statistically different $ED_{50}$ in the future. Histologically, vacuolization was seen between the lamellar sheets of collagen fibers. Stromal denaturation appears to be present throughout the damaged area[16].

### 3.3 Skin Thickness

The skin of Yucatan mini-pigs and Yorkshire pigs are structurally similar to humans (See Figure 1). The skin of the Yucatan mini-pig is thicker than any location found on the Yorkshire pig. The human data was pooled but the pig data was not due to significant differences in thickness at each location for each breed[10,11]. The thickness of the Yucatan mini-pig flank was determined to be 68 ± 34 micrometers in thickness. The Yorkshire flank was 47 ± 19 micrometers. The two breeds of pig were statistically different in thickness at the 95% confidence level.

Human skin thickness for the face, neck and arm averaged 67 micrometers[11]. Our values compared well with those listed by the International Commission on Radiological Protection (ICRP) for the arm and leg of 40 to 60 micrometers[18]. A statistical comparison of human skin to Yorkshire pig flank found that the two were statistically different in thickness at the 95% confidence level. Yucatan mini-pig flank was determined to be statistically identical to human face, neck and arm thickness[11].

The normalized melanin fraction in Yucatan mini-pigs was 45.4% in the flank, while Yorkshire pigs were found to have 0.8%. Human normalized melanin content was 23.7% (face), 16.3% (neck), and 26.0% (arm). The skin of the Yucatan mini-pig has a much greater proportion of melanin in epidermal cells than the Yorkshire pig. Melanin distribution in humans is closer to that of the Yucatan mini-pig than to the Yorkshire pig, although human melanin does not extend into the layers of the stratum granulosum as with the Yucatan mini-pig[11].

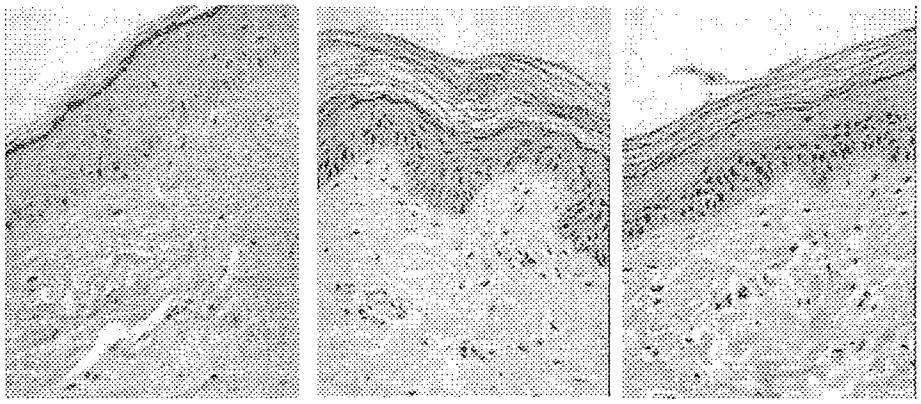

**Figure 1. Human, Yucatan mini-pig, and Yorkshire pig skin, 10x**

### 3.4 Skin

Statistically significant $ED_{50}$ results are not yet available for skin. Quantitatively, we can report that Yucatan mini-pigs require much higher energy densities ($J/cm^2$) to induce a lesion as compared to Yorkshire pigs. Thus far in our study the most readily apparent differences between the two breeds are the acute appearance of erythematous skin lesions in the Yucatan mini-pigs and the delayed formation of erythematous skin lesions in Yorkshire pigs after laser exposures. Lesion development appears to begin at or near the basal layer of the epidermis and is the source of underlying dermal tissue damage in each breed of pig[14]. The stratum corneum and lucidum appear to be transparent to 1540 nm laser injury at the spot size and energy density used in this study.

## 4. DISCUSSION

### 4.1 Cornea

The preliminary $ED_{50}$ value for in-vivo cornea is estimated at 33 $J/cm^2$. Although this $ED_{50}$ is not statistically significant, we believe it to be within 30 to 90 $J/cm^2$ for a spot size of 0.0013 $cm^2$ (at $1/e^2$). Above this energy density, lesions were always achieved. Histological examination showed that laser energy is not absorbed in the tear layer, or epithelial tissue, contrary to some theories[1]. We suspect that laser energy is absorbed within the stroma resulting in thermal damage which propagates toward the epithelial layers of the eye. The deposition of energy in the stroma causes distension of collagen within the affected area, and elongation of the epithelial cells. No direct laser damage has been seen in epithelial cells to date. This result is in extremely good agreement with Egbert and Maher's theory[2], but in complete disagreement with Allen and Polhamus[1].

### 4.2 Corneal Equivalents

The $ED_{50}$ for corneal buttons is estimated to be significantly higher than that for in-vivo cornea. We expect to develop a scaling factor or other techniques to correlate CE's and in-vivo cornea in the future as statistically significant data becomes available. Note that the $ED_{50}$ for CE's is analyzed only at acute exposure. CE's are not monitored at 1 and 24 hours, since they are returned within a few hours post exposure to the University of Illinois for analysis. Histologically, only a few

differences between corneal tissue and CE's have been found. We suspect that the inability of the CE's to respond systemically, as the in-vivo cornea would, accounts for the majority of differences between the two tissues. As in corneal tissue, CE's present with extensive stromal damage and no epithelial damage. Figure 2 shows a histological comparison of in-vivo acute injury and CE damage. Our results seem to imply that an increase in spot size requires an increase in energy density ($J/cm^2$) to achieve the $ED_{50}$.

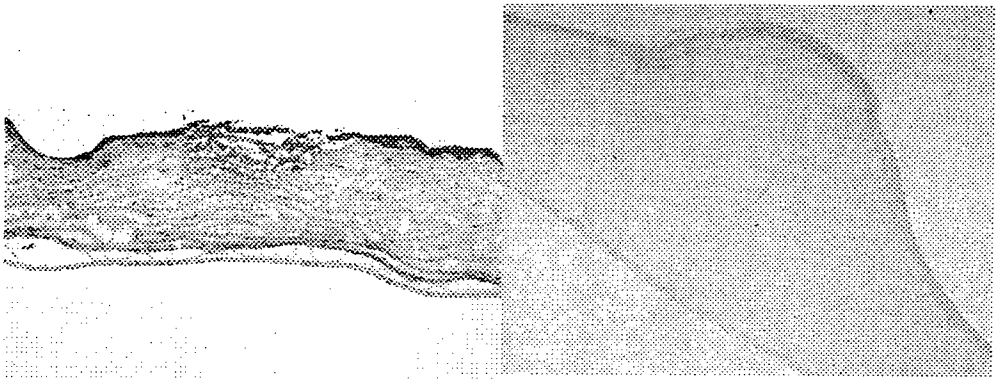

**Figure 2. Corneal Equivalent (left, 63×) and Acute Rabbit Cornea Laser Injury (right, 4×).**

**4.3 Skin Thickness**

The Yorkshire pig skin and Yucatan mini-pig skin differ significantly in thickness, melanin concentration, and quantity of hair. These characteristics make the Yucatan mini-pig more similar to humans than the Yorkshire pig. Melanin granules are readily visible in the epidermis, especially in the stratum basale, stratum spinosum, and the deep layers of the stratum granulosum in the Yucatan mini-pig and similarly in human skin. Although our skin samples were from lightly pigmented persons, their skin was still better represented by the Yucatan mini-pig than the Yorkshire pig, both in thickness and melanin content[11]. This is significant in that we suspect pigmentation plays a role in the damage mechanism of skin, based on the different responses of Yorkshire pig and Yucatan mini-pig models.

**4.4 Skin**

Yorkshire and Yucatan mini-pigs differ in the way that laser induced skin lesions present[14]. Acute lesions are seen in the Yucatan mini-pig, whereas they are not in the Yorkshire pig. Additionally, the Yucatan mini-pig requires higher energy densities ($J/cm^2$) to achieve the $ED_{50}$ in comparison to the Yorkshire pig at identical spot sizes. Since the lesions require differing time periods to formation, this is thought to be an indication of dissimilar laser tissue interaction methodology within each breed. We suspect that melanin absorbs the photon energy and that thermal damage results from energy deposition in the melanin, resulting in immediate thermal damage to Yucatan mini-pig tissue. On the other hand the Yorkshire skin may absorb energy in a longer path length such that more tissue is damaged. It might appear that the mediating effects of melanin granules are not a significant factor for Yorkshire pigs as it is in the Yucatan mini-pig. Histologically, the penetration depth in both models appears to be to the basal layer.

## 5. CONCLUSION

### 5.1 Cornea and CE

Allen and Polhamus[1] indicate that water absorption is the primary means of energy deposition in the cornea for 1540 nm wavelength pulses. The absorption of 1540 nm laser energy would presumably occur in the tear layer external to the epithelium of the cornea and in the epithelium. Contrary to this theory, energy absorption appears to occur in the stroma of the cornea at 1540 nm. Egbert and Maher[2] predict energy absorption in the stroma based purely on tissue thermal properties rather than water thermal propagation. This theory agrees well with our histological results. Egbert and Maher go on to describe how epithelial damage will occur as energies are increased above the threshold for damage. This theory only partially explains the location of energy deposition within the stroma. Assuming corneal tissue can be approximated by physiological saline, a practical assumption if water absorption is assumed to be the mechanism of 1540 nm light absorption in the cornea, then the penetration depth of the laser should be significantly greater than the thickness of the cornea (corneal thickness is estimated to from0.5 to 0.6 mm).

Unusual preliminary results have also been obtained with CE's. Beatrice et al[19] reported that increasing spot size will require a lower energy density ($J/cm^2$) to achieve the $ED_{50}$ in retina. The cornea lacks any focusing ability like the retina, but increasing spot size might still be expected to produce a lower $ED_{50}$. Although we have only two data points, which are not yet statistically significant, our data appears contradictory. Increasing spot size for the CE's requires more energy ($J/cm^2$) to achieve the $ED_{50}$.

### 5.2 Skin

The difference between the $ED_{50}$ of the Yorkshire pig and the Yucatan mini-pig seem to be significant at this time. Only one previous skin study appears to have been performed by Lukashev et al[7]. The reported $ED_{50}$ was 6.5 $J/cm^2$ for 2.5 ms pulses and 3.5 $J/cm^2$ for 100 ns pulses with a spot size of 2 mm. They also report that above 2 mm spot size, there is no experimental evidence for dependence on spot size. Theoretical calculations performed[19] indicate that at diameters greater than 0.4 mm there is no spot size dependence. Our preliminary data suggest that the $ED_{50}$ for skin is significantly greater than that reported by Lukashev et al[7] and that $ED_{50}$ is spot size dependant at 0.5 and 0.2 mm contrary to their calculations. We postulate that their assumption that "only water absorbs the 1540 nm laser energy" is not completely correct. Water and another absorbing medium, such as melanin, we theorize to be the primary absorber of energy. This explanation also satisfies the differing $ED_{50}$ we see in the two breeds of pig.

## ACKNOWLEDGMENTS

This research was supported by the Air Force Office of Scientific Research under Grant # FQ8671-9900412 (PMB # G487HQ-04), the Uniformed Services University of the Health Sciences Departments of Preventive Medicine and Biometrics and Laboratory Animal Medicine.

## REFERENCES

1. R.G. Allen, G.D. Polhamus, "Ocular thermal injury from intense light" in Laser applications in medicine and biology, M.L. Wolbarsht ed., Plenum Press, New York, 1989, p. 266

2. D.E. Egbert, E.F. Maher, Corneal damage thresholds for infrared laser exposure: Empirical data, model predictions, and safety standards, USAF School of Aerospace Medicine, SAM-TR-77-29, Brooks AFB TX, 1977, p. 17-18
3. W. T. Ham, H. A. Mueller, "Ocular effects of laser infrared radiation," J. Laser App. **3**:**3**, pp. 19-21, 1991.
4. E. Stuck, D. J. Stuck, E. S. Beatrice, "Ocular effects of laser radiation from 1.06 to 2.06 u," Health Phys. **40** pp. 835-846, 1981.
5. D.J. Lund, M.B. Landers, G.H. Bresnick, J.O. Powell, J.E. Chester, C. Carver, "Ocular Hazards of the Q-switched Erbium Laser" Investigative Opthamology, Volume 9, Number 6, p.463-470, June 1970.
6. P.S. Avdeev, Yu. D. Berezin, P. Gudakovskii, V.R. Muratov, A.G. Murzin, V.A. Fromzel, "Experimental Determination of Maximum Permissible Exposure to Laser Radiation of 1.54 um wavelength", Soviet Journal of Quantum Electronics, Volume 8, Number 1, p. 137-139, January 1978.
7. A. V. Lukashev, S. E. Sverchkov, V. P. Solovyev, B. I. Denker, V. V. Engovatov, "Laser safety standard for skin at 1540 nm. New experiment and estimations." SPIE Vol. 2974, pp. 148-156, 1997
8. The animals involved in this study were procured, maintained and used in accordance with the Animal Welfare Act and the "Guide for the Care and Use of Laboratory Animals" prepared by the Committee on Care and Use of Laboratory Animals of the Institute of Laboratory Animal Resources, National Research Council. The Uniformed Services University of the Health Sciences has been fully accredited by the Association for the Assessment and Accreditation of Laboratory Animal Care, International since 1982.
9. T. Eurell, DVM, PhD, University of Illinois at Urbana-Champaign College of Veterinary Medicine, Urbana, Illinois.
10. T. A. Eggleston, Michael A. Mitchell, T. E. Johnson, W. P. Roach, "Comparison of *in vivo* skin models for near infrared laser exposure," Proceedings SPIE, Vol. 3590, p. 356-360, 1999.
11. T. A. Eggleston, M. A. Mitchell, T. E. Johnson, R. L. Becker, and W. P. Roach, "Comparison of in vivo skin models for near infrared laser exposure," submitted to *Laboratory Animal Sciences*, 1999.
12. D. J. Finney, *Probit Statistical Analysis Software*, Cambridge University Press, 1971.
13. T.E. Johnson, T.A. Eggleston, D. Fletcher, K. Lopez, P.J. Rico, M.A. Mitchell, W.P. Roach, "Determination of single-pulse exposure threshold ($ED_{50}$) for 1400 - 2000 nm lasers," Proceedings SPIE, Vol. 3601, p. 55-58, 1999.
14. P.J. Rico, M.A. Mitchell, T. E. Johnson, W. P. Roach, " ED50 determination and histological characterization of porcine dermal lesions produced by 1540 nm laser radiation pulses," Proceedings SPIE, Vol. 3907, 2000.
15. C.P. Cain, G.D. Noojin, D.X. Hammer, R.J. Thomas, B.A. Rockwell, "Artificial eye for in-vitro experiments of laser light interaction with aqueous media," J. Biomedical Optics, 2(1), pp. 1-7, 1997
16. D.J. Fletcher, T.E. Johnson, M.A. Mitchell, T.E. Eurell, P.J. Rico, W. P. Roach, "Corneal equivalents: a replacement model for in-vivo 1540 nm laser exposure studies," Proceedings SPIE, Vol. 3907, 2000
17. This protocol was reviewed by the Uniformed Services University of the Health Sciences' Institutional Review Board, and approved for execution on November 6, 1998 as an exempt human use study.
18. ICRP, "The biological basis for dose limitation in the skin," Annals of the ICRP 22, Pergamon Press, Oxford, 1991.
19. Beatrice, E.S., and G.D. Frisch, "Retinal laser damage thresholds as a function of image diameter," Arch. of Environ. Health, V27, November 1973, pp. 322-326.

# Optoacoustic measurements during µs-irradiation of the retinal pigment epithelium

Georg Schüle[1], Gereon Hüttmann[1], Johann Roider[3], Christopher Wirbelauer[2], Reginald Birngruber[1], Ralf Brinkmann[1]

[1]Medical Laser Center Lübeck, Lübeck, Germany
[2]Department of Ophthalmology, University of Lübeck, Germany
[3]Department of Ophthalmology, University of Regensburg, Germany

## ABSTRACT

The selective microphotocoagulation is a new technique to damage the retinal pigment epithelium (RPE), which is desired for treatment of several retinal diseases. By applying a train of µs laser pulses it is possible to selectively destroy these cells and simultaneously spare the adjoining photoreceptor and neural tissue. We applied µs laser pulses of a Nd:YLF laser (527nm), at a repetition rate of 500Hz to porcine RPE. The light is absorbed in the RPE and by thermoelastic expansion, an optoacoustic (OA) signal will be generated which could be measured by an ultrasonic transducer. With this setup, the baseline temperature increase at the RPE, during irradiation can be determined, since the optoacoustic pressure signal depends on the temperature of the irradiated RPE. We found a linear dependence of the OA amplitude to the RPE sample temperature. At higher irradiance we prooved the formation of microbubbles and bubble collapse in the RPE with OA techniques.

**Keywords:** optoacoustic, retinal pigment epithelium, selective photocoagulation, microbubbles, Grueneisen parameter, RPE

## 1. INTRODUCTION

The selective RPE cell treatment is a promising method in ophthalmology for a variety of diseases, which are associated with a dysfunction of the RPE cells[1]. In contrast to conventional methods for RPE cell destruction with cw (200ms) laser irradiation it allows to spare the photoreceptor tissue, thus maintaining full vision in the treated area. This allows the treatment in proximity of the fovea[1-2]. So far, 65 patients with different macular diseases have been treated with this new technique. The RPE cell destruction was proved by fluorescein angiography. Temperature calculations show[3], that during the laser pulse a high peak temperature will be generated at the absorbing melanosomes inside the RPE cells in the µs time scale (figure 1). Due to the thermal relaxation time of the melanosomes, heat could only penetrate over several µm. The high temperature at the melanosomes will damage the

Correspondence: e-mail: schuele@mll.mu-luebeck.de
tel:+49-451-500-6517
fax: +49-451-505486
www.mll.mu-luebeck.de

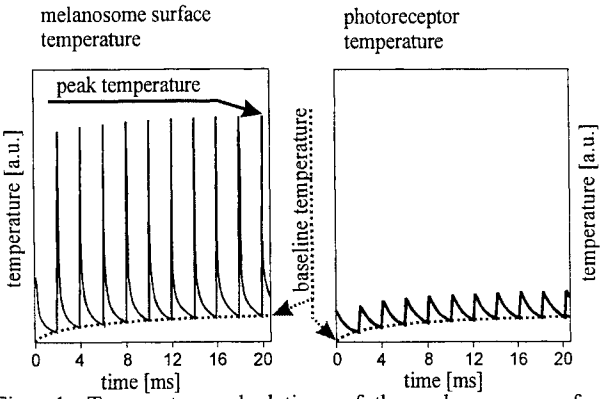


Figure1: Temperature calculations of the melanosome surface and the photoreceptor tissue during irradiation with repetitive µs laser pulses. During laser pulse high peak temperature will be generated at the mesanosome surface. At the photoreceptors, the temperature peaks are much lower due to the fact, that the laser pulses are shorter than the heat conduction time for the distance of 5µm. Induced by the train of laser pulses the baseline temperature increases in both cases.



In *Laser-Tissue Interaction XI: Photochemical, Photothermal, and Photomechanical*, Donald D. Duncan, Jeffrey O. Hollinger, Steven L. Jacques, Editors, Proceedings of SPIE Vol. 3914 (2000)
1605-7422/00/$15.00

RPE cell. The temperature peaks at the adjacent photoreceptor are much lower. However, due to the high repetition rate, a baseline temperature is build up in the RPE. This effect is on the ms time scale, thus heat diffusion can reach other tissue layers like the photoreceptors as shown in figure 1. This makes the baseline temperature to an important factor, which interfere with the selective RPE cell destruction. Until now this baseline temperature increase was not measured although it is very important for the selectivity of the treatment.

The formation of microbubbles around the strong absorbing melanosomes inside the RPE has been reported for laser pulses shorter than $10^{-8}$ s in experimental[4] and theoretical studies[5-6]. In this case the RPE cell damage is most likely induced by mechanical effects such as cell membrane disruption[4] from the microbubbles or by laser induced stress waves[7]. For longer laser pulses (>$10^{-4}$ s), the RPE cells are assumed to be thermally denaturated.

Objective of this study was to determine the baseline temperature increase and the formation of microbubbles in porcine RPE with optoacoustic techniques. These techniques have been used for temperature monitoring in canine liver[8] and for the proof of microbubbles around melanosomes[9].

## 2. MATERIAL AND METHODS

### 2.1 Setup

A frequency doubled, pulse stretched Nd:YLF laser[12] (527nm, 1.5µs pulse duration) was used as irradiation source. The fiber tip with top head beam profile was imaged with an ophthalmic laser slit lamp (Zeiss, 30 SL/L) to the sample which was fixed in a water filled cuvette (fig.1). Beam diameter at the sample was 156µm. The OA signals were received with an ultrasonic broadband transducer (Valpey-Fisher, VP-1093, 0-10 MHz) and recorded by a transient recorder (TEK/Sony, RTD710). The distance between sample and transducer was approximately 3 mm. The temperature inside the cuvette was measured near the sample by a thermocouple (Type J).

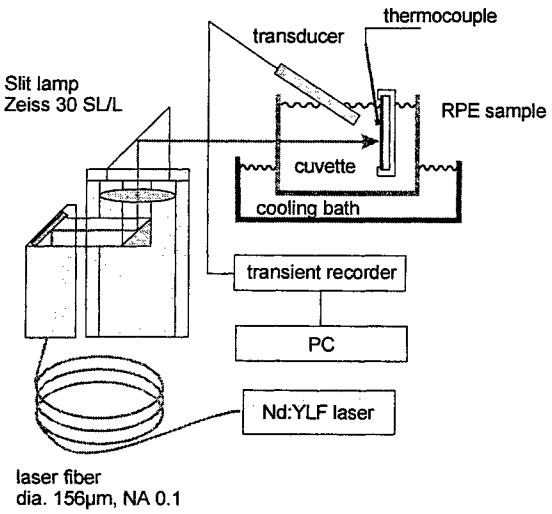


Figure 1: Setup for optoacoustic measurements during irradiation of porcine RPE with µs-laser pulses.

### 2.2 Optoacoustic techniques

Thermoelastic stress waves are based on thermal expansion of an energy absorbing medium. Under condition that the laser pulse duration is shorter than the thermal relaxation time of the target volume, the induced pressure $P$ is given as[10]

$$P = \alpha \Gamma F_0 \quad (1)$$

with $F_0$ =radiant exposure, $\alpha$ =absorption coeff. , $\Gamma$ = Grueneisen parameter of the absorbing medium. $\Gamma$ can be expressed by the following material properties[10].

$$\Gamma = \frac{\beta}{\rho} C_v \kappa_\tau \quad (2)$$

with $\beta$ =thermal expansion coeff., $\rho$ = density, $C_v$ = spec. heat capacity, $\kappa_\tau$ = isothermal compressibility. These parameters vary in dependence of temperature. For small temperature variations of several degrees $\Gamma$ can be written as [11]

$$\Gamma(T) = \Gamma_0 + \Gamma_1 T \quad (3)$$

where $T$ is the absolute medium temperature. In this case the pressure $P$ goes linear with the temperature at constant radiant exposure.

$$P(T) = \alpha(\Gamma_0 + \Gamma_1 T) F_0 \quad (4)$$

There are some limitations to apply this to our experimental conditions. The laser pulse duration is in the order of the thermal relaxation time of the absorbing melanosome in the RPE cells. The assumption of an instantanious heating, which is needed for deriving equation *1* is not fulfilled. Also the acoustic relaxation time is much shorter than the laser pulse duration. During the laser pulse the pressure can propagate out of the heated volume and the resutling stress wave differs in amplitude and in shape. With our setup it is therefore only possible to measure the pressure signal in relative units. We have to add an experimental constant $C_{exp}$ to equation *4* which include the transducer sensitivity, the distance between sample and transducer and the amplitude loss due to the unfulfilled acoustic confinement. Equation *4* could then expanded to

$$P_{exp}(T) = C_{exp}\alpha(\Gamma_0 + \Gamma_1 T)F_0 \quad (5)$$

At constant radiant exposure $F_0$, it can be reduced to two constants

$$P_{exp}(T) = A + BT \quad (6)$$

As we measure only the pressure in relative units it is not possible to calculate the absolute temperature form our OA data. However, it is possible to determine the baseline temperature increase based on the temperature dependence of the measured pressure signals.

From water it is known, that for temperatures exceeding 80°C the pressure increases less than linear with temperature, thus the Grueneisen parameter becomes a high order function of the temperature. High temperatures are also expected during irradiation of RPE. The absorbing melanosomes could heat up over 80°C at higher radiant exposures.

### 2.3 Sample preparation

The experiments were performed with enucleated porcine eyes. After equatorial dissection the vitreous gel, the neural, and the photoreceptor tissue were carefully removed. The sample with RPE as superficial layer was fixed in a holder system and covered with physiological saline solution.

### 2.4 Sample irradiation

For a calibration of the temperature dependence of the OA-signal on RPE, we measured the pressure signal for different temperatures of the PRE sample. The sample cuvette with warm physiological solution (45°C) was cooled down by the cooling bath. At constant radiant exposure of 50 mJ/cm², a repetition rate of 1 Hz, the optoacoustic pressure signal was recorded during cooling. A typical OA signal is shown in figure 3. The RPE sample temperature was measured with a thermocouple near the sample surface. As OA signal value we used the integral over the first positive bipolar wave to reduce noise from the pressure signal (fig. 3).

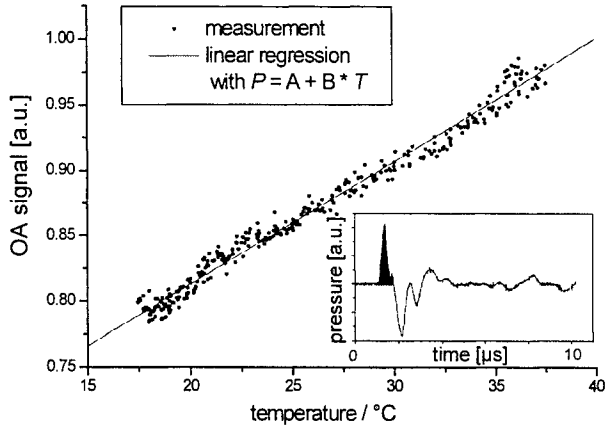


Figure 3: OA signal versus temperature. The pressure increases linear with temperature. Averaging over 17 samples with $P$=A+B$T$ lead to values of A=-0.57(14) and B=0.0109(19). As OA signal value the integral over the positive bipolar wave was used to reduce noise from the optoacoustic signal.

The clinical used treatment parameter for selective photocoagulation are 100 laser pulses at repetition rate of 500 Hz. For this parameter it is important to know the increased baseline temperature induced by the train of laser pulses. During the first laser pulse, the temperature around the melanosome absorber increases. An optoacoustic signal will be generated. In the following time, the heat diffuses to the surrounding tissue, but a small temperature increase in the irradiated area remains, when the next laser pulse follows after 2 ms. This means an increased start temperature for this laser pulse, which leads to a higher optoacoustic signal at constant pulse energy, according to eq. *5*.

## 3. RESULTS AND DISCUSSION

### 3.1 Temperature dependence of the OA signal of porcine RPE

The OA signal emitted from irradiated RPE increases linear with the RPE temperature (fig. 3). Averaging over 17 samples leads to values of $A = -0.57 \pm 14$ and $B = 0.0109 \pm 19$ for the linear regression with $P = A + BT$. With this data as calibration values it is possible to calculate the temperature increase from the pressure increase during irradiation with a train of laser pulses.

As the OA signal is linear with temperature the heating of the melanosome at this radiant exposure is lower than 40 °C. A nonlinear dependence will be result if the melanosome temperature reach the nonlinear Grueneisen parameter region over 80°C.

### 3.2 Temperature measurements on RPE

At 500 Hz repetition rate, 1.5µs laser pulse duration and a radiant exposure of 160 mJ/cm² every single pressure signal was recorded. By analyze the OA signals, it is possible to calculate (eq. *6*) the temperature increase with the data from the calibration measurement.

As described above, the OA signal should increase with increasing pulse number due to the higher baseline temperature. This was also found experimentally (fig. 4). By analyzing every single OA signal from each laser pulse, it is possible to determine the temperature increase. The first pulse start at the sample temperature. With the known pressure-temperature dependence the following pressure amplitudes could directly converted to absolute temperatures.

The baseline temperature increased about 30 °C (fig. 5). At this radiant exposure the melanosome temperature is three times higher than in the pressure-temperature dependence experiment due to the threefold pulse energy. In this case a linear dependence of the Grueneisen parameter on the temperature could not securely be assumed. If the melanosome temperature is in the nonlinear region, the real baseline temperature increase is somewhat higher than calculated. In this case the results show a lower estimation of the real temperature.

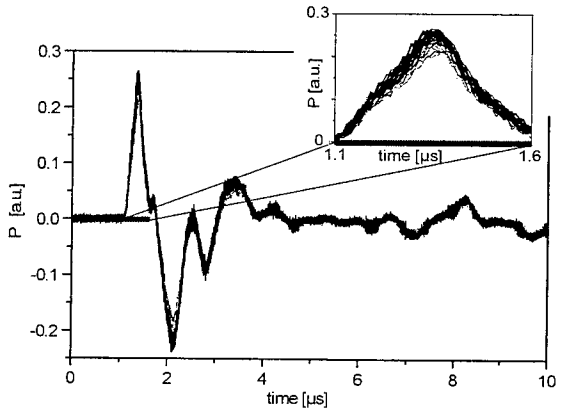


Figure 4: Superimposed optoacoustic signals during irradiation with a train of 100 laser pulses at rad. exp. of 160 mJ/cm² and 500 Hz repetition rate. The OA signal is a bipolar wave and very stable over the 100 pulses. Only the pressure maximum increases slightly, due to the baseline temperature increase of the RPE. In the magnification of the positive bipolar wave, the lower line is from the first laser pulse, and the topmost line from the last pulse.

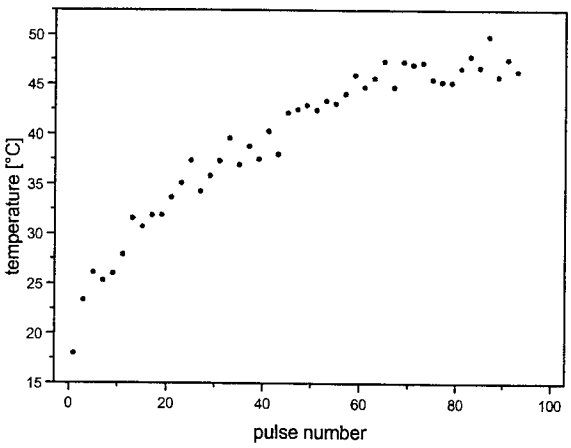


Figure 5: From the measured OA signal calculated baseline temperature increase of irradiated RPE. (100 laser pulses, 500Hz repetition rate, 160 mJ/cm², 156 µm spot size). The final temperature increase is approximately 30 °C.

### 3.3 Formation of microbubbles in RPE cells

Increasing the radiant exposure to 300mJ/cm² a disturbance at the end of the bipolar optoacoustic wave appears (fig. 6). This can be interpreted as the formation of microbubbles around the absorbing melanosome. Slightly above the threshold radiant exposure, the microbubble formation could not be determined from a single OA signal. The disturbance of the thermoelastic bipolar signal is very weak. Only by superimposing several OA signals the formation could be visualized. This is comprehensible, as we irradiate simulaneously 500 RPE cells with about 200 melanosomes inside each cell. At the microbubble threshold we have a large pure thermoelastic bipolar signal from the main part of the 100.000 melanosomes and the bubble formation signal of probably several microbubbles. Therefore also the disturbance did not start very significant as known from other optoacoustic bubble collapse experiments[13].

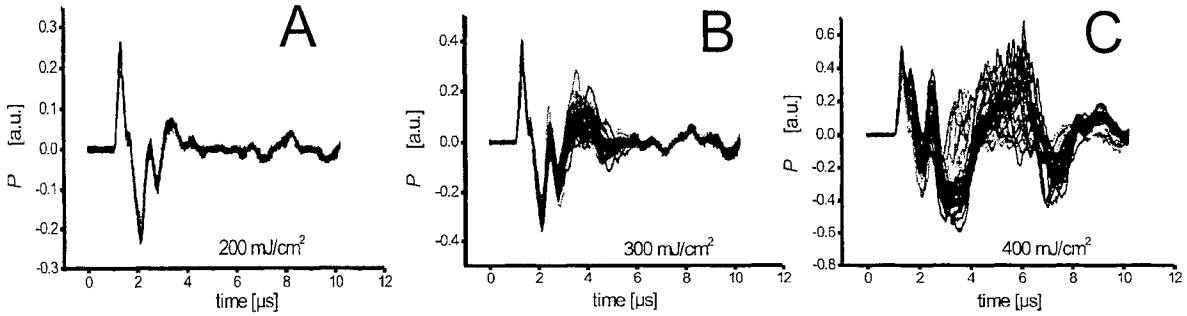


Figure 6: Change of the OA signal with increasing radiant exposures. The 100 optoacoustic signals from the laser pulse train were superimposed.
A: Radiant exposure 200mJ/cm². The signal is pure thermoelastic.
B: Radiant exposure 300mJ/cm². At the end of the thermoelastic bipolar wave signal fluctuations appear, which are explained by the formation of microbubbles.
C: Radiant exposure 400mJ/cm². The signal deviations from the bubbles are larger than the thermoelastic signal.

At higher radiant exposure of 400 mJ/cm² the disturbance is higher than the thermoelastic bipolar wave. At 450 mJ/cm² a second peak is observed, which can be interpreted as a bubble collapse (fig. 7). With increasing pulse number the delay time between the first pressure peak and the collapse signal increases. An increasing bubble size due to the higher baseline temperature at higher pulsenumber can explain this observation. We measured delay times up to 35µs at even higher irradiations.

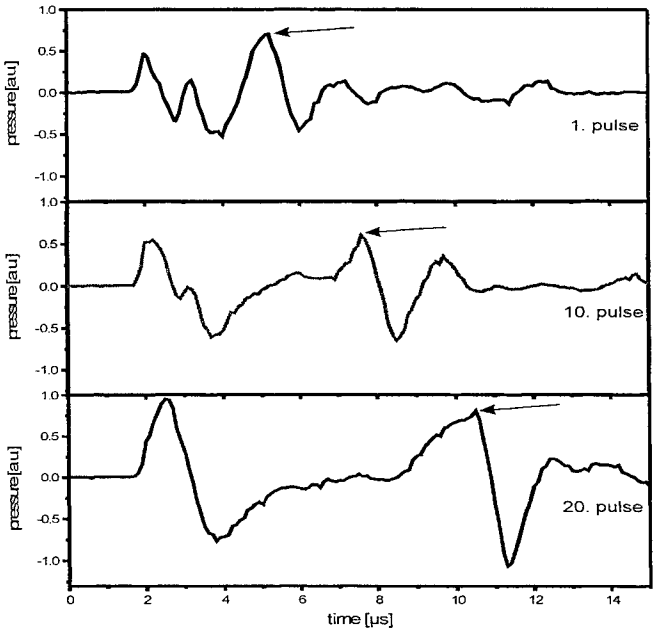


Figure 7: Optoacoustic signals at radiant exposure of 450 mJ/cm². After the bubble formation signal (first positive peak) a secound pressure peak (arrow) appears which could be assumed as bubble collapse. The delay time between bubble formation signal and collapse signal increase over the number of pulses.

### 3.4 Optoacoustic measurements during treatment

During clinical treatment a contact glass is placed on the patient's cornea to couple the laser radiation into the eye. We modified a standard contact glass with a piezzo electric transducer. With this optoacoustic contact glass we were able to measure the OA signals during treatment (fig. 8). The represented signals were measured at a radiant exposure of 600 mJ/cm² with a retinal spot diameter of 200 µm. In this first experiments, a pressure peak increase due to a baseline temperature increase was also found.

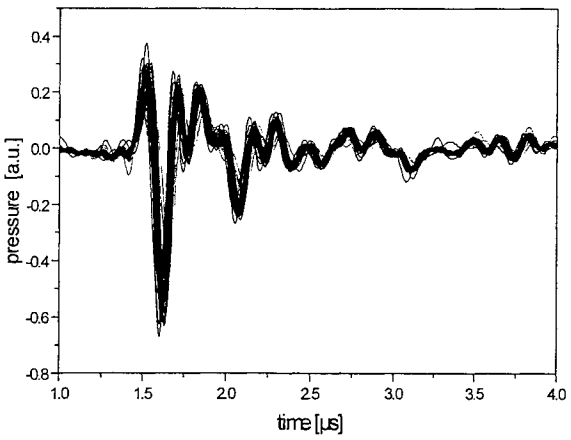


Figure 8: Measured OA signals during patient treatment. The pressure peak increases with pulse number, compareable to the in-vitro measurement.

## 4. CONCLUSIONS

With optoacoustic techniques it is possible to determine the baseline temperature increase in the RPE during irradiation with a train of laser pulses. The formation of microbubbles and the bubble collapse in porcine RPE was also determined optoacoustically. Using an optoacoustic contact glass, measurements can also be performed in vivo during treatment. This will lead to a better understanding of the effects involved in the selective photocoagulation of the RPE.

## ACKNOWLEDGMENTS

The authors would like to thank Dr. K. Giese from the Institute for Medical Physics and Biophysics Göttingen for technical assistance and fruitful discussions and the German Ministry of Education, Science, Research and Teaching (BMBF) for financal fund (No. 13N7309).

## REFERENCES

1. J. Roider, F. Hillenkamp, T. Flotte, R. Birngruber, *Microphotocoagulation: Selective effects of repetitive short laser pulses*, Proc. Natl. Acad. Sci., Vol. 90, pp. 8643-8647, 1993
2. J. Roider, R. Brinkmann, C. Wirbelauer, H. Laqua, R. Birngruber, *Retinal sparing by selective retinal pigment epithelial photocoagulation*, Arch. Ophthalm., Vol. 117, pp. 1028-1033, 1999
3. J. Rioder, *Entwicklung eines neuen Konzepts zur räumlichen Begrenzung von okulären Laserkoagulationen mit repetierenden kurzen laserpulsen*, habilitation, University Lübeck, 1996
4. D. J. Pane, T. R. Jost, J. J. Elliott, B. G. Eilert, L. Lott, K. Lott, G. D. Noojin, R. A. Hopkins, C. P. Lin, B. A. Rockwell, *Cavitation thresholds in the rabbit retina pigmented epithelium*, Proc. SPIE, Vol. 3601, pp. 27-31, 1999
5. B. S. Gerstman, C. R. Thompson, S. L. Jaques, M. E. Rogers, *Laser induced bubble formation in the retina*, Laser in Surg. Med., **18**, pp. 10-21, 1996
6. J. Sun, B. S. Gerstman, *Modeling of pressure generation by lasers in melanosomes; How to avoid stress confinement and bolw up a meanosome*, Proc. SPIE, Vol. 3601, pp.43-54, 1999
7. A. G. Doukas, T. J. Flotte, *Physical characteristics and biological effects of laser-induced stress waves*, Ultrasound in Med. Biol., Vol. 22, **2**, pp. 151-164, 1996

8. R. O. Esenaliev, A. A.Oraevsky, K. V. Larin, I. V. Larina, M. Motamendi, *Real-time optoacoustic monitoring of temperature in tissues*, Proc. SPIE, Vol.3601, pp. 268-275, 1999
9. C. P. Lin, M. W. Kelly, *Cavitation and acoustic emission around laser-heated microparticles*, Appl. Phys. Lett., Vol. 72, **22**, pp. 1-3, 1998
10. R. S. Dingus, R. J. Scammon, *Grueneisen-stress induced ablation of biological tissue*, Proc. SPIE, vol. 1427, pp. 45-54, 1991
11. G. Paltauf, H. Schmidt-Kloiber, *Microcavity dynamics during laser-induced spallation of liquids and gels*, Appl. Phys. A, **62**, pp. 303-311, 1996
12. R. Brinkmann, J. Rögener, C. P. Lin, J. Roider, R. Birngruber, G. Hüttmann, *Selective RPE-Photodestruction: Mechanism of cell damage by pulsed laser irradiance in the ns to μs time regime*, Proc. SPIE, Vol. 3601, pp. 59-65, 1999
13. A. Vogel, W. Lauterborn, *Acoustic transient generation by laser-produced cavitation bubbles near solid boundaries*, J. Acoust. Soc. Am., **84** (2), pp. 719-731 1988

## SESSION 9

# Laser Ablation

# Hydrodynamic modeling of tissue ablation with a free-electron laser

Stephen R. Uhlhorn[a, b], Richard A. London[b], Anthony J. Makarewicz[b], and E. Duco Jansen[a]

[a]Vanderbilt University, Department of Biomedical Engineering
Box 351631, Station B, Nashville, TN 37235, USA
[b]Lawrence Livermore National Laboratory
P.O. Box 808, Livermore, CA 94551, USA

## ABSTRACT

The Vanderbilt University free-electron laser (FEL) provides a continuously tunable ($\lambda = 2 - 10\,\mu m$) source of pulsed IR radiation with a pulse structure unlike those of conventional lasers (a macropulse of 5 $\mu$s consisting of a train of 1 ps micropulses at a frequency of 3 GHz). A numerical hydrodynamic code at Lawrence Livermore National Laboratory, known as LASTIS3D, was used to model the ablation of tissue using the FEL. This study investigates the role of the FEL pulse structure by comparing the results from simulations using a time-averaged energy deposition and a pulsetrain energy deposition.

**Keywords:** free electron laser, tissue ablation, hydrodynamic modeling

## 1. INTRODUCTION

The Vanderbilt University free electron laser is a continuously tunable source of pulsed mid-IR radiation with a wavelength range of $\lambda = 2 - 10\,\mu$m. Previous studies have suggested that by tuning the FEL to the vibrational mode of the amide-II bonds in protein ($\lambda = 6.45\,\mu$m) the FEL is well suited for precise tissue cutting and ablation with minimal collateral damage.[1] This original study has been followed by several investigations into the role of the FEL wavelength in tissue ablation,[2–5] however, none of these studies have considered the effect of the FEL pulse structure in tissue ablation. Previously reported[6] experimental results have been largely inconclusive, in part due to the ultrashort duration of the micropulses.

A diagram of the pulse structure of the FEL is seen in Figure 1. It consists of a macropulse of 4–6 $\mu$s at a repetition rate of up to 30 Hz. The macropulse is the envelope of a high frequency (3 GHz) train of micropulses with a duration of about 1 ps, separated by approximately 350 ps. This pulse structure results in a laser that is capable of both high peak (10 MW) and average (1 W) powers. If a laser pulse is shorter than the time necessary for heat to diffuse out of an irradiated volume, it is said to be thermally confined. Likewise, if the pulse is shorter than the time necessary for a stress wave to propagate out of the irradiated volume, it is said to be inertially confined. A diagram of these confinement conditions in water for many common laser systems appears in Figure 2. In it, the penetration depth $\delta$ is plotted against the pulse duration $\tau_L$ for the pulses of some common laser systems. The condition for thermal confinement is given by the line $\tau = \delta^2/4\alpha$, where $\alpha$ is the thermal diffusivity of the medium. As the pulse duration is further decreased, the condition for inertial confinement given by the line $\tau = \delta/\sigma$, where $\sigma$ is the speed of sound in the medium. It can be seen from Figure 2 that the FEL macropulse is thermally confined at all penetration depths except those below $\approx 1$ $\mu$m, which is only seen at wavelengths near the strong water absorption peak at $\lambda = 3.0$ $\mu$m. Further, both the FEL micropulses (1 ps) and the micropulse separation (350 ps) are short compared to the inertial confinement time for all penetration depths. This raises the possibility that large amplitude stress waves may be generated by the FEL micropulse structure.

In order to investigate the effects of the micropulse structure on a sufficiently short time scale, we turned to theoretical modeling using a numerical hydrodynamic code called LATIS3D that is being developed at Lawrence Livermore National Laboratory (LLNL). The current study investigated the effect of the FEL micropulse structure on the laser-induced stress waves. We hypothesize that the results of ablation with the FEL can not be solely attributed to wavelength tunability and specific absorption in amide bands.

Further author information: (Send correspondence to S.R.U.)
S.R.U.: E-mail: stephen.uhlhorn@vanderbilt.edu



In *Laser-Tissue Interaction XI: Photochemical, Photothermal, and Photomechanical*, Donald D. Duncan, Jeffrey O. Hollinger, Steven L. Jacques, Editors, Proceedings of SPIE Vol. 3914 (2000)
1605-7422/00/$15.00

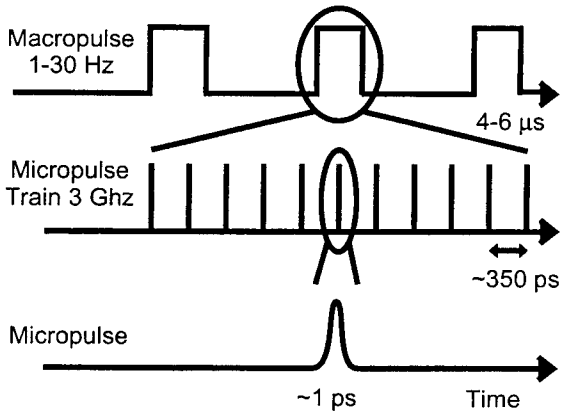


**Figure 1.** Pulse structure of the FEL.

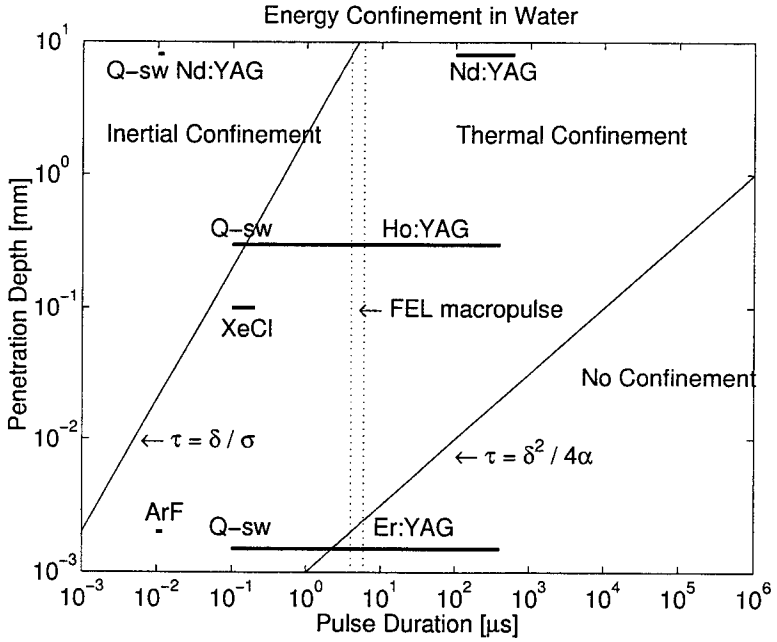


**Figure 2.** Confinement regions in water as a function of pulse duration for various laser pulses including the FEL macropulse which lies between the two vertical dotted lines. Modified from Welch et al.[7]

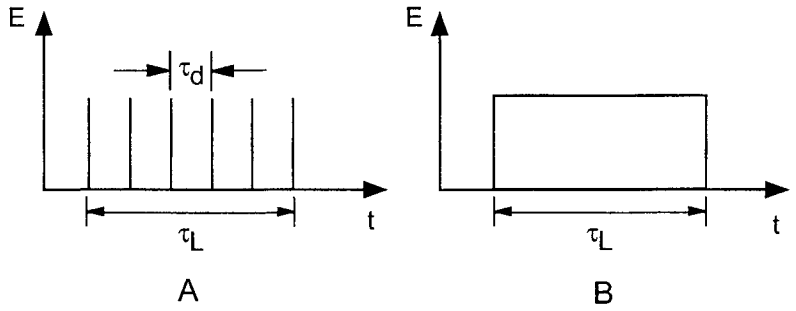


**Figure 3.** Time-dependent energy depostion schemes for the model simulations. A) pulsetrain and B) time-averaged deposition. $\tau_L$ is the laser pulse duration and $\tau_d$ is the delay between micropulses.

## 2. MODELING METHODS

LATIS3D is a subset of Kull, a larger simulation code at LLNL. Kull is a comprehensive physics package, based on finite volumes and written in the computer language C++, that includes light transport, fluid dynamics, materials response, and heat transfer modeling. The current study only considers the hydrodynamic response of the material, which is calculated using the standard thermodynamic conservation equation for mass, momentum, and energy:

$$\frac{\partial \rho}{\partial t} = -\rho \vec{\nabla} \cdot \vec{v}, \tag{1}$$

$$\frac{\partial \rho v^k}{\partial t} = -\frac{\partial P}{\partial x^k} - \rho v^k \vec{\nabla} \cdot \vec{v} + \rho \vec{g}_k, \tag{2}$$

$$\frac{\partial \rho \varepsilon}{\partial t} = -P \vec{\nabla} \cdot \vec{v} - \rho \varepsilon \vec{\nabla} \cdot \vec{v}. \tag{3}$$

We used a tabular equation of state of water to model the tissue and only sub-threshold fluences were initially used, that is, the water temperature was kept below the point of vaporization. The stress waves in the medium are generated by a time-dependent energy source deposition with a Beer's Law absorption distribution. Only one dimensional propagation is considered by making the laser spot radius $r$ much larger than the penetration depth $\delta$. Two types of laser irradiation schemes were considered: 1) a pulsetrain energy deposition that is similar to the pulse structure of the FEL and 2) a time-averaged energy deposition that had a total energy input equivalent to the pulsetrain, but delivered at a constant power level. These two pulse deposition schemes are illustrated in Figure 3. Although the numerical model is in one dimension only, the total energy delivered for both the pulsetrain deposition (Figure 3a) and the time-averaged deposition (Figure 3b) is equivalent to $E_{tot} = 50$ $\mu$J deposited over pulse duration $\tau_L = 50$ ns in a laser spot radius $r = 100$ $\mu$m and the penetration depth $\delta = 10$ mum, which is approximately the penetration depth of water at $\lambda = 6.45$ mum. The pulse duration $\tau_L = 50$ ns was chosen to maintian a sub-ablation threshold fluence given typical energies contained in an FEL micropulse. For the pulsetrain deposition, it is assumed that the individual micropulses are absorbed instantaneously, that is, the micropulse duration is short compared to the inertial confinement time. The energy contained within one micropulse was E = 0.3 $\mu$J, with a delay between micropulses $\tau_d = 333$ ps and a total of n = 150 pulses delivered. The numerical mesh consisted of 20 zones/$\mu$m.

## 3. RESULTS

The results from the model simulations appear in Figures 4, 5, and 6. Figure 4 shows the stress waved generated from both the pulsetrain and time-averaged energy deposition described in section 2. For both schemes, we see that the peak stress amplitudes are comparable, however in the pulsetrain deposition, it appears that there is a high frequency noise imposed on the stress waves. By looking at an expanded scale (Figure 5), we can see that the high frequency noise is well correlated with the micropluses. There are 150 pressure transients present and time delay between them is exactly the same as the delay between delivered micropulses (333 ps).

This correlation between the pressure transients and the delivered pulses is more clearly seen in Figure 6. In this case, the total energy was the same as the previous simulations ($E_{tot} = 50$ $\mu$J) and was delivered over the same pulse

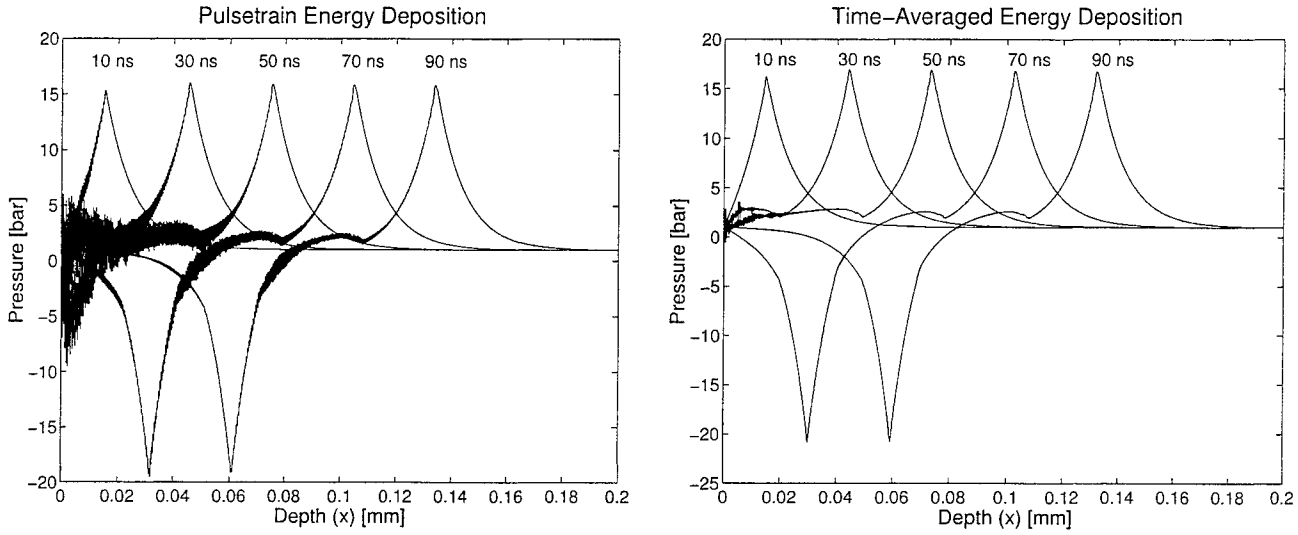


**Figure 4.** Pressure amplitude as a function of tissue depth at multiple times for both the pulsetrain and time-averaged energy deposition schemes. The numerical grid is 200 $\mu$m deep.

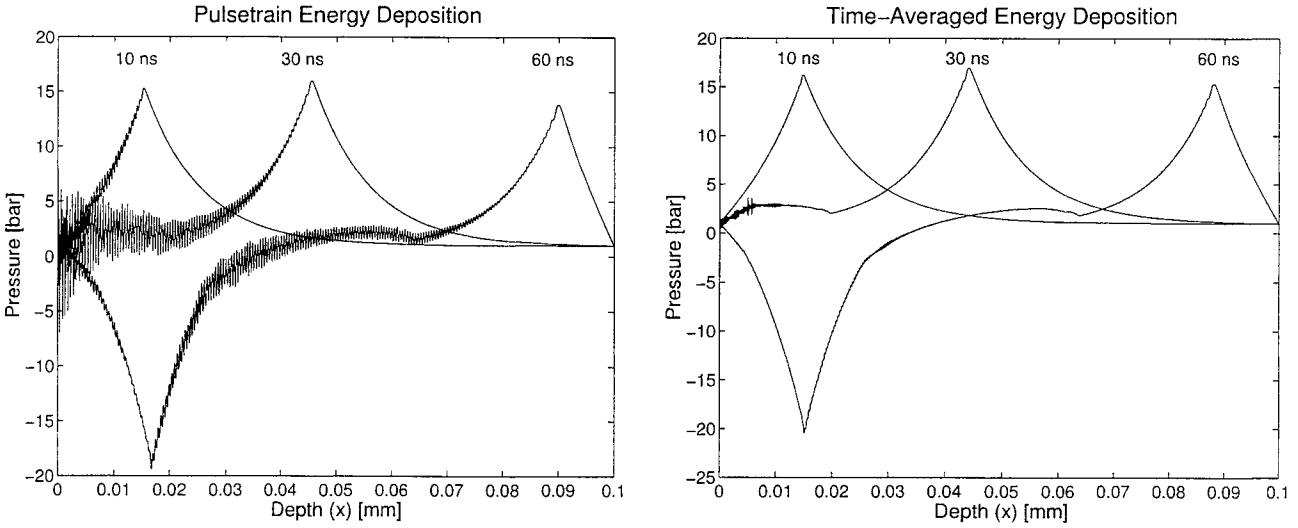


**Figure 5.** Pressure amplitude as a function of tissue depth at multiple times for both the pulsetrain and time-averaged energy deposition schemes. The numerical grid is 100 $\mu$m deep.

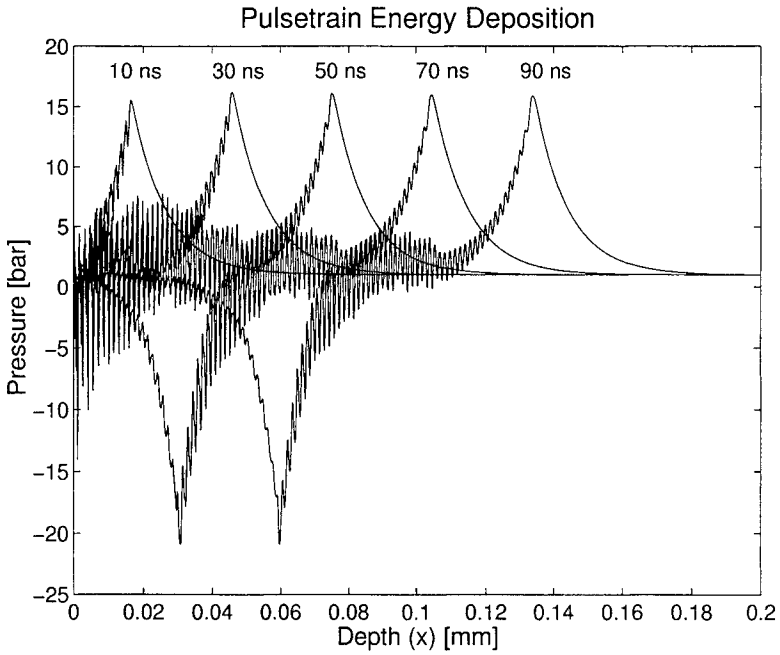


**Figure 6.** Pressure amplitude as a function of tissue depth at multiple times for the pulsetrain energy deposition scheme. The numerical grid is 200 $\mu$m deep.

duration ($\tau_L = 50$ $\mu$s). However, the number of micropulses was reduced to n = 50 and the delay between pulses was increased to $\tau = 1$ ns. Again, we see that the pressure transients are well correlated with the micropulses delivered, both in the total number (50) and in the delay between each micropulse (1 ns).

## 4. DISCUSSION

In comparing the results from the pulsetrain and time-averaged energy depositions, we see that the peak stress wave amplitudes generated are the same, which is exactly what one would expect given that the average radiant exposure ($E_{tot}/\tau_L$) is constant for both cases. However, for the pulsetrain deposition, we see that large local pressure transients are generated. These local pressure transients create large pressure gradients that are on the order of $\frac{dP}{dx} = 300$ bar/$\mu$m. Such large pressure gradients, which have both a compressive and tensile component, may effect tissue on a cellular level by tearing cell membranes and other microstructures.

The data that has been presented shows that the micropulse structure has an effect on the stress waves that are generated by laser exposure. This suggests that the results of ablation with the FEL can not be solely attributed to wavelength tunability and the selective absorption of multiple tissue components.

## ACKNOWLEDGMENTS

This work was performed under the auspices of the U.S. Department of Energy by University of California Lawrence Livermore National Laboratory under contract No. W-7405-Eng-48 and was supported by the Office of Naval Research (Grant No. N00014-94-1-1023).

## REFERENCES

1. G. Edwards, R. Logan, M. Copeland, L. Reinisch, J. Davidson, B. Johnson, R. Maciunas, M. Mendenhall, R. Ossoff, J. Tribble, J. Werkhaven, and D. O'Day, "Tissue ablation by a free-electron laser tuned to the amide II band," *Nature* **371**, pp. 416–419, 1994.
2. D. L. Ellis, N. K. Weisberg, J. S. Chen, G. P. Stricklin, and L. Reinisch, "Free electron laser wavelength specificity for cutaneous contraction," *Lasers in Surgery and Medicine* **25**, pp. 1–7, 1999.

3. J. M. Auerhammer, R. Walker, A. F. G. van der Meer, and B. Jean, "Dynamic behavior of photoablation products of corneal tissue in the mid-ir: a study with felix," *Applied Physics B* **68**, pp. 111–119, 1999.
4. M. Ostertag, J. T. McKinley, L. Reinisch, D. M. Harris, and N. H. Tolk, "Laser ablation as a function of the primary absorber in dentin," *Lasers in Surgery and Medicine* **21**, pp. 384–394, 1997.
5. J. Tribble, D. C. Lamb, L. Reinisch, and G. Edwards, "Dynamics of gelatin ablation due to free-electron-laser irradiation," *Physical Review E* **55**(6), pp. 7385–7389, 1997.
6. S. R. Uhlhorn, S. Harrison, H. S. Pratisto, and E. D. Jansen, "Tissue ablation with the free-electron laser: Contributions of wavelength and pulse structure," in *Laser-Tissue Interaction X*, S. L. Jacques, ed., vol. 3601, pp. 256–261, SPIE, (Bellingham, WA, USA), 1999.
7. A. J. Welch and M. J. C. van Gemert, eds., *Optical-Thermal Response of Laser-Irradiated Tissue*, ch. 21, pp. 709–763. Plenum Press, New York, 1995.

# Laser-tissue interaction with high-power fiber lasers operating in the mid-infrared wavelength region

Mark Pierce*, Stuart Jackson, Mark Dickinson, Paul Golding, Terence King,
Laser Photonics Research Group, Department of Physics & Astronomy,
University of Manchester, Manchester, UK. M13 9PL.

Philip Sloan
University Dental Hospital of Manchester, Higher Cambridge Street,
Manchester, UK. M15 6FH.

## ABSTRACT

We describe the results of preliminary studies on the interaction of continuous wave (cw), mid-infrared fiber laser light and soft biological tissues. An Er,Pr:ZBLAN fiber laser operating at a wavelength of 2.71 μm was used at 800 mW output power, a Tm-doped silica fiber laser at 1.98 μm provided up to 5 W output power, and a Yb:Er-doped silica fiber laser at 1.5 μm was used at 800 mW output power. Surface changes in tissue samples are described qualitatively and quantitatively, ablation velocity in tissue is measured, where observed, at the 800 mW power level, and sample sections are described with reference to histologically recognisable markers of thermal damage. The basic science described prepares the way toward ultimate clinical evaluations and applications of these new laser sources.

**Keywords:** fibre laser, diode-pumping, cladding-pumping, tissue ablation, erbium, thulium, ytterbium.

## 1. INTRODUCTION

Lasers operating in the mid-infrared wavelength region have demonstrated the ability to precisely and efficiently interact with both hard and soft biological materials. Applications such as dentistry[1], dermatology[2], orthopaedics[3], neurosurgery[4] and ophthalmology[5] are increasingly using laser sources as alternatives to traditional tools for high-precision tissue shaping and removal. Accurate ablation is made possible by strong coupling of optical energy to the water content of tissue, with absorption increasing with wavelength in the mid-IR to a maximum at around 3 μm [6]. The absorption spectrum of water exhibits fundamental and harmonic OH absorption bands at around 3 μm, 1.9 μm and 1.4 μm. This study examines the nature of laser-tissue interaction with newly developed fiber laser sources operating around these important wavelengths.

Use of the fiber laser geometry has become increasingly popular in recent years for a number of reasons. The guiding structure of the fiber confines pump light very effectively, which, on absorption by active ions doped into the fiber core, enables highly efficient, low threshold laser operation. High output beam quality is attained as a consequence of using fibers with a small core diameter, often supporting only the lowest order laser mode. Thermal problems encountered with power scaling of lasers using bulk media are reduced as a result of heat dissipation over a long length of fiber with a large surface area to volume ratio.

The requirement of a pump source with high beam quality for coupling light to the core of single mode fibers would, apparently, eliminate the desirable option of diode laser pumping. However, use of the cladding-pumping technique[7] circumvents this restriction, as pump light is launched into the larger, pump cladding of the fiber, interacting with the core on propagation along the fiber length. High powers may be launched in this way, potentially offering pump limited output, whilst using an offset



In *Laser-Tissue Interaction XI: Photochemical, Photothermal, and Photomechanical*, Donald D. Duncan, Jeffrey O. Hollinger, Steven L. Jacques, Editors, Proceedings of SPIE Vol. 3914 (2000)
1605-7422/00/$15.00

core maximises pump light absorption. The use of diode lasers already employed in clinical centres offers the potential for these compact fiber laser systems to be incorporated in a cost effective manner.

## 2. MATERIALS AND METHODS

### 2.1 Fiber laser sources

Three recently developed fiber lasers were used in this study. An Er,Pr:ZBLAN fiber (KDD, Japan), provided up to 1.7 W, nearly single-transverse-mode, cw output at a wavelength of 2.71 μm. This laser was developed following extensive theoretical analysis intended to overcome problems associated with excited-state absorption (ESA) and output power saturation in the erbium-doped fluoride fiber[8]. Successful power scaling was achieved by using a fiber containing a high concentration of erbium ions with a praseodymium co-dopant, in conjunction with double-clad diode pumping. A diode concentrator unit (Diomed Ltd., Cambridge, UK), combining the output from sixteen 2 W AlGaAs diode lasers was used, capable of providing up to 22.4 W total incident pump power at a wavelength of 790 nm. The 200 μm x 50 μm spot size at the focus of the diode pump source was oriented with the 200 μm x 100 μm rectangular cross section of the fiber pump cladding. Details of this fiber laser design and operation are reported elsewhere[9].

A Tm-doped silica fiber (Optoelectronics Research Centre, University of Southampton, UK), was used to generate laser light in the 2 μm wavelength region. Up to 5 W cw power was obtained using the same pump laser parameters described above. All experiments described with this laser in the present study were carried out at a wavelength of 1.98 μm, but tuneable output was available between 1.880 and 2.033 μm by adjustment of the fiber length. Further details regarding this fiber laser are reported elsewhere[10].

Approximately 1.4 W of cw output at a wavelength of 1.5 μm was obtained from a Yb:Er-co-doped double-clad silica fiber[11], (National Optics Institute, Sainte-Foy, Canada). In these experiments, the fiber was pumped with a high power Nd:YAG laser, however, it should be noted that diode-pumped Yb:Er-co-doped silica fiber lasers have been demonstrated to provide output powers in excess of 10 W.

### 2.2 Tissue samples

Chicken breast, liver and porcine muscle tissue samples were obtained on the day of experiment and refrigerated until one hour prior to experiment. Samples were mounted on an X-Y-Z translation stage and irradiated in air. A single 35 mm focal length $CaF_2$ lens was used to focus fiber laser output onto the tissue surface, providing incident spot size of approximately 150 μm. Laser power was monitored regularly with a Coherent 210 power meter. Surface changes in tissue samples were evaluated under an optical microscope, immediately following laser exposure, whilst specimens were also stored for histological analysis. Samples were routinely processed, fixed in paraffin wax, sectioned and stained with hematoxylin and eosin (H&E). The ablation velocity in tissue was determined by measuring the time taken for the laser to perforate samples of measured thickness. The point of perforation was detected by placing a power meter behind the tissue sample.

## 3. RESULTS

### 3.1 Gross evaluation

Visible changes at chicken breast tissue sample surfaces were recorded during irradiation with each fiber laser at 800 mW incident power. At all three wavelengths, a region of dehydrated, whitened tissue instantaneously formed at the beam focus, rapidly growing in size with exposure time. The diameter of this thermally affected zone is indicated in figure 1 as a function of exposure time, for the 2.71 μm and 1.98 μm lasers. In both cases, the range of thermally altered tissue initially grows rapidly, as energy is deposited in a volume close to the tissue surface. With increasing exposure time, the rate of growth of this zone decreases as tissue water is removed, decreasing local thermal conductivity resulting in reduced conduction of heat to surrounding areas. The extent of thermal effects is lower with the 2.71 μm wavelength at all exposure times as a result of stronger absorption at this wavelength. Energy is absorbed in a smaller tissue volume than at 1.98 μm, resulting in a reduced zone of interaction.

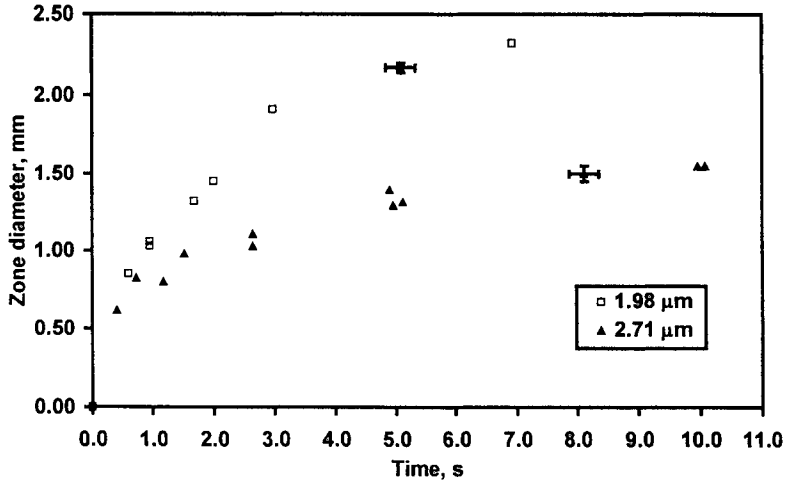


Figure 1. Diameter of the visibly affected zone at the surface of chicken breast tissue samples, as a function of fiber laser exposure time. Data shown represent 800 mW cw irradiation at 1.98 μm and 2.71 μm wavelengths.

As exposure continued with the near- 2 and 3 micron lasers, the interaction proceeded through up to three distinct stages. With the 1.98 μm laser, water vaporisation and bubbling was observed at around 5 s, accompanied by a popping sound and visible rupture of the tissue surface. With continued irradiation, the ablation front proceeded into the tissue. At around 10 s, the onset of tissue browning was noted, with char formation and carbonisation at the ablation crater edge. The 2.71 μm laser-tissue interaction followed the same stages, but with a more rapid onset of ablation and char formation. The 1.5 μm fiber laser failed to produce any ablative effect, resulting only in continued tissue whitening, dehydration and indications of shrinkage.

Figure 2a indicates the time taken for the laser to penetrate tissue samples of varying thickness, at each of the 1.98 μm and 2.71 μm wavelengths. Thin tissue samples were penetrated quickly, but as the ablation front moved into thicker samples, the ablation velocity was reduced considerably. Factors contributing to this include a reduced irradiance as the ablation front moves beyond the beam focus, absorption of laser energy in crater walls and absorption and scatter by ejected debris. Whilst the 2.71 μm laser demonstrated an ablation velocity of 0.80 $mm.s^{-1}$ compared to 0.27 $mm.s^{-1}$ with the 1.98 μm laser for shallow holes (fig. 2b), the narrower ablation channel formed by the 2.71 μm laser made it increasingly difficult for debris to escape, slowing the advance of the ablation front at deeper levels. The 1.5 μm laser failed to penetrate even the thinnest samples during 80 s exposure at the same, 800 mW power level.

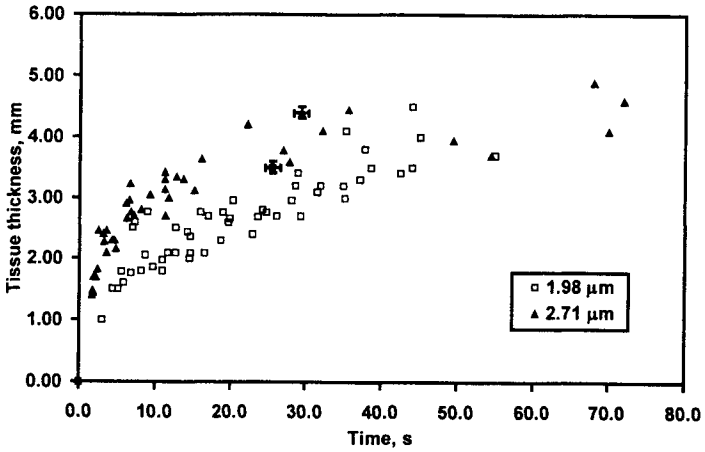


Figure 2a. Time taken for cw 1.98 µm and 2.71 µm fiber lasers to penetrate chicken breast tissue samples up to 5 mm thickness, at 800 mW incident power.

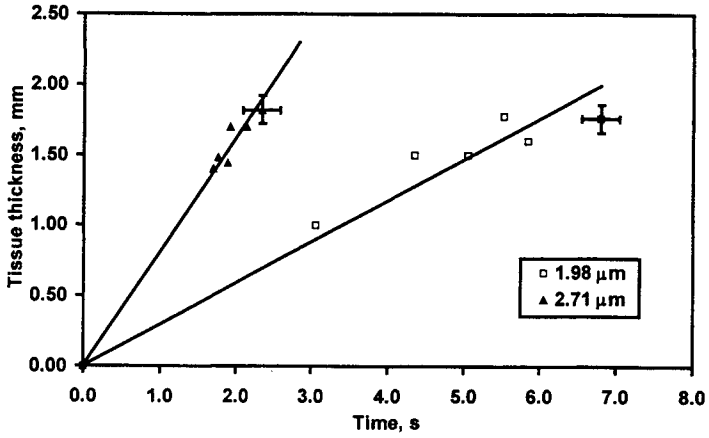


Figure 2b. Time taken for cw 1.98 µm and 2.71 µm fiber lasers to penetrate thinnest chicken breast tissue samples at 800 mW incident power.

### 3.2 Histologic evaluations

Tissue samples processed for histology were inspected for indications of laser induced damage. Chicken breast samples irradiated with the 1.5 µm fiber laser are presented in figure 3. Following 5 s exposure at 600 mW, minimal effects were observable in H&E stained sections viewed under routine light microscopy, with no evidence of tissue removal or ablation having taken place, (figure 3, left). However, when the same field of view was inspected with transmission polarising microscopy, a thermally affected zone was clearly seen, as indicated by a loss of tissue birefringence, (figure 3, right).

Figure 4 shows routinely stained sections of slots cut in porcine muscle tissue with the 1.98 µm fiber laser at 5 W incident power. The slot presented on the left was formed by traversing the sample across the focus of the laser beam at 0.25 $mm.s^{-1}$, producing a lesion approximately 1200 µm wide and 2300 µm in depth. A dark layer of carbonised tissue is present at the inside edge, with a 300 µm wide region of vacuolated tissue also in evidence. Normal tissue is seen to clearly define the edge of the lesion, with muscle fibers appearing more densely packed over an approximately 200 µm region extending into the tissue. In contrast, on traversing the tissue across the beam at 25 $mm.s^{-1}$, lesions were formed with minimal damage at the margins, as seen in the section on the right.

Samples exposed to the 2.71 µm fiber laser also revealed well defined holes and slots with remnants of vacuolated tissue in ablation craters and minimal collateral damage. Figure 5 shows histological

sections of holes formed in chicken breast and liver on the left and right, respectively, following 0.5 s laser irradiation. Significantly, there is no char formation or carbonisation to be seen.

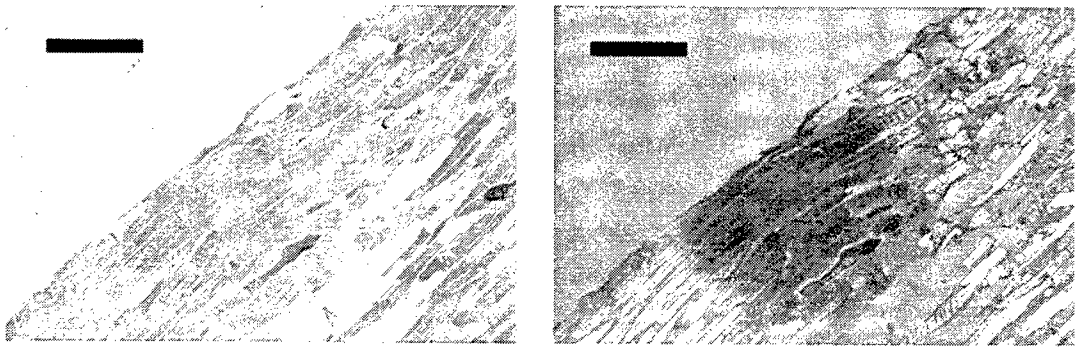

Figure 3. Histologic sections (H & E stain) of chicken breast tissue following 5 s cw exposure to the 1.5 μm fiber laser at 600 mW incident power, spot size ~150 μm. Left: minimal change is observable when inspected with routine light microscopy. Right: the same field of view under transmission polarising microscopy demonstrates a thermally affected zone, indicated by loss of tissue birefringence. Scale bars = 500 μm.

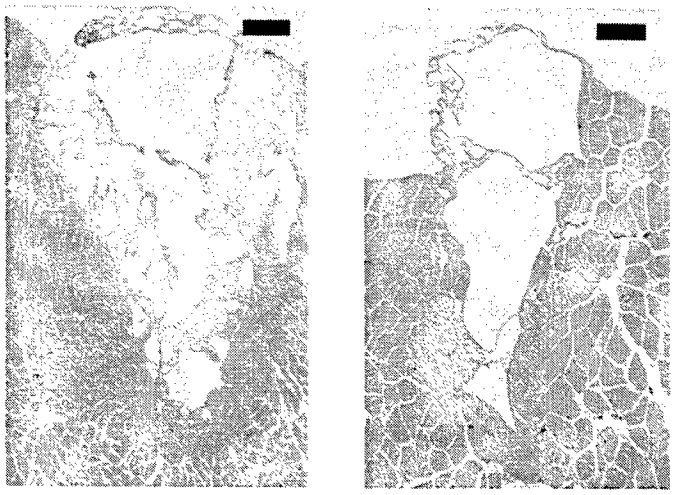

Figure 4. Histologic sections of porcine muscle tissue exposed to 1.98 μm cw fiber laser irradiation at 5 W incident power. Left: sample translated across the 150 μm beam focus at 0.25 $mm.s^{-1}$, scale bar = 300 μm. Right: sample translated across beam focus at 25 $mm.s^{-1}$, scale bar = 100 μm.

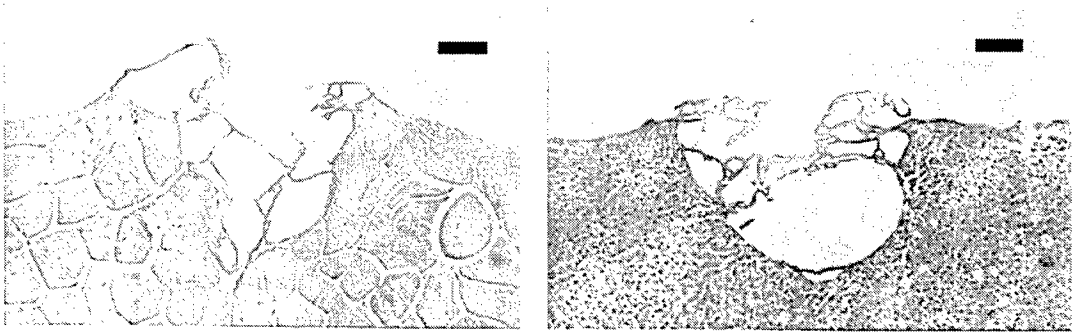

Figure 5. Histologic sections of chicken breast (left) and liver (right) tissue exposed to 2.71 μm cw fiber laser irradiation at 800 mW incident power for 0.5 ± 0.1 s, scale bar = 75 μm.

## 4. DISCUSSION

Preliminary laser-tissue interaction studies have been carried out with three newly developed, cw laser sources operating in the mid-infrared wavelength region. This study aims to compare the effects of these lasers both with each other, and with lasers currently established in medical practice. Continuous wave ablation of soft tissue has been described previously at Nd:YAG, argon ion and diode laser wavelengths [12-14] as a three-phase process, characterised by an increase in subsurface temperature and pressure, explosive vaporisation or "popcorn", and cyclic carbonisation. Formation of this strongly absorbing carbonised layer is required for tissue removal as a consequence of the low absorption coefficients in the visible and near-infrared spectral regions. It has been demonstrated here that at the more strongly absorbed wavelengths encountered in the 2 and 3 μm regions, soft tissue ablation may proceed without the presence of char, leaving normal tissue at boundaries of holes and slots. Future *in vivo* research is required to indicate the significance of this in terms of tissue healing and regeneration. Results presented here are consistent with McKenzie's three-zone model of cw ablation with the 10.6 μm $CO_2$ laser [15], providing a comparable absorption coefficient. Three zones of damage were revealed by histology; a carbonised zone, a vacuolated zone, and a sub-boiling coagulated zone, as shown in figure 4 (left). In general, by limiting the exposure time, carbonisation and char formation can be avoided, figure 4 (right).

Whilst there are few reported studies on laser-tissue interaction with cw sources at the 2 and 3 μm wavelengths, pulsed erbium and holmium doped bulk lasers have been widely investigated [16-20]. A pulse length shorter than the tissue thermal relaxation time will restrict thermal effects to a minimum[15], but on further reduction may involve generation of potentially damaging stress waves [21]. 250 μs pulses from Er:YAG and Er:YSGG lasers at wavelengths of 2.94 μm and 2.79 μm respectively, confined thermal effects to tens of microns in soft tissues, and to less than 10 μm with 40 ns Q-switched pulses, but with evidence of mechanical tearing in certain tissues [16, 17]. Thermal damage produced by the fiber lasers described here was restricted to a few hundreds of microns extending laterally from the irradiated site, greater than that produced by pulsed mid-IR lasers, but this is to be expected with exposure times longer than required for thermal confinement. There was no evidence of tensile stress induced tissue damage generated by pressure transients, a consequence of cw irradiation with exposure times far longer than required for stress confinement.

Whilst the resulting effect in tissue of cw laser irradiation at the 2.71 μm and 1.98 μm wavelengths was fundamentally similar, the consequence of relatively weak absorption at 1.5 μm was demonstrated by the inability to penetrate tissue samples during 80 s exposure at the 800 mW power level. This laser produced a purely thermal heating effect insufficient to raise tissue temperature to ablation threshold, but capable of inducing loss of tissue birefringence, indicating significant temperature elevation nonetheless.

The nature of interaction is strongly dictated by operating near the fundamental and harmonic peaks in the water absorption spectrum. However, it has been previously acknowledged that the dynamic, temperature-dependent optical properties of water must be considered when assessing the response of tissue to high-intensity laser irradiation. Both the 3 μm and the 2 μm absorption bands shift to shorter wavelengths as temperature rises, due to weakening of the hydrogen bond structure in water[22]. Walsh and Cummings[23] demonstrated that the Er:YAG laser cuts more deeply than the Er:YSGG laser, contradicting predictions based on the static, low-intensity absorption coefficient of water[6]. Based on these findings, the 2.71 μm wavelength of the erbium-doped fiber laser described here may also be expected to produce shallower cuts than a laser operating near the low-intensity water absorption peak at 2.94 μm. Whether these dynamic changes significantly affect the cw ablation process is unclear, but these issues will become increasingly relevant as fiber lasers proceed to be used in pulsed mode.

## 5. CONCLUSIONS

In conclusion, we have demonstrated the nature of interaction *in vitro,* between three recently developed cw, mid-infrared fiber lasers and soft tissues. Differences in the resultant effects in soft tissues can be explained by consideration of absorption coefficients at the three wavelengths examined. The effects demonstrated ranged from clean incision to non-ablative heating, suggesting a number of clinical outcomes may be realised. The small size, efficiency, inherent capability for fiber delivery and high output beam quality of these sources offer clear benefits for medical applications. Future studies will lead the way toward clinical evaluation and application of these, and other, fiber laser sources.

## ACKNOWLEDGMENTS

We gratefully acknowledge Sue Holland for the histological processing and Dr. Howard Carter, both of the University Dental Hospital of Manchester.

This project was partly funded by the UK Engineering and Physical Sciences Research Council Department of Trade and Industry Link - Solid State Lasers for Applications in Medicine (SSLAM).

## REFERENCES

1. Wigdor HA, Walsh JT, Featherstone JDB, Visuri SR, Fried D, Waldvogel JL, "Lasers in dentistry," *Lasers Surg Med* **16**, pp. 103-133, 1995.

2. Alster TS, "Clinical and histologic evaluation of six erbium:YAG lasers for cutaneous resurfacing," *Lasers Surg Med* **24**, pp. 87-92, 1999.

3. Vangsness CT, Watson T, Saadatmanesh V, Moran K, "Pulsed Ho:YAG laser meniscectomy: effect of pulsewidth on tissue penetration rate and lateral thermal damage," *Lasers Surg Med* **16**, pp. 61-65, 1995.

4. Verdaasdonk RM, van Swol CFP, "Laser light delivery systems for medical applications," *Phys Med Biol* **42**, pp. 869-894, 1997.

5. Azzolini C, Gobbi PG, Brancato R, Trabucchi G, Codenotti M, "New semiconductor laser for vitreoretinal surgery," *Lasers Surg Med* **19**, pp. 177-183, 1996.

6. Hale GM, Querry MR, "Optical constants of water in the 200-nm to 200-μm wavelength region," *Appl Opt* **12**, pp. 555-563, 1973.

7. Po H, Cao JD, Laliberte BM, Minns RA, Robinson RF, Rockney BH, Tricca RR, Zhang YH, "High power neodymium-doped single transverse mode fibre laser," *Electron Lett* **29**, pp. 1500-1501, 1993.

8. Pollnau M, "The route toward a diode-pumped 1-W erbium 3-μm fiber laser," *IEEE J Quantum Electron* **33**, pp. 1982-1990, 1997.

9. Jackson SD, King TA, Pollnau M, "Diode-pumped 1.7-W erbium 3-μm fiber laser," *Opt Lett* **24**, pp. 1133-1135, 1999.

10. Jackson SD, King TA, "High-power diode-cladding-pumped Tm-doped silica fiber laser," *Opt Lett* **23**, pp. 1462-1464, 1998.

11. Jackson SD, King TA, "Efficient high power operation of a Nd:YAG-pumped Yb:Er-doped silica fibre laser," *Opt Commun* **172**, pp. 271-278, 1999.

12. Verdaasdonk RM, Borst C, van Gemert MJC, "Explosive onset of continuous wave laser tissue ablation," *Phys Med Biol* **35**, pp. 1129-1144, 1990.

13. LeCarpentier GL, Motamedi M, McMath LP, Rastegar S, Welch AJ, "Continuous wave laser ablation of tissue: analysis of thermal and mechanical events," *IEEE Trans Biomed Eng* **40**, pp. 188-200, 1993.

14. Youell PD, Dickinson MR, King TA, "Investigations into the interaction of a high power semiconductor diode laser with biological tissue," in *Laser Interaction with Hard and Soft Tissue*, van Gemert MJ, Steiner RW, Svaasand LO, Albrecht HJ, Editors, Proc. SPIE 2077, pp. 109-117, 1993.

15. McKenzie AL, "Physics of thermal processes in laser-tissue interaction," *Phys Med Biol* **35**, pp. 1175-1209, 1990.

16. Frenz M, Pratisto H, Könz F, Jansen ED, Welch AJ, Weber HP, "Comparison of the effects of absorption coefficient and pulse duration of 2.12-μm and 2.79-μm radiation on laser ablation of tissue," *IEEE J Quantum Electron* **32**, pp. 2025-2036, 1996.

17. Dickinson MR, Charlton A, King TA, Freemont AJ, Bramley R, "Studies of Er:YAG laser interactions with soft tissue," *Lasers Med Sci* **6**, pp. 125-131, 1991.

18. Walsh JT, Flotte TJ, Deutsch TF, "Er:YAG laser ablation of tissue: Effect of pulse duration and tissue type on thermal damage," *Lasers Surg Med* **9**, pp. 314-326, 1989.

19. Domankevitz Y, Lee MS, Nishioka NS, "Effects of irradiance and spot size on pulsed holmium laser ablation of tissue," *Appl Opt* **32**, pp. 569-573, 1993.

20. van Leeuwen TG, Jansen ED, Motamedi M, Borst C, Welch AJ, "Pulsed laser ablation of soft tissue," in *Optical-thermal response of laser irradiated tissue*, Welch AJ, van Gemert MJC, Editors, pp. 709-763, Plenum, New York, 1995.

21. Cummings JP, Walsh JT, "Tissue tearing caused by pulsed laser-induced ablation pressure," *Appl Opt* **32**, pp. 494-503, 1993.

22. Jansen ED, van Leeuwen TG, Motamedi M, Borst C, Welch AJ, "Temperature dependence of the absorption coefficient of water for mid-infrared laser radiation," *Lasers Surg Med* **14**, pp. 258-268, 1994.

23. Walsh JT, Cummings JP, "Effect of the dynamic optical properties of water on midinfrared laser ablation," *Lasers Surg Med* **15**, pp. 295-305, 1994.

---

* Correspondence: phone +44 (0)161 275 4292, fax +44 (0)161 275 4293, email mp@fs4.ph.man.ac.uk

SJ is now with the Optical Fibre Technology Centre, Australian Photonics CRC,
101 National Innovation Centre, Australian Technology Park, Eveleigh NSW 1430, Australia.

# Laser tissue interaction of a continuous wave 2μm, 3μm cascade oscillation fiber laser: sharp incision with controlled coagulation layer thickness

Tsunenori Arai*[a], Tetsumi Sumiyoshi[b], Kyota Naruse[c], Miya Ishihara[a], Shunichi Sato[d], Makoto Kikuchi[a], Tadashi Kasamatsu[b], Hitoshi Sekita[b], and Minoru Obara[c]

[a]Dept. of Med. Eng., National Defense Medical College, Tokorozawa, Saitama 359-8513 Japan
[b]Opt-Elec. Comp. Labs., Opt-Elec. and High-Freq. Device Labs, NEC Corp
[c]Dept. of Elec., Facult. of Sci. and Tech., Keio University
[d]Div. of Biomed. Info. Sci., National Defense Medical College Res. Inst.

## ABSTRACT

We studied coagulation layer controlled incision with newly developed continuous wave 2μm, 3μm cascade oscillation fiber laser in vitro. Since this laser device simultaneously oscillates 2μm and 3μm radiation, we could change tissue interaction by arranging power ratio of 2μm to 3μm radiation. About one watt of total irradiation power with various power ratios was focused to extracted fresh porcine myocardium or anesthetized rabbit on an automatic moving stage to obtain line incision. Macro photograph and microscopic histology were used to observe tissue interaction phenomenon. The incised specimen showed that precise cutting groove with thin coagulation layer was attained by 3μm based radiation, mean while addition of 2μm radiation to 3μm radiation made coagulation layer thicker. A heat conduction simulator using finite-element method was used to qualitatively explain obtained coagulation layer thickness. This precise incision with controllable side coagulation layer may effective to control bleeding during incision, for instance, for skin, liver, and kidney incisions. Pure continuous wave radiation of 2μm and 3μm may eliminate stress wave induced tissue damage which is frequently found in Ho:YAG and/or Er:YAG tissue interactions. Moreover, sapphire fiber might offer flexible power delivery to this new laser to establish endoscopic application and/or to improved beam handling.

Keywords: Fiber laser, Cascade oscillation, Mid-infrared laser, Incision, Coagulation, Laser therapy.

## 1. INTRODUCTION

Carbon dioxide laser scalpel and Nd:YAG laser coagulator have been popular instrument in surgical operations. However, variable functioned laser system which can change its cutting and coagulating characteristics has never been developed in spite of cheap electric surgical unit can easily vary its cutting/coagulating function. The reason of difficulty to develop the multi-functioned laser surgical system may be attributed to fixed tissue interaction at certain fixed laser wavelength. To achieve the multi-function system, multiple wavelength or variable wavelength system has been studied. However, there has been no practical system because these multiple or variable wavelength laser system should be bulky and/or expensive. Moreover, it is difficult to prepare a flexible waveguide for these systems because the wavelength for cutting and the wavelength for coagulation are widely separated[1].

We aim to develop a compact sophisticated variable functioned laser surgical scalpel system using the multiple wavelength concept. Our aim is to obtain sharp cutting characteristics with variable coagulation layer thickness(i.e. variable hemostatic capability). In order to realize this function, we employed 3μm and 2μm infrared radiation. Water absorption spectra shows strongest absorption (absorption coefficient:10000$cm^{-1}$) on 3μm band due to OH radical fundamental vibrational

*Correspondence:Email:tsuneari@ndmc.ac.jp;Telephone:81 42 995 1596;Fax:81 42 996 5199



In *Laser-Tissue Interaction XI: Photochemical, Photothermal, and Photomechanical*, Donald D. Duncan, Jeffrey O. Hollinger, Steven L. Jacques, Editors, Proceedings of SPIE Vol. 3914 (2000)
1605-7422/00/$15.00

absorption. This 3μm radiation may be the best cutting wavelength in infrared. To append coagulation capability to this sharp cutting, we chose a wavelength which has medium absorption coefficient (20-80cm$^{-1}$) so that we employed 2μm band. To avoid stress tissue damage, we prefer continuous radiation rather than pulsed radiation.

We newly developed a compact high power and high efficiency all solid-state fiber laser system using $Ho^{3+}$ doped fluorozirconate-based fiber with particular 1.15μm excitation wavelength to obtain 3μm and 2μm continuous radiation simultaneously. We studied laser tissue interaction of this $Ho^{3+}$ doped fluorozirconate-based fiber in vitro. We applied heat conduction estimation to explain variable coagulation layer thickness of this laser.

## 2. MATERIAL AND METHOD

### 2.1.HOLMIUM ION DOPED FLUOROZIRCONATE-BASED FIBER LASER

The $Ho^{3+}$ doped fluorozirconate-based fiber laser which operate continuous cascade oscillation with 1.15μm Raman fiber optical source excitation has been developed co-author Sumiyoshi et al[2-3]. Fig. 1 shows energy diagram of $Ho^{3+}$ ion. The transition from $^5I_6$ to $^5I_7$ level can emits 3μm band radiation, however, long life time of $^5I_7$ level(lower laser level for 3μm radiation) makes this 3μm laser system inefficient. The transition from $^5I_7$ to $^5I_8$ level emits 2μm band radiation. Since $^5I_8$ level is grand state, this 3 level laser system for 2μm band is also inefficient. Since these 3μm laser system and 2μm laser system are arranged in series, you may get cascade oscillation when intensive selective excitation to $^5I_7$ level and effective cooling to reduce $^5I_8$ level are simultaneously achieved. Sumiyoshi et al. employed 1.1μm band optical excitation using a Yb doped silica Raman shifter from 800nm band continuous wave diode laser driver. They also employed $Ho^{3+}$ doped fiber laser configuration to obtain efficient cooling with intensive excitation. The excitation efficiency was very high because the single mode emission from above 1.1μm band light source is easily collimated into multi-mode infrared fiber made of fluorozirconate-based($ZrF_4$-$BaF_2$-$LaF_3$-$AlF_3$-NaF: ZBLAN) glass. Consequently we could obtain all solid state laser system.

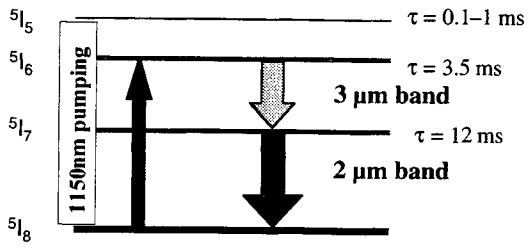


Fig. 1 The energy diagram of $Ho^{3+}$ ion and the cascade oscillation with our unique pumping.

### 2.2 EXPERIMENTAL SET-UP

The experimental set-up is illustrated in Fig.2. This set-up photograph is shown in Fig.3. The Yb doped silica based fiber pumped with the continuous wave laser diode emitted 1.15μm emission of 5W to the $Ho^{3+}$ ZBLAN fiber laser. Using 2.5m fiber with 5W of 1.15μm pumping power, we obtained 3W total output (3μm:1.4W, 2μm 1.6W). Emission wavelengths from this laser device were 2.93μm for $^5I_6$ to $^5I_7$ transition and 2.06μm for $^5I_7$ to $^5I_8$ transmission, respectively. We obtained this 3W combined laser output using 2.5m-long, 10μm -core diameter ZBLAN fiber. $Ho^{3+}$ ion dope density was 2500ppmw. The power ratio between 3μm band and 2μm band was almost 1. The efficiency against 1.15μm pumping light was 65%(slope).

The winded ZBLAN fiber laser around a reel in a black colored box located upper level of the system (see Fig.3). The black colored box on the lower level was diode laser driver for 1.15um light source. The lower and upper box were connected Yb doped silica fiber(Raman shifter). The 3μm, and 2μm beams emitted horizontally from upper level. We used

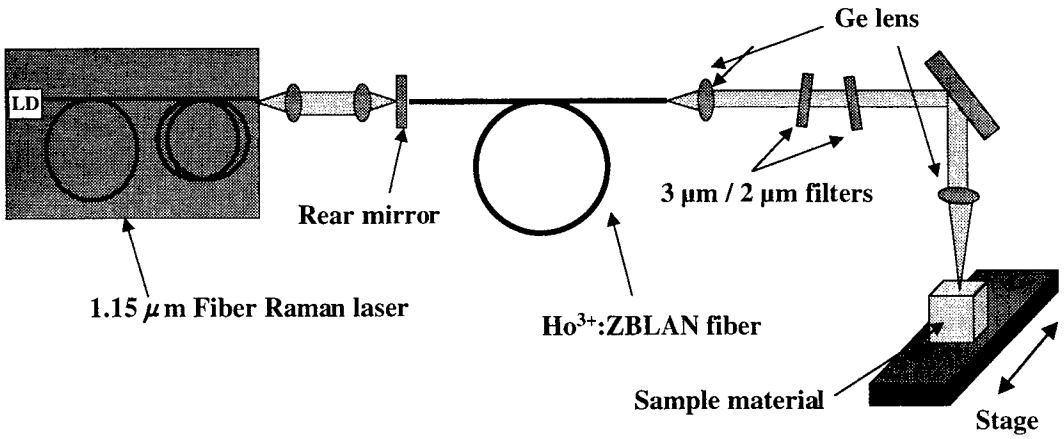


Fig. 2 Schema of experimental set-up

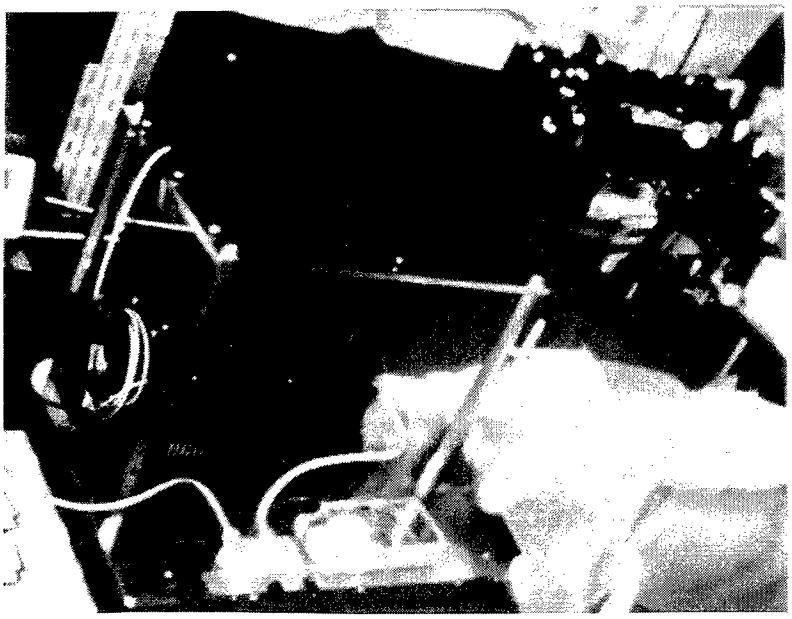

Fig. 3 The photograph of experimental set-up.

the filers which had different transmissions for 2μm and 3μm to arrange 2μm /3μm power ratio. The laser beam was turn down by a gold coated reflector and 70mm F.L. Ge lens for collimating. We employed total power 0.9W laser beam for tissue interaction experiments varying 2μm /3μm power ratio by filter arrangement. The sample materials put on the one axis automatic stage to move the laser beam to make line incision.

Japanese white rabbits were totally anesthetized by pentobarbital sodium. The rabbit hair was eliminated by a safety shaver to prepare cutting experiment. The rabbit liver was surgically exposed by median incision. Porcine myocardium cubes for in vitro experiment were cut down from extracted fresh porcine heart which was given from an abattoir. The ablated samples were fixed by formaldehyde solution or glutaraldehyde solution. In the case of formaldehyde fixation, hematoxylin-eosin staining was applied to make specimen for microscopic observation. In the case of glutaraldehyde fixation, the fixed sample was median cut at the ablated crater and observed by a fiber-optic stereoscopic microscope. There was no difference on incision depth between these two method, however observed coagulation layer thickness by the glutaraldehyde fixation/stereoscopic microscope procedure was thicker than that of the formaldehyde fixation/H.E. stain/microscope procedure.

## 3.RESULTS AND DISCUSSIONS

### 3.1 CUTTING CAPABILITY OF 2.93 MICRO METER CONTINUOUS RADIATION

We determined cutting capability of 2.93μm continuous radiation comparing to continuous $CO_2$ laser(10.6μm). This incision depth vs beam traveling speed data is summarized in Table 1. The sample was porcine myocardium. The laser powers were kept to 0.9W. Although collimating optical configurations for each laser beam were litter different, 2.93μm radiation showed superior cutting capability against $CO_2$ laser. The ratio of 2.93μm radiation cutting capability to 10.6μm was about 1.3 to 1.5.

| Beam traveling [mm/s] | incision depth [mm] λ:2.93μm | λ:10.6μm |
|---|---|---|
| 0.15 | 2.20 | 1.70 |
| 0.25 | 1.80 | 1.30 |
| 0.50 | 1.10 | 0.74 |
| 0.75 | 0.75 | 0.59 |

Table 1 Comparison of cutting capability between 2.93μm continuous radiation and 10.6μm continuous radiation.

Beam power:0.9W, sample:myocardium. Focusing parameter for 2.93μm: 70mm F.L. and 180μm diameter at F.P. Focusing parameter for 10.6μm: 100mm F.L. and 240μm diameter at F.P.

Fig. 4 shows the microscopic photograph of the H.E. stained myocardium specimen with 2.93μm cutting groove. The cutting conditions of this specimen corresponds to 0.75mm/s beam traveling in Table 1. Thermal damaged zone thickness which was recognized by thick colored zone by the H.E. stained specimen was up to 100μm. Since the beam traveling speed was slow, the thermal damaged zone thickness might be governed by thermal conduction rather than optical penetration.


Fig. 4 Microscopic observation of H.E. steined specimen ablated by 2.93μm radiation.

### 3.2 CONTROL OF CUTTING/COAGULATING CAPABILITY BY POWER RATIO CHANGE

We demonstrated the controllability of cutting/coagulating capability by the power ratio change of 2.93μm and 2.06μm radiation. Fig. 5 shows the dependence of the power ratio on incised depth and coagulation layer thickness. in vivo animal experiment using rabbit liver. When 2μm radiation ratio was increasing, cutting capability was decreasing with increasing coagulation layer thickness. The scattering of plots in Fig.5 indicate influence of bleeding. Therefore, the data scattering was small when we used low 2μm radiation ratio, because deep incision induced chance of bleeding. We successfully demonstrated that control of cutting/coagulating capability by power ratio change of 2.93μm and 2.06μm radiation.

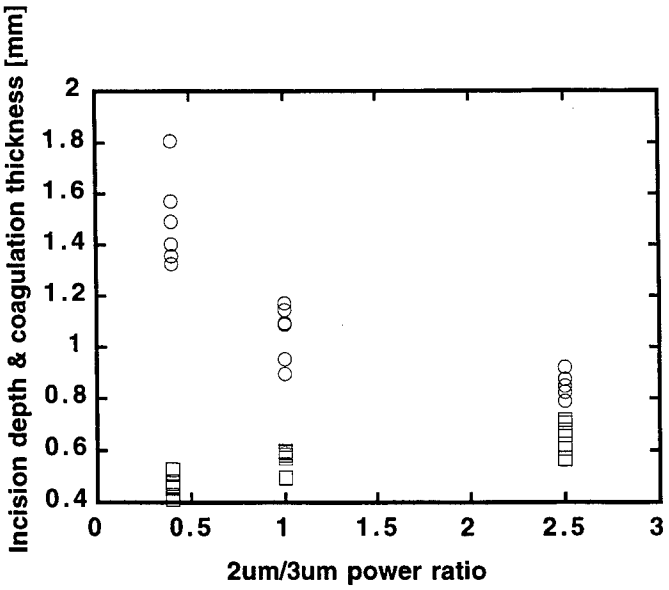


Fig. 5 Dependence of the power ratio on incised depth and coagulation layer thickness. Beam power:1.4W, beam traveling: 1mm/s, sample:rabbit liver in situ.

Fig. 6 indicates visual observation of cutting groove cross-section on myocardium.. Beam power was 0.9W with 0.25mm/s beam travelling. In Fig. 6, Right to left, the 2μm/3μm power ratios are 7.2, 0, respectively.

Fig. 6 Photograph of visual observation of cutting groove cross-section on myocardium.
Right to left, the 2μm/3μm power ratios are 7.2, 0, respectively. Beam power:0.9W with 0.25mm/s beam travelling.

### 3.3 THERMAL CONDUCTION ESTIMATION

To understand this variable function by changing power ratio, we calculate thermal conduction by market-available QuickTherm™ software (Res. of Computation. Mechanics, Inc., Tokyo, Japan), a 2-dimensional heat-conduction simulator with a finite-element method. We assumed that heat conduction occurs sequentially after thermal ablation(mass loss, i.e., cutting groove formation). Then, the irradiation intensity which used in calculation was set to 1/30 of original intensity, because we assumed energy fraction of heat deposit (finally) to tissue was 0.6 and we also assumed that sharp groove shape reduced irradiation intensity. Using thermal characteristics of water with arranging variable heat capacity corresponds to tissue coagulation, we obtained Fig.7 for 2.93μm radiation and Fig.8 for 14% 2.93μm light addition in 2.06μm radiation. These conditions correspond to Fig.6. The mesh size of the finite-element model surface was set at least 1/4 of 2.06μm light penetration. Since 2.93μm light penetration is very small, 2.93μm radiation heat deposition was set on the surface nodes. The bright area which is about 70 degree is obviously restricted in Fig. 7 than Fig.8. Our heat conduction calculation offers qualitative tendency to thermal damage layer thickness with changing 2.06/2.93μm power ratio. We should use the complete simulation model which contains thermal ablation, deformation, etc. to understand the quantitative evaluation of cutting/coagulating function change.

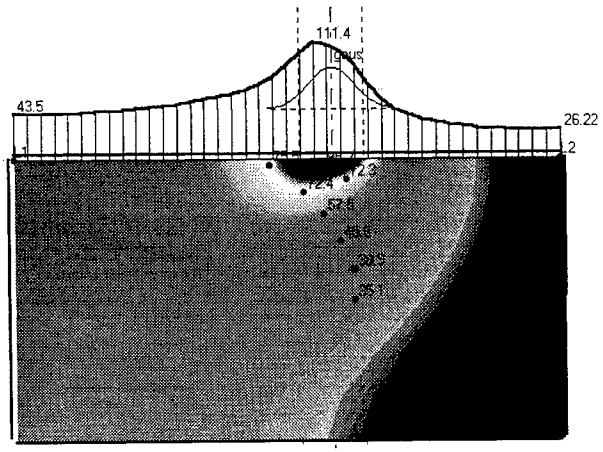


Fig. 7 Estimated thermal distribution for 2.93μm radiation. Beam power:0.9w, beam travelling:0.25mm/s.

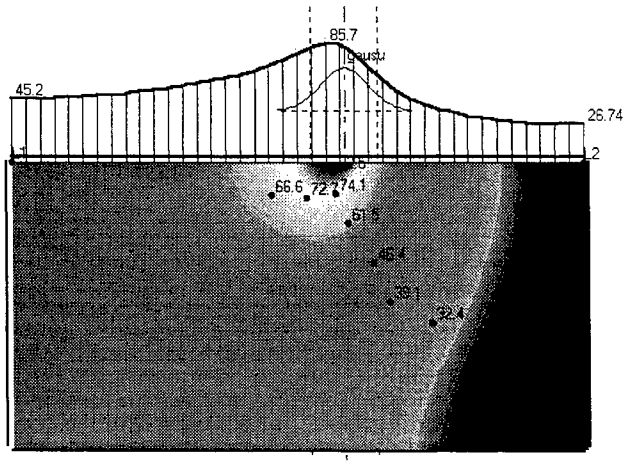


Fig. 8 Estimated thermal distribution for 2μm/3μm power ratio of 7.2. Beam power:0.9w, beam travelling:0.25mm/s.

### 3.4 APPLICATIONS OF THE HOLMIUM ZBLAN FIBER LASER TO MEDICAL TREATMENT

As shown in our results, the major characteristics of the cascade oscillation $Ho^{3+}$ ZBLAN fiber laser is sharp cutting like $CO_2$ laser scalpel with variable coagulation layer thickness. Therefore, this laser tissue interaction is helpful to plastic surgery of head, neck and face region, where precise incision with controlled blood bleeding and cosmetic scaring suppression is necessary. We also recommended to apply liver, kidney, and tongue surgery with parenchymatous bleeding.

The other particular characteristics of our laser is acoustic damage free thermal ablation in 2μm and 3μm region because of continuous laser radiation in both 2μm and 3μm band. There have been many 2μm and 3μm laser treatment systems by flash lamp pumping Ho lasers and Er lasers. The emissions of these equipment are spike shaped pulsed radiation with 200 to 250μs in total duration. In living tissue, pulsed radiation of these mid-infrared laser from a silica fiber make a water vapor bubble. This bubble is available to enhance cutting capability to put stress force around the bubble in its expansion phase. However, excess stress force may induce dissection of tissue. Moreover, in collapse phase of the bubble, the intensive shockwave occurs from the bubble, so that sometimes it affect acoustic tissue damage. Our novel continuous-

wave high-efficiency cascade oscillation system offers unique safe laser tissue interaction to medical applications.All solid sate laser system may be helpful to reduce maintenance cost and/or running cost. Moreover, this compact fiber and diode laser based system may be fabricated up to 1 square feet volume.

We have various method to establish the flexible fiber delivery of our 2μm, 3μm cascade oscillation system. The advanced technology of mid-infrared flexible optical transmission line in recent years make it possible to deliver our laser emissions. Power scalability of this laser may depend on damage threshold of the ZEBLAN fiber end. We could predict that we may construct total power 10W class laser without any conceptual change in the laser system.

## 4. SUMMARY

We studied coagulation layer controlled incision with newly developed continuous wave 2μm, 3μm cascade oscillation fiber laser in vitro. Since this laser device simultaneously oscillates 2μm and 3μm radiation, we could change tissue interaction by arranging power ratio of 2μm to 3μm radiation. About one watt of total irradiation power with various power ratios was focused to extracted fresh porcine myocardium or anesthetized rabbit on an automatic moving stage to obtain line incision. Macro photograph and microscopic histology were used to observe tissue interaction phenomenon. The incised specimen showed that precise cutting groove with thin coagulation layer was attained by 3μm based radiation, mean while addition of 2μm radiation to 3μm radiation made coagulation layer thicker. A heat-conduction simulator using finite-element method was used to qualitatively explain obtained coagulation layer thickness. This precise incision with controllable side coagulation layer may effective to bleeding controlled incision, for instance, skin, liver, and kidney incisions.

## ACKNOWLEDGEMENT

This work was supported in part by the Grant-in-Aid for Cancer Research(10-37) from the Ministry of Health and Welfare(Japan).

## REFERNCES

1. T. Arai and M. Kikuchi:The variable-function fiberoptic laser apparatus using Nd:YAG and carbon monoxide lasers, in Advances in Nd:YAG Laser Surgery, S. N. Joffe and Y. Oguro ed., Springer-Verlag, New York, 1987, pp. 294-301.
2. T. Sumiyoshi and H. Sekita, "Dual-wavelength continuous-wave cascade oscillation at 3 μm and 2 μm with a holmium-doped fluoride-glass fiber laser," Opt. Lett., vol. 23, No. 23, pp.1837-1839, 1998.
3. T. Sumiyoshi, H. Sekita, T. Arai, S. Sato, M. Ishihara, and M. Kikuchi, "High-power continuous-wave 3- and 2-μm cascade $Ho^{3+}$:ZBLAN fiber laser and its medical applications," IEEE J. Slect. Topics in Quant. Electron. 5, pp. 936-943, 1999.

# SESSION 10

# Laser-Tissue Interaction

# Human Cell Viability to Laser Pulse and Ion Transport Processes

Dmitri Lapotko*[a], Tat'yana Romanovskaya[b]

[a] Luikov Heat and Mass Transfer Institute, Minsk, Belarus, 220072

[b] International Sakharov Environmental University, Minsk, Belarus,

## ABSTRACT

We have studied experimentally the problem of cell viability during laser-tissue interaction: how the cell viability can be regulated under certain laser regime. Many modern laser therapeutic techniques assume that cells should survive laser therapy or even to become activated (laser stimulation of immune system). An influence of ion balance was studied for human Red Blood Cells (RBC) during in vitro measurements of single RBC viability after laser pulse. Single cell viability was measured optically with Laser Viability Test which is based upon interpretation of cell photothermal response to pump pulse (532 nm, 10 ns, 10 – 50 μJ at 12 μm diameter). According to our experiments laser-induced cell damage occurs at different laser energy levels within one cell population (heterogeneity of cell viability) and besides is donor-dependent. The latter result means that laser therapeutic dose should be adjusted individually. For solutions of the ions $Na^+$, $K^+$, $Ca^{++}$ and $Mg^{++}$ we have found strong dependence of cell viability upon the process of ion transport through the cell membrane which was regulated by variation of concentration and composition of above mentioned ions. An increase of $Na^+$ or $K^+$ concentration causes a decrease of RBC laser viability.

**Keywords:** blood cell ,viability, photodamage, ion, photothermal

## 1. INTRODUCTION

We consider the problem of viability of various human cells during their interaction with laser radiation: how the viability can be provided and controlled. Many modern laser therapeutic techniques assume that cells should survive laser therapy or even such therapy is used to control cell functional activity(immune stimulation for example). Most of laser-based studies of this problem are connected mainly with regimes which are destructive for cells and cell damage is considered as a main issue. Such approach is inherited from surgery and aims to kill the cells. As a result the studies of laser-tissue interaction covers the regimes of radiation which assumes destruction of living cells or tissues[1, 2, 3].
Those studies suggested few mechanisms of cell damage by laser radiation: thermal [3, 4, 5, 6], acoustical[1] and chemical[5,6].
Cell viability control should be done with methods which do not affect cell viability properties during diagnostic procedure. Furthermore for correct results cell should be maintained under natural condition. But the most recognized methods as fluorescent require introduction into the cells of various fluorochromes which alter cell functions and viability.

This problem can be solved with photothermal method which allows direct studies of the sample in 'as is' condition using only natural absorbing properties. Studies of functional activities and monitoring of living cells requires that cells should survive laser radiation. Thus the latter may be considered as a load factor when being delivered properly into a single cell. Such load has thermal and mechanical origin due to light absorption by natural cell chromophores. With optical non-invasive registration of cell response we come to the idea of photothermal cytometry [7, 8, 9, 10].

* Correspondence: Email: ld@ ns1.hmti.ac.by; telephone: (375172) 842 483; Fax:(375172) 842 486



In *Laser-Tissue Interaction XI: Photochemical, Photothermal, and Photomechanical*, Donald D. Duncan, Jeffrey O. Hollinger, Steven L. Jacques, Editors, Proceedings of SPIE Vol. 3914 (2000)
1605-7422/00/$15.00

Main tasks of this study were:
1.to evaluate parameters which can be used to measure cell viability to laser load for individual patients;
2.to consider experimentally how some basic biochemical factors may influence cell viability.

Red blood cell (RBC) were chosen for the following reasons:
- RBC in functional terms has limited ability to restore its structure, to maintain energy balance and ion transport through the membrane. Besides RBC does not produce proteins neither incorporates DNA and therefore is considered to be rather stable and predictable cell.
- in a visible range of wavelengths RBC has strongest absorption of its main component – hemoglobin - and therefore may be considered as most vulnerable cell. Thus in terms of safety of laser doses RBC is a good target cell.

## 2. METHODS AND MATERIALS

### 2.1. Laser Viability Test

The method for a living cell population analysis is based on a single cell viability control after irradiation with laser pulse. The traditional techniques for cell functional analysis require considerable amount of the sample solution and are not fast. In the case of pulsed laser illumination of a single cell the latter becomes a subject of thermal and mechanical load due to light absorption by cellular components. Thus a load test can be considered in which the response of each cell to a laser pulse is analyzed if we can avoid total cell ablation being the only result of irradiation. Apparent advantages of such approach are that the load factor can be controlled precisely through the laser pulse parameters, load is delivered into a certain cell, minimal sample quantities are required. If the entire procedure is automated, the method may provide express cell diagnostics. The influence of thermal factors upon cells has been the subject of continuous studies[11, 12], because the functional state of the cells depends upon temperature. The present situation with research of cell thermal properties is well established for long (from minutes to several days) exposures to heat [13, 14, 15]. But exposure to heat during the laser-cell interaction is much shorter ($10^{-9}$-$10^{-3}$s for a pulsed laser). The study of thermal effects in cells under such conditions is rather complicated, but it is important for the effective application of laser techniques, where heat action or photodamage may occur. However, there are no techniques that would allow the studies of non-stationary short thermal processes in a single living cell. Suggested photothermal method is applied for investigation of living cells.

Two processes that follow the light pulse absorption are considered as loading factors for the cell. The thermal load that emerges in nanoseconds and acts inside the cell during $10^{-6}$-$10^{-4}$ s. This factor may lead to cell lysis. Mechanical load caused by a pressure wave. It acts during $10^{-9}$-$10^{-8}$ s after the initial T-jump and causes membrane deformation. This deformation may also result in a cell damage. The cell is illuminated by a CW-laser probe beam with the power and wavelength satisfying noninvasive conditions. A photothermal signal is defined as the normalized ratio of the probe beam power P as the detector plane:

$$S(t) = \frac{\Delta P(t)}{P}, \qquad (1)$$

where P is the probe beam power measured prior to cell illumination by the pump pulse.

The quantity S - a photothermal (PT) signal - presents an integral response of the cell on the action of the pump pulse. This response describes the relative change in the refractive index due to thermal and pressure factors after pumplaser pulse absorption.

For a certain cell population with known absorption properties, cell damage occurs when the pump pulse energy E approaches some critical level. The cell is considered to be damaged when optically detectable irreversible changes of the cell shape, volume and structure occur. After irradiation the cell with one pump pulse

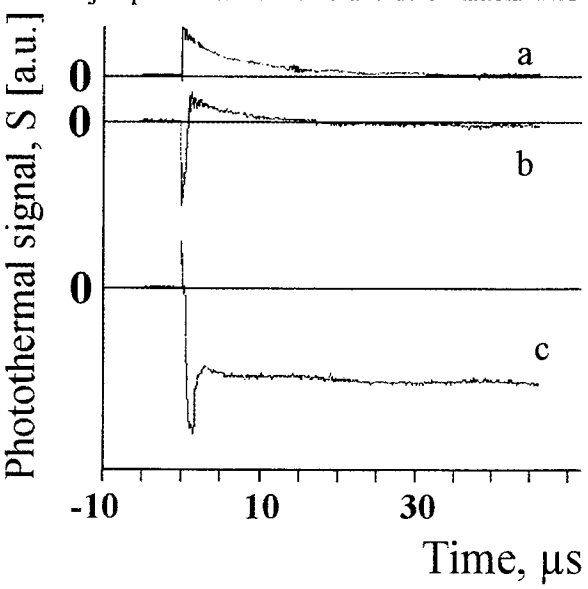


Figure1. Photothermal responses of human red blood cells. Pump pulse:, λ = 532 nm, 10 ns

we may treat it as being intact or damaged cell according to its photothermal response (Fig. 1). When the probe beam signal recovers to its original state after illumination, the cell is considered to survive the pulse (case 'a', Fig. 1 ). If it performs irreversibly (cases 'b' and 'c') the cell is considered to be damaged. Fast sharp negative peak has a width within 1 mcs. We suggest that such short photothermal signal is associated with the damage to membrane. This was verified during visual control of the cells: we had always observed either RBC lysis during 1-10 s or cell burst. When N cells within one population are consequently irradiated with one pulse of the same energy, we can measure viability index VI(E) for this population:

$$I = \frac{N_d}{N}, \tag{2}$$

where $N_d$ is the number of damaged cells.
Whole procedure is defined as Laser Viability Test - LVT. The smaller is V, the higher the average cell viability.

### 2.2.Experimental set up

Technical realization of the viability test is shown at Fig.2. All set up is based upon optical microscope.
The cell plane is defined as the surface of cell monolayer. Its vertical position almost coincides with the bottom of the quvette where the cells lay fixed after having been injected into the quvette (see below).

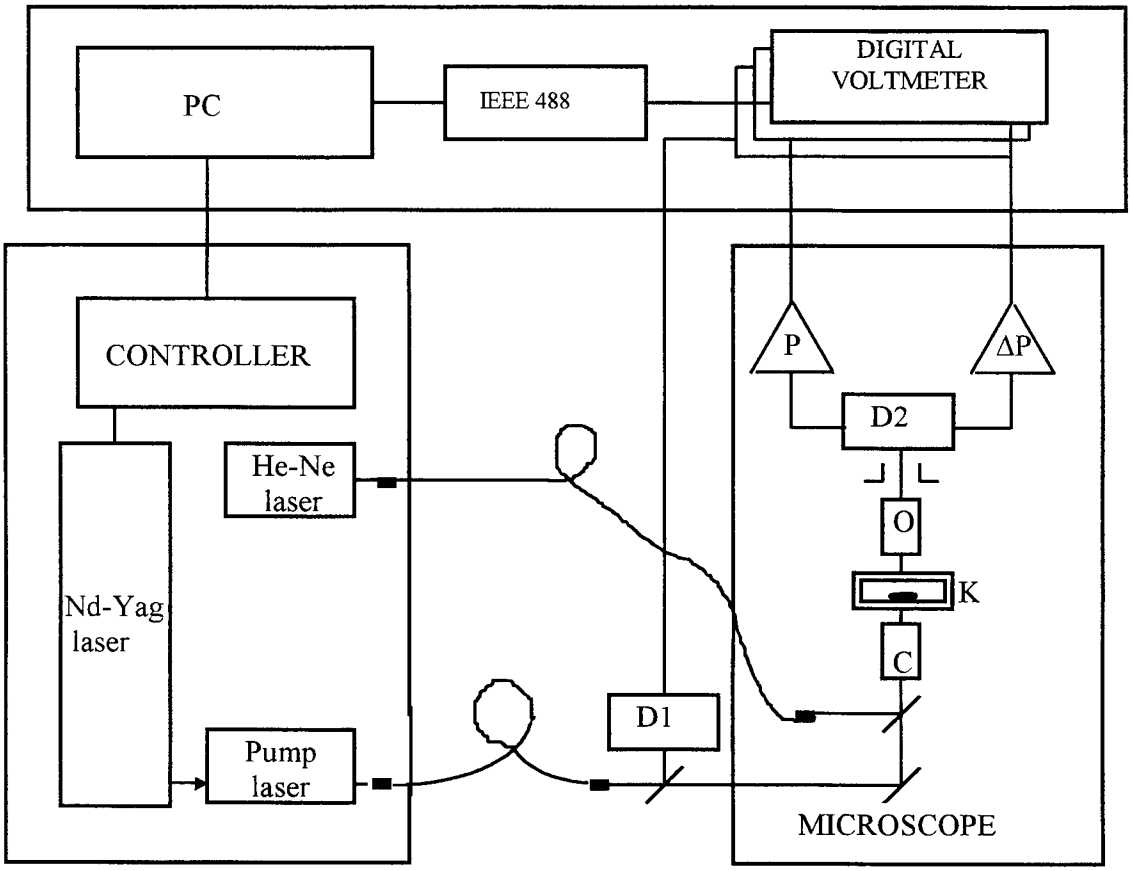


Figure 2. An experimental set up. D1 - pump energy meter, D2 - probe beam detector with axial diaphragm and two preamplifiers: for the base level signal (P) and for the impulse signal (ΔP); O - microobjective;C - microscope condenser; K - the cassette with sample quvettes, the cassette is fixed on a microscope stage

The probe beam registration path includes a microobjective 20×0.4 (LOMO, St.Peterburg, Russia), the pump radiation stop-filter, detector diaphragm (0.5 mm) and a custom built photo-diode detector with a preamplifier. The detector was specially built for this setup on the basis of a PIN-diode FD-256 (Polyarone, Ukraine) and was mounted inside the microscope MBI-15 (LOMO, Russia) with 1 mm diaphragm at a distance of 35 cm from the microobjective.

The preamplifier has two signal outputs. Through one, a fast component $\Delta P$ (100 Hz ÷ 50 MHz) is available. The other is designed to measure the constant level of probe laser power P. Both signals are acquired by the host PC through digital voltmeters and IEEE-488 interface. Finally, the following data are available:

- the probe beam level P;
- the photothermal signal $S(t)= \Delta P(t)/P$, with it peak value and duration;
- the pump pulse energy $E_o$ and wavelength $\lambda$.

The pump pulse energy is measured at the microscope input. The beam geometry is stable and the beam diameter at the sample plane is almost twice larger than the RBC diameter. Thus, we provide equal conditions during laser irradiation of various cells. The human RBC have been acquired from the venous blood of a healthy donor. Photothermal signal from each cell is analyzed by the program which makes the counts of damaged cells and calculates viability index and other data.

## 3. EXPERIMENTAL RESULTS

### 3.1.Viability of the Red Blood Cells under normal conditions

The blood samples of 27 normal donors of various age (20-40 years old) and sex were studied. In each sample 100-150 cells were tested to obtain viability index. The viability of RBC was studied as a function of pump wavelength, energy (Fig. 3). To investigate the mechanism of cell damage, we have studied the dependence of the viability index VI on the pump energy and spectral distribution of the destructive energy levels $E_d \rightarrow E_d(\lambda)$. The function VI(E) is measured at 532 nm (Fig. 3).
For a certain cell population no cell is damaged by the pulse with the energy below some limit and no cell survives the pulses with the energy above the other limit. In the gap between two limits the behavior of the cell viability follows the rule: the higher the energy - the greater the damage. Under certain conditions of the cell irradiation we consider the pulse energy to be the main factor of damage (of course for a fixed pump wavelength).
The values of the pump energy were determined for various pump wavelengths (Fig. 4).

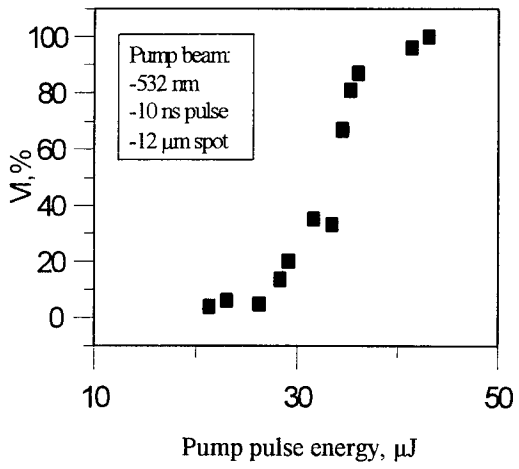


Figure 3. The dependence of human RBC viability (V1) upon pump pulse energy E (532 nm, 5 ns)

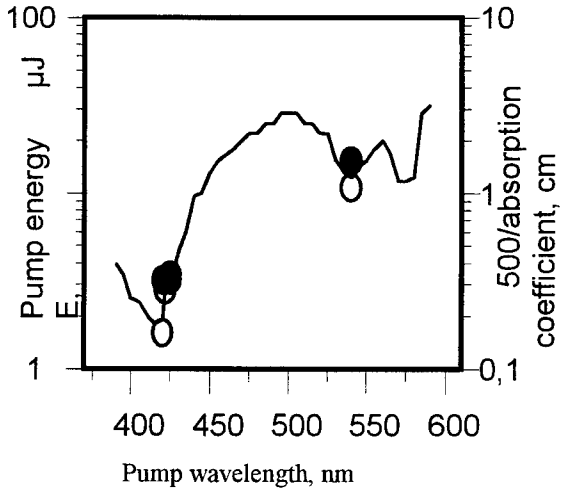


Figure 4. Human Red Blood Cell destruction pump energies $E_0$ at 420 nm (3 cell populations) and 532 nm (averaged for10 cell populations) acquired for low damage region (0<VI<0.3 (o)) and high damage region (0.6<VI<1 (●)). The solid line is the inverted absorption spectrum of the same whole blood

Two spectral regions which contain the peaks of hemoglobin (Hgb) absorption were studied. For several human RBC populations with 100 cells in each we measured the functions VI($E_o$) at two pump wavelengths: 417 nm and 532 nm.Then we determined characteristic energies for two V ranges:
- low damage (V<0.3);
- high damage (0.6<V<1).

The pairs of energy values obtained were presented as a spectrum (Fig. 4). The spectrum coincides with the inverted absorption spectrum of the same blood as measured by a Beckman DU-70 spectrophotometer (Beckman Inc, CA, USA).

The both results may indicate the thermal nature of cell damage. Hgb inside a cell provides light absorption and thermal shock generation. Thermal and pressure shocks act on the cell membrane where initial destructive processes are likely to occur. The degree of the membrane resistance to such kind of a load should depend upon the state of a certain cell, because the state of the membrane generally depends upon the state of the cell. We suggest a thermal (or at least heat-dependent) damage process. We have introduced two more parameters to describe the functional properties of the cell population: the degree of heterogeneity H and the relative energy E(50) causing 50 % damage level:

$$H = \frac{V_2 - V_1}{E_2 - E_1}, \tag{3}$$

$$E_{50} = E_1 + (E_2 - E_1) \times \frac{50 - V_1}{V_2 - V_1}, \tag{4}$$

where $V_2$, $V_1$ – viability indexes of cell population on pump pulse 40 ($E_2$) and 30 ($E_1$) μJ.

Viability parameter (V) was found to be independent of main RBC absorbing factor – Hb concentration. We have found no correlation between the viability and standard hematological parameters as: hematokrit, Hb concentration, mean concentration of Hb in a single cell (MCHC).

Also we found no correlation between LVT parameters and blood groups (A, B, 0) and age or sex of the donor. In our experiments alternation of these hematological parameters was within normal range though the LVT-parameters for normal donors showed significant alternations (Fig. 5) with indication for two subgroups of donors: 20 % of populations have high heterogeneity and differ significantly in terms of cell viability and 80 % of populations have homogeneous cells. We may consider the value for H to be in the range 2.5 – 5.0 for normal cells. If the heterogeneity of cell population exhibits other value for H this may indicate a high number of cells with abnormal viability properties.

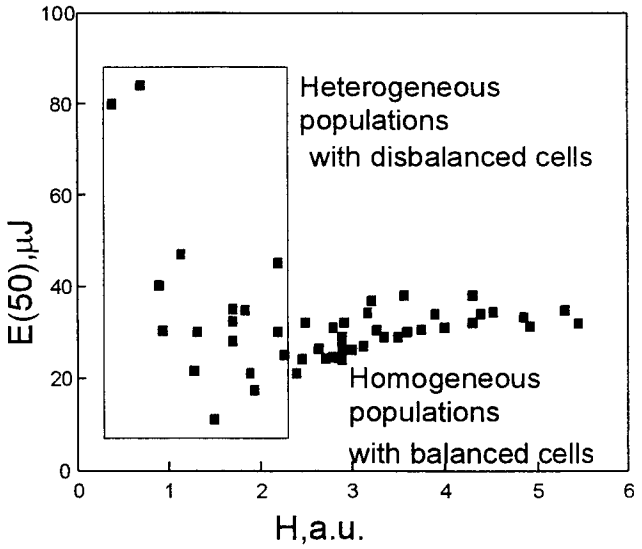


Figure 5. Normal human Red Blood Cell population diagram: 50 % destruction energy level (E(50)) versus population heterogeneity (H), each dot represents one population

### 3.2. Influence of the ions on RBC viability

Cell functional state was studied for in vitro models with human Red Blood Cells under various conditions of ion transport and balance. Laser pump wavelength for all further experiments was fixed at 532 nm. According the results presented above the main absorbing component in the cell is Hb. This wavelength is within absorbing band but and is far enough from the peaks of absorption where absorbing properties depends strongly upon state of Hb (for example oxy-Hb and met-Hb). Thus the load being induced in the cell will not depend upon the change of absorption coefficient due to alteration of Hb forms.

First the influence of osmotic pressure was considered. Osmotic situation was controlled through the concentration of extracellular ions as $Na^+$ and $K^+$ which are the main ions for osmosis. Cells viability was measure for isotonic (0.15 M), hypotonic (0.1 M) and hypertonic (0.22 M) solutions of NaCl (Fig.6). We observed certain increase of RBC viability in hypotonic solution. Parallel control of cell resistivity with standard clinical technique yielded 0-5% lysis for same samples.

Cell ion balance depends upon degree of ion channels activation. The role of various ion channels was studied in experiments with several ions: $Ca^{2+}$, $K^+$ and $Mg^{2+}$ . These ions are responsible for cell natural activity and there are certain ion channels for them. Introduction into isotonic solution of K ions caused the decrease of RBC laser viability (Fig.6). But if we maintain isotonic environment only with K it causes the increase of cell viability (Fig.7). The ions of $Mg^{2+}$ when being added into isotonic solution do not affect cell laser viability at all (Fig.7). As for the ions of $Ca^{2+}$ when added in concentration 3 mcM they caused certain increase of cell viability (Fig.7). This result may indicate that the biological property that is measured in these tests is connected with activity of ATP-aza for $Na^+$, $K^+$ and $Ca^{++}$, and also with the state of ion channel proteins. This idea is confirmed by the results of experiments with $Mg^{2+}$ (2.0 mM): the absence of any differences in viability is caused by minimal activity Mg-dependent ATP-aza for RBC.

With the solutions of the ions as $Na^+$, $K^+$, $Ca^{2+}$ and $Mg^{2+}$ we have found strong dependence of cell viability upon the process of ion transport through the cell membrane [16, 17, 18, 19, 20]. An increase of $Na^+$ or $K^+$ concentration causes a almost linear decrease of RBC resistance against laser load (Fig. 6, 7). For the same solutions significant increase of cell resistance was observed after some amount of $Ca^{++}$ was added (3 mcM).

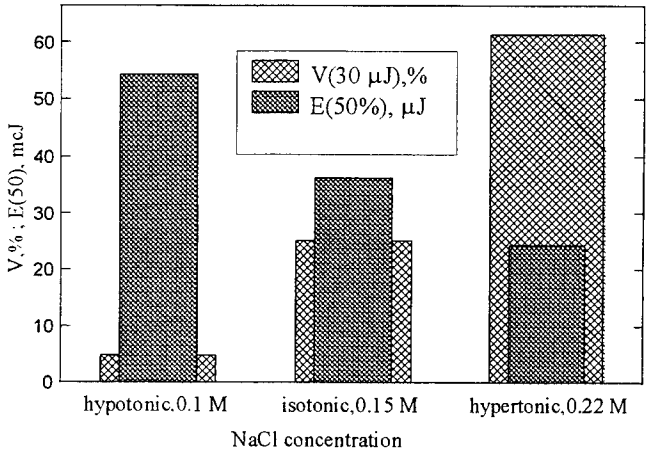


Figure 6. LVT-parameter of RBC in solution with different concentration of $Na^+$

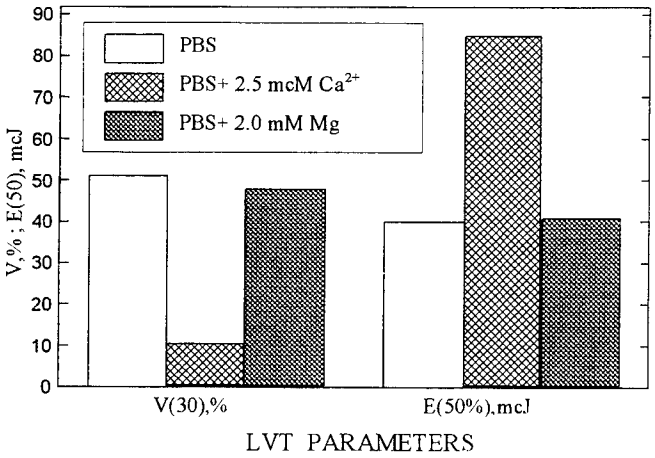


Figure 7. LVT-parameter of RBC in solutions with t $Ca^{2+}$ and $Mg^{2+}$

## 4. DISCUSSION

### 4.1. Damage mechanism

For RBC their resistivity to laser load depends upon membrane properties. RBC membrane is very dynamic structure. Acoustical component of laser load may destroy membrane directly. For example 10-11 nm hole which emerges after complement system activation provides cell lysis [21, 22]. Thermal component of laser load may act first at proteins and transport systems. For the degree of thermal load (an order of 0.1-1.0 °C) which is realized in our experiments there no certain damage mechanism described in literature. We may only assume that relatively small thermal load (protein denaturation occurs at 50-60 °C) can trigger some cascades which are responsible for the ion channels permeability. Recent data being obtained for some signal mechanisms in different cells may confirm this assumption.

### 4.2. Cell viability versus ion balance

Osmotic pressure is the main factor for stability of live cell. An influence of this factor on RBC is well known [16,17]. For laser load an osmotic pressure was found also to be the main factor for cell viability. The fact that cell viability increases due to $Ca^{2+}$ and also due to maintains of isotonic environment with $K^{+}$ ions shows that viability depends upon water and electrolyte balance of the cell which is controlled through the ion channels. As the processes of ion transport are similar for various cell types we may suggest ion mechanism of regulation of cell laser viability is applicable to other cell types.

We have found that the spread of cell viability under certain laser regime depends upon the differences in cell functional state. This can be associated with occasional side effects of laser therapy for certain patients: their cell laser viability may be different. Such individual effects may require optimization of cell viability through some ion – based methods prior to the laser treatment. We have found that such parameters as V, H and E(50%) describe structural and functional state of cell population. Thus the laser viability test may provide preliminary diagnostics for any patient with indications for laser therapy to avoid or anticipate negative side effects of the latter.

## 5. CONCLUSIONS

The studies of live human Red Blood Cells with Laser Viability Test allow to conclude that:
- laser viability of RBC depends upon ion transport processes and can be controlled by pharmaceutical means;
- there is a natural variation of cell viability among various donors which may require individual optimization of laser therapies;
- Laser Viability Test provides diagnostics of cell functional properties and may be used in combination with therapeutic methods for their more safe and predictable application through preliminary dose evaluation.

## REFERENCES


1. M.J.C.Germet, A.J.Welch, "Clinical Use of Laser-Tissue Interactions", *IEEE Eng. in Med. and Biol. Mag.*, **4,** pp.10-13, 1989.
2. J.C.Martin, J.H.Jett, "Photodamage, a basis for super high speed cell selection", *Cytometry*, **2,** p.114, 1981.
3. J.A. Parrish, "Effects of Lasers on Biological Tissue: Options For Specificity in Laser", *Photobiol. and Photomed. Proc. of the Two-Week Cours,* pp.17-27, 1985.
4. A.Kumar, S.R Cud., S.M.Gokhale, V.Bhakuni, C.M.Gupta, "Heat-induced alternations in Monkey erythrocyte membrane phospholipid organization and skeletal protein structure and interactions", *Biochim. Biophys. Acta*, **1030**, pp. 269-278, 1990.
5. W.Kusera, W.Meier, D.Lerche, "Influence of heat-induced changes in the mechanical properties of the membrane on the filterability of human erythrocytes", *Biomed-Biochim. Acta*, **45**, pp. 353-358, 1986.
6. J.Utoh, H.Harasaki, "Damage to erythrocytes from long-thermed heat stress", *Clin. Sci.*, **82**, pp.9-11, 1992.
7. D.Lapotko, G.Kutchinsky, E.Scoromnic, T.Romanovskaya, "Photothermal methods in analytical cytology: single living cell studies", *Bulletin of the Stefan university: Laser optoacoustics and photothermal phenomena*, **11**, pp.65-70, 1999.
8. D. Lapotko, G. Kuchinsky, T..Romanovskaya, H.Scoromnik, "Photothermal Method For Cell Viability Control", *Book of Abstracts: X international conference on Photoacoustica and Photothermal Phenomena*, pp.467-468, Rome, 1998.

9. D. Lapotko, G. Kuchinsky, T..Romanovskaya, H.Scoromnik, "Photothermal Cytometry and Microscopy ", *Book of Abstracts: X international conference on Photoacoustica and Photothermal Phenomena*, eds.F.Scudieri, M.Bertolotti, pp.489-490, Rome, Italy, 1998.
10. D.Lapotko, G.Kuchinsky, H. Antonishina, H.Scoromnik, "Laser viability method for red blood cells state monitoring", *Proc. SPIE, Vol. 2628, Optical and Imaging Techniques for Biomonitoring*, eds. Hans-Jochen Foth, Renato Marchesini, Halina Podbielska, Herbert Schneckenburger, Michel Robert-Nicoud, pp. 340-348.
11. J.A.Bloom, W.W.Webb, "Photodamage to intact erythrocyte membranes at high laser intensities: methods of assay and suppression", *J.Histochem. Cytochem.*, **32**, pp. 608-616, 1984.
12. "In vitro effects of argon laser radiation on blood: quantitative and morphologic analysis", *J. Am. Coll. Cardiol.*, **5**, pp. 231-237, 1985.
13. "Pathologic analysis of photothermal and photomechanical effects of laser-tissue interactions", *Photochem. Photobiol.*, **53**, pp. 825-835, 1991.
14. S.L.Thomsen, J.A. Schwartz, R.Joseph, J. A. Pearce, B.Rae, T.J.McMurray, "Temperatures associated with thermally induced red blood cell changes in tissues irradiated in vivo", *Proc. SPIE, Vol. 2130, Diagnostic and Therapeutic Cardiovascular Interventions IV*, ed. G.S. Abela, pp. 156-163.
15. B.S.Polla, R.R.Anderson, "Thermal injury by laser pulses: protection by heat shock despite failure to induce heat-shock response", *Lasers Surg. Med.*, **7**, pp. 398-404, 1987.
16. P.von Sengbush, *Molecular-und Zellbiologie*, Springer-Verlag, Berlin, Heidelberg, New York, 1979.
17. I.M.Glynn, S.J.D.Karlish, "The sodium pump", *Ann.Rev.Physiol.*, **37**, pp.13, 1975.
18. R.Johnsson, "Effect of pentoxifylline on red cell flexibility and cation transport in healthy subjects and patients with hereditary spherocytosis", *Scand. J. Haematol.*, **23**, pp. 81-87, 1979.
19. F.Meng, Y.Chen, S.Ge, "Erythrocyte membrane during shock stage in burned rats", *Chung Hua Cheng Hsing Shao Shang Wai Ko Tsa Chih* , **10**, pp.134-137, 1994.
20. P.Lijnen, D.Groeseneken, M.Laermans, G.Lommelen, Y.Piccart, A. Amery, "Methodological assessment of assays for intracellular concentration and transmembrane fluxes of sodium and potassium in erythrocytes of man", *Methods Find. Exp. Clin. Pharmacol.*, **6**, pp. 293-301, 1984.
21. M.D.P.Boyle, T.Borsos, "The terminal stages of immune hemolysis - a brief review", *Mol. Immunol.*, 17, pp.425-432, 1980.
22. J.H.Humphrey, R.R.Dourmachkin, "The lesions in cell membranes caused by complement", Adv. Immunol, **18**, pp.75-115, 1969.

# Photodynamic Modulation of Immune Properties of Blood Cells

Dmitri Lapotko[a], Tat'yana Romanovskaya[b], Vladimir Zharov[c]

[a] Luikov Heat and Mass Transfer Institute, Minsk, Belarus, 220072

[b] International Sakharov Environmental University, Minsk, Belarus

[c] Moskow Bauman State University of Technology, Moskow, Russia

## ABSTRACT

The mechanisms of therapeutic action of laser radiation with and without photosensitizers were studied experimentally at cell level for living leukocytes. Single cell response to action of pathogens and to laser-based therapeutic processes was measured with photothermal (PT) image microscope. We have monitored cell functional properties during phagocytosis of bacteria S.aureus by human leukocytes. Laser therapy was applied in vitro to cell suspense and to the mixture of cells and microbes in three regimes:
- low-power(30-50 mW/cm$^2$) CW-laser radiation at 633 nm and at 670 nm;
- photoactivated with 670 nm laser radiation Chlorin E6 at 0.2 mg/l (PDT);
- photoactivated with 670 nm laser radiation aluminuim disulfonated phthalocyanine (Photosens) at 0.2 mg/l (PDT).
For all three regimes an increase of bactericidal effect was found only when the cells are involved into interaction with microbes. No bactericidal effect in the wide range of drug doses was found during direct application of PDT to bacteria in vitro. The best effect was found when the cells are treated with laser radiation only. Also laser radiation restored cell properties. As a result we suggest that immune stimulation depends more upon physical factors (laser) rather than upon pharmaceutical (photosensitizers).

**Keywords:** photothermal, photosensitizer, bacteria, blood cell, phagocytosis, immune system

## 1. INTRODUCTION

Therapeutic action of laser radiation in non-destructive regime is based on the effects that are induced in tissues due to absorption of laser radiation. Such effects are a result of direct laser-cell interaction or may include the third component – the medicine – which is used to regulate first scheme. The latter method is more known as photodynamic therapy (PDT) or photochemotherapy. At present various therapeutic techniques have a good clinical background but still the understanding of cellular mechanisms of laser – tissue interaction is quite limited. Such situation slows the development of laser-based therapeutic methods and instrumentation. Clinical (or animal) trials still are considered as a most effective approach for evaluation of therapeutic effect.

We have studied experimentally action of PDT and low-power laser radiation at cell level in vitro. The damage to the host caused by inflammatory process depends not only upon activity of the pathological process but also upon degree of immune system activation. It means that the microbes may stimulate stronger than optimal defense inflammatory reaction which need to be optimized. This caused the growth of interest in therapeutic methods which immune modulation capabilities [1,2,3,4,5].

Photosensitizers (PS) were investigated as new antibacterial drugs during the last 25 years with little practical output [1, 22], especially compared with their success in oncology. The results obtained by various groups are based on bacteriological models in vitro where cells are not considered or laser radiation levels are destructive for living cells. The microbiocidal effect of PS was investigated and described for a wide spectra of the drugs: herbal, bacterial, hematoporphyrin derivatives and synthetic [6, 7, 8]. The mechanism of PS action is associated with free radicals production and penetration of the drug through cell wall, disorganization of membrane peptides, DNA damage etc [9, 12, 14, 15, 16].

* Correspondence: Email: ld@ ns1..hmti.ac.by; Telephone: 375 172 842 483; Fax: 375 172 842 486



In *Laser-Tissue Interaction XI: Photochemical, Photothermal, and Photomechanical*, Donald D. Duncan, Jeffrey O. Hollinger, Steven L. Jacques, Editors, Proceedings of SPIE Vol. 3914 (2000) 1605-7422/00/$15.00

The effect was shown to depend upon PS chemical structure, as a result there are variations in PS efficiency which depend upon the type of microbes and microbial growth stages [15, 19, 23]. The efficiency of PS action was shown to depend also upon the drug dose and laser radiation parameters [13, 17, 19, 20, 22]. Photodynamic regimes which provide microbiocidal effect (but not the microbiostatical effect) have a damage effect to the host cells [15, 18, 21, 24]. The latter makes difficult a successful application of PS against infective agents and for sterilization purposes. This can be improved through the evaluation of more selective PDT regimes and drugs which will be safe for cells and at the same time effective enough to kill the microbes. Another question of interest is the influence of photoactivated PS on immune status of the host. These questions need to be studied for application of PS against infections and for immune system modulation.

The development of low-power laser (LPL) therapeutic methods is still based on empirical approach. The effects of laser radiation are generally non-linear, dose dependent and strongly depends upon initial host state [25]. Its applications will be more safe and effective providing understanding the cellular mechanisms of laser-cell interaction. The mechanisms of LPL action at cell level are presented by through several assumptions as which are based on:
- modulation of metal components activity;
- action through transformation of cell bio-polymers;
- action through transformation of water structure.

This work is an attempt of direct experimental study of laser action on living blood cells – leukocytes- at a single cell level. The basic reasons for this study were as:
- we need to register cell response to laser impact in terms of cell functional properties;
- the function of leukocytes is to provide an immune response of the host;
- new applications of PDT against infections and for immune system stimulation should be studied at cell level.

We have studied the changes of single living cells properties during their interaction in vitro with LPL, drugs (photosensitizers) and bacteria. The goals of our experiments were:
- to model in vitro laser therapeutic regimes(with and without photoactivated drugs) for intact cells and for the cases of infection;
- to evaluate an efficiency of LPL and PDT regimes in terms of cell properties and bactericidal effect;
- to evaluate cellular mechanisms of laser-cell interaction for non-destructive regimes of laser radiation.

Cytometric data were acquired with photothermal (PT) laser microscope [26,27]. The method and device allow differential single living cell monitoring in a real time regime. Parameters of photothermal images of each cell were acquired and analyzed statistically for cell population. The advantages of photothermal method for cytological applications are:
- it allows the study of a living cell;
- heterogeneous populations of cells can be studied through multi-parameter processing of cell data;
- monitoring of living cell population parameters during application of some therapeutic or pathogen factor is possible.

## 2. METHODS AND MATERIALS

### 2.1. Model for cell activation in vitro

#### 2.1.1. The cells

All the cell were used in experiments as the suspension of human leukocytes including: lymphocytes –16%, monocytes – 6%, eosinophils –2%, neutrophils –76%. Such composition is very close to real situation during inflammation when all the types of leukocytes are involved in host defense reaction. The cell suspension was obtained from normal donor after 1-hour incubation of whole blood with 3% solution of $Na_2EDTA$. The Red Blood Cells were lysed out with hypotonic solution of distilled water. Cell concentration was adjusted at $1.8\times10^6$ cell/ml in PBS solution at pH 7.35.

#### 2.1.2. Laser radiation

Cell suspensions were irradiated in vitro by CW-lasers at 632.8 nm and at 670 nm at a power density of 30-50 $mW/cm^2$. Irradiation time varied from 45 s to 30 min, during modeling of phagocytosis irradiation time was 5min for all experiments. These regimes of irradiation had not shown any cytologically detectable cell damage or the changes of cell viability and therefore are considered as safe for the cells.

### 2.1.3. Photosensitizers

We have used two drugs – Chlorin E6 and Photosens (aluminuim disulfonated phthalocyanine).
Photosensitizer concentration was 0.2 mg/l which is similar to therapeutic dose in oncology. This dose in vitro corresponds to the in vivo dose because in our model cell concentration is much lower than natural and besides there are no drug-binding proteins. Preliminary monitoring of the cells with optical microscope during 2 hours revealed no cytologically distinguishable cell damage at this concentration. Incubation time for the drugs was 5 min to provide endocytosis of photosensitizer.

### 2.1.4. Bacteria

In all experiments we have used 24-hour cultures S.aureus type Cowan 1. Bacteria–cell ratio was maintained as 5:1. Incubation time with the cells was 20 min at 37 °C.

### 2.1.5. Experimental procedure

Experimental procedure included the following steps:
- cell suspense was pre-incubated with the drugs for 5 min;
- bacteria were added and the suspense was irradiated with laser for a certain time;
- incubation with bacteria was for 20 min;
- cell properties were measured.

All models, sample and experiment descriptions are summarized in Table 1

Table 1
Specifications for experiments

| MODEL | SAMPLE NUMBER | ELLS | BACTERIA | DRUG (type/concentration, mg/l) | LASER (wavelength, nm/ dose,min) |
|---|---|---|---|---|---|
| Stimulation of immune response with PDT | | | | | |
| Control – intact cells | 1 | leukocytes | - | - | - |
| Natural phagocytosis | 2 | leukocytes | S.aureus | - | - |
| Laser-based PDT | 3 | leukocytes | S.aureus | - | 670/5 |
| Drug-based PDT | 4 | leukocytes | S.aureus | Photosens/0.2 | 670/5 |
| Drug-based PDT | 5 | leukocytes | S.aureus | Chlorin e6/0.2 | 670/5 |
| Bactericidal PDT without cells | | | | | |
| Control – intact bacteria | 6 | - | S.aureus/E.coli | - | - |
| Laser-based PDT | 7 | - | S.aureus/E.coli | - | 670/5 |
| Drug-based PDT | 8 | - | S.aureus/E.coli | Photosens/0.002-2.0 | 670/5 |
| Drug-based PDT | 9 | - | S.aureus/E.coli | Chlorin e6/0.002-2.0 | 670/5 |
| Mechanism of laser action on a cell | | | | | |
| Dose effect | 10 | leukocytes | - | - | 633/0.75-25 |
| Dose effect | 11 | leukocytes | - | - | 670/0.75-25 |
| Thermal load effect | 12 | leukocytes | - | - | - |

## 2.2. Cell diagnostics

### 2.2.1. Photothermal microscopy

The detailed technique for photothermal PT) imaging was described[26, 27]. Photothermal image is defined as visualized response of cell to non-specific thermal and mechanical load being induced in the cell using pump laser pulse absorption by cell natural chromophores (fig.1). Photothermal image represents only the absorbing structure of a sample at the pump laser wavelength and its background for non-absorbing areas is zero. Also, its sensitivity to light absorption is much higher than the sensitivity of a light microscope.

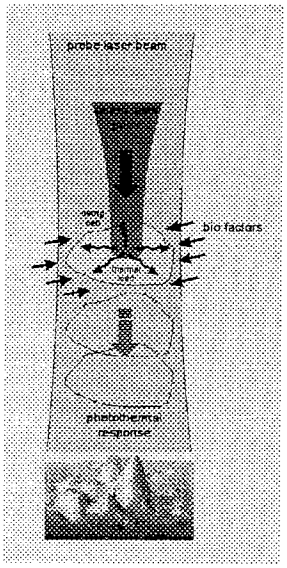


Figure 1. Definition of photothermal imaging: single cell optical monitoring

An algorithm of PT-imaging (fig. 2) includes acquisition of two probe laser images, one prior to the excitation of a cell with the pump pulse and the other within thermalisation time after sample was irradiated with the pump pulse. A differential image is a photothermal image of a sample.

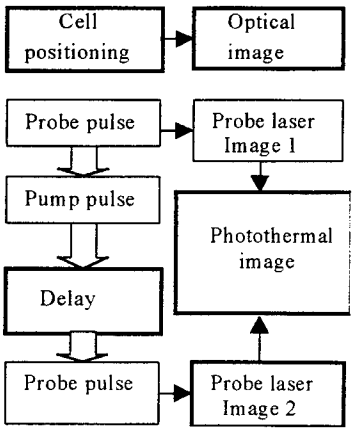


Figure 2. An algorithm of PT-imaging

Providing various delay times between two images, a temporal sequence of PT-images at various relaxation stages can be obtained. The sample is pumped by the pulsed Nd-Yag laser at 532 nm with a pulse duration of 10 ns with variable pump energy of 10-400 μJ. The source of probe beam is a dye laser at a wavelength 630 nm, energy 0.01 mcJ, duration approximately 10 ns and delay with respect to the pump pulse of 6 ns.

For cell suspension holding and positioning multi-sample chamber have been designed. The chamber includes a steel case where up to three microcuevettes with cell suspension can be fixed. Each cuevette is 10 mm long, with outer cross section 1×1.5 mm and capillary rectangular channel 100×400 μm. In comparison with standard glass slides the cuevette provides safer and more stable environment for cells. Several samples can be studied during one experiment. The amount of suspension required for a cuevette is less than 1 μl. Three types of images can be acquired from each sample(single cell): white light optical image, probe laser optical image and photothermal image. The time required for cell automatic recognition, positioning to the center of laser beams and acquisition of three images is less than 1s.

### 2.2.2. Cell population analysis

The main source of information about cell is its photothermal (PT) image. PT-image of each single cell is subject of further analysis. The goal of this analysis is to express in quantitative terms any detected changes in cell functional and structural state. This was done through the evaluation of 15 PT-image parameters that describe:

- image dimensions: Area of a sample S, Effective diameter d, Normalized perimeter Pnr,
- geometry of an image: Signal eccentricity Eksi, Ekss, central momentum B1;
- PT-signal distribution(structure): Mean image amplitude Mi and radial mean Mir, Dispersion of an image amplitude Sigma and dispersio of radial distribution of PT-signal Sir, Asymmetry coefficient Ax and its radial version Axr, Excess coefficient Ex and its radial analog Exr.

Detailed description of these parameters can be found in [26,27,28]. Due to a high sensitivity of this method, an ability to measure properties of each single cell in the population and because of high degree of heterogeneity of the populations, an interpretation of acquired results may be complicated. To simplify primary analysis of results (cell image parameters) and to increase their reliability we have used a reference approach. Several populations of cells (at least two) were studied in all experiments and one was always used as the reference population: cells which are not exposed to action of factors that are applied to the other populations being studied(intact cells). When the reference population is used, the parameters experiment are the same for all samples. Such regime allows also a normalization of image parameters by the corresponding values for the reference cells. Thus we may quantitatively analyze the cells in terms of their difference from the reference (control) cells. All results after automatic calculation of parameters are presented as histograms for each image parameter. For general estimation of all parameters we introduced two reference values that are calculated for each parameter either for one specific cell or for cell population(marked as "i") :

- deviation of the mean values of cell parameters from those of control cell (population):

$$DEVIATION(i) = (MEAN(i) - MEAN(control)) / MEAN(control)$$

- histogram overlap coefficient (HOC):

$$HOC(i) = (SQUARE.H(i) - SQUARE.H(control)) / SQUARE.H(CONTROL)$$

The more are DEVIATION and HOC for a given cell image parameter the more it is different from control cell or cell population. When these values are calculated for all image parameters they can be graphically presented in a spectrum-like manner which is defined as *cell profile*. Thus cell or population reference analysis is done through comparison of cell image parameters in the form of histograms, diagrams and profiles.

### 2.2.3. Control (cytological and bacteriological) methods

Besides photothermal diagnostics of the cells their bactericidal and cytological properties were measured also with standard biological techniques. It was done to verify photothermal data and to obtain independent complementary information on cell functional state.

The basic parameters for cell phagocytosis were measured with optical microscope by counting the concentration of phagocytes(*phagocytic index* – FI(cell). Phagocytic Index is defined as percentage of the cells which can phagocyte microbes among all neutrophils in population. It is measured by visual counts of cells in Gimsa stained smears[29].

The *mean number of phagocyted microbes* in one cell - FI(bac) - is measured as microscopy counts of total amount of ingested by cells microbes divided by total amount of active phagocytes[29].

Cell viability during phagocytosis and PDT or LPL treatment was measured as the *concentration of native cells* - C(cell) – after their treatment with PDT, microbes, drugs etc.

Control of bactericidal effect after application of PDT or LPL procedures was done through the counts of microbe concentration – the number of *Colony Forming Units* (CFU). The cells were lysed and washed out from the mixture of cells and intact microbes with PBS. Then the microbes were cultivated during 24h in MPA. CFU counts were made after 24h.

## 3. RESULTS AND DISCUSSION

### 3.1. Modulation of phagocytosis with Photo-Dynamic Therapy( PDT) and Low-Power Laser (LPL ).

Gram-positive microbes (S.aureus) were studied with leukocytes to model phagocytosis under treatment with photoactivated Chlorin E6 and Photosens. As can be seen from fig. 3 and 2 (sample 2) after 20 min of phagocytosis of S.aureus a subpopulation of cells emerges among initially intact cells. This subpopulation may be caused by an increase of cell functional and structural heterogeneity during phagocytosis.

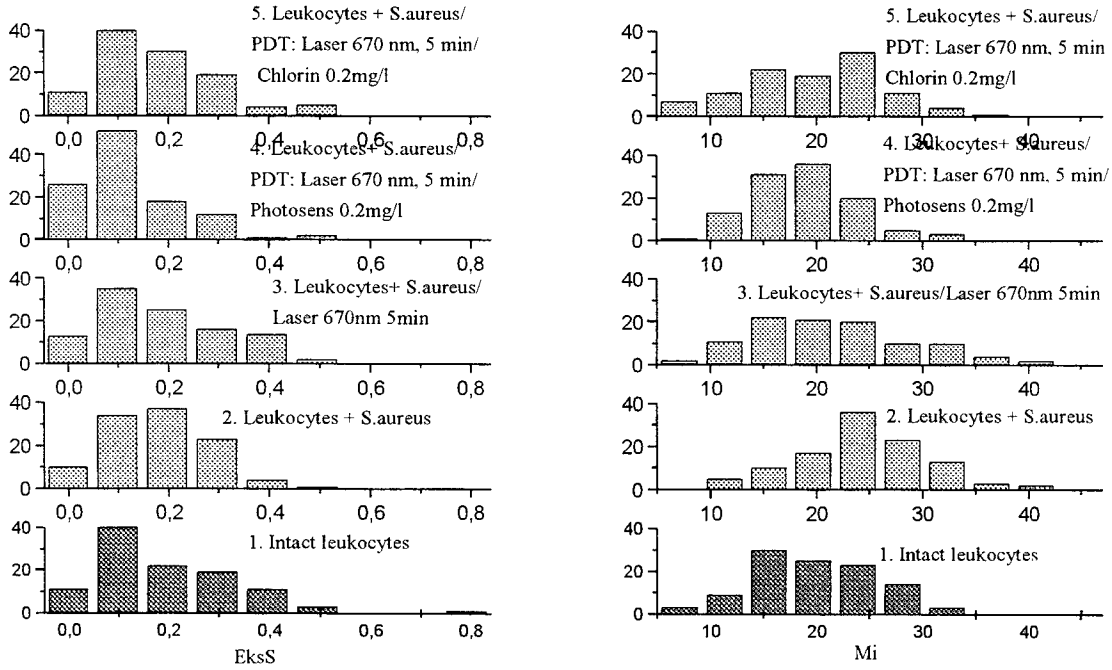


Figure 3. Influence of three regimes of PDT in vitro on cell properties during phagocytosis: histograms of photothermal image parameters EksS (Signal eccentricity) and Mi (Mean signal amplitude) for several populations of human leukocytes. Vertical axis: cell counts.

For leukocytes the phagocytosis is a complex and multi-stage reaction and affects many cell functions[31]. Those functions include cell migration with energy losses, membrane activation with phagosome production, intracellular ferments activation resulting in microbe killing. Thus we can conclude about significant changes in the parameters of leukocytes and other cells population after adding bacteria. Those changes were observed almost for all PT-image parameters thus indicating that there is a big difference in cell structural and functional state before and during phagocytosis.

The influence of the both laser and photoactivated drugs (Chlorin E6 and Photosens) was similar in terms of PT-parameter changes (Fig. 4). In all three cases we have observed stable restoration of cell parameters in comparison with the case of natural phagocytosis.

Parallel cytological experiments revealed an increase of cell bactericidal properties after the treatment with all three laser-based methods (laser, photoactivated chlorin e6 and photoactivated Photosens): FI(cell) and FI(bac) for the laser-treated samples increase (Fig. 5). Concerning the cell viability the most hostile for cell was Photosens and the most secure regime was found for the treatment with LPL. This comparison is rather relative because significant cell loss was observed for the case of natural phagocytosis.

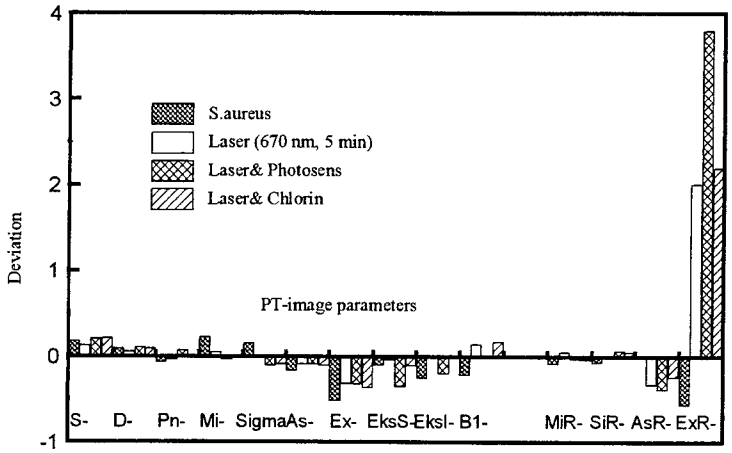


Figure 4. Phagocytosis of S.aureus by human leukocytes with and without PDT (in vitro): photothermal profiles of cell populations.
Vertical axis: deviation from mean values of control population.

Therapeutic effects of all three regimes were analyzed for all obtained on cells data: photothermal parameters, bactericidal effect and cell viability. Such approach shows that application of laser without any photoactivated drugs has maximum effect (regime of LPL). In this case we have observed minimal deviation of PT-parameters from control (Fig. 2), minimal cell loss and maximal bactericidal effect. We suggest that in vivo application of LPL may produce the similar therapeutic effect. Although therapeutic regimes should be adjusted individually according to initial structural and functional state of immune-competent cells of the host. Cellular concentration of natural porphirins may be one of the main factors for correct regime choice. Such preliminary cell diagnostics may be realized with photothermal cytometry methods.

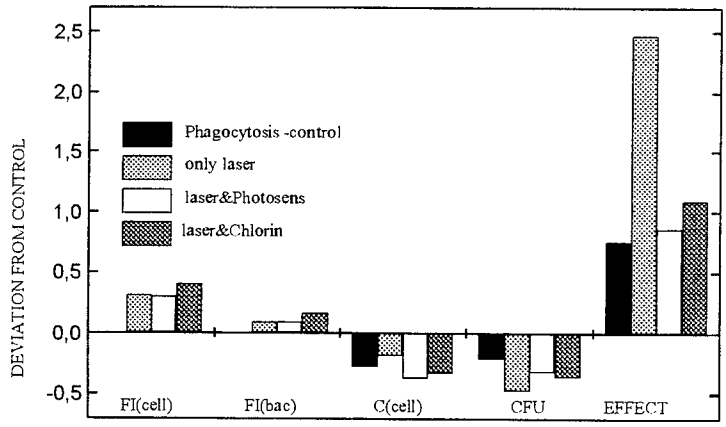


Figure 5. Phagocytosis of S.aureus by human leukocytes with and without PDT (in vitro): deviation of the mean cytological and bacteriological parameters from control: FI(cell) - phagocytic index, FI(bac) – mean number of phygocyted microbes as per one cell, C(cell) – native cell concentration, CFU – colony forming units,
EFFECT – integrated criterion for phagocytosis.

To understand the mechanism of PDT and LPL action on cells we have measured independently bactericidal effect in the samples with microbes only when no cells are involved (Table 2) and compared the results to three initial samples.

Microbe suspense (10) was incubated with the drugs for 10 min and then was irradiated for 5 min with CW laser at 670 nm. There were three drug doses: 0.002, 0.2 and 2 mg/l. The measurement of bactericidal effect in this experiment for the microbes is based on a visual count of colony forming units (CFU) after 24h cultivation in MPA.
Application of photoactivated drugs did not show any microbiocidal effect (Table 2).

Table 2
Bactericidal effect of photosensitizers without cells

| MODEL | DRUG DOSE mg/l | BACTERIA CONCENTRATION CFU/ml | |
|---|---|---|---|
| | | S.aureus ($\times 10^5$CFU/ml) | E.coli ($\times 10^5$CFU/ml) |
| 1. Intact microbes | | 76,2 ± 5,76 | 61,4 ± 2,97 |
| 2. Chlorin e6 | 2,0 mg/l | 75,8 ± 4,2 | 62,4 ± 2,07 |
| | 0,2 mg/l | 775,6 ± 5,55 | 60,6 ± 3,97 |
| | 0,002 mg/l | 75,6 ± 3,85 | 62 ± 1,58 |
| 3. Photosens | 2,0 mg/l | 80,8 ± 4,66 | 62,6 ± 1,34 |
| | 0,2 mg/l | 77,2 ± 6,1 | 61,6 ± 5,22 |
| | 0,002 mg/l | 76,2 ± 2,77 | 63,4 ± 1,52 |

This means that there were no direct effects of photosensitizer on bacteria with the doses of drug and laser radiation being used. Therefore bactericidal effect is provided through phagocytosis and not through a direct action of laser radiation or the drugs on microbes. Activation of phagocytic activity of cells is associated with modulating effect of PDT. Modulating effect of PDT on cells results in:
- general decrease of population heterogeneity and decrease of deviation from the properties of intact cells;
- increase of functional activity of the leukocytes.
There are at least several mechanisms of cell activation in vitro which are associated with above mentioned phenomena:
- increase of phagocyte adherence;
- increase of membrane reparative properties;
- activation of cellular bactericidal systems resulting in $NO^-$ and $O^-_2$ production.
LPL and PDT influence on cell phagocytic activity depends also upon metal-protein components concentration which are natural (endogenous) chromophores. When their concentration is low or their state is modified we can provide stimulating effect by adding exogenous chromophores – photosensitizers. This assumption is confirmed by our results and also by our previous studies of laser stimulation [27, 28]. We found no additive effect of laser radiation and photoactivated drugs. Such result can be explained by threshold nature of light absorption and concurrence between endogenous and exogenous photosensitizers.

The modulating mechanism is a subject of further investigations of PS action at cell-molecular level. It was established that the action of a photosensitizer induces amount of free-radicals which damage macro-molecules and cell membranes. There is a possibility that low doses of free radicals may stimulate or optimize some metabolic processes during phagocytosis. It has been shown that PS action is connected with selective uptake by cells which have a high level of protein and DNA synthesis [12, 14, 16]. In some recent studies [27] other photosensitizers have been considered in terms of their immunotropic action. New method for treating infections was patented - photopheresis – which is claimed to have immune-stimulating properties towards immune-competent cells[5]. This information is in line with our results and with an assumption about immune modulating effect of PDT and LPL at cell level. In any case prior to PDT/LPL administration cytometric diagnostics will be required for optimization of therapeutic regime.

### 3.2. Mechanism of laser action

The mechanisms of laser radiation action on leukocytes was studied in several additional experiments (Table 1). The purpose of these experiments was:
- to measure basic dependence of intact cell properties upon radiation wavelength and dose. Such investigations have a certain background and in our case it was done for comparative purposes and for verification of our in vitro models;
- to find other than laser physical factors which action has similar effect on living cells and thus to find some direct confirmation to existing theories about laser action mechanism.

For a dose and wavelength effect studies we have used the 670 nm wavelength as a basic in terms of our previous experiments. The second wavelength was 633 nm as a most frequently used in therapeutic devises. For the both wavelengths we have found that PT-parameters are dose dependent (Fig. 6). The dose was regulated by exposition time. For the parameters S, Mi, Sigma, Asr, Exr an increase of LPL dose has appeared to suppress effect of laser action. Similar effects of cell reaction (of the changes in cell functional and structural state) are well known for various factors [31,32]. But they often are ignored at therapeutic level because there is usually no way for cell functional state diagnostics. We assumed that one of physical factors which action is well investigated at cellular and clinical levels may be the cause for the cell activation during laser–cell interaction. This factor has thermal origin. Thermal model for human leukocyte activation was experimentally studied in vitro (fig. 7). Cell suspense was exposed to 45 °C during 1 min. Such short exposition should prevent from the cell damage which can be induced by longer heating [32,33,34,35]. As a rule leukocytes can be suppressed due to heat shock protein production after exposure to the temperature 45-48 °C during the hours [35,37]. Our short-time hyperthermia model corresponds to positive effects of therapeutic application of a heat. Also we should note that clinical applications of thermal and laser factors are quite similar and cover a wide range of tasks.

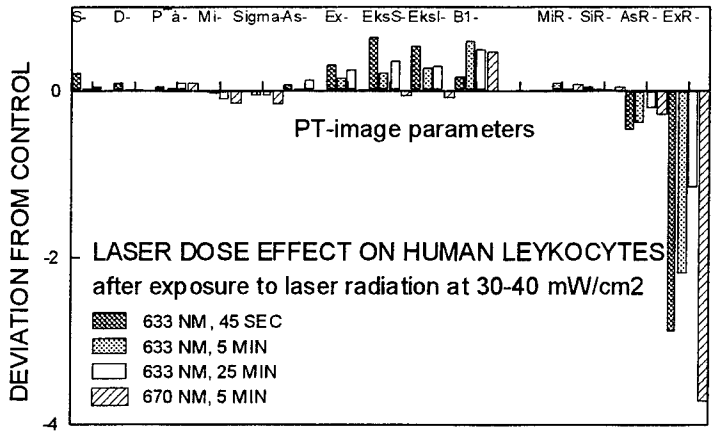


Figure 6. Photothermal profiles of human leukocytes under action in vitro of PDT:dose and wavelength effects.
Vertical axis: deviation from mean values of control population.

Photothermal investigation of cell properties revealed very close character of PT-profiles obtained from heat- and laser-treated cells (Fig. 7). This result is additional proof for concurrent action of endogenous and exogenous photosensitizers.

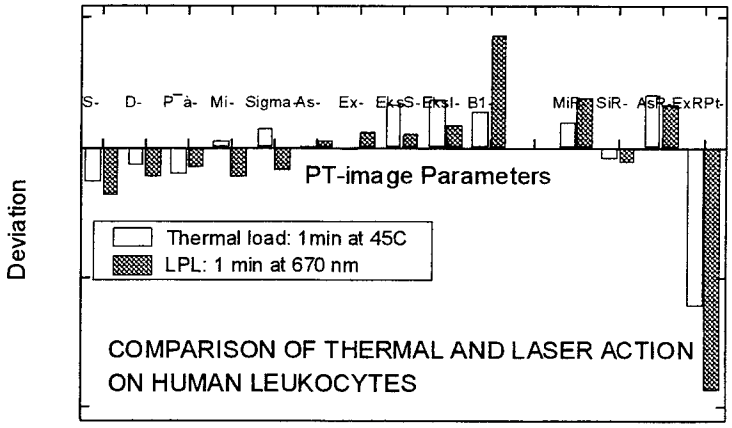


Figure 7. Photothermal profiles of human leukocytes under action in vitro of LPL and of thermal load (1 min at +45 °C). Vertical axis: deviation from mean values of control population

The mechanisms of thermal therapeutic action are well empirically developed at macro level. The cellular mechanism of thermal activation is still the subject for discussions. It was found that optimal temperature rise stimulates metabolic processes and diffusion through membrane in cells. Also such processes as lipid molecules phase transitions, protein conformation were found to be temperature – dependent [37]. This means that thermal factor modulates molecular lability of many membrane components. Such modulation is accompanied by the changes of biochemical parameters which characterize cell functional state: level of ferments activation, intracellular $Ca^{2+}$ level change [38], etc. The effect of thermal modulation as it appears at macro level will depend strongly about two factors:

-initial functional state of the cells that are subject of heat action;

-actual distribution of temperature in tissue and inside the cell.

Various combinations of these two factors can cause almost contrary effects at macro level under the same doses of heat being applied. All above can be applied for explanation of the mechanism of LPL too. Although there is a difference between action of laser radiation from action of thermal factor: primary acceptors of laser radiation are specific chromophores (endogenous photosensitizers). Metabolic changes that follow laser impact depend upon initial state of chromophore molecules. When they change all further cascade of processes will change too resulting in activation of specific functional properties of the cell. This specifity of laser-cell interaction may explain selective therapeutic effects of lasers in some cases (prolongated phisiological effects for example). Further development of this idea is connected with selective activation of specific chromophore molecules for the modulation of cellular response in desired direction. Providing a realization of this principle the laser-based therapy will become a tool for selective treatment through the modulation of most adequate immune reaction. Technically this can be done either by the use of an optimal for a certain endogenous chromophore laser wavelength and energy or by application of specialized drugs (as exogenous chromophores) and laser radiation to activate those drugs inside the cells.

## 4. CONCLUSIONS

The results of the described experiments showed that immune competent cells are the main component in realization of photodynamic stimulation of defense systems. The main activation and modulation factor for such cells is laser radiation. The use of combination of laser and drugs (PDT) is also possible but pharmaceutical factor may damage the cells and therefore requires more control during PDT administration. For this reason and also according to our results a «direct» bactericidal application of PDT in vivo may have a little sense – drug concentrations will be too high and too dangerous for a host. Concerning the mechanism of laser stimulating or modulating action on cell properties we have demonstrated new approach for its direct investigation. However a suggested approach (in vitro modeling of therapeutic regimes with photothermal cell state control) allows now to check and optimize individually photodynamic regime prior to clinical use.

## REFERENCES


1. V.P. Zharov, D.O. Leviev, A.V. Lutikov, V.I. Chuvilkin, " Development of combined photo-drug therapy for treatment of infected and inflammatory processes", *Proc. of the IV Intern. Conf. on New Information Technology in Medicine*, Yalta-Gurzuf, Crimea, Ukraina, pp.174-178, 1998.
2. V.P. Zharov, D.O. Leviev, A.M.. Shoshensi, A.V. Luticov, "Photo-drug therapy of infected wound", *Proc. of the VIII-th Intern. Conf. on Laser in Science, Technology and Medicine*, Pskov, Russia, pp. 28-30, 1997.
3. V.P. Zharov, A.S. Latyshev, "Laser combined medical technologies from Russia", *J. of Laser Appl.*, **11**, pp.80-90. 1999.
4. J.B. Hudson, G.H. Towers, "Therapeutic potential of plant photosensitizers", *Pharmacol. Ther.*, **49**, pp.181-222, 1991.
5. S.N. McLaughlin, B.C. Stouch, J.B. Zeldis, "Photopheresis treatment of leukocytes", [Oncologic, Endocrine & Metabolic] Patent *fast-alert,* 1997.
6. T.A. Dahl, O. Valdes-Aguilera, W.R. Midden, D.C. Neckers, "Partition of Rose Bengal anion from aqueous medium into a lipophilic environment in the cell envelope of Salmonella thyphimurium: implications for cell-type targeting in photodynamic therapy", *J. Photochem.Photobiol.*, **4**, pp. 171-184,1989.
7. S. Gross, A. Brandis, L. Chen, V. Rosenbach-Belkin, S. Roehts, A. Scherz, Y. Salomon, "Protein-A-mediated targeting of bacteriochlorophyll-IgG to Staphylococcus aureus: a model for enhanced site-specific photocytotoxicity". *Photochem. Photobiol.*, **66**, pp.872-878, 1997.
8. G. Jori, G. Bertoloni, M. Merchat, P. Giacomoni, "Use of porphine cationic derivative salts as Gram-negative bacteria photosensitizers", [Anti-infectives] Patent *fast-alert*, 1996.
9. E. Cassuto, N. Gross, E. Bardwell, P. Howard-Flanders, "Genetic effects of photoadducts and photocross-links in the DNA of Phage lambdal exposed to 360 nm light and trimethiylpsoralen or khellin", *Biochim. Biophys. Acta*, **475**, pp. 589-600, 1977.
10. A. Minnock, D.I. Vernon, J. Schofield, J. Griffiths, J.H. Parish, S.T. Brown, " Photoinactivation of bacteria. Use of a cationic water-soluble zinc phthalocyanine to photoinactivate both gram-negative and gram-positive bacteria", *J. Photochem. Photobiol. B*, **32**, pp.159-164, 1996.
11. A. Eisenstark, "Bacterial genes involved in response to near-ultraviolet radiation", *Adv. Genet.*, **26**, pp.99-147, 1989.
12. B. Epe, M. Pflaum, S. Boiteux, "DNA damage induced by photosensitizers in cellular and cell-free systems", Mutat. Res.. **299**, pp.135-145, 1993.
13. J.S. Friedberg, R.G. Tompkins, S.L. Raketraw, S.W. Warren, A.J. Fischman, M.L. Yarmush, "Antibody-targeted photolysis. Bacteriocidal effects of Sn (IV) chlorin e6-dextran-monoclonal antibody conjugates", *Ann. N Y Acad. Sci.* **618**, pp. 383-393, 1991.

14. H. Li, O.S. Fedorova, A.N. Grachev, W.R. Trumble, G.A. Bohach, L. Czuchajowski, "A series of meso-tris (N-methyl-pyridiniumyl)-(4-alkylamidophenyl) porphyrins: synthesis, interaction with DNA and antibacterial activity", *Biochim. Biophys. Acta.*, **20**, pp. 252-260, 1997.
15. A.Iu. Fomichev, V.P. Zorin, T.E. Zorina, S.N. Cherenkevich, "Photodamage of gram-positive and gram-negative bacterial cells in the presence of chlorin e6", *Mikrobiologiia*, **60**, pp.507-511, 1991.
16. T.E. Zorina, A.Iu. Fomichev, S.N. Cherenkevich, "Damage photosensitized by chlorine e6 in bacteria with various defects of the DNA repair system", *Mikrobiologiia*, 57, pp.1007-1010, 1988.
17. M. Merchat, J.D. Spiekes, G. Bertoloni, G. Jori, "Studies on the mechanism of bacteria photosensitization by meso-substituted cationic porphyrins", *J. Photochem. Photobiol. B*, **35**, pp.149-157, 1996.
18. F.W. Van der Meulen, K. Ibrahim, H.J. Sterenborg, L.V. Alphen, A. Maikoe, J. Dankert, " Photodynamic destruction of Haemophilus parainfluenzae by endogenously produced porphyrins", *J. Photochem. Photobiol. B*, **40**, pp. 204-208, 1997.
19. P. Martinetto, M. Gariglio, G.F. Lombard, B. Fiscella, F. Boggio, "Bactericidal effects induced by laser irradiation and haematoporphyrin against gram-positive and gram-negative microorganisms", *Drugs Exp. Clin. Res., 12*, pp. 335-342, 1986.
20. Y. Nitzan, H.M. Wexler, S.M. Finegold, "Inactivation of anaerobic bacteria by various photosensitized porphyrins or by hemin", *Curr. Microbiol.*, **29**, pp.125-131, 1994.
21. F.R. Venezio, C. DiVincenzo, R. Sherman, M. Reichman, T.C. Origitano, K. Thompson, O.H. Reichman, "Bactericidal effects of photoradiation therapy with hematoporphyrin derivative", *J. Infect. Dis.*, **151**, pp.166-169, 1985.
22. M. Wainwright, "Photodynamic antimicrobial chemotherapy (PACT) ", *J. Antimicrob. Chemother.*, **42**, pp. 13-28, 1998.
23. M. Wilson, J. Dobson, S. Sarkar, "Sensitization of periodontopathogenic bacteria to killing by light from a low-power laser", *Oral. Microbiol. Immunol.*, **8**, pp. 182-187, 1993.
24. M. Wilson, J. Pratten, "Lethal photosensitisation of Staphylococcus aureus", *Microbios.*, **78**, pp.163-168, 1994.
25. E.Ernst , V.Fialka, *Schweiz. Med.Wschr.*, **123**, pp. 949-954, 1993.
26. D. Lapotko, G. Kuchinsky, "Photothermal microscopy for cell imaging and diagnostics", *J. Proc. SPIE, Optical biophysics*, **2390** pp. 89-100, 1995.
27. D. Lapotko, G. Kuchinsky, M. Potapnev, D. Pechkovsky, "Photothermal image cytometry of human neutrophils", *Cytometry*, **24**, pp.198-203, 1996.
28. D.Lapotko, T.Romanovskaya, G.Kutchinsky, V. Zharov, " Photothermal studies of modulating effect of photoactivated chlorin on interaction of blood cells with bacteria", *Cytometry*, **37**, pp.320-326, 1999.
29. D.Lapotko, V. Zharov, T.Romanovskaya, G.Kutchinsky, G.Vorojtsov, "Photothermal microscopy study of photodynamic inactivation of bacteria in the presence of living blood cells", *Proc. SPIE*, **3592**, pp. 101-109, 1999.
30. H.Friemel, *Immunologische Arbeitsmethoden*, Jena, 1984.
31. S.J. Klebanoff, "Cytodial mechanism of phagocytic cells", *Ser. Rev.*, **11**, pp 721-736, 1980.
32. V.S. Letokhov, "Effects of transient local heating of spatially and spectrally heterogeneous biotissue by short laser pulses", *Nuovo Cimento*, **13**, pp. 939-948, 1991.
33. T.Karu, "Primary and secondary mechanisms of action of visible to near-IR radiation on cells", *J. Photochem. Photobiol. B.*, **49**, pp.1 - 7, 1999.
34. R.D. Nelson, S.R. Hasslen, D.H. Ahrenholz, L.D. Solem, "Mechanisms of loss of human neutrophil chemotaxis following thermal injury", *J. Burn. Care Rehabil.*, **8**, pp. 496-502, 1987.
35. M. Braquet, P.Lavaud, D. Dormont, R.Garay, R. Ducousso, J.Guilbaund, M.Chignard, P. Borgeat, P. Braquet, "Leukocytic functions in burn-injured patients", *Prostaglandins*, **29**, pp. 747-764, 1985.
36. H. Yang, R. Mitchel, I. Lemaire, "The effects of in vitro hyperthermia on natural killer activity from lung, blood and spleen", *J. Clin. Lab. Immunol.*, **32**, pp. 117-122, 1990.
37. F.Elvinger, P.J. Hansen, R.P. Natzke, "Modulation of function of bovine polymorphonuclear leukocytes and lymphocytes by high temperature in vitro and in vivo", *Am. J. Vet. Res.*,**52**, pp. 1692-1698, 1991.
38. E.D. Wieder, M.H.Fox, "The role of intracellular free calcium in the cellular response to hyperthermia", *Int. J. Hyperthermia*, **11**, pp. 733-742, 1995.

## SESSION 11

# Tissue Optics

# Focusing light into biological tissue - How effective is it?

Lihong V. Wang
Optical Imaging Laboratory, Biomedical Engineering Program
Texas A&M University, College Station, Texas 77843-3120
URL: http://oilab.tamu.edu; Email: LWang@tamu.edu

## ABSTRACT

Focusing light into a turbid medium was studied with Monte Carlo simulations. Focusing was found to have a significant impact on the absorption distribution in turbid media when the depth of the focal point (the distance between the focal point and the surface of the turbid media) was less than or comparable with the transport mean free path. Focusing could significantly increase the peak absorption and narrow the absorption distribution. As the depth of the focal point increased, the peak absorption decreased, and the depth of peak absorption increased initially but quickly reached a plateau that was less than the transport mean free path. A refractive-index-mismatched boundary between the ambient medium and the turbid medium deteriorated the focusing effect, increased the absorption near the boundary, lowered the peak absorption, and broadened the absorption distribution.

## INTRODUCTION

The study of applications of laser and incoherent light in biomedicine for both therapeutic and diagnostic purposes is an active research field. It is possible to treat lesions selectively without damaging the surrounding normal tissues by use of selective interactions between light and biological tissue. The selectivity, related to one or more of the characteristics of laser light, includes the wavelength selectivity of light absorption by certain tissue types where the monochromatic property of laser light is employed or the thermal or stress confinement selectivity where the short pulse width of laser light is used. It is also possible to diagnose disease noninvasively by use of the optical properties of biological tissues. The optical properties include index of refraction, absorption coefficient, scattering coefficient, and scattering anisotropy. The spectra of the optical properties are related to the molecular conformation of biological tissues and hence should be sensitive indicators of the physiological status of biological tissues.

One of the fundamental goals in the study of laser-tissue interaction is to understand and simulate light transport in optically turbid biological tissues, by use of various theoretical models. In these models the optical properties of biological tissues are the input parameters, and the light distribution in the tissues or re-emitted from the tissues is calculated. Several methods are usually used in the modeling. The first method starts from the radiative transfer equation. The radiative transfer equation is usually too complex to solve analytically and is often simplified by a diffusion approximation. The radiative transfer equation with the approximation is usually solved by finite-element or finite-difference methods.[1,2] The second method is based on the Monte Carlo technique. Other methods include discrete random-walk model[3] and path-integral technique.[4] Diffusion theory is quick but inaccurate in predicting the light distribution near the light source and boundaries. In many applications, especially the therapeutic applications, knowledge about the light distribution near the source is very important. On the contrary, the Monte Carlo method is accurate but slow owing to its statistical nature.

In this work, we studied light distribution in turbid media when a focused optical beam was used to enhance the peak absorption inside the media. Monte Carlo technique was employed for its accuracy and flexibility in dealing with complex configurations. Although focusing optical beams has been well studied in confocal microscopy for imaging applications,[5] our goal was to investigate the internal light absorption toward therapeutic applications.



In *Laser-Tissue Interaction XI: Photochemical, Photothermal, and Photomechanical*, Donald D. Duncan, Jeffrey O. Hollinger, Steven L. Jacques, Editors, Proceedings of SPIE Vol. 3914 (2000)
1605-7422/00/$15.00

## METHOD

Monte Carlo simulations of light transport in tissues have been implemented previously for simple tissue geometry.[6–13] To compute light distributions according to the tissue geometry and optical properties, including refractive index $n$, absorption coefficient $\mu_a$, scattering coefficient $\mu_s$, and anisotropy factor $g$, we have written a Monte Carlo program in C for tissues with buried objects and focused optical beams. We used the delta-scattering technique[14] for photon tracing to greatly simplify the algorithm because this technique allows a photon packet to be traced without directly dealing with photon crossings of interfaces between different types of tissues.

A Cartesian coordinate system was set up for the simulation. The origin of the coordinate system was the center of the incident optical beam on the surface of the turbid medium. The $z$ axis was the normal of the surface pointing toward the inside of the turbid medium. The $xy$ plane was therefore on the surface of the turbid medium.

For a focused optical beam of a radius $\rho_f$, the irradiance was assumed to be uniform on the surface of the turbid medium (Fig. 1), and the radial position of a photon packet was sampled by

$$\rho = \rho_f \sqrt{x_\rho}, \tag{1}$$

where $\xi_\rho$ was a uniformly distributed random number between 0 and 1 ($0 \le \xi_\rho \le 1$). The azimuthal angle of the photon packet was sampled by

$$\theta = 2\pi\, \xi_\theta, \tag{2}$$

where $\xi_\theta$ was another uniformly distributed random number between 0 and 1 ($0 \le \xi_\theta < 1$). The Cartesian coordinates of the incident point were

$$x = \rho \cos(\theta), \tag{3}$$

$$y = \rho \sin(\theta), \tag{4}$$

If the depth of the focal point in the turbid medium was $z_f$, the directional cosines were set to

$$u_x = -x/\sqrt{r^2 + z_f^2}, \tag{5}$$

$$u_y = -y/\sqrt{r^2 + z_f^2}, \tag{6}$$

$$u_z = z_f/\sqrt{r^2 + z_f^2}, \tag{7}$$

If the ambient medium and the turbid medium had the same index of refraction, the directional cosines did not need to be changed when the photon packet entered the turbid medium. Otherwise, the directional cosines were changed based on the Snell's law, and the specular reflection was taken into account based on the Fresnel equations. Once the photon packet was launched into the turbid medium, the photon packet was traced with the delta-scattering technique.

The tissue system in the simulation had multiple types of tissue such as epidermis and dermis, which were assumed to have the same index of refraction. The interaction coefficient (also known as the total attenuation coefficient) of the $i$th tissue type, defined as the sum of $\mu_a$ and $\mu_s$, was denoted by $\mu_i$. The delta-scattering technique applied to light transport in turbid media is briefly summarized as follows.

1. Define an upper-bound interaction coefficient $\mu_m$, where $\mu_m \ge \mu_i$ for all $i$. In this study, $\mu_m$ was set to the maximum $\mu_i$ among all tissue types.
2. Select a step size $R$ between two consecutive interactions based on the upper-bound interaction coefficient,

$$R = -\ln(\xi_R) / \mu_m, \tag{8}$$

where $\xi_R$ was a uniformly distributed random number between 0 and 1 ($0 < \xi_R \le 1$). Then, determine the tentative next collision site $\boldsymbol{r}_k'$ by

$$\boldsymbol{r}_k' = \boldsymbol{r}_{k-1} + R\, \boldsymbol{u}_{k-1}, \tag{9}$$

where $\boldsymbol{r}_{k-1}$ was the current site, and $\boldsymbol{u}_{k-1}$ was the direction of the flight. The direction of the flight was determined according to the probability distributions of the deflection (polar) angle and azimuthal angle at each interaction site.[10]

3. Play a rejection game:
   a. Get another random number $\xi_a$, which was uniformly distributed between 0 and 1 ($0 < \xi_a \le 1$).
   b. If $\xi_a \le \mu_i(\boldsymbol{r}_k')/\mu_m$, i.e., with a probability of $\mu_i(\boldsymbol{r}_k')/\mu_m$, accept this point as a real interaction site ($\boldsymbol{r}_k = \boldsymbol{r}_k'$).

c. Otherwise, do not accept $\boldsymbol{r}_k'$ as a real interaction site but select a new path starting from $\boldsymbol{r}_k'$ with the unchanged direction $\boldsymbol{u}_{k-1}$ (i.e., set $\boldsymbol{r}_{k-1} = \boldsymbol{r}_k'$ and return to Step 2).

At each real interaction site, a fraction $\mu_a/(\mu_a + \mu_s)$ of the photon packet was absorbed, and the rest was scattered. The tracing continued until either the weight of the photon packet was below a preset threshold or the packet exited the tissue system. The weight threshold was set to $10^{-4}$ in this study. A sub-threshold photon packet experienced a "Russian roulette" to conserve energy. Since step 3 was very efficient, the delta-scattering technique was comparable with the standard Monte Carlo simulation methods in computational speed. The detailed treatment of photon tracing after step 3 was similar to that in Ref. 10 and will not be repeated here.

During the tracing of each weighted photon,[10] the light absorption, reflection, or transmission were correspondingly scored into different arrays according to the spatial positions of the photon. Multiple photons were traced to achieve an acceptable statistical variation. For this study, two to ten million photons were traced.

It is assumed in the delta-scattering technique that all the tissues in the simulation have the same index of refraction, although the ambient medium (e.g., air) is allowed to have different index of refraction from the tissues. Since most soft tissues have similar indices of refraction, this limitation does not pose a problem in our simulation.

This Monte Carlo program was used to simulate the optical absorption for the two types of configurations shown in Fig. 1. Figure 1(a) shows an optical beam focused into a homogeneous turbid medium. Figure 1(b) shows an optical beam focused into a blood vessel buried 0.015 cm deep in a skin model unless stated otherwise. The refractive index of the ambient medium was chosen to be either $n_a = 1$ or $n_a = 1.4$. In Fig. 1(a), the optical properties of the turbid medium were $n_t = 1.4$, $\mu_a = 0.1$ cm$^{-1}$, $\mu_s = 100$ cm$^{-1}$, and g = 0.9. In Fig. 1(b), the optical properties of the epidermis were $n_t = 1.4$, $\mu_a = 19$ cm$^{-1}$, $\mu_s = 480$ cm$^{-1}$, and g = 0.787. The optical properties of the dermis were $n_t = 1.4$, $\mu_a = 2.2$ cm$^{-1}$, $\mu_s = 210$ cm$^{-1}$, and g = 0.787. The optical properties of the blood vessel were $n_t = 1.4$, $\mu_a = 266$ cm$^{-1}$, $\mu_s = 473$ cm$^{-1}$, and g = 0.995. These optical properties for the skin model represented the realistic optical properties of the skin components at the wavelength of 532 nm.[15] The thickness of the epidermis was 0.006 cm (60 μm). The dermis was considered semi-infinite in this simulation. The blood vessel was modeled as an infinitely long cylinder perpendicular to the schematic with a diameter of 0.006 cm (60 μm). The distance between the center of the cylinder and the surface of the turbid medium was varied. When focusing was applied, the depth of the focal point always matched the depth of the center of the blood vessel.

## RESULTS AND CONCLUSIONS

The distributions of the absorption density in the homogeneous turbid medium as shown in Fig. 1(a) were simulated. The absorption density was in the units of cm$^{-3}$ representing the absorption probability density of the incident photons per unit volume. If the light source was continuous wave, the absorption density multiplied by the incident power yielded the power deposition density in W/cm$^{-3}$. If the light source was pulsed, the absorption density multiplied by the incident energy yielded the energy deposition density in J/cm$^{-3}$.

When the indices of refraction between the ambient medium and the turbid medium were matched, $n_a = n_t = 1.4$. The depth of the focal point varied among $z_f = 0.05$, 0.1, 0.2, and ∞ cm while the radius of the beam on the surface was fixed. When $z_f = \infty$, the incident beam was collimated and unfocused. The sizes of the grid elements for the Monte Carlo simulations in the $x$, $y$, $z$ directions were 0.05 cm, 0.05 cm, and 0.025 cm, respectively. It can be seen that focusing had a dramatic effect on the absorption distribution in the turbid medium. As the depth of the focal point increased, the peak absorption density decreased, the focus became blurred, and the pattern of absorption expanded. The key parameter was the transport mean free path defined as $1/[\mu_a + \mu_s(1 - g)]$, which was 0.099 cm. Therefore, the focusing had a significant effect when the depth of the focal point was less than or comparable with the transport mean free path.

When the indices of refraction between the ambient medium and the turbid medium were mismatched, $n_a = 1.0$ and $n_t = 1.4$. The depth of the focal point was $z_f = 0.1$ cm based on propagation in air. Two reasons affected the absorption distribution in the mismatched scenario. First, the beam was defocused by the mismatched interface between the ambient medium and the turbid medium. Second, the mismatched

boundary increased the internal light reflection and reduced light reflection into the ambient medium. Therefore, more light was absorbed near the boundary, and the light absorption was more spread out.

The absorption distribution was simulated when the focusing was corrected such that the unscattered light rays would reach the same point at $z_f = 0.1$ cm based on propagation in the turbid medium. This focus correction for mismatched index of refraction could be accomplished by use of specially designed external focusing optics.

Figure 2 shows the one-dimensional absorption distributions along the vertical line through the center of the light beam. Figure 2(a) demonstrated the effect of the depth of the focal point $z_f$. As the depth of the focal point $z_f$ increased, the peak absorption decreased, and the depth of peak absorption increased initially but quickly reached a plateau. Even if the depth of the focal point $z_f$ increased beyond 0.1 cm, the depth of peak absorption was less than 0.1 cm, which was approximately the transport mean free path. Therefore, focusing the depth of peak absorption significantly more than one transport mean free path into a turbid medium would prove to be inefficient although the peak absorption with a focused beam was greater than the peak absorption with an unfocused beam.

Figure 2(b) shows that the uncorrected focusing with a mismatched boundary had the lowest peak absorption because of defocusing. The corrected focusing with a mismatched boundary had the highest peak absorption because of the increased internal reflection at the boundary. For many therapeutic applications of light, such as the port wine stain treatments, the ratio between the absorption at the boundary and the peak absorption inside the tissues is the most significant parameter because it determines how well the skin surface can be preserved while the internal lesions are treated. Therefore, we plotted the normalized absorption distributions in Fig. 2(c). The focusing into index-matched turbid medium had the lowest surface-to-peak ratio of absorption, which was nearly 50%. The uncorrected focusing with a mismatched boundary had the highest surface-to-peak ratio of absorption, which was approximately 85%, and had the broadest distribution. The corrected focusing with a mismatched boundary had a slightly lower surface-to-peak ratio of absorption but had a much narrower distribution than the uncorrected counterpart .

The distributions of the absorption density in the skin model as shown in Fig. 1(b) were also simulated. The radius of the optical beam $\rho_f$ was fixed. Several scenerios were simulated: (a) Matched indices of refraction between the ambient medium and the turbid medium, and $z_f = \infty$ (unfocused). (b) Matched indices, and $z_f = 0.015$ cm. (c) Mismatched indices, and $z_f = \infty$. (d) Mismatched indices, and $z_f = 0.015$ cm without focus correction. (e) Mismatched indices, and $z_f = 0.015$ cm with focus correction. The 0.006-cm diameter blood vessel was buried 0.015 cm deep. The radius of the optical beam $\rho_f$ was 0.075 cm.

Figure 3(a) shows the one-dimensional distributions along the vertical line through the center of the optical beam. Additionally, the one-dimensional distributions of the absorption density were plotted for more deeply buried blood vessels under the matched boundary condition in Figs. 3(b) and (c). The sizes of the grid elements for the Monte Carlo simulations were 0.002 cm in all the $x$, $y$, $z$ directions. Since the blood was much more absorbing than the other components in the skin model, the absorption density in the blood vessel was greater than that in the epidermis and dermis even when the beam was not focused. Under both matched and mismatched boundary conditions, focusing into the shallow blood vessel dramatically increased the absorption density in the blood vessel even when the optical beam was defocused by the mismatched boundary. Note that the depth of the blood vessel for Fig. 3(a) was approximately one transport mean free path as calculated by $\mu_{te}' d_e + \mu_{td}' d_d$, where $\mu_{te}'$ and $\mu_{td}'$ were the sum of the absorption coefficient and the reduced scattering coefficient for the epidermis and dermis, respectively, $d_e$ was the thickness of the epidermis, and $d_d$ was the distance between the bottom of the epidermis and the center of the blood vessel. As the distance between the center of the cylinder and the surface of the turbid medium was doubled and quadrupled, the effect of focusing decreased dramatically [Figs. 3(b) and (c)]. This was in agreement with the studies on focusing light into homogeneous turbid media.

A short-pulsed laser is often used to reach the so-called "thermal confinement" condition for localized treatment, where the laser pulse width is much shorter than the thermal relaxation time of the medium being treated. In thermally confined treatments, the above simulated absorption probability density can be converted into the energy absorption density by multiplying it with the pulse energy of the laser. The absorbed optical energy is converted into heat and causes an abrupt temperature rise. The instantaneous temperature rise is proportional to the local absorption density. For example, by use of a focused beam with a matched boundary [Fig. 2(c)], the surface temperature rise would be only ~50% of the peak temperature rise inside the turbid medium. For a buried highly absorbing blood vessel, the surface temperature rise

would be much lower than the peak temperature rise in the vessel when the beam is properly focused into the blood vessel.

## SUMMARY and DISCUSSION

Focusing light into a homogeneous turbid medium had a significant impact on the absorption distribution in the turbid medium when the distance of the focal point from the surface of the turbid medium was less than or comparable with the transport mean free path. Focusing increased the peak absorption and narrowed the absorption distribution significantly. As the depth of the focal point $z_f$ increased, the peak absorption decreased, and the depth of peak absorption increased initially but quickly reached a plateau that was less than the transport mean free path. Therefore, focusing the peak absorption significantly more than one transport mean free path into a turbid medium would prove to be inefficient although the peak absorption with a focused beam was greater than the peak absorption with an unfocused beam.

A mismatched boundary between the ambient medium and the turbid medium deteriorated the focusing effectiveness, increased the absorption near the boundary, lowered the peak absorption, and broadened the absorption distribution. The focus correction improved the surface-to-peak ratio of absorption slightly but narrowed the absorption distribution significantly.

Focusing into a shallowly buried absorbing object was very effective. But the effectiveness was reduced significantly when the depth of the buried object was increased to more than one transport mean free path.

This study provides some guidance for improving clinical treatments of superficial lesions such as port wine stains. If the depth of the lesions are measured with techniques such as optical coherence tomography or high-frequency ultrasonography, the laser beam can be focused toward the lesions such as the vessel network for improved localization of energy. Of course, focusing into wrong locations surrounding the lesions would cause adverse effects. One of the techniques that may assist the focus aiming is photo-acoustic imaging.[16] If the power of the treatment laser is reduced to a diagnostic (non-therapeutic) level, the laser can be used as the optical source for photo-acoustic imaging. The photo-acoustic signal is used to optimize the focusing such that an maximal amount of energy is absorbed by the lesions compared with the surrounding normal tissue. Once the focusing is completed, the laser power can be restored to the therapeutic level for treatments.

## ACKNOWLEDGMENTS

This project was sponsored in part by the National Institutes of Health grants R29 CA68562 and R01 CA71980, and the National Science Foundation grant BES-9734491.

## FIGURES

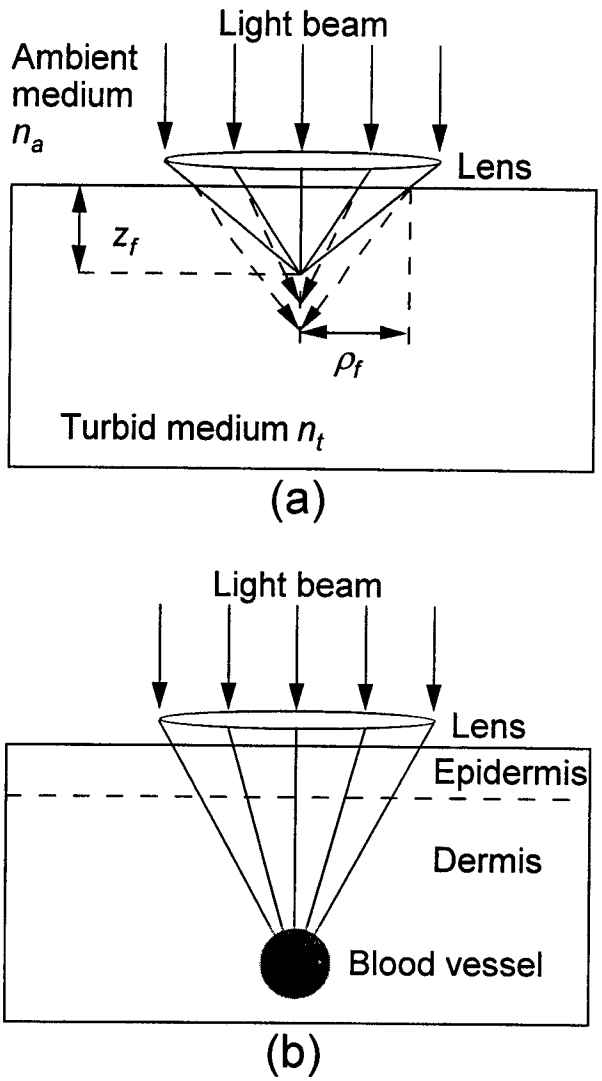


Fig. 1. (a) Schematic of focusing an optical beam into a turbid medium, where $z_f$ was the depth of the focal point in the turbid medium, $\rho_f$ was the radius of the optical beam on the surface of the turbid medium, $n_a$ was the index of refraction of the ambient medium, and $n_t$ was the index of refraction of the turbid medium. Focusing is illustrated for both matched boundary condition (solid converging lines) and mismatched boundary condition (dashed lines with arrows). (b) Schematic of a skin model containing the epidermal and dermal layers. A 0.006-cm (60-μm) diameter blood vessel was buried 0.015 cm deep in the dermis unless stated otherwise. The thickness of the epidermis was 0.006 cm (60 μm).

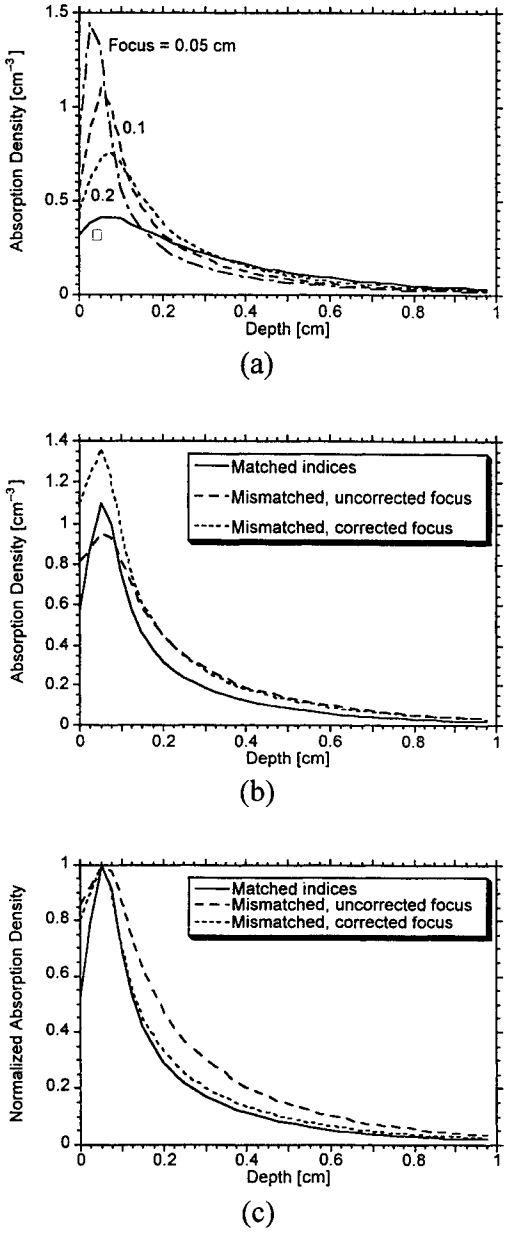


Fig. 2. One-dimensional depth distributions of the absorption density in the turbid medium under various conditions [see Fig. 1(a)]. (a) Comparison in the case of matched indices of refraction between the ambient medium and the turbid medium. (b) Comparison among the absorption density curves showing the effects of mismatched indices and focus correction. (c) Comparison among the normalized absorption density curves showing the effects of mismatched indices and focus correction.

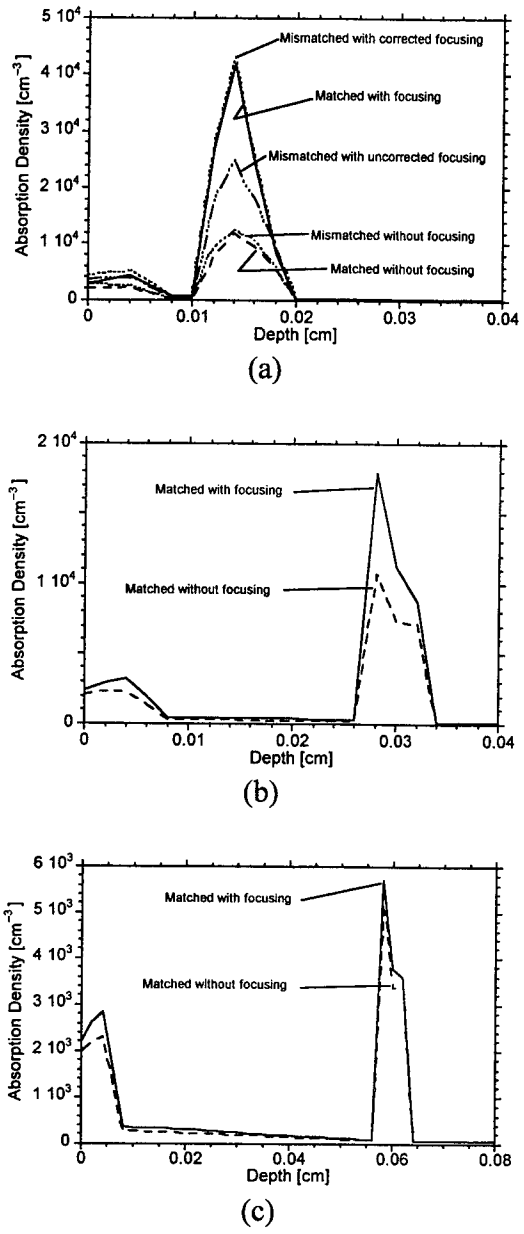


Fig. 3. One-dimensional depth distributions of the absorption density in the skin model under various conditions [see Fig. 1(b)]. (a) Both the effects of matched indices of refraction and focusing were considered. The distance between the center of the cylinder and the surface of the turbid medium was 0.015 cm. (b) The effect of focusing under matched boundary condition was studied when the distance between the center of the cylinder and the surface of the turbid medium was 0.030 cm. (c) The effect of focusing under matched boundary condition was studied when the distance between the center of the cylinder and the surface of the turbid medium was 0.060 cm.

## REFERENCES


1. A. H. Hielscher, R. E. Alcouffe, and R. L. Barbour, "Comparison of finite-difference transport and diffusion calculations for photon migration in homogeneous and heterogeneous tissues," Phys. Med. & Biol. **43**, 1285-1302 (1998).
2. M. Schweiger and S. R. Arridge, "The finite-element method for the propagation of light in scattering media - frequency domain case," Med. Phys. **24**, 895-902 (1997).
3. A. H. Gandjbakhche, G. H. Weiss, R. F. Bonner, and R. Nossal, "Photon path-length distributions for transmission through optically turbid slabs," Phys. Rev. E **48**, 810-818 (1993).
4. L. T. Perelman, J. Wu, I. Itzkan, and M. S. Feld, "Photon migration in turbid media using path integrals," Phys. Rev. Lett. **72**, 1341-1344 (1994).
5. A. Singh and K. P. Gopinathan, "Confocal microscopy - a powerful technique for biological research," Current Science **74**, 841-851 (1998).
6. B. C. Wilson and G. A. Adam, "Monte Carlo model for the absorption and flux distributions of light in tissue," Med. Phys. **10**, 824-830 (1983).
7. S. T. Flock, B. C. Wilson, D. R. Wyman, and M. S. Patterson, "Monte-Carlo modeling of light-propagation in highly scattering tissues I: model predictions and comparison with diffusion-theory," IEEE Trans. Biomed. Eng. **36**, 1162-1168 (1989).
8. S. A. Prahl, M. Keijzer, S. L. Jacques, and A. J. Welch, "A Monte Carlo model of light propagation in tissue," in *Dosimetry of Laser Radiation in Medicine and Biology*, G. J. Muller and D. H. Sliney, eds., Proc. Soc. Photo-Opt. Instrum. Eng. **IS 5**, 102-111 (1989).
9. S. L. Jacques and L.-H. Wang, "Monte Carlo modeling of light transport in tissues," in *Optical Thermal Response of Laser Irradiated Tissue*, A. J. Welch and M. J. C. van Gemert, eds., (Plenum Press, New York, 1995), pp. 73-100.
10. L.-H. Wang, S. L. Jacques, and L.-Q. Zheng, "MCML - Monte Carlo modeling of photon transport in multi-layered tissues," Comp. Meth. and Prog. in Biomed. **47**, 131-146 (1995). The MCML/CONV software package may be downloaded from URL: http://people.tamu.edu/~lwang.
11. A. Sassaroli, C. Blumetti, F. Martelli, L. Alianelli, D. Contini, A. Ismaelli, and G. Zaccanti, "Monte Carlo procedure for investigating light propagation and imaging of highly scattering media," Appl. Opt. **37**, 7392 - 7400 (1997).
12. E. Okada, M. Firbank, M. Schweiger, S. R. Arridge, M. Cope, and D. T. Delpy, "Theoretical and experimental investigation of near-infrared light propagation in a model of the adult head," Appl. Opt. **36**, 21 - 31 (1997).
13. L.-H. Wang, S. L. Jacques, and L.-Q. Zheng, "CONV - Convolution for responses to a finite diameter photon beam incident on multi-layered tissues," Comp. Meth. and Prog. in Biomed. **54**, 141-150 (1997).
14. I. Lux and L. Koblinger, *Monte Carlo Particle Transport Methods: Neutron and Photon Calculations* (CRC Press, Boca Raton, 1991).
15. C. Sturesson and S. Andersson-Engels, "Mathematical modeling of dynamic cooling and pre-heating, used to increase the depth of selective damage to blood vessels in laser treatment of port wine stains," Phys. Med. Biol. **41**, 413-428 (1996).
16. C. G. A. Hoelen, F. F. M. Demul, R. Pongers, and A. Dekker, "Three-dimensional photoacoustic imaging of blood vessels in tissue," Opt. Lett. **23**, 648-650 (1998).

# Monte Carlo Simulation of Light Propagation in Skin Tissue Phantoms Using a Parallel Computing Method

D. Wu[a], S. S. Zhao[b], J. Q. Lu[a*], X. H. Hu[a]
[a]Department of Physics, East Carolina University, Greenville, NC 27858
[b]AT&T Labs, 200 S. Laurel Ave., Middletown, NJ 07748

## ABSTRACT

In Monte Carlo simulations of light propagating in biological tissues, photons propagating in the media are described as classic particles being scattered and absorbed randomly in the media, and their path are tracked individually. To obtain any statistically significant results, however, a large number of photons is needed in the simulations and the calculations are time consuming and sometime impossible with existing computing resource, especially when considering the inhomogeneous boundary conditions. To overcome this difficulty, we have implemented a parallel computing technique into our Monte Carlo simulations. And this movement is well justified due to the nature of the Monte Carlo simulation. Utilizing the PVM (Parallel Virtual Machine, a parallel computing software package), parallel codes in both C and Fortran have been developed on the massive parallel computer of Cray T3E and a local PC-network running Unix/Sun Solaris. Our results show that parallel computing can significantly reduce the running time and make efficient usage of low cost personal computers. In this report, we present a numerical study of light propagation in a slab phantom of skin tissue using the parallel computing technique.

**Keywords:** Tissue scattering, Monte Carlo simulation, parallel computing

## 1. INTRODUCTION

The scattering of light by turbid media has been studied extensively in the past.[1] However, the existing theoretical models are still not satisfactory for explaining the experimental data in many important applications related to the light propagation in highly scattering turbid media such as the biological materials. Understanding the interaction between light and biological materials is critical in development of new optical methods for biomedical imaging applications. For this purpose, it is essential to develop efficient modeling tools in the investigation of interaction between laser radiation and turbid media.

In a turbid medium, light is scattered and absorbed due to the inhomogeneities and absorption characteristics of the medium. When the medium becomes highly scattering, multiple scattering effects become dominant, and one widely used approach to solve this type of problem is the radiative transport theory [1] which concerns transport of light energy. Within the framework of radiative transfer theory, light propagating in a turbid medium is treated as a large number of photons, with no phase and polarization characterizations, that undergo random scattering and absorption. However, the radiative transfer equation can not be solved analytically without approximations except for a few cases with simple boundary conditions. Several approximations have been developed. Among them are the first-order solution,[2] the discrete ordinates method, [2] the Kubelka-Munk two-flux and four-flux theory, [3] and the diffusion theory.[4, 5] These methods all have their limits.

Light transportation in turbid medium can be statistically simulated by various Monte Carlo methods.[6,7] Using a simple model of random walk, a Mote Carlo method can be applied to solve radiative transfer problems accurately with virtually any boundary conditions. However, the heavy demand of computation time of the Monte Carlo simulation to reduce statistical error has impeded the wide applications of the method. Recently, we have developed a new Monte Carlo method through a "time slicing" algorithm to directly calculate light distribution in turbid medium such as biological tissues.[8-10] This method is capable of direct calculation of the light distribution with inhomogeneous boundary conditions. Two examples of the inhomogeneous boundary conditions are: a converging laser beam incident on a tissue phantom with a plane surface in which the incident angle varies with the photon location, and a tissue phantom with rough interfaces in which the incident angle

* Correspondence: Email: luj@mail.ecu.edu; URL: http://bmlaser.physics.ecu.edu; Tel: 252-328-1856; Fax: 252-328-6314

In *Laser-Tissue Interaction XI: Photochemical, Photothermal, and Photomechanical*, Donald D. Duncan, Jeffrey O. Hollinger, Steven L. Jacques, Editors, Proceedings of SPIE Vol. 3914 (2000)
1605-7422/00/$15.00

varies with fluctuating direction of the surface normal even for a collimated beam. To take the advantage of the rapid progress in personal computers (PC) with ever increasing computation power and decreasing cost, we have established a PC cluster for parallel computing to fully appreciate the potentials of the recently developed Monte Carlo method within a modest research budget.

In this paper we report our initial results in carrying out efficient Monte Carlo simulations on light distribution in biological tissue phantom by implementing parallel computing techniques, and we show that it can dramatically reduce the program running time. The material of the paper is organized as following. After a brief summary of the Monte Carlo simulation in tissue scattering in next section, the implementation of the parallel computing is then discussed, and the results of Monte Carlo simulations of a converging laser beam propagating through a tissue slab using the parallel method is then presented afterward.

## 2. MONTE CARLO SIMULATION OF TISSUE SCATTERING

In this section we will give a brief summary of a recently developed Monte Carlo simulation method in study the scattering and propagation of a converging laser beam in highly scattering medium.[8-10] In the present case the medium is a slab, as shown in Figure 1.

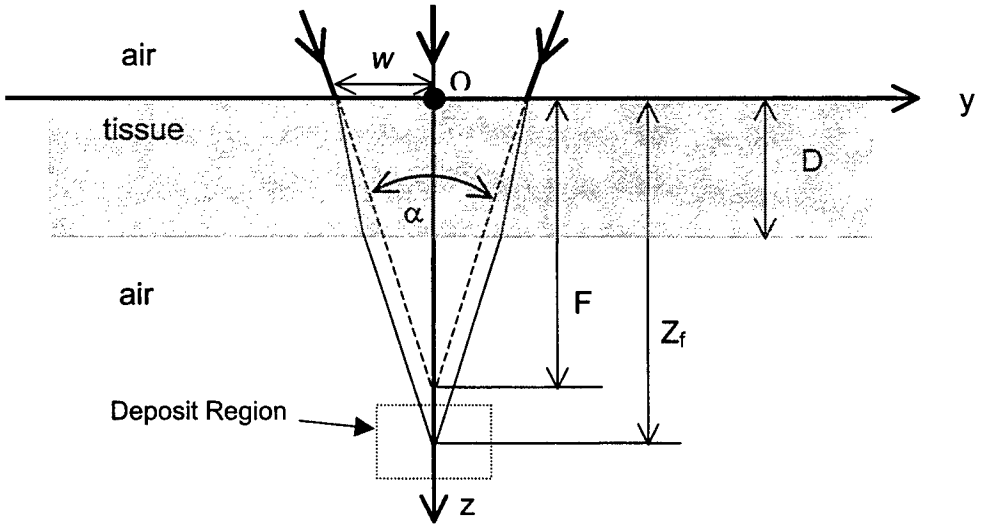


**Fig. 1** Schematic of a focused laser beam propagating through a tissue slab. Where α is the cone angle and $w$ is the radius of the beam at the entrance surface. The tissue slab has a thickness of $D$ and an index of refraction of $n$. The dashed line indicates the focal point in the absence of the tissue slab that is located at a distance $F$ below the entrance surface. In the presence of the slab, the beam will be focused in a spreading line along z-axis centered at a distance $Z_f$ below the entrance surface.

The converging beam is incident on the tissue phantom from the air, it has a cone angle of α and a radius of $w$ at the air-tissue interface, and its focal point in the absence of the tissue slab is located at a distance $F$ below the exit surface. In the presence of the slab, the beam will be focused in a spreading line along z-axis centered at a distance $Z_f$ below the entrance surface. A Cartesian coordinate system is used for the simulation with the origin set on the beam axis at the entrance surface or the $xy$-plane. The tissue slab is assumed to be macroscopically homogeneous with a thickness of $D$. It is optically characterized by an index of refraction $n$, scattering coefficient $\mu_s$, absorption coefficient $\mu_a$, and anisotropy factor $g$. The propagation of a photon in the phantom is described by its position and propagating direction, where the position is described by the Cartesian coordinates, and propagation direction is described by a set of moving spherical coordinates ($\phi$, $\psi$) attached to the photon. The boundary condition at the $z = 0$ plane for each photon contained in the beam are decided by its position at the entrance surface ($x_0$, $y_0$) and its incident angle. The incident angle of each photon is to be calculated according to its distance $\rho_0 =$

$\sqrt{x_0^2 + y_0^2}$ from the z-axis and the distance between the focal point of the beam in the absence of the slab and the entrance surface, $F$. At the entrance surface, a photon will either be refracted or reflected according to a probability decided by the Fresnel reflectivity at the photon's incident angle. The reflected photons are not considered further.

If a photon pass through the entrance surface, it starts to propagate inside the material in the direction of the refraction angle until scattered or absorbed. When a scattering occur, the scattering angle, $\phi_s$, i.e. the angle between the propagation directions before and after scattering, is randomly chosen from a distribution governed by the Henyey-Greenstein phase function.[11] The azimuthal angle, $\psi_s$, is randomly chosen to determine the projection of the new direction of the scattered photon in the plane perpendicular to the original one. Both of the angles can be found from the following equation: [7]

$$\varphi_s = \cos^{-1}\left(\frac{1}{2g}\left[1 + g^2 - \left(\frac{1-g^2}{1-g+2gRND}\right)^2\right]\right) \tag{1}$$
$$\psi_s = 2\pi RND$$

where RND is a random number ranging from 0 to 1. If the photon direction before scattering is given by $(\phi,\psi)$, the photon direction after scattering, $(\phi',\psi')$, can be related to $(\phi,\psi)$ and $(\phi_s, \psi_s)$ as [7]

$$\varphi' = \cos^{-1}(\cos\varphi_s \cos\varphi + \sin\varphi_s \sin\varphi \cos\psi_s), \tag{2}$$

$$\psi' = \begin{cases} \psi + \tan^{-1}(\sin\varphi_s \sin\psi_s / \alpha), & for \quad \alpha > 0 \\ \psi + \tan^{-1}(\sin\varphi_s \sin\psi_s / \alpha) + \pi, & for \quad \alpha < 0 \end{cases}, \tag{3}$$

$$\alpha = \cos\varphi_s \sin\varphi - \sin\varphi_s \cos\psi_s \cos\varphi . \tag{4}$$

The distance traveled by a photon between successive scattering events, $L_s$, is randomly chosen from an exponential distribution function and given by $L_s = -\ln(1 - RND)/\mu_s$ with a mean value $< L_s >= 1/\mu_s$.[7] If a photon travels in a direction $(\phi,\psi)$ after a scattering event at (x, y, z) and the next scattering occurs at point (x', y', z') of a distance $L_s$ away, the coordinates of these two points are related through the following relations

$$\begin{aligned} x' &= x + L_s \sin\varphi \cos\psi \\ x' &= y + L_s \sin\varphi \sin\psi \\ z' &= z + L_s \cos\varphi \end{aligned} \tag{5}$$

As for the photon absorption, we used an approach different from previously published ones [6,7] for its offering a clear and intuitive way to the direct calculation of light distribution. For any photon which passed through the entrance surface, a life-time traveled distance in the medium, $L_a$, is first determined to predetermine the distance the photon may travel in the medium before it is absorbed. For an arbitrary photon, $L_a$ is randomly chose according to an exponential distribution function and given by $L_a = -\ln(1 - RND)/\mu_a$ with a mean $< L_a > = 1/\mu_a$ [7].

In this paper we are interested in the distribution of the transmitted light near the geometric focal point at $z = Z_f$ of the refracted incident beam for a cw incident beam. To obtain the light distribution, a cubic region surrounding the focal point (which is indicated by the deposit region in Fig.1) is selected and divided into cubic grid cells, and each cell has a register which will count the number of photons falling in the cell. According to a "time-slice" method,[8] the total number of photons falling into one cell from an impulse beam can be used to calculate the steady-state number of photons in that cell for a cw beam. Thus the registers of the cells will provide the photon density distribution in the deposit region.

We track each photon along its 3-d trajectory and record its total traveled distance, $L$, in the medium at each scattering event. Before the photon is allowed to propagate further, $L$ is compared with the predetermined $L_a$. If $L > L_a$, the photon is then eliminated as a result of absorption. Otherwise the photon's position is further checked to determine if it is on a boundary of the considered region in the turbid material. When the photon is on the air-phantom boundary, it will be either reflected back into the material, with a probability equal to the Fresnel reflection coefficient, or refracted into the air. If it is refracted into the free-space region above the tissue, it will not be tracked further. If it is refracted into the free-space region below the slab, i.e. the transmission region, it will be further checked to see if it falls into the deposit region where its presence will be recorded by the registers in each cell as it passes through. The photon will also be eliminated if it reaches other borders of the considered region. If the photon survives these tests it will be allowed to propagate further until one of the eliminating conditions is met. The procedures are repeated to the next photon until all the photons contained in the beam are depleted.

## 3. PARALLEL COMPUTING

The Monte Carlo simulations described above offers a flexible yet rigorous approach toward modeling of light transportation inside turbid media within the framework of the radiative transfer theory. Furthermore, its capability of handling of difficult boundary conditions related to the propagation of converging laser beam and rough interfaces has provided an extremely useful tool in understanding the interplay between the coherent and the diffuse components of the light transmitted through biological tissues.[9,10] However, this method requires large-scale computation to achieve satisfactory accuracy for its statistical nature and thus greatly needs the adoption of high performance computing techniques. But on the other hand, the tracking of individual photons are independent processes because of the nature of the radiative transfer framework. These operational features of the Monte Carlo simulations of light transportation in turbid media make itself a very good candidate for parallel computing.

To adopt parallel computing techniques for our Monte Carlo simulations, two parallel computing models can be used: either on a massively parallel processing architecture computer or a cluster of PCs. With the wide availability of parallel computing software packages and high power PCs with low cost, the latter is more attractive. Among the current parallel computing interface models we selected the message passing model over the share memory model for the its suitability to heterogeneous networks of workstations or PCs. The message passing is a paradigm used widely on parallel computers, especially scalable parallel computers with distributed memory. While several implementation methods exist for the message passing model, two stand out because of their efficiency, portability, and easy to use. These are the PVM – the Parallel Virtual Machine and MPI – the message Passing Interface. We have successfully converted our sequential program into parallel code using PVM, and our discussions and results presented here are associated with PVM, and the effort to use MPI is currently in progress.

**PVM:** PVM is a free software package that can be downloaded from Oak Ridge National Lab web site. It allows a programmer to create and access a concurrent computer system made from networks of loosely coupled processing elements. This ability to bring together diverse computer architectures under a central control enables the PVM users to divide a simulation problem into subtasks and assign each subtask to be executed on the processor architecture that is best suited for the subtask. PVM allows messages passing between machines that do not share data representations.

**Workload distribution:** To perform parallel processing, it is necessary to distribute the workload across the networked processing elements (PE). There are two main programming approaches that codes are written under PVM: master/worker and hostless. We choose the former approach to conduct our parallel processing. Under the master/worker paradigm, one task is used as the master. The sole purpose of the master task is to create all other tasks for solving the problem, to coordinate the input of initial data to each task and collect the output of results from each task. In our case, the photons contained in the incident beam are divided into multiple groups by the master program and each group is sent to a task that may run on a different PE. In each task, after receiving its group of the incident photons from the master program, the trajectories of each photon will be tracked, and any deposit into the deposit area is recorded and will be sent back to the master program when the task finishes its tracking procedure. The master will append the deposit results to the existing data from finished tasks, it will also send the PE another task to be executed until all simulations finish. Then the master program will conduct the final summarization of the deposit from all the tasks, and carry out certain required statistical calculations before terminating the program.

**Cray T3E:** We have conducted part of Monte Carlo simulations reported here on the massive parallel computer Cray T3E at North Carolina Super Computer Center (NCSC) where PVM is readily available and easy to use.

**PC cluster:** To make our parallel codes more accessible for regular users, we have established a local network of PC's to execute bulk of the simulation jobs. The PC cluster consists of fifteen Pentium PCs with Celeron CPU of 433, 466 and 500MHz and each PC has 128MB memory. The local network is served with a 100 Mbit/s network hub and the Solaris 7 operating system (the UNIX operating system for Intel x86 processors) from the Sun Microsystem. PVM is used on this network to implement the parallel process using each PC as a PE. With this local network we were able to significantly raise the simulation speed and reduce CPU time, and to perform large scale code testing and transfer large part of our numerical simulations from the CRAY supercomputers at NCSC to this dedicated PC cluster with a very modest cost.

**Random number generators (RNG):** One of the major challenge in our implementation of parallel computing for the Monte Carlo simulations is to find an appropriate RNG. As discussed in the previous section, calculating light distribution in the tissue phantom relies on photon tracking which contains many random processes. The scattering frequency, the scattering angle and the life-time travel length as well as the reflection at the interfaces are randomly chosen from corresponding

distributions, and a good RNG is essential for obtaining accurate statistical results. Beside the standard requirements for a good RNG, an appropriate RNG needed in our simulation must be able to generate a sequence of random numbers satisfying statistical tests for randomness, uniformly distributed in the full range from 0 to 1, not correlated, and have long period within the acceptable error ranges. As we move from sequential to parallel computing, additional requirements arise that are especially important for executing parallel computing:

- The sequences of random numbers generated on each PE should satisfy the requirements of a good sequential generator.
- There should be no correlation between the sequence on different PE.
- It should generate same sequence for different PEs.

In the early days of parallel computing, two techniques were often used to derive parallel RNG from serial RNG: sequence splitting and the leapfrog method. Both of them have been reported to have their problems [12, 13]. To avoid the problems associated with both of the above approaches, recent research has lead to development of parallel random number generators based on parameterization.[14]

For our initial calculations, we employ the sequence splitting method to generate the random numbers from a tested sequential generator. We designate a task to control the distribution of random numbers among the tasks of tracking different photons. The control task initiates a block of seeds for master program for each task it spawn, and it will supply more for the same task if needed. This method does lead to a problem, though, in which it is impossible to pre-determinate accurately the number of random numbers a photon tracking task needs during the process. So the block of seeds passed to a task may not be all used up by it. Because of this problem, we found that the results of simulating a converging laser beam varies slightly if the task number differs. Results with different optical parameters shown in this paper are obtained using the same number of task to maintain the consistency and it is to demonstrate the feasibility of the parallel calculation light distribution in tissue phantom. Currently, efforts to make use of a package using the parameterization method, the Scalable Parallel Random Number Generator (SPRNG),[15] is underway.

## 4. RESULTS

In this section we present our results on Monte Carlo simulation of tissue scattering using the parallel computing method described in the previous sections. Here we consider a converging laser beam, with a Gaussian profile at the entrance surface, propagating through a slab of tissue phantom made of intralipid solution, as shown in Fig. 1.

To understand the results better, let us first exam the components of the light propagating inside a turbid medium. When a beam of light is incident on a turbid medium, most of the photons will be scattered before they emerge from the medium and thus form the scattered part of the transmitted light. And a very small portion of the photons will come out without scattering (the unattenuated part), if the optical pathlengths involved are not too large. Within the scattered part, some photons are scattered in the forward direction for only a few times and was named quasi-ballistic or the snake component, the rest forms the diffuse component since their distribution can be well described by a diffusion equation.[2, 16] Both unattenuated and quasi-ballistic photons have their trajectories either unchanged or slightly modified from the original. In a configuration of a converging beam propagating through a slab of turbid medium, the ballistic component will be brought together near the focal point to form a peak.[8] The quasi-ballistic component will mostly provide a photon density near the focal point and thus contribute to the background near the peak and decrease quickly away from the focal point. For the diffuse component, the photons which have been multiply scattered, will form a rather uniform background in the focal plane. If we name the radiance inside the medium as $I(\vec{r},\hat{s})$, it can be divided into the coherent part $I_c$ and the scattered part $I_d$: $I(\vec{r},\hat{s}) = I_c(\vec{r},\hat{s}) + I_d(\vec{r},\hat{s})$.[2] The coherent radiance, i.e., the unattenuated part, is reduced according to:

$$\frac{dI_c(\vec{r},\hat{s})}{ds} = -\mu_t I_c(\vec{r},\hat{s}), \tag{6}$$

where $\mu_t$ is the attenuation coefficient defined as $\mu_t = \mu_s + \mu_a$. The unattenuated photons arriving near the focal point in our simulation can then be compared to that expected from Eq. (6). For a cw converging Gaussian beam with $N_0$ photons per unit time transmitted through a tissue slab of thickness D, according to Eq. (6) the number of unttenuated photons in the transmitted light arriving at the focal point is given by:

$$N_{uatt} \simeq (1-R_1)(1-R_2)N_0 e^{-\mu_t D} - N_0 \frac{\mu_t D w}{\sqrt{2}F}\int_{t_0}^{\infty} e^{-t^2} dt, \tag{7}$$

where $t_0 = \sqrt{2}F / w + \mu_t Dw / 2F$, and $R_1$, $R_2$ are the reflectivity at the entrance and exit surfaces of the slab, respectively. For the cases we considered in this paper with $F = 63mm$ and $w = 4.86mm$, we find $F >> w$, and therefore the second term in Eq. (7) can be neglected. So we have

$$N_{unatt} \simeq (1 - R_1)(1 - R_2) N_0 e^{-\mu_t D}. \tag{8}$$

This provides the expected photon density peak at the focal point. Eq. (8) also indicates that the coherent part of the incident radiance is attenuated exponentially with the optical depth $\mu_t$ D. Thus, measuring of this peak against the slab thickness can lead to the determination of the attenuation coefficient $\mu_t$, or *vice versa*.

To study such dependence of the peak height on $\mu_t$, we carried out simulations of a converging laser beam propagating through a slab of diluted intralipid solution using the parallel technique. Through the simulations, the slab thickness is fixed at $D = 17mm$ while $\mu_t$ is changed from 0.546 ($mm^{-1}$) to 1.092 ($mm^{-1}$) through the variation of the concentration of the solution slab. The optical parameters of intralipid solution are given by an albedo of $\mu_s/\mu_a = 0.9666$, and a refractive index $n=1.33$ and $g=0.48$.[17] We chose the transverse dimension of the slab in the $xy$-plane to be of $50mm \times 50mm$ to accommodate the simulation, and the parameters of the incident Gaussian beam to have radius $w = 4.86mm$, cone angle $\alpha = 8.82°$ and focal length $F = 63mm$. The unattenuated photons distribute along a spreading line in the z-axis centered at $z = Z_f = 67.3mm$, which is referred to as the focal point. The grid cells of the deposit region are cubic with $50\mu m$ sides and the region occupies a $(16mm)^3$ cube centered at the focal spot.

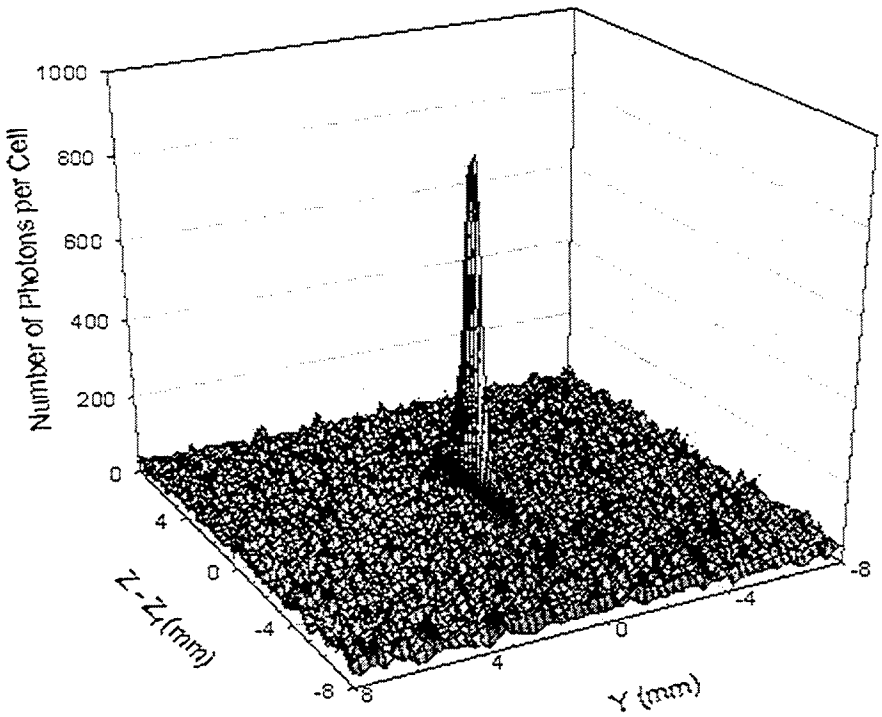


**Fig. 2** Parallel computing results of Monte Carlo simulation of the photon density distribution in $yz$-plane near the focal point for a converging laser beam transmitting through a tissue phantom slab with $\mu_t = 0.936(mm^{-1})$. The peak formed by unattenuated photons is located at the focal point $z = Z_f = 67.3mm$ and $y = 0$.

Results for all the values of $\mu_t$ up to 1.09 ($mm^{-1}$) show a well-defined peak formed by the unattenuated photons at the focal point of the beam and a uniformly fluctuating background around the peak. Because of the photon of the incident beam are treated as a spherical wave in our Monte Carlo simulations, the unattenuated photons propagates toward the z-axis after

emerging from the slab and form a peak at the focal point. This peak in photon density has a significant width along the z-axis because of the aberrations of the wavefront suffered at the plane interfaces of the slab while appear as a single point at the focal point in the *xy*-plane. Figs. 2 and 3 show the light distribution in the *xy*-plane and *xz*-plane corresponding to the case of $\mu_t = 0.936(mm^{-1})$. To obtain these results, a total of $1.14 \times 10^9$ photons are injected at the entrance surface of the slab phantom to produce a photon density in background and peak with negligible statistical fluctuations. Considering the reflection at the entrance surface, a total of $1.115 \times 10^9$ photons enter the slab and are tracked by the program. Twenty tasks are used in the parallel calculation, and it takes the PC cluster about 9 hours to finish.

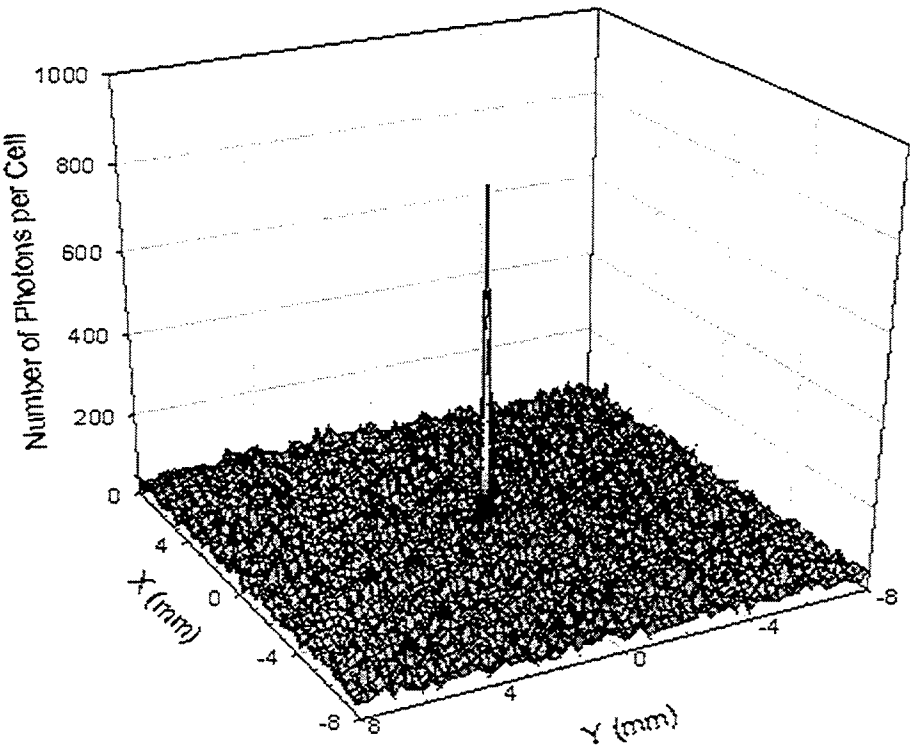


**Fig. 3** Same as Fig. 2 except in the *xy*-plane at the focal point $z = Z_f = 67.3mm$.

Fig. 4 shows the dependence of the number of unattenuated photons arrived at the focal point on the attenuation coefficient $\mu_t$ when $\mu_t$ is changed from 0.546 $(mm^{-1})$ to 1.092 $(mm^{-1})$. The unattenuated photons at the focal point is obtained by subtracting the background formed by the diffusely scattered photons from the observed peak. To do that, we first obtain the photon density, or the number of photons per cell at the focal point, $N_f$, from the light distribution deposition in the *yz*-plane, and $N_f$ includes both unattenuated and diffusely scattered photons. The diffusely scattered photon density $N_b$, i.e. the background in the photon density near the focal point, is obtained by averaging the number of photons per cell over the cells in the *xy*-plane excluding the single cell where the peak is located. A simple treatment like this is well justified. First: the deposit region is small enough so that the background is relatively flat. Second: due to the geometric optical approximation adopted in the Monte Carlo simulation, all the unattenuated photons are focused to a single cell in the *xy*-plane at $z = Z_f$, so by excluding that single cell, the xy-plane distribution is dominated by that of the diffusely scattered photons near the focal point. In this way we can obtain the unattenuated photons at the focal point by $N_{unatt} = (N_f - N_b)$ for each slab of $\mu_t$. The results shown in Fig. 4 (solid circle) are in excellent agreement with the radiative transfer theory prediction (the solid line) given by Eq. (8). This proves directly that the photon density peak at the focal point consists of the unattenuated photons on top of the diffusive background formed by the multiply scattered photons.

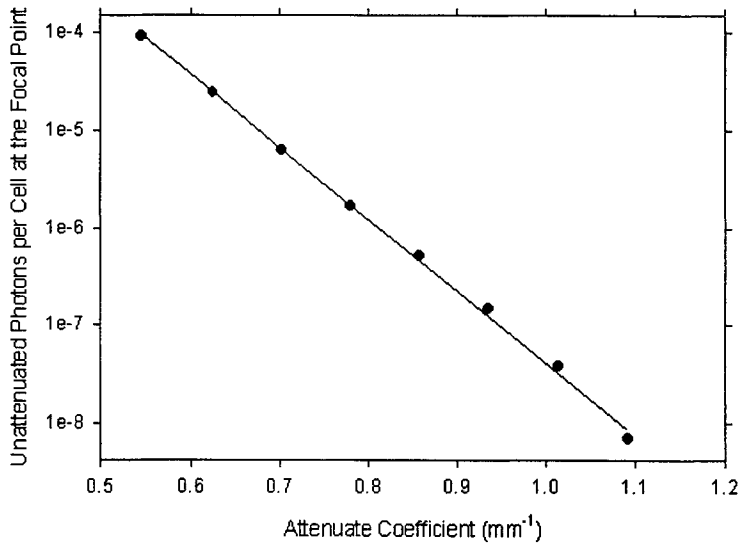


**Fig. 4** Parallel computing results of Monte Carlo simulation of the dependency of unattenuated photons near the focal point on the attenuate coefficient $\mu_t$. The solid circles are the simulation results, while the straight is the predicted value from Eq. (8).

To produce a background in the photon number per cell with negligible fluctuation, there is a minimum for the number of photons $N_0$ required for the incident beam even when $\mu_t$ is small. In our cases shown in Fig. 4 it is $N_0 = 3.5 \times 10^8$ for $\mu_t \leq 0.858 mm^{-1}$. And as $\mu_s$ increases, more photons are needed to reduce statistical fluctuation for the peak at the focal point. For example, the number $N_0$ is increased to $1.14 \times 10^9$ for $\mu_t = 0.936 mm^{-1}$, $2.2 \times 10^9$ for $\mu_t = 1.014 mm^{-1}$, and $5.6 \times 10^9$ for $\mu_t = 1.092 mm^{-1}$ for the results shown in Fig. 4. The steep increase in the total number of tracked photon as a result of large optical depth clearly demonstrates the urgent need to adopt the parallel computing technique for conducting high performance computation in the biomedical optics.

In summary, we have adopted the parallel computing technique in our simulation of light propagating in highly turbid media of biological tissues. Our results have shown that the parallel technique can be implemented into Monte Carlo simulations to calculate light distribution with inhomogeneous boundary conditions. With nearly no overhead cost in the CPU time for distributed parallel computing and the rapid increase in the performance/cost ratio of PC, this approach offers excellent opportunity in the near future to conduct large-scale Monte Carlo simulations for the modeling of light-tissue interaction. For example, the expansion of the current work to include surface roughness is in progress and will be reported elsewhere.

## ACKNOWLEDGMENTS

This work was partly supported by National Science Foundation under grant #PHY-9973787, National Institute of Health under grant # R15GM/OD55940-01, and North Carolina Super Computer Center through the allocation on Cray T3E.

## REFERENCE

1. S. Chandrasekhar, *Radiative Transfer*, (Oxford University Press, London, 1960)
2. A. Ishimaru, *Wave Propagation and Scattering in Random Media*, vol.1 and vol.2 (Academic, New York, 1978)
3. S. Wan, R. R. Anderson, J. A.Parrish, "Analytical modeling for the optical properties of the skin with *in vitro* and *in vivo* applications," *Photochem. Photobiol.*, **34**, 493-499 (1981)
4. C.C. Johnson, "Optical diffusion in blood," *IEEE Trans. Biomed. Engineer.*, **17**, 129-134 (1970)

5. M. de Belder, J. de Kerf, J. Jespers, R. Verbrugge, "Light diffusion in photographic layers: its influence on sensitivity and modulation transfer," *J. Opt. Soc. Am.*, **55**, 1261-1268 (1965)
6. B.C. Wilson, G.Adams, "A Monte Carlo model for the absorption and flux distribution of light in tissue," *Med. Phys.*, **10**, 824-830 (1983)
7. M. Keijzer, S.T. Jacques, S.A. Prahl, A.J. Welch, "Light distribution in artery tissue: Monte Carlo simulation for finite-diameter laser beams," *Lasers Surg. Med.*, **9**, 148-154 (1989)
8. Zhi Song, Ke Dong, Jun Q. Lu, X. H. Hu, "Monte Carlo Simulations of Laser Pulse Propagation in Biological Tissues," *Applied Optics,* **38**, 2944 -2949(1999).
9. Ke Dong, Zhi Song, Jun Q. Lu, X.H. Hu, "Monte Carlo Simulation of Converging Laser Beams Propagating in Skin Tissue Phantoms", *Proceedings of SPIE*, **3590**, (1999)
10. Jun Q. Lu, X. H. Hu, Z. Song, K. Dong, "Simulation of light scattering in biological tissues: the coherent component," *Proceedings of SPIE*, **3601**, 474-481 (1999)
11. L. G. Henyey, J. L. Greenstein, "Diffuse radiation in the galaxy," *Astroph. J.*, **93**, 70-83 (1941)
12. A. De Matteis and S. Pagnutti, "Parallelization of random number generators and long-range correlations," *Parallel Computing*, **15**, 155-164 (1990)
13. P. L'Ecuyer and S. Cot'e, "Implementing a random number package with splitting facilities," *ACM Trans. On Mathematical Software*, **17**, 98-111 (1991)
14. O. E. Percus and M. H. Kalos, "Random Number generators for MIMD parallel processors," *Journal of Parallel and Distributed Computing*, **6**, 477-497 (1990)
15. M. Mascagni, "SPRNG: A Scalable Library for Pseudorandom Number Generation," Proceeding of the 9th SIAM Conference on Parallel Processing for Scientific Computing, MS11, March 22-24 (1999)
16. B. B. Das, F. Liu, R. R. Alfano, "Time-resolved fluorescence and photon migration studies in biomedical and model random media", *Rep. Prog. Phys.*, **60**, 227-292 (1997).
17. H.J. van Staveren, C.J.M. Mose, J. van Marle, S.A. Prahl, M.J.C. van Germert, "Light scattering in intralipid-10% in the wavelength range of 400-1100 nm", *Appl. Opt.*, **30**, 4507-4514 (1991)

# DERIVING OPTICAL PROPERTIES IN THE NEAR INFRARED USING AN INVERSE MONTE CARLO PROGRAM

Karl Pope[1], Lihong Wang[2]
1. Candela Corporation, 530 Boston Post Road, Wayland, MA 01778
2. Texas A&M University, 3120 TAMU, Collage Station, TX 77846-3120

**ABSTRACT:**

An Inverse Monte Carlo program was developed based on a scaleable Monte Carlo algorithm. This program determines the skin optical ($\mu_a$ and $\mu_s$) properties in vivo using reflectance and thermal measurements as inputs from different skin types, very light to very dark. Some basic assumptions are made: 1) epidermal thickness is close to 100 μm, 2) the scattering in the epidermis is the same or similar to the dermal scattering, 3) the dermal absorption and scattering coefficients are similar between individuals. Experimental measurements of reflectance and temperature were taken. These were input into a pair of Inverse Monte Carlo programs that generated the optical properties for the different skin types. A single layer Inverse Monte Carlo model was employed to determine the optical properties of the dermis. A 2-layer Inverse Monte Carlo program was used to determine the epidermal optical properties.

**KEYWORDS:** Inverse Monte Carlo, Optical Properties, Near Infrared, In vivo

## INTRODUCTION

Monte Carlo (MC) modeling was adapted from field of physic's studies of x-ray scattering[1-3] for biomedical applications in order to describe the distribution of light in tissue[4]. To apply Monte Carlo modeling to light-tissue interactions there is a growing need to better define the optical properties of tissue *in vivo*. While the sophistication of MC models increased to include, for example, multi-layers[5] and edge effects[6], the need for accurate absorption and scattering coefficients, $\mu_a$ and $\mu_s$ for varying skin types, has only increased.

Many different methods have been used to collect and analyze optical properties and have been described in great detail in other papers [7, 8]. With few exceptions[9, 10] most of this work has been done *ex vivo*. Once tissue is removed from the body it begins to undergo changes such as dehydration, cell death, changes in blood content and transformation of state of Hb. The time between preparation and measurements as well as the thickness of the sample will affect the outcome to some extent. In addition, there has been little work done looking at different skin types, light skin vs dark skin.

The problem that motivated this work was that optical properties from different sources[8, 11] {http://omlc.ori.edu/news/ and http://www.medhpys.ucl.ac.uk/research/borg} had significantly different values. When optical properties from these sources were input into a Standard MC (SMC) program and followed by a finite element model of thermal diffusion the output of reflectance and temperature rise did not correspond to what was measured in our lab. Since our development work is sensitive to the effects of the amount of melanin in skin, very white to very dark skin (Fitzpatrick Skin Types I to VI), the ability to construct MC models that take skin type into account is of great interest.

The goal of this paper is to describe a method of obtaining optical properties *in vivo* on different skin types from 2 easily obtained measurements; total reflectance and temperature rise.

## METHOD

Figure 1 is a flow chart of the procedure that was carried out. Two types of data were collected *in vivo*, total reflection and the peak temperature after a laser pulse. Reflection measurements were taken using an



In *Laser-Tissue Interaction XI: Photochemical, Photothermal, and Photomechanical*, Donald D. Duncan, Jeffrey O. Hollinger, Steven L. Jacques, Editors, Proceedings of SPIE Vol. 3914 (2000)
1605-7422/00/$15.00

integrating sphere setup as shown in Figure 2. The laser, a Candela GentleLASE PLUS™ (Wayland, MA) with a wavelength of 755 nm and a 3 ms pulse duration was used in these experiments. A high-speed silicon photo-detector (Det210, ThorLabs Newton NJ) was used to collect the output. The voltage was normalized using Spectralon (Lapsphere, North Sutton, NH) reflectance standards, 99% and 75%, and calibrated to energies using a power meter. Variations in laser energy were normalized using a beam splitter and an energy meter (Ophir Nova meter and Ophir detector FL250, Danvers, MA). Reflectance data was collected from the inner forearm of each volunteer. Skin types varied from very white to very black, Fitzpatrick Skin Type I to VI.

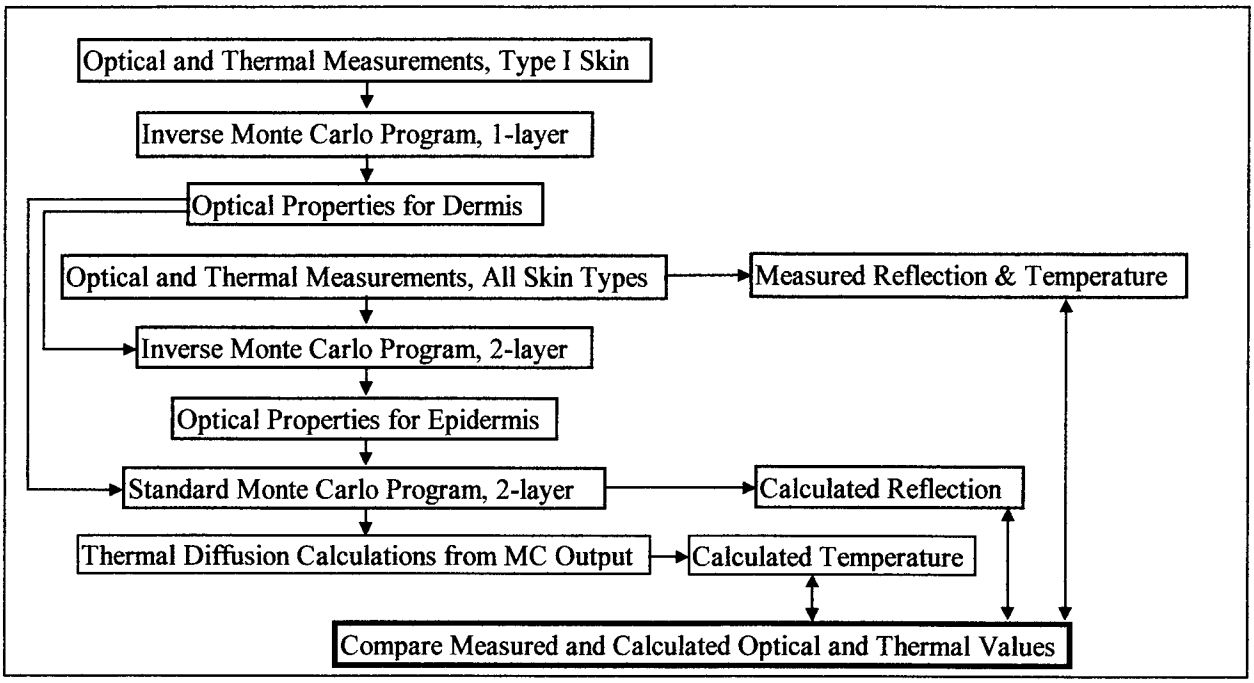


Figure 1: Flow chart of data collection, generation, and verification.

Skin temperature data were collected using a thermal camera, (Infametrics, Model 600, Bedford MA). Infametrics software was used to acquire temperature data on a single pixel at video frame rates (60 Hz). The GentleLASE PLUS laser was used at low fluence levels, 3 to 10 J/cm$^2$, 3 ms laser pulse, to heat the skin without collateral damage. A beam splitter was used to sample the laser output power and correct for pulse to pulse variations. Three thermal measurements were taken at different spots on the inner arm of each volunteer and averaged.

Two Inverse Monte Carlo (IMC) programs, a 1- and 2-layer model, were employed to determine the optical properties from the reflection and temperature measurements. The 1- layer IMC model assumes that the reflection and temperature inputs are from a very white skinned individual, Fitzpatrick Skin Type I, and its' output are assumed to be the dermal optical properties. In the near IR the absorption in skin is dominated by melanin and to a lesser extent, blood. In Type I skin there is very little melanin present and the majority of the absorption is likely to occur in the dermis. So for very white skin the absorption coefficient ($\mu_a$) is dictated by the dermis. The epidermis is approximately 90 ±30 μm and at wavelengths in the near infrared region there are not significant numbers of scattering events. It is therefore assumed that scattering in skin is dominated by the dermis. This is thought to be true for all skin types. The anisotropy was assumed to be 0.876 in these calculations

Diffuse reflection from a Monte Carlo program is defined by the ratio of $\mu_s/\mu_a$. The 1-layer IMC program first uses the measured diffuse reflectance from Type I skin, to iteratively calculate the ratio of $\mu_s/\mu_a$. Next, The 1-layer IMC program uses the measured peak temperature from Type I skin to determine a unique $\mu_{a\,(derm)}$. The laser pulse duration at 3 ms was determined to be sufficiently short that the system was considered to be thermally

confined. Finally, after $\mu_{a\ (derm)}$ is known then $\mu_{s\ (derm)}$ can be calculated from the previously determined ratio of $\mu_s/\mu_a$.

Assuming that dermal properties do not change significantly between people, the optical properties obtained from the 1-layer IMC model can then be input as the dermal properties in the 2-layer IMC model for darker skin types. The 2-layer IMC program was next used to determine the epidermal absorption coefficient, $\mu_{a\ (epi)}$ using the assumption that scattering is dominated by the dermis, the epidermal scattering coefficient was set to be the same as those of the dermis ($\mu_{s\ (derm)} = \mu_{s\ (epi)}$).

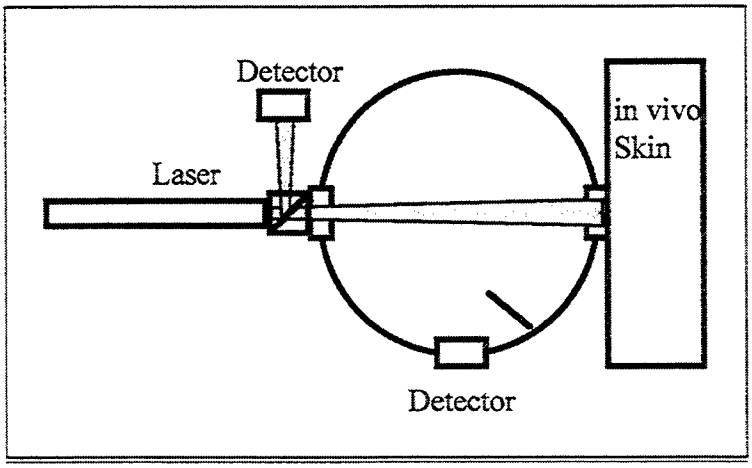


Figure 2: The collection geometry for reflection measurements using a laser and integrating sphere

The 2-layer IMC program collects only the calculated diffuse reflection data from the run. The 2-layer IMC program utilizes the measured diffuse reflection and adjusts the $\mu_{a\ (epi)}$ that was input to the program until the calculated diffuse reflection matches the measured value.

## RESULTS

The measured reflectance from very white skin, Fitzpatrick Skin Type I, was 59.2%. After a 10 J/cm$^2$, 3 ms laser pulse at 755 nm, the maximum temperature of 35.5° C was measured using a 8 to 12 μm thermal camera. Using the 1-layer IMC model the values of $\mu_{a\ (derm)} = 0.410$/cm and $\mu_{s\ (derm)} = 231$/cm were calculated. Inputting these estimates into the 2-layer IMC for the optical properties of the dermal layer, an epidermal $\mu_{a\ (epi)} = 0.405$/cm was calculated.

To validate the program, these optical properties from the Skin Type I were used in a Standard Monte Carlo (SMC) program. The calculated reflection was 58.8%, which compares favorably with measured value of 59.2%. When a thermal diffusion model was applied to the output of the Monte Carlo the skin temperature is calculated to reach 35.3° C, again close to the measured 35.5° C. This is a circular test, with the values of the epidermis and the dermis set to the same value, thus simulating the 1-layer model. The output is then used in a SMC and thermal diffusion model and the reflection and temperature results should match the starting values. This process validated the general concept and programming for skin Type I.

Testing a medium skin color, Fitzpatrick Skin Type III, the measured reflectance was 49.5%. After a 10 J/cm$^2$, 3 ms laser pulse at 755 nm, the maximum temperature was measured at 49.3° C. Using the same optical properties for the dermal layer as those derived from the Skin Type I, an epidermal $\mu_{a\ (epi)} = 3.82$/cm was calculated from the 2-layer IMC program. The Type III optical properties were then put into a SMC program. The calculated reflection was 51.3%, which compares favorably with the measured value of 49.5%. When a thermal diffusion model is applied to the output of the Monte Carlo the skin temperature is calculated to reach 74.8° C, which is not close to the measured 49.3° C.

Finally when testing very dark skin, Fitzpatrick Skin Type VI, the measured reflectance was 27.9%. After a 3 J/cm$^2$, 3 ms laser pulse at 755 nm, the maximum temperature of 52.6° C was measured. Using the same optical properties for the dermal layer as those derived from the Skin Type I, an epidermal $\mu_a$ = 19.0/cm was calculated from the 2-layer IMC model. The optical properties derived from the Type VI skin were put into a SMC program and the calculated reflection was 31.9% compared to the measured value of 49.5%. When a thermal diffusion model is applied to the output of the Monte Carlo the skin temperature is calculated to reach 70.7° C, which is not close to the measured 52.6° C. It should be noted here that only 3 J/cm$^2$ was used in the thermal measurements on the Type VI whereas 10 J/cm$^2$ was used for the Type I and III. In the thermal model temperature increase is proportional to the fluence. For Type VI skin in this simulation, a 10 J/cm$^2$ laser pulse would have resulted in a final measured and calculated temperature of 75° C and 137° C respectively.

## Discussion

Abstracting optical properties from *ex vivo* skin has been studied extensively, but using optical and thermal measurements from *in vivo* skin provides a new and unique approach. This method has the advantage that the measurements are easy to obtain and there are few complicating factors that must be addressed to achieve optical properties.

The results from the 1-layer IMC program on very light skin showed a highly scattering tissue with low absorption, $\mu_s$ = 231/cm and $\mu_a$ = 0.410/cm respectively. When these numbers were used in a SMC program and followed by a thermal diffusion model, the reflection and final temperature results were closely related to the experimental measurements. This validated the programming of the IMC algorithm for skin Type I.

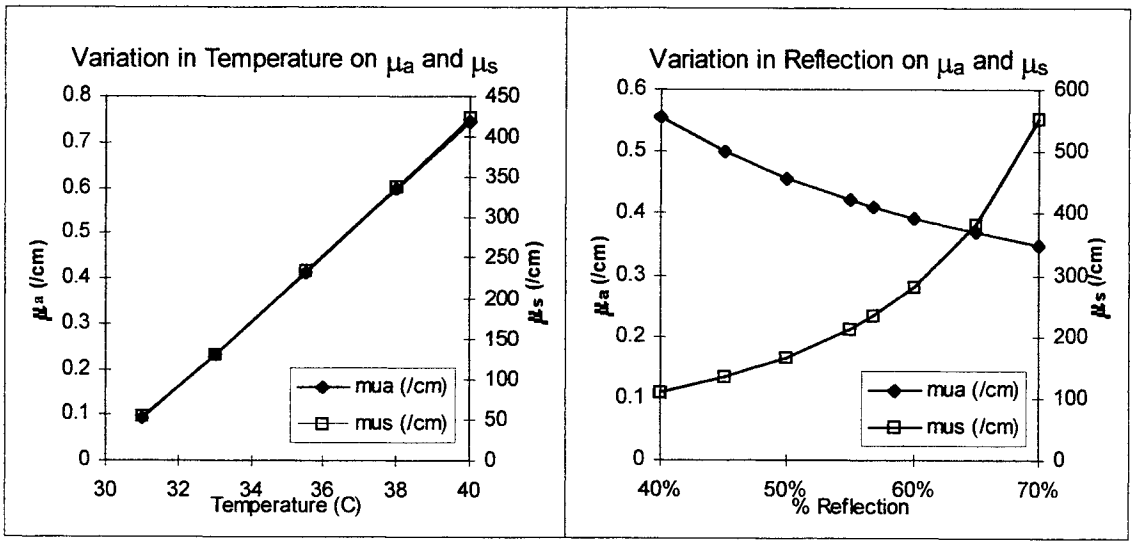


Figure 3 & Figure 4: The effect on changes of temperature and percent reflection on $\mu_s$ and $\mu_a$ is shown. Increases in temperature measurements cause the calculated $\mu_s$ and $\mu_a$ to increase. Increases in percent reflection cause $\mu_s$ to increase but $\mu_a$ to decrease.

The Results from the 2-layer IMC model when employed on darker skin types was not as encouraging. When the resulting output optical properties from the 2-layer IMC program were run through the standard Monte Carlo model and thermal diffusion model, the reflection and final temperature were overestimated for both the medium and very dark skin types. However, the calculated reflection values were close to the measured ones, which was expected since the measured reflectance was used as an input to the IMC program.

To understand the source of the thermal error, the effect of under or over estimating the measured values for either the total reflection or final temperature, were considered. For changes in the final peak temperature, Figure 3, $\mu_s$ and $\mu_a$ move together, as the final temperature increases so does the $\mu_s$ and $\mu_a$. For variations in the

reflection, Figure 3, $\mu_s$ and $\mu_a$ change in opposite directions. For example, changing the reflection from 55% to 60% would require a decrease in the $\mu_a$ but increase the $\mu_s$ and the converse is true if the reflection was changed from 55% to 50%.

Given these trends, we hypothesize that the measured peak temperatures were too low. One possible reason is that the thermal camera sampling rate is only 60 Hz and the camera cannot be triggered with the laser. It was not possible to determine if the thermal camera was recording the peak temperature or some later point as the skin had already started cooled. By employing temperatures that were lower than the true skin surface temperatures, both $\mu_s$ and $\mu_a$ are underestimated for the 1 layer model. If higher $\mu_{s\ (derm\ \&\ epi)}$ and $\mu_{a\ (derm)}$ were used in the 2-layer IMC, then the final calculated $\mu_{a\ (epi)}$ would be lower for all skin types, thus leading to better validation of the experimental results. Obtaining more accurate peak temperatures should be performed to verify this hypothesis.

This general model has shown promise but refinements are necessary. More accurate methods need to be developed for measuring or calculating temperature.

## REFERENCES


1. Ennow, K., and Jessen, K. A., Spectral measurements and Monte Carlo calculations of scattered radiation from therapeutic radiation sources, *Acta Radiol Ther Phys Biol, 14*, 262 (1975).
2. Santoro, R. T., Alsmiller, R. G., Jr., and Chandler, K. C., Calculation of the effects caused by bone present in phantoms irradiated by negatively charged pions, *Med Phys, 1*, 303 (1974).
3. Muthukrishnan, G., and Gopinath, D. V., Charged-particle transport in one-dimensional systems, *Radiat Res, 95*, 1 (1983).
4. Wilson, B. C., and Adam, G., A Monte Carlo model for the absorption and flux distributions of light in tissue, *Med Phys, 10*, 824 (1983).
5. Wang, L., Jacques, S. L., and Zheng, L., MCML--Monte Carlo modeling of light transport in multi-layered tissues, *Comput Methods Programs Biomed, 47*, 131 (1995).
6. Keijzer, M., Jacques, S. L., Prahl, S. A., and Welch, A. J., Light distributions in artery tissue: Monte Carlo simulations for finite-diameter laser beams, *Lasers Surg Med, 9*, 148 (1989).
7. Marchesini, R., Clemente, C., Pignoli, E., and Brambilla, M., Optical properties of in vitro epidermis and their possible relationship with optical properties of in vivo skin, *J Photochem Photobiol B, 16*, 127 (1992).
8. Simpson, C. R., Kohl, M., Essenpreis, M., and Cope, M., Near-infrared optical properties of ex vivo human skin and subcutaneous tissues measured using the Monte Carlo inversion technique, *Phys Med Biol, 43*, 2465 (1998).
9. Star, W. M., Light dosimetry in vivo, *Phys Med Biol, 42*, 763 (1997).
10. Zeng, H., MacAulay, C., McLean, D. I., and Palcic, B., Reconstruction of in vivo skin autofluorescence spectrum from microscopic properties by Monte Carlo simulation, *J Photochem Photobiol B, 38*, 234 (1997).
11. Welch, A. J., and van Gemert, M. J. C., *Optical-thermal response of laser-irradiated tissue*, Plenum Press, New York (1995).

# Optical property measurements in mammalian cartilage

Steen J. Madsen*[a], Eugene A. Chu[b] and Brian J.F. Wong[b,c]

[a]Dept. of Health Physics, University of Nevada, Las Vegas, 4505 Maryland Pkwy., Box 453037, Las Vegas, NV 89154

[b]Beckman Laser Institute and Medical Clinic, University of California, Irvine, CA 92715

[c]Dept. of Otolaryngology – Head and Neck Surgery, University of California, Irvine

## ABSTRACT

The optical properties of porcine nasal cartilage have been determined at a wavelength of 632.8 nm using two different techniques. A single integrating sphere method was used to measure diffuse reflectance and diffuse transmittance, while total attenuation was determined from separate measurements of collimated transmission. Optical properties (absorption and scattering coefficients, and scattering anisotropy) were obtained by comparing measured results with predictions of Monte Carlo computer simulations. An estimate of the validity of the optical properties was obtained by measuring the optical penetration depth in bulk cartilage tissue.

The optical properties of porcine nasal cartilage are characterized by low absorption ($0.14 \pm 0.05$ cm$^{-1}$) and high scatter ($304 \pm 47$ cm$^{-1}$). The scattered light is highly forward peaked as indicated by the mean cosine of the scattering angle ($0.973 \pm 0.005$). Based on these results, the calculated optical penetration depth was in good agreement with that measured in bulk tissue. The results presented here are compared to those obtained in mammalian cartilage tissue by other investigators.

**Keywords:** Cartilage reshaping, tissue optics, optical properties

## 1. INTRODUCTION

In the past few years there has been a heightened interest in the use of lasers to deform cartilage. The plastic deformation of cartilage via laser-mediated stress relaxation was introduced by Sobol et al in 1993[1] who observed that laser irradiation of cartilage specimens under mechanical deformation resulted in permanent reshaping without carbonization or ablation. Laser-induced temperature elevations can thus be used to reshape autologous donor cartilage grafts into mechanically stable shapes, and could quite possibly be used to reconstruct complex anatomic structures without significant loss or waste of harvested tissue[2]. The reshaping process is reversible and adaptable for use in minimally invasive procedures. Unlike traditional surgical techniques, laser-mediated cartilage reshaping requires no suturing, carving or morselization to relieve or balance the elastic forces within the cartilage[2].

To prevent irreversible thermal damage to the cartilage during the reshaping procedure, a method is required to determine when to terminate irradiation. Since changes in the optical properties of laser irradiated cartilage reflect alterations in mechanical and thermal properties, optimal cartilage reshaping may be accomplished using the backscattered light from a probe laser as a feedback control signal[2]

Accurate laser reshaping of cartilage requires knowledge of the light distribution in tissue which, in turn, depends on its optical properties. The fundamental optical properties of interest are: the absorption

*Correspondence: Email: steenm@ccmail.nevada.edu; Telephone: 702.895.1805; Fax: 702.895.4819

In *Laser-Tissue Interaction XI: Photochemical, Photothermal, and Photomechanical*, Donald D. Duncan, Jeffrey O. Hollinger, Steven L. Jacques, Editors, Proceedings of SPIE Vol. 3914 (2000)
1605-7422/00/$15.00

coefficient ($\mu_a$), scattering coefficient ($\mu_s$) and scattering anisotropy (g). Measurements of the optical properties of various cartilage tissues have been attempted by several investigators[3-7]. The wide range of optical properties measured by different groups is most likely due to differences in: (1) cartilage tissue, (2) measurement techniques, and (3) light propagation models. A wide variety of measurement techniques and light propagation models have been used. For example, Kubelka-Munk theory has been used to obtain $\mu_a$ and $\mu_s$ from single integrating sphere measurements of diffuse reflectance ($R_d$)[3], while diffusion theory has been used to determine $\mu_a$ and the transport scattering coefficient ($\mu'_s = \mu_s (1-g)$) from single integrating sphere measurements of $R_d$ and from measurements of the optical penetration depth ($\delta$)[7]. Bagratashvilli et al[6] used a 1-D diffusion model to evaluate $\mu_a$, $\mu_s$ and g from single integrating sphere measurements of $R_d$ and diffuse transmittance ($T_d$), and from collimated transmission measurements of the total attenuation coefficient ($\mu_t = \mu_a + \mu_s$). Finally, a number of investigators have used an inverse adding-doubling (IAD) algorithm to obtain fundamental optical properties from double-integrating sphere (DIS) measurements of $R_d$, $T_d$ and $\mu_t$[4,5]. Each technique has certain advantages and drawbacks. In general, the choice of measurement technique and light propagation model is dictated by the level of accuracy required – the higher the degree of accuracy desired, the more complex the technique.

In this paper, the optical properties of cryopreserved porcine nasal cartilage at a representative visible wavelength (632.8 nm) are presented. Although it is unlikely that lasers of this particular wavelength will be used in cartilage reshaping, it is nevertheless an important wavelength since the probe laser is likely to be a low cost diode or helium-neon laser. The optical properties of cartilage tissue at the probe wavelength are important since changes in these properties constitute the feedback signal for optimal cartilage reshaping. Furthermore, this is a common wavelength used by many investigators to probe cartilage tissue and thus provides a means for comparison of data with those of others. The accuracy of the optical properties presented in this study using integrating sphere, total attenuation measurements and Monte Carlo computer simulations is discussed by way of comparison to those determined by others using different techniques.

## 2. MATERIALS AND METHODS

### 2.1. Cartilage tissue

Fresh porcine nasal cartilage was obtained from a local abattoir. Cartilage was stripped of soft tissue and cut into rectangular shapes of thickness ranging from 1.5 to 2.5 mm using a custom-built guillotine microtome. The tissue was cryopreserved until measurements could be performed. Measurements were performed on cartilage from five different animals. The number of specimens measured per animal ranged from 3 to 14.

### 2.2. Total attenuation measurements

The technique used to measure total attenuation has been described extensively elsewhere[8]. Briefly, a lock-in detection technique was used to measure light transmitted through cartilage tissue sandwiched between glass slides. To minimize the possibility of detecting scattered light, the samples were positioned 150 cm from the detector and a 1.0 mm aperture was placed over the photodiode detector. Measurements were made on cartilage tissue ranging in thickness from 50 to 400 μm. The total attenuation coefficient was found from Beer's Law:

$$\mu_t = \frac{1}{t} \ln\left(\frac{I}{I_o}\right) \tag{1}$$

where I is the measured intensity with the sample between source and detector, $I_o$ is the intensity with a water sample, and t is the pathlength of the cuvette.

### 2.3. Reflectance and transmittance measurements

A single integrating sphere technique was used to measure diffuse reflectance and transmittance[8]. The sphere (Labsphere, North Sutton, NH) was 15.2 cm in diameter and included two opposing beam ports with diameters of 2.54 cm. A third port (dia. = 1.27 cm), located at 90° to the other ports, was used to mount a photodiode detector (New Focus Inc., Santa Clara, CA). Diffuse transmittance was measured by placing the sample in front of the entrance port and covering the open exit port with a highly reflective plug. To measure diffuse reflectance, the reflective plug was removed and the sphere was rotated 180°. Four reflectance and transmittance measurements were performed for each sample.

### 2.4. Monte Carlo model

For a detailed description of the Monte Carlo program, the interested reader should consult Peters et al.[9] In addition to various geometrical parameters characteristic of the experimental setup, the input to the Monte Carlo program included estimates of g, the albedo ($a = \mu_s/\mu_t$), and the measured $\mu_t$. For a given set of input values (g, a, and $\mu_t$), the Monte Carlo program outputs values of diffuse reflectance ($R_c$) and transmittance ($T_c$). Simulations were run for a grid of input values. When the calculated values ($R_c$ and $T_c$) matched the measured ones ($R_d$ and $T_d$), simulations were terminated and the matched a and g noted. In this way, it was possible to determine uniquely the optical properties of the cartilage specimen.

Acceptably small errors in $R_c$ and $T_c$ were obtained with 5000 incident photons per simulation. In almost all cases, relative errors were within 2 %. Each 5000 photon simulation required approximately 10 to 20 s of CPU time on a DEC Alpha Workstation 200 (Digital Equipment Corp., Maynard, MA).

### 2.5. Optical penetration depth measurements

The details of these measurements have been described elsewhere[8]. Briefly, bulk cartilage tissue was illuminated with a broad beam and the diffusely transmitted intensity was recorded as a function of cartilage thickness. If the cartilage is sufficiently thick such that the light distribution in the tissue can be described by diffusion theory, then the transmitted intensity will decrease exponentially with thickness according to the following expression:

$$I_{n+1} = I_n e^{-t/\delta} \tag{2}$$

where $I_n$ and $I_{n+1}$ are the transmitted intensities through n and n + 1 layers of tissue, t is the thickness, and $\delta$ is the optical penetration depth:

$$\delta = \left[3\mu_a\left(\mu_a + \mu'_s\right)\right]^{-1/2} \tag{3}$$

## 3. RESULTS AND DISCUSSION

The optical properties of porcine nasal cartilage determined in this study, and in a previous investigation[8] are summarized in the first two rows of Table I. The results of other investigators are shown for comparative purposes. The results obtained by our group clearly show that the optical properties of porcine nasal cartilage are characterized by low absorption and high forwardly directed scatter. Although direct comparison of $\mu_s$ and g is not possible, the $\mu_a$ and $\mu'_s$ values determined by our group are in excellent agreement with those of Youn et al.[5] and Descalle et al.[7] The excellent agreement in absorption coefficients is somewhat surprising since this parameter is difficult to determine accurately in scatter-dominated tissues, such as porcine cartilage.

Table I Optical properties of representative cartilage tissue at 632.8 nm

| Tissue | Method | $\mu_a$ ($cm^{-1}$) | $\mu_s$ ($cm^{-1}$) | g | $\mu'_s$ ($cm^{-1}$) | $\delta$ (cm) | Reference |
|---|---|---|---|---|---|---|---|
| Porcine Nasal Cart | (a) | 0.14 ± 0.05 | 304 ± 47 | 0.973 ± 0.005 | 8.2 ± 1.3 | 0.53 ± 0.20** | (8) |
| Porcine Nasal Cart | (b) | | | | | 0.52 ± 0.1 | (8) |
| Porcine Nasal Cart | (c) | 0.21 ± 0.07 | | | 6.3 ± 2.4 | 0.49 ± 0.20** | (5) |
| Porcine Nasal Cart | (d) | 0.53 ± 0.44 | 31.9 ± 1.6 | 0.62 ± 0.05 | 12.1 ± 0.8 | 0.22 ± 0.03** | (6) |
| Porcine Shoulder Cart. | (e) | 0.17 ± 0.02 | | | 10.6 ± 2.0 | 0.43 ± 0.07** | (7) |
| Equine Art. Cart. | (e) | 0.5 ± 0.1 | 80 ± 5 | 0.8* | 16 ± 1.0 | 0.20 ± 0.03** | (3) |
| Rabbit Cart. | (c) | 0.33 ± 0.05 | 214 ± 0.2 | 0.909 ± 0.005 | 19.4 ± 1.1 | 0.23 ± 0.02** | (4) |

* Best guess
** Penetration depths calculated from $\mu_a$ and $\mu_s$'
(a) Single integrating sphere, collimated transmission, and Monte Carlo
(b) Fluence attenuation measurements and diffusion model
(c) Double integrating sphere and inverse adding-doubling algorithm
(d) Single integrating sphere, collimated transmission, and 1-D diffusion model
(e) Single integrating sphere and Kubelka-Munk model

In this study, determination of the fundamental optical properties was accomplished, in part, through total attenuation measurements of thin samples. Such measurements are notoriously difficult in highly scattering tissues, especially if the scatter has a significant forwardly directed component. In collimated total attenuation measurements, the thickness of the tissue specimen should be such that only a single scattering even occurs. Based on the results described here, this condition is satisfied in specimens of thickness less than approximately 30 μm. However, due to the consistency of cartilage tissue, it is extremely difficult to obtain specimens of thickness below 100 μm as the tissue tends to flake or snap during the sectioning process. Since the average tissue thickness was approximately ten times greater than that required for single interactions, great care was taken to minimize the probability of detecting scattered light. For example, a large sample-to-detector separation (150 cm) was chosen and a 1-mm-diameter pinhole was placed over the detector aperture. In order to determine whether this geometrical arrangement was sufficient for scatter rejection, detector signals were acquired as a function of sample-detector separation. Transmitted intensities remained constant down to separations of 100 cm. Based purely on geometrical arguments then, our setup was optimized for scatter rejection. However, due to the high scattering anisotropy, it may be possible for photons to reach the detector via small angle scattering along the optical axis. This will result in an increase in the transmitted signal and, hence, a decrease in the measured attenuation coefficient. To investigate this further, a series of measurements of transmitted intensity as a function of thickness was performed (Figure 1). As illustrated in Fig. 1, there was no significant deviation from linearity over tissue thicknesses ranging from 50 to 300 μm. We are thus reasonably confident of having eliminated multiply scattered photons from our setup.

There are significant discrepancies between our data and the results of Bagratashvili et al.[6]. Specifically, the results of the latter group are characterized by high absorption, low scatter and low scatter anisotropy. The reasons for this discrepancy are unknown, however, it should be noted that Bagratashvili et al. used somewhat thick specimens in their total attenuation measurements (300 to 900 μm). The authors also point out that their technique is limited, to some extent, by poor accuracy[6]. Interestingly, although both $\mu_s$ and g are lower than those obtained in other studies of porcine cartilage, the transport scattering coefficient

obtained by Bagratashvili et al. is in good agreement with those of others (see Table I for comparison). Of further interest is the finding of Bagratashvili et al. that there are no significant differences in the optical properties of porcine and human nasal cartilage, thus providing justification for using porcine nasal cartilage in light propagation studies.

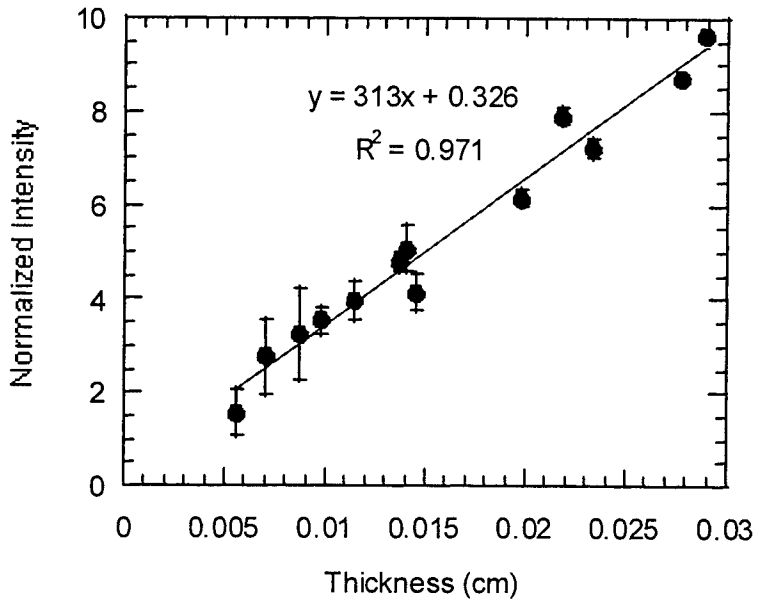


Figure 1. Attenuation as a function of cartilage thickness. The normalized intensity is given by: $-\ln (I/I_o)$. The total attenuation coefficient is given by the slope of the fitted line[8].

The results of Ebert et al.[3] are also characterized by relatively high absorption, however, the validity of comparing their results to those obtained by our group is not known since their measurements were performed on equine articular cartilage. Cartilage from different animals appear different under visible illumination, in fact, cartilage from different parts of the same animal may appear different to the naked eye, suggesting differences in their optical properties[8]. The Kubelka-Munk model used by Ebert et al. is limited to the extent that it can only provide absorption and scattering coefficients. This is a limitation since accurate modeling of light distributions in tissue requires knowledge of the transport scattering coefficient. In this case, the transport scattering coefficient can only be obtained by making a reasonable guess for the value of g (0.8 in this case[3]). It is interesting to note that a g-value of 0.9 would have resulted in a $\mu'_s$ of 8 $cm^{-1}$ which is in good agreement with the values obtained for porcine nasal cartilage (Table I).

The results of Beek et al.[4] disagree somewhat with those obtained by our group, however, as discussed previously, this may be a reflection of the fact that different animals were studied. A further complication is the observation that the technique used by Beek et al (double integrating sphere/inverse adding-doubling) may be somewhat inaccurate in cases where the samples are characterized by low absorption and high scatter[9]. The inaccuracies are due to light losses from the sides of the sample and the exit port of the transmittance sphere. The losses at the exit port are especially severe for tissues of high g values, such as porcine nasal cartilage. Exit port losses of 15 % or more are not uncommon[10]. The light losses are manifested as overestimations in $\mu_a$ and an erroneous dependence of the optical properties on specimen thickness. Furthermore, DeVries et al.[10] have found that, for $g > 0.94$, the IAD algorithm fails to converge to a unique solution. Thus, the validity of this technique may be suspect in tissues of high g-values.

An estimate of the validity of the optical properties determined by our group was obtained from measurements of the optical penetration depth in bulk cartilage tissue. Light fluence was measured as a function of depth in cartilage under conditions where the diffusion approximation is valid. As illustrated in

Fig. 2, the optical penetration depth (0.52 ± 0.1 cm) is in good agreement with that calculated by substituting the derived optical properties into equation (3) (0.53 ± 0.20). Thus, the fundamental optical properties ($\mu_a$, $\mu_s$ and g) measured by our group can be used with some measure of confidence to predict the optical fluence distribution in porcine nasal cartilage.

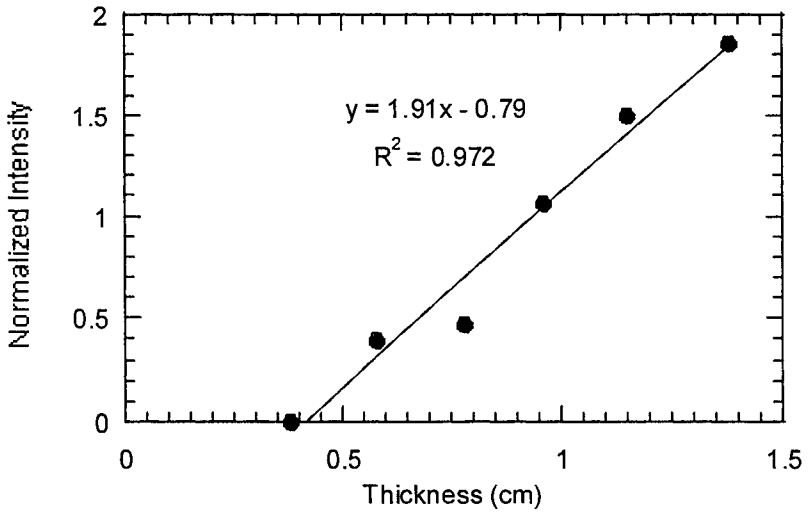


Figure 2. Attenuation as a function of sample thickness for broad beam irradiation of thick cartilage specimens. The normalized intensity is given by: - ln ($I_{n+1}/I_n$). The optical penetration depth is equal to 1/slope of the fitted line.

## 4. CONCLUSIONS

Accurate determination of the optical properties of mammalian cartilage tissue is difficult due to its high albedo and forwardly directed scatter. Careful consideration should be given to the choice of both experimental technique and light propagation model. In terms of porcine cartilage, the results presented here are in good agreement with those of other studies. In summary, the results of our studies, and those of others, suggest that porcine nasal and shoulder cartilage are characterized by absorption and transport scattering coefficients in the range of 0.1 to 0.3 $cm^{-1}$ and 6.0 to 12.0 $cm^{-1}$, respectively. Due to the close similarity between porcine and human cartilage tissue, these findings may be extended to human cartilage with some measure of confidence.

## ACKNOWLEDGEMENTS

The authors thank Dr. Doug Wyman for providing the original Monte Carlo code. Steen Madsen is grateful for the support of the UNLV Office of Research.

## REFERENCES

1. E. Sobol, V. V. Bagratashvili, and A. Omel'chenko, "Laser shaping of cartilage," Proc. SPIE, **2128,** pp. 43-49, 1994.
2. B. J.F. Wong, T. E. Milner, B. Anvari, A. Sviridov, A. Omel'chenko, V. V. Bagratashvili, E. Sobol, and J. S. Nelson, "Measurement of radiometric surface temperature and integrated backscattered light intensity during feedback-controlled laser-assisted cartilage reshaping," Lasers Med. Sci. **13,** pp. 66-72, 1998.
3. D. W. Ebert, C. Roberts, S. K. Farrar, W. M. Johnston, A. S. Litsky, and A. L. Bertone, "Articular cartilage optical properties in the spectral range 300-850 nm," J. Biomed. Optics **3,** pp. 326-333, 1998.

4. J. F. Beek, P. Blockland, P. Posthumus, M. Aalders, J. W. Pickering, H. J. C. M. Sterenborg, and M. J. C. van Gemert, "*In vitro* double-integrating-sphere optical properties of tissues between 630 and 1064 nm," Phys. Med. Biol. **42,** pp. 2255-2261, 1997.
5. J.-I. Youn, "Laser-mediated cartilage reshaping: thermal, optical and quasi-elastic light scattering studies," M.Sc. thesis, University of Texas at Austin, 1999.
6. N. V. Bagratashvili, A. P. Sviridov, E. N. Sobol, and M. S. Kitai, "Optical properties of nasal septum cartilage," Proc. SPIE, **3254,** pp. 398-406, 1998.
7. M.-A. Descalle, S. L. Jacques, S. A. Prahl, T. J. Laing, and W. R. Martin, "Measurements of ligament and cartilage optical properties at 351 nm, 365 nm and in the visible range (440-800 nm)," Proc. SPIE **3195,** pp.280-286, 1998.
8. S. J. Madsen, E. A. Chu, and B. J. F. Wong, "The optical properties of porcine nasal cartilage," IEEE J. Select. Topics. Quant. Elect. **5**, pp. 1127-1133, 1999.
9. V. G. Peters, D. G. Wyman, M. S. Patterson, and G. L. Frank, "Optical properties of normal and diseased human breast tissues in the visible and near infrared," Phys. Med. Biol. **35**, pp. 1317-1334, 1990.
10. G. DeVries, J. F. Beek, G. W. Lucassen, and M. J. C. van Gemert, "The effect of light losses in double integrating spheres on optical properties estimation," IEEE J. Select Topics Quant. Elec. **5,** pp. 944-947, 1999.

# Retrieval of optical properties of skin from measurement and modelling the diffuse reflectance

Lucien F.A. Douven and Gerald W. Lucassen*,
Personal Care Institute, Philips Research, Prof. Holstlaan 4,
5656AA Eindhoven, The Netherlands

## ABSTRACT

We present results on the retrieval of skin optical properties obtained by fitting of measurements of the diffuse reflectance of human skin. Reflectance spectra are simulated using an analytical model based on the diffusion approximation. This model is implemented in a simplex fit routine. The skin optical model used consists of five layers representing epidermis, capillary blood plexus, dermis, deep blood plexus and hypodermis. The optical properties of each layer are assumed homogeneously distributed. The main optical absorbers included are melanin in epidermis and blood. The experimental set up consists of a HP photospectrometer equipped with a remote fiber head. Total reflectance spectra were measured in the 400-820nm wavelength range on the volar under arm of 19 volunteers under various conditions influencing the blood content and oxygenation degree. Changes in the reflectance spectra were observed. Using the fit routine changes in blood content in the capillary blood plexus and in the deep blood plexus could be quantified. These showed different influences on the total reflectance. The method can be helpful to quantitatively assess changes in skin color appearance such as occurs in the treatment of port wine stains, blanching, skin irritation and tanning.

**Keywords:** diffuse reflectance, layered skin model, diffusion approximation, skin color, Monte Carlo, hemoglobin, effective absorption, blood concentration, oxygenation.

## 1. INTRODUCTION

The subject of this paper is retrieval of optical properties of skin by modelling and measurement of the diffuse reflectance of human skin characterising its visual appearance. Optical properties are obtained by adjustment of these properties in a fit routine that optimises for least squares differences between measured and calculated diffuse reflectance spectra using an analytical model. Quantification of skin colour and interpretation of skin colour changes in terms of physiological parameters are important in (laser) medicine, dermatology, and cosmetics.
Recently, Svaasand et al.[1] used stationary diffusion theory in a planar, layered skin model to simulate the skin diffuse reflectance spectrum in case of collimated illumination. Using analytical expressions for the wavelength dependence of the optical properties of skin and its chromophores a fast calculation method was developed. The model was used to assess parameters characterising the visual appearance of normal and port-wine stain skin, as well as skin colour changes induced by laser treatments. Others have used Monte Carlo methods in more realistic skin and blood vessel geometries to simulate the light distribution in skin and port-wine stain skin models, see for example Keijzer[2], Smithies and Butler[3], Lucassen *et al.*[4], Pfefer *et al.* [5]. The advantage of the analytical model is its short calculation time (seconds) compared to hours needed for Monte Carlo simulations.

In this paper Svaasand's approach is extended to a five layer skin model containing epidermis, superficial plexus, dermis, deep blood plexus, and hypodermis. In this model the main absorbing chromophores melanin and blood are homogeneously distributed. Following Verkruysse *et al.*[6] the optical properties of blood are corrected for the effect of non-homogeneous distribution in vessels.
We compare the derivations for the diffuse reflectance coefficient under diffuse and collimated illumination from diffusion theory following Keijzer[2] with that given by Svaasand *et al.*[1] (collimated illumination). We apply these models to study the skin colour changes due to heating, and pressure controlled arterial and venous occlusion. These changes are experimentally investigated by measuring the diffuse reflectance of in vivo skin by means of a photospectrometer. The results obtained from calculations are compared with the measured diffuse reflectance spectra. In order to assess the validity of the diffusion approximation also Monte Carlo simulations are performed.

* Correspondence: Prof. Holstlaan 4, 5656AA Eindhoven, The Netherlands; E-mail:Gerald.Lucassen@philips.com
Tel:+31-40-2743648; Fax:+31-40-2744288



In *Laser-Tissue Interaction XI: Photochemical, Photothermal, and Photomechanical*, Donald D. Duncan, Jeffrey O. Hollinger, Steven L. Jacques, Editors, Proceedings of SPIE Vol. 3914 (2000)
1605-7422/00/$15.00

## 2. METHODS

### 2.1. Layered optical skin model

In order to simulate the reflectance of light from skin in both the diffusion and Monte Carlo approach, a skin model consisting of five layers is employed. This is an extension of the two and three layer skin models of Svaasand *et al.*[1] The epidermis, dermis and fat layers are assumed flat with homogeneous optical properties. The dermis layer consists of three distinct layers that can contain different concentrations of blood. The first layer of the dermis accounts for the superficial blood plexus and the capillary loops located in the upper dermis, and the third layer of the dermis accounts for the deep blood plexus in the lower dermis, see Fig. 1.

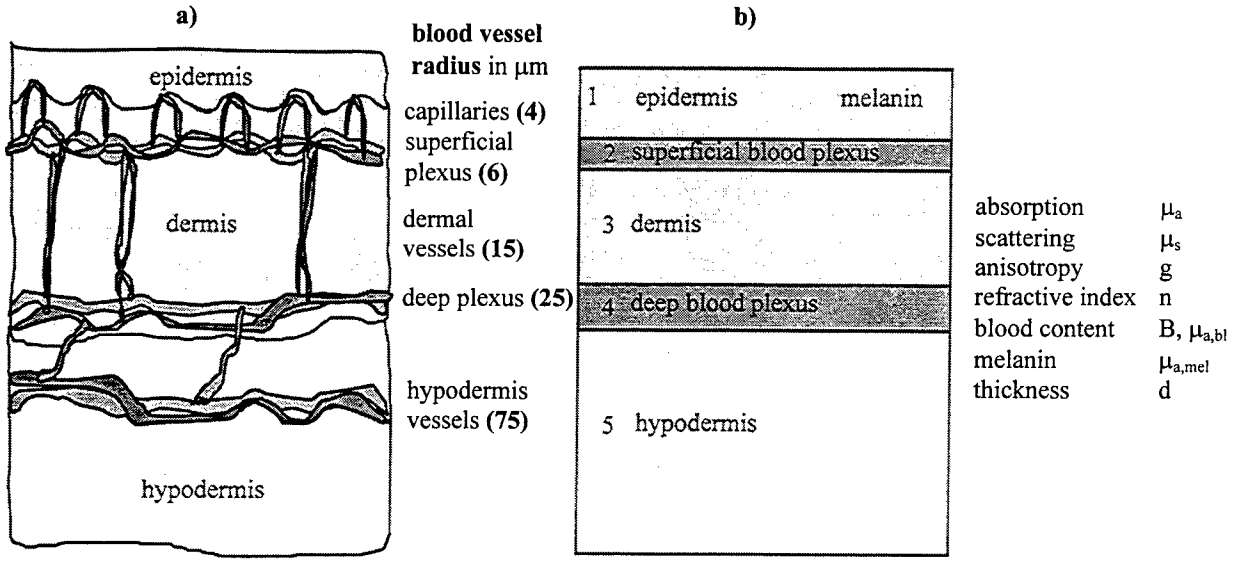


**Figure 1.** *a) Schematic of the skin structure after Refs 9-11 and b) layered skin model. Each layer has its own optical properties: absorption, scattering, anisotropy factor, refractive index and layer thickness. The main absorbing chromophores are melanin in epidermis and blood. The superficial and deep blood plexi in the dermis are separate blood layers.. Typical blood vessel sizes[11] are indicated in a).*

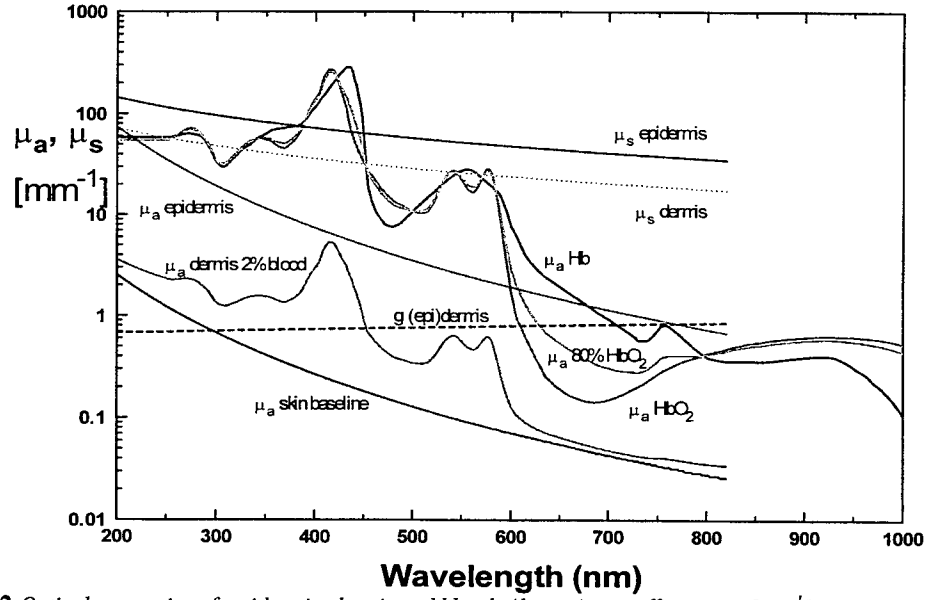


**Figure 2** *Optical properties of epidermis, dermis and blood. Absorption coefficient $\mu_a$ [$mm^{-1}$], scattering coefficient $\mu_s$ [$mm^{-1}$], and anisotropy factor g. Blood absorption data from compilation of data from Welch and van Gemert[7], and Jacques[8].*

Melanin is assumed homogeneously distributed in the epidermal layer. (Oxy)hemoglobin in blood is homogeneously distributed in all layers. To account for the irregular shape of the epidermal-dermal interface a small concentration of blood is taken into account for the bloodless epidermis.

## 2.2. Optical properties of skin chromophores

### 2.2.1. Oxyhemoglobin and hemoglobin

The absorption data for 100% oxyhemoglobin ($HbO_2$) and 100 % hemoglobin ($Hb$) in blood were taken from a compilation of data available from van Welch and van Gemert [7] and Jacques [8] (See Fig.2). Following Svaasand[1] we empirically fitted these data using Gaussian band shapes with amplitudes $a_j$ , bandwidths $b_j$ and center wavelengths $\lambda_j$ to get an analytical expression (See also Table B1, Appendix B)

$$\mu_a^{HbO_2}(\lambda), \mu_a^{Hb}(\lambda) = 25H\sum_{J=1}^{11} a_j \exp[-(\frac{\lambda-\lambda_j}{b_j})^2] \ , \tag{1}$$

with $H$ the hematocrit and $\lambda$ in [nm]. Some discrepancies exist when comparing the data for (oxy) hemoglobin of Welch and van Gemert [7], and Jacques [8] and those of Hillenkamp [12]. Svaasand [1] used a fit to the Hillenkamp data of 80% $HbO_2$ based on eight Gaussian bands.

The scattering data for oxyhemoglobin and hemoglobin are adapted from Svaasand *et al.*[1]. In the wavelength range 400-820 nm the scattering coefficient is taken to be inversely proportional to the wavelength and scaled to the value at 685 nm.

$$\mu_s^B(\lambda) = 440.72H(1-H)(1.4-H)\left(\frac{685}{\lambda}\right) \ , \tag{2}$$

The anisotropy of scattering for oxyhemoglobin and hemoglobin is assumed constant over the wavelength range considered

$$g^B(\lambda) = 0.995 \ , \tag{3}$$

Recently, Roggan [13] investigated optical properties of whole circulating human blood in the 400-2500 nm wavelength range using a double integrating sphere set-up. Their data for (oxy)hemoglobin are in reasonable agreement with the data above. Scattering in the 400-500 nm range shows a deviation from the reciprocal wavelength dependence. For the moment we will neglect this and use equation (2).

### 2.2.2. Composite optical properties of blood

The absorption of blood is calculated from the analytical expressions for $HbO_2$ and $Hb$.

$$\mu_a^B(\lambda) = p^{Oxy}\mu_a^{HbO_2}(\lambda) + (1-p^{Oxy})\mu_a^{Hb}(\lambda), \tag{4}$$

where $p^{Oxy}$ is the oxygenation degree of the blood. Thus $p^{Oxy}$ = 0.8 means 80 % $HbO_2$ and 20% $Hb$.

### 2.2.3. Correction for non-homogeneous distribution of blood in skin

In our skin model the blood is assumed homogeneously distributed which is a crude simplification of the real case where blood is discretely distributed in vessels. This has consequences for the effective absorption of light, see Verkruysse *et al.*[6]. The effective absorption of blood is reduced when the penetration depth of light in blood becomes small compared to the vessel radius ($R$), when blood in the center of the vessel does not contribute to absorption. Verkruysse *et al.* introduce correction factors which can be used to correct for this effect. In our study we use their expressions yielding a correction factor $C$. The correction factor depends on the product $\xi$ of the blood absorption coefficient and vessel radius $\xi = \mu^B{}_a R$.

*2.2.4 Melanin*

The absorption coefficients for melanin are taken from Svaasand *et al.*[1].

$$\mu_a^M(\lambda) = \mu_{a,m,694}\left(\frac{694}{\lambda}\right)^4 \ , \tag{5}$$

with $\mu_{a,m,694}$ the average melanin absorption at $\lambda$ = 694 nm. Typical values for $\mu_{a,m,694}$ range from ca. 0.3mm$^{-1}$ for fair Caucasian skin to ca. 2.5 mm$^{-1}$ for African skin, see Norvang *et al.*[14].

### 2.3. Composite optical properties of layered skin model

The composite optical properties for the layers $i$ = 1..5 are given by the following expressions; first, the absorption coefficient reads

$$\mu_{a,i}(\lambda) = B_i C_i \mu_a^B(\lambda) + (1 - B_i)\mu_a^T(\lambda) + M_i \mu_a^M(\lambda), \tag{6}$$

where $B_i$ is the blood concentration in layer $i$, $C_i$ is the correction factor in layer $i$, $M_i$ = 1 for $i$=*1*(epidermis), $M_i$ = 0 for $i$ =2,...,5, and $\mu_a^T$ is the absorption coefficient for skin tissue without chromophores.
Next, the expression for the composite scattering coefficient of each layer reads

$$\mu_{s,i}(\lambda) = B_i C_i \mu_s^B(\lambda) + (1 - B_i)\mu_{s,i}^T(\lambda), \tag{7}$$

where and $\mu_{s,i}^T$ the scattering coefficient of skin tissue without chromophores, is written as

$$\mu_{s,i}^T(\lambda) = \mu_s^{E,D,H}\left(\frac{577}{\lambda}\right), \quad E(i=1), \quad D(i=2..4), \quad H(i=5), \tag{8}$$

Finally, the expression for the composite mean cosine of the scattering angle of each layer reads

$$g_i(\lambda) = \frac{B_i C_i \mu_s^B(\lambda) g^B + (1 - B_i)\mu_{s,i}^T(\lambda) g^T(\lambda)}{\mu_{s,i}}, \tag{9}$$

where $g^T$ the mean cosine of the scattering angle of skin tissue without chromophores, is written as

$$\begin{aligned} g^T(\lambda) &= 0.62 + 29 \cdot 10^5 \lambda, \qquad i = 1,...,4 \\ g^T(\lambda) &= 0.9 \qquad\qquad\qquad\quad i = 5 \end{aligned} \tag{10}$$

with $\lambda$ in nm, Svaasand *et al.*[1].

### 2.4. Diffusion approximation

In general the transport of light in a scattering medium can be described with the equation of radiative transfer, Case and Zweifel[15]. The so-called diffusion approximation yields a simplified set of two first order differential equations formulated in the fluence rate $\Psi$ (W/mm$^2$) and the radiative flux $F$ (W/mm$^2$)

$$F = -\frac{1}{3\mu_{tr}}\frac{d\Psi}{dz} + \frac{\mu_s g}{\mu_{tr}} q_c, \tag{11}$$

$$\frac{dF}{dz} = -\mu_a \Psi + \mu_s q_c, \tag{12}$$

where $\mu_a$ is the absorption-, $\mu_s$ the scattering coefficient, $g$ the mean cosine of the scattering angle, $\mu_{tr} = \mu_a + \mu_s (1 - g)$ the transport coefficient, and $q_c$ the collimated source term. Eliminating the radiative flux from these equations yields a second order differential equation (diffusion equation) formulated in $\Psi$, see e.g. Keijzer[2].

The diffusion approximation is only valid in case the transport of light in the medium is dominated by scattering, and in case the scattering is mainly isotropic:

$$\frac{\mu_a}{\mu_s} << 1 - g^2, \tag{13}$$

For skin the validity of this condition will be tested over the entire range of wavelengths considered: 400-820nm. Furthermore the accuracy of this approximation is poor in case of large gradients (boundaries, discontinuities). However, the advantage of this approach is that, in case of simple geometries, it yields analytical solutions. So it provides a very fast means to gain insight in the phenomena occurring.

The skin is modeled as a one-dimensional, semi-infinite, layered structure that is homogeneous in the lateral directions. The one-dimensional, stationary diffusion equation is employed to describe the transport of light in a 1-dimensional multi-layered geometry. Two approaches are followed. The first approach is based on Keijzer's[2] general 3-dimensional diffusion approximation. A distinction is made between perfectly diffuse- and collimated illumination of the skin. In the second

approach the two-layer model derived by Svaasand *et al.*[1] for collimated illumination was generalized for an arbitrary number of layers.

The reader can find derivations of the diffuse reflectance for the layered models for diffuse and collimated illumination in Appendix A. Here only the end results will be given.

*Layered Keijzer model for perfectly diffuse illumination*
The diffuse reflectance $\gamma_d^K$ in Keijzer's approach for *diffuse* illumination is given by

$$\gamma_d^K = \frac{C_{1,1}^K + C_{2,1}^K}{2AP_{inc}} - \frac{1-R_2}{1+R_2}(1-R_{s1}), \tag{14}$$

where $C_{1,1}^K$ and $C_{2,1}^K$ are determined by the boundary conditions (see Appendix A). $A = (1 + R_2)/(1 - R_1)$ is a constant, with $R_1$ and $R_2$ hemispherical moments of the Fresnel reflection coefficient. $R_{s1}$ accounts for the fraction of incident light at the skin's surface that is specularly reflected. $P_{inc}$ is the incident power flow at the skin surface generated by the light source, where $(1-R_{s1})\,P_{inc} = 2\pi L_0$.

*Layered Keijzer model for collimated illumination*
The diffuse reflectance $\gamma_c^K$ in Keijzer's approach for *collimated* illumination is given by

$$\gamma_c^K = \frac{C_{1,1}^K + C_{2,1}^K + C_{3,1}^K}{2AP_{inc}}, \tag{15}$$

where $C_{1,1}^K$, $C_{2,1}^K$ and $C_{3,1}^K$ are determined by the boundary conditions and the particular solution of the diffusion equation (eq. A1).

*Layered Svaasand model for collimated illumination*
The diffuse reflectance $\gamma_c^S$ in Svaasand's approach for *collimated* illumination is given by

$$\gamma_c^S = \frac{C_{1,1}^S + C_{2,1}^S + C_{3,1}^S}{2AP_{inc}}, \tag{16}$$

where $C_{1,1}^S$, $C_{2,1}^S$ and $C_{3,1}^S$ are determined by the boundary conditions and the particular solution of the diffusion equation (eq. A1).
Note that we have used the reflectance $\gamma_c^S$ with respect to the amount of incident light, whereas in the definition given by Svaasand the diffuse reflectance was defined with respect to the amount of light transmitted to the skin which differs a factor $(1-R_{s1})$ in $\gamma_c^S$.
For each case the the total reflectance $\Gamma_{d,c}^{K,S}$ is given by adding $R_{s1}$ to the expression of the diffuse reflectance given in Eqs. (14) to (16)

On comparison of the model for collimated illumination based on Keijzer's approach and Svaasand's model some differences are observed. These include the right-handside of the diffusion equation, the boundary condition at $z = 0$, and the interface condition forcing continuity of (the normal component of) the radiative flux. These differences are caused by different treatment of the collimated source term $q_c$ that is present in equations (11) and (12). Firstly, in Keijzer's derivation this term reads

$$q_c^K = (1-R_{s1})P_{inc}\exp(-\mu_t z), \tag{17}$$

whereas in Svaasand's derivation the source term is given by

$$q_c^S = (1-g)(1-R_{s1})P_{inc}\exp(-\mu_{tr} z). \tag{18}$$

Secondly, Svaasand *et al.* omit the collimated source term in equation (11).

We compared simulations of reflectance spectra on the basis of the Keijzer and Svaasand models to Monte Carlo calculations in a similar 5 layer model using program code in detail described by Lucassen *et al.*[4]. The outcome of these simulations is that all simulated spectra agree qualitatively very well. In case of diffuse illumination the Keijzer model slightly underpredicts the Monte Carlo results over the entire wavelength range. The deviation decreases from ca. 0.05 to 0.02 in the range from 400 to 600 nm, and decreases further to ca. 0.01 at 800 nm. In case of collimated illumination the deviation between the Monte Carlo model and the Keijzer model is less than 0.01 over the entire range (400-800 nm). The deviation between the Monte Carlo model and the Svaasand model is ca. 0.02 in the range 400-600 nm.

It was mentioned that the diffusion approximation is valid in case the transport of light is dominated by (isotropic) scattering, i.e. inequality (13) must hold or alternatively the factor $\mu_a / (\mu_s( 1 - g^2))$ should be much less than unity. Fig. 3 shows $\mu_a / (\mu_s( 1 - g^2))$ as a function of wavelength for each of the five layers in the layered skin model. From this graph it can be seen that this condition tends to be violated in the range 400-600 nm, especially for the layers in the model that contain the highest concentration of chromophores (layers 1,2, and 4 respectively). This corresponds with the fact that deviations between Monte Carlo and diffusion approximation results are highest in the range 400-600 nm.

## 3. EXPERIMENTAL

The experimental set-up for measuring the diffuse reflectance of skin consists of a HP8452 photospectrometer with holographic grating and photodiode array detector with a 2 nm spectral resolution. Data acquisition time is 0.1 sec. An integrating sphere accessory with light entrance port area of 22 mm diameter and a handheld fiber optic probe with integrating cylinder head accessory with 10 mm diameter light port are used. These accessories each have a Halogen lamp (6W) inside to provide a diffuse illumination through the light port onto the skin. The diffuse reflectance is captured in the integrating cylinder and fed back to the spectrometer. In case of the handheld probe the light from the integrating cylinder to the spectrometer is transmitted through a glass fiber. The wavelength range covered is 400-820 nm. Calibration is

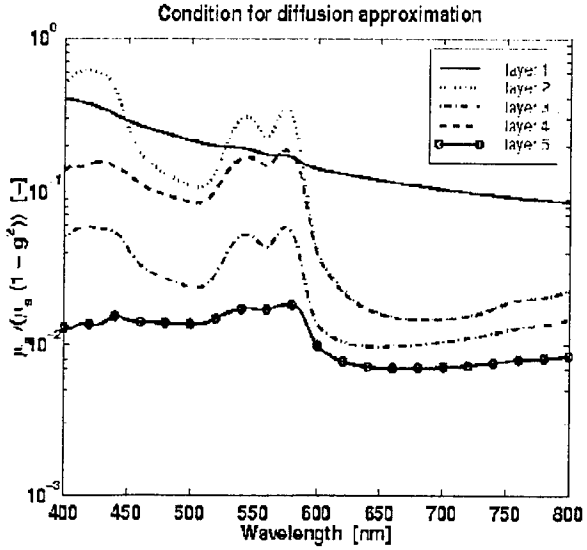


**Figure 3**. *Diffusion approximation is valid for* $\mu_a / \mu_s(1-g^2) << 1$ .

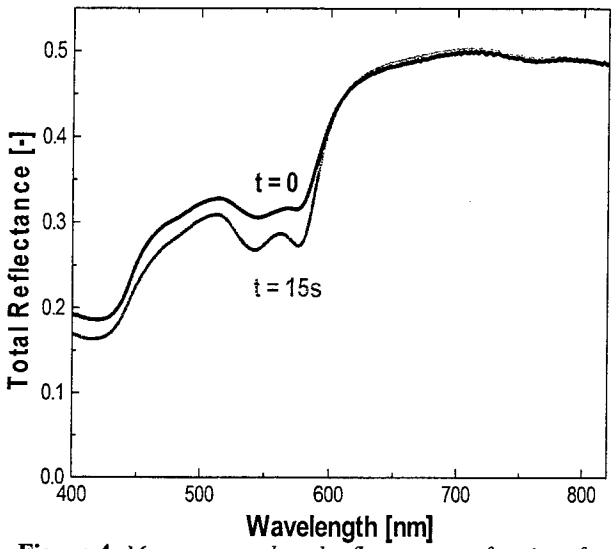


**Figure 4.** *Mean measured total reflectance as a function of wavelength at t=0 and after heating t=15s.*

performed using 99% reflection standards. To prevent heating the fiber probe housing was cooled using a fan. The reflectance data were stored on a PC for later processing. The handheld probe was spring loaded in order to control the pressure of the probe on the skin. To increase reproducibility the circumference of the probe was marked on the skin allowing for easy replacement of the probe on the same skin location. To test reproducibility all measurements were repeated 3-5 times. Typical standard deviations of 2-5% are obtained.

Due to the smaller measuring port area of the hand held probe head compared to the port area of the integrating sphere the hand-held probe captures less light that remits the skin. This results in a lower measured reflectance for wavelengths larger than about 600 nm. We corrected the fiber probe spectra for this effect. The following procedure was employed. Total reflectance was measured on the volar forearm skin of 5 subjects, both with the integrating sphere accessory ($\Gamma_{d,is}$) and the hand-held probe accessory ( $\Gamma_{d,hp}$). The ratio $\rho_d = \Gamma_{d,is} / \Gamma_{d,hp}$ ,which is wavelength dependent, is used to correct the measured spectra $\Gamma_{d,corr}(\lambda) = \Gamma_{d,meas}(\lambda) * \rho_d(\lambda)$. The ratio $\rho_d$ is close to unity for he lower wavelengths (400-600nm) and amounts to 1.1 –1.15 for larger wavelengths (600-820nm). This is due to increased penetration depth for higher wavelengths (in the 400-820nm range).

### 3.1. Measurement of skin color changes due to skin heating and occlusion of blood supply

Measurements were performed on both the right and left volar aspect of the forearm of 19 Caucasian volunteers (7 female, 12 male, 22-40years). We used the lamp heat of the probe to induce heating the skin by keeping the fiber probe against the skin volar forearm skin for 15 seconds, recording a diffuse reflectance spectrum each second. We used a pressure cuff placed around the upper arm to perturb the blood flow in the forearm. A spectrum was measured at the start of the experiment. Next the cuff pressure was kept at 70 mbar for 1 minute, followed by a reflectance measurement. Finally the cuff pressure is raised to 120 mbar. After one minute the last reflectance measurement is done. At a cuff pressure of 70 mbar, the venous flow will be partly blocked, and at a cuff pressure of 120 mbar, venous flow has stopped and arterial supply has diminished. As a consequence blood concentrations will increase and oxygenation of the blood will be affected.

### 3.2. Fit procedure

Measured reflectance spectra are fitted using the diffusion approximation, see equations (14) to (16). In the experiments considered here, it is assumed that the induced changes will only affect blood concentrations $B_i$. In case of the occlusion experiment also blood oxygenation $p^{OXY}$ will be expected to change (The complete list of parameters in the five layered skin model can be found in Tables B2 and B3, Appendix B). A Nelder-Mead simplex direct search method was employed in the fit procedure.

## 4. RESULTS

In Figure 4 the measured mean total reflectance is shown. Next the measured total reflectance is corrected by multiplication by the factor $\rho_d$ subsequently the diffuse reflectance $\Gamma_d$ is calculated by subtraction of the specularly reflected light (assuming $n_a = 1$ and $n_s = 1.4$, Svaasand et al.[1], $\gamma_d = \Gamma_{d,corr} - R_{s1}$.

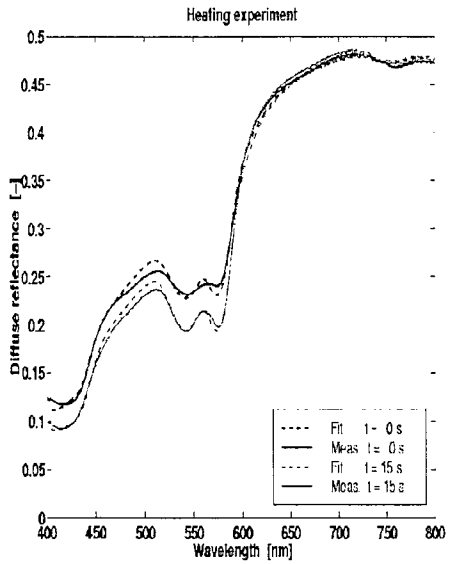


**Figure 5.** *Mean measured diffuse reflectance (solid lines) as a function of wavelength at t=0 and at t=15s). The fits (dahed) according to the diffusion approximation ($\gamma_d^K$)*

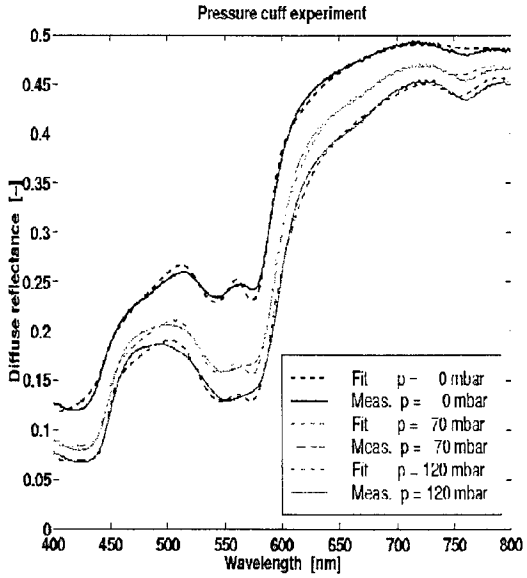


**Figure 6.** *Mean measured diffuse reflectance(solid lines) as a function of wavelength at p=0, 70 and at p=120mbar cuff pressure. The fits (dashed) according to the diffusion approximation ($\gamma_d^K$).*

In the fit procedure both diffuse reflectance spectra ($t = 0$, and $t = 15$s) are fit simultaneously in a single run. A distinction is made between parameters that are fixed to a set value ($R_i$, $d_i$, $H$, $n_s$), parameters that are fit but equal for both spectra ($\mu_{s,577,i}$, $p^{OXY}$, $\mu_{a,m,694}$, $\mu_a^T$) and parameters that are fit differently per spectrum ($B_i$).

Figure 5 shows the measured and fitted diffuse reflectance, both at $t = 0$ and $t = 15$s. The resulting fit parameters are shown in Table B2 (Appendix B). The data of the difference spectrum: $\gamma_d$(t=15) - $\gamma_d$ (t=0) were analysed statistically. It was found by a one way ANOVA analysis on the data at $\lambda = 540$ and 576 nm that there was no side effect (left/right), however women and men reacted significantly different ($p = 0.006$ at $\lambda = 540$ nm, and $p = 0.004$ at $\lambda = 576$ nm respectively): women showing a more pronounced reaction to the heating.

For spectra of the occlusion of blood experiment the fit procedure was done on all three spectra simultaneously. In this experiment the oxygenation parameter was treated differently. Firstly, seperate oxygenation parameters are introduced: $P^{OXY}_{12}$ for layer 1 and 2, and $P^{OXY}_{345}$ for layers 3 to 5. Secondly, both parameters are now considered to be different for each spectrum.
In Figure 6 the mean measured diffuse reflectance curves are shown along with the fitted results. Fit parameters are listed in Table B3, Appendix B.

## 5. DISCUSSION

### 5.1. Heating experiment

In the skin heating experiment the reflectance is lowered essentially (~20 %) in the 400 to 600 nm wavelength range after 15 seconds of heating. The decreased reflectance points to an increased absorption of light (mainly by blood) in the upper layers of the skin. Note that this effect was significantly higher in women ($n = 7$) than in men ($n = 12$). From the fits and Table B2 it can be inferred that the most pronounced change occurs in the blood concentration of layer 2 (the superficial blood plexus). Furthermore we see a slight increase in blood concentration in the epidermal capillaries and in the dermis layer, and a decrease in the deep blood plexus and the hypodermis layer.
The 540 nm and 578 nm bands are more pronounced in the spectrum at $t = 15$ s compared to the spectrum at $t = 0$ s. This subtle change in the shape of the spectrum can be explained by the following: at the start of the experiment not all the capillaries are filled with red blood cells. During the heating especially the smaller blood vessels in layer 2 are filled with red blood cells thereby changing the effective absorption by the blood. Verkruysse *et al.*[6] have shown that absorption of light by blood vessels of different sizes has a pronounced effect on the shape of the reflectance spectrum in the 400-600 nm spectral range. This means that at the start of the experiment the effective absorption is mainly due to larger vessels which have a flattening effect on the 540 and 578 nm oxyhemoglobin absorption bands. At the end of the experiment more smaller vessels in layer 2 are filled with blood giving the bands a sharper appearance. At this stage we have used fixed vessel radii and oxygenation degree for both sets ($t = 0$ and $t = 15$ s) because we focused on the overall effect of changed blood concentration in the different skin layers. We are currently investigating refining the extraction of physiologic parameters taking into account the coupling of blood volume changes with blood concentration and vessel sizes.

From the fact that the measured reflectance spectra closely match above 600 nm we would expect that there is no change in blood absorption in the deeper layers of the skin. A total decrease of the reflectance over the entire 400-800 nm spectral range is expected when the concentrations in the deeper layers change as we have concluded from separate forward calculations varying the blood concentrations in the different layers. However, this does not follow from our fits on the present data, where the calculated blood concentrations in the fourth and fifth layer are substantially lowered. It should be noted that as only little light will penetrate in layers four and five, these parameters have less influence on the resulting fit result than the parameters concerned with the upper layers.

### 5.2. Pressure cuff experiments

In the pressure cuff experiments two major effects play a role:

- Blood concentrations increase in all skin layers. At 70 mbar the flow in the venous system will be partly blocked; at 120 mbar venous flow will be totally blocked. Supply of blood will be partly blocked at 70 and 120 mbar, respectively.
- As the normal inflow of oxygen rich blood and outflow of oxygen poor blood of the underarm are perturbed, the overall oxygen state of the blood will change.

The measurements at cuff pressures at 70 mbar and 120 mbar show a total decrease in reflectance over the entire spectral range. This agrees with the fact that more light is absorbed by the presence of more blood in the upper and deeper skin layers. The two peaks according to oxyhemoglobin tend to disappear into a single band. This points to an increased contribution of (deoxy)hemoglobin which is also evident from the pronounced hemoglobin band at 760 nm, and, less clearly visible, the reflectance minimum shift from 412 nm to 430 nm corresponding with the Soret hemoglobin absorption band.

From the fits and Table B3 it follows that the blood concentration $B_i$ in all layers increase, most drastically in layer 2. Along with the increased blood concentrations, the oxygenation degree of the blood in the two upper layers decreases from 65% to 31%, while in the deeper layers the oxygenation degree drops from 88% to 69%. These fit parameters indicate that the superficial blood plexus is filled up and oxygen is best released in the upper layers. In the deeper layers the oxygenation degree decreases by accumulation of oxygen poor blood.

The results of the two experiments described above show the possibility of extracting detailed information on the physiological parameters of the skin. The added value of modelling is that changes in the physiological state of e.g. blood concentration and oxygenation degree can be quantified. Assessment of the physiological parameters that induce the skin colour changes on the basis of e.g. the $L^*$ $a^*$ $b^*$ values alone is very difficult. The changes in $L^*$ $a^*$ $b^*$ values for the pressure cuff experiment show a decrease in $L^*$ from 59.5 to 53.0 at 70 mbar and to 49.8 at 120 mbar, an increase in $a^*$ from 9.9 to 12.7 and 13.4, and a decrease in b* from 16.6, to 15.0 and 13.6. The colour distance defined *by* $\Delta E = (\Delta L^{*2} + \Delta a^{*2} + \Delta b^{*2})^{0.5} = 5.53$ at 70 mbar and $\Delta E = 10.74$ at 120 mbar. These parameters clearly show that skin in this experiment gets less bright, less blue, and more red. The large colour distances 5.5 and 10.7 (compared to the minimal colour difference of $\Delta E = 0.4$ that can be distinghuished by the naked eye) indicate that these changes in skin colour are clearly visible.

## 6. CONCLUSION

We extended Svaasand's analytical approach to simulate skin reflectance to a five layer skin model using first order diffusion approximation (P1) of the transport equation. Following Keijzer's formalism we derived expressions for the diffuse reflectance under diffuse and collimated illumination. We compared the calculated diffuse reflectance spectrum with simulated spectra using the Monte Carlo method. The diffuse reflectance under diffuse illumination is underestimated in the P1 approximation, whereas a close match is found under collimated illumination when compared to the Monte Carlo results. Svaasand's model for collimated illumination gives slightly higher values in the 400-600 nm spectral range. The analytical models were incorporated in a Nelder-Mead simplex fit program to extract skin parameters from measured diffuse reflectance spectra.
From fits to the measured spectra in the two experiments we found good agreement with expected results. In the heating experiment, essentially the blood concentration in the superficial skin layer increased, and the spectral shape of the oxyhemoglobin bands sharpen due to the contribution of small blood vessels to the total absorption. In the pressure cuff experiment, we found increased blood concentrations in all layers, but most in the superficial blood plexus, and a decrease in oxygenation state of the blood in the upper skin layers.

Although we employ a very simplified model for the complex skin and make use of first order approximations to model the reflectance we have shown that such models yield quantitative information on physiological parameters that influence the visual appearance of skin under different conditions. We think that further development of these models in combination with non-invasive reflectance measurements will help us to gain knowledge on the optical response of skin, which is not available from other existing methods.

## 7. REFERENCES


1. L.O. Svaasand, L.T. Norvang, E.J. Fiskerstrand, E.K.S. Stopps, M.W. Berns, and J.S. Nelson, "Tissue Parameters Determining the Visual Appearance of Normal Skin and Port-wine Stains", *Lasers in Medical Science*, **10**, pp55-65, 1995.
2. M. Keijzer, *Light Transport for Medical Laser Treatments*, PhD thesis, Delft University of Technology, 1993.
3. D.J. Smithies, and P.H. Butler, "Modelling the distribution of laser light in port-wine stains with the Monte Carlo method", *Physics in Medicine and Biology*, **40**, pp701-733, 1995.
4. G.W. Lucassen, W. Verkruysse, M. Keijzer, and M.J.C van Gemert, "Light distributions in Port-Wine Stain Model containing multiple cylindrical and curved blood vessels", *Laser in Surgery and Medicine*, **18**, pp345-357, 1996.
5. T.J. Pfefer, J.K. Barton, D.J. Smithies, T.E. Milner, J.S. Nelson, M.J.C. van Gemert, and A.J. Welch, "Laser Treatment of Port Wine Stains: 3-D simulation using biopsy-defined geometry in an optical-thermal model", SPIE Proceedings, 3245, 1998.

6. W. Verkruysse, G.W. Lucassen, J.F. de Boer, D.J. Smithies, J.S. Nelson, and M.J.C. van Gemert, "Homogeneous versus discrete absorbing structures in turbid media", *Physics in Medicine and Biology*, **42**, pp51-65, 1997.
7. A.J. Welch, and M.J.C. van Gemert, eds., *Optical-thermal response of laser irradiated tissue*, Plenum Press, NY, 1995.
8. S.L. Jacques, "Origins of tissue optical properties in the UVA, Visible and NIR regions", *Advances in Optical Imaging and Photon Migration*, R.R. Alfano and J.G. Fujimoto ,Vol.2., pp364-370, 1996.
9. H.R. Jakubovich, and A.B. Ackerman, *Dermatology,* Moschella, S.L., and H.J. Hurley, Philadelphia, W.B. Saunders Company, 1992.
10. G.F. Odland, "Structure of the skin", in *Physiology, Biochemistry and Molecular Biology of the Skin,* L.A. Goldsmith, Vol II, Oxford University Press, Oxford, pp. 3-62, 1991.
11. T.J. Ryan, "Cutaneous Circulation", *Physiology, Biochemistry, and Molecular Biology of the Skin*, Goldsmith, L.A. Vol II, Oxford University Press, Oxford, pp. 1019-1084, 1991.
12. F. Hillenkamp, "Interaction between laser radiation and biogical systems", *Lasers in Biology and Medicine* F. Hillenkamp, R. Pratesi, and C. Sacci, New York, Plenum Press, 57, pp61, 1979.
13. A. M. Roggan, Friebel, K. Dörschel, A. Hahn, and G. Müller, "Optical properties of circulating human blood", Proc. SPIE Vol. 3252, 1998.
14. L.T. Norvang, T.E. Milner, J.S. Nelson, M.W. Berns, and L.O.Svaasand, "Skin pigmentation characterised by visible reflectance measurements", *Lasers in Medical Science*, **12**, pp99-112, 1997.
15. K.M. Case and P.F. Zweifel, *Linear Transport Theory*, Addison-Wesly Publishing Co, 1967.
16. J.H. Joseph and W.J. Wiscombe, "The delta-Eddington approximation for radiative flux transfer", *Journal of Atmospheric Sciences*, **33**, pp2452-2459, 1976.

## APPENDIX A: DERIVATION OF THE DIFFUSE REFLECTANCE

In the following the derivations for the cases diffuse illumination -Keijzer will be denoted a) , collimated illumination – Keijzer denoted b) and collimated –Svaasand denoted c). The diffusion equation of a semi-infinite n-layered structure reads

$$\frac{d^2\Psi_i}{dz^2} - k_i^2\Psi_i = 0 \quad , \tag{A1a}$$

$$\frac{d^2\Psi_i}{dz^2} - k_i^2\Psi_i = -3\mu_{s,i}(\mu_{tr,i} + \mu_{t,i}g_i)2\pi L_0 \exp(-\mu_{t,i}z)Q_i(\mu_{t,1},.....,\mu_{t,i}) \, , \tag{A1b}$$

$$\frac{d^2\Psi_i}{dz^2} - k_i^2\Psi_i = -3\mu_{s,i}\mu_{tr,i}(1-g_i)2\pi L_0 \exp(-\mu_{tr,i}z)Q_i(\mu_{tr,1},.....,\mu_{tr,i}) \, , \tag{A1c}$$

for $z_{i-1} \le z \le z_i$, $i = 1,...,n$ and where the quantity $Q_i(\mu_{tr,1},...,\mu_{tr,i})$ is defined as

$$Q_i(\mu_{tr,1},.....,\mu_{tr,i}) = \begin{cases} 1, & for \quad i = 1, \\ \prod_{j=1}^{i-1} \exp(-(\mu_{tr,j} - \mu_{tr,j+1})z_j, & for \quad i = 2,...,n \end{cases} \tag{A2}$$

$\Psi_i$ is the fluence rate in layer $i$ bounded by coordinates $z_{i-1}$ and $z_i$ respectively, and $k_i = \sqrt{3}\ \mu_{a,i}\ \mu_{tr,i}$. Note that $z_0 = 0$ is the skin-air interface, and $z_n = \infty$; the thickness of layer $i$, $d_i = z_i - z_{i-1}$.

*Boundary conditions:* The following boundary conditions apply at these surfaces, Keijzer [2]:

$$\Psi_1(0) - Ah_i \left.\frac{d\Psi_1}{dz}\right|_{z=0} = \frac{8\pi}{1-R_1}L_0, \tag{A3a}$$

$$\Psi_1(0) - Ah_i \left.\frac{d\Psi_1}{dz}\right|_{z=0} = -6\pi\mu_{s,i}g_iAh_iL_0, \tag{A3b}$$

$$\Psi_1(0) - Ah_i \left.\frac{d\Psi_1}{dz}\right|_{z=0} = 0, \tag{A3c}$$

For all three case the other boundary condition reads

$$\lim_{z\to\infty} \Psi_n(z) = 0 \, , \tag{A4}$$

$A = (1 + R_2)/(1 - R_1)$, $h_i = 2/(3\,\mu_{tr,i})$, and $L_0$ the radiance of the diffuse light source transmitted to the skin. The factors $R_j$, j=1,2 are the so-called hemispherical moments of the Fresnel reflection factor (from skin to air) defined as:

$$R_j = (j+1)\int_{\theta_s}^{\pi/2} R(\theta_s)\cos^j\theta_s \sin\theta_s d\theta_s, \tag{A5}$$

where the Fresnel reflection factor (for transport from skin to air) $R(\theta_s)$ can be written as

$$R(\theta_s) = \begin{cases} \left(\dfrac{n_s - n_a}{n_s + n_a}\right)^2, & for \quad \theta_s = 0 \\ \dfrac{1}{2}\left(\dfrac{\sin^2(\theta_s - \theta_a)}{\sin^2(\theta_s + \theta_a)} + \dfrac{\tan^2(\theta_s - \theta_a)}{\tan^2(\theta_s + \theta_a)}\right), & for \quad 0 < \theta_s < \theta_c \\ 1, & for \quad \theta_s \geq \theta_c \end{cases} \tag{A6}$$

where $n_s$ is the refractive index of skin, $n_a$ is the refractive index of air, and $\theta_c = \arcsin(n_a/n_s)$, $n_s \geq n_a$, is the so-called critical angle.

*Interface conditions:* At the interfaces $z = z_i$ for $i=1,...n-1$, the following conditions must hold: continuity of the fluence rate and continuity of (the normal component of) the radiative flux.

The first condition is the same for the three cases and can be written as

$$\Psi_i(z_i) = \Psi_{i+1}(z_i) \qquad for \quad i = 1,...n-1 \tag{A7}$$

The second condition is different per case and reads

$$\left.\frac{1}{3\mu_{tr,i}}\frac{d\Psi_i}{dz}\right|_{z=z_i} = \left.\frac{1}{3\mu_{tr,i+1}}\frac{d\Psi_{i+1}}{dz}\right|_{z=z_i}, \tag{A8a}$$

$$\left.\frac{1}{3\mu_{tr,i}}\frac{d\Psi_i}{dz}\right|_{z=z_i} = \left.\frac{1}{3\mu_{tr,i+1}}\frac{d\Psi_{i+1}}{dz}\right|_{z=z_i} + \left(\frac{\mu_{s,i}g_i}{\mu_{tr,i}} - \frac{\mu_{s,i+1}g_{i+1}}{\mu_{tr,i+1}}\right)2\pi L_0, \tag{A8b}$$

$$\left.\frac{1}{3\mu_{tr,i}}\frac{d\Psi_i}{dz}\right|_{z=z_i} = \left.\frac{1}{3\mu_{tr,i+1}}\frac{d\Psi_{i+1}}{dz}\right|_{z=z_i}, \tag{A8c}$$

for $i = 1,...,n-1$.

The analytical solution of the diffusion equation yields:

$$\Psi_i(z) = C_{1,i}^K \exp(-k_i z) + C_{2,i}^K \exp(k_i z), \tag{A9a}$$

$$\Psi_i(z) = C_{1,i}^K \exp(-k_i z) + C_{2,i}^K \exp(k_i z) + C_{3,i}^K \exp(-\mu_{t,i} z), \tag{A9b}$$

$$\Psi_i(z) = C_{1,i}^S \exp(-k_i z) + C_{2,i}^S \exp(k_i z) + C_{3,i}^S \exp(-\mu_{tr,i} z), \tag{A9c}$$

where

$$C_{3,i}^K = -3\mu_{s,i}\frac{\mu_{tr,i} + g_i\mu_{t,i}}{\mu_{t,i}^2 - k_i^2} Q_i(\mu_{t,1},.....,\mu_{t,i})(1 - R_{s1})P_{inc}, \tag{A10b}$$

$$C_{3,i}^S = -3\mu_{s,i}\frac{\mu_{tr,i}(1 - g_i)}{\mu_{tr,i}^2 - k_i^2} Q_i(\mu_{tr,1},....., \mu_{tr,i})(1 - R_{s1})P_{inc}, \tag{A10c}$$

The $2n$ constants $C_{1,i}^{K,S}$ and $C_{2,i}^{K,S}$ can be determined by employing the boundary conditions (A3) and (A4) and the interface conditions (A7) and (A8).

The diffuse reflectance and the total reflectance are given by (with respect to incident light)

$$\gamma_d^K = \frac{\Psi_1(0)}{2AP_{inc}} - \frac{1 - R_2}{1 + R_2}(1 - R_{s1}), \tag{A11a}$$

$$\gamma_c^K = \frac{\Psi_1(0)}{2AP_{inc}}, \tag{A11b}$$

$$\gamma_c^S = \frac{\Psi_1(0)}{2AP_{inc}}, \tag{A11c}$$

and for the total reflectance $\Gamma_{d,c}^{K,S} = \gamma_{d,c}^{K,S} + R_{s1}$ . (A12)

where $R_{s1}$ accounts for the fraction of incident light at the skin's surface that is specularly reflected (see definition $R_1$ in equation (A4), and $P_{inc}$ is the incident power flow at the skin surface generated by the light source, where $(1-R_{s1})\ P_{inc} = 2\pi L_0$. The diffusion approximation can be improved by employing the so-called δ-Eddington phase function, Joseph and Wiscombe [16]. This is implemented by adaptation of the scattering properties according to

$$\mu_{s\delta} = \mu_s(1-g^2), \qquad g_\delta = \frac{g}{1+g} . \tag{A13}$$

Note that $\mu_{tr}$ and $\mu_s(1-g)$ are invariant under this transformation. Therefore the δ-Eddington correction is trivial for the perfectly diffuse illumination case, as well as for Svaasand's approach.

## APPENDIX B: TABLES

**Table B1**. Coefficients $\lambda_j$, $a_j$ and $b_j$ in the expression for the absorption coefficient for oxyhemoglobin $HbO_2$, (deoxy)hemoglobin $Hb$ resulting from a fit to the data of Welch and van Gemert [7] and Jacques [8].

| | $HbO_2$ | | | $Hb$ | | |
|---|---|---|---|---|---|---|
| $j$ | $\lambda_j$ nm | $a_j$ $mm^{-1}$ | $b_j$ nm | $\lambda_j$ nm | $a_j$ $mm^{-1}$ | $b_j$ nm |
| 1 | 268 | 5.88 | 23.41 | 265 | 5.46 | 25.74 |
| 2 | 315 | 2.88 | 70.71 | 315 | 0.64 | 56.57 |
| 3 | 350 | 2.59 | 31.82 | 325.4 | 0.99 | 247.49 |
| 4 | 395 | 8.43 | 14.07 | 360 | 3.43 | 51.48 |
| 5 | 414 | 23.49 | 12.30 | 380 | 2.63 | 35.36 |
| 6 | 430 | 5.38 | 17.68 | 389.4 | 1. 56 | 10.61 |
| 7 | 435.7 | 1.67 | 99.00 | 410 | 11.59 | 11.74 |
| 8 | 530 | 0.78 | 35.36 | 430 | 30.64 | 11.31 |
| 9 | 542.5 | 2.72 | 16.97 | 555 | 2.45 | 35.00 |
| 10 | 575 | 3.21 | 11.31 | 755 | 0.04 | 15.00 |
| 11 | 907 | 0.07 | 159.1 | 900.5 | 0.04 | 84.85 |

**Table B2.** Parameters in layered skin model: estimated values by fit on mean data of heating experiment.

| Layer $i$ | $B_i(t=0)$ % | $B_i(t=15)$ % | $\mu_{s,577,i}$ $mm^{-1}$ | | | |
|---|---|---|---|---|---|---|
| 1 | 0.77 | 0.89 | 29.5 | $p^{OXY}$ | 83.2 | % |
| 2 | 1.69 | 9.10 | 11.7 | $\mu_{a,m,694}$ | 0.283 | $mm^{-1}$ |
| 3 | 1.41 | 1.46 | 11.7 | $\mu_a^T$ | 0.0158 | $mm^{-1}$ |
| 4 | 3.25 | 2.39 | 11.7 | | | |
| 5 | 1.32 | 0.33 | 16.2 | | | |

**Table B3.** Parameters in layered skin model: estimated values by fit on mean data of pressure cuff experiment.
$\mu_{a,m,694} = 0.271 mm^{-1}$ , $\mu_a^T = 0.0134\ mm^{-1}$

| Layer $i$ | $B_1(p=0)$ % | $B_i(p=70)$ % | $B_i(p=120)$ % | $p^{OXY}$ % | $p^{OXY}$ % | $p^{OXY}$ % | $\mu_{s,577,1}$ $mm^{-1}$ |
|---|---|---|---|---|---|---|---|
| 1 | 0.92 | 1.63 | 1.94 | 65.7 | 32.8 | 25.9 | 31.7 |
| 2 | 1.07 | 10.29 | 19.11 | | | | 10.5 |
| 3 | 1.43 | 2.77 | 3.54 | 88.3 | 76.8 | 69.1 | 10.5 |
| 4 | 3.19 | 2.39 | 2.18 | | | | 10.5 |
| 5 | 1.35 | 1.33 | 1.56 | | | | 16.6 |

# Spatially resolved diffuse reflectance with laser Doppler imaging for the simultaneous in-vivo measurement of tissue perfusion and metabolic state

Kevin R. Forrester[1a], Roxane Shymkiw[a], John Tulip[b], Craig Sutherland[a], David Hart[a], and Robert Bray[a]

[a]University of Calgary, Calgary, Alberta, Canada T2N-4N1

[b]University of Alberta, Edmonton, Alberta, Canada, T6G- 2M7

## ABSTRACT

**Laser Doppler Imaging (LDI) has become an established technique for the two dimensional measurement of tissue perfusion but the uncertainty of photon penetration depth leads to ambiguous interpretation of what fraction of the tissue microcirculation is being sampled. This study investigates a diffuse reflectance technique for measuring tissue optical properties during LDI perfusion measurement for the simultaneous determination of photon penetration depth and tissue metabolic state.**

**LDI and diffuse reflectance spectroscopy measurements were made on surgically exposed ligaments in pregnant and non-pregnant rabbits. Photon penetration depths are reported. It was observed that anisotropic scattering occurs due to the ordered alignment of collagen fibers within ligament. Tissue perfusion in the ligaments of pregnant animals was significantly lower than in non-pregnant animals. Tissue hemoglobin concentration and oxygenation, and percent vascularization are also reported showing no statistical difference between the ligaments in pregnant and non-pregnant rabbits. A significant difference was observed in the photon scattering coefficient between the pregnant and non-pregnant groups suggesting a change in fibril spacing and/or orientation, most likely caused by an increased laxity in the ligaments of the pregnant animals. These investigations compare well with previous biochemical and biomechanical information obtained on ligaments.**

**Keywords:** laser Doppler imaging, diffuse reflectance spectroscopy, blood flow, metabolic state

## 1. INTRODUCTION

### 1.1 Laser Doppler imaging

Tissue microcirculation plays an essential role in the regulation of metabolic, haemodynamic, and thermal processes. A tissue's physiological state can vary over both long and short term intervals, where inadequate tissue perfusion can result from vascular disease or injury[1]. For these reasons, physiologists and clinicians are interested in monitoring the blood flow and distribution of the microvascular network rapidly, repeatedly and with minimal invasiveness.

Blood flow can be measured using several techniques that depend on direct observation, e-m flowmetry, plethysmography, thermal, or radioisotope methods. However, these techniques are often too slow and disturb the tissue's normal state. Optical techniques such as laser Doppler flowmetry (LDF) have become a

[1] Direct correspondence to Kevin Forrester. Email: kforrest@ucalgary.ca; telephone: (403) 220 7866; fax: (403) 270 0617



In *Laser-Tissue Interaction XI: Photochemical, Photothermal, and Photomechanical*, Donald D. Duncan, Jeffrey O. Hollinger, Steven L. Jacques, Editors, Proceedings of SPIE Vol. 3914 (2000) 1605-7422/00/$15.00

popular method for perfusion measurement because they can measure blood flow in the microcirculation with rapid response times and minimal invasiveness[2, 3, 4].

In LDF fiber optics are used to deliver laser light to and from the tissue surface. The fibers are attached to a probe placed in contact with the tissue and a continuous, real-time recording of perfusion is made. Because LDF is an optical technique the perfusion measurement depends on the optical properties of the tissue and is limited to a relative measurement with a varying response between tissue types. Also, because LDF can only sample a small region, the spatial variation in a tissue's heterogeneous structure makes the perfusion measurement site and tissue specific[5]. For these reasons, it is commonly recognized that LDF is best suited to monitoring temporal variations in stimuli-response experiments over specific tissues and at specific tissue sites.

In the early 1990s LDF technology was expanded to produce a Doppler technique that could record the spatial distribution of tissue perfusion. This technique has become known as laser Doppler perfusion imaging (LDI)[6, 7]. An LDI measurement is analogous to making a two dimensional sequence of single point LDF measurements across the tissue surface. To produce an automated scan the fiber optic probe is discarded and replaced with a remote optical system using a collimated laser beam, scanning-mirror, and bare photodiode (see figure 1). The scanning mirror directs a collimated laser beam across the surface of a tissue where penetrating photons scatter off internal structures. While most of the photons are scattered only by the stationary tissue matrix, retaining their original frequencies, some photons eventually collide with moving red blood cells to become spectrally broadened by Doppler shifting. The spectrally broadened photons "beat" with the non-shifted photons on the surface of a photodiode producing a modulation in its output current. The signal processing used in LDI is essentially the same as that used in LDF, where the first moment in the spectrum of Doppler shifted frequencies is used to generate an index related to tissue perfusion[8].

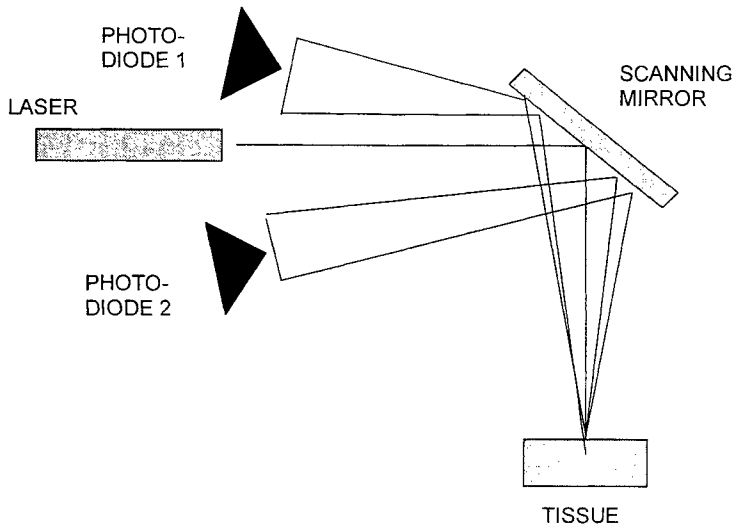


Figure 1: Schematic diagram showing the optical components used in LDI.

The spatial measurement in LDI has certain advantages over LDF, where perfusion maps can be analyzed to determine average tissue perfusion or the two-dimensional structuring of tissue microcirculation[9]. Also, in a comparison of LDI with colored microspheres our group has demonstrated that an average tissue perfusion can be used to compensate for tissue heterogeneity such that the perfusion measurement of a particular tissue can be compared between different animals[10]. This work has validated a method for monitoring the progress of disease (or injury) by comparing tissue perfusion between physiologically different animal groups. However, this model for studying disease and injury is valid only if the average optical properties of the tissue remain relatively constant between animal groups.

In this investigation, tissue perfusion and metabolic state of pregnant and non-pregnant rabbit ligaments are measured *in-vivo* to evaluate LDI and diffuse reflectance spectroscopy (DRS) as a method for quantifying physiologic and metabolic changes that occur during pregnancy. This study also demonstrates how the simultaneous measurement of tissue optical properties can be used to assist in the physiological interpretation of perfusion sampling volumes.

### 1.2 Diffuse reflectance measurement and spectroscopy

Light interaction with tissue is wavelength dependent and determined by the tissue absorption and reduced scattering coefficients, $\mu_a$ and $\mu_s'$, respectively[11]. These coefficients are used to define the effective attenuation coefficient $\mu_{eff} = [3\mu_a(\mu_a + \mu_s')]^{1/2}$, which in turn is used to determine the effective penetration depth of laser light within tissue

$$\delta_{eff} = 1/\mu_{eff} . \tag{1}$$

The effective penetration depth is the radial distance at which light fluence from a point source diminishes by 37 percent and is a useful parameter for determining the region of microcirculation sampled by a laser Doppler measurement.

Light absorption within tissue is determined by the species and concentration of its light absorbing molecules (chromophores) and is represented as a sum

$$\mu_a = (\ln(10))\sum_i \varepsilon_i C_i , \tag{2}$$

where $\varepsilon_i$ and $C_i$ are the extinction coefficient and concentration for the $i$th chromophore, respectively. If the chromophore extinction coefficients are known and a sufficient number of wavelengths are used, equation 2 can be solved and the concentration for each chromophore population can be determined[11].

In ligament tissue the only significant chromophores contributing to absorption in the visible to NIR wavelengths are oxy and deoxy-hemoglobin. With only two unknowns, two equations are sufficient to derive the exact concentrations of oxy- and deoxy- hemoglobin. For the two wavelengths used in this study, 633 and 780 nm, equation (2) can be written as

$$\mu_a^{633} = \ln(10)\left(\varepsilon_{Hb}^{633}[Hb] + \varepsilon_{HbO2}^{633}[HbO_2]\right) \tag{3}$$

$$\mu_a^{780} = \ln(10)\left(\varepsilon_{Hb}^{780}[Hb] + \varepsilon_{HbO2}^{780}[HbO_2]\right). \tag{4}$$

From the total hemoglobin concentration calculated using equations 3 and 4, and the molecular weight of the tetrahaem molecule (64,500 g/mol), the percent vascularization of tissue volume can be determined

$$PV = 100 \times \left(\frac{64{,}500\,g/mol}{150\,g/liter}\right)([Hb] + [HbO_2]), \tag{5}$$

where the concentrations are given in units of molars (mol/liter) and 150 g/liter is the normal physiological concentration of hemoglobin in whole blood.

The percent oxygenation of hemoglobin within the tissue is determined by taking the ratio of oxyhemoglobin over total hemoglobin

$$PO_2 = [H_bO_2]/([H_b] + [H_bO_2]) \tag{6}$$

To perform the DRS measurement we have adopted a technique similar to the one used by Farrell and co-workers[12]. This technique works particularly well with the geometry of an LDI measurement. It models the tissue as a semi-infinite half space using a "method of images" method to approximate the top surface boundary condition.

The diffusion model generates an analytical expression for the diffuse reflectance as a function of radial distance between the source point and an arbitrary point located on the tissue surface

$$R(\rho, z_0) = \frac{a'}{4\pi}\left[z_0\left(\mu_{eff} + \frac{1}{r_1}\right)\frac{e^{-\mu_{eff} r_1}}{r_1^2} + (z_0 + 2z_b)\left(\mu_{eff} + \frac{1}{r_2}\right)\frac{e^{-\mu_{eff} r_2}}{r_2^2}\right], \tag{7}$$

where

$$r_1 = \left[(z - z_0)^2 + \rho^2\right]^{1/2}, \tag{8}$$

$$r_2 = \left[(z + z_0 + 2z_b)^2 + \rho^2\right]^{1/2}, \tag{9}$$

and

$$a' = \mu_s' / (\mu_a + \mu_s') \tag{10}$$

The x and y coordinates define the plane of a flat tissue surface located at z = 0 with z positive downward (see figure 2). The model approximates the light source using a single point located a distance $z_0 = 1/\mu_t'$ below the tissue surface. The position $z_b$ is an extrapolated boundary located along the z-axis where the fluence is forced to zero. It is related to the tissue's diffusion coefficient and internal reflection parameter (see Farrell and co-workers for more information[12]).

During a DRS measurement the tissue surface is irradiated by a laser source and a fiber optic probe is used to spatially resolve the diffusely reflected light (see figure 2). A profile of light intensity as a function of radial distance is measured and tissue absorption and reduced scattering coefficients are extrapolated by matching equation 7 to the experimental data using a least-squared curve fitting procedure[13].

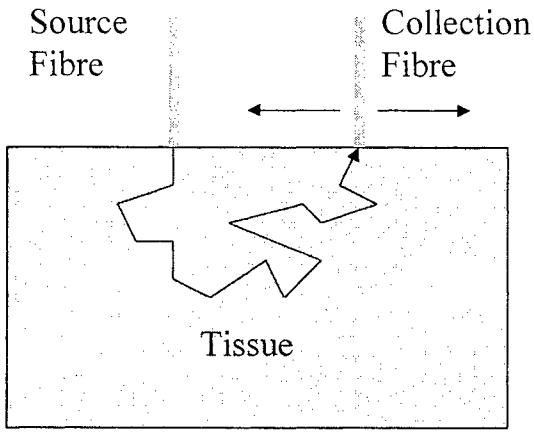


Figure 2: Schematic depicting the geometry of a diffuse reflectance spectroscopy measurement. A typical path for a photon scattered within the tissue matrix is also included.

Using the equations 3 to 6 and the tabulated values for oxy and deoxy-hemoglobin extinction coefficients[14], the effective penetration depth, concentrations of oxy and deoxy-hemoglobin, percent oxygenation, and percent vascularization of ligament tissue can be determined for pregnant and non-pregnant rabbits.

## 2. MATERIALS AND METHODS

Experiments were performed on 6 female, skeletally immature New Zealand white rabbits (3.8-5.4 kg) of which 3 were primagravid (day 29 of pregnancy) and 3 were virgin controls. Surgical procedures consisted of premedicating the animals with a 0.18-ml i.v. dose of acepromazine maleate and anaesthetizing with urethane (1g/kg i.p.). To prepare the animal for LDI scans and diffuse reflectance measurement skin and soft tissue surrounding the left and right joint capsule were dissected to expose both medial collateral ligaments. The remaining background of the preparation was masked with black velvet cloth, ensuring a zero background at the anatomic margins of the MCL. LDI scans were performed on the exposed tissue and immediately after scanning diffuse reflectance profile measurements were made. The animal was then sacrificed and a final LDI scan was taken post mortem for a "biological zero" perfusion measurement.

A commercial LDI[2] with a HeNe laser source of 633nm and 2mW nominal power and a laser diode source of 830 nm and 1 mW nominal power was used. The LDI scanner head contains the lasers and necessary optics for directing a collimated laser beam towards the tissue surface and collecting the returning light. For these experiments a laser Doppler sampling time of 10 ms was used resulting in a bandwidth with lower and upper cutoff frequencies of 100Hz and 15 kHz, respectively. The instrument measures total reflected light intensity and Doppler-shifted reflected light (raw flux). Total light intensity values were used to normalize the raw flux signals. LDI perfusion maps were analyzed using MLDIV2[3] software. A schematic of the commercial LDI and an example of its operation are given in figure 3.

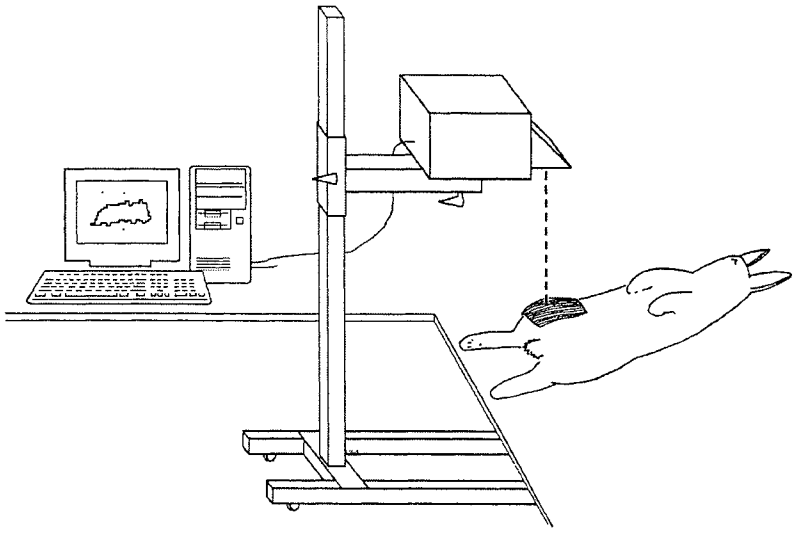

Figure 3: Schematic of the LDI instrument and the surgical technique for measuring tissue perfusion in the rabbit ligament.

The diffuse reflectance instrumentation used 633 and 780 nm wavelength lasers with output power of 5.5 and 2.2 mW, respectively. Tissue illumination and light collection was achieved using two fiber optic probes with 600 μm hard-core silica fibers of 0.39 NA, transmitting in the UV to NIR spectrum. Positioning of the probes on the tissue surface was achieved using an armature system capable of translational and rotational motion. During the measurement the location of the source fiber was held constant and positioned normal to the tissue surface. A radial profile of diffuse reflectance was produced by translating the position of the collection fiber across the tissue surface while making light intensity measurements at several specified locations using a Melles Griote 13 PDC 001 Universal Power Meter with silicon photodiode directly coupled to the detection fiber.

The diffuse reflectance profiles were converted to tissue optical coefficients using a C program designed to fit the diffusion dipole algorithm (equation 7) to the measured data points using a least squared procedure. Program output produced the effective penetration depths as well as the absorption and reduced scattering coefficients. The sum of the squares of the difference between the logarithm of the measured data and the modeled data ($\Sigma$) was also produced to estimate the confidence level of the in-vivo measurement. Using the absorption coefficients another program was used to determine the oxy and deoxy-hemoglobin concentrations, oxygenation level, and percent vascularization of tissue volume.

The mean values for the optical and physiological properties for the pregnant and non-pregnant animal groups were determined. Both groups were compared for statistical differences using an unpaired Student's t-test.

[2] Moor Instruments Ltd., Devon, England, U.K.
[3] Moor instruments Ltd., Devon, England, U.K.

## 3. RESULTS

Some medial collateral ligaments contain large lateral blood vessels overlying the ligament structure. These show up as heterogeneous structures within the LDI images or as "bumps" in the diffuse reflectance profiles. Although these vessels interfered with the measurement it was necessary to leave them intact because they fed the smaller vascular network of the ligament. The presence and location of these vessels varied between animals and was a biological variance that could not be controlled. However, by averaging LDI perfusion images and carefully choosing an appropriate location for the diffuse reflectance measurement these effects were minimized. For these reasons the sum of the squares value was used to determine the confidence of the measurement. Figure 4 shows a diffuse reflectance profile measured for one of the rabbit ligaments using the 633-nm wavelength source. The matched curve from diffusion theory is also shown. For this particular measurement a reasonably good fit was obtained ($\Sigma$ = .04) generating a reduced scattering coefficient of 0.92 $mm^{-1}$ and an absorption coefficient of 0.015 $mm^{-1}$.

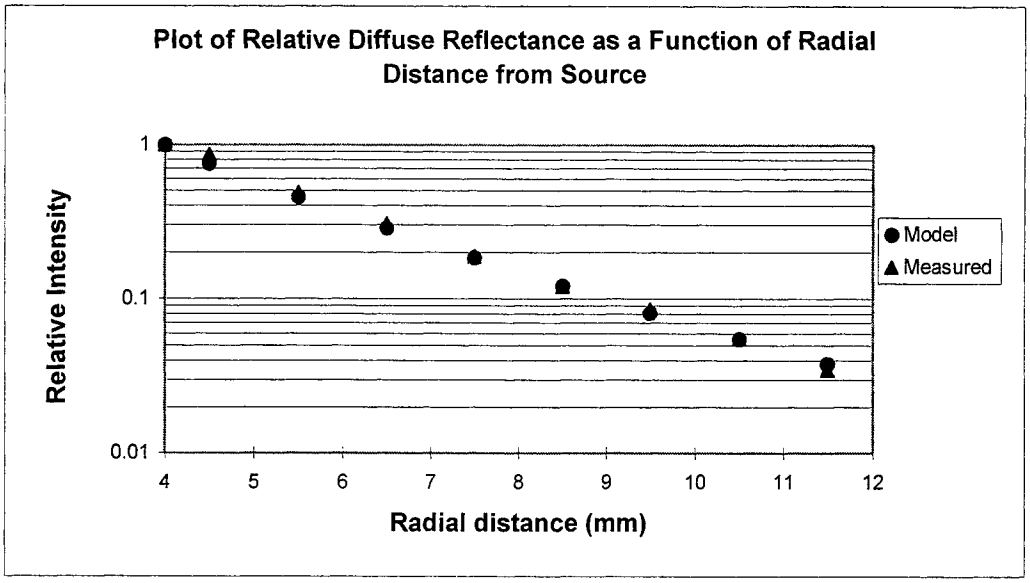


Figure 4: Measured diffuse reflectance profile of a medial collateral ligament at 633 nm over a distance range of 4 - 11.5 mm (triangle). The matched curve from diffusion theory with $\mu_s' = 0.92$ $mm^{-1}$ and $\mu_a = 0.015$ $mm^{-1}$ is also shown (circles).

The mean values for the optical properties at 633 and 780 nm wavelengths for pregnant and non-pregnant rabbit ligaments are given in table 1. The average $\Sigma$ values from the least-squares method are also included. A non-paired student's t-test was used to test for significant differences between the pregnant (n=5) and non-pregnant (n=4) rabbit groups. A significant difference between the reduced scattering coefficients at 633 nm (P = 0.02) and 780 nm (P = 0.03) was observed.

The mean values of the optically determined physiological parameters for both pregnant and non-pregnant rabbit groups are given in table 2. These parameters include the hemoglobin concentrations and percent oxygenation, as well as percent vascularization of tissue volume. Live and post mortem LDI perfusion values measured at 633-nm wavelength and averaged over the entire ligament are also included. Only the live perfusion values showed a significant difference between the pregnant (n= 5) and non-pregnant groups (n= 4) for (P< 0.01).

Table 1: Table of pregnant and non-pregnant ligament tissue optical coefficients at 633 and 780 nm wavelengths.

| | λ = 633 nm | | λ = 780 nm | |
|---|---|---|---|---|
| | Pregnant | Non-Pregnant | Pregnant | Non-Pregnant |
| $\mu_a$ ($mm^{-1}$) | .013 (±.006) | .012 (± .008) | .007 (± .003) | .008 (±.002) |
| $\mu'_s$ ($mm^{-1}$) | .896* (± .050) | .812* (± .016) | .858** (± .043) | .785** (± .038) |
| $\delta_{eff}$ (mm) | 5.66 (± 1.65) | 6.66 (± 2.38) | 7.99 (± 2.07) | 7.27 (± 0.83) |
| $\Sigma$ | .153 (± .142) | .124 (± .083) | .061 (± .036) | .072 (± .029) |

$\mu_a$ absorption coefficient
$\mu'_s$ reduced scattering coefficient
$\delta_{eff}$ effective penetration depth
$\Sigma$ sum of the squares of the difference between the logarithm of the measured and modeled data points.
* statistically significant (P = .02)
** statistically significant (P = .03)

Table 2: Table of optically determined physiological properties of ligament tissue for pregnant and non-pregnant rabbits.

| | Pregnant | Non-Pregnant |
|---|---|---|
| Tissue Perfusion (P.I.) (live) | 222.9* (± 35.9) | 416.3* (± 39.6) |
| Tissue Perfusion (P.I.) (dead) | 19.4 (± 3.8) | 27.3 (± 7.9) |
| $[H_b]$ (mM) | .007 (± .007) | .009 (± .008) |
| $[H_bO_2]$ (mM) | .038 (± .019) | .040 (± .015) |
| Percent Oxygenation | 81.6 (±21.1) | 82.1 (± 17.7) |
| Percent Vascularization | 1.94 (±.70) | 2.09 (± .60) |

P.I. average perfusion index
$[H_b]$ deoxyhemoglobin concentration
$[H_bO_2]$ oxyhemoglobin concentration
mM milli-Molars
* statistically significant (P < .01 )

## 4. DISCUSSION AND CONCLUSIONS

The DRS measurements in this study used radiance profiles along the longitudinal axis of the MCL, where relatively large effective penetration depths at both wavelengths were measured. This is because ligament tissue is a highly organized structure with a preferred direction for collagen orientation along its longitudinal axis. This anisotropic structuring produces a larger scattering component in the transverse directions leading to a "light-guide" effect along the direction of collagen alignment. We believe this "light-guide" effect is a realization of the same physical process behind a similar optical technique used for measuring tissue collagen architecture called small angle light scattering (SALS), where the ordered alignment of collagen fibers produces asymmetrical diffraction patterns in transmitted, collimated laser light[15]. This observation has provided valuable information for interpreting future LDI measurements made in ligament tissue, where the anisotropic scattering and large longitudinal penetration demonstrates how optical properties influence the shape and resolution of the perfusion measurement.

One of the benefits of tissue spectroscopy over conventional absorption spectroscopy is that it also provides information on tissue scattering properties. The statistical difference observed between the scattering coefficients for pregnant and non-pregnant ligament suggests that some type of tissue restructuring occurs during pregnancy. Much of the scattering within a tissue occurs at the boundaries between tissue components with different indices of refraction. These boundaries are typically the aqueous-lipid membranes surrounding and within each cell, or at the boundaries between collagen fibrils and the extracellular-matrix. A change in water content and distribution can alter the separation between tissue components and change the scattering effects at boundaries between different tissue types and components. However, a separate biochemical investigation within this model has indicated that tissue water content does not change during pregnancy (unpublished data within our group). Another explanation for the measured difference between pregnant and non-pregnant groups is that the collagen structure itself has changed. Collagen in its relaxed state has a "wavy" pattern that straightens under tissue loading. Using biomechanical testing an increased laxity has been observed in the MCLs of pregnant rabbits compared to age-matched control animals[16,17]. However, high load behavior of the tissue was unaffected. An increased tissue laxity would suggest a more

pronounced collagen wave structure, which could influence photon scattering events. In light of no detectable change in water content of ligaments from pregnant animals, as well as no changes in high load (collagen-dependent) behavior of the tissues, the change in laxity and collagen organization could be the result of water and proteoglycan distribution in the tissue.

The results from this study suggest that DRS could provide a method for measuring tissue structure and a technique for monitoring the tissue restructuring associated with disease and injury. Where collagen architecture correlates with a tissue's biomechanical properties, this technique could also lead to a minimally invasive method for measuring some of the biomechanical properties of tissue.

LDI measured a decrease in the average tissue perfusion in the ligaments of pregnant animals compared to age-matched non-pregnant animals. Although tissue perfusion is related to both the velocities of the moving red blood cells as well as their concentrations, one might suspect that a decrease in tissue perfusion would be supported by an observed decrease in percent vascularization. But the spectroscopic information obtained from the DRS measurements revealed no significant difference between pregnant and non-pregnant animal groups.

Until we are able to refine our DRS technique to account for the anisotropic and heterogeneous structure of this tissue we are very cautious in interpreting the spectroscopic information we obtained from these investigations. For example, while calculating hemoglobin concentration, two of the nine data points had to be removed because they produced a negative value. These data points had unusually high $\Sigma$ values and we believe this effect was caused by the heterogeneous vascular structures within the tissue. To use tissue spectroscopy as an effective method for comparing physiological differences between animal groups the technique will most likely require an averaging procedure similar to that used in LDI, where several measurements must be made across a tissue surface. Nevertheless, of the remaining seven data points the values for percent oxygenation of hemoglobin are within expected physiological parameters and the percent vascularizations are comparable to percent vascularizations calculated using India ink and carmine red injection techniques[18, 19]. These results are encouraging because dye injection techniques for measuring percent vascularization are terminally invasive, in-vitro procedures.

The results from this study suggest that spatially resolved diffuse reflectance provides supplementary information to an LDI measurement of tissue perfusion. Using DRS with wavelengths identical to those used in LDI produces an immediate determination of laser penetration depths that can be used to estimate the regions of microcirculation sampled by a multiple wavelength LDI measurement. Also, spectroscopic analysis of a DRS measurement provides additional metabolic information, such as oxy and deoxy-hemoglobin concentrations, tissue oxygenation and percent vascularization. A technique combining DRS with LDI for the continuous monitoring of tissue perfusion and metabolic state would have significant clinical impact in the study of tissue disease and injury.

## ACKNOWLEDGEMENTS

This work was funded through grants obtained from the Medical Research Council of Canada (MRC), the Alberta Heritage Foundation for Medical Research (AHFMR), the Whitaker Foundation, and University Technologies International Inc. (UTI). Special thanks to Pat Irwin for helpful discussions and to Jason McDougall for assisting in the surgeries. I would also like to acknowledge the Oregon Medical Laser Center for its resourceful web-site (http://omlc.ogi.edu/).

## REFERENCES

1. R. C. Bray, "Blood supply of ligaments: A brief overview", *Int. Orthop.* **3,** pp. 39-48, 1995.
2. D. Watkins, and G. A. Holloway, "An instrument to measure cutaneous blood flow using the Doppler shift of laser light", *IEEE Trans. Biomed. Eng.* **25,** pp. 28-33, 1978.
3. G. E. Nilsson, T. Tenland, and P. A. Oberg, "A new instrument for continuous measurement of tissue blood flow by light beating spectroscopy", *IEEE Trans. Biomed. Eng.* **27,** pp. 597-604, 1980.
4. G. E. Nilsson, "Signal processor for laser Doppler flowmeters". *Medical and Biological Engineering and Computing.* **22,** pp. 343-348, 1984.

5 A. P. Shepherd, G. L. Riedel, J. W. Kiel, D. J. Haumschild, and L. C. Maxwell, "Evaluation of an infrared laser Doppler flowmeter", *Am. J. Physiol.* **252,** pp. G832-G839, 1987.

6. T. J. H. Essex, and P. O. Byrne, "A laser Doppler scanner for imaging blood flow in skin", *J. Biomed. Eng.* **14,** pp. 189-194, 1991.

7. K. Wardell, A. Jakobsson, and G. E. Nilsson, "Laser Doppler perfusion imaging by dynamic light scattering", *IEEE Trans. Biomed. Eng.* **40,** pp. 309-316, 1993.

8. R. F. Bonner, R. Nossal, S. Havlin, and G. H. Weiss, "Model for photon migration in turbid media", *J. Opt. Soc. Am.* **4, No. 3,** pp. 423-432, 1987.

9. K. Forrester, M. Doschak, and R. C. Bray, "In-vivo comparison of scanning technique and wavelength in laser Doppler perfusion imaging: Measurement in knee ligaments of adult rabbits", *Medical and Biological Engineering and Computing.* **35,** pp. 581-586, 1997.

10. R. Bray, K. Forrester, J. McDougall, A. Damji, and W. R. Ferrell, "Evaluation of laser Doppler imaging to measure blood flow in knee ligaments of adult rabbits", *Medical and Biological Engineering and Computing.* **34,** pp. 227-231, 1996.

11 A. J. Welch, and M. J. C. van Gemert, *Optical-thermal response of laser irradiated tissue,* Plenum Press, New York, 1995.

12. T. J. Farrell, M. S. Patterson, and B. Wilson, "A diffusion theory model of spatially resolved, steady-state diffuse reflectance for the noninvasive determination of tissue optical properties in-vivo", *Medical Physics.* ***19,*** **No. 4,** pp. 879-888, 1992.

13. P. R. Bevington, *Data reduction and error analysis for the physical sciences,* McGraw-Hill, New York, 1969

14. S. Prahl, *Tabulated molar extinction coefficient for hemoglobin in water,* (http://omlc.ogci.edu/), Oregon Medical Laser Center.

15. M. S. Sacks, and C. J. Chuong, "Characterization of collagen fiber architecture in the canine diaphragmatic central tendon", *J. of Biomech. Eng.* **114,** pp. 183-190, 1992.

16. C. B. Frank, D. A. Hart, and N. G. Shrive. "Molecular biology and biomechanics of normal and healing ligaments" (Invited Review). *Osteoarthritis and Cartilage (Special Issue edited by V. Mow and S. L-Y. Woo), Osteoarthritis and Cartilage.* 7, pp. 130-140, 1999.

17. D. A. Hart, C. Reno, C. B. Frank and N. G. Shrive. "Pregnancy affects cellular activity, but not tissue mechanical properties, in the healing rabbit MCL", *J. Orthop. Res.* In press, 1999.

18. K. Eng, R. M. Rangayyan, R. C. Bray, C. B. Frank, L. Anscomb, and P. Veale, "Quantitative analysis of the fine vascular anatomy of articular ligaments", *IEEE Trans. Biomed. Eng.* **39, No. 3,** pp. 296-306, 1992

19. J. J. McDougall, and R. C. Bray, "Vascular volume determination of articular tissues in normal and anterior cruciate ligament-deficient rabbit knees", *The Anatomical Record,* **251**, pp. 207-213, 1998.

# Spatially resolved diffuse reflectance for the determination of tissue optical properties and metabolic state.

Kevin R. Forrester[1a], Roxane Shymkiw[a], Grace Yeung[a], Pat Irwin[a], John Tulip[b], and Robert Bray[a]

[a]University of Calgary, Calgary, Alberta, Canada T2N-4N1

[b]University of Alberta, Edmonton, Alberta, Canada, T6G- 2M7

## ABSTRACT

**A multiple wavelength diffuse reflectance instrument was evaluated for the in-situ measurement of tissue optical properties. A diffusion dipole model with a non-linear least-squares fitting procedure was used to generate optical properties from the radial profiles of diffuse reflectance measurements. The diffusion model was compared with Monte Carlo simulations showing acceptable agreement for a range of distances far enough away from the source point. Instrumentation was evaluated by experimental measurement of tissue simulating phantoms where measured optical properties were compared to those obtained using a collimated transmission setup. The results showed agreement to within 5-10%. The optical properties of rabbit ligament and tendon are reported where anisotropic scattering due to collagen alignment was observed. This study represents the first known measurement of rabbit ligament and tendon optical properties and the use of diffuse reflectance to measure the "lightguide" effects of collagen alignment.**

**To evaluate instrument response to changes in tissue oxygenation levels the optical properties of human skin were measured before and during arterial occlusion. During arterial occlusion absorption at 633 nm increased while absorption at 810 nm remained relatively constant. These results are consistent with the deoxygenation of hemoglobin that occurs during occlusion.**

**Keywords:** diffuse reflectance spectroscopy, Monte Carlo, collagen, light guide, metabolic state

## 1. INTRODUCTION

The study of light propagation and distribution in tissue is necessary for the effective application of optical diagnostic and therapeutic techniques. For example, when laser Doppler techniques are used for measuring tissue blood perfusion an uncertainty in the photon sampling depth leads to ambiguous interpretations in the fraction of microcirculation that contributes to the Doppler signal[1, 2].

It has been suggested that the wavelength dependence of photon penetration depths can be used in multiple wavelength laser Doppler techniques for a discriminative measurement of tissue microcirculation[1, 3]. However, for an effective application of this technique a better understanding of the propagation and distribution of light in tissue during a laser Doppler measurement is required.

[1] Direct correspondence to Kevin Forrester. Email: kforrest@ucalgary.ca; telephone: (403) 220 7866; fax: (403) 270 0617

In *Laser-Tissue Interaction XI: Photochemical, Photothermal, and Photomechanical*, Donald D. Duncan, Jeffrey O. Hollinger, Steven L. Jacques, Editors, Proceedings of SPIE Vol. 3914 (2000)
1605-7422/00/$15.00

This study investigates a minimally invasive optical diagnostic technique that measures tissue optical properties from the same diffusely reflected laser light used in a multiple-wavelength Doppler measurement. Spatially resolved diffuse reflectance (DR) instrumentation is developed along with Monte Carlo and tissue phantom techniques for instrument evaluation and calibration.

One of the significant advantages with using a multiple wavelength diffuse reflectance technique is the potential for measuring tissue structure and metabolic state[4]. The DR instrument is evaluated for its ability to measure tissue structure in in-vitro articular tissues, while its potential for monitoring metabolic change is investigated by measuring changes in hemoglobin oxygenation during arterial occlusion in in-vivo skin tissue. The purpose of these investigations is to develop a technique to supplement multiple wavelength laser Doppler measurement of tissue perfusion with a simultaneous measurement of tissue optical properties and metabolic state.

### 1.1 Optical Properties of Tissue

Light-tissue interactions with absorbing molecules (chromophores) and scattering components produce the spectral characteristics observed in a diffuse reflectance measurement, where each tissue contains its own specific composition of chromophores that in turn can vary with metabolic changes. Some of the more prominent chromophores are hemoglobin and myoglobin, where a tissue's absorption can depend strongly on its blood content and oxygenation status.

Although absorption provides the unique spectral characteristics of tissue, scattering strongly influences light propagation and remission. This is an essential point in tissue spectroscopy, distinguishing it from simple absorption spectroscopy. Scattering usually depends on tissue structure, where boundaries between mismatching refractive indices of tissue layers and components lead to reflective or refractive scattering of light.

The optical properties of tissue are characterized by the radiative transport equation and are defined quantitatively as the average number of absorption and scattering events occurring per unit path length of photon travel. They are represented as $\mu_a$ and $\mu'_s$, respectively. The parameter, $\mu'_s$, is called the reduced scattering coefficient. It represents isotropic scattering but for visible to NIR wavelengths light scattering in tissue is anisotropic having a strong forward scattering component. As a result, a third parameter, $g$, must be included to represent the true scattering in tissue with respect to the reduced scattering, $\mu'_s = \mu_s (1-g)$, where $g$ is the average cosine of the scattering angle and is usually between 0.9 to 0.97. Two other important optical parameters of tissue are the effective attenuation coefficient[5]

$$\mu_{eff} = \left[3\mu_a\left(\mu_a + \mu_s(1-g)\right)\right]^{1/2}, \tag{1a}$$

and the transport scattering mean free path[4]

$$mfp' = 1/\left(\mu'_s + \mu_a\right). \tag{1b}$$

The inverse of the effective attenuation coefficient gives the effective penetration depth and is defined as the distance at which light fluence from a point source is decremented by 37 percent. (This is the optical parameter that has particular significance in interpreting laser Doppler measurements.)

### 1.2 Models for photon transport

Unlike absorption spectroscopy, where a direct derivation of the attenuation coefficient is possible from a transmission measurement and Beer's law, the challenge with tissue diagnostic techniques are that an indirect, iterative method must be used to generate the optical properties. To do this numerical techniques or analytical models that accurately characterize the photon source while satisfying appropriate tissue boundary conditions are used. Several iterations of optical properties are modeled and compared to the measured data using a non-linear least-squares testing procedure. Using this technique the best estimate of the absorption and reduced scattering coefficient are generated.

The Monte Carlo method is a numerical technique simulating the "random walk" of photons in a medium that contains absorption and scattering potentials[6]. This method can simulate various light source/detector configurations for finite tissue geometries. It is a flexible yet rigorous application of the radiative transport equation and provides a very descriptive approach but is statistical in nature, requiring a large number of photons and a significant amount of computer processing time. As a result, it is ineffective for optical diagnostic measurements that require the real-time generation of biological parameters but provides a useful tool for training neural networks or testing the analytical models that can generate optical parameters in real time[7, 8].

Most tissue spectroscopy instruments use a diffusion model to produce tissue optical properties[9]. Although these models are based on approximations to the radiative transport equation, they are used in diagnostic instrumentation because they can generate optical coefficients in the relatively short interval of time necessary for clinical applications.

To measure tissue optical properties we have adopted a diffusion model and diffuse reflectance method originally developed by Farrell and co-workers[4]. However, the instrumentation used for this study differs from the original method by using multiple wavelength laser sources rather than a monochromator/white light source and is capable of using a remote detection method as well as the contact fiber optic method used by Farrell and co-workers.

The diffusion model generates an analytical expression for the diffuse reflectance as a function of radial distance ($\rho$) between the source point and an arbitrary point located on the tissue surface

$$R(\rho, z_0) = \frac{a'}{4\pi}\left[ z_0\left(\mu_{eff} + \frac{1}{r_1}\right)\frac{e^{-\mu_{eff} r_1}}{r_1^2} + \left(z_0 + 2z_b\right)\left(\mu_{eff} + \frac{1}{r_2}\right)\frac{e^{-\mu_{eff} r_2}}{r_2^2}\right], \tag{2}$$

where

$$r_1 = \left[\left(z - z_0\right)^2 + \rho^2\right]^{1/2}, \tag{3}$$

$$r_2 = \left[\left(z + z_0 + 2z_b\right)^2 + \rho^2\right]^{1/2}, \tag{4}$$

and

$$a' = \mu_s' / \left(\mu_a + \mu_s'\right) \tag{5}$$

The x and y coordinates define the plane of a flat tissue surface located at z = 0 with z positive downward (see figure 2). The model approximates the light source using a single point located a distance $z_0$ = 1 mfp′ below the tissue surface. The position $z_b$ is an extrapolated boundary located along the z-axis where the fluence is forced to zero. It is related to the tissue's diffusion coefficient and internal reflection parameter (see Farrell and co-workers for more information[4]).

## 2. MATERIALS AND METHODS

### 2.1 Collimated transmission measurements

The diffuse reflectance instrumentation was tested on three different mixtures of tissue simulating phantoms. The absorption and scattering components used in these phantoms were calibrated using a collimated transmission apparatus.

The collimated transmission setup was based on the optical arrangement for a normal absorption spectrophotometer. The setup consisted of a 1.22 cm thick cuvette containing samples of varying concentrations of absorbers/scatterers in solution. Collimated laser-light, at various wavelengths, was transmitted through the center of the cuvette. The transmitted light was then passed through a pinhole aperture to eliminate scattered photons from being detected. The spatially filtered light was then detected using an integrating sphere and photodiode (see figure 1). Intensity measurements were normalized for each wavelength to light transmission through a reference sample of distilled water.

For measurements of collimated, unscattered light the attenuation coefficient can be calculated from Beer's law:

$$\mu_t = -\frac{1}{t}\ln\left(\frac{T_c}{T_0}\right) = e|C|, \qquad (6)$$

where $e$ is the extinction coefficient ($mm^{-1}$/(one percent concentration)). $T_c$ and $T_0$ are the collimated transmission intensities measured on the sample of concentration |C| and the reference sample, respectively.

By measuring the collimated transmission on samples of increasing concentration and using equation 6 to plot the results the attenuation coefficient for 1 mm of travel through a solution containing a one percent concentration of absorber or scatterer can be determined from the slope[10, 11].

In this study methylene blue[2], India ink[3], and intralipid[4] were calibrated. The methylene blue was in powder form and the concentrations used in the transmission measurements are based on a solution of 0.3 g of methylene blue dissolved in 300 ml of distilled water.

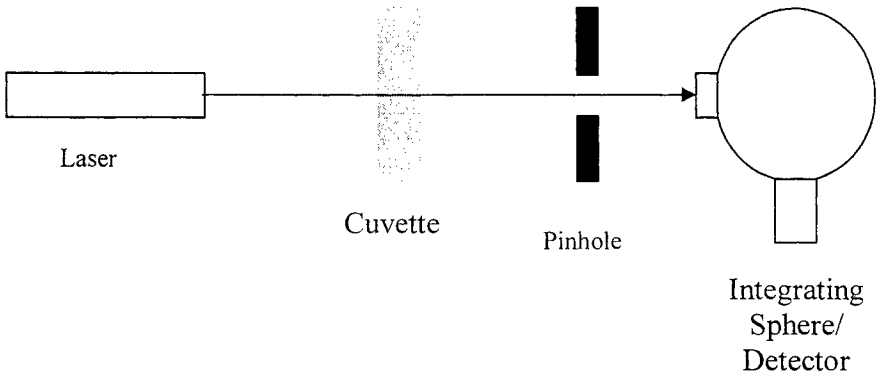


Figure 1: Experimental setup for absorption spectrophotometer. Cuvette thickness is 1.22 cm. Pinhole diameter is 1.1 mm. Detector is an integrating sphere and photodiode.

**2.2 Diffuse reflectance instrumentation**

The diffuse reflectance instrument uses a fiber optic probe attached to an armature positioning system to transmit light directly to the tissue surface. Multiple laser sources are coupled to the fiber optics to achieve several wavelength measurements (543, 633, 780, 810 nm). The instrumentation can be adapted to use a remote or contact system for spatially resolving and collecting diffusely reflected light exiting the tissue surface. The contact system uses another fiber optic probe with light output directly coupled to a silicon photodiode. Light intensity is measured using a Melles Griote 13 PDC 001 Universal Power Meter. The fiber optics used for both source and detection probes are 600μm hard core silica fibers of 0.39 NA transmitting in the UV to NIR spectrum. One-dimensional profiles of the diffuse reflectance are produced using a translational stage built into the armature system of the detection probe. Several light intensity measurements are made at specific points of distance between the source and collection fibers (see figure 2).

The remote operation for the diffuse reflectance instrumentation is achieved by using a CCD camera and frame grabber card. Diffuse reflectance exiting the tissue is spatially resolved using a TV lens (see figure 2). To prevent CCD saturation while ensuring sufficient signal to noise ratios, light levels are controlled using a variable aperture and exposure setting. Multiple frames are captured and averaged to improve the signal to

[2] 90% dye content; Fischer Scientific Company, Fair Lawn, New Jersey
[3] 100% carbon, black pigment – no dyes; Hunt Manufacturing Company, Statesville, N.C.
[4] 10 % stock solution; Pharmacia Inc., Mississuaga Ontario

noise ratio. Diffuse reflectance profiles are generated from the averaged image using a "line profile" image analysis procedure.

The diffuse reflectance profiles were converted to tissue optical coefficients using a C program designed to fit the diffusion dipole algorithm (equation 2) to the measured data points using a least squared procedure[12]. Program output produced the effective penetration depths as well as the absorption and reduced scattering coefficients. The root mean square of the difference between the logarithm of the measured data and the modeled data ($\sigma$) was also produced to estimate the confidence level of the in-vivo measurement.

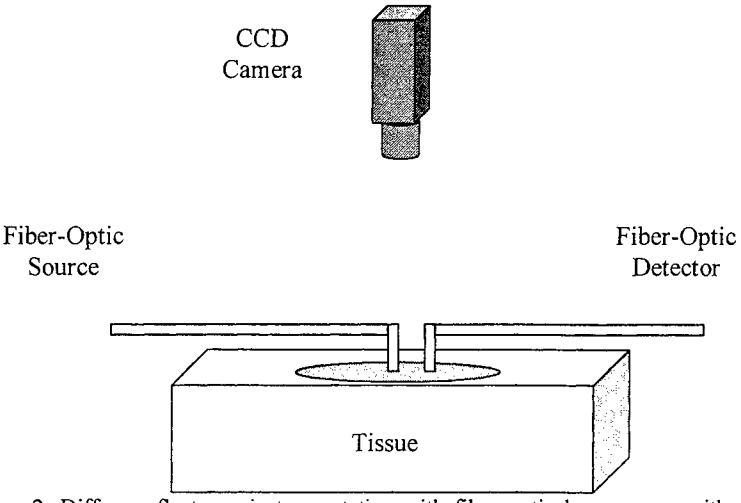


Figure 2: Diffuse reflectance instrumentation with fiber optic laser source with optional remote detection technique (CCD camera) or contact probe (fiber optic detector).

### 2.3 Monte Carlo model

A Monte Carlo model was used to evaluate the performance of the diffusion model algorithm. The Monte Carlo program is based on a previously written code designed for modeling multi-layered tissues[6]. A semi-infinite tissue was modeled with a surface boundary between air and tissue. Photons were launched into the tissue from an infinitesimal source point located immediately above the surface. The optical coefficients generated by the diffusion algorithm were compared to the Monte Carlo optical input parameters using several ranges for the radial distance, $\rho$. The $\sigma$ value and the differences between the optical parameters were used to determine the range of radial distances where the diffusion model gives acceptable results.

### 2.4 Tissue phantom measurements

Three tissue phantoms were mixed for diffuse reflectance measurements. Phantom 1 consisted of a 2% dilution of the 10% intralipid solution in distilled water. Phantoms 2 and 3 contained the same mixture of intralipid with a 0.2 and 0.4 concentration of methylene blue, respectively. The total volume for each tissue phantom mixture was 500 ml. To simulate a semi-infinite tissue, each phantom was placed in an open flat black container to minimize surface reflection. The contact diffuse reflectance method was used where the probes were positioned directly above the phantom surface (see figure 2). Diffuse reflectance profiles were measured by holding the source fibre stationary and adjusting the distance between the source and collection probe from 4 - 15.5 mm.

Intralipid was used as a scattering component, where its contribution to absorption was assumed to be negligible. Methylene blue was considered a perfect absorber for 543 and 633 nm wavelengths but results from the collimated transmission experiments demonstrated it to have a poor absorption at NIR wavelengths. Although India ink was found to be a strong absorber for the entire range of wavelengths used in this study it has a scattering component that isn't entirely negligible[13]. Consideration for this component complicates

phantom mixing. Therefore, India ink and the NIR wavelengths (780 and 810 nm) were omitted from diffuse reflectance measurements of tissue phantoms.

The optical coefficients derived from the diffuse reflectance measurement were compared to the "optical" concentrations of intralipid and methylene blue within the phantom mixtures. The diffusion model used a scattering parameter of g= 0.8 and g = 0.85 for the 543 and 633 nm wavelengths[14], respectively, and an index of refraction equivalent to water, n = 1.33.

To evaluate the remote detection technique reflectance measurements using the CCD camera were compared with the contact fiber optic probe. Measurements were performed on a tissue phantom with the same mixture as phantom 1. However, these experiments used another batch of intralipid that was not calibrated with the collimated transmission setup.

### 2.5 In-vitro measurements

In-vitro diffuse reflectance measurements were performed on fresh articular tissues of an adult female New Zealand White rabbit using the 543, 633, and 810 nm wavelengths. Immediately after sacrifice, the left and right medial collateral ligaments (MCL) and patellar tendons (PT) were excised and placed horizontally on a black background with the surface of the tissue facing upward. Saline was applied at regular intervals to prevent tissue dehydration. The contact fiber optic probe was used where source and collection fibres were placed directly above and normal to the tissue surface. Diffuse reflectance profiles where made along the longitudinal axis of the ligament. To investigate anisotropic scattering behavior in articular tissue, both lateral and longitudinal measurements were made on the patellar tendon.

### 2.6 In-vivo measurements

In-vivo measurements were performed on the skin of a human forearm at 633 and 810 nm wavelengths before and during occlusion of the brachial artery. For these measurements the source fiber optic probe was positioned directly above and normal to the surface of the skin and the remote CCD camera detection system was used.

## 3. RESULTS

### 3.1 Monte Carlo model

The Monte Carlo simulation used a scattering coefficient of 10.0 $mm^{-1}$, an absorption coefficient of 0.01 $mm^{-1}$, an index of refraction of n = 1.4, and a scattering phase function of g = 0.9. The diffusion algorithm was tested for a range of distances in the radial profiles of the Monte Carlo output. Intensities were normalized at the initial point in the range of distances. The results are given in table 1 where the percent difference between the optical coefficients generated by the diffusion model and the "true" Monte Carlo optical coefficients are given in parenthesis. To represent the "goodness" of the fit the table also includes the $\sigma$ values. The Monte Carlo diffuse reflectance profile with matched diffusion model for the profile range of 4 – 19.6 mm is shown in figure 3.

Table 1: Table of optical properties generated by the diffusion model for Monte Carlo diffuse reflectance profiles produced using $\mu_a$= 0.01 $mm^{-1}$, $\mu_s$ = 10.0 $mm^{-1}$, $g$ = 0.9, and n = 1.4 as input optical parameters.

| **Profile range (mm)** | **2 – 19.6** | **3 – 19.6** | **4 – 19.6** |
|---|---|---|---|
| $\mu_s$ **($mm^{-1}$)** | 9.90 (1)* | 10.91 (9.1)* | 11.00 (10)* |
| $\mu_a$ **($mm^{-1}$)** | 0.009 (10)* | 0.0089 (11)* | 0.0089 (11)* |
| $\sigma$ | 0.076 | 0.032 | 0.026 |

$\sigma$ root mean square of the difference between the logarithm of the measured and modeled data points

* percent differences between the diffusion model and Monte Carlo optical coefficients are included in parenthesis.

The results from the Monte Carlo comparison demonstrates that the optical coefficients generated by the diffusion algorithm are only accurate to within 10 percent of the "true" values. Although the $\sigma$ value improves as the initial point in the radial profile is moved further away from the source point, the accuracy of the model does not change. The higher accuracy in the model for the 2-19.6 mm range is a random artifact caused by normalizing the reflectance profiles at a distance too close to the source where the diffusion model begins to deviate significantly from the Monte Carlo profile. This is confirmed by the poor $\sigma$ value for this range.

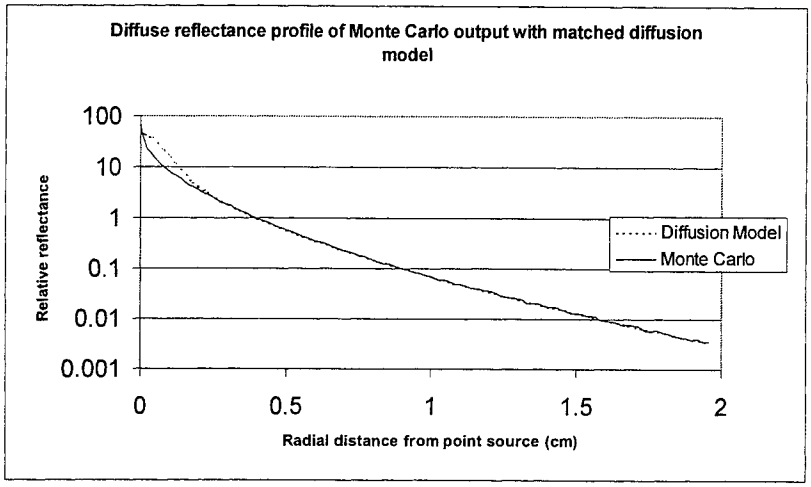


Figure 3: Diffuse reflectance profile for Monte Carlo output and matched diffusion model normalized to unity at $\rho$ = 4 mm. The Monte Carlo model used a scattering coefficient of 10.0 $mm^{-1}$, an absorption coefficient of 0.01 $mm^{-1}$, an index of refraction of n = 1.4, and a scattering phase function of g = 0.9.

### 3.2 Collimated transmission measurements

The results for the attenuation coefficients determined for 1 percent concentrations of phantom components of methylene blue, intralipid, and India ink at 543, 633, 780, and 810 nm are given in table 2. The attenuation coefficients for methylene blue at the 780 and 810 nm wavelengths were omitted because of its poor ability to absorb at these wavelengths.

Table 2: Table of attenuation coefficients, $\mu_t$ ($mm^{-1}$) for tissue phantom components in 1 percent solutions.

| Wavelength(nm) | Intralipid | Methylene Blue | India Ink |
|---|---|---|---|
| 543 | 0.494 | 0.0476 | 0.0241 |
| 633 | 0.357 | 0.2049 | 0.0217 |
| 780 | 0.187 | - | 0.0164 |
| 810 | 0.1724 | - | 0.0148 |

### 3.3 Tissue phantom measurements

The measured diffuse reflectance profiles for the three tissue phantoms at 633 nm with matched diffusion model are given in figure 4. Diffusion model output and diffusion measurements were scaled to unity at $\rho$ = 4 mm. The absorption and scattering parameters generated by the model are given in table 3 and are compared with calculated optical coefficients using the phantom component concentrations and the extinction coefficients obtained from the transmission measurements (table 2). The results show very close agreement between transmission and diffuse reflectance measurement techniques for both red and green wavelengths (5 – 10 percent).

The diffuse reflectance profiles of a 2 % intralipid tissue phantom using the CCD camera and fiber optic probe detector are presented in figure 5. The profiles are normalized to unity at the 3 mm distance showing a reasonably good overlap in profile intensities for distances greater than 3 mm. The optical properties

generated by the diffusion algorithm for profile ranges from 3 – 15 mm and 4 – 15 mm are given in table 4. Although the tissue phantom used for this comparison contained the same mixture as phantom 1, the discrepancy between the measured scattering coefficients are probably the result of using a different batch of intralipid.

Table 3: Comparison of tissue phantom optical coefficients ($mm^{-1}$) at 543 nm and 633 nm wavelengths derived using the collimated transmission and diffuse reflectance techniques.

| | Phantom 1 | | Phantom 2 | | Phantom 3 | |
|---|---|---|---|---|---|---|
| **633 nm** | $\mu_s$ | $\mu_a$ | $\mu_s$ | $\mu_a$ | $\mu_s$ | $\mu_a$ |
| **Transmission** | 0.72 | 0 | 0.72 | 0.040 | 0.72 | 0.080 |
| **Diffuse Model** | 0.74 | 0 | 0.74 | 0.036 | 0.75 | 0.065 |
| **543 nm** | $\mu_s$ | $\mu_a$ | $\mu_s$ | $\mu_a$ | $\mu_s$ | $\mu_a$ |
| **Transmission** | 0.98 | 0 | 0.98 | 0.009 | 0.98 | 0.019 |
| **Diffuse Model** | 0.97 | 0 | 0.95 | 0.009 | 0.95 | 0.019 |

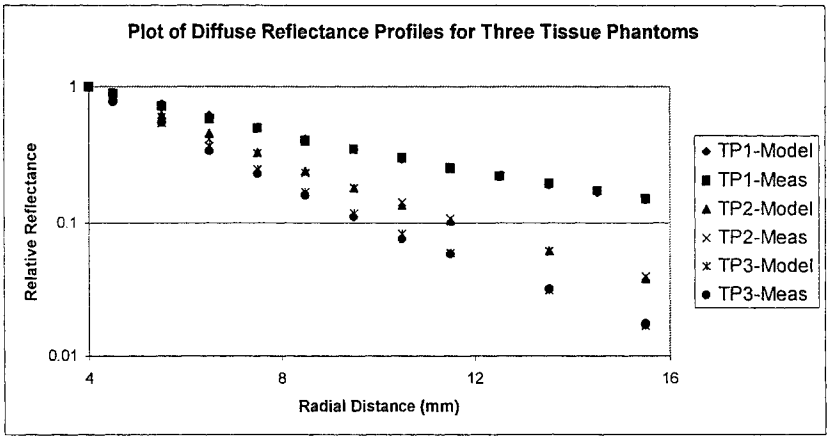


Figure 4: Diffuse reflectance profiles for the three tissue phantoms showing the effects of increasing the concentration of the absorption component (0%, 0.2 %, 0.4 % of methylene blue solution) while maintaining a constant scattering component (2 % solution of 10 % intralipid). Modeled data points are included where g = 0.8 and n = 1.33 is assumed.

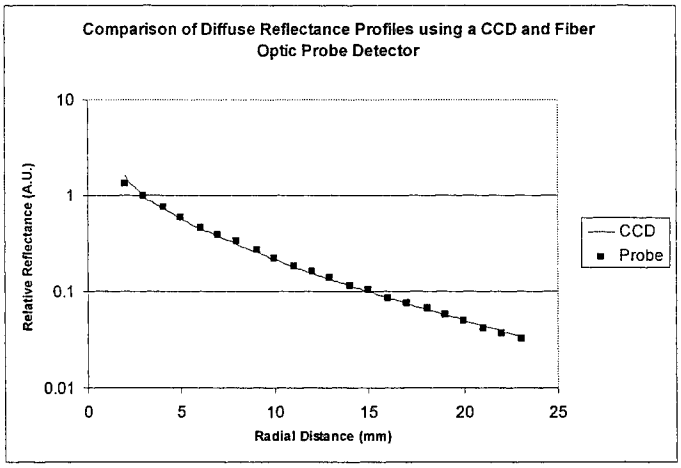


Figure 5: Comparison between diffuse reflectance profiles measured using a CCD and fiber optic probe detector. A tissue phantom containing a 2 % solution of 10 % intralipid was used. Modeled data points are included where g = 0.8 and n = 1.33 is assumed.

Table 4: Comparison between the CCD camera and fiber optic probe detector. Measurements are made on a 2 percent solution of 10 percent intralipid, where a scattering phase function of g=0.8 and an index of refraction of n= 1.33 are assumed. Ranges of 3 – 15 mm and 4 – 15 mm are investigated

| | CCD (3–15 mm) | Probe (3-15mm) | CCD (4-15mm) | Probe (4-15mm) |
|---|---|---|---|---|
| $\mu_s$ (mm$^{-1}$) | 0.92 | 0.89 | 0.84 | 0.80 |
| $\mu_a$ (mm$^{-1}$) | 0 | 0 | 0.002 | 0.008 |

### 3.4 In-vitro measurements

Optical properties along the longitudinal direction in the ligament and along the longitudinal and lateral directions in the tendon are presented in table 5. Lateral measurements at 543 nm were not possible because of the high attenuation of light propagation in this direction. Also, due to the finite lateral dimension of the MCL a reasonable range for the diffuse reflectance profile was not possible and lateral measurements in this tissue were omitted but a similar anisotropic attenuation of light was observed. Negligible absorption coefficients were measured along the longitudinal axis of the patellar tendons for all wavelengths. This produced unrealistically high values for the effective photon penetration depths. It was assumed that this was a breakdown of the diffusion model due to the "light-guiding" properties within the tendon and these values were omitted from the table. The diffuse reflectance profiles for the right MCL are shown in figure 6.

Table 5: Optical coefficients for the left and right medial collateral ligaments (MCL) and patellar tendons (PT). Diffuse reflectance measurements were made along the longitudinal axis of the ligament and along the longitudinal and lateral directions in the patellar tendon. (An index of refraction of n = 1.4 was assumed).

| | | left MCL | right MCL | left PT (long.) | right PT (long.) | left PT (lat.) | right PT (lat.) |
|---|---|---|---|---|---|---|---|
| **543 nm** | | | | | | | |
| | $\mu_s'$ (mm$^{-1}$) | 1.10 | 1.18 | 0.70 | 0.97 | - | - |
| | $\mu_a$ (mm$^{-1}$) | 0.082 | 0.086 | ~ 0.001 | ~ 0.001 | - | - |
| | $\delta_{eff}$ (mm) | 1.85 | 1.75 | - | - | - | - |
| **633 nm** | | | | | | | |
| | $\mu_s'$ (mm$^{-1}$) | 1.00 | 0.86 | 0.25 | 0.27 | 1.53 | 1.56 |
| | $\mu_a$ (mm$^{-1}$) | 0.048 | 0.039 | ~ 0.001 | ~ 0.001 | 0.21 | 0.30 |
| | $\delta_{eff}$ (mm) | 2.57 | 3.08 | - | - | 0.95 | 0.77 |
| **810 nm** | | | | | | | |
| | $\mu_s'$ (mm$^{-1}$) | 0.96 | 0.81 | 0.32 | 0.22 | 1.42 | 1.43 |
| | $\mu_a$ (mm$^{-1}$) | 0.030 | 0.032 | 0.003 | ~ 0.001 | 0.24 | 0.32 |
| | $\delta_{eff}$ (mm) | 3.35 | 3.52 | - | - | 0.86 | 0.77 |

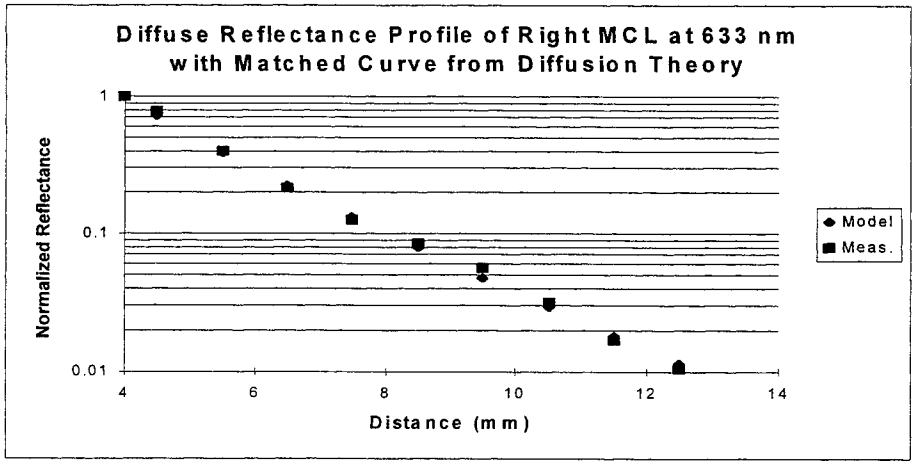


Figure 6: Diffuse reflectance profile of the right medial collateral ligament at 633 nm over a distance range of 4 -12.5 mm. The matched curve from diffusion theory with $\mu_s' = 0.86$ mm$^{-1}$ and $\mu_a = 0.039$ mm$^{-1}$ is also shown.

### 3.5 In-vivo measurements

Diffuse reflectance measurements were performed on human forearm skin at 633 and 810 nm wavelengths before and during occlusion of the brachial artery (figures 7 and 8). The profile for the 633 nm wavelength shows a steeper decline during arterial occlusion. This is due to an increased absorption of the 633 nm photons as hemoglobin becomes deoxygenated. The profile at 810 nm remains relatively constant before and during arterial occlusion. This is because 810 nm is relatively close to an isobestic point in the extinction spectra where oxy- and deoxy- hemoglobin have almost the same extinction coefficient[15].

The optical coefficients generated from the diffusion model are given in table 6 where both wavelengths show a slight decrease in the scattering coefficient during occlusion. It is uncertain whether this is due to a measurement artifact or if physiological processes occurring during occlusion are altering light scattering within the tissue. At 633 nm the absorption coefficient during occlusion is roughly 3 times that before occlusion. At 810 nm the absorption coefficient slightly increased after occlusion but remained relatively constant.

Table 6: Optical coefficients of forearm skin before and during arterial occlusion at 633 and 810 nm wavelengths. (An index of refraction of n = 1.4 was assumed).

| | | before occlusion | during occlusion |
|---|---|---|---|
| **633 nm** | $\mu_s'$ **(mm$^{-1}$)** | 0.573 | 0.483 |
| | $\mu_a$ **(mm$^{-1}$)** | 0.021 | 0.064 |
| **810 nm** | $\mu_s'$ **(mm$^{-1}$)** | 0.558 | 0.498 |
| | $\mu_a$ **(mm$^{-1}$)** | 0.013 | 0.015 |

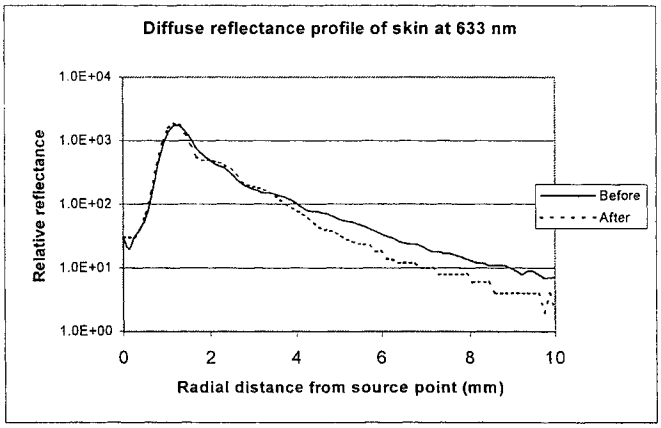


Figure 7: Diffuse reflectance profile of forearm skin at 633 nm before and after arterial occlusion.

## 4. DISCUSSION AND CONCLUSION

Although Monte Carlo simulations are not practical for clinical applications, they provide a non-experimental method for testing and validating analytical models. The results obtained from matching the diffusion algorithm to the Monte Carlo simulation indicate that the diffusion model begins to fail for intensity profiles measured at close ranges (~ 2 *mfp'*). For intensity profiles measured at radial distance greater than this the diffusion model matched the Monte Carlo profile very well but the accuracy of the generated optical coefficients does not improve (roughly 10 percent). If these results are indicative of real tissue measurements then caution should be exercised because the diffusion model may generate a reasonably good fit to the intensity profiles but the accuracy of the measurement could be out by as much as 10 percent.

The tissue phantom investigations showed a slightly better agreement between the diffusion model and the results from the transmission technique (5 – 10 %). These phantom measurements also confirmed that remote detection (CCD) and contact detection (fiber optic probe) techniques give relatively similar results.

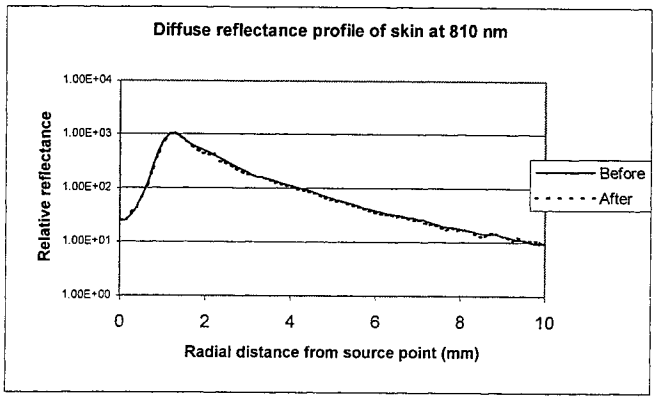


Figure 8: Diffuse reflectance profile of forearm skin at 810 nm before and after arterial occlusion.

The in vitro measurements demonstrated that longer wavelengths give consistently larger penetration depths within ligament and tendon tissue. This is probably due to the absorption spectrum of hemoglobin where absorption is stronger at shorter wavelengths. For measurements made in the patellar tendon larger scattering and absorption coefficient were observed along the lateral dimension of the tissue compared to the longitudinal dimension. This is caused by the regular fibril structuring in ligament and tendon where collagen fibers align themselves along the direction of applied biomechanical forces. Because photon propagation within these structures is dominated by scattering off the boundaries between collagen and the interstitial fluid, collagen architecture can be measured using an in-vitro technique called small angle light scattering[16]. This anisotropic scattering produces the light-guiding effects that are observed in the reflectance profiles. As a result, DR measurement could provide an effective in-vivo technique for the optical measurement of collagen architecture and tissue structure.

The in-vivo measurements performed in this investigation have demonstrated that the DR model and instrumentation is sensitive to changing levels in hemoglobin oxygenation. With the use of more wavelengths the absolute concentrations of oxy and deoxy-hemoglobin can be determined along with the remaining populations of tissue chromophores.

These preliminary studies have established a diffuse reflectance instrumentation for the measurement of tissue structure and metabolic state with a source and detection geometry that is compatible with multiple wavelength Laser Doppler imaging for future measurement of tissue perfusion and metabolic state.

## ACKNOWLEDGEMENTS

This work was funded through grants obtained from the Medical Research Council of Canada (MRC), the Alberta Heritage Foundation for Medical Research (AHFMR), the Whitaker Foundation, and University Technologies International Inc. (UTI). Special thanks to Catherine Leonard and Tyler Ivie for assisting with animal and tissue preparation. I would also like to acknowledge L. Wang (Laser Biology Research Laboratory, University of Texas M.D. Anderson Cancer Center) and S. Jacques (Oregon Medical Laser Center) for providing the original Monte Carlo source code used in this research.

## REFERENCES

1. K. Forrester, M. Doschak, and R. C. Bray, "In-vivo comparison of scanning technique and wavelength in laser Doppler perfusion imaging: Measurement in knee ligaments of adult rabbits", *Medical and Biological Engineering and Computing.* **35,** pp. 581-586, 1997.
2. R. Bray, K. Forrester, J. McDougall, A. Damji, and W. R. Ferrell, "Evaluation of laser Doppler imaging to measure blood flow in knee ligaments of adult rabbits", *Medical and Biological Engineering and Computing.* **34,** pp. 227-231, 1996.

3. A. N. Obeid, D. M. Boggett, N. J. Barnett, G. Dougherty, and P. Rolfe, "Depth discrimination in laser Doppler skin blood flow measurement using different lasers", *Medical and Biological Engineering and Computing",* **26,** pp. 415-419, 1988.
4. T. J. Farrell, M. S. Patterson, and B. Wilson, "A diffusion theory model of spatially resolved, steady-state diffuse reflectance for the noninvasive determination of tissue optical properties in-vivo", *Medical Physics.* ***19*****, No. 4**, pp. 879-888, 1992.
5. A. J. Welch, and M. J. C. van Gemert, *Optical-thermal response of laser irradiated tissue,* Plenum Press, New York, 1995.
6. L. H. Wang, S. L. Jacques, and L. Q. Zheng, "Monte Carlo modeling of photon transport in multi-layered tissues", *Comput. Methods Programs Biomed.* **47**, 131-146, 1995.
7. T. J. Farrell, M. S. Patterson, J. E. Hayward, B. C. Wilson, and E. R. Beck, A CCD and neural network based instrument for the non-invasive determination of tissue optical properties in-vivo", *Proc. SPIE,* **2135, pp.** 117-128.
8. L. Wang, X. Zhao, and S. L. Jacques, "Computation of the optical properties of tissues from light reflectance using a neural network", *Proc. SPIE,* **2134A,** pp. 391-399, 1994.
9. B. C. Wilson and S. L. Jacques, "Optical reflectance and transmission of tissues: Principles and applications", *IEEE J. Quant. Electron.* ***26,*** 2186-2199, 1990.
10. C. J. M. Moes, M. J. C. van Gemert, W. M. Star, J. P. A. Marijnissen, and S. A. Prahl, "Measurements and calculations in a scattering and absorbing phantom at 633 nm", *Applied Optics,* **28, No. 12,** pp. 2292-2296, 1991.
11. H. J. van Staveren, C. J. M. Moes, J. van Marle, S. A. Prahl, and M. J. C. van Gemert, "Light scattering in intralipid-10% in the wavelength range of 400-1100 nm", *Applied Optics,* **30, No. 31,** pp. 4507-4514, 1991.
12. P. R. Bevington, *Data reduction and error analysis for the physical sciences,* McGraw-Hill, New York, 1969
13 S. J. Madsen, M. S. Patterson, and B. C. Wilson, "The use of India ink as an optical absorber in tissue-simulating phantoms", *Phys. Med. Biol.,* **37, No. 4,** pp. 985-993, 1992.
14. S. T. Flock, S. L. Jacques, B. C. Wilson, W. M. Star, and M. J. C. van Gemert, "Optical properties of intralipid: A phantom medium for light propagation studies", *Lasers in Surgery and Medicine*, **12**, pp. 510-519, 1992.
15. S. Prahl, *Tabulated molar extinction coefficient for hemoglobin in water*, (http://omlc.ogci.edu/), Oregon Medical Laser Center.
16. M. S. Sacks, and C. J. Chuong, "Characterization of collagen fiber architecture in the canine diaphragmatic central tendon", *J. of Biomech. Eng.* **114**, pp. 183-190, 1992.

# Propagation of polarized light beams through biological tissues

Steven L. Jacques, Jessica R. Ramella-Roman

Oregon Graduate Institute, Portland OR 97225
Oregon Medical Laser Center, 9205 SW Barnes Rd, Portland OR 97225

## ABSTRACT

The rate of randomization of linearly polarized light as a collimated polarized beam passes through scattering media was characterized by a diffusivity ($\chi$) [radians$^2$/mean free path] in the angle space ($\theta$) describing orientation of the linear polarization: probability of orientation at an angle $p(\theta) = \exp(-\theta^2/(2\sigma^2))/(\sigma \text{ sqrt}(\pi/2))$ where $\sigma = \chi\tau$ and $\tau$ is the mean free path ($\mu_s L$) where $\mu_s$ is the scattering coefficient [cm$^{-1}$] and L is sample thickness [cm]. The media studied were polystyrene microsphere solutions, liver, muscle, and skin. The $\chi$ for microspheres ranged from 0.80-0.03 ffor 300-6000 nm diameter, and was 0.28 for skin, 0.06 for muscle, and 0.003 for liver.

**Key words:** optical imaging, birefringence, skin, muscle, liver

## 2. INTRODUCTION

An imaging system for visualizing cancer in skin and other superficial tissue layers (esophagus, lung, cervix, colon, etc.) is being developed using polarized light [1]. The camera acquires two images based on reflected light from a tissue illuminated with polarized light, one image with collected light passing through a polarizer oriented parallel to the illumination light and one image with collected light passing through a polarizer oriented perpendicular to the illumination light. The difference of the two images cancels any randomized light due to multiple scattering. The illumination light is delivered obliquely to the surface and surface glare due to specular reflectance is reflected obliquely and misses the camera. Only the initial superficially reflected polarized light contributes to the image based on the difference of the two images.

To address the issue of how deep such polarization images extend into tissues, we studied the rate of randomization of linearly polarized light in a transmission-mode experiment. Light transmission through either polystyrene microsphere solutions or through biological tissues (skin, muscle, liver) was studied.

The results were analyzed in terms of a diffusivity ($\chi$) [radians$^2$/mean free path] or [rad$^2$/mfp] in the angle space describing the orientation of the linear polarization.

In *Laser-Tissue Interaction XI: Photochemical, Photothermal, and Photomechanical*, Donald D. Duncan, Jeffrey O. Hollinger, Steven L. Jacques, Editors, Proceedings of SPIE Vol. 3914 (2000)
1605-7422/00/$15.00

## 2. MATERIALS AND METHODS

### 2.1 Materials

Two kinds of materials were tested: (1) polystyrene microspheres in water solution, and (2) biological tissues. The microspheres were from various suppliers and ranged in size from 380-1070 μm in diameter. The tissues were pig liver, chicken breast muscle and pig skeletal muscle, and pig skin from both albino and pigmented pigs. Fresh tissues (unfrozen) were sliced into thin sections and compressed slightly between the glass plates of an adjustable cuvette to a known thickness, L [cm].

### 2.2 Experimental setup

Figure 1 shows the basic setup. A horizontally polarized collimated laser beam was passed through a horizontal polarizer to verify the orientation of the polarization, then through the sample cuvette containing either microphere solutions or a tissue slab, then through a second analyzing polarizer that was oriented either parallel to the incident beam (horizontal to table) or parallel to the incident beam (vertical) to reach a photodetector. The rear surface of the sample cuvette was always in the same position although the thickness of the cuvette was adjustable. Hence the optical depth, $\tau = \mu_s L$ [dimensionless] of the microsphere solution or tissue sample could be adjusted. The two measurements were labeled $I_{par}$ and $I_{per}$. Normalization by the incident beam ($I_o$) yielded dimensionless values $I_{par}/I_o$ and $I_{per}/I_o$. The transmitted light consisted of (1) unscattered light, exp(-τ), and (2) a fraction of the scattered light passing through the 2-mm aperture that limited the amount of scattered light that reached the detector. The goal of the measurement was to observe the transition from incident parallel light (horizontal) into randomly polarized light.

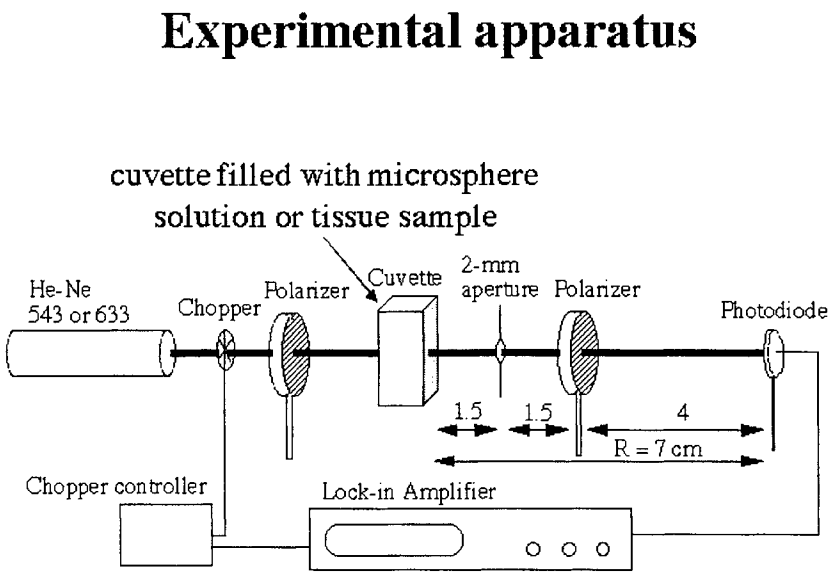


Fig. 1: Experimental apparatus. Horizontally polarized laser beam passes through a sample cuvette and a second analyzing polarizer that can be oriented either horizontal (parallel to incident beam) or vertical (perpendicular to incident beam) before reaching a photodetector. The 2-mm aperture limits but does not completely eliminate the amount of multiply scattered light that reaches the photodetector.

## 2.3 Analysis

The transmitted values of $I_{par}/I_o$ and $I_{per}/I_o$ were analyzed to fit the following approximate expression:

$$I_{par}/I_o = \exp(-\tau) + (1 - \exp(-\tau))\, f \exp(-\mu_{atten}L)\, (1/2)(1 + \exp(-\chi\tau/2)$$

$$I_{par}/I_o = (1 - \exp(-\tau))\, f \exp(-\mu_{atten}L)\, (1/2)(1 - \exp(-\chi\tau/2)$$

where

$I_o$ is the incident parallel polarized light (horizontal to table),
$\tau$ is the mean free path equal to $\mu_s L$ [dimensionless],
$\mu_s$ is the scattering coefficient [$cm^{-1}$],
L is the sample thickness [cm],
f is the fraction of transmitted scattered light that is collected by the detector,
$\mu_{atten}$ is an attenuation comparable to $\mu_{eff}$ but includes cuvette boundary effects,
$\chi$ is the diffusivity [radian2/mean free path].

The above expressions are based on the concept that incident polarized light will scatter in a forward direction and its orientation of polarization will become only slightly rotated from its original orientation. In a tissue, if the fibers (collagen or actin-myosin) are randomly oriented, then the rotation of polarization will not favor either clock-wise or counterclock-wise rotation but rather will rotate in either direction. The result is a diffusion of the orientaton of linear polarization in the angle space $\theta$ depicted in Fig. 2. The diffusivity $\chi$ characterizes the rate of this diffusion process.

If fibers are oriented, then rotation of polarization should prefer one direction of rotation and the process is not accurately described by a diffusion process. Collagen fibers of skin dermis are randomly oriented. Actin-myosin fibers of muscle are oriented. The pig skeletal muscles were cut perpendicular to the fibers to avoid any preferred orientation. The chicken muscle samples were soft and fibers were easily disorganized by the compression in the cuvette. No attempt to orient chicken muscle fibers was made.

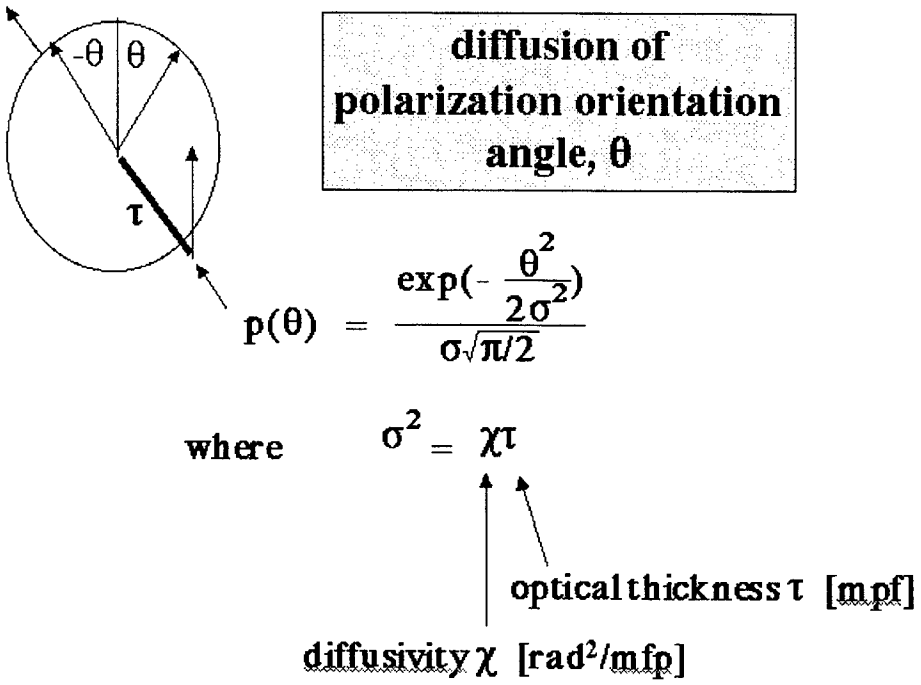


Fig. 2: Linearly polarized light passing through an optical depth ($\tau$) of randomly oriented media will scatter causing the orientation of polarized light to rotate in the $+\theta$ and $-\theta$ angle directions. The process is described by a diffusion equation shown in the figure which depends on a diffusivity $\chi$.

## 3. RESULTS

Figure 3 shows the idealized behavior of transmission measurements versus optical depth for a range of diffusivity values. The upper figure shows the behavior of $I_{par}/I_o$ and $I_{per}/I_o$. $I_{par}/I_o$ initially falls from unity exponentially as $\exp(-\tau)$, but then approaches the value of $I_{per}/I_o$. Both $I_{par}/I_o$ and $I_{per}/I_o$ then attenuate as $\exp(-\mu_{atten}L)$. The lower figure shows the behavior of the degree of linear polarization (Pol):

$$Pol = (I_{par} - I_{par})/(I_{par} + I_{par})$$

Pol is initially unity then falls to zero at a rate that depends on the diffusivity $\chi$.

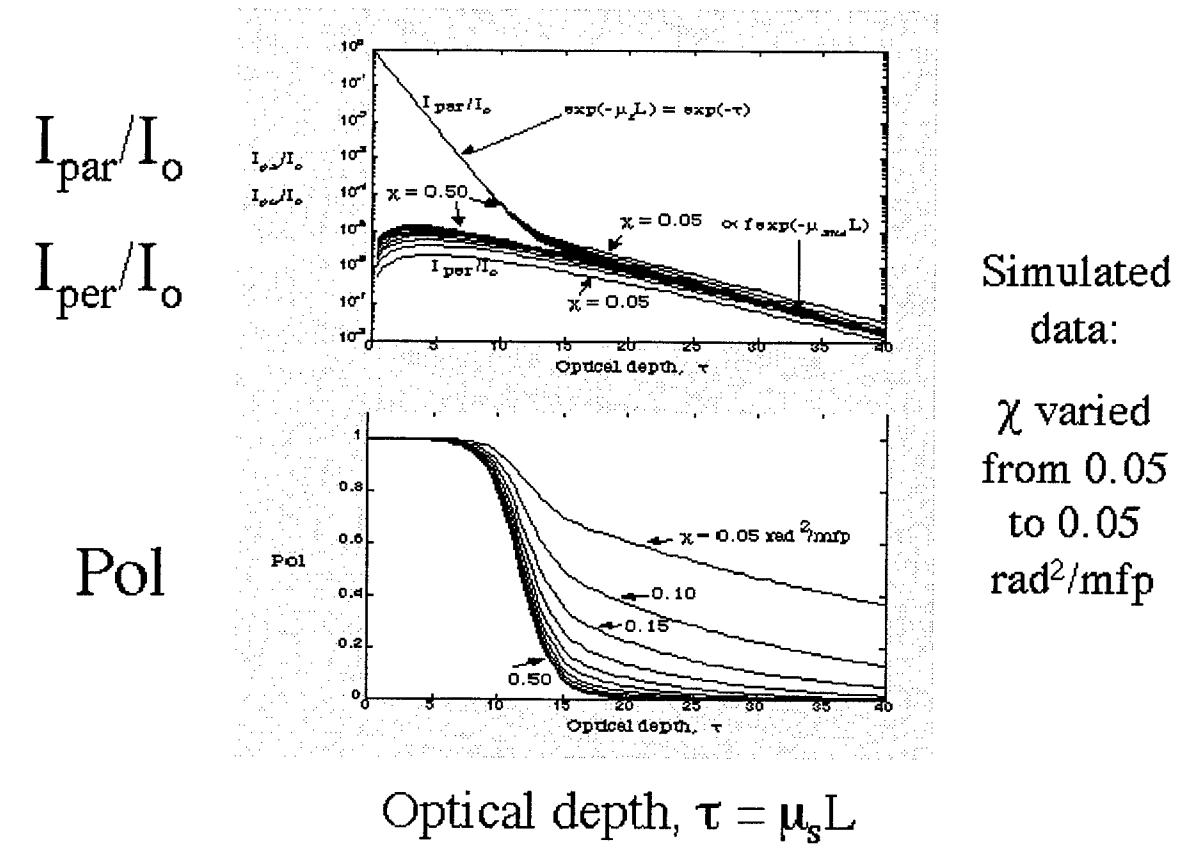


Fig. 3: The idealized behavior of transmission versus optical depth for a range of diffusivity ($\chi$) values.

Figures 4 and 5 show typical experimental data. Figure 4 shows a result for a 482-nm-diameter microsphere demonstrating rapid depolarization. Figure 5 shows a result for chicken liver demonstrating very slow depolarization.

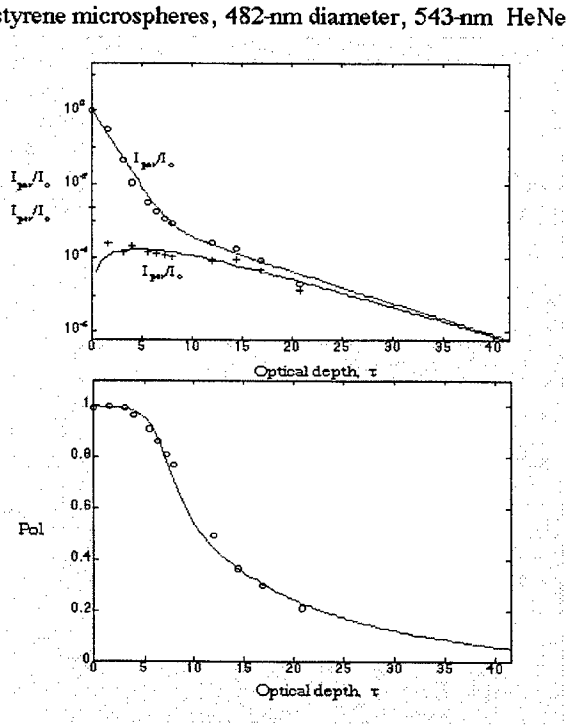


$\chi = 0.070$ rad$^2$/mfp

Fig. 4: Transmission and degree of linear polarization for light passing through a polystyrene microsphere solution of increasing optical depth (482-nm-dia. sphere, 543-nm HeNe laser).

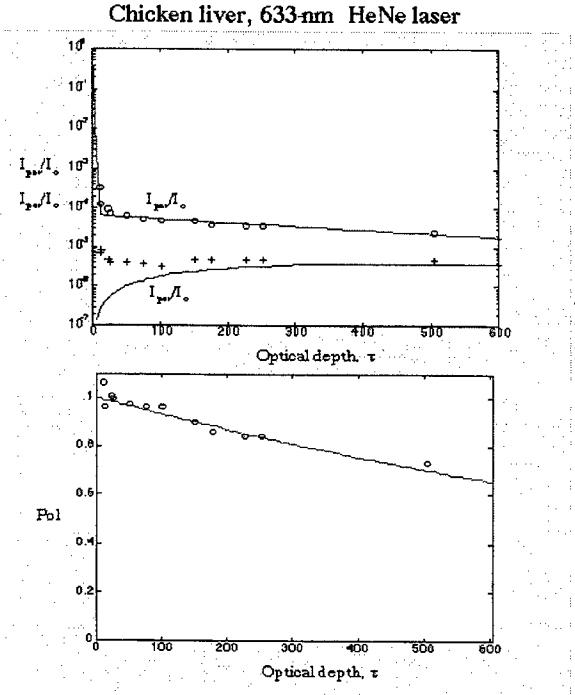


$\chi = 0.00070$ rad$^2$/mfp

Fig. 5: Transmission and degree of linear polarization for light passing through chicken liver of increasing optical depth (chicken liver, 633-nm HeNe laser).

A final summary of all the measurements for the microsphere solutions and the liver, muscle, and skin are shown in Fig. 6. The experimental results from the work of Jarry et al. [2] were also analyzed and the deduced $\chi$ values are plotted for comparison. The key result is the large dynamic range of $\chi$ values for tissues, with low $\chi$ for liver, moderate $\chi$ for muscle, and the highest $\chi$ for skin.

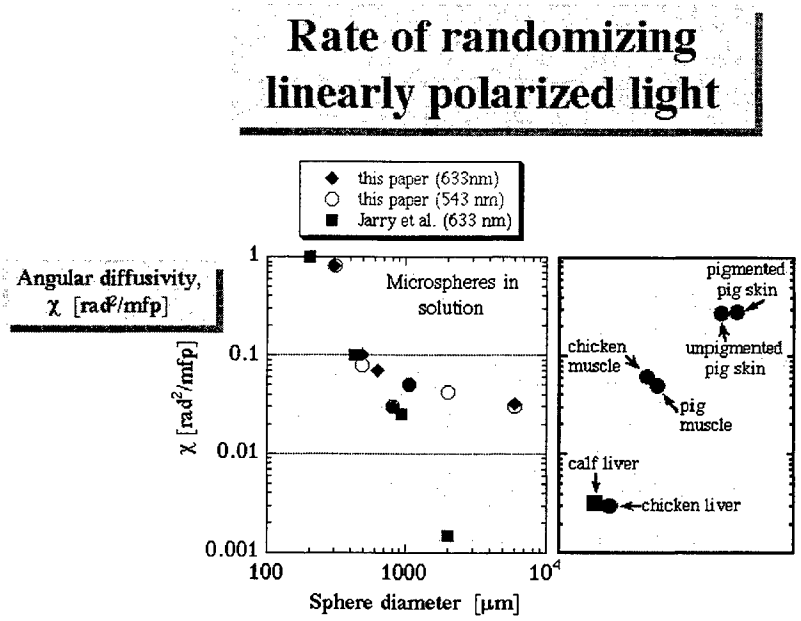


Fig. 6: Summary of the diffusivity $\chi$ for polysytene spheres versus diameter and for various tissues. The data of Jarry et al. [2] were also analyzed and are included in the figure.

## 4. CONCLUSIONS

The birefringence of the collagen and actin-myosin fibers in the skin and muscle appear to be responsible for the strong randomization of the linearly polarized light. Liver has little birefringence and does not efficiently randomize linearly polarized light.

For skin, the angular diffusivity of 0.28 $rad^2$/mfp causes Pol to drop to nearly zero after 10 mfp. In the reflectance mode of the polarized light camera, this suggests that Pol drops to zero at a depth of 5 mfp due to the combined path in and out of the tissue. For a red wavelength (633 nm), the scattering coefficient is about 187 $cm^{-1}$ so $1/\mu_s$ is 53 μm. Therefore polarization images should extend 5(53) or 265 μm beyond the epidermis into the dermis composed of collagen fibers. Since the epidermis is about 60-100 μm in thickness, the expected depth of imaging in skin is about 326-367 μm.

## 5. REFERENCES


1 Jacques SL, K Lee, Polarized video imaging of skin. SPIE Proc. 3245D, Cutaneous Applications of Lasers in Dermatology, Plastic Surgery, and Tissue Welding, San Jose, CA. Feb. 26-28, 1998.

2 Jarry G, E. Steimer, V. Damaschini, M. Epifanie, M. Jurczak, R. Kaiser, Coherence and polarization of light propagating through scattering media and bioloigcal tissues. Applied Optics 37:7357-7367, 1998.


## 6. ACKNOWLEDGEMENTS


This work is supported by the NIH (RO1-80985-01).

## SESSION 12

# Beam Propagation in Random Media I

Invited Paper

# DOUBLE-PASSAGE RESOLUTION EFFECTS AND THEIR APPLICATIONS TO IMAGING IN RANDOM MEDIA*

Reuven Mazar and Alexander Bronshtein
Department of Electrical and Computer Engineering,
Ben-Gurion University of the Negev,
P.O.Box 653, Beer-Sheva, Israel 84105

**Abstract**

In wave-based remote sensing of distant objects embedded in a random medium a high-frequency electromagnetic wave is scattered by object discontinuities, and portions of the scattered radiation can traverse the same random inhomogeneities as the initial incident field, leading to an anomalous intensity distribution. Here, we present a possible realization for the resolving properties of an object using the double-passage effects and construct the intensity response at the image plane of an optical system, resulting from backward reflection from a target having discontinuities. The object plane – image plane relations are formulated and manageable algorithms are obtained by using the random propagators of the Stochastic Geometrical Theory of Diffraction. The resolving properties of periodic spatial objects are investigated.

## 1. Formulation of the problem

In high-frequency location and remote sensing experiments through a random medium the propagating field can be reflected or diffracted by targets or embedded obstacles, and the scattered field species can traverse the same random inhomogeneities as the incident one. Statistical dependence of the forward-backward propagating events leads to the so-called double-passage effects related to the anomalous distribution of the backscattered intensity, particularly to local intensity enhancement not observed along unidirectional paths [1-7]. Such situations can occur in medical imaging, nondestructive evaluation and remote sensing experiments in various environments. Anomalies in the distribution of the backscattered radiation suggest the application of double-passage to the remote imaging of distant objects [8-14].
The theoretical analysis of double-passage effects is rather complicated. Because of the need to correlate the forward-backward propagating fields, the desired solution has to preserve the random information accumulated along the propagation path from the source to the scatterer. Here we adopt the approach of the Stochastic Geometrical Theory of Diffraction (SGTD) [15-18] and formulate the double passage relations for a simple "source plane – target – source plane" configuration. The propagation geometry is given in Fig.1. The medium is characterized by the refractive index $N(\mathbf{R}) = 1 + \tilde{n}(\mathbf{R})$ which consists of a homogeneous background part and a weak random part $\tilde{n}(\mathbf{R})$. The field from an isotropic point source located at the point $S(\mathbf{r} = 0, \sigma = -\sigma_0)$ propagates in the $-\sigma$ direction and is scattered backwards from the plane $\sigma = -\sigma_s$ by the object with reflection coefficient $K(\mathbf{r})$. The one-directional propagation according to the SGTD is described by the propagator

*Also published in *Proc. of SPIE* Vol. 3927



In *Laser-Tissue Interaction XI: Photochemical, Photothermal, and Photomechanical*, Donald D. Duncan, Jeffrey O. Hollinger, Steven L. Jacques, Editors, Proceedings of SPIE Vol. 3914 (2000)
1605-7422/00/$15.00

$$g(\mathbf{p}_2,\mathbf{s}_2,\sigma_2\,|\,\mathbf{p}_1,\mathbf{s}_1,\sigma_1)=\left(\frac{k}{2\pi}\right)^m\int_{-\infty}^{\infty}d^m\rho d^m\eta\exp\{ik\boldsymbol{\eta}\cdot[\mathbf{p}_2-\mathbf{p}_1-\boldsymbol{\rho}(\sigma_2-\sigma_1)]\}\exp[ik\boldsymbol{\rho}\cdot(\mathbf{s}_2-\mathbf{s}_1)]$$

$$\times\exp\left\{ik\int_{\sigma_1}^{\sigma_2}d\zeta\left(\tilde{n}[\mathbf{p}_1+\boldsymbol{\rho}(\zeta-\sigma_1)+\frac{\mathbf{s}_2}{2}+\frac{\boldsymbol{\eta}(\zeta-\sigma_2)}{2},\zeta]-\tilde{n}[\mathbf{p}_1+\boldsymbol{\rho}(\zeta-\sigma_1)-\frac{\mathbf{s}_2}{2}-\frac{\boldsymbol{\eta}(\zeta-\sigma_2)}{2},\zeta]\right)\right\}, \qquad (1)$$

where m=2 is for the three-dimensional problem, and m=1 is for the two-dimensional one.

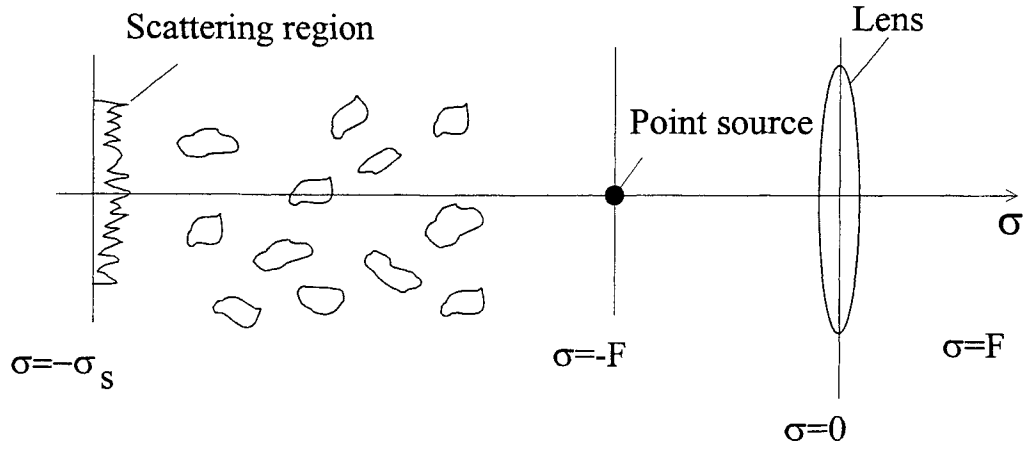


**Fig1:** Double-passage imaging configuration

Using this propagator the propagation relation for the described source-object configuration can be written in the following form:

$$\langle\Gamma_{ref}(\mathbf{p}_0,\mathbf{s}_0,-\sigma_0)\rangle=\int_{-\infty}^{\infty}d^m p_S d^m s_S K\left(\mathbf{p}_S+\frac{\mathbf{s}_S}{2}\right)K^*\left(\mathbf{p}_S-\frac{\mathbf{s}_S}{2}\right)$$

$$\times\langle g(\mathbf{p}_0,\mathbf{s}_0,-\sigma_0\,|\,\mathbf{p}_S,\mathbf{s}_S,-\sigma_S)g(0,0,-\sigma_0\,|\,\mathbf{p}_S,\mathbf{s}_S,-\sigma_S)\rangle\,. \qquad (2)$$

Because of the double-passage of the forward-backward radiation through the same random regions, we expect that at the source plane an anomalous angular intensity distribution will be created. To resolve these anomalies, we place at $\sigma=0$ a spatial filter, a lens of focal length F so that $\sigma_0=F$, and analyze the image at the image plane $\sigma=F$. The action of such a lens-filter is described by the propagator:

$$g_F(\mathbf{p}_3,\mathbf{s}_3,\sigma_3 \mid \mathbf{p}_2,\mathbf{s}_2,\sigma_2) = \left(\frac{k}{2\pi F}\right)^m \exp\left\{-\frac{ik}{F}(\mathbf{p}_3\cdot\mathbf{s}_2+\mathbf{p}_2\cdot\mathbf{s}_3)\right\}. \tag{3}$$

At the focal plane of the lens we obtain the following TPRF:

$$\Gamma_F(\mathbf{p}_3,\mathbf{s}_3,\sigma_3) = \int_{-\infty}^{\infty}\!\!\cdots\!\int d^m p_2 d^m s_2 g_F(\mathbf{p}_3,\mathbf{s}_3,\sigma_3|\mathbf{p}_2,\mathbf{s}_2,\sigma_2)\Gamma(\mathbf{p}_2,\mathbf{s}_2,\sigma_2). \tag{4}$$

For the propagator $g_F(\mathbf{p}_3,\mathbf{s}_3,\sigma_3 \mid \mathbf{p}_2,\mathbf{s}_2,\sigma_2)$ we use a solution (19) of Ref.16, and assume that the fluctuations of the refractive index represent an isotropic homogeneous Gaussian random field, which is delta-correlated along the propagation direction:

$$B_n(\mathbf{r}_1-\mathbf{r}_2,\sigma_1-\sigma_2) = \langle \tilde{n}(\mathbf{r}_1,\sigma_1)\tilde{n}(\mathbf{r}_2,\sigma_2)\rangle = A_n(\mathbf{r}_1-\mathbf{r}_2)\delta(\sigma_1-\sigma_2), \tag{5}$$

where the function $A_n(\mathbf{r}_1-\mathbf{r}_2)$ describes correlation in the plane transverse to the propagation direction. Using the above assumptions, the averaging of the product of the two-scale propagators in the propagation relation (2) can be performed. The result of the product <g(*)g(*)> is presented by the following expression:

$$\begin{aligned}\langle g(\mathbf{p}_0,\mathbf{s}_0,-F \mid \mathbf{p}_S,\mathbf{s}_S,-\sigma_S)g(0,0,-F \mid \mathbf{p}_S,\mathbf{s}_S,-\sigma_S)\rangle = \\ = \left(\frac{k}{2\pi}\right)^m \exp\left\{\frac{ik}{2\Delta\sigma}[\mathbf{p}_0-2\mathbf{p}_s]\cdot[\mathbf{s}_0-2\mathbf{s}_s]\right\}\int_{-\infty}^{\infty}\!\!\cdots\!\int d^m\rho d^m\eta \exp\{ik\boldsymbol{\eta}\cdot[\mathbf{p}_0-\boldsymbol{\rho}\Delta\sigma]\} \\ \times \exp\left(\frac{ik\boldsymbol{\rho}\cdot\mathbf{s}_0}{2}\right)\exp\left\{-k^2\int_0^{\Delta\sigma} d\zeta f_s(\mathbf{s}_0,\mathbf{s}_s,\boldsymbol{\rho},\boldsymbol{\eta},\zeta)\right\}\end{aligned} \tag{6}$$

with the function $f_s$ defined as:

$$\begin{aligned}f_s(\mathbf{s}_0,\mathbf{s}_s,\boldsymbol{\rho},\boldsymbol{\eta},\zeta) = 2A_n(0) - A_n[\mathbf{s}_0+\boldsymbol{\eta}(\zeta-\Delta\sigma)+(\mathbf{s}_s-\mathbf{s}_0)(1-\zeta/\Delta\sigma)/2] \\ - A_n[\boldsymbol{\eta}(\zeta-\Delta\sigma)-(\mathbf{s}_s-\mathbf{s}_0)(1-\zeta/\Delta\sigma)/2] \\ - A_n[\boldsymbol{\rho}\zeta+\mathbf{s}_s(1-\zeta/\Delta\sigma)+\mathbf{s}_0\zeta/(2\Delta\sigma)] \\ - A_n[\boldsymbol{\rho}\zeta-\mathbf{s}_s(1-\zeta/\Delta\sigma)-\mathbf{s}_0\zeta/(2\Delta\sigma)] \\ + A_n[\boldsymbol{\rho}\zeta+\mathbf{s}_0/2+\boldsymbol{\eta}(\zeta-\Delta\sigma)] + A_n[\boldsymbol{\rho}\zeta-\mathbf{s}_0/2-\boldsymbol{\eta}(\zeta-\Delta\sigma)].\end{aligned} \tag{6a}$$

In the case of the incoherent reflection, the scattering region correlation function is given by:

$$K\left(\mathbf{p}_s+\frac{\mathbf{s}_s}{2}\right)K^*\left(\mathbf{p}_s-\frac{\mathbf{s}_s}{2}\right) = S(\mathbf{p}_s)\delta(\mathbf{s}_s). \tag{7}$$

Combining Eqs. (2), (3) - (7) and setting $\mathbf{p}_0=\mathbf{r}$, $\mathbf{s}_0=0$, we obtain for the average intensity distribution in the plane F after the lens:

$$I(\mathbf{r},F) = \left(\frac{k}{2\pi F}\right)^m \int_{-\infty}^{\infty}\!\!\cdots\!\int d^m p_s d^m\eta d^m\rho S(\mathbf{p}_s)\exp\{-ik\boldsymbol{\eta}\cdot[\mathbf{p}_s+\mathbf{r}\frac{\Delta\sigma}{F}+\boldsymbol{\rho}\Delta\sigma]-k^2\int_0^{\Delta\sigma} d\zeta f_0(\boldsymbol{\eta},\boldsymbol{\rho},\zeta)\}. \tag{8}$$

Or expressing $S(\mathbf{p}_s)$ as a form of spectral integral:

$$S(\mathbf{p}_s) = \left(\frac{1}{2\pi}\right)^m \exp\left(-\frac{p_s^2}{D^2}\right) \int_{-\infty}^{\infty} \ldots \int S(\boldsymbol{\alpha}) \exp(i\boldsymbol{\alpha} \cdot \mathbf{p}_s) d^m\alpha , \tag{9}$$

and performing the integrations we represent (8) in an alternative form:

$$I(\mathbf{r}, F) = \frac{D}{4\pi}\left(\frac{k}{2\pi F}\right)^m \int_{-\infty}^{\infty} \ldots \int d^m\eta d^m\alpha d^m\rho \exp\left[-\frac{(\boldsymbol{\eta} - \boldsymbol{\alpha}/k)^2 (kD)^2}{4}\right] \hat{S}(\boldsymbol{\alpha})$$

$$\times \exp\{-k^2 \int_0^{\Delta\sigma} d\zeta f_0(\boldsymbol{\eta}, \boldsymbol{\rho}, \zeta)\} \exp\{-ik\boldsymbol{\eta} \cdot [\mathbf{r}\frac{\Delta\sigma}{F} + \boldsymbol{\rho}\Delta\sigma]\} , \tag{10}$$

where $\Delta\sigma = \sigma_s - F$, D is the characteristic size of the scattering region and the scattering function $f_s$ is defined as:

$$f_0(\boldsymbol{\eta}, \boldsymbol{\rho}, \zeta) = 2A_n(0) - A_n[\boldsymbol{\eta}(\zeta - \Delta\sigma)] - A_n(\boldsymbol{\eta}\Delta\sigma) - A_n[(\boldsymbol{\rho} + \frac{\boldsymbol{\eta}}{2})\zeta] - A_n[(\boldsymbol{\rho} - \frac{\boldsymbol{\eta}}{2})\zeta]$$

$$+ A_n[(\boldsymbol{\rho} + \frac{\boldsymbol{\eta}}{2})\zeta - \boldsymbol{\eta}\Delta\sigma] + A_n[(\boldsymbol{\rho} - \frac{\boldsymbol{\eta}}{2})\zeta + \boldsymbol{\eta}\Delta\sigma] . \tag{11}$$

In many practical cases it would be useful to obtain the response for a bounded two-dimensional periodic scattering function:

$$S(p_s) = \frac{1}{2}\chi \exp\left(-\frac{p_s^2}{D^2}\right)\{\exp(i\alpha p_s) + \exp(-i\alpha p_s)\}, \tag{12}$$

where $\chi$ is the scattering amplitude. The intensity distribution for such a distribution at the focal plane of the lens takes the following form:

$$I(r, F) = \frac{k\chi D}{4\sqrt{\pi}F} \int_{-\infty}^{\infty} \int d\eta d\rho \left\{\exp\left[-\frac{(\eta - \alpha/k)^2 (kD)^2}{4}\right] + \exp\left[-\frac{(\eta + \alpha/k)^2 (kD)^2}{4}\right]\right\}$$

$$\times \exp\left\{-ik\eta\left[r\frac{\Delta\sigma}{F} + \rho\Delta\sigma\right]\right\} \exp\{-k^2 \int_0^{\Delta\sigma} d\zeta f_0(\eta, \rho, \zeta)\} . \tag{13}$$

The expression in (13) represents the intensity pattern at the image plane resulting from the incoherent contribution of the periodic scattering pattern under double-passage conditions. In the absence of random refractive index fluctuations ($A_n(r)=0$) the scattering function $f_0=0$, and the integrations in (13) can be performed leading to a constant intensity value.

In the general case investigation of the results of the double-passage imaging algorithm presented by Eq. (13) requires evaluation of multidimensional integrals. We choose here a random medium characterized by a Gaussian correlation function

$$A_n(r) = A_n(0) \exp\left(-\frac{r^2}{\ell_n^2}\right), \tag{14}$$

and introduce scaled coordinates

$$r = \ell_n \bar{r}, \quad \alpha = \bar{\alpha}/\ell_n, \quad \sigma = k\ell_n^2 \bar{\sigma}, \quad F = k\ell_n^2 \bar{F}, \tag{15}$$

and scattering parameter

$$\gamma = k^3 A_n(0)\ell_n^2 . \tag{16}$$

Rescaling the integration variables, the intensity distribution in (13) becomes:

$$I(\bar{r}, \Delta\bar{\sigma}) = \frac{\chi \bar{D}}{4\sqrt{\pi} k^2 \ell_n^3 \bar{F}} \int_{-\infty}^{\infty} \int d\bar{\eta} d\bar{\rho} \left\{ \exp\left[ -\frac{(\bar{\eta} - \bar{\alpha})^2 \bar{D}^2}{4} \right] + \exp\left[ -\frac{(\bar{\eta} + \bar{\alpha})^2 \bar{D}^2}{4} \right] \right\}$$
$$\times \exp\left\{ -\gamma \int_0^{\Delta\bar{\sigma}} dt f_n(\bar{\eta}, \bar{\rho}, t) \right\} \exp\left[ -i\bar{\eta} \left( \bar{r} \frac{\Delta\bar{\sigma}}{\bar{F}} + \bar{\rho}\Delta\bar{\sigma} \right) \right], \tag{17}$$

with the normalized scattering function

$$f_n(\bar{\eta}, \bar{\rho}, t) = \{2A_n(0) - A_n[\bar{\eta}(t - \Delta\bar{\sigma})] - A_n(\bar{\eta}\Delta\bar{\sigma}) - A_n[(\bar{\rho} + \bar{\eta}/2)t] - A_n[(\bar{\rho} - \bar{\eta}/2)t]$$
$$+ A_n[(\bar{\rho} + \bar{\eta}/2)t - \bar{\eta}\Delta\bar{\sigma}] + A_n[(\bar{\rho} - \bar{\eta}/2)t + \bar{\eta}\Delta\bar{\sigma}]\} / A_n(0) . \tag{17a}$$

In some cases the expression in (17) can be evaluated analytically. The simplest situation is when the scattering can be described in the perturbation regime.

## 2. Perturbation regime

For $\gamma\Delta\bar{\sigma} << 1$, the exponential scattering term can be expanded into the perturbational series. Leaving the first two terms, we obtain

$$I(\bar{r}, \Delta\bar{\sigma}) = I_0 + I_1 \tag{18}$$

$$I_0 = \frac{\chi D\sqrt{\pi}}{k^2 \ell_n^3 \bar{F} \Delta\bar{\sigma}} \exp\left( -\frac{\bar{\alpha}^2 \bar{D}^2}{4} \right) \tag{18a}$$

$$I_1 = \frac{\gamma\chi \bar{D}}{4\sqrt{\pi} k^2 \ell_n^3 \bar{F}} \int_{-\infty}^{\infty} \int d\bar{\rho} d\bar{\eta} \left( \exp\left\{ -\frac{(\bar{\eta} + \bar{\alpha})^2 \bar{D}^2}{4} \right\} + \exp\left\{ -\frac{(\bar{\eta} - \bar{\alpha})^2 \bar{D}^2}{4} \right\} \right)$$
$$\times \int_0^{\Delta\bar{\sigma}} d\zeta P_2(\bar{\eta}, \bar{\rho}, \zeta) \exp\{-i\bar{\eta}[(\bar{r}/\bar{F} + \bar{\rho})\Delta\bar{\sigma}]\} , \tag{18b}$$

$$P_2(\bar{\eta}, \bar{\rho}, \zeta) = \bar{A}_n[(\bar{\rho} + \bar{\eta}/2)\zeta - \bar{\eta}\Delta\bar{\sigma}] + \bar{A}_n[(\bar{\rho} - \bar{\eta}/2)\zeta + \bar{\eta}\Delta\bar{\sigma}]$$
$$- \bar{A}_n[(\bar{\rho} + \bar{\eta}/2)\zeta] - \bar{A}_n[(\bar{\rho} - \bar{\eta}/2)\zeta] \tag{18c}$$

Expressing the correlation functions in the scattering function $P_2$ in a spectral form

$$\overline{A}_n(x) = \frac{1}{2\pi}\int_{-\infty}^{\infty} d\kappa \Phi_n(\kappa)\exp(i\kappa x) \tag{19}$$

and performing the integrations, leads to the following result for $I_1$:

$$I_1 = \frac{\chi\gamma\overline{D}\Delta\overline{\sigma}}{2\sqrt{\pi}k^2\ell_n^3\overline{F}}\int_0^1 d\zeta\int_{-\infty}^{\infty} d\kappa\Phi_n(\kappa)\left(\exp\left\{-\frac{(\kappa\zeta+\overline{\alpha})^2\overline{D}^2}{4}\right\}+\exp\left\{-\frac{(\kappa\zeta-\overline{\alpha})^2\overline{D}^2}{4}\right\}\right)$$
$$\times\left\{\cos\left(\frac{\kappa^2\zeta^2}{2\Delta\overline{\sigma}}\right)-\cos\left[\kappa^2\zeta\left(\frac{\zeta}{2\Delta\overline{\sigma}}-1\right)\right]\right\}\exp\left(-i\kappa\overline{r}\zeta/\overline{F}\right). \tag{20}$$

For large $\overline{D}$ the exponential terms act as delta-functions and this expression can be simplified. The result is:

$$I(\overline{r},\Delta\overline{\sigma}) = I_0 + H_1(\overline{\alpha},\Delta\overline{\sigma})\exp\left\{-\frac{(\overline{r}\Delta\overline{\sigma}/\overline{F})^2}{\overline{D}^2}\right\}\cos\left(\overline{\alpha r}\frac{\Delta\overline{\sigma}}{\overline{F}}\right), \tag{21}$$

$$H_1(\overline{\alpha},\Delta\overline{\sigma}) = \frac{2\chi\gamma\Delta\overline{\sigma}}{\sqrt{\pi}k^2\ell_n^3\overline{F}}\int_0^1\frac{d\zeta}{\zeta}\Phi_n\left(\frac{\overline{\alpha}}{\zeta}\right)\sin\left[\frac{\overline{\alpha}^2\Delta\overline{\sigma}}{2}\left(1-\frac{1}{\zeta}\right)\right]\sin\left[\frac{\overline{\alpha}^2\Delta\overline{\sigma}}{2\zeta}\right]. \tag{21a}$$

In Fig. 2, we present variation of the spectral coefficient with $\alpha$ for $\overline{\sigma} = 1, 2, 3$.

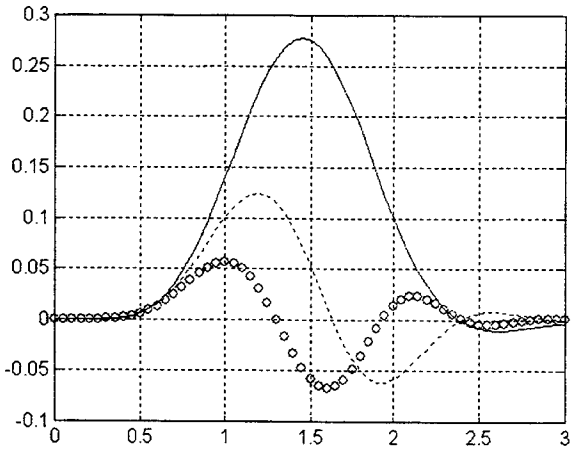


**Fig. 2:** Variation of the response coefficient $H_1(\overline{\alpha},\Delta\overline{\sigma})$ with $\overline{\alpha}$. Solid line - $\overline{\sigma} = 1$, dashed line - $\overline{\sigma} = 2$, circles - $\overline{\sigma} = 3$.

## 3. Arbitrary scattering conditions

In order to evaluate the integral (17) for arbitrary scattering conditions, we note that there are two characteristic scales in this integral. One is specified by the first exponential term being of the order of the inverse of the scattering region $\overline{D}$ and the another defined by the scattering exponential. This exponential defines the following important region for the variable $\overline{\eta}$ :

$$\gamma \int_0^{\Delta\overline{\sigma}} dt\, f_n(\overline{\eta}, \overline{\rho}, t) = 2 . \tag{22}$$

For $\overline{\rho} >> \overline{\eta}$ this equation becomes:

$$\gamma \int_0^{\Delta\overline{\sigma}} dt\{2A_n(0) - A_n[\overline{\eta}(t - \Delta\overline{\sigma})] - A_n(\overline{\eta}\Delta\overline{\sigma})\} = 2 . \tag{23}$$

For $\overline{D}^{-1} << \overline{\eta}_c$, the action of the first Gaussian exponential term in Eq. (17) is equivalent to the delta function, which leads to the following result:

$$I(\overline{r}, \Delta\overline{\sigma}) = \frac{\chi}{k^2 \ell_n^3 \overline{F}} \int_{-\infty}^{\infty} d\overline{\rho} \exp\left\{ - \frac{\left( \overline{r} \frac{\Delta\overline{\sigma}}{\overline{F}} + \overline{\rho}\Delta\overline{\sigma} \right)^2}{\overline{D}^2} \right\} \exp\left\{ -\gamma \int_0^{\Delta\overline{\sigma}} dt f_n(\overline{\alpha}, \overline{\rho}, t) \right\} \cos\left[ \overline{\alpha} \left( \overline{r} \frac{\Delta\overline{\sigma}}{\overline{F}} + \overline{\rho}\Delta\overline{\sigma} \right) \right] . \tag{24}$$

In Figs. 3a,b, we present the backscattered intensity variation with r/F as calculated from Eq. (24). We note that the resolution is observed for different values of $\alpha$ in wide spatial regions.

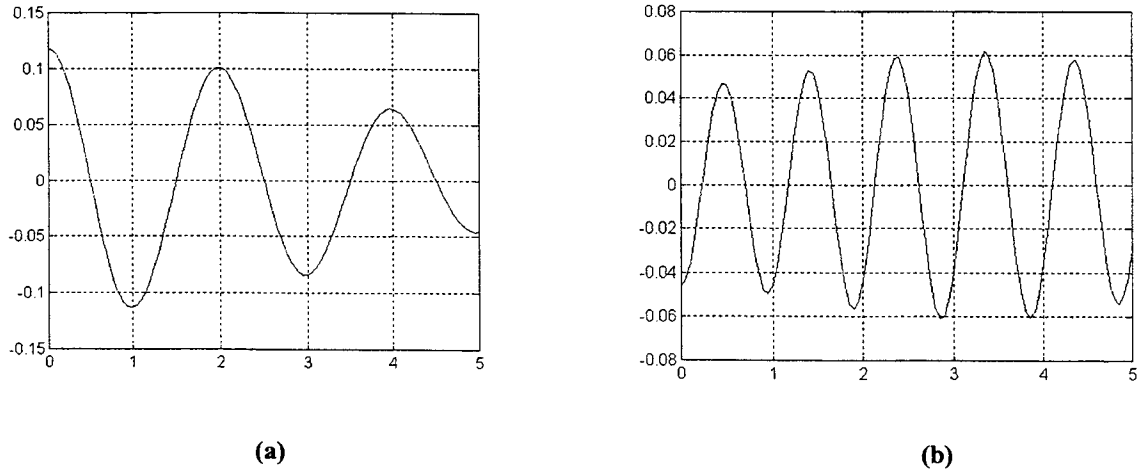


**(a)** **(b)**

**Fig. 3:** Backscattered intensity patterns as functions of r/F at $\overline{\sigma} = 1$ for a) $\overline{\alpha} = \pi$ and b) $\overline{\alpha} = 2\pi$ .

In the opposite case $\overline{D}^{-1} >> \overline{\eta}_c$, the important contribution is given by the scattering term. In this case the function $F(\overline{\eta}, \overline{\rho}, t)$ can be replaced by its expansion into powers of $\overline{\eta}$. Keeping only the terms up to the second order and performing the $\overline{\eta}$ -integration leads to the following expression:

$$I(\overline{r}, \overline{\alpha}, \Delta\overline{\sigma}) = \frac{\chi \overline{D}}{2\sqrt{\gamma \Delta\overline{\sigma} k^2 \ell_n^3 \overline{F}}} \int_{-\infty}^{\infty} \frac{d\overline{\rho}}{\sqrt{\overline{D}^2 + 4\gamma\Omega(\overline{\rho}, \Delta\overline{\sigma})}}$$

$$\times \exp\left\{ - \frac{\gamma \Omega(\overline{\rho}, \Delta\overline{\sigma})\overline{\alpha}^2 \overline{D}^2 + \left( \overline{r} \frac{\Delta\overline{\sigma}}{\overline{F}} + \overline{\rho}\Delta\overline{\sigma} \right)^2}{\overline{D}^2 + 4\gamma \Omega(\overline{\rho}, \Delta\overline{\sigma})} \right\} \cos\left[ \frac{\overline{\alpha} \overline{D}^2 \left( \overline{r} \frac{\Delta\overline{\sigma}}{\overline{F}} + \overline{\rho}\Delta\overline{\sigma} \right)}{\overline{D}^2 + 4\gamma \Omega(\overline{\rho}, \Delta\overline{\sigma})} \right] \quad (25)$$

with function $\Omega(\overline{\rho}, \Delta\overline{\sigma})$ defined as

$$\Omega(\overline{\rho}, \Delta\overline{\sigma}) = \frac{2}{3} |A_n^{(2)}(0)| (\Delta\overline{\sigma})^3 - [A_n(0) - A_n(\overline{\rho}\Delta\overline{\sigma})](\Delta\overline{\sigma}) . \quad (26)$$

Analyzing this expression we note that for the strong scattering regime the periodic properties of the backscattered intensity pattern disappear.

The expressions in Eqs. (21), (24) and (25) represent the backscattering effects resulting from a periodic function with a spatial period $\overline{\alpha}$. Using the above results, the backscattering pattern of the arbitrarily shaped object can be obtained by multiplying these equations by the spectrum of the object function and performing the inverse spectral transform.

## Acknowledgement

This research was supported by The Israel Science Foundation founded by the Israel Academy of Sciences and Humanities

## References:


1. A. G. Vinogradov, Yu. A. Kravtsov, and V. I. Tatarskii, " Amplification effect of backscattering by bodies placed in a medium with random inhomogeneities", Radiophys. and Quantum Electronics, **16**, 818-823, (1973).

2. A. S. Gurvich, and S. S. Kashkarov, "Amplification of scattering in a turbulent medium", Radiophysics and Quantum Electronics, **20**, 794-796, (1977).

3. S. S. Kashkarov, "Amplification of the mean intensity of backscattering in a turbulent atmosphere", Radiophys.and Quantum Electronics, **26**, 36-40, (1983).

4. Y. A. Kravtsov and A. I. Saichev, "Effects of double passage of waves in randomly inhomogeneous media", Sov.Phys.Uspekhi, **25** , 494-508, (1982).

5. Y. A. Kravtsov and A. I. Saichev, "Properties of coherent waves reflected in turbulent medium", J.Opt.Soc.Am.,**A2** , 2100-2105, (1985).

6. V. P. Aksenov and V. L. Mironov, "Phase approximation of the Huygens-Kirchhoff method in problems of reflection of optical waves in the turbulent atmosphere", J.Opt.Soc.Am., **69**, 1609-1619,(1979).

7. E. Jakeman, "Enhanced backscattering through a deep random phase screen", J.Opt.Soc.Am., **A5**,1638-1648,(1988).

8. T. Mavroidis, J. C. Dainty, and M. J. Northcott, "Imaging of coherently illuminated objects through turbulence: plane-wave illumination", J.Opt. Soc.Am.,**A7**, 348-355, (1990).

9. D. N. Ghosh Roy and Gilwon Yoon, "Double-passage recovery of an object embedded in a random medium", Opt. Lett., **17**, 553-555, (1992).

10. T. Mavroidis, J. C. Dainty, "Imaging after double passage through a random screen", Opt. Lett., **15**,857-859, (1990).

11. T. Mavroidis, C. J. Solomon, and J. C. Dainty, "Imaging a coherently iluminated object after double passage through a random screen", J.Opt.Soc.Am. **A8**, 1003-1013, (1991).

12. C. L. Solomon, R. G. Lane, T. Mavroidis, and J. C. Dainty, "Double passage imaging through a random screen using a non-redundant aperture", J. Modern. Opt., **38**, 1993-2008, (1991).

13. A. N. Bogaturov, A. A. D. Canas, J. C. Dainty, A. S. Gurvich, V. A. Mayakin,C. J. Solomon, and N. J. Wooder, "Observation of the enhancement of coherence by backscattering through turbulence", Opt. Comm., **87**, 1-4, (1992).

14. C. J. Solomon and J. C. Dainty, "Use of polarisation in double passage imaging through a random screen", Opt. Comm., **87**, 207-211, (1992).

15. R. Mazar and L. B. Felsen , "Stochastic geometrical theory of diffraction", J.Acoust.Soc.Am.,**86**, 2292-2308, (1989).

16. R. Mazar, "High-frequency propagators for diffraction and backscattering in randommedia", J.Opt.Soc.Am.,**A7**, 34-46, (1990).

17. R. Mazar and A. Bronshtein, "Double passage analysis in random media",Waves in Random Media, **1**, pp.341-362, (1991).

18. R. Mazar and A. Bronshtein, "Multiscale solutions for the high-frequency propagators in an inhomogeneous background random medium", J.Acoust.Soc.Am., **91**, pp.802-812, (1992).

**Invited Paper**

# Wigner Phase Space Distributions and Coherence Tomography

J. E. Thomas, F. Reil, K. F. Lee, A. Wax, and S. Bali

Physics Department, Duke University, Durham, NC 27708-0305

## ABSTRACT

We demonstrate the measurement of path-length-resolved optical phase space distributions as a new framework for exploring the evolution of optical coherence in a turbid medium. This method measures joint transverse position and momentum (i.e., angle) distributions of the optical field, resolved by optical path length in the medium. The measured distributions are related to the Wigner phase space distribution function of the optical field, and can provide complete characterization of the optical coherence in multiple scattering media. Optical phase space distributions are obtained as contour plots which enable a visual as well as quantitative method of characterizing the spatial coherence properties and wavefront curvature of the input and scattered fields. By using a broad-band source in a heterodyne detection scheme, we observe transmission and backscatter resolved by path length in the random medium, effectively providing timing resolution. New two-window heterodyne detection methods permit independent control of position and momentum resolution with a variance product that surpasses the uncertainty limit associated with Fourier transform pairs. Hence, high position and angular resolution can be simultaneously achieved. These techniques may provide new venues for using optical coherence in medical imaging.

**Keywords:** Multiple scattering, turbid media, enhanced backscatter, coherence, Wigner distributions, angular distributions, heterodyne detection, optical coherence tomography, superluminescent diode

## 1. INTRODUCTION

Optical imaging via light scattering offers a wide variety of methods for characterizing changes in tissue structure for early detection and diagnosis of disease [1]. However, light propagating in tissue is subject to severe multiple scattering which limits the ability to image structure. For this reason, many groups have explored the problem of light propagation in highly scattering media [2]. Besides measuring changes in the intensity, time gating has been used to separate ballistic and diffuse scattering components [3]. Also, the change in the polarization of the incident light has been explored as a means of imaging tissue subsurfaces [4]. An important question is whether additional imaging information is available from the spatial *coherence* of the scattered field and how to extract this information.

To address this question, we have developed a general heterodyne method for measuring Wigner phase space distributions which are Fourier transform related to the spatial coherence $\langle \mathcal{E}^*(x)\mathcal{E}(x')\rangle$ of the scattered field $\mathcal{E}(x)$. The measurements determine not only the position distribution of the intensity, but the correlations between the angle and position of the scattered light field. By contrast, OCT (optical coherence tomography) measures only the position dependence of the mean scattered field $\langle \mathcal{E}(x)\rangle$ [5,6]. Analogous to OCT, our method employs a broad-band light source to select the optical path within the scattering medium [7]. Hence, we obtain the depth-resolved correlation between the position and angle of the scattered light to measure the evolution of the optical coherence. Potentially new imaging information is contained in these position-correlated angular distributions.

Angular distributions alone, i.e., position integrated phase space distributions, have already been shown to provide a means of determining cell size distributions and internal structure [8]. Small spatial features yield large angle scattering, while large features yield forward scattering. In lowest order, the angular distribution of the scattered light is related to the spatial structure by the scattering amplitude $f$,

$$f_{\mathbf{k}}(\mathbf{k}') \simeq \frac{k^2}{4\pi}\int \mathbf{dr}\frac{n^2(\mathbf{r})-n_0^2}{n_0^2}\exp[i(\mathbf{k}-\mathbf{k}')\cdot\mathbf{r}] \tag{1}$$

Here, $k = 2\pi/\lambda$ is the wave vector in the medium for the incident light, $n(\mathbf{r})$ is the spatially varying index of refraction within the cell, and $n_0$ is the mean index of the cell cytoplasm. The most significant feature of Eq. 1 is that the shape of the angular distribution is Fourier transform related to the spatial structure. For small angle scattering, $|\mathbf{k}-\mathbf{k}'| = 2k\sin(\theta/2) \simeq k\theta$, and the scale of the scattering angle is then of order $\theta \simeq 1/(kD)$, where $D$ is the size of the spatial feature. Even in the small angle region, where $\theta < 0.1$ rad, the angular distributions

In *Laser-Tissue Interaction XI: Photochemical, Photothermal, and Photomechanical*, Donald D. Duncan, Jeffrey O. Hollinger, Steven L. Jacques, Editors, Proceedings of SPIE Vol. 3914 (2000)
1605-7422/00/$15.00

contain spatial information down to micron and submicron scales. Typical cell sizes are the order of a few tens of microns, and cells contain nearly spheroidal nuclei and other organelles embedded in the cytoplasm that can be distinguished in the angular distribution. For spherically symmetric scatterers, Eq. 1 is readily shown to be equivalent to the Rayleigh-Gans approximation [8]. Normally, the nucleus has a higher index of refraction than that of the surrounding cytoplasm, $n_0$, and is the largest feature in the cell. In cancerous tissue, the nuclei have been known to swell from a normal size of $\simeq$ 5 microns to fill almost the entire cell volume. This leads to a highly forward peaked angular distribution. In epithelial tissue, indirect information on the angular distribution and cell size has been obtained by measuring the wavelength dependence of the scattering cross section. This enables cancerous cells to be distinguished from cells with normal nuclei [9].

While angular distributions have been shown to be quite useful in obtaining information on the spatial structure of cells in epithelial tissue, there is great interest in extending this method to deeper tissue where severe multiple scattering occurs. In many imaging applications, for example, in detection of tumor precursors, it is important to determine both the angular distribution and the location of the scatterers simultaneously, i.e., the optical phase space distribution.

In this paper, we show that optical phase space distributions provide a natural framework for characterizing the propagation of optical coherence in multiple scattering media. In optical phase space measurement, we obtain correlated information about the position at which a light field is measured and the local angle of propagation. As depicted in Fig. 1, the field $\mathcal{E}(x_0)$ measured at position $x_0$ propagates nominally along the **z** direction. The normal to the surface of the wavefront makes an angle $\theta_0$ with the **z** direction. The corresponding transverse momentum (wavevector) $p_0 = \theta_0\, k$, where $k = 2\pi/\lambda$ and $\lambda$ is the optical wavelength. Hence, optical phase space measurement

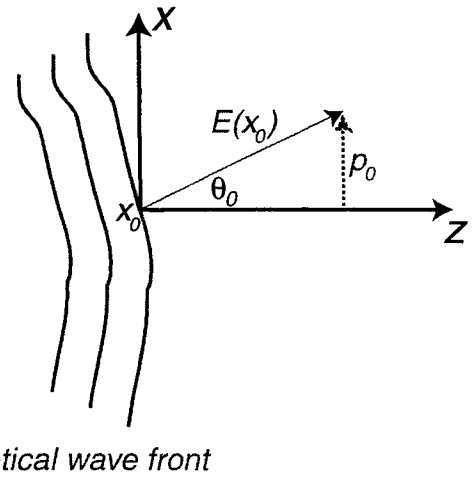


**Figure 1.** Transverse position and transverse momentum measurement.

corresponds precisely to exploring the propagation of spatially localized angular distributions. Using two-window heterodyne detection methods, as described below, we obtain independent control of the position and momentum resolution. This enables simultaneous localization in position and momentum with a variance product that *surpasses* the uncertainty limit associated with Fourier transform pairs. Thus, it is possible to obtain high position resolution while simultaneously maintaining the high angular resolution. By employing low coherence sources, we measure phase space distributions resolved by path length in the medium, effectively providing timing resolution. In applications where joint angle and position information is needed, optical phase space measurement may offer new methods for improving tomographic imaging, such as in tissue differentiation and in suppressing direct backscatter.

Optical phase space distributions are intimately related to Wigner phase space distributions for wave fields which were introduced by Wigner in 1932 [10]. These distributions play a role closely analogous to classical phase space distributions in position and momentum. For a wave field varying in one spatial dimension, $\mathcal{E}(x)$, the Wigner phase

space distribution is given by

$$W(x,p) = \int \frac{d\epsilon}{2\pi} e^{i\epsilon p} \langle \mathcal{E}^*(x+\epsilon/2)\mathcal{E}(x-\epsilon/2)\rangle, \tag{2}$$

where $x$ is the position, $p$ is a wavevector (momentum), and $\langle \ldots \rangle$ denotes a statistical average. It is easy to show that $\int dp\, W(x,p) = \langle |\mathcal{E}(x)|^2 \rangle$, the position distribution of the intensity, and $\int dx\, W(x,p) = \langle |\mathcal{E}(p)|^2 \rangle$, the corresponding momentum distribution. These results suggest that $W(x,p)$ is analogous to a classical phase space distribution in $x$ and $p$. However, Eq. 2 shows that the Wigner distribution is Fourier transform related to the two-point mutual coherence function, and therefore is sensitive to the spatially varying phase and amplitude of the field. Therefore, optical phase space distributions offer an attractive framework in which to study the propagation of optical coherence through random media. In addition, these phase space distributions provide an intuitive, yet rigorous, particle-like description of the underlying wave propagation.

The rest of the paper is organized as follows. We first describe the general heterodyne scheme for measuring optical phase space distributions using a broad band light source. Next, we present path-resolved phase space measurements for transmission through a dense turbid medium. We isolate the contributions of ballistic and low order scattered light. Then, we present phase space measurements for backscattered light resolved by path length in the medium, showing the evolution of the coherent component. Finally, we demonstrate a new two-window detection method which achieves independent control of the position and momentum resolution.

## 2. SCHEME

The scheme of the heterodyne experiments has been described previously [11–13]. In the experiments, Fig. 2, a beam from a coherent or low coherence source is split into an input beam to the sample and a local oscillator (LO) beam that is offset in frequency by 10 MHz using acousto-optic modulation. In our experiments, the source used is

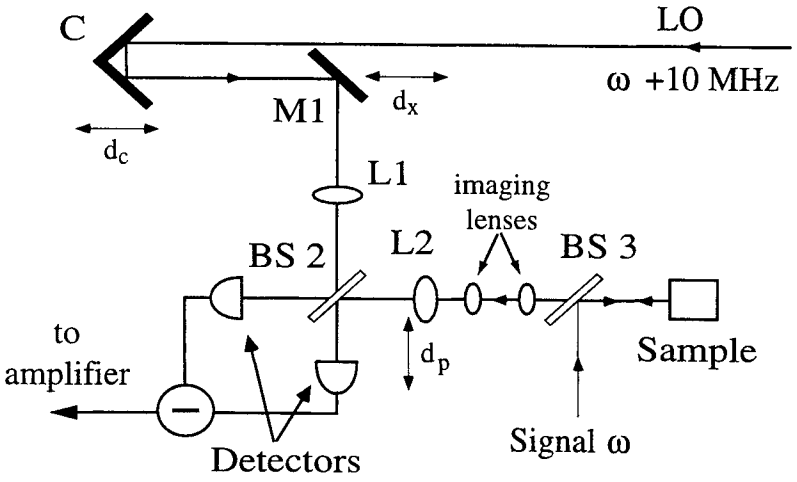


**Figure 2.** Scheme for Heterodyne Measurement of Optical Phase Space Distributions.

a low-coherence superluminescent diode (SLD). The LO and signal beams are each passed through an achromatic input lens (L1 and L2 respectively, $f = 6$ cm) and mixed at a 50-50 beam splitter BS2. Technical noise is suppressed using balanced detection. The rms voltage at 10 MHz is measured with an analog spectrum analyzer.

An important feature of the experiments is that the analog output of the spectrum analyzer is squared using a low-noise multiplier to obtain the mean square voltage at 10 MHz. Hence, the multiplier output is proportional to the power spectrum at 10 MHz. The multiplier output is fed to a lock-in amplifier which effectively subtracts the power spectra with the signal on and off. Thus, electronic noise and LO shot noise power spectra are subtracted in real time and the lock-in output is then directly proportional to the signal power spectrum and hence to the mean square beat amplitude at 10 MHz, $|V_B|^2$.

In order to generate phase space contour plots of the signal field we scan the central position of the LO beam ($d_x$ scan, via translation of M1, for position $x$ information) and the relative angle between the LO and signal beams ($d_p$ scan, via translation of L2, for momentum $p$ information). For a Gaussian LO beam, the position resolution is determined by the diameter of the LO beam while the momentum resolution is limited by the corresponding diffraction angle. Since the LO only detects light scattered into the LO mode, scanning the center position and relative angle of the LO maps out the phase space distribution of the signal field.

Since a low coherence source is used, the LO and signal optical paths must be equal within the coherence length of the source. In this case, the position of a corner mirror C is adjusted by $d_c$ to maintain the relative path length between the LO and signal beams as the mirror M1 is scanned. In addition, it is not difficult to show that as the lens L2 is scanned over a distance $d_p$, the path length of the signal arm to the detectors changes. In this case, to maintain a fixed optical path difference $\Delta L'$ between the LO and signal arms, $d_c$ must be precisely adjusted so that $\Delta L' = 2d_c - d_x + d_p^2/(2f) - d_x d_p$ has a constant value [13]. Adjustment of the corner mirror position $d_c$ is accomplished using a precision computer controlled translator which has 50 nm resolution.

From a theoretical standpoint it is important that the mean square beat amplitude $|V_B|^2$ can be written in terms of the spatial overlap of the LO and signal Wigner distributions [11,12]. In one dimension, one has

$$|V_B|^2(d_x, d_p) \propto \int dx\, dp\, W_{LO}(x - d_x, p + k\, d_p/f)\, W_S(x,p). \tag{3}$$

Here, $x$ is a transverse position and $p$ is a transverse wavevector, and $k = 2\pi/\lambda$. The fields are measured in the planes of the input lenses L1 and L2. From Eq. 3, we see that the mean square beat signal is the convolution integral of the LO and signal field Wigner phase space distributions. Hence, the mean square beat signal that is obtained in real time in the experiments is a *smoothed* Wigner distribution [11]. $W_S$ is measured over a range in position of $\pm 1$ cm, and over a range in momentum of $\pm 300$ mrad. A phase space contour plot of this smoothed phase space distribution is obtained by measuring the beat intensity as a function of the shift in the center of the LO phase space distribution. This contour plot yields information about the Wigner phase space distribution, $W_S(x,p)$, of the signal beam.

## 2.1. Path-Length-Resolved Optical Phase Distributions for Transmitted Light

For transmission measurements, the beamsplitter BS3 in Fig. 1 is omitted and the signal beam is transmitted directly through the sample. As described below, the two imaging lenses take the Wigner distribution of the light emerging from the output plane of the sample and reproduce it in the measurement plane of lens L2.

We have measured the optical phase space distribution for the field transmitted through a turbid medium consisting of latex microspheres (n=1.59) in a mixture of 25% glycerol and 75% water [14]. This mixture is chosen to produce neutral buoyancy for the microspheres. The index of refraction for the medium ($n_0 = 1.36$) results in a relative refractive index of 1.17 for the latex microspheres compared to the medium. Large spheres are specifically selected to give highly forward peaked scattering. The spheres used in this experiment have a radius of 4.9 $\mu$m. The Mie solution for the above parameters gives a total scattering cross section $\sigma_S$ that is 2.3 times the geometrical cross section, i.e., $\sigma_S = 181\,\mu\text{m}^2$. It is assumed that there is no absorption.

At high concentrations of scatterers ($\rho \geq 1.5 \times 10^7/\text{cm}^3$), the magnitude of the scattered intensity transmitted through the sample becomes greater than that for the ballistic light. In propagating through the sample, which is 1 cm thick, the ballistic light is attenuated by a factor of $e^{-27.2}$ for this concentration. While the ballistic light is still present, it has a peak magnitude lower than that of the scattered light. In the experiments, the input power is a fraction of a milliwatt and the detection sensitivity is less than $10^{-16}$ W.

Fig. 3 shows the measured optical phase space distributions for two different path delays. When the LO and signal paths are matched to within the coherence length of the source $\Delta L' = 0$, we can see the distribution is dominated by the ballistic light indicated by the arrow in Fig. 3(a). By introducing a delay of 100$\mu$m in the LO path, we see that low order scattered light dominates the contour plot (Fig. 3(b)).

Fig. 3 shows that the high sensitivity of the detection method and the high angular and position resolution enable isolation of the ballistic and low order scattered components of the phase space distribution. The ballistic component exhibits a phase space distribution similar to that of the input beam. By contrast, even for small changes in the optical path from that of ballistic light, the phase space contour broadens. However, the 50 mrad angular

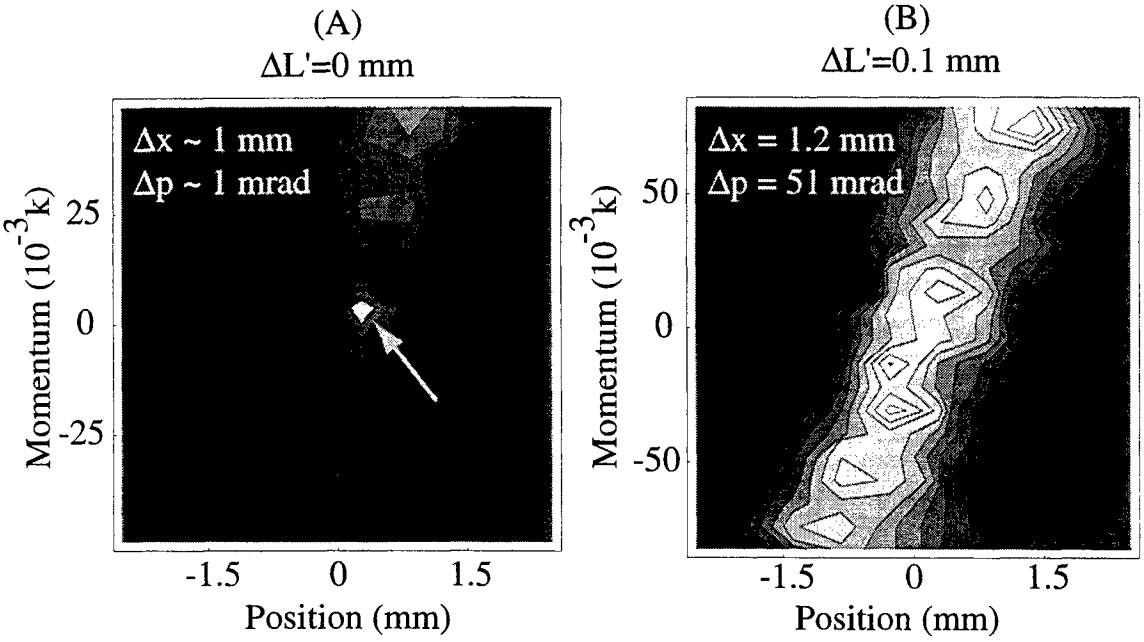


**Figure 3.** Measured optical phase space distributions (x,p) at fixed LO path delay. (a) $\Delta L' = 0$ (b) $\Delta L' = 0.1$ mm concentration $\rho = 1.5 \times 10^7/\text{cm}^3$

resolution demonstrated in Fig. 3(b) would still be useful for resolving angular distributions from localized scatterers. Note that the slope of the phase space plot in Fig. 3 (b) is a result of wavefront curvature for light diverging from a localized source: As the input beam propagates through the medium, light scattered with positive (negative) transverse momentum emerges from the medium shifted to the right (left) in position.

### 2.2. Path-Length-Resolved Optical Phase Space Distributions for Enhanced Backscatter

We have also obtained phase space distributions for backscattered light. For this case, the heterodyne set-up is configured to measure optical phase space distributions for partially coherent light backscattered from a turbid sample, Fig. 2 . The low-coherence light in the signal arm at center frequency $\omega$ is directed to the turbid medium by a beamsplitter BS3. The light scattered by the sample in the reverse direction passes through the beamsplitter BS3 to lens L2 through a standard 4f imaging lens system [15]. This system enables measurement of the Wigner distribution of the backscattered light at the input plane of the medium. Thus, the phase space distribution of the backscattered light can be mapped out in position and momentum for various path lengths (i.e., various penetration depths, or propagation times) in the medium, by scanning M1, L2 and C in conjunction.

It is important to know the coherence properties of the partially coherent source beam itself as a reference against which to compare the backscattered light [16]. We measure the optical phase space distribution for the source simply by replacing the sample with a mirror. Thus, using the same heterodyne set-up, we can obtain quantitative information on the spatial and longitudinal coherence of the source beam, as well as its wavefront curvature [13]. Using this method we obtain the following beam parameters for the SLD light source: beam width 0.9 mm, transverse coherence length 4 mm, wavefront curvature 480 mm. In extracting these values from the data we assume the low-coherence beam is described by a Gaussian-Schell model [17].

Optical phase space distributions were measured for light backscattered from the turbid sample, for LO path delays $\Delta l'$ ranging from 0 to 1 mm. Here, $\Delta l' \equiv 0$ corresponds to the input face of the sample, where the path length in the medium is zero. Fig. 4 (a) shows the measured optical phase space distribution for a path length in the medium of $\Delta l'/n_0 = 7\,\mu$m which is less than the longitudinal resolution for our source. Figures 4 (b) and (c) show the corresponding distributions for $\Delta l'/n_0 = 0.15$ mm and 0.44 mm, respectively. A distinct variation is observed in Figures 4 (a-c). For the longer path delays, the momentum distribution of the central coherent component

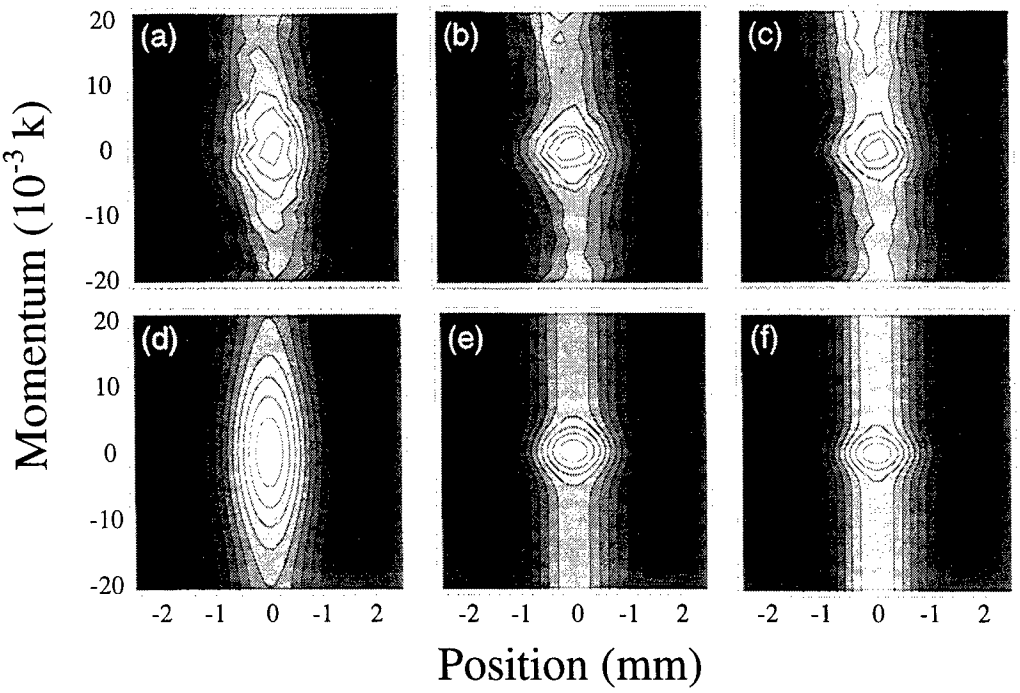


**Figure 4.** Optical phase space distributions for enhanced backscattering for different path lengths in a random medium. The path length is given by $\Delta l'/n_0$, where $\Delta l'$ is the path delay between the LO and signal beams and $n_0 = 1.36$ is the mean refractive index: (a,b,c) shows the measured distributions for $\Delta l'/n_0 = 7\,\mu$m, 0.15 mm, and 0.44 mm, respectively. (d,e,f) show the corresponding predictions using our model. (Momentum given in units of the optical wavevector, $k = 2\pi/\lambda$).

narrows and a bright spot appears localized at zero transverse momentum and zero position. This is the enhanced backscattering peak. The gray bands extending in momentum correspond to the diffuse background.

We model the optical phase space distributions by calculating the mean square beat amplitude $|V_B|^2$, Eq. 3, using an approximate Wigner function of the backscattered light. We assume a diffusion approximation for the propagation probability and include contributions to the field from self-interfering and time-reversed paths. This theoretical model will be described in a future publication. Using the parameters obtained for the source yields the predictions shown in Fig. 4 (d,e,f). The model is found to be in good agreement with the data except for the shortest delays, where the diffusion approximation for the propagation probability breaks down.

### 2.3. Two-Window Detection Methods

A deficiency of the optical phase space method described in the previous sections is that the position and momentum resolution are not independent: The position resolution is determined by the LO beam diameter $w$ while the angular resolution is constrained to be $\lambda/(\pi w)$ and can not be independently controlled. Hence, we measure Wigner distributions that have been smoothed by the phase space resolution of the LO. To measure "true" Wigner distributions, we require $w << d$ to accurately measure spatial features of size $d$, as well as $\lambda/(\pi w) << \lambda/(\pi d)$ to measure the corresponding angles.

To solve this problem, we replace the single Gaussian LO field in our heterodyne scheme by a *phase coherent* superposition of two fields: One is a focused Gaussian beam of width $a << d$ and the other is a collimated beam of width $A >> d$ [18]. This method exploits the use of multiple detection windows to *surpass the uncertainty limit* for Fourier transform pairs [19]. The LO field is

$$\mathcal{E}_{LO}(x) = \mathcal{E}_0 \left[ \exp\left(-\frac{x^2}{2a^2}\right) + \beta \exp\left(-\frac{x^2}{2A^2}\right) \exp(i\theta) \right]. \tag{4}$$

In this case, the phase ($\theta$)-dependent part of the Wigner function for the LO takes the form

$$W_{LO}(x,p) \propto \exp\left(\frac{2x^2}{A^2} - 2a^2p^2\right) \cos(2xp+\theta) \simeq \cos(2xp+\theta), \tag{5}$$

where the last form assumes that the range of the momentum and position integration in Eq. 3 is limited by the Wigner distribution of the signal field.

In the experiments, the LO field is obtained by combining on a beam splitter two fields of widths $a$ and $A$, which differ in frequency by 5 kHz, so that $\theta = (2\pi \times 5 \text{ kHz})\ t$. One output of the beam splitter is used to phase lock the 5 kHz beat to the reference channel of a lock-in amplifier. As in our previous method, the rms beat amplitude is measured with an analog spectrum analyzer with a bandwidth of 100 kHz centered at 10 MHz. The output of the spectrum analyzer is squared in real time with a low noise multiplier, the output of which is sent to the lock-in amplifier. Substituting Eq. 5 into Eq. 3 we find that the lock-in outputs for the in- and out-of-phase quadratures then directly determine the real and imaginary parts of the quantity

$$\begin{aligned} S(x_0,p_o) &= \int \frac{dx'\,dp'}{\pi} \exp[2i(x'-x_o)(p'-p_0)]\, W_S(x',p') \\ &= \langle \mathcal{E}^*(x_0)\,\mathcal{E}(p_0)\rangle \exp(ix_0p_0). \end{aligned} \tag{6}$$

Here $x_0 = d_x$ is the center position of the LO fields and $p_0 = -k\,d_p/f$ is the center momentum.

Eq. 6 is readily inverted to yield the Wigner function of the signal field by a linear transformation. Using the reality of $W_S(x,p)$, we obtain

$$\begin{aligned} W_S(x,p) &= \int \frac{dx_o\,dp_0}{\pi} \cos[2(x-x_0)(p-p_0)]\, S_R(x_0,p_0) \\ &+ \int \frac{dx_o\,dp_0}{\pi} \sin[2(x-x_0)(p-p_0)]\, S_I(x_0,p_0). \end{aligned} \tag{7}$$

$S_R$ and $S_I$ are the real and imaginary parts of Eq. 6, i.e., the in- and out-of-phase quadrature signals which are simultaneously measured, as shown in Fig. 5 below.

Using a coherent He-Ne source, we have generated an LO field with $a = 200\,\mu$m and $A = 5$ mm. First, we measure the $x-p$ correlation function and recover the Wigner distribution for a Gaussian signal beam of 1/e width 0.85 mm. The simultaneously measured spatial and momentum widths agree with predictions to within 5%, clearly demonstrating independent control of the position and momentum resolution. Further, the theoretical and experimental Wigner distributions are in excellent agreement.

Fig. 5 shows the experimental and theoretical $x-p$ correlation function obtained for the same Gaussian signal beam, blocked in the center by a $d = 1$ mm wire in the plane of the input lens L2 of Fig. 2. The real and imaginary parts of the $x-p$ correlation function, Fig. 5 (a,b) clearly show the wire, and exhibit positive and negative regions in phase space demonstrating the phase sensitivity. Note that the recovered Wigner phase space distribution (c) exhibits *negative* regions, in agreement with predictions. The period of the oscillation as a function of $p$ bears a Fourier transform relation to the diameter $d$ of the wire. The negative region assures that the position distribution $|\mathcal{E}(x)|^2 = \int dp\, W(x,p)$ is zero for $|x| < d/2$ as it should be.

Currently, we are employing the two-window method with a broad band light source to measure path-length resolved Wigner distributions for enhanced backscatter. This method will enable spatial resolution smaller than a single coherence area with adequate momentum resolution to fully resolve the angular distribution.

## 3. CONCLUSIONS

We have demonstrated heterodyne measurement of path-length-resolved optical phase space distributions for light transmitted through and backreflected from a multiple scattering medium. The heterodyne method permits a broad band source to be used which has a short longitudinal coherence length. This provides a simple means of obtaining very high effective timing resolution ($\leq$ 20 fs with a 40 nm bandwidth) for selection of optical path-lengths in the medium. We have demonstrated that the heterodyne method has a dynamic range of thirteen orders of magnitude and subfemtowatt sensitivity.

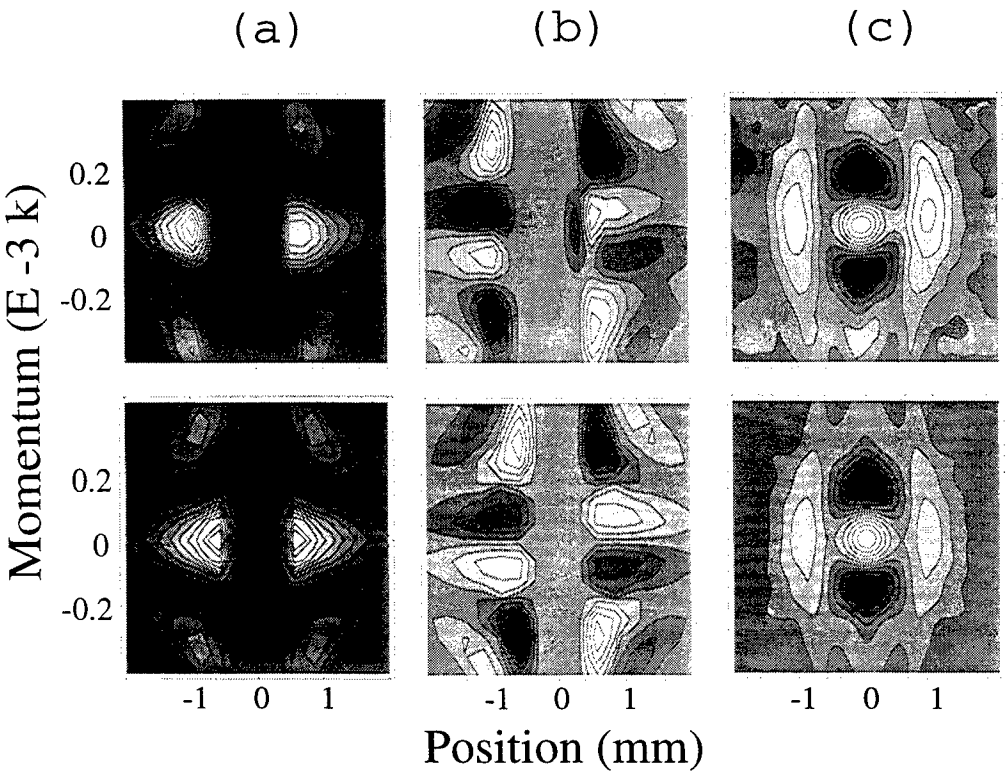


**Figure 5.** Measured (Top) and theoretical (Bottom) $x - p$ correlation function for a Gaussian beam blocked in the center by a 1 mm diameter wire. a) Real part; b) Imaginary part; c) Recovered Wigner distribution. Note that black regions denote negative values.

The measured optical phase space distributions provide a visual as well as quantitative technique to study the evolution of optical coherence as it propagates in a random medium. The same method is used to characterize quantitatively the coherence properties of both the source and scattered fields, enabling detailed comparison between theory and experiment. By using two-window heterodyne detection methods and a broad band source for path-length-selection, it will be possible to measure Wigner phase space distributions for localized spatial regions which are smaller than a single coherence area. In this case, new theoretical insights may be required to describe the measurements.

The phase space data show the importance of joint position and angular measurement for isolating the contributions of ballistic and low order scattered light. These components are useful for imaging since they retain relatively narrow angular distributions after propagation. In highly scattering media, where the ballistic component is highly attenuated, path-length-resolved low order scattered light may be used to measure the angular scattering characteristics of spatially localized cells. This may be important for sensitive detection of diseased tissue. However, further study is required to understand how path-length-selection modifies the measured angular distributions.

## ACKNOWLEDGMENTS

This research has been supported by the National Institute of Health and in part by the National Science Foundation.

## REFERENCES

1. J. C. Hebden, S. R. Arridge, and D. T. Delpy, Phys. Med. Biol. **42**, 825-840 (1997).
2. See for example, R. R. Alfano, S. G. Demos, S. K. Gayen, Ann. NY Acad. Sci., **820**, 248 (1997), and references therein.

3. K. M. Yoo, F. Liu, and R. R. Alfano, Phys. Rev. Lett. **64**, 2647 (1990).
4. S. L. Jacques and L. Kenneth, Proc. SPIE **3245**, 356-362 (1998).
5. A. F. Fercher, "Optical Coherence Tomography," *J. Biomed. Opt.* **1**, 157-173 (1996).
6. J. A. Izatt, M. D. Kulkarni, K. Kobayashi, M. S. Sivak, J. K. Barton, and A. J. Welch, "Optical Coherence Tomography for Biodiagnostics," *Optics and Photonics News* **8** (5), 41-47, 65 (1997).
7. Heterodyne imaging with broad band light in a random medium has been demonstrated by A. Schmidt, R. Corey, and P. Saulnier, Opt. Lett. **20**, 404-406 (1995).
8. J. Beuthan, O. Minet, J. Helfmann, M. Herrig, and G. Muller, Phys. Med. Biol. **41**, 369 (1996).
9. L. T. Perelman, V. Backman, M. Wallace, G. Zonios, R. Manoharan, A. Nusrat, S. Shields, M. Seiler, C. Lima, T. Hamano, I. Itzkan, J. Van Dam, J. M. Crawford, and M. S. Feld, Phys. Rev. Lett. **80**, 627 (1998).
10. E. P. Wigner, "On the quantum correction for thermodynamic equilibrium," Phys. Rev. **40**, 749-759 (1932).
11. A. Wax and J. E. Thomas, Opt. Lett. **21**, 1427 (1996).
12. A. Wax and J. E. Thomas, J. Opt. Soc. A **15**, 1896 (1998).
13. A. Wax, S. Bali, and J. E. Thomas, Opt. Lett. **24**, 1188 (1999).
14. See erratum, A. Wax and J. E. Thomas, Proc. of SPIE **3598**, 2-9 (1999); ibid **3726**, 494-501 (1999).
15. C. Scott, *Introduction to Optics and Optical Imaging* ( IEEE Press, Piscataway, NJ, 1998), pp. 310.
16. Characterization of different broad band sources is demonstrated in A. Wax, S. Bali, G. A. Alphonse, and J. E. Thomas, J. Biomed. Opt. **4**(4), 482-489 (1999).
17. L. Mandel and E. Wolf, *Optical Coherence and Quantum Optics* (Cambridge University Press, New York, 1995).
18. K. F. Lee, F. Reil, S. Bali, A. Wax, and J. E. Thomas, Opt. Lett. **24**, 1370 (1999).
19. L. Cohen, *Time-Frequency Analysis* (Prentice Hall PTR, Englewood Hills, NJ, 1995).

Invited Paper

# Propagation of the optical Wigner function in random multiple-scattering media

M. G. Raymer and Chung-Chieh Cheng

Oregon Center for Optics and Department of Physics

University of Oregon, Eugene, OR 97403

## ABSTRACT

The transverse spatial coherence of light evolves as the light traverses a random, multiple-scattering medium. For near-forward scattering, the wave-transport process can be described by a wave-transport equation for the spatial-angular Wigner function of the light, which is related to the spatial coherence function. Using a novel variable-shear Sagnac interferometer, we measured the Wigner function of initially coherent light after propagation through a multiple-scattering medium. We find good agreement between the wave-transport theory and the experimental results.

**Keywords:** optical coherence, Wigner function, multiple scattering, shearing interferometer

## 1. INTRODUCTION

The transport of light in random, multiple-scattering dielectric media occurs in a wide variety of physical situations. Of special interest in recent years is the transport of light in biological tissue, since this forms the basis of a variety of optical imaging techniques that are playing an increasing role in medical diagnostics.[1]

A crucial aspect of this problem is the spatial coherence properties of light that has been multiply scattered while traveling through a dense random medium. While it has been long recognized that such coherence lies at the base of any theoretical approaches to understanding propagation in such media,[2,3] there has not been until recently a reliable method by which to measure directly the spatial coherence properties of the optical field. With the development of phase-space tomography,[4] and more recently Sagnac variable-shearing interferometry [5,6,7] and heterodyne detection schemes, [8] such measurements are now providing new information about optical transport.[7,8]

Here we review our recent efforts to test quantitatively a proposed transport equation for the spatial Wigner function (WF) of a light beam in a random dielectric. We find that this transport theory is quite robust. Within the range of our tests it properly models the evolution of the Wigner function and the two-point spatial coherence function (SCF) of light propagating in a near-forward scattering medium over a distance of up to 13 optical mean-free paths. Moreover, when applied to light propagating through a thin medium, of order of one mean-free path in length, the transport theory correctly explains the rather complicated observed form of the SCF. [7] This transport theory has also been subjected to various tests by the group of J. Thomas.[8]



In *Laser-Tissue Interaction XI: Photochemical, Photothermal, and Photomechanical*, Donald D. Duncan, Jeffrey O. Hollinger, Steven L. Jacques, Editors, Proceedings of SPIE Vol. 3914 (2000)
1605-7422/00/$15.00

We discuss a way in which measurements of the transmitted Wigner function (Fourier transform of the SCF) might be used for reconstruction of the interior structure of a random medium. The basic idea is that transport of the WF is more fundamental than transport of the corresponding specific intensity. The specific intensity (energy flux per unit area per solid angle) is the quantity that appears in conventional radiometry and optical energy transport theory. [3] The conventional Boltzmann transport equation for specific intensity is the basis of recent experimental medium reconstruction techniques based on photon-transport.[9] Nevertheless, this approach is limited in that it averages over the coherence (or phase) properties of the light, thereby throwing away potentially useful information. The conventional approach is a special case of our more general approach. Our approach, based on transport of the WF, contains more information about the medium than does the conventional transport approach. As such, reconstruction techniques based on the WF transport may be able to provide better constrained inverse solutions for determining the interior structure of a medium. Such a scheme was proposed by our group [10] and independently by the group of S. John,[11] who also pointed out the importance of the nonlocal nature of wave transport, a point we do not consider here.

We first point out that the specific intensity is a theoretical quantity that does not obey a fundamental transport equation, contrary to conventional wisdom. Derivations of the conventional Boltzmann transport equation for specific intensity follow a heuristic, phenomenological approach. The specific intensity $I(\vec{r},\hat{k})$ is, by definition, a positive quantity [12,13]:

$$I(\vec{r},\hat{k}) = \frac{d^2\Phi}{d\Omega \; dA_S \; \cos\theta} \quad , \tag{1}$$

with units of $Wm^{-2}sr^{-1}$. $dA_S$ is a surface area element in space located at position $\vec{r}$ which radiates an energy flux $d\Phi$ into an element of solid angle $d\Omega$ pointing in the $\hat{k}$-direction ($|\hat{k}| = 1$). The angle between $\hat{k}$ and the unit vector $\hat{n}$ normal to the surface $dA_S$ is $\theta$ $(0 \le \theta < \pi/2)$. The wave uncertainty relation, $dA_S \cdot d\Omega \ge \lambda^2$ (where $\lambda$ is wavelength), prevents simultaneous existence of the limits $dA_S \to 0$ and $d\Omega \to 0$. Therefore the specific intensity is in fact not a well-defined quantity according to standard calculus. It must be viewed as a coarse-grained quantity which only approximately obeys the conventional Boltzmann transport equation (which itself breaks down when a significant degree of coherence is present in the light). This raises the question, "What is the more fundamental quantity that is averaged over in phase space in order to yield the specific intensity?" This fundamental quantity is the Wigner function.

## 2. WIGNER FUNCTION AND ITS TRANSPORT EQUATION

The Wigner function (WF) is a quasi-distribution representing simultaneous position and angle information about the light flux. Because such a concept cannot be rigorously defined due to the wave nature of light, as we noted above, the WF must be a quasi-distribution rather than a true distribution. As such, it may take on negative values.

The WF is defined by a Fourier transform of the spatial coherence function (SCF), which is related to the mutual coherence function. The SCF is given by

$$\Gamma(\vec{x}_\perp, \vec{s}_\perp, z) = \langle E(\vec{x}_\perp + \vec{s}_\perp/2, z)\, E^*(\vec{x}_\perp - \vec{s}_\perp/2, z) \rangle, \tag{2}$$

where $E(\vec{x}_\perp;z)$ is the scalar electric field and the bracket indicates an ensemble average over all possible realizations of $E(\vec{x}_\perp;z)$, each being associated with a particular configuration of the environment, which is subject to spatial and/or temporal fluctuations. Here we consider only time-independent fields for simplicity, and denote a spatial location by $(\vec{x}_\perp;z)$, where $z$ is the propagation axis and $\vec{x}_\perp=(x,y,0)$ is the transverse position vector.

The transverse WF is given by the 2-D Fourier transform

$$W(\vec{x}_\perp,\vec{k}_\perp,z)=\int\frac{d^2s_\perp}{(2\pi)^2}\exp(-i\vec{s_\perp}\cdot\vec{k}_\perp)\ \Gamma(\vec{x}_\perp,\vec{s}_\perp,z), \tag{3}$$

where $\vec{k}_\perp=(k_x,k_y,0)$ is interpreted as the transverse k-vector. The WF is analogous to a joint density function for spatial and angular energy densities, as can be seen by considering its marginal integrals:

$$\int W(\vec{x}_\perp,\vec{k}_\perp,z)d^2k_\perp=\Gamma(\vec{x}_\perp,0,z)=\left\langle\left|E(\vec{x}_\perp;z)\right|^2\right\rangle, \tag{4}$$

which is the spatial energy density, and

$$\int W(\vec{x}_\perp,\vec{k}_\perp,z)d^2x_\perp=\left\langle\left|\tilde{E}(\vec{k}_\perp;z)\right|^2\right\rangle, \tag{5}$$

which is the angular energy density [$\tilde{E}(\vec{k}_\perp;z)$ is the 2-D Fourier transform of $E(\vec{x}_\perp;z)$].

For a medium composed of randomly distributed, discrete scatterers embedded in an otherwise homogeneous medium, an approximate transport equation for the WF has been proposed. [8,11,14] It reads

$$\left(\mathrm{v}\partial_z+\frac{\mathrm{v}}{k}\vec{k}_\perp\cdot\nabla_{\vec{x}_\perp}\right)W(\vec{x}_\perp,\vec{k}_\perp;z)=\int d^2\vec{k'}_\perp\,\tilde{F}(\vec{k}_\perp-\vec{k'}_\perp)W(x_\perp,\vec{k'}_\perp;z)\ , \tag{6}$$

where v is the speed of light in the medium, and

$$\tilde{F}(\Delta\vec{k}_\perp)=-\mathrm{v}\mu_T\,\delta^2(\Delta\vec{k}_\perp)+\frac{\mathrm{v}N}{k^2}\frac{d\sigma(\Delta\vec{k}_\perp)}{d\Omega} \tag{7}$$

and $d\sigma(\vec{k}_\perp-\vec{k'}_\perp)/d\Omega=\left|f(\vec{k}_\perp-\vec{k'}_\perp)\right|^2$ is the differential scattering cross section of a single discrete scattering object in the medium, for scattering from $\vec{k'}_\perp$ to $\vec{k}_\perp$, and $f(\vec{k}_\perp-\vec{k'}_\perp)$ is the corresponding scattering amplitude. The number density of scatterers is $N$. The total, angle-integrated scattering cross section (plus any absorption present) is incorporated into the attenuation coefficient $\mu_T$.

Equation (6) is identical in form to the Boltzmann transport equation of conventional optical transport theory. This strengthens our earlier identification of the WF as a quasi-joint density function. The main difference between these two formalisms is in the important fact, mentioned above, that the WF is related directly to the spatial coherence function, which represents the wave-like properties of the

light. In contrast, the specific intensity contains no direct wave information. One may, therefore, refer to Eq.(6) as a wave transport equation.

Equation (6) is, in general, difficult to solve. However, if one considers the situation where the light field is scattered through only small angles by the random medium, then most of the scattered light propagates in the near-forward direction. This may be call generically near-forward scattering (snake-light scattering [15]). In this case one can assume that the light scattered into large angles is weak compared to the near-forward light, and the correlation between the near-forward light and the wide-angle light is weak. Then the WF of the total light field and the integral kernel can be separated approximately into two parts:

$$W \approx W_N + \eta W^{(1)} \quad , \qquad \tilde{F} \approx \tilde{F}_N + \eta \tilde{F}^{(1)} \tag{8}$$

where $W_N$ and $\tilde{F}_N$ are the near-forward parts, $\eta$ is a small perturbation parameter and $W^{(1)}$, $F^{(1)}$ are the first-order corrections corresponding to the wide-angle scattering. Then Eq.(6) can be separated into a zero-order (in $\eta$) equation, i.e.,

$$\left( \mathrm{v}\partial_z + \frac{\mathrm{v}}{k}\vec{k}_\perp \cdot \nabla_{\vec{x}_\perp} \right) W_N(\vec{x}_\perp, \vec{k}_\perp; z) = \int d^2\vec{k}'_\perp \, \tilde{F}_N(\vec{k}_\perp - \vec{k}'_\perp) W_N(x_\perp, \vec{k}'_\perp; z) \quad , \tag{9}$$

and a set of higher-order equations.[16] The angular range within which this approximation is valid is somewhat arbitrary, as long as it is sufficiently narrow. We find it convenient to define this angle as being equal to the collection angle of our optical system. This angle is several times wider than the angular width of the main forward peak in the scattering cross section, for the particular type of medium we use (see below).

The differential scattering cross section of a single spherical object in the medium is evaluated numerically using Mie theory. The near-forward part of the Mie differential scattering cross section can be approximated by a Gaussian function with respect to the angle [8,17]:

$$\left(\frac{d\sigma}{d\Omega}\right)_N \approx \frac{\sigma_N}{\pi\theta_0} \exp\left[ -\left|\Delta\vec{k}\right|^2 / \left(k^2\theta_0^2\right) \right] \quad , \tag{10}$$

where $\left|\Delta\vec{k}_\perp\right| = \left|\vec{k}_\perp - \vec{k}_\perp'\right| \approx k\sin\theta \approx k\theta$ is the magnitude of the change of transverse wave vector, and $\theta_0$ is the 1/e half-width estimated from the Mie cross section. We take the scattering cross section $\sigma_N$ into the near-forward angles to equal the Mie cross section integrated over the collection angle $\theta_C$ (= 140 mrad) of our optical system.

The transport equation (9) can be solved in integral form to yield, in terms of the SCF, [2, 8]

$$\begin{aligned} \Gamma(\vec{x}_\perp, \vec{s}_\perp, z) = \int d^2\vec{q} \exp[i\vec{q}\cdot\vec{x}_\perp] \exp\left[ \frac{-1}{\mathrm{v}} \int_0^z dz' \, F_N\left(\vec{s}_\perp - \vec{q}(z-z')/k\right) \right] \bullet \\ \bullet \int \frac{d^2\vec{x}'_\perp}{(2\pi)^2} \exp[-i\vec{q}\cdot\vec{x}'_\perp] \Gamma(\vec{x}'_\perp, \vec{s}_\perp - \vec{q}z/k, 0) \end{aligned} \quad , \tag{11}$$

where $F_N$ is defined as the Fourier transform of Eq.(7), using Eq.(10). The WF is obtained by inserting this solution into Eq.(3).

In our experiments we used as the input light field a collimated Gaussian beam,

$$E(\vec{x}_\perp, z=0) = \sqrt{\frac{1}{\pi a^2}} \exp\left[-\left|\vec{x}_\perp\right|^2 / 2a^2\right] , \tag{12}$$

with a beam width $a = 140\mu m$. This determines the form of the boundary condition $\Gamma(\vec{x}_\perp, \vec{s}_\perp, 0)$. Below we use Eq.(11) to predict the WF from the transport theory and compare it with results from our experiments.

## 3. VARIABLE-SHEAR SAGNAC INTERFEROMETER

To record the WF of a light wave following propagation through a multiple-scattering medium, we have designed and constructed an improved version of a variable-shear, common-path (Sagnac) interferometer, first introduced by Iaconis and Walmsley.[5] We have improved the design of the interferometric imaging system so that it can measure a complex SCF with greater light collection efficiency than in the previous design, with no additional astigmatism introduced by the shearing operation. The main innovations are the use of a free-space shearing method, a telescopic imaging system, and a four-phase-shifting method for acquiring the data. These are described in detail in [7].

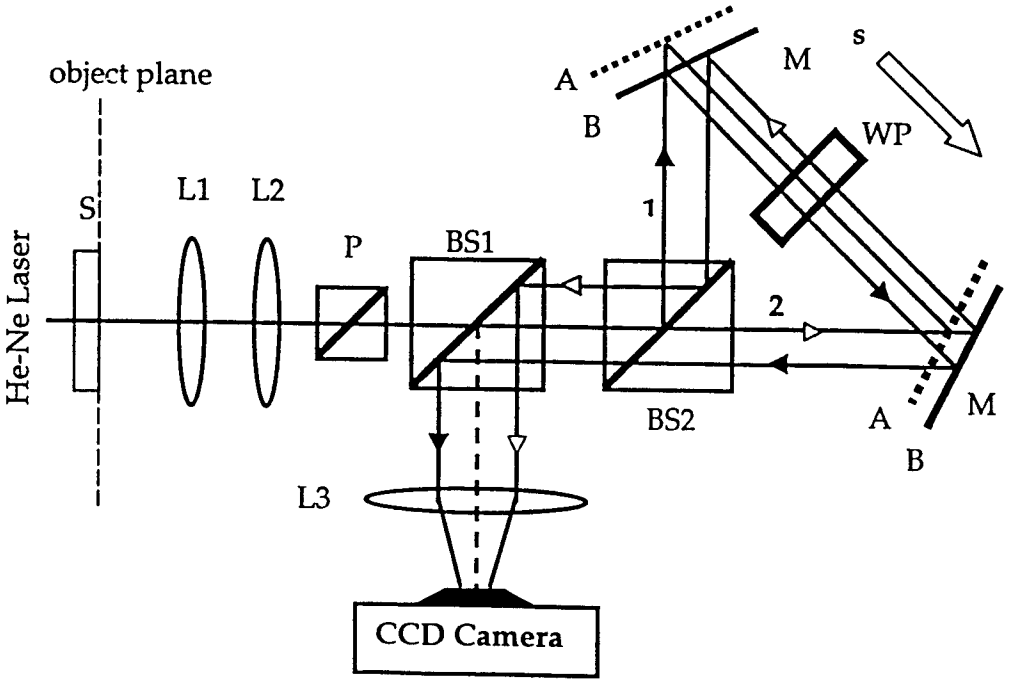


Figure 1. The shearing Sagnac interferometer measures the SCF of the light at the object plane. S: Scattering medium or source, BS: nonpolarizing 50/50 beam splitters, M: Mirror, P: Polarizer, L: Lens, WP: Wave plate set.

Figure 1 shows our system. Light from the sample or source (S) leaves the object plane, is collected by lenses L1, L2, then is linearly polarized by a polarizing cube (P), and passes through a nominal 50/50 non-polarizing beam splitter (BS1) before entering the Sagnac interferometer through the second beam splitter (BS2). The light is equally split into clockwise- and counterclockwise-travelling beams, which undergo shears of equal magnitude, but opposite sign, before recombining at BS2, where interference takes place. After reflecting partially from BS1 the light is imaged onto the CCD camera where its interferogram is recorded.

In our design the shears are introduced by moving a pair of mirrors (M) parallel to the propagation axis of the middle portion the triangular ring. Figure 1 illustrates the mirrors moving from a position "A" to position "B" by a common translation stage and the subsequent optical paths followed by a single ray in the two cases. This free-space shearing introduces no additional astigmatism.

A phase shift between the two sheared beams is introduced by using the wave-plate set (WP), shown in Figure 1, to perform phase-shifting interferometry. The basic concept is to orient the polarization directions of the two counter-propagating beams inside the triangular ring so one beam passes with its polarization parallel to the fast axis of the wave plate, and the other beam passes with polarization parallel to the slow axis. In this way four different phase shifts between the beams are introduced in turn, the interferograms for each are recorded, and pixel-by-pixel computations on the interferograms are performed afterwards in order to extract the SCF.[7] The WF is then obtained from the SCF by a simple fast Fourier transform.

## 4. MEASUREMENT OF WIGNER FUNCTION OF MULTIPLY SCATTERED LIGHT

To study the Wigner function (WF) of light we used a linearly polarized, continuous-wave He-Ne laser ($\lambda = 632.8nm$) as the source of input light to a medium composed of polystyrene microspheres (mean diameter 46 $\mu m$, standard deviation 0.64 $\mu m$, refractive index = 1.59) suspended in a solidified gelatin/water mixture ($n_0$=1.42) between two glass plates. This leads to a Mie cross section with $\theta_o$ = 5.8 mrad. The ensemble averaging of spatial configurations was achieved by moving the sample transversely over a range $\pm$5mm while collecting data over a long CCD camera exposure.

To investigate how the coherence properties of the light change with depth into a medium, we kept the volume fraction (VF) of the microsphere suspension at 2% and changed the thickness of the medium. The characteristics of a scattering medium can be specified by the optical distance (OD), which equals $\mu_T L$, where $\mu_T$ is the total extinction coefficient of the ballistic (unscattered) beam, and $L$ is the thickness of the medium [18]. We studied four cases: L = 0.1 cm, 0.3 cm, 0.5 cm and 1 cm, and the corresponding OD at 2% VF are 1.34, 4.02, 6.70, and 13.4, respectively. In a non-absorptive medium, $\mu_T \approx \mu_S$, where $\mu_S$ is the total elastic scattering coefficient. The OD can be interpreted as the average number of scattering events occurring in the medium when light traverses it.

Figures 2-5 shows how the WF evolves from the case with small OD to the case with large OD. The results have the following interpretation. The central peak of the WF in Fig. 2 and Fig. 3, which is narrow in k-space, corresponds to the ballistic (unscattered) component of the light traversing the medium, whereas the broad (in k) peak corresponds to the scattered component. As the thickness of the medium increases, the ballistic light decays while the scattered light grows. When the OD reaches 6.70 the scattered light is dominant and there is a significant spread of the WF in k-space. Notice that the range of the k-axis in Fig. 2 and 3 is about seven times smaller than the one in Fig. 4 and Fig. 5, indicating that the light spreads in k-space quickly as the OD of the medium increases from 4.02 to 6.70.

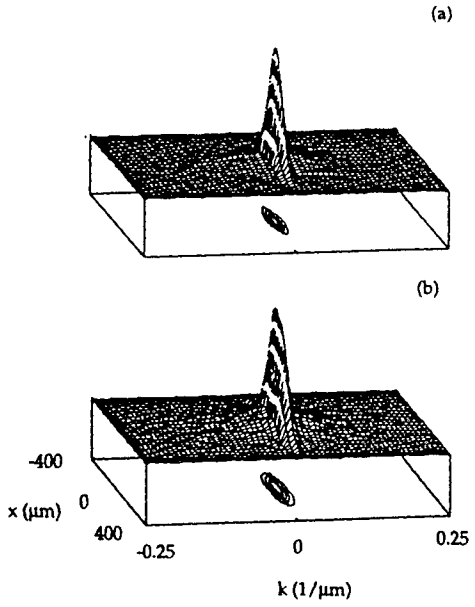


Figure 2

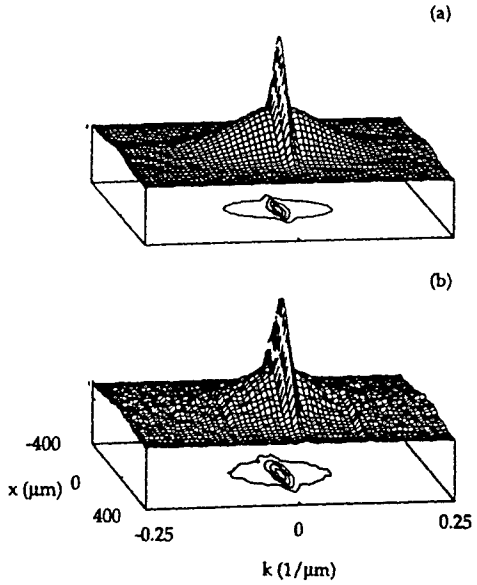


Figure 3

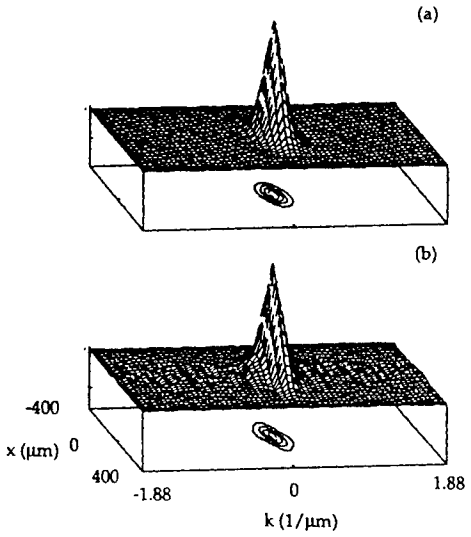


Figure 4

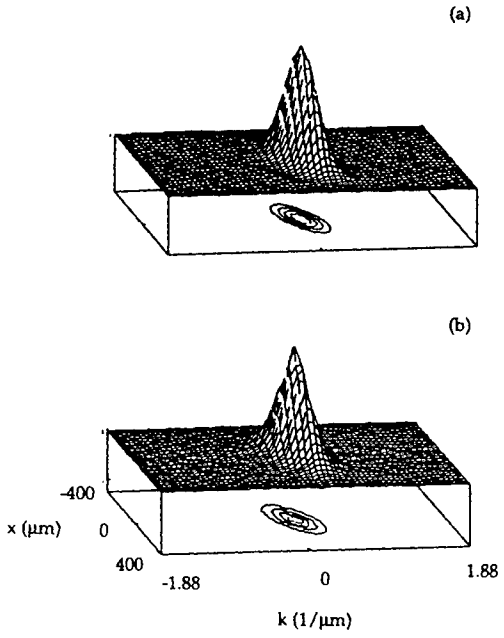


Figure 5

Figures 2 – 5. Wigner function for various optical distances (OD). In each, (a) is theory and (b) is measured. Fig.2: OD = 1.34. Fig.3: OD = 4.02. Fig.4: OD = 7.60. Fig5: OD = 13.4.

## 5. DISCUSSION

The substantial agreement between our measurements and theory (with no free parameters) seen in Fig. 2-5 is, we believe, convincing evidence that the wave transport equation for the WF provides an excellent description of near-forward wave transport in a random medium over a wide range of conditions. This raises the question of whether this equation can be used to advantage for reconstructing the interior structure of a dense medium from measurements on light that have has passed through it. Currently, successful reconstruction methods include photon-diffusion (or transport) tomography [1,9] and optical coherence tomography.[19]

We propose a modified form of photon diffusion tomography in which the WF is measured rather than optical intensity or specific intensity. One would search numerically for a medium's internal structure that reproduces, through solutions of Eq.(6), the observed WF data. We argue that such a scheme could possibly constrain the internal structure more strongly than the analogous method based on the transport equation for the specific intensity. Implementation of this method could be carried out now only for media that are predominantly near-forward scattering, since the transport equation has only been solved so far in that case. Also, it is in that case that the transverse coherence area of the transmitted light is sufficiently large to make allow accurate measurement of the WF. This restricts the method to media that are dominated by scatterers that are large compared to a wavelength. In fact, many biological tissues do not satisfy this condition. Therefore the present method must be generalized to include wider-angle scattering before a successful imaging method for such tissue can be developed. The technique could possibly be applied to reflection as well as transmission geometries.

## ACKNOWLEDGEMENTS

We thank John Thomas and Steve Jacques for helpful discussions. This work was supported by the Army Research Office and by DOE through the Oregon Medical Laser Center.

## REFERENCES

1. See, for example, *Optical Tomography, Photon Migration, and Spectroscopy of Tissue and Model Media: Theory, Human Studies, and Instrumentation*, Part 1 and 2, B. Chance, R. Alfano, eds., Proc. SPIE 2389 (1995).
2. A. Ishimaru, *Wave Propagation and Scattering in Random Media*, vol. II (Academic Press, NewYork,1978), Chap. 20.
3. L. Mandel and E.Wolf, *Optical Coherence and Quantum Optics* (Cambridge, New York, 1995), Chap. 4.
4. D. McAlister, M. Beck, L. Clarke, A. Mayer and M. G. Raymer, Opt. Lett. **20**, 1181 (1995).
5. C. Iaconis and I. A. Walmsley, Opt. Lett. **21**, 1783 (1996).
6. Chung-Chieh Cheng and M. G. Raymer, Phys. Rev. Lett. **82**, 4807 (1999), and references therein.
7. Chung-Chieh Cheng, M. G. Raymer, and H. Heier, "A variable lateral-shearing Sagnac interferometer with high numerical aperture for measuring the complex spatial coherence function of light" (Journal of Modern Optics, in press).

8. A. Wax, J. E. Thomas, J. Opt. Soc. Am. A 15, 1896 (1998); A. Wax, S. Bali, J.E. Thomas, Opt. Lett., .24, 1188 (1999).
9. A. Hielscher and R. Alcouffe, in *Proc. Photon Propagation in Tissue II*, eds., D. A. Benaron, B. Chance, and C. J. Muller (SPIE vol. 2925, 1996).
10. M. G. Raymer, C. Cheng, D. M. Toloudis, M. Anderson, and M. Beck, *in Advances in Optical Imaging and Photon Migration*, 1996 Technical Digest 9Optical Society of America, Washington, DC, 1996), pp. 236-238.
11. S. John, G. Pang, and Y. Yang, J. Biomed. Opt. **1**, 180 (1996).
12. S. Chandrasekhar, *Radiative Transfer* (Oxford, New York, 1950).
13. L. Mandel and E.Wolf, *Optical Coherence and Quantum Optics* (Cambridge, New York, 1995), Chap. 4.
14. J. E. Thomas, private communication (1996).
15. L. Wang, et al., Science **253**, 769 (1991).
16. Chung-Chieh Cheng and M. G. Raymer, "Propagation of Transverse Optical Coherence in Random Multiple-Scattering Media" (submitted to Phys. Rev. A, 2000).
17. Chung-Chieh Cheng, "Propagation of Transverse Optical Coherence in Random Multiple-Scattering Media" (PhD dissertation, Univ. of Oregon (1999)).
18. See Ref. [2], vol. I, Chap.4.
19. H. D. Huang, E. A. Swanson, C. P. Lin, J. S. Schuman, W. G. Sinson, W. Chang, M. R. Hee, T. Flotte, K. Gregorry, C. A. Puliafita, and J. G. Fujimoto, *Science*, **254**, 1178-1181 (1991).

## SESSION 13

# Beam Propagation in Random Media II

# A path integral model of light scattered by turbid media*

Michael J. Wilson

Department of Medical Physics, University Hospital, Birmingham, UK

## ABSTRACT

Imaging techniques involving transillumination require detailed knowledge of radiation path(s) between source and detector. When imaging with near infra-red in tissue this is particularly problematic due to the high scattering cross section. The population of 'direct path' photons is so small that information must be gathered from the much larger (but still small) population of 'snaked path' photons.

Path Integral (PI) models set out to find the most likely of these paths, not by random sampling as in Monte Carlo based techniques, but directly: A cost function (Lagrangian) is constructed based on the physics of the scattering processes/ absorption and integrated along the photon path to generate a total cost (Action). This is minimised using variational calculus to extract the most likely path.

Whilst the PI approach is not new, the work presented here is novel in constructing the Lagrangian using local path descriptors. This allows explicit inclusion of an absorption term and also lends itself to arbitrary numbers of constraints on intermediate 'visit' points, path directions, and overall path length. Scaling symmetries are used to further reduce the computational expense of the method.

**Keywords:** path integral, forward model

## 1. INTRODUCTION

The propagation of light within a highly scattering medium is of interest in many fields such as atmospheric scattering of light, photo dynamic therapy and near infra-red tomography. Monte Carlo analysis is frequently used to model these problems. The Monte Carlo method essentially computes the photon density within a volume element by counting the number of randomly selected photon histories (or paths) that intersect that element. The actual number of photon paths is of course, infinite and the Monte Carlo technique is based on the assumption that a finite set of randomly selected paths will be 'representative' of the true (infinite) population. In the context of the Monte Carlo approach the path integral technique* may be seen as an extreme form of variance reduction. Instead of finding the most likely paths by random sampling the path integral formalism sets out to identify them directly. The literature on this subject is still very limited[2–7] and all practical implementations centre around the approximate method due to Perelman.[3] The path integral model presented here is derived from first principles and does not include Perelman's approximation.

## 2. THEORY

A photon path is characterised by its interactions with the medium through which it propagates. If it is constrained to lie within a single plane and interactions consist exclusively of elastic scattering events such a path may be completely described by the local rate of change of the angle of the path tangent $\frac{d\theta(l)}{dl} = \theta'(l)$ as a function of distance $l$ along the path.

To find the most likely path from $A$ to $B$ (Figure 1) it is necessary to construct $P_{A\to B}[\theta'(l)]$, the probability of the path described by $\theta'(l)$, and then find the $\theta'(l)$ that maximises $P_{A\to B}$. It should be noted that $P_{A\to B}[\theta'(l)]$ is a *functional* i.e. it is a function whose independent variables have increased in number until they have become a continuum of points, in this case represented by the curve $\theta'(l)$. In the present case this may be illustrated directly since $\theta'(l)$ has already been shown to be discontinuous with only $2N-1$ independent variables: $\theta_1, \theta_2 \cdots \theta_{N-1}, l_1, l_2 \cdots l_N$.

Further author information: (Send correspondence to M.J.W.)

M.J.W.: E-mail: michael.wilson@university-b.wmids.nhs.uk

*Path integral formulations of physical processes began with the Lagrangian formulation of classical mechanics and Feynman has developed the field as an alternative description of quantum mechanics.[1]

*Also published in *Proc. of SPIE* Vol. 3927



In *Laser-Tissue Interaction XI: Photochemical, Photothermal, and Photomechanical*, Donald D. Duncan, Jeffrey O. Hollinger, Steven L. Jacques, Editors, Proceedings of SPIE Vol. 3914 (2000) 1605-7422/00/$15.00

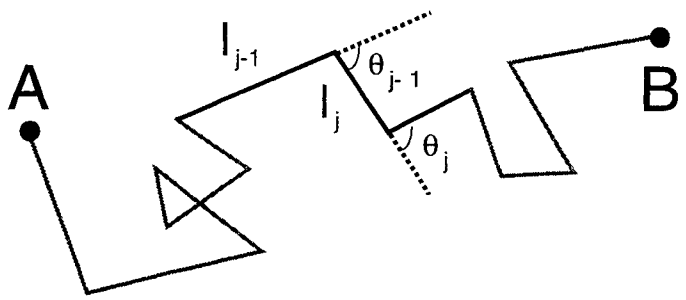


**Figure 1.** Variables used to describe an $N$ step path from $A$ to $B$.

Thus the functional $P_{A\to B}[\theta'(l)]$ may be thought of as the limiting case of the multivariate probability distribution $P_{A\to B}(\theta_1, \theta_2 \cdots \theta_{N-1}, l_1, l_2 \cdots l_N)$.† This may be written as the product of a series of vertex and propagator terms.

$$P_{A\to B}(\theta_1, \theta_2 \cdots \theta_{N-1}, l_1, l_2 \cdots l_N) \prod_{i=1}^{N-1} dl_i d\theta_i dl_N = \prod_{i=1}^{N-1} e^{-\mu_t l_i} dl_i \mu_s p(\theta_i) d\theta_i e^{-\mu_t l_N} dl_N \tag{1}$$

This may be used to derive the functional dependence of $P_{A\to B}$ by examination of the limit as $N \to \infty$ i.e. a 'smooth' photon path. Taking logs to deal with products (in Equation 1) as summations :

$$\begin{aligned} \lim_{N\to\infty} \ln(P_{A\to B}) &= \lim_{N\to\infty} \sum_{i}^{N} -\mu_t l_i + N\ln(\mu_s dl) + (N-1)\ln(d\theta) + \cdots + \sum_{i}^{N-1} \ln(p(\theta_i)) \\ &= -\mu_t L + constant + \lim_{N\to\infty} \sum_{i}^{N-1} \ln(p(\theta_i)) \end{aligned} \tag{2}$$

The final (summation) term in Equation 2 requires some expansion to proceed. It should be remembered that the phase function $p(\theta_i)$ cannot take the Henyey-Greenstein form since the problem has been limited to two dimensions. Under this circumstance it would seem reasonable to adopt a phase function representing a 'slice' through the Henyey-Greenstein distribution.

$$p(\theta) \propto \frac{1}{(1+g^2-2g\cos\theta)^{\frac{3}{2}}} \tag{3}$$

Allowing the number of interactions $N$ to increase without limit on a finite segment of path is, of course, quite artificial and unphysical. However, it is legitimised by allowing the set of finite scattering angles $\theta_i$ to tend towards infinitesimal quantities. It should be borne in mind that, over a physical path scale $\sim \frac{1}{\mu_s}$, these infinitesimals should total a scattering angle consistent with Equation 3. This process offers the considerable advantage of allowing the phase function to be expanded in the small angle limit. Since the phase function is symmetric a quadratic represents the lowest order of expansion possible. Given the form of Equation 2 it would be convenient if $p(\theta)$ had a Gaussian form. To this end we equate quadratic co-efficients of Gaussian and Henyey-Greenstein forms to give:

$$\frac{1}{2\sigma^2} = \frac{3g}{2(1-g)^2} \tag{4}$$

Substituting this approximation into Equation 2 gives:

†The convention of reserving square brackets [ ] for the dependent 'curves' of functionals, and rounded brackets ( ) for the dependent variables of functions, will be adopted throughout.

$$\lim_{N\to\infty} \ln(P_{A\to B}) \;=\; -\mu_t L + constant - \lim_{N\to\infty} \sum_{i}^{N-1} \frac{3g}{2(1-g)^2}\theta_i^2$$

Adopting a slight change in notation, writing $\delta\theta_i$ in place of $\theta_i$ to signal its tendency towards an infinitesimal, this becomes:

$$\lim_{N\to\infty} P_{A\to B} \propto \exp\left(-\mu_t L - \lim_{N\to\infty} \sum_{i}^{N-1} \frac{3g}{2(1-g)^2}\delta\theta_i^2\right) \tag{5}$$

The constant multiplier required to make Equation 5 an equality is not relevant to this discussion. The intention is to discover a path that maximises $P_{A\to B}$ and the exponent term is the only element of importance in this regard. In an attempt to cast the exponent as a path integral $\delta\theta_i^2$ may be replaced by the quantity $\left(\frac{\delta\theta_i}{\delta l_i}\right)^2 \delta l_i^2$ which gives $\lim_{N\to\infty}\sum_i^{N-1}\delta\theta_i^2 \to dl\int_A^B\left(\frac{d\theta}{dl}\right)^2 dl$ , an infinitesimal quantity - clearly something has gone wrong. In fact the previously mentioned note of caution (i.e. deflection angles should be physical on a path scale $\sim \frac{1}{\mu_s}$) has been overlooked. It suggests that the infinitesimal $dl$ outside the integral should be replaced by $\frac{1}{\mu_s}$, forcing quantities integrated along the path to receive unit weight over path segments of this scale. This effectively undoes the artificial device of allowing the number of interactions to increase indefinitely and returns the expression for $P_{A\to B}$ to a more physical footing.

$$P_{A\to B} \;\propto\; \exp\left(-\mu_t L - \frac{3g}{2\mu_s(1-g)^2}\int_A^B \left(\frac{d\theta}{dl}\right)^2 dl\right) \tag{6}$$

*or* :

$$P_{A\to B} \;\propto\; \exp\left(-\int_A^B (\mu_t + \frac{3g}{2\mu_s(1-g)^2}\left(\frac{d\theta}{dl}\right)^2)dl\right) \tag{7}$$

These expressions for (relative) path probability take the form $\exp(-S[\theta(l)])$ where $S[\theta(l)]$ is a functional. The most probable path is the one that minimises $S$. In this respect $S$ is analogous to 'Hamilton's first principal function' (usually referred to as the 'action') in Classical Mechanics. The term inside the integral is therefore analogous to a Lagrangian. The problem of minimising $S$ to find the most likely path may be solved using the methods of variational calculus. However, there is some advantage in recasting the problem before constructing the Euler-Lagrange equation. The substitution $\frac{1}{R} = \frac{d\theta}{dl}$, where $R$ is called the radius of curvature of the path, gives:

$$S[R(l)] = \int_0^L \left(\mu_t + \frac{3g}{2R^2(l)\mu_s(1-g)^2}\right) dl \tag{8}$$

and since $\frac{dl}{R} = d\theta$ we may choose to parameterize the path in terms of $\theta$ rather than $l$. This gives:

$$S[R(\theta)] = \int_{\theta_A}^{\theta_B} \left(\mu_t R(\theta) + \frac{3g}{2R(\theta)\mu_s(1-g)^2}\right) d\theta \tag{9}$$

Where $\theta_A$ and $\theta_B$ define the start and end directions for the path respectively.

We now construct the Euler-Lagrange differential equation satisfied by the path $R(\theta)$ that minimises $S[R(\theta)]$.

$$\left[\frac{\partial}{\partial R} - \frac{d}{d\theta}\left(\frac{\partial}{\partial R'}\right)\right] L(R, R', \theta) = 0 \tag{10}$$

where $L$ is the Lagrangian for the problem and, as has already been shown (Equation 9), depends only upon $R$ :

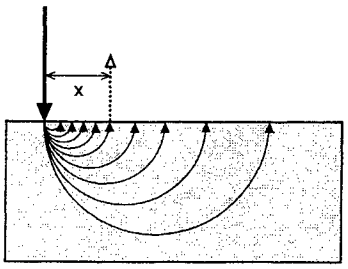


**Figure 2.** Simple illustration of the path integral method. The most likely path with exit radius $x$ is assumed to be circular arc of radius $\frac{x}{2}$ for all $x$.

$$L(R) = \mu_t R + \frac{3g}{2R\mu_s(1-g)^2} \tag{11}$$

Because of this $\frac{d}{d\theta}\left(\frac{\partial L}{\partial R'}\right) = 0$ and the Euler-Lagrange equation is not a differential equation at all. It says, quite directly, that $R$ must satisfy:

$$\begin{aligned} \mu_t - \frac{3g}{2\mu_s(1-g)^2R^2} &= 0 \\ \Rightarrow R &= \sqrt{\frac{3g}{2\mu_s\mu_t(1-g)^2}} \end{aligned} \tag{12}$$

This appears to be saying something rather paradoxical: The most likely unconstrained path from any point $A$ to any other point $B$ is always a circle of fixed radius $R$ (dependent only on the scattering properties of the medium). This is paradoxical because the path that minimises $S$ is obviously a straight line ($R = \infty$)[‡]. Actually, the problem as posed is implicitly constrained - the path must turn through an angle $\theta_B - \theta_A$. If $\theta_B - \theta_A = 0$ (as would be the case for a straight line) $R$ is indeterminate from Equation 9. If the path is required to curve, i.e. $\theta_B - \theta_A \neq 0$, then there is no paradox and the circular arc is an acceptable solution. (If we had stuck with Equation 8 we would have obtained this result directly since there is no implicit direction change in this form for the action.)

## 2.1. A simple illustration

To put the result into a physical perspective, consider a narrow beam of light incident on a thick (thick enough to be considered infinite) slab of scattering medium. How will the light 'reflected' [§] from the slab be distributed as it leaves the slab at the entry face? Such light must follow paths that turn through an angle of greater than $\frac{\pi}{2}$ radians, and probably more so that the path is not suppressed by virtue of being so long. If we assume that they actually turn through $\pi$ radians [¶] the above result says that the most likely path for such reflected light is a half circle of radius '3 or 4' times the diffusion length of the medium. What happens closer to and further from the input beam cannot yet be decided but, to illustrate the path integral method, it will be assumed that when paths are constrained to exit at particular radii that they too turn out to be circular arcs as shown in Figure 2. (It will be shown later this is simply not the case. However the approximation is not too bad and, for the present, we are only concerned with illustration.)

[‡]It may also seem paradoxical because the solution doesn't allow passage to any other point $B$, only the vanishing subset on the circular path that returns to $A$. This is not, however, a fair criticism since the problem was unconstrained and therefore 'unaware' that solutions might be required to visit any particular point.

[§]reflected light here meaning light having entered the slab that leaves via the entry face

[¶]The choice of $\pi$ is a fudge at this stage - we only know that the most probable solution that turns through a given angle is the arc of a circle. The only way to get photons out of the medium is to choose an angle $\pi$. (If we didn't prescribe the angle we would get a different path and, it turns out, a more probable one. See Section 2.4)

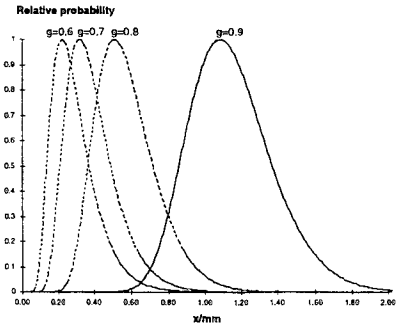


**Figure 3.** The probability of normal reflection $P_x$ arising from a simple path integral model (see Figure 2). Curves are plotted for several values of $g$ and each profile is self normalised to a maximum reflection probability of 1.

Under this simple model the action $S$ for each selected path is particularly straightforward to calculate. The radius of curvature $R$ is simply $\frac{x}{2}$ independent of $\theta$ (see Figure 2) and the total angle through which each path turns is $\theta_B - \theta_A = \pi$ radians. From Equation 9 this gives a path action of $S(x)$:

$$S(x) = \mu_t \frac{x}{2} + \frac{3g}{\mu_s(1-g)^2 x} \tag{13}$$

and a relative probability $P_x$:

$$P_x \propto \exp(-S(x)) = \exp(-\mu_t \frac{x}{2} - \frac{3g}{\mu_s(1-g)^2 x}) \tag{14}$$

Figure 3 shows $P_x$ for various values of $g$. An important feature of these curves is that each shows a radius of maximum exit probability. This arises from the interplay of two distinct and competing 'physical' processes: Firstly, photons are rarely scattered through large angles and so paths with small radii of curvature (tightly curved) are suppressed. The action term containing $\frac{d\theta}{R}$ achieves this: Secondly, photons rarely propagate for large distances without being absorbed and so long paths are suppressed. The action term containing $Rd\theta$ achieves this. Paths that exit close to the input beam may be short but they are also very tightly curved and this turns out to be the dominant factor giving such paths a relatively low probability. Paths that exit far from the input beam may have little curvature but they are also very long and are unlikely for that reason. Somewhere in between, these effects balance and there is a most likely path. Exactly where this balance occurs will depend on the relative weights of the two terms and this, of course, is determined by the scattering parameters $\mu_t, \mu_s$ and $g$. Figure 3 shows that as $g$ increases the path curvature expression suppresses ever more gentle radii of curvature and pushes the 'peak' away from the entry point. For increasing $\mu_t/\mu_s$ (not shown) the opposite is true.

## 2.2. Introducing constraints

The use of semi-circular paths as constrained solutions has provided an instructive overview of the path integral method, but it was only a guess. To proceed, the problem of path constraint must be properly addressed. The angle through which the path must turn has already been included implicitly. In addition (as in the above problem) we should like to constrain the path to end at a particular displacement $(x_B - x_A, y_B - y_A)$ from the start position.

We would like therefore to minimise $S$ subject to the constraints:

$$\begin{aligned} \int_{\theta_A}^{\theta_B} \frac{dx}{d\theta} d\theta &= x_B - x_A \\ \int_{\theta_A}^{\theta_B} \frac{dy}{d\theta} d\theta &= y_B - y_A \end{aligned}$$

i.e.

$$\begin{aligned}\int_{\theta_A}^{\theta_B} R\sin\theta d\theta &= x_B - x_A \\ \int_{\theta_A}^{\theta_B} R\cos\theta d\theta &= y_B - y_A \end{aligned} \tag{15}$$

To accommodate these constraints we must add arbitrary multiples ($\eta$ and $\xi$) of them to our Lagrangian $L$ to give the following Euler-Lagrange equation for the path:

$$\left[\frac{\partial}{\partial R} - \frac{d}{d\theta}\left(\frac{\partial}{\partial R'}\right)\right](L + \eta R\sin\theta + \xi R\cos\theta) = 0 \tag{16}$$

Substituting for $L$ from Equation 11 gives:

$$\mu_t - \frac{3g}{2R^2\mu_s(1-g)^2} + \eta\sin\theta + \xi\cos\theta = 0 \tag{17}$$

Rearranging for $R$ and substituting the Lagrange multipliers $\eta$ and $\xi$ with $\rho$ and $\phi$ (where $\eta\sin\theta + \xi\cos\theta = \mu_t\rho\cos(\theta+\phi)$) to provide a more compact notation gives:

$$R(\theta) = \frac{1}{1-g}\sqrt{\frac{3g}{2\mu_t\mu_s}}\frac{1}{\sqrt{1+\rho\cos(\theta+\phi)}} \tag{18}$$

Therefore, the most likely path for a photon starting off at an arbitrary angle $\theta_A$ from a point $(x_A, y_A)$ and ending at an angle $\theta_B$ at a point $(x_B, y_B)$ has the Cartesian form:

$$\begin{aligned} x(\theta) &= x_A + \int_{\theta_A}^{\theta} \frac{1}{1-g}\sqrt{\frac{3g}{2\mu_t\mu_s}}\frac{\sin\theta}{\sqrt{1+\rho\cos(\theta+\phi)}}d\theta \\ y(\theta) &= y_A + \int_{\theta_A}^{\theta} \frac{1}{1-g}\sqrt{\frac{3g}{2\mu_t\mu_s}}\frac{\cos\theta}{\sqrt{1+\rho\cos(\theta+\phi)}}d\theta \end{aligned} \tag{19}$$

And the values of $\rho$ and $\phi$ for any particular set of path constraints must be determined from the simultaneous equations:

$$\begin{aligned} x_B - x_A &= \int_{\theta_A}^{\theta_B} \frac{1}{1-g}\sqrt{\frac{3g}{2\mu_t\mu_s}}\frac{\sin\theta}{\sqrt{1+\rho\cos(\theta+\phi)}}d\theta \\ y_B - y_A &= \int_{\theta_A}^{\theta_B} \frac{1}{1-g}\sqrt{\frac{3g}{2\mu_t\mu_s}}\frac{\cos\theta}{\sqrt{1+\rho\cos(\theta+\phi)}}d\theta \end{aligned} \tag{20}$$

Although analytical solutions for $x$ and $y$ exist in terms of elliptic functions it is not possible to solve for $\rho$ and $\phi$ in closed form. Another subtlety of Equation 19 is the parameterization of the path in terms of $\theta$. Although the start and end values of $\theta$ are prescribed, it is generally *not* the case that $\theta$ along the path will be bounded by these values. This is exemplified by the problem of a path that is required to start and end with the same $\theta$ as shown in Figure 4. If $\theta$ along the path were to be bounded by $\theta_A$ and $\theta_B = \theta_A$, in this situation it would not be able to change direction. The actual variation for the computed path is shown in Figure 5. Note that the minimum value of $\theta$ along the path corresponds to a point of inflection. Here the radius of curvature becomes infinite and changes sign. It would appear that this single excursion in the value $\theta$ represents the most complex form of solution (although no attempt has been made to verify the hypothesis theoretically). This effectively introduces another path parameter $\theta_{max/min}$ that must be found alongside the Lagrange multipliers $\rho$ and $\phi$.

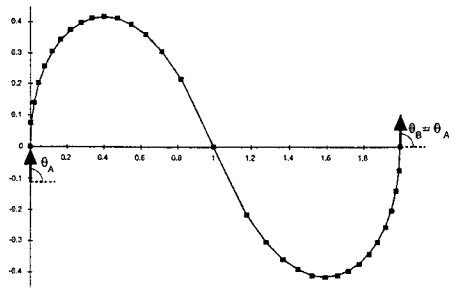

**Figure 4.** Most probable path for a photon constrained to begin at $(0,0)$ with $\theta = \frac{\pi}{2}$ and end at $(2,0)$ travelling in the same direction.

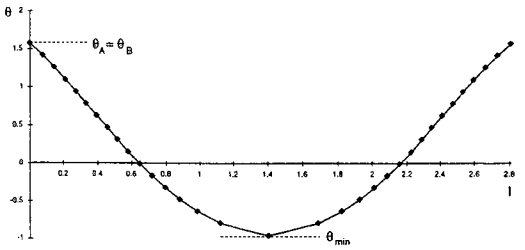

**Figure 5.** The tangent angle $\theta$ of the path shown in Figure 4 plotted as a function of distance $l$ along the path.

## 2.3. Numerical solution

For these reasons the solution of problems using this particular path integral method has been approached purely numerically. Apart from facilitating the inclusion of the extra parameter $\theta_{max/min}$, this route has the additional advantage of allowing the implicit constraint $\theta_B$ to be relaxed (i.e. allowed to take the most favorable value) if the problem demands.[‖]

To construct numerical solutions that minimise the action $S$ (Equation 9) we return to the notion that a functional may be represented as a multi-variate distribution. Previously the set of variables $\{\theta_1, \theta_2 \cdots \theta_{N-1}, l_1, l_2 \cdots l_N\}$ was chosen but, given the foregoing discussion, we now consider the set $\{R_1, R_2 \cdots R_{N-1}, \theta_1, \theta_2 \cdots \theta_{N-1}\}$. The significance of the variables in this alternative scheme is illustrated in Figure 6.

This set lends itself to minimisation of a discrete form of Equation 9:

[‖]It is assumed that $\theta_A$ will always be specified for the simple one step ($A$ to $B$) type of problem discussed so far. However, if the method is extended to multiple steps (Section 2.5) then $\theta_A$ for an intermediate step will need to match the $\theta_B$ of the previous step and thus may also need to remain unconstrained.

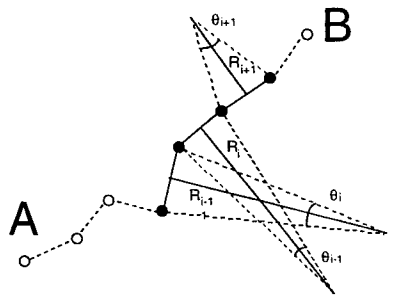


**Figure 6.** Multivariate path descriptors

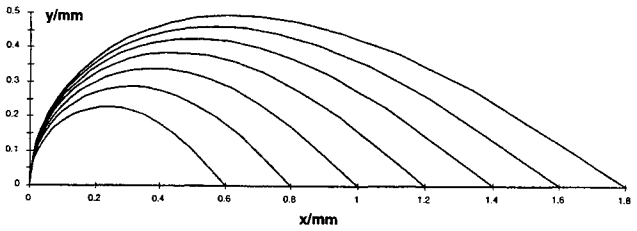


**Figure 7.** Most probable paths for photons entering a scattering medium normally at $x = 0$ and required to exit at radius $x$. The exit angle is not constrained.

$$\begin{aligned} S[R(\theta)] &= \int_{\theta_A}^{\theta_B} \left( \mu_t R(\theta) + \frac{3g}{2R(\theta)\mu_s(1-g)^2} \right) d\theta \\ &\simeq \sum_i \mu_t R_i \theta_i + \frac{3g}{2R_i\mu_s(1-g)^2}\theta_i \end{aligned} \tag{21}$$

Ordinarily in a problem of this kind the next stage would be to identify a set of starting values for $\{R_1, R_2 \cdots R_{N-1}, \theta_1, \theta_2 \cdots \theta_{N-1}\}$ (i.e. an approximate path) and then feed these into a numerical procedure. This would attempt to adjust each of the path variables so as to make $S$ smaller and (hopefully) after a number of such iterations no further adjustment would be possible: The routine would have converged and the most likely path would have been identified. However, when (as in this case) the number of variables is large, this approach is usually only successful if the starting guess is pretty close to the solution. Fortunately, the solution of the Euler-Lagrange problem (Equation 18) is highly prescriptive. For a given set of angular steps from $\theta_A$ to $\theta_B$ it identifies all of the associated radii of curvature. Only three parameters can be used to vary the prescription: the reduced Lagrange multipliers $\rho$, $\phi$ and $\theta_{max/min}$. ($\theta_{max/min}$ is sometimes needed to construct the set of angular steps in two stages, $\theta_A \rightarrow \theta_{max/min}$ and $\theta_{max/min} \rightarrow \theta_B$, as described earlier. With only three parameters to vary, the numerical approach is not only much more stable (i.e. likely to converge on the solution even with a poor starting approximation) but is also much quicker.

To compute the photon paths in the context of this work, the optimization of path parameters was performed using standard conjugate-gradient based iterative methods.

### 2.4. A more refined illustration

Returning to the simple illustration given earlier (Section 2.1), we are now in a position to refine the calculation of most probable paths based on a model that constrains photons to exit at a certain radius, but allows any exit angle (rather than assume all paths to be semi-circular and therefore all to exit at an angle $\pi$.)

Figure 7 shows a series of such paths. Notice that although the radius of curvature of each path falls below that of its corresponding semi-circle, this curvature is not sustained. The expense (in terms of increased action) of this local increase in curvature is more than offset by the increased radius of curvature it affords towards the end of the path *and* the resultant decrease in path length and smaller exit angle (i.e. the total deflection is always considerably less than $\pi$).

The relative probabilities of these paths are plotted alongside the corresponding probability profile generated by the semi-circle model in Figure 8. Apart from the noticeably increased width of the 'semi-circular' distribution the curves are in close agreement as to the most likely exit radius. However, the self normalisation of each curve masks a gross discrepancy in the relative probabilities of the two path types. The semi-circular paths are roughly $180,000$ times less probable than their 'free' path counterparts. **

**The action of the most probable semi-circular path is about 12 units larger than the most probable path making it $\simeq e^{12}$ times less likely.

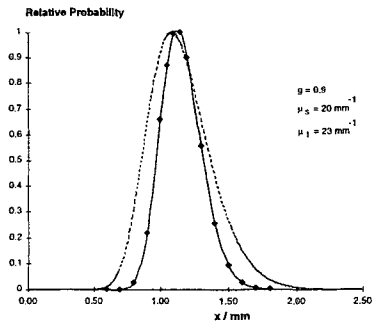


**Figure 8.** Relative probabilities for paths shown in Figure 7 together with the corresponding profile from the simple semi-circular model (dashed line).

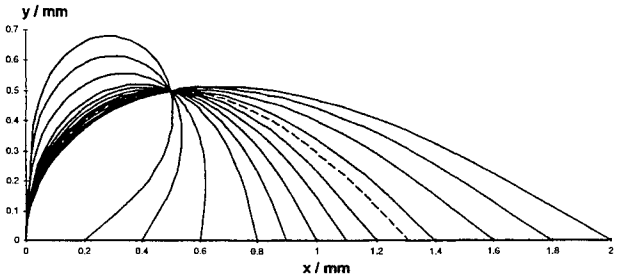


**Figure 9.** Most probable paths constrained to enter normally at $(0,0)$, pass through the intermediate point $(0.5,0.5)$ and exit freely (i.e. $\theta$ unconstrained) at $(x,0)$.

## 2.5. Intermediate point constraints

Thus far the path integral technique has been allowed to select the most probable route (consistent with boundary conditions) from the set of all possible routes between start and end points $A$ and $B$.

If we are particularly interested in the sub-population of photons that pass through a specific intermediate point $C$ within the medium (perhaps because we are interested in the effects of a change in the medium properties at $C$) we need to further constrain the path. However, rather than return to the Lagrangian and add the new constraint with a new Lagrange multiplier etc., we can divide the new 'two step' problem into two familiar 'one step' problems: one from $A$ to $C$ and one from $C$ to $B$. The only extra complexity is that the starting conditions for the second path segment must match the end point conditions of the first i.e. both $\theta$ and $R$ should match at $C$. These additional requirements (i.e. in addition to the two sets of $\rho$ and $\phi$ to be found) appear in place of the extra Lagrange multipliers that would have resulted from the more direct approach. The virtue of this approach is that path segments share the same form and therefore the same numerical algorithm may be used for each. In this way the method may be extended to find paths that visit any number of pre-specified intermediate points.

A series of paths calculated using this two stage approach is shown in Figure 9. All paths enter normally at $(0,0)$ and are required to pass through the point $(0.5,0.5)$, which lies deeper within the medium than any point on the most probable unconstrained path. The corresponding path probabilities (relative to the most likely) are shown in Figure 10 together with the unconstrained profile (the same optical scattering characteristics were used in the solution of each problem). This shows that photons having passed through the point $(0.5,0.5)$ are more likely to exit at a larger radius than those that take (more probable) shallower routes. The most probable exit radius has moved from $x \simeq 1.15mm$ to $x \simeq 1.31mm$. Again the normalised profiles mask the relative probabilities of the two types of path: The most favoured of the constrained paths is approximately 6.9 times less likely than its unconstrained counterpart.

## 2.6. Path length (or time) constraints

In some fields, the relative contributions of photons having traversed paths of differing lengths is of importance. The constraint of path length would, therefore, provide a further extension to the utility of the path integral model.

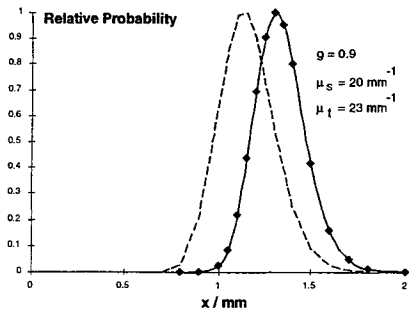


**Figure 10.** Probability profile of paths shown in Figure 9 together with the unconstrained profile (dashed line).

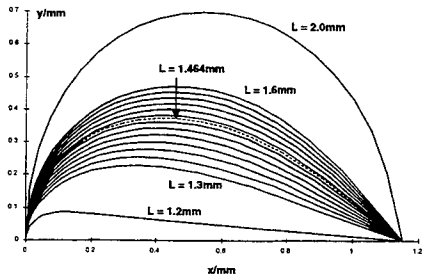


**Figure 11.** Series of paths with various total path lengths but otherwise similarly constrained.

Examination of Equation 9 (or 8) shows that the action for a path already contains $L$ in the form $\int \mu_t R d\theta = \mu_t L$. If we are to fix the value of $L$, this part of the action will clearly remain the same from one path to the next and so may be dropped. However, to include $L$ as a constraint, the usual procedure of adding an undetermined multiple (of the constraint) to the action effectively resurrects the term in the form $\int \epsilon R d\theta$, where $\epsilon$ is the Lagrange multiplier:

$$S[R(\theta)] = \int_{\theta_A}^{\theta_B} \left( \epsilon R(\theta) + \frac{3g}{2R(\theta)\mu_s(1-g)^2} \right) d\theta \tag{22}$$

Somewhat curiously, the problem of finding a path whose total length is fixed is exactly the same as the problem without the constraint except that we are allowed to tinker with the attenuation co-efficient until the balance between curvature and propagation terms is such that $L$ is the favoured path length! Of course $\epsilon$ merely appears in the same place as did $\mu_t$ previously but the treatment of $\epsilon - \mu_s$ as a pseudo-attenuation co-efficient is compelling (especially since the curvature component doesn't depend on $\mu_a$ [††] ).

Figure 11 shows a series of paths each required to enter normally and exit at any angle at approximately $(1.15, 0)$ - the most likely exit point for the unconstrained problem. However, each path is required to take on a particular value for $L$. The relative probabilities of these paths are shown in Figure 12.

## 3. POTENTIAL APPLICATIONS

### 3.1. Optical Calculations

To use the PI method to make, for example, a calculation of time dependent reflectance might seem straightforward. One might consider the photon paths that enter at some fixed angle and exit at some constrained radius $r$ with a particular exit angle $\theta$ and certain total path length $L$. Integration of path probabilities over all $r$ and $\theta$ would thus give a measure of the probability of the path length $L$. Of course it is not entirely clear that the path parameters $r$ and $\theta$ are either necessary or indeed sufficient. Such issues remain to be explored.

[††] If it did depend on $\mu_a$ we might still regard $\epsilon$ as a tool for 'cranking up' the attenuation but only as it applied to the propagation term - happily it doesn't! The physical analogy only breaks down when $\epsilon$ is required to be less than $\mu_t$ and the pseudo-attenuation becomes negative so as to promote long paths.

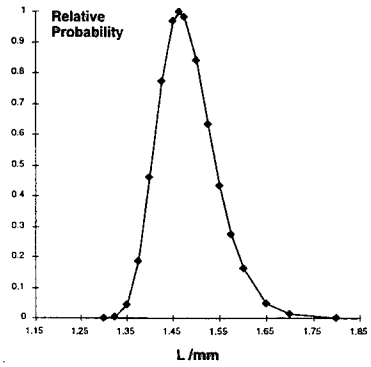


**Figure 12.** Relative probabilities of paths in Figure 11

One symmetry of the PI method that might provide an important simplification of the calculation process is that of scaling i.e. if a path is found for $r_1$ and $\theta_1$ at some particular $L_1$ then the relative probability of the path will be given by an expression of the form

$$p(L_1, r_1, \theta_1) \propto \exp(-S^1_{curvature} - S^1_{distance}) \tag{23}$$

where $S_{curvature} \propto \int \frac{d\theta}{R}$ and $S_{distance} \propto L$. If such a curve is scaled by a factor $f$ then the scaled curve will represent a solution for the case $r_2 = fr_1$, $\theta_2 = \theta_1$ and $L_2 = fL_1$. The corresponding probability is thus given by:

$$p(L_2, r_2, \theta_1) \propto \exp(-\frac{S^1_{curvature}}{f} - fS^1_{distance}) \tag{24}$$

However such an approach requires some care. Whereas an equivalent Monte Carlo based calculation would select photon histories effectively at random, the facility within a PI based approach to allow systematic path selection on the basis of predetermined parameters also introduces a potential for bias. The problem of path degeneracy (i.e. the local 'density' of similar paths surrounding any given path) must be considered.

### 3.2. Optical Tomography

One area where constrained paths of this type might find ready application is in the field of forward modeling for optical tomography.[8–11] The basic tomographic problem centers around the desire to deduce a cross-sectional map of (in this case) an optical parameter (such as absorption co-efficient) from a series of transmission measurements.[12] Under these circumstances it is imperative to have a good model for the effect that each cross-sectional element will have on each external measurement (i.e. a forward model). Figure 13 illustrates how the path integral model might be used to address this problem. To estimate the sensitivity within the region marked by the square for example (under the particular source/detector configuration shown), a series of paths may be constructed based on some system of constraints. Figures 13 (a) and (b) illustrate possible strategies based on variation of path angles at either the source or probed region, but there are obviously many other possibilities. The combined probabilities of these paths may then be used as a measure of the local sensitivity.

Optical tomographic techniques often attempt to refine the information available from transmission measurement by temporal sorting i.e. photons that take a relatively short period of time to reach the detector will have travelled along shorter, straighter paths thus providing higher quality spatial information about the intervening medium.[13,14] The addition of path length constraints to the sensitivity calculations might facilitate this.

The great (potential) advantage of this approach is one of speed. A Monte Carlo based algorithm can provide very accurate answers if it is allowed to generate enough paths. However, to intersect the least sensitive of regions with sufficient frequency may take a very long time. The systematic selection process of the path integral approach promises the same precision, for any region (however insensitive), without the time penalty.

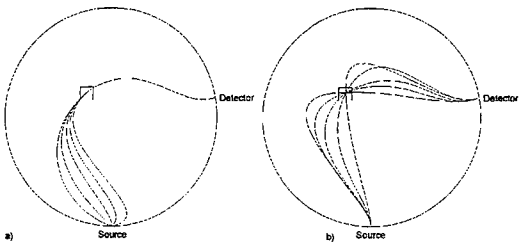


**Figure 13.** Forward modelling in optical tomography using a path integral based approach

## 4. CONCLUSIONS

Whilst the application of the path integral formalism to photon migration is not new, the introduction of local co-ordinate path descriptors has overcome the need for the approximate methods of other formulations and also allows a rich mechanism for dealing with constrained problems. However, there are still some questions that need to be addressed before the path integral method can be properly evaluated alongside Monte Carlo models. Central among these is the question of path degeneracy weighting i.e. whilst the method can identify and compare the probabilities of isolated paths, at present it takes no account of the likely density of similar paths. It is hoped that these questions can be addressed and that the path integral formalism may be developed as a general optical modelling tool.

## ACKNOWLEDGMENTS

Many thanks for the valuable assistance and facilities provided by Dr. Ruikang Wang of the Optical Imaging Group, Dept. of Biomedical Engineering, Keele University, UK. This work was funded (in part) by a research grant from the West Midlands Regional Health Authority (UK).

## REFERENCES

1. R. P. Feynman and A. R. Hibbs, *Quantum Mechanics and Path Integrals*, ch. 12-6. McGraw Hill Book Company, 1965.
2. J. Tessendor, "Radiative transfer as a sum over paths," *Physical Review A* **34**, pp. 872–878, 1987.
3. L. T. Perelman, J. Wu, I. Itzkan, and M. S. Feld, "Photon migration in turbid media using path integrals," *Physical Review Letters* **72**, pp. 1341–1344, 1994.
4. L. T. Perelman, J. Wu, Y. Wang, I. Itzkan, R. R. Dasari, and M. S. Feld, "Time-dependent photon migration using path integrals," *Physical Review E* **51**, pp. 6134–6141, 1995.
5. A. Y. Polishchuk and R. R. Alfano, "Fermat photons in turbid media: an exact analytic solution for most favorable paths - a step toward optical tomography," *Optics Letters* **20**, pp. 1937–1939, 1995.
6. S. L. Jacques and X. Wang, "Path integral description of light transport versus monte carlo and diffusion theory," *Proc. SPIE: Optical tomography and spectroscopy of tissue* **2979**, pp. 488–499, 1997.
7. S. L. Jacques, "Path integral description of light transport in tissue," *Ann N Y Acad Sci* **838**, pp. 1–13, 1998.
8. S. R. Arridge, M. Cope, and D. T. Delpy, "The theoretical basis for the determination of optical pathlengths in tissue: temporal and frequency analysis," *Phys. Med. Biol.* **37**, pp. 1531–1560, 1992.
9. D. T. Delpy, "Optical spectroscopy for diagnosis," *Physics World* , pp. 34–39, 1994.
10. S. R. Arridge, "Photon-measurement density functions. part 1: Analytical forms," *Applied Optics* **34**, pp. 7395–7049, 1995.
11. S. R. Arridge and M. Schweiger, "Photon-measurement density functions. part 2: Finite-element-method calculations," *Applied Optics* **34**, pp. 8026–8037, 1995.
12. H. H. Barrett and W. Swindell, *Radiological Imaging. The theory of image formation, detection, and processing. Vol. 2*, ch. 11. Academic Press, 1981.
13. D. T. Delpy, M. Cope, P. van der Zee, S. Arridge, S. Wray, and J. Wyatt, "Estimation of optical pathlength though tissue from direct time of flight measurement," *Physics in Medicine and Biology* **33**, pp. 1433–1442, 1988.
14. M. S. Patterson, B. Chance, and B. C. Wilson, "Time resolved reflectance and transmittance for the non-invasive measurement of tissue optical properties," *Applied Optics* **28**, pp. 2331–2336, 1989.

Invited Paper

# Modeling the optical coherence tomography geometry using the extended Huygens-Fresnel principle and Monte Carlo simulations

Peter E. Andersen*[a], Lars Thrane[a], Harold T. Yura[b], Andreas Tycho[c], and Thomas M. Jørgensen[a]

[a]Optics and Fluid Dynamics Dept., Risø National Laboratory
P. O. Box 49, DK-4000 Roskilde, Denmark

[(b)] Electronic Technology Center, The Aerospace Corporation
P. O. Box 92957, Los Angeles, CA 90009, USA

[(c)] Research Center COM, Technical University of Denmark,
DK-2800 Kgs. Lyngby, Denmark

## ABSTRACT

We have developed a new theoretical description of the optical coherence tomography (OCT) geometry for imaging in highly scattering tissue. The new model is based on the extended Huygens-Fresnel principle, and it is valid in the single and multiple scattering regimes. The so-called shower curtain effect, which manifests itself in standard OCT systems, is an inherent property of the extended Huygens-Fresnel model. We compare the theoretical analysis with experiments carried out on samples consisting of aqueous suspensions of microspheres and solid phantoms. We calculate the signal-to-noise ratio, and provide an estimation of the maximum attainable probing depth for shot-noise limited detection. Furthermore, we investigate the focusing of the Gaussian probe beam in the tissue using Monte Carlo simulations, and compare it to the extended Huygens-Fresnel model. Finally, we simulate the operation of the OCT system using a specially adapted Monte Carlo simulation code.

**Keywords:** optical coherence tomography; extended Huygens-Fresnel principle; Monte Carlo simulations; multiple scattering

## 1. INTRODUCTION

Since the first paper describing the use of the optical coherence tomography (OCT) technique for noninvasive cross-sectional imaging in biological systems,[1] various theoretical models of the OCT system have been developed. The primary motivation has been optimization of the OCT technique based on these models thereby improving the imaging capabilities. The first theoretical models were based on single-scattering theory.[2,3] These models are restricted to superficial layers of highly scattering tissue in which only single scattering occurs.

At larger probing depths, which is also covered by OCT systems, the light is also subject to the effects of multiple scattering. Therefore, efforts have been concentrated on including these effects in the theoretical modeling. The effects of multiple scattering have been investigated experimentally,[4] and the impact on the interpretation of OCT signals has been discussed. The effects of multiple scattering were treated by the same authors by using a hybrid Monte Carlo/analytical model.[5] Multiple scattering effects were also analyzed by using methods of linear systems theory[6,7] combined with Monte Carlo simulations.[6] The extended Huygens-Fresnel principle has also been applied to the investigation of multiple scattering effects.[8] However, Schmitt and Knüttel[8] excluded the important shower curtain effect,[9,10] which is the key to understanding the effects of multiple scattering. Hence, their results should not be used when considering multiple scattering effects. As shown by the above-mentioned investigations, the primary effects of multiple scattering are a reduction of the imaging contrast and resolution of the OCT system, and a less steep slope of the signal intensity depth profile than the slope given by the single-backscatter model.[4,7]

For a more comprehensive overview of the literature and applications, the reader is referred to Ref. 11 or Ref. 12. The application of OCT in connection with endoscopes seems to be another area in rapid growth.[13] Finally, polarization effects and tissue birefringence have also been treated more intensely, since the first paper by Hee *et al.*[14] Recent papers show promise

*Correspondence: Email: peter.andersen@risoe.dk; WWW: http://www.risoe.dk; Telephone: +45 4677 4555; Fax: +45 4677 4565



In *Laser-Tissue Interaction XI: Photochemical, Photothermal, and Photomechanical*, Donald D. Duncan, Jeffrey O. Hollinger, Steven L. Jacques, Editors, Proceedings of SPIE Vol. 3914 (2000)
1605-7422/00/$15.00

of new applications of OCT.[15] It should be noted that the above-mentioned theoretical investigations may be extended to include polarization effects, especially models based on the extended Huygens-Fresnel principle.

Since the first investigations[16,17] on using Monte Carlo simulations (MCS) for describing light propagation in highly scattering media, its applicability has increased significantly due to the advent of powerful computers and efficient code. Previously, MCS has been utilized to model OCT systems.[5,7,18] However, these investigations were carried out without taking into account the focusing of the sample beam commonly used in OCT. Smithies *et al.* [19] presented an analysis of the signal attenuation in OCT systems including focusing of the sample beam. However, the sample beam was focused to the geometrical focal point. More recently, Song *et al.*[20] presented their numerical results, which clearly shows the capability of MCS in modeling OCT systems. However, their results are obtained for a sample beam essentially focused to a point as in Ref. 19. As will be shown below in the present paper, such modeling may be too crude an approximation to model this particular OCT geometry adequately.

In this paper, we present a new theoretical description of the OCT technique when used for imaging in highly scattering tissue.[21,22] The description is based on the extended Huygens-Fresnel principle first described by Lutomirski and Yura[23] for beam propagation in the turbulent atmosphere. We show that our theoretical model, based on this principle and the use of mutual coherence functions, describes the performance of the OCT system in both the single and multiple scattering regimes. In a standard OCT system[1] with diffuse backscattering from the tissue discontinuity being probed, and a distance between the focusing lens and the tissue, the so-called shower curtain effect[9,10] is present. Note that this effect has been omitted in previous theoretical models.[8] We demonstrate that inclusion of this effect is of utmost importance in the calculation of the heterodyne signal and thereby for the system performance. The main result is that inclusion of the shower curtain effect leads to a strong increase in the heterodyne signal. Experimental data verifying the theoretical results are presented. We then use the model to calculate the maximum probing depth for the case of shot-noise limited detection. The analytical model is compared to MCS,[24] which includes two important improvements with respect to previous models: firstly, Gaussian focal point spread, and secondly, inclusion of the tissue discontinuity reflection characteristics. Comparisons between experimental data, the analytical model and the new MCS code[24] are carried out. The purpose of carrying out this comparison is to show the advantage of using the extended Huygens-Fresnel principle over MCS when describing the operation of OCT systems.

## 2. EXTENDED HUYGENS-FRESNEL PRINCIPLE USED IN OCT

In section 2.1, the derivation of the heterodyne signal based on the extended Huygens-Fresnel (EHF) principle[23] and mutual coherence functions is outlined. For the detailed derivation, the reader is referred to Thrane *et al.*[22] Numerical results are presented demonstrating the importance of the so-called shower curtain effect.[9,10] Section 2.2 discusses the experimental investigation verifying the use of EHF for describing light propagation in the OCT geometry. Section 2.3 outlines the calculation of the maximum probing depth for an OCT system with shot-noise limited detection based on our theoretical model.[25] Finally, in section 2.4 it is shown how our model may be used to investigate system performance, i.e., as a design tool.

### 2.1. Theoretical model

A conventional OCT system[1] consists of a superluminescent diode (SLD), a Michelson interferometer with moveable reference mirror, and a photodetector. The rotationally symmetric sample arm geometry of the OCT system is shown in Fig. 1. The tissue discontinuity being probed arises from a refractive index discontinuity between two tissue layers ($n \neq n_l$ in Fig. 1). Therefore, the discontinuity is characterized by a Fresnel reflection coefficient $R_d$, and placed at a depth $z$ in the tissue. A lens with focal length $f$ is placed at a distance $d$ from the tissue surface. In the system of interest, the focal plane coincides with the tissue discontinuity. Furthermore, the reference arm optical path length in the Michelson interferometer is matched to the focal plane optical depth.

In the case of human skin, light scattering in the bulk tissue is predominantly in the forward direction for the

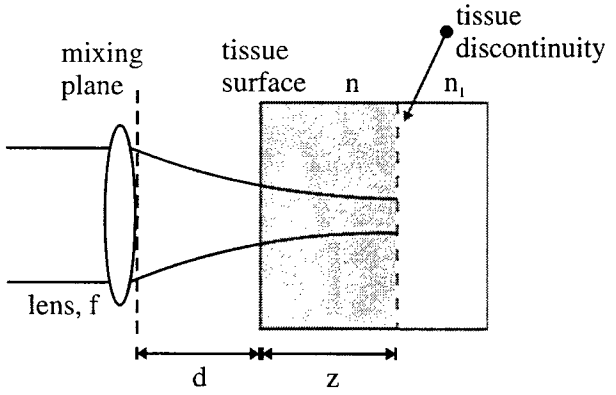

Fig. 1. The sample arm geometry of the OCT system.

wavelengths of interest in the NIR region.[26] Hence, bulk backscattering may be neglected, and the extended Huygens-Fresnel principle[23] is used to describe the light propagation in the bulk tissue. This is justified by the fact that the extended Huygens-Fresnel principle is based on the paraxial approximation and therefore valid for small-angle forward scattering. In particular, it can be shown that the paraxial approximation is valid up to ~30° (i.e., ~0.5 rad).[27] Because most tissues are characterized by rms scattering angles below this limit, the extended Huygens-Fresnel principle may be used to describe light propagation in tissue retaining both amplitude and phase information. The bulk tissue absorption is neglected.[26] Thus, the bulk tissue is characterized by a scattering coefficient $\mu_s$, a root mean square scattering angle $\theta_{rms}$ or asymmetry parameter[28] $g$ related through $g=\cos\theta_{rms}$, and a mean index of refraction $n$. Furthermore, the bulk tissue is modeled as a material with scatterers randomly distributed over the volume of interest. Note that in the present analysis polarization effects are not included.

By mixing the sample field reflected at the discontinuity in the tissue at depth $z$ with the reference field on the photodetector of the OCT system, the heterodyne signal current $i(z)$ is obtained. In the calculation of the mean square heterodyne signal current $\langle i^2(z)\rangle$, which is proportional to the heterodyne signal power, mutual coherence functions (MCFs) are used. For simplicity, the heterodyne mixing plane coincides with the lens plane, see Fig. 1. The MCF of the sample field in the mixing plane is determined by using the extended Huygens-Fresnel principle expressed in terms of the *ABCD* matrix elements of the optical system.[29] Furthermore, it is assumed that the statistical properties of the bulk tissue and the tissue discontinuity are independent, and that the propagation to the tissue discontinuity is statistically independent from the corresponding reflected propagation path. Finally, diffuse backscattering[9] from the tissue discontinuity is assumed. Using Gaussian-shaped beams, the following expression for the mean square heterodyne signal current is obtained[22]

$$\langle i^2(z)\rangle = \frac{\alpha P_R P_S \sigma_b}{\pi w_H^2}\left[\exp\{-2\mu_s z\} + \frac{2\exp\{-\mu_s z\}\left(1-\exp\{-\mu_s z\}\right)}{1+\frac{w_S^2}{w_H^2}} + \left(1-\exp\{-\mu_s z\}\right)^2 \frac{w_H^2}{w_S^2}\right] \equiv \langle i^2\rangle_0 \Psi(z). \qquad (1)$$

The quantity $\langle i^2\rangle_0 = \alpha^2 P_R P_S \sigma_b / \pi w_H^2$ is the mean square heterodyne signal current in the absence of scattering, and the terms contained in the brackets is the heterodyne efficiency factor $\Psi(z)$. Physically, $\Psi(z)$ can be looked upon as the reduction in the heterodyne signal-to-noise ratio due to the scattering of the tissue. The first term in the brackets of Eq. (1) represents single scattering. The corresponding third term is the multiple scattering term, and the second term is the cross term. The constant $\alpha$ is a conversion factor for power to current. The quantities $P_R$ and $P_S$ are the powers of the reference beam and the sample input beam in the lens plane, respectively. The factor $\sigma_b = 4\pi R_d/k^2$ is the effective backscattering cross section, where $k=2\pi/\lambda$, and $\lambda$ is the center wavelength of the source in vacuum. Finally, $w_H$ and $w_S$ are the $1/e$ irradiance radius of the sample beam in the plane of the tissue discontinuity in the absence and presence of scattering, respectively. When the focal plane coincides with the tissue discontinuity, the quantities $w_H$ and $w_S$ are given by[22]

$$w_H^2 = \left(\frac{f}{kw_0}\right)^2; \qquad \frac{w_H^2}{w_S^2} = \frac{1}{1+\left(\frac{2w_0}{\rho_0(z)}\right)}, \qquad (2)$$

where $w_0$ is the $1/e$ intensity radius of the reference beam and the sample input beam in the lens plane, and $\rho_0(z)$ is the lateral coherence length of the reflected sample field in the mixing plane. For lateral separations much less (greater) than $\rho_0(z)$, the field can be considered to be mutually coherent (incoherent). Because of the diffuse backscattering from the tissue discontinuity, $\rho_0(z)$ is determined only by the propagation back through the tissue from the tissue discontinuity to the mixing plane. Consequently, $\rho_0(z)$ is the lateral coherence length of a point source located in the tissue discontinuity plane, and observed in the mixing plane. For the geometry of interest, this quantity is given by[22]

$$\rho_0(z) = \sqrt{\frac{3}{\mu_s z}}\frac{\lambda}{\pi\theta_{rms}}\left(1+\frac{nd(z)}{z}\right), \qquad (3)$$

where $d(z)=f-z/n$. The second term in the brackets of Eq. (3) indicates that the lateral coherence length increases with increasing distance between the tissue surface and the mixing plane. This well-known dependence of the lateral coherence length on the position of the scattering medium relative to the observation plane, is the so-called shower curtain effect.[9,10] In general, the shower curtain effect implies that the lateral coherence length obtained for the case when the scattering medium is close to the radiation source is larger than the case when the scattering medium is close to the observation plane. The effect is well known for light propagation through the atmosphere as discussed by Dror *et al.*,[10] but has been omitted in previous theoretical OCT models.[8] Hence, their results[8] should not be used when considering multiple scattering effects, which is evident from the following paragraphs. However, due to the finite distance between the focusing lens and the tissue, the effect is inevitably present in practical OCT systems and could facilitate system optimization.

The reflection characteristics of the tissue discontinuity play a vital role for the shower curtain effect. If the tissue discontinuity is characterized by specular reflection, instead of diffuse backscattering, the expression for the heterodyne efficiency factor is given by[22]

$$\Psi(z)=\left[\exp\{-2\mu_s z\}+\left(1-\exp\{-2\mu_s z\}\right)\frac{w_H^2}{w_S^2}\right] \tag{4}$$

with

$$\rho_0(z)=\sqrt{\frac{1}{2\mu_s z}}\frac{\lambda}{\pi\theta_{rms}}. \tag{5}$$

It is obvious from Eq. (5) that the shower curtain effect is not present in the case of a specular reflection at the tissue discontinuity, in contrast to the case of diffuse backscattering. However, it is important to note that it is diffuse backscattering which actually occurs in the case of (skin) tissue.

The heterodyne efficiency factor $\Psi(z)$ is shown as a function of depth $z$ of the tissue discontinuity in Fig. 2 for typical parameters of human skin tissue with diffuse backscattering and the shower curtain effect included (dashed) and specular reflection (solid), respectively. For comparison, the case of diffuse backscattering with exclusion of the shower curtain effect (dash-dot) and the case of pure single scattering (dotted) are shown. At shallow depths single backscattering dominates. Due to multiple scattering, the slope is changed and $\Psi(z)$ becomes almost constant for three cases (curve 1-3). The important difference is, however, that the change of slope occurs at different depths. This is due to the shower curtain effect leading to

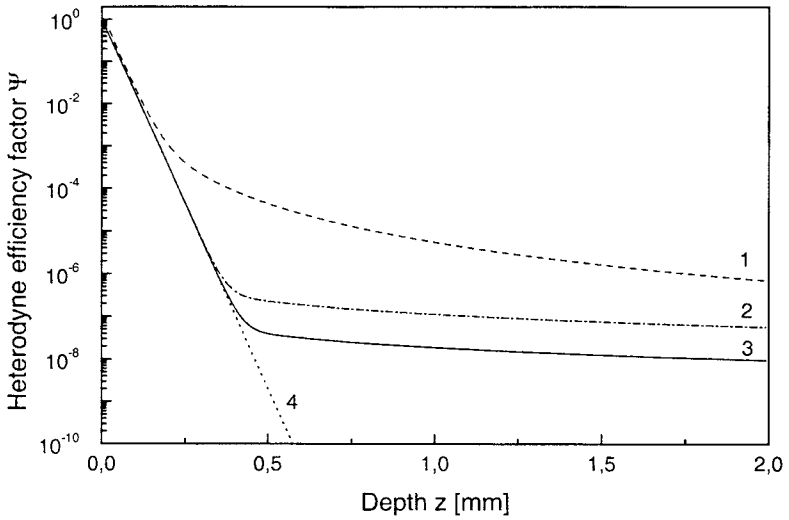


Fig. 2. The heterodyne efficiency factor $\Psi(z)$ as a function of depth $z$ for diffuse backscattering with the shower curtain effect included (curve 1), and for specular reflection (curve 3). Curve 2 is calculated for diffuse backscattering but with the shower curtain effect excluded, and curve 4 is the case of pure single (back-) scattering ($\lambda$=814 nm, $\mu_s$=20 mm$^{-1}$, $g$=0.955 ($\theta_{rms}$=0.3 rad), $n$=1.4, $f$=5 mm, and $w_0$=0.5 mm). From Ref. 30.

an appreciable enhancement of $\Psi(z)$, and with it the heterodyne signal, which is obtained by comparing curve 1 and 2 in Fig. 2.

### 2.2. Experimental results

The above theoretical analysis is verified by measurements on samples consisting of aqueous suspensions of microspheres, and solid phantoms as discussed in Refs. 22 and 30. For these experiments, a conventional OCT setup[1] comprised by a superluminescent diode (SLD) with a center wavelength of 814 nm (22.8 nm spectral bandwidth (FWHM), 1.9 mW output power), a fiber-optic Michelson interferometer with moveable reference mirror, and a silicon photodetector is used.

In the first experiment, the samples consist of latex (polyvinyltoluene) microspheres with a mean diameter of 2.04 μm (std. dev. 2.2 %) suspended in distilled, deionized water. Mie theory[28] is used to calculate $g$ and the scattering cross section $\sigma_s$, using the sphere diameter, the index of refraction (1.59 @ 589 nm (25°C)), and the specific weight (1.05 g/ml) of the microspheres, together with the index of refraction (1.33) and the specific weight (1.00 g/ml) of water. When $\sigma_s$ is known, the concentration of microspheres needed to obtain a specific $\mu_s$ may be found. The samples are placed in a 0.5 mm (internal thickness) glass cuvette with a changeable back plate. In the experiments, both a Si and a glass plate giving diffuse backscattering and specular reflection, respectively, are used to define the probed liquid-back plate discontinuity. The interferogram of a single scan is analyzed to determine the maximum amplitude of the envelope, and by averaging a number of scans, their mean value is used in the determination of the heterodyne efficiency factor.

Fig. 3 shows the theoretical predictions and measurements of the heterodyne efficiency factor $\Psi$ as a function of the scattering coefficient $\mu_s$ for the case of diffuse backscattering (dashed (no fit) and solid (fitted curve) lines; squares) and specular reflection (dash-dot line; circles) at the discontinuity. As shown in Fig. 3, excellent agreement between theory and experiment in the case of specular reflection is obtained. In the case of diffuse backscattering, the experimental data shows deviations from theory (dashed line; no fit). However, there is no doubt that the experimental results show a clear deviation from what would be obtained in the absence of the shower curtain effect (i.e., specular reflection). At $\mu_s$=7 mm$^{-1}$, the experimental value of the heterodyne efficiency factor is a factor of about 5 larger than the value that would be obtained in the absence of the shower curtain effect. Hence, it is clearly demonstrated that the shower curtain effect *increases* the heterodyne signal through enhanced spatial coherence of the multiple scattered light. Mismatch of the focal and discontinuity planes, and the strong fluctuations of the interference signal caused by the motion of the scattering microspheres, may be the reasons for the deviation from the theoretical curve.

In the second experiment, the geometry is identical to the one shown in Fig. 1. Solid phantoms consisting of scattering microspheres (approximate diameter size 10 μm) in polymer are used as the scattering medium with thickness $z$. The optical

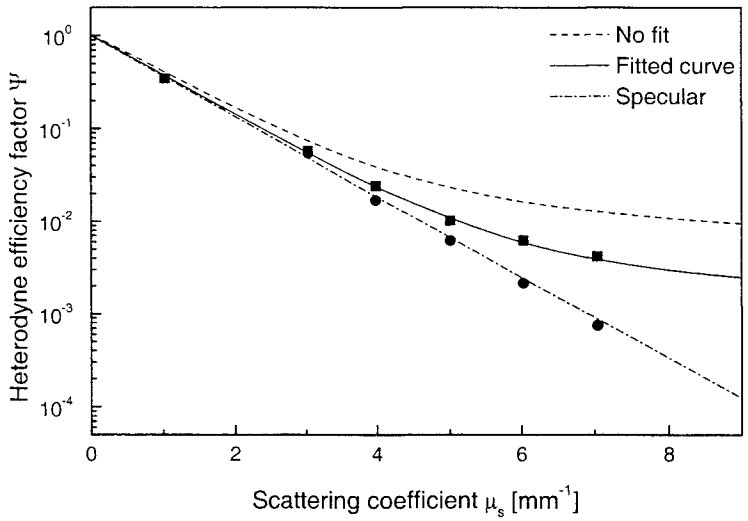


Fig. 3. The theoretical curves and measurements of the heterodyne efficiency factor $\Psi$ as a function of the scattering coefficient $\mu_s$ for the case of diffuse backscattering (dashed (no fit) and solid (fitted curve);■) and specular reflection (dash-dot;●) at the discontinuity. The probing depth $z$ is 0.5 mm, and the typical standard deviation for the squares (■) is ±7.8 % ($\lambda$=814 nm, $g$=0.929 ($\theta_{rms}$=0.38 rad), $n$=1.33, $f$=16 mm, and $w_0$=0.125 mm). From Ref. 25.

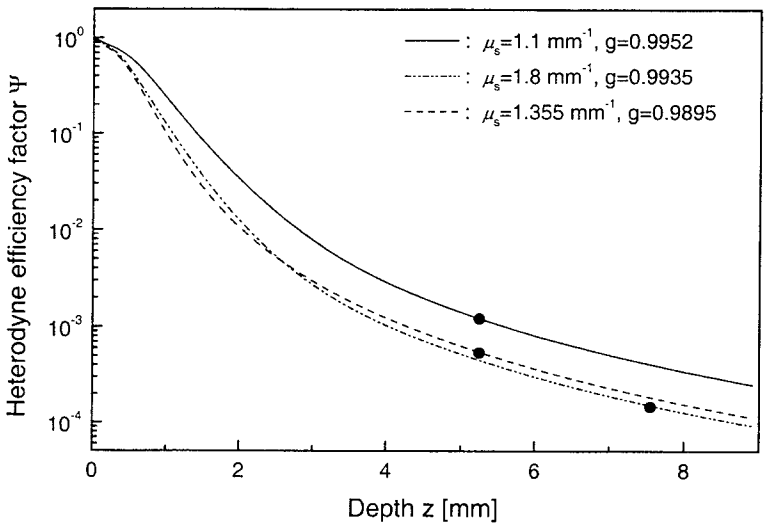


Fig. 4. The theoretical curves and measurements of the heterodyne efficiency factor Ψ as a function of sample depth for three solid phantoms ($\lambda$=814 nm, $n$=1.5, $f$=16 mm, and $w_0$=0.125 mm). Experimental data is represented by circles (●).

parameters of the solid phantoms, i.e., the asymmetry parameter, the scattering coefficient, and the absorption coefficient, were determined by carrying out integrating sphere and collimated transmission measurements.[31] All phantoms used for these experiments had a negligible absorption. The probed discontinuity is defined by the phantom-air interface. This discontinuity is giving a diffuse backscattering. Fig. 4 shows the theoretical curves and the measurements of the heterodyne efficiency factor Ψ as a function of sample depth with the scattering coefficient and asymmetry parameter[28] $g$ as parameters. The theoretical curves are created by fitting to the experimental points using $g$ as the only fitting parameter. The values of $g$ obtained in this way are shown in the inset, and they are less than 0.25% from the values determined by the integrating sphere setup. Hence, good agreement between theory and experiment has been demonstrated.

### 2.3. Maximum probing depth

In the present section, the maximum probing depth for an OCT system is calculated using the theoretical model based on EHF and assuming shot-noise limited detection. The details of derivation may found in Thrane *et al.*[25]

Assuming shot-noise-limited operation, the only significant source of noise is the shot-noise caused by the reference beam. For a photoconductive detector the mean square noise power $N$ can be expressed as $N = i_N^2 R_l = 2\alpha q G^2 R_l B_w P_R$,[32] where $\alpha$ is a conversion factor from power to current, $q$ the electron charge, $R_l$ is the resistance of the load, $G$ is the gain associated with the current amplifier, and $B_w$ is the system bandwidth. The corresponding mean heterodyne signal power $S(z)$ is given by[33] $S(z) = \langle i^2(z) \rangle G^2 R_l$, where $\langle i^2(z) \rangle$ is given by Eq. (1). Hence, the mean signal-to-noise ratio $SNR(z)$ is given by

$$SNR(z) = \frac{S(z)}{N} = SNR|_0 \, \Psi(z). \tag{6}$$

In the absence of scattering the signal-to-noise ratio is given by $SNR|_0 = (\eta P_s / 2h\nu B_w)(\sigma_b / \pi w_H^2)$, where $\eta$ is the detector quantum efficiency, $h\nu$ the photon energy, and $\sigma_b$ the effective backscattering coefficient of the probed tissue defined above. In the case of interest where the focal plane coincides with the tissue discontinuity, the signal-to-noise ratio is given by $SNR|_0 = (2\eta P_s / h\nu B_w)(w_0 / f)^2 R_d$.

The calculation of the maximum probing depth $z_{max}$ is based on the minimum acceptable signal-to-noise ratio.[25] In these calculations, the value 3 has been used as the minimum acceptable signal-to-noise ratio, i.e., $SNR(z_{max}) = 3$. Thus, in order to determine the maximum probing depth, the following equation must be solved with respect to $z_{max}$:[25]

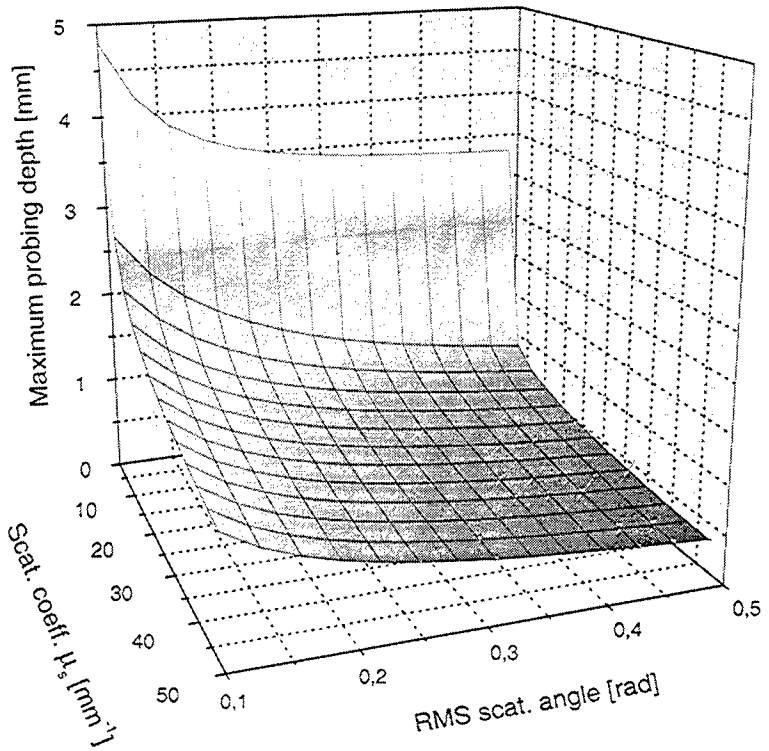


Fig. 5. The maximum probing depth $z_{max}$ as a function of the scattering coefficient $\mu_s$ and the rms scattering angle $\theta_{rms}$ (the asymmetry parameter $g=\cos\theta_{rms}$) with focal length f=16 mm, $1/e$ beam radius $w_0$=125 μm, and tissue discontinuity reflection coefficient $R_d=10^{-4}$.

$$\frac{2\eta P_s}{h\nu B_w}\left(\frac{w_0}{f}\right)^2 R_d \Psi\left(z_{max}\right) = 3 \tag{7}$$

where $\Psi$ is given by either Eq. (1) or Eq. (4) depending on the reflection characteristics of the probed discontinuity. As can be seen from Eq. (7), our calculation of the maximum probing depth is based on the design variables of the OCT system, the detector characteristics, and the optical properties of the tissue.

The dependence of $z_{max}$ on the scattering coefficient $\mu_s$ and the rms scattering angle $\theta_{rms}$ (the asymmetry parameter $g=\cos\theta_{rms}$) is shown in Fig. 5 with focal length $f$=16 mm, $1/e$ beam radius $w_0$=125 μm, and tissue discontinuity reflection coefficient $R_d=10^{-4}$. Fig. 6 shows the maximum probing depth $z_{max}$ as a function of the scattering coefficient $\mu_s$ for a typical OCT system.[25] In the calculations, the following parameters have been used: λ=814 nm, $g$=0.955, $n$=1.4, $f$=16 mm, $w_0$=0.125 mm, $P_s$=650 μW, $B_w$=10 kHz, $\eta$=0.8, and $R_d$=0.05%. The solid curve represents the case found in tissue where the probed discontinuity is giving a diffuse backscattering and the shower curtain effect is present. The dashed curve represents three different cases which all give the same dependence of the maximum probing depth on the scattering coefficient. The three different cases are diffuse backscattering at the discontinuity with exclusion of the shower curtain effect, specular reflection at the discontinuity, and pure single backscattering. It is important to note that the shower curtain effect, which is a multiple scattering effect, alone is responsible for the marked difference between the solid and the dashed curves. This demonstrates that multiple scattering and the shower curtain effect are important effects to consider when calculating the maximum probing depth in tissue.

### 2.4. System optimization

The primary motivation for the development of OCT models is optimization of the OCT technique based on these models, thereby improving the imaging capabilities. In this section, the important role of the shower curtain effect when focusing on system optimization in terms of maximum signal power is discussed.

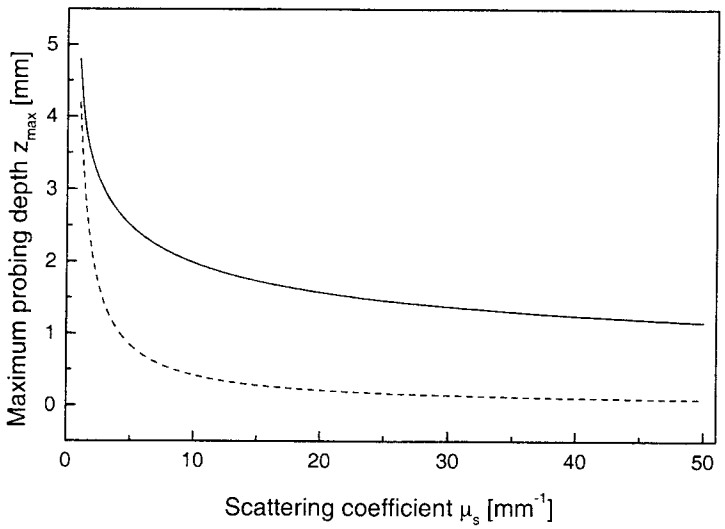


Fig. 6. The maximum probing depth $z_{max}$ as a function of the scattering coefficient $\mu_s$ for a typical OCT system ($\lambda$=814 nm, $g$=0.955, $n$=1.4, $f$=16 mm, $w_0$=0.125 mm, $P_s$=650 μW, $B_w$=10 kHz, $\eta$=0.8, and $R_d$=0.05%). Solid curve: diffuse backscattering at discontinuity and shower curtain effect included. Dashed curve: represents three different cases yielding similar results; (i) diffuse backscattering at discontinuity and the shower curtain effect excluded, (ii) specular reflection at discontinuity, and (iii) pure single backscattering (taken from Ref. 25).

In Fig. 7, the normalized signal power, or the normalized mean square heterodyne signal current, is shown as a function of the focal length $f$ for three different scattering coefficients $\mu_s$ (2, 10, and 15 mm$^{-1}$) and diffuse backscattering with the shower curtain effect included. The probing depth is $z$=0.5 mm in this case. For the purpose of system optimization in terms of maximum signal it is obvious from Fig. 7 that the optimal choice of focal length is to keep it as short as possible. However, as a direct consequence of the shower curtain effect, the advantage of choosing a short focal length decreases with increasing value of the scattering coefficient, or the optical depth $\mu_s z$, which is obtained from Fig. 7. This is because the shower curtain effect is a multiple scattering effect thus playing a crucial role in a medium with a high scattering coefficient. For a sufficiently high scattering coefficient, in this case about 15 mm$^{-1}$, we reach a point where the choice of focal length does not affect the OCT signal.

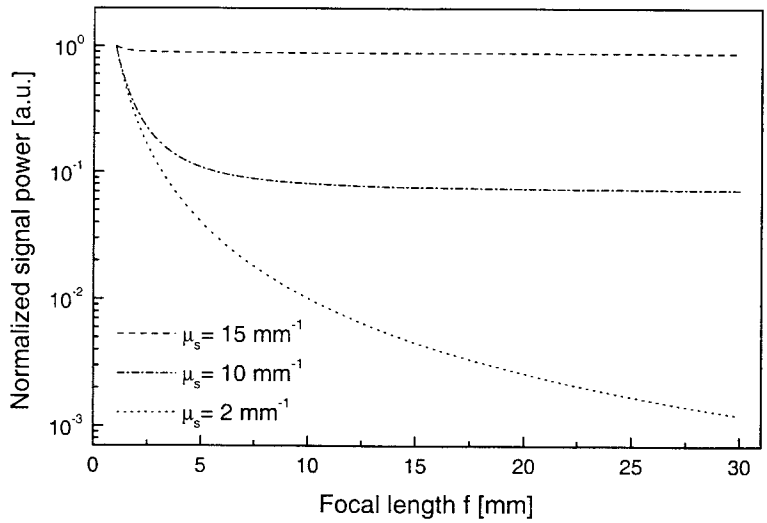


Fig. 7. The normalized signal power as a function of the focal length $f$ for three different scattering coefficients $\mu_s$ and diffuse backscattering with the shower curtain effect included. The probing depth $z$=0.5 mm ($\lambda$=814 nm, $g$=0.955 ($\theta_{rms}$=0.3 rad), $n$=1.4, and $w_0$=0.5 mm). From Ref. 30.

## 3. MONTE CARLO SIMULATIONS

Monte Carlo simulations (MCS) have proven their feasibility in terms of predicting the distribution of light in random media.[16,17] Most studies, in which MCS have been applied, are concerned with the distribution of the intensity rather than the complex field, i.e. amplitude and phase. The two latter parameters are essential in order to include the coherence properties and thereby considering interference effects. However, by using a method that keeps track of the path length of each photon interacting with random media, the use of MCS is extended to handle propagation of essentially coherent beams. Recently, this has been discussed in the literature.[18-20]

Most OCT systems combine coherence gating with focusing of the sample beam in order to attain the highest possible longitudinal rejection of scattered, incoherent light and a high lateral spatial resolution. Previous MCS models either excluded sample beam focusing or simply modeled the focused beam by a so-called pencil beam. The purpose of our work, described below, has been to develop a MCS code for modeling the OCT system including Gaussian shaped beam focused with a true focus. In the present model, the focusing has been modeled by using a hyperboloid of one sheet. Simulations carried out on non-scattering media revealed perfect match to a Gaussian focal point. Furthermore, the reflectance characteristics of the discontinuity being probed at a certain depth in the tissue are investigated. In particular, two important cases are treated: firstly specular reflection, and secondly diffuse reflection. The latter characterizes reflection of light from rough surfaces,[34] which is the case when considering biological tissues. Moreover, this also facilitates the study of the capability of the MCS code to describe the shower curtain effect.[9,10] For a detailed description of the MCS code that has been developed, the reader is referred to Tycho *et al.*[24] Finally, the present section is primarily concerned with comparing our MCS output to other well-established models, e.g. the extended Huygens-Fresnel principle,[22] and experimental data.

### 3.1. MCS code and extensions

The MCS code that has been developed[24] is based on the "Monte Carlo for multi-layered media" software implementation written by Jacques and Wang.[35] The code has, however, been modified to incorporate the focusing of a Gaussian shaped laser beam being injected into the tissue. This important feature is accomplished by using the fact that the surface of the $1/e$-intentsity of that on the axis for a Gaussian beam is well approximated by a hyperboloid of one sheet, and that such a surface can be described by a set of straight lines.[24] Furthermore, by keeping track of the path length experienced by the individual photons, the code has been modified to simulate the mixing process with the reference beam at the photodetector as is the case in the OCT system. Finally, a choice between various scattering phase functions, e.g. the Henyey-Greenstein function[35] or a Gaussian shaped function, has been incorporated into the code.

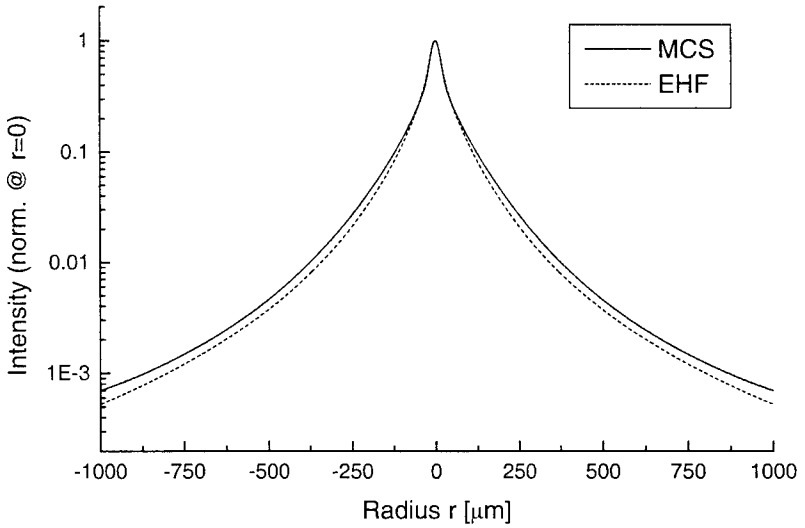


Fig. 8. Normalized lateral intensity profile (normalized at $r$=0) of a focused beam (Gaussian distribution) as a function of distance $r$ at a depth of $z$=0.7 mm into the tissue: MCS (solid line) and EHF (dashed line). The remaining parameters are: scattering coefficient $\mu_s$=7 mm$^{-1}$, asymmetry parameter $g$=0.9, refractive index $n$=1.4, source wavelength $\lambda$=814 nm, $1/e$ radius $w_0$=125 μm, and focal length $f$=16 mm.

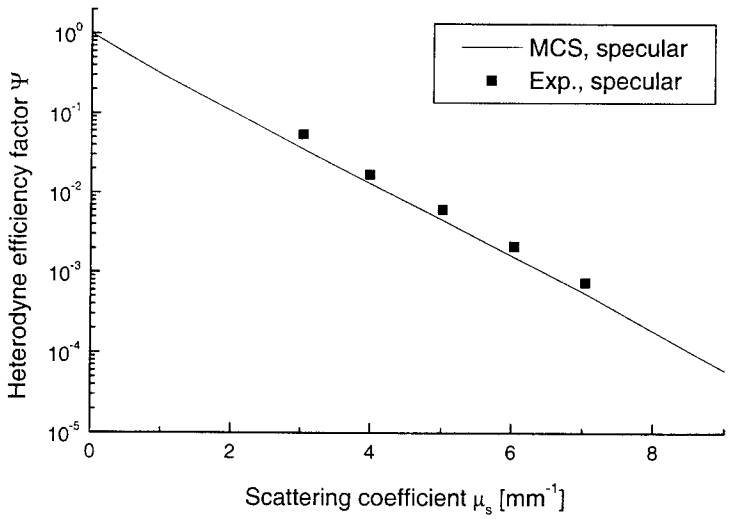


Fig. 9. Monte Carlo simulation of the heterodyne efficiency factor $\Psi$ as a function of the scattering coefficient $\mu_s$. The discontinuity is characterized by specular reflection: MCS (solid line) and experimental data (squares). Remaining parameters given in Fig. 8.

### 3.2. Numerical results and comparison

In Fig. 8, the normalized lateral intensity profile as a function of distance $r$ is shown after propagating 700 μm into a tissue characterized by an optical depth of $\mu_s z$=4.9 ($\mu_s$=7 mm$^{-1}$), an asymmetry parameter of $g$=0.9, and refractive index of 1.4. The wavelength of the source is λ=814 nm with $1/e$ radius $w_0$=125 μm. The focal length of the sample beam focusing lens is $f$=16 mm. These parameters represent the experimental setup that previously was used to investigate the use of the EHF model in OCT.[22] In Fig. 8, the MCS simulation using the Henyey-Greenstein scattering phase function[35] is compared with the extended Huygens-Fresnel principle (using similar scattering phase function). Evidently, good agreement between the two models is obtained. Note that other sets of parameters have been simulated with similar results.

By simulating the detection process of the OCT system as described in Tycho *et al.*[24], the heterodyne efficiency factor $\Psi$, described in section 2.1 above, has been calculated for various values of the scattering coefficient $\mu_s$. The remaining parameters are similar to those used in Fig. 8. Fig. 9 shows the simulated heterodyne efficiency factor as a function of the scattering coefficient with fixed sample probing depth $z$=0.5 mm. For these simulations, the discontinuity is assumed to have a specular reflection. Furthermore, experiments[22] carried out on aqueous scattering phantoms are shown. As expected, a straight-line dependence is observed in this case (see also Fig. 3a). However, in Fig. 9 it is important to realize the good agreement between the MCS using specular reflection and experimental data.

Finally, the heterodyne efficiency factor has been calculated for the case of diffuse reflectance of the probed discontinuity. The parameters used in this simulation are identical to those stated above. The result is shown in Fig. 10, where the heterodyne efficiency factor is plotted as a function of the scattering coefficient. The solid line represents the diffusely reflecting discontinuity and the dashed line the specularly reflecting discontinuity from Fig. 9. The latter curve shows the expected straight-line slope in a log-plot. However, the diffusely reflecting discontinuity causes the heterodyne efficiency factor to level off from a straight-line slope as evident in Fig. 10. This behavior is a result of the previously discussed shower curtain effect (section 2.1), which manifests itself in OCT systems. Note that such behavior has been verified experimentally as shown in Fig. 3a. The MCS for the diffusely scattering discontinuity has not yet been matched satisfactorily to the EHF model or experimental data, which probably is due to inadequate modeling of the discontinuity characteristics in the MCS. Currently, investigations are undertaken to simulate the diffusely reflecting surface properly.

The use of MCS has successfully explained numerous experiments involving light propagation in random media demonstrated throughout the literature. Hence, MCS has deservedly gained its reputation as a reference point standard. However, adequate modeling requires a large number of photon packages resulting in lengthy calculations. The above comparison of the EHF model, which is an analytical model requiring little computational effort, and MCS shows that the analytical model provides as much insight as the MCS. Therefore, at least when modeling the operation of OCT systems, our results suggest that using the extended Huygens-Fresnel principle is advantageous over MCS.

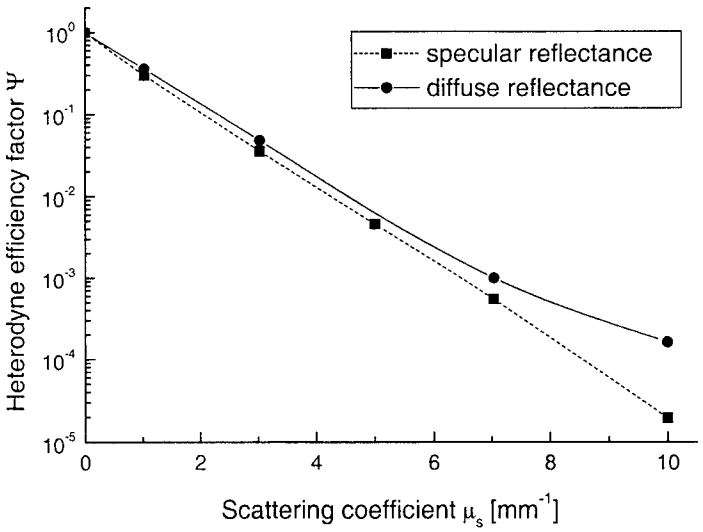


Fig. 10. Monte Carlo simulation of the heterodyne efficiency factor $\Psi$ as a function of the scattering coefficient $\mu_s$: MCS with diffuse reflectance (solid line and circles); MCS with specular reflectance (dashed line and squares). Remaining parameters given in Fig. 8.

## 4. CONCLUSION

A new theoretical model of the optical coherence tomography (OCT) geometry for imaging in highly scattering tissue has been presented. The model is based on the extended Huygens-Fresnel principle, and it is valid in the single and multiple scattering regimes. The so-called shower curtain effect, an inherent property of the extended Huygens-Fresnel model, is shown to be essential for calculating the OCT heterodyne signal, when multiple scattering effects are dominating and the probed discontinuity yields a diffuse reflection (rough surface). Using the new model, a method for calculating the maximum probing depth is outlined, and an OCT system with shot-noise limited detection has been investigated. Moreover, the model may be used for optimization of the OCT system. In particular, the optimization reveals that in cases where multiple scattering dominates the magnitude of the detected signal power is practically independent of the choice of numerical aperture, which is due to the shower curtain effect.

Monte Carlo simulations (MCS) have been applied to investigate the operation of an OCT system with a focused sample beam. The code is capable of handling various scattering phase functions. As a novelty, the point-spread of the focused beam has been included. The focusing of the beam has been modeled by using a hyperboloid of one sheet. Furthermore, the reflection characteristics of the probed discontinuity have been investigated. In particular, specular reflection and diffuse reflection, i.e. reflection from a rough surface, have been investigated, respectively. For the latter case, it is known that the so-called shower curtain effect is of utmost importance when considering multiply scattered light, which is the case in most OCT systems. Comparisons between MCS, the extended Huygens-Fresnel principle, and experiments demonstrate that our MCS code adequately describes the operation of the OCT system for specular reflections from the probed discontinuity. Moreover, the MCS code reveals the influence of the shower curtain effect.

The use of MCS has successfully explained numerous experiments involving light propagation in random media demonstrated throughout the literature. Hence, MCS has deservedly gained its reputation as a reference point standard. However, adequate modeling requires a large number of photon packages resulting in lengthy calculations. The above comparison of the EHF model, which is an analytical model requiring little computational effort, and MCS shows that the analytical model provides as much insight as the MCS. Therefore, at least when modeling the operation of OCT systems, our results suggest that using the extended Huygens-Fresnel principle is advantageous over MCS.

## ACKNOWLEDGMENTS

Peter E. Andersen acknowledges the financial support from The Danish Technical Research Council under grant no. 9901433. Lars Thrane acknowledges the financial support from The Danish Technical Research Council under grant no. 9601565.

## REFERENCES


1. D. Huang, E. A. Swanson, C. P. Lin, J. S. Schuman, W. G. Stinson, W. Chang, M. R. Hee, T. Flotte, K. Gregory, C. A. Puliafito, and J. G. Fujimoto, "Optical Coherence Tomography", Science **254**, pp. 1178-1181, 1991.
2. J. M. Schmitt, A. Knüttel, and R. F. Bonner, "Measurement of optical properties of biological tissues by low-coherence reflectometry", Appl. Opt. **32**, pp. 6032-6042, 1993.
3. J. M. Schmitt, A. Knüttel, A. S. Gandjbakhche, and R. F. Bonner, "Optical characterization of dense tissues using low-coherence interferometry", *Proc. SPIE* **1889**, pp. 197-211, 1993.
4. M. J. Yadlowsky, J. M. Schmitt, and R. F. Bonner, "Multiple scattering in optical coherence microscopy", Appl. Opt. **34**, pp. 5699-5707, 1995.
5. M. J. Yadlowsky, J. M. Schmitt, and R. F. Bonner, "Contrast and resolution in the optical coherence microscopy of dense biological tissue", *Proc. SPIE* **2387**, pp. 193-203, 1995.
6. Y. Pan, R. Birngruber, J. Rosperich, and R. Engelhardt, "Low-coherence optical tomography in turbid tissue: theoretical analysis", Appl. Opt. **34**, pp. 6564-6574, 1995.
7. Y. Pan, R. Birngruber, and R. Engelhardt, "Contrast limits of coherence-gated imaging in scattering media", Appl. Opt. **36**, pp. 2979-2983, 1997.
8. J. M. Schmitt and A. Knüttel, "Model of optical coherence tomography of heterogeneous tissue", J. Opt. Soc. Am. A **14**, pp. 1231-1242, 1997.
9. H. T. Yura, "Signal-to-noise ratio of heterodyne lidar systems in the presence of atmospheric turbulence", Optica Acta **26**, pp. 627-644, 1979.
10. I. Dror, A. Sandrov, and N. S. Kopeika, "Experimental investigation of the influence of the relative position of the scattering layer on image quality: the shower curtain effect", Appl. Opt. **37**, pp. 6495-6499, 1998.
11. A. F. Fercher, "Optical coherence tomography", J. Biomed. Opt. **1**, pp. 157-173, 1996.
12. J. M. Schmitt, "Optical coherence tomography (OCT): A review", IEEE J. Select. Topics in Quantum Electronics **5**, pp. 1205-1215, 1999.
13. M. E. Brezinsky, J. G. Fujimoto, "Optical coherence tomography: High resolution imaging in nontransparent tissue", IEEE J. Select. Topics in Quantum Electronics **5**, pp. 1185-1192, 1999.
14. M. R. Hee, D. Huang, E. A. Swanson, and J. G. Fujimoto, "Polarization-sensitive low-coherence reflectometer for birefringence characterization and ranging", *J.* Opt. Soc. Am. B **9**, pp. 903-908, 1992.
15. J. F. de Boer, S. M. Srinivas, B. H. Park, T. H. Pham, Z. Chen, T. E. Milner, and J. S. Nelson, "Polarization effects of optical coherence tomogtaphy of various biological tissues", IEEE J. Select. Topics in Quantum Electronics **5**, pp. 1200-1204, 1999.
16. B. C. Wilson and G. Adams, "A Monte Carlo model for the absorption and flux distributions of light in tissue", Med. Phys. **10**, pp. 824-830, 1983.
17. M. Keijzer, S. L. Jacques, S. A. Prahl, and A. J. Welch, "Light distributions in artery tissue: Monte Carlo simulations for finite-diameter laser beams", Lasers Surg. Med. **9**, pp. 148-154, 1989.
18. G. Yao and L. V. Wang, "Monte Carlo simulation of an optical coherence tomography signal in homogeneous turbid media", Phys. Med. Biol. **44**, pp. 2307-2320, 1999.
19. D. J. Smithies, T. Lindmo, Z. Chen, J. S. Nelson, and T. E. Milner, "Signal attenuation and localization in optical coherence tomography studied by Monte Carlo simulation", Phys. Med. Biol. **43**, pp. 3025-3044, 1998.
20. Z. Song, K. Dong, X. H. Hu, and J. Q. Lu, "Monte Carlo simulation of converging laser beam propagating in biological materials", Appl. Opt. **38**, pp. 2944-2949, 1999.
21. L. Thrane, H. T. Yura, S. G. Hanson, and P. E. Andersen, "Optical Coherence Tomography of Heterogeneous Tissue: Calculation of the Heterodyne Signal", in CLEO/Europe'98 Technical Digest, paper CTuE6, p. 58, Glasgow, Scotland, 14-18 September 1998.
22. L. Thrane, H. T. Yura, and P. E. Andersen, "Analysis of optical coherence tomography systems based on the extended Huygens-Fresnel principle", to be published in J. Opt. Soc. Am. A, March 2000.
23. R. F. Lutomirski and H. T. Yura, "Propagation of a Finite Optical Beam in an Inhomogeneous Medium", Appl. Opt. **10**, pp. 1652-1658, 1971.
24. A. Tycho, T. M. Jørgensen, and L. Thrane, "Investigating the focusing problem in OCT: comparison of Monte Carlo simulations, the extended Huygens-Fresnel principle and experiments", to appear in *SPIE Proc.* **3915** (published 2000).

25. L. Thrane, H. T. Yura, and P. E. Andersen, "Calculation of the maximum obtainable probing depth of optical coherence tomography in tissue", to appear in *SPIE Proc.* **3915** (published 2000).
26. M. J. C. van Gemert, S. L. Jacques, H. J. C. M. Sterenborg, and W. M. Star, "Skin Optics", IEEE Transactions on Biomedical Engineering **36**, pp. 1146-1154, 1989.
27. A. E. Siegman, *Lasers*, section 16.1, University Science Books, Mill Valley, California, 1986.
28. C. F. Bohren and D. R. Huffman, *Absorption and Scattering of Light by Small Particles*, John Wiley & Sons, New York, 1983.
29. H. T. Yura and S. G. Hanson, "Optical beam wave propagation through complex optical systems", J. Opt. Soc. Am. A **4**, pp. 1931-1948, 1987.
30. L. Thrane, H. T. Yura, and P. E. Andersen, "Optical Coherence Tomography: New Analytical Model and the Shower Curtain Effect", to appear in *SPIE Proc.* **4001** (published 2000).
31. S. A. Prahl, "The adding-doubling method", Chap. 5 in *Optical-Thermal Response of Laser-Irradiated Tissue (eds. A. J. Welch and M. J. C. van Gemert)*, Plenum Press, New York, 1995.
32. C. M. Sonnenschein and F. A. Horrigan, "Signal-to-noise relationships for coaxial systems that heterodyne backscatter from the atmosphere", Appl. Opt. **10**, pp. 1600-1604, 1971.
33. D. L. Fried, "Optical heterodyne detection of an atmospherically distorted signal wave front", Proc. IEEE **55**, pp. 57-67, 1967.
34. J. W. Goodman, "Statistical properties of laser speckle patterns", Chap. 2 in *Topics in Applied Physics Vol. 9 (ed. J. C. Dainty)*, Springer Verlag, Berlin, 1975.
35. S. L. Jacques and L. Wang, "Monte Carlo modeling of light transport in tissues", Chap. 4 in *Optical-Thermal Response of Laser-Irradiated Tissue (eds. A. J. Welch and M. J. C. van Gemert)*, Plenum Press, New York, 1995.

Invited Paper

# Coherent and Polarization Imaging: Novel Approaches in Tissue Diagnostics by Laser Light Scattering

Dmitry A. Zimnyakov [a], Valery V. Tuchin [a], Roman A. Zdrajevsky [b], Yury P. Sinichkin [a]

[a] Saratov State University, Astrakhanskaya, 83, 410026, Saratov, Russia,
[b] Saratov Technical State University, Polytechnicheskaya, 77, 410054, Saratov, Russia

## ABSTRACT

Different techniques for diagnostics and visualization of the inhomogeneous scattering media by means of the statistical analysis of spatial-temporal fluctuations of scattered light are considered:
1) polarization diagnostics and imaging based on the application of the polarization degree as visualization parameter;
2) imaging techniques on the basis of measurements of the contrast of multiply scattered speckles induced by partially coherent light scattering in the probed object;
3) modification of the speckle imaging technique based on the statistical analysis of time-integrated electronic images of the speckle patterns under coherent light illumination.
Comparison of these methods with traditional approaches to the diagnostics and imaging of macroscopically inhomogeneous multiply scattering objects is made. Experimental results obtained with phantom scattering media and illustrating the potentialities of the discussed approaches are presented.

**Keywords:** imaging, speckle, polarization, contrast, path distribution.

## 1. INTRODUCTION

In the last two decades certain potentialities of application of visible and near-infrared (NIR) light in medical diagnostics stimulated a great number of theoretical and experimental studies dedicated to various fundamental and applied problems of the tissue-light interaction. Different methods of tissue probing and imaging by use of continuos-wave or modulated laser light have been developed and modified for clinical applications in a relatively short period of time due to the significant research activity in this field. The major problem which causes the significant difficulties in reconstruction of optical images of inner structure of human tissues and organs and requires the development of sophisticated algorithms of data acquisition and processing is the multiple scattering of the probe laser light by the disordered and weakly ordered tissue structures. On the other hand, potential ability of optical methods to extract a significant amount of information about structure and functional activity of the probed object makes them a very attractive tool for biological and medical applications. There are several examples of optical technologies with use of visible and NIR laser light as applied to the tissue structure analysis and functional imaging:
1) diffusing-wave spectroscopy in applications to diagnostics and imaging of the dynamic scattering systems (such as ensembles of blood cells and other bio-flows in the living tissues) [1,2];
2) time-domain and frequency-domain methods based on the applications of high-frequency modulated laser light for object probing; pulse-modulated probe-light and time-gating detection technique are used in the first case and, respectively, harmonic modulation of the probe light in combination with heterodyne processing of the detected signal are used in the later case [3,4];
3) low-coherent interferometry, also known as optical coherence tomography (OCT) (there is a lot of theoretical and experimental studies in this field; see, e.g., Ref. 5);
4) CW transillumination, or NIR regional imaging technique based on the measurements of spatial distributions of scattered light intensity obtained with the continuos-wave light sources and reconstruction of the scattering object image by means of appropriate algorithms of inverse problem solution (such algorithms are usually based on the application of the diffusion theory of light transport through multiply scattering media) [6];
5) methods based on measurements of spatial distributions of statistical moments of speckle intensity fluctuations (such as contrast) of multiply scattered light in the case of application of partially coherent light sources [7].
It should be noted, however, that the majority of methods appertaining to the above listed wide groups of the techniques require very expensive and complicated hardware arrangement (such as fast-processing digital correlators, sources of the ultra-short light pulses and opto-electronic equipment for their processing, etc.) for their applications. On the other hand, some simple and relatively non-expensive optical methods could be successfully used for certain specific purposes (such as

In *Laser-Tissue Interaction XI: Photochemical, Photothermal, and Photomechanical*, Donald D. Duncan, Jeffrey O. Hollinger, Steven L. Jacques, Editors, Proceedings of SPIE Vol. 3914 (2000)
1605-7422/00/$15.00

regional imaging and low-resolution tissue topography and tomography, analysis of the functional activity of tissues, rapid diagnostics and screening of the wide groups of patients, etc.) in medical diagnostics. These methods can be based on the analysis of the decay of such properties of laser light as polarization and coherence due to its propagation in multiply scattering tissues.

The goal of this work is the comparative analysis of the following methods of optical diagnostics of tissue structure:
- by using the polarization degree of multiply scattered laser light as imaging parameter;
- by measurements of the contrast of multiply scattered speckles induced by partially coherent source;
- by application of time-integrating speckle photography of the dynamic speckle patterns induced by optical mixing of multiple scattered non-stationary optical field.

The efficiency of the first two approaches is analyzed in comparison with such simple and widely applied method of inhomogeneous media probing as CW transillumination technique by carrying out the Monte-Carlo simulation and experiments with phantom scattering objects. Phenomenological approach based on the concept of pathlength distribution of the partial components of scattered optical field is used for the description of scattered field formation in the case of multiple scattering of probe beam in the analyzed object; pathlength statistics is described by the probability density function of the effective optical paths $\rho(s)$ (see, e.g., Ref. 8); all characteristics of the scattered optical field which are considered as imaging parameters in this study (polarization degree; speckle contrast in the case of partially coherent illumination and contrast of the time-integrated speckle patterns obtained by optical mixing) can be expressed as the integral transforms of $\rho(s)$ or its autocorrelation with correspondingly chosen kernels.

## 2. POLARIZATION DIAGNOSTICS OF MACROSCOPICALLY INHOMOGENEOUS MEDIA IN THE CASE OF TRANSITION FROM SINGLE TO MULTIPLE SCATTERING MODE

### 2.1. Phenomenological description of depolarizing properties of multiply scattering media

Decay of the initial polarization of the probe beam due to its multiple scattering can be expressed in terms of polarization degree and, respectively, this value can be considered as visualization parameter in the case of scattering media probing by use of the coherent light. One of the most convenient approaches for analytical description of depolarizing properties of multiply scattering probed objects is based on the phenomenological concept of distribution of effective optical paths which characterize partial components of scattered optical field. In particular, if linearly polarized probe beam with initial $x$-orientation of electric field propagates through optically dense random medium, we can consider alternate statistically independent polarization channel characterized by linear polarization with electric vector directed along $y$-axis. Thus, intensities of co-polarized ($x$-direction) and cross-polarized ($y$-direction) components of scattered field and, respectively, its polarization degree can be expressed as:

$$
\begin{aligned}
&< I_x >= \frac{I_0}{2} \int_0^\infty \left( 1 + exp\left\{ s/\xi \right\} \right) \rho(s) ds; \\
&< I_y >= \frac{I_0}{2} \int_0^\infty \left( 1 - exp\left\{ - s/\xi \right\} \right) \rho(s) ds; \\
&P = \frac{< I_x > - < I_y >}{< I_x > + < I_y >} = \frac{\int_0^\infty exp\left\{ - s/\xi \right\} \rho(s) ds}{\int_0^\infty \rho(s) ds},
\end{aligned}
\tag{1}
$$

These expressions have been obtained by the modification of equations for temporal autocorrelation functions of co-polarized and cross-polarized components of scattered optical field [9] if time delay is taken equal to 0. Here $\rho(s)$ is probability density function of effective optical paths; $s$ is the effective pathlength characterizing the arbitrary selected partial component of scattered field; $\xi$ is depolarization length which depends on optical properties of scattering medium.

For probe coherent beam averaging $< >$ should be carried out over all possible configurations of ensemble of elementary scatterers if small-aperture photodetector is used.
In the case of "discrete" scattering media consisting of the ensembles of randomly distributed scattering particles normalized depolarization length, which is estimated as the ratio $\tilde{\xi} = \xi / l^*$, depends in the complicated manner on the optical properties of the elementary scatterers such as effective value of size parameter $\langle ka \rangle$ and real and imaginary parts of their refractive index with respect to background medium; $k$ is the wavenumber of the probe light, $a$ is the characteristic size of the elementary scatterer (e.g., radius for spherical particles). Mean transport length $l^*$ is the characteristic spatial scale of the scattering medium which corresponds to full stochastization of the direction of probe light propagation [10]. Another dimensionless parameter of the scattering medium is the effective number of scattering events causing polarization decay: $\tilde{N} = \xi / l = \tilde{\xi} / (1 - g)$, where $l$ is the mean scattering length. For discrete scattering media such as ensembles of randomly distributed scattering particles $l = \mu_s^{-1} = (n\sigma)^{-1}$, where $\mu_s$ is the scattering coefficient, $\sigma$ is the scattering cross-section of the isolated scattering particle and $n$ is the volume concentration of scattering particles; $l$ and $l^*$ are related with each other as $l^* = l/(1-g)$.

Rigid analytical calculation of probability density function $\rho(s)$ is possible only for the small number of scattering systems with simple geometry if pure diffusion mode of probe light propagation through scattering object takes place [8]. It is well-known fact that in the intermediate case of light transport through scattering media, when $l^*$ is comparable with the characteristic size of scattering object (for example, slab with $L \sim l^*$) and contributions of non-scattered ("ballistic") and low-step scattered components become significant, Monte-Carlo simulation gives the better results in comparison with the different analytical approaches based on the various forms of modification of radiative transfer equation.

**3.2. Path statistics analysis by means of Monte-Carlo simulation: procedure description and results**
In order to compare polarization imaging technique with such universally adopted method as CW transillumination technique the following scattering model has been accepted. Macroscopically homogeneous scattering slab with near-zero absorption has been considered as turbid object masking the embedded inhomogeneity (absorbing half-plane). Distance between half-plane and slab surfaces is equal to $L/2$. Collimated point-like probe source used to locate the edge of the model inhomogeneity is placed on the slab surface and the beam axis is perpendicular to both interfaces and absorbing half-plane. Transmitted light is collected by on-axis detection system placed behind the slab; efficiency of light collection is determined by the distance between detector aperture and output interface, numerical aperture of detector and its size. Standard set of parameters such as scattering coefficient $\mu_s = l^{-1}$, absorption coefficient $\mu_a$ and mean value of the cosine of scattering angle $g$ has been used to characterize the optical properties of the masking medium. Henvey-Greenstein function has been applied to simulate the angular distribution of light scattered by the single particle – elementary scatterer. Optical pathlength statistics has been analyzed for each given position of the edge of absorbing half-plane with respect to source-detector axis for different detection conditions:
1) finite-sized "isotropic" detector (i.e., with isotropic angular dependence of sensitivity) is placed on the output interface;
2) detector with given numerical aperture is placed on the given distance from the output interface so all the partial components of the scattered field leaving the slab and propagating in free space inside the "detection cone" will form the detector response (e.g., this case corresponds to the detection system which includes the fiber-optical light collector).

It is necessary to note that in these cases optical pathlength statistics will strongly differ from that for "ideal" detection conditions (when isotropic point-like detector is used). Indeed, for such detection conditions $\rho(s)$ can be obtained by the integration of the "local" probability density of optical paths for each interface point over the whole area inside the "detection cone" (or across the detector aperture in the first case) with an appropriate weighting function which takes into account the efficiency of the light collection in the dependence on the detection angle. Thus, analyzing parameters of pathlength distribution (e.g., most probable value of effective optical path $s_m$) for diffusion mode of light transport it is easy to see that this value strongly depends on the source-detector separation $\Delta L$ (as $\sim (\Delta L)^2$). Correspondingly, light collection from finite-sized area of the output interface of scattering slab will cause the "broadening" of probability density

function $\rho(s)$ and increase of statistical moments of $s$ distribution in comparison with "ideal" detection conditions for on-axis source-detector combination.

Boundary reflections on the slab interfaces have been taken into account by using Fresnel formulas for arbitrary polarization of the propagating light. Probability density functions of the effective optical paths of partial components were reconstructed during the simulation by using the procedure of distribution of groups of transmitted "photons" over the set of pathlength bins.

Typical changes of the probability density function of effective optical paths with an increase of $\Delta X$ (separation between half-plane edge and source axis), which are caused by cut-off of the part of scattered field components absorbed by the phantom inhomogeneity, are shown in Fig. 1 for different values of scattering coefficient and factor of anisotropy of the background scattering medium (normalized value of absorption coefficient was taken equal to $0.1L^{-1}$ in all cases). Logarithmic plot is used to show all graphs because of the significant predominance of low-step scattered components with $s \sim L$ in comparison with "diffusing" components of scattered field in case of weak scattering (when the mean transport length of the background scattering medium is of the order of slab thickness). Non-scattered, or "ballistic" component with $s = L$ is not shown on these pictures; "isotropic" detector with circle aperture is placed on the output interface of slab in the on-axis position ( $x' = y' = 0$ ).

Thus, simulation results show that in the case of small values of anisotropy factor ( $g$ = 0.3) form of probability density function of effective optical paths $\rho(s)$ is more sensitive in comparison with the case of anisotropic scattering ( $g$ = 0.8) to the variations of inhomogeneity position with respect to beam axis (especially in the short-path part of $s$ distributions; see Fig.1,c,d, curves □ and O). Curves formed by open triangles correspond to pure diffusion mode of the light propagation between source and detector, when low-step scattered components are totally "overlapped" by inhomogeneity (large positive values of $\Delta X$ ).

For large positive values of $\Delta X$ (and, respectively, for predominating diffusion mode of light transport through slab) decay of initial polarization with an increase of $\Delta X$ is determined by the form of pathlength distribution tail (i.e., scaling behavior of $\rho(s)$ in the region of large $s$ ). When $s$ increases, decay of pathlength density $\rho(s)$ is determined by two concurring factors:

1) "diffusion" decay of $\rho(s)$ manifested approximately as power-law decrease;

2) exponential decay as the manifestation of generalized Bougier's law due to non-zero absorption.

It should be noted that for hypothetical non-absorbing finite-sized media with predominating diffusion of the probe light in the scattering volume decay tendency of $\rho(s)$ is determined by the boundary conditions. In terms of "classical" diffusion approach these conditions are taken into account in the generalized form by introducing so-called extrapolation length, which in turn depends on total reflection coefficient of scattering medium.

### 3.3. Experimental approbation of the polarization imaging technique for intermediate scattering regime

Experimental setup used for evaluation of the quality of "images" of the phantom inhomogeneity (edge of absorbing half-plane) in the dependence on optical properties of background scattering medium is schematically shown in Fig. 2. He-Ne laser with linearly polarized output was used as the source of the probe beam 1. Electromechanical modulator of the probe light intensity 2 (chopper) was applied in combination with lock-in amplifier of photo-electric signal to provide the better signal-to-noise ratio in polarization degree measurements, modulation frequency was equal to 1 kHz. Probe beam was passed through the flat glass cuvette 3 ( $L$ = 40 mm) filled by the phantom scattering medium (diluted milk). Phantom absorber (half-plane) 4 was placed in the middle part of cuvette; half-plane is perpendicular to the probe beam axis.

Scattered light was passed through the manually rotated polarizer 5 and collected by the multi-mode fiber 6 (core diameter is 400 μm, numerical aperture is 0.20) placed in the on-axis position (with respect to probe beam) behind the phantom scatterer (cuvette). Separation between cuvette and fiber tip was equal to 40 mm.

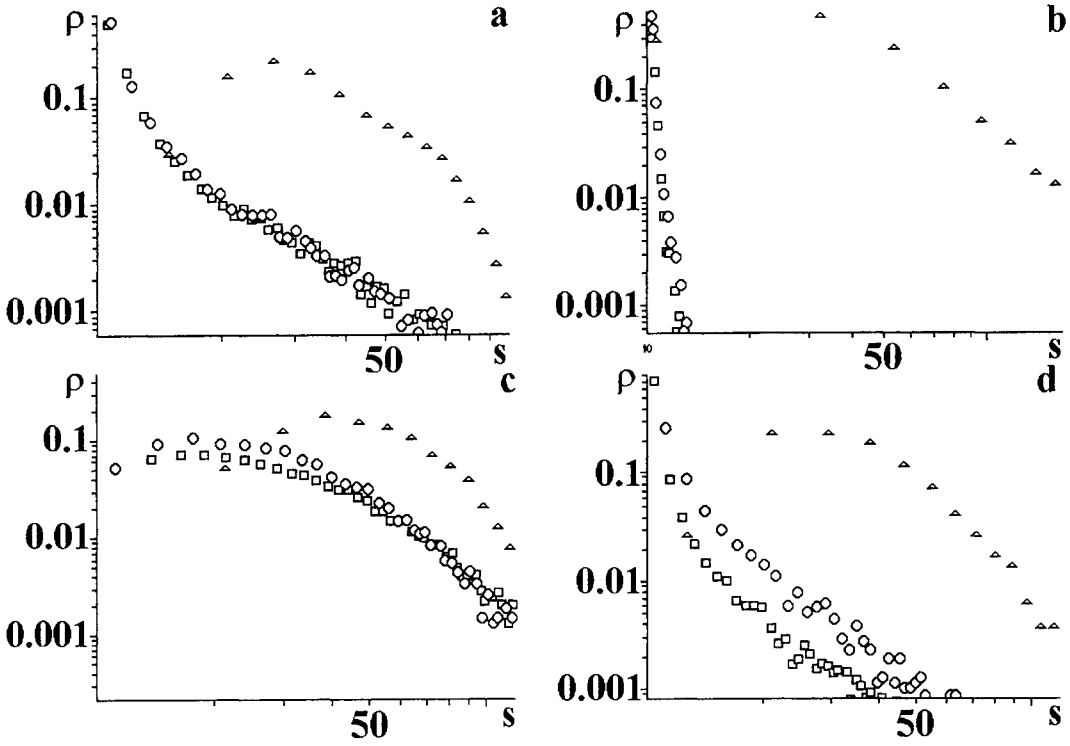


Fig.1. Fragments of probability density functions of effective optical paths (results of Monte-Carlo simulation). a - $g = 0.8$; $\mu_s = 10\,L^{-1}$, b - $g = 0.8$; $\mu_s = 2\,L^{-1}$; c - $g = 0.3$; $\mu_s = 10\,L^{-1}$, d - $g = 0.3$; $\mu_s = 2\,L^{-1}$. □ - $\Delta X = -L$; O - $\Delta X = 0$; Δ - $\Delta X = 0.5\,L$. Values of effective optical path are normalized by the slab thickness $L$.

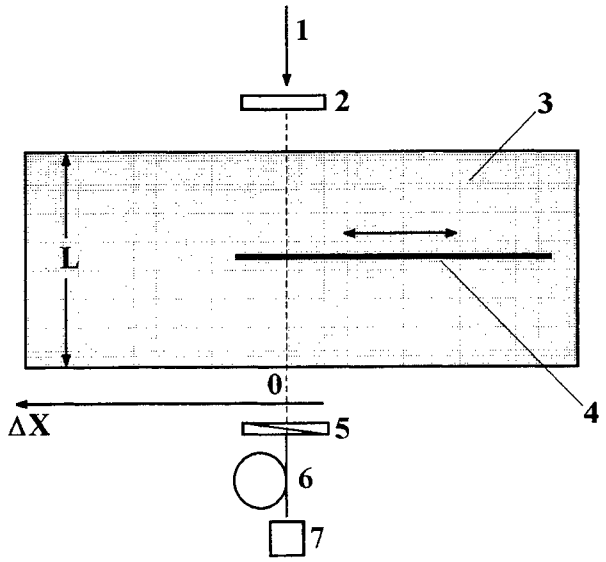


Fig. 2. Schematic sketch of experimental setup used to study the potentialities of the polarization imaging.

Typical dependencies of the normalized intensity of scattered probe light detected by fiber-optical light collection system on the position of the half-plane edge are shown in Fig.3,a for different concentrations of the phantom scattering medium

(diluted milk). Similar dependencies of the polarization degree on edge position are presented in Fig.3,b. Presence of maxima of $P$ in the region of small negative values of $\Delta X$ is one of the typical peculiarities of these curves. Such behavior can be simply explained by the influence of absorbing half-plane position on the interrelation of non-scattered and scattered parts of polarized light passed through the slab. Relative contribution of the ballistic and low-step scattered components which preserve the initial polarization state of probe light is maximal for edge positions corresponding to the maximal values of polarization degree.

Depolarization length as free parameter has been used to fit the obtained experimental dependencies of $P$ on $\Delta X$ for different concentrations of the phantom scattering medium (milk); distributions of effective optical paths were obtained from Monte-Carlo simulation. Because of the absence of systematic reliable results of optical measurements of diluted milk as scattering medium the following two-stage fitting procedure has been applied:

1) at first, interrelation of transport length of diluted milk and its concentration has been obtained by using the criterion of best fitting of experimental dependencies of normalized intensity on $\Delta X$ (Fig.3,a); value of $g$ = 0.6 taken to provide Monte-Carlo simulation procedure has been chosen as typical value corresponding to some scattering substances such as water suspensions of fat drops (e.g., Intralipid); for milk suspensions used in our experiments we have obtained the following interrelation between scattering coefficient and volume concentration of the diluted milk: $\mu_s[mm^{-1}] \approx 0.082\, c[\%];$

2) obtained interrelation of $\mu_s$ and $c$ (and, respectively, of the mean transport length and $c$ for given value of anisotropy factor) for diluted milk has been used to simulate pathlength distributions and to fit the experimentally obtained dependencies $P = \varphi(\Delta X)$ with $\xi_L$ as free parameter by using the above described algorithm.

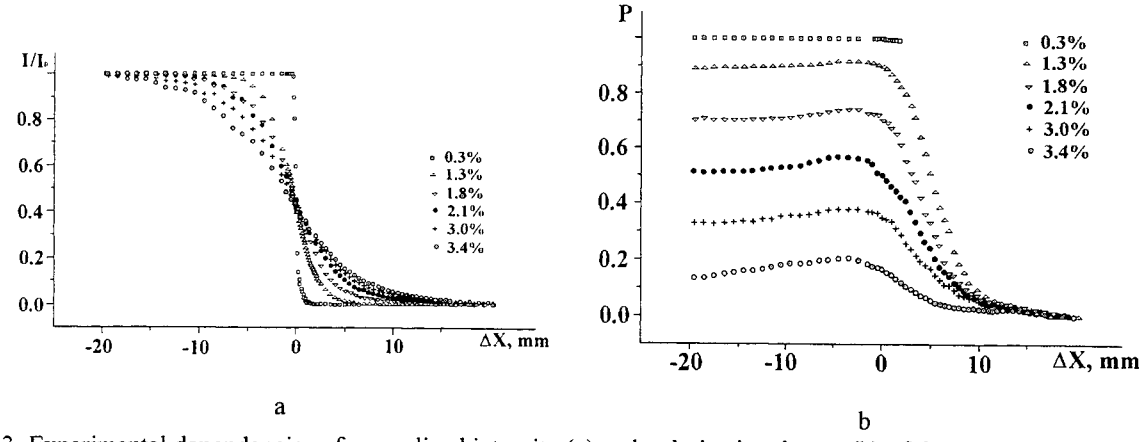


Fig.3. Experimental dependencies of normalized intensity (a) and polarization degree (b) of the transmitted light on position of half-plane edge for different concentrations $c$ of the background scattering medium (diluted milk).

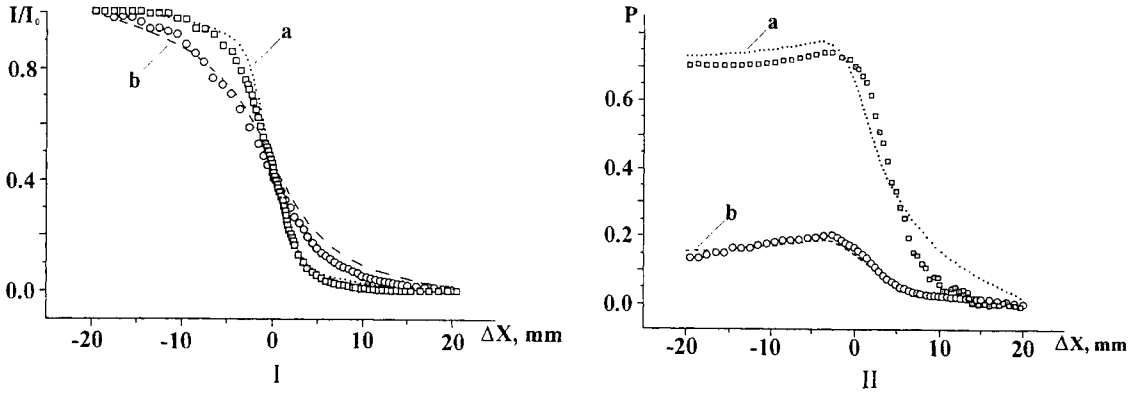


Fig. 4. Fitting of empirical dependencies $I / I_0 = f(\Delta X)$ (I) $P = \varphi(\Delta X)$ (II) by using the results of Monte-Carlo simulation. □ and fitting curve (a) - $c$ = 1.8 %; O and fitting curve (b) - $c$ = 3.4 %.

Results of fitting procedure for two concentrations of diluted milk differing approximately in two times are presented in Fig. 4,I,II. Value of $\xi_L$ providing the best fit for polarization degree for different concentrations of diluted milk is equal to $\approx 1.2l^*$. It is necessary to note that such small value of depolarization length in comparison with mean transport length is typical for ensembles of small scattering particles (so-called Rayleigh scattering mode, value of size parameter is much less than 1). Thus, the reasonable suggestion is that, despite the polydispersity of the ensemble of fat drops in the diluted milk, the predominating contribution in the polarization decay of transmitted light is due to the small-sized part of the ensemble of scattering particles.

Divergence of experimental data and fitting curves $P = \varphi(\Delta X)$ (Fig.4,II) which takes place for positive values of $\Delta X$ exceeding $\Delta X \approx (0.1 \div 0.2)L$ is observed in the case of weakly scattering background medium and caused by the certain overestimation of contribution of simulated pathlength density $\rho(s)$ in the formation of polarization state of scattered light. This is rather due to the failure of model of exponential decay of polarization degree in the dependence on propagation path in case of weak scattering ( $L/l^* \leq 1$ ).

Thus, dependencies of normalized intensity and polarization degree on the edge position can be interpreted as the "edge-spread functions" which determine distortions of the image of the phantom inhomogeneity obtained by means of CW transillumination method and polarization imaging technique. For given illumination and detection conditions these distortions are caused the by multiple scattering in the masking background medium. To quantify the quality of images of the probed object obtained in such a way for different values of scattering coefficient of background medium the following parameters can be introduced:

1) the image contrast estimated as ratio $(P_{max} - P_{min})/(P_{max} + P_{min})$;

2) the image "sharpness" $\Delta\tilde{X}^{-1}$ estimated as the inverse of normalized value of half-plane edge displacement between two positions, one of which corresponds to 0.9 of maximal value of visualization parameter, and other, respectively, – to 0.1 of maximal value.

Fig. 5 illustrates the effect of edge image broadening with an increase of concentration of diluted milk and, respectively, of the scattering coefficient of background medium when normalized intensity of transmitted light (□) and its polarization degree (O) are applied as visualization parameters. Thus, negative exponential kernel in Eq. 1 leads to the larger values of sharpness of polarization images because of the cut-off of long-path contributions in the detected scattered field. We can conclude that for intermediate scattering regime (mean transport length is comparable with the slab thickness and contributions of ballistic and low-step scattered components are adequately significant) visualization and location of absorbing inhomogeneity by using the measurements of polarization degree can be more appropriate in comparison with CW transillumination technique. Thus, efficiency of polarization imaging increases with an increase of the scattering coefficient of background medium; for used scattering conditions ratio of $(\Delta\tilde{X}^{-1})_P$ ("polarization" imaging) to $(\Delta\tilde{X}^{-1})_{I/I_0}$ reaches the value approximately equal to 1.5 and more for milk concentrations exceeding (2.5÷3.0) %.

It is necessary to note that, despite the seeming simplicity of the used phenomenological model with negative exponential decay of polarization of scattered field partial components (Eq.1) it adequately describes behavior of first-order statistical moments of scattered field and their combinations (such as mean intensity and polarization degree) with the changes of pathlength distributions even for typically non-diffusion light transport regimes through the probed object (up to the significant predominance of the ballistic and low-step scattered components of transmitted light). Also, analysis has been carried out only for the case of absorbing phantom inhomogeneity embedded in the scattering slab, but it can be expected that polarization location and imaging technique will provide the adequately reliable results for other types of macro-inhomogeneities (i.e., scatterers) and scattering geometry. More commonly, maximal sensitivity of the polarization degree as location or imaging parameter to the variations of pathlength distributions should be expected if the modal value of $s$ distribution is of the order of depolarization length and relation $s_{mod} \approx \xi$ can be accepted as the criterion of applicability of the discussed technique.

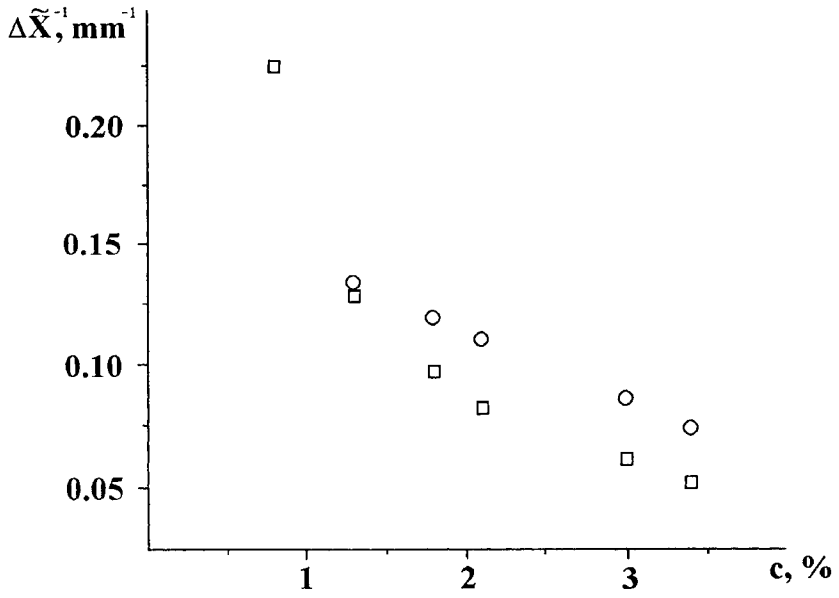


Fig.5. The dependence of image "sharpness" on concentration of the background scattering medium; □ - normalized intensity as visualization parameter; O - polarization degree as visualization parameter.

One of the important questions is the appropriate choice of the initial polarization state of the probe beam in the dependence on optical properties of background scattering medium: for Rayleigh scatterers characterized by small effective value of size parameter $ka << 1$ linear polarization of the probe beam is preferable in comparison with circular polarization because of the larger values of $\xi_L$. On the contrary, application of the probe beam with circular polarization will give the better results in the case of location of macro-inhomogeneities embedded in turbid media with strongly anisotropic scattering $ka >> 1$ due to the following relation: $\xi_C >> \xi_L$ (see, e.g., Ref. 11).

## 3. SPECKLE CONTRAST MEASUREMENTS AND CW TRANSILLUMINATION TECHNIQUE: COMPARATIVE ANALYSIS FOR SOME PARTIAL CASES

Stochastic interference in the case of coherent light propagation in the disordered multiply scattering systems leads to the formation of speckle patterns. For same scattering conditions, if the partially coherent light source with finite coherence length is used, observed speckles will have the less level of amplitude fluctuations in comparison with that for monochromatic light source. The most appropriate parameter for characterization of suppression of speckle modulation of scattered optical fields with a decrease of coherence length of the used light source is the observed speckle contrast expressed as the ratio $\sigma_I / < I >$, where $\sigma_I$ is the root mean square value of the speckle intensity fluctuations and $< I >$, correspondingly, - their mean value. Thus, multiply scattering media can be considered as the multiple-beam interferometer with continuos distribution of random phase delays between interfering beams in each interference channel and contrast of the observed interference patterns is determined by the statistical properties of the ensemble of phase delays, which in turn depend on the effective optical path statistics. It is necessary to note that depolarization due to the multiple scattering also causes the contrast decay (in particular, superposition of two non-correlated fully developed speckle patterns with orthogonal directions of linear polarization and contrast values equal to 1 induce resulting speckle pattern with value of contrast equal to $\approx 0.707$), but these effects can be easily eliminated by polarization filtering of the scattered optical field. Method of probing of inhomogeneous multiply scattering media by means of the speckle contrast analysis has been proposed by Thompson, Webb and Weiner [7]; they have presented theoretical analysis of relation between effective optical path statistics, coherence function of the used light source and observed contrast of multiply scattered speckles together with the experimental results obtained for phantom scatterers with macro-inhomogeneities.

It is important to compare the efficiency of the discussed approach and such traditional visualization technique as CW transillumination method. In order to analyze the influence of the effective optical path statistics on the image formation in the case of application of transmitted light intensity and speckle contrast as visualization parameters expression for the contrast of multiply scattered speckles has been obtained by using the random walk approach for the discrete scatter model.

**3.1. Phenomenological description of the formation of multiply scattered speckles: the random walk approach**

One of the convenient ways to describe the formation of random interference patterns due to the multiple scattering of the probe coherent light in the disordered media is to interpret these patterns as the result of superposition of non-correlated partial contributions caused by the sequences of scattering events. In this case coordinate-dependent part of complex amplitude of scattered field in arbitrary chosen point can be expressed by using the scalar approximation as:

$$E(\bar{r}) = \sum_k a_k \exp\{j\phi_k(\bar{r})\}, \tag{2}$$

where phase of each partial contribution can be written as: $\phi_k = 2\pi s_k / \lambda$. Here $s_k$ is the effective optical path of $k$-th contribution; $\lambda$ is the wavelength of the probe light in the scattering medium. Using the simplifying assumption about the equality of $a_k = 1$ we can obtain the value of intensity in the observation point as:

$$I(\bar{r}) = |E(\bar{r})|^2 = E(\bar{r})E^*(\bar{r}) = \sum_k \sum_{k'} \cos\{2\pi(s_k - s_{k'})/\lambda\}. \tag{3}$$

It is easy to see that averaging over all possible combinations of statistically independent $s_k$ and $s_{k'}$ gives the value of mean intensity in the observation point $< I(\bar{r}) >$ equal to $N$, where $N$ is the number of contributions. In further analysis, replacing the summation over $k$ and $k'$ by the summation over new index $l$, we express "instantaneous" value of intensity corresponding to current configuration of scattering sites as:

$$I(\bar{r}) = N + 2\sum_l \cos(2\pi\Delta s_l / \lambda), \tag{4}$$

where summation over $l$ is carried out from 1 to $(N^2 - N)/2$. In this notation statistical properties of the intensity fluctuations are controlled by the distribution of the pathlength differences $\Delta s_l$. Second term in the equation (4) can be considered as the result of interference between $k$ and $k'$ components of scattered field. Thus, if the partially coherent source is used for the probing of the scattering medium and this source is characterized by the normalized coherence function $g(\Delta s)$, then equation (4) should be replaced by the following expression:

$$I(\bar{r}) = N + 2\sum_l \cos(2\pi\Delta s_l / \lambda)|g(\Delta s_l)|. \tag{5}$$

Taking into account the statistical independence of pathlength differences and calculating the mean value of $I^2(\bar{r})$, we can obtain:

$$\langle I^2(\bar{r})\rangle = N^2 + 4N\left\langle \sum_l \cos(2\pi\Delta s_l / \lambda)|g(\Delta s_l)|\right\rangle + 4\left\langle \sum_l \cos^2(2\pi\Delta s_l / \lambda)|g(\Delta s_l)|^2\right\rangle +$$

$$+ 4\left\langle \sum_l \sum_{l'} \cos(2\pi\Delta s_l / \lambda)\cos(2\pi\Delta s_{l'} / \lambda)|g(\Delta s_l)||g(\Delta s_{l'})|\right\rangle =$$

$$= N^2 + 4\left\langle \sum_l \cos^2(2\pi\Delta s_l / \lambda)|g(\Delta s_l)|^2\right\rangle,$$

where $l \neq l'$.

Taking the number of partial contributions $N \to \infty$ and considering the transition from the discrete model of scattering medium which is characterized by the finite number of contributions, to the "continuos" description, we can introduce the probability density function of the pathlength differences $\rho(\Delta s)$ and write the second-order statistical moment of the scattered light intensity as:

$$\left\langle I^2(\bar{r})\right\rangle \approx \left\langle I\right\rangle^2 + 2\left(\left\langle I\right\rangle^2 - \left\langle I\right\rangle\right)\int_0^\infty \cos^2(2\pi\Delta s/\lambda)\left|g(\Delta s)\right|^2 \rho(\Delta s)d(\Delta s). \quad (6)$$

Probability density function of the pathlength differences $\rho(\Delta s)$ is related with probability density function of effective optical paths $\rho(s)$ as:

$$\rho(\Delta s) \sim \int_0^\infty \rho(\xi)\rho(\xi + \Delta s)d\xi,$$

i.e., $\rho(\Delta s)$ can be expressed as autocorrelation of $\rho(s)$. Thus, contrast of the multiply scattered speckle pattern can be expressed as:

$$V = \sqrt{\left\langle I^2(\bar{r})\right\rangle / \left\langle I(\bar{r})\right\rangle^2 - 1} \approx \sqrt{\int_0^\infty \left\{1 + \cos(4\pi\Delta s/\lambda)\right\}\left|g(\Delta s)\right|^2 \rho(\Delta s)d(\Delta s)}. \quad (7)$$

For fully coherent illumination source with $|g(\Delta s)|$ equal to 1 for all possible values of the pathlength differences contrast value introduced as (7) is equal to 1 independently on pathlength statistics. On the contrary, for broadband light sources $V \approx 0$. In the intermediate case, when coherence length of the used light source is comparable with spatial scales characterizing the ensemble of the pathlength differences (e.g., root mean square or modal value), speckle contrast varies between 1 and 0.

### 3.2. Monte-Carlo simulation of visualization of hidden inhomogeneity by means of CW transillumination technique and speckle contrast analysis

Monte-Carlo simulation has been carried out to analyze the influence of the effective optical path statistics on the efficiency of inhomogeneity imaging by means of the CW transillumination technique and the speckle contrast analysis. Simulation procedure was in general similar to algorithm described in section 2.2; Henvey-Greenstein distribution has been applied to describe the scattering anisotropy. The following model of inhomogeneous scattering object has been accepted: infinite slab consisting of the strongly scattering and weakly absorbing macroscopically homogeneous substance contains the macro-inhomogeneity such as sphere with differing optical properties (scattering coefficient, absorption coefficient and (or) anisotropy factor). Location of this inhomogeneity is carried out by use of the movable detection system consisting of point-like collimated illumination source and three detectors with circle aperture; one of them is placed in on-axis position on the opposite surface of the slab (transillumination geometry); the second one is centered in the source detection point and the third one is also placed on the input interface and shifted on the distance $L/2$ with respect to source position. In general, in this study we analyzed the influence of inhomogeneity position on the statistics of the effective optical paths for transillumination geometry. Fig. 6 shows the dependencies of normalized intensity of the transmitted light in the detection point and value of speckle contrast estimated in the accordance with equation (7) on the inhomogeneity position with respect to probe beam axis. Coherence function $g(\Delta s)$ is assumed to have the Gaussian form: $g(\Delta s) = exp\left(-\Delta s^2/l_C^2\right)$, where $l_C$ is the coherence length. Two different types of spherical inhomogeneity were simulated: the absorbing sphere, which is characterized by the same value of the scattering coefficient as background medium but the larger value of $\mu_a$, and the scattering sphere with opposite relation between scattering and absorption coefficients. Accepting the image contrast for its quality characterization as the ratio of difference of maximal and minimal values of imaging parameter to its mean value in the region of inhomogeneity location we can see that "shadow images" obtained by using the normalized intensity of the transmitted light as visualization parameter is characterized by the larger values of image contrast in comparison with that for speckle contrast as visualization parameter. The noticeable fact is that scattering and absorbing inhomogeneities produce the opposite influence on the measured parameters of the transmitted light: in the case of overlapping of source axis by the absorbing sphere decrease of the transmitted intensity is accompanied by an increase of speckle contrast (see curves marked by open circles in Fig. 6) because of the cut-off of the part of long-path contributions due to the increasing local absorption. On the contrary, eclipse of the part of transmitted light by the scattering sphere causes the simultaneous decrease of speckle contrast and normalized intensity (see curves marked by open squares in Fig.6).

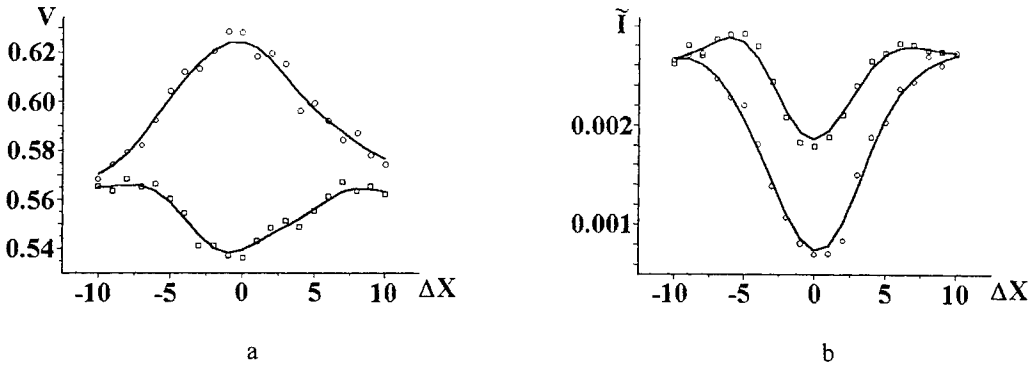


Fig. 6. Dependencies of the speckle contrast (a) and normalized intensity (b) on the inhomogeneity position (results of MC simulation). Parameters of background medium: $\mu_s'$ = 1; $\mu_a$ = 0.001; $g$ = 0.3; $L$ = 10. Sphere radius is equal to 3.5. Open circles correspond to absorbing sphere ($\mu_s'$ = 1; $\mu_a$ = 0.1; $g$ = 0.3) and open squares – to scattering sphere ($\mu_s'$ = 2; $\mu_a$ = 0.001; $g$ = 0.3). Value of $l_c$ was taken to be equal ≈ 6.3.

**4.3. Experiments with phantom scatterrers**

Experimental comparison of CW transillumination technique and visualization by use of the speckle contrast analysis in application to imaging of the macro-inhomogeneities hidden in the multiply scattering media has been carried out by using the phantom scattering object such as rectangular Teflon plate with cylindrical channel filled by the water solution of black ink as absorbing substance (see Fig. 7, a). Setup used to provide these experiments is schematically shown in Fig. 7, b. Single-mode He-Ne laser 1 is used as an illumination source; phantom scatterer was placed on the translation stage; CCD camera with 3-mm diameter aperture diaphragm was placed at illuminating beam axis closely behind the output surface of Teflon plate; no any lens for speckle image formation has been used between output surface and CCD photo-sensitive area. Electrim camera EDC-1000L has been used in our experiments; recorded 256-gray scale images of speckle patterns in the detection plane have been processed to estimate their mean value and variance for given position of the phantom scatterer with respect to illuminating source and detector. In some experiments film-like polarization filter was placed between aperture diaphragm and output surface of scatterer to enhance the speckle contrast of the recorded images.

Fig. 8 shows the dependencies of the normalized mean intensity of recorded speckle patterns on the inhomogeneity (absorbing channel) position for different concentrations of ink in the absorbing substance. Fig. 9, a displays the dependence of normalized mean intensity on channel position in the case of large concentration of absorber; similar dependencies for speckle contrast (with polarization filter and without it) are shown in Fig. 9, b. Thus, considering the obtained curves as the "shadow images" of the inhomogeneity we can see that image contrast is less in the case of speckle contrast as imaging parameter; application of polarization filter allows to improve the value of speckle contrast, but the image quality remains practically the same. Decrease of absorbance of inhomogeneity leads to the full vanishing of the "shadow image" of inhomomogeneity on the dependence of $V$ on channel position $X$ (only the random oscillations of the speckle contrast with the uniform distribution of its mean value for all given positions of the channel are typical for small concentrations of absorber). These results are in qualitative agreement with the results of Monte-Carlo simulation presented in Section 3.2.

The interesting feature is the behavior of experimentally obtained dependencies $I / I_0 = f(X)$ in the region of small concentrations of absorber (Fig. 8). Decrease of absorption of substance which fills the channel causes the appearance of local maximum of intensity of transilluminating light in the region of inhomogeneity "shadow". Amplitude of this local peak strongly depends on the absorption coefficient of inhomogeneity and peak vanishes with the increase of absorber concentration. If channel filled by distilled water is probed, when "shadow images" has the specific form (see curve marked by down triangles on Fig. 8); such behavior is rather caused by the peculiarities of the spatial distribution of the diffusing light intensity in the vicinity of the non-scattering channel boundary.

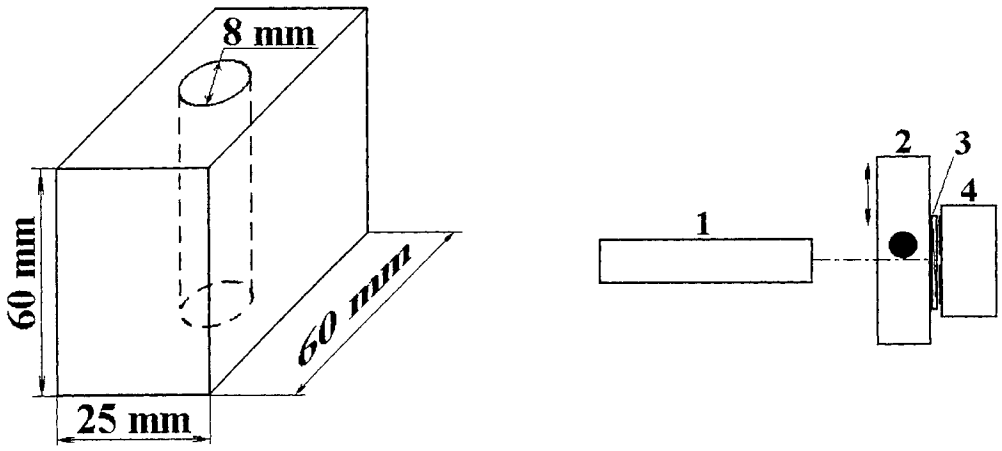


a b

Fig. 7. a – phantom scatterer used for the speckle contrast experiments. b – schematic sketch of the experimental setup.

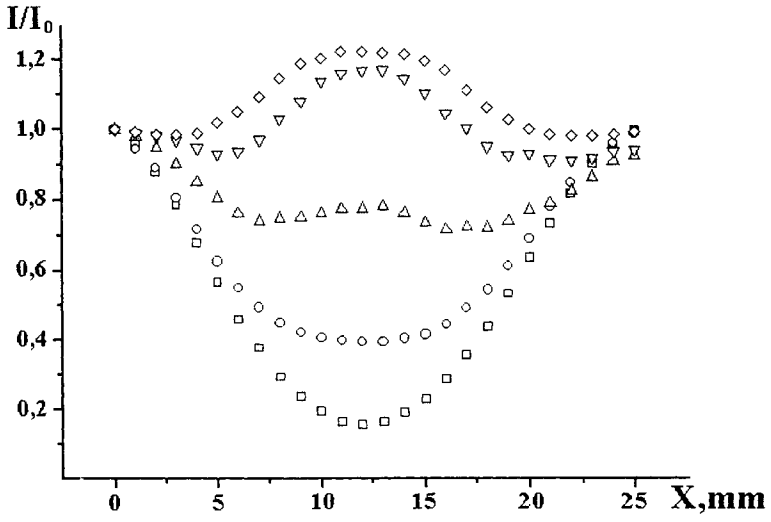


Fig. 8. Dependencies of normalized intensity on the absorbing channel position. Diamonds – empty channel; down triangles – channel filled by distilled water; up triangles – ink concentration $3.5\times10^{-4}$ %; circles - $3.2\times10^{-3}$ %; squares - $6.7\times10^{-3}$ %.

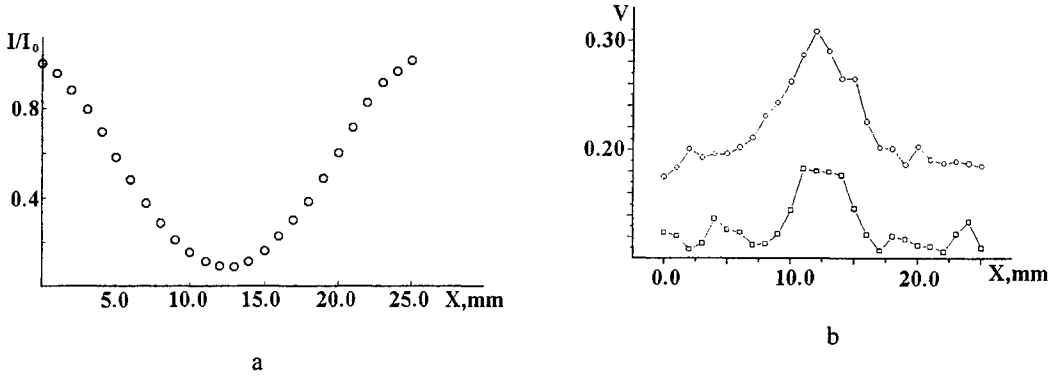


Fig. 9. Comparison of normalized intensity (a) and speckle contrast (b) as imaging parameters (ink concentration 0.02%).

## 4. TIME-INTEGRATING ELECTRONIC PHOTOGRAPHY OF THE DYNAMIC SPECKLE PATTERNS AS THE TOOL FOR MULTIPLY SCATTERING MEDIA PROBING

Suppression of the stochastic interference modulation of the observed scattered fields can also be caused by the broadening of the probe light spectral bandwidth due to scattering by the non-stationary random media. Application of integrating detectors with finite detection time causes the decay of observed contrast if the correlation time of the speckle intensity fluctuations due to the probed media dynamics is comparable with the detector aperture time. Relation between coherence time of the used light source and average time delay of the light propagation in the probed multiply scattering medium should allow to observe full speckle modulation in the case of motionless probed medium. Another feature of this approach is the analysis on the statistical moments of scattered field intensity obtained by not temporal but spatial averaging (e.g., by means of the time-integrating speckle photography). It is necessary to note that modification of such technique named as LASCA (LAser Speckle Contrast Analysis) has been developed by J.D. Briers *et al.* for blood capillary microcirculation monitoring in the upper layers of living tissues (see, e.g., Ref. 12). Here we will discuss another modification of the time-integrating electronic speckle photography in applications to multiple scattering media probing.

The basic principles of the discussed approach are illustrated by the schematic sketch presented in Fig. 10, a. A couple of multi-mode optical fibers is used for probing of multiply scattering media in the back-scattering regime. Probe light from laser source 1 is passed through the fiber A and penetrates into the scattering medium; part of backscattered light is collected by the second fiber (B). Scattering medium is scanned by these coupled fibers; dynamic speckle pattern which is induced by the backscattered optical field causes the excitation of set of propagating modes in the light-collecting fiber and provides the dynamic speckle pattern on its output recorded by CCD camera. Fixed image of the dynamic speckle pattern is characterized by the value of contrast equal to ratio of root mean square value of the speckle intensity and its mean value. Contrast value $V(T)$ depends on the exposure time used to record the image of analyzed speckle pattern. Decay of time-dependent contrast with an increase of exposure time depends on the correlation time of the speckle intensity fluctuations in the fixed detection point which are caused by the scattering medium motion with respect to the illumination and detection point. In the case of statistically homogeneous fluctuating speckle pattern normalized value of $V(T)$ can be expressed as:

$$V(T) = \frac{1}{T}\int_0^T \tilde{g}_2(\tau)d\tau,$$

where $\tilde{g}_2(\tau) = \left\langle \{I(t+\tau) - < I >\}\{I(t) - < I >\} \right\rangle \Big/ \left\langle \{I(t) - < I >\}^2 \right\rangle$.

Without the losses of generality, applying simplifying assumptions about excitation of the propagating modes in the light-collecting fiber and formation of the recorded dynamic speckle pattern due to the optical mixing we can conclude that normalized intensity correlation function $\tilde{g}_2(\tau)$ can be approximately expressed by using the temporal correlation function

of the scattered field fluctuations on the output surface of the probed medium: $\tilde{g}_2(\tau) \sim \left| g_1^{bs}(\tau) \right|^2$. On the other hand, for certain scattering conditions field correlation function $g_1^{bs}(\tau)$ can be expressed as Laplace transform of the probability density function $\rho(s)$ which characterizes the scattering medium for given illumination and detection conditions (see, e.g., Ref.13):

$$g_1^{bs}(\tau) \sim \int_0^{\infty} exp\left( -\frac{k_0^2 \left\langle \Delta \bar{r}^2(\tau) \right\rangle s}{3l^*} \right) \rho(s) ds ,$$

where $k_0$ is the wave-number of the probe light in the scattering medium, $\left\langle \Delta \bar{r}^2(\tau) \right\rangle$ characterizes the variance of the displacement of scattering particles for the observation time $\tau$. Thus, presented approach can be used as the analytical background in order to obtain the relation between local optical characteristics of the probed medium and contrast decay parameters. It is obvious that effective depth of the scattering medium probing depends on the separation between fibers A and B.

Fig. 10, b, c shows the typical recorded fragments of static (b) and dynamic (c) speckle patterns if phantom scattering medium such as 5.5-mm thick polypropylene slab is probed by a pair of closely disposed 400 μm diameter fibers; in the latter case speckle dynamics corresponds to scan velocity equal to 3.5 mm/s. Logarithmically scaled plots of the normalized variance of intensity for the recorded speckle patterns versus exposure time are presented in Fig. 10 for different phantom scatterers with slab geometry. We can see that decay behavior of $\sigma^2(T)/\sigma^2_{stat}(T)$ (where $\sigma^2_{stat}(T)$ is the intensity variance for the static speckle patterns) with an increase of $T$ can be approximated by an inverse linear law: $\sigma^2(T)/\sigma^2_{stat}(T) \approx K/T$, where parameter $K$ depends on scattering properties of the probed medium (i.e., mean transport length), illumination and detection conditions (at first, separation between illumination and detection fiber) and scan velocity and can be used as the imaging parameter.

Comparing the discussed approach with traditional correlation spectroscopy techniques in the case of application for location of structural and dynamic inhomogeneities in the multiply scattering media, we can see that speckle contrast analysis for the time-integrated images of the dynamic speckle patterns is the significantly faster procedure than the later ones due to the quasi-parallel character of the image formation. On the other hand, major restriction of this technique is related with the small efficiency of recording and acquisition of images of the speckle patterns induced by fiber-optical mixing of the scattered light for large separations between illuminating and mixing fibers.

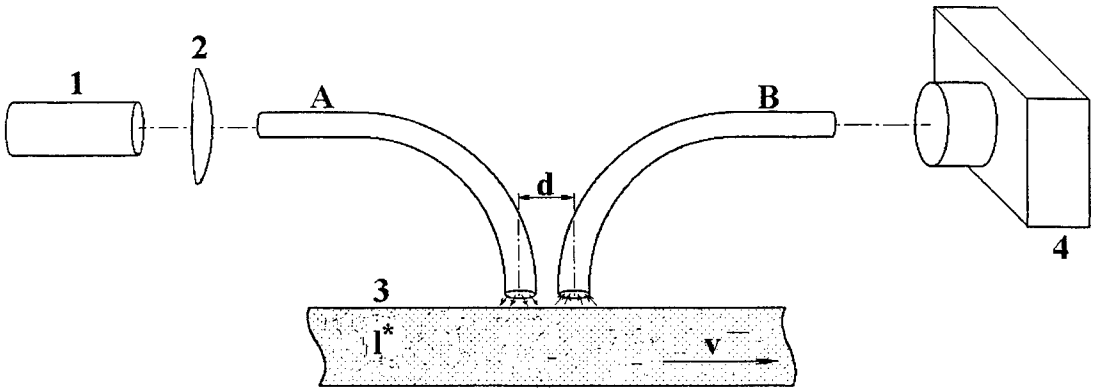


a

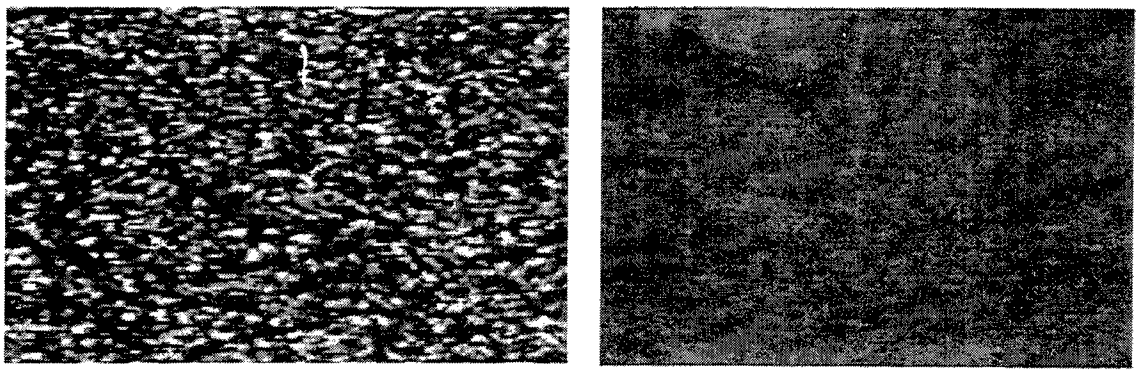

b c

Fig. 10. a – schematic sketch illustrating the basic principles of scattering media probing by means of electronic speckle photography of the time-integrated dynamic speckle patterns; 1 – single-mode laser; 2 – focusing lens; 3 – probed medium; 4 – CCD camera; A – illuminating multi-mode fiber; B – light collecting and mixing multi-mode fiber. b, c – typical images of the recorded speckle patterns induced by scattered light passed through the light-mixing system (multi-mode fiber B) (exposure time is equal to 5 ms).

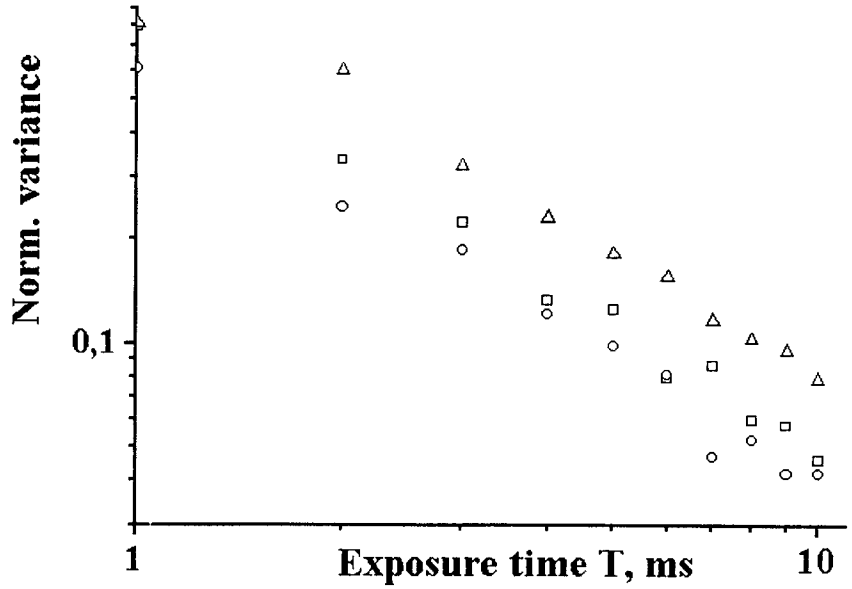


Fig. 11. Normalized variance of the intensity of time-integrated speckle patterns in the dependence on exposure time. Phantom samples: up triangles – sample consisting of $SiO_2$ spheres (0.5 μm) in polystyrene matrix ( $\mu_s$ = 30 $cm^{-1}$); squares – Teflon; circles – polystyrene. Scan velocity is equal to 4 mm/s.

## 5. CONCLUSIONS

Thus, applicability of each of the above discussed techniques is limited by the scattering conditions determined mainly by the relation between characteristic spatial scale controlling the decay of corresponding imaging parameter during the probe light propagation into the scattering medium and parameter characterizing the effective pathlength distribution (or distribution of pathlength differences, in the case of usage of partially coherent source and speckle contrast as imaging parameter). One of the prospective directions is the application of the local control of tissue optical properties (e.g., by

administration of special immersion agents) [14] in combination with polarization monitoring of the structure of optically cleared tissue; in this case maximal sensitivity of polarization degree as imaging parameter to the local variations of optical properties can be achieved by the appropriate choice of the wavelength and initial polarization state of the probe light.
Method of scattering media probing by means of speckle contrast analysis with low-coherent source seems to be relatively low-sensitive to the changes of optical properties of scattering object within the analyzed area but final decision about its applicability for these purposes requires the further investigations.

Considered technique of time-integrating electronic photography of the dynamic speckle patterns in combination with optical mixing of the backscattered optical field seems to be adequately attractive for monitoring and functional imaging of upper layers of living tissues. In particular, combination of the analysis of speckle patterns in the case of scanning by moving fibers and for the fixed position allows to exclude the contribution of motionless scatterers and to share the influence of blood microcirculation and tissue structure on the formation of recorded speckle patterns. This gives the certain possibilities of multifunctional monitoring of living tissues.

## 6. REFERENCES


1. A. Yodh, B. Chance, "Spectroscopy and imaging with diffusing light", *Physics Today* ***48***, pp. 34-40, 1995.
2. D.A. Boas, L.E. Campbell, A.G. Yodh, "Scattering and imaging with diffusing temporal field correlations", *Phys. Rev. Lett,* ***75***, pp. 1855-1858, 1995.
3. M.S. Patterson, B. Chance, B.C. Wilson, "Time resolved reflectance and transmittance for the non-invasive measurement of tissue optical properties", *Applied Optics* ***28***, pp.2331-2336, 1989.
4. B.W. Pogue, M.S. Patterson, "Frequency-domain optical absorption spectroscopy of finite tissue volumes using diffusion theory", *Phys. Med. Biol,* ***39***, pp. 1157-1180, 1994.
5. A.F. Fercher, "Optical coherence tomography", *J. Biomed. Opt.* ***1***, pp.157-173, 1996.
6. R.M. Danen, Y. Wang, X.D. Li, W.S. Thayer, A.G. Yodh, "Regional imager for low-resolution functional imaging of the brain with diffusing near-infrared light", *Photochemistry and Photobiology* ***67***, pp.33-40, 1998.
7. C.A. Thompson, K.J. Webb, A.M. Weiner, "Imaging in scattering media by use of laser speckle", *JOSA A* ***14***, pp. 2269-2277, 1997.
8. S.R Arridge., M. Cope, D.T. Delpy, "The theoretical basis for the determination of optical pathlengths in tissue: temporal and frequency analysis", *Phys. Med. Biol.* ***37***, pp.1531-1560, 1992.
9. F.C. MacKintoch, J.X. Zhu, D.J. Pine, D.A. Weitz, "Polarization memory of multiply scattered light", *Phys. Rev. E* ***40***, pp. 9342-9345, 1989.
10. A. Ishimaru, "Diffusion of light in turbid material", *Applied Optics* ***28***, pp. 2210-2215, 1989.
11. D. Bicout, C. Brosseau, A.S. Martinez, J.M. Schmitt, "Depolarization of multiply scattering waves by spherical diffusers: influence of the size parameter", *Phys. Rev. E* ***49***, pp. 1767-1770, 1994.
12. J.D. Briers, S. Webster, "Laser speckle contrast analysis (LASCA): a non-scanning, full-field technique for monitoring capillary blood flow", *J. Biomed. Opt. 1,* pp.174-179, 1996.
13. F.C. MacKintosh, S. John, "Diffusing-wave spectroscopy and multiple-scattering of light in correlated random media", *Phys. Rev. B* ***40***, pp. 2382-2406, 1989.
14. V.V. Tuchin, I.L. Maksimova, D.A. Zimnyakov et al., "Light propagation in tissues with controlled optical properties", *J. Biomed. Opt. 2*, pp.401-417, 1997.

# Optical Diffusion of Focused Beam Wave Pulses in Discrete Random Media*

Arnold D. Kim[a] and Akira Ishimaru[b]

[a]Department of Applied Mathematics, University of Washington, Seattle, WA 98195, USA

[b]Department of Electrical Engineering, University of Washington, Seattle, WA 98195, USA

## ABSTRACT

In this paper we present a theoretical study of focused beam wave pulse propagation and diffusion in highly scattering discrete random media. By using Wigner distributions, we calculate an explicit closed-form expression for the reduced intensity of focused beam waves. From this analysis, we find that the extent to which the reduced intensity focuses depends upon the attenuation it experiences from scattering and absorption. We then solve the diffusion equation for continuous wave sources and delta function input pulses to examine the spatial and temporal spreading of beam wave pulses. Through numerical approximations to the obtained solutions, we find that focusing effects of the diffuse intensity are negligible. Finally, we compare these results to those of collimated beam waves and pulsed plane waves. Through these comparisons, we determine that the spatial spreading of focused beams is similar to that of collimated beams, and the temporal spreading of the focused beam wave pulse is similar to that of plane wave pulses.

**Keywords:** Optical diffusion, radiative transport, focused beams, Wigner distributions.

## 1. INTRODUCTION

Optical beam wave propagation in discrete random media has attracted considerable amounts of interest among those working in optical imaging of biological media, and optical communication and remote sensing through fog and rain. For these applications, a thorough knowledge of the spatio-temporal spreading of the beam wave pulse is necessary. There has been much theoretical work done on these problems using the parabolic equation technique[1,2] where the scattering is mainly confined to the forward direction. However, for discrete random media where particle sizes vary on the order of a wavelength or smaller, scattering occurs over large angles and the parabolic approximation is not valid. Therefore, one must use the theory of radiative transport to investigate these problems.

The theory of radiative transport models classical wave propagation in discrete random media.[1] This theory describes the transport of energy that is emitted, scattered and absorbed in a medium containing a random distribution of scattering particles.[3] In the limit when a significant amount of multiple scattering takes place with little absorption, the diffuse component of the specific intensity develops a nearly isotropic angular distribution and the corresponding radiative transport equation reduces to a simpler diffusion equation for the angularly averaged diffuse intensity.[4–7] This approach to studying highly scattering random media has lead to a number of fundamental results that have been successfully applied to biomedical optics,[8] for example.

The Wigner distribution was originally constructed to examine quantum mechanical systems in phase space.[9] It is also a useful tool for studying classical wave propagation since its properties are very similar to those of the specific intensity of transport theory. Because the Wigner distribution is constructed from the fundamental wave field, it provides one with a mathematical tool to bridge fundamental wave fields to the specific intensity of the phenomenological theory of radiative transport. This relationship of the Wigner distribution to transport theory is well known and has been studied by a number of authors.[10–12]

After giving a brief overview of optical diffusion in random media, we examine focused beam waves and their corresponding Wigner distributions in order to determine the correct form for the reduced intensity. Then we calculate the solution to the diffusion equation for continuous wave sources and delta function input pulses. From these investigations, we examine the temporal and spatial spreading of the pulse.

Further author information: (Send correspondence to Arnold D. Kim)
Department of Applied Mathematics; Box 352420; University of Washington; Seattle, WA 98195-2420; Phone: (206) 221-5167, Fax: (206) 685-1440, E-mail: adkim@amath.washington.edu

*Also published in *Proc. of SPIE* Vol. 3927

In *Laser-Tissue Interaction XI: Photochemical, Photothermal, and Photomechanical*, Donald D. Duncan, Jeffrey O. Hollinger, Steven L. Jacques, Editors, Proceedings of SPIE Vol. 3914 (2000)
1605-7422/00/$15.00

## 2. THE THEORY OF RADIATIVE TRANSPORT

Radiative transport theory models classical wave propagation in a scattering and absorbing medium.[3] The fundamental quantity of transport theory is the specific intensity, $I(\bar{\mathbf{x}}, \hat{\mathbf{s}}, t)$, which depends on a position vector, $\bar{\mathbf{x}} = (x_1, x_2, x_3)$, time, $t$, and a unit directional vector, $\hat{\mathbf{s}}$. It is a non-negative and real-valued function for all space and directions. The specific intensity in the narrow-band limit is governed by the space-time radiative transfer equation,

$$\frac{1}{c}\frac{\partial}{\partial t} I(\bar{\mathbf{x}}, \hat{\mathbf{s}}, t) + \hat{\mathbf{s}} \cdot \nabla I(\bar{\mathbf{x}}, \hat{\mathbf{s}}, t) + \gamma_t I(\bar{\mathbf{x}}, \hat{\mathbf{s}}, t) = \frac{\gamma_s}{4\pi} \int_{4\pi} p(\hat{\mathbf{s}}, \hat{\mathbf{s}}') I(\bar{\mathbf{x}}, \hat{\mathbf{s}}', t) d\Omega(\hat{\mathbf{s}}'), \tag{1}$$

where $c$ is the constant wave speed, $\gamma_t$ is the extinction coefficient, $\gamma_s$ is the scattering coefficient, $p(\hat{\mathbf{s}}, \hat{\mathbf{s}}')$ is the phase function and $d\Omega(\hat{\mathbf{s}}')$ is the differential element on the unit sphere in direction $\hat{\mathbf{s}}'$. Upon obtaining a solution to the radiative transport equation, we can calculate the average intensity by integrating the specific intensity over all directions,

$$\frac{1}{4\pi} \int_{4\pi} I(\bar{\mathbf{x}}, \hat{\mathbf{s}}, t) d\Omega(\hat{\mathbf{s}}) = U(\bar{\mathbf{x}}, t). \tag{2}$$

This average intensity is proportional to the energy density. A quantity that is often used in biomedical optics applications is the radiant energy fluence rate defined as

$$\Psi(\bar{\mathbf{x}}, t) = 4\pi U(\bar{\mathbf{x}}, t) = \int_{4\pi} I(\bar{\mathbf{x}}, \hat{\mathbf{s}}) d\Omega(\hat{\mathbf{s}}). \tag{3}$$

In addition, we can calculate the flux vector by integrating the product of the specific intensity and the direction vector over all directions,

$$\int_{4\pi} I(\bar{\mathbf{x}}, \hat{\mathbf{s}}, t)\, \hat{\mathbf{s}}\, d\Omega(\hat{\mathbf{s}}) = \mathbf{F}(\bar{\mathbf{x}}, t). \tag{4}$$

### 2.1. The Diffusion Approximation

The specific intensity is normally expressed as the sum of the reduced intensity, $I_{ri}$, and the diffuse intensity, $I_d$. When the specific intensity undergoes a significantly large amount of scattering, its reduced intensity exponentially decays according to the extinction theorem and its diffuse component's angular distribution becomes nearly isotropic or nearly independent of $\hat{\mathbf{s}}$. This limiting process towards an isotropic specific intensity is the main assumption of the diffusion approximation.[1,4–7] From this assumption, we can expand the diffuse intensity into an asymptotic series of Legendre functions,

$$I_d(\bar{\mathbf{x}}, \hat{\mathbf{s}}, t) \sim U(\bar{\mathbf{x}}, t) + \frac{3}{4\pi} \mathbf{F}(\bar{\mathbf{x}}, t) \cdot \hat{\mathbf{s}} + \cdots \tag{5}$$

leading to a diffusion equation for the average intensity of the form,[7]

$$\frac{1}{c}\frac{\partial}{\partial t} U(\bar{\mathbf{x}}, t) - D\nabla^2 U(\bar{\mathbf{x}}, t) + \gamma_a U(\bar{\mathbf{x}}, t) = \gamma_s U_{ri}(\bar{\mathbf{x}}, t). \tag{6}$$

The diffusion coefficient, $D = \ell_{tr}/3$, is defined in terms of the transport mean free path, $\ell_{tr}$. The scattering coefficient is denoted by $\gamma_s$ and the absorption coefficient, $\gamma_a$, is related to the total and scattering coefficients by $\gamma_a = \gamma_t - \gamma_s$. The right hand side is proportional to the average reduced intensity denoted by $U_{ri}(\bar{\mathbf{x}}, t)$. From the solution of the diffusion equation, we can compute the diffuse flux vector by the approximate equality[7]

$$\mathbf{F}(\bar{\mathbf{x}}, t) \cong -cD\nabla U(\bar{\mathbf{x}}, t). \tag{7}$$

For a continuous wave source, the corresponding diffusion equation is

$$-D\nabla^2 U(\bar{\mathbf{x}}) + \gamma_a U(\bar{\mathbf{x}}) = \gamma_s U_{ri}(\bar{\mathbf{x}}). \tag{8}$$

Although there exist many discrepancies among various researchers regarding the "proper" form of the diffusion equation, its boundary conditions and its coefficients,[13–16] we have chosen to adhere to the commonly used diffusion theory presented in a recent review by van Rossum and Nieuwenhuizen.[7] In this proceeding, we intend to keep the analysis and results as general as possible so that they can be easily adapted to other diffusion theories. Discrepancies between the variety of different diffusion theories most often occur at early times proximal to sources where the diffusion approximation is not valid.[16] Therefore, we shall restrict our attention to long times and large distances away from the source where all diffusion theories seem to agree with reasonably well with each other.[16]

## 3. THE REDUCED INTENSITY FOR FOCUSED BEAM WAVES

A scalar, time-harmonic wave field of a high-frequency Gaussian beam wave with a quadratic phase front propagating in the $\hat{z}$ direction takes the form[17]

$$\phi(\bar{\mathbf{x}}_T, x_3) = \frac{A_o}{\alpha\beta(x_3)} \exp\left[-\frac{x_T^2}{\beta(x_3)} + ik_o n x_3\right]. \tag{9}$$

The beam wave parameters are defined as

$$\alpha = 1/W_o^2 + ik_o/2R_o, \quad \text{and} \quad \beta(x_3) = 1/\alpha + i2x_3/k_o n,$$

where $W_o$ is the beam waist, $k_o$ is the free space propagation constant, and $R_o$ is the phase front's radius of curvature.

To consider these focused beam waves in the theory of radiative transport and thus, the diffusion approximation, we must understand the behavior of the reduced intensity of these beam waves. In anticipation of using the Wigner distribution of this wave field to derive the reduced intensity, we consider propagation in a lossy medium with a complex refractive index, $n = n' + in''$. For the reduced intensity, the attenuation of the wave field is due to extinction and the expression, $\gamma_t = 2k_o n''$, relates the imaginary part of the refractive index used above to the extinction coefficient.[4]

### 3.1. The Wigner Distribution

The Wigner distribution was originally constructed as an auxiliary phase-space distribution function for quantum mechanical systems.[9] However, it is also useful as a tool for studying classical wave propagation, and there exists a relationship between the Wigner distribution and the specific intensity that is well established.[10–12] Let us summarize some of these important relationships.

The Wigner distribution of a time-harmonic wave field, $\phi(\bar{\mathbf{x}})$, is defined as

$$\mathcal{W}(\bar{\mathbf{x}}, \bar{\mathbf{k}}) = (2\pi)^{-3} \int_{\mathbb{R}^3} d^3\bar{\mathbf{y}} \exp[i\bar{\mathbf{k}} \cdot \bar{\mathbf{y}}]\, \phi^*(\bar{\mathbf{x}} + \bar{\mathbf{y}}/2)\phi(\bar{\mathbf{x}} - \bar{\mathbf{y}}/2). \tag{10}$$

Integrating the Wigner distribution with respect to the wave vector, $\bar{\mathbf{k}} = (k_1, k_2, k_3)$, yields the energy density of the wave,

$$\int_{\mathbb{R}^3} \mathcal{W}(\bar{\mathbf{x}}, \bar{\mathbf{k}})\, d^3\bar{\mathbf{k}} = |\phi(\bar{\mathbf{x}})|^2. \tag{11}$$

Calculating the first moment of the Wigner distribution with respect to the wave vector yields the Poynting vector,

$$\int_{\mathbb{R}^3} \mathcal{W}(\bar{\mathbf{x}}, \bar{\mathbf{k}})\, \bar{\mathbf{k}}\, d^3\bar{\mathbf{k}} = \frac{1}{2i}\left[\phi^*(\bar{\mathbf{x}})\nabla\phi(\bar{\mathbf{x}}) - \phi(\bar{\mathbf{x}})\nabla\phi^*(\bar{\mathbf{x}})\right]. \tag{12}$$

Furthermore, the Wigner distribution is a real-valued function for all $\bar{\mathbf{x}}$ and $\bar{\mathbf{k}}$.

With these properties, one may be inclined to interpret the Wigner distribution as a wave-vector dependent energy density that is equivalent to the specific intensity, but the Wigner distribution is not a non-negative function, in general. Therefore, the Wigner distribution cannot be entirely interpreted as this wave-vector dependent energy density. However, the Wigner distribution becomes a non-negative function in the high-frequency asymptotic limit.[12] For example, consider a plane wave with constant amplitude, $A_o$, propagating in free space in the $\hat{\mathbf{s}}$ direction,

$$\phi(\bar{\mathbf{x}}) = A_o \exp[ik_o \hat{\mathbf{s}} \cdot \bar{\mathbf{x}}]. \tag{13}$$

Upon substituting this plane wave expression into the definition of the Wigner distribution, we obtain

$$\mathcal{W}(\bar{\mathbf{x}}, \bar{\mathbf{k}}) = |A_o|^2 \delta(\bar{\mathbf{k}} - k_o\hat{\mathbf{s}}). \tag{14}$$

Similarly, a high-frequency wave with a slowly varying complex amplitude, $A(\bar{\mathbf{x}})$, and phase, $S(\bar{\mathbf{x}})$, is

$$\phi^{(\epsilon)} \sim A(\bar{\mathbf{x}}) \exp[iS(\bar{\mathbf{x}})/\epsilon] \quad \text{as } \epsilon \to 0^+, \tag{15}$$

where $\epsilon$ is a small, positive parameter used to evaluate the high-frequency limit. The high-frequency asymptotic Wigner distribution[12] takes the form

$$\mathcal{W}(\bar{\mathbf{x}}, \bar{\mathbf{k}}) \sim |A(\bar{\mathbf{x}})|^2\, \delta(\bar{\mathbf{k}} - \nabla S(\bar{\mathbf{x}})). \tag{16}$$

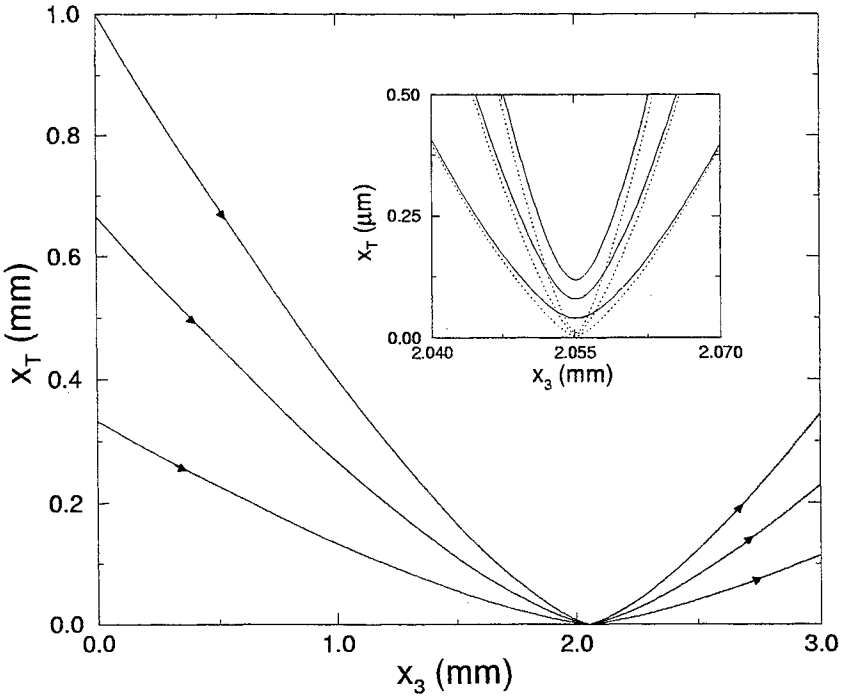


**Figure 1.** Ray paths of the Wigner distribution starting from $x_T = W_o/3, 2W_o/3$ and $W_o$. Here $W_o = 1\,mm$, $R_o = 1.5\,mm$, $n' = 1.37$ and $\lambda = 467\,nm$. Dotted lines correspond to propagation in free space and solid lines correspond to propagation with $\gamma_t = 42\,mm^{-1}$. The inset plot is a close-up showing the defocusing due to extinction.

### 3.2. Wigner Distribution of Focused Beam Waves

By rearranging terms in the beam wave defined in (9), we find that the amplitude is

$$A(\bar{\mathbf{x}}) = \frac{A_o}{\alpha\beta(x_3)} \exp\left[-f_r(x_3)\frac{x_T^2}{W_o^2} - k_o n'' x_3\right]. \tag{17}$$

In addition, we find the phase is

$$S(\bar{\mathbf{x}}) = k_o n' x_3 - f_i(x_3)\frac{x_T^2}{W_o^2}. \tag{18}$$

Here, we define

$$f_r(x_3) = \mathrm{Re}\left[\frac{Wo^2}{\beta(x_3)}\right] = d^{-1}(x_3)\left(1 + \frac{x_3}{n' z_o}\frac{n''}{n'}\frac{1 + z_o^2/R_o^2}{1 + n''^2/n'^2}\right), \tag{19}$$

$$f_i(x_3) = \mathrm{Im}\left[\frac{Wo^2}{\beta(x_3)}\right] = d^{-1}(x_3)\left(\frac{z_o}{R_o} - \frac{x_3}{n' z_o}\frac{1 + z_o^2/R_o^2}{1 + n''^2/n'^2}\right), \tag{20}$$

$$z_o = k_o W_o^2/2, \tag{21}$$

and

$$d(x_3) = 1 + \frac{x_3^2}{n'^2 z_o^2}\frac{1 + z_o^2/R_o^2}{1 + n''^2/n'^2} + 2\frac{x_3}{n' z_o}\frac{1}{1 + n''^2/n'^2}\left(\frac{n''}{n'} - \frac{z_o}{R_o}\right). \tag{22}$$

Upon substituting these expressions above as well as $n'' = \gamma_t/2k_o$ into the high-frequency asymptotic form of the Wigner distribution, we obtain

$$\mathcal{W}(\bar{\mathbf{x}}, \bar{\mathbf{k}}) = \frac{|A_o|^2}{d(x_3)} \exp\left[-f_r(x_3)\frac{2x_T^2}{W_o^2} - \gamma_t x_3\right] \delta\left(\bar{\mathbf{k}}_T + f_i(x_3)\frac{2\bar{\mathbf{x}}_T}{W_o^2}\right) \delta\left(k_3 - k_o n' + \frac{df_i(x_3)}{dx_3}\frac{2x_T^2}{W_o^2}\right). \tag{23}$$

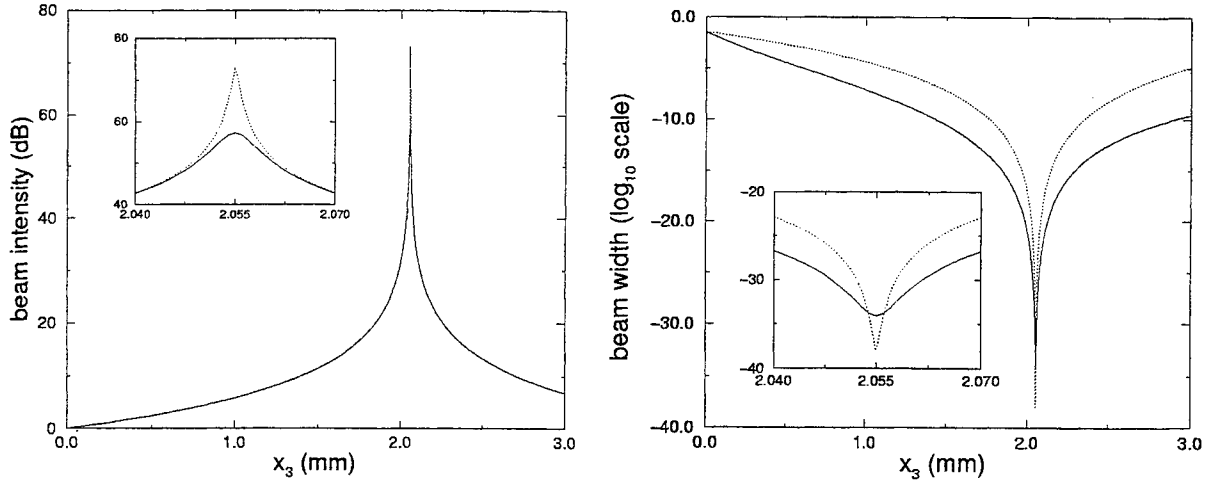


**Figure 2.** On-axis beam intensity without exponential decay from extinction (left plot) and beam width (right plot) of the Wigner distribution. Here the beam wave parameters are the same as in Figure 1. Dotted lines correspond to propagation free space and solid lines correspond to propagation in a medium with $\gamma_t = 42\,mm^{-1}$. Insets in both plots are close-ups that show the effect of extinction on focusing.

In (23), the argument of the transverse wave-vector distribution leads to the ray path equation,

$$\delta\left(\bar{\mathbf{k}}_T + f_i(x_3)\frac{2x_T}{W_o^2}\right) \qquad \Rightarrow \qquad \bar{\mathbf{k}}_T = k_o \sin\theta = -f_i(x_3)\frac{2x_T}{W_o^2} = \frac{dx_T}{dx_3}. \tag{24}$$

For a particular radial distance given at $x_3 = 0$, the solution to the differential equation above yields the ray path. Some sample ray paths are given in Figure 1. Here, we have chosen the beam wave parameters to correspond to narrow beam waves in biological media.[18] As the extinction coefficient increases, the ray paths deviate from the ray paths in free space and widen the focusing spot size.

From the expression of the Wigner distribution given in (23), we determine the on-axis beam intensity, $b(x_3)$, and the beam width, $w(x_3)$, to be

$$b(x_3) = \frac{|A_o|^2}{d(x_3)}\exp(-\gamma_t x_3) \qquad \text{and} \qquad w^2(x_3) = \frac{W_o^2}{2f_r(x_3)}. \tag{25}$$

In the expression for beam intensity, we easily see that it attenuates exponentially due to extinction. However, in order to fully understand the effect of extinction on the intensity and width, we plot some typical beam intensities (without the exponential decay factor due to extinction) and beam widths in free space and with extinction in Figure 2. As the extinction coefficient increases, deviations the from free space case are seen again near the focal distance that inhibit focusing. In Figure 3 we plot the beam intensity with the exponential decay due to extinction for a variety of extinction coefficients.

### 3.3. The Reduced Average Intensity

The result for the high-frequency asymptotic Wigner distribution given in (23) is proportional to the reduced intensity of transport theory. Recall that the average intensity is proportional to the energy density,[1]

$$|\phi(\bar{\mathbf{x}})|^2 = \frac{1}{c}\int_{4\pi} I(\bar{\mathbf{x}}, \hat{\mathbf{s}})\, d\Omega(\hat{\mathbf{s}}) = \frac{4\pi}{c}U(\bar{\mathbf{x}}). \tag{26}$$

The asymptotic form of the Wigner distribution in the high frequency limit (16) is easy to integrate over all $\bar{\mathbf{k}}-$space and yields,

$$\int_{\boldsymbol{R}^3} \mathcal{W}(\bar{\mathbf{x}}, \bar{\mathbf{k}}) d^3\bar{\mathbf{k}} = |A(\bar{\mathbf{x}})|^2 = \frac{|A_o|^2}{d(x_3)}\exp\left[-f_r(x_3)\frac{2x_T^2}{W_o^2} - \gamma_t x_3\right] = |\phi(\bar{\mathbf{x}})|^2, \tag{27}$$

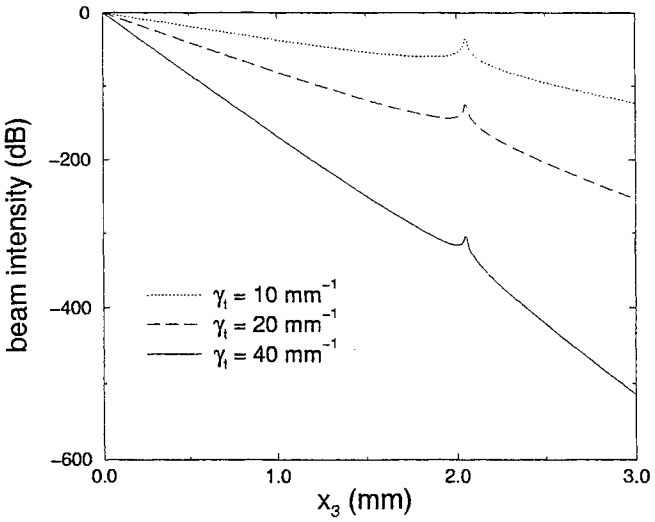


**Figure 3.** Effect of extinction on the on-axis beam intensity. The beam parameters are the same as figure 1 and 2.

where we have substituted $n'' = \gamma_t/2k_o$. Therefore, we can easily see from these expressions that the average reduced intensity is related the $\bar{\mathbf{k}}$–integrated Wigner distribution by a constant factor of $4\pi/c$.

## 4. FOCUSED BEAM WAVE DIFFUSION

As a beam wave propagates in a random medium, the reduced intensity exponentially decays due to scattering and absorption. Then the distribution of power that is scattered feeds into diffuse intensity. In a highly scattering medium with little absorption, the average diffuse intensity can be approximated by the diffusion approximation. In this section, we solve the diffusion equation in which the results from previous section are used as source terms.

### 4.1. Spatial Behavior

To study the spatial behavior of the diffuse average intensity, let us consider the diffusion equation with a continuous wave source,

$$\nabla^2 U(\bar{\mathbf{x}}) - \kappa U(\bar{\mathbf{x}}) = -\eta U_{ri}(x_T, x_3). \tag{28}$$

Here, we define $\kappa = \gamma_a/D$ and $\eta = \gamma_s/D$. To simplify this calculation, we normalize the average reduced intensity, (27) so that it takes on a value of unity at $(x_T, x_3) = (0, 0)$ yielding

$$U_{ri}(x_T, x_3) = \frac{1}{d(x_3)} \exp\left[-f_r(x_3)\frac{2x_T^2}{W_o^2} - \gamma_t x_3\right]. \tag{29}$$

By applying the Hankel transform of order zero on (28), we obtain

$$\frac{\partial^2}{\partial x_3^2}\hat{U}(k_T, x_3) - (\kappa + k_T^2)\hat{U}(k_T, x_3) = -\eta a_o \hat{U}_{ri}(k_T, x_3), \tag{30}$$

where we define the Hankel transform of order zero as

$$\hat{f}(k_T) = \mathcal{H}_o[f(x_T)] = \int_0^\infty dx_T\, x_T\, J_o(k_T\, x_T) f(x_T), \tag{31}$$

and $J_o(x)$ is the Bessel function of order zero. Since the two-dimensional Fourier transform of a radially symmetric function is related to the Hankel transform of order zero by

$$\frac{1}{(2\pi)^2}\int_{I\!R^2} d^2\bar{\mathbf{x}}_T \exp\left[i\bar{\mathbf{k}}_T \cdot \bar{\mathbf{x}}_T\right] f(x_T) = \frac{1}{2\pi}\mathcal{H}_o\left[f(x_T)\right] = \frac{1}{2\pi}\hat{f}(k_T), \tag{32}$$

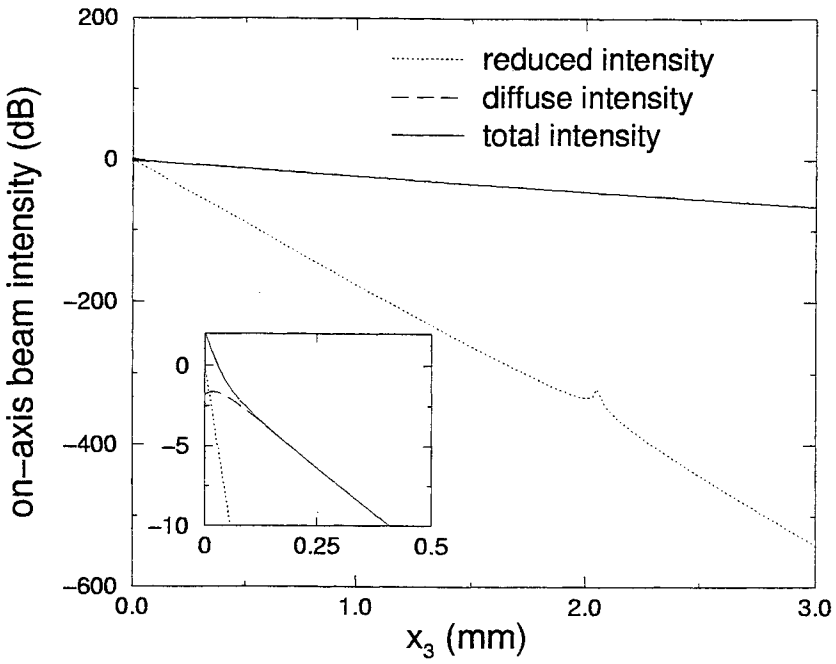


**Figure 4.** Numerical calculation of the solution of the continuous wave diffusion equation given in (37). This plot shows the on-axis averaged total intensity (solid curve) as well as the reduced intensity (dotted curve). The inset shows a detail of the plot including the average diffuse intensity. Here we consider an albedo value of 0.98 and asymmetry parameter value of 0.80. The other parameters are the same as in Figure 1.

we find that

$$\hat{U}_{ri}(k_T, x_3) = \frac{1}{4}\frac{W_o^2}{d(x_3) f_r(x_3)} \exp\left[-\frac{k_T^2 W_o^2}{8 f_r(x_3)} - \gamma_t x_3\right]. \tag{33}$$

Therefore, the solution to (30) is

$$\hat{U}(k_T, x_3) = \int_0^\infty d\zeta\, G(k_T, x_3 - \zeta)\hat{U}_{ri}(k_T, \zeta), \tag{34}$$

where the Green's function,

$$G(k_T, x_3 - \zeta) = \frac{1}{2\sqrt{\kappa + k_T^2}} \exp\left[-\sqrt{\kappa + k_T^2}|x_3 - \zeta|\right] \tag{35}$$

satisfies

$$\frac{\partial^2}{\partial x_3^2} G(k_T, x_3 - \zeta) - (\kappa + k_T^2) G(k_T, x_3 - \zeta) = -\delta(x_3 - \zeta). \tag{36}$$

Here we have assumed that the source function is only non-zero for positive propagation distances. Finally, we can recover the solution in the physical domain by inverse Hankel transforming the result from (34),

$$U(x_T, x_3) = \int_0^\infty dk_T\, k_T\, J_o(k_T\, x_T) \int_0^\infty d\zeta\, G(k_T, x_3 - \zeta)\hat{U}_{ri}(k_T, \zeta) \tag{37}$$

To understand the behavior of the diffuse intensity as it propagates in the medium, we numerically compute the solution given by (37). From our analysis of the reduced intensity, we found that the attenuation due to extinction impeded focusing effects. In the diffusion limit, since directional information of the beam source is lost due to

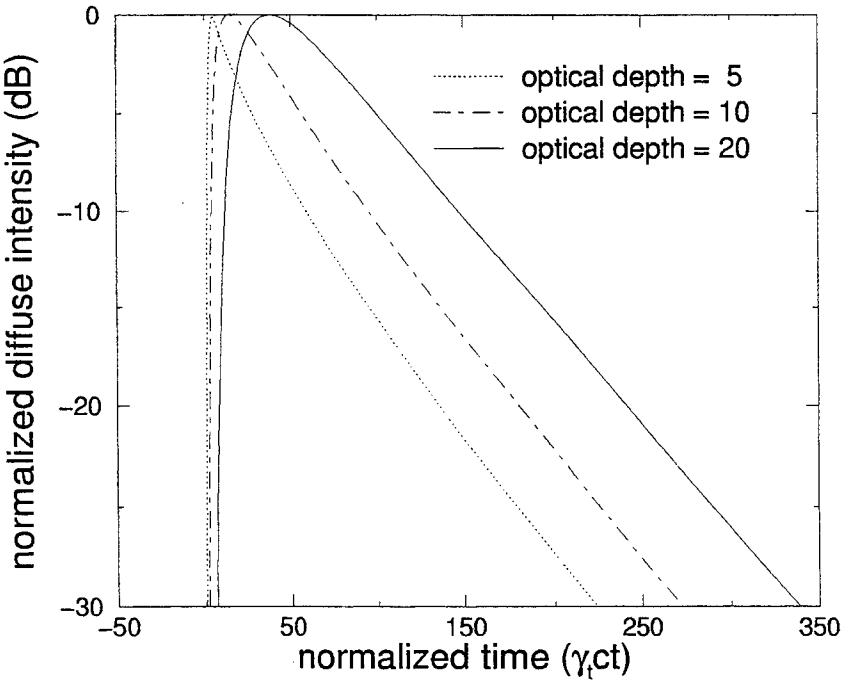


**Figure 5.** On-axis ($x_T = 0$), average diffuse intensity temporal responses to a delta function input pulse given by (40). These pulse responses are normalized to their peak intensity and plotted on a time scale normalized with the extinction coefficient and constant wave speed as $t/T_o = \gamma_t ct$. For this medium, the albedo value is 0.98 and the asymmetry parameter value is 0.80. The other parameters are the same as in figure 1. These pulse responses are computed at optical depths of 5, 10 and 20 or at approximately $0.12\,mm$, $0.24\,mm$ and $0.48\,mm$, respectively.

significant amounts of multiple scattering, one can expect that focusing would be even more greatly impeded.[19–22] In fact, from our numerical calculations, we find that the effects of focusing on the average diffuse intensity are hardly noticeable. In Figure 4, we show some results from a sample calculation for a medium with albedo equal to 0.98 and mean scattering cosine equal to 0.80. The beam wave parameters for these calculations are the same as the ones used for the reduced intensity study.

In Figure 4, we plot the average total intensity at beam-center as a function of distance. As a reference, we also plot the average reduced intensity at beam-center. The inset of this figure shows the transition that the total intensity makes as the reduced intensity attenuates from scattering and absorption. Although one cannot entirely assume that the diffusion approximation is valid this close to the source, the overall qualitative behavior demonstrated in this figure seems intuitively correct. At the focal length ($\sim 2.055\,mm$ for these particular parameters), the total intensity is effectively equal to the average diffuse intensity since the average reduced intensity suffers from a significant amount of attenuation from scattering and therefore, the diffusing beam does not seem to undergo any focusing effects.

Numerically investigating the spatial spreading as the beam propagates into the medium, we find that beam width increases linearly with propagation distance. This linear growth is a significant departure from the average reduced intensity's beam width (see Figure 2) which spans several orders of magnitude as it propagates in the medium.

### 4.2. Temporal Behavior

To study the temporal behavior of focused beam wave pulses in a diffusing medium, let us consider the diffusion equation with a delta function input pulse,

$$\frac{1}{c}\frac{\partial}{\partial t}U(x_T, x_3, t) - D\nabla^2 U(x_T, x_3, t) + \gamma_a U(x_T, x_3, t) = \gamma_s U_{ri}(x_T, x_3, t)\delta(t - x_3/c). \tag{38}$$

Here, we are assuming a narrow-band limit whereby the reduced intensity's spectrum is supported locally about the carrier frequency.[4,16] By applying the Fourier Transform on (38), we obtain

$$\nabla^2 U(x_T, x_3, \omega) - (\kappa + i\omega/cD)U(x_T, x_3, \omega) = -\frac{1}{2\pi}\eta U_{ri}(x_T, x_3)\exp(-i\omega x_3/c), \tag{39}$$

where $\omega$ is the frequency. Notice that this diffusion equation in the frequency domain takes the same form as (28). Therefore, we can easily write the solution as

$$U(x_T, x_3, \omega) = \int_0^\infty dk_T\, k_T\, J_o(k_T\, x_T) \int_0^\infty d\zeta\, G_c(k_T, x_3 - \zeta, \omega)\hat{U}_{ri}(k_T, \zeta)\exp\left[-i\omega\zeta/c\right], \tag{40}$$

where the Green's function,

$$G_c(k_T, x_3 - \zeta, \omega) = \frac{1}{2\sqrt{\kappa + i\omega/cD + k_T^2}}\exp\left[-\sqrt{\kappa + i\omega/cD + k_T^2}\,|x_3 - \zeta|\right], \tag{41}$$

is a complex function that parametrically depends on frequency. Although some special care must be taken in choosing a branch of the square root functions within the Green's function given above, only a relatively simple modification to the numerical code used to approximation the continuous wave case is needed to consider the pulse case in the frequency domain. Upon computing the spectrum of the diffuse intensity, one can recover the pulse in the time-domain using Fast Fourier Transforms.

As pulses propagate in a scattering medium, one expects that the pulse spreads in time due to scattering.[2] In Figure 5, we plot numerical calculations of (40) along the beam center, $x_T = 0$ at various optical depths. The medium is the same as the one studied in the continuous wave case. The pulse responses have sharp rise and long tails typical of pulses propagating in a diffusing random medium.[16] As pulses propagate deeper into the medium, they undergo a significant amount of temporal spreading. For these calculations we measure the temporal pulse width at $-3\,dB$ below the peak intensity, and find that the pulse spreads nearly linearly with respect to the optical depth.

## 4.3. Comparison With Collimated Beam and Plane Waves

From the numerical results described above, we find that focused beam wave pulses spread significantly in space and time as they propagate deeper into the medium. Furthermore, these numerical results seem to demonstrate that the effects of focusing in highly-scattering random media are negligible. To fully understand whether focusing effects are evident for focused beam pulses in diffusing media, let us compare the results presented above for spatial spreading to collimated beam waves and temporal spreading to pulsed plane waves.

### 4.3.1. Collimated Beam Diffusion

To examine spatial spreading, let us revisit the diffusion equation with a continuous collimated beam wave source. Picking up from (30), we examine Hankel transform of the reduced intensity of a collimated beam wave,

$$\hat{U}_{ri}(k_T, x_3) = \frac{1}{4}\frac{W_o^2}{\tilde{d}(x_3)\tilde{f}_r(x_3)}\exp\left[-\frac{k_T^2 W_o^2}{8\tilde{f}_r(x_3)} - \gamma_t x_3\right]. \tag{42}$$

The parameters,

$$\tilde{f}_r(x_3) = \tilde{d}^{-1}(x_3)\left(1 + \frac{x_3}{n'z_o}\frac{\varepsilon}{1+\varepsilon^2}\right) \qquad \text{and} \qquad \tilde{d}(x_3) = 1 + \frac{x_3^2}{n'^2 z_o^2}\frac{1}{1+\varepsilon^2} + 2\frac{x_3}{n'z_o}\frac{\varepsilon}{1+\varepsilon^2}, \tag{43}$$

are evaluated in the collimated beam limit of $R_o \to \infty$. Following Ito[21,22] we assume that the ratio of the extinction coefficient to the wave number is very small which motivates defining the small parameter $\varepsilon = \gamma_t/(2k_o n') \ll 1$. Upon evaluating the asymptotic limit as $\varepsilon \to 0^+$, we obtain,

$$\hat{U}_{ri}(k_T, x_3) \sim \frac{W_o^2}{4}\exp\left[-\frac{k_T^2 W_o^2}{8} - \gamma_t x_3\right] + \mathcal{O}(\varepsilon). \tag{44}$$

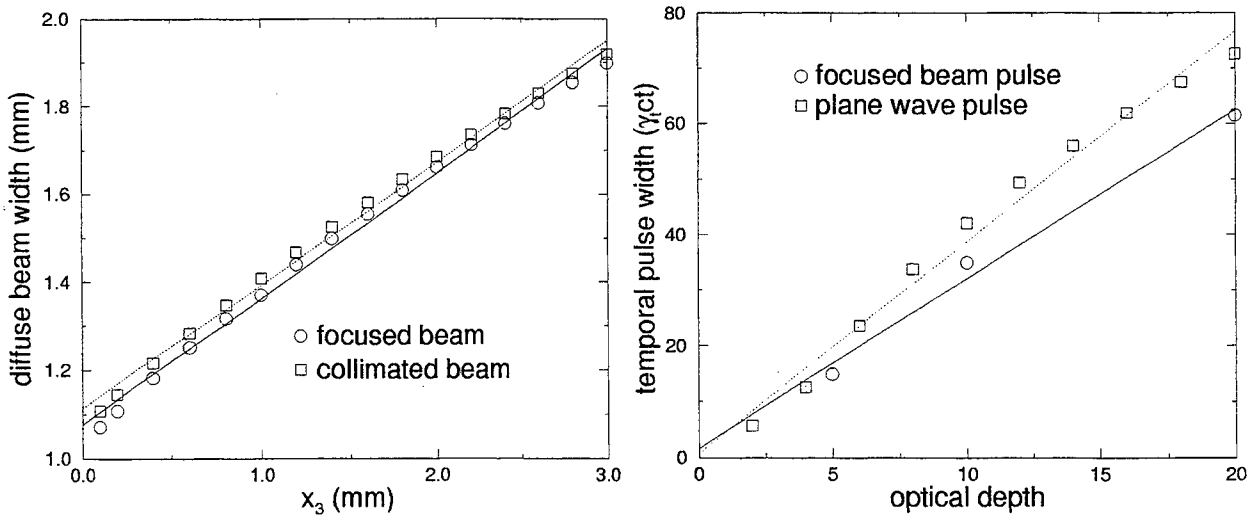


**Figure 6.** Comparisons of the diffuse intensity's spatial spreading with collimated beams (left plot) and temporal spreading with plane wave diffusion (right plot).

This asymptotic expression greatly simplifies the $x_3$-dependence in the average reduced intensity, and upon solving (34), we obtain,

$$\hat{U}(k_T, x_3) = \frac{W_o^2}{8\sqrt{\kappa + k_T^2}} \exp\left[-\frac{1}{8}k_T^2 W_o^2\right] \left( \frac{\exp[-\gamma_t z] - \exp[-\sqrt{\kappa + k_T^2}\, z]}{\sqrt{\kappa + k_T^2} - \gamma_t} + \frac{\exp[-\gamma_t z]}{\sqrt{\kappa + k_T^2} + \gamma_t} \right), \tag{45}$$

which can be substituted into (37) to yield the desired solution.

From the previous section, we determined that the focused beam width grows linearly as a function of the propagation distance. We find from numerical calculations that the collimated beam spreads linearly as a function of distance as well. In fact we find that the difference of beam spread of the diffuse component of the focused beam wave defined as

$$\langle x_T^2 \rangle = \int U(x_T, x_3) x_T^2 dx_T \Big/ \int U(x_T, x_3) dx_T \tag{46}$$

from that of the collimated beam is qualitatively negligible. A sample comparison can be seen in the left plot of Figure 6.

### 4.3.2. Plane Wave Diffusion

To examine temporal spreading, let us reconsider the diffusion equation with a plane wave delta function input source. Starting from (39) with a plane wave source whose reduced intensity is normalized to unity at $x_3 = 0$, we have the following differential equation,

$$\frac{\partial^2}{\partial x_3^2} U(x_3, \omega) - (\kappa + i\omega/cD) U(x_3, \omega) = -\frac{1}{2\pi} \eta \exp\left[-(1 + i\omega/c) x_3\right]. \tag{47}$$

The solution in the frequency domain can be written as

$$U(x_3, \omega) = \frac{\eta}{2\pi} \int_0^\infty d\zeta \, g_c(x_3 - \zeta, \omega) \exp\left[-(1 + i\omega/c)\zeta\right], \tag{48}$$

where

$$g_c(x_3 - \zeta, \omega) = G_c(x_T = 0, x_3, \omega) = \frac{1}{2\sqrt{\kappa + i\omega/cD}} \exp\left[-\sqrt{\kappa + i\omega/cD}\, |x_3 - \zeta|\right] \tag{49}$$

By numerical quadrature and Fourier transform methods, we can compute the resultant solution in the time-domain.

In Figure 6, we compare the temporal spreading of the plane wave pulse to the focused beam wave. Although rates of spreading are different, the spread of the focused beam pulse is qualitatively the same as the plane wave pulse. Therefore, the temporal spread of focused beam wave pulses is qualitatively similar to the temporal spread of plane wave pulses.

## 5. CONCLUDING REMARKS

In this paper, we have derived a high-frequency asymptotic expression for the reduced intensity of focused beam waves using Wigner distributions. This expression was then used to investigate focused beam pulses in highly scattering media using the diffusion approximation. From the solutions obtained from the diffusion equation, we found that these focused beams spread linearly in space in a similar way to collimated beams and spread linearly in time in a similar way to plane waves.

One aspect of this investigation that was not considered involves addressing the variety of diffusion theories available. Each diffusion theory can yield drastically different results[16] from the others. These discrepancies would most likely get amplified for boundary-value problems since posing physically exact boundary conditions in the diffusion approximation is not always possible and subject to a variety of treatments. In order to address the applicability of the various diffusion theories, we feel that one must closely examine the transition that waves make as they go from a transport theory description to a diffusive one. From understanding this transition, one can diagnostically determine the validity of applying a diffusion approximation and pose physically correct boundary conditions. In future studies, we will address this issue more carefully.

## ACKNOWLEDGMENTS

The authors would like to acknowledge their support from the Office of Naval Research, the National Science Foundation and the Army Research Office. A. D. Kim would specifically like to acknowledge his support for this work through a NSF VIGRE research assistantship.

## REFERENCES

1. A. Ishimaru, *Wave Propagation and Scattering in Random Media*, IEEE Press, New York, 1997.
2. A. Ishimaru, "Pulse propagation, scattering and diffusion in scatterers and turbulence," *Radio Science* **14**(2), pp. 269–276, 1979.
3. S. Chandrasekhar, *Radiative Transfer*, Dover, New York, 1960.
4. A. Ishimaru, "Diffusion of a pulse in densely distributed scatterers," *J. Opt. Soc. Am.* **68**, pp. 1045–1050, 1978.
5. A. Ishimaru, "Diffusion of light in turbid material," *Appl Opt.* **28**(12), pp. 2210–2215, 1989.
6. K. Furutsu, "Diffusion equation derived from space-time transport equation," *J. Opt. Soc. Am.* **70**(4), pp. 360–366, 1980.
7. M. C. W. van Rossum and T. M. Nieuwenhuizen, "Multiple scattering of classical waves: microscopy, mesoscopy, and diffusion," *Rev. Mod. Phys.* **71**(1), pp. 313–371, 1999.
8. A. Yodh and B. Chance, "Spectroscopy and imaging with diffusion light," *Physics Today* , pp. 34–40, March 1995.
9. E. Wigner, "On the quantum correction for thermodynamic equilibrium," *Physical Review* **40**, pp. 749–759, June 1932.
10. H. Bremmer, "General remarks concerning theories dealing with scattering and diffraction in random media," *Radio Science* **8**(6), pp. 511–534, 1973.
11. R. Fante, "Relationship between radiative-transport theory and maxwell's equations in dielectric media," *J. Opt. Soc. Am.* **71**, pp. 460–468, 1981.
12. L. Ryzhik, G. Papanicolaou, and J. B. Keller, "Transport equations for elastic and other waves in random media," *Wave Motion* **24**, pp. 327–370, December 1996.
13. S. Ito, "Comparison of diffusion theories for optical pulse waves propagated in discrete random media," *J. Opt. Soc. Am. A* **1**(5), pp. 502–505, 1984.
14. A. Ishimaru, "Difference between ishimaru's and furutsu's theories on pulse propagation in discrete random media," *J. Opt. Soc. Am. A* **1**(5), pp. 506–509, 1984.

15. A. Polishchuk, S. Gutman, M. Lax, and R. Alfano, "Photon-density modes beyond the diffusion approximation: scalar wave diffusion," *J. Opt. Soc. Am. A* **14**(1), pp. 230–234, 1997.
16. A. D. Kim and A. Ishimaru, "Optical diffusion of continuous-wave, pulsed, and density waves in scattering media and comparisons with radiative transfer," *Appl. Opt.* **37**(22), pp. 5313–5319, 1998.
17. A. Ishimaru, *Electromagnetic Wave Propagation, Radiation and Scattering*, Prentice Hall, Englewood Cliffs, New Jersey, 1991.
18. M. Keijzer, S. Jacques, S. Prahl, and A. Welch, "Light distributions in artery tissue: Monte carlo simulations for finite diameter laser beams," *Appl. Opt.* **28**(12), pp. 2331–2336, 1989.
19. A. Ishimaru, Y. Kuga, R. Cheung, and K. Shimizu, "Scattering and diffusion of a beam wave in randomly distributed scatters," *J. Opt. Soc. Am.* **73**(2), pp. 131–136, 1983.
20. J. Ying, F. Liu, and R. Alfano, "Spatial distrubtion of two-photon-excited fluorescence in scattering media," *Appl. Opt.* **38**(1), pp. 224–229, 1999.
21. S. Ito, "Diffusion of collimated, narrow beam waves in discrete random media," *Appl. Opt.* **34**(30), pp. 7106–7112, 1995.
22. S. Ito, "Theory of beam light pulse propagation through thick clouds: effects of beamwidth and scatterers behind light source on pulse broadening," *Appl. Opt.* **20**(15), pp. 2706–2715, 1995.

# Confocal Imaging of Biological Tissues Using Second Harmonic Generation

Beop-Min Kim[1], Patrick Stoller[1], Karen Reiser[2], Jürgen Eichler[3], Ming Yan[1], Alexander Rubenchik[1], Luiz Da Silva[1]

[1]Medical Technology Program, Lawrence Livermore National Laboratory, Livermore, CA
[2]University of California Medical Center at Davis, Davis, CA
[3]Technische Fachhochschule-Berlin, Berlin Germany

## Abstract

A confocal microscopy imaging system was devised to selectively detect second harmonic signals generated by biological tissues. Several types of biological tissues were examined using this imaging system, including human teeth, bovine blood vessels, and chicken skin. All these tissues generated strong second harmonic signals. There is considerable evidence that the source of these signals in tissue is collagen. Collagen, the predominant component of most tissues, is known to have second order nonlinear susceptibility. This technique may have diagnostic usefulness in pathophysiological conditions characterized by changes in collagen structure including malignant transformation of nevi, progression of diabetic complications, and abnormalities in wound healing.

## Introduction

The predominant structural protein in animals is collagen, a macromolecule comprising at least 17 genetically distinct forms. Collagen types are generally classified as either fibrillar or nonfibrillar. Fibrillar collagens, such as types I, II, and III, comprise the major structural collagens of the body. They are characterized at the molecular level by a triple helical structure, and at the supramolecular level by ordered arrays of fibrils and bundles [1]. They lack inversion symmetry which is a necessary condition for second order nonlinear susceptibility. The second order nonlinearity of the collagen is responsible for generation of light at twice the excitation frequency (second harmonic generation) when interacting with intense laser pulses [2]-[5]. The development of ultrashort pulse laser technology has made it feasible to analyze harmonic generation in collagen nondestructively. Recently, it was reported that femtosecond laser pulses generate second harmonic light in collagen more effectively without damaging the target tissues than picosecond or nanosecond pulses [5]. Since collagen is the only significant source of second harmonic signals in tissues, nonlinear optical imaging offers the possibility of obtaining structural information about collagen with exceptionally high signal-to-noise ratios. In the present study, we report the

In *Laser-Tissue Interaction XI: Photochemical, Photothermal, and Photomechanical,* Donald D. Duncan, Jeffrey O. Hollinger, Steven L. Jacques, Editors, Proceedings of SPIE Vol. 3914 (2000)
1605-7422/00/$15.00

development of a nonlinear optical imaging system capable of nondestructive analysis of biological samples, in which we combine the resolution of confocal microscopy with the specificity of second harmonic signal detection. We further report that this system can be successfully used on a diverse range of soft and hard biological tissues, including tooth, skin, and blood vessel.

**Materials and Methods:**

We used a Ti:Sapphire (Spectra-Physics Tsunami) ocscillator pumped by a 5 W, frequency-doubled Nd-YAG (Spectra-Physics Merlin) laser to produce 100 fs, 800 nm pulses at a repetition rate of 82 MHz. The laser beam passes through a 1.5 kHz optical chopper for lock-in amplification of the signal. The laser intensity is controlled using a half-wave plate and a birefringent calcite crystal. The laser beam is focused onto a sample mounted on a translation stage using a 20 mm focal length microscope objective (Mitutoyo) with a numerical aperture of 0.42. This produces a focal spot with approximately 1 micron diameter and an approximate beam waist of 10 microns.

The back-scattered light is collected by the same microscope objective and transmitted through the dichroic mirror that reflects the input beam onto the sample. The signal is focused through a 50 micron pinhole using an f = 50 mm lens, collimated by another lens, and then reflected onto a photomultiplier tube (PMT) using a series of dichroic mirrors that reject two-photon fluorescence and first-harmonic light. The use of a confocal detection system allows improved depth resolution by eliminating SHG generated away from the focal spot.

Some of the back-scattered first-harmonic light is reflected at one of the calcite crystal interfaces and detected using a photodiode. The PMT and photodiode signals are lock-in amplified using the reference signal from the optical chopper. A Labview program is used to move the motorized translation stage and to collect data from the lock-in amplifiers.

Chicken skin (kept frozen at -80°) was obtained from previous studies. Human tooth samples, containing carious lesions, were obtained from UCSF School of Dentistry. Bovine artery was dissected from commercially obtained bovine shanks. For analysis, all samples were clamped between two glass slides and mounted on the translation stage. Samples were kept moist with physiological saline. Several scans were performed on each sample in order to determine reproducibility of results.

**Experimental Results**

*Hard Tissue (dentin)*: We made several scans of the surface of a tooth at the boundary between healthy dentin and cavity. Fig. 1(a) below shows the strong contrast

between dentin and cavity in the second harmonic signal. Fig. 1(b) gives the first harmonic signal obtained from the same scan. While the contrast ratio in the SHG scan is 180:1 between dentin and cavity, it is only 5:1 in the first harmonic scan.

*Bovine Arteries*: Arteries were analyzed in several ways. We cut out a thin (about 2 mm) cross-section of the artery (Fig. 2) and performed several one-dimensional scans across the surface, moving from the hole in the center to the outer edge. Fig. 3 is an illustration of the cross-section of an artery [1]. As shown in Fig. 4, the SHG signal is weaker near the endothelium, the elastic lamina and the tunica media, which is a layer composed mostly of soft muscle tissues. The SHG intensity rapidly increases as the beam focus approaches the adventitia, which is rich in collagen content. The signal from the adventita is by no means uniform; the large fluctuations in the SHG signal suggest that our detection technique is able to resolve features on the scale of a few microns. When we repeated the scan (Fig. 4(a) and 4(b)), we found that results were highly replicable, suggesting that fluctuations in signal intensity represent determinant features and not random noise. The repeated scans also confirmed that the high intensity laser pulses do not appear to damage the artery tissue.

*Chicken Skin*: We performed two-dimensional scans on chicken skin (Fig. 5). Fluctuation in SHG intensity gave the appearance of a layered structure with distinct structural features, especially near the left side of the scan. There are also features about 50 microns deep (chicken surface not shown in the figure) and about 10 to 20 microns across in the SHG scan. The features are separated by about 10 to 20 microns. We use the peak in the first harmonic signal that occurs when the focus of the beam crosses the glass slide-chicken skin interface to indicate the location of the surface. This technique confirms that we are observing second harmonic generation from just inside the chicken skin and not from the surface.

## Discussion

In the present study we have shown that it is possible to obtain second harmonic images from a variety of biological tissues using confocal microscopy linked to a femtosecond laser. Such images have very high-resolution (on the order of microns) and high replicability. We also found that there was no evidence of tissue destruction. We were able to perform two-dimensional scans, similar to those described by Guo et al. [6,7] in which imaging is simultaneously obtained along the surface and into the sample.

These studies suggest that detailed studies of collagen are feasible using second harmonic analysis. A major advantage of this technique is high specificity, since light is generated only from material that possesses second order nonlinear susceptibility. Thus,

targeted imaging is possible even when this nonlinear material is embedded inside turbid media. As demonstrated by our preliminary studies and by other studies in the literature, collagen can be selectively imaged inside the tissue. The intensity of the second harmonic signal is highly dependent on the chirality of the collagen fibrils, a structural feature that is known to change in specific pathologic conditions. For example, conditions involving partial degradation of collagen, increased nonenzymatic glycation, and/or glyco-oxidative damage result in a decrease in chiral structure. We might therefore expect to see decreased SHG intensity in diabetes, aging, and during neoplastic transformation of nevi into melanoma. Conversely, conditions such as hypertrophic scarring and scleroderma, which are characterized by an increase in enzymatically mediated crosslinking, result in an increase in chirality, and we would therefore expect to see an increase in SHG intensity.

## ACKNOWLEDGMENTS

This work was performed at Lawrence Livermore National Laboratory under the auspices of the U.S. department of Energy under contract No. W-7405-ENG-48.

## References

1. D. W. Fawcett, *A Textbook of Histology* (Chapman and Hall, New York, 1994), p. 133.
2. I. Freund, M. Deutsch, and A. Sprecher, "Connective tissue polarity: optical second-harmonic microscopy, cross-beam summation, and small-angle scattering in rat-tail tendon," *Biophys. J.* **50**, 693-712 (1986).
3. G. B. Altshuler, N. R. Belashenkov, G. A. Martsinovski, and A. A. Solounin, "Nonlinear transmission and second-harmonic generation in dentin in the field of ultrashort Nd-laser pulses," in *Advanced Laser Dentistry*, G. B. Altshuler, R. J. Blankenau, and H. A. Wigdor, eds., Proc. SPIE **1984**, 6-10 (1995).
4. V. Hovanessian and A. Lalayan, "Second-harmonic generation in biofiber-containing tissues," in *Proceedings of the International conference on Lasers'96* (Society for Optical and Quantum Electronics, McLean, VA., 1996), pp. 107-110.
5. B.-M. Kim, J. Eichler, and L. B. Da Silva, "Frequency doubling of ultrashort pulses in biological tissues," *Appl. Opt.* **38**, 7145-7150 (1999).
6. Y. Guo, P. P. Ho, H. Savage, D. Harris, P. Sacks, S. Schantz, F. Liu, N. Zhadin, and R. R. Alfano, "Second-harmonic tomography of tissues," *Opt. Lett.* **22**, 1323-1325 (1997).
7. Y. Guo, P. P. Ho, A. Tirksliunas, F. Liu, and R. R. Alfano, "Optical harmonic generation from animal tissues by the use of picosecond and femtosecond laser pulses," *Appl. Opt.* **35**, 6810-6813 (1996).

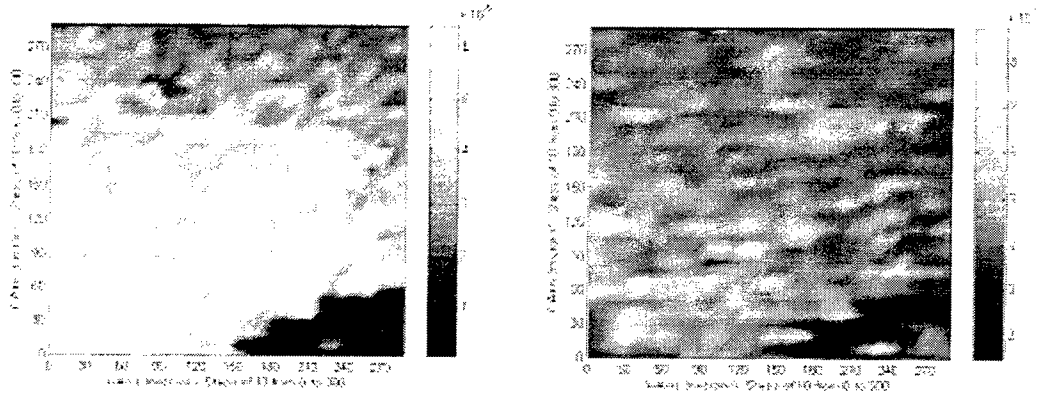

Fig. 1. (a) SHG scan of cavity/dentin boundary. (b). First harmonic scan of the cavity/ dentin boundary. The cavity is located in the lower-right corner of the scan.

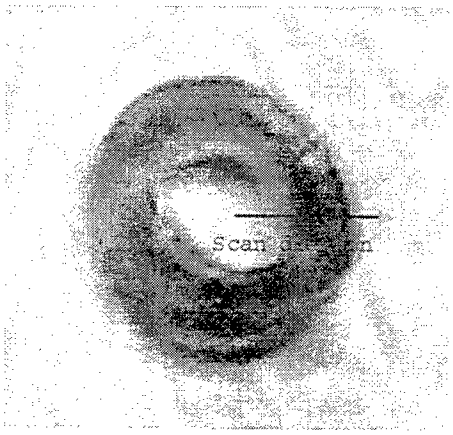

Fig. 2. Photograph of bovine artery cross-section showing scan direction.

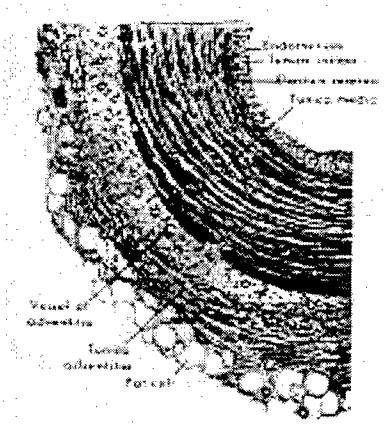

Fig. 3. Illustration of structure of artery [1].

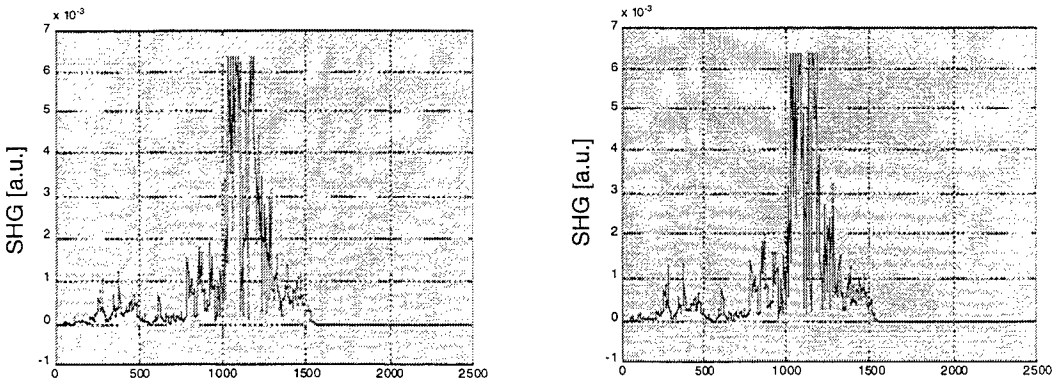


Figure 4. (a) Scans of cross-section of bovine artery. x = 0 microns corresponds to the center area and x around 1500 microns corresponds to the outer edge. Note that the lock-in amplifier saturated; the highest peaks actually indicate a higher signal than recorded (b). Repeat of scan shown in Fig. 4(a). Note that the same features can be observed in both scans.

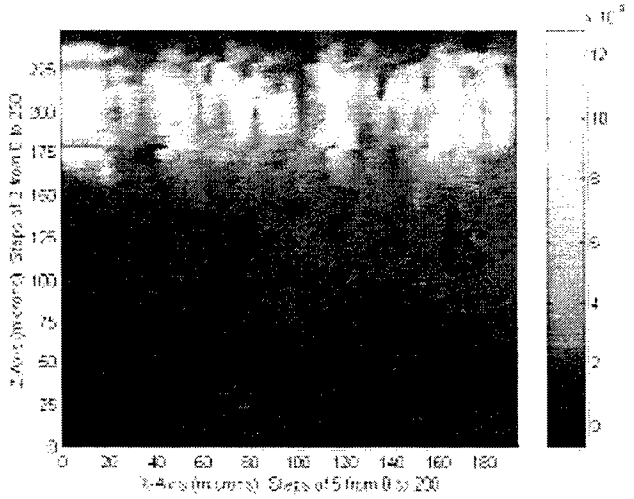

Figure 5. Confocal scan of chicken skin. x-axis is along the surface and positive z-axis points along the normal to the skin surface. The surface is at about 250 microns; lower values of z are inside the chicken skin.

## SESSION 14

# Beam Propagation in Random Media III

Invited Paper

# The Aerosol of the Marine Environment *

Stuart G. Gathman
Science and Technology Corporation
SPAWAR System Center, San Diego CA

## ABSTRACT

The aerosol found in the lowest kilometer over the world's ocean is quite different than that found over land. It includes several unique components of marine origin in addition to a background component, which can be similar to that found over land. Large marine aerosol can have significant interaction with infrared propagation in this region and are thus very important for naval applications. This paper will discuss some of the author's research in this area with special emphasis on the aerosol of interest to the Navy. The topics will include the aerosol found from shipboard level to altitudes above the marine inversion, aerosol found in the boundary layers between the wave tops and shipboard level and the effect of surf produced in the coastal regions. This paper will also describe some aspects of recent series of experiments sponsored by the Office of Naval Research called EOPACE (Electro Optical Propagation in A Coastal Environment). This program has concentrated on looking at the history of the sea salt aerosol produced by the breaking of waves in a surf zone as it interacts with the micrometeorology in the ocean atmospheric surface layer.

**Keywords:** marine aerosol, surf, EO propagation, whitecaps, EOPACE, MAPTIP

## 1. BACKGROUND

The world's navies have a particular interest in determining the aerosol distribution throughout the lower layers of the ocean atmosphere where most of their operations take place. The aerosol in these layers provide an extremely varied component of the marine atmosphere where they contribute to the deterioration in the propagation of electrooptical energy. The ocean atmospheric environment is different from most land based environments in that it is relatively homogeneous for large regions at least when compared with an equivalent land situation in which there are many different structures, elevations, temperatures and sources of aerosol. Land regions inject into the atmosphere large quantities of different types of natural and manmade aerosol whereas the aerosol generated at the ocean surface is composed of sea-salt and water. Air motions can also be more complicated over land than over the ocean because of orographic effects and diurnal variations of land surface temperature which are functions of soil composition, time of day and location. The ocean is, on the other hand, a huge thermal heat sink and tends to stay at a relatively constant temperature. Its composition is also very constant when compared with the land.

The major molecular constituents of the atmosphere, both over the ocean and over land, tend to be constant with the exception of water vapor. Variations in water vapor content cause large variations in absorption except in certain frequency windows where propagation is possible. Modern computer codes used to predict propagation characteristics accurately describe the interaction of electrooptical energy with these molecular effects. Although the natural molecular composition of the air is relatively constant, the aerosol concentration in the marine boundary layer can vary by orders of magnitude and remains a major unknown in the propagation of EO, electrooptical, signals.

Aerosols interact with EO energy propagation by scattering and absorbing the photons as they travel along the propagation path. The amount of extinction and absorption of EO energy can be calculated from Mie theory. This however requires knowledge of the aerosol size distribution and the assumption that the scatterers are spherical in shape and that their composition (i.e. layering and index of refraction) is known.

## 2. INTRODUCTION

Aerosol in the different parts of the size spectra have different residence times in the atmosphere. Some of the smallest particles can be caught up with turbulent mixing and transported many thousands of miles from their source of generation, such as the transport of Saharan dust reported by Prospero[1]. Other populations of small aerosols are the end results of chemical combinations of naturally occurring trace constituents in the atmosphere as modeled by Fitzgerald et al[2,3]. The very

*Also published in *Proc. of SPIE* Vol. 3927



In *Laser-Tissue Interaction XI: Photochemical, Photothermal, and Photomechanical*, Donald D. Duncan, Jeffrey O. Hollinger, Steven L. Jacques, Editors, Proceedings of SPIE Vol. 3914 (2000)
1605-7422/00/$15.00

largest particles produced on the breaking of water waves fall rapidly back into the sea. The criterion of the time that an aerosol resides in the atmosphere can be used to distinguish roughly between different aerosol types.

If the dwell time of a particular size class of aerosol is short, we can say that the aerosol is probably of oceanic origin and was produced by either one of two methods. The jet drop mechanism[4] is the process where air bubbles bursting on a water surface produce an upward shooting jet of water on the breakup of the bubble. This jet becomes unstable and breaks up into several droplets each of which have upward momentum propelling it tens of centimeters into the air just above the water surface. Once in this region, turbulent air motions mix them in various ways throughout the marine boundary layer. The air bubbles are introduced into the ocean by breaking waves which entrap air beneath the surface. Visual evidence of this are whitecaps and breaking surf. A more violent process of getting sea water into the air is that of the shearing off of wave tops by wind interaction as described by Monahan et. al.[5]. Aerosol of oceanic origin thus have a droplet nucleus composed mainly of sea water and are thus hygroscopic. Thus the size of an aerosol particle changes as the relative humidity of the environment about the droplet changes. Aerosol in the smallest size parts of the spectrum, on the other hand, have probably been transported to the site by advection from more distant regions.

## 3. MARINE AEROSOL OF THE OPEN OCEAN

The navy aerosol model, NAM[6], can be used to determined the aerosol size distribution in various parts of the world's ocean. It was formed from a statistical analysis of many aerosol size distributions available in the literature of the time. These data

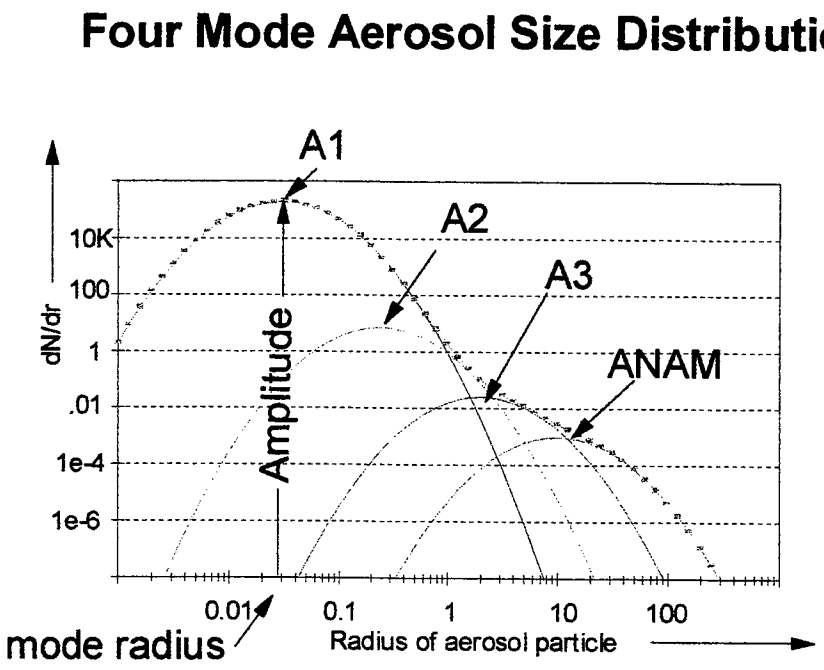


**Figure 1:** A four mode lognormal function used to represent the aerosol size distribution over the ocean. The NAM model used only the first three modes for describing the aerosol size distribution. The Advanced Navy Aerosol Model, ANAM[7], uses the fourth mode for describing the very large aerosol close to the wave tops.

were mostly from deck level measurements (taken at about 10 meters above the water surface.) More recent improvements add vertical utility to the model predictions. This original model and those following define the marine aerosol size distribution as a set of lognormal curves superimposed upon each other to represent the total distribution. All of the sets of aerosol represented by a particular lognormal function are assumed similar in their properties.

A typical size distribution represented by the most recent member of the family of navy aerosol models is shown in figure 1. The size distribution here is plotted with the y axis representing "dN/dr" of the distribution where N is the concentration of the aerosol which have the radius of "r." The lognormal function on the left-hand side of the plot (with its amplitude labeled

A1) represents the entire small aerosol population. Obviously the extreme complexity of the structure of the small aerosol, with variations in chemical composition and fine structure in the size distribution, are glossed over in this approximation which represents the "effective" small aerosol size distribution. This approximation is especially justified when the calculation of the optical properties of infrared wavelengths are needed. This is because Mie theory predicts that spheres with sizes comparable to the wavelength in question are more effective in scattering than are the smaller ones. The assumption is also made that these small background aerosol are well mixed throughout the lower atmosphere and thus, unlike large aerosol produced at the sea surface, exhibit minimal vertical variation in concentration.

The second function, with the labeled amplitude of A2, is known as the residual ocean produce mode of aerosol and it is related to the average wind speed over a 24 hour period of time. The third mode, A3, is known as the fresh aerosol and it is related to the current wind speed. Finally, the component labeled ANAM is that mode related to the very large aerosol which exists close to the wave tops. All but the A1 component have vertical variation and are functions of altitude. This vertical structure is related to mixing and other meteorological processes.

The total size distribution is the superposition of all of the individual lognormal components and can be expressed by an equation as:

$$\frac{dN(z)}{dr} = \sum_{i=0}^{4} \frac{A_i(z)}{f_i} \cdot \exp\left\{ C_i \cdot \left[ \log\left( \frac{r}{(r_{0i} \cdot f_i)} \right) \right]^2 \right\} \qquad (1)$$

where each of the four lognormal function is designated by the three parameters $A, r_0$ and C with subscripts, 1,2,3 and 4 to designate the particular lognormal function in question. The whole aerosol size distribution represented by the set of lognormal functions can thus be described by a limited number of parameters. Some of these parameters are found by experiment to be constant while others are empirically related to simultaneous meteorological events. The function "f" is used to describe the hygroscopic growth of the aerosol with respect the relative humidity surrounding the particles.

## 4. ELECTRO OPTICAL CALCULATIONS

Mie theory was used to calculate the volume extinction, scatter and absorption coefficients at a band of wavelengths from ultraviolet to 40 microns from a model population of spherical droplets of known chemical composition. These are functions of the wavelength, the radius of the sphere, and the index of refraction of the sphere. The volume extinction coefficient is expressed in equation 2 as an integration over the whole population of aerosol sizes. A volume absorption coefficient can be calculated in a similar way except that the Mie coefficient, $Q_{abs}$, must be used instead of $Q_{ext}$. The volume extinction coefficient is expressed as:

$$\beta_{ext} = \frac{\pi}{1000} \int Q_{ext} \cdot \frac{dN}{dr} \cdot r^2 \cdot dr \qquad (2)$$

If we now substitute the lognormal formulation for dN/dr into equation 2 above, our formulation of the size distribution in terms of the sum of these lognormal type functions becomes:

$$\beta_{ext} = \frac{\pi}{1000} \int Q_{ext} \sum_{i=0}^{3} \frac{A_i}{f_i} \cdot \exp\left[ -1 \cdot \left\{ \log\left( \frac{r}{r_{0i} \cdot f_i} \right) \right\}^2 \right] \cdot r^2 dr \qquad (3)$$

The Dave[8] code was adopted to calculate $Q_{ext}$ for these calculations. The integration and the summation can be switched so that the result becomes the sum of several integrals.

$$\beta_{ext} = \frac{\pi}{1000} \sum_{i=0}^{3} \frac{A_i}{f_i} \cdot \int Q_{ext} \cdot \exp\left[ -1 \cdot \left\{ \log\left( \frac{r}{r_{0i} \cdot f_i} \right) \right\}^2 \right] \cdot r^2 dr \qquad (4)$$

This has the advantage that the integrals can be pre-calculated to the required precision and their values stored in tables if necessary. If the dry aerosol nucleus of a particular chemistry (say sea salt) is soluble then f is function of relative humidity other wise it has a value of 1.0. The index of refraction is determined after the method of Hänel[9] where indices are calculated by using the ratio of the volumes of the water and the soluble nucleus in each hygroscopic droplet. These might be different for each population group of the model.

## 5. RESIDENCE TIME

Close to the surface, freshly produced jet drop and/or sea spray aerosol are found. Their concentration is strongly related to the efficiency of aerosol production mechanisms such as bubble mediated production and the direct wave tearing, both of which are functions of wind speed. The actual concentration results from a complex interplay of various processes such as production, subsequent upward lifting in the turbulent airflow just above the surface and downward gravitational fall.

Calculations involving just a few important processes taking place over the ocean surface can be used to get a simple picture of the actual concentrations at various altitudes of aerosol of different sizes. The following analysis[10] shows the time evolution of a column of air into which aerosol of different sizes are injected. The following simple equation describes the processes of turbulence and gravitational fall acting on the aerosol of a single size class in a column of air moving with a constant velocity in the direction of wind. The equation describes the time history of the concentration of particles $N_k$ of the "$k^{th}$" class which experience a size dependent settling velocity $V_k$. The turbulence in the atmosphere is represented by a turbulent diffusion function which is height dependent and described by K(z). The equation representing the concentrations of these aerosol is shown below.

$$\frac{dN_k}{dt} = \frac{\partial}{\partial z} \cdot K(z) \cdot \frac{\partial N_k}{\partial z} + V_k \frac{\partial N_k}{\partial z} \qquad (5)$$

The generation rate of these aerosol are introduced into the model space by the bottom boundary condition of the column. At time equals zero, all of the concentrations in the model grid are equated to zero. At the one hour model time after the start of the calculation a source of marine aerosol was turned on for one hour and then turned off for the rest of the calculation time.

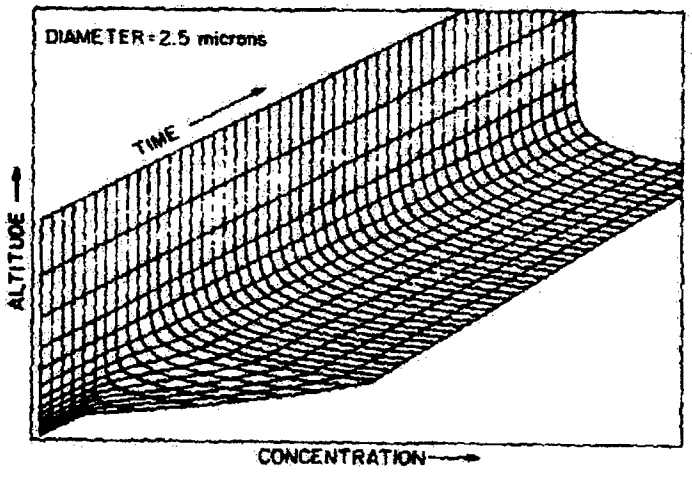


**Figure 2:** 3D surface depicting the concentration of aerosol of 2.5 micron diameter during the scenario discussed in the text.

The results are shown for two diameters of interest, i.e. 2.5 microns (figure 2) and 20 microns (figure 3). The results are shown as three dimensional surfaces which have the concentration on the x axis with increases going to the right from a zero level back plane. The altitude is shown along the vertical y axis and time goes back into the page. These figures give a visual indication of what happens to the marine aerosol as it is introduced into the marine boundary layer. In figure 2, we see a time history of the small 2.5 micron diameter aerosol. The figure shows the building up of the concentration especially near the surface immediately after the generator is turned on. During this time it is being mixed upward as time progresses. After the source is turned off, however, these small aerosol remain airborne for considerable lengths of time.

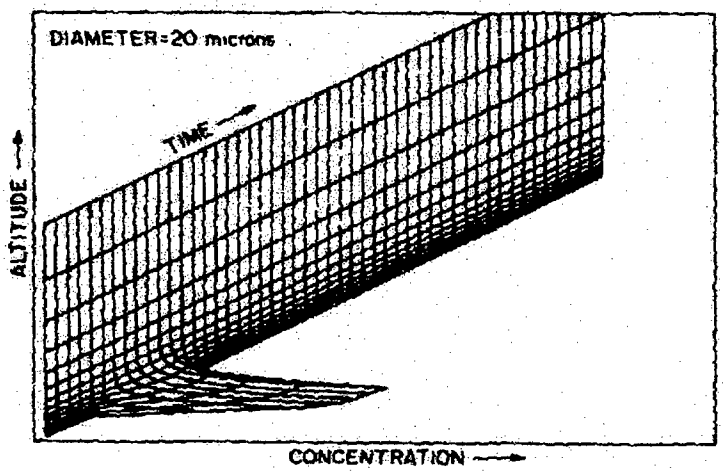


**Figure 3:** 3D surface depicting the concentration of aerosol of 20 micron diameter during the scenario discussed in the text.

A contrasting view is shown for the figure representing the larger aerosol with diameters of 20 microns. In figure 3 the aerosol is again generated between hours 1 and 2 as was done in the case of figure 2. In this case however it falls back to the ocean surface despite the mixing processes taking place. This is an illustration of how different sized populations of the navy aerosol model are suspended in the atmosphere longer than others.

## 6. EXTENSIONS OF THE BASIC NAM

Additions to NAM have extended its application from only deck level predictions to a broader scope of applications. Most of the original data used in the development of NAM was taken in the open ocean environment making the model to be principally useful at deck level for the open ocean scenario. A need arose to extend the model to higher in order to determine the propagation properties along slant paths. The need resulted in the effort of building NOVAM, Navy Ocean Vertical Aerosol Model[11,12]. It was based on the NAM as a kernel and is identical to NAM at an altitude of 10 meters. It provides information on the optical/IR properties of the aerosol at any altitude from ship deck level to above the marine boundary layer. NOVAM uses as its input information from profiles of temperature and humidity and surface meteorological data. Shown above in figure 4 is an example of a NOVAM extinction profile obtained during the KEY-90[13] experiments off of the Florida Keys. The in-situ extinction profile data plotted in the figure are from Mie calculations from aerosol size distribution measurements made from an aircraft making a spiral descent and from a boat on the water's surface.

Remote sensing data is also shown in the figure as the thin line that represents the profile of the estimated extinction from a downward looking LIDAR located in a plane flying overhead at 6 kilometers. The NOVAM prediction is shown as the heavy dark line. The input to NOVAM was the surface meteorological data from the boat and from the profile data obtained from the aircraft making the spiral. The model does not attempt to describe the situations within clouds (as seen

in this example when the spiraling aircraft penetrated a small cloud in making its profile). Likewise, if precipitation is present, the model is not capable of determining the optical and IR properties of the precipitation.

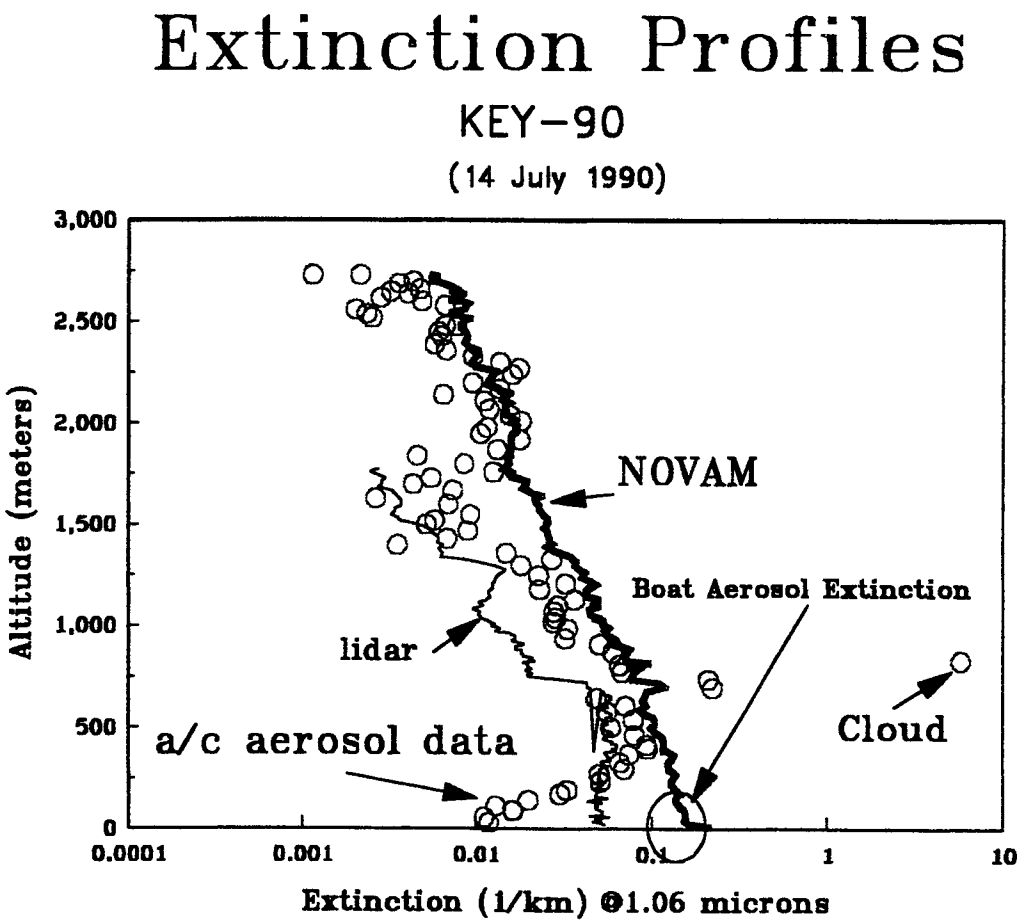


**Figure 4:** A composite plot of various types of extinction data taken during KEY-90 on 14 July 1990 for a wavelength of 1.06 micrometers. The small circles are the data calculated from the aircraft aerosol size distribution measurements. The large circle at the surface is the extinction calculation from an hour average of the boat aerosol size distribution measurement. The thin line is the NRL LIDAR extinction estimate at approximately the same time and place. Finally, the thick line is the NOVAM estimate of extinction at 1.06 microns for the particular set of surface and radiosonde data available at the site. Note that the aircraft inadvertently entered a cloud in the process of making its profile and a few large extinction values are noted in the data.

## 7. SMALL BACKGROUND AEROSOL OF LAND ORIGIN

In addition to those aerosol formed over the open ocean other types of aerosol have been found . Additional sources of aerosol are produced near the littoral zone and can have a significant effect on the propagation of EO energy. Local land based aerosol generation sources are factories and other man made sources. These aerosols tend to be smaller sized and thus have longer residence time in the atmosphere than large marine aerosol. They are eventually mixed into general background aerosol as they are advected out to sea. Close to the sources, however, they exhibit plume like structures as they drift down wind.

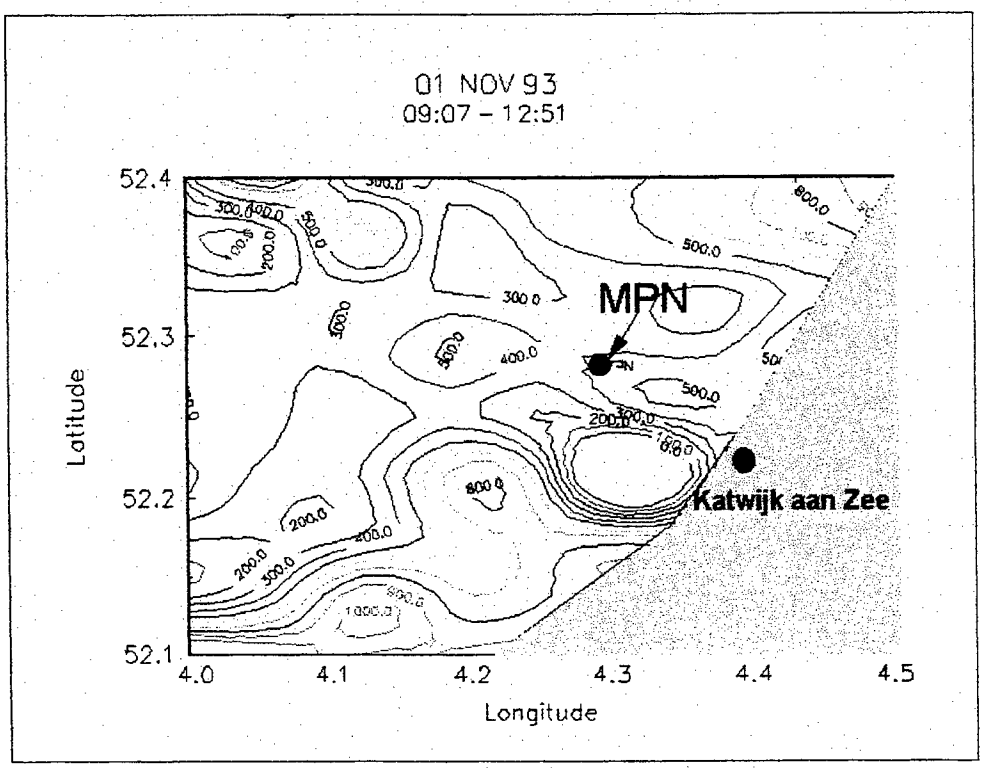


**Figure 5:** A contour map from the MAPTIP experiment on 1 November 1993 when the meteorological measurements of the region indicated that there were indeed local winds bringing coastal aerosols from the shore into the littoral region. On that day the wind direction was from about 100 degrees. The land in the figure is the Dutch coast.

Most of the small background aerosol are not produced by wind/wave interaction but are either produced in-situ in the marine atmosphere with an in situ genesis process or transported many miles from their generation sites by advection. The in situ genesis process refers to the many physical and chemical processes describing the life cycles of the small non sea salt aerosol in the marine atmosphere see Fitzgerald et.al.[2,3]. These sources are relatively uniform in extent and are the main type of background aerosol found over the open ocean. A second class of aerosols are those being advected downwind from land areas. In these cases, it seems that especially large clouds of various kinds of aerosol can be found in the littoral zones near industrial areas. The structure of these aerosol clouds may be striking near land but they eventually lose their identity as these air masses are advected to sea. An example[14] of this was shown in figures 5 and 6 .

These contour maps were from the Marine Aerosol Properties and Thermal Imager Performance, MAPTIP[15], experiment off of the Dutch coast. A small aircraft flying at a constant altitude (below 150 meters) in a star shaped flight pattern did the mapping shown in these figures. The MAPTIP experiment had as one of its key observation points an offshore research platform labeled MPN on these figures. MPN is located about 9 km from shore. During the aircraft flights, the concentration of aerosol was measured by an aerosol size spectrometer and the data is presented here as a set of contour maps. Two opposite conditions are presented to illustrate the differences in an "on shore wind," figure 6, and an "off shore wind," figure 5. These experiments show clearly that the aerosol in the littoral zone can be dominated by land and/or surf produced aerosol when the wind comes from the shore.

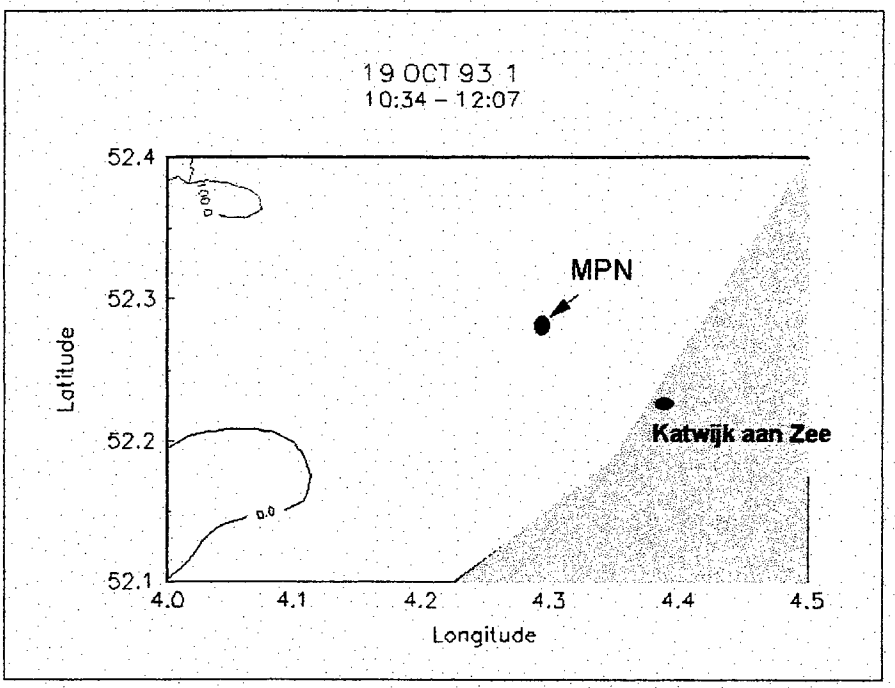


**Figure 6:** An aerosol concentration map made 19 Oct.1993 when the wind was toward the shore. The small isolated pockets of aerosol seen here may or may not be from ships traversing the region but it is felt that they could also be from noise sources either in the data itself or from the interpolation needed in the contouring of the irregular data.

## 8. SURF PRODUCED AEROSOL

There is also in the coastal zone a component of large sea salt aerosol which has been observed to have been transported tens of kilometers out to sea under certain meteorological conditions. These aerosol are large and associated with the breaking of surf on the beach area. Observations from the recent Electro Optical Propagation Assessment in a Coastal Environment, EOPACE[16], experiments have shown the occurrence and importance of this source of aerosol in the littoral zone.

Special visual and LIDAR observations have shown for the first time the structured format that plumes of aerosol make as they are produced by lines of breaking surf and transported aloft by thermal and turbulent processes. Quantification and prediction of these aerosol was first shown in a paper by Gathman and Smith[17] who predicted the extinction of the aerosol produced by breaking surf by using existing forecasts of oceanic swell off shore of San Diego. Swell is different than wind driven waves in that breaking swell can produce aerosol with no local wind. This is because they are produced by distant storms at sea which may not affect the weather at a particular spot on shore but the swells never the less eventually may propagate to the coastline. Thus the source strength of these surf driven aerosol is not a function of the local wind. On the other hand, the advection of these aerosol by the local wind is of high importance in determining how and where they are transported into the littoral zone. It is in this region where, under certain meteorological situations, they can greatly effect the propagation of IR energy.

The experimental setup used was an instrumented boat positioned just outside of the breaking surf and turned headed into the wind for its measurement of the aerosol content of the marine atmosphere prior to the addition of the surf aerosol. On shore, a similar aerosol spectrometer was positioned to measure the same air sample after the addition of the surf aerosol. Thus, if the instruments are calibrated, the difference between them would be the aerosol produced by the surf and brought to the downwind instrument. The same situation holds for the offshore breeze. At this time the boat instrument would be able to measure the total aerosol (background plus surf generated) whereas the beach instrument would measure only the background component. The effect of the on and offshore breeze on the surf component of the aerosol is strong, often overriding the general wind flow of the area. The usual time for the offshore wind is during the evening and night hours as the land cools

and the coastal aerosol is blown back out to sea. On the other hand, during the day there is usually an onshore breeze when the land heats up bringing air in from the ocean. This causes the surf aerosol to be blown over the shore and land.

Figure 7 shows some average aerosol spectrums obtained by the two spectrometers used in this study. The top picture shows the calibration comparison results when both of the instruments were located together on the cliff overlooking the Pacific Ocean at the Navy laboratory at Point Loma, California. The instruments are distinguished by the style of the marks used. The plus sign "+" indicates the shore instrument and the "X" indicates boat instrument data. It is seen that the two instruments agree reasonably well when in the comparison mode. When, however, the instruments are located on the boat

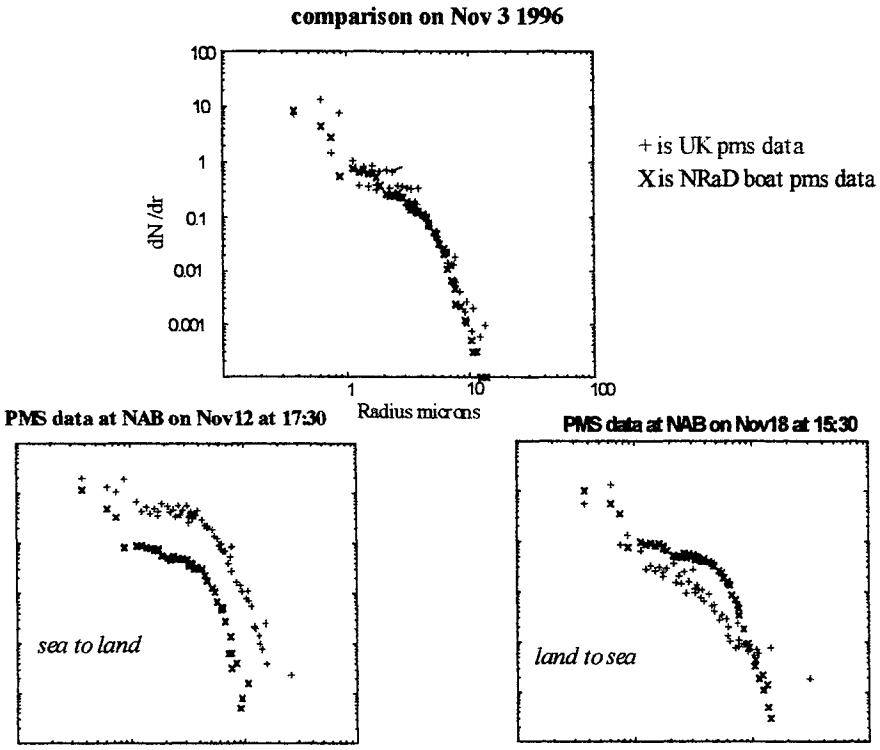


**Figure 7:** Simultaneous aerosol size distribution measurements from the boat and the beach under various conditions. The top figure shows the comparison between the two instruments prior to the experiment the two instruments prior to the experiment.

and the beach during the condition of an onshore breeze, it is seen that the land measurements are an order of magnitude higher than are the boat measurements. On the other hand, during the few episodes in which after dark measurements were made and in which an offshore breeze was in operation, the situation looked like that shown in the lower right hand side of the figure.

It appears that there is some discrepancy between the two spectra in the lower right hand plot. Here the data from the boat appears to be less than from the land measurement at the very largest sizes. This happens even though the boat is measuring both the background aerosol plus the surf aerosol. It is possible that the airflow about the boat and box tended to discriminate against the largest aerosol, and this instrumental factor would account for the crossing of these lines at the far end of the spectrum.

There is, however, enough aerosol to in all of these measurements to actually difference the data so that we can determine what the spectra of aerosol looks like when it is produced by the surf.

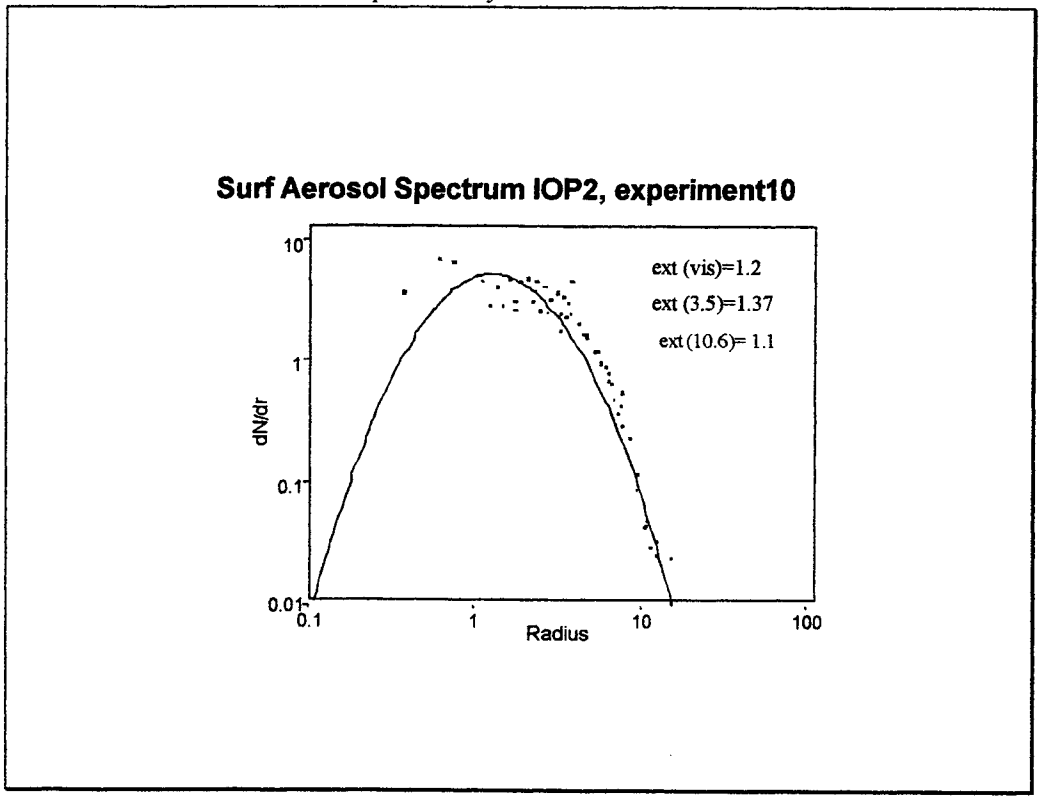


**Figure 8** A plot of the difference between the aerosol size spectrum on a log log scale. The individual points seem to follow the shape of the well known lognormal curve. The best fit lognormal is shown here as a solid line and is represented by only three parameters. Mie theory was used to determine the extinction at three useful wavelengths from these surf produced aerosol and the results are printed on the curve.

The important feature here is the difference between the background aerosol and the aerosol concentration after the surf aerosol is added. A sample of this difference is plotted in figure 8 for one of the EOPACE experiments. Fortunately, this difference (represented by the points in the figure) appears to be able to be adequately represented by a lognormal type of function. This function has three parameters which each can be expressed by functions containing information concerning the exact shape of the lognormal. The previous series of navy aerosol models successfully used this form of function to express the variation in shapes of the individual components of the size distribution. Each of the parameters has a graphical significance which simplifies their use. For instance in the following equation, "A" represents the amplitude or maximum value that the function has "$r_0$" represents the radius at the graphical peak of the plot. The third parameter, "C," is related to the sharpness of the curve. Since the surf generated aerosol is hygroscopic, the growth or swelling factor is represented by the function "f" which is a function of the relative humidity. This allows the description of the surf aerosol size distribution to be represented by the well known lognormal function as:

$$\frac{dN}{dr} = A \cdot \exp(-C \cdot (Log(r/(r_0 \cdot f))^2) \qquad (7)$$

Gathman and Smith then calculated the extinction based on the Mie theory integration of the dN/dr function above and found that the extinction was an increasing function of the predicted swell height. The extinction values expressed in (1/km) are shown in the figure.

## 9. CONCLUSIONS

This paper describes the marine aerosol both over the open ocean and over the littoral zones of the world's ocean. The open ocean aerosol has been presented as a model which describes the aerosol at deck level together with a set of equations for the determination of extinction and absorption of energy from these aerosol. Extensions to the deck level model both upward to altitudes above the marine boundary layer and downward to the tops of the waves are illustrated. In addition, other sources of energy in the coast regions due to advection of land formed aerosol and surf produced aerosol are discussed. Concentrations of marine aerosol are variable, and therefore accurate calculations of the propagation of EO energy along paths in the oceanic environment needs to include the effects of these aerosol.

## ACKNOWLEDGMENTS

The work presented in this paper has been supported over the years by the U.S Navy's Office of Naval Research for which the author is beholden. The author would also like to express thankfulness to Dr. J.H. Richter and Dr. D.R. Jensen of Spawar Systems Center- San Diego without whom most of the work described in the paper could not have been accomplished.

## REFERENCES

1) J.M. Prospero, "Saharan Dust Transport over the North Atlantic Ocean and Mediterranean", chapter in *The Impact of Desert Dust from Northern Africa Across the Mediterranean*, S. Guerzoni and R. Chester eds. Kluwer Academic Publishers, 1995.
2) J.W. Fitzgerald, W.A. Hoppel, and F. Gelbard, "A one-dimensional sectional model to simulate multicomponent aerosol dynamics in the marine boundary layer I. Model description," *J. Geophys. Res.* D, **103**, pp. 16085-16102, 1998.
3) J.W. Fitzgerald, J.J. Marti, W.A. Hoppel, G.M. Frick and F. Gelbard, "A one-dimensional sectional model to simulate multicomponent aerosol dynamics in the marine boundary layer, II. Model application," *J. Geophys. Res.* D, **103**, pp. 16103-16177, 1998.
4) D.C. Blanchard, "The Electrification of the atmosphere by particles from bubbles in the sea", in *Progress in Oceanography Vol 1*, M. Sears, editor, A Pergamon Press Book, The MacMillan Co., NY. pp. 71-202, 1963.
5) Monahan, E.C., D.E. Spiel and K.L. Davidson, "A Model of marine aerosol generation via whitecaps and wave disruption", in *Oceanic Whitecaps*, E.C. Monahan and G. MacNiocoill, editors, D. Reidel Publishing Co., Dordrecht, p 167, 1983.
6) S. G. Gathman, "Optical properties of the marine aerosol as predicted by the Navy aerosol model", *Optical Engineering*, vol. **22**, #1, p 057, 1983.
7) S.G. Gathman and A.M.J. van Eijk, "A Preview of the Advanced Navy Aerosol Model," *Proceedings of the 1997 Battlespace Atmospheric Conference, December 1997*, Eds. K.D. Anderson and J.H Richter, Space and Naval Warfare Systems Center, San Diego, Technical Document 2989, 1997.
8) J.V. Dave, "Subroutines for computing the parameters of the electromagnetic radiation scattered by a sphere", IBM report # 320-3237, 1968.
9) G. Hänel, "The properties of atmospheric aerosol particles as functions of the relative humidity at thermodynamic equilibrium with the surrounding moist air", in *Advances in Geophysics*, 19, 73-188 Edited by H, E, Landsberg and J. Van Mieghem, Academic Press, New York. ., (1976)
10) S.G. Gathman, "A Time-Dependent Ocean Aerosol Profile Model", *NRL Report # 8536*, Naval Research Laboratory, Washington D.C., 20375, 1982.
11) S.G. Gathman, "A preliminary Description of NOVAM, the Navy Oceanic Vertical Aerosol Model", *NRL report 9200*, Naval Research Laboratory, Washington D.C. 20375, 1989.
12) S.G. Gathman, and K.L. Davidson, "The Navy Oceanic Vertical Aerosol Model", *Technical Report #1634*, NCCOSC RDT&E DIV, San Diego, CA 92152-5001, 1993.
13) S.G. Gathman, D.R. Jensen, W.P. Hooper, J.E. James, H.E. Gerber, K. Davidson, M. H. Smith, I.E. Consterdine, G. de Leeuw, G.J. Kunz and M.M. Moorman (1993)"NOVAM evaluation utilizing electro-optics and meteorological data from KEY-90", *Technical Report #1608*, NCCOSC, RDT&E div. San Diego, CA 92152-5000.
14) S.G. Gathman and D.R. Jensen, "Aerosol characteristics in a coastal region (results from MAPTIP)", *Atmospheric Propagation and Remote Sensing IV*, J.C. Dainty editor, SPIE vol. 2471, 1995

15) D.R. Jensen, G. de Leeuw, and A.M.J. van Eijk, "Work Plan for the Marine Aerosol Properties and Thermal Imager Performance Trial (MAPTIP)", *Technical Report #2573*, NCCOSC, RDT&E div. San Diego, CA 92152-5000, 1993.
16) D.R. Jensen, C.R. Zeisse, K. M. Littfin, S.G. Gathman, "EOPACE (Electrooptical Propagation Assessment in Coastal Environments) Overview and Initial Accomplishments", *Propagation and Imaging through the Atmosphere*, L.R. Bissonnette and C. Dainty editors, SPIE vol. 3125, p98. 1997.
17) S.G. Gathman and M. H. Smith, "On the nature of surf generated aerosol and their effect on electro-optical systems", *Propagation and Imaging through the Atmosphere*, L.R. Bissonnette and C. Dainty editors, SPIE vol. 3125, p98. 1997.

Correspondence: Email: sgathman@msn.com, FAX (418) 730 4908

**Invited Paper**

# Adapting atmospheric LIDAR techniques to imaging biological tissue

J. Fred Holmes[1]*[a], Steven L. Jacques[o], John M. Hunt[a]

[a]Oregon Graduate Institute of Science & Technology, 20000 NW Walker Road, Beaverton, OR, 97006

[o]Oregon Medical Laser Center, 9205 SW Barnes Road, Portland, OR, 97225

## ABSTRACT

Optical radar (LIDAR) is being used to remotely probe the atmosphere. Quantities that can be sensed on a path resolved basis include temperature, pressure, number density for specific molecules and atmospheric winds. We believe that the techniques used can be scaled down and used to analyze tissues in medical optics applications. As our first project using atmospheric optics technique, we are building a Heterodyne, Optical, Coherent tomography (HOCT) system for imaging tissue. This system will be described.

Key words: tissue; imaging; coherent; heterodyne.

## 1.INTRODUCTION

Optical radar (LIDAR) is being used to remotely probe the atmosphere[1]. Quantities that can be sensed on a path resolved basis include temperature, pressure, number densities for specific molecules (using differential absorption LIDAR [DIAL]), and atmospheric winds. The techniques used make these measurements at long range. However, we believe that they can be scaled down and used to analyze tissue structures and perhaps to measure temperature, pressure, chemical presence and fluid flow in medical optics applications. Most atmospheric LIDARS are mono-static (transmitter and receiver optical axis are the same) and pulsed, which yields range resolved (10's of meters) results using "time of flight" to separate the signals from different ranges. This will not work for medical optics applications because of the need for range resolution of 10's of microns.

However, by using a bistatic (transmitter and receiver optical axes are not the same) coherent LIDAR operating continuous wave (CW) with heterodyne detection[2-7], the range resolution can be made small enough to meet the requirement of medical optics through the geometry of the system and the need for the back propagated local oscillator (LO) to match the transmitted optical beam wave front. This will happen where the two optical axes cross, as illustrated in figure 1. Although signal will enter the receiver from scattering along a good portion of the transmitted beam path, only scattering in the vicinity of where the optical axes cross will coherently mix with the LO and provide an electrical signal. We have analytically determined the path resolution in the z direction (into the sample) and the x-y direction (parallel to the surface). Some results for the z direction are shown in figures 2 and 3. The parameters used in the calculation were: transmitted beam radius = 0.01m; local oscillation beam radius 0.01m; transmitted beam and local oscillator (back propagated) focused at 0.5m; 0.6328 micron wavelength; and a transmitter receiver separation of 0.12m. The results are encouraging in that the z-axis resolution (full width, half maximum) is about 60 microns and no effort has been made to optimize the solution. The x-y resolution is determined by the focused spot radius, which is 10 microns. The sensitivity falls off very rapidly in the z direction as can be seen in figure 3, which plots log base 10 of the relative, received signal.

[1] *Correspondence: email: jfred@ece.ogi.edu; Telephone: 503-748-1132; Fax: 503-748-1406



In *Laser-Tissue Interaction XI: Photochemical, Photothermal, and Photomechanical*, Donald D. Duncan, Jeffrey O. Hollinger, Steven L. Jacques, Editors, Proceedings of SPIE Vol. 3914 (2000)
1605-7422/00/$15.00

## 2. PROJECT

As our first project using atmospheric optics techniques for medical applications, we are building a Heterodyne Optical Coherent Tomography (HOCT) system to image tissue. Its purposes would be similar to OCT but the way it works is quite different and may have some advantages. The OCT uses a highly incoherent source with a short coherence length and coherent detection to achieve range resolution. The HOCT uses a highly coherent source and a combination of geometry and coherent detection to achieve range resolution. The OCT uses homodyne detection. However, the HOCT uses heterodyne detection and this may have several advantages.

The heterodyne signal is a sinusoid (100 KHz) plus additive noise. The sinusoid amplitude and phase, track the optical signal amplitude and phase[8-10]. The maximum likelihood estimator for a sinusoid plus noise is the discrete Fourier transform which we will implement using the Fast Fourier Transform (FFT)[11]. This will directly yield not only the optical signal amplitude but also the phase, which carries additional information about the tissue. Because of the sensitivity of the processing (can operate with negative signal to noise ratios) and the fact that with heterodyne detection the phases of the optical signal and LO do not need to be matched, the HOCT system may be able to probe deeper into the tissue than the OCT.

A tentative design that is in the process of being built and tested is described in the next section. As mentioned earlier, the design has not been optimized from a resolution standpoint and that needs to be done. Once the system has been built it will be tested for resolution on known targets and then on tissue samples working in collaboration with the Department of Dermatology at Oregon Health Sciences University (OHSU).

## 3. EXPERIMENTAL SYSTEM

The experimental system is shown in figure 1. The source is a vertically polarized laser and as shown, will start with a HeNe gas laser. The output of the laser is split into two parts by a beam splitter. One part is transmitted and the other is used as an optical local oscillator. The transmitted beam is directed through an optical isolator that helps prevent reflections in the transmitter from contaminating the local oscillator. The beam is then passed through an accusto-optic modulator (AOM), which shifts the optical frequency by 39.95MHz, and then through a wave plate holder. We can use a quarter wave plate for circular polarization, no plate for vertical polarization and a half wave plate for horizontal polarization. Since we are using coherent detection, the LO has to be polarized the same as the transmitter. The transmitter beam is then 10x beam expanded and focused on the region to be probed.

The LO beam that was split off is passed through an AOM where the optical frequency is shifted by 40.05MHz. The AOM in the LO path provides isolation[12] between the transmitter and LO and allows us to operate with a heterodyne frequency of 100kHz (difference of transmitter and LO frequencies). The LO Beam is then directed through a wave plate to match the polarization of the transmitted beam. We can also use these wave plates to measure depolarization caused by the target materials. A 10x beam expander is used to match the LO beam size to the transmitted beam.

The signal scattered from the sample is added to the LO using a beam splitter and then both are focused onto a detector. The electrical signal from the detector is amplified, filtered, digitalized and processed using the FFT to obtain the amplitude and phase of the signal scattered from the tissue.

## REFERENCES


1. A. Amsmann, R. Neuber, P.Rairoux and U. Wandinger (eds.), "Advances in Atmospheric Remote Sensing with Lidar", (Selected papers of the 18th International Laser Radar Conference, Berlin, 22-26 July 1996), Springer, 1996.

2. J. Fred Holmes and Badih J. Rask, "Range Resolved, 3-D Optical Remote Sensing of Atmospheric Winds Using a CW Lidar", in Advances in Amospheric Remote Sensing with Lidar, A. Amsmann, R. Neuber, P. Rairoux and U. Wandinger (eds.), Springer-Verlag, Berlin, 1997.

3. J. Fred Holmes and Chunyan Zhou, "Path Resolved, Optical Remote Sensing of the Strength of Turbulence Using a Psuedo Random Code Modulated CW Lidar and Coherent Optical Processing", 9th Conference on Coherent Laser Radar, June 23-27, 1997, Linkoping, Sweden.

4. J. Fred Holmes and B. John Rask, "Path resolved Doppler Wind Measurement System Using a Coherent, CW Pseudo Random Code Modulated, $C0_2$ Laser," Coherent Laser Radar Topical Meeting, July 23-27, 1995, Keytsone, Colorado.

5. (Invited) J. Fred Holmes and Badih J. Rask, "Coherent, CW, pseudo random code modulated lidar for path resolved optical remote sensing," SPIE meeting on Atmospheric Propagation and Remote Sensing III, April 5-8,1994, Orlando, Florida.

6. Farzin Amzajerdian and J. Fred Holmes, "Time Delayed Statistics and Signal to Noise Ratio Reduction Factor for a Bistatic Coherent Lidar Operating in Atmospheric Turbulence," Applied Optics, **30**, 20, July 1991.

7. J. Fred Holmes, "Enhancement of Backscattered Intensity for a Bistatic LIDAR Operating in Atmospheric Turbulence," ICO Topical Meeting on Atmospheric, Volume, and Surface Scattering and Propagation, August 27-30, 1991, Florence, Italy.

8. J. Fred Holmes, John S. Peacock and Douglas C. Draper, "Optical remote sensing of surface roughness through the turbulent atmosphere," Applied Optics, **33**, 20, November 1994.

9. Douglas C. Draper, J. Fred Holmes, and John Peacock, "An Unwrapped Phase Distribution Model for Speckle/Turbulence, "Applied Optics, **31**, 20, June 1992.

10. Douglas Draper, J. Fred Holmes, John S. Peacock and John M. Hunt, "Techniques for Measuring Optical Phase Beyond Principal Values in the Atmosphere," Proceedings of the Conference on Lasers and Electrooptics, April 24-28, 1989, Baltimore Maryland.

11. D.C. Rife and R.R. Boorstyn, "Single Tone Parameter Estimation From Discrete-Time Observations," IEEE Trans. Inform. Theory, IT-20, **No. 5** (September 1974), pp.591-598.

12. J. Fred Holmes, Farzin Amzajerdian, and John M. Hunt, "Improved Optical Local Oscillator Isolation Using Multiple Acoustooptic Modulators and Frequency Diversity," Optics Letters, 12, **No.8** page 637, August 1987.

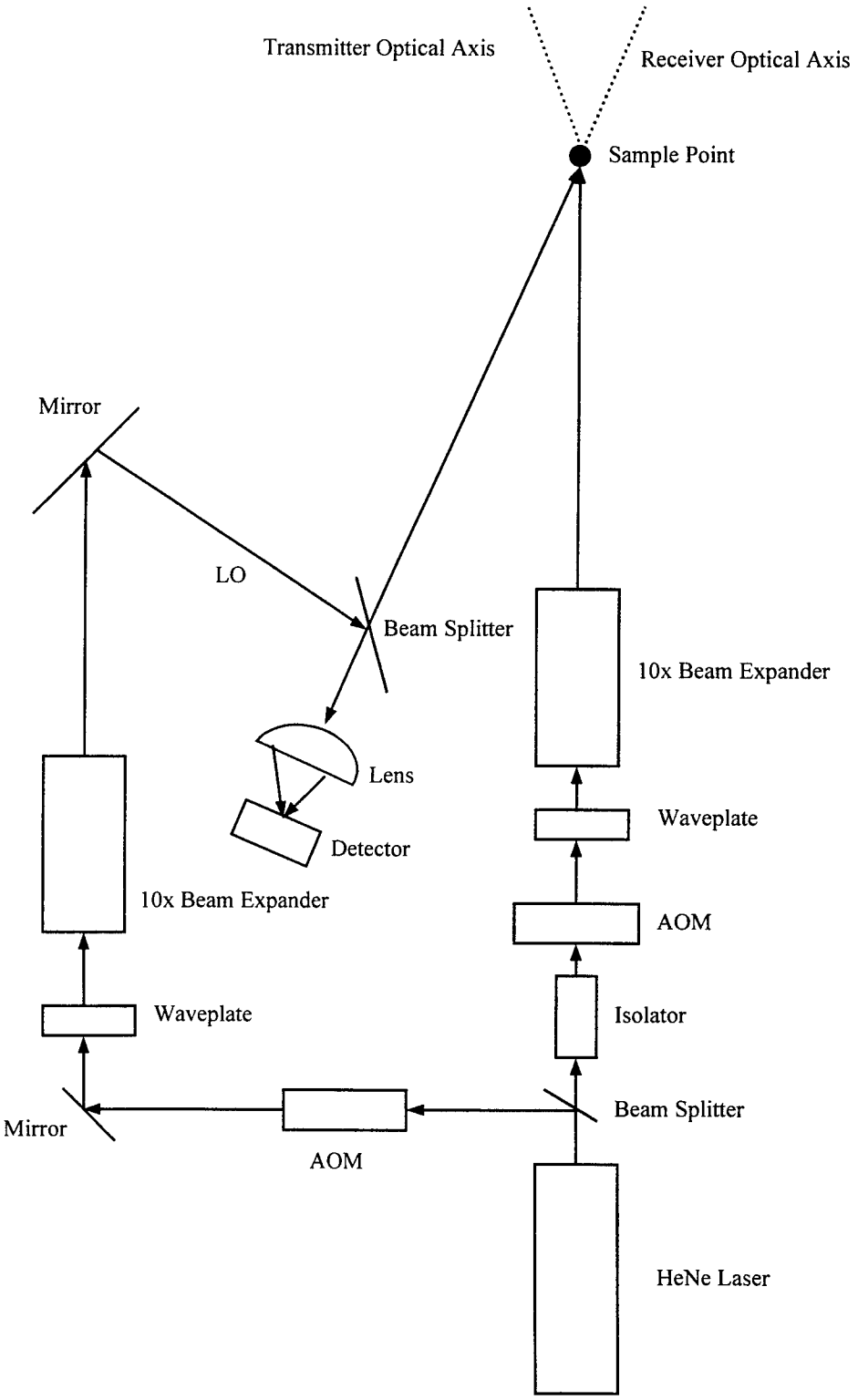


Figure 1. - Heterodyne Coherent Optical Tomography System

Figure 2

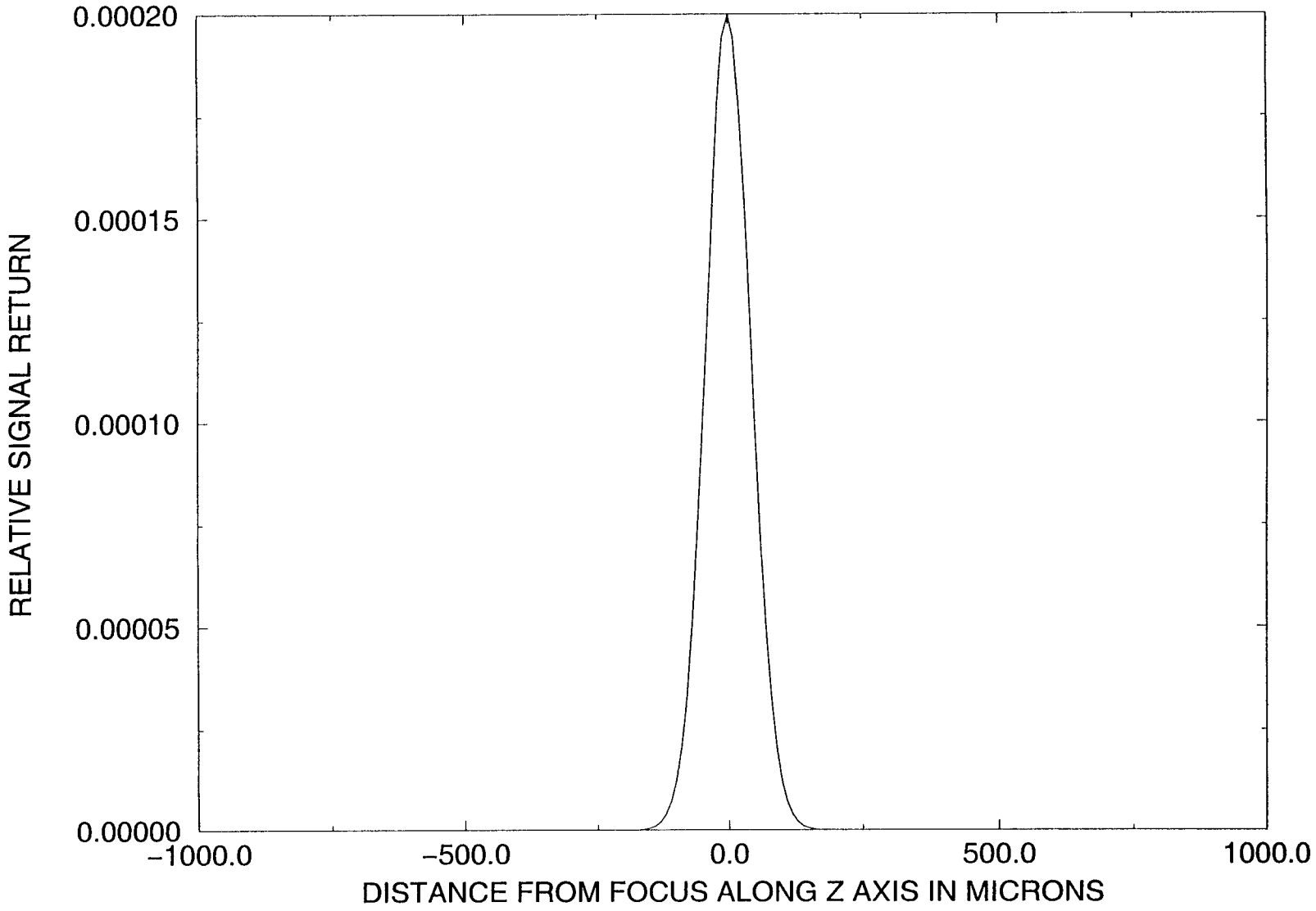
0.00020
0.00015
0.00010
0.00005
0.00000
RELATIVE SIGNAL RETURN
-1000.0
-500.0
0.0
500.0
1000.0
DISTANCE FROM FOCUS ALONG Z AXIS IN MICRONS

Figure 3

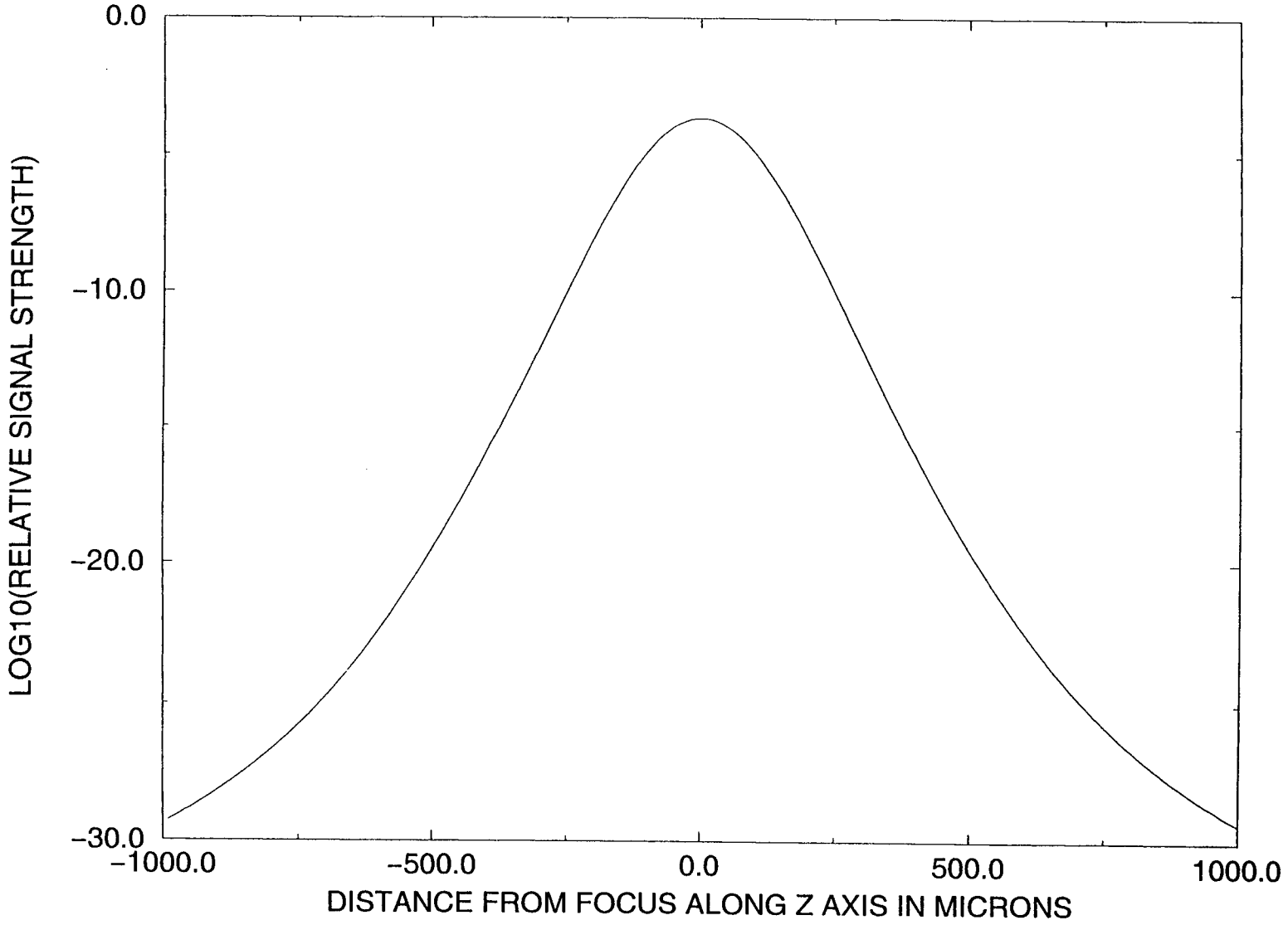
0.0
-10.0
-20.0
-30.0
LOG10(RELATIVE SIGNAL STRENGTH)
-1000.0
-500.0
0.0
500.0
1000.0
DISTANCE FROM FOCUS ALONG Z AXIS IN MICRONS

# Vertical profiles of aerosol and optical turbulence strength and their effects on atmospheric propagation.*

N.S.Kopeika and A.Zilberman

Dept. Electrical and Computer Engineering,

Ben-Gurion Univ. of the Negev,

POB 653, Beer-Sheva 84105, Israel

## ABSTRACT

On a basis of a multiple-forward-scatter propagation model the atmospheric aerosol contributions to laser beam widening for a horizontal propagation path is estimated and compared with beam widening caused by turbulence. It is shown that the beam widening caused by atmospheric aerosols is significant, often even more significant than that caused by turbulence.

**Keywords**: laser beam propagation, atmospheric aerosol, turbulence, multiple scattering, beam widening.

## 1. INTRODUCTION

As a laser beam propagates through the atmosphere, it is affected by atmospheric turbulence and aerosol particles.
The turbulence of the atmosphere modifies the laser light passing through it in various ways. The laser beam spot at the target can wander, increase in diameter (beam widening), and acquire substantial amplitude and phase modulation (scintillation). Simultaneously, atmospheric aerosols result in laser beam extinction and additional widening. As a result, the power density arriving at the target plane is reduced.
It is interesting to compare the contributions of scattering by aerosol particles and turbulence in beam widening. This is an important part of system analysis, which is necessary to take into account in laser system design.
For this, we used aerosol and turbulence strength model profiles presented in the literature and calculated laser beam widening for horizontal propagation at different elevations from 2 to 20 km. A laser wavelength of 532 nm is assumed. In general, the shorter the wavelength, the more destructive the effects of a high intensity laser beam. This can be important in laser weaponry.

## 2. AEROSOL DISTRIBUTION AND TURBULENCE PROFILES

Aerosols in the planetary boundary layer (up to 2-3 km) generally have a bimodal size distribution in the size range of optically effective particle radii, i.e., the accumulation particle mode is at around 0.05-0.2 μm in radius and the large particle mode around 1.5-3 μm for volume size distribution. Maximal values of the individual modes change corresponding to different seasons or different atmospheric conditions. The boundary layer aerosols have high total particle concentration due to optical depth $\tau$ = 0.7-3 for 10 km horizontal path. The tropospheric aerosols above the boundary layer are assumed to have the same composition but the size distribution is modified by eliminating the large particle component. The optical depth due to them is 0.1-0.4 for 10 km horizontal path. In the stratospheric region from 10 to 30 km, measurements have shown a background aerosol that has a rather uniform global distribution. For particles a few tenths of a micron in size, one finds a significant maximum in concentration in the altitude range from about 18 to 20 km. This aerosol layer seems to be worldwide. The stratospheric aerosol concentration is very strongly influenced by particles from volcanic eruptions and meteoric dust. When passing from background to volcanic or polar stratospheric clouds conditions, the effective radius undergoes a change from approximately 0.15 to 0.6 μm. Simultaneously, the variable stratospheric aerosol layers can be observed. Such behavior is in good agreement with a large set of observation made by several groups[1,2,3]. Based on

*Also published in *Proc. of SPIE* Vol. 3927



In *Laser-Tissue Interaction XI: Photochemical, Photothermal, and Photomechanical*, Donald D. Duncan, Jeffrey O. Hollinger, Steven L. Jacques, Editors, Proceedings of SPIE Vol. 3914 (2000)
1605-7422/00/$15.00

observations of stratospheric aerosol behavior, different aerosol size distribution models have been employed to fit the observed size distribution[4]: gamma, log normal, power law. The most commonly used of these is the log normal distribution because it reproduces well the bell-shaped dispersion of observed aerosol distributions and clearly predicts particles both larger and smaller that are actually found in the air:

$$N(r) = \frac{dN}{dr} = \frac{N_0}{r\sqrt{2\pi}\ln\sigma}\exp\left[-\frac{\ln^2(r/r_0)}{2\ln^2(\sigma)}\right], \tag{1}$$

where $N_0$ is the total number of particles per unit volume and $r_0$ and $\sigma$ are the distribution geometric radius and width, respectively. The background or "moderate" volcanic aerosol distribution at 18-20 km can be fitted well by this distribution with parameters[3] $N_0 = 20$ cm$^{-3}$, $r_0 = 0.09$ μm, and $\sigma = 1.8$. This aerosol size distribution is shown in Fig.1. It should be noted that the volcanic aerosol can have a second mode in the micrometer size range. Also, in Fig.1. is shown the tropospheric aerosol distribution at 5 km altitude[5]. Here $N_0 = 300$ cm$^{-3}$, $r_0 = 0.08$ μm, and $\sigma = 1.95$.

To describe the varying strength of optical turbulence as a function of altitude several turbulence profile models for both day and night conditions have been developed. The most widely used models are the Hufnagel-Valley (H-V) model and the SLC Day and Night models[6]. For calculations we will use the SLC Day model.

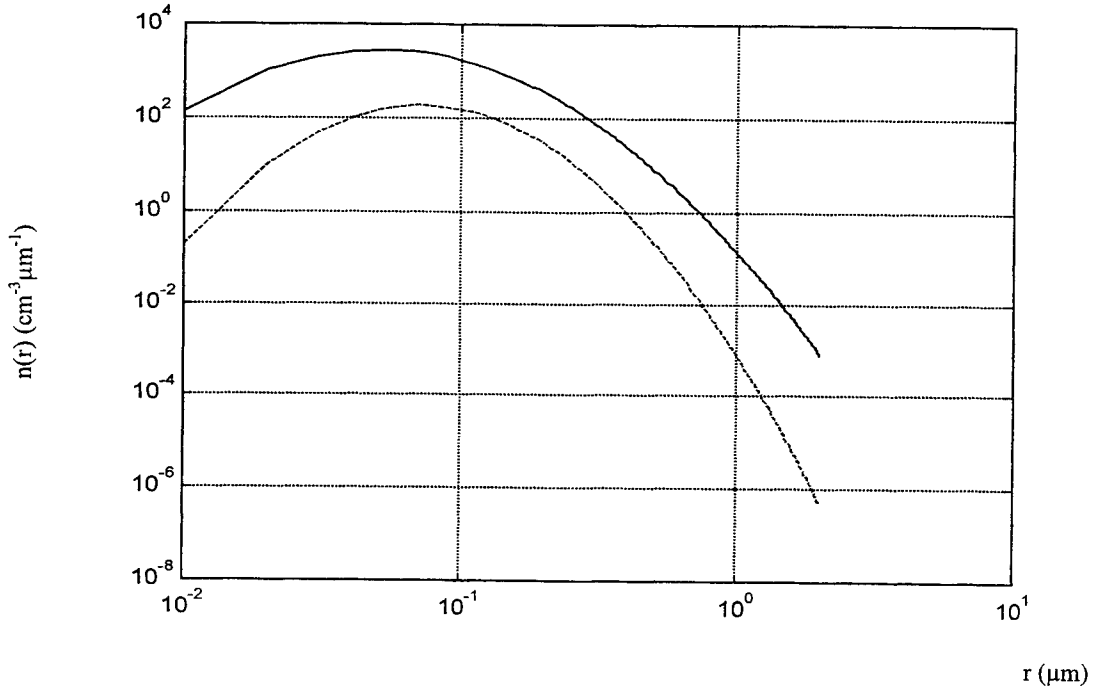


Fig.1. Typical stratospheric aerosol size distribution for moderate volcanic conditions at 20 km altitude (dotted curve). Tropospheric aerosol size distribution model at 5 km altitude (solid curve).

## 3. AEROSOL AND TURBULENCE BEAM WIDENING

The general characteristics of wave propagation through a particulate medium may be classified into the following three regions: first-order scattering, multiple scattering, and diffusion. The first-order scattering theory is applicable to the case in which the optical depth is much less than unity. We don't examine this case.

The calculations developed here do not take the diffusion into account but deal with multiple scattering only.

In multiple scattering processes the photons undergo many scattering events before reaching the target. A collimated laser beam, therefore, suffers spatial and angular widening in addition to attenuation.
Assuming that the laser beam radiance profile is represented by a Gaussian functional form the resulting beam spread is given by[7]

$$W(z) = \left(W_S^2(z) + W_d^2(z)\right)^{1/2}, \tag{2}$$

where $W_d$ is the beam spread due to diffraction effects and $W_s$ is the contribution to the beam width due to forward multiple scattering[8,9],

$$W_S^2 = \frac{z^2 \cdot \tau \cdot \theta_0^2}{3}, \tag{3}$$

where $z$ is the distance to target and $\tau$ is the optical depth.
Alternatively, the beam widening $W_s$ can be found from the beam spread angle[10] $\theta_S = \sqrt{2}/k\rho_0$, where $\rho_0 = \left(3/\alpha_s z k^2 \theta_0^2\right)^{1/2}$ is the spatial coherence length of the field, $k = 2\pi/\lambda$ is the wave number, and $\alpha_S$ is the effective scattering coefficient, $\alpha_S = \sigma_S \phi$, where $\sigma_s$ is the scattering coefficient of the medium and $\phi$ is the forward-scattering efficiency. Both methods yield similar results but the second method is not so as sensitive to particle size and may be used for aerosols of radius comparable to incident wavelength.
The parameter $\theta_0$ is the rms scatter angle associated with the scatter medium under the small angle scattering approximation, equal to

$$\theta_0^2 = 2\pi \int_0^\infty P(\theta)\theta^3 d\theta, \tag{4}$$

where $P(\theta)$ is the angular scattering phase function, that is, the intensity of radiation scattered in the direction given by the scattering angle $\theta$. Multiple scattering depends on both the scattering cross section as a function of range and the scattering phase function as a function of range.
The phase function can be approximated as a Gaussian function of scattering angle for forward-scattering events. This choice is convenient because, after a series of small-angle scatterings, the spatial (or angular) distribution of photons remains Gaussian. The phase function is specified by two parameters: a value at a scattering angle of zero, *P(0)*, and a mean-square angular width $\theta_0^2$. The parameters of the Gaussian approximation can be defined as

$$P(\theta) = \frac{1}{\pi\theta_0^2} \exp\left[-\frac{\theta^2}{\theta_0^2}\right], \tag{5}$$

with $\theta_0 = 1/\left[\pi P(0)\right]^{1/2}$, where *P(0)* is the phase function of the medium evaluated at
$\theta = 0$. It can be found from Mie theory assuming that the complex refractive index of the particles is 1.44-0.0*i* for all values of radii (stratospheric aerosol). Stratospheric aerosols are very probably essentially spherical and homogeneous due to their liquid nature (~75% solution of sulfuric acid), and, therefore, Mie scattering theory can be applied with some degree of confidence. The actual formulae for Mie scattering are well known[11,12].
The beam geometry parameter $W_d$ due to diffraction effects which causes the spot size radius of the beam to increase along the propagation path. A collimated Gaussian beam is assumed. Thus, the spot size on the target distance $z$ from the transmitter in free space is given by

$$W_d(z) = W_0\left(1 + \left(\frac{2z}{kW_0^2}\right)^2\right)^{1/2}, \tag{6}$$

where $W_0$ is the initial beam radius.

Wave front distortion in the optical wave induced by atmospheric turbulence results in a beam widening beyond that due to diffraction.
The effective beam spot size deriving from turbulence effects, under assumption of the Kolmogorov power law spectrum, is[6]

$$W_e(z) = W_d(z)\left[1 + 1.33\sigma_1^2\left(\frac{2z}{kW_d^2(z)}\right)^{5/6}\right]^{1/2}, \tag{7}$$

where $\sigma_1^2$ is the Rytov variance, which is $\sigma_1^2 = 1.23C_n^2 k^{7/6} z^{11/6}$.
Inner scale and outer scale effects on the effective beam spot size can also be taken into account in certain conditions using other spectrum models. Thus, for the stratosphere the von Karman spectrum can be used. The effective beam spot radius is[6]

$$W_e(z) = W_d(z)\left\{1 + 3.537\sigma_1^2\Lambda^{5/6}\left[\frac{(1+0.31\Lambda Q_m)^{5/6}}{(\Lambda Q_m)^{5/6}} - 0.359(\Lambda Q)^{1/6}\right]\right\}^{1/2}, \tag{8}$$

where $\Lambda = \frac{2z}{kW^2}$, $Q_m = \frac{zk_m^2}{k}$, $Q_0 = \frac{zk_0^2}{k}$, $k_m = 5.92/l_0$, $k_0 = 1/L_0$, where $l_0$ and $L_0$ are the turbulence inner and outer scales respectively.
The inner scale is on the order of centimeters or more in the troposphere and stratosphere. Depending on the spectrum model, inner scale effects may increase or decrease the spot size.
In Fig.2 is shown the calculated laser beam spot size versus horizontal distance in free space, with and without the individual turbulence and particle scattering contributions, at 20 km altitude.

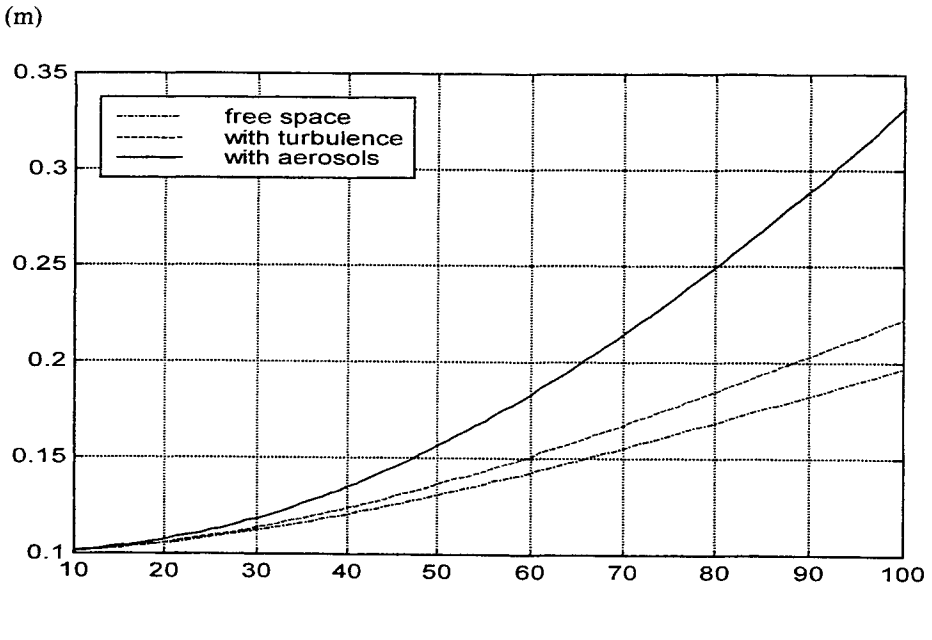


Fig.2. Laser beam spot size (m) as a function of horizontal distance at 20 km altitude. $C_n^2 = 1.41e-18\ \mathrm{m}^{-2/3}$ (Daytime SLC model), $\lambda =$ 532 nm. The initial beam radius $W_0 = 10$ cm.

The aerosol size distribution is assumed to be as in Fig.1 and laser wavelength is 532 nm. In Fig.3 is shown the beam spot size vs horizontal distance at 5 km altitude. The beamspread from turbulence is calculated from the von Karman spectrum (8). The beam spot size radius at zero range is $W_0 = 10$ cm.

From these Figs we see that propagating through atmospheric turbulence causes the laser beam to widen more than it would from diffraction. However, the beam widening by aerosols is significant, even more so than that caused by turbulence.

It should be noted that here we used the small angle approximation for beam radiance profile. The small-angle approximation is a reasonable assumption for strongly forward scattering, which occurs for the case of particles larger than the incident wavelength. For the background stratospheric conditions this assumption may not be valid. Although in ref[12], as an example of angle-dependent scattering by a sphere, a water droplet with radius of about 260 nm illuminated by light of wavelength 550 nm was chosen, the predominance of forward scattering even for rather small particles was emphasized. On the other hand, for small particles and long-path propagation with optical depth greater than about unity, the diffusion must be taken into account. This is to be included in future work.

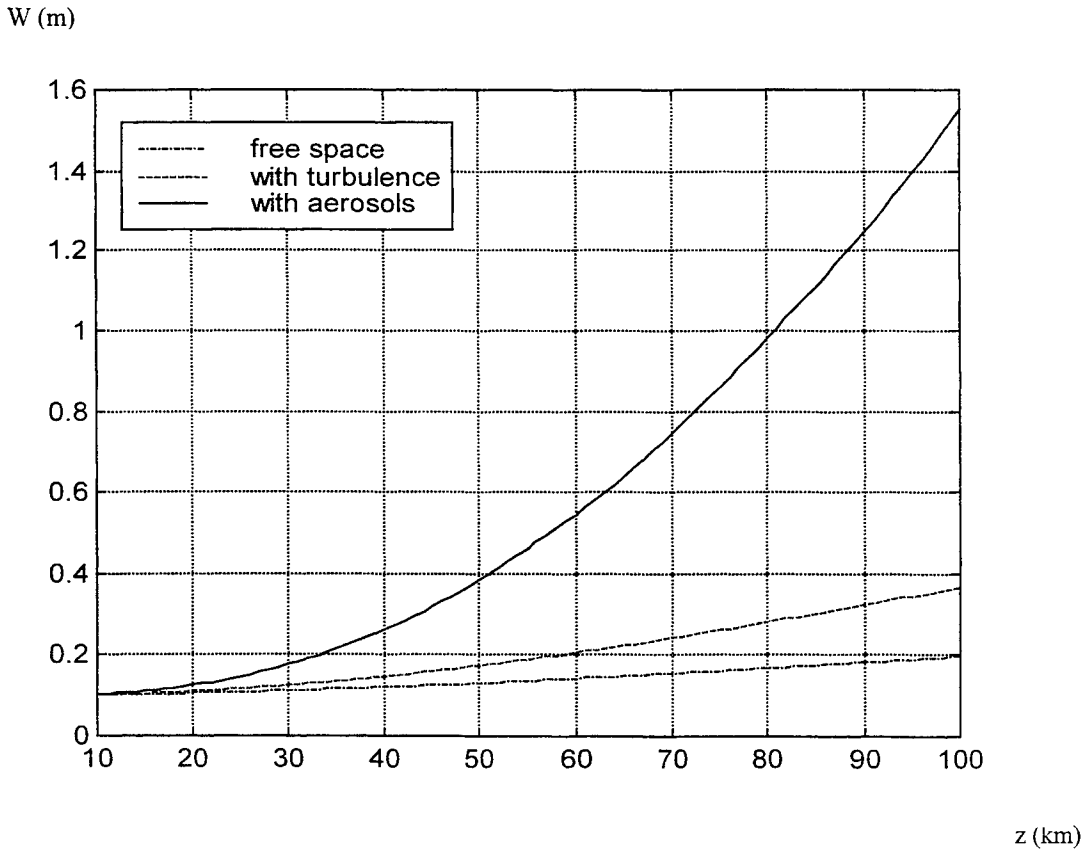


Fig.3. Laser beam spot size (m) as a function of horizontadistance at 5 km altitude. $C_n^2 = 7e-18$ $m^{-2/3}$ (Daytime SLC model), $\lambda =$ 532 nm The initial beam radius $W = 10$ cm.

To estimate the contribution of the turbulence and aerosols at the energy losses in the target, we can calculate the irradiance $I(z)\,(W/m^2)$ or path loss $(dB)$ in the target plane located at range $z$ from transmitter:

$$I(z) = \frac{P_t \exp(-\tau)}{\pi W^2(z)}, \tag{9}$$

where $P_t$ is the total output power of the laser, $\tau$ is the optical depth, and $W(z)$ is the radius of the laser beam in the target plane due to the direct unscattered beam (6) and the beamwidth broadened according to the turbulence (8) and aerosol (2) contributions.

In Figs 4 and 5 is shown the path loss as a function of the target plane distance in free space with an exponential path loss and with the individual turbulence and particle scattering contributions to beam broadening at 5 and 20 km elevation altitude. We see that the energy losses of the scattered beam by aerosols may be much more significant than that caused by turbulence.

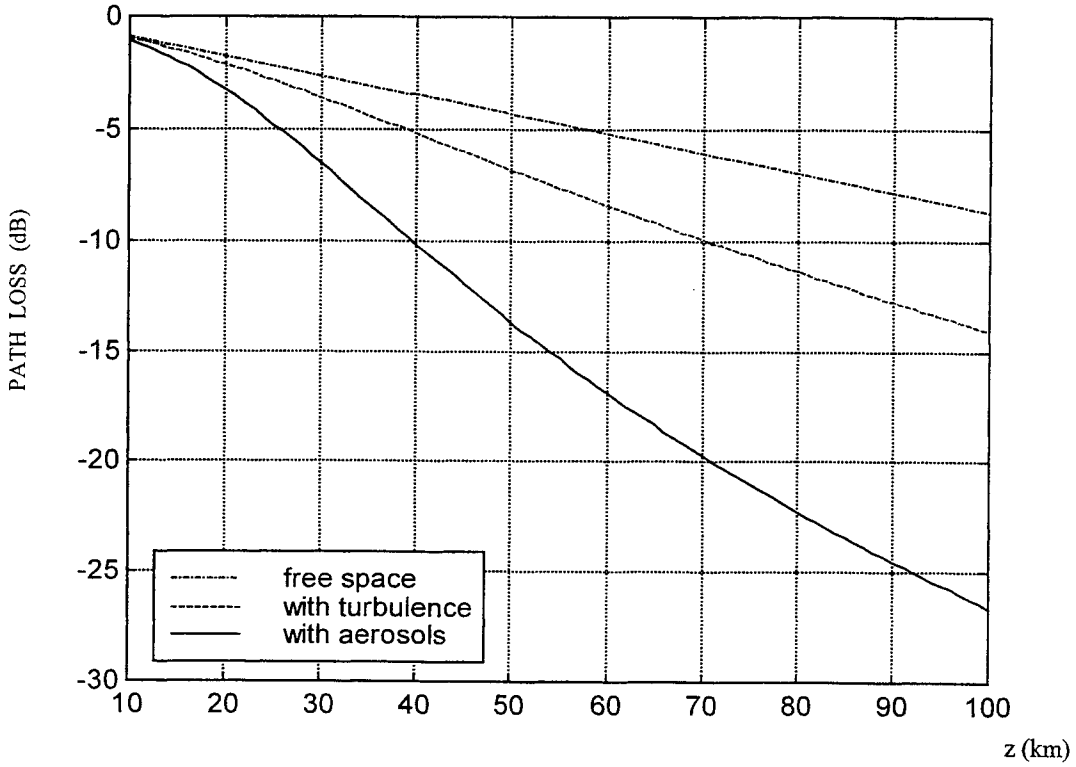


Fig. 4 Path loss vs horizontal distance to target at 5 km altitude.

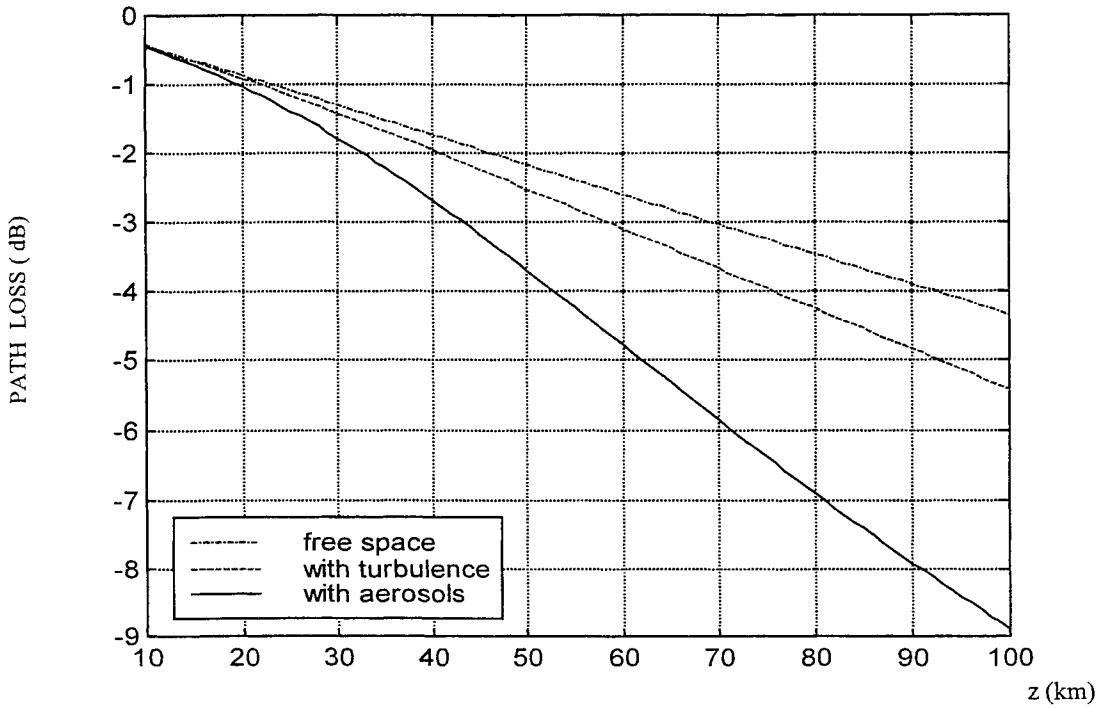


Fig. 5 Path loss vs horizontal distance to target at 20 km altitude.

## 4.CONCLUSIONS

Calculations for aerosol beam widening developed here cannot be valid in all cases because assumptions of strong multiple-forward-scattering and small angle approximation are not always true. This depends on the atmospheric conditions and aerosol loading. However, the results presented here for known typical aerosol loading show that aerosol contributions to laser beam widening may be significant, even more so than that of turbulence, and must be taken into account for laser system design. To estimate this contribution for different aerosol loadings another approach is needed.

In future work a Monte Carlo method for aerosol beam widening calculation is planned to be used. This should allow us to obtain results for other wavelengths and elevations where the small angle approximation may not be valid.

In addition, a three wavelength (1064, 532, 355 nm) lidar has been developed at BGU to measure for the first time vertical profiles of both aerosol loading and turbulence at the same location almost simultaneously. Such data will make the calculations here much more reliable.

## REFERENCES

1. U. Wandinger, A. Ansmann, J. Reichardt, and T. Deshler, "Determination of stratospheric aerosol microphysical properties from independent extinction and backscattering measurements with Raman lidar," App. Opt. 34, No. 36, pp. 8315-8329, 1995.
2. M. R. Gross, T. J. McGee, U. N. Singh, and P. Kimvilakani, "Measurements of stratospheric aerosols with a combined elastic-Raman-backscatter lidar," Appl. Opt. 34, No. 30, pp. 6915-6924, 1995.
3. R. G. Pinnick, J. M. Rosen, and D. J. Hofmann, "Stratospheric aerosol measurements. III. Optical model calculations," J. Atmos. Sci. 33, pp. 304-313, 1976.

4. P. B. Russell, T. J. Swissler, M. P. McCormick, W. P. Chu, J. M. Livingson, and T. J. Pepin, "Satellite and correlative measurements of the stratospheric aerosol. I. An optical model for data conversion," J. Atmos. Sci. 38, pp. 1279-1294, 1981.
5. G. A. d'Almeida, P. Koepke, and E. P. Shettle, *Atmospheric Aerosols: Global Climatology and Radiative Characteristics*, A. Deepak Publishing, 1991.
6. L. C. Andrews and R. L. Phillips, *Laser Beam Propagation through Random Media*, SPIE Optical Engineering Press, Bellingham, 1998.
7. A. Deepak, A. Zardecki, U. O. Farrukh, and M. A. Box, "Multiple scattering effects of laser beams traversing dense aerosols," in *Atmospheric Aerosols: Their Formation, Optical Properties, and Effects*, A Deepak ed., Spectrum Press, Hampton, 1982.
8. R. F. Lutomirski, "Atmospheric degradation of electrooptical system performance," Appl. Opt. 17, No. 24, pp. 3915-3921, 1978.
9. G. C. Mooradian, M. Geller, L. B. Stotts, D. H. Stephens, and R. A. Krautwald, "Blue-green pulsed propagation trough fog," Appl. Opt. 18, No. 4, pp. 429-441, 1979.
10. W. S. Ross, W. P. Jaeger, J. Nakai, T. T. Nguyen, and J. H. Shapiro, "Atmospheric optical propagation – an integrated approach," Opt. Eng. 21, No. 4, pp. 775-785, 1982.
11. H. C. van de Hulst, *Light Scattering by Small Particles*, 2nd edition, Dover, New York, 1981.
12. C. F. Bohren and D. R. Huffman, *Absorption and Scattering of Light by Small Particles*, New York, 1983.

# Mean Fade Time of an Optical Communication Channel Under Moderate-To-Strong Atmospheric Turbulence.*

M. A. Al-Habash
Department of Mathematics and
Florida Space Institute
University of Central Florida, Orlando, Florida 32826

L. C. Andrews
Department of Mathematics and
Center for Research and Education in Optics and Lasers.
University of Central Florida, Orlando, Florida 32816

R. L. Phillips
Director, Florida Space Institute
Department of Electrical and Computer Engineering
University of Central Florida, Orlando, Florida 32816

## ABSTRACT

Interest in the use of optical communications over terrestrial links has greatly increased during the last several years. In many applications, the path is horizontal so the index of refraction structure parameter can be taken as constant. In addition, optical communication channels offer a number of advantages over conventional RF channels. However, due to the short wavelength, the reliability of an optical link can be seriously degraded over that of an RF system by atmospheric scintillation. In particular, scintillation can cause severe fading of the channel. In our analysis here we assume that the refractive index structure parameter $C_n^2$ is constant and use our recently developed gamma-gamma model and the well known lognormal model to consider the fading statistics associated with a spherical wave model for simplicity. The results are similar to a Gaussian-beam wave with perfect pointing. Our analysis show that compared to the gamma-gamma model, the lognormal model predicts optimistic values of probability of fade, underestimate the number of fades per second and consequently does not measure the mean fade time correctly.

**Keywords:** Terrestrial links, optical communications, fade probability, mean fade time, frequency of fade.

## 1. INTRODUCTION

The possibility of using high-data-rate optical transmitters for satellite communication channels has generated interest in laser communication systems over the last three decades. The future for laser satellite communications at optical frequencies depends primarily on its ability to provide distinct advantages as compared with microwaves systems. These advantages include but not limited to smaller antennas, less mass and volume, less operating power, intrinsic narrow beam and high gain nature of lasers, and the absence of regulatory restrictions for frequency use and bandwidths. Most of these advantages are consequences of the short wavelengths associated with optical waves. However, because of the very short wavelengths, the reliability of an optical communication link can be seriously degraded over

Correspondence: Email: ammarica@lorien.creol.ucf.edu; WWW: http://www.creol.ucf.edu/~ammarica;
Telephone 407 823 2418;

*Also published in *Proc. of SPIE* Vol. 3927



In *Laser-Tissue Interaction XI: Photochemical, Photothermal, and Photomechanical*, Donald D. Duncan, Jeffrey O. Hollinger, Steven L. Jacques, Editors, Proceedings of SPIE Vol. 3914 (2000)
1605-7422/00/$15.00

that of an RF system by the much greater irradiance (intensity) fluctuations or scintillation, caused by atmospheric turbulence. In the design of any laser communications system with an atmospheric channel, therefore, it is important to understand the optical signal fade characteristics that result from atmospherically induced scintillation. In a binary communication channel, for example, these periods of fades in the signal strength represent periods of extremely high error rate. For the vast majority of applications under weak scintillation, it is believed that the lognormal model provides adequate estimation of the probability and the frequency of fades.[1,2,3] However, as was shown in a previous work[4,5] the lognormal model is not the best PDF to describe the laser beam intensity even in weak turbulence conditions. The invalidity of the lognormal model to describe the irradiance of a laser beam propagating through atmospheric turbulence has also been established by Hill, Frehlich and Otto.[6] Although other models have been suggested as an alternative to the lognormal PDF , like the Rician PDF , the lognormal modified PDF and the Beckmann PDF, these models do not have a closed form probability density function (PDF) or cumulative distributions function (CDF). The uniqueness of the gamma-gamma model is attributed to the fact that it not only accurately describes the irradiance of a laser beam in all atmospheric conditions, but it has a closed form PDF and CDF as well. With that in mind, this paper shows that by using the gamma-gamma model to calculate the probability and the frequency of fade, for a spherical wave propagating through atmospheric turbulence, we get substantially different results than these obtained by the lognormal model. Therefore, the use of the lognormal model to calculate the above statistics may lead to erroneous results.

The use of large transmitter and receiver apertures has been theoretically predicted to result in a substantial reduction of laser beam scintillation under certain conditions. Such effects had been recognized[3,6] in astronomical measurements that showed that the aperture averaging annihilate the fastest fluctuations in the irradiance power spectrum reducing the scintillation of the collected light. Here we also investigate the effect of the aperture averaging, and consequently the reduction of the scintillation index, on the probability of fade and the frequency of fades calculated by the gamma-gamma PDF and the lognormal models.

Anticipating that the immediate application of this work is most useful for an optical terrestrial link, we choose $C_n^2 = 2.4\text{X}10^{-13}$, $\lambda = 1.55\,\mu m$ and keep these values fixed as we consider two different distances $L = 300$ and $1000\,m$, which corresponds to $\beta_0^2 = 0.21$ and $1.91$ respectively, where $\beta_0^2 = 0.5\,C_n^2\,k^{7/6}L^{11/6}$. For each distance, we calculate the probability of fade for the gamma-gamma and the lognormal models, $P(I \leq I_T)$, as seen by a point detector ($D = 0$) and by a $5\,cm$ radius aperture ($D = 5\,cm$). The results are shown in figures 1 and 4. Also, for both distances and both models we calculate the mean fade time, $< n(I_T) >$, for $D = 0$ and $5\,cm$. The results are shown in figures 2 and 5. Eventually we take the ratio of $P(I \leq I_T) / < n(I_T) >$ to estimate the mean fade time, the results are shown in figures 3 and 6.

## 2. THE GAMMA-GAMMA MODEL

The gamma-gamma model was developed by assuming that small scale irradiance fluctuations are modulated by large scale irradiance fluctuations of the optical wave as it propagates through the atmospheric turbulence.[4] To model this modulation process described above, we assume that the normalized irradiance is defined by $I = xy$, where $x$ arises from large scale turbulent eddies and $y$ from statistically independent small scale eddies. Therefore, we assume that the intensity has a gamma distribution with a mean $x$. That is

$$p(I/x,\alpha) = (\frac{\alpha}{x})^{\alpha}\ \frac{I^{\alpha-1}}{\Gamma(\alpha)}\ e^{\frac{-\alpha I}{x}} \tag{1}$$

where $\alpha > 0$. We also assume that the mean intensity $x$ has a gamma distribution with a mean equal to $\delta = < I(r, L >$ and $\beta > 0$, that is

$$p(x\,;\beta\,,\delta\,) = (\frac{\beta}{\delta})^{\beta}\ \ \frac{(x)^{\beta-1}}{\Gamma(\beta)}\ e^{-\beta\frac{x}{\delta}} \tag{2}$$

Therefore, the modulated intensity is given by

$$p(I;\,\alpha,\beta,\delta) = \int_0^{\infty} (\frac{\beta}{\delta})^{\beta}\ \ \frac{x^{\beta-1}}{\Gamma(\beta)}\ e^{-\beta\frac{x}{\delta}}\,(\frac{\alpha}{x})^{\alpha}\ \ \frac{I^{\alpha-1}}{\Gamma\,(\alpha)}\ e^{\frac{-\alpha I}{x}}\,dx,\ \ I>0 \tag{3}$$

and can be simplified to

$$p(I|\,\alpha,\beta) = \frac{2(\beta\,\alpha\,)^{\frac{1}{2}(\beta+\alpha)}}{\Gamma\,(\beta)\,\Gamma\,(\alpha\,)}\,(\frac{I}{<I(r,L>})^{\frac{1}{2}(\beta+\alpha)-1}\,K_{\beta-\alpha}(2\sqrt{\alpha\beta\frac{I}{<I(r,L>}}) \tag{4}$$

Under the above assumptions, the normalized variance of irradiance, commonly called the scintillation index, is defined by

$$\sigma_I^2\ =\ <x^2>\ <y^2>\ -1 \tag{5}$$

$$=(1+\sigma_x^2)\,(1+\sigma_y^2)-1$$

$$=\sigma_x^2+\sigma_y^2+\sigma_x^2\,\sigma_y^2 \tag{6}$$

where $\sigma_x^2$and $\sigma_y^2$ are the normalized variances of the large scale and small scale irradiance fluctuations and <> denotes an ensemble average. We can further express the normalized variances $\sigma_x^2$and $\sigma_y^2$ in the form

$$\sigma_x^2 = exp\,(\sigma_{lnx}^2)-1,\quad \sigma_y^2 = exp(\sigma_y^2)-1 \tag{7}$$

which allows us to rewrite

$$\sigma_I^2 = exp\,(\,\sigma_{lnx}^2+\sigma_{lny}^2)-1 \tag{8}$$

and consequently to write the gamma-gamma parameters as

$$\frac{1}{\alpha}=\sigma_x^2=exp(\sigma_{lnx}^2)-1 \tag{9}$$

$$\frac{1}{\beta}=\sigma_y^2=exp(\sigma_{lny}^2)-1 \tag{10}$$

Under weak irradiance fluctuations, we can identify the sum $\sigma_{lnx}^2 + \sigma_{lny}^2$ with the conventional log irradiance variance $\sigma_{lnI}^2$.

## 3. THE PROBABILITY AND FREQUENCY OF FADE

### 3.1 The Lognormal Model

The *fraction fade time* describes the percentage of time the irradiance of the received wave is below some given threshold value. Here we assume the irradiance fluctuations are an ergodic process where ensemble averages are equal to time averages. Based on the above results the fractional fade time or *probability of miss* (fade) as a function of threshold level becomes the cumulative probability for the irradiance

$$P(I \le I_T) = \int_0^{\infty} p(I)\, dI = = \frac{1}{2}\left\{1 + erf\left[\frac{\frac{1}{2}\sigma_I^2(L) + \frac{2r^2}{W_e^2} - 0.23\, F_T}{\sqrt{2}\,\sigma_I^2(L)}\right]\right\} \tag{11}$$

where $ln\,(\frac{I_T}{<I(0,L)>}) = -\,0.23\, F_T$. The expected number of fades per second is then given by

$$< n(I_T) > \; = \nu_0\, exp\left[\frac{\frac{1}{2}\sigma_I^2(L) \; - \; 0.23\, F_T}{2\;\sigma_I^2(L)}\right] \tag{12}$$

where the quasi frequency is defined by[8,9,10,11]

$$\nu_0 = \frac{1}{2\pi}\sqrt{\frac{-\,B_I''(0)}{B_I(0)}} \tag{13}$$

where $B_I(\rho)$ is the covariance function of irradiance. Knowing the probability of fade and the expected number of fades per second, the mean fade time is simply a ratio of these quantities given by

$$< t(I_T) > \; = \frac{Pr(I \le I_T)}{< n(I_T) >} \tag{14}$$

### 3.2 The Gamma-gamma Model

We have shown that the closed form cumulative distribution function, CDF, is[5]

$$F\,(\tfrac{I_T}{<I(0,L)>}\,|\,\alpha,\beta) = \tfrac{\pi}{sin\,(\pi(\alpha-\beta))}\;\tfrac{1}{\Gamma(\beta)\,\Gamma(\alpha)}$$

$$\left\{\tfrac{(\alpha\,\beta\,\frac{I_T}{<I(0,L)>})^{\beta}}{\beta\;\Gamma\,(\beta-\alpha+1)}\;{}_1F_2(\beta\,;\beta+1,\beta-\alpha+1,\alpha\,\beta\,\tfrac{I_T}{<I(0,L)>})\right.$$

$$- \frac{(\alpha\beta \frac{I_T}{<I(0,L)>})^{\alpha}}{\alpha\,\Gamma(\alpha-\beta+1)}\, {}_1F_2(\alpha;\alpha+1,\alpha-\beta+1,\alpha\beta\frac{I_T}{<I(0,L)>})\Big\} \tag{15}$$

where ${}_1F_2$ is the generalized hypergeometric function and $\alpha$ and $\beta$ for a zero inner scale spherical wave case are given by equations (9) and (10). The quantities $\sigma^2_{lnx}$ and $\sigma^2_{lny}$, including the aperture averaging effect, are given by[12,13]

$$\sigma^2_{lnx} = \frac{0.196\,\sigma_1^2}{(1+0.18\,d^2+0.186\,\sigma_1^{12/5})^{7/6}} \tag{16}$$

$$\sigma^2_{lny} = \frac{0.204\,\sigma_1^2\,(1+0.23\,\sigma_1^{12/5})^{-5/6}}{1+0.9\,d^2+0.207 d^2\,\sigma_1^{12/5}} \tag{17}$$

with $d = \sqrt{\frac{kD^2}{4L}}$ and $D$ is the actual aperture diameter, $k$ is the optical wave number, and $L$ is the propagation distance. Hence, the expected number of fades (surges) per second for the gamma-gamma distribution is given by

$$< n(I_T) > = \frac{\sqrt{8\pi}\,(\beta\,\alpha)\nu_0\,\sigma_I}{\Gamma(\beta)\,\Gamma(\alpha)}\,(\frac{\beta\,\alpha\,I}{< I(0,L) >})^{\frac{1}{2}(\beta+\alpha)-1}\,K_{\beta-\alpha}(2\sqrt{\alpha\beta\frac{I}{< I(0,L) >}}) \tag{18}$$

where the quasi frequency is defined by (11). The mean fade time in this case is also defined by (12).

## 4. RESULTS

With the raising need for relatively short terrestrial links, and anticipating the need to characterize the performance of a channel under certain optical atmospheric conditions, we specialize our results to two different distances along the propagation path of the beam, namely 300m and 1000m. We plotted the probability of fade, the number of fades per second and the meant fade time using the lognormal PDF and the gamma-gmma PDF for a point detector and a 5 cm diameter detector. The results clearly illustrate differences between the two PDF models.

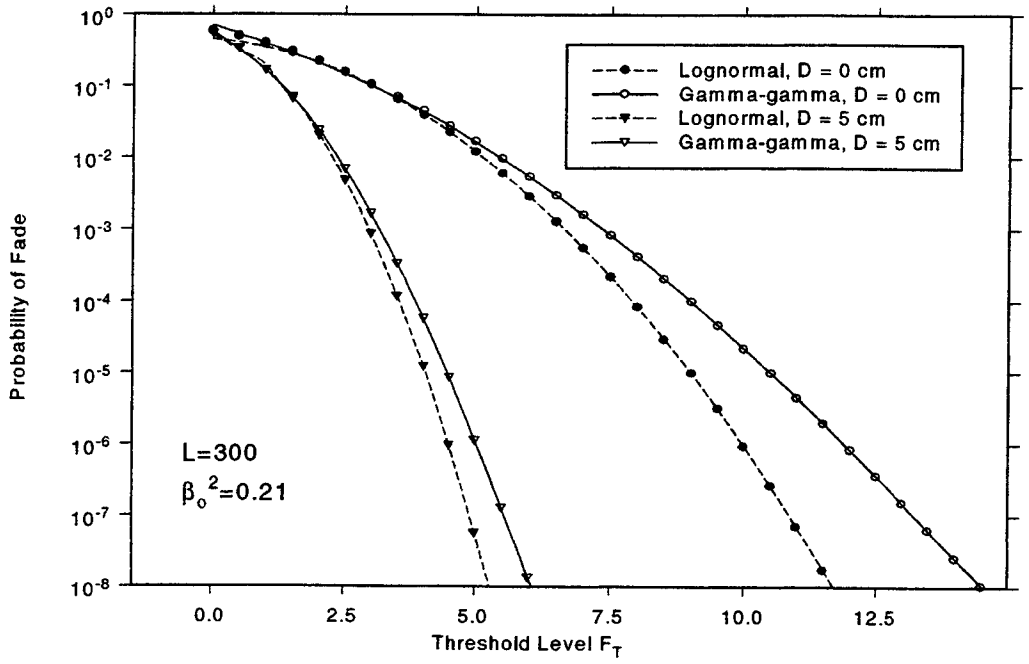


**Figure 1:** A Log plot of the probability of fade.

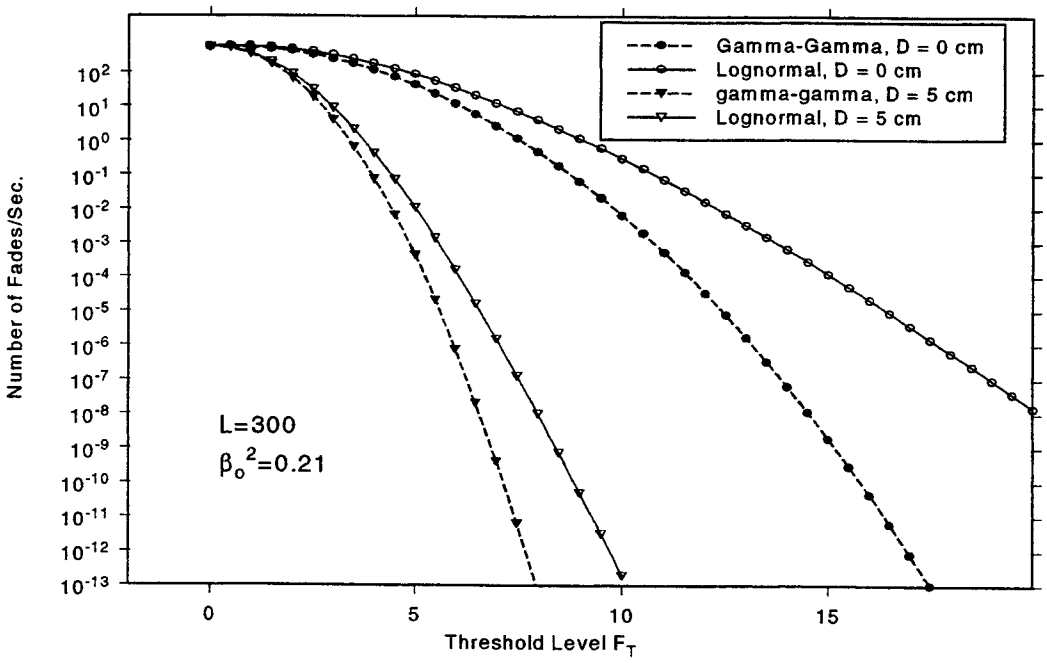


**Figure 2:** A Log plot of the number of fades per second.

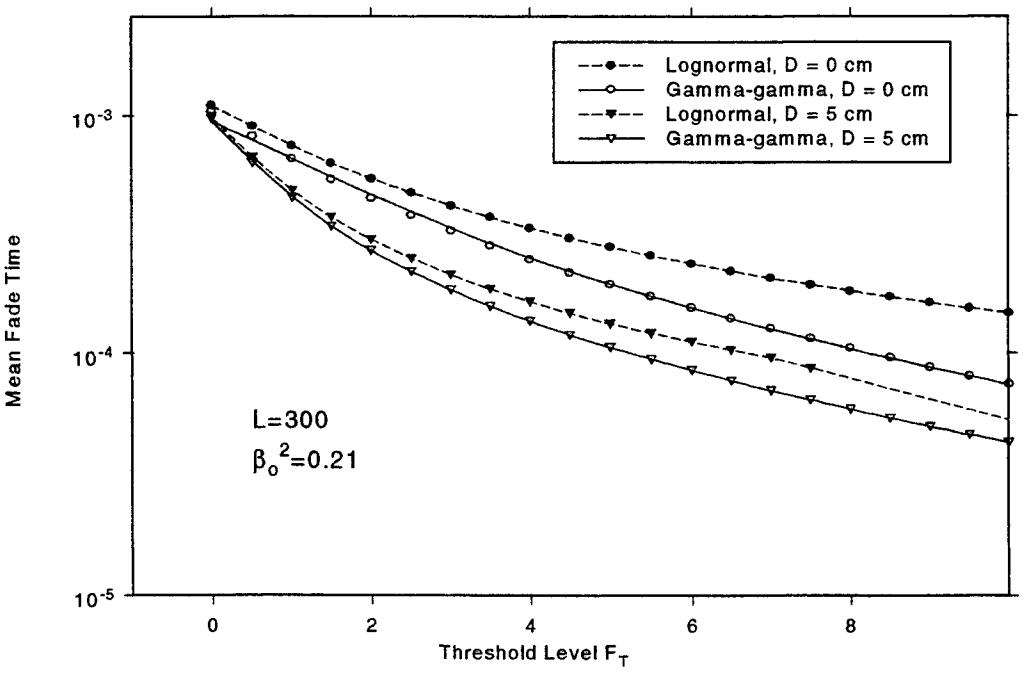


**Figure 3:** A Log plot of the mean fade time.

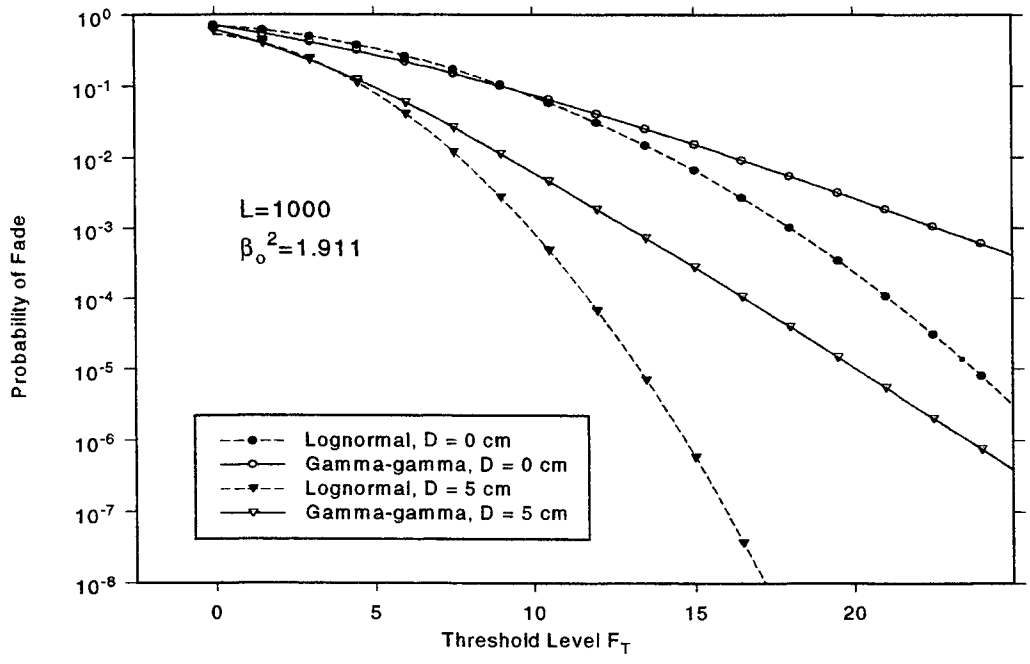


**Figure 4:** A Log plot of the probability of fade.

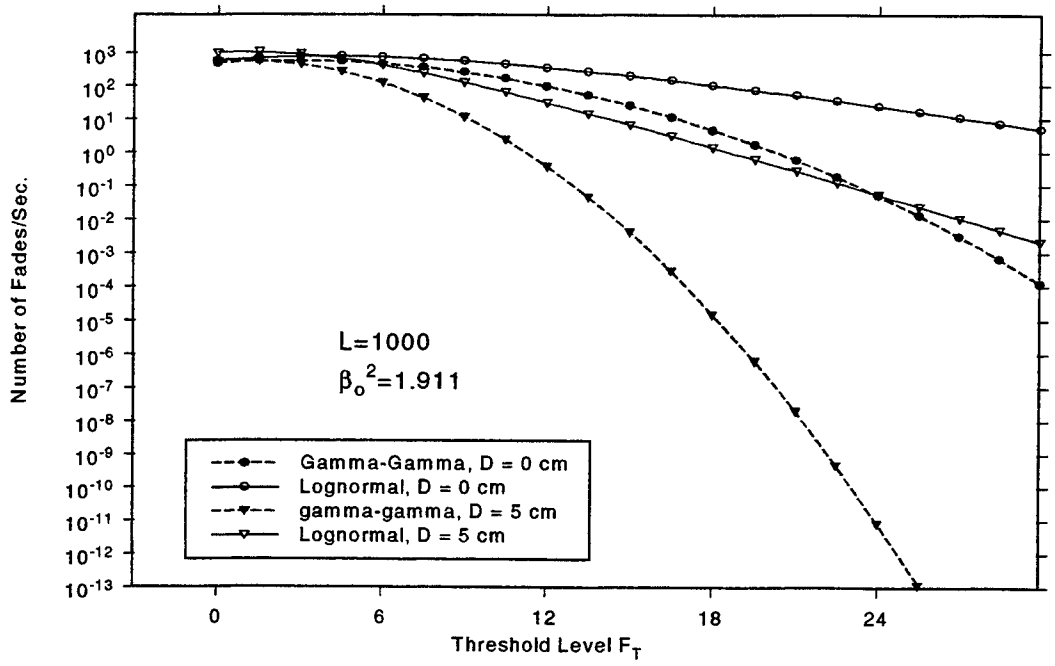


**Figure 5:** A Log plot of the number of fades per second.

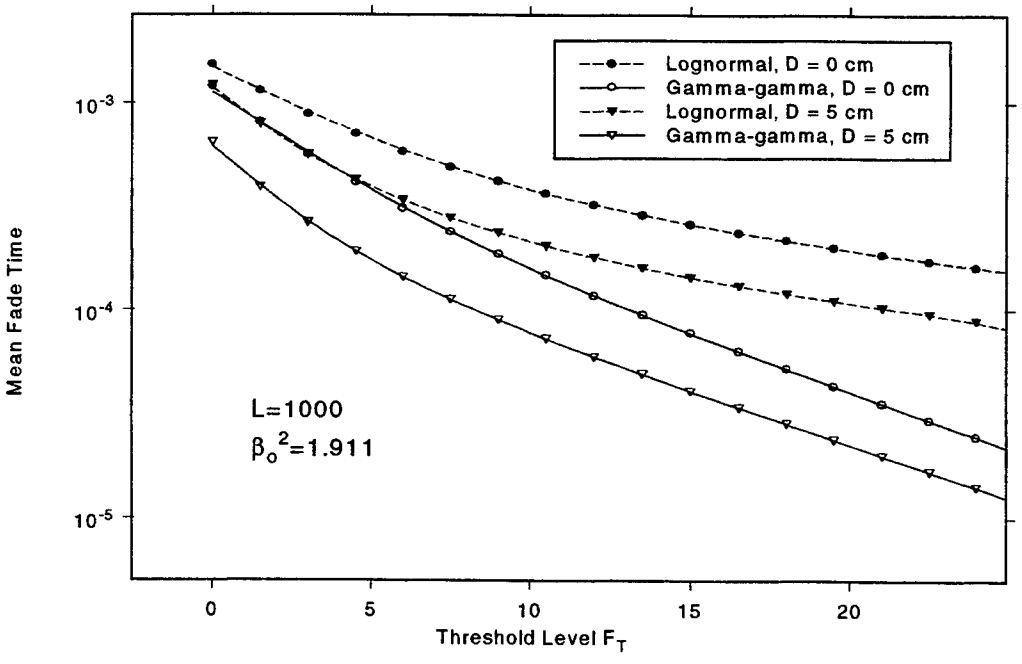


**Figure 6:** A Log plot of the mean fade time.

## 5. CONCLUSION

We have calculated the probability of fade, the frequency of fade and the mean fade time using the gamma-gamma and the lognormal model, for the same atmospheric conditions, but for two different propagation distances and two different receiver sizes. The results are shown in figures 1 through 6. It is clear, from figure 1 and 4 that the probability of fade can be drastically reduced by using a larger size aperture. It is also clear that in all cases, the log normal model predicts optimistic values for the probability of fades compared to those obtained by the gamma-gamma model, especially in the weak region. The optimistic values of the lognormal PDF has also been recognized by Hill[7]. The lognormal model also underpredicts the number of fades per second in all cases. The mean fade times predicted by the lognormal model are close to those predicted by the gamma-gamma model, nevertheless, these estimates are still one and two orders of magnitude larger than these predicted by the gamma-gamma model.

## ACKNOWLEDGMENTS

Funding for this work was partially provided by the Ballistic Missile Organization's (BMDO) Innovative Science and Technology Directorate and administrated by the Space and Naval Warfare Systems Center, San Diego, CA under contract NO. N66001-97-C-6008.

## REFERENCES

1. P. Beckmann, *Probability in Communication Engineering,* Harcourt, Brace, and World, New York, 1967.
2. L. C. Andrews, and R. L. Phillips, *Laser Beam Propagation Through Random Media*, SPIE, Washington, 1998.
3. D. L. Fried, "Aperture averaging of scintillation," *J. Opt. Soc. Am.* **57**, 169-175, 1967.
4. M. A. Al-Habash L. C. Andrews and R. L. Phillips,"Mathematical model for the irradiance PDF of a laser beam propagation through turbulent media," *J. Opt. Soc. Am. A* (submitted).
5. M. A. Al-Habash, *New Mathematical Model For The Intensity of a Laser Beam Propagating Through Atmospheric Turbulent Media,* master's thesis, University of Central Florida, 1998.
6. R. J. Hill, R.G. Frehlich, and W. D. Otto, "The probability distribution of irradiance scintillation," *NOAA Tech. Memo. ERL ETL-274,* NOAA Environmental Research Laboratories, Boulder, Colorado, 1996.
7. R. J. Hill and R.G. Frehlich, "Probability distribution of irradiance for the onset of strong scintillation," *J. Opt. Soc. A* **14**, 1530-1540, 1997.
8. D. Middelton, *An Introduction to Statistical Communication Theory*, Peninsula Publishing, Los Altos, 1987.
9. A. Papoulis, *Probability, Random Variables, and Stochastic Processes,* McGraw-Hill, New York, 1965.
10. S. O. Rice, "The mathematical analysis of random noise," *Bell Sys. Tech. J.* **23**, 282-332, 1994; **24**, 46-156, 1945.
11. S. O. Rice, "Statistical properties of a sine wave plus random noise," *Bell Sys. Tech. J.* **27**, 109-158, 1948.
12. L.C. Andrews, R. L. Phillips, C. Y. Hopen, and M. A. Al-Habash, "A new theory of optical scintillation," *J. Opt. Soc. Am. A.* **16**, 1417-1429, 1999.
13. L. C. Andrews, R. L. Phillips and C.Y. Hopen, "Aperture averaging of optical scintillation: power fluctuations and the temporal spectrum," Waves in Random Media (to appear).

## SESSION 15

# Beam Propagation in Random Media IV

Invited Paper

# Virtues of Mueller matrix detection of objects embedded in random media

George W. Kattawar[1]
Department of Physics, Texas A&M University, College Station, TX, 77843-4242

## ABSTRACT

We will present a brief introduction to Mueller matrix imaging (MMI) from cradle to adolescence and then show how it can be effectively used for detection of objects embedded in a highly scattering medium when ordinary radiance imaging might fail. We will show which elements and combination of elements are important for gaining the highest contrast against the background continuum. The mapping of certain combinations of Mueller matrix elements into an equivalent human visual system will also be discussed.

**Keywords:** Mueller matrix, Stokes vector, polarimetry, multiple scattering, radiative transfer, imaging, Monte Carlo

## 1. INTRODUCTION

### 1.1. Why do polarimetry?

Since the earth is constantly being bathed in polarized light from simple Rayleigh scattering, it seems only natural that many organisms that find their home both in the sea and on land would be endowed with polarization vision and are thus able to detect the orientation of the electric vector at their photoreceptors.. The early work of von Frisch established the fact that the honeybee, *Apis mellifera,* was indeed sensitive to polarized light. More recent work by Waterman[1] has shown that certain arthropods having compound multifaceted eyes and squids and octopuses having single lens camera eyes are also sensitive to polarized light. In fact just recently scientists at the Marine Biological Laboratory in Woods Hole, Mass. have shown that squids have developed a polarization sensitive visual system which allows them to "see" the almost transparent plankton on which they feed. Bernard and Wehner[2] have done a study of the neural mechanism for electric vector detection . They have shown how different polarizationally sensitive receptors cooperate to unambiguously determine the direction of vibration of the electric vector. They also showed that color vision (CV) in humans was similar to polarization vision (PV) in invertebrates if one used in addition to radiance, which is common to both, hue or dominant wavelength (CV) to correspond to orientation of the plane of polarization (PV) and saturation or spectral purity (CV) to correspond to degree of linear polarization (PV). It therefore seems only natural that a great deal of information is waiting to be uncovered by using complete polarization analysis which leads us into the study of the Mueller matrix.

### 1.2. Mueller matrix/ Stokes vector formulation

Proper treatment of the Stokes vector formulation requires very careful consideration of reference frames. Referring to Fig.1, the incident beam is denoted by $I_i$ and it along with the z axis define a plane called the meridian plane in which the radiance can be resolved into two orthogonal components denoted by $I_l$ and $I_r$ where the subscripts l and r refer to vibrations of the electric field parallel and perpendicular to the meridian plane respectively. If we let **l** and **r** denote unit vectors in the meridian plane and perpendicular to it respectively and the sense is chosen so that **rxl** is in the direction of propagation then the electric field can be resolved into components as follows

$$\mathbf{E} = E_l \mathbf{l} + E_r \mathbf{r} \tag{1}$$

where $E_l$ and $E_r$ are complex oscillatory functions. The four component Stokes vector can now be defined as follows:

[1] Correspondence: Email: kattawar@tamu.edu; Telephone: 409-845-1180; Fax: 409-845-2590



In *Laser-Tissue Interaction XI: Photochemical, Photothermal, and Photomechanical*, Donald D. Duncan, Jeffrey O. Hollinger, Steven L. Jacques, Editors, Proceedings of SPIE Vol. 3914 (2000)
1605-7422/00/$15.00

$$
\begin{aligned}
I &= E_l E_l^* + E_r E_r^* = I_l + I_r \\
Q &= E_l E_l^* - E_r E_r^* = I_l - I_r \\
U &= E_l E_r^* + E_r E_l^* \\
V &= i\left(E_l E_r^* - E_r E_l^*\right)
\end{aligned}
\tag{2}
$$

where the asterisk denotes complex conjugation. It is clear that they are all real numbers and satisfy the relation

$$
I^2 = Q^2 + U^2 + V^2 \tag{3}
$$

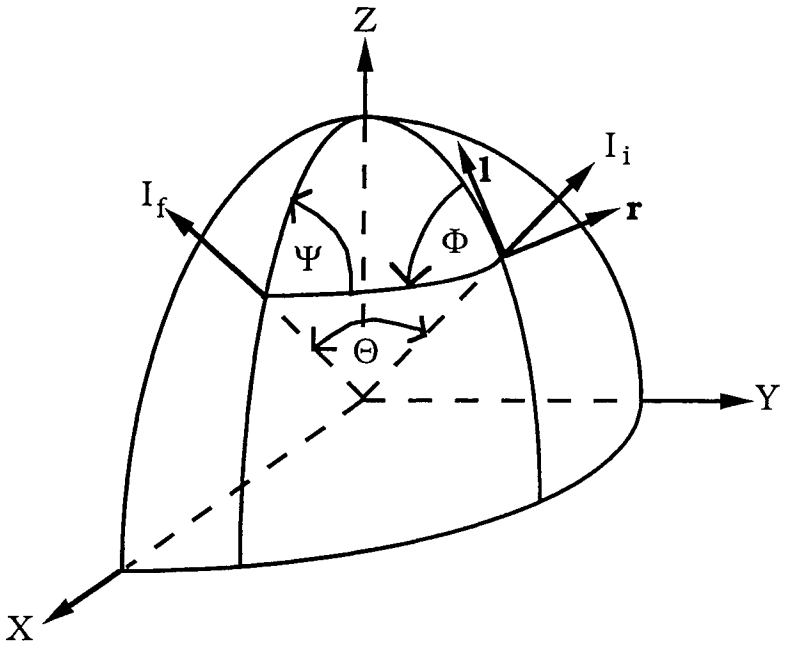


Fig. 1 Geometry showing reference planes for both incident and scattered beams as well as rotation angles $\Phi$ and $\Psi$ and scattering angle $\Theta$.

One of the very important transformations which must be handled any radiative transfer technique is the placing of the Stokes vector in the proper frame of reference for both scattering and possible Fresnel reflection from a stochastic interface. If we rotate the **l** axis *clockwise* by an angle $\phi$ and now refer the Stokes vector to the **l'** system, the transformation to do this is easily derived to be

$$
\begin{pmatrix} I' \\ Q' \\ U' \\ V' \end{pmatrix} = \begin{pmatrix} 1 & 0 & 0 & 0 \\ 0 & \cos 2\phi & \sin 2\phi & 0 \\ 0 & -\sin 2\phi & \cos 2\phi & 0 \\ 0 & 0 & 0 & 1 \end{pmatrix} \begin{pmatrix} I \\ Q \\ U \\ V \end{pmatrix} \tag{4}
$$

The rotation matrix leaves I, $Q^2+U^2$ and V invariant. The rotation matrix $\mathbf{R}(\phi)$ has some other interesting properties, namely:

$$
\begin{aligned}
\mathbf{R}(-\phi) &= \mathbf{R}(\pi - \phi) \\
\mathbf{R}(\phi_1)\mathbf{R}(\phi_2) &= \mathbf{R}(\phi_1 + \phi_2) \\
\mathbf{R}^{-1}(\phi) &= \mathbf{R}(-\phi)
\end{aligned}
\tag{5}
$$

Several quantities which are of particular importance are the *degree of polarization*, $(Q^2+U^2+V^2)^{1/2}/I$, the *degree of linear polarization*, $(Q^2+U^2)^{1/2}/I$, the *degree of circular polarization* V/I, the *orientation* ($\chi$) of the polarization ellipse where $\tan 2\chi = U/Q$ and the *ellipticity*(ratio of semiminor to semimajor axis of polarization ellipse),= $\tan\beta$ where $\sin 2\beta = V/I$

The quantity that transforms the Stokes vector when an interaction occurs is called the Mueller matrix. It is a 4x4 matrix which determines everything optically one can determine from a system of elastic scatterers. We will denote this matrix by $\mathbf{M}(\Theta,\phi)$, where the arguments will soon be explained. This matrix is derived from the more fundamental scattering amplitude matrix which is defined as follows. If the incoming electromagnetic wave scatters from an object, then we can relate the incident fields (denoted by the subscript i) to the scattered fields ( denoted by the subscript f) by

$$\begin{pmatrix} E_{lf} \\ E_{rf} \end{pmatrix} = \frac{e^{ikr}}{-ikr} \begin{pmatrix} S_2 & S_3 \\ S_4 & S_1 \end{pmatrix} \begin{pmatrix} E_{li} \\ E_{ri} \end{pmatrix} \tag{6}$$

Now every element of the Mueller matrix involves quadratic forms of the complex scattering amplitudes $S_i$. It should be noted, that since each scattering amplitude has both an amplitude and a phase but noting that only relative phase is important, there are only seven independent parameters which implies that there must be be nine relations connecting the sixteen elements of the Mueller matrix[3]. We have also shown that these equalities become inequalities when ensemble averaging is done either over orientation, size, morphology, or optical properties. These inequalities provide a sine qua non for testing the validity of single scattering Mueller matrix measurements. For example one of these inequalities which is extremely useful is

$$\sum_{i,j=1}^{4} \overline{M}_{ij}^2 \le 4 \tag{7}$$

The quantity $\overline{M}_{ij}$ is called the reduced Mueller matrix, which is the Mueller matrix normalized to $M_{11}$.
Since the Mueller matrix is always specified with respect to a particular frame of reference, we must be able to transform from the meridian plane to the frame for which the Mueller matrix is referenced. To see how this is done let us again refer to Fig.1. The incident Stokes vector $\mathbf{I}_i$ and the z axis determine the initial meridian plane where the **l** and **r** directions are shown and the direction of propagation is given by **r**x**l**. The initial Stokes vector first has to be rotated *counterclockwise* by the angle $\Phi$ which will reference it to the scattering plane and then be acted upon by the Mueller matrix $\mathbf{M}(\Theta,\Phi)$. To put it back into the final meridian plane we must rotate it *counterclockwise* by the angle $\Psi$ which will place the final Stokes vector in the proper reference frame for the next interaction. Symbolically this sequence is represented as

$$\mathbf{I}_f = \mathbf{R}(-\Psi)\,\mathbf{M}(\Theta,\Phi)\,\mathbf{R}(-\Phi)\,\mathbf{I}_i \tag{8}$$

When one is considering scattering from an ensemble of particle orientations, symmetries in the particle induce significant simplifications in the full Mueller matrix. Let us first see the two fundamental symmetry operations which can be performed on a particle shown in Fig. 2. What is important to note about these fundamental symmetry operations is the effect on the scattering amplitude matrix. The changes in this matrix are what induce the simplifications in the Mueller matrix.

One of the most useful symmetries we will encounter is when the ensemble of scatterers contains particles and their mirror images in equal number and in random orientation or the particles have a plane of symmetry and are randomly oriented. In this case the Mueller matrix reduces to the following form containing only six parameters.

$$\begin{pmatrix} m_{11} & m_{12} & 0 & 0 \\ m_{12} & m_{22} & 0 & 0 \\ 0 & 0 & m_{33} & m_{34} \\ 0 & 0 & -m_{34} & m_{44} \end{pmatrix} \tag{9}$$

It should be noted that only for spheres is $m_{22} = m_{11}$; therefore, this element is a good indicator for aspherical particles.

In order to carry the concept of a single scattering Mueller matrix (SSMM) into an effective multiple scattering Mueller matrix (MSMM). We need to consider the measurements necessary to generate a Mueller matrix. A very nice description of

these measurements was presented by Bickel and Bailey[4] which we have shown in Fig.3. These are precisely the measurements that will be used when the Mueller matrix is displayed for a physical system.

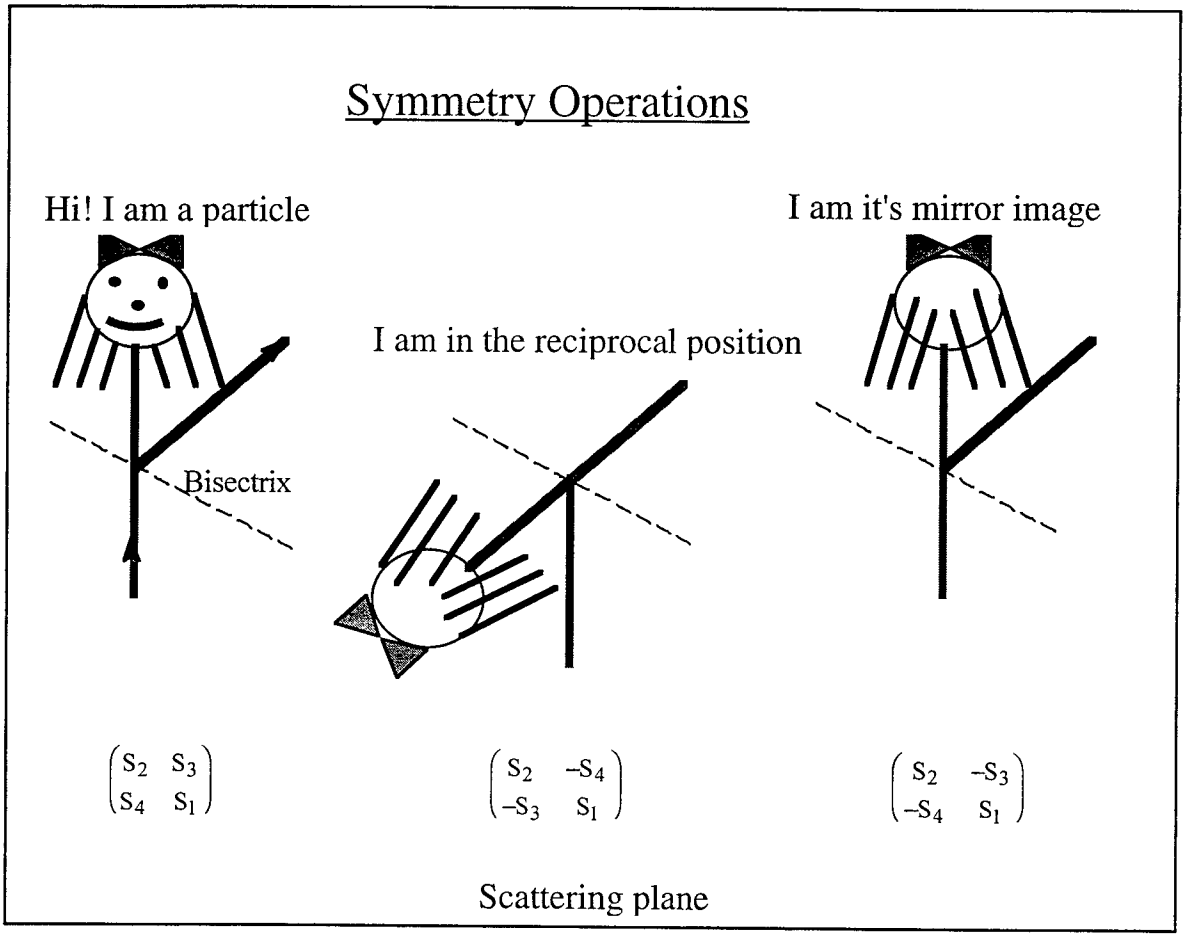


Fig. 2 These are the two fundamental symmetry operations on a particle from which all others can be derived. The bisectrix shown in the figure bisects the incident and scattered beams. The reciprocal position is defined to be a 180° rotation about the bisectrix. The mirror image symmetry is the mirror reflection of the particle in the scattering plane

## 2. COMPUTATIONAL METHODS

We have developed a Monte Carlo program which will calculate the effective or MSMM for any target embedded in any inhomogeneous medium with arbitrary scattering and absorbing properties which can also include a stochastic dielectric interface. This program uses state-of-the-art variance reduction schemes to optimize the results. One of these programs was written specifically for plane parallel calculations for computing the MSMM for a coupled atmosphere/ocean system. This program uses a novel statistical estimation technique which allows us to compute continuum radiances without averaging over finite solid angle bins. Since these codes are very complicated, checking them can be very laborious and time consuming. Fortunately my colleague Dr. Eleonora Zege has developed a completely different technique using what is called

| | | | |
|---|---|---|---|
| $S_{11}$ (OO) | $S_{12}$ (HO-VO) | $S_{13}$ (PO-MO) | $S_{14}$ (LO-RO) |
| $S_{21}$ (OH-OV) | $S_{22}$ (HH-VV)- (HV+VH) | $S_{23}$ (PH-MV)- (PV+MH) | $S_{24}$ (LH-RV)- (LV+RH) |
| $S_{31}$ (OP-OM) | $S_{32}$ (HP-VM)- (HM+VP) | $S_{33}$ (PP-MM)- (PM+MP) | $S_{34}$ (LP-RM)- (LM+RP) |
| $S_{41}$ (OL-OR) | $S_{42}$ (HL-VR)- (HR+VL) | $S_{43}$ (PL-MR)- (PR+ML) | $S_{44}$ (LL-RR)- (RL+LR) |

Fig3. Diagram showing the input polarization (first symbol) and output analyzer orientation (second symbol) to determine each element of the MSMM denoted by $S_{ij}$. For example, HV denotes horizontal input polarized light and a vertical polarization analyzer. The corresponding symbols denoting polarization are V, vertical; H, horizontal; P, +45°, M, -45°; R, right handed circular polarization; L, left handed circular polarization; and O, open or no polarization optics. This set of measurements was first deduced by Bickel and Bailey[4].

the multicomponent approach[5,6] This technique is extremely fast and can yield highly accurate results. We have compared the two approaches for the situation where we have two media separated by a water interface where each medium scatters according to a Henyey Greenstein volume scattering function with an asymmetry factor g=0.75. The medium above the interface has an optical depth of 0.15 and the medium below the interface has an optical depth of 1.0. The interface has a refractive index of 1.338 typical of ocean water. The solar beam is incident at an angle of 60° from the vertical. The rest of the reduced Mueller matrix is taken as Rayleigh scattering. In Fig.4 we show a comparison of the two results for the degree of polarization for detectors at the top of the atmosphere, just above and just below the interface, and at the bottom of the ocean. As can be seen the agreement is extremely good. There are several noteworthy features of these curves. First it should be noted that there are several places where the degree of polarization goes to zero. These are called neutral points and are points where Q, U, and V are all simultaneously zero. Another interesting feature is that there is still significant polarization even at the ocean bottom. This is why many marine organisms can exhibit polarotaxis.

In order to accurately emulate target detection using the MSMM, we must first have good data on the SSMM for the various objects we would like to detect. Unfortunately, there is not a plethora of SSMM data available for either natural or anthropogenic materials; therefore we would like to test state-of-the-art polarimetric surface models as well as develop our own Monte Carlo surface model to emulate rough surface scattering from both metallic and dielectric surfaces.

There have been several surface reflectance models which have been used to emulate rough surface scattering. One of the simplest models was that developed by Videen, et.al.[7] This is a simple facet model which uses geometric optics but neglects more than one facet interaction which eliminates it as a model for getting cross polarization components which do occur when light is scattered from rough surfaces. A more sophisticated model is one recently developed by Wolff[8]. This model utilizes basic radiative transfer theory and treats a smooth dielectric as a plane-parallel layer where subsurface scattering by the inhomogeneities is isotropic so that one can use Chandrasekhar H-function theory[9] to obtain closed form expressions for diffuse reflection. This model; however, neglects polarization completely.

A crude attempt to include polarization effects was made by O'Donnell and Knotts[10]. They computed the Mueller matrix of a one-dimensional rough surface and found it to contain only four unique elements which provided important insight into prevalent scattering mechanisms.

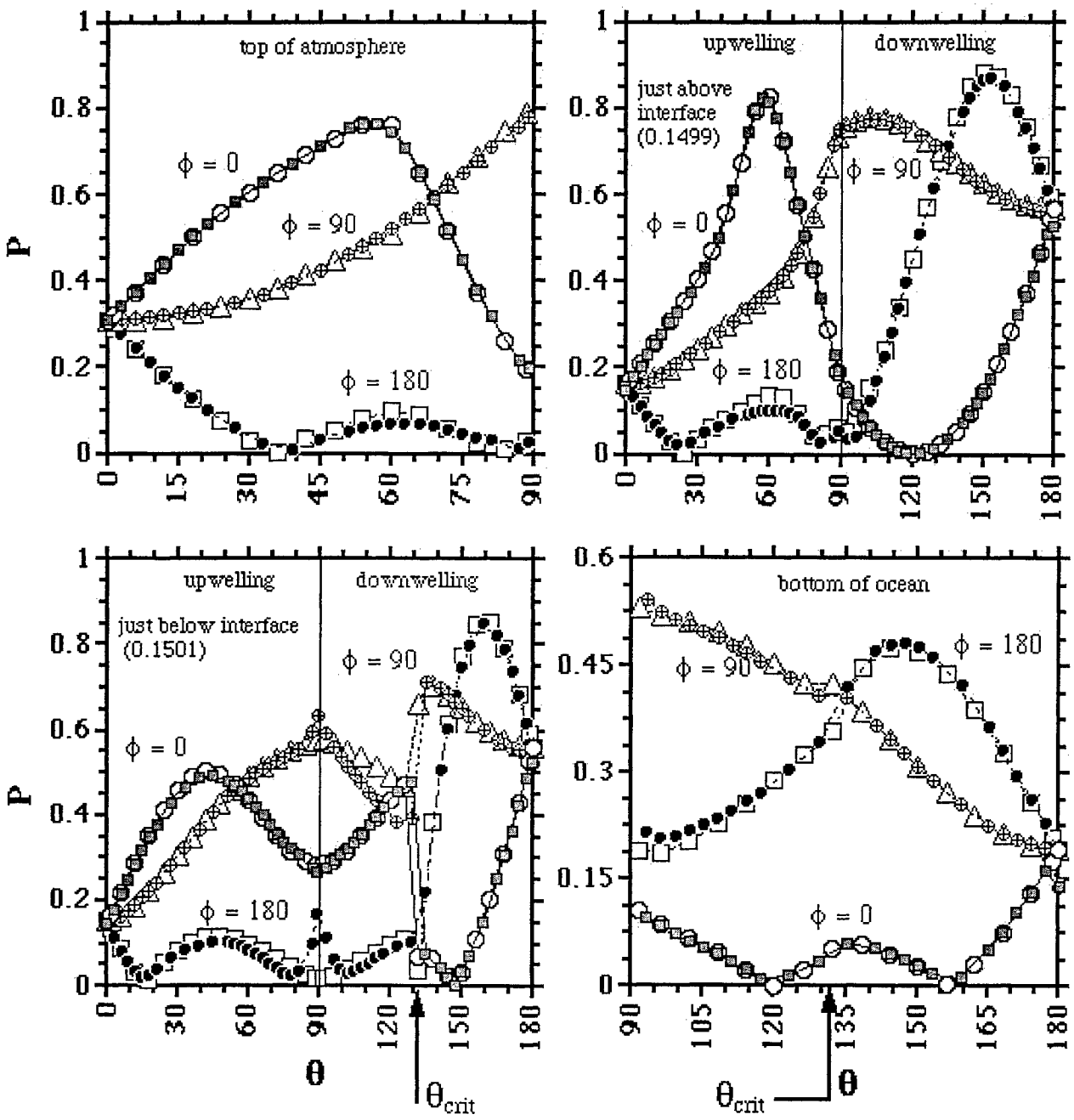


Fig. 4 Degree of polarization vs. detector polar angle for an atmosphere-ocean system with Henyey-Greenstein ($g=\langle\mu\rangle=0.75$) scattering in both layers. The single scattering albedo is 1.0 for both layers and the refractive index is 1.338 for the ocean. A dielectric interface separates the layers at an optical depth of 0.15. Radiation is incident at the top of the atmosphere at an angle of 60°. $\theta_{crit}$ is the critical angle for the interface and the azimuthal angle $\phi$ shows the azimuth of the detector relative to the azimuthal angle of the sun taken to be 0°. Shaded symbols are data from a new estimation Monte Carlo Code and the unshaded symbols are data from the multicomponent approach sent to us by Dr. Zege.

## 3. VIRTUES OF MUELLER MATRIX IMAGING

One of the first studies of simple polarization imaging was done by Walraven[11]. He used a 35 mm camera equipped with a polarizing filter to obtain radiance, degree of linear polarization and orientation of the plane of polarization. Plotting the same scene with each of these parameters, he found that new and very useful information could be obtained beyond what was present in a simple radiance image. For example, he found that the image obtained using the degree of polarization looked somewhat like the radiance image but had a much stronger dependence on surface properties than the radiance image. He also found it to be a very good mechanism for identifying man-made objects. On the other hand, the orientation of the plane of polarization was quite sensitive to surface textures and surface orientation as well as illuminated and shadowed areas. More recently, a group at Nichols Research Corporation has taken photographs with certain polarizing optical elements of an automobile against a wooded background to show how certain elements can enhance different features. Fig. 5 was kindly provided to me by Brad Blume of Nichols Research Corporation.

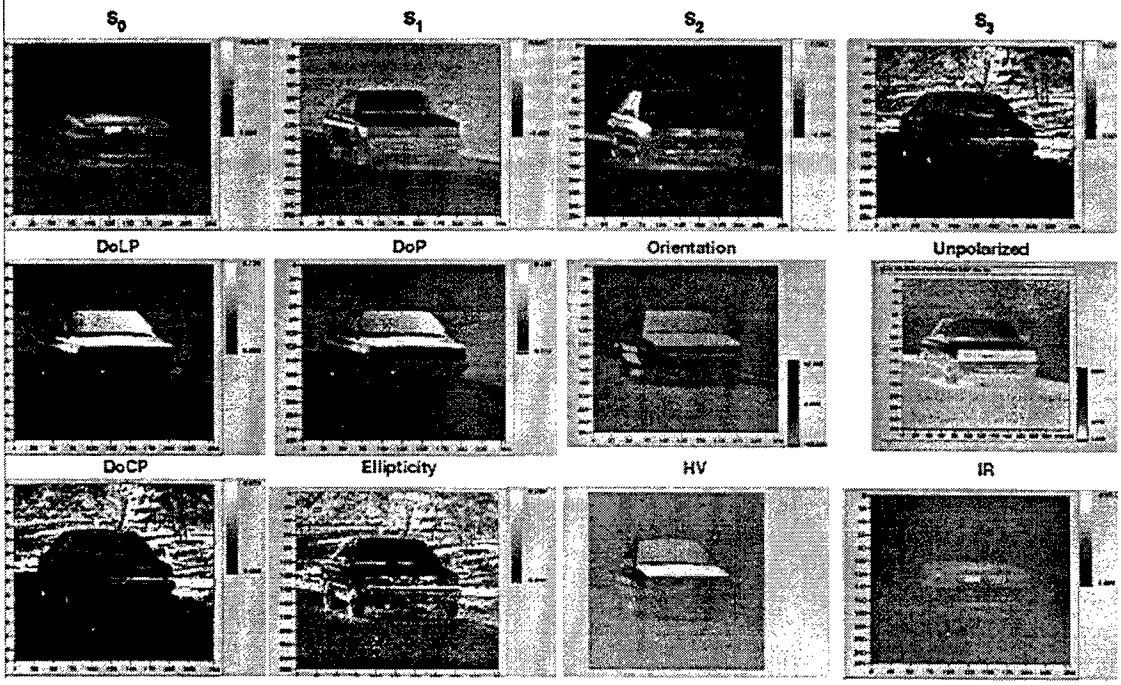


Fig. 5 This data was collected using an Amber MWIR InSb imaging array 256x256. The polarization optics consisted of a rotating quarter wave plate and a linear polarizer. Images were taken at eight different positions of the quarter wave plate (22.5 degree increments) over 180 degrees. The data was reduced to the full Stokes vector using a Fourier transform data reduction technique. The $S_0$ term is the radiant intensity, $S_1$ is the amount of radiation that is polarized in the 0/90 degree orientation; $S_2$ is the amount of radiation that is polarized in the +/-45 degree orientation, and $S_3$ is the amount of radiation that is right or left circularly polarized. The other products are all derived from the Stoke vector quantities. The equations are:

DOP = Degree of polarization = $\sqrt{S_1^2 + S_2^2 + S_3^2} / S_0$; DOLP = Degree of linear polarization = $\sqrt{S_1^2 + S_2^2} / S_0$

DOCP = Degree of circular polarization = $|S_3| / S_0$; Orientation of plane of polarization = $\theta = \frac{1}{2}\tan^{-1}(S_2 / S_1)$

Ellipticity = Ratio of semiminor to semimajor axis of polarization ellipse = $\frac{b}{a} = \tan\left(\frac{1}{2}\sin^{-1}(S_3 / S_0)\right)$

HV= Horizontal minus vertical polarization states and IR = midwave IR image

What is particularly interesting about this set of infrared (3-5μm) images is that each combination of Mueller matrix elements brings out different features of the scene. What is particularly noteworthy is the fact that using the elliptical polarization information enormously enhances the vegetation in the background. In fact the sharpest image overall is the one mapping the ellipticity.

It has recently been shown[12] that simple polarization imagery can be used to effectively enhance images of objects underwater where simple radiance imaging failed to yield enough contrast. This system was extremely simple and employed nothing but a video camera equipped with a fixed polarizer and a twisted nematic liquid crystal (TNLC) to rotate the transmission axis of the polarization analyzer by the simple application of an AC voltage . The advantage of using TNLC is that there are no moving parts to contend with. It should also be noted that this system used only the natural ambient light field for illumination.

In another more complicated system Cariou, et. al.[13] used sixty four measurements with combinations of polarizers and retarders to show that by using a pulsed laser one could greatly improve contrast of targets in ocean water by looking at certain elements of the Mueller matrix. In addition he also showed that by summing the squares of all sixteen elements of the Mueller matrix one could gain valuable information on the turbidity (extinction coefficient) of the water.

A few recent studies have demonstrated that information on the properties of a turbid medium can be measured by shining a polarized laser beam onto a sample and then analyzing the state of polarization of the diffusely backscattered light. The investigated applications of this technique include the measurements of the average particle size, the scattering coefficients and the anisotropy factor of particle suspensions[14], cloud diagnostics[15,16], the study of biological materials[17-19], and the measurements of the average photon path length[20]. Hielscher *et al.*[21] generalized the concept of an effective Mueller matrix and measured the two-dimensional Mueller matrix of backscattered light. A more recent paper by Rakovic, *et.al*[22],.extended this work to include a theoretical, computational, and experimental verification of the use of incoherent scattering theory to explain the patterns seen in polarized light backscattering from suspensions of polystyrene spheres. Some of the results in this paper are shown in Fig. 6.

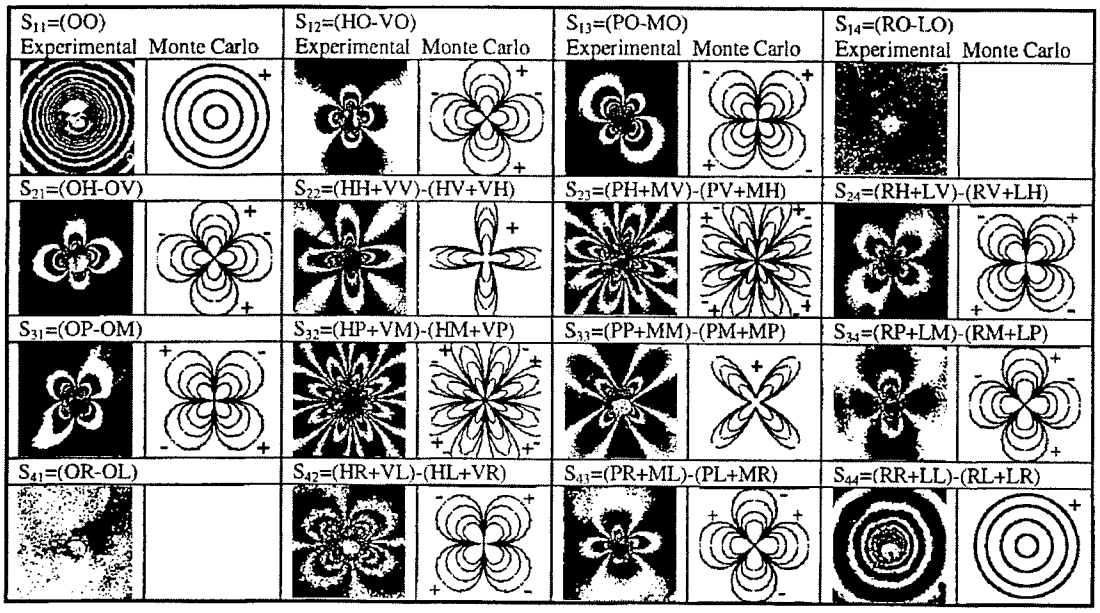


Fig.6 Experimental and Monte Carlo backscattering Mueller matrix. The phantom was comprised of a 0.05-wt% suspension of polysterene spheres (of diameter 2.02 μm) in deionized water. The approximate size of each image is 1.6cm x 1.6cm. Light wavelength was 632.8 nm. The normalized absolute values corresponding to the contours of the theoretical matrix elements are $S_{11}$: 266, 111, 69, 49 x $10^{-4}$; $S_{12}$, $S_{21}$, $S_{13}$, $S_{31}$: 15, 6, 2.5, 1 x $10^{-4}$; $S_{22}$, $S_{33}$: 38, 20, 14, 10 x $10^{-4}$; $S_{23}$ , $S_{32}$: 26, 15, 10, 6 x $10^{-4}$; $S_{24}$, $S_{34}$, $S_{42}$, $S_{43}$: 10, 5, 2, 1 x $10^{-4}$; $S_{44}$: 129, 60, 38, 28 x $10^{-4}$. The smaller values correspond to the contours located farther from the center of each plot.

What is extremely significant about these images is the fact that they can be preidcted from first principle symmetry properties of the single scattered Mueller matrix. For example if the SSMM has the following form

$$\begin{pmatrix} M_{11} & M_{12} & M_{13} & M_{14} \\ M_{12} & M_{22} & M_{23} & M_{24} \\ -M_{13} & -M_{23} & M_{33} & M_{34} \\ M_{14} & M_{24} & -M_{34} & M_{44} \end{pmatrix} \tag{10}$$

then the MSMM will contain only seven independent elements and the rest can be obtained by simple rotations. These symmetry relations hold under quite general conditions. For example the scattering medium should be invariant under rotations around the initial laser beam direction and should contain an ensemble of identical (possibly asymmetric) scattering particles in random orientations. They also hold if both the scattering particles and the scattering medium are optically active. The symmetry relations will break down only if the scattering particles are all virtually different and cannot be classified in several ensembles of identical particles. These results can be shown symbolically as

$$\begin{pmatrix} S_{11} & S_{12} & S_{12}(\pi/4) & 0 \\ S_{12} & S_{22} & S_{23} & S_{24} \\ -S_{13} & -S_{23} & -S_{22}(\pm\pi/4) & S_{24}(-\pi/4) \\ 0 & S_{24} & -S_{34} & S_{44} \end{pmatrix} \tag{11}$$

The seven independent elements are $S_{11}$, $S_{12}$, $S_{14}$, $S_{22}$, $S_{23}$, $S_{24}$ and $S_{44}$. Element $S_{13}$ is simply $S_{12}$ rotated by 45°.This result is also true in Fig. 6. The reader should verify the other symmetries and compare them to Fig. 6.

Another application of Mueller matrix imaging is demonstrated with the following model developed by Rakovic and Kattawar. It consists of a circular target with three annuli with different reflecting reduced Mueller matrices but with the same albedo. It is shown in Fig. 7 below. All distances are measured in terms of mean free path lengths. A sophisticated Monte Carlo program was written to perform the simulation and the medium had a very forward scattering volume scattering function. We found that a good parameter to calculate was the depolarization index (DI) which was used by Gerligand[23] in analyzing polarimetric images of a cone. It is defined as

$$DI = 1 - \sqrt{\left( \sum_{i,j=1}^{4} S_{ij}^2 / S_{11}^2 - 1 \right) / 3} \tag{12}$$

It gives a rough idea of how much completely polarized light is scattered from the surface with a reduced degree of polarization. And is closely related to the average depolarization of the exiting radiation. In Fig. 8 we show a result of the simulation where the target has been placed at a distance of four mfp from the illuminating beam and the detector. The program to generate the GUI images was provided by colleagues at NRL at Stennis, Mississippi. The image in the upper left shows just the radiance and it can be seen that the contrast with the scattering medium is lost. The target would thus be undetectable with just radiance imaging. In the next image in the upper right, we see the DI image of the same scene and notice that regions 1 and 2 of the target are clearly seen; however, region 3 is starting to blend with the background continuum. The reason for this is due to the fact that the backscattering Mueller matrix for this painted region is similar to the backscattering from water (Rayleigh scattering). Now in the image in the lower left we interchange regions 2 and 3 on the target and we now notice that all three annuli can be distinguished. In the final figure in the lower right regions 1 and 3 have been interchanged and we can still see the three annuli with different polarimetric properties. These results demonstrate the power of polarimetric imaging compared to ordinary radiance imaging

## 4. CONCLUSIONS

We have shown that Mueller matrix imaging can be a very powerful tool for target identification and image analysis. It should be used in conjunction with ordinary radiance imaging. The power in the method is that it reveals features not normally seen in the human visual system. We feel that this method will be used routinely in such diverse fields as astronomy, ocean optics, tissue optics, and atmospheric remote sensing of biological aerosols.

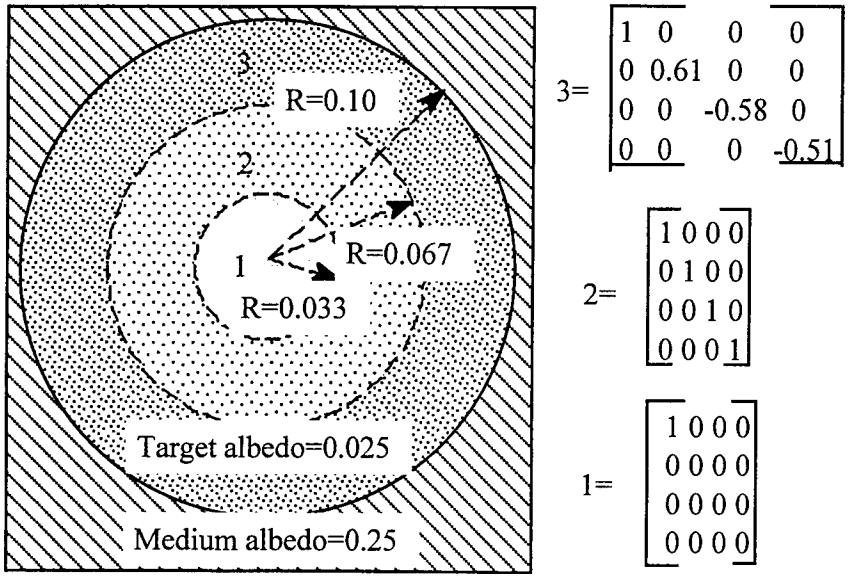


Fig.7 The target used in the simulation consisted of three annuli each having different polarization properties as shown by the corresponding reduced Mueller matrices shown on the right. Region 1 completely depolarizes the incident light; region 2 leaves the polarization unchanged; and region 3 describes the backscattering from a painted surface. The target albedo is uniform across the annuli and the medium albedo is a factor of ten larger than the target albedo.

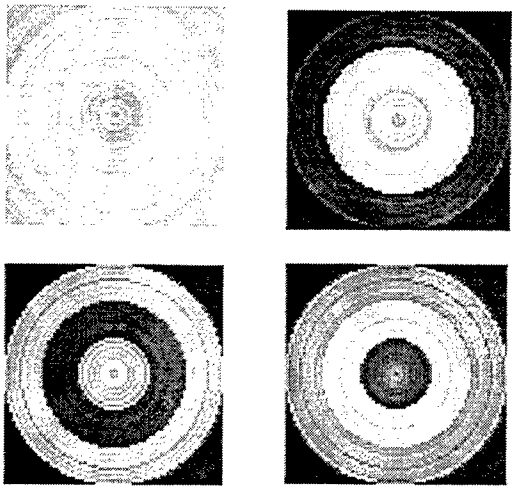

Fig. 8 Detected signal of a target embedded in a highly forward scattering medium such as ocean water with three different annuli each with different polarimetric properties. The target distance is 4 mfp. The image in the upper left is just the normal radiance. The one in the upper right is for the region ordering of 1, 2 , 3 from the center outwards as shown in Fig. 7. The one in the lower left is when regions 2 and 3 have been interchanged giving the sequence 1, 3, 2 and the one in the lower right has regions 1 and 3 interchanged giving the sequence 3, 2, 1.

## ACKNOWLEDGMENTS

This research was partially supported by the Office of Naval Research under contract N00014-95-1-0275

## REFERENCES


1. T. H. Waterman, *Plansts Stars and Nebulae studied with photopolarimetry*, 482-494, The University of Arizona Press, 1973.
2. G. D. Bernard and R. Wehner, "Functional Similarities Between Polarization Vision and Color Vision", *Vision Res.* **17**,1019-1028, 1977.
3. E. S. Fry and G. W. Kattawar, "Relationships between elements of the Stokes matrix", *Applied Optics* **20**, 2811-2814, 1981.
4. W. S. Bickel and W. M. Bailey, "Stokes vectors, Mueller matrices, and polarized scattered light", *Am. J. Phys.* **53**, 468-478, 1985
5. E. P. Zege, I.L. Katsev and I.N. Polonsky, "Multicomponent approach to light propogation in clouds and mists", *Applied Optics*, **32**, 2803-2812, 1993.
14. E. P. Zege and L. I. Chaikovskaya, "New approach to the radiative transfer problem", *JQSRT*, **55**, 19-31, 1996.
15. 9. G. Videen, JY. Hsu, W. S. Bickel, and W. L. Wolfe, "Polarized light scattered from rough surfaces", *J. Opt. Soc. Am. A.* **9**,1111-1118, 1992.
16. L. B. Wolff, "Diffuse-reflectance model for smooth dielectric surfaces", *J. Opt. Soc. Am. A*, **11**, 2956-2968, 1994.
17. S. Chandrasekhar, *Radiative Transfer*, (Dover, New York, 1960)
10. K. A. O'Donnell and M.E. Knotts, "Polarization dependence of scattering from one-dimensional rough surfaces", *J. Opt. Soc. Am. A*, **8**, 1126-1131, 1991.
11. W alraven, "Polarization imagery", *Opt. Eng.*, **20**, 014-018, 1981
12. N. Shashar, T. W. Cronin, G. Johnson, and L.B. Wolff, "Portable imaging polarized light analyzer", *SPIE* **2426**, 28-35, 1994.
13. J. Cariou, B. Le Jeune, J. Lotrian, and Y. Guern, "Polarization effects of seawater and underwater targets", *Applied Optics* **29**, 1689-1695, 1990.
14. A. H. Hielsher, J. R. Mourant, and I. J. Bigio, "Influence of particle size and concentration on the diffuse backscattering of polarized light from tissue phantoms and biological cell suspensions," *Appl. Opt.* **36**, 125-135, (1997.
15. A. I. Carswell and S. R. Pal, "Polarization anisotropy in lidar multiple scattering from clouds," *Appl. Opt.* **19**, 4123-4126, 1980.
16. S. R. Pal and A. I. Carswell, "Polarization anisotropy in lidar multiple scattering from atmospheric clouds," *Appl. Opt.* **24**, 3464-3471, 1985.
17. S. L. Jacques, M. Ostemeyer, L. Wang, and D. Stephens, "Polarized light transmission through skin using video reflectometry: toward optical tomography of superficial tissue layers", in Lasers in Surgery: Advanced Characterization, Therapeutics, and systems VI, R.R. Anderson, ed., *Proc. SPIE* **2671**, 199-220, 1996.
18. S. G. Demos and R.R. Alfano, "Optical oalrization imaging", *Appl. Opt.* **36,** 150-155, 1997.
19. A. H. Hielsher, A. A. Eick, J. R. Mourant, and I. J. Bigio, "Biomedical diagnostic with diffusely backscattered linearly and circularly polarized light", Biomedical Sensing Imaging and Tracking Technologies II, T. Va-Dinh, R. A. Lieberman, and G. G. Vuvek, eds. *Proc. SPIE* **2976**, 298-305, 1997.
20. M. Dogariu and T. Asakura, "Photon pathlength distribution from polarized backscattering in random media", *Opt. Eng.* **35,** 2234-2239, 1996.
21. A. H. Hielsher, A. A. Eick, J. R. Mourant, D. Shen, J.P. Freyer, and I. J. Bigio, "Diffuse backscattering Mueller matrices of highly scattering media", *Opt. Exp.* **1**, 441-454, 1997.
22. M. J. Rakovic, G. W. Kattawar, M. Mehrubeoglu, B. D. Cameron, L. V. Wang, S. Rastegar, and G. L. Cote, "Light backscattering polarization patterns from turbid media: theory and experiment" , *Appl. Opt.*, **38** , 3399-3408, (1999).
23. P-Y. Gerligand, M. H. Smith and R. A. Chipman, "Polarimetric images of a cone", *Opt. Exp.* **4**, 420-430, 1999

# Mueller Matrix imaging of targets in turbid media

Milun J. Raković and George W. Kattawar

Department of Physics, Texas A&M University, College Station, Texas 77843-4242

## ABSTRACT

We present a theoretical analysis on the use of polarized light in the detection of a model target in a scattering and absorbing turbid medium. Monte Carlo numerical simulations are used in the calculation of the effective Mueller matrix which describes the scattering process. Contrasts between various parts of the target and background are analyzed in the images created by ordinary radiance, by elements of the Mueller matrix and by the depolarization index. It is shown that the application of polarized light has distinct advantages in target detection and characterization when compared to the use of unpolarized light.

**Keywords:** polarization, backscattering, multiple scattering, turbid media

## 1. INTRODUCTION

The use of polarimetry in ocean optics is still in its infancy although it has been used in astronomy for many years (for a nice list of references see Gehrels[1]). The use of Mueller matrix imaging has been shown to be very effective in analyzing the scattering from suspensions in turbid media.[2–5] Pezzanti and Chipman[6] have used it effectively in analyzing optical systems as well as the point spread matrix of a point object. Cariou et al[7] have shown that polarization contrast could be obtained using a pulsed laser on immersed targets. They were also able to show that by using all elements of the backscattering Mueller matrix one could monitor the turbidity of the medium. It this paper we continue our work on Mueller matrix imaging[8] and show how it can effectively be used to not only detect but also determine features of a target in different turbid media such as seawater and perhaps even biological tissue.

Under the assumption that the light scattering is incoherent we developed a Monte Carlo program which allows simultaneous calculation of all 16 elements of the effective Mueller matrix which completely describes the scattering process. Contrasts between various parts of the target and background are analyzed in the images created with the use of the light radiance as well as of the elements of the Mueller matrix and depolarization index. It will be shown that the use of polarized light in target detection has distinct advantages over the use of unpolarized light. In Sect. 2 we develop our method and in Sect. 3 we present the results of numerical calculations. Sect. 4 contains some concluding remarks.

## 2. BACKSCATTERING MUELLER MATRIX

### 2.1. Models for targets and turbid media

We start by defining the scattering system (medium, incoming light beam, targets and detector) which is assumed to simulate a detection process, and then define the effective scattering Mueller matrix which describes the process. The incoming light beam is collimated, i.e., it consists of parallel rays orthogonal to the target, see Fig. 1a. The target is immersed in a scattering medium which is assumed to occupy the lower half-space, $z \leq 0$. The beam illuminates the target as well as the vicinity around it. All rays are initially directed along the negative z-axis, and have the same $x - z$ reference plane. This allows us to specify a polarization state for the incoming beam, i.e. a common polarization state for all initial rays. The point detector is located at the origin of the coordinate system, and the target is located at a specified distance from the detector.

Optical properties of scattering medium are described by the phase function, the single scattering albedo and the single scattering reduced Mueller matrix. When simulating the medium such as sea water we have used the standard formula[9]

$$p(\theta) = \frac{p_0 \theta_0}{(\theta_0^2 + \theta^2)^{3/2}}, \tag{1}$$

Further author information: (Send correspondence to M.J.R.)
M.J.R.: E-mail: milun@rainbow.physics.tamu.edu

In *Laser-Tissue Interaction XI: Photochemical, Photothermal, and Photomechanical*, Donald D. Duncan, Jeffrey O. Hollinger, Steven L. Jacques, Editors, Proceedings of SPIE Vol. 3914 (2000)
1605-7422/00/$15.00

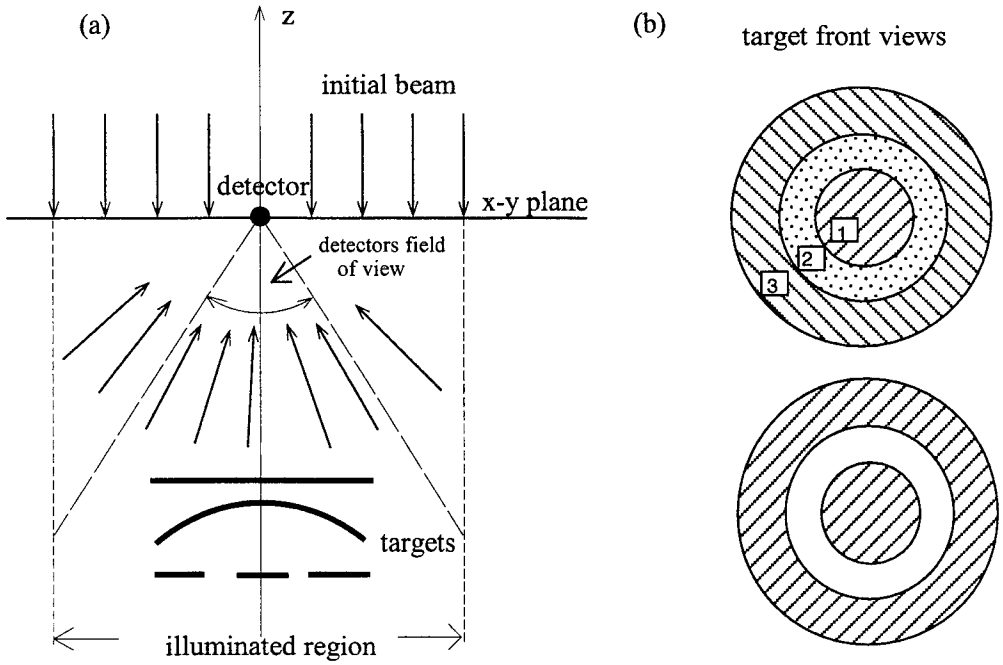


**Figure 1.** a) Geometry of the scattering system. b) A target as a reflector with three optically different regions and a target as a union of two disjoint reflectors.

where $\theta_0 = 0.06$ and the normalization constant $p_0$ was determined by the condition $2\pi \int_0^{2\pi} p(\theta)\sin(\theta)d\theta = 1$. The single scattering reduced Mueller matrix for such medium was chosen to be the one corresponding to Rayleigh scattering:

$$\mathbf{M}^{sc}(\theta) = \begin{pmatrix} 1 & b(\theta) & 0 & 0 \\ b(\theta) & 1 & 0 & 0 \\ 0 & 0 & d(\theta) & 0 \\ 0 & 0 & 0 & d(\theta) \end{pmatrix}, \quad b(\theta) = \frac{-1+\cos^2\theta}{1+\cos^2\theta}, \quad d(\theta) = \frac{2\cos\theta}{1+\cos^2\theta}. \tag{2}$$

This choice is justified by the results of measurements by Voss and Fry,[10] which showed that the reduced Mueller matrix for ocean water is very similar to that of Rayleigh scattering.

When simulating a turbid medium such as biological tissue we have used the same single scattering Mueller matrix while the phase function was the familiar Henyey-Greenstein function:

$$p(\theta) = \frac{1-g^2}{4\pi(1+g^2-2g\cos(\theta))^{3/2}} \tag{3}$$

where $g = <\cos\theta>$ is the anisotropy parameter.

In our simulations we have used two different models for targets. The first model with possible application in underwater target detection was defined as a Lambertian reflector in the shape of a flat disk or more generally of a rotational paraboloid, Fig. 1a, i.e. the target surface is determined by

$$z = -d_t - \alpha\rho^2, \quad 0 \le \rho \le R, \quad d_t, \alpha \ge 0, \tag{4}$$

where $d_t$ is the target-detector distance, $R$ is the target radius and parameter $\alpha$ defines the shape of the target. It has rotationally symmetric optical (polarization) properties, i.e its reduced Mueller matrix $\mathbf{M}_t$ is at most a function of the polar radius and not of the polar angle of the points on the target. More specifically our target is divided into three regions, i.e. annuli defined by the inequalities $\rho < R/3$, $R/3 < \rho < 2R/3$ and $2R/3 < \rho < R$, see Fig. 1b, and each of the zones had different optical properties. To each of these regions corresponds one of the three reduced Mueller matrices which, with respect to the scattering plane, have the forms:

$$\mathbf{M}_t^d(\theta) = diag(1,0,0,0), \quad \mathbf{M}_t^1(\theta) = diag(1,1,1,1), \quad \mathbf{M}_t^p(\theta) = diag(1,0.61,-0.58,-0.51). \tag{5}$$

We see that $\mathbf{M}_t^d$ completely depolarizes the light, $\mathbf{M}_t^l$ leaves the polarization unchanged, while $\mathbf{M}_t^p$ describes the backscattering from a painted metal surface.[11] To study the resolution of the detecting process we have also defined the target as a union of two disjoint flat Lambertian reflectors, one of which is a disk and another is a concentric annulus around it, both with the same polarization properties, see Fig. 1.

The second target model was defined as an inhomogeneity in the scattering medium, i.e. we have assumed that certain regions of the three-dimensional space had different polarization properties while the phase function and scattering probabilities were the same as in the rest of the scattering medium. This type of target may have possible applications in the imaging of biological tissues.

Let $\mathbf{F_0}$ be the Stokes vector corresponding to the light irradiance of the incident beam with respect to the $x-z$ reference plane. Due to (multiple) light scattering from the medium and/or target, the detector receives the light from all possible directions, see Fig. 1a. Let $\mathbf{I}(\theta,\phi)$ be the Stokes vector describing the angular distribution of the radiance at the detector, i.e. it corresponds to the ray coming back to the detector from the direction defined by spherical angles $\theta,\phi$. For the reference plane let us choose the corresponding meridian plane, i.e., the plane defined by the ray direction and the $z$-axis. (Note that different rays hit the target from different directions and necessarily have different reference planes.) Then

$$\mathbf{I}(\theta,\phi)=\mathbf{M}(\theta,\phi)\mathbf{F}_0 \tag{6}$$

where, by definition, $\mathbf{M}$ is the effective backscattering Mueller matrix which completely describes the scattering process. In addition to angles, $\mathbf{M}$ depends on the extinction coefficient of the medium $c$, single scattering albedo of the medium $\varpi_0$, distance between target and detector, and albedo of the target. Also, as a functional, it depends on the reduced single scattering Mueller matrices of the medium and target.

Since the medium is assumed to be homogeneous and since the target (i.e. its reduced Mueller matrix) is rotationally symmetric, the scattering system possesses axial symmetry which leads to the factorization of the effective backscattering Mueller matrix which takes the form

$$\mathbf{M}(\theta,\phi)=\tilde{\mathbf{M}}(\theta)\mathbf{R}(-\phi),\quad \mathbf{R}(\phi)=\begin{pmatrix}1&0&0&0\\0&\cos 2\phi&\sin 2\phi&0\\0&-\sin 2\phi&\cos 2\phi&0\\0&0&0&1\end{pmatrix}. \tag{7}$$

where $\mathbf{R}$ is the standard rotational matrix and the ("radial") Mueller matrix $\tilde{\mathbf{M}}$ depends only on $\theta$.

## 2.2. Monte Carlo method: Summation over trajectories

The matrix $\mathbf{M}$ is a solution of the radiative transfer equation[12] with appropriate boundary conditions. In principle, one can try to solve this equation by using an iterative procedure or some other approximation method. Here we shall use the Monte Carlo method to calculate numerically the effective backscattering Mueller matrix. Essentially, we represent $\mathbf{M}$, Eq. (6), as a sum over an ensemble of a large number of randomly chosen "photon trajectories". To simulate the incoming light beam described above, all trajectories have initial directions along the negative $z$-axis, while starting positions cover some neighborhood of the origin in the $x-y$ plane which is larger than the actual target area. The trajectories are defined by the collection of points, $\mathbf{r}_i^j$, $i=1,2,...,n$ (index $j$ enumerates the trajectories), where the light scatterings take place, and with initial and final points, $\mathbf{r}_0^j=(x_0^j,y_0^j,0)$ and $\mathbf{r}_{n+1}^j=0$, respectively. Fig. 2 shows several examples of such trajectories.

To each trajectory we associate its weight $w^{(j)}$ and (reduced) Mueller matrix $\mathbf{M}^{(j)}$. (Recall that if $\mathbf{M}$ is a Mueller matrix, the corresponding reduced matrix is $\mathbf{M}/M_{11}$.) The weight $w^{(j)}$ is proportional to the probability of the corresponding trajectory, therefore it is a product of the attenuation factor $\exp(-l^{(j)}c)$ and $n$ factors $\varpi_i p(\theta_i)$, where $l^{(j)}$ is the length of the $j$-th trajectory, $\varpi_i$ is the scattering albedo corresponding to the $i$-th scattering and $p(\theta_i)$ is the angular probability (density) of the $i$-th scattering. The matrix $\mathbf{M}^{(j)}$ has the form $\mathbf{M}^{(j)}=\mathbf{R}_n\mathbf{M}_n^{(j)}\mathbf{R}_{n,n-1}\mathbf{M}_{n-1}^{(j)}...\mathbf{R}_{21}\mathbf{M}_1^{(j)}\mathbf{R}_1$ where $\mathbf{M}_i^{(j)}$ is the reduced single scattering matrix describing the $i$-th scattering (of the $j$-th trajectory); $\mathbf{R}_{i,i-1}$ are the rotational matrices which make transitions between pairs of the consecutive scattering planes, while $\mathbf{R}_1$ is the rotational matrix which makes the transition from the $x-z$ reference plane to the scattering plane of the first scattering and $\mathbf{R}_n$ is the rotational matrix which makes transition from the

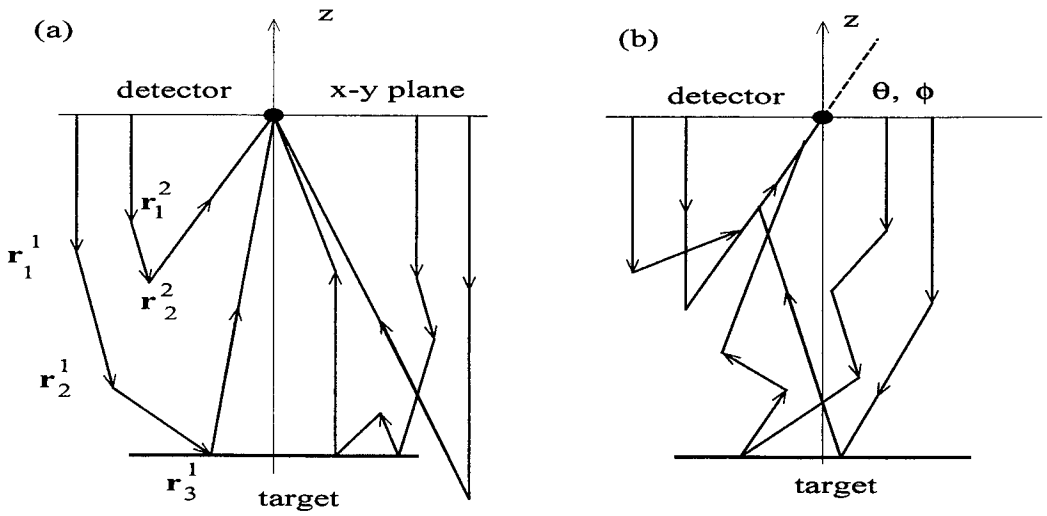


**Figure 2.** a) Several scattering trajectories reaching the detector from various directions. b) Several scattering trajectories which all reach the detector from the same direction defined by spherical angles $\theta, \phi$.

$n$-th scattering plane to the meridian plane defined by the final direction of the trajectory. Now, the effective Mueller matrix is approximately given by

$$\mathbf{M}(\theta, \phi) = \sum_j w^{(j)} \mathbf{M}^{(j)}, \tag{8}$$

where the sum runs over the large number of trajectories which all arrive at the detector from the same direction defined by $\theta$ and $\phi$, see Fig. 2b.

To calculate numerically the above sum in a straightforward manner, one has to generate a large number of randomly chosen trajectories which all start from a certain neighborhood of the origin in the $x-y$ plane and all have initial directions along the negative $z$-axis. Some of the trajectories will eventually hit the detector (with or without possible reflection from the target) and contribute to the sum in Eq. (8). In this form the method would hardly produce any results, i.e. there will be very few trajectories reaching the detector even for an enormously large initial ensemble. To circumvent this difficulty we have used two methods to modify this straightforward procedure.

In the first method, in order to reduce the number of low probability trajectories, one modifies the process of generating trajectories. Instead of randomly choosing free paths between consecutive scatterings, i.e. lengths $|\mathbf{r}_{i+1} - \mathbf{r}_i|$, and scattering angles $\theta_i$, one samples these quantities. In other words, in the course of generating trajectories, one chooses lengths of the consecutive free paths so that at the end of the algorithm the probability distribution over all free paths (for the large number of trajectories) coincides with $c\exp(-cl)$. And similarly for the scattering angles we use appropriate phase functions $p(\theta)$. To compensate for this change, one has to omit the attenuation factor as well as the angular probabilities in the definition of the weight $w$ associated with the trajectory, i.e. $w$ becomes just a product of single scattering albedos $\varpi_i$ which correspond to consecutive scatterings (from medium and/or target).

However, even with this improvement very few trajectories will reach the detector (in fact formally, the set of trajectories reaching the pointlike detector is of measure zero). Therefore, essential for success of the Monte Carlo numerical calculation is the improvement of the method which we now describe.

## 2.3. The method of the representative trajectories or "estimation" procedure

We begin by emphasizing that throughout this section whenever we refer to the scattering from the target we shall always mean the target of the first type as defined in Sect. 2.1, i.e. the target as a reflecting surface. On the other hand, the scattering from the medium will also include the scattering from the target of the second type since it was defined as an inhomogeneity in the polarization properties of the scattering medium.

As we explained earlier to each trajectory which is to contribute to the sum in Eq. (8) we associate the weight $w^{(j)}$, and the reduced Mueller matrix $\mathbf{M}^{(j)}$. These quantities are defined in the following way. To each scattering point along the ($j$-th) trajectory, $\mathbf{r}_i^{(j)}$, we associate a matrix, $\mathbf{M}_i^{(j)}$, and weight $w_i^{(j)}$, using an inductive procedure. To the starting point $\mathbf{r}_0^{(j)}$ (which lies in the $x-y$ plane) we associate $\mathbf{M}_0^{(j)} = \mathbf{1}$ and $w_0^{(j)} = 1$. Suppose that $\mathbf{M}_i^{(j)}$ and $w_i^{(j)}$ ($i = 0, 1, ..., k$) are already defined, then, $\mathbf{M}_{k+1}^{(j)} = \mathbf{M}^{sc}(\theta_k)\mathbf{R}(\phi_k)\mathbf{M}_k^{(j)}$ and $w_{k+1}^{(j)} = \varpi_k w_k^{(j)}$. Here $\theta_k$ and $\varpi_k$ are the scattering angle and the single scattering albedo of the $k$-th scattering (occurring at the point $\mathbf{r}_k^{(j)}$, which can be in the medium or on the target). $\mathbf{M}^{sc}(\theta_k)$ is the reduced single scattering Mueller matrix corresponding to the $k$-th scattering. $\mathbf{R}(\phi_k)$ is the rotational matrix which makes transitions between two consecutive scattering planes. If it happens that the trajectory in question eventually hits the detector, i.e. if for some $n$, $\mathbf{r}_{n+1}^{(j)} = 0$, then the product $w_n^{(j)}\mathbf{R}_n\mathbf{M}_n^{(j)}$ enters the sum Eq. (8) for the angles $\theta, \phi$ defined by the vector $\mathbf{r}_n^{(j)}$ (and again $\mathbf{R}_n$ is the rotational matrix which makes transitions from the $n$-th scattering plane to the meridian plane defined by the final direction of the trajectory).

Very few, if any, trajectories actually hit the detector, however, one can (instead of waiting for such trajectories to happen) use each trajectory (generated as above) to calculate contributions to the sum in Eq. (8) in the following way. Suppose that in the course of generating say, the $j$-th trajectory, we have reached the $i$-th scattering point $\mathbf{r}_i^{(j)}$ which is located in the scattering medium (i.e. it *does not* lie on the targets surface) and that we have calculated the corresponding weight $w_i^{(j)}$ and Mueller matrix $\mathbf{M}_i^{(j)}$. Then, before generating the next scattering point $\mathbf{r}_{i+1}^{(j)}$, we can calculate ("estimate") the contributions corresponding to all possible trajectories which can reach the detector from the point $\mathbf{r}_i^{(j)}$ *without any additional scatterings from the medium* and add them up with appropriate weighting factors to the sum, Eq. (8). In this way, each generated trajectory becomes a representative of the whole class of different trajectories which give contribution to the sum in Eq. (8). Each member of the class has the same scattering points from the medium as the representative trajectory and differs from it only by the segment in which it reaches the detector, see Fig. 3. In this way the Monte Carlo method becomes effective: we generate a large number of trajectories none of which actually reaches the detector but we use them to calculate contributions to the effective Mueller matrix, Eq. (8), of an even larger number of trajectories. We shall now consider the actual determination of the terms in the sum, Eq. (8).

Let us again assume that we have reached the $i$-th scattering point $\mathbf{r}_i^{(j)}$ (located in the scattering medium) and that we have determined the corresponding weight $w_i^{(j)}$ and Mueller matrix $\mathbf{M}_i^{(j)}$, see Fig. 3b. Consider first the direct path from $\mathbf{r}_i^{(j)}$ to the origin (detector). Together with the so far generated trajectory it defines one of the members in the sum Eq. (8) with the contribution proportional to:

$$\mathbf{m}_i^{(j)} = \varpi_0 \exp(-c|\mathbf{r}_i^{(j)}|) w_i^{(j)} p(\theta_s)\mathbf{R}_m\mathbf{M}^{sc}(\theta_s)\mathbf{R}_s\mathbf{M}_i^{(j)}. \tag{9}$$

Here, $\varpi_0$ is the single scattering albedo of the medium, $p(\theta_s)$ and $\mathbf{M}^{sc}(\theta_s)$ are the single scattering phase function and reduced Mueller matrix of the medium calculated at the scattering angle $\theta_s$. $\mathbf{R}_s$ is the rotational matrix which makes a transition from the scattering plane of the $(i-1)$st scattering to the (scattering) plane defined by vectors $\mathbf{r}_{i-1}^{(j)}$ and $\mathbf{r}_i^{(j)}$, while $\mathbf{R}_m$ is the rotational matrix which makes the final transition to the meridian plane defined by the vector $\mathbf{r}_i^{(j)}$. In actual numerical calculation $\mathbf{M}$ is a matrix function defined on a discrete set of pairs $\theta_k, \phi_k$ which define a grid on the (unit) sphere with the center at the origin, the grid being defined by the small solid angle $\delta\Omega$ corresponding to the finite resolution of the detector. Therefore, the term in Eq. (9), after being divided by the factor $|\mathbf{r}_i^{(j)}|^2\delta\Omega$, gives a contribution to the matrix $\mathbf{M}$ for the pair of angles $\theta_k, \phi_k$ from the grid point which is the closest to the angles defined by the direction of the vector $\mathbf{r}_i^{(j)}$.

Consider now another type of trajectory associated with the scattering point $\mathbf{r}_i^{(j)}$. Fig. 3b shows that besides the direct path there is a two parameter family of trajectories which, without any additional scattering from the

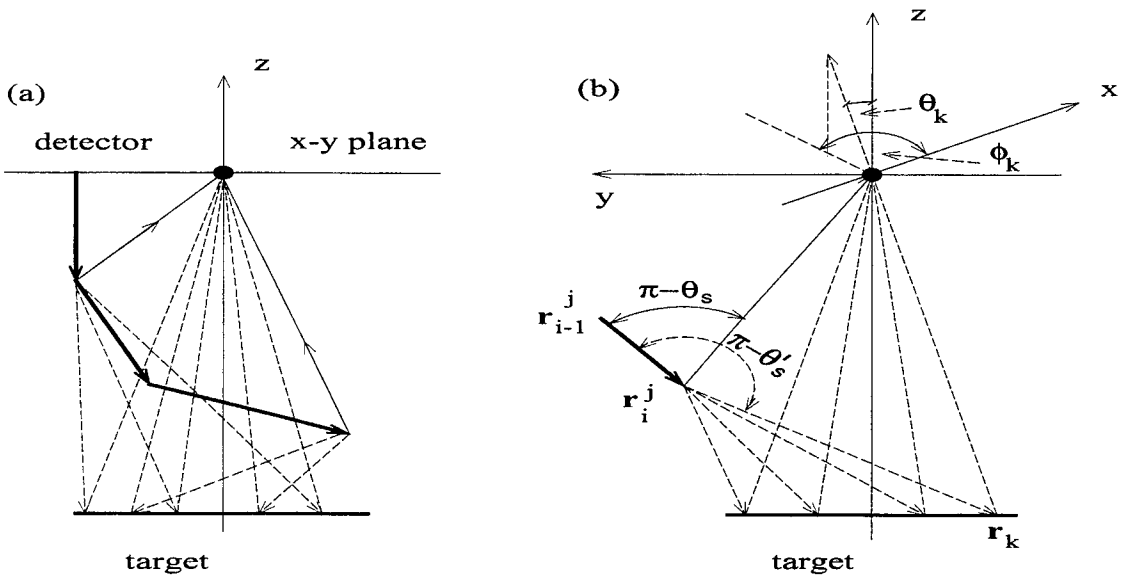


**Figure 3.** a) An example of the "representative" trajectory, thick solid line, and the corresponding class of trajectories used in the estimation procedure. Two of these trajectories, thin solid lines, miss the target, while the dashed trajectories hit the target before reaching the detector. b) Possible paths (with no additional scatterings from the medium) connecting the scattering point $\mathbf{r}_i^j$ and the detector: direct path (thin solid line) and paths via target reflection (dashed lines).

medium, connect $\mathbf{r}_i^{(j)}$ with the origin via reflection from the target. These trajectories give contribution to the matrix $\mathbf{M}$ for all directions (angles $\theta_k, \phi_k$) which are enclosed by the solid angle $\Omega$ through which the target is seen from the detector, see Fig. 3b. For example, a term in the sum Eq. (8) generated by the scattering point $\mathbf{r}_i^{(j)}$ which corresponds to the angles $\theta_k, \phi_k$ from Fig. 3b is proportional to

$$\mathbf{t}_i^{(j)} = \varpi_0 \exp(-c|\mathbf{r}_i^{(j)} - \mathbf{r}_k|) p(\theta_s') \varpi_t \frac{\exp(-c|\mathbf{r}_k|)}{|\mathbf{r}_i^{(j)} - \mathbf{r}_k|^2} \frac{p_t(\theta_k)\cos(\theta'')}{\cos(\theta_k)} w_i^{(j)} \mathbf{R}_m \mathbf{M}_t \mathbf{R}_t \mathbf{M}^{sc}(\theta_s') \mathbf{R}_s \mathbf{M}_i^{(j)}. \tag{10}$$

Here, $\varpi_t$ is the target albedo, $p_t(\theta)$ and $\mathbf{M}_t$ are the angular probability distribution and reduced Mueller matrix describing reflection from the target, and $\mathbf{R}_s$, $\mathbf{R}_t$ and $\mathbf{R}_m$ are the rotational matrices with similar roles as in Eq. (9); $\theta''$ is the angle between the vector $\mathbf{r}_i^{(j)} - \mathbf{r}_k$ and the $z$-axis.

The above analysis has divided the trajectories into two disjoint classes, one consisting of trajectories whose *last* scattering before reaching the detector was from the medium, the corresponding terms are $\mathbf{m}_i^{(j)}$, Eq. (9), and the other consisting of trajectories whose *last* scattering was from the target, the corresponding terms are $\mathbf{t}_i^{(j)}$, Eq. (10). In this way the Eq. (8) takes the form

$$\mathbf{M}(\theta, \phi) = \frac{\pi R_0^2}{N_m} \sum \frac{\mathbf{m}_i^{(j)}}{|\mathbf{r}_i^{(j)}|^2 \delta\Omega} + \frac{\pi R_0^2}{N_t} \sum \mathbf{t}_i^{(j)} \tag{11}$$

where the sums run over those $(i, j)$ pairs whose corresponding trajectories reach the target from the direction defined by angles $\theta$ and $\phi$. $R_0$ is the radius of the incident beam and $N_m$ and $N_t$ are the numbers of trajectories in the corresponding sums. Note again, that in the case of the target of the second type, only the first sum in Eq.(11) contributes, i.e. in that case all trajectories have the last scattering from the medium, and the medium and "target" differ only in the single scattering matrix $\mathbf{M}^{sc}$ in Eq.(9).

## 3. RESULTS

We have applied the method of the previous section to several target/medium configurations. In the first several examples the scattering medium had optical properties close to those of sea water, i.e. we used the phase function Eq.(1). The medium and target albedos were $\varpi_0 = 0.25$ and $\varpi_t = 0.025$.

Fig. 4 shows the results for the flat target i.e. the simple disk ($\alpha = 0$ in Eq.(4)), at a distance of $d_t = 2$ mfp (mean free paths) from the source. The radius of the incoming collimated light beam is 0.4 mfp. The sequence of target Mueller matrices from center outwards is 1 (depolarizing), 2 (polarization preserving), and 3 (painted surface), see Eq.(5). In Fig. 4a the radiance is plotted as a function of the polar distance $\rho$ in the plane containing the target (instead as a function of $\theta$). We see that the radiance cannot distinguish any structure within the target since it has a uniform albedo. It should also be noted that as soon as we leave the target at a distance of 0.1 mfp, the radiance very rapidly approaches its continuum value but the contrast is still quite good for the target detection. In Figs. 4b - 4d we show the same type of plot but this time it is for the normalized radial Mueller matrix elements $\tilde{M}_{22}$, $\tilde{M}_{33}$, and $\tilde{M}_{44}$. The elements show sharp contrast across the target (except $\tilde{M}_{22}$ between regions 2 and 3) with the largest occurring for $\tilde{M}_{44}$. On the other hand, the contrast between the paint boundary and the continuum disappears in element $\tilde{M}_{44}$ and it is small for elements $\tilde{M}_{22}$ and $\tilde{M}_{33}$. The reason for this lies in the fact that the backscattering Mueller matrix for the Rayleigh scattering continuum is $\mathbf{M}^{sc}(\theta = \pi) = diag(1, 1, -1, -1)$, which is similar to that of paint, see Eqs. (2) and (5). Note that the approach to the continuum values of $\approx \pm 1$ is slow.

Next, we study the dependence of depolarization index $DI$ on polar distance $\rho$. The depolarization index is defined by[13]

$$DI = 1 - \sqrt{(SM - 1)/3} \tag{12}$$

where $SM$ is the normalized sum of the squares of the radial Mueller matrix elements, $SM = \sum \tilde{M}_{ij}^2(\rho)/\tilde{M}_{11}^2(\rho)$. We see that in the case of complete depolarization of the signal $SM = 1$ and $DI = 1$, while $DI = 0$ when $SM = 4$, i.e. when Mueller matrix preserves the light polarization.

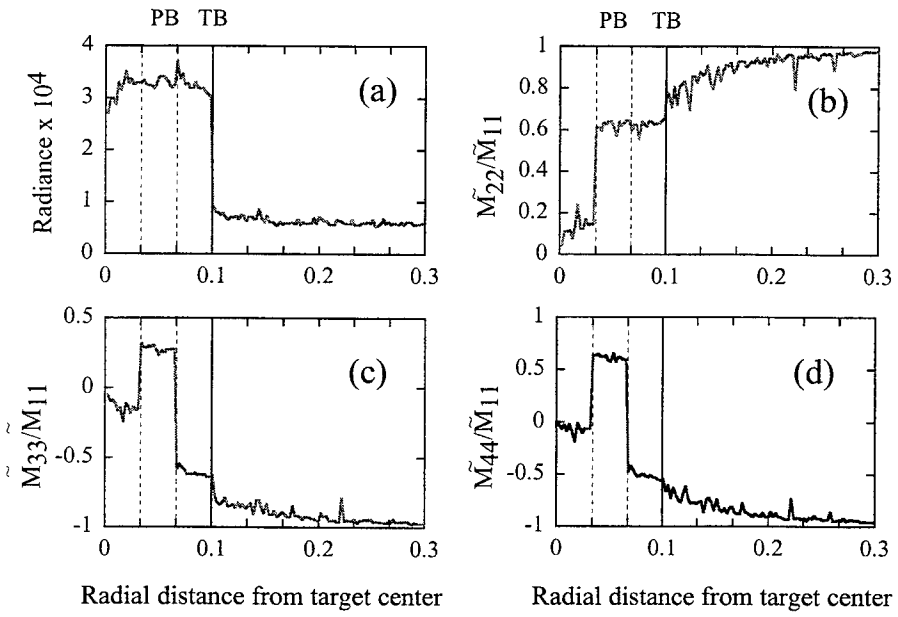


**Figure 4.** Detected signal as a function of the radial distance from the target center. Target is disk-shaped and at a distance of 2 mfp from the detector. The sequence of the target regions is 1- depolarizing, 2 - polarization preserving, and 3 - painted surface. Dashed vertical lines correspond to polarization boundaries (PB) inside the target, while solid vertical lines correspond to target - medium boundary (TB). a) Scalar radiance for the case of unpolarized incoming light beam of unit irradiance, or equivalently, the matrix element $M_{11}(\rho, \phi) = \tilde{M}_{11}(\rho)$. b) - d) Normalized diagonal matrix elements.

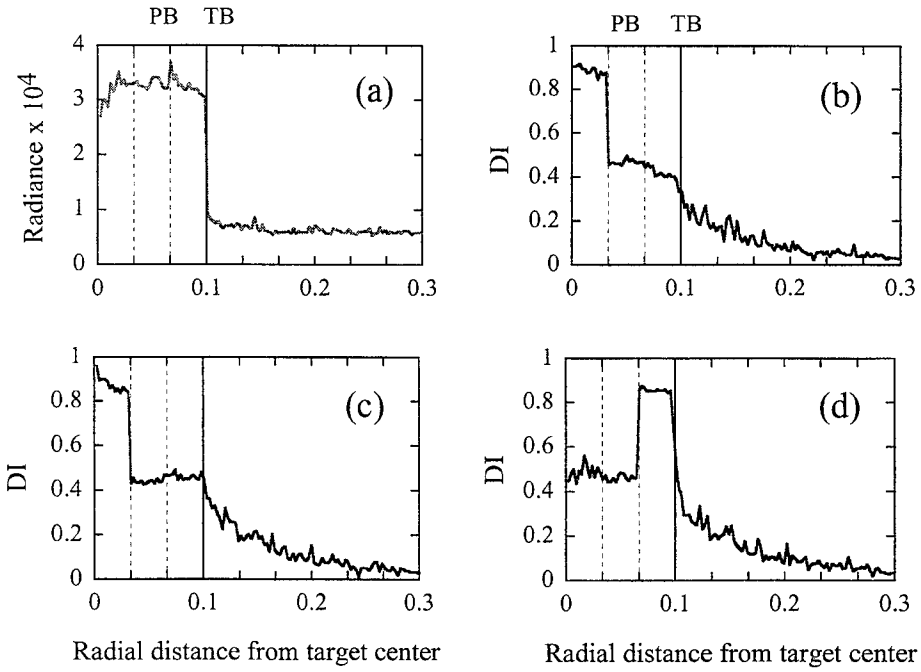


**Figure 5.** Detected signal as a function of the radial distance from the target center. Target distance is 2 mfp. Depolarization index is plotted for the sequences of the target regions: b) 123, c) 132 and d) 321.

In Fig. 5 for the same target distance we compare DI with the scalar radiance. In Fig. 5b for the same target sequences as in Fig. 4, DI shows the sharp contrasts between regions 1 and 2, no contrast between regions 2 and 3 and small but noticeable contrast between region 3 and the continuum. What makes $DI$ a useful quantity is the fact that the approach to the continuum value of 0.02 is quite slow and is not reached even out to a distance of 0.25 mfp. The very important result here is the fact that we know there is an object present long before we actually "see" it. In other words we have amplified the cross section of the target by at least an order of magnitude by sampling this quantity. From Figs. 4 and 5a, we see that in order to detect as many boundaries as possible it is useful to measure all Mueller matrix elements and study certain combinations of these elements, e.g. $DI$. However, our calculations showed that the contribution to $SM$ (and therefore to $DI$) that came from off-diagonal Mueller matrix elements was negligible. In other words, at least for the target-medium configuration studied in this work, the target and its structure could be detected by using diagonal matrix elements and the depolarization index $DI$.

Figs. 5c and 5d show the depolarization index $DI$ as a function of the polar distance $\rho$, for the same target distance but for different sequences of target regions. We se that when the regions are arranged in the order 1-3-2, Fig. 5c, $DI$ has the similar features as in Fig. 5a, while when the sequence is 3-2-1, Fig. 5d, $DI$ shows sharp contrasts between regions 2 and 1, and between the target and medium, i.e. region 1 and continuum.

Fig. 6 shows the results for the same target which is now moved to a distance of 4 mfp, and the radius of the incoming light beam is in this case 0.2 mfp. In Fig. 6a we see that we have lost all contrast between target and continuum using just the radiance. However, in Figs. 6b for the target arrangements 1-2-3 $DI$ shows clear contrast between regions 2-3 and 3-C and small contrast between regions 1-2. The approach to the continuum beyond 0.1 mfp is quite rapid. It is also interesting to note that the largest value of $DI$ is roughly 0.18 whereas in the previous case where the target distance was 2 mfp it was up to roughly 0.9. This quantity can be used as an indicator of the amount of multiple scattering between the target and the observer. Figs. 6c and 6d show that in the case of target arrangements 1-3-2 and 3-2-1, the depolarization index $DI$ can be effectively used to locate all boundaries.

In Fig. 7, the target distance is 3 mfp, however the target of roughly the same size (i.e. the same $R = 0.1$) is now a paraboloid with $\alpha = 16$. (Note that in Fig. 7, the quantities are plotted again as functions of the radial distance, which in this case is the distance from the target center of the points which uniquely define the direction of the backscattered light and lie in the plane $z = -d_t$.) Fig. 7a shows that the scalar radiance, in addition to loosing

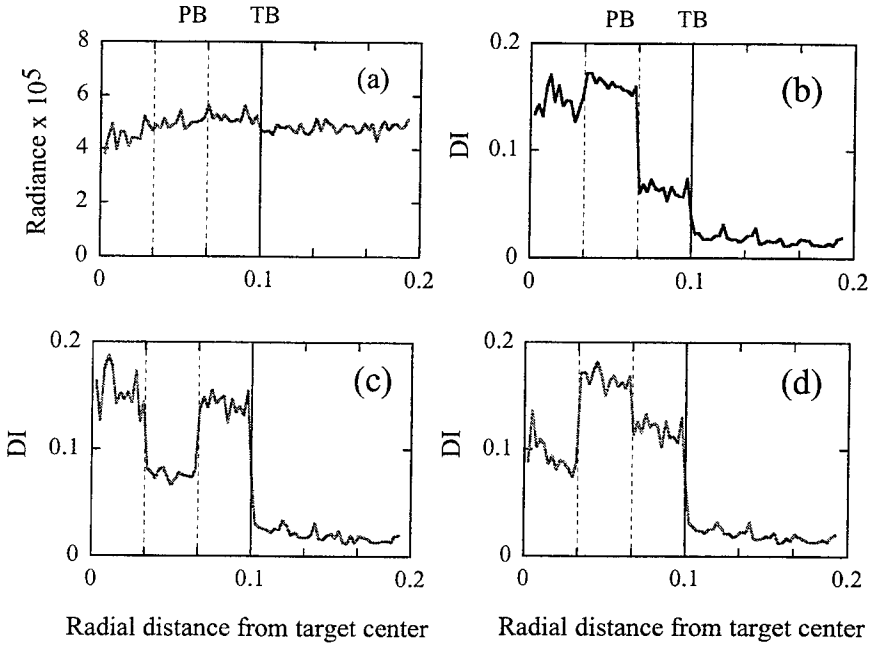


**Figure 6.** Detected signal as a function of the radial distance from the target center. Target distance is 4 mfp. Depolarization index is plotted for the sequences of the target regions: b) 123, c) 132 and d) 321.

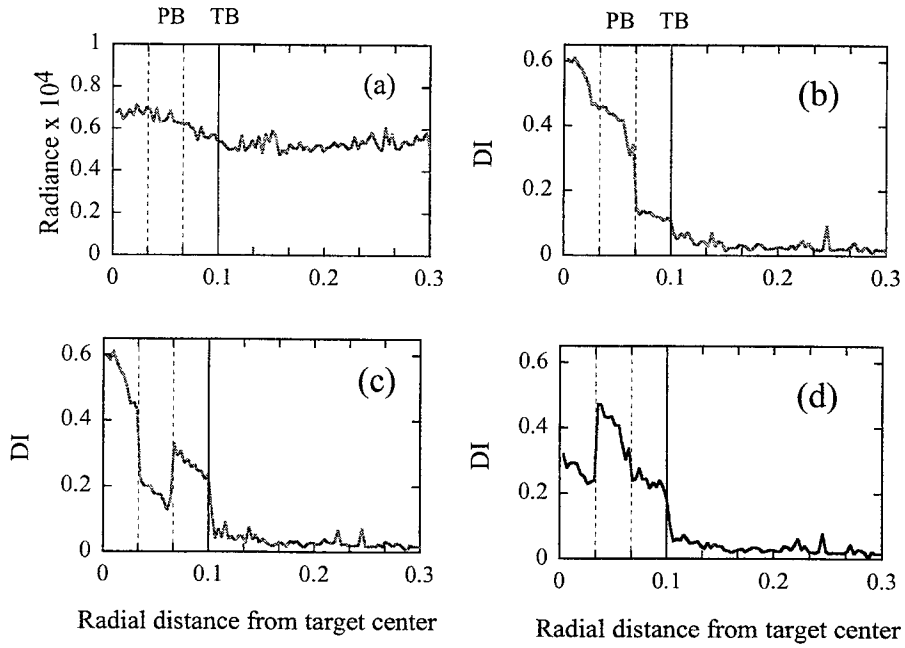


**Figure 7.** Detected signal for the paraboloid target at a distance of 3 mfp. Depolarization index is plotted for the sequences of the target regions: b) 123, c) 132 and d) 321.

the target-medium contrast, also gives very vague estimate of a target size. On the other hand, Figs. 7b - 7d show that $DI$ is still, with variable success, capable of detecting the size and the structure of the target.

To study the resolution of the detecting process in our next example the target consists of two disjoint flat Lambertian reflectors, one of which is a disk and another is a concentric annulus around it, and they both completely depolarize the light, see Fig. 1. Radius of the disk is 0.033 mfp, and the inner and outer radii of the annulus are 0.067 and 0.1 mfp respectively. The radius of the incoming collimated light beam is 0.2 mfp. The phase function of the medium is in this case Henyey-Greenstein, Eq.(3) with the anisotropy parameter $g = 0.9$. The medium and target albedos are $\varpi_0 = 0.999$ and $\varpi_t = 0.1$. The radius of the incoming collimated light beam is 0.2 mfp. Fig. 8 shows the detected signal as a function of radial distance across the target for the two different target distances. In Figs. 8a and 8b the target distance is 2 mfp while in Figs. 8c and 8d the distance is 3 mfp. Figs. 8a and 8c show scalar radiances while Figs. 8b and 8d show the depolarization index. In all plots we compare the detected signal with the signal that would be detected with no targets present. For smaller target distance, Figs. 8a and 8b, both scalar radiance and depolarization index show contrast between the two targets and and the background and again DI announces the presence of the targets beyond its geometric boundary, and together data in Figs. 8a and 8b suggest that the target at hand has a "hole". As expected, for larger target distance, Figs. 8c and 8d, scalar radiance does not detect anything while DI still detects target and its features.

Finally, in our last example the "target" is of quite a different type. It is actually a spherical region in the space which possesses different polarimetric properties than the rest of the scattering medium with which it is surrounded. Both the medium and the "target" have the same single scattering albedo $\varpi = 0.999$ and the Henyey-Greenstein phase function. The single scattering Mueller matrix of the medium is given by Eq. (2). The sphere with different optical properties has a radius 0.1 mfp and its center is at a distance 1 mfp from the detector. The radius of the incoming collimated light beam is again 0.2 mfp. For the single scattering Mueller matrix of the sphere two extreme cases are chosen, $\mathbf{M}_t^d$ which depolarizes, and $\mathbf{M}_t^1$ which preserves polarization, see Eq. (5). Fig. 9 shows the detected signal as a function of radial distance from the center of the sphere (in the plane orthogonal to the incoming beam

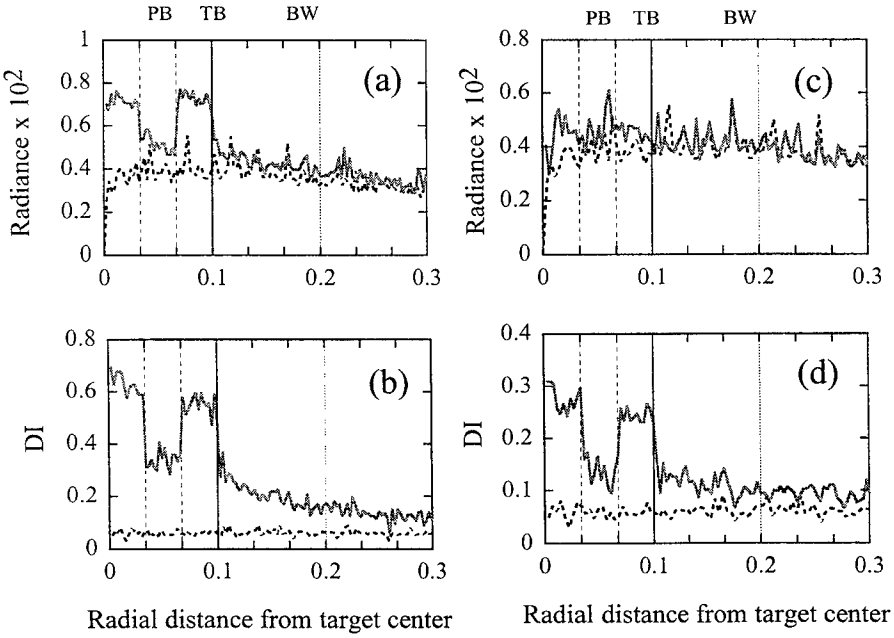


**Figure 8.** Detected signal as a function of the radial distance from the target center. The target is flat and consists of a disk and a concentric annulus, both being Lambertian reflectors which depolarize the light. Dashed vertical lines correspond to polarization boundaries (PB) inside the target, the solid vertical lines correspond to target - medium boundary (TB), while dotted vertical lines designate the incoming beam width (BW). Target distance is 2 mfp in plots a) and b) and 3 mfp in plots c) and d). In all plots dashed curves correspond to the signal with no targets present.

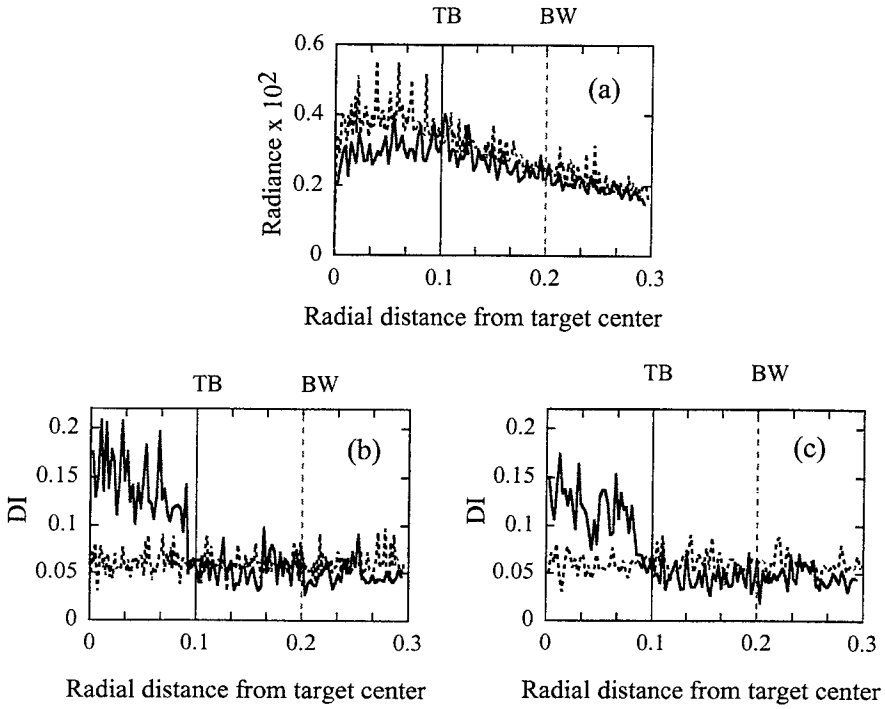


**Figure 9.** Detected signal as a function of the radial distance from the target center: a) scalar radiance, and (b), (c) depolarization index. The target is a sphere which depolarizes light (b), or preserves polarization, (c). The solid vertical lines correspond to target - medium boundary (TB), while dotted vertical lines designate the incoming beam width (BW). In all plots dashed curves correspond to the signal with no inhomogeneity present.

which contains the center). Fig. 9a shows scalar radiance while Figs. 9b and 9c show the depolarization index for the cases of a depolarizing and polarization preserving sphere, respectively. In all plots we compare the detected signal with the signal with no inhomogeneity present. We see that while radiance fails to detect anything, DI again signals the existence of the "target" in both mentioned cases.

## 4. CONCLUSION

We have shown that Mueller Matrix Imaging (MMI) can be used very effectively in determining target size and composition even under very low radiance conditions. It can be particularly useful for camouflage detection in underwater imaging and may be useful for tumor detection in biological tissue. It appears that only the diagonal elements of the Mueller matrix and the depolarization index are important for imaging contrasts. A truly added bonus to MMI imaging is that by monitoring the depolarization index the presence of a target can be detected far beyond its geometric boundary.

## ACKNOWLEDGMENTS

This research was partially supported by the Office of Naval Research under contract N00014-95-1-0275.

## REFERENCES

1. T. Gehrels, ed., *Planets, Stars and Nebulae*, The University of Arizona Press, Tucson, 1974.
2. A.H. Hielscher, A.A. Eick, J.R. Mourant, D. Shen, J.P. Freyer and I.J. Bigio, "Diffuse backscattering Mueller matrices of highly scattering media", *Opt. Exp.* **1**, pp. 441-454, 1997.
3. M.J. Raković and George W. Kattawar, "Theoretical analysis of polarization patterns from incoherent backscattering of light", *Appl.Opt.* **37**, pp. 3333-3338, 1998.

4. B.D. Cameron, M.J. Raković, M. Mehrubeoglu, G. Kattawar, S. Rastegar, L.V. Wang and G.L. Coté, "Measurement and Calculation of the Two-Dimensional Backscattering Mueller Matrix of a Turbid Medium", *Opt. Lett.* **23**, pp. 485-487, 1998.
5. M.J. Raković, G.W. Kattawar, M. Mehrubeoglu, B.D. Cameron, L.V. Wang, S. Rastegar and G.L. Coté " Light Backscattering Polarization Patterns from Turbid Media: Theory and Experiment", *Appl.Opt.* **38**, pp. 3399-3408, 1999.
6. J.L. Pezzaniti and R.A. Chipman, "Mueller matrix imaging polarimetry", *Opt.Eng.* **34**, pp. 1558-1568, 1995.
7. J. Cariou, B. Le Jeune, J. Lotrian, and Y. Guern, "Polarization effects of seawater and underwater targets", *Appl. Opt.* **29**, pp. 1689-1695, 1990.
8. G.W. Kattawar and M.J. Raković, "Virtues of Mueller Matrix imaging for underwater target detection", *Appl. Opt.* **38**, pp. 6431-6438, 1999.
9. J.W. McLean and K.J. Voss, "Point spread function in ocean water: comparison between theory and experiment", *Appl. Opt.* **30**, pp. 2027-2030, 1991.
10. K.J. Voss and E.S. Fry, "Measurement of the Mueller matrix for ocean water", *Appl. Opt.* **23**, pp. 4427 - 4439, 1984.
11. G.D. Lewis, D.L. Jordan and P.J. Roberts, "Backscattering target detection in a turbid medium using polarization discrimination", *Appl. Opt.* **38**, pp. 3937 - 3944, 1999.
12. S. Chandrasekhar, *Radiative transfer*, Oxford University Press, London, 1950.
13. P-Y. Gerligand, M.H. Smith and R.A. Chipman, "Polarimetric images of a cone", *Opt. Exp.* **4**, pp. 420-430, 1999.

# Poster Session

# A new computer code for calculation of radiation and heat fields in laser irradiated tissues

Alexander V. Lappa* [a,b], Alla S. Anikina[a,b], Vladimir A. Kamalov[a,b]
[a]Chelyabinsk State Institute of Laser Surgery, pr. Pobedy 287, Chelyabinsk, 454021, Russia
[b]Chelyabinsk State University, Br. Kashirinykh, 129, Chelyabinsk, 454021, Russia

## ABSTRACT

A non-stationary two-dimensional computer code for modelling of radiation and heat transport in heterogeneous biological tissues irradiated with laser is presented. Radiation transport is considered in the kinetic model, radiation transport equation is solved by the Monte Carlo method. Heat transport is considered in the heat conduction model, the heat equation is solved by a combination of Galerkin and the finite element methods. The code has passed a number of tests including comparisons with analytical solutions, numerical calculations of other authors, and with experimental results. The code can be used for working out and designing of laser surgical and therapeutic procedures. As well it can be used in inverse problem of experimental determination of optical and thermal parameters of biological tissues.

**Keywords:** laser, radiation, temperature, the Monte Carlo method, the finite element method, tissue.

## 1. INTRODUCTION

The information about radiation and heat fields in laser irradiated biological tissues is important for laser surgery, photo and thermotherapy. It is very desirable for institute of such speciality to have a computer code for evaluation of such fields. A few created codes[1-5] do not cover the demands of the institutes both in respect of accuracy and availability.

In this work we present our code for calculation of non-stationary two-dimensional distributions of different radiation characteristics and temperature in heterogeneous turbid media (biological tissue, first of all), irradiated with laser. The calculations are performed in two stages: radiation and heat ones. On the first stage we use the kinetic model of light transport and the Monte Carlo method, on the second stage - the heat equation model and a combination of the finite elements and Galerkin's methods.

## 2. MODEL OF MEDIUM

We use a two-dimensional axial symmetry model of a medium. The heterogeneous medium is represented as a cylinder consisting of homogeneous ring zones of rectangular section (fig. 1) with their optical and thermophysical parameters. Such geometry is in good agreement with cylindrical symmetry of laser beams and allows sufficiently adequate modelling of radiation and heat effects in a lot of real tissues.

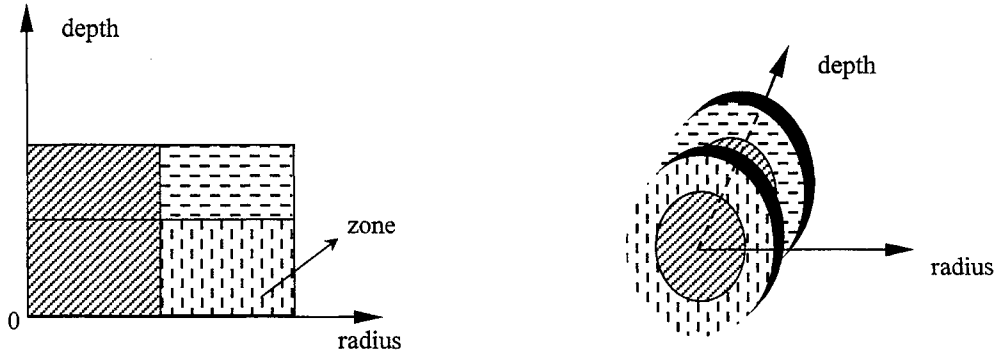


Fig. 1. Model of heterogeneous medium.

* Correspondence: e-mail: lappa@cgilh.chel.su or lappa@cgu.chel.su



In *Laser-Tissue Interaction XI: Photochemical, Photothermal, and Photomechanical,* Donald D. Duncan, Jeffrey O. Hollinger, Steven L. Jacques, Editors, Proceedings of SPIE Vol. 3914 (2000)
1605-7422/00/$15.00

## 3. RADIATION TRANSPORT MODEL

We use the kinetic model, one of the most adequate models of optical radiation transport in scattering and absorbing media. In this model the radiation transport is interpreted as the process of multiple scattering of photons on randomly distributed inclusions of medium. The basic characteristic of radiation field is the differential energy flux density (differential intensity) $I(\boldsymbol{r}, \Omega, t)$ in a point $\boldsymbol{r}$, in a direction $\Omega$, at a time $t$. It satisfies to the radiation transport equation, quasi-stationary in our case (photon time life in medium is negligible, $t$ is a parameter):

$$\Omega \nabla I(\mathrm{r},\Omega,t)+\mu(\mathrm{r},t)\, I(\mathrm{r},\Omega,t)-\int \mu_s(\mathrm{r},t)\, p(\mathrm{r},\Omega\cdot\Omega')\, I(\mathrm{r},\Omega',t)\, d\Omega' = S(\mathrm{r},\Omega,t), \tag{1}$$

where $\mu \equiv \mu_a + \mu_s$, $\mu_s$, $\mu_a$ are coefficients (macroscopic cross sections) of interaction, scattering and absorption, resp., $p$ is the indicatrix of scattering (distribution of photon scattering angle $\theta = \arccos(\Omega', \Omega)$, $S$ is the source function (differential power density of radiation emitted by the source). As the indicatrix we use the Heney-Grinstein function, traditional for biooptics:

$$p(\cos\theta) = \frac{1-g^2}{4\pi\left(1-2g\cos\theta+g^2\right)^{3/2}} \tag{2}$$

where g is the anisotropy factor (the average cosine of scattering angle). As boundary conditions we accept those following Fresnel's formulas for light reflection and refraction on border of zones with different refractive indexes $n$. So, the data necessary for radiation transport modelling are the source function $S$ and medium optical parameters $\mu_a$, $\mu_s$, $g$, $n$ for each zone.

## 4. HEAT TRANSPORT MODEL

The main ways of heat transport inside any object are heat conduction, convection and thermal radiation transport. The latter is negligible in the temperature range to be considered. We take into account the thermal conduction in medium and the convection in boundary conditions. This model approximately describes thermal processes in tissues with capillary blood flow, which is taken into account in transport coefficients. The mathematical representation of the model is the non-stationary heat equation for each zone $V_i$ (open domain in $\boldsymbol{R}^3$) of the medium $V = \sum_i V_i$ (over all the zones) with the heat sources from laser radiation, calculated on the radiation stage, and initial and boundary conditions which allow zone-zone and medium-environment interactions:

$$c\rho \frac{\partial T}{\partial t} = k\Delta T + Q \tag{3}$$

$$T\big|_{t=0} = T_0 \tag{4}$$

$$(\theta\, k\boldsymbol{n}\cdot\nabla T + \beta T - \psi)\big|_{\Gamma} = 0 \tag{5}$$

$$\left(k_A \boldsymbol{n}_{AB}\cdot\nabla T_A - k_B \boldsymbol{n}_{AB}\cdot\nabla T_B\right)\big|_{\Gamma_{AB}} = 0 \tag{6}$$

$$(T_A - T_B)\big|_{\Gamma_{AB}} = 0 \tag{7}$$

$$Q(\boldsymbol{r},t) = \mu_a(\boldsymbol{r},t)\int_{4\pi} I(\boldsymbol{r},\Omega,t)\, d\Omega$$

where $T=T(\boldsymbol{r},t)$ is the medium temperature to be calculated in a point $\boldsymbol{r}$ at an instant $t$; $c, \rho, k$ are specific heat capacity, mass density and thermal conductivity, resp., (they are constant over a zone and possibly are dependent on time); $Q = Q(\boldsymbol{r},t)$ is the heat source, the power density of laser radiation absorbed by medium in a point $\boldsymbol{r}$ at an instant $t$; $\Gamma$ is the outside (medium-environment) border of medium $V$; $\Gamma_{AB}$ is the border between adjacent zones $A$ and $B$; $\boldsymbol{n}$, $\boldsymbol{n}_{AB}$ is the outside normal to $\Gamma$ and $A$ to $B$ normal to $\Gamma_{AB}$ ; $T_A$, $k_A$, $T_B$, $k_B$ are the temperatures and the thermal conductivities in

zones $A$ and $B$; $\theta$, $\beta$, $\psi$ are parameters determining a kind of outside boundary conditions. By choosing these parameters we take into account the following physical conditions on the outside border $\Gamma$:

- conservation of temperature ($\theta=0$, $\beta=1$, $\psi$ is the temperature); (8)
- conservation of thermal flow ($\theta=1$, $\beta=0$, $\psi$ is the flow); (9)
- heat exchange under the Newton law ($\theta=1$, $-\beta$ is the heat-transfer coefficient, $\psi/\beta$ is the environment temperature near boundary $\Gamma$. (10)

The conditions (6,7) provide the physical requirements on the inside borders: continuity of temperature and heat current density.

## 5. CALCULATION OF RADIATION FIELDS

Solution of the radiation transport equation (1) is carried out by the analog Monte Carlo method[6]. The photon trajectories are simulated in full accordance with the given source function $S$, optical parameters $\mu_a$, $\mu_s$ and indicatrix (2) with the given factor g. When a photon achieves a boundary of a zone (inside or outside), it undergoes either reflection or diffraction according to Fresnel's formulas. For estimation of space distribution of absorbed power density (heat source $Q$) we divide each zone of medium into small ring cells of rectangular section (fig. 2), and during simulation of photon trajectories we determine absorbed energy in the each cell. Absorbed power density in a cell is accepted a constant equal to average value of the density over the cell. In addition to $Q$ we can estimate other radiation characteristics: space and angular distributions of flux and current density of photon energy, reflection and transmission characteristics and other functionals of differential intensity $I$.

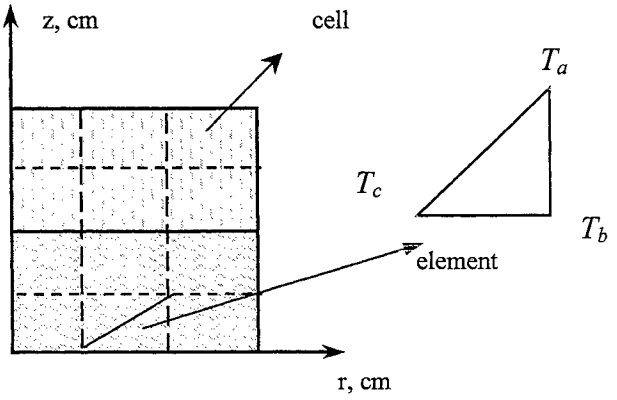

Fig. 2. Discretization of 2-zone domain.

## 6. CALCULATION OF HEAT FIELDS

The non-stationary temperature field $T(\mathbf{r},t)$, the solution of eq. (3), is calculated step by step in time, beginning from initial condition (4). Let $\tau_1$ be an instant time when the temperature field $T_1(\mathbf{r})=T(\mathbf{r},\tau_1)$ have already been determined. For determination of the field $T_2(\mathbf{r})=T(\mathbf{r},\tau_2)$ at the next instant $\tau_2=\tau_1+\tau$, $(\tau>0)$ approximate the time dependence of the field $T(\mathbf{r},t)$, $\mathbf{r}\in V$, on interval $(\tau_1,\tau_2)$ by the linear function:

$$T(\mathbf{r},t)\approx T_{1,2}(\mathbf{r},t)\equiv N_1(t)T_1(\mathbf{r})+N_2(t)T_2(\mathbf{r}), \tag{11}$$

where $N_1(t)$, $N_2(t)$ are the linearly independent basic functions:

$$N_1(t)=\frac{\tau_2-t}{\tau},\quad N_2(t)=\frac{t-\tau_1}{\tau}$$

Since the dependence $T_{1,2}$ is not correct absolutely the residual of eq. (3)

$$\varepsilon(\mathbf{r},t)=\frac{\partial T_{1,2}}{\partial t}-\frac{k}{c\rho}\Delta T_{1,2}-\frac{Q}{c\rho},\quad t\in(\tau_1,\tau_2),\ \mathbf{r}\in V,$$

is not equal to zero at any field $T_2$. For determination of $T_2$ we minimize the residual in sense of Galerkin's method: we

find $T_2$ from the orthogonality condition:

$$\int_{\tau_1}^{\tau_2} N_2(t)\varepsilon(\boldsymbol{r},t)\,dt = 0 \quad \text{for all point } \boldsymbol{r} \text{ of the medium } V.$$

As a result we obtain the following equation for determination of the field $T_2$

$$\tilde{k}\Delta T - \alpha T + \tilde{Q} + \frac{\tilde{k}}{2}\Delta T_1 = 0\ , \tag{12}$$

where $T \equiv T_2$, $\tilde{k} = \frac{\tau}{3}k$, $\tilde{Q} = \frac{c\rho}{2}T_1 + \frac{\tau}{2}Q$, $\alpha = \frac{c\rho}{2}$. The same boundary conditions (5)-(7) must be used.

So, we reduce a non-stationary problem to sequence of stationary problems. For solving the equation (12) with the boundary conditions (5)-(7) we use the finite element method[7]. It is based on minimization of a variational functional for the corresponding problem. The functional for the problem (12), (5)-(7) with boundary conditions (8) has the form:

$$\chi = \sum_i \int_{V_i} \frac{1}{2}\left[\tilde{k}(\nabla T)^2 - 2\tilde{Q}T + \alpha T^2 + \tilde{k}\nabla T\cdot\nabla T_1\right]dV, \tag{13}$$

where the summation is taken over all zones of the medium $V$. The minimization must be performed in the class of functions $T(\boldsymbol{r})$ continuous over the all zones and its boundaries under conditions (7), (8): $T|_\Gamma$ is fixed (no variation).

The functional for the same problem under boundary condition (9), (10) has another form:

$$\chi = \sum_i \int_{V_i} \frac{1}{2}\left[\tilde{k}(\nabla T)^2 - 2\tilde{Q}T + \alpha T^2 + \tilde{k}\nabla T\cdot\nabla T_1\right]dV - \\ - \int_\Gamma \left(\frac{\beta}{2}T^2 - T\psi + \frac{\tilde{k}}{2}T\boldsymbol{n}\cdot\nabla T_1\right)d\Gamma \tag{14}$$

The continuity of $T$ over zones and boundaries must be provided at minimization.

For minimizaton of the functionals the domain $V$ is divided on finite number of ring elements with triangular cross sections. We use the same system of cells as in calculation of the heat source function $Q$ in the radiation stage (fig. 2). The cell sizes are a subject of choice. They must be small enough to provide a sufficient approximation of both functions $Q$ and $T$. Within each of the elements the unknown temperature $T$ is represented by the linear combination of temperatures $T_a$, $T_b$, $T_c$ in nodes $\boldsymbol{r}_a$, $\boldsymbol{r}_b$, $\boldsymbol{r}_c$ of the element:

$$T(\boldsymbol{r}) = \varphi_a(\boldsymbol{r})T_a + \varphi_b(\boldsymbol{r})T_b + \varphi_c(\boldsymbol{r})T_c, \tag{15}$$

$$\varphi_i = \frac{1}{2S}(a_{1i} + a_{2i}r + a_{3i}z),\ a_{1i}=r_jz_k-r_kz_j,\ a_{2i}=z_j-z_k,\ a_{3i}=r_k-r_j,\ i, j, k = a, b, c,$$

where $(r, z)$ are cylindrical coordinates of vector $\boldsymbol{r}$, $S$ is the area of element cross section.

Using the approximation (15) in the functionals (13), (14) varying them under the indicated conditions we obtain the final system of the linear equations:

$$\boldsymbol{K}\,\boldsymbol{T} = \boldsymbol{F}$$

where $\boldsymbol{T}$ is a column of temperatures in the element nodes at the end of considered time step, the values to be calculated;
$\boldsymbol{K}$ is a matrix dependent on node coordinates, on the medium parameters $k$, $c$, $\rho$, on the duration of time step $\tau$, and on the heat-transfer coefficients if the boundary condition (10) is considered;
$\boldsymbol{F}$ is a column dependent on heat source function in the elements, on the known node temperatures at the beginning of the time step, on parameters $k$, $c$, $\rho$, $\tau$, on the node coordinate, and on the parameter $\psi$ in boundary conditions.

## 7. RESULTS

The described algorithm is realized as a computer code in FORTRAN. The code passed a number of tests including comparison of our results with analytical solutions, numerical calculations made with other codes, and with experimental data. Some of these comparisons are presented on fig. 3-6.

The fig.3 shows the excellent agreement between our and MCML[8] calculations of the main radiation characteristic (absorbed power density) in a typical laser geometry.

The fig. 4 demonstrates the full agreement between calculated and analytical temperatures in a simple non-stationary heat problem.

We had a good agreement in more complicated problem, including non-stationary two-dimensional transport both radiation and heat (fig.5). We compared our results with data calculated with the LITT code[2]. The data is given by authors of LITT in private communication.

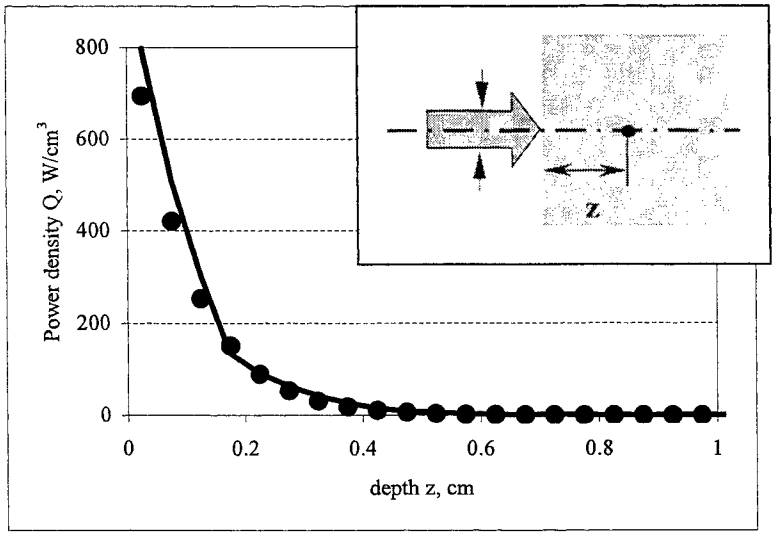


Fig. 3. Absorbed power density of laser radiation in semi-infinite homogenous medium at different depths on the beam axis. Beam profile is cylindrical flat, diameter $d$=0.1cm, power equals to 1 W. Medium parameters are: $\mu a$= 10.0 $cm^{-1}$, $\mu s$= 1.0 $cm^{-1}$, $g$=0.9, $n$=1.5. Solid line shows our data, points are data calculated with the MCML code.

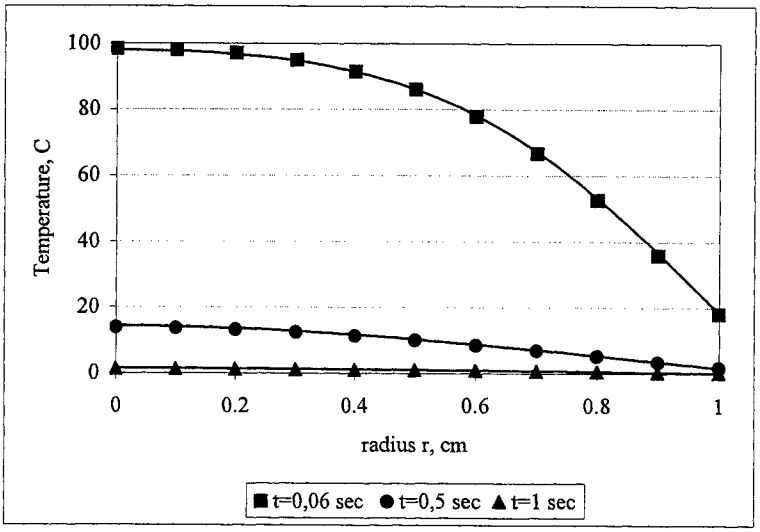


Fig.4. Temperature at 3 instants t within an infinite homogenous cylinder of radius 1 cm placed in a medium of fixed temperature 0 °C. The heat-transfer coefficient equals to 10 W/cm$^2$·K. Substance parameters are: $\rho$=1g/cm$^3$, $k$=1 W/cm·K, $c$=1 J/g·K. Solid lines are the data calculated by our code, points are analytical data.

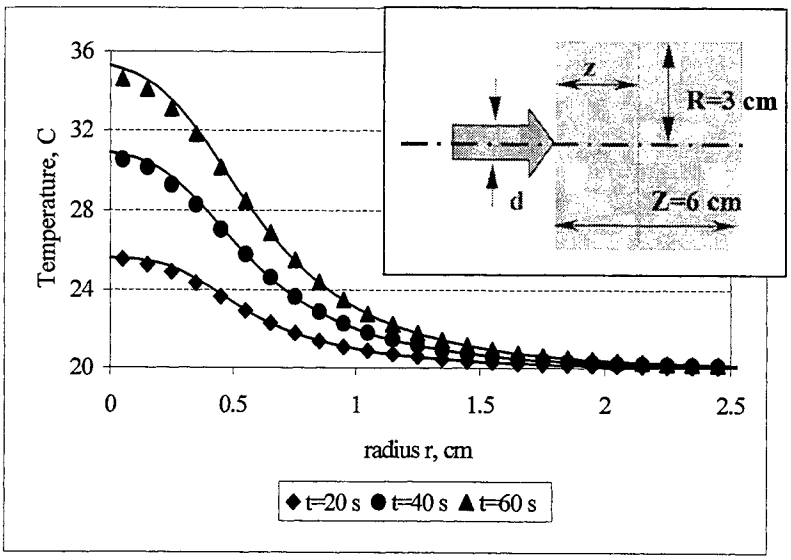


Fig.5. Temperature at 3 instant times within finite homogenous cylinder at the plane z=0.55 cm, irradiated by cylindrical monodirectional laser beam. Profile of the beam is flat, diameter d=1cm, power equals to 5 W. The frontal cylinder surface (z=0) is isolated (no heat exchange), the rest surfaces are in a contact with a medium of fixed temperature 20 °C; heat-transfer coefficient equals to 1.0 W/cm$^2$·K. At initial instant t=0 the temperature over whole cylinder was a constant (20 °C). Substance parameters are: $\mu a$= 0.2 cm$^{-1}$, $\mu s$= 50.0 cm$^{-1}$, $g$=0.95, $n$=1.4, $k$=0.0048 W/(cm·K), $\rho$=1.075 g/cm$^3$, $c$=3.4882 J/(g·K). Solid lines are our calculations, points are calculations by the LITT code.

On fig. 6 we compare our numerical calculations with analytical and experimental data in a heat problem with a point heat source in infinite homogeneous medium. Measurements were performed with an original setup created by us for determination of the termophysical parameters: the specific heat capacity $c$ and the thermal conductivity $k$. A potato of size about 10 cm, was used as the medium in the experiment. An electric heat source of size about 1 mm was placed into the centre of the potato, temperature was measured by mean of thermocouples of sizes 0.3 mm. The comparisons allowed us to determine the range of source-detector distance and the time interval where the finiteness of medium and source is not significant, and it is possible to use analytical solutions in the inverse problem (determination of $c$ and $k$).

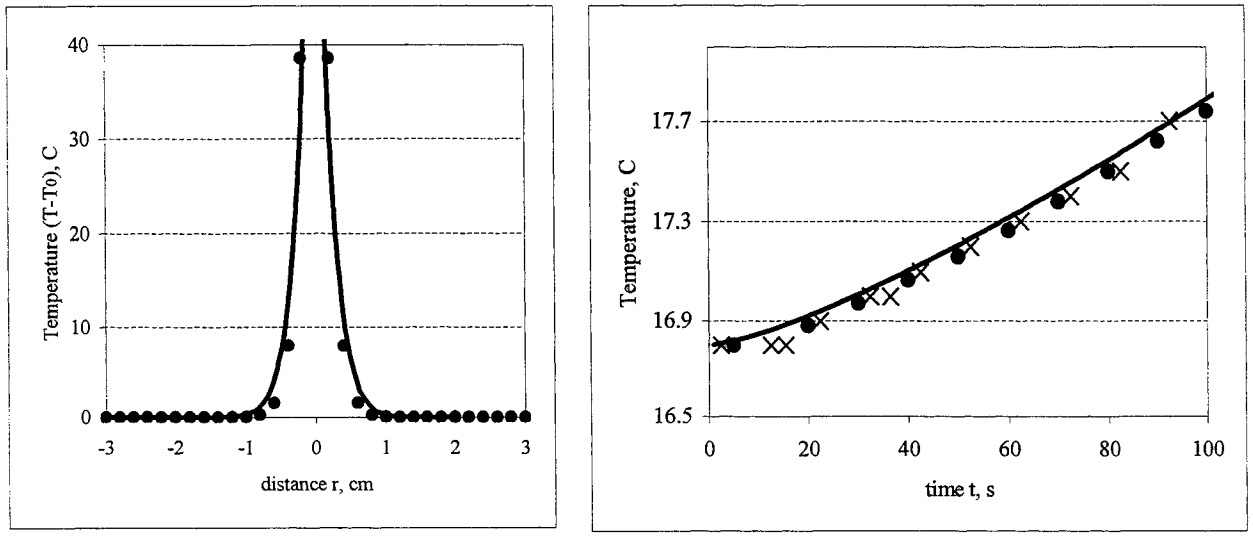


Fig. 6. Temperature in infinite homogeneous medium from a point heat source of fixed power 0.5 W. The left figure is the dependence on source distance $r$ at an instant $t$=15 s, the right one is the dependence on time at a fixed source distance $r$=0.85 cm. At initial instant $t$=0 the temperature over whole medium was a constant ($T_0$= 16.8 °C). Substance is a potato with the parameters $\rho$=1.1 g/cm$^3$, $k$=0.01 W/(cm·K), $c$=4.4 J/(g·K) (our own measurements). Solid lines are calculations, points are analytical solution, crosses are our experimental data (see text).

Some capabilities of our code are illustrated with Fig. 7, 8 where modelling results of thermal action of He-Ne laser on skin in two operating modes (continuous and pulse) are presented. The modelling of such sort allows us not only to find out the parameters of laser irradiation as a preliminary, but to study, justify, and may be reveal the effects of laser action. In particular, the presented calculations demonstrate the effect of heat localisation for the pulse operating mode in comparison with the continuous. It is interesting to note that the localisation is not accompanied by temperature increase (see fig.8).

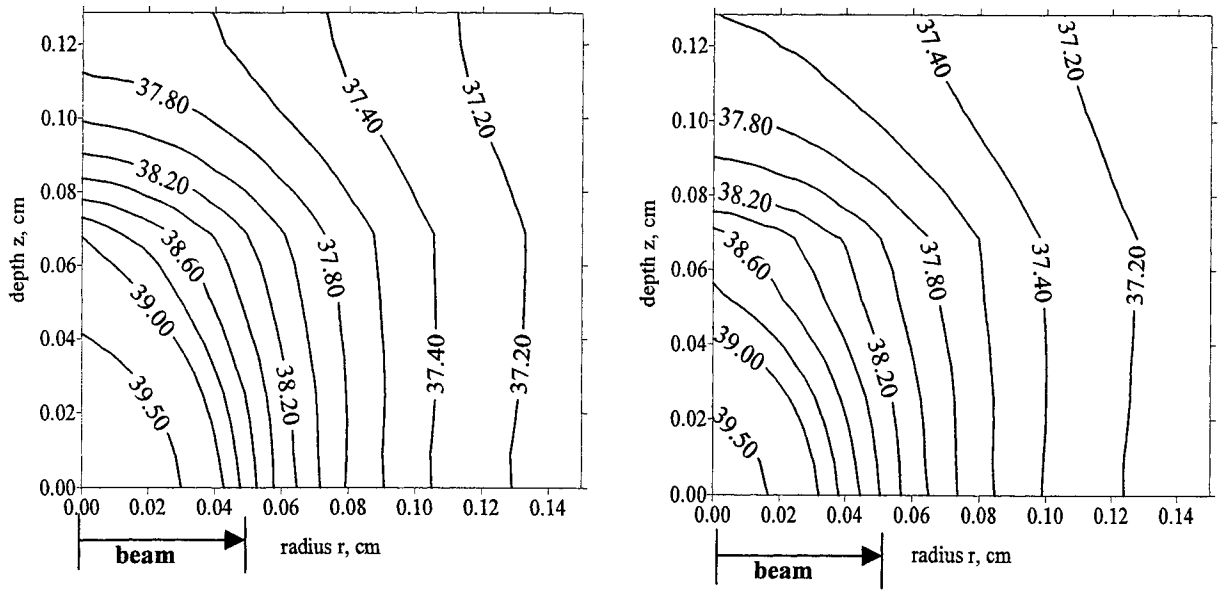


Fig. 7. Isotherms in skin irradiated by cylindrical monodirectional beam of He-Ne laser for the continuous (the left) and the pulse (the right) operating modes at an instant 1.5 s after the laser on. Profile of the beam is flat, diameter equals to 0.1cm, average power 25 mW at both modes, pulse duration 0.02 s, frequency 10 Hz. Initial temperature equals 37 °C. Heat exchange between the skin and environment is left out of account. Skin model is 4 layers one with the following parameters[5]:

| Layer | thickness, mm | $\mu_a$, 1/cm | $\mu_s$, 1/cm | $g$ | $n$ | $k$, $10^{-3}$ W/cm·K | $\rho$, g/cm$^3$ | $c$, J/(g·K) |
|---|---|---|---|---|---|---|---|---|
| 1.Epidermis | 0.065 | 4.3 | 107.0 | 0.79 | 1.5 | 2.66 | 1.6 | 3.7 |
| 2. Derma | 0.565 | 2.7 | 187.0 | 0.82 | 1.4 | 4.98 | 1.0 | 3.2 |
| 3. Blood | 0.09 | 25.0 | 400.0 | 0.98 | 1.35 | 5.30 | 1.0 | 3.6 |
| 4. Derma | 0.565 | 2.7 | 187.0 | 0.82 | 1.4 | 4.98 | 1.0 | 3.2 |

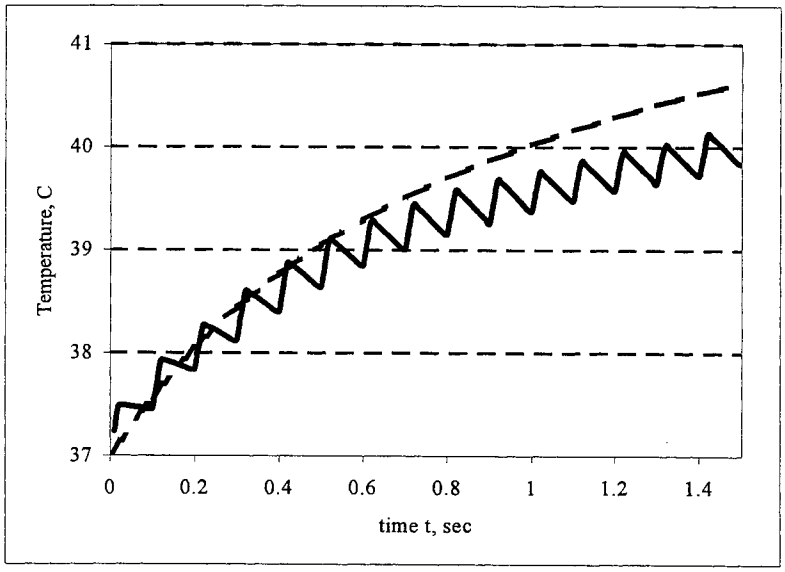


Fig.8. Time dependence of temperature at a point on frontal surface of skin on beam axis in the same problem as in fig.7. The continuous mode results are shown by dotted line, the pulse one by solid.

## 8. CONCLUSION

There are many cases where the presented code is useful. It allows simulation of laser surgical operations and laser procedures of thermotherapy and biostimulation, solving direct and inverse problems of the optics and the thermophysics of biological tissues. In the next code version we are going to use the accelerated local Monte Carlo estimate of radiation characteristics[9]. This estimate allows us to calculate more accurately the strongly non-uniform radiation fields. We also intend to involve more adequate models of blood flow and to apply other modifications.

## REFERENCES


1. R.A. London et. al.,"Laser tissue interaction modeling with the LATIS computer program",UCRL-LR-105821-96-3.
2. A. Roggan, G. Mueller, "Dosimetry and computer based irradiation planning for laser-induced interstitial thermotherapy (LITT)", *Laser-induced interstitial thermotherapy,* Mueller G., Roggan A., pp. 114-156, SPIE Press, Bellingham, 1995.
3. M.J. Rossacci, C.A. Di Marzio, S.C. Lindberg., "A 3-d model for laser heating of a heterogeneous turbid medium", SPIE Proc., **2970**, pp.144-155, 1997.
4. J.W. Berger, "Thermal modelling of micropulsed diode laser retinal photocoagulation", Lasers in Surgery and Medicine **20**, pp. 409-415, 1997.
5. Yu.N. Tcherbakov, A.N. Yakunin, I.V. Yaroslavskiy, V.V. Tuchin, "Modeling of heat processes in the interaction of non coagulated radiation with multi-layer tissue", *Optics and Spectroscopy,* **76(5)**, pp. 845-850, 1994 (in Russian).
6. S.M. Ermakov, *The Monte Carlo method and associated problems*, Nauka, Moscow, 1979 (in Russian).
7. L.J. Segerlind, *Applied Finite Element Analysis*, John Willey and Sons Inc., 1976.
8. L. Wang et al., *Monte Carlo modelling of light transport in multi-layered tissues in standard C*, University of Texas, M.D. Anderson Cancer Center, 1992.
9. A.V. Lappa, V.A. Kamalov, A.E. Potapov, I.E. Shipitsin, "Accelerated local Monte Carlo estimate in calculation of laser radiation fields in tissue", SPIE Proc., **3726**, pp. 151-156, 1998.

# Refractive index of biotissue and its thermal response

Hui Li,* Shusen Xie, Lei Lin

Biomedical Optics Laboratory, Department of Physics

Fujian Teachers University, Fuzhou, Fujian 350007, China

## ABSTRACT

The main significance about the refractive index of bio-tissue, its measurement methods and its thermal properties in particular are presented in this paper. Most of bio-tissue can be regarded as random dispersed medium which inhomogeous dimension is about the order of micrometers. In order to describe the optical behaviors of bio-tissue, we have to use the imaginary scattering and absorption properties. Meanwhile, an apparent index of refraction, or average refractive index has to be introduced to solve various boundary and temporal problems. Two possible measurement methods in which the experimental creativity is reflected are provided. We applied one of experimental setups to study the thermal response of refractive index of bio-tissue. Experimental results suggest that the index be temperature dependent on the process of heating. The tissues used in these experiments were porcine muscles. These measurements were taken at the 632.8nm. The index of refraction keeps stable levels ($1.364 \pm 0.001$) below 36 Celsius degrees and ($1.387 \pm 0.005$) above 60 Celsius degrees, respectively, but increases with an increase in temperature from 36 to 60 Celsius degrees. The heating and cooling procedures are irreversible in optical property of tissue.

**Key words**: bio-tissue, refractive index, optical property, specular reflectivity, thermal response

## 1. INSTRUCTION

Although the preliminary theories of light propagation in tissue have been constructed, tissue optics has not come that far [1]. On the one hand such a situation comes from the variety and complexity of bio-tissue, the effective research concepts and technical means are lacking on the other hand. One of the most important reasons, in author's opinion, is what the refractive index of tissue is. How to measure it *in vivo* and even *in vitro*? Unfortunately, these problems are neglected somewhat despite the fact that many researchers seem to rely on the inferred values of refractive index. However, it does not make no difference whether the concept of refractive index exists or not in tissue optics. In fact, some errors are often committed in the researches on optical properties of bio-tissue especially in experimental measurements so long as the refractive index is disregarded. For these reasons, the main significance about the refractive index of bio-tissue, its measurement methods and its thermal properties in particular are presented in this paper.

## 2. CONCEPT OF REFRACTIVE INDEX OF BIOTISSUE

The first definition of refractive index come from the refractive phenomena when a light beam goes through the interface between two different homogeneous transparent materials. By numerous experiments, the refractive law was discovered. The ratio of sine of incident angle and refractive angle is a constant, i.e., the refractive index if the incident material is the vacuum, independent of incident angle. Here, the definition is experienced, equivalent to the law of refraction. Based on the Huygens' principle, the refractive and reflective laws can be explained and the physical meaning of refractive index is defined as the ration of the phase speed of light in vacuum to that of the material. According to optical electromagnetic theory, the refractive index $n = \varepsilon^{1/2}$ ( $\varepsilon$ is the dielectric constant) if the material is nonferromagnetic. What is more, Fresnel equations deduced from Maxwell' theory can also show the energy distribution and phase relations of reflection and refraction. This definition is more intrinsic. And due to the last definition, the refractive index earns original meanings.

The electromagnetic theory of light encompasses wave optics, which, in turn, encompasses geometrical optics. Except for the

* E-mail: *hli@fjtu.edu.cn*

In *Laser-Tissue Interaction XI: Photochemical, Photothermal, and Photomechanical*, Donald D. Duncan, Jeffrey O. Hollinger, Steven L. Jacques, Editors, Proceedings of SPIE Vol. 3914 (2000)
1605-7422/00/$15.00

certain optical phenomena that are quantum mechanical in nature, optical electromagnetic theory provides the most complete treatment of light within the confines of classical optics. In optical conditions, biological tissues are reasonably considered to be dielectrics. Therefore, from a fundamental viewpoint, a rigorous treatment would consider the propagation of an electromagnetic wave through a spatially and temporally varying dielectric medium. However, especially for real tissues, it is clear that the task is formidable, if not totally impossible. In fact, it is a dead end because most biological tissues are turbid or inhomogeneous in celluar structures.

In the microscopic viewpoint (or cellular dimension: the same order of magnitude as the wavelength >> typical size of atom, ), $\varepsilon$ has physical meaning. Nevertheless, it is known that the scattering characteristics of tissues due to microscopic fluctuations in refractive index. Hence, $n = \varepsilon^{1/2}$ may be called micro-index, i.e., the original meaning of refractive index which has different values at different spacial points. It is almost useless for the fact that it can not tell us more except for its original meaning.

Following the various structures of bio-tissue, it is suggested that the optical complexity and particularity of bio-tissue be characteristically described by microscopic(atomic or molecular size $\sim 10^{-9}$ m), semi-microscopic(wavelength or biological cell size$\sim 10^{-6}$m) and macroscopic (interaction distance between light and bio-tissue or mean free path ($MFP$)$\sim 10^{-4}$m ) scales, respectively. According to such a viewpoint, most of bio-tissue can be regarded as random dispersed medium which inhomogeous dimension is about the order of micrometers. And a simplified model about light propagation in bio-tissue is drawn schematically from the ready-made neutron transport theory. Consequently, a concept about average refractive index comes into prominence. In other words, it is impossible and unnecessary as well to determine the refractive index in bio-tissue at original senses due to the inhomogeneous structure of bio-tissue. An alternative to describe the optical behaviors of bio-tissue uses the imaginary scattering and absorption properties. Meanwhile, an apparent index of refraction, or average refractive index has to be introduced to solve various boundary and temporal problems. This is the significant conclusion that average refractive index should be independent on the absorption coefficient, scattering coefficient and angle distribution of scattering and be as the fourth optical property of bio-tissue.

The average refractive index of tissue and its dispersive properties account for specular reflection at tissue boundaries and for the speed of light in tissue. (By the way, it should be noted the refractive index in transport equation be the "group" one. However, the difference between phase velocity and group velocity is often omitted.[7] For this reason, the dispersive properties of biotissue should be also taken seriously) . Therefore, the refractive index of tissue means the average refractive index. With the concept, the complicated problems can be transformed to simple ones and thus solved easily. At best this concept represent the macroscopic response of rather idealized tissue.

The importance of the refractive index was expounded by some researchers[2-4] based on some qualitative analysis and numerical calculations of light propagation. It can been seen that the subsurface fluence rate is strongly dependent on the refractive index. In addition, the influence of the refractive index on light and temperature distribution in laser irradiated bio-tissue has been demonstrated by a rigorous method of discrete ordinates and a finite element solution as well. The conclusions show that the presence of optical discontinuity due to an air-tissue interface forces the maximum peak intensity to move from subsurface to the surface, which leads to an increase in the total fluence rate and the temperature near the surface. By the way, at last, there is a boundary matched or mismatched problem in experimental measurement. The response of light probe in bio-tissue is a function of the refractive indices of both probe and biotissue.

## 3. METHODS TO DETERMINE THE REFTRACTIVE INDEX

Because most tissue samples are soft, optical turbid and highly scattering, previous methods of measuring the refractive index of transparent materials have to be abandoned. If possible, the only promising is the approach to utilize the *Fresnel* reflection, i.e. the total internal reflection or specular reflection methods. Howevèr, there are two obstacles. The first trouble, that is, scattering effect on the specular reflection, must be overcome. The second one, due to the soft of tissue, is how to determine the direction of specular reflection. As long as both of the problems have their answers, the refractive index is available. It is also noted that an experimental result is basically the average refractive index if the area of detecting is much larger than wavelength, that is, homogenous.

There are two ways to reach the success. One is to determine the critical angle of total internal reflection just like the method [5,6] we developed before. In principle, *Bolin*'s method [7] also belongs to the method of total internal reflection. Another is to

measure the specular reflectivity just like the method [8] introduced by ours.

The first method based on the total internal reflection. There is a theoretical core in which the amplitude of the incident light wave decays rapidly in the second medium, becoming negligible at a distance perpendicular to the interface of only a few wavelengths. Note that the mean free path (MFP), which describes the characteristic distance between scattering and/or absorption events for light in bio-tissue, is $\sim 10^{-4}$ m for most bio-tissue types, which is much longer than the wavelengths available. Therefore, when total internal reflection takes place, statistically significant scattering does not occur if tissue is used as the second medium. This conclusion has the limit of statistical homogeneity reach the characteristic macroscopic dimension just as the said above. The dependence of the internal reflectivity on the angle of incidence is measured to determine the critical angle and therefore the refractive index of biotissue.

The other method is an improved specular method in which the direction of incident light is not perpendicular to the interface but close to the critical angle of total internal reflection. That the specular reflectivity changes sharply near the critical angle implies that a high measuring sensitivity be reached easily. Another outstanding advantage is that the experimental use is particularly straightforward. We applied this experimental setup in Fig. 1, to study the thermal response of refractive index of bio-tissue. A He Ne laser at 633nm is used in experimental setup. In order to let power meter receive the specular light only, two diaphragms are applied to decrease the scattering effects. The prism provides a planar platform so as to direct the specular reflection from sample. The incident laser beam should be polarized to the transverse electric or magnetic polarization when the incident angle deviates the zero degree much more. The direction of incident laser beam depends on the refractive index accuracy of result we expected. Based on the well-known *Fresnel*'s formula, the curve of relation between refractive index and reflectivity can be obtained. From the curve it is concluded that a high accuracy can be reached when the reflectivity is near the total reflection. It is obvious that the specular reflectivity changes sharply near the critical angle of total internal reflection. This implies that a high measuring sensitivity be reached easily. However, due to the stability (5%~8%) of output of laser, the advantage of high accuracy has not been brought into full play. An optoelectronic receiver with dual-channel divider is being made.

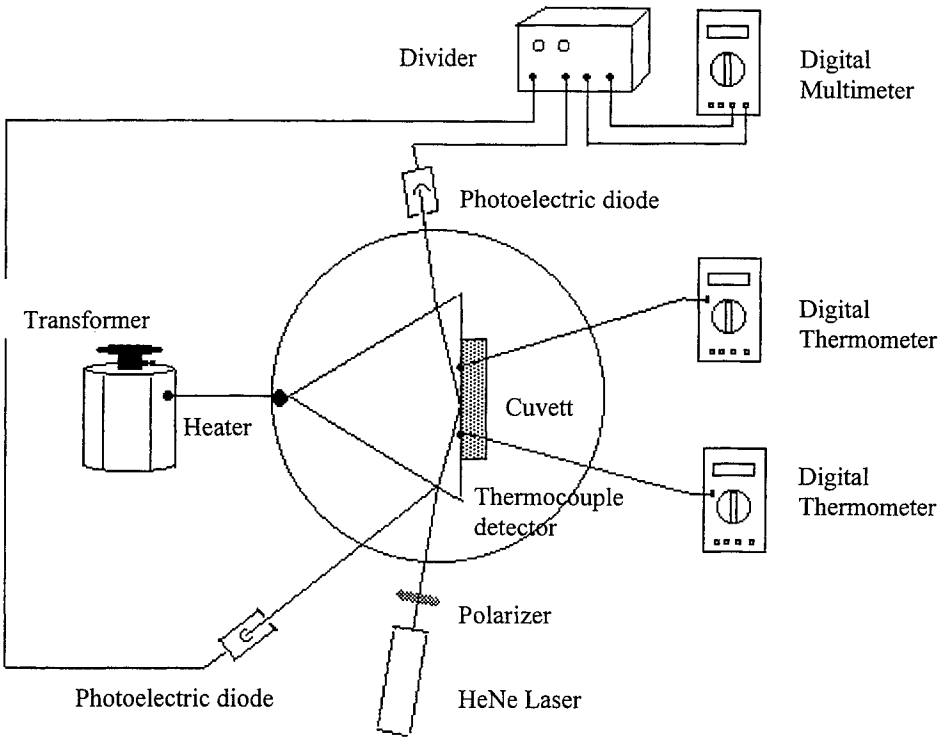


Fig.1 Schematic of the measurement apparatus for index of refraction as function of temperature

A flat heater is contacted on the prism and a tiny heat electric couple is hold between a sample and the prism. By slowly increasing the output power of the heater, the temperature of the sample and the prism as well was increased from approximately 20 to 70℃ at rates between 0.2 at higher temperature and 3℃ at lower temperature per minute. The temperature was measured with thin well-calibrated $\pm 0.2$℃. In order to have the high accuracy be brought into full play, an optoelectronic receiver with dual-channel divider is designed to compensate the stability of output of laser. Less than 1% instability was obtained by the dual-channeled divider when the output power of laser was about 10% in fluctuation. The change of refractive index of the prism is less than $10^{-6}$ approximately in the range of the temperature. Therefore, the thermal effects on the experimental system can be reasonable disregarded.

## 3. MEASUREMENT RESULTS

The tissues used in these experiments were porcine muscles. Tissue was harvested and used within 5 hours after the animals were sacrificed. Prior to usage, tissue specimens were fresh and not undergone any pretreatment.

We report the results of index of refractive measurements as a function of temperature for approximately 20 to 70℃. These measurements were taken at the 632.8nm. The index of refraction keeps stable levels ($1.364 \pm 0.001$) below 36℃ and ($1.387 \pm 0.005$) above 60℃, respectively, but increases with an increase in temperature from 36 to 60℃. During a temperature descent after heating, the evolvement of refractive index is determined by the climax of temperature reached. The heating and cooling procedures are irreversible in optical property of tissue. Such results are consistent to the biological observation and can be explained by the cellular response to temperature.

The plots comes from 4 samples with the same kind of porcine muscle tissue are illustrated in Fig. 2, which implied that the differences among different samples with the same kind be left out account.

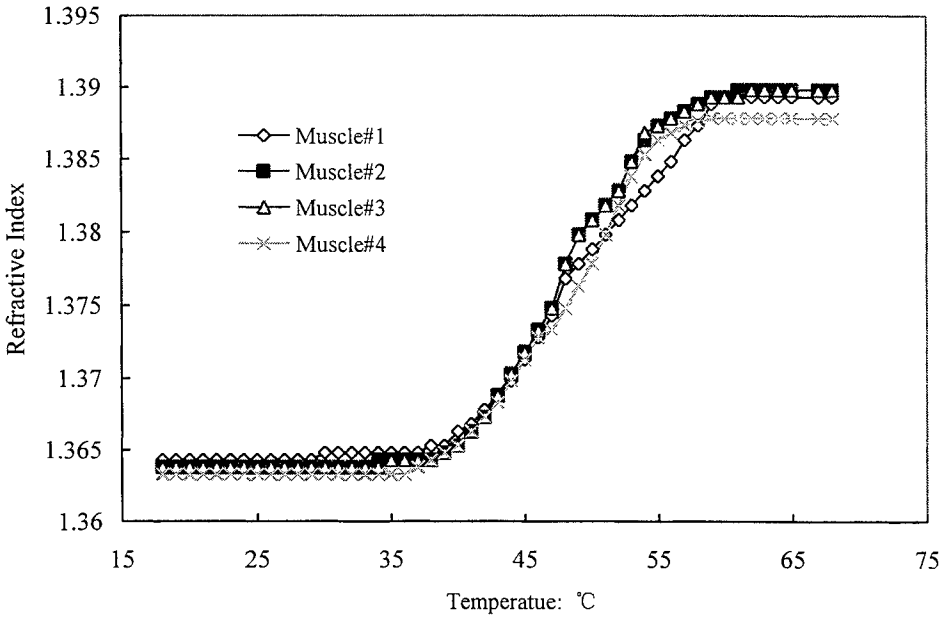


Fig. 2 Refractive indices of 4 samples of porcine muscles changed with temperature

Fig. 3 shows the plots of the refractive index of porcine muscle tissue as a function of temperature during an ascent and then a descent at different climax, respectively. As seen from these graphs, the heating and cooling procedures are irreversible. There are two stable states which imply that the micro structures of biological tissue keep rather stability below animal heat 37℃ and above 60℃ at the range of 20-70℃. It is very interesting that the irreversible procedure is consistent with the

descriptions of biological tissue heat interaction studies 8 which points out that animal heat is about 37℃ and the coagulated process begins to operate above 60℃ due to proteinic deformation. These experimental results can be explained by the cellular response to temperature.

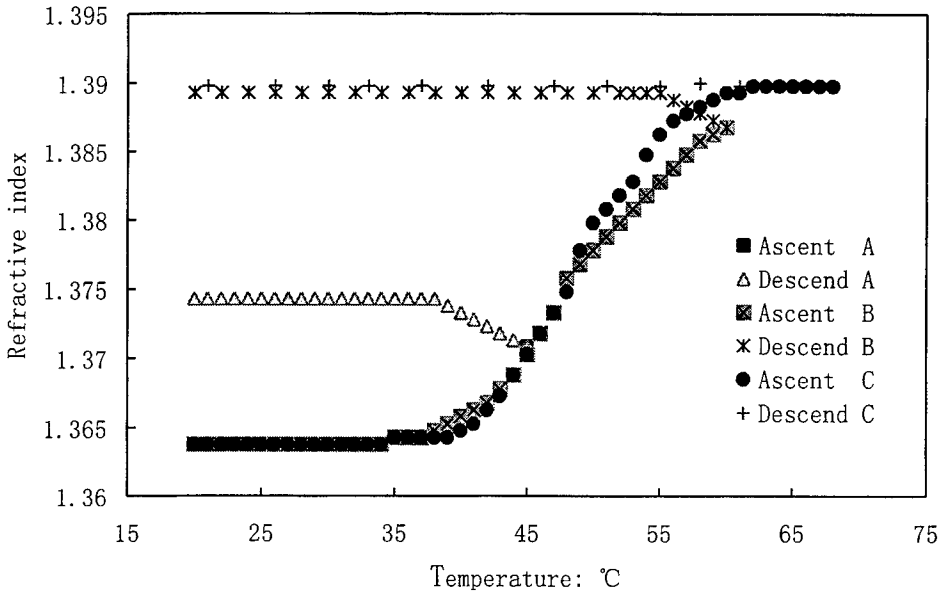


Fig.3 The plots of the refractive index of porcine muscle tissue as a function of temperature during a rise and descent at different climax, respectively.

## 4. IN CONCLUSION

We think that a concept of apparent index of refraction be introduced to tissue optics. An average refractive index can be the apparent one as the additional optical parameter of biological tissue. Among the biological tissue-laser interactions, the thermal effects play a key role. In authors' opinion, besides the dispersive relations of refractive index, the temperature properties of refractive index is the most important just for the common fact of that there is a laser-induced temperature rise during laser irradiation.

A specular reflection method is promising to study the detailed change of refractive index of biological tissue during the different conditions. We have completed the measurements of the relation between refractive index and temperature of porcine tissue. Our results suggest that the refractive index of biological tissue be temperature dependent on the process of heating. During a rise of temperature in the range of 20～70℃, the index of refraction keeps stable levels below 36℃ and above 60℃, respectively, but increases with an increase in temperature from 36 to 60℃. On the other hand, during a temperature descent after heating, the evolvement of refractive index is determined by the climax of temperature the tissue sample reached. In a word, the heating and cooling are irreversible procedures in which there are two stable states.

It is pointed out that the specimen preparations and the controls of experimental conditions are "narrow neck of bottle" on the road to learn more knowledge about refractive index of bio-tissue. In order to find conditions for optimal treatment, precise relationships between physical characteristics such as temperature and the refractive index must be further exploited for each wavelength of interest.

## ACKNOWLEDGMENTS

This work was supported in part by the National Natural Science Foundation of China under Grant No.69778029, in part by the Fujian International Cooperation of Science & Technology under Grant No. 98-I-5, and in part by the Fujian Provincial Natural Science Foundation of China under Grant No. A97019.

## REFERENCES


1. A. J. Welch and M. J.C. Van Gemert ed. Optical-Thermal Response of Laser-Irradiated Tissue, Plenum Press, New York 1995;
2. R. Anderson, H. Beck, *et al* "Pulsed photothermal radiometry in tubid media: internal reflection of backscattered radiation strongly influences optical dosimetry," *Applied Optics*, 28, pp.2256-2272, 1989.
3. M. Motamedi, Sohi Rastegar, et al,"Light and temperature distribution in laser irradiated tissue:the influence of anisotropic scattering and refractive index," *Applied Optics* 28, pp2230-2237, 1989.
4. R. C. Haskell, L. O. Svaasand, *et al*, "Boundary conditions for the diffusion equation in radiative transfer," *J. Opt. Soc. Am.* A 11, pp2727-2741, 1994.
5. Hui Li and Shusen Xie, "Measurement method of the refractive index of biotissue by total internal reflection," *Applied Optics* 35, pp1793-1795, 1996.
6. Hui Li, Shusen Xie, Yishen Qiu, "Using the focused light to determine the refractive index of materials," SPIE Proceedings, Vol. 2899:496-499, 1996.
7. F. P. Bolin, L. E. Preuss, R. C. Taylor, and R. J. Ference, "Refractive index of some mammalian tissues using a fiber optic cladding method," *Applied Optics* 28, pp2297-2303, 1989.
8. Li Hui, Lu Zukang, Xie Shusen,Lin Lei, "Measurement and accuracy analysis of refractive index using a specular reflectivity close to the total internal reflection," in Automated Optical Inspection for Industry: Theory, Technology, and Applications / SPIE Proceedings, Vol. 3558:491-497, 1998.

# Refractive index of human whole blood with different types in the visible and near-infrared ranges

Hui Li*, Lei Lin, Shusen Xie

Biomedical Optics Laboratory, Department of Physics

Fujian Teachers University, Fuzhou350007, China

## ABSTRACT

Knowledge of the optical properties of human whole blood has always been of great interest for medical applications. The aim of this study was to provide the dispersive relations of refractive index of human whole blood with different types in the visible and near-infrared ranges and other conditions. In order to overcome the scattering effect, we applied an unusual method based on total internal reflection. A focused light, a semicylindrical lens in contact with tissues and a linear CCD camera are used in the experimental apparatus. The critical angle and therefore the refractive index can be obtained from the spacial distribution of internal reflective light. A monochrometer is chosen as the light source, the chromatic dispersion curve of materials can be determined directly and quickly. A set of values has been presented that relates the refractive index to wavelength and types of whole, undiluted blood. Our results suggest that the refractive dispersions be almost the same in the visible and near-infrared ranges no matter which blood type it belongs to. In addition, the relationship can be described by Cauchy's formula.

**Key words:** refractive index, whole blood, blood type, focused light beam, semicylindrical lens, total internal reflection

## 1. INSTRUCTION

The development of methods for assessing the optical properties of biological tissue is not yet finished. So far, few of results in vivo for medical applications are available. In fact, the human data in vitro are also lack even if some methods were put forward already. How to determine the optical properties with a straight, practical and noninvasive method has been a rather difficult problem for a long time [1].

In our opinion, the possible alternate approach is a combination of the data in vitro and those of whole blood. One of the reasons is due to that the blood constitutes, together with the geometry of the tissue, the optical properties of the tissue. The main difference between a biological tissue in vivo and in vitro rests on how much of whole blood is. The former contains full of blood but the latter does not. Moreover, the properties of whole blood in vitro are reasonable considered as the same ( or at least likely to be equivalent ) to those in vivo. Therefore, as the first step, it is desired to understand all of optical properties of human whole blood in order to complete the promising approach. The spectral absorption of human blood was investigated intensively. Some attempts to explore the scattering properties had been made [2]. In addition, some researches about the scattering and absorption at 632.8nm changes due to slow heating had been done [3].

As for the refractive index of biological tissue, however, little information is obtained despite the fact that the refractive index is one of the most important optical properties of biological tissue. For example, the dispersive relation in the visible and near-infrared ranges possesses a special significance for medical application. Because most tissue samples are soft, optical turbid and highly scattering, it is a tough task to measure the refractive index of biological tissue. Perhaps for this reason, the problems with relative to the refractive index are neglected somewhat. In particular, many researchers seem to have to rely on the inferred values. A few attempts were made to improve the situation. Bolin et al [4]reviewed some attempts and put forward a method with an optical fiber with the cladding replaced by tissues. Several years ago, we developed a method based on total internal reflection to measure the refractive index of tissue[5]. And then, an improved method[6]with a focused light beam had been performed.

By the improved method we developed, it is possible to provide the dispersive relations of refractive index of biological tissue. In this presentation, dispersion measurement was made and some data of four human whole blood types are given.

* Email: *hli@fjtu.edu.cn*

In *Laser-Tissue Interaction XI: Photochemical, Photothermal, and Photomechanical*, Donald D. Duncan, Jeffrey O. Hollinger, Steven L. Jacques, Editors, Proceedings of SPIE Vol. 3914 (2000)
1605-7422/00/$15.00

## 2. METHODS AND MATERIAL

In 1995, we developed a new experimental device [5] to determine the refractive index of biological tissue, in which a collimated narrow laser beam and a semicylindrical lens in contact with materials are used. After that, some improvements were completed. Thereinto, a focused light beam is substituted for the laser beam. The method [6] is based on the total internal reflection, belonging to angle-determined approach. However, the geometry of light and the detective unit are different from the previous methods and techniques used widely. The key is to apply a focused beam incident and focused upon the surface separating the two different materials. The focused beam can not only provide the incident rays with different incident angles but also make the detective area very small so as to suit to a tiny sample. When the angles over the cone of focused beam include the critical angle of total internal reflection, total internal reflection takes place for the part of incident rays which incident angles are equal to or larger than the angle of total internal reflection. The other part of incident rays will be partly refracted into the medium with lower refractive index. Therefore, the angle distribution of reflective intensity is non-linear to that of incident focused beam in its cone. There is a turning point correspond to the critical angle of total internal reflection in the spacial distribution of reflective light. The dependence of the internal reflective intensity on the angle of incidence is directly measured by a linear CCD camera. The critical angle and therefore the refractive index can be obtained from the spacial distribution of internal reflective light.

In order to avoid the second refraction and to simplify the relation of measurement, the semicylindrical lens is used as the carrier contacted with a sample in the experimental apparatus. The material of semicylindrical lens depends on the kind of sample and the specific conditions. The care must be taken in keeping the intimate contact between the semicylindrical lens and the sample. That the interface is solid-liquid contact can satisfy the conditions very well. In addition, the focal spot formed through a lens by a point or linear source with monochromatic light must be placed on the axis of semicylindrical lens.

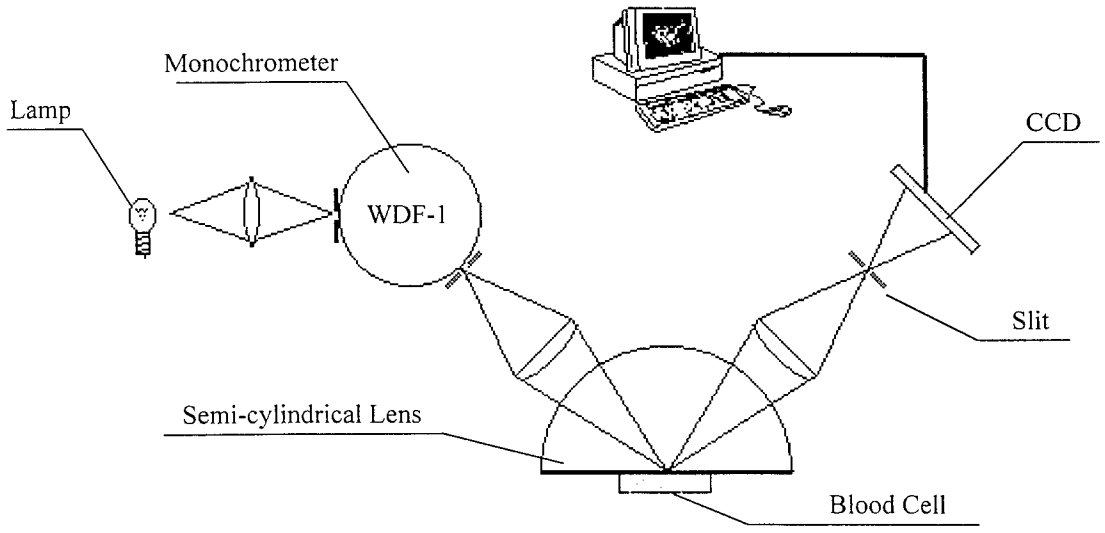


Fig.1 Optical schematic of the measurement apparatus for the dispersion of human whole blood in the visible and near-infrared ranges

Due to using the focused beam, it is possible to measure a very small sample. Also due to that, a scanner of incident angle is not needed. As a result, the mechanical structure of experimental device is very simple and reliable. Because the linear CCD camera is used as light detector, the experimental data is easily of collecting, processing and controlling by a computer. The experimental accuracy is expected to reach 0.1%-0.5%. It is by the arrangements of total internal reflection and aperture restrictor that the method can be applied to biological tissue.

If the the wavelength of light source is scanned in a spectral range, the dispersive properties of sample can be directly measured. When a monochrometer chosen as the light source, the dispersion measurements can be fast done directly. It is very important to measure directly The dispersive property of material is unable to be measured directly so far. Otherwise, the experiential dispersion formula has to be used provided that the refractive indices at several wavelengths are known. However, it should be verified if the dispersion formula is feasible or not, because the optical properties (e.g. absorption) of biological tissue are deeply depended on the wavelength.

The experimental device is very simple, as shown in Fig. 1. The systemic calibration had been made with pure water and alcohol in advance. In particular, the dispersive curve of semicylindrical lens should be carefully prepared.

The samples came from nine healthy volunteer blood donors ( Chinese, male and female ) with type A, B and O, respectively. Each type was provided by 3 of different donors. Each sample contained about 3 ml. After sampling, each blood sample was mixed with a standard anticoagulation in order to prevent coagulation. The samples were kept in the refrigerator. Prior to usage, the temperature of blood samples is at 27-28℃ approximately. The samples were routinely tested and met the regulations for transfusion, but the detailed results about the concentration of red and white blood cells, haemoglobin, platelet and other standard parameters were not available. What is more, from the name tags attached to the samples we could not distinguish the male from female. And neither do the ages of donors.

## 3. RESULTS AND DISCUSSION

We report the results of index of refractive measurements as a function of wavelength from 370nm to 850nm. The average experimental error is less than 0.01. Figs. 2-4 show the plots of the refractive dispersions of whole blood with type A, B and O, respectively. As seen from these graphs, the differences among the different donors with the same blood type are limited in the experimental error. Furthermore, it is very interesting that there is little difference among the different types. The approximate Cauchy's formula is as follows:

$$n = 1.357 + \frac{6.9 \times 10^{3}}{\lambda^{2}} + \frac{7.6 \times 10^{8}}{\lambda^{4}} \qquad (\lambda: \text{nm})$$

where $n$ represents the refractive index of whole blood, and $\lambda$ represents the wavelength. And the accuracy of $n$ is about 1.5%. That is, $\Delta n$ equals to 0.02 at most.

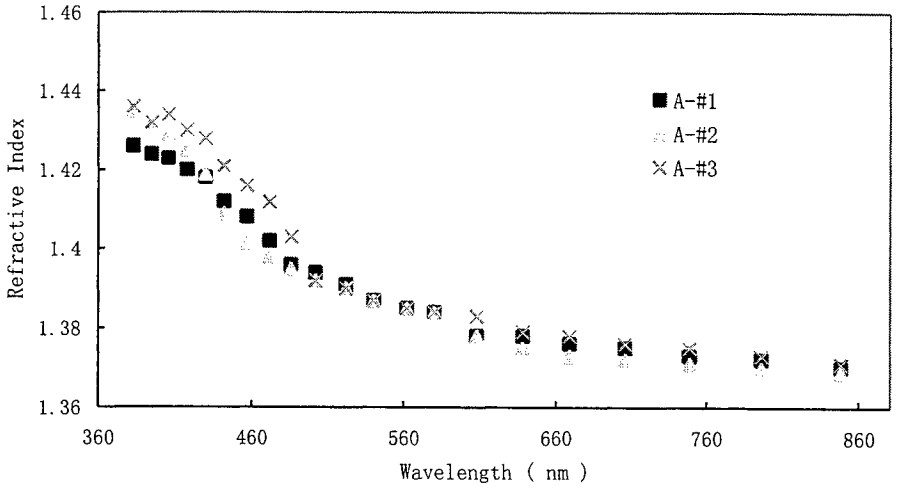


Fig. 2 The refractive dispersions of 3 healthy donors with blood type A

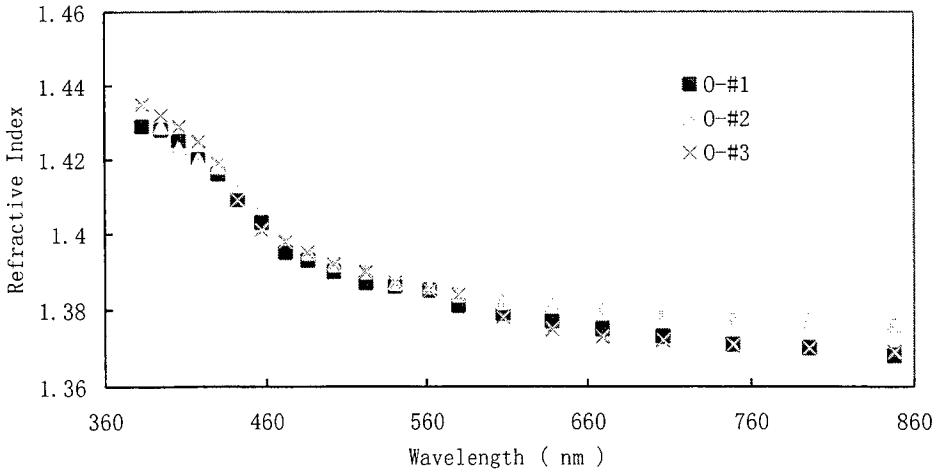


Fig. 3 The refractive dispersions of 3 healthy donors with blood type O

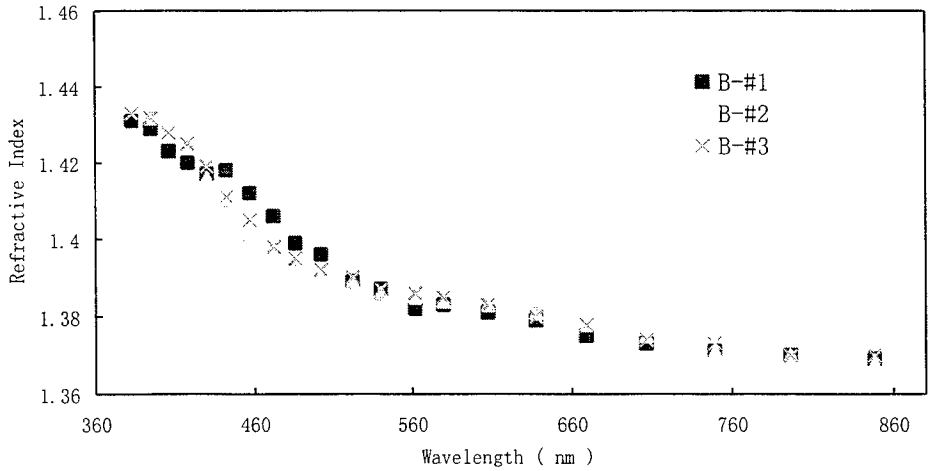


Fig. 4 The refractive dispersions of 3 healthy donors with blood type B

In order to confirm the common relationship, it seems to be worthy of a lot of measurements under different blood conditions in future. We are continuing to undergo the research work. Further results will be reported on a coming separate paper.

## 4. IN CONCLUSION

Based on the unusual method we developed, the relation between refractive index and wavelength of different blood types had been determined directly. Our results suggest that the refractive dispersions of human whole blood be almost the same in the visible and near-infrared ranges no matter which type it belongs to. In addition, the relationship can be described by Cauchy's formula.

## ACKNOWLEDGMENTS

This work was supported in part by the National Natural Science Foundation of China under Grant No.69778029, and in part by the Fujian Provincial Natural Science Foundation of China under Grant No. A990010.

## REFERENCES

1. A.J. Welch and M.J.C. Van Gemert ed. Optical-Thermal Response of Laser-Irradiatied Tissue, Plenum Press, New York 1995.
2. J. M. Steinke and A. P. Shepherd, "Comparison of Mie theory and the light scattering of read blood cells," Applied Optics 27, 4027-4033(1988);
3. Annika M. K. Nilsson, Gerald W. Lucassen, Wim Verkruysse, Stefan Andersson-Engels, and Martin J. C. Van Gemert, Optical properties of human whole blood-changes due to slow heating," SPIE Proceedings, Vol. 2923:24-34(1996);
4. F.P.Bolin et al,"Refractive index of some mammalian tissues using a fiber optic cladding method," Applied Opt 28(12): 2297-2303(1989).
5. Hui Li and Shusen Xie,"Measurement method of the refractive index of bio-tissue using total-internal-reflection," Applied Optics 35(10): 1793-1795, (1996).
6. Hui Li, Shusen Xie, Yishen Qiu, "Using the focused light to determine the refractive index of materials," SPIE Proceedings, Vol. 2899:496-499(1996).

# Light scattering model for biological tissue*

Shusen Xie, Hui Li, Lei Lin
Biomedical Optics Lab, Department of Physics,
Fujian Teachers University, Fuzhou, 350007, China

## ABSTRACT

We suggest that the optical model of a tissue is constructed by different size particles and the corresponding density in a liquid just like some phantoms of tissues. Due to the fact that the nonhomogenous dimension is about the order of several and hundred micrometers,, the Fraunhofer diffraction and process are applicable to biological tissue. We define n(r) as the number of particles per unit volume in tissue with radiuses between r and r + d r, i.e. n(r) is an unnormalized probability density function. We have verified that all of scattering properties of tissue can be obtained as long as the equivalent particle size distribution function n(r) is measured. In particular, the relation between $\mu_s$ and $S(\theta)$ is dependent on the n(r). The equivalent particle size distribution is feasible for experimental methods and techniques, as well as necessary for scattering principle. Furthermore, the equivalent particle size distribution provide not only a new understanding about the scattering properties of tissue but also a new approach to obtain the scattering coefficient and phase function. In addition, this scheme is helpful to design more precision tissue-simulating phantoms.

**Key words:** biological tissue, optical model, light scattering, equivalent particle density, size distribution

## 1.INTRODUCTION

The fundamental tasks of tissue optics are determination of optical radiation energy within biotissue under certain condition and development of methods for measuring the optical properties of tissue in vivo[1]. For the purpose, the model of light transport in tissue should be established. Although the photon transport model that is similarly to neutron transport theory should be improved, it is very helpful to solve the light profile question under the condition of optical properties of biotissue is known. However, the optical properties of tissue and methods are known limited. For the reason, we study the description of light scattering property, and introduce an equivalent particle size distribution as parameter available to describe the optical scattering properties of tissue. At the same time, the new method of measuring scattering coefficient and the phase function.

## 2.BASIC OPTICAL MODEL OF BIOTISSUE

As we well known, every practical physics problem should be changed into corresponding math model, and the valuable model must be soluble. Now, one of fundamental purposes of tissue optics is to study the light transport rule in biotissue for

*Supported by the National Natural Science Foundation of China under Grant No.69778029, and the Fujian Provincial Science Committee Subject of International Science and Technology Cooperation Plan 98-I-5.



In *Laser-Tissue Interaction XI: Photochemical, Photothermal, and Photomechanical*, Donald D. Duncan, Jeffrey O. Hollinger, Steven L. Jacques, Editors, Proceedings of SPIE Vol. 3914 (2000)
1605-7422/00/$15.00

visible and near infrared region. Because the spectrum that ranges from 600nm to 1300nm is "therapy window", the spectrum has important role for many known and potential optical therapy and optical diagnosis. It is the reason of emphasis visible light and near infrared light.

Most of biotissue are turbid, high scattering, for complex structure of biotissue. A tissue can be reasonably considered as a medium in which the formation and the physical parameters randomly change in the range of cell scale or wavelength order of magnitude. For the optical properties, the object that is described as "inhomogeneous" is refractive index, the reason of high light scattering of biotissue is the inhomogeneous of refractive index at the scale of cell. As to practical biotissue, its optical properties are difficult to describe by electromagnetism field theory. Even if all details of biotissue refractive index are available, and the existence and unique of solution are certainly, the hope of obtaining the rule of light profile in tissue by solve Maxwell equation group is limited.

Based on the properties of biotissue, neutron transport theory can be used to present a simple interaction model of light and biotissue and distract the major optical properties of tissue. In other words, the physics presence that is light transport in tissue and form a light profile can be simulated by particle transport. The quantity density of particle equals to the light energy. The assumed particles can be thought as packets of photons (independent to the nature of optics) that is equivalent to the aggregation of photons. The tissue should be thought as absorbers and scatterers distributed randomly over the volume, it is according to the structure of biotissue. The absorption coefficient $\mu_a$ , scattering coefficient $\mu_s$ and phase function $S(\theta)$ (or anisotropy factor g) can be measured by experiments to show the undulation of refractive index of tissue. The physics optics concepts such as diffraction and polarization etc. would not appear at the model, only the basic optical parameters that are measured by experiment are involved in the model. For utilizing the model in various biotissue or inhomogeneous tissue, the concept of average refractive index must be introduced. In fact, such a model has been founded, the tissue has to be represented as a liquid with absorbers and scatterers randomly distributed over the volume. The average refractive index is the refractive index of liquid. For the inhomogeneous of tissue, the basic parameter that is measured by experiment is statistical average value.

So, the Boltzmann transport equation of photon and Monte Carlo model can be implemented, and then the spatial and temporal distributions of light fluence rate and other physical variables such as reflectance and transmission are available on the light irradiation and boundary conditions. This is a rigorous method that composes the experiment and mathematic model. All of questions in tissue optics are studied on the bases.

## 3.NEW LIGHT SCATTERING MODEL OF BIOTISSUE

The annotation of tissue optical model shows the coarseness of the description of light scattering, because the light scattering phenomenon is deduced only from all the same scatterers (particles). This scheme is too simple for complicated tissues. It is easy to understand that optical properties of a tissue are determined by microscopic structures of the tissue. For this reason, we suggest that the optical model of a tissue is constructed by different size particles and the corresponding density in a liquid. In other words, the imaginative particles in a tissue are not the same kind and have a size distribution. By the way, the particles do not represent the real various cells and should be considered as an equivalent scatterers.

According to Mie scattering theory, there is an important conclusion that scattering of big particles is independent with relative refractive index of particles, the scattering can be described by Fraunhofer diffraction of circular aperture or circular

screen. The scattering cross-sectional area is double what the geometric cross-sectional area of particle is. So, in polar coordinates, for big particle with r radius and incidence of plane wave, the light intensity distribution versus angle is

$$I(\theta) = I_0 \frac{x^2}{4\pi}[\frac{2J_1(x\sin\theta)}{x\sin\theta}]^2 \tag{1}$$

where, $x = \frac{2\pi}{\lambda}r$, $J_1$ is the first-order Bessel function of the first kind.

If introduce

$$\begin{aligned} F(\theta)d\theta &= \frac{\int_0^{2\pi} I(\theta)\sin\theta d\varphi d\theta}{\int_0^{2\pi} d\varphi \int_0^{\pi} I(\theta)\sin\theta d\theta} \\ &= \frac{I(\theta)\sin\theta d\theta}{\int_0^{\pi} I(\theta)\sin\theta d\theta} \end{aligned} \tag{2}$$

where $\varphi$ expresses the rolling angle of the plane with scattering light and axis around the axis, then $F(\theta)d\theta$ represents the proportion of diffraction light flux between $\theta$ and $\theta + d\theta$ to total diffraction light flux, as the condition of diffraction light within $d\theta$ area of $\theta$. Then, $F(\theta)$ can be understood as possibility density function of angle distribution of diffraction light on the wavelength and the size of particle.

Despite of the complicated structures in biotissue, fortunately, there is evidence that an ensemble of irregularly shaped particles that are larger than the wavelength gives rise to a diffraction pattern similar to that of an ensemble of spheres whose cross-sectional areas are equal to those of the irregularly shaped particles. Therefore, due to the fact that the inhomogeneous dimension is about the order of several and hundred micrometers, e.g., the diameters of human cells within the range from blood cell about 7$\mu$m to egg 150 $\mu$m, the above Fraunhofer diffraction and process are applicable to biological tissue. In fact, the well-known strong forward-scattering patterns observed by many researchers also support this assumption. In a word, the sizes of equivalent particles of tissues are much larger than the wavelength of visible and near-infrared region.

It is necessary to emphasize the corresponding scattering cross-sectional area $\sigma$ and scattering coefficient, the reciprocal of scattering cross-sectional area is the times that a photon scattered by median within unit area. The scattering coefficient means light attenuation percentage per unit length due to scattering. For the reason, the scattering percentage per unit volume or the number of equivalent particles $n$ is the product of scattering coefficient and the reciprocal of scattering cross-sectional area, that is

$$n = \mu_s \cdot (\frac{1}{\sigma}) \tag{3}$$

If the radius of equivalent scattering particle is $r$, then the geometric cross-sectional area is $\pi r^2$, the corresponding scattering cross-sectional area is

$$\sigma(r) = 2\pi r^2 \tag{4}$$

*n(r)* is assumed as probability density function at the radius *r*, then the probability function of photon scattered by biotissue particle with radius r along unit length is

$$\mu_s(r) = \sigma(r)n(r) \tag{5}$$

Therefore, total scattering probability in the tissue can be obtained by

$$\mu_s = \int \mu_s(r)dr = \int \sigma(r)n(r)dr \tag{6}$$

We define the angular dependency of probability distribution function of scattered photon for a given wavelength and the radius *r* of equivalent particle as $F(r,\theta)$. It can be concluded from Eqs. (1) and (2) that

(7)

Therefore, for many equivalent particles with various size, the average probability of photon scattered with the angle between $\theta$ and $\theta + d\theta$

$$S(\theta)d\theta = \frac{[\int n(r)F(r,\theta)dr]d\theta}{\int n(r)dr} \tag{8}$$

where

$$S(\theta) = \frac{\int n(r)F(r,\theta)dr}{\int n(r)dr} \tag{9}$$

which is the scattering probability density function, or phase function mentioned above.

Thus, it can be concluded from Eqs. (6) and (9) that all of scattering properties of tissue can be obtained as long as the equivalent particle size distribution function is measured, and the scattering coefficient and phase function can be obtained. In other words, the meaning of *n(r)* describeds more essential scattering than $\mu_s$ and $S(\theta)$. This discovery will be helpful to correct the misunderstanding widely among literature and papers[1] in which $\mu_s$ and $S(\theta)$ are regarded as independent parameters.

## 4.DISCUSSION

The above recognizance of scattering parameters of biotissue is not only necessary for theory, but also feasible for experimental methods and techniques. There are many methods[6,7] to determine the real particle sizes and their distribution. We have measured human whole blood in elementary under available condition. The whole results of the experiment will report in other paper. The new scattering model that is presented in the paper will be discussed as follow.

(1) Due to the fact that we need here is not real particle size distribution but scattering properties, the equivalent particle size distribution should be determined by light scattering method.

(2) If the equivalent particle is of an only radius r, the scattering coefficient is simply given scattering cross-section

multiplied particle density. If the diameter of particle is D, and the volume concentration C, the scattering coefficient is 3C/D. The phase function is determined by Eqs. (2).

## 5.CONCLUSIONS

In this paper we have got the new optical scattering model of biotissue. The innovations are as follows:

(1) $\mu_s$ is related to $S(\theta)$ by Fraunhofer diffraction approximation and equivalent particle size distribution function *n(r)*, $\mu_s$ and $S(\theta)$ are correlative parameters in nature, and are unified by *n(r)*, then the scattering characteristic of biotissue is recognized;

(2) we present the new method of measuring scattering characteristic and the feasibility of designing more precise tissue-simulating phantoms.

In conclusions, the equivalent particle size distribution provides not only a new understanding about the scattering properties of tissue but also a new approach to study the scattering problem of biotissue. Base on the idea, much work of theory and experiment can be carried out.

## REFERENCES


1. A.J. Welch and M.J.C. Van Gemert ed. Optical-Thermal Response of Laser-Irradiated Tissue, Plenum Press, New York, 1995;
2. S.A. Prahl, M.Keijzer, S.L. Jacques, "A Monte Carlo model of light propagation in tissue," SPIE Institute Series IS5, pp102-111, 1989;
3. M.Born and E. Wolf, Principles of Optics (Macmillan, New York 1964);
4. H.C. Van de Hulst, Light Scattering by Small Particles (Dover, New York 1981);
5. J.R. Hodkinson,"Light scattering and extinction by irregular particles larger than the wavelength," in Elecromagnetic Scattering, M. Kerker, ed.(Macmillan, New York, 1963),pp. 87-100;
6. H.G. Barth, Modern Methods of Particle Size Analysis (John Wiley & Sons, New York, 1984);
7. Song Feijun and E.D. Hirleman, "Principle of measuring particle size distribution by laser non-imaging method," Physics, 17 (1987) 85 (in Chinese).
8. Shusen Xie, A.E. Profio, and K-H Shu, "Design of the optical phantom of tissue for photodynamic therapy research," Proc. SPIE 1616: 246-251 (1991);
9. V.P. Maltsev, A.V. Chemyshev, K.A. Sem'yanov, and E. Soini, "Absolute real-time measurement of particle size distribution with the flying light-scattering indicatrix method," Applied Optics 35(18): 3275-3280 (1996).

# Light activation of immune system. Part I. Influence on G-class antibodies

Vladimir P. Zharov*[a], Vladimir S. Gevondyan[b], Natalya M. Gevondyan†[b], Sergey A. Ermilov[a], Alla M. Volynskaya[b]

[a]Bauman Moscow State Technical Univ., Moscow, 107005, Russia

[b]Shemyakin & Ovchinnikov Institute of Bioorganic Chemistry Russian Academy of Sciences, Moscow, 117871, Russia

## ABSTRACT

The experimental evidences for photochemical mechanism of light activation of immune system are presented. The experiments were made in vitro using serums from normal blood, from blood of people with secondary immunodeficiency containing low-avidity IgG (up to 75-90%), and pure IgG buffer solutions obtained from the same serums. LED arrays and halogen lamps with narrow spectral filters from UV to IR were used as optical monochromatic sources. We have discovered that light can activate immune system by IgG transformation from low-avidity state to high-avidity one. This change has multistage irreversible character and depends on light wavelength and intensity. The estimations of optical effects were made by determination of IgG functional activity and quaternary antibody structure through the number of accessible functional protein residues in the IgG buffer solutions. Both methods showed very correlated results. Each IgG avidity transformation stage correlated with definite change of antibody spatial structure that, to our opinion, corresponds to the phenomenon pass through the several intermediate metastable forms, which are maintained by different intermolecular bonds. The bioaction spectrum of discovered effects is also presented.

**Key words:** Light, immune system, photoactivation, avidity, IgG, LED

## 1. INTRODUCTION

In the modern medicine the popularity of physiotherapeutic methods is gradually approaching the one of the traditional medical therapy. Among them the application of low-intensity lasers and LEDs of different spectral bands is very promissory. Such optical sources have been found very useful in different medical fields including dermatology, neurology, PDT of tumors, etc.[1] Nowadays an intensive development of new methods as well as an extension of low-intensity optical radiation is being made. For example, optical radiation is now used at the PDT of infectious diseases[2,3], phototherapeutic LED treatment of lymphedemas after the mastectomy[4], etc.

But many of the mechanisms of light - biological object interaction still remain undiscovered. This causes difficulties in comprehension of the observed clinical phenomena both for a biomedical engineer and for a doctor, and consequently delays the development and application of new medical equipment and methods. Moreover, in many cases the therapeutic application of optical radiation has just an empiric character, and the changes, which occur at the system and organism levels are usually the only feedback of such a treatment. It means that up to now there practically no any objective methods for the efficient control of phototherapeutic treatment. Therefore, any fundamental research concerned with the peculiarities of light - living structure interaction would have doubtlessly a great importance.

Today we have a lot of information on biostimulative action of the low-intensity laser radiation leading to the changes in the antioxidant system, stimulation of the cell membrane structure, amplification of the reparation processes in skin, neural and

* Correspondence: E-mail: zharov@mx.bmstu.ru; Telephone: 7-095-2636791; Fax: 7-095-2679893

† Correspondence: E-mail: gevond@ibch.siobc.ras.ru

In *Laser-Tissue Interaction XI: Photochemical, Photothermal, and Photomechanical*, Donald D. Duncan, Jeffrey O. Hollinger, Steven L. Jacques, Editors, Proceedings of SPIE Vol. 3914 (2000)
1605-7422/00/$15.00

bone tissues, acceleration of the trophic ulcer healing, improvement of microcirculation, tissue edema reduction, positive influence on the development of abscessed and inflammatory processes, and immunomodulative effect[5-8]. The last has been studied least, but it is very important, because the immune system affection always precedes and predetermines the development of many pathological processes in different organs and tissues.

According to the above-mentioned information, the main goal of this research was to do the experimental estimations of the influence of low-intensity monochromatic radiation on the immune system. Particularly, we've considered such influence on the structure and functional activity of G-class antibodies, which play the very important role in the pathogenesis of secondary immunodeficiencies (SI).

## 2. CRITERIA FOR THE ESTIMATION OF IMMUNITY STATUS

Choosing the method of objective control of the immune system reaction on optical radiation we have considered our recent research. This research has shown that the disfunction of antibody processing mechanisms, which are responsible for the formation of quaternary protein structure is the dominant factor in the SI development[9,10].

It is well known that antibodies interact with pathogens at earlier stages, generate immune clusters and induce a selective immune response accompanied by the developing local inflammatory processes in points of the etiotropic agents penetration, they represent a highly sensitive indicator that reflects objectively the generation of the immune response to the aggression of pathogens and other agents.

A fundamental function of antibodies is their protective activity, i.e. an ability to attract molecular and cellular natural protective mechanisms to the immune response. This function can be realised due to a specific polyvalence interaction of antibodies with the antigen, which depends on true and functional affinity of antigen-binding domains as well as owing to the antibody ability to involve molecular and cellular protective mechanisms through the effector domains in the immune response. Hence antibodies are a decisive and powerful factor of acquired immunity.

Yet, not all antigen-specific antibodies were found to have equal protective activity: some of them provide protection from pathogens, the others do not. Some antigens are specific of opsonic activity with regard to bacteria; the others do not affect phagocytosis. A similar situation is also a characteristic of infectious diseases.

Recently it has been found that some antibodies differ in their functional activity due to the peculiarities of their trinary and quaternary structure[9,10]. A new earlier unknown form of B-cell immune deficiency (ID) has been discovered. It is a characteristic of the predominating biosynthesis of G-class low-avidity antibodies unable to produce the protective effect[11-14]. This ID form occurs at early stages of the pathology evolution and precedes clinical manifestations of immune deficiency syndromes (infection, allergy, etc.)[8]. Its pathogenesis is associated rather with a dysfunction of the mechanisms of antibody posttranslation modification in the rough endoplasmic reticulum and Golgi's complex than with disorders in proliferation and differentiation processes of antigen-affine B-lymphocyte clones to plasma cells[9,15,16]. As a result of the processing in plasmacytes, the secreted antibodies acquire an optimum structure that provides not only their selective polyvalent binding with antigens but also good coupling of antigen-binding and effector domains through which effector (protective) functions of antibodies are implemented.

Disorders in the processing mechanisms in plasma cells lead to the predominating biosynthesis of low-avidity antibodies which differ from high-avidity antibodies in the availability of intermolecular interdomain bonds thus restricting the macromolecule structure dynamics[9].

Basing on the distinctions between high-avidity and low-avidity antibodies at the level of their quaternary structure, we were the first to develop a diagnostic test system that enables to identify a proportion of high-avidity and low-avidity normal antibodies in blood serum and secretions and hence to monitor objectively the activity and a disfunction degree of B-cell immunity (Patent of Russian Federation, 1999)[8-10,17]. The principle of the test system operation is based on the detection of low-avidity antibodies in the serological test after their transformation to the reactive ones.

The method given the possibility to differentiate IgG samples on their avidity has also been developed. It is based on the determination of peculiarities in the antibody quaternary structure (Patent of Russian Federation)[8-10].

The high diagnostic and prognostic significance of the information obtained by the system was established in the clinical study of patients with different ID-associated diseases (acute and chronically relapsing infections of upper respiratory tracts of viral and bacterial etiology, pollinoses, urticaria, atopic dermatitis, bronchial asthma, leukosis, tumoral diseases, hepatitis B, C, AIDS, etc.)[8]. As a rule, the acute condition of a disease was preceded by predominant biosynthesis of low-avidity antibodies, and the stage of remission - of high-avidity antibodies. At the same time, the comparative analysis of results obtained by standard methods of assessment of the state of B-system immunity proved to be less informative, creating sometimes a false notion of well-being in this part of immune system.

The avidity test has been also found a very informative and high-sensitivity tool for the estimation of therapeutic efficiency. Moreover, earlier it has been shown that the process of antibody maturation in plasma cells can be actively influenced by some immunocorrectors[16]. Under their action the secretion of high-avidity antibodies has increased with a pronounced clinical remission in patients having ID associated diseases.

It's well known that the phototherapeutic treatment of patients with chronic infectious diseases often gives the considerable positive clinical effect. So, it has been supposed that this effect could be explained either by the direct influence of optical radiation on the quaternary structure of low-avidity G-class antibodies, or by the mediated action of optical radiation through the mechanisms responsible for the formation of quaternary structure and avidity of antibodies secreted in plasma cells[16].

Therefore, in this research the influence of low-intensity optical radiation on the structure and functional activity of low-avidity antibodies secreted at the patients with SI has been studied. The main tasks of this work included: determination of the IgG avidity change in immunodeficient blood serums with dominant low-avidity antibodies in dependence on the dose of optical irradiation; detection of the similar curves for the structural change of the low-avidity IgG received from the tested blood serums of immunodeficient patients; investigation of the optical radiation wave length and intensity influence on the character of structure-functional change in the low-avidity antibodies.

## 3. MATERIALS AND METHODS

The research has been performed on the antibodies in blood serums from healthy people and patients with acute and chronically recidivous infections of the viral and bacterial etiology with apparent disorders of the cellular and humoral immunity. The sharp reduction of high-avidity antibodies up to 12-25% ( at the normal level of 80-100%) as well as the growth (up to 75-90%) of low-avidity antibodies unable to implement the protective function have been found at all the patients, independently of the nature of etiotropic agents and clinical symptoms.

Moreover, the IgG samples received from the same blood serums by the traditional methods of antibody purification[18] have been studied. The rate of low-avidity and high-avidity normal antibodies in blood serums and the functional antibody activity have been controlled before and after the irradiation using the above-mentioned test system for express diagnostics of immunodeficiencies (Patent of Russian Federation)[8,17]. The efficiency of optical irradiation has been determined basing on the percentage growth of high-avidity antibodies and their titres with the simultanious reduction of the low-avidity antibody level. The influence of optical radiation on the IgG quaternary structure and their transformation to the high-avidity state have been controlled by the quantitative analysis (using some chemical markers) of the reactive and masked functional protein residues (Patent of Russian Federation)[9,10]. The latter become reactive as a result of the breaking of additional nonvalent bonds in the low-avidity antibodies. The method of this analysis is an analogue of the one developed for the investigation of multidomain proteins[19,20].

The LED array and the halogenous lamp with multifiber optical guide and installed optical filters restricted the radiation in the demanded spectral band have been used as the sources of optical radiation (Fig.1). In one case the irradiation has been performed using a part of the LED photomatrix system especially designed for the steady irradiation of rather extended superficial pathologies, including the whole human body (V.P. Zharov "Photomatrix medical systems." International notification PCT/RU99/00111 on the Russian patent from 04/10/98). The peculiarity of such a photomatrix system is the possibility to use different LED kits with definite spectral and power characteristics chosen according to the applied medical task. The influence on the immune system, the extended infectious wound treatment combined with the PDT, dermatological applications, weight photoregulation, and some others could be mentioned among those applied medical tasks. In the other case, the radiation of the wide spectral band has been delivered from the lamp to the biological sample using a multifiber light guide. The demanded spectral bands have been set by the interference and ordinary optical filters.

The additional IR optical rejector has been fixed to avoid the sample heating. The application of such optical sources has allowed to change the intensity of optical radiation in the rather wide range from 0.1 to 100 mW/cm$^2$ on the surface of up to several thousands square centimeters in the 10-20 nm spectral band.

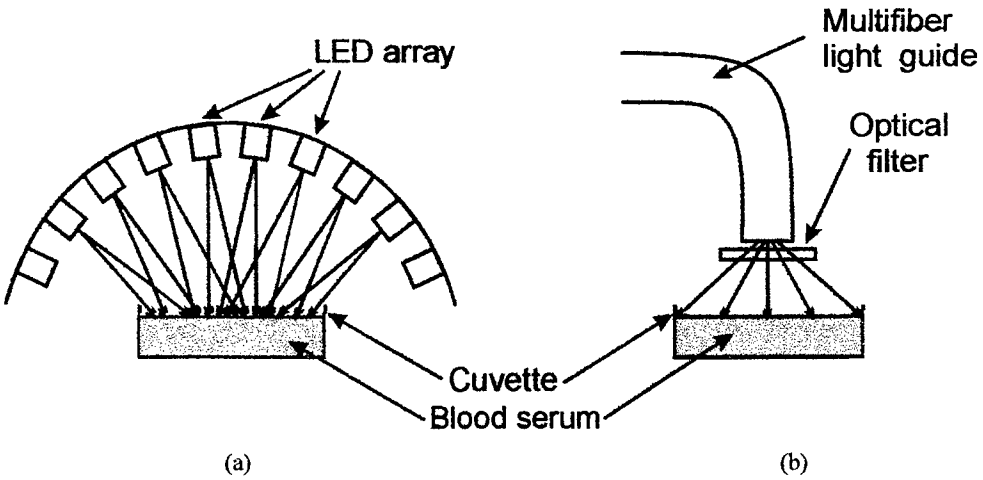


Fig.1 Two methods of the serum and IgG solution irradiation using the LED array (a) and the lamp with multifiber light guide (b).

The monochromatic optical radiation with $\lambda$ = 670 nm and $\lambda$ = 630 nm has been used at the first stage of experiments. Partly, this choice could be explained in terms of the high popularity of optical sources with spectral characteristics close to the above-mentioned in photomedicine, namely, in the laser therapy and PDT. Particularly, the He-Ne laser with $\lambda$ = 632,8 nm is often used in those medical applications.

The samples of blood serums and water IgG solutions (IgG concentration about 8 mg/ml) have been placed into the Petri dishes (hight - 10 mm, diameter - 35 mm). The transparent side surfaces of the Petri dishes have been isolated by an opaque film to avoid the undesirable lightening of the sample. The sample has been placed so that the heterogeneity of its superficial illumination was less than 7%, according to the measured spatial distribution of radiation. Besides that, a weak mixing at a magnetic stirrer has been introduced to improve the homogeneity of irradiation. A control sample placed at the same conditions, but without its irradiation has been used in the experiments for the proper comparison. During the irradiation of investigated sample (volume - 3 ml) a small part has been periodically taken for the analysis. It is should be noticed that in the visible spectral range the sample was enough transparent that has been confirmed by the spectrophotometric measurements of the IgG absorption (Fig.2). The strongest absorption, as it can be assumed, appears in the UV interval.

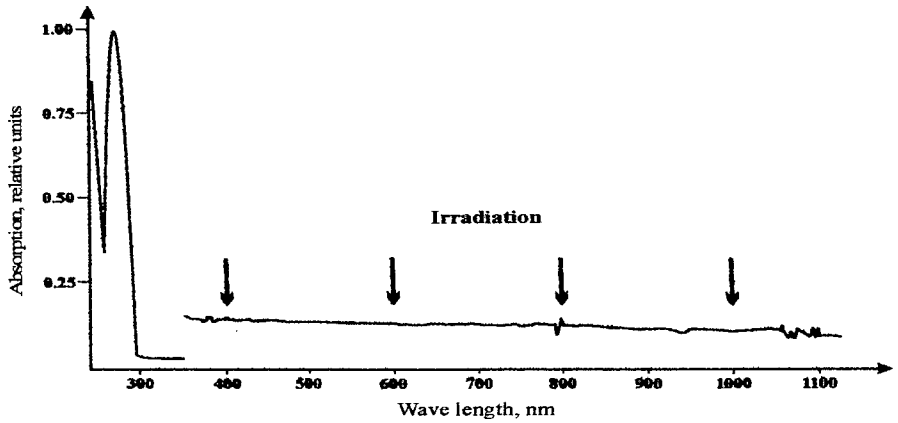


Fig.2 IgG absorption spectrum in the water solution. Ultraspec 2000 (Pharmacia) spectrophotometer. IgG concentration - 0,5 mg/ml. To improve the resolution of absorption the sensitivity of recorder was adjusted at the 350-1100nm wave length band.

## 4. EXPERIMENTAL RESULTS

The first task of research was to obtain the kinetic dependence showing the change of antibody avidity in blood serums and low-avidity IgG water solutions as a function of irradiation time. The irradiation has been done by the monochromatic light with relatively low intensity, when the obvious thermal effects could be eliminated. For example, one of the measured functions is shown at the Fig.3.

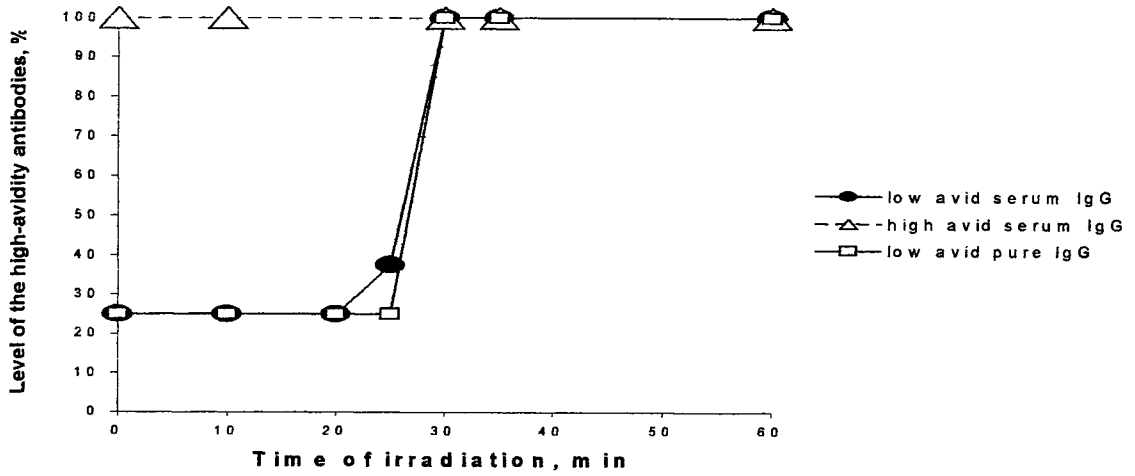


Fig.3 Dependence of the average antibody avidity on the time of their irradiation with LED matrix in the blood serums and IgG water solutions with different initial avidity.

It can be seen that in case of the low initial antibody avidity the progressive growth of high avidity antibodies from 12-25% to 100% with the simultanious reduction of low-avidity antibodies from 75-85% to 0% takes place during the irradiation. It is important to notice that the irradiation of both blood serums from healthy donors and high-avidity IgG solutions received from these serums hasn't led to any functional antibody change under the same conditions and parameters of radiation. The data presented at the Fig.3 are the average dependences, which have been found at the preliminary stage of research with few detected points. The more detailed investigation of the phenomenon/irradiation time dependences let us discover that the transformation of low-avidity molecule status to the high-avidity one has several clear stages with rather sharp transformation bounds (see Fig.4a). The same picture of multistage activation has been discovered during the irradiation of low-avidity IgG obtained from the serums. The increase of accessibility of functional protein residues to the chemical markers during the irradiation of low-avidity IgG solutions was the evidence that the antibody structural change strongly correlated with the change of their functional activity (Fig.4b). As it's turned out the results of the measurements of antibody avidity in blood serums coincide, limited to the experimental error, with the ones in IgG samples. It is an additional proof that in these experiments namely IgG are the target of optical radiation.

Later on it is proposed to name the time demanded for 100% transformation of low-avidity antibodies to the high-avidity state as the time of photoactivation $\tau_A$.

The next step has been the investigation of $\tau_A$ dependence on the irradiation intensity. The lamp with a kit of calibrated optical filters has been used in these experiments. Some of the experimental results presented at the Fig.5 for several values of intensity show that the parameter $\tau_A$ reduces with the increase of radiation intensity. The same results have been also found for the other spectral intervals.

As it seems to us, in this case it is more visual from both physical and biological points of view to use a reverse parameter $\eta = \tau_A^{-1}$, named the rate of photoactivation, instead of $\tau_A$. The dependence of $\eta$ and $E_f = \tau_A * E$ (power of photoactivation) on the intensity of irradiation (E) is considered at the Fig.6 to compare the character of the found phenomenon at the two close wave lengths. It can be seen from the diagram that in case of $\lambda = 630$ nm the phenomenon approaches the satiation whereas

at $\lambda = 670$ nm it constantly increases. It is evidently connected with the different mechanisms of the phenomenon realization even at the two close wavelengths.

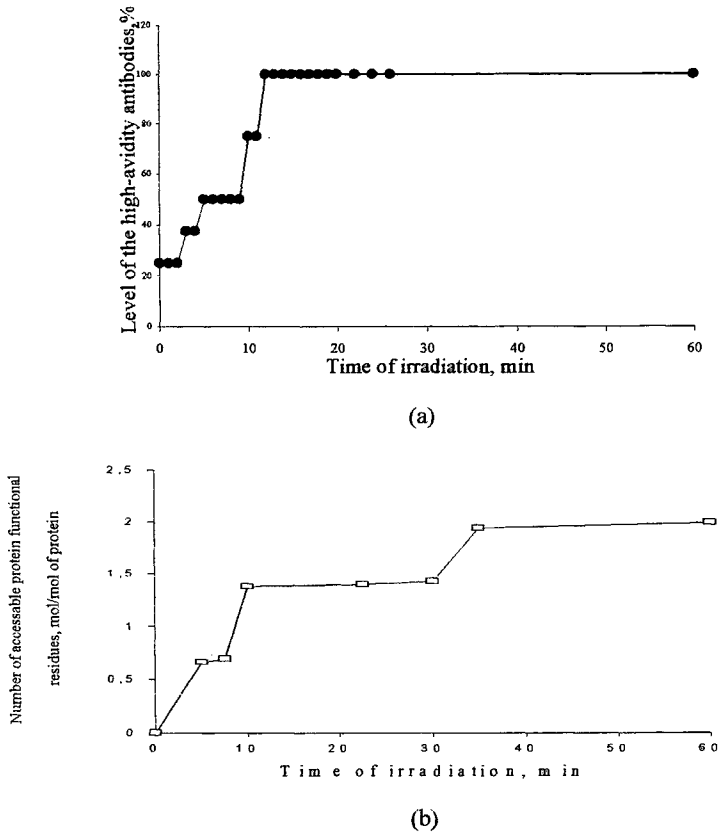


Fig.4 Time-dependent photoactivation of low-avidity antibodies. Functional serum IgG activation (a). Pure IgG structural change (b).

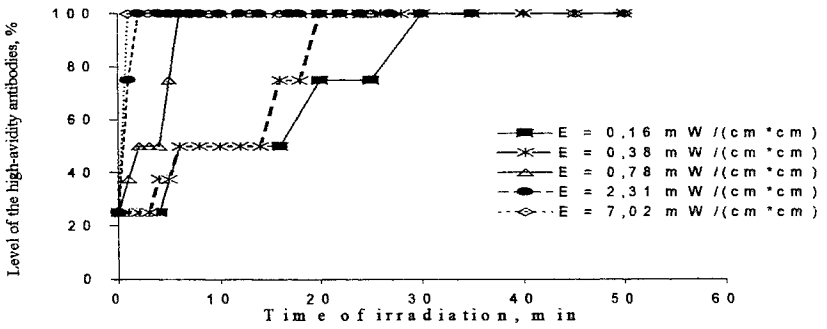


Fig.5 Change of the level of high-avidity IgG in serums of patients with SI irradiated at different light intensity. $\lambda = 630$ nm $\pm$ 15 nm.

The next task was the estimation of the found phenomenon of low-avidity antibody transformation to the high-avidity state at different spectral bands. As it has been already mentioned, these spectral bands were set by the optical filters fixed at the tip of the light guide. The spectral characteristics of these filters are shown at the Fig.7. because of the rather wide spectral widths of the filters, the bioaction spectrum is revealed as a gistogram where only the wave lengths at the maximum of

radiation are pointed. All the data are normalized at the same average intensity of 0.68 mW/cm$^2$ for each spectral band. The Fig.7 shows that the definite spectral selectivity of the phenomenon can be observed.

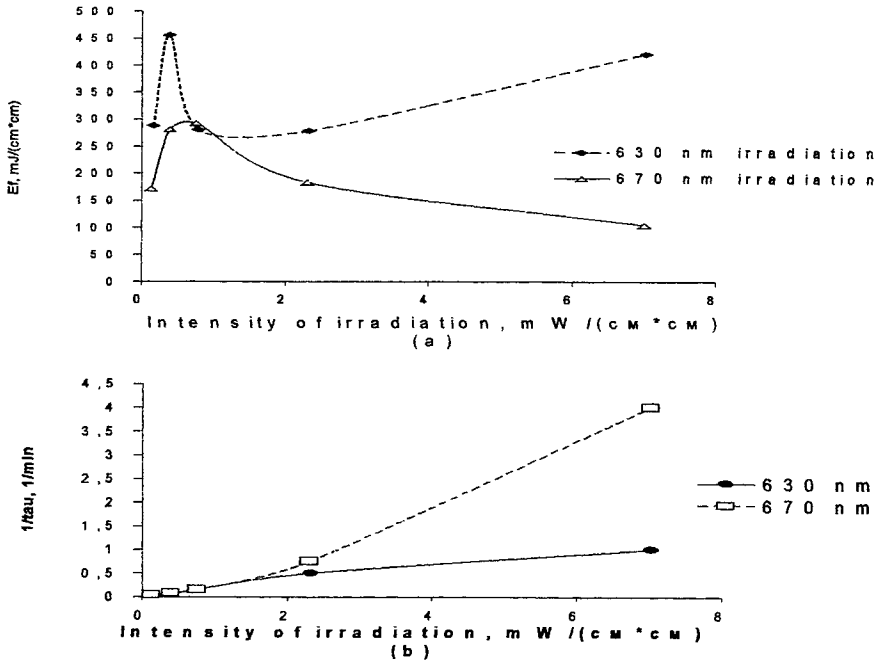


Fig.6 Dependence of $E_f$ (a) and $\eta$ (b) parameters of the low-avidity serum IgG on the intensity of irradiation.

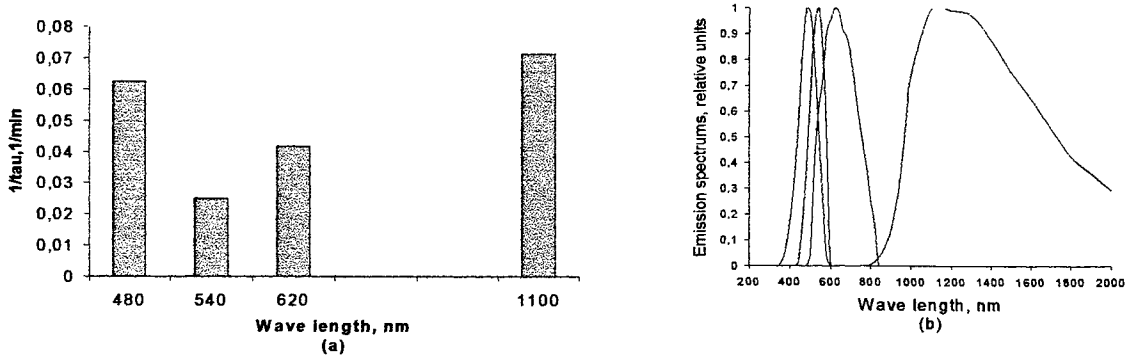


Fig.7 Bioaction spectrum (a) and spectral characteristics of the utilized optical filters (b).

## 5. DISCUSSION

The investigation of blood serums from healthy people predominantly containing high-avidity antibodies and high-avidity IgG water solutions received from these serums has shown that low-intensity optical radiation doesn't lead to any essential structural change of the antibodies. Namely, such an affection doesn't change the accessibility of the protein functional residues to the chemical markers, doesn't influence the avidity, functional affinity and antibody protective properties. This fact evidences that the quaternary structure of high-avidity antibodies is tolerant to the low-intensity optical radiation.

The investigation of blood serums from patients with acute and chronically recidivous infections of viral and bacterial etiology with the sharply reduced level of high-avidity antibodies up to 12-25% (at 80-100% of normal level) has shown

that the low-intensity (0.1-1.0 mW/cm$^2$) optical radiation induces the structural and functional change in low-avidity antibodies both at a blood serum and at an IgG water solution. The consequent selective breaking of additional nonvalent molecular bonds happens only in the low-avidity antibodies at the definite value of power of photoactivation. The latter depends on the wavelength, intensity, and time of irradiation. The selective breaking of nonvalent bonds leads to the transformation of molecule from one metastable state to another. At the last transformation the low-avidity antibodies acquire the properties of high-avidity ones. The transformation of low-avidity antibodies to the high-avidity ones has a steady and irreversible character. The irradiated blood serums and IgG solutions keep their properties for several months. The numerous irradiation of blood serums from sick people and low-avidity IgG samples at the one-time doses of optical radiation less than $E_f$, but at the summary dose greatly exceeded the one hasn't induced the structural and functional change in IgG. The multistage change of the functional protein residue accessability in addition to the multistage change of the antibody functional properties evidences that at least two kinds of nonvalent bonds with different energetic characteristics exist in the low-avidity antibodies. The identical values of $\tau_A$ and $E_f$ of the blood serums and IgG solutions let us suppose that namely the low-avidity antibodies are the direct target of optical radiation.

At the same time the other mechanisms of the phenomenon realization may probably exist in the systems containing chromophores and other photobiologically active compounds. This may be the direct absorption of optical radiation by different chromophores incorporated in the biomolecules or by the soluted substances including the same chromophores and even by the soluted oxygen. The different character of the phenomenon/irradiation time dependences at two close wavelengths of 630 nm and 670 nm evidences for the benefit of the latter hypothesis. It is supposed[5] that the direct absorption by soluted oxygen is possible at 630 nm when the redox processes are become activated and influence the conformational transformation.

Nowadays pre-clinical studies of the developed biotechnology for phototreatment of ID-associated diseases have been started. The first results have clearly shown the evident difference between the optimal parameters of optical radiation for the photoactivation of low-avidity antibodies in vitro and in vivo.

## 6. CONCLUSION

For the first time emerged possibility of the detection of effects made by the low-intensity optical radiation at the molecular level in a homogenous system has allowed to formulate the novel view in the understanding of the photoimmunocorrection mechanisms. The found phenomenon of breaking of nonvalent bonds in low-avidity IgG leading to the structural and functional change of antibodies gives a basis to consider the protein molecules as direct acceptors of optical radiation.

Thus, in this research there have been received the clear evidences of influence of optical radiation on the very important part of the human immune system responsible for the integration of the molecular and cellular mechanisms of organism protection and for the efficiency of the whole immune response. Consequently, it opens the real possibility for the development of scientifically based targeted individual procedures of immunocorrection.

It seems interesting that the found dependence of immune system on the light illumination could explain the empiric data on the immune response intensification during the sun bathing procedures from the one hand, and on its weakening at the deficiency of illumination from the other. Moreover, it can be supposed that the flu epidemics happen namely at the periods of reduction of the average daily solar illumination. For example, at the periods of great cloudiness, i.e. in the fall or spring. It may become proved that light, besides the vision, has far stronger influence on our organism, including the regulation of sleep, mood, weight and sexual behaviour[13]. In this case, one of the ways of such influence can be the interaction of light with peripheral blood and lymph through the thin skin layer, especially in the nearest IR range, where the depth of effective light penetration approaches several millimeters.

## REFERENCES


1. Edited by A.N. Chester, S. Mortellucci, A.M. Scheggi, *Laser Systems for Photobiology and Photomedicine*, p.303, Plenum Press, New York and London, 1991.

2. V.P. Zharov, D.O. Leviev, V.N. Tzarev, "Influence of the photodynamic effect on the microorganisms", *Proseed. of the II symposium on the photodynamic therapy,* Moscow, Russia, 1999.

3. V.P. Zharov, A.S. Latyshev, D.O. Leviev, "Photomedicine with laser drug delivery technologies", *Proceed. SPIE in Novel Laser Methods in Medicine and Biology*, **3829**, pp.141-154, 1999.

4. V.P. Zharov, A.S. Latyshev, "Laser combined medical technologies from Russia", *J. Laser Application*, **11**, #2, pp.80-90, 1999.

5. T. Karu, "Primary and secondary mechanisms of action of visible to near-IR radiation on cells", *J. Photochem. Photobiol.*, **B: 49**, pp.1-17, 1999.

6. V.S. Gevondyan, N.M. Gevondyan, I.S. Muzyka, A.M. Volynskaya, S.A. Ermilov, V.P. Zharov, "Enhancement of IgG antibody protective activity by low-intensive optical radiation", *Proceedings of VII International Conference and Scientific Discussion Club "New Information Technology in Medicine and Ecology"*, pp.121-123, Ukraine, Crimea, Gurzuf, May, 31-June 11, 1999.

7. V.S. Gevondyan, S.A. Ermilov, N.M. Gevondyan, A.M. Volynskaia, V.P. Zharov, "Influence of low intensive optical radiation on humoral immunity", *Biomedical Radioelectronics*, #5, pp.32-35, Moscow, Russia, 1999.

8. N.M. Gevondyan, V.S. Gevondyan, V.P. Zharov., I.B. Trofimova, N.A. Didkovsky, I.K. Malashenkova, A.M. Volynskaia, S.A. Ermilov, T.B. Kasatova, "Test System for Express Diagnostics of Secondary Immunodeficiencies. Alternative Ways of Immunocorrection, Methods and Equipment", *Seminar Presentation of scientific and Technical Innovation Projects. Biotechnologies-99*, pp.68-69, Pushchino, Russia, 1999.

9. N.M. Gevondyan, V.S. Gevondyan "Structure-functional particularities of antibody G class: in the rate and at pathology", *Proceedings in: IV International conferences and Scientific Discussion Club: New Information Technology in Medicine and Ecology*, pp.121-123, Gurzuf-Crimea-Ukraine, 1998.

10. V.S. Gevondyan, N.M. Gevondyan, "New Approaches to Conformational Dynamic Changes in the IgG Molecule and Functional Activity of Secreted Antibodies G-class", *The Protein Society Second European Symposium*, **6**, supl.1, 353, p. 104, Cambridge, April 12-16, 1997.

11. V.S. Gevondyan, N.M. Gevondyan, "A Novel type of immunodeficiency for B-lymphotropic retrovirus infection", *Abstract in FASEB journal. Experimental Biology '97*, **11**, #3, A535, p.3098, New Orleans, 1997.

12. V.S. Gevondyan, N.M. Gevondyan, "Diagnostics and pathogenesis of secondary immunodeficiency and associate with them diseases", *Works IV International conferences and Discussion Scientific Club: "New information technologies in medicine and ecology"*, **1**, pp.190-192, Ukraine, Crimea, Yalta-Gurzuff, 1998.

13. R.E. Efendiyev, N.M. Gevondyan, V.S. Gevondyan, "Suppression of B-System Immunity Induced by Exogenic Lipid Peroxides", *FASEB journal*, **10**, #3, p.20, 1996.

14. V.S. Gevondyan, N.M. Gevondyan, "Ecological Stress and Functional Deficiency of the Immunity B-System", *FASEB journal*, **10**, #3, p.742, 1996.

15. I.S. Muzyka, N.M. Gevondyan, V.S. Gevondyan, "The Efficiency of Posttranslational Modification in Plasmic Cell and Avidity of Antibodies", *The Protein Society Second European Symposium*, **6**, sup.11, 141, p.68, Cambridge, April 12-16, 1997.

16. V.S. Gevondyan, N.M. Gevondyan, "Role of the antibody processing disfunction in the pathogenesis of secondary immunodeficiences and the associated diseases. The ways of immunocorrection", *V Russian national congress "Man and Medicine"*, p.556, Moscow, Russia, 1998.

17. V.S. Gevondyan, N.M. Gevondyan, "Avidity of Secreted Antibodies - Indicator of the Functional Activity and the Suppression Level of the B-cell Immunity", *Protein Folding and Design*, p.70, National Institutes of Health, Bethesda, Maryland, 1996.

18. M. Page, R. Thorpe, "IgG Purification", *Methods in Mol. Biol. Immunochemical Protocols*, Edited by J.D.Pound, **80**, pp. 98,100, 1998.

19. N.M. Gevondyan, A.V. Grinberg, V.S. Gevondyan, "The study of structure-functional organization features in the pig kidney Na,K-ATPase at different conformational states", *Annals of the N.Y.Academy of Sciences*, pp.364-367, 1997.

20. N.M. Gevondyan, V.S. Gevondyan, E.E. Gavrilyeva, N.N. Modyanov, "Analysis of free sulfhydryl groups and disulphide bonds in Na,K-ATPase", *FEBS Letters*, **255**, №2, pp.265-268, 1989.

# Formation of Nitric Oxide under action of UV and visible light on S-nitrosocompounds

Ivan Stepuro*[a], Raisa Adamchuk[a], Slavomir Anufrik[b], Vitaly Stepuro[b], Sergey Maskevich[b]

[a]Institute of Biochemistry, Grodno, 230017, Belarus

[b]State University of Grodno, Grodno, 230023, Belarus

## ABSTRACT

It has been shown that NO is released under the exposure of the aqueous solutions of S-nitrosocompounds as well as blood plasma proteins and whole blood of healthy donors to UV and visible light. The NO release from degrading S-nitrosocompounds was monitored both spectrophotometrically (by nitrosohemoglobin formation) and using the quenching of pyrene fluorescence by nitric oxide. In addition to NO, thyil radicals which dismutate to disulfides, were formed under anaerobic conditions. In the presence of oxygen, peroxide compounds, cysteine acid derivatives and S-nitrocompounds are formed apart from disulfides, and NO is mainly converted to $NO_2^-$. It is suggested that NO releasing under the action of UV and visible light from physiological depots induces vascular relaxation, which enhances the blood flow.

**Keywords:** S-nitrosoglutathione, S-nitrosocysteine, NO, UV and visible light, nitrite, nitrosohemoglobin, methemoglobin

## 1. INTRODUCTION

Nitric oxide has recently been recognized to have important physiological roles as vascular regulator[1] in neuronal communication[2] and in nonspecific defense against bacterial infection by macrophages.[3]

There are physiological depots of NO in organism. They are, first of all, S-nitrosothiols and S-nitrosoproteins[4], dinitrosyl complexes with Fe(II) ions and glutathione molecules[5], and possibly nitrosyl complexes with Fe cations of hemecontaining proteins, such as hemoglobin (Hb), mioglobin (Mb)[6].

One of physiological effects of visible irradiation is relaxation of blood vessels. This effect resembles the vessel relaxation under endothelium-derived relaxing factor (EDRF) and depends on the presence of NO donors. S-nitrosothiols and S-nitrosoproteins, which dissociate under UV irradiation to release NO, are supposed to play a role of photosensitive donors[4]. Nitroso-Hb can be a possible compound releasing NO under exposure to visible light. The authors had shown that irradiating nitrosohemoglobin (HbNO) by the light of HeCd laser the complex is dissociated to produce free NO which can be responsible for the beneficial therapeutic effect[6].

Our work was initiated to demonstrate that under action of UV an visible light S-nitrosocompounds and particularly S-nitrosoproteins dissociate and produce NO in anaerobic conditions and NO derived reactive intermediates in the presence of oxygen.

## 2. METHODS

S-nitrosogluthione (GSNO) and S-nitrosocysteine (CysNO) were synthesized as reported by Saville.[7] Briefly, a reaction mixture containing glutathione or L-cysteine was incubated with an equimolar amount of sodium nitrite under acidic conditions (pH=2.0) for 15 min. To the reaction mixture NaOH was added to give a final pH of 7.5. The concentration of RSNO was determined spectrophotometrically at 545 nm ($\varepsilon$=13.0 $M^{-1}$ $cm^{-1}$).[8]

S-nitrosocompounds (S-nitrosothiols and S-nitrosoproteins) were also obtained under the action of ultrasound (880 KHz, 2.0 $W/cm^2$) on aqueous solutions of low-molecular-weight thiols and proteins (human serum albumin, Hb) respectively. The formation of S-nitrosocompounds were recorded spectrophotometrically[9].

* Correspondence: Email: stepuro@grsu.unibel.by

In *Laser-Tissue Interaction XI: Photochemical, Photothermal, and Photomechanical*, Donald D. Duncan, Jeffrey O. Hollinger, Steven L. Jacques, Editors, Proceedings of SPIE Vol. 3914 (2000)
1605-7422/00/$15.00

Hydrogen peroxides as well as glutathione and cysteine peroxides were measured spectrophotometrically using catalase[10]. The concentration of $NO_2^-$ was determined with the use of the Griess reagent[11] from a calibration curve with standard $NO_2^-$ concentrations. The number of sulfhydryl groups in the thiol solutions after the exposure to ultrasound were recorded with the Ellman's reagent using the molar extinction coefficient ~13600 $M^{-1}cm^{-1}$.[9] The NO release observed in photochemical degrading S-nitrosocompounds was controlled by pyrene fluorescence quenching or nitrosohemoglobin formation[12,13]. To detect NO the desaturation device shown in Fig.1 was used.

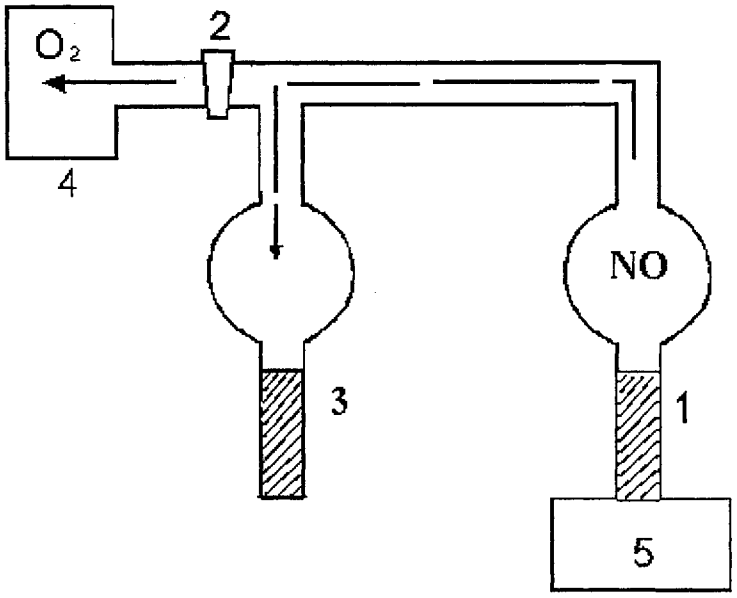


Fig. 1. Scheme of evacuated device for spectrophotometrical registration of NO. It consists of rectangular glass cuvette (L=1 cm) (1); valve, connecting the evacuated device either with forvacuum pump or with atmosphere (2); glass cuvette (L=1 cm) (3); forvacuum pump (4); magnetic mixer (5). After the air removal the evacuated device was placed into spectrophotometer sample-holder with built-in magnetic mixer.

Aqueous solution of S-nitrosocompound (1- 10 μM) was located in glass cuvette (1) and oxyHb in phosphate buffer (pH 7.0, 0.05 M) -in cuvette (3). Then using forvacuum pump air was removed changing the pressure from atmospheric to 0.2 torr. Photochemical reaction was initiated by the action of UV-VIS radiation on compound in cuvette (1). Nitrogen (λ=337 nm) and argon ion (λ=514 nm) lasers were used as light sources.

The release of NO was controlled also by pyrene fluorescence quenching. In this case pyrene solution in buthanol was located in cuvette (3). Fluorescence spectra were recorded using SFL spectrofluorometer (Solar, Belarus). The single-photon-counting decay instrument[14] was used to measure fluorescence lifetimes. Samples were excited by flash lamp pulses with a typical duration of 1 ns. Nonlinear least squares method with the Marquardt algorithm was employed for fluorescence decay data analysis[15].

## 3. RESULTS

After the exposure of the aqueous solutions of glutathione or cysteine to ultrasound, we observed a new band with a maximum at 340 nm in the absorption spectrum and a weaker absorption band at 540 nm (Fig.2). The absorption spectrum was identical to the spectrum of S-nitrosothiols resulting from chemical synthesis.

Under the action of UV-VIS irradiation fast degradation of GSNO was observed (Fig. 3). The photolysis of S-nitrosocompounds was accompanied by release of NO and a formation of thyil radicals which subsequently dismuted to disulfides. The concentration of NO, recorded shectrophotometrically by the production of HbNO (Fig.4), coincided with the amount of degraded S-nitrosothiols.

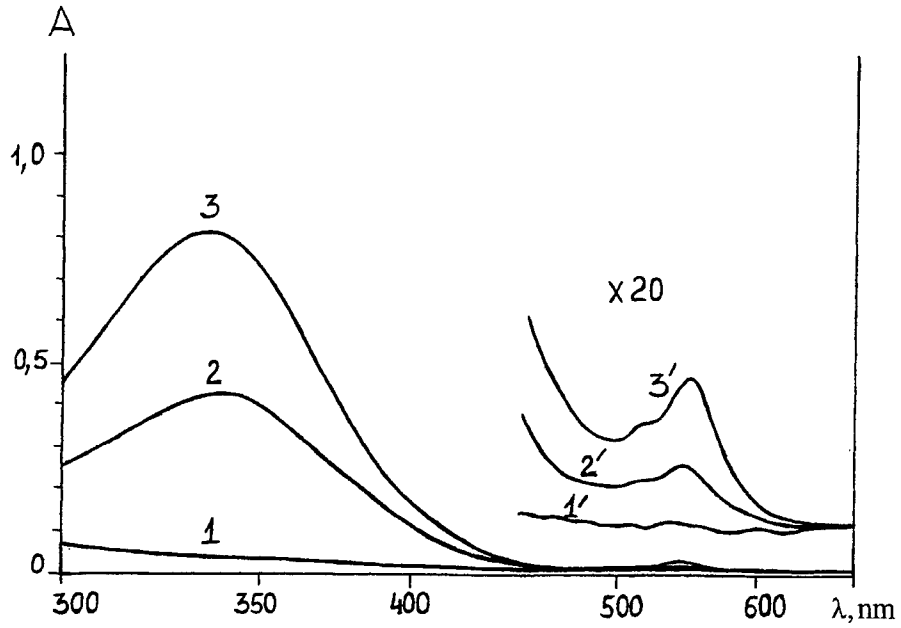


Fig. 2. Absorption spectra of glutathione (1,3) and cysteine (2) in aqueous solutions after the exposure to ultrasound in nitrogen (1) or air (2,3) atmosphere. Glutathione and cysteine concentrations were 10 mM. The time of the ultrasound action (880 kHz, intensity of 2 W/cm$^2$ ) on aqueous thiol solutions was 30 min.

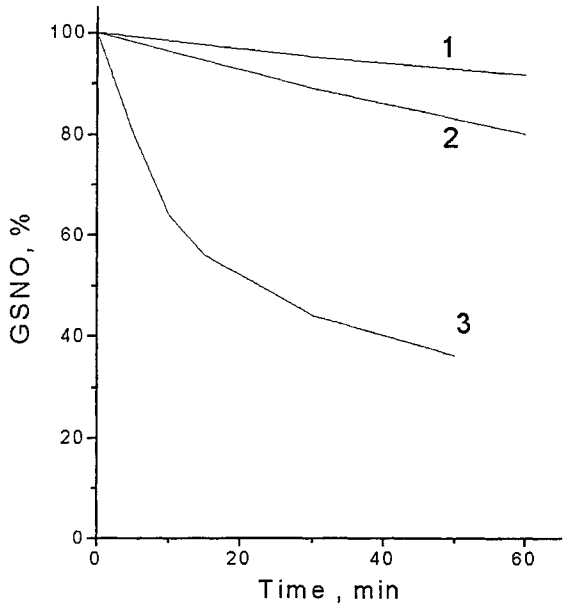


Fig.3. Kinetics of spontaneous decay of S-nitrosoglutathione in darkness (1) and photodissociation kinetics of S-nitrosoglutatione under action of visible (2) and UV-radiation (3) in vacuum. Intensity of defocused light 150 W/m$^2$

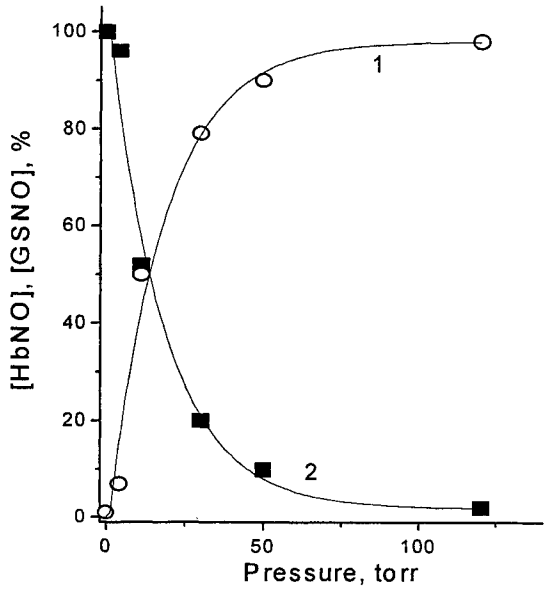


Fig. 4. Kinetics of oxiHb oxidation in metHb (1) and nitrosoHb formation from deoxiHb under action of NO (2) at differnt air pressures. NO flow was obtained under action of UV-irradiation on GSNO. Concentrations of metHb and HbNO were measured after 1 hour of irradiation of GSNO solution

We developed fast and sensitive method of NO registration, based on the property of NO molecules to quench fluorescence. It is known that fluorescence intensity depends on quencher concentration [Q] according to Stern-Volmer equation

$$I_0/I=1+k_q\tau[Q]$$

where $I_0$, I - fluorescence intensity in the absence and presence of quencher, $k_q$ -bimolecular rate constant of quenching, $\tau$ - emission lifetime in the absence of quencher.

As a fluorescent molecule we chose pyrene possessing long fluorescence lifetime $\tau \approx 300$ ns (Fig. 5.). Assuming that bimolecular quenching rate $k_q$ for NO is about $10^{10}$ $M^{-1}$ $s^{-1}$ one can easily measure the concentration of dissolved NO.

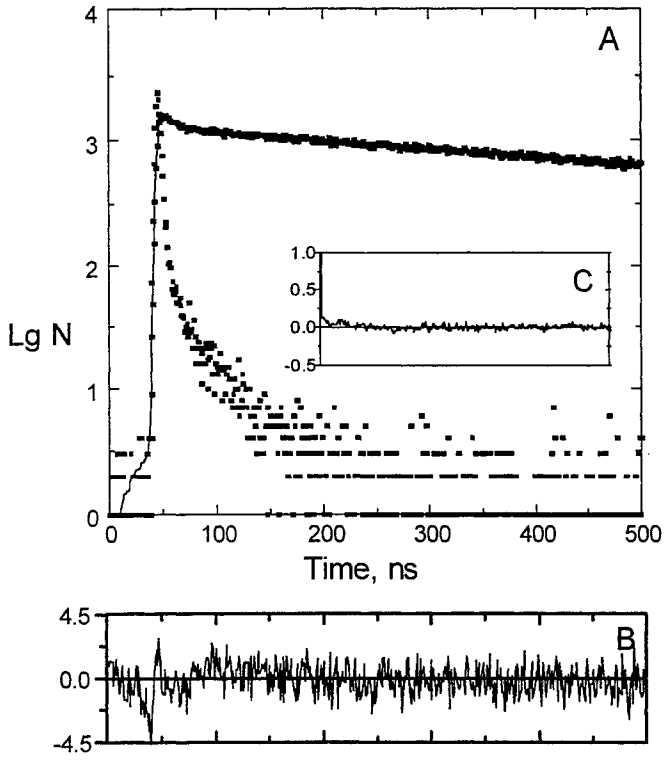


Fig.5. Fluorescence decay of pyrene ($10^{-5}$ M) in butanol. Decay lifetime is $\tau$= 307±5 ns. $\lambda_{ex}$=337 nm, $\lambda_{em}$=390 nm. A- experimental and calculated decay curve: dots correspond to experimental data, solid curve is the result of approximation with monoexponential function; B- distribution of weighted residuals; C- autocorrelation function of weighted residuals.

We showed that amount of dissolved in buthanol NO was approximately 10 times greater than in water at normal conditions and was equal to 4.0±0.5 mM.

The quantum yield of S-nitrosocompound photolysis was very high and approached to 1.0. From the results obtained it can be suggested that under anaerobic conditions the principal photodissociation process in S-nitrosocompounds is breaking of the RSNO bond to form thyil radicals and nitrogen oxide.

$$RSNO + h\upsilon \rightarrow RS^{\cdot} + NO \quad (1)$$

$$RS^{\cdot} + RS^{\cdot} \rightarrow RSSR \quad (2)$$

In the presence of oxygen, the process of S- nitrosocompound photolysis became complicated. One could see that when the partial oxygen pressure increased the NO content decreased. And since the air pressure of 75 torr NO was virtually completely converted to $NO_2$. Hence in air atmosphere nitrogen oxide is mainly converted to $NO_2$.

$$2NO + O_2 \rightarrow 2NO_2 \quad (3)$$

Molecules of nitrogen dioxide interact with each other to form $N_2O_4$, that produce in water nitrites and nitrates

$$2NO_2 \rightarrow N_2O_4 + H_2O \rightarrow NO_2^- + NO_3^- + 2H^+ \quad (4)$$

At low partial pressure of oxygen P(air)<75 torr nitric oxide can react with $NO_2$.

$$2NO_2 + 2NO \rightarrow 2N_2O_3 \quad (5)$$

The produced anhydride of nitrous acid is converted to nitrite after the interaction with water.

$$2N_2O_3 + 2H_2O \rightarrow 4NO_2^- + 4H^+ \quad (6)$$

As follows from the equations (3-4), the increase in concentration of protons is equal to the concentration of NO reacting with oxygen. The proton concentration was controlled spectrophotometrically using pH-dependent dye (phenolphthalein).

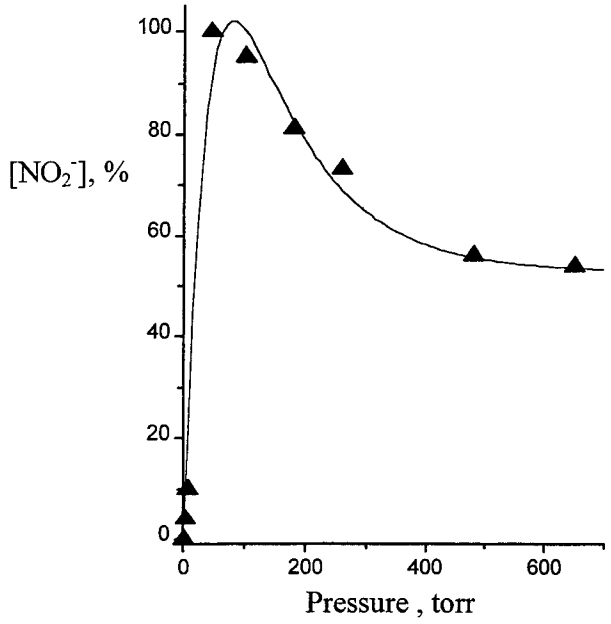


Fig.6. Efficiency of $NO_2^-$ formation at different air pressure. NO flow resulted from UV-irradiation of GSNO aqueous solution in desaturator cuvette. [GSNO] = $10^{-3}$ M. Exposure time- 1 hour.

Nitrites concentration depends significantly on NO - $O_2$ ratio (Fig.6). Maximal efficiency of nitrite formation at air pressure 80- 100 torr relates to preferrable production of $N_2O_3$, which completly transforms to nitrite (5,6). When oxygen content is higher and exceeds NO concentration only $NO_2$ formation is observed, which results both in nitrites and nitrates (3,4). This can be an explanation of nitrites yield decrease at high partial oxygen pressure (Fig.6).

In addition to the disulfide production (2) peroxycompounds, cysteic acid derivatives and S-nitrocompounds ($RNO_2$) were formed during photolysis in air (6). Probably, the thyil radicals produced in the primary photochemical reaction (1) interacted with $O_2$ and $NO_2$ and formed the following compounds

$$RS + O_2 \rightarrow RSOO \quad (7)$$

$$RS + NO_2 \rightarrow RSNO_2 \quad (8)$$

For instance, in air, GSNO exposed to laser irradiation ($\lambda$=337 nm) produced nitroglutathione ($GSNO_2$) having an absorption maximum at 298-300 nm and induced optical activity at that band[16].

Thus NO is released under the exposure of the aqueous solutions of S-nitrosocompounds as well as blood plasma proteins and whole blood of healthy donors to UV and visible light. In the absence of oxygen NO binds to Hb and forms nitrosohemoglobin (HbNO). When NO interacted with $HbO_2$ one can see methemoglobin Hb(III) production. HbNO and Hb(III) formation under action of NO on water solution of Hb at different air pressure is shown in Fig. 4. HbNO is formed only at pressures below 100 torr. Therefore one can expect only venous vessels relaxation mediated by NO, released under action of UV and visible light.

## 4. CONCLUSION

The results obtained indicate that the photosensitive donors of NO, S-nitrosothiols and S-nitrosoproteins, circulating in the blood channel under the action of UV and visible light can release NO which is known to cause blood vessel relaxation. In oxygen atmospere NO is mainly oxidized to nitrite. The physiologic effects induced by irradiation will probably vary for arterial and venous blood both due to different oxygen saturation and as a consequence of different Hb to $HbO_2$ ratio.

## 5. ACKNOWLEDGEMENTS

This work was supported by the Fundamental Reserch Foundation of Belarus.

## 6. REFERENCES

1 S.M. Moncada, R.M. Palmer, E.A. Higgs. *Biochem.Pharmacol.* **38**, pp. 1709-1713, 1989.
2 K. Shibuki, D. Okada, *Nature*, **349**, pp. 326-328, 1991.
3 G.M. Rubanyi, E.H. Ho, E.H. Cantor, *Biochim.Biophys.Res.Commun.*, **181**, pp. 1392-1397, 1991.
4 J.S. Stamler, O. Jaraki, J. Osborne, D.I Simon, J. Keanei, J. Vita, D. Singel, C.R. Valeri, C.R. Loscalzo, *Proc. Natl. Acad. Sci.USA* **89**, p.7674, 1992
5 Boese M, Mordvintcev PI, Vanin AF, Busse R, Mulsch A *J Biol Chem* **270**,:p.29244, 1995.
6 G.G. Borisenko, A.N. Osipov, K.D. Kazarinov, Yu.A. Vladimirov, *Biochemistry(Moscow)* **62,** p.774, 1997.
7 B.Saville, *Analyst* **83,** p.670, 1958.
8 G.Scorza, D.Pietraforte and M. Minetti *Free Radical Biol. and Medicine* ,**22,** p.633, 1997.
9 I.I. Stepuro, A.A. Solodunov, S.N. Sokolovskaya, *Biofizika*, **40,** p.1158, 1995.
10 Gebicki, S., and Gebicki, J. *Biochem. J.*, **289**, pp.743-749, 1993.
11 L.C. Green, D.A. Wagner, J. Glogowski, P.Skipper, J.S. Wishnok, S.R. Tannenbaum, *Anal.Biocem.* **126,** p.131, 1982.
12 I.I. Stepuro, N.A. Chaikovskaya, B.P. Vodoevich, V.V. Vinogradov, *Biochemistry(Moscow)* **64,** p.106, 1999.
13 .I.I. Stepuro, N.A. Chaikovskaya, T.Piletskaja, A.A. Solodunov, *Pol. J Pharmacol* **46**, p.601, 1994.
14 G.A. Gachko, L.N. Kivach, S.A. Maskevich, "Automatic pulse spectrofluorimeter," *J. Prikl. Spectr.* **47**, pp. 335-339, 1987.
15 O'Connor D.V. O'Connor and D. Phillips, *Time-correlated Single Photon Counting*, Academic Press, London, 1984.
16 I.I. Stepuro, N.A. Chaikovskaya, A.A. Solodunov, and A.N. Artsuckevich, *Biochemistry (Moscow)* **62**, p.960, 1997.

# Viability of Porcine Nasal Septal Cartilage Grafts Following Nd:YAG ($\lambda$=*1.32* $\mu m$) Laser Radiation

Kenneth K.H. Chao [a,b], Brian J.F. Wong [b,c], Hong K. Kim [b,d], Thomas E. Milner [e], Chung-Ho Sung [b], Emil N Sobol [f], J. Stuart Nelson [b]

[a] Univ. Of Texas Health Science Center at San Antonio, San Antonio, TX 78284

[b] Beckman Laser Institute, Univ. of California/Irvine, Irvine, CA 92715

[c] Dept. of Otolaryngology – Head and Neck Surgery, Univ. of Califonria/Irvine, Orange, CA 92668

[d] United States Peace Corp, P.O. Box 50, SAMPA, BAR, Ghana, West Africa

[e] Dept. of Electrical and Computer Program, Univ. of Texas at Austin, Austin, TX 78705

[f] Center for Technological Lasers, Russian Academy of Sciences, Troitsk, Moscow reg., 142092, Russia

## ABSTRACT

Mechanically deformed morphologic cartilage grafts undergo a temperature dependent phase transformation during sustained laser irradiation that results in reshaping of the specimen. While thermal, optical, and mechanical properties of cartilage undergoing laser heating have been previously investigated, the viability of these irradiated grafts has yet to be examined closely until now. In this study, chondrocyte viability following laser irradiation was determined by measuring the incorporation of radiolabelled sulfate (Na $^{35}SO_4^{-2}$) into proteoglycan (PTG) macromolecules. Proteoglycans are highly sulfated and are the principal molecular constituents of cartilage matrix. Their synthesis directly reflects chondrocyte viability. By measuring the scintillation counts of $^{35}SO_4^{-2}$ uptake and normalizing the value by the total protein content of each specimen we can determine the level of PTG synthesis rats following laser reshaping. Regional baseline PTG synthesis rates as a function of location was determined by dividing each specimen into six regions. All regions except the most cephalic are demonstrated similar PTG synthesis rates. The most cephalic region exhibited a significantly greater PTG synthesis rates.. In order to establish a positive control for this study, specimens were immersed in boiling saline water for approximately 40 minutes. The boiled specimens demonstrated a fivefold increase in normalized radioisotope uptake and suggest that the non-specific uptake of radioactive $Na^{35}SO_4^{-2}$ is caused by structural alterations in the collagen matrix caused by extensive thermal exposure. To avoid this thermal artifact, another positive control was established using nitric oxide was to induce apoptosis of the chondrocytes, resulting in significantly lower PTG synthesis compared to untreated tissue. Cartilage specimens (25 x 10 x 2 mm) were irradiated with light emitted from an Nd:YAG laser (25 W/cm2, $\lambda$ = 1.32 $\mu$m) while radiometric surface temperature, internal stress, and backscattered light were simultaneously recorded. Individual specimens underwent either one, two, or three sequential laser exposures with the duration of each exposure determined in real-time from observation of characteristic changes in integrated backscattered light intensity that correlate with thermal mediated stress relaxation. A five-minute time interval between each irradiation was given to allow the cartilage to return to thermal equilibrium. Average laser exposure for each irradiation sequence was recorded (5, 8.3, 12.2 sec). PTG synthesis decreased with increasing laser exposure, but was noted to remain above baseline levels for NO treated tissue. To further refine these results and minimize the effect of regional tissue variations, 7 mm diameter discs excised from the most cephalic portions and a middle region of the pig nasal septal cartilages were irradiated. A reduction of PTG synthesis rates was noted with each successive irradiation, suggesting that laser mediated cartilage reshaping acutely does not eliminate the population of viable chondrocytes. The degree of reduction in PTG synthesis is dependent upon the time-temperature dependent heating profile created during laser irradiation, and carefully monitored dosimetry is necessary to ensure chondrocyte viability.

In *Laser-Tissue Interaction XI: Photochemical, Photothermal, and Photomechanical*, Donald D. Duncan, Jeffrey O. Hollinger, Steven L. Jacques, Editors, Proceedings of SPIE Vol. 3914 (2000)
1605-7422/00/$15.00

**Keywords**: Cartilage reshaping, laser, viability, regional variability, nitric oxide, plastic surgery, Nd:YAG laser, photothermal interactions, proteoglycans, phase transformation

## 1. INTRODUCTION

Classic surgical techniques modify the shape of cartilage by cutting, suturing, or scoring the specimen, and these methods possess a variety of limitations such as excessive graft waste and donor site morbidity. Recently laser irradiation has been used to reshape cartilage into new stable structures without these limitations[1]. Previous investigations have characterized the biophysical changes accompanying laser reshaping; cartilage undergoes a temperature dependent phase transformation accompanied by alterations in optical, thermal, and mechanical properties[2]. Although histological evaluations suggest that chondrocyte viability is preserved, no biochemical studies following laser reshaping have been reported. Consequently, the clinical efficacy and risk potentials of this novel surgical technique have yet to be assessed.

In this study, we determine the effect of sustained Nd:YAG laser irradiation on viability of porcine nasal septal cartilage using laser parameters employed for feedback-controlled reshaping[4-6]. Cartilage is a complex macromolecular tissue that performs several functions in a living organism from maintaining structural support and load bearing to providing functional and aesthetic shape. The major constituents of cartilage are collagen (primarily type II) and proteoglycans. Proteoglycans are highly sulfated macromolecules (100-200 MD) that act like sponges and attract water molecules, causing the cartilage to be highly shock absorbent and durable[8]. These macromolecules are primarily responsible for the mechanical properties of cartilage and are exclusively synthesized by chondrocytes[9]. Our study first investigated the regional-dependent variation in PTG synthetic rates in the porcine nasal septal cartilage. Further, baseline PTG synthesis rates of cartilage specimens subjected to a variety of positive (total cell death) and negative (native) control environments were assessed. We evaluated PTG synthesis rates of cartilage slabs following laser irradiation. Finally, the effects of regional variation by comparing post-irradiation viability between two regions of distinctly different baseline PTG synthesis rates were determined.

## 2. MATERIALS AND METHODS

### 2.1 Experimental setup

Nasal septal cartilages were extracted from freshly euthanized pigs obtained from a regional packing house (Clougherty Packing Company, Vernon, CA) as previously described[3-6]. Each cartilage was divided into 6 regions from the most cephalic portion to the caudal region near the snout. Disc-shaped samples from each region were excised with a 7 mm trochar and bioassayed to determine baseline proteoglycan synthesis rates. Samples were also placed in positive (total cell death) and negative (native) control environments and evaluated biochemically. Rectangular slabs (23 x 11 x 2 mm) were fashioned using a custom guillotine in each region. They were then irradiated while monitoring biophysical properties as previously described[4]. Viability was determined biochemically following the laser exposure. Disc samples from two regions with distinctly different PTG synthesis rates were irradiated under near-adiabatic conditions. Those samples were then assessed for PTG synthesis rates. Figure 1 summarizes the study.

### 2.2 Assessment of regional variation

Our preliminary observations suggested that nasal septal cartilage exhibited a regional variation in proteoglycan synthesis. To determine such differences in synthesis rates, the entire porcine nasal septal cartilage was divided into six distinct anatomical regions and numbered them from the most cephalic (Region 1) to the most caudal (Region 6) (Figure 2). Discs from each region (7 mm diameter by 2 mm in thickness) were obtained and kept in normal saline solution briefly prior to being placed in an individual well of a 24-well plate filled with Delbecco's minimal essential medium (DMEM)(Sigma, St. Louis, MO) treated with antibiotics (10 mg/L of amphotericin B (Sigma, St. Louis, MO) and 200 mg/L of gentamicin (Sigma, St. Louis, MO)). These discs were then incubated at 37°C, 7.5% $CO_2$ for 36 hours prior to being assayed for PTG synthesis rates as described in section 2.6.

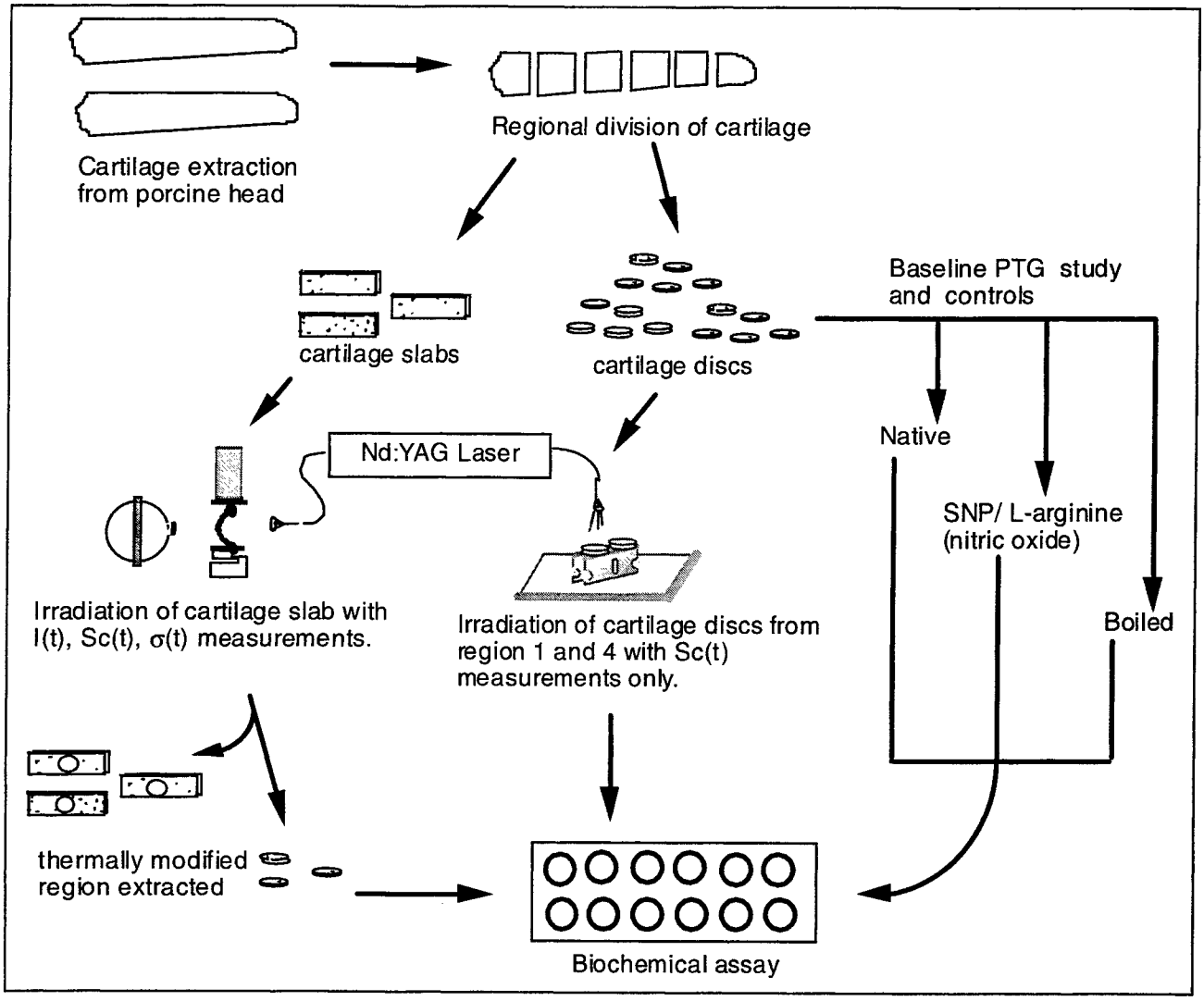


Figure 1. Step-by-step schematics of experiment

### 2.3 Controls

As it was necessary to compare the viability of sequential laser irradiations to controls representing the upper and lower ranges of chondrocyte viability, three additional protocols were used. For negative controls (native), non-modified, native cartilage discs extracted with a 7 mm trochar were placed in individual wells of a 24-well plate filled with 1.5 ml DMEM growth media treated with antibiotics (10 mg/L of amphotericin B and 200 mg/L of gentamicin) and incubated at 37°C, 7.5% $CO_2$ for 36 hours. For positive controls, cartilage discs (7 mm diameter and 2 mm thick) were either a) induced

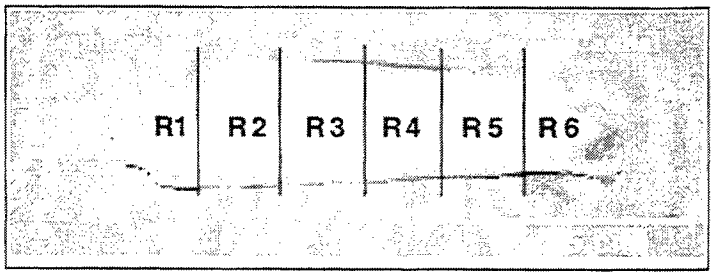


Figure 2. Regional separation of nasal septal cartilage

to undergo apoptosis in 1.5 ml DMEM treated with both 2 mM sodium nitroprusside (Sigma, St. Louis, MO) and 5 mM L-arginine (Sigma, St. Louis, MO) for 36 hours or b) thermally denatured in a boiling saline bath for 40 minutes. After the chemical or physical treatment, both samples were then transferred into individual wells filled with 1.5 ml DMEM with antibiotics and incubated at 37°C, 7.5% $CO_2$ for 36 hours. All samples from each of the three protocols were then assessed biochemically for PTG synthesis rates as noted in section 2.6

### 2.4 Laser irradiation and biophysical measurements

The goal of this study is to determine the viability of nasal septal cartilage following laser irradiation and to establish a dose-dependent correlation between cartilage viability and the amount of laser exposure. Cartilage from regions 2 to 6 was cut into uniform rectangular slabs (23 x 11 x 2mm) using a custom guillotine microtome. Region 1 was not used because it exhibited a proteoglycan synthesis rate that was much different from all the other regions. All other regions had consistently lower PTG synthesis rates similar to each other. Each slab was secured to the apparatus illustrated in figure 3a.

Integrated backscattered light [I(t)], radiometric surface temperature [$S_c(t)$], and internal stress [$\sigma(t)$] were measured as previously described[4-6]. Each cartilage slab was irradiated by an Nd:YAG laser ($\lambda$ =1.32 mm, 50 Hz PPR, New Star Lasers, Auburn, CA). Laser spot size was measured with thermal paper and had an average diameter of 5.09 mm. Laser power (25 W/cm$^2$) was calibrated with a pyroelectric meter (Model 10A-P, Ophir Optronics, Jerusalem, Israel). Integrated backscattered light intensity, radiometric surface temperature, and internal stress signals [$\sigma(t)$] were acquired using an analog-digital converter and a personal computer. The fractional changes in integrated backscattered light intensity ($\Delta I(t)/Io$) were determined by recording the change in I(t) relative to the baseline integrated backscattered light intensity signal Io.

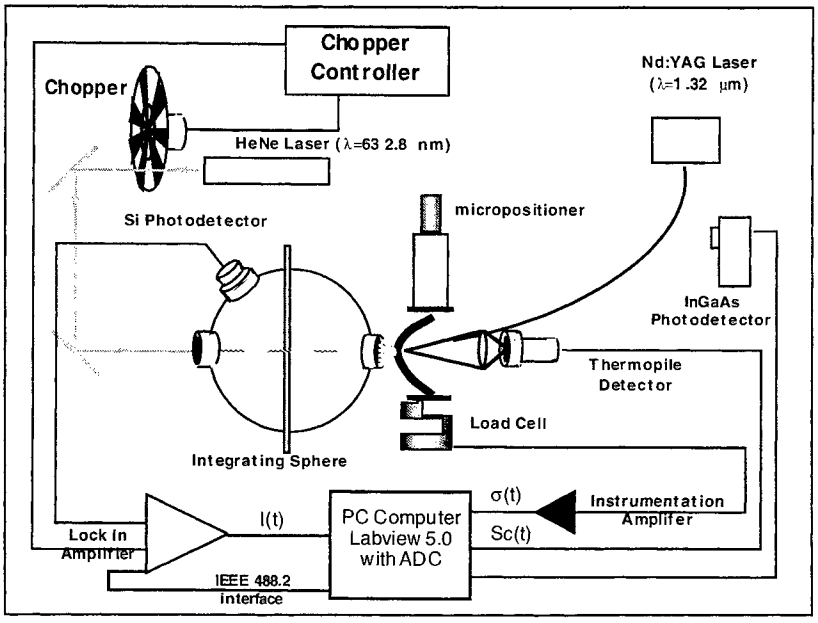


Figure 3a. Schematic of apparatus used to irradiate cartilage slabs. Integrated backscattered light intensity I(t), internal stress $\sigma(t)$, and radiometric surface temperature $S_c(t)$.

Each specimen was irradiated once, twice or three times with a five minute interval between successive laser exposures to permit thermal relaxation and cooling. Laser irradiation was terminated when the peak light scatter measurement [$\Delta I(t)/Io$] was clearly identified on the lock-in amplifier digital readout, indicating the onset of stress relaxation[4]. Optical, mechanical, and thermal properties were continuously recorded during laser irradiation and cooling interval.

Following laser irradiation, the irradiated regions were excised using a 7 mm trochar biopsy punch. The discs were maintained in normal saline solution and then placed into tissue culture media and incubated as noted in section 2.2 above.

### 2.5 Irradiations of cartilage discs

In order to minimize variation in results due to regional tissue variation, the experiment outlined in section 2.4 was repeated using samples from only region 1 (most caudal) and region 4 (near the middle). We selected two regions of distinct PTG synthesis rates to see whether regional variation plays a factor in dose-response effect of laser reshaping. As only a small quantity of tissue is available from each specific regions, discs (7mm diameter) were used (instead of slabs) so more

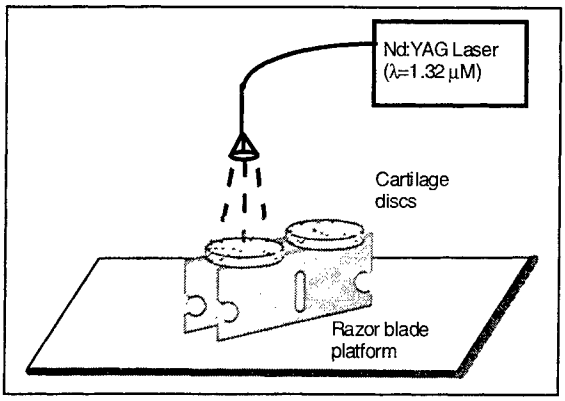


Figure 3b. Diagram of setup used to irradiate cartilage discs. Samples from region 4 and 1 were irradiated. Only Sc(t) was recorded.

experiments could be performed from tissue within a given region. As the small size and shape of these discs preclude the use of the apparatus used in section 2.4, only real-time temperature measurements could be recorded. Laser exposure time intervals for the first, second, and third laser pulses were determined from the average values obtained in section 2.4. The average laser exposure time intervals 5.2, 8.3, and 12.2 seconds corresponding to the first, second, and third laser pulses, respectively.

Discs were suspended on top of two razor blade edges to minimize conductive heat losses to the surroundings as illustrated in Figure 3b. Laser parameters were identical to those used in section 2.4 above. Following irradiation, the discs were placed in tissue culture and incubated as in section 2.2 above.

### 2.6.1 Radiolabel studies

After the 36 hours incubation, 1 ml DMEM with $^{35}SO_4^{-2}$ (at an activity of 10 uCi/ml) was added to each well and incubated for an additional 72 hours. Each cartilage discs were then rinsed several times with PBS until all non-specific radioisotope activity was reduced to background levels. Fresh growth media was again placed into each well for 4-6 hours. The discs then are washed three times in PBS. One ml of papain solution was prepared in 1x PBS(-) containing Papain at 1.35 units/ml, Na2-EDTA at 5 mM and Cysteine-HCl at 5mM at pH 6.0 and is added to each well. The digestion was carried out at 60°C in a dry oven overnight.

### 2.6.2 Determination of $^{35}S$ uptake total protein content

For assessment of $^{35}S$ uptake, 100 ul of papain digested cell suspension is added to 10 ml of Ecoscint (National Diagnostics, Atlanta, GA) and the radioactivity is measured from a Beckman LS5801 liquid scintillation counter (Beckman Instrument, Fullerton, CA). The counter is set up with 14°C as standard and cpm as unity on channel 1 with a window setting extended to 670. For total protein content, 1ml bicinchoninic acid (BCA)(Pierce, Rockford, Il) working solution (50 parts of Reagent A (base reagent with sodium carbonate, sodium bicarbonate, BCA detection reagent and sodium tartrate in 0.2N NaOH) with 1 part of Reagent B(4% Copper sulfate solution), was mixed with 10ul of each sample and incubated at 37°C for 30 minutes before measurement at 562 nm. Bovine serum albumin (BSA) was used as the standard for the assay. Standard concentration solutions were prepared in papain solution varying from 1ug/ml to 100ug/ml. The scintillation counts for a given specimen were normalized with respect to tissue protein content. $^{35}SO_4^{-2}$ uptake was determined and calculated over time to give us an average PTG synthesis rate.

## 3. RESULTS

Figure 4 depicts the regional variation in baseline PTG synthesis rates [normalized counts per minutes (CPM)] in the porcine nasal septal cartilage. Scintillations counts show that the most cephalic region (region 1) of the septal cartilage exhibited greater PTG synthesis rates than the other more proximal segments. Those other regions demonstrated consistently similar levels of PTG synthesis rates. Figure 6 illustrates proteoglycan synthesis rates of negative (native, non-irradiated samples) and positive controls (nitric oxide-treated and boiled cartilage tissue). NO-treated samples exhibited minimal PTG synthesis rates while boiled specimens exhibited apparent PTG synthesis rates similar to native cartilage.

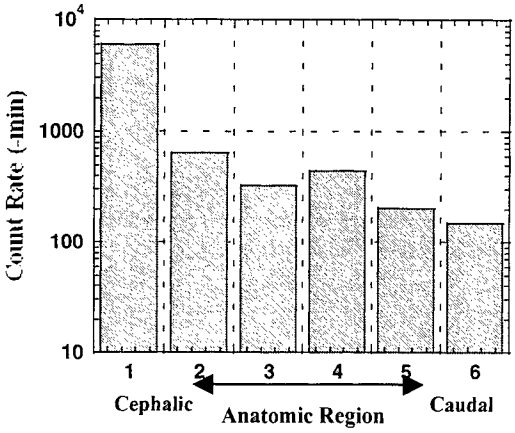


Figure 4. Regional variation in PTG synthesis rates. Rates based on scintillation counts per minute.

During laser irradiation, changes in optical, mechanical, and thermal properties that accompany laser irradiation were observed and recorded. Figure 5 illustrates the time variation the percentage changes in integrated backscattered light intensity [ΔI(t)/Io x 100%] and internal stress [σ(t)] during sequential laser irradiations from a representative sample. These observations are consistent with the results noted previous studies[3-6]. Radiometric surface temperature is not included in this figure in order maintain clarity. Average peak temperatures attained in each successive laser irradiation increased incrementally (57°, 70°, and 85° C for first, second and third laser pulse, respectively) expected since the average duration of each successive laser exposures in reaching phase transformation lengthened (5, 8.3, 12.2 seconds, respectively). It should be noted that laser irradiation was terminated when the peak in I(t) was observed on the lock-in amplifier signal monitor, and hence the duration of laser irradiation exceeds the time required to observe a peak in ΔI(t)/Io and σ(t). Peaks for ΔI(t)/Io and δ(t) occurred concurrently in the first two laser irradiations while peak for ΔI(t)/Io following the third irradiation was observed prior to the crest in δ(t). All are consistent with previous studies[5].

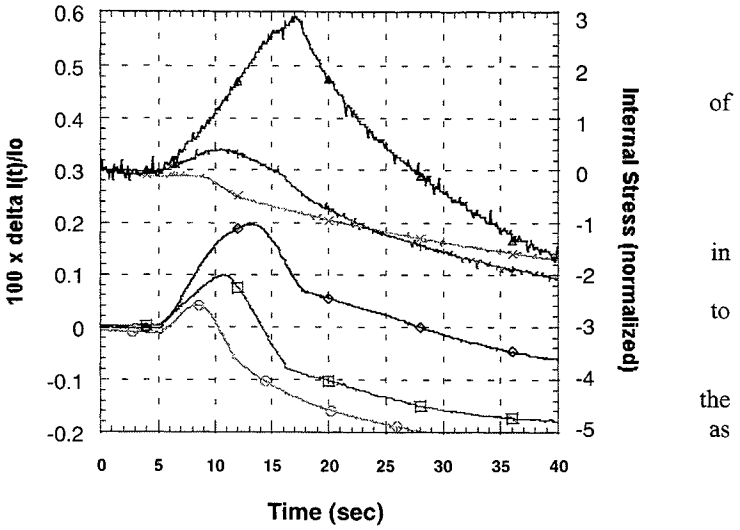


Figure 5. Simultaneous measurement of ΔI(t)/Io (left), σ(t) (right) during laser irradiation of cartilage slabs. $S_c(t)$ not displayed.

As illustrated in figure 6, biochemical assay following feedback-controlled laser irradiation showed that PTG synthesis rates decreased with each successive irradiation. Specimens exposed to three successive pulses exhibited PTG synthesis rates near NO-treated levels, but never reached at or below the same levels. Comparison between the two positive control types revealed a difference in baseline PTG synthesis with the boiled samples exhibiting a higher rate than the NO-treated cartilages. Figure 7 illustrates the PTG synthesis from two distinct regions of the cartilage (regions 1 and 4) after irradiation with fixed laser exposure durations for one, two, and three pulse sequences. Again, the PTG synthesis rates decreased with increasing laser irradiation. However, it is also clear from these results that regional variation does play a factor in baseline rates, as exemplified by the consistently higher PTG synthesis after each successive firing displayed in region 1 compared to region 4.

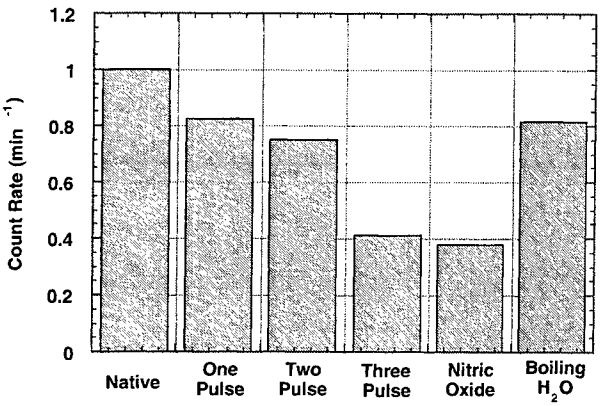


Figure 6. Average PTG synthesis rates following sequential laser irradiations. Both negative and positive controls (NO-treated and boiled samples) are displayed to compare the results. Samples from all regions except Region 1 were used.

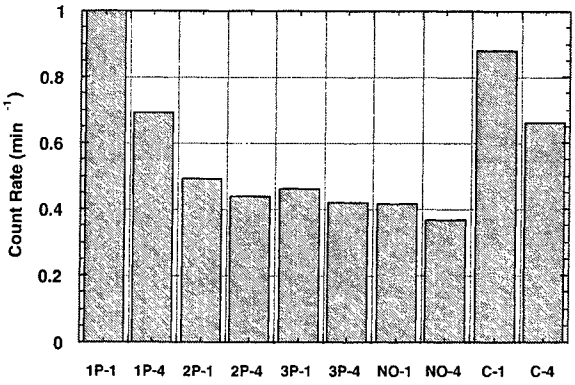


Figure 7. Average PTG synthesis rates of sequentially irradiated cartilage discs from two distinct regions (1 and 4). 1P, 2P, 3P = one pulse, two pulse, three pulse, respectively. NO = nitric oxide treated. C= native. Last digit represents region of cartilage.

## 4. DISCUSSION

Laser heating results in the acceleration of stress relaxation in mechanical deformed cartilage grafts which result in a stable shape change and the characteristic optical, thermal, and mechanical changes accompanying this process have been identified. Recently, a prototype feedback controlled cartilage reshaping device has been constructed which uses dynamic measurements of these biophysical properties to reshape cartilage[4-6]. Despite characterization of the physical changes accompanying cartilage reshaping, tissue viability has not been extensively studied albeit limited histological studies have been performed[12]. Our objective was to determine the viability of cartilage samples following laser irradiation using a pulse-chase radio-isoptope technique.

Chondrocyte viability was evaluated biochemically by measuring proteoglycan synthesis. Although many other approaches can be used to assess tissue viability ranging from DNA and genetic analyses to histological investigations, we opted to us a pulse chase technique using $Na^{35}SO_4^{-2}$ as it is used extensively by orthopedic and biomechanic researchers. In cartilage, proteoglycans are synthesized exclusively by the chondrocytes; these macromolecules exhibit a high degree of sulfation and turn over rapidly as their biologic half-life is very short[8]. Any compromise in chondrocyte viability would alter proteoglycan synthesis rates. A potential source of artifact associated with this method is that nonspecific uptake of the radioisotope by the tissue matrix may occur which may result in elevated measurements. With heating, protein denaturation may also result in changes in tissue matrix porosity and effect uptake of the radioisotope. The high $^{35}SO_4^{-2}$ levels measured in cartilage samples boiled for 40 minutes underscore this point. We emphasize that thermal modification from laser irradiation, however, does not appear to cause significant alterations in tissue matrix that would cause aberrant $^{35}SO_4^{-2}$ uptake as exhibited in boiled samples. Histological studies have showed that only chondrocytes on the superficial layers of the cartilage matrix were adversely affected while other levels did not exhibit any signs of degeneration in controlled, short-pulsed laser exposures[12, 15].

Porcine nasal cartilage was selected, as it is inexpensive, easily available in large quantities, and relatively large in size. Further, porcine nasal cartilage is similar to its human counterpart in gross appearance, texture, and mechanical properties. However, the physiological and biochemical characteristics were largely unknown. Our first step was to determine whether there are variations in proteoglycan synthesis rates throughout the different regions of the cartilage. The most cephalic portion of the cartilage (region 1) displayed markedly higher PTG synthesis rates than other tissue regions. Further, we observed a gradual decrease in the radioisotope uptake towards the more caudal regions (towards region 6) (Figure 4). Region 1 is the most cephalic portion of the septum and it articulates with the osseous nasal septum. We

speculate that this region is an area of more active cartilage growth, though differences in chondrocyte density or matrix architecture also play a role. Nevertheless, these findings establish that regional variations in the pig septal cartilage do exist and that future investigations focusing on cellular or biochemical septal cartilage properties must take this into consideration.

The establishment of a positive control (no living tissue) is a vexing issue. Our initial approach involved boiling the cartilage tissue in saline for 40 minutes. This resulted in a $^{35}SO_4^{-2}$ uptake rates paradoxically higher than those measured in native tissue. We speculate that the prolonged heating caused alterations in tissue matrix structure resulting in higher nonspecific uptake of the radioisotope. We sought an alternative method of eliminating all viable chondrocytes.

Recent studies on nitric oxide (NO) induced apoptosis in chondrocytes prompted our interest in using this agent to establish a positive control. NO is thought to induce chondrocyte apoptosis by directly inhibiting specific enzyme(s) within the cell that leads to morphological, ultrastructural changes, and DNA fragmentation[7]. One leading theory points to the disruption of normal tricarboxylic acid (TCA) cycle, leading to oxidative stress. Although the exact mechanism of nitric oxide-induced apoptosis remains a mystery, studies have already showed conclusive histological and microscopic proof of its actions. Cytokine such as Il-1 have also been linked to cause apoptosis in cartilage tissue, but recent studies showed that nitric oxide operated as the intermediary for these effectors[10,11]. Nitric oxide can be introduced exogenously by donor molecules such as sodium nitroprusside (SNP), which carry the NO once it is ionized in aqueous solution. Other agents, such as L-arginine, can induce endogenous production of nitric oxide within tissue by stimulating enzymes called inducible nitric oxide synthase (iNOS)7. Those two agents combined generate large quantities of nitric oxide that in turn activate a chain of events leading to chondrocyte cellular death. Our study using nitric oxide confirmed the expected results. All specimens treated with nitric oxide displayed minimal $^{35}SO_4^{-2}$ uptake.

PTG synthesis rates decreased with increasing sequential laser exposures though PTG synthesis always exceeded levels measured in nitric oxide treated controls (even after three pulses). This suggests that cartilages remains viable using laser parameters and irradiation sequences that likely would be employed clinically. Histological studies have showed that only chondrocytes on the superficial layers of the cartilage matrix were adversely affected while other levels did not exhibit signs of degeneration in controlled, short-pulsed laser exposures[12, 15]. In this study, real-time measurements of changes in tissue optical properties were used to terminate laser exposure; laser irradiation was terminated after observation of a peak in I(t) on the lock-in amplifier monitor. As illustrated in Figure 4, the maxima of I(t) and $\sigma(t)$ are highly correlated, and are observed prior to the cessation of laser irradiation. Hence, the proteoglycan synthesis rates measured in this study correlate with observed changes in tissue biophysical properties accompanying stress relaxation.

As illustrated in figure 7, 7 mm diameter cartilage discs were used instead of slabs in order to minimize the effect of regional differences in tissue proteoglycan synthesis rates. As the discs are much smaller than the cartilage slabs used in section 2.4, more specimens can be obtained from a given region of a septal cartilage, thus minimizing the effect of regional variation of tissue properties (section 2.2). To further reduce experimental error due to the slight variation in laser exposure time that results from using real-time measurement of backscattered light to terminate laser radiation, we exposed each laser disc to the set of laser pulse durations. The length of each laser pulse duration for the first, second, and third laser exposure was determined from the average pulse durations measured in section 2.4. Using discs permitted efficient and rapid irradiation of many specimens as they were arranged and supported by two parallel razor blade edge. Unfortunately, the small size of the discs precluded the measurement of dynamic changes in $\sigma(t)$ and I(t); only Sc(t) was recorded.

The experiment also compared two regions (1 and 4) with different baseline biochemical activity; region 1 exhibited significantly high PTG synthesis activity while region 4 exhibited moderate activity. As noted in Figure 7, both regions, although distinctly different in baseline (native) biosynthetic activity, demonstrated similar reduction in PTG synthesis rates. When the results of section 2.4 are compared to those obtained in section 2.5, it is clear that the irradiated discs had consistently lower PTG synthesis rates than slabs irradiated with corresponding laser parameters and exposures. In fact, PTG synthesis rates in disc- shaped specimens irradiated two or three times were similar to rates measured in NO-treated controls. One possible explanation for this observation may be that thermal relaxation (cooling) occurs more slowly in the discs shaped specimens than in the slabs. Radial heat conduction to non-irradiated cartilage tissue occurs in the relatively large slabs. In contrast, little heat flow occurs in the disc as the diameter of the laser spot and disc are nearly the same. It takes longer for the disc to cool. PTG synthesis rates, and thus chondrocyte viability, is sensitive to the geometry of the specimen. Future clinical studies must take into account. Application of an exogenous cooling agent (cryogen spray), use of material with high thermal conductivity, or perhaps immersion in saline may provide a way to help disperse the heat following laser irradiation.

## 5. CONCLUSION

Laser-mediated, non-ablative cartilage reshaping is a novel alternative to standard open surgical techniques. Current reconstructive and aesthetic operations of the head and neck region generally require an autologous cartilage graft and physical manipulation (scoring, cutting, suturing) to achieve the desired remodeling. The substitution of a scalpel for a laser to reshape cartilage brings the potential of a less invasive approach that requires minimal graft waste. With advances in endoscopic and minimally invasive technology that have diminished the utility of true open surgeries, this technique can potentially decrease operative complications and minimize donor morbidity. Identification of characteristic optical, mechanical, and thermal properties during laser reshaping will aid in establishing reliable feedback control. Cartilage viability related to laser interactions, however, has not been well characterized. First, we needed to determine normative data on proteoglycan synthesis rates. Regional variation in proteoglycan synthesis in porcine nasal septal cartilage was assessed, and a positive control or chondrocyte death using nitric oxide was also developed. This information should be taken into consideration in any study that evaluates cartilage tissue biochemical properties following thermal modification. The primary objective of this study is to determine whether cartilage remained physiologically viable following feedback-controlled laser reshaping. . It should be stressed that overall chondrocyte activity does not appear to be lost when the same laser parameters and feedback signals previously used to reshape cartilage were employed. Our findings demonstrate that cartilage biosynthetic activity remained viable even after sequential irradiations

## ACKNOWLEDGMENTS

This work was supported in part by the Office of Naval Research (N00014-94-0874), National Institutes of Health (1 K08 DC 00170-01, AR-43419, RR-01192, and HL-59472), The Whitaker Foundation (WF- 21025), and the Department of Energy (95-3800459).

We are grateful to Kevin Mee, Xavier Dao, Amir Karamzadeh, and Linda Li for their technical assistance, Joey Kimball and Darren Gray for construction of the cartilage guillotine microtome, and to B. Samuel Tanenbaum for his suggestions and comments.

## REFERENCES

1. E. Sobol, V. Bagratashvilli, A. Omel'chenko, A. Sviridov, "Laser shaping of cartilage", *SPIE Proceedings 1994*; 2128:43-49.
2. B.J.F. Wong, T.E. Milner, H.K. Kim, S. Telenkov, C. Chew, T. Kuo, D. Smithies, E. Sobol, J.S. Nelson, "Critical Temperature Transitions in Laser Mediated Cartilage Reshaping", *SPIE Proceedings 1998*:3245:161-172.
3. Z. Wang, M.W. Pankratov, D.F. Perrault, S. Shapshay, "Laser-Assisted Cartilage Reshaping: In-Vitro and In-Vivo Animal Studies", *SPIE Proceedings 1995*;2395:296-302.
4. B.J.F. Wong, T.E. Milner, H.K. Kim, J.S. Nelson, E. Sobol, "Stress Relaxation of Porcine Septal Cartilage During Nd:YAG ($\lambda$ = 1.3mm) Laser Irradiation: Mechanical, Optical, and Thermal Responses", *Journal of Biomedical Optics*, 1998;3:409-414.
5. C. Chew, B.J.F. Wong, T.E. Milner, H. Kim, A. Gomez, J.S. Nelson, E. Sobol, "Feedback Controlled Cartilage Reshaping with Nd:YAG Laser: Effect of pH Variation", *SPIE Proceedings 1998*; 3245:206-216.
6. B.J.F. Wong, T.E. Milner, B. Anvari, A. Sviridov, A. Omel'chenko, V.V. Bagratashvili, E. Sobol, J.S. Nelson, "Measurement of Radiometric Surface Temperature and Integrated Back-Scattered Light Intensity During Feedback Controlled Laser-Assisted Cartilage Reshaping", *Lasers in Medical Science* 1998;3245:161-172.
7. F.J. Blanco, R.I. Ochs, H.Schwarz, et al. "Chondrocyte Apoptosis Induced by Nitric Oxide", *American Journal of Pathology*, 1995, Jan 146(1):75-85.
8. P.J. Roughley, E.R. Lee, "Cartilage Proteoglycans: Structure and Potential Functions", *Microscopic Research and Technique*, 1994;28:385-397.

9. Muir, "The chondrocyte, architect of cartilage: Biomechanics, structure, function, and molecular biology of cartilage matrix macromolecules", *BioEssays 1996*;17:2970:380-391.
10. D. Taskiran, M. Stefanovic-Racic, H. Georgescu, C. Evans, "Nitric Oxide Mediates Suppression of Cartilage Proteoglycan Synthesis by Interleukin-1", *Biochemical and Biophysical Research Communications*, 1994;200(1):142-147.
11. M. Stefanovic-Racic, D. Taskiran, H. Georgescu, C.H. Evans, "Modulation of Chondrocyte Proteoglycan Synthesis by Endogenously Produced Nitric Oxide", *Inflammation Research,* 1995;44(2):S216-S217.
12. E. Helidonis, M. Volitakis, I. Naumidi, G. Velegrakis, J. Bizakis, P. Christodoulou, "The Histology of Laser Thermo-Chondro-Plasty", *American Journal of Otolaryngology,* 1994;15(6):423-428.
13. E. Sobol, M. Kitai, N. Jones, A. Sviridov, T. Milner, B.J.F. Wong, "Theoretical Modeling of Heating and Structure Alteration in Cartilage Under Laser Radiation with Regard of Water Evaporation and Diffusion Dominance", *Proceedings SPIE* 1998;3254:54-63.
14. E. Helidonis, E. Sobol, G. Kavvalos, J. Bizakis, P. Chrstodoulou, G. Velegrakis, J. Segas, V. Bagratashvili, "Laser Shaping of Composit Cartilage Grafts", *American Journal of Otolaryngology*, 1993;14(6):410-412.
15. E. Sobol, V. Bagratashvili, A. Sviridov, A. Omel'chenko, M. Katai, "Study of Cartilage Reshaping with Holmium Laser", *Proceedings SPIE*, 1996;2623:544-547.
16. A. Heldonis, E. Sobol, G. Velegrakis, J. Bizakis, "Shaping of Nasal Septal Cartilage with the Carbon Dioxide Laser – a Preliminary Report of an Experimental Study", *Lasers in Medical Science*, 1994;9:51-54.

## Part B

# OPTICAL TECHNOLOGIES TO SOLVE PROBLEMS IN TISSUE ENGINEERING

# SESSION 16

# Bone Engineering

Invited Paper

# Engineered Matrices for Bone Regeneration

Shelley R. Winn, Yunhua Hu, Amy Pugh, Leanna Brown,
Jesse T. Nguyen, Jeffrey O. Hollinger

Oregon Health Sciences University, Dept. of Surgery,
School of Medicine, Portland, OR 97201

## ABSTRACT

Traditional therapies of autografts and allogeneic banked bone can promote reasonable clinical outcome to repair damaged bone. However, under certain conditions the success of these traditional approaches plummets, providing the incentive for researchers to develop clinical alternatives.

The evolving field of tissue engineering in the musculoskeletal system attempts to mimic many of the components from the intact, healthy subject. Those components consist of a biologic scaffold, cells, extracellular matrix, and signaling molecules. The bone biomimetic, i.e., an engineered matrix, provides a porous structural architecture for the regeneration and ingrowth of osseous tissue at the site of injury. To further enhance the regenerative cascade, our strategy has involved porous biodegradable scaffolds containing and releasing signaling molecules and providing a suitable environment for cell attachment, growth and differentiation. In addition, the inclusion of genetically modified osteogenic precursor cells has brought the technology closer to developing a tissue-engineered equivalent. The presentation will describe various formulations and the methods utilized to evaluate the clinical utility of these biomimetics.

**Keywords:** biomaterials, biomimetic, bone grafting, phase separation, scaffold, tissue engineering

## 1. INTRODUCTION

Bone can repair itself provided the damage is not too extensive. When the damage is beyond a "critical" limit, therapeutic interventions, such as autografting and banked allogeneic bone are required[1]. However, these therapies are associated with an unsatisfactory rate of success providing an incentive for researchers to develop clinical alternatives.

Our strategy has been geared toward developing alternatives for bone regeneration by engineering matrices that are biomimetics for the tissues to be replaced[2,3]. Thus, targets for the ideal bone biomimetic should: 1) exhibit compatibility that is equivalent to the autograft; 2) provide a suitable environment for cell attachment, recruitment, expansion and differentiation; and 3) be convenient for the surgeon to handle and remain localized to the site of implantation.

A variety of biomaterials have provided the foundation for osteoconductive scaffolds, that is, scaffolds which permit the ingrowth and regeneration of tissue at osseous sites (reviewed in[4]). The present studies are



In *Laser-Tissue Interaction XI: Photochemical, Photothermal, and Photomechanical*, Donald D. Duncan, Jeffrey O. Hollinger, Steven L. Jacques, Editors, Proceedings of SPIE Vol. 3914 (2000)
1605-7422/00/$15.00

focused on the homopolymers of polylactide within a family of biocompatible, biodegradable polymers known as the poly(alpha-hydroxy acids). These materials have close to a 30-year history exhibiting clinical efficacy and safety as sutures[5], thus, the poly(alpha-hydroxy acids) enjoy a clear advantage with respect to regulatory issues when developed as potential matrices to be engineered as osteoconductive scaffolds. We will present methodologies to engineer matrices by phase separation using a multi-solvent system, followed by freeze-drying, which permits the desired microstructure for use as scaffolds in bone regeneration.

## 2. MATERIALS AND METHODS

The candidate matrices engineered for bone regeneration were comprised of two types of a homopolymer of poly (D, L-lactide), i.e., PL, within the family of poly(alpha-hydroxy acids). The first type of PL was a high molecular weight, MW 670 kDa, 0.8 dL/g inherent viscosity, a generous gift from THM Biomedical, Inc., (Duluth, MN), which was originally supplied by Sofamor Danek, Memphis, TN. The second type of PL exhibited a molecular weight of 100 kDa, 0.73 dL/g inherent viscosity, supplied by Alkermes, Inc., Wilmington, OH, and is also known as MEDISORB®. All solvents and reagents were ACS grade. The PL was purified by dissolving in methylene chloride, precipitated in absolute methanol, and dried under vacuum.

Following purification, dioxane, which was refluxed and distilled over sodium metal, was utilized at either 100%, or a combination of 95% dioxane / 5% water, to dissolve the 670 kDa and 100 kDa PL at concentrations of 0.010 and 0.015 g/mL (room temperature). In addition, the 100 kDa PL was further dissolved at a concentration of 0.030 g/mL. Each PL solution (80 mL) was poured into a crystallizing dish with a 15 cm diameter and frozen at (-) 20 °C. The solvent was removed by freeze-drying under vacuum (<50 mTorr) for 3 days at 0 °C. The PL sheets formed were warmed to 23, 30 and 37 °C each for 12 hrs to ensure solvent removal. Discs 8 mm in diameter were prepared from PL sheets, packaged 8-10/container and sterilized with hydrogen peroxide plasma gas (58%) in a Sterrad® 100 Sterilizer. Residual dioxane was measured with gas chromatography containing a mass spectroscopic detector.

Several techniques were utilized to characterize scaffold microstructure. These included scanning electron microscope images to assess pore size and the porosity morphology (i.e., do the pores exhibit a closed pore or an interconnecting open-pore meshwork). Mercury intrusion porosimetry analysis provided data for the percent porosity. In addition, degradation profiles have been characterized by assessing percent weight loss of the scaffolds at various intervals when maintained in phosphate buffered saline (0.05M, pH 7.4) at 37°C. Also, we routinely assess the cytocompatibility of engineered matrices in an osteogenic cell culture system and have utilized these materials as *in situ* scaffolds to deliver osteoinductive factors, as well as, fabricated tissue-engineered bone biomimetics[2].

## 3. RESULTS

The phase separation / sublimation process was able to produce PL foam structures that were highly porous and could exhibit interconnected pores under specific conditions. Variations in parameters such as solvent composition, polymer concentration, and polymer molecular weight were observed to influence the scaffold microstructure.

TABLE 1 illustrates the influence of solvent composition on the pore size and morphology of the scaffold microstructures. The scaffolds in TABLE 1 were fabricated from concentrations of 0.010 g/mL for the 670 kDa PL and 0.030 g/mL for the 100 kDa PL. Scaffold microstructures fabricated from the 100 kDa PL concentrations of 0.010 and 0.015 g/mL were weak and difficult to handle.

TABLE 1. The Effect of Solvent Composition on the Morphology of PL Foams

| PL | Solvent Composition (v/v%) | Pore Size Range in SEM (μm) | Morphology |
|---|---|---|---|
| 670 kDa | 100% Dioxane | 130 - 200 | Closed Pore |
| 100 kDa | 100% Dioxane | 100 - 180 | Closed Pore |
| 670 kDa | 95% Dioxane/5% Water | 100 - 250 | Open Pore, *INT |
| 100 kDa | 95% Dioxane/5% Water | 40 - 200 | Open Pore, *INT |

*INT = interconnecting porous structure

The influence of solvent composition on the morphology of the PL foams can be further illustrated in Figure 1. The use of 100% pure dioxane resulted in the formation of closed pore structures (A). The addition of 5% water (B) resulted in a modified structure that exhibited an open, interconnected porous structure that is a preferred morphology for osteoconductive scaffolds. The addition of 5% water did not negatively impact the strength or handling characteristics of the porous scaffold. However, if too much water was added to the solvent composition, e.g., 10%, the resulting structure exhibited an open pore structure with weak strength, poor handling characteristics and loose particulate matter. Measurements of residual dioxane were at the lower limit of detection and the PL disks did not exhibit cytotoxicity in the osteogenic cytocompatibility assay.

A. 100% Dioxane

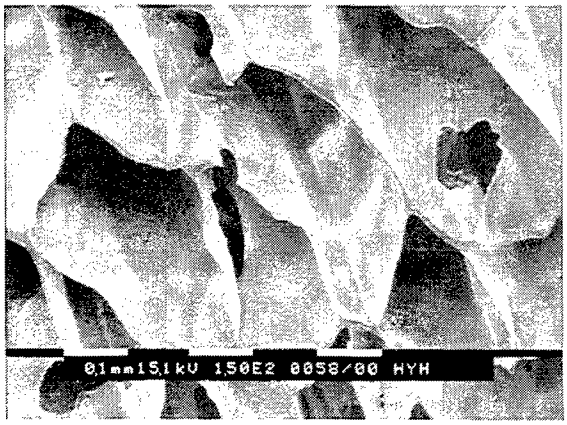


B. 95% Dioxane + 5% Water

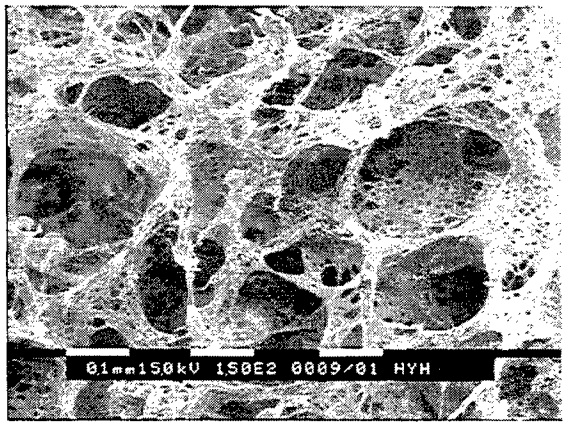


Figure 1. The effect of solvent composition on the morphology of PL foam scaffolds.

TABLE 2 summarizes the mercury intrusion porosimetry analysis from the PL porous scaffolds fabricated with a solvent composition of 95% dioxane / 5% water. The scaffolds in TABLE 2 were fabricated from concentrations of 0.010 g/mL for the 670 kDa PL and 0.030 g/mL for the 100 kDa PL, hence a larger bulk density is observed with the 100 kDa PL porous foam scaffolds. Essentially, the total pore area and percent porosity was equivalent for the polymer systems; however, a significant difference was observed for the median pore diameters.

TABLE 2. Summary of Mercury Intrusion Porosimetry Analysis of the PL Porous Foam Scaffolds

| PL | Total Pore Area ($m^2/g$) | Median Pore Diameter (μm) | Porosity (%) | Bulk Density (g/mL) |
|---|---|---|---|---|
| 670 kDa | 1.113 | 118 | 92.2 | 0.0438 |
| 100 kDa | 1.013 | 63 | 91.4 | 0.0672 |

Figure 2 presents the porosimetry analysis demonstrating the pore size distributions for the 670 kDa and 100 kDa PL porous foam scaffolds. The 670 kDa foam exhibited a median pore diameter peak at 118 μm, while the median diameter peak for the 100 kDa PL is at 63 μm.

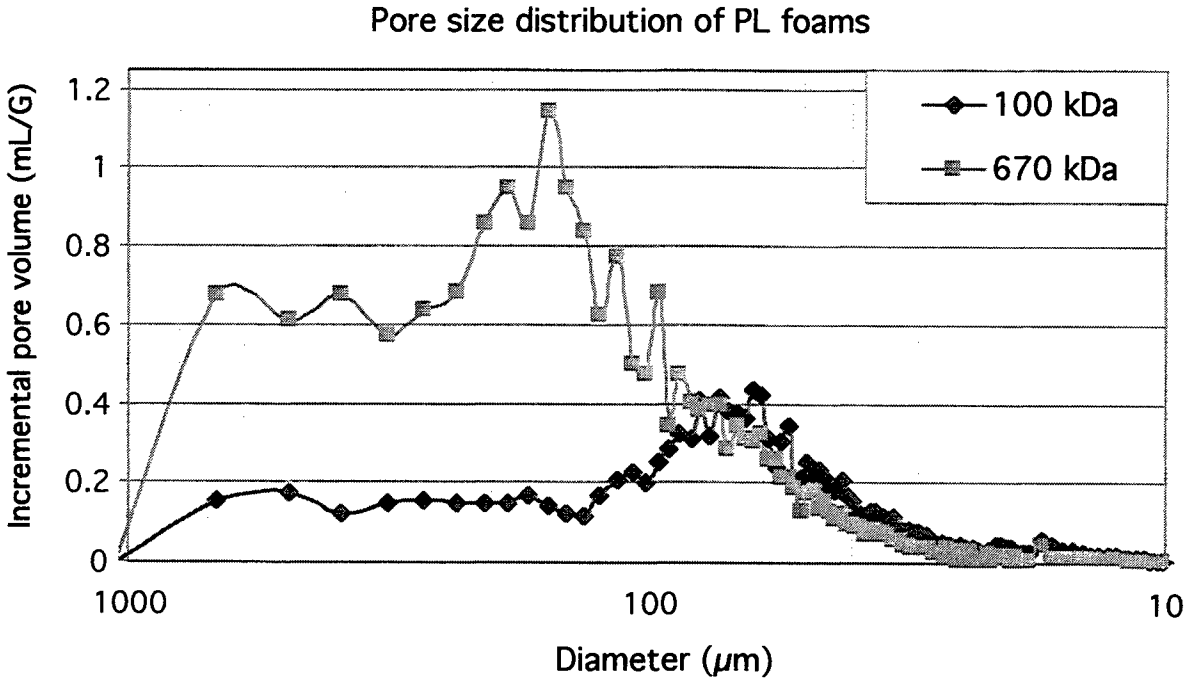


Figure 2. Porosimetry data for the 100 kDa and 670 kDa PL porous foam scaffolds.

The analysis of pore volumes indicated that nearly 50% of the void space was represented by a pore size in the 100 - 250 μm range for the 650 kDa PL, while the 100 kDa pore volumes exhibited pore sizes in the range of 40 - 200 μm.

The rate of degradation of the 670 kDa and 100 kDa PL porous foam scaffolds in phosphate buffered saline has been characterized for at least 12 months when maintained at 37°C. The 670 kDa foams exhibit a 10 ± 1% loss of weight after 12 months *in vitro*, while the 100 kDa foams exhibit a 48 ± 4% weight loss over the same interval.

We have routinely assessed the cytocompatibility of the 670 kDA and 100 kDa PL engineered matrices in an osteogenic cell culture system[6]. Briefly, the cytocompatibility of bone-graft substitutes are evaluated in the presence of osteogenic cells by compartmentalizing biomaterials from direct cell contact in a dual chamber transwell® configuration or by evaluating direct cell/biomaterial interactions. When tested in this osteogenic cell culture system, no adverse effects on cell proliferation or the osteogenic potential of the cultured cells was observed with the 670 or 100 kDa PL foams. Lastly, both types of the PL foams have been utilized as *in situ* scaffolds to deliver osteoinductive factors, such as bone morphogenetic protein-2, and additionally, inclusion of osteoprecursor cells within the porous foam scaffolds has been evaluated as a tissue-engineered bone biomimetics[2].

## 4. DISCUSSION

The present studies describe a phase separation multi-solvent system, followed by a sublimation process, to fabricate highly porous and interconnected poly(lactic acid), i.e., PL, foam scaffolds for use in bone tissue regeneration. Modifications to some of the parameters, such as solvent composition, polymer concentration, and polymer molecular weight were optimized to arrive at a targeted foam microstructure. For materials used in bone grafting, as well as guided tissue regeneration, highly porous microstructures with an interconnected, communicating network, a large surface area and uniform pore size is essential. Optimum pore size for bone grafting is in the range of 100 – 350 μm which exhibits a porosity greater than 90%[7]. Preferred foam compositions exhibiting an interconnecting open-pore structure, with a porosity greater than 90%, were fabricated with a solvent composition of 95% dioxane / 5% water. Analyses of these preferred compositions with scanning electron microscopic images and mercury intrusion porosimetry indicated a pore size range of 100 - 250 μm for the 670 kDa PL, and a pore size range of 40 - 200 μm for the 100 kDa PL. The cytocompatibility assay demonstrated that the porous foam scaffolds were non-toxic and did not release any leachables that were potentially hazardous to osteogenic cell cultures. Furthermore, osteoprecursor cells seeded into the preferred foam structures exhibited the ability to attach, propagate and differentiate into a calcified structure.

Porous matrices comprised of natural and synthetic polymers have been fabricated by a number of methods, including solvent evaporation, phase separation, solvent cast-particulate leaching, emulsion freeze-drying, membrane lamination, melt molding and extrusion. However, solvent casting and phase separation, if performed alone, typically produce structures exhibiting small pores. Solvent cast-particulate leaching has been shown to result in a desired pore size range, however, significant loss of any bioactive molecule incorporated into the foam

would occur during the leaching process. The vast majority of other techniques would likewise require significant modifications.

The PL porous scaffolds have been utilized to engineer matrices for bone regeneration. Bone regeneration with an engineered matrix should be convenient for the surgeon, and should demonstrate the ability to localize, position, and sustain combinations of cueing molecules (e.g., BMPs), DNA plasmids or cells at the wound site[8]. Most important, the engineered matrix must provide the role of a substrate, which provides a site for attachment and differentiation of host pluripotent cells. In addition to offering convenient and easy handling, providing the role as a substrate and vehicle for the sustained delivery of cueing molecules, the PL scaffolds have recently been infiltrated with various cell types to develop a true tissue-engineered bone biomimetic[2].

Recent efforts in our laboratory have been geared toward establishing BMP-responsive osteoprecursor cell lines (OPCs) that could be incorporated in the PL tissue-engineered scaffolds to supplement the host osteogenic cell population[9]. These OPCs have been delivered within the 670 kDa PL porous scaffolds to restore critical-sized defects (CSDs) in an athymic rat calvaria model[2]. Moreover, the scope for our current bone biomimetic tissue-engineered construct incorporates OPCs containing BMP genes to provide a mini bioreactor to constituitively express BMP activity. These types of tissue-engineered constructs containing BMP-producing cells should minimize the therapeutic dose of BMPs required in a clinical carrier (currently mg quantities) and still effectively recruit locally responsive cells to differentiate into osteoblasts. This later point is especially important in the geriatric patient population with limited numbers of functioning osteoblasts[10].

The present studies demonstrate the ability to fabricate highly porous and interconnected poly(lactic acid) foam scaffolds for use in bone tissue regeneration. Future work will focus on surface modification of the preferred foam structure to further enhance cell attachment and differentiation. Surface-modified structures will be attained by chemically grafting attachment motifs to enhance cellular affinity. In addition, localized gene delivery methods for sustained delivery of growth and/or differentiating factors will be evaluated by incorporating DNA into the foam and assessing sustained release and the ability of the local reactive cells in a wound environment to take-up the DNA and express the transgene.

## ACKNOWLEDGEMENTS

This work was supported by NIH grant numbers RO1-DE11416-03 and RO1-DE13018-01. The authors wish to thank our colleagues David Buck and Richard V. Sipe from the OHSU and Dr. David Grainger and Guy Beauregard from Colorado State University.

## REFERENCES


1. M.J. Yaszemski, R.G. Payne, W.C. Hayes, R. Langer and A.G. Mikos, "Evolution of bone transplantation: Molecular, cellular and tissue strategies to engineer human bone", *Biomaterials* , **17**, pp. 175-185, 1996.
2. S.R. Winn, J.M. Schmitt, D. Buck, Y. Hu, D. Grainger and J.O. Hollinger, "A tissue engineered bone biomimetic to regenerate calvarial critical-sized defects in athymic rats", *J Biomed Mater Res* , **45**, pp. 414-421, 1999.
3. S.R. Winn, H. Uludag and J.O. Hollinger, "Carrier systems for bone morphogenetic proteins", *Cln Orthop Rel Res* , **367(S)**, pp. 95-106, 1999.
4. S.R. Winn, H. Uludag and J.O. Hollinger, "Sustained release emphasizing recombinant human bone morphogenetic protein-2", *Advanced Drug Deliv Rev* , **31**, pp. 303-318, 1998.
5. C.C. Chu, "The degradation and biocompatibility of suture materials", In: *Critical Reviews in Biocompatibility*. C.C. Chu (ed.) Boca Raton, CRC Press, 1985, pp. 261-322.
6. S.R. Winn and J.O. Hollinger, "An osteogenic cell culture system to evaluate the cytocompatibility of OsteoSet®, a calcium sulfate bone void filler", *Biomaterials* , pp. in press.
7. J.O. Hollinger and K. Leong, "Poly(alpha-hydroxy acids): Carriers for bone morphogenetic proteins", *Biomaterials* , **17**, pp. 187-194, 1996.
8. J.O. Hollinger and J.P. Schmitz, "Macrophysiologic roles of a delivery system for vulnerary factors needed for bone regeneration", *Annals NY Acad Science* , **831**, pp. 427-437, 1997.
9. S.R. Winn, G. Randolph, H. Uludag, S.C. Wong, G.A. Hair and J.O. Hollinger, "Establishing an immortalized human osteoprecursor cell line: OPC1", *J Bone Min Res* , **14**, pp. 1721-1733, 1999.
10. R. Quarto, D. Thomas and T. Liang, "Bone progenitor cell deficits and age-associated decline in bone repair capacity", *Calcif Tissue Int* , **56**, pp. 123-129, 1995.

Invited Paper

# Endoscopes Integrated into Instruments for Spinal Surgery

E. Frank, J. Hollinger, S Winn

Oregon Health Sciences University, Portland, Oregon 97201

## ABSTRACT

With minimally invasive approaches the visual path to guide instruments becomes constricted. Often one is unable to visualize adequately interaction of the instrument with tissue. We have incorporated 1.2-mm diameter 10,000 pixel fiberoptic endoscopes into instruments for spinal surgery. With these instruments one has a direct view of the instrument's interaction with the surgical anatomy.

We have studied a variety of endoscopic instruments including malleable forceps, retractors and punches in over 40 cases of lateral disc herniations, migrated disc fragments and spinal stenosis. The instruments provided excellent visualization of spinal structures. The size and effect of the pathologic process could be readily evaluated, as could neural decompression. Operative times were not significantly increased and there were no complications attributable to the instruments.

This preliminary work documents that "seeing instruments" can be safely used and add to our appreciation of operative anatomy. It is suggested that these instruments may provide more complete decompression through a more limited, less invasive, access. Further study of these instruments may provide better understanding of their overall utility.

**KEYWORDS**: Endoscope, instruments, spine surgery

## INTRODUCTION

When one uses a surgical instrument one is guided by visual information, the tactile feel of the instrument, the sound of the instrument interacting with tissue and in rare occasions the smell of the interaction of the instrument with tissue

In *Laser-Tissue Interaction XI: Photochemical, Photothermal, and Photomechanical,* Donald D. Duncan, Jeffrey O. Hollinger, Steven L. Jacques, Editors, Proceedings of SPIE Vol. 3914 (2000)
1605-7422/00/$15.00

(e.g. coagulator or drill). Of these, the visual interaction is perhaps the most important.

The visual orientation of an instrument requires a wide, direct visual pathway between the operators' eye and the tissue that the instrument is acting upon (Figure 1). In most cases this visual field is wide enough to permit binocular vision. Recently, as surgeons endeavor to limit surgical exposures for "less invasive" procedures, the visual pathways are constricted and are often longer, limiting visualization of the interaction of the instrument with tissue. As the visual pathway is constricted and extended, one is less able to "angle" ones observation to get a wide view at the depths of the exposure. There has been an attempt to overcome these obstacles utilizing the operative microscope. The interoccular distance is shorter with the operative microscope and a binocular view can be obtained through a constricted approach. But, the ability to angle the microscope to see lateral aspects of the visual field is limited as the depth of the approach increases.

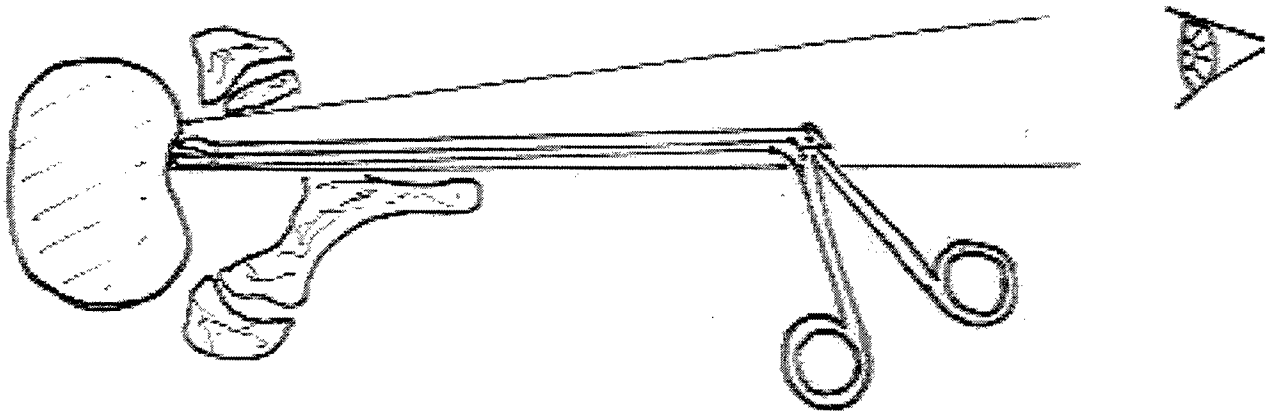

FIGURE 1

We have attempted to further overcome the limitations of limited field of view and depth of field by moving the surgeons eye to the tip, or working end of the instrument with the aid of a small endoscope (suggested by the work of Finn et al. [1]) (Figure 2). By remotely visualizing the working end of the instrument one overcomes some of the limitations of narrower, longer visual pathways.

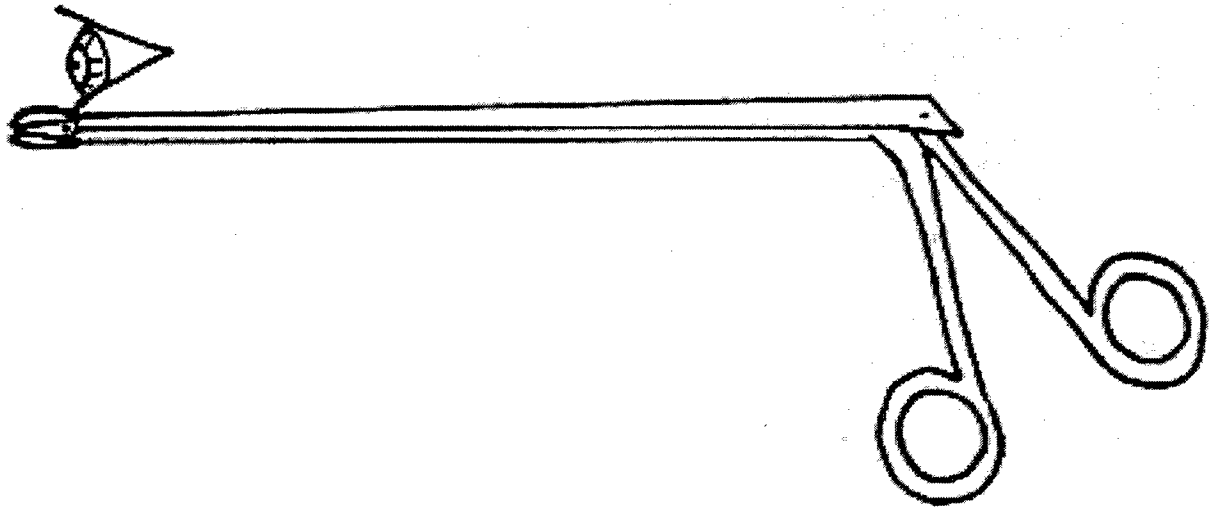

FIGURE 2

## MATERIALS AND METHODS

We have integrated small, standardized fiberoptic endoscopes into instruments commonly used for spinal surgery. The endoscopes have 10,000 pixels, a 70-degree field of view and a depth of field of 0.5 to 1.5 mm. In all cases, the endoscope allows the working end of the instrument to be visualized.

The endoscope has an optical adapter to interface with the cameras on standard operative endoscopic towers used in operating rooms for knee arthroscopy and thoracoscopy. The image is displayed on a television monitor and by visual projection glasses worn by both the primary surgeon and the assistant surgeon.

There are several instruments used for endoscopy. The endoscopic pituitary forceps consist of a malleable pituitary forceps (Aesculap FD426R) including the above-mentioned channel added for the endoscope (Figure 3) [2]. The tips of the forceps are small permitting removal of small bits of tissue (Figure 4). The endoscope channel is malleable permitting flexibility. This type of instrument is especially helpful in working in areas where larger diameter, rigid instruments cannot access, either under the spinal dura or within the neuroforamina (Figure 5).

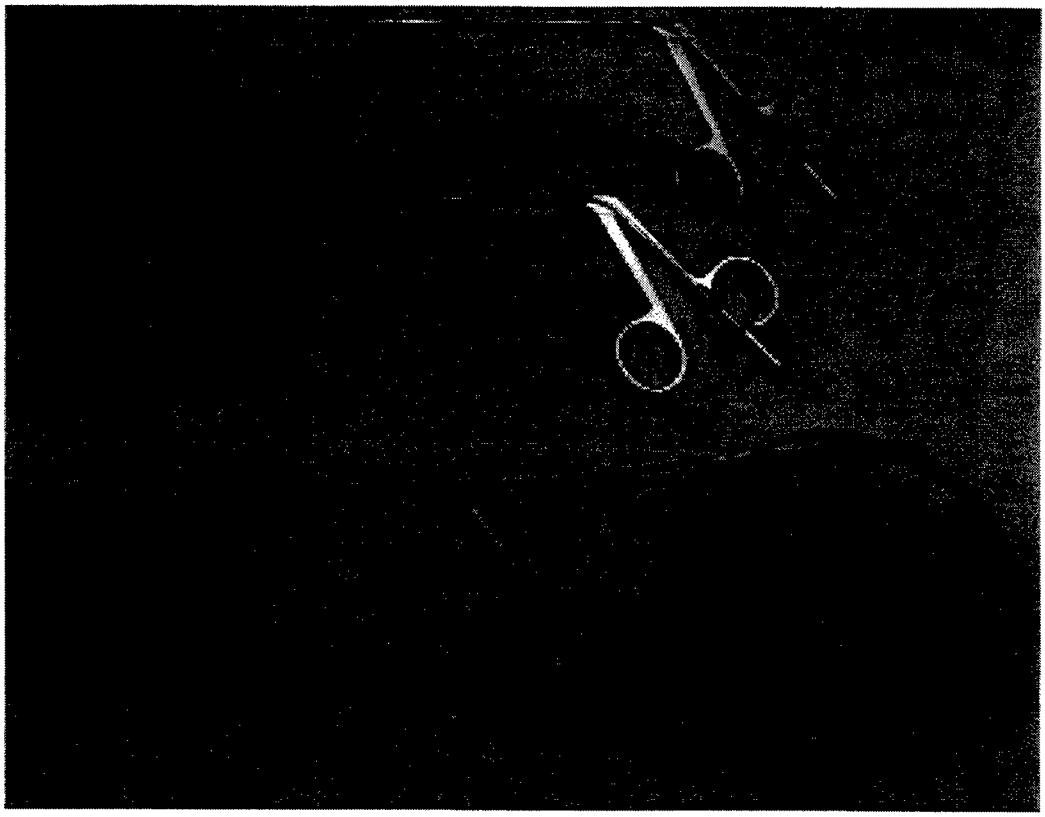

FIGURE 3 Malleable pituitary and endoscope

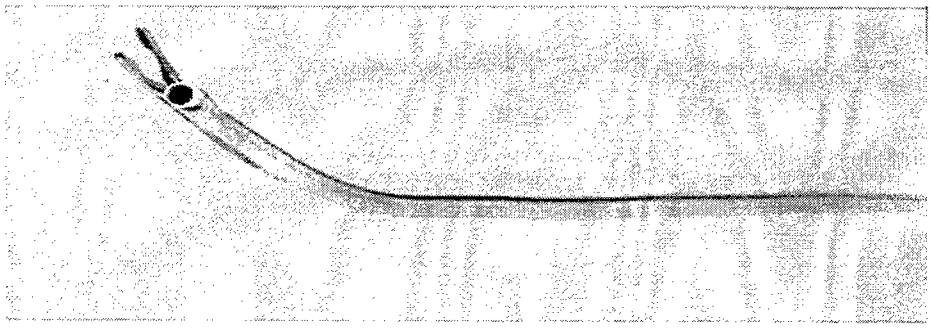

FIGURE 4 Tip of the pituitary showing the endoscope channel

FIGURE 5 the malleable pituitary in the foramen

The endoscopic stenosis retractor consists of a modified nerve root retractor with a channel to fit the small fiberoptic endoscope (Figure 6) [3]. The channel ends 5 mm from the tip of the retractor blade and angles laterally, allowing the endoscope to focus in the lateral recess (Figure 7). Using this instrument, the surgeon can retract the spinal dura and nerve root while looking into the lateral recess where disc material and ligamentous material may compress the nerve root. In this case the endoscopic instrument permits surgical observation around a corner. This capability previously did not exist.

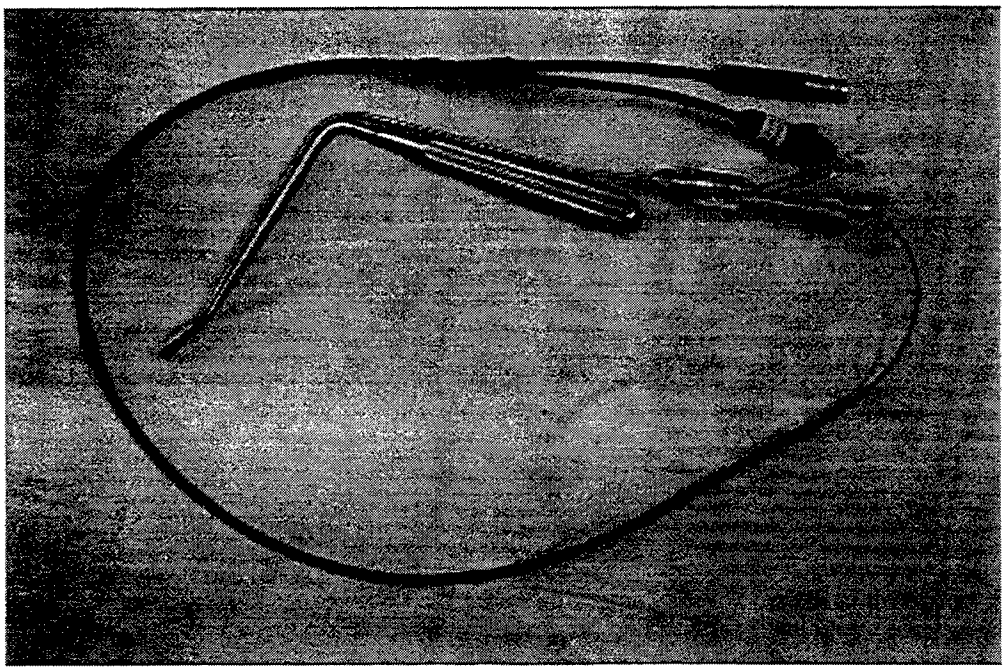

FIGURE 6 the root retractor with endoscope

FIGURE 7 the retractor retracting the dura

The endoscopic curved kerrison ronguer consists of a modified curved kerrison rongeur (described by Beatty[4]) with a channel to fit a small malleable endoscope (Figures 8,9). The overall profile of the instrument is small enough to be inserted and used within the lateral recess (Figure 10). The kerrison has a 30 degree angle

(determined by cadaver studies) to insure the foramen can be reached using a standard laminectomy.

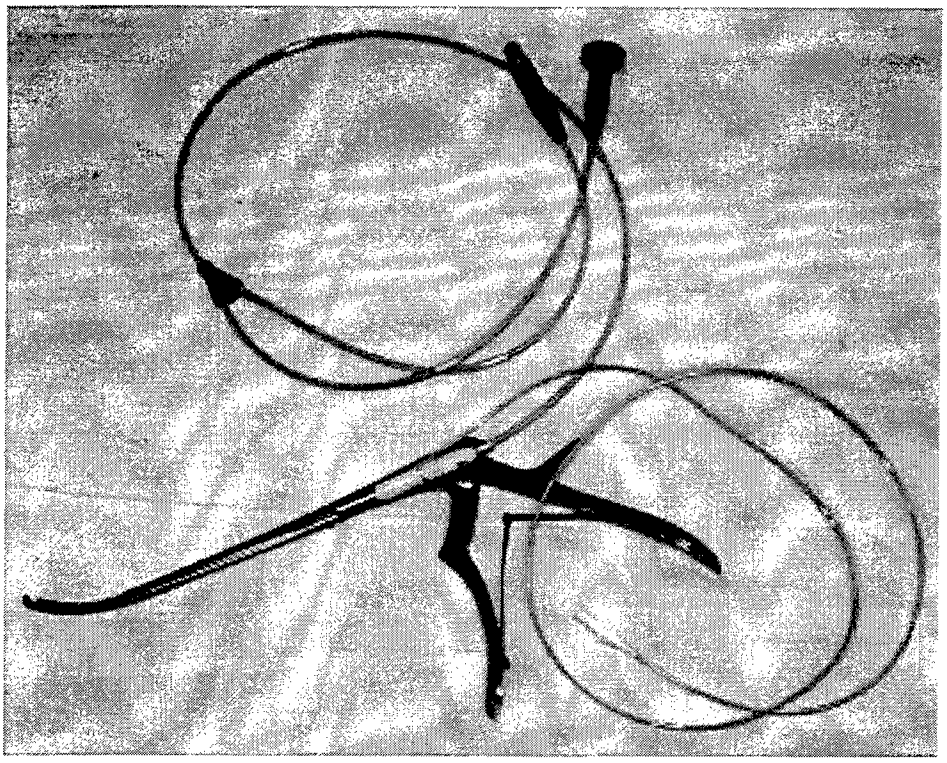

FIGURE 8 the kerrison punch and endoscope

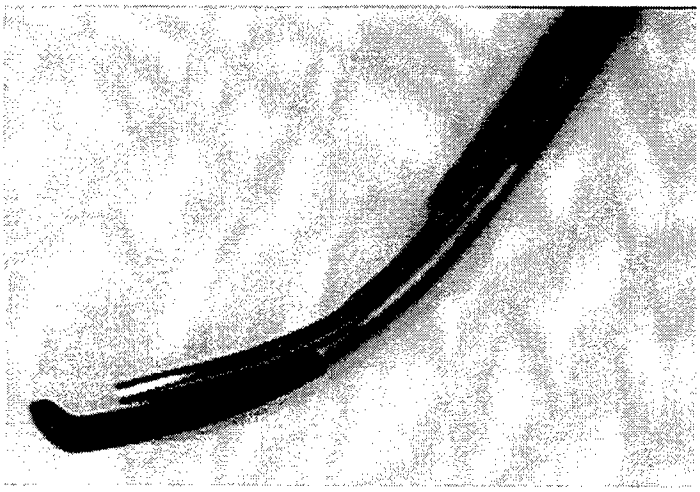

FIGURE 9 the tip of the kerrison with the endoscope channel

FIGURE 10 the kerrison in the foramina

We have used these instruments during the surgery for forty patients with lateral disc herniations, migrated disc fragments and spinal stenosis.

## RESULTS

All of the instruments provided excellent visualization and surgical access. Initially, there was a problem keeping the lens of the endoscopes clean. When the instruments were first used, the lens would fog due to a temperature difference between the instrument and patient body temperature. This was solved with a commercially available emulsion to coat the lens. In a bloody operative field, the lens will become obstructed. We have found that a suction instrument along with the instrument overcomes this problem for the most part. We are currently redesigning the endoscopic retractor to contain an internal suction.

The malleable pituitary instrument enabled recognition of pertinent anatomy in the lateral recess and removal of lateral disc fragments (Figure 11). The endoscopic retractor gave an excellent view of the lateral recess and allowed monitoring activity of instruments, such as the nerve hook (Figure 12).

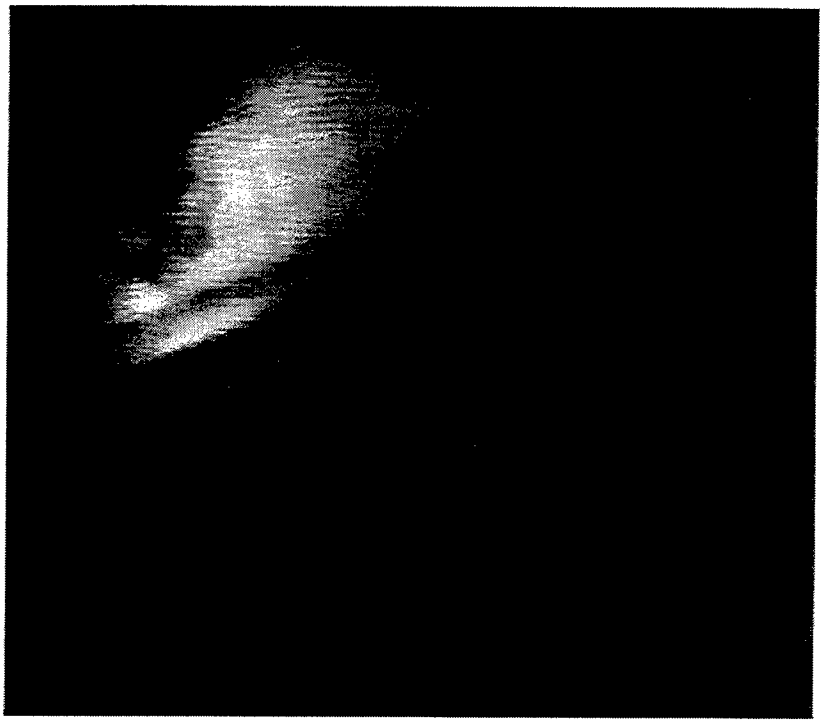

FIGURE 11 the pituitary is under the nerve root

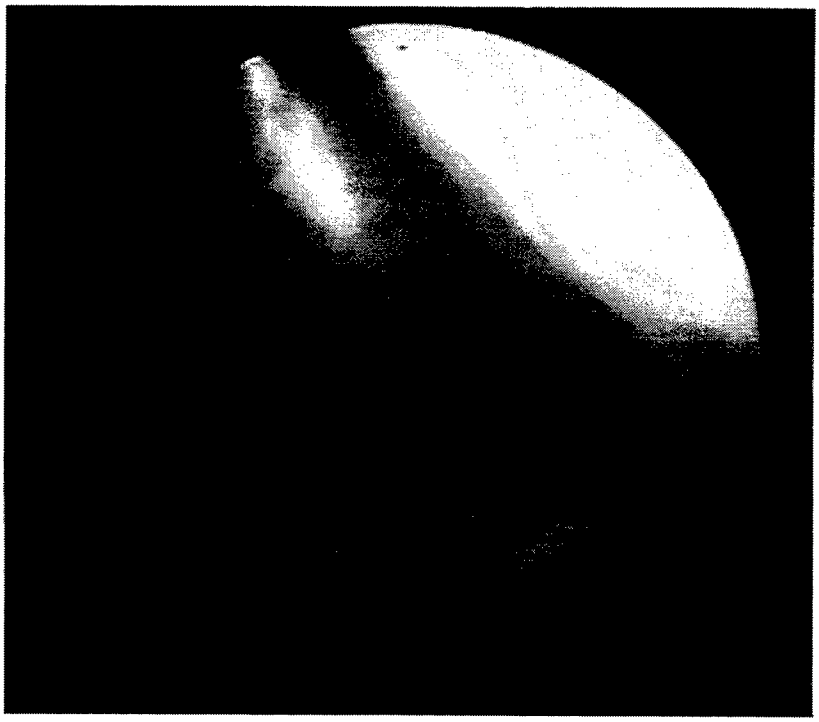

FIGURE 12 A nerve hook adjacent to the white nerve root

Perhaps the most useful instrument was the curved rongeur. Bone and ligament compressing the nerve root could be removed (Figure 13).

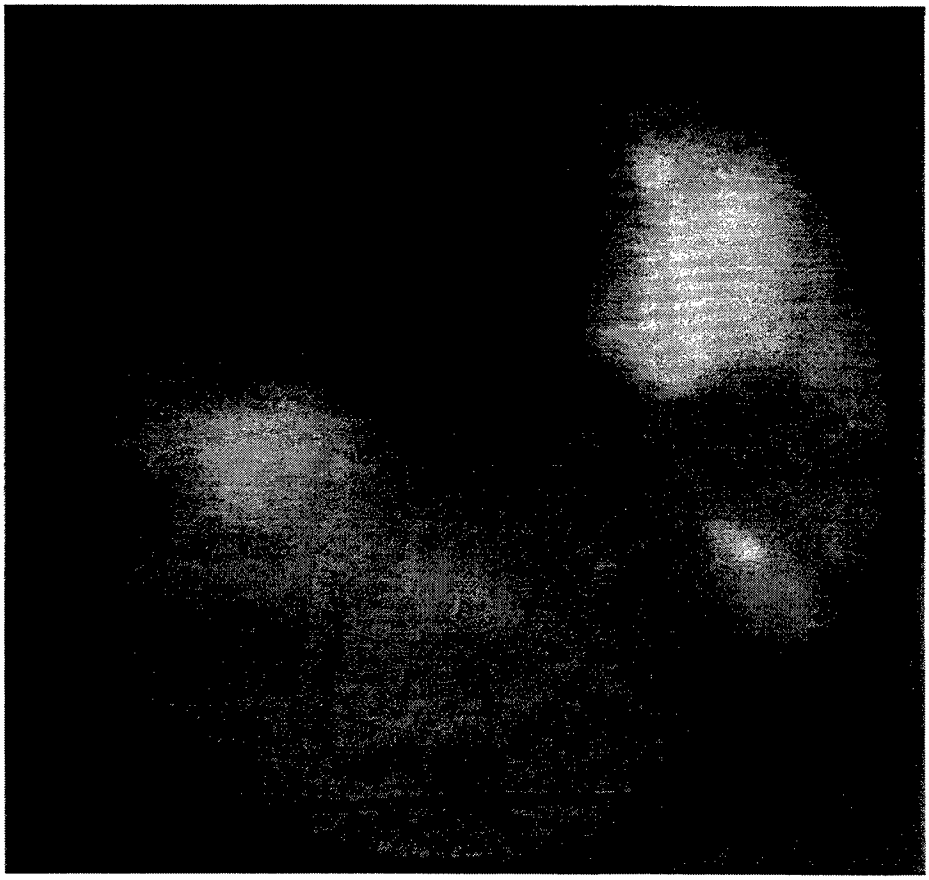

FIGURE 13 the punch-removing ligament

Of the patients operated upon with lateral disc herniations, one required a second procedure for removal of further disc herniation several months after the original procedure. No patients with migrated fragments required a second operation. In the group with spinal stenosis, two patients had some residual intermittent nerve root symptomatology, but did not require further surgery.

There were no intraoperative complications such as hemorrhage, dural tears or neural damage. The operative times were not significantly increased. We have not found any delayed complications, such as increased postoperative bleeding, nerve dysfunction or spinal instability.

## DISCUSSION

We believe that the endoscopic instruments discussed above overcome some of the stated limitations induced by minimal operative approaches. They allow visualization around corners in the operative field, previously not possible. Moreover, we have had to relearn spinal anatomy because we are now looking from the inside out rather than from the outside in.

One aspect of operative visualization that has not been solved is binocular vision. Attempts to use two small endoscopes attached to an instrument resulted in a very bulky instrument that was inconvenient to use. Recently, attempts have been made to construct a binocular endoscope that is about the same size as the endoscope that we are using. It will be interesting to see if this might be employed with our instruments.

Objectively, the surgical cases reviewed have proven that instruments with integral endoscopes can be used safely and effectively for spinal procedures. They allow one to see surgical anatomy in ways we have not appreciated before. Subjectively, we think that they might enable us to do better surgery (less invasive, better decompression of the neural elements) than we have been able to do before.

Further experience with these instruments and more advanced technology will enhance instrument design permitting surgical improvement and diversity of applications.

## ACKNOWLEDGMENTS

We would like to acknowledge Miles Finn, Ph.D. for his support in these experiments

## REFERENCES

1) Haines S, Camarata P, Finn m, Poss T: Prototype instruments for endoscopic microsurgery: Technical note. Minim Invasive Neurosurgery 38: 167-169, 1995.

2) Frank EH: Removal of a Lateral Disc Herniation using a Malleable Endoscopic Forceps. Neurosurg. 41:311-313, 1998.

3) Beatty RA: Formaneotomy Rongeur. Spine 16:1388-89, 1991.

4) Frank EH, Hsu PK: An Endoscopic Retractor for Spinal Stenosis Surgery. Submitted Minimally Invasive Neurosurgery.

# SESSION 17

# Ultrastructure

# Optical assessment of tissue heterogeneity in biomaterials and implants

Steven L. Jacques

Oregon Medical Laser Center, 9205 SW Barnes Rd, Portland OR 97225

## ABSTRACT

Optical techniques can assess the heterogeneity and structural layers of biomaterials and implants. Such assessment can assist engineering of tissue patches and implants by assessing implant structure, monitoring the implant fabrication process, controlling the machining of the implant, and monitoring in vivo the body's host response to the implant. Optical scattering can quantify the granularity of a biomaterial on the scale of 0.1-10 μm. Optical coherence tomography can map heterogeneity on the scale of 2-20 μm. Optoacoustic imaging can image absorbing heterogeneities on the scale of 20 μm - 10 mm (or more). Diffusion optical tomography can image absorbing and scattering heterogeneities on the scale of 5 mm - 5 cm (or more). The opportunities for optical techniques in preparing biomaterials and implants are discussed.

**Key words:** optical diagnostics, imaging, tissue engineering, biomaterials

## 1. DISCUSSION

Optical techniques can assess the hetereogeneity and structural layers of biomaterials and implants. Such assessment can assist engineering of tissue patches and implants by assessing implant structure, monitoring the implant fabrication process, controlling the machining of the implant, and monitoring in vivo the body's host response to the implant.

**Optical scattering** can quantify the granularity of a biomaterial on the scale of 0.1-10 μm. The ultrastructure of tissues presents structures that are on the scale on the wavelengths of light. Consequently, the behavior of light scattering is dependent on the size distribution of tissue ultrastructure.

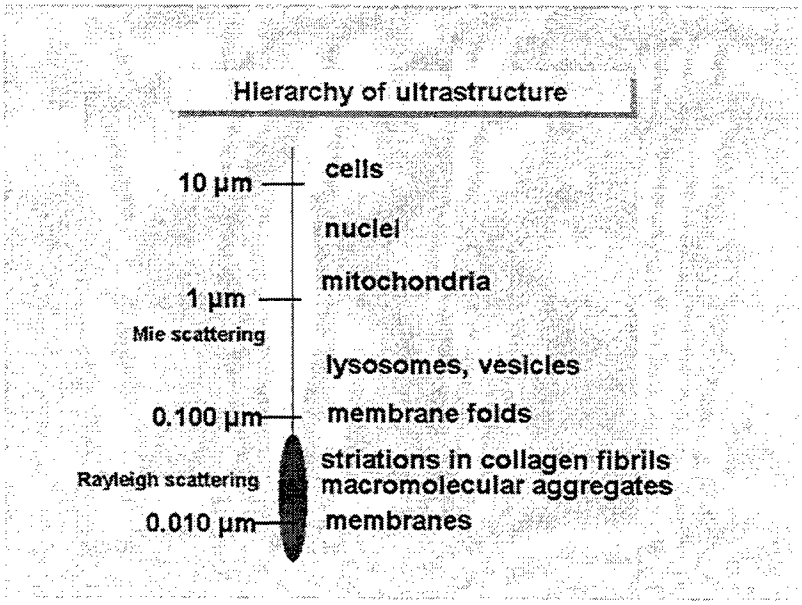




In *Laser-Tissue Interaction XI: Photochemical, Photothermal, and Photomechanical*, Donald D. Duncan, Jeffrey O. Hollinger, Steven L. Jacques, Editors, Proceedings of SPIE Vol. 3914 (2000)
1605-7422/00/$15.00

**Optical coherence tomography** (OCT) can map heterogeneity on the scale of 2-20 μm. OCT uses a superluminescent diode light source whose coherence length is on the order of 10-20 μm. Sub-ps pulsed laser systems can achieve broader bandwidths and hence shorter coherence lengths, down to about 2 μm. An interferometric system matches the distance to a vibrating mirror to the distance to a depth within a tissue, and the signal acquired by the detector is associated with this depth within the tissue. Hence, a vibrating mirror selects a oscillating depth within the tissue yielding a z-scan of the tissue structure. Typically, OCT images extend over a depth of about 0.5-2 mm with 2-20 μm resolution.

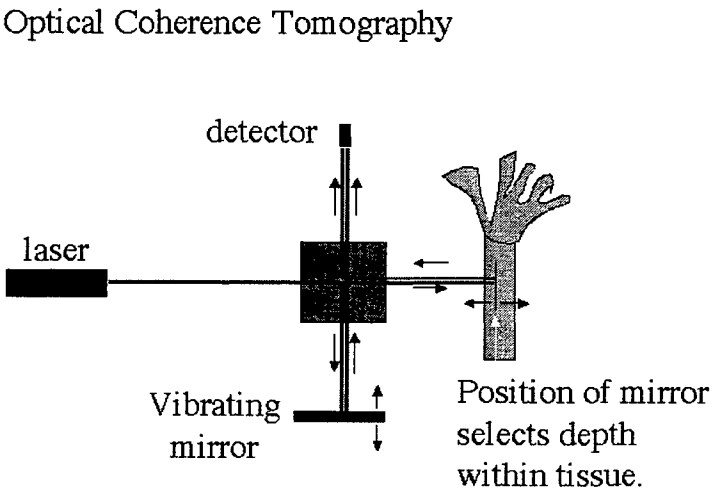


**Optoacoustic imaging** can image absorbing heterogeneities on the scale of 20 um - 10 mm (or more). A pulsed laser irradiates tissue and the light diffuses into the tissue. Where light is strongly absorbed by an absorbing object such as a blood vessel, the energy deposition causes thermoelastic expansion that generates a sound wave which propagates to an array of acoustic detectors on the tissue surface. The time of arrival of the sound at a detector specifies the distance of the object from that detector. Backprojection of the acoustic signals allows reconstruction of the absorbing object within the tissue.

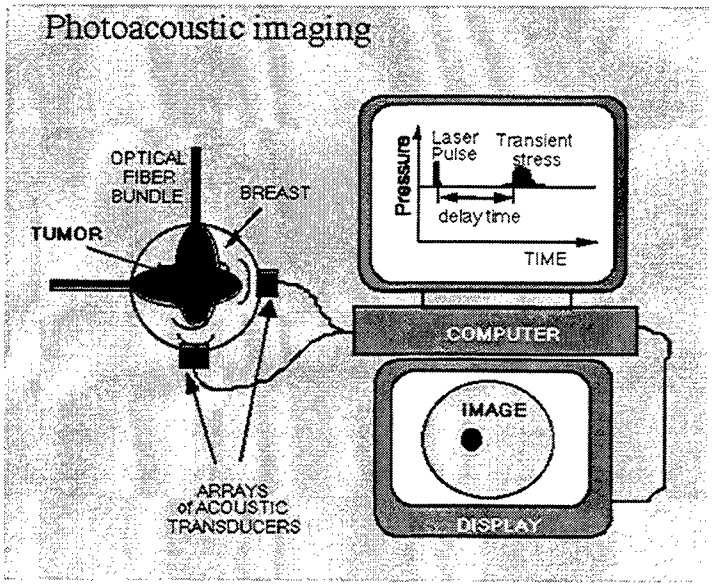

**Diffuse optical tomography** can image absorbing and scattering hetereogeneities on the scale of 5 mm - 5 cm (or more). Light diffuses into tissue, interacts with an absorbing or scattering object, and the perturbation caused by the object reradiates out toward the tissue surface where photodetectors acquire the signal.

There are 3 goals in optical measurements: (1) Detection, (2) Localization, and (3) Characterization. Sometimes one needs only to detect the presence of an object. Sometimes one needs to localize that object, and this is often the goal of "imaging". Sometimes one needs to characterize the object, for example by specifying the spectral signature of an object using fluorescence or reflectance or IR Raman spectroscopy, in order to identify the state of the object, for example normal versus cancerous.

The types of optical measurements fall roughly into two categories: (1) perturbation methods , or the "ninja in the woods at night" problem, and (2) hidden source problems, or the "ninja in the woods at night with a candle" problem. Clearly the latter is the better situation.

The following partial list of optical techniques indicates whether the method is a "perturbation" method or a "hidden source" problem.

- Diffusion Optical Tomography — Perturbation method
- Time gated transmission — Perturbation method
- Reflectance spectral imaging — Perturbation method
- Raman spectral imaging — Hidden Source
- Fluorescence spectral imaging — Hidden Source
- Fluorescence lifetime imaging — Hidden Source
- Optical Coherence Tomography — Hidden Source
- Photoacoustic imaging — Hidden Source
- Ultra-sound modulated light transmission — Hidden Source

In summary, there are a variety of optical techniques, each with its own scale of imaging resolution. The goals of optical measurements include detection, localization, and characterization. Optical techniques usually can be described as a perturbation method or a hidden source method.

## Goal 1: Detection

"There's a magic coin in one of these haystacks."

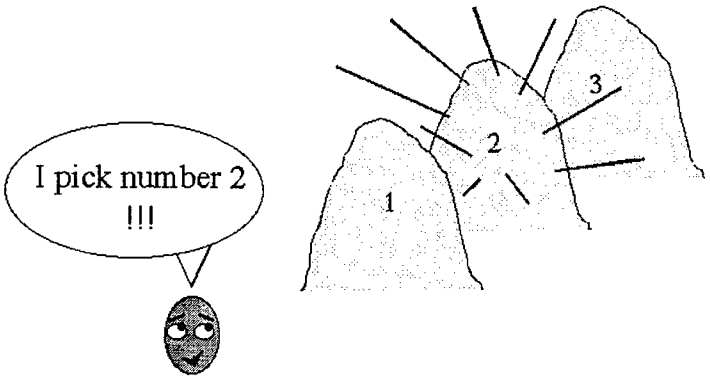


## Goal 2: Localization

"There's a magic coin in this haystack."

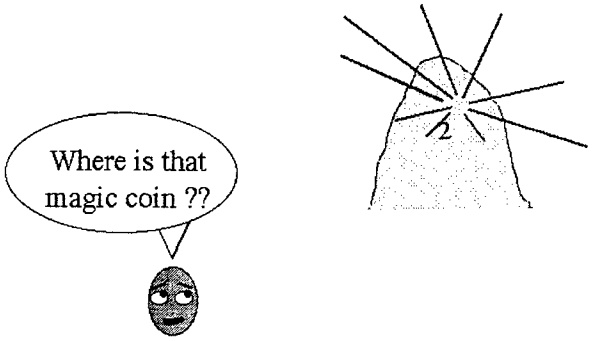


## Goal 3: Characterization

"or maybe there's a handgrenade in this haystack."

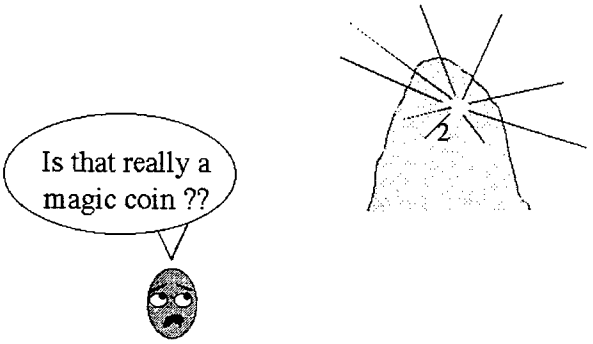

## Perturbation methods

= ninja in woods at night

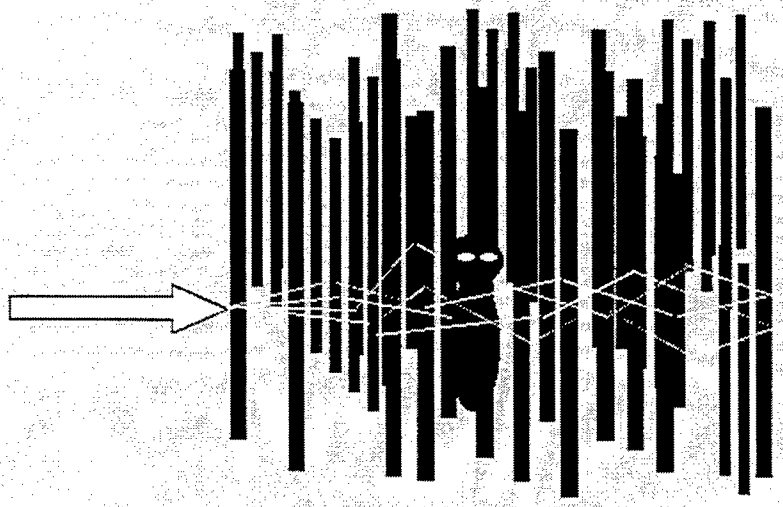

## Hidden source methods

= ninja in woods at night with a candle

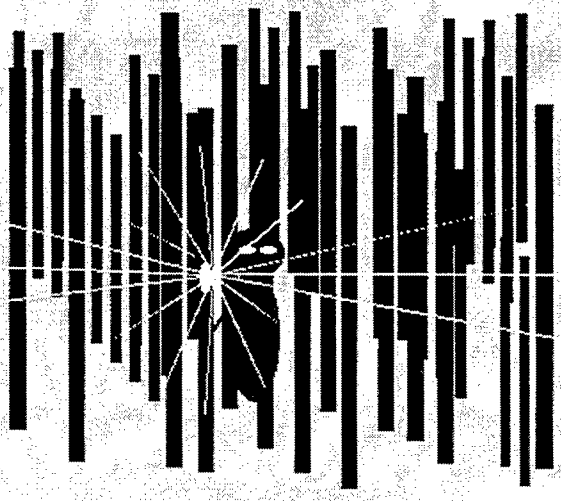

# Optical coherence tomography imaging of collagenous tissue microstructure

Kristi A. Hansen*, Jennifer K. Barton, Jeffrey A. Weiss

Biomedical Engineering Program, University of Arizona, Tucson, AZ 85721

## ABSTRACT

The engineering of new biomaterials requires an in-depth understanding of the structure and function of the native tissues. Optical coherence tomography (OCT) is a non-destructive technique that allows the visualization of the microstructure of biological tissues. The aim of this study was to determine if OCT could be used to identify geometric properties of tendons such as crimp pattern. Freshly harvested tendon tissue was imaged with OCT during the application of incremental axial strain. Loads were simultaneously recorded during imaging. Results revealed that birefringent banding perpendicular to the collagen fiber axis could be visualized and measured. This crimp banding disappeared at a very low strain. Birefringent banding parallel to the collagen fiber axis was also seen and it was observed that the number of parallel bands increased as strain increased. Stress-strain data was calculated and found to lie within the expected range. These results indicate that OCT may prove to be a useful tool for the non-destructive analysis of tissue microstructure.

**Keywords:** OCT, collagen, crimp, birefringence

## 1. INTRODUCTION

To engineer new biomaterials or induce the generation of new tissue, the properties and processes of the native tissue must first be understood. The relationship between tissue microstructure and continuum level function has long been a topic of interest in biomechanics and tissue engineering. Mechanical properties of biological tissues depend on structural organization and features, from the microscopic to macroscopic level. Due to the difficulties in accurately visualizing the microstructure, studies of structure-function relations in biological soft tissues are often difficult or impossible. Although histological methods can provide some microstructural information, the techniques require destruction of the tissue and often alter the relationship between tissue components.

Tendons and ligaments are small flexible pieces of fibrous connective tissue. Tendons join muscle to bone and ligaments join bone to bone, transmitting force and guiding movement. These soft tissues are commonly injured and heal by scarring, which results in altered interior tissue organization and inferior mechanical properties when compared to control tissues. Surgical reconstruction or replacement is often required. Understanding the behavior of tendons and ligaments is important in order to prevent injuries, optimize reconstruction, and improve replacements. Both tendons and ligaments are composed mainly of type I collagen. Collagen molecules form into microfibrils that aggregate to form subfibrils. A number of subfibrils form fibrils, which associate into fibers or fascicles[1]. Fascicles finally assemble to form tendons and ligaments. Fascicles can be viewed under polarized light to reveal a longitudinal waveform or crimp pattern. In rat tail tendon fascicles, the crimp pattern on the surface was observed to disappear under low stress[2,3]. It is generally accepted that the stress-strain curve for collagenous tissue is not linear, but consists of three regions, the first of which is called the toe region, in which collagen fibers gradually straighten[4]. It is believed that the transition from the toe region to the second region, which is linear, is the point at which the crimp pattern has completely straightened or disappeared. The third region is again non-linear, due to the onset of internal failure, and ends at complete failure. It is of interest to note that the physiological function of tendon is mostly confined to the toe region[5].

Recent attention has been given to non-destructive techniques used to quantify the microstructure of soft tissues. Sacks, Smith, and Hiester[6] developed a small angle light scattering device that can measure fiber orientation in soft tissues of less than 500 μm thickness with an angular resolution of approximately 1 degree and a spatial resolution of +/- 254 μm.

* Correspondence: Email: khansen@u.arizona.edu; WWW: http://www.ece.arizona.edu/~BMEoptics; Telephone: 520 626 8175

In *Laser-Tissue Interaction XI: Photochemical, Photothermal, and Photomechanical*, Donald D. Duncan, Jeffrey O. Hollinger, Steven L. Jacques, Editors, Proceedings of SPIE Vol. 3914 (2000)
1605-7422/00/$15.00

Magnetic resonance diffusion tensor techniques have been used to measure fiber orientation in canine myocardium[7] and the lamellar structure of the intervertebral disc[8]. Others have developed non-invasive techniques to investigate the composition of the different layers of skin[9]. Optical Coherence Tomography (OCT) provides a relatively inexpensive, non-destructive alternative for the analysis of soft tissue microstructure, with resolution that is potentially superior to the aforementioned techniques in three dimensions (on the order of 15 μm)[10]. OCT is an optical analogue to ultrasound, utilizing reflected near-infrared light instead of sound. The intensity of reflected low coherence light is measured, using a Michelson interferometer to determine its spatial origin (Figure 1). It is a recently developed technology that has been used to image many biological tissues *in vitro* or *in vivo*, including skin[11], retina[12], oviduct[13], aorta[14] and tendon[15].

The birefringent nature of collagen enables the visualization of crimp pattern under polarized light in the form of light and dark bands perpendicular to the collagen fiber axis. Birefringence previously seen in OCT images, however, appears to be indicative of tissue state[16]. Collagenous tissues observed under polarization sensitive OCT (PS-OCT) lose birefringence when they are damaged[17] or disorganized[18]. Boer[15] used PS-OCT to image fresh bovine tendon, revealing banding parallel to the fiber axis. Tendons are highly organized even in their relaxed state, resulting in the appearance of birefringence effects in OCT images, even using OCT that is not polarization sensitive. As tendon is stretched, the fibers straighten and become more perfectly aligned with the tendon axis. This has been reported to correlate with changes in the crimp pattern of the collagen.

Nondestructive and potentially noninvasive measurement of the ultrastructure of collagenous soft tissues would provide a unique method for the evaluation of normal and healing tissues and the efficacy of treatment regimens. The technique could also be used to determine microstructural parameters for constitutive models of the tissue material behavior[19,20]. The objectives of this work were to assess the feasibility of quantifying the crimp pattern of tendons under different states of strain. Our hypotheses were that OCT imaging would allow visualization of tendon crimp pattern because of its birefringent nature, and that the birefringence would be extinguished as successively increasing increments in tensile strain were applied to the tendons.

## 2. METHODS

### 2.1. Optical coherence tomography

The OCT system used to image tendons in this study was recently built by the investigators and is similar to one described by Izatt[10] (Figure 1). The system has axial resolution of 15 μm in air and lateral resolution of approximately 15 μm. Acquisition time varies depending on the number of pixels in the image. Based on an image 512 x 100 pixels, acquisition time is approximately 7 seconds. The system uses a superluminescent source with a center wavelength of 1295 nm. Cross-sectional scans are taken into the tissue one to two millimeters and along the tissue the desired length, dependent on the movement of a motorized stage (Figure 2).

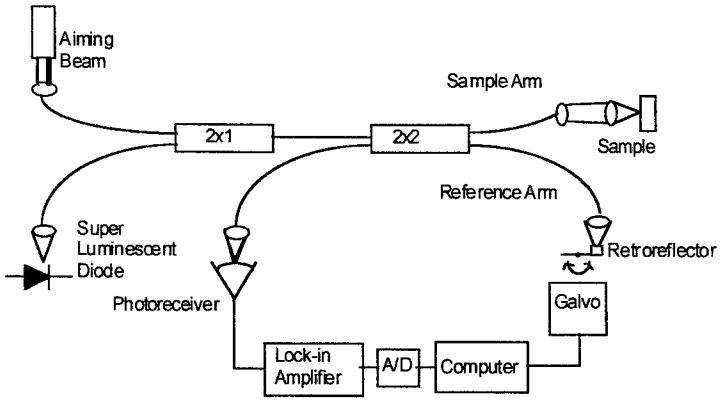


**Figure 1:** OCT system. Backscattered light from the sample and translating retroreflector interferes when the pathlength is within the coherence length of the source.

### 2.2. Tissue preparation

Tendons from the forelimb of a mature sheep were obtained immediately following slaughter. Rat tail tendons from four Sprague Dawley rats were obtained immediately following sacrifice. All tendons were kept continuously moist with 0.9% buffered saline during harvest and preparation, and images were acquired within 48 hours of sacrifice. Sheep tendons were excised from the surrounding tissue and trimmed to a length of approximately 35 mm. The tendons were gripped in stainless steel clamps and mounted in a custom-built stretching apparatus (Figure 2). The skin was removed from the rat tails and pieces of tendon were carefully dissected away from the proximal end of the tail. Single fascicle specimens were teased out of the tendon section. All rat tail fascicles were secured with cyanoacrylate between two small pieces of rubber to increase the gripping area and avoid tissue damage at the clamped area. Nylon thread markers were attached transverse to the collagen fiber direction of the tissue with cyanoacrylate, on specimens longer than 20 mm (Figure 2, inset). Each end was then placed in a metal clamp, allowing for a small amount of slack to keep from prematurely stretching the tissue. The stretching apparatus was then attached to the motorized stage and the saline bath was filled to just cover the tissue.

### 2.3. Mechanical testing

The sheep tendons were used in the initial development and validation of the experimental protocol, while the rat tendons were used to correlate crimp with the stress-strain behavior of the tissue. The width and thickness of rat tail specimens were measured using digital calipers and the cross-sectional area was determined using the assumption of elliptical cross-sectional geometry. Thickness measurements were later verified using values determined from the OCT images. The nylon markers formed a gage length for strain measurements using images acquired by the OCT system (Figure 2). In rat tail fascicle specimens that were shorter than 20 mm, clamp edges were imaged to form the gage length. One clamp was attached to a translation stage and the other was fixed to a stationary plate. A micrometer adjusted the position of the translation stage to apply strain to the clamped tissue. The stretching apparatus was attached to a computer-controlled motorized stage to allow movement along the collagen fiber axis for OCT image acquisition. The zero-load length of the tissue was established by consecutively applying and removing a small tare load via adjustment of the micrometer. The clamp-to-clamp distance was then measured with calipers. An image of the tissue with zero-load length was acquired in the vertical plane with the OCT system. Using the measured zero-load length, the rat tail fascicle was consecutively stretched to lengths corresponding to 1, 2, 3, 4 and 5% clamp-to-clamp strain or 30-50 μm increments. The exact tissue-level strain for the rat tail fascicles was later determined from the change in distance between the nylon thread markers in the OCT images. A 100 lb. load cell (Transducer Techniques, Temecula, CA), integrated into the stretching apparatus, was connected to an amplifying circuit and then interfaced with a data acquisition system. The load was continuously monitored and recorded during the application of each strain increment, and an OCT image was acquired for each strain increment when the change in load dropped below a value of 0.03 N/sec. Engineering stress, $\sigma$, was calculated at each strain increment using the initial cross-sectional area $A_0$ and the measured load $F$ as $\sigma = F/A_0$.

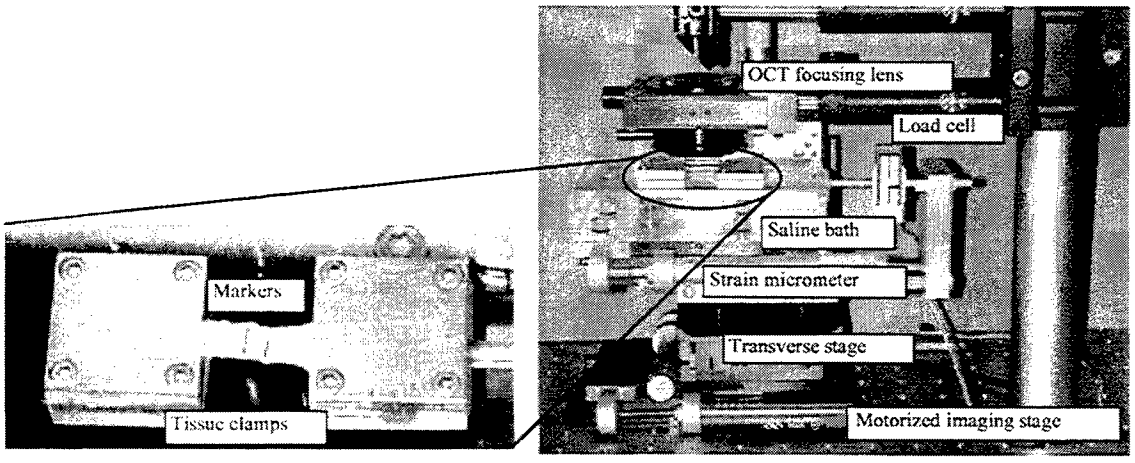


**Figure 2:** Stretching apparatus with enlarged top view of tissue clamps holding sheep tendon.

### 2.3. Data analysis

Strain and crimp period were measured using image analysis software (Scion Inc., Frederick, MD). Marker-to-marker distances were measured to determine the strain on the tissue portion being imaged. Engineering strain was calculated as $\varepsilon = \Delta L/L_0$, where $L_0$ is the marker-to-marker distance on the unstrained tissue and $\Delta L$ is the difference between the strained marker-to-marker distance and $L_0$. Crimp period, identified by one dark and light band pair, was measured over the imaged length and ranges were reported.

## 3. RESULTS

### 3.1. Crimp pattern and birefringence changes

Preliminary tests on sheep tendons show how the ultrastructure of the tendon differed under different strain conditions. In Figure 3, both vertical and horizontal banding is seen in the interior of the tendon. The vertical banding is believed to represent the collagen birefringence due to crimp, while the vertical banding is likely a part of the structural organization of the tendon. As strain was applied to the tissue, the vertical banding gradually disappeared from the images (Figure 4). The dark region in the top center of the tissue is due to dehydration of the tissue. The black nylon markers placed on the top surface of the tissue absorb the light and cause the thick dark vertical stripes seen in the images. All images show x and z scales in millimeters and the intensity scale in decibels.

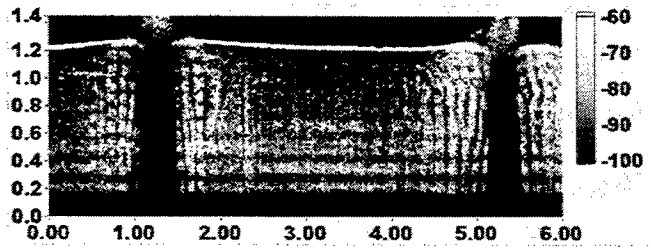


**Figure 3:** Sheep tendon before strain application. Vertical banding indicative of collagen crimp pattern is apparent.

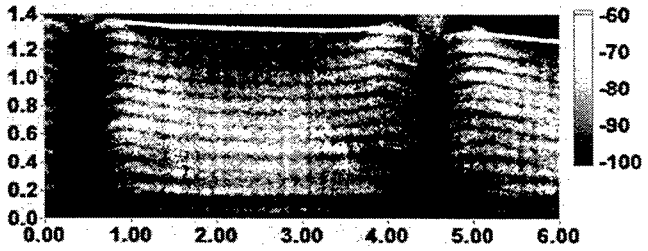


**Figure 4:** Sheep tendon after application of 2.4% strain. Vertical banding disappeared and horizontal banding became more apparent.

Figure 5 represents typical images resulting from the rat tail fascicle tests, as a sequence. Measurable crimp period ranged from 100 μm to 200 μm in Figures 5A–C. Crimp period in Figure 5D ranged from 100 μm to 160 μm. Crimp banding disappeared in Figure 5E. There is little change between images A, B, and C, the first two increments of strain. All three images show distinct vertical and horizontal banding. The third increment shows decreased visibility of crimp banding and an additional bright horizontal band appears. Larger crimp periods seen in the previous images have disappeared and only small crimp periods remain in Figure 5D. In the final image the crimp banding can no longer be distinguished and the new horizontal band in the previous image has increased in thickness.

### 3.2. Stress-strain data

Stress strain data for single fascicle tests is plotted in Figure 6. Values are within the expected range.

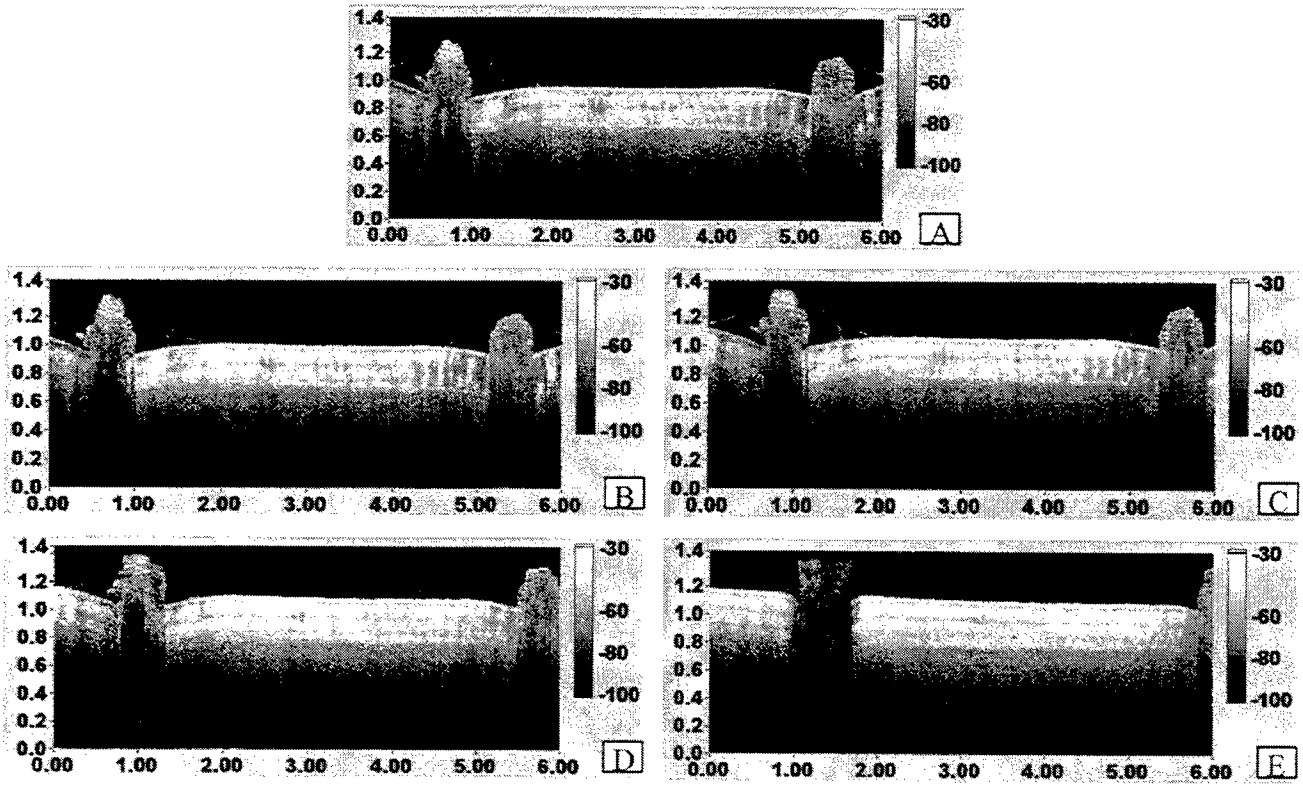


**Figure 5A-E:** Change in birefringent banding with increasing strain. Clamp-to-clamp strain: A) 0.0%, B) 0.4%, C) 0.8%, D) 1.3%, E) 1.7%.

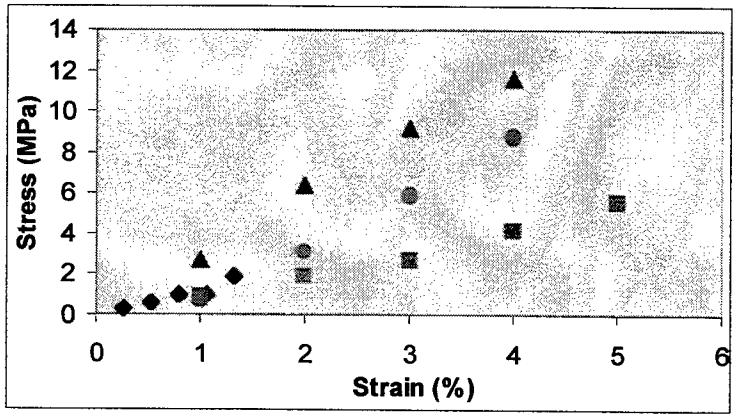


**Figure 6:** Stress-strain data for tests of rat tail tendon fascicles.

## 4. DISCUSSION

This study demonstrated that OCT imaging can visualize microstructural details of collagenous tissues. In particular, the crimp pattern of tendons was readily visible in the OCT images, and changes in the crimp pattern were seen as the tissue was stretched. Preliminary OCT images of sheep tendon showed the horizontal banding like that seen by other researchers[15]

using PS-OCT to look at bovine tendon, and in addition revealed the vertical birefringent banding indicative of crimp pattern. Knowing that crimp pattern is believed to disappear at low strain, we desired to find if OCT could image this process. Also, understanding that birefringent horizontal banding indicates tissue state or level of organization, we wanted to see if the horizontal banding changed as the tendon was strained. Prior to these tests, we introduced a polarization-rotating element into the sample arm of the system. Changes in the banding appearance were observed as the element was rotated, assuring us that the banding observed was indeed a polarization effect.

Figure 5A-E shows the progressive change in birefringent banding of rat tail tendon fascicle. Relaxed crimp period measurements are in the same range as the 120 μm measurement made by Diamant[3]. We attribute the change in the appearance of the banding to the removal of the crimp. We attribute the increased brightness and number of horizontal bands to the increased level of organization that strain induces in the tissue by pulling the fibrils into more parallel alignment with the tensile axis.

A comparison of clamp-to-clamp and marker-to-marker strain was not presented herein. Under very low strain measurements, the two measurements correlate well. At higher strains, the measurements differed in some of the tests. It was observed that the markers in these tests were adhered to the very thin fascia that covered the fascicle. The stretching of this fascia often did not appear to correlate with the stretching of the tendon tissue beneath it, accounting for the difference in measurements. Clamp-to-clamp strain values were used in these cases. In future work the thin fascia will be removed prior to testing.

Stress-strain data for the rat tail tendon fascicles was within the range reported in the literature[21] of 0 to 20 MPa for strains of 0 to 5%. This suggests that our stress and strain measurements were accurate and provide a good reference between collagen crimp period, applied strain and resulting stress in the tissue. This information, combined with images taken at smaller strain increments, can provide accurate detail on the state of the tissue as it passes through the toe region and transitions into the linear region. Three-dimensional images would be even more useful in determining tissue state, measuring crimp period and measuring cross-sectional areas. Work is presently in progress to develop a real-time OCT imaging system that would then be capable of taking continuous images as tissue is mechanically loaded.

## ACKNOWLEDGEMENTS

This work was supported in part by a grant from the National Science Foundation (KAH, JKB) and a Whitaker Foundation Biomedical Research Grant (JAW).

## REFERENCES

1. J. Kastelic, A. Galeski, and E. Baer, "The multicomposite structure of tendon," Connective Tissue Research, **6**:11-23, 1978.
2. B. J. Rigby, N. Hirai, J.D. Spikes, H. Eyring, "The mechanical properties of rat tail tendon," Journal of General Physiology, **43**:265-289, 1959.
3. J. Diamant, A. Keller, E. Baer, M. Litt, and R. G. C. Arridge, "Collagen; ultrastructure and its relation to mechanical properties as a function of ageing," Proceedings of the Royal Society of London. Series B: Biological Sciences, **180**:293-315, 1972.
4. Y. Lanir, E. L. Salant, and A. Foux, "Physico-chemical and microstructural changes in collagen fiber bundles following stretch in-vitro," Biorheology, **25**:591-603, 1988.
5. A. Viidik, C. C. Danielsen, and H. Oxlund, "On fundamental and phenomenological models, structure and mechanical properties of collagen, elastin and glycosaminoglycan complexes," Biorheology, **19**:437-451, 1982.
6. M. S. Sacks, D. B. Smith, and E. E. Hiester, "A small angle light scattering device for planar connective tissue microstructural analysis," Annals of Biomedical Engineering, **25**:678-689, 1997.
7. E. W. Hsu, A. L. Muzikant, S. A. Matulevicius, R. C. Penland, and C. S. Henriquez, "Magnetic resonance myocardial fiber-orientation mapping with direct histological correlation," American Journal of Physiology, **274**(5 Pt 2):H1627-34, 1998.
8. E. W. Hsu and L. A. Setton, "Diffusion tensor microscopy of the intervertebral disc anulus fibrosus," Magnetic Resonance in Medicine, **41**:992-999, 1999.
9. P. J. Caspers, G. W. Lucassen, R. Wolthuis, H. A. Bruining, and G. J. Puppels, "In vitro and in vivo Raman spectroscopy of human skin," Biospectroscopy, **4**(5 Suppl):S31-39, 1998.
10. J. A. Izatt, M. D. Kulkarni, S. Yazdanfar, J. K. Barton, and A. J. Welch, "*In vivo* bi-directional color Doppler flow imaging of picoliter blood volumes using optical coherence tomography," Optics Letters, **22**:1439-1441, 1997.
11. J. M. Schmitt, M. Yadlowsky, and R. F. Bonner, "Subsurface imaging of living skin with optical coherence microscopy," Dermatology, **191**:93-98, 1995.

12. M. R. Hee, J. A. Izatt, E. A. Swanson, D. Huang, C. P. Lin, J. S. Schuman, C. A. Puliafito, and J. G. Fujimoto, "Optical coherence tomography of the human retina," Archives of Ophthalmology, **113**:325-332, 1995.
13. J. M. Herrmann, M. E. Brezinski, B. E. Bouma, S. A. Boppart, C. Pitris, J. F. Southern, and J. G. Fujimoto, "Two- and three-dimensional high-resolution imaging of the human oviduct with optical coherence tomography," Fertility and Sterility, **70**:155-158, 1998.
14. M. E. Brezinski, G. J. Tearney, B. E. Brett, S. A. Boppart, M. R. Hee, E. A. Swanson, J. F. Southern, J. G. Fujimoto, "Imaging of coronary artery microstructure with optical coherence tomography," American Journal of Cardiology, **77**:92-93, 1996.
15. J. F. de Boer, T. E. Milner, M. J. C. van Gemert, and J. S. Nelson, "Two-dimensional birefringence imaging in biological tissue by polarization-sensitive optical coherence tomography," Optics Letters, **22**:934-936, 1997.
16. M. J. Everett, K. Schoenenberger, B. W. Colston, Jr., and L. B. Da Silva, "Birefringence characterization of biological tissue by optical coherence tomography," Optics Letters, **23**:228-230, 1998.
17. S. M. Srinivas, J. F. de Boer, B. H. Park, K. Keikhanzadeh, H. L. Huang, Z. Chen, J. S. Nelson, "Determination of burn depth by polarization sensitive optical coherence tomography," in *Coherence Domain Optical Methods in Biomedical Science and Clinical Applications III*, Valery V. Tuchin, Joseph A. Izatt, Editors, Proceedings of SPIE Vol. 3598, 70-78, 1999.
18. X. Li, J. Herrmann, R. Ghanta, C. Pitris, W. Drexler, C. Jesser, D. Stamper, D. Golden, S. Martin, J. G. Fujimoto, M. Brezinski, " OCT imaging of osteoarthritic cartilage: structure, polarization sensitivity, and clinical feasibility," in *Coherence Domain Optical Methods in Biomedical Science and Clinical Applications III*, Valery V. Tuchin, Joseph A. Izatt, Editors, Proceedings of SPIE Vol. 3598, 152-157, 1999.
19. M. K. Kwan and S. L. Woo, "A structural model to describe the nonlinear stress-strain behavior for parallel-fibered collagenous tissues," ASME Journal of Biomechanical Engineering, **111**:361-363, 1989.
20. C. Hurschler, B. Loitz-Ramage, R. Vanderby, Jr., "A structurally based stress-stretch relationship for tendon and ligament," ASME Journal of Biomechanical Engineering, **119**:392-399, 1997.
21. J. P. Price, G. O. Njus, T. A. Conway, "Ultrastructural properties of rat tail tendon," Biomedical Engineering Conference. Proceedings of the 1996 Fifteenth Southern, 456-459, 1996.

Invited Paper

# Laser Ultrasonic Techniques for Assessment of Tooth Structure

D.W. Blodgett[1] and K.C. Baldwin
The Johns Hopkins University Applied Physics Laboratory
Laurel, MD 20723

## ABSTRACT

Dental health care and research workers require a means of imaging the structures within teeth in vivo. For example, there is a need to image the margins of a restoration for the detection of poor bonding or voids between the restorative material and the dentin. With conventional x-ray techniques, it is difficult to detect cracks and to visualize interfaces between hard media. This is due to the x-ray providing only a 2 dimensional projection of the internal structure (i.e. a silhouette). In addition, a high resolution imaging modality is needed to detect tooth decay in its early stages. If decay can be detected early enough, the process can be monitored and interventional procedures, such as fluoride washes and controlled diet, can be initiated which can help the tooth to re-mineralize itself. Currently employed x-ray imaging is incapable of detecting decay at a stage early enough to avoid invasive cavity preparation followed by a restoration with a synthetic material. Other clinical applications include the visualization of periodontal defects, the localization of intraosseous lesions, and determining the degree of osseointegration between a dental implant and the surrounding bone.

A means of assessing the internal structure of the tooth based upon use of high frequency, highly localized ultrasound (acoustic waves) generated by a laser pulse is discussed. Optical interferometric detection of ultrasound provides a complementary technique with a very small detection footprint. Initial results using laser-based ultrasound for assessment of dental structures are presented. Discussion will center on the adaptability of this technique to clinical applications.

**Keywords:** laser-based ultrasonics, in-vivo tooth structure assessment, dental diagnostics

## 1. INTRODUCTION

The benefits of ultrasonics to examining soft tissue structures, particularly the abdominal region, brain, and eyes have long been known[1]. In these applications typically one or more acoustic contact transducers is used to generate and detect the acoustic waves in the structure. These procedures are simplified, at least in regards to the examination of teeth, with the relatively large dimensions that are being examined, the slower acoustic wave velocity (allowing lower frequency acoustic waves to be used for equivalent acoustic wavelengths), and a readily available acoustic coupling material for the transducer to the soft tissue. Soft tissue, unlike hard tooth enamel and dentin, is largely composed of water, making water a very efficient coupling material.

Attempts to adapt these conventional ultrasonic techniques to the examination of the internal structure of a tooth have met with little success[1,2,3,4]. One of the major obstacles was and is finding a suitable couplant for the transducer to the tooth for in-vivo measurements. Without proper coupling, it is difficult to transfer acoustic energy into the tooth. Early investigators[2,3] attempted using water, as with soft tissue structures, but the results were not convincing. Reich *et al.* [4] overcame this problem by replacing water with mercury. Although proving superior in coupling efficiency, it would never be suitable for clinical applications. Barber *et al.* [1] overcame this coupling difficulty by using a small aluminum buffer rod to transfer the acoustic energy from the contact transducer to the tooth. They estimated a transmission efficiency of almost 87% using this technique as compared to only 5% using water. Another area of concern addressed by Barber *et al.* [1], was the temporal resolution of ultrasonic probes as dictated by the excitation pulse length of the contact transducer. Previous researchers had used ultrasonic transducers operating between 10 and 20 MHz [3,4]. Barber *et al.* [1], by using a specially designed transducer,

[1] Correspondence: Email: david.blodgett@jhuapl.edu; Telephone: 443-778-7368 (Baltimore, MD) or 240-228-7368 (Washington D.C.); Fax: 443-778-6779/240-778-6779



In *Laser-Tissue Interaction XI: Photochemical, Photothermal, and Photomechanical*, Donald D. Duncan, Jeffrey O. Hollinger, Steven L. Jacques, Editors, Proceedings of SPIE Vol. 3914 (2000)
1605-7422/00/$15.00

generated a single pulse with a 10 nsec rise time that was repeated at a 2 kHz repetition rate. This pulse width corresponds to a maximum acoustic frequency, $f_{max}$, of about 1/10nsec = 100 MHz. The increased frequency content generated by this specially designed transducer allowed the researchers to clearly resolve the dentino-enamel and dentino-pulp interfaces of human and bovine incisors. The one limitation of Barber's system was the coupling of the aluminum buffer rod with the tooth surface. In order to ensure proper coupling of the acoustic energy to the tooth, a small flat spot had to be ground on the tooth surface. In addition to making this technique unsuitable for clinical applications, the large contact area (3.2 mm diameter) limited the spatial resolution of the probe. For assessing anomalies in a tooth, such as poor bonding or voids between the restorative material and the dentin, one requires a detection footprint smaller than the anomaly itself.

One means of increasing the spatial resolution of a contact transducer is to use a spherical transducer that focuses the beam onto the sample (tooth) surface. This is the basis for the acoustic microscope, which is the acoustic equivalent of the optical microscope [5]. Peck *et al.* [6] took advantage of the increased spatial resolution of the acoustic microscope to detect small caries lesions in sections of human enamel. In addition, they were able to quantify the anisotropic nature of the enamel via variations in the Raleigh velocity. However, as with the previous work by Barber *et al.* [1], special polishing of the tooth samples was required, again making the technique ill-suited for clinical applications.

Laser generation of ultrasound provides a non-contact, non-invasive method of generating high frequency (broad-band) ultrasound [7]. In laser generated ultrasound, a short-pulse laser is used, in place of a contact transducer, to excite acoustic waves in the specimen. Due to the absorption of pulse energy at or near the surface of the specimen, temperature gradients are established within the material producing a rapidly changing strain field. This strain field, in turn, radiates energy as elastic (ultrasonic) waves. At low pulse energies, this is an entirely thermoelastic process resulting in no damage to the material under test. An advantage of this technique over the previous methods is that no special surface preparation of the tooth is required. In addition, by focusing the laser beam onto the surface of the tooth, a very small contact (generation) area can be achieved. Spot size diameters on the order of tens of microns are routinely achieved. For clinical applications, one could imagine optical fiber delivery of the optical pulse to the tooth.

Optical interferometric detection of the ultrasound provides a complementary technique for remote sensing of ultrasonic waves [7,8]. As shown in Fig. 1, the surface displacement from the ultrasonic arrival varies the path length of one arm of the Michelson-type interferometer with respect to a reference arm. This path difference causes a corresponding phase difference between the wavefronts of the two arms of the interferometer. When the optical wavefronts are mixed, the phase difference becomes a variation in intensity, which can be measured directly. One drawback of the Michelson-type interferometer is that the test sample must provide a specular reflection. This is not possible without special preparation of the tooth's surface. However, Fabry-Perot and Mach-Zender interferometers are well suited for diffusely reflecting surfaces and adaptable to optical fiber delivery.

In this paper, ultrasonic waveforms from both human teeth and special tooth phantoms are presented. The tooth phantoms model both a healthy tooth and a tooth with amalgam restoration. Results from these tooth phantoms aids in the interpretation of the ultrasonic waveforms from the human teeth. A Nd:YAG pulsed laser was used for ultrasound generation in both the tooth phantoms and the real tooth. All ultrasonic wave detection was accomplished using a Michelson-type interferometer.

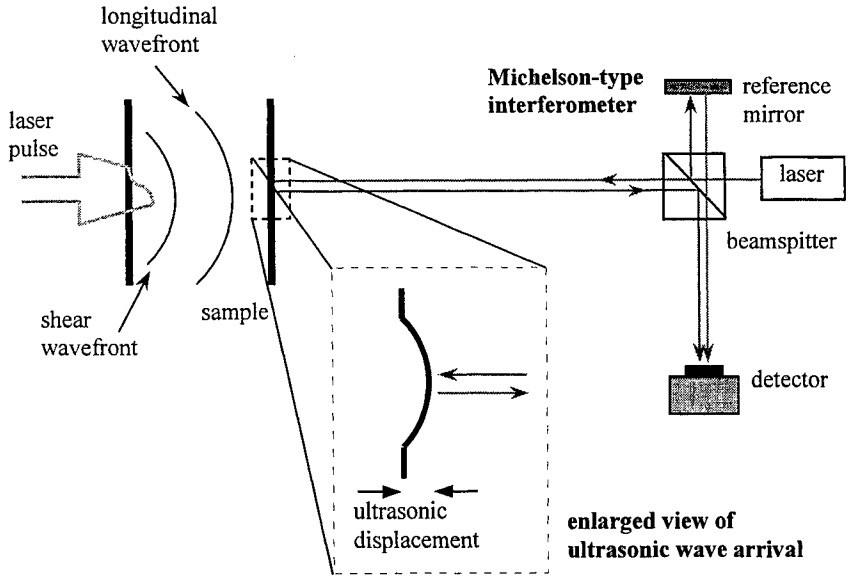


Fig. 1. Ultrasonic measurement scheme using a pulsed-laser for ultrasound generation and a Michelson-type interferometer for ultrasound detection.

## 2. ACOUSTIC MODELLING OF TOOTH STRUCTURE

### 2.1 Acoustic Wave Propagation

The generation and detection of ultrasonic waves provides a method for characterizing the bulk and surface properties of a material by interrogating a specimen with high frequency acoustic waves [7]. Up to three bulk acoustic waves can propagate in a material, each with its own characteristic velocity. As an ultrasonic wave propagates, the amplitude decreases due to geometrical spreading, attenuation from absorption, and scattering from discontinuities. Measurement of wave speeds, attenuation, and scattering provide the information needed to quantify the bulk properties of the material. Some applications for ultrasonics are provided in Table 1.

| Property | Measurements |
|---|---|
| *Dimensional* | thickness and density |
| *Compositional* | impurity levels |
| *Microstructural* | grain size, anisotropy, number and distribution of phases |
| *Mechanical* | elastic moduli |
| *Inspection* | defects, discontinuities, interfaces, bonds |

Table 1. Application of ultrasonics to material property measurements [7].

The propagation of elastic plane waves in an anisotropic material is described using Christoffel's equation[9,10,11] by

$$\left|C_{ijkl} l_j l_l - \rho v^2 \delta_{ik}\right| = 0. \tag{1}$$

This equation provides an analytic relation between the phase velocity, v, of the elastic waves and the elastic moduli, $C_{ijkl}$. The direction cosines are specified by $l_i$ (with i = 1, 2, or 3), $\rho$ is the material density, and $\delta_{ik}$ is the Kronecker delta function.

Although the anisotropic nature of tooth enamel is well documented [6,12], we will proceed, as with previous researchers [1,13], assuming the enamel, dentin, and pulp are elastically isotropic. For isotropic materials, only two bulk waves must be considered, longitudinal and shear. It can be shown through Christoffel's equation that the velocity of these two waves is given by

$$v_{long} = \sqrt{\frac{C_{11}}{\rho}} = \sqrt{\frac{E}{\rho}} \quad \text{and} \quad v_{shear} = \sqrt{\frac{C_{44}}{\rho}} = \sqrt{\frac{\mu}{\rho}}. \tag{2}$$

where E is the elastic modulus and $\mu$ is the shear modulus. The acoustic velocities for the various components of a tooth are listed in Table 2. When assessing any multi-phase structure, such as a tooth, both the acoustic velocity and acoustic impedance of each layer must be considered. The acoustic impedance, Z, is defined as

$$Z = \sqrt{E\rho} = \rho v_{long}. \tag{3}$$

When an acoustic wave travels from one medium to another (i.e. from the enamel to the dentin), a portion of the wave is reflected and the remaining portion transmitted (assuming no other losses). The intensity of the reflected acoustic radiation, $I_r$, assuming plane wave propagation, at the interface between two different mediums with acoustic impedances of $Z_1$ and $Z_2$, is given by

$$I_r = \left(\frac{Z_2 - Z_1}{Z_2 + Z_1}\right)^2 I_i \tag{4}$$

and the intensity of the transmitted acoustic radiation, $I_t$, is

$$I_t = I_i - I_r, \tag{5}$$

where $I_i$ is the intensity of the incident radiation. Knowledge of the relative reflected and transmitted intensities at each material interface in a tooth structure aids in the interpretation of the final ultrasonic waveform.

| Layer | $V_{long}$ [m/s] | $V_{shear}$ [m/s] | Density $\rho$ [kg/m$^3$] | Acoustic Impedan Z [x10$^6$ kg/m$^2$s] |
|---|---|---|---|---|
| ***Enamel*** | *6250* | *3100* | *3000* | *18.8* |
| Aluminum | 6300 | 3100 | 2700 | 17.0 |
| ***Dentin*** | *3800* | *1900* | *2000* | *7.6* |
| Tin | 3300 | 1700 | 1740 | 24.2 |
| Borosilicate glass | 5300 | 3000 | 3570 | 18.9 |
| ***Pulp*** | *1570* | *800* | *1000* | *1.57* |
| Neoprene | 1560 | 1380 | 1300 | 2.03 |
| ***Amalgam*** | *4350* | *2260* | *7750* | *33.7* |
| copper | 4700 | 2300 | 9670 | 41.6 |

Table 2. Acoustic velocity and impedance for the different layers in a tooth as well as acoustically similar materials.

### 2.2 Tooth Phantom Construction

One means of better understanding the acoustic signature obtained from an actual tooth structure is to construct a tooth phantom. A typical cross section of a healthy tooth is shown in Fig. 2a. In this figure, the enamel, dentin, and pulp are clearly marked. In addition, a tooth with amalgam "restoration" is shown in Fig. 2b. These cross-sections are similar to those chosen by Ghorayeb *et al.* [13] for their finite element study. To simplify construction, a separate tooth phantom was designed for three different acoustic "paths" through the two tooth sections (these paths are marked on the teeth). The characteristic structure of a tooth phantom is shown in Fig. 2c. Each layer represents a material with similar acoustic properties to either the enamel, dentin, pulp, or amalgam

Materials with similar acoustic velocities and impedances to the different components of a real tooth are listed in Table 2. Good matches were found for enamel, pulp, and amalgam. Only dentin proved difficult to match. As shown in Table 2, tin has very similar acoustic velocities but much higher acoustic impedance. This larger impedance does not provide the desired interface characteristics between the different components of the tooth phantom. Borosilicate glass, on the other hand, has much faster acoustic velocities, but more comparable acoustic impedance. To compensate for the increased velocities, a comparatively thicker glass piece was used.

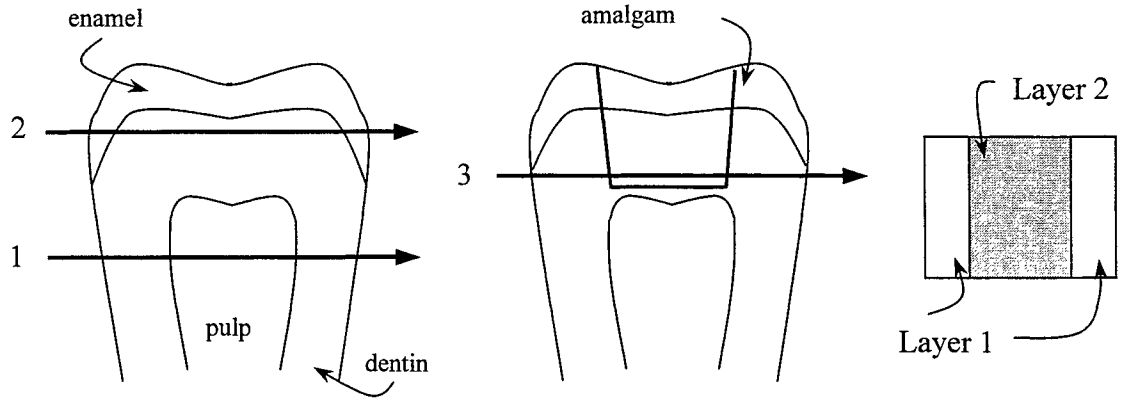

Fig. 2. Cross section of a) a healthy tooth b) a tooth with an amalgam "restoration" and c) layered composition of representative tooth phantom.

| Real Tooth | | Tooth Phantom | | |
|---|---|---|---|---|
| **Components** | **$I_R$** | **Components** | **Thickness [mm]** | **$I_R$** |
| dentin/pulp/dentin | 0.432 | glass/neoprene/glass | 3.3/4.74/3.3 | 0.502 |
| enamel/dentin/enamel | 0.18 | aluminum/glass/aluminum | 2/6.6/2 | 0.026 |
| dentin/amalgam/dentin | 0.399 | glass/copper/glass | 3.3/4/3.3 | 0.296 |

Table 2. Comparison of reflected acoustic radiation at various interfaces for a real tooth and the four teeth phantoms.

## 3. EXPERIMENTAL CONFIGURATION

### 3.1 Ultrasound Generation Considerations

Efficient ultrasound generation depends upon the material's absorption characteristics at the pulsed laser's wavelength [7]. Work by Zuerlein *et al.* [14] and Duplain *et al.* [15] have shown that enamel and dentin have a strong absorption in the 9-11μm region due to the phosphate in the carbonated hydroxyapatite (CAP). Zuerlein *et al.* [14] determined absorption coefficients of 5500, 8000, 1125, and 825 $cm^{-1}$ at 9.3, 9.6, 10.3, and 10.6 μm, respectively. These correspond to absorption depths between 1.25 and 12 μm. Previous work by Blodgett and Baldwin [16] has shown that one can successfully generate ultrasound with a pulsed $CO_2$ laser (10.6 μm) at absorption depths of around 10 μm.

For this work, ultrasound generation in the tooth phantoms and real tooth was accomplished using a pulsed Nd:YAG laser (18 ns pulse width @1.064 μm). The measured temporal profile of the Nd:YAG pulse is given in Fig. 3. Previous work has shown that tooth enamel and dentin have very low absorption coefficients at 1.064 μm[17]. Therefore, to allow for effective ultrasound generation, a piece of metallic tape was placed on the tooth. Most metals have a very high absorption coefficient at 1.064 μm. The tape was thin enough, that it did not distort the detected ultrasonic waveform. The metallic tape was also used on glass/neoprene/glass (dentin/pulp/dentin) and glass/copper/glass (enamel/dentin/enamel) tooth phantoms. No metallic tape was required for the aluminum glass/aluminum tooth phantom (dentin/amalgam/dentin).

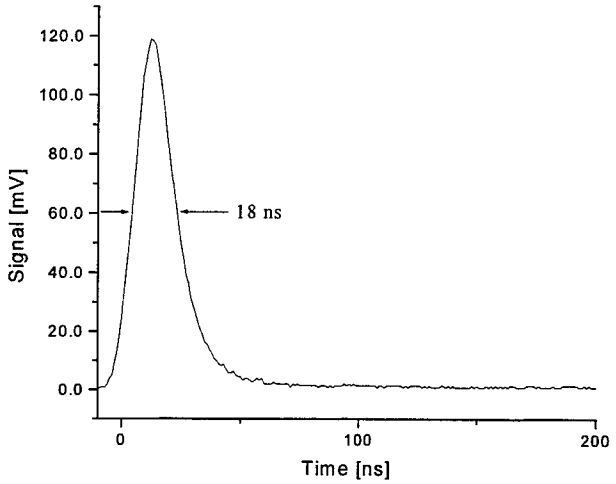


Fig. 3. Measured temporal pulse from Nd:YAG laser.

### 3.2 Ultrasound Detection Considerations

A path-stabilized Michelson-type interferometer was used to detect the ultrasonic wave arrivals in the tooth and tooth phantoms [7,8]. An interferometer design was chosen that allowed the division of optical power between the reference and object arms to be controlled through use of a polarization based scheme [7]. Using this configuration, the optical power reflected by the specimen can be increased enough to provide an adequate signal level. Michelson interferometers require a specular reflection from the surface of the object. To obtain this type of reflection, a piece of mylar silvered tape was placed on both the teeth and the teeth phantoms. The mylar tape is thin enough that it does not affect the ultrasonic waveform. For in-vivo measurements, one would either use an interferometer better suited to diffusely reflecting surfaces such as a Fabry-Perot [1] or choose a laser wavelength for a Michelson-type interferometer at which enamel/dentin is highly reflective.

### 3.3 Experimental Setup

The complete experimental configuration is shown in Fig. 4. A single mode Nd:YAG laser, manufactured by Laser Photonics, was used to generate the ultrasound. Laser power was controlled using a Glan-Thompson polarizer to ensure all measurements were made in the thermoelastic regime. The laser source used in the interferometer was a Coherent 532, 150mW frequency doubled Nd:YAG laser ($\lambda$ = 532nm). An optical beam dump was used to limit the total power to the interferometer, avoiding saturation of the optical detectors.

Ultrasound measurements were taken in an epicentral configuration (source and receiver on opposite sides). The output of the interferometer was passed to a high-speed digitizing oscilloscope for recording the ultrasonic event. The capture of the ultrasonic waveform was triggered by a high-speed photodetector, which saw a sampling of the output pulse of the pulsed laser.

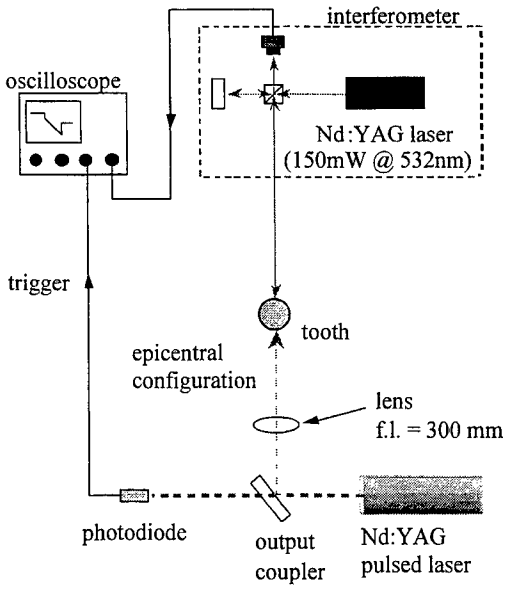


Fig. 4. Experimental setup for laser ultrasonic system.

## 4. RESULTS

### 4.1 Baseline Results

Shown in Fig. 5 is a measured thermoelastic ultrasonic waveform in single piece of steel (6 mm thick). In this figure, the first longitudinal and shear wave arrivals are clearly visible, as are subsequent reflections of the longitudinal wave from the front and back surfaces of the sample. Scattered light from the pulsed laser marks the beginning of the ultrasonic waveform. This waveform is provided as a baseline for the subsequent waveforms. For comparison, the measured ultrasonic waveforms for the three tooth phantoms are shown in Figs. 6-8. Each of these waveforms is distinctly different due to the variations in the elastic properties of the different layers of the tooth phantoms.

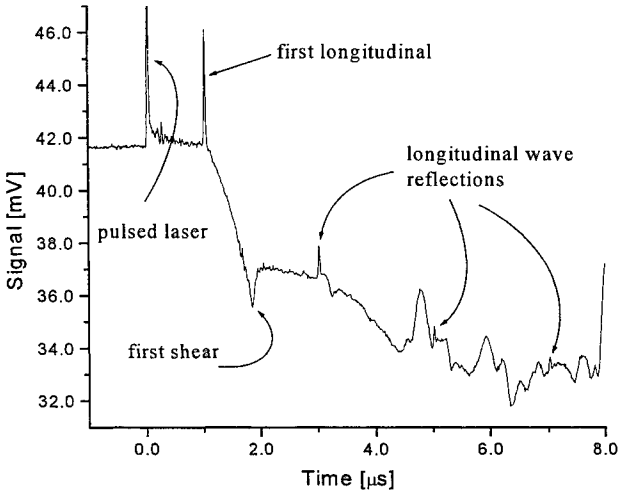


Fig. 5. Thermoelastic ultrasonic waveform in steel.

### 4.2 Tooth Phantom Results

The ultrasonic waveform for the glass/neoprene/glass (dentin/pulp/dentin) tooth phantom is shown in Fig. 6. The first longitudinal wave arrival (long 1) corresponds to a single pass of the longitudinal wave through the phantom. Each of the successive longitudinal arrivals (long 2-4) is separated by 1.3 μs, which corresponds to an additional round trip time of the longitudinal wave through one of the glass layers. This shows that the glass is effectively acting as an etalon for the acoustic wave, which is made possible with the relatively large reflection coefficient at the glass/neoprene interface, $I_r = 0.502$.

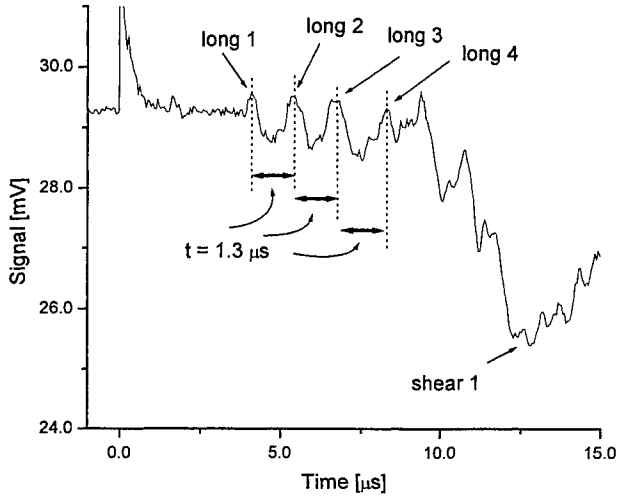


Fig. 6. Ultrasonic waveform for glass/neoprene/glass (dentin/pulp/dentin) tooth phantom.

The ultrasonic waveform for the aluminum/glass/aluminum (enamel/dentin/enamel) tooth phantom is shown in Fig. 7. The first longitudinal arrival (long 1) is clearly identified by the initiation of the negative slope in the waveform. The second longitudinal arrival is also marked, although it is only barely visible due to the small reflection coefficient at the aluminum glass interface. In this waveform, there are two shear arrivals visible. The "spikes" that appear after the second shear wave arrival are believed due to edge effects. Edge effects occur when the acoustic waves reflect off the sides of the sample. This effect must be considered when assessing the internal structure of teeth, which can have a fairly small cross-section.

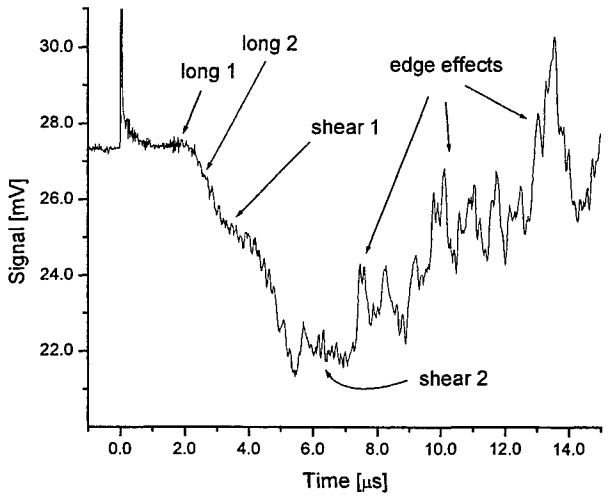


Fig. 7. Ultrasonic waveform for aluminum/glass/aluminum (enamel/dentin/enamel) tooth phantom.

The ultrasonic waveform for the final tooth phantom is shown in Fig. 8. As before, the first longitudinal corresponds to the direct path across the sample. The secondary longitudinal represents an additional round trip in the glass and the third longitudinal arrival represents an additional round trip in the copper. An interesting feature is a longitudinal arrival that is marked as "unknown". This does not correspond to any known paths between the different layers of the tooth phantom. One possible explanation is a poor bond between the different layers that is redirecting (reflecting) a longitudinal wave back to the detection site. This is the type if artifact that one would look for in assessing the internal structure of a tooth.

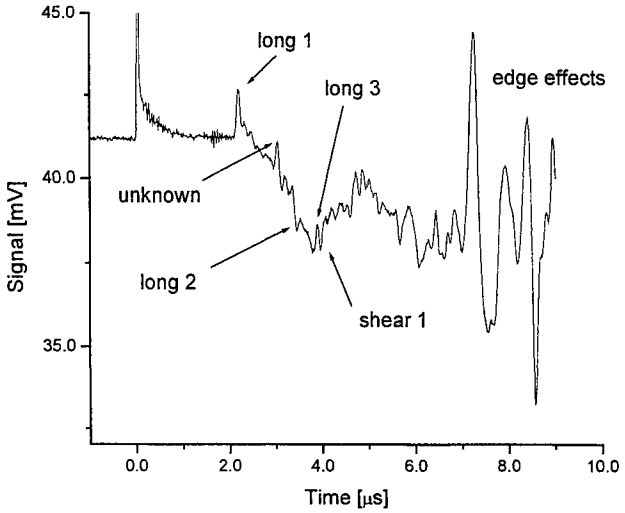


Fig. 8. Ultrasonic waveform for glass/copper/glass (dentin/amalgam/dentin) tooth phantom.

**4.3 Human Bicuspid Results**

Three measurements were taken at different locations on a human bicuspid with an amalgam restoration. The location of these measurements is shown in Fig. 9 with the approximate thickness of the tooth at that location marked. Also included in this figure are the corresponding three ultrasonic waveforms. The ultrasonic waveform shown in Fig. 9a has four distinct longitudinal arrivals prior to the first shear arrival. As with the tooth phantoms, these arrivals are believed due to reflections between different layers in the tooth. In this figure, the time difference between the first two longitudinal arrivals is 0.54 μs. If this arrival were due to a reflection from an enamel/dentin or an enamel/amalgam interface, then the corresponding thickness of the enamel would be about 1.7 mm, which is quite believable. The remaining reflections may correspond to reflections from enamel/dentin or dentin/amalgam interfaces. It is difficult to assess what the thickness is of other layers in this section of the tooth are without additional ultrasonic measurements.

The ultrasonic waveform in Fig. 9b only has three longitudinal arrivals. This indicates that there is probably one less interface for reflections to occur. Since the amplitude of the reflections are smaller, it is most likely that the amalgam restoration is not this deep in the tooth.

The third ultrasonic measurement, shown in Fig. 9c, was taken even closer to the bottom of the tooth. In this waveform, only one longitudinal and shear arrival are clearly visible. This indicates that there is only one layer in this section of the tooth, which is surprising since one would expect to find some pulp. If there were only dentin in this region, then the thickness of the tooth could be estimated using the longitudinal velocity in dentin, $v_{long}$, and the longitudinal arrival time, $t_{long}$, by

$$\text{thickness} = v_{long} t_{long} = \left(3800\frac{\text{m}}{\text{s}}\right)(1.97\mu\text{s}) \qquad (6)$$
$$= 7.5\text{mm}.$$

This is much thicker than the measured 5 mm thickness of this section of the tooth. This is only possible if there is a layer with a slower acoustic velocity in this section of the tooth, which is most likely pulp. The lack of reflections from the dentin/pulp interface may be due to a degradation of the pulp.

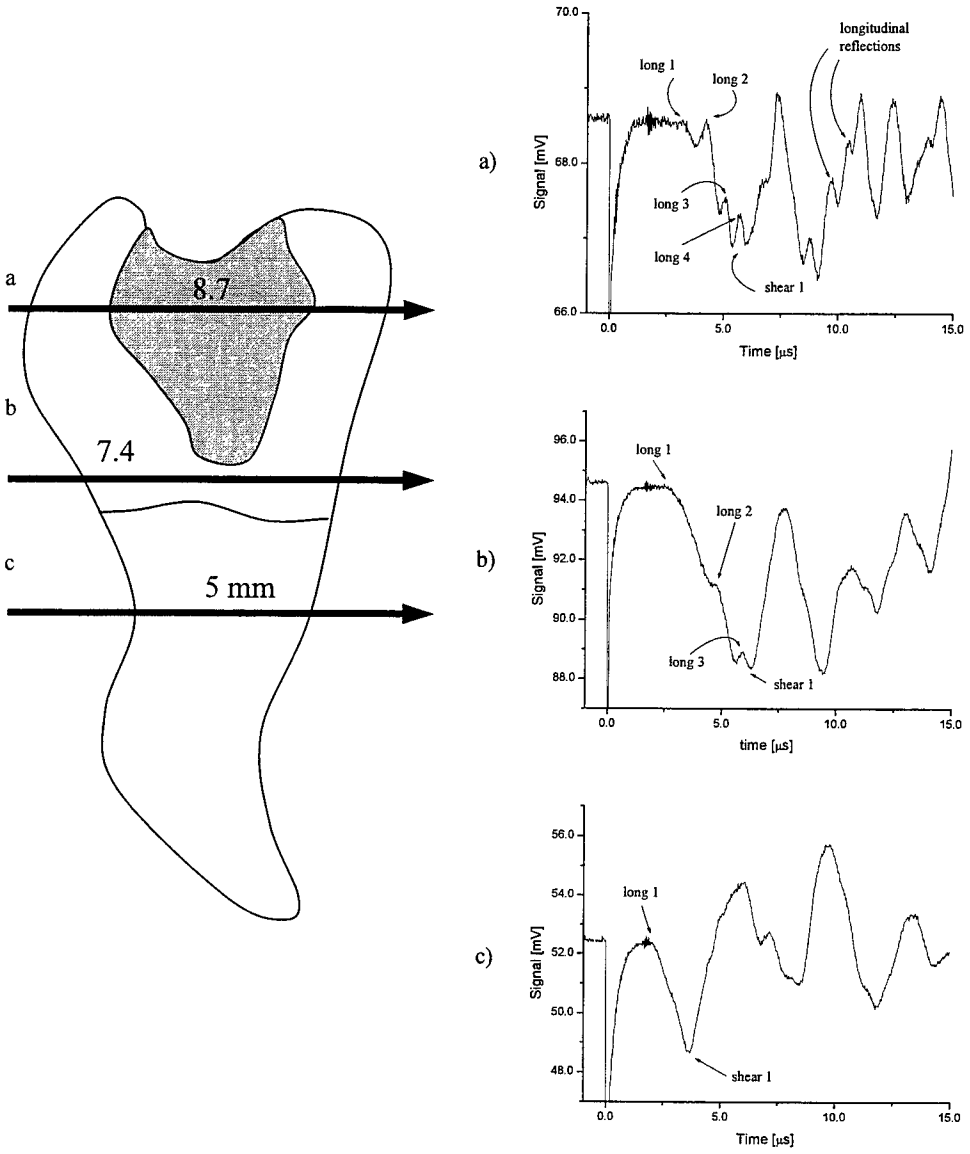


Fig. 9. Approximate cross-section of human bicuspid with the three ultrasonic measurement locations marked. The corresponding ultrasonic waveforms are listed a) through c).

## 5. SUMMARY

The application of laser ultrasonics to the in-vivo assessment of the internal structure of teeth has been presented. Tooth phantoms, that modeled different interfaces found within real teeth, were constructed. Ultrasonic measurements on these phantoms showed that high-frequency ultrasound were clearly able to resolve the interfaces between the different layers. Measurements were also taken on a human bicuspid with an amalgam restoration. As with the tooth phantoms, interfaces within the human biscuspid were clearly visible.

## ACKNOWLEDGEMENTS

This research was funded under a Johns Hopkins University/Applied Physics Laboratory IR&D program.

## REFERENCES


1. Barber, F. E., Lees, S., and Lobene, R. R., "Ultrasonic Pulse-Echo Measurements in Teeth," *Arch Oral Biol*, V 14, pp. 745-760, 1969.
2. G. Baum, I. Greenwood, S. Slawski, and R. Smirnov, "Observation of internal structures of teeth by ultrasonography", *Science*, 139, pp495-496, 1963.
3. G. Kossof and C.J. Sharpe, "Examination of the contents of the pulp cavity in teeth", *Ultrasonics*, 4, pp77-83, 1966.
4. F.R. Reich, B.B. Brenden, and N.S. Porter, "Ultrasonic imaging of teeth", *Report of Battelle Memorial Institute*, Pacific Northwest Laboratory, 1967.
5. G.S. Akino, *Acoustic Waves: Devices, Imaging, & Analog Signal Processing*, Prentice-Hall, 1987.
6. Peck, S. D., Rowe, J. M., and Briggs, G. A. D., "Studies on Sound and Carious Enamel with the Quantitative Acoustic Microscope," *J. Dent. Res.*, V. 68, pp. 107-112, 1998.
7. Scruby, C., Drain, L., *Laser Ultrasonics: Techniques & Applications*, Adam Hilger, New York, 1990.
8. Wagner, J.W., "Optical Detection of Ultrasound," in *Physical Acoustics*, W.P.Mason and A.D. Pierce, Editors , Academic Press, New York, Vol. 19, pp. 201-266, 1990.
9. R.E. Green, *Treatise on Materials Science and Technology, Vol. 3: Ultrasonic Investigation of Mechanical Properties*, Academic Press, New York, 1973.
10. M.J.P. Musgrave, *Crystal Acoustics*, Holden-Day, 1970.
11. B.A. Auld, *Acoustic Fields and Waves in Solids Vol. I*, Krieger Publishing Company, Florida, 1990.
12. D. Fried, W. Seka, R. Glena, and J. Featherstone, "Thermal response of hard dental tissues to 9- through 11-μm $CO_2$ laser irradiation", *Opt. Eng.* 35(7) pp1976-1984, 1996.
13. Ghorayeb, S. R., Xue, T, and Lord, W., "A Finite Element Study of Ultrasonic Wave Propagation in a Tooth Phantom," *J. Dent. Res.*, V. 77, pp. 39-49, 1998.
14. M. Zuerlein,D. Fried, J. Featherstone, and W. Seka, "Optical properties of dental enamel in the mid-IR determined by pulsed photothermal radiometry", *IEEE J. Sel. Top. Q. Elect*, 5(4), pp1083-1089, 1999.
15. G. Duplain, R. Boulay, and P.A. Belanger, "Complex index of refraction of dental enamel at $CO_2$ laser wavelengths", *Appl. Optics*, 26(20), pp4447-4451, 1987.
16. D.W. Blodgett and K.C. Baldwin, "High-Temperature Mechanical Characterization of Single-Crystal Sapphire Using Laser-Based Ultrasonics" *SPIE Conf. on Window and Dome Materials*, pp51-59, 1999.
17. J. White, J. Neev, H. Goodis, and M. Berns, "Surface temperature and thermal penetration depth of Nd:YAG laser applied to enamel and dentin", SPIE Vol. 1643, *Laser Surgery*, pp423-436, 1992.

**Invited Paper**

# The Role of Evanescent Waves in Three-Dimensional Near Field Imaging

David G. Fischer

National Center for Microgravity Research on Fluids and Combustion
NASA Glenn Research Center
21000 Brookpark Rd.
Cleveland, OH 44135

## Abstract

The structural information carried by the evanescent components of the scattered field is discussed for the case of a single homogeneous plane wave incident on a weakly scattering *three-dimensional* medium. It is shown that, unlike the homogeneous components of the scattered field, the evanescent components are related to the three-dimensional Fourier transform of the dielectric susceptibility through a generalized Radon transform. The region of the three-dimensional Fourier space that is accessible from evanescent wave measurements is discussed, as well as the spatial resolution attainable in a typical multiple-view scattering experiment.

## 1. Introduction

Near-field imaging is a discipline that has gained a great deal of exposure in recent years due to its ability to resolve sub-wavelength structure in optically thin media [1-4]. It has many variants, including total internal reflection microscopy (TIRM) [5,6] and near-field scanning optical microscopy (NSOM) [3,4], but common to all is the use of evanescent waves for illumination and/or detection. Image interpretation is often difficult, however, owing to the complex interaction between the incident field and the sample, as well as between the scattered field and the near-field probe.

This is especially true when near-field techniques are applied to relatively thick samples. Even when the scattering is linear, the detected field is not related simply to the sub-wavelength structure of the object, as it for thin media. Specifically, for thin media, both the homogeneous and evanescent components of the scattered field are related to the transverse Fourier structure of the dielectric susceptibility of the object through a one-to-one mapping. For thick media (i.e. true three-dimensional media), this is no longer true. Whereas a one-to-one mapping still exists for the homogeneous components of the scattered field, it has recently been shown [7] that the evanescent components of the scattered field are related to the three-dimensional Fourier transform of the susceptibility through a generalized Radon transform (i.e. a many-to-one mapping).

In this paper, we discuss this result in detail. We present, for the case of homogeneous plane wave incidence, the generalized Radon transform relating the evanescent components of the scattered field to both the high *transverse* spatial frequency components and the low and high *longitudinal* spatial frequency components of the

In *Laser-Tissue Interaction XI: Photochemical, Photothermal, and Photomechanical*, Donald D. Duncan, Jeffrey O. Hollinger, Steven L. Jacques, Editors, Proceedings of SPIE Vol. 3914 (2000)
1605-7422/00/$15.00

susceptibility. We also examine the Fourier information that is accessible from evanescent wave measurements in a typical scattering experiment. While we will not specifically consider here the case of evanescent plane wave incidence (which is most direct related to TIRM and the conversion of evanescent waves to homogeneous ones at a near-field probe), it can shown [7] that a reciprocal transform exits that relates the homogeneous components of the scattered field to the Fourier transform of the susceptibility.

## 2. Angular Spectrum Representation of the Scattered Field

We begin by reviewing the angular spectrum representation of the scattered field. Consider the geometry shown in figure 1, in which a monochromatic plane wave of frequency $\omega_0$ is incident in the direction $\mathbf{s}_0$ on a localized scattering medium of dielectric susceptibility $\eta(\mathbf{r})$.

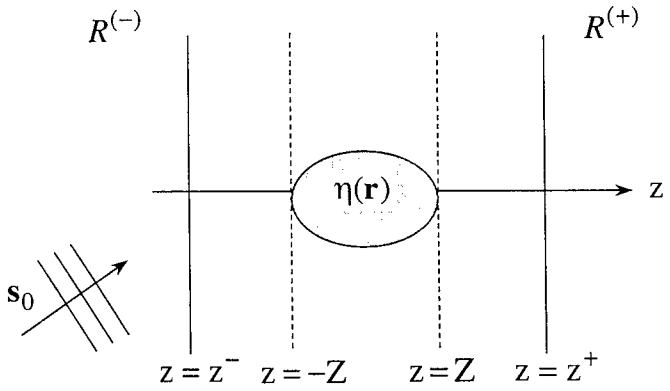


**Figure 1.** Scattering geometry.

If the medium is weakly scattering, the scattered field is given to first order in the susceptibility by the expression

$$U^{(s)}(\mathbf{r}) = \frac{k_0^2}{4\pi}\int_D \frac{\exp(ik_0|\mathbf{r}-\mathbf{r}'|)}{|\mathbf{r}-\mathbf{r}'|}\eta(\mathbf{r}')U^{(i)}(\mathbf{r}')d^3r'. \quad (1)$$

This is the well-known first Born approximation to the scattered field [8].

The scattered field may be alternatively expressed as an angular spectrum of plane waves. For this purpose, we make use of the Weyl expansion for an outgoing spherical wave, which is given by [9]

$$\frac{\exp(ik_0|\mathbf{r}-\mathbf{r}'|)}{|\mathbf{r}-\mathbf{r}'|} = \frac{ik_0}{2\pi}\int_D \frac{1}{s_z}\exp\{ik_0[\mathbf{s}_\perp\cdot(\rho-\rho') + s_z|z-z'|]\}d^2s_\perp\,, \tag{2a}$$

where

$$\mathbf{s}_\perp = (s_x, s_y, 0)\,, \tag{2b}$$

$$s_z = \begin{cases} (1-s_\perp^2)^{1/2} & \text{when } s_\perp^2 \le 1 \\ i(s_\perp^2-1)^{1/2} & \text{when } s_\perp^2 > 1, \end{cases} \tag{2c}$$

$\mathbf{r} = (x,y,z)$, $\mathbf{r}' = (x',y',z')$, $\rho = (x,y,0)$, and $\rho' = (x',y',0)$. Substituting equation (2a) into equation (1), we obtain the following angular spectrum representation for the scattered field in the half spaces $R^{(+)}$ $(z > Z)$ and $R^{(-)}$ $(z < -Z)$:

$$U^{(s)}(\mathbf{r},\mathbf{s}_0) = \int_{-\infty}^{\infty}\int_{-\infty}^{\infty} a^{(\pm)}(\mathbf{s}_\perp;\mathbf{s}_0)\exp[ik_0(\mathbf{s}_\perp\cdot\rho) \pm s_z z]d^2s_\perp\,, \tag{3}$$

where $a^{(\pm)}$, the spectral amplitude function, has the form

$$a^{(\pm)}(\mathbf{s}_\perp;\mathbf{s}_0) = \frac{ik_0^3}{8\pi^2 s_z}\int_D \eta(\mathbf{r}')\exp\{-ik_0[(\mathbf{s}_\perp - \mathbf{s}_{0\perp})\cdot\rho' + (\pm s_z - s_{0z})z']\}d^3r'. \tag{4}$$

The spectral amplitude function may also be related to the scattered field in the planes $z = z^{\pm}$ by Fourier inversion of equation (3), viz.

$$a^{(\pm)}(\mathbf{s}_\perp;\mathbf{s}_0) = \exp(\mp ik_0 s_z z^{\pm})\tilde{U}(k_0\mathbf{s}_\perp, z^{\pm};\mathbf{s}_0)\,, \tag{5}$$

where

$$\tilde{U}(\mathbf{f}, z^{\pm};\mathbf{s}_0) = \frac{1}{(2\pi)^2}\int_{z=z^{\pm}} U(\rho, z^{\pm})\exp(-i\mathbf{f}\cdot\rho)d^2\rho \tag{6}$$

is the two-dimensional Fourier transform of the scattered field in the planes $z = z^{\pm}$. Those plane wave (or spectral) components for which $s_\perp^2 \le 1$ are known as homogeneous waves, and they propagate into the half-spaces $R^{(+)}$ and $R^{(-)}$. Those plane wave components for which $s_\perp^2 > 1$ are known as evanescent waves, and they decay exponentially with increasing distance from the scattering medium [9].

## 3. Homogeneous Components of the Scattered Field

For the homogeneous components of the scattered field, $\mathbf{s}$ is real and the spectral amplitude function [cf. Equation (4)] is given by [8]

$$a_h^{(\pm)}(\mathbf{s}_\perp;\mathbf{s}_0) = \frac{i\pi k_0^3}{s_z}\tilde{\eta}\left[k_0(s_x - s_{0x}), k_0(s_y - s_{0y}), k_0(\pm s_z - s_{0z})\right], \tag{7}$$

where $\tilde{\eta}(\mathbf{K})$ is the three-dimensional spatial Fourier transform of the dielectric susceptibility, viz.

$$\tilde{\eta}(\mathbf{K}) = \frac{1}{(2\pi)^3}\int_D \eta(\mathbf{r})\exp(-i\mathbf{K}\cdot\mathbf{r})d^3r. \tag{8}$$

Equation (7) illustrates that, for a weakly scattering medium, there is a one-to-one mapping between the spectral amplitudes of the homogeneous components of the scattered field and the low spatial frequency components of the dielectric susceptibility. Specifically, for a fixed direction of incidence $\mathbf{s}_0$, the homogeneous spectral amplitudes are mapped onto the surface of a sphere of radius $k_0$ centered at $-k_0\mathbf{s}_0$ in the three-dimensional Fourier space of the dielectric susceptibility (figure 2). As $\mathbf{s}_0$ is varied, those surfaces fill a sphere of radius $2k_0$ centered at the origin (known as the Ewald limiting sphere). Consequently, the homogeneous components of the scattered field allow the susceptibility to be reconstructed with a resolution of $\lambda_0/2$.

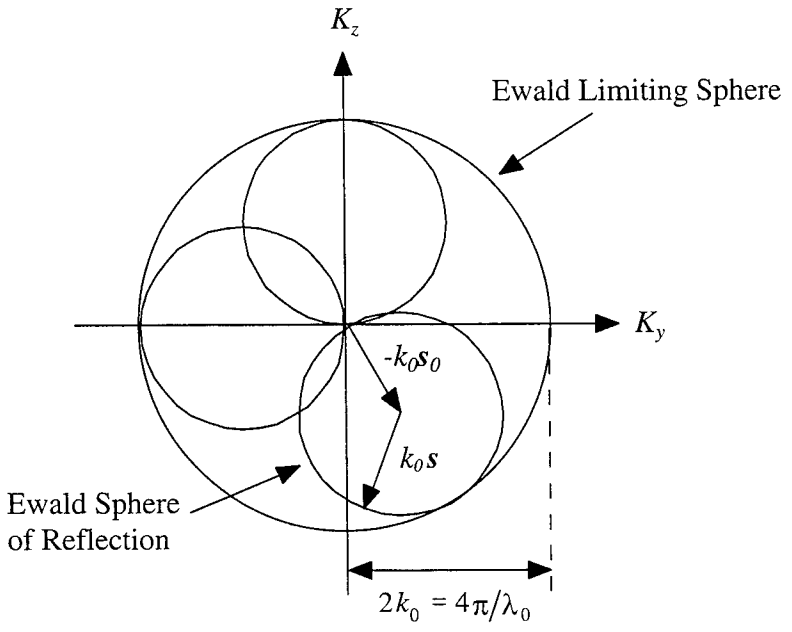


**Figure 2.** Ewald Limiting Sphere

## 4. Evanescent Components of the Scattered Field

It follows from the last section that in order to obtain object detail smaller than $\lambda_0/2$ (band-limited extrapolation aside), the evanescent components of the scattered field must be measured and incorporated into the reconstruction procedure. This, in turn, requires that the measurement plane be located within a wavelength of the object, since the evanescent components decay exponentially with increasing distance and are quickly masked by noise. Any improvement in resolution, however, depends critically on the information carried by the evanescent components of the scattered field, and it is this point that we now address.

The spectral amplitudes of the evanescent components of the scattered field are formally given by equation (7), except that $s_z$ is now purely imaginary. They are proportional to the analytic continuation of $\tilde{\eta}(\mathbf{K})$ into the complex $K_z$ plane, viz.

$$a_e^{(\pm)}(\mathbf{s}_\perp;\mathbf{s}_0) = \frac{\pi k_0^3}{|s_z|}\tilde{\eta}\left[k_0(s_x - s_{0x}), k_0(s_y - s_{0y}), k_0(\pm i|s_z| - s_{0z})\right]. \tag{9}$$

While correct, this relationship provides little physical insight into the connection of the evanescent spectral amplitudes to the actual three-dimensional Fourier components of the dielectric susceptibility. Alternatively, it has recently been shown [7] that the evanescent components of the scattered may be expressed as

$$a_e^{(\pm)}(\mathbf{s}_\perp,\mathbf{s}_0) = \frac{k_0^3}{2|s_z|}\int_{-\infty}^{\infty}\tilde{\eta}\left[k_0(s_x - s_{0x}), k_0(s_y - s_{0y}), K_z\right] I_e^{(\pm)}(K_z;s_z,s_{0z})\,dK_z, \tag{10}$$

where

$$I_e^{(\pm)}(K_z;s_z,s_{0z}) = \frac{\exp\left\{\left[k_0|s_z| \pm i(k_0 s_{0z} + K_z)\right]Z\right\}}{k_0|s_z| \pm i(k_0 s_{0z} + K_z)}. \tag{11}$$

Equation (10) relates the spectral amplitudes of the evanescent components of the angular spectrum representation of the scattered field to the three-dimensional Fourier components of the dielectric susceptibility. We see that there is no longer a one-to-one correspondence between the spectral amplitudes and the Fourier components of the dielectric susceptibility. This is so because, as a result of the superposition integral, the spectral amplitude of a given evanescent component of the scattered field (the one labeled by $\mathbf{s}_\perp$, for example) is dependent on all those Fourier components of the dielectric susceptibility having spatial frequencies $K_x = k_0(s_x - s_{0x})$, $K_y = k_0(s_y - s_{0y})$, and (arbitrary) $K_z$. The strength of the contribution is determined by the weighting function $I_e^{(\pm)}$. In order to see the effect of the weighting function, let us examine its (normalized) modulus:

$$\left|\frac{I^{(\pm)}(K_z;s_z,s_{0z})}{I^{(\pm)}(-k_0 s_{0z};s_z,s_{0z})}\right| = \left[\frac{(k_0|s_z|)^2}{(k_0|s_z|)^2+(k_0 s_{0z}+K_z)^2}\right]^{1/2}. \qquad (12)$$

It is clear that the normalized weighting function is peaked at $K_z = -k_0 s_{0z}$ and has a full-width half-maximum of $2\sqrt{3}k_0|s_z|$. It is plotted in figure 3 as a function of $K_z / k_0$ for $s_z = 0.5i$ and $s_{0z} = 1$.

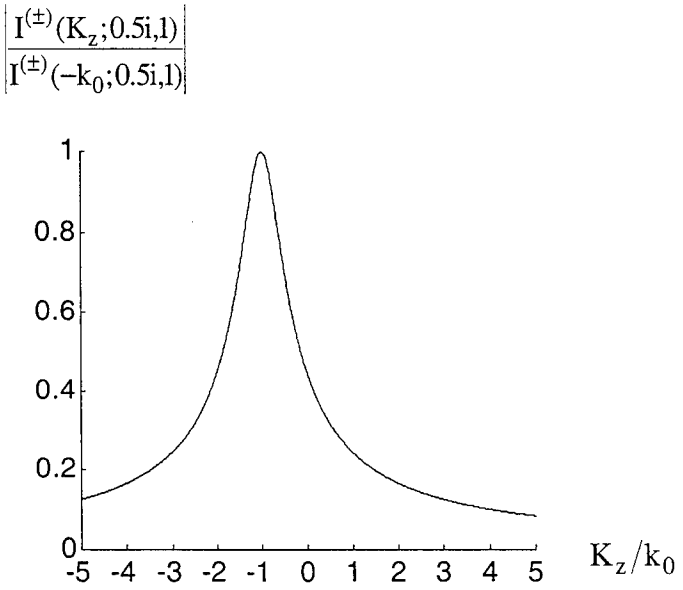


**Figure 3.** The normalized weighting function

As a result of the many-to-one mapping [equation (10)], a given evanescent component potentially carries more information than a given homogeneous component. *This information consists of high transverse spatial frequency information and both low and high longitudinal spatial frequency information.* Furthermore, the larger the value of $|s_\perp|$ ($s_\perp^2 > 1$) and hence $|s_z|$ (i.e. the more evanescent a particular angular spectrum component), the greater the "effective" number of three-dimensional Fourier components of the susceptibility that contribute to its spectral amplitude.

With the wealth of Fourier information present in the evanescent spectral amplitudes, it is natural to inquire about using the evanescent components of the scattered field to determine the structure of the dielectric susceptibility. This question is best answered if we view equation (10) as a generalized projection integral (i.e. a generalized

Radon transform) in which the three-dimensional Fourier components are projected along the $K_z$ axis. Taking a cue from conventional tomography, let us fix $|\mathbf{s}_\perp|$ and $|\mathbf{s}_{0\perp}|$ (so that the weighting function $I_e^{(+)}$ depends solely on $K_z$) and only consider the evanescent components in the forward half-space $R^{(+)}$. In this case, if we vary the directions of $\mathbf{s}_{0\perp}$ and $\mathbf{s}_\perp$, we obtain the projection along the $K_z$ axis of all of those Fourier components that lie within a cylindrical shell, oriented along the $K_z$ axis, of inner radius $k_0\left(|\mathbf{s}_\perp| - |\mathbf{s}_{0\perp}|\right)$ and outer radius $k_0\left(|\mathbf{s}_\perp| + |\mathbf{s}_{0\perp}|\right)$ (i.e. we obtain an annular projection). If a different value of $|\mathbf{s}_\perp|$ is chosen, we obtain a second (coaxial) annular projection of the same annulus width $2k_0|\mathbf{s}_{0\perp}|$. This process can be repeated any number of times, limited only, in practice, by measurement noise. If we take $|\mathbf{s}_\perp|^{(i)} = |\mathbf{s}_\perp|^{(i-1)} + 2|\mathbf{s}_{0\perp}|$, $(i = 2,...,N)$, where $|\mathbf{s}_\perp|^{(i)}$ is the fixed value of $|\mathbf{s}_\perp|$ in the $i^{th}$ measurement set, we obtain a contiguous set of annular projection data for which the weighting function $I_e^{(+)}$ is different for each annulus (figure 4). The inner radius of the composite annulus (in 2D) or cylindrical shell (in 3D) is $K_{min} = k_0\left(|\mathbf{s}_\perp|^{(1)} - |\mathbf{s}_{0\perp}|\right)$ and the outer radius is $K_{max} = k_0\left(|\mathbf{s}_\perp|^{(N)} + |\mathbf{s}_{0\perp}|\right)$, where $|\mathbf{s}_\perp|^{(1)} > 1$. If we repeat the measurement procedure for every possible object orientation, we obtain a multi-view set of projection data.

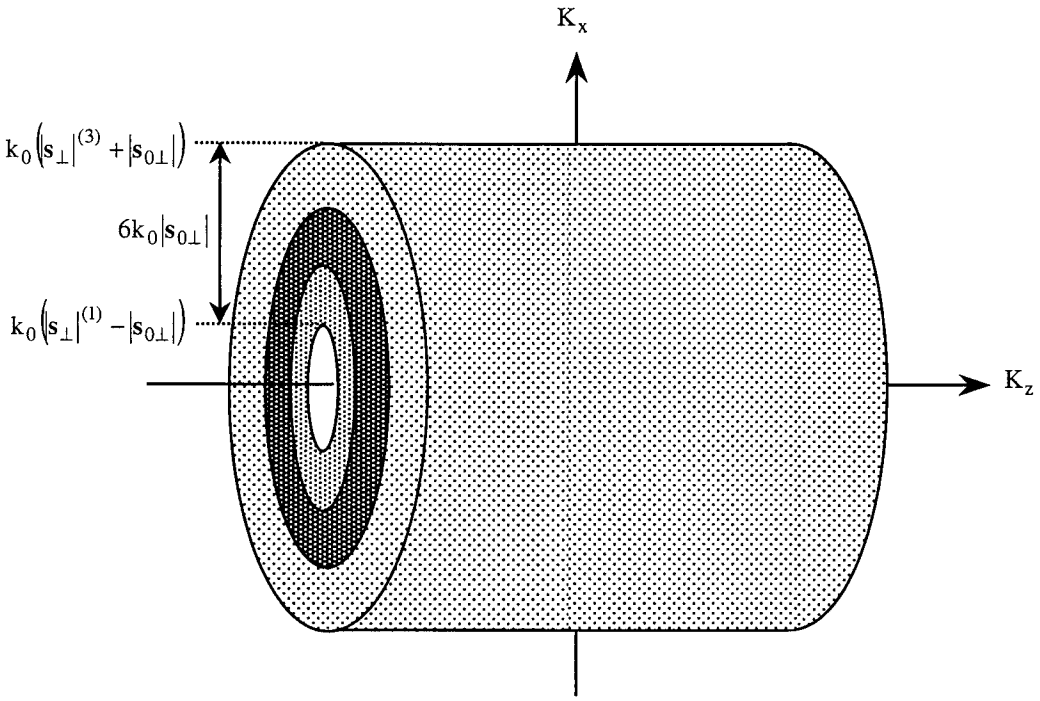


**Figure 4.** Illustrating the annular projections obtained in the Fourier space of the dielectric susceptibility via equation (10)

The cylinder of missing low-frequency Fourier data $\sqrt{K_x^2 + K_y^2} \le K_{min}$ is not a concern, since typically $K_{min} \le 2k_0$ and those components can be determined from the homogeneous waves (see section 3). The upper limit, $K_{max}$ (which ultimately determines the spatial resolution), is a function of the distance between the measurement plane and the object, as well as of the measurement noise. Let us define the noise decay factor (NDF) as the minimum relative evanescent wave amplitude allowed by the measurement noise. It is related to the maximum value of $|s_z|$ (corresponding to the most evanescent measurable scattered field component) by the expression:

$$\mathrm{NDF} = \exp\left(-k_0 |s_z|_{max} \Delta z_m\right), \tag{13}$$

where $\Delta z_m$ is the distance between the measurement plane and the object. It follows that $K_{max}$ is given by

$$\begin{aligned} K_{max} &= k_0\left(|s_\perp|_{max} + |s_{0\perp}|\right) \\ &= \sqrt{\left(\frac{\mathrm{NDF}}{\Delta z_m}\right)^2 + k_0^2} + k_0 |s_{0\perp}|. \end{aligned} \tag{14}$$

As an example, if NDF = 0.1, $\Delta z_m = \lambda_0/10$, and $|s_{0\perp}| = 0.5$, then $K_{max} = 4.3k_0$ and the resolution is roughly increased by a factor of two over the typical figure. Further improvements in resolution can be obtained by better suppressing the noise and decreasing the distance $\Delta z_m$.

## 5. Conclusion

Near-field imaging techniques are attractive due to the possibility of achieving sub-wavelength resolution. The images that are obtained are, in many instances, difficult to interpret for a variety of reasons, most directly linked to the complexity of the interaction between the probe field and the object. To provide direction in interpretation, simple models are often employed, such as the thin sample model. This model is convenient since many of the structures investigated can, in fact, be modeled as two-dimensional structures. In many cases (when the object under investigation has even modest transverse spatial frequency content [7]), the thin sample model breaks down and two-dimensional diffraction theory, even as only a tool for improved understanding, is inappropriate.

A more appropriate pedagogical model would be a *three-dimensional*, linear scattering model. To this point however, few studies have been made of the structural information carried by the evanescent components of the scattered field. In this paper, we have addressed this very problem in an attempt to gain insight into the more general case of near-field imaging. We showed, for the case of homogeneous plane wave incidence that, unlike the one-to-one mapping that exists between the low spatial frequency

components of the susceptibility and the homogeneous components of the scattered field, *the evanescent components of the scattered field are related to the high transverse spatial frequency components and both the low and high longitudinal spatial frequency components of the dielectric susceptibility through a generalized Radon transform (i.e. projection integral).* In addition, we illustrated, for a typical single-view measurement set, the region of the Fourier space of the susceptibility that is accessible from measurements of the evanescent components of the scattered field, and we derived an expression for the multiple-view resolution as a function of measurement noise and object-detector separation. We found that, even with conservative choices for the experimental parameters, measurement of the evanescent components of the scattered field leads to a significant improvement in resolution.

## References


[1] Betzig, E. and Trautman, J., 1992, *Science* **257**, 189-195.

[2] Durig, U., Pohl, D. W., and Rohrer, F., 1986, *J. Appl. Phys.* **59**, 3318-3327.

[3] Courjon, D. and Bainer, C., 1994, *Rep. Prog. Phys.* **57**, 989-1028.

[4] Girard, C. and Dereux, A., 1996, *Rep. Prog. Phys.* **59**, 657-699.

[5] Temple, P. A., 1981, *Appl. Opt.* **20**, 2656-2664.

[6] Courjon, D., Vigoureux, J., Spajer, M., Sarayeddine, K., and Leblanc, S., 1990, *Appl. Opt.* **29**, 3734-3740.

[7] Fischer, D. G., *J. Mod Opt.* (in press).

[8] Wolf, E., 1969, *Opt. Commun.* **1**, 153-156.

[9] Mandel, L., and Wolf, E., 1995, **Optical Coherence and Quantum Optics** (Cambridge: Cambridge University Press), sec. 3.2.

# Evaluation of Tissue Optical Properties from Light Distribution Images

Cheng-Lun Tsai*, Ming Chang†, Jui-Hsiang Hsieh, Yi-Fong Yang, and Yi-Sheong Chou

Dept. of Biomedical Engineering, Chung-Yuan Christian University, Jung-Li 32023, Taiwan
†Dept. of Mechanical Engineering, Chung-Yuan Christian University, Jung-Li 32023, Taiwan

## ABSTRACT

Images of light distribution in biological soft tissue were used to study the optical characteristics of tissue. The light distribution image was taken under a microscope with light injected through a pinhole close to the edge of the top surface. Images taken on skin, fat, and muscle tissues were compared to study the effect of cellular structure and temperature on the light intensity distribution. Monte Carlo simulation with the same conditions was also performed to simulate the light intensity distribution in tissue for comparison. The anisotropy scattering of light in tissue is affected by the tissue microscopic structure, such as the direction of muscle tissue fibers. The change in optical properties of fat and muscle tissue with temperature was observed. The two-dimensional light distribution images offer more information than general reflectance and transmission measurements. By matching the simulated light intensity distribution with the light distribution image, the optical properties of biological tissue could be estimated. This method might be applied in tissue engineering as an economic way for evaluating the microscopic structure of tissue.

**Keywords:** Anisotropy factor, tissue optics, light intensity distribution, Monte Carlo simulation

## 1. INTRODUCTION

The progress in optical and optoelectrical technologies is a great help to the development of biomedical optics. Optical measurement has advantages of minimal invasive and no electrical safety problem. It is becoming a safe measurement option in medical applications. Most of these applications require some knowledge of light path and the distribution of light in tissue. For instance, we need to know the light path in tissue to tell which part of tissue is really measured by a reflective oxygen saturation sensor. In photodynamic therapy, the activated area has to match the size of tumor to have a good treatment result. A proper control of dose relies on a good estimation of light intensity distribution in tissue.[1, 2] The light path and distribution in tissue are determined by the optical property of tissue, and the property is characterized by a few coefficients for simplicity.[3, 4, 5] The most typically coefficients are light absorption, scattering, and anisotropic coefficients. These optical coefficients are generally evaluated from the transmission and reflectance of a thin piece of tissue sample.[6, 7, 8, 9, 10] When light is injected into a biological tissue, we can not directly measure the inside light intensity distribution without interfere the distribution. What can only be seen is the diffusive reflectance back to the surface. The reflectance intensity distribution on the surface of tissue can also be used to estimate the optical coefficients of tissue.[7, 11] Then, these coefficients are used in different kinds of mathematical models to simulate the light path or intensity distribution inside the tissue.[12, 13, 14] However, the simulation results are very difficult, if not impossible, to be verified. Furthermore, optical coefficients that are reported by different researchers by using different measurement and estimation methods show a great variation.[7, 15, 16, 17] In some cases, three parameters may be not enough to characterize the optical property of tissue. Since it is difficult to carry out a measurement of light distribution inside a tissue to verify the result of simulation, we can simulate the light distribution under the condition that is easier to perform the measurement.

Similar to the measurement of spatial distribution of reflected light on the surface, the light distribution can be taken on the cross section surface by moving the light source very close to this surface. The light distribution on this surface also can be easily simulated by modify the conditions. Monte Carlo method was used in this study to compare the cross section of light intensity distribution in both situations.[18] In this study, biological soft tissue with different contents and microscopic structures were studied. It also has been reported that the optical properties of biological tissue were affected by temperature. The scattering property of dermis increases as temperature increases, whereas the scattering property of subdermis decreases as temperature increases. But, their absorption coefficients are not affected.[9] Temperature of tissue was also controlled in this study to show its effects.

* Correspondence: Email: clt@medical.be.cycu.edu.tw, Telephone: 886 3 456 3171 ext. 4509;
Fax: 886 3 456 3171 ext. 4599



In *Laser-Tissue Interaction XI: Photochemical, Photothermal, and Photomechanical*, Donald D. Duncan, Jeffrey O. Hollinger, Steven L. Jacques, Editors, Proceedings of SPIE Vol. 3914 (2000)
1605-7422/00/$15.00

## 2. METHODS AND MATERIALS

The approach taken in this study was to inject light into tissue sample through a small pinhole that is very close to the front surface of tissue rather than at the center of the top surface, see Fig. 1. The dimension of aluminum sample holder is 20 mm by 20 mm by 10 mm inside, and the diameter of the pinhole is 0.5 mm. The inner surface of the sample holder was painted black to absorb light and reduce reflection. Since we only take the image of light distribution with very low power of light source, about 100 μW. The volume of sample tissue is large enough to be assumed that sample is a quarter infinite space. Which means the reflection from the tissue-holder boundary is assumed to be negligible. The sample holder was placed under a microscope (Leitz Laborlux S) for observation. The view of field was about 3 mm by 3 mm. A heating plate was put underneath the holder to worm up tissue sample. A temperature sensor and controller (Omron, E5CS-X) were used to control the temperature of sample. With this arrangement, the light intensity distribution could be observed similar to a cross section view. To avoid the speckle on image, light source used in this study was a high luminance red LED (665 nm). Images were taken either by a photo camera (Leica MPS52 and Kodak Elite 100) or video camera (Electrophysics 7290A) with image acquisition card (Matrox Meteor). To study the difference between the light distribution with light injected at the center of the top surface with that of light injected close to the edge of the top surface. Monte Carlo simulation was coded with similar conditions. The optical coefficients used in the simulation were based on the values published in literature. To compare the light distribution in a more quantitative way, equal intensity curves were found from both the measurement and simulated light distribution images, as shown in Fig. 2. The curves can be expressed in a length vs. angle plot and approximate by a Gaussian curves. This will be easier to see the difference between the results of simulation and measurement.

Tissue samples used in this study include pork, fat tissue, and skin tissue. Sample was purchased from local supermarket. Since these tissue have different microscopic structures. It should be reasonable to assume that the scattering and anisotropic characteristics of these tissues are also different. In pork tissue, these coefficients might even change with fiber direction. Muscle fibers in pork are well aligned compared to the collagen fiber in skin tissue. Light propagate in muscle tissue could be affected by the direction of muscle fibers. To study the effect, port sample was cut with different angle (roughly 0°, 30°, 60°, and 90°) to the direction of muscle fiber. When these samples were put in the sample holder, the light would be injected with an angle to the direction of muscle fiber. To characterize the change in anisotropic coefficient, $g$, with fiber direction in simulation, we assume that the anisotropic coefficient is a function of the angle ($\theta$) between the fiber direction and the moving direction of photon. Since, the typical anisotropic value of muscle tissue is about 0.9, the value of $g(\theta)$ was assumed to range from 0.75 to 0.95. The value used in Monte Carlo simulation was calculated by using the following equation:

$$g(\theta) = 0.2 * \cos(\theta) + 0.75 \quad (1)$$

Fat tissue is made of fat cells with big fat droplets in the cells. These fat cells tightly stacked together to form fat tissue. Its microscopic structure has no obvious dependence on direction. Therefore, the anisotropic coefficient was

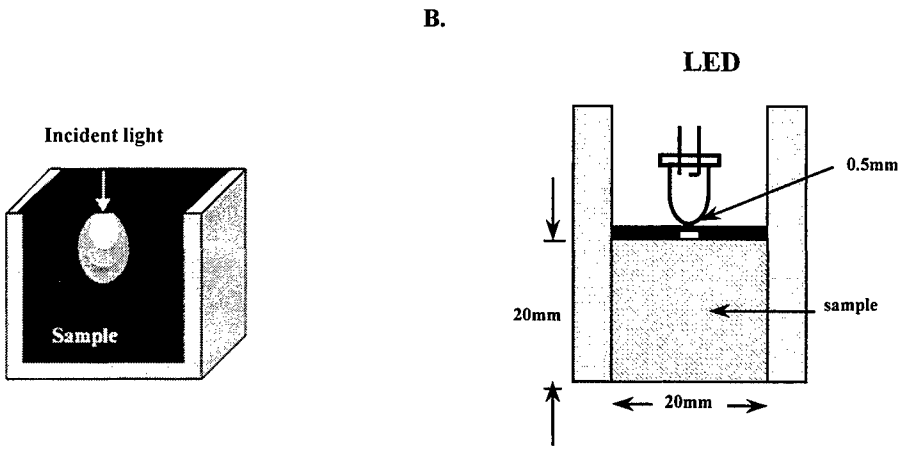


Fig. 1. **A.** Scheme of the tissue sample holder with light injected through a pinhole close to edge of the top surface. **B.** Front view of the tissue sample holder and the LED light source.

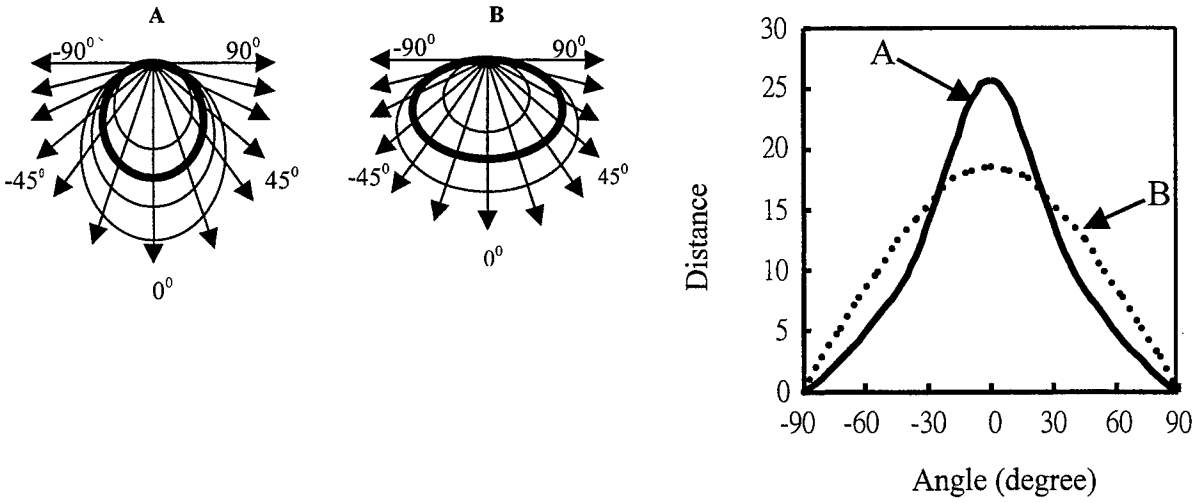


Fig. 2. Schemes of two different light intensity distribution images and the equal intensity curves, A and B. Comparison of the two equal intensity curves in a distance vs. angle plot.

treated as direction independent. Fat tissue has a strong light scattering property and looks white at room temperature. The light distribution in fat tissue should be more diffusive than muscle tissue. However, the scattering coefficient has been reported to change with temperature.[9] Because fatty acid is melted at body temperature, it looks slightly transparent with a lower scattering property. In this study, the temperature of tissue sample was also heated up to 40°C to compare the light intensity distribution with that at 25°C.

Skin tissue has a layered structure; the thickness of epidermis layer is only about 150 μm. The dermis layer is about 1 mm thick and constructed mainly by collagen fiber bundles with different diameters. The collagen fibers in skin tissue are randomly arranged without specific direction. This structure gives it a very strong light scattering characteristic to reflect most of the visible light that shines on our skin. Because skin is very thin, it is difficult to take the cross section image of light distribution in a single piece of skin tissue. To solve this problem, several pieces of skin tissue were stacked together to form a thick and bulky tissue sample.

## 3. RESULTS

Light intensity distribution images in pork with the direction of muscle fiber in 0°, 30°, 60°, and 90° to the incident direction of light are shown in Fig. 3. These images are 3.25 mm by 3.25 mm in size. Light was injected into pork tissue in perpendicular to the upper edge right at the center. The incident light beam is about 0.5 mm wide which is the same as the diameter of the pinhole. Images were taken with different exposure time (4, 7, and 10 minutes) to show the distribution of different light intensity level. Therefore, the images of light distribution expand with longer exposure time. The direction of muscle fibers could be seen with a close look on the images with long exposure time. Small circles in the images are air bubbles trapped on the surface covered by a cover glass. Compared with the images of pork, light distributions in fat and skin tissue are very more like diffusive distribution even very close to the incident site, see Fig. 4. Results of Monte Carlo simulation are shown in Fig. 5 and Fig. 6. The size of pictures is 10 mm by 10 mm. Pictures in Fig. 5 are the cross section view of simulated light distribution when the light is injected through a 0.5 mm pinhole at the center of top surface. Whereas, pictures in Fig. 6 were simulated with light injected through a 0.5 mm pinhole close to the edge of tissue top surface. The absorption, scattering, and anisotropic coefficients used in two types of condition were the same. These values were chosen from the values surveyed by Cheong.[7] The temperature effects on light distribution in pork and fat tissue are shown in Fig. 7, Fig. 8, and Fig. 9. Temperature of tissue samples was heated up to 27°C and 40 °C in these experiments. The lower plots in Fig. 7, Fig, 8, and Fig. 9 show the equal intensity pixels on the upper images of light intensity distribution. These equal intensity points were fit by Gaussian curves and shown in distance vs. angle plots. This makes the comparison much easier and more quantitatively.

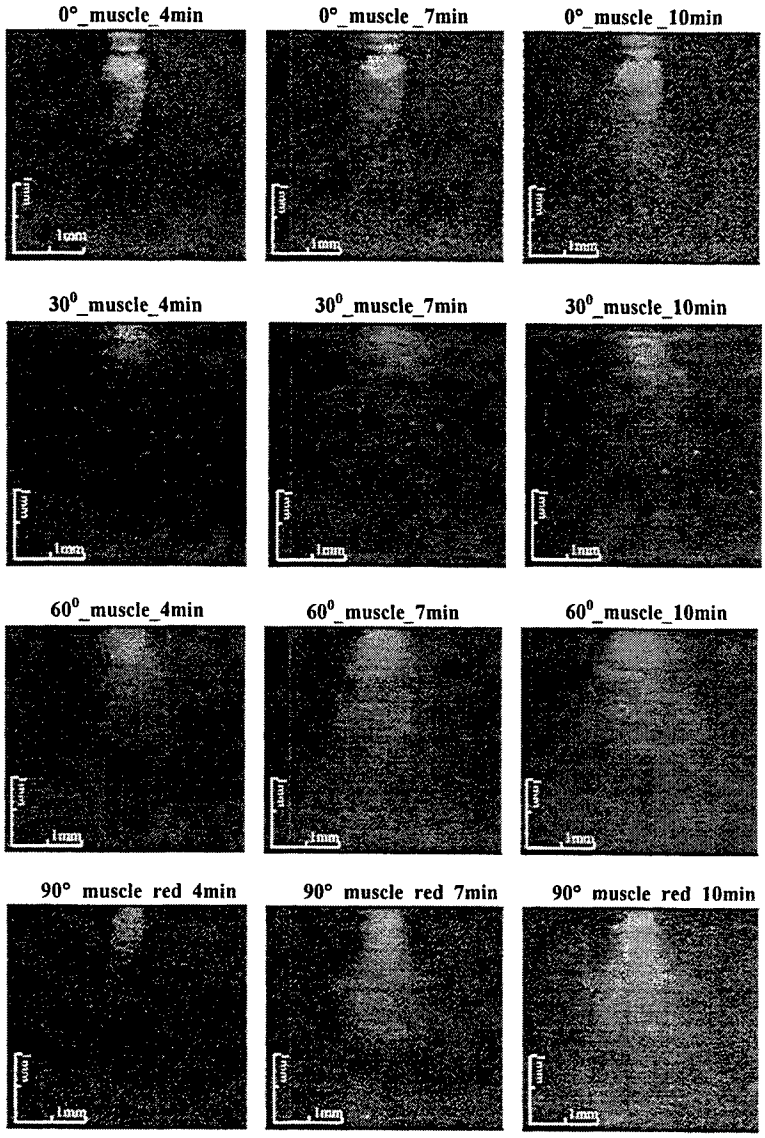


Fig. 3. Light distribution images in pork taken with different exposure time (4, 7, or 10 minutes) and different muscle fiber directions. Muscle fiber direction was in 0°, 30°, 60°, or 90° to the direction of light source.

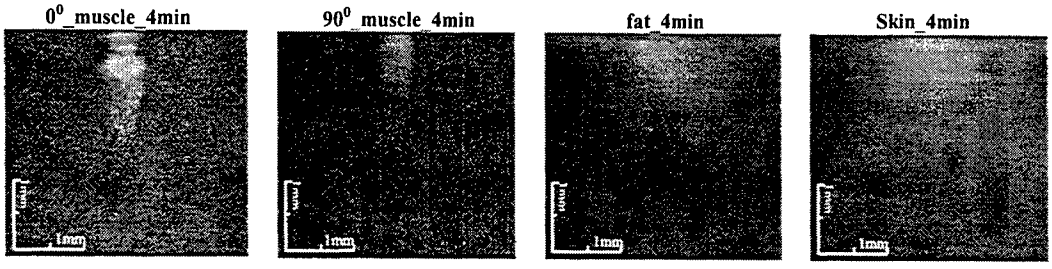


Fig. 4. Light distribution images in pork, fat, and skin tissue taken with 4 minutes of exposure.

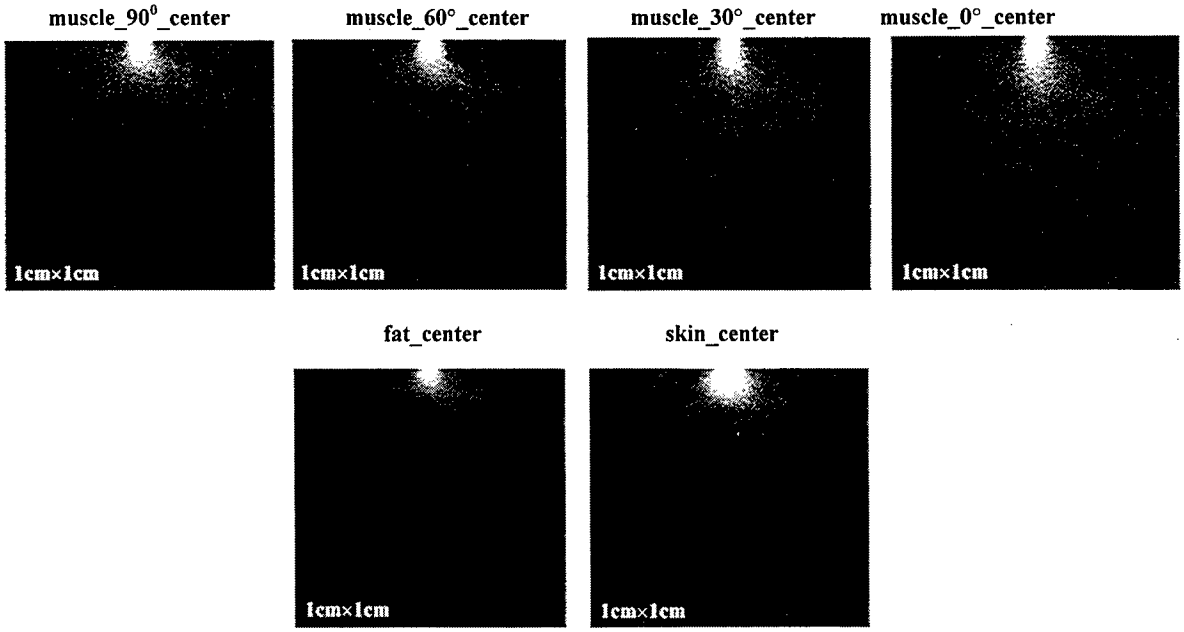


Fig. 5. Monte Carlo simulation of light distribution in muscle, fat, and skin tissue with light injected at the center of the top surface. Muscle fiber direction was 90°, 60°, 30°, or 0° to the direction of light source. The distribution images shown here are on the surface of sample tissue.

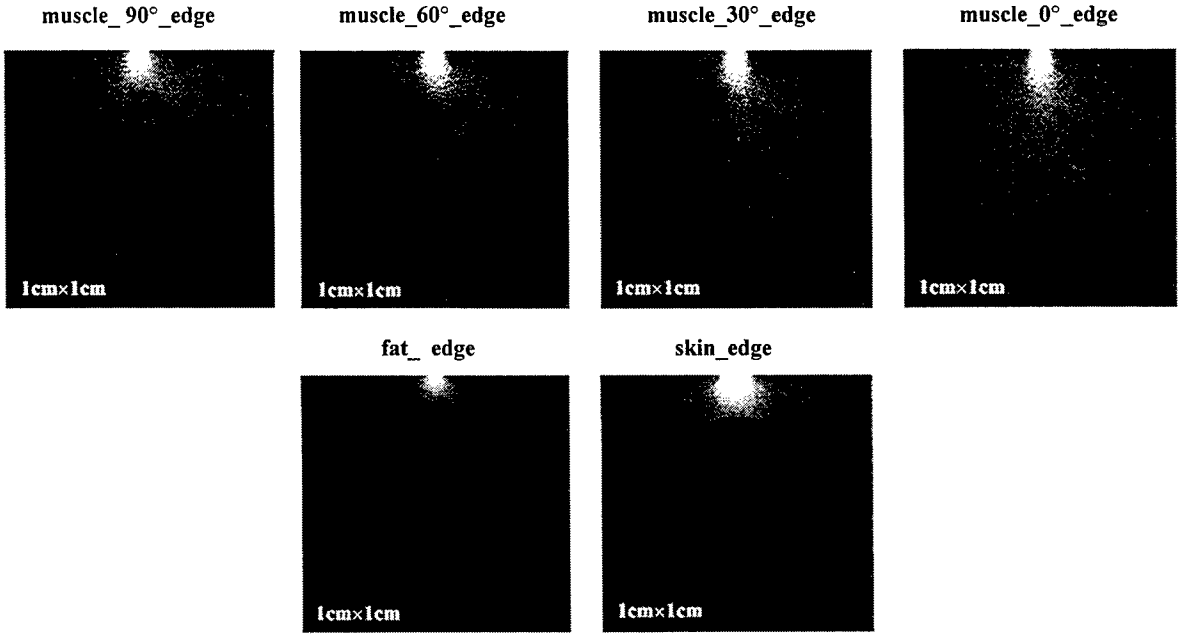


Fig. 6. Monte Carlo simulation of light distribution in muscle, fat, and skin tissue with light injected close to the edge of the top surface. Muscle fiber direction was 90°, 60°, 30°, or 0° to the direction of light source. The distribution images shown here are through the center of sample tissue.

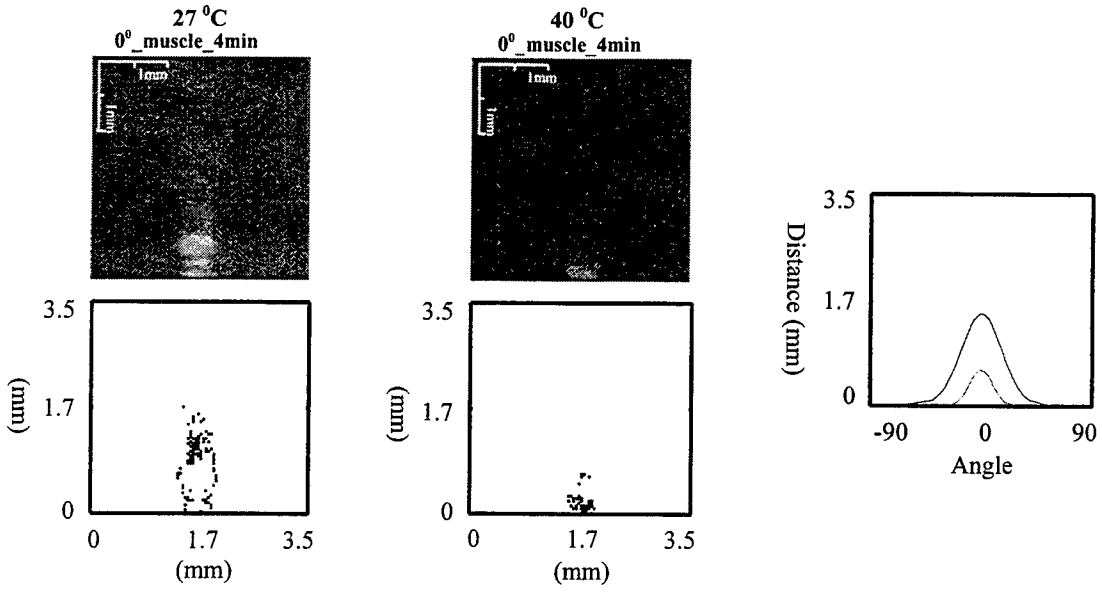


Fig. 7. Images of light distribution in pork at 25°C and 40°C with 4 minutes of exposure. Muscle fiber direction is in parallel with the direction of light source. Equal intensity distributions are shown below. The equal intensity points were fit with Gaussian curves for comparison, as shown on the right.

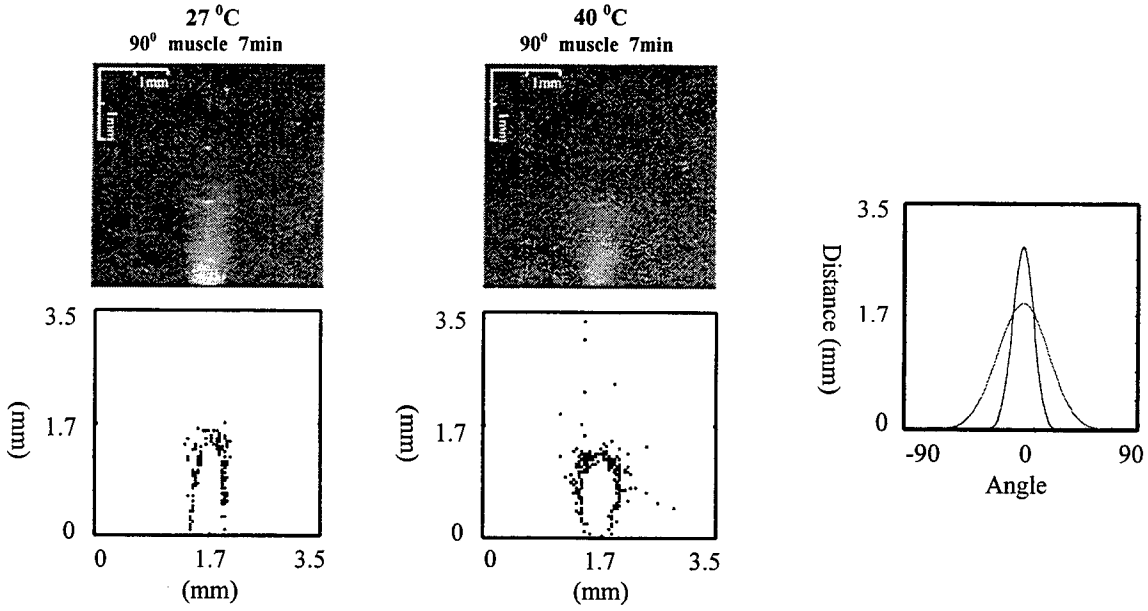


Fig. 8. Images of light distribution in pork at 25°C and 40°C with 7 minutes of exposure. Muscle fiber direction is perpendicular to the direction of light source. Equal intensity distributions are shown below. The equal intensity points were fit with Gaussian curves for comparison, as shown on the right.

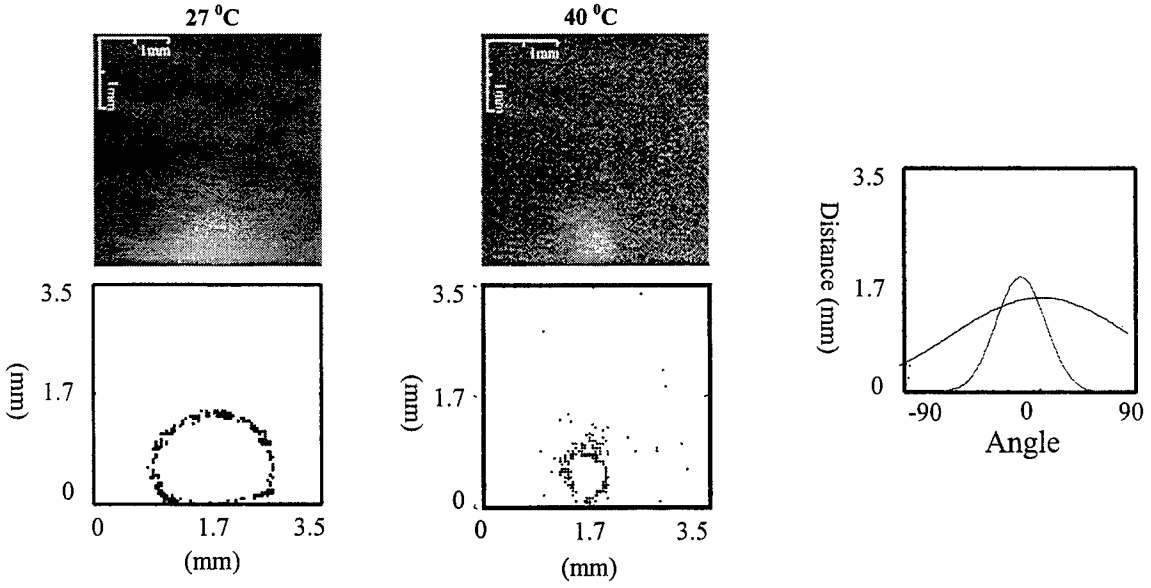


Fig. 9. Images of light distribution in fat tissue at 25°C and 40°C with 7 minutes of exposure. Equal intensity distributions are shown below. The equal intensity points were fit with Gaussian curves for comparison, as shown on the right.

## 4. DISCUSSION

Because the video camera does not have a large enough of dynamic range, images were taken by photo camera with different exposure time to show the light distribution with different intensity. To cover this very large of dynamic range, the exposure time was controlled to inspect the distribution at different scales. The distribution close to the incident site is best observed with a short exposure time, but the distribution at deep region could not be seen, as shown in Fig. 3. With a longer exposure time, light intensity close to the incident site would saturate the film and no detail could be seen there. However, the intensity distribution at deeper region could be better seen. Theoretically, biological tissue has a strong forward scattering characteristic. The effect of anisotropic factor is better shown on the light distribution close to the incident site. Because of multiple scattering effect, light distribution becomes diffusive at deep region. The effect of anisotropic factor also is not so obvious. For pork tissue, a slightly tilted light distribution could be seen in the 30° and 60° images with 4 minutes of exposure. Fig. 4 shows that the distribution images of fat and skin tissue are very close to the diffusive distribution. This may be because these two kinds of tissue have stronger scattering properties than that of pork. Fat and skin tissues also do not have a very obvious directional dependent of microscopic structure. Their light distribution images are more uniform in all direction.

The Monte Carlo simulation results in Fig. 5 and Fig. 6 show that the cross section view of light distribution with light injected at the center is very similar to that with light injected close to the edge of tissue sample. This allows us to use the side injection distribution to study the real light distribution inside the tissue. In general, the distribution of side injection is shallower than that of center injection. This is because a great part of the injected photons escaped from the front surface before it penetrated deep into tissue. Therefore, the light distribution in Fig. 5 spread out more than that in Fig. 6.

Pork tissue has a wider light distribution at 40°C than that at 27°C, as shown in Fig 7 and Fig. 8. When temperature was increased, pork tissue generally would look white. This means when temperature of pork is increased, the scattering coefficient of pork increases and/or the anisotropic coefficient decreases. The strong scattering property make the light in pork spread out more than that at lower temperature. On the other hand, fat tissue has a wider distribution at 27°C than at 40°C, see Fig. 9. This is because fatty acid is melt at 40°C and the scattering property is lower. So, light penetrated deeper in tissue without being scattered away from the front surface.

## 5. CONCLUSION

In this study, we developed a method to study the light intensity distribution in biological soft tissue. The side view of light distribution images in this study show that this method could be valuable for studying the optical characteristics of biological soft tissue. It is also a more direct way to determine the optical properties of tissue. The microscopic structure of soft biological tissue has a great variation from sample to sample, and at different positions. Therefore, light distribution in tissue also varies on different samples and at different measurement sites. Although, the results shown here are mostly qualitative, it is also possible to estimate the optical coefficients of tissue quantitatively by using inverse method. That is to modify the simulation coefficients until the results match the images of experiments. With more measurement and simulation, the representative values and their ranges could be found.

## ACKNOWLEDGMENTS

This study is partially supported by the National Science Council of Taiwan (NSC-89-2213-E-033-020) and by the special grant from the Engineering School of Chung-Yuan Christian University.

## REFERENCES

1. A. M. K. Nilsson, R. Berg, and S. Anderson-Engles, "Measurements of the optical properties of tissue in conjunction with photodynamic therapy," *Appl. Opt.* **34**, pp. 4609-4619, 1995.
2. L. O. Svassand and R. Ellingsen, "Optical penetration in human intracranial tumors," *Photochem. Photobiol.* **41**, pp. 73-76, 1985.
3. R. R. Anderson, and J. A. Parrish, "The optics of human skin," *J. Invest. Dermatol.* **77**, pp. 13-19, 1981.
4. M. J. C. van Gemert, S. L. Jacques, H. J. C. M. Sterenborg, and W. M. Star, "Skin optics," *IEEE Trans. on Biomed. Eng.* **36**, pp. 1146-1154, 1989.
5. B. C. Wilson, and S. L. Jacques, "Optical reflectance and transmission of tissues: Principles and applications," *IEEE J. Quantum Electron.* **26**, pp. 2186-2199, 1990.
6. E. Chan, T. Menovsky, and A. J. Welch, "Effects of cryogenic grinding on soft-tissue optical properties," *Appl. Opt.* **35**, pp. 4526-4532, 1996.
7. W. F. Cheong, S. A. Prahl, and A. J. Welch, "A review of the optical properties of biological tissues," *IEEE J. Quantum Electron.* **26**, pp. 2166-2185, 1990.
8. R. Graaff, A. C. M. Dassel, M. H. Koelink, F. F. M. de Mul, J. G. Aarnoudse, and W. G. Zijlstra, "Optical properties of human dermis *in vitro* and *in vivo*," *Appl. Opt.* **32**, pp. 435-447, 1993.
9. J. Laufer, R. Simpson, M. Kohl, M. Essenpreis, and M. Cope, "Effect of temperature on the optical properties of *ex vivo* human dermis and subdermis," *Phys. Med. Biol.* **43**, pp. 2479-2489, 1998.
10. J. W. Pickering, S. A. Prahl, N. V. Wierinhen, J. F. Beek, H. J. C. M. Sterenborg, and M. J. C. van Gemert, "Double-integrating-sphere system for measuring the optical properties of tissue," *Appl. Opt.* **32**, pp. 399-410, 1993.
11. A. Kienle, L. Lilge, M. S. Patterson, R. Hibst, R. Steiner, and B. C. Wilson, "Spatially resolved absolute diffuse reflectance measurements for noninvasive determination of the optical scattering and absorption coefficients of biological tissue," *Appl. Opt.* **35**, pp. 2304-2312, 1996.
12. Y. Hasegawa, Y. Yamada, M. Tamura, and Y. Nomura, "Monte Carlo simulation of light transmission through living tissues," *Appl. Opt.* **30**, pp. 4514-4520, 1991.
13. E. Okada, M. Firbank, M. Schweiger, S. R. Arridge, M. Cope, and D. T. Delpy, "Theoretical and experimental investigation of near-infrared light propagation in a model of the adult head," *Appl. Opt.* **34**, pp. 21-31, 1997.
14. J. M. Schmitt, G. X. Zhou, E. C. Walker, and R. T. Wall, "Multilayer model of photon diffusion in skin," *Opt. Soc. Am.* A **7**, pp. 2141-2153, 1990.
15. S. J. Matcher, M. Cope, and D. T. Delpy, "*In vivo* measurements of the wavelength dependence of tissue-scattering coefficients between 760 and 900 nm measured with time-resolved spectroscopy," *Appl. Opt.* **36**, pp. 386-396, 1997.
16. S. A. Prahl, I. A. Vitkin, U. Bruggemann, B. C. Wilson, and R. R. Anderson, "Determination of optical properties of turbid media using pulsed photothermal radiometry," *Phys. Med. Biol.* **37**, pp. 1203-1217, 1992.
17. C. R. Simpson, M. Kohl, M. Essenpreis, and M. Cope, "Near-infrared optical properties of *ex vivo* human skin and subcutaneous tissues measured using the Monte Carlo inversion technique," *Phys. Med. Biol.* **43**, pp. 2465-2478, 1998.
18. S. L. Jacques, and Wang L., "Chapter 4: Monte Carlo modeling of light transport in tissues," in optical-thermal response of laser-irradiated tissue, edited by A. J. Welch, and M. J. C. van Gemert, pp. 73-100, 1995.

# SESSION 18

# Tissue Mechanics

# Characterisation of Mechanical Behaviour of Human Skin *In Vivo*

Lucien F.A. Douven*[a], Riske Meijer[b] and CeesW.J. Oomens[b]

[a]Personal Care Institute, Philips Research Laboratories, Eindhoven, The Netherlands
[b]Dept. of Mechanical Engineering, Eindhoven University of Technology, The Netherlands

**ABSTRACT**

**Purpose:** In this paper characterization of the biomechanical properties of human skin in vivo is studied both experimentally and by numerical modelling. These properties can be important in the evaluation of skin condition (e.g. ageing) as well as skin disorders.
**Methods:** In this study we focus on the static behaviour of the dermis. Important features are stress-strain non-linearity and anisotropy; both are mainly determined by the collagen fibre network present in the dermis. A suitable constitutive model was developed by Lanir[1].
An experimental set-up was developed and used to stretch the skin in vivo. Two pads are attached to the skin which are driven apart during the experiment. The forces and displacements of the pads are measured. A field of markers (6x12) is applied to the skin's surface between the pads. The displacement history of the markers can be determined by image analysis. Both measured forces and displacement histories are input that is used to estimate the unknown material parameters in Lanir's skin model. A numerical simulation model of the experiment (finite element method) is combined with an estimation algorithm (constrained sequential maximum-likelihood approach) to determine estimates of the material parameters.
**Results:** Estimates of the skin parameters could be determined. However the procedure also shows that the skin model applied exhibits modelling errors.

**Keywords:** skin, mechanical properties, collagen, numerical-experimental method, parameter estimation.

## 1 Introduction

The purpose of this work is to characterise the in-plane mechanical behaviour of human skin *in vivo*. The overall mechanical behaviour of skin under macroscopic deformation is inhomogeneous, viscoelastic, non-linear and anisotropic. This complex behaviour of skin can be attributed to its specific structural properties. Only few constitutive models are formulated in a general three-dimensional theory based on thermodynamic considerations. The constitutive model employed by Lanir[1] is such a model, and it fully accounts for the viscoelastic, non-linear and anisotropic behaviour of skin. It is a model based on structural arguments, assuming that the tissue's response is the sum of the responses of its constituents. Hence, if the constituents' structure, their mechanics and interactions are known, the overall response can be evaluated. However, structural models often contain many parameters which, in the case of implementation in a finite element code, can result in an increase of the computing effort. In order to reduce the computing effort, we will neglect the viscoelastic behaviour in the present study.

For the determination of the parameters of Lanir's Skin Model a mixed numerical-experimental method based on the identification method of Hendriks[2,3] is applied. This method has been applied successfully in numerous investigations concerning the mechanical behaviour of complex materials[4-6]. It is based on the confrontation of measured data from an experiment with calculated data obtained from a finite element model, eventually leading to an estimation of the material parameters of a constitutive model. These parameters include the stiffness, the orientation distribution, and the undulation of the collagen fibres.

In the next section Lanir's Skin Model is described. The application of the numerical-experimental method is described in Section 3. The results are listed in Section 4 and discussed in Section 5. Finally, in Section 6, some conclusions are drawn.

* Correspondence: Prof. Holstlaan 4, 5656 AA Eindhoven, The Netherlands; Email: Lucien.Douven@philips.com; Telephone: +31 40 2742888; Fax: +31 40 2744288



In *Laser-Tissue Interaction XI: Photochemical, Photothermal, and Photomechanical*, Donald D. Duncan, Jeffrey O. Hollinger, Steven L. Jacques, Editors, Proceedings of SPIE Vol. 3914 (2000)
1605-7422/00/$15.00

# 2 Lanir's Skin Model

The assumptions for the constitutive model of skin according to Lanir are described in Section 2.1. The constitutive equation is outlined in Section 2.2 and in Sections 2.3 and 2.4 some additional elaboration is given.

## 2.1 Assumptions

Skin has a stratified structure consisting of three main layers: a surface layer called epidermis (thickness ca. 0.1-0.3 *mm*), beneath this, a dense connective tissue layer called dermis (thickness ca. 1-2 *mm*), and a fatty layer called hypodermis or subcutis. The epidermis and dermis are connected in a wavy and fingerlike-folded way ensuring that the epidermis can not glide over the dermis. The dermis is loosely connected to the hypodermis. The dermis is an order of magnitude thicker than the epidermis and is assumed to dominate the in-plane mechanical behaviour of the skin. The main constituents of the dermis are collagen and elastin fibres embedded in a matrix of semi-fluid amorphous material. From scanning electron microscopy of skin sections it can be observed that collagen fibres are undulated and form an irregular meshwork oriented roughly parallel to the skin surface[7,8].

The mechanical behaviour of skin is assumed to be dominated by the dermis; the influence of the epidermis and hypodermis are neglected. In Lanir's Skin Model, the structure is defined in terms of the orientation of fibres[1]. In order to reduce the computing effort, a two-dimensional (plane stress) model is considered. In flat tissues, the orientation distribution of each fibre type, $k$, can be described by a density distribution function $R_k(\theta)$, where the argument is the polar angle $\theta$ (see Section 2.3). In this study two fibre types are considered: collagen ($k$=$c$), and elastin ($k$=$e$).
The following assumptions are made in employing Lanir's Skin Model (with elastic behaviour of all components):

- Each fibre is thin and perfectly flexible. It has no compressive strength and if contracted will buckle under zero load. The fibres that are undulated do not carry load until they are completely straightened.
- If a fibre is stretched, it is subjected to a uniaxial strain that is the tensorial transformation of the overall strain in the fibre's direction (affine deformation).
- The fibres are linear elastic under stretch.
- Upon stretching, the fraction of fibres that are straightened and stretched increases, causing increased resistance against stretch.
- Skin is incompressible.
- The unfolding and rotating of the fibres during deformation squeezes the matrix. The matrix's response is through hydrostatic pressure only.

## 2.2 Constitutive Model

The stress-strain relation is described with:

$$\sigma = \tau - p\boldsymbol{I}\,, \tag{1}$$

where $\sigma$ is the Cauchy stress tensor, $\tau$ the so-called extra stress tensor, $p$ a hydrostatic pressure, and $\boldsymbol{I}$ the second order unit tensor. The mechanical behaviour of the fibres is accounted for in $\tau$ and the contribution of the ground-substance in $p$. The stress-strain relation defined by Lanir[1] for an in-plane continuous fibre distribution is given by:

$$\sigma = J^{-1}\sum_k S_k \int_0^{\pi} (R_k(\theta) f_k^*(\lambda(\vec{r}_0))\boldsymbol{F}\cdot\frac{\partial\lambda(\vec{r}_0)}{\partial\boldsymbol{E}}\cdot\boldsymbol{F}^c)d\theta - p\boldsymbol{I}\,, \tag{2}$$

with:

- $\boldsymbol{F}$ the deformation tensor, and $J=\det(\boldsymbol{F})$ a measure for the volume strain,
- $\vec{r}_0$ a unit vector tangent to the fibre in reference configuration defined by:
  $$\vec{r}_0(\theta) = \cos(\theta)\vec{e}_x + \sin(\theta)\vec{e}_y\,, \tag{3}$$
- $\lambda(\vec{r}_0)$ the elongation ratio, i.e. the ratio of the current length and the length in the reference state of the fibres orientated in the direction $\vec{r}_0$ in the reference state,
- $\boldsymbol{E} = 1/2(\boldsymbol{F}^c.\boldsymbol{F} - \boldsymbol{I})$ the Green-Lagrange tensor (Note that the term $\partial\lambda(\vec{r}_0)/\partial\boldsymbol{E}$ can be expressed as $\lambda^{-1}(\vec{r}_0)\vec{r}_0\vec{r}_0$),
- $R_k(\theta)d\theta$ the fraction of all fibres of type k orientated between $(\theta)$ and $(\theta+d\theta)$ in the reference state. The function $R_k(\theta)$ should satisfy the normalisation condition:

$$\int_0^{\pi} R_k(\theta)d\theta = 1, \tag{4}$$

- $S_k$, the volume fraction of fibre type $k$,
- $f_k^*(\lambda(\vec{r}_0))$ the load per unit undeformed cross-sectional area, which also accounts for the undulation of fibres according to a normal distribution $N(\mu_k, \sigma_k)$ (see Section 2.4).

This model is implemented[9] in the finite element code MARC[10], using a mixed finite element formulation. A quadrilateral element is used, with displacements interpolated bilinear (4 vertex nodes) and the hydrostatic pressure interpolated constant (1 centre node). The incompressibility constraint is forced using the penalty function method.

## 2.3 Fibre Orientation Distribution Functions

The following orientation distribution function is chosen for the collagen fibres[11]:

$$R_c(\theta) = A \cdot \cos^4(\theta - C_2) + B \qquad \text{with } 0 \le \theta \le \pi, \tag{5}$$

where $A$ and $B$ are constants. By requiring that the function is symmetric, cyclic, smooth and should satisfy the normalisation condition for density distribution functions (note Equation (3)), Equation (5) attains the following form:

$$R_c(\theta) = 1/\pi + C_1(\cos^4(\theta - C_2) - 0.375). \tag{6}$$

The restriction $R(\theta) \ge 0$ for all $\theta$ imposes limits on $C_1$, namely $0 \le C_1 \le 0.849$. The orientation associated with the angle $C_2$ ($0 \le C_2 \le \pi$) is the direction of physical symmetry of the fibrous structure or the preferred fibre orientation. The parameter $C_1$ is a measure for the anisotropy. The orientation distribution of elastin is assumed to be isotropic and can thus be defined by:

$$R_e(\theta) = 1/\pi. \tag{7}$$

The numerical integration of the fibre orientation distribution functions is done by means of the trapezoidal rule using 24 intervals.

## 2.4 Stress-Elongation Law for Undulated Fibres

The assumptions that fibres are perfectly thin and flexible, have no compressive strength, and if stretched are linear elastic, lead to the following stress-elongation relation for straightened fibres:

$$f_k(\lambda) = \begin{cases} 0 & \text{for } 0 < \lambda \le 1 \\ K_k(\lambda - 1) & \text{for } \lambda > 1 \end{cases}, \tag{8}$$

with $K_k$ the stiffness of fibre type $k$. The elastin fibres are assumed to be already strained in reference configuration[12,13].

In order to incorporate the undulation behaviour of the collagen fibres[7,8], the stress-elongation relation is adjusted. The undulation of collagen fibres is assumed to be normally distributed and expressed in the undulation density distribution function given by:

$$D_{c,\vec{r}_0}(x) = \frac{1}{\sigma_{c,\vec{r}_0}(2\pi)^{1/2}} \exp\left(\frac{-(x - \mu_{c,\vec{r}_0})^2}{2\sigma_{c,\vec{r}_0}^2}\right), \tag{9}$$

where $x$ is the elongation ratio of the collagen fibres in the deformed state, $\mu_{c,\vec{r}_0}$ the mean elongation ratio defined as the length at which the collagen fibres become straightened divided by the fibre length along $\vec{r}_0$ in the undulated, unstrained state and $\sigma_{c,\vec{r}_0}$ its standard deviation.

Suppose $a_{c,\vec{r}_0}$ is the fraction of collagen fibres orientated in direction $\vec{r}_0$ that is already straightened in reference configuration. Then, the total load per unit unstrained cross-sectional area contributed by all collagen fibres in direction $\vec{r}_0$, with different straightening strain, can be formulated as:

$$f_c^*(\lambda(\vec{r}_0)) = a_{c,\vec{r}_0} f_k(\lambda) + \int_{x=1}^{\lambda} D_{c,\vec{r}_0}(x) f_c\left(\frac{\lambda}{x}\right) dx, \tag{10}$$

with $f_c\left(\frac{\lambda}{x}\right)$ obeying the relationship given by Equation (8).

# 3 Numerical-Experimental Method

The method chosen for characterising the mechanical behaviour of skin is based on the combination of three elements[2,3]:

1) measurements of (field) data from an experiment,
2) finite element modelling of the experiment,
3) an iterative scheme to obtain estimates for the material parameters of the constitutive model employed.

The application of these three elements is described in the next sections.

## 3.1 Experimental Set-up

In the present study, uniaxial, *in vivo* stretch tests are performed, where pads attached to the skin surface are used to induce deformation. Structural characterisation of tissues can be performed by biaxial stretch tests on *in vitro* samples. In this case it was found that most information is gathered by performing uniaxial tests (lateral strain is kept zero by the biaxial test set-up) at mutually perpendicular directions inclined by 22.5° (0.4 *rad*) to the specimens axes of material symmetry[11]. Although, the *in vivo* loading situation does not correspond exactly with a biaxial loading of a flat membrane we will adopt this approach. Since the direction of Langer's Lines coincides with the preferred orientation of the collagen and elastin fibres in the dermis, these lines give an indication of the axes of material symmetry of the skin[14,15]. For the experiments the skin at the volar forearm near the elbow was chosen, because skin at that place is flat and anisotropic[14,16,17]. Furthermore the epidermis at the volar side of the arm is relatively thin and therefore has only little influence on the mechanical behaviour of skin. The loose cells of the relatively stiff surface layer[12] of the epidermis, the stratum corneum, are removed by using scrub-cream and tap-water in order to enhance the attachment of the pads to the skin. Besides, hydrating the stratum corneum will soften it and decrease its influence on the overall mechanical behaviour of skin. Note that (mechanical) skin properties depend on anatomical site and also on inter-individual differences, see e.g.[12,15].

In order to obtain deformation field information, a number of markers is applied to the surface of the skin under investigation. The marker pattern consists of 12×6 markers, equidistantly spaced by 2 *mm*, with a diameter of approximately 0.4 *mm*, see Figure 1. The marker pattern is applied to the skin by means of a template and white oil paint. If skin is stretched *in vivo*, an undefined, rather large area is deformed. In order to limit the deformation to a defined area, the skin under investigation is mechanically isolated from its surrounding area by gluing a rigid plastic frame on it.

To impose a certain state of deformation to the skin, a small surface tensile device is used. The pads (6×5 $mm^2$) of the device are glued to the skin using cyanoacrylate resin. An electric motor translates the pads in opposite directions by means of a spindle. Using the measuring and controlling software package Labview (National Instruments, 1992), the displacements of the pads can be prescribed in an arbitrary way. The force on each pad is measured and registered by the Labview program in the direction of its displacement with an accuracy of 0.01 *N* using strain gauged leaf springs.

A CCD camera with a 105 *mm* focal distance lens is placed perpendicularly above the marker pattern at a working distance of about 700 *mm*. With this CCD camera, connected to a super-VHS video recorder and an on-line video screen, the markers can be observed. From the video recording, images at different states of deformation are taken and the individual marker positions are determined using the image analysis software package Quantimet 500+ (Leica, 1994). The standard deviation of the reconstructed marker positions proved to be 0.004 *mm* for the x-coordinate and 0.003 *mm* for the y-coordinate at a working distance of 580 *mm*[18,19]. Correction for a different working distance of 700 *mm* used in the present case yields a standard deviation of 0.005 *mm* for the x-coordinate and 0.004 *mm* for the y-coordinate.

In Figure 1 the skin under investigation isolated by the frame is shown. The length of the area of skin enclosed by the frame is 40 *mm*, which is large enough to prevent wrinkling of the skin between the pads and the frame. Markers are placed on the frame and the pads in order to reconstruct their positions (see Section 3.2). The pads are moved in the direction of the arrows. The outlines of the camera view are represented by the dash-dotted rectangle.

The pads are glued to the surface of the skin of the volar fore arm (near the elbow) of the 33-year-old male subject. In the first experiment, the skin is stretched perpendicular to the direction inclined by approximately 22.5° to the direction of Langer's Lines. This experiment will further be called the transverse experiment, because the direction of stretching is approximately transverse to the long axis of the forearm. In the second experiment, called the longitudinal experiment, the frame and the direction of stretching are rotated by 90°. Both experiments are executed on the same location on the right volar forearm of the subject, on consecutive days. Removal of the glued pads will only affect the surface layer of the skin

(stratum corneum). As this layer is very thin and also softened by hydration at the start of our experiment, this will not affect our measurements.

The initial distance between the pads is approximately 12.6 *mm*. The pads are moved apart in four steps of 1 *mm* each (except the last step of the longitudinal experiment was 0.5 *mm*) with a constant velocity of 0.20 *mm/s*. Thus the final distance between the pads is 16.6 *mm* and 16.1 *mm* in the transverse and longitudinal experiment respectively. After each step, the skin is given time to relax in order not to measure the viscous response of the skin. The relaxation time needed increases with increasing load. The reaction forces during the longitudinal experiment are higher and not fully relaxed at the end of each relaxation period. However, longer relaxation periods are not used in view of the well-being of the test person. The ambient conditions during the experiments are: 23 *°C* and 33% *RH*.

From the video recording, five pictures are taken: one before the first deformation step and one at the end of each relaxation period. Using the displacements of the eight markers on the frame (see Figure 1), a correction for small movements of the test person can be made. The corrected marker positions of the transverse experiment are shown in Figure 2.

## 3.2 Finite Element Modelling

As the fibre distributions in skin are assumed to be mainly two-dimensional, a two-dimensional finite element model of each experiment is made. It is obvious that as the skin is loaded only on the surface, the displacements will not be homogeneously throughout the thickness. This means that the stiffness of the skin will be underestimated by employing a two-dimensional model. All the measured marker positions at the reference state become nodes in the finite element model. The geometry of the frame defines the edge of the finite element model. The locations of the pads are reconstructed using the positions of the markers at the corners of the pads. The space without markers is divided into elements connected to the nodes of the elements defined by the positions of the markers.

The arbitrary thickness of the finite element model is 1.51 *mm* (measured thickness of epidermis plus dermis at the volar forearm of the test person by means of 20 *MHz* ultrasound echography, see e.g.[20]). The part of the mesh forming a pad is assumed rigid. The edge of the finite element model, defined by the frame is assumed fixed. The measured displacements of the pads are prescribed to the rigid modelled skin under the pads. The sum of the calculated nodal reaction forces on a pad in the y-direction corresponds to the y-component of the measured force on a pad. Figure 3 shows the finite element meshes of the transverse experiment at the undeformed state and at deformation state 4 (using parameters that are estimated in Section 4).

## 3.3 Parameter Estimation

The essential part of the identification method is the iterative procedure that is used to adjust the parameters of the constitutive equation of Lanir's Skin Model (see Equation (2)). In the next section the parameters of Lanir's Skin Model to be estimated are selected. In Section 3.3.2 an iterative scheme to obtain estimates for the parameters is described. This scheme is tested in Section 3.3.3.

### 3.3.1 Parameters of Lanir's Skin Model

Lanir's Skin Model contains a large number of parameters. Since the computing effort increases with the number of parameters, a limitation of the set of parameters to be estimated is desired. In order to decide which parameters can be fixed, a literature survey is done.

The fraction of collagen and elastin fibres in human skin, $S_c$ and $S_e$ respectively, are determined well in previous studies[12] and therefore fixed in the estimations. Values for the stiffness of collagen and elastin fibres, $K_c$ and $K_e$ respectively, are also known from the literature[21], however with unknown accuracy. The mean undulation ratio of collagen fibres, is roughly guessed at 1.25 by Manschot[12]. The collagen fibre distribution is known to be preferably orientated in the direction of Langer's Lines[15]. However, the exact direction of Langer's Lines differs between subjects.

Based on some preliminary finite element calculations, it was observed that the variation of the stiffness of elastin, $K_e$, and the standard deviation of the mean undulation of collagen fibres, $\sigma_c$, do not influence the calculated reaction forces significantly. Therefore these parameters are also fixed in the estimations. Thus, the parameters of Lanir's Skin Model to be estimated are the collagen fibre stiffness, $K_c$, its mean undulation, $\mu_c$, and the parameters defining the collagen fibre

orientation distribution, $C_1$ and $C_2$ of Equation (6). The fixed and expected values of the parameters of Lanir's Skin Model are given in Table I.

### 3.3.2 Iterative Scheme

In order to adjust the parameters the residuals, i.e. the differences between the measured and the calculated data, are used. The algorithm employed in this research is based on a constrained sequential maximum-likelihood approach[18]. The minimisation procedure used takes possible equality and inequality constraints into account.

For estimating the four non-fixed parameters, the measured reaction forces as well as the marker displacements are needed in the estimation process. These two types of experimental data differ in number (8 (4 increments x 2 pads) forces vs. 576 (4 increments x 72 markers x 2 coordinates) displacements), value and dimension, making it difficult to determine appropriate values for their weights in the estimation process. If the forces and displacements are weighed equally, the estimation times are long and the estimation results are bad. Therefore, more information about the influence of these four parameters on the reaction forces and the marker displacements is gathered from a numerical parameter study, where the influence of each parameter on the calculated reaction forces and the marker positions is determined.

From the parameter study, it appears that the reaction forces are mainly characterised by the collagen stiffness, $K_c$, and particularly by its mean undulation, $\mu_c$. The marker displacements are mainly characterised by the collagen fibre orientation distribution parameters, $C_1$ and $C_2$, and by $\mu_c$. The marker displacements are influenced by $C_1$ and $C_2$ in mutually perpendicular directions, while in most cases $\mu_c$ influences the marker displacements in almost the same direction as $C_1$. The influence of $K_c$ on the marker displacements can be neglected. Therefore, $C_1$ and $C_2$ can only be estimated well from the marker displacements, if $\mu_c$ is known. It is expected that a rough estimate for $\mu_c$ can be made, using the measured reaction forces and that $K_c$ can be estimated based on the reaction forces only. Therefore, the estimation in a two-step cycle, schematically presented in Figure 4, seems appropriate to steer the estimation process.

First, $K_c$ and $\mu_c$ are estimated using the measured reaction forces on each pad at the end of each relaxation period. In our experience using the experimental data of successive states of deformation in each estimation step has proved to be effective. Next, $C_1$ and $C_2$ are estimated using the measured marker coordinates of each state of deformation, and using the last estimated values for $K_c$ and $\mu_c$. Because of excessive computation times, the number of estimation cycles is limited to two.

To initialise the estimation sequence, an initial guess for the parameters to be estimated is needed. To study whether the estimation process converges to a local minimum, the estimation process is repeated for another set of initial guesses. The values of the initial guesses are based on the literature values given in Table I. The two estimation processes each starting with different initial guesses will be called Case I and Case II, respectively. The values chosen for each initial guess for the parameters $C_1$ and $C_2$ have relatively small influence on the reaction forces in the finite element model. Therefore the first parameters to be estimated, $K_c$ and $\mu_c$, will be characterised better. As stated above a good first estimation of $\mu_c$ is important for the estimation of the parameters $C_1$ and $C_2$.

For numerical reasons the parameter $K_c$ is scaled in the estimation process, by dividing its value by 100. Based on physical and numerical arguments, the constraints for the different parameters are set to:

$$\begin{aligned} 0.001 \le K_c/100 \le 2.000 \quad & N/mm^2/100 \\ 1.100 \le \mu_c \le 1.700 \quad & - \\ 0.001 \le C_1 \le 0.848 \quad & - \\ 0.001 \le C_2 \le 3.141 \quad & rad \end{aligned} \tag{11}$$

### 3.3.3 Accuracy of the Estimated Parameters

In order to get an indication of the accuracy of the two-step estimation process, the transverse experiment is simulated using a given set of parameters: $K_c/100$=1 $N/mm^2/100$, $\mu_c$=1.4, $C_1$=0.6, $C_2$=0.4 *rad*, and the other parameter values used can be found in Table I. The calculated forces and displacements are used in the estimation process, employing the following initial guesses for the parameters to be estimated: $K_c/100$=0.5 $N/mm^2/100$, $\mu_c$=1.5, $C_1$=0.4, $C_2$=0.2 *rad*. To investigate the effect of the modelling error introduced by the numerical integration of the fibre orientation distribution functions in 24 intervals, the test data are generated more accurately using 60 intervals. The generated data are provided with random normal distributed

noise with a standard deviation of 0.010 $N$ for the generated reaction forces and 0.005 $mm$ for the generated marker coordinates. In order to assess the accuracy of the parameters during the estimation, the measure $\chi^2$ is introduced. This measure is defined by:

$$\chi^2 = (\underset{\sim}{h}(\underset{\sim}{\hat{x}}) - \underset{\sim}{y})^T \underline{R}^{-1} (\underset{\sim}{h}(\underset{\sim}{\hat{x}}) - \underset{\sim}{y}), \tag{12}$$

where $\underset{\sim}{y}$ is the column of measured data, $\underset{\sim}{h}(\underset{\sim}{\hat{x}})$ the column of calculated data with the estimated column of parameters $\underset{\sim}{\hat{x}}$, and $\underline{R}^{-1}$ is a diagonal matrix with diagonal values $10^8$.

Furthermore, the individual values of the residuals, $\underset{\sim}{h}(\underset{\sim}{\hat{x}}) - \underset{\sim}{y}$, give an indication of the reliability of the parameters and the constitutive model employed. From the reaction forces the arithmetic mean of the residual force on both pads, $\bar{r}_f$, for each state of deformation is determined. In the ideal case of no modelling errors, the residual reaction force for each state of deformation should be of the same order of magnitude as the measuring error. For the residual marker positions, a positive value implies a deviation of the calculated position compared to the measured position in positive $x$- or $y$-direction. In the ideal case of no modelling errors, the distribution of the residual field should be random, and the order of magnitude of the residuals should be equal to the measuring error. From the residual marker positions, the arithmetic means and the sample standard deviations of each deformation state for the $x$- and $y$-direction are determined, respectively indicated by $\bar{r}_x$, $\bar{r}_y$, $s_x$ and $s_y$.

The estimation results ($K_c/100$=0.849 $N/mm^2/100$, $\mu_c$=1.383, $C_1$=0.603, $C_2$=0.399 $rad$) and the residuals from the simulated experiment showed a stable solution for the set of parameters after two estimation cycles. The accuracy by which the parameters $\mu_c$, $C_1$ and $C_2$ are estimated is about 1%. The accuracy of the estimated parameter $K_c$ is about 15%. The measure $\chi^2$ resulting after the second estimation step of $K_c$ and $\mu_c$ is one order of magnitude larger than the expected minimal value, and $\chi^2$ resulting after the second estimation step of $C_1$ and $C_2$ is in the same order of magnitude than the expected minimal value. The residual reaction forces as well as the residual marker positions are of the same of magnitude as the generated noise on the data. The residual displacement field is randomly orientated. For these reasons it is concluded that the remaining deviation of parameter $K_c$ does not contribute to significant modelling errors. Using 24 intervals in the numerical integration of the fibre orientation distribution functions does not lead to significant modelling errors either.

# 4 Results

In the next two sections the results of the estimations based on the transverse and the longitudinal *in vivo* experiment are listed.

## 4.1 Estimation Results of the Transverse Experiment

The estimation results of the transverse experiment for the two cases are summarised in Table II. For both cases, the measure $\chi^2$ resulting after the second estimation step of $K_c$ and $\mu_c$ is two orders of magnitude larger than the expected minimal value: $\chi^2_{\min} = 8.0 \cdot 10^4$, and $\chi^2$ resulting after the second estimation step of $C_1$ and $C_2$ is three orders of magnitude larger than the expected minimal value: $\chi^2_{\min} = 1.2 \cdot 10^6$ (These minimal values are obtained when the residuals equal the measurement errors.). The residuals for both cases of the transverse experiment are summarised in Table III. From this table, it can be observed that the mean residual reaction forces are of the same order of magnitude as the accuracy of the force measurement (0.01 $N$), except for state 2. It can also be observed that the standard deviations of the residual marker positions are about an order of magnitude larger than expected (0.005 $mm$ in the $x$-direction, and 0.004 $mm$ in the $y$-direction respectively). The residual marker positions for Case I of deformation states 1 and 4 of the transverse experiment are shown in Figure 5. It can be seen that the residuals of the marker positions are not orientated randomly, but exhibit a structure, which is similar for Case II.

### 4.2 Estimation Results of the Longitudinal Experiment

The longitudinal experiment is used for the verification of the estimated parameters of the transverse experiment. The longitudinal experiment was carried out on the same piece of skin as the transverse experiment, therefore the collagen fibre distribution estimated from the transverse experiment may be used. The values for the parameters $C_1$ and $C_2$ of Case I are used because of the smaller residuals. The values for the parameters $C_1$ and $C_2$ of Case I are used in the longitudinal experiment. Thus, the value for the fibre distribution parameter, $C_1$, is set to 0.552 and the preferred orientation angle, $C_2$, is set to 1.953 *rad* (0.382 + $\pi$/2 *rad*).

The estimation results of the longitudinal experiment for two different initial guesses are summarised in Table IV. The residuals for the two cases of the longitudinal experiment are summarised in Table V. From this table, it can be observed that the mean residual reaction forces are of the same order of magnitude as the measuring error of the force measurement. Figure 6 shows the residual marker positions of deformation state 4. The figures are similar for Case I.

## 5 Discussion

In section 3.3.3 the proposed two step estimation procedure is validated in case of a simulated 'experiment'. The number of iterations is limited to two. Results show that $C_1$ and $C_2$ can be estimated from the 'measured' displacement field, starting from different initial estimates. From the 'measured' forces, $\mu_c$ can be determined to within 1%, but $K_c$ has not yet converged to its true value. This can be explained by the fact that the mean collagen fibre undulation is 1.4. In combination with a maximum global stretch of only 30%, and the main orientation of the collagen fibres being perpendicular to the direction of stretch (transverse experiment), this implies that only a small fraction of the collagen fibres is stretched and exhibit their intrinsic stiffness.

The results of the actual experiments show that after two iterations $\mu_c$ is estimated at a value of 1.42-1.43 for both initial estimates in the transverse as well as the longitudinal experiment. The estimates for $K_c$ vary between 51-86 $N/mm^2$, while the value for $\chi^2$ is about equal for all cases. Here, the same phenomenon is observed as in the simulated 'experiment': $K_c$ can not be determined very accurately because the global level of strain in our experiments is not sufficient to stretch a substantial fraction of the collagen fibres. Because these experiments are performed in vivo, it is not easy to improve on this. The level of global strain must be limited in order not to damage the volunteer's skin, and the stress levels created in the skin would be so high that the attachment of the pads to the surface of the skin would fail.

Besides that the residual marker positions are larger than the measuring error, some other observations can be made from the tables and figures mentioned in Section 4. The difference in the residuals of both cases is small for both experiments, which may indicate that the solution (estimates) for the parameters is converged. The structures of the residuals of the marker positions of the two experiments differ significantly. Further, the residuals of the marker positions increase with increasing load.

Summarising, it can be stated that the constitutive model used for the characterisation of the mechanical behaviour of human skin *in vivo* exhibits modelling errors. Below, a number of most probable modelling errors are listed:

- Lanir's Skin Model is restricted to the characterisation of the dermis; the influence of the epidermis and hypodermis are neglected.
- Lanir's Skin Model may have invalid assumptions: the interaction between the fibres and the matrix is not taken into account.
- The assumption that the epidermis moves exactly the same as the dermis upon deformation.
- The fact that the skin is not fully relaxed at the end of the last relaxation periods while the model employed only takes elastic behaviour into account.
- The assumption that the deformations are homogeneous throughout the thickness of the skin.

## 6 Conclusion

The experimental set-up, the implemented skin model and the two-step estimation process are useful tools to increase the knowledge of the in-plane mechanical behaviour of human skin *in vivo*. Resulting from the estimations using the data from the transverse and the longitudinal *in vivo* experiments at the inner side of the test persons arm, the collagen fibre mean undulation $\mu_c$, is approximately 1.42 and the collagen fibre stiffness $K_c$, ranges from 50 to 90 $N/mm^2$. Resulting from the estimations using the data of the transverse experiment parameter $C_1$ is approximately 0.55 and $C_2$ is about 0.40 *rad*. The

estimated values for the collagen fibre stiffness and the parameter $C_2$ do not differ significantly from values found in previous studies (see Table I). The parameters $\mu_c$ and $C_1$ had not been determined in earlier research.

However, the implemented skin model still exhibits modelling errors. Therefore, it is recommended to take the influence of the epidermis and the interaction between the fibres and the matrix into account in future research. It is strongly believed that further improvement of mechanical skin models will only be possible by using (optical) imaging techniques that can measure sub-surface skin deformations.

## REFERENCES


1. Y. Lanir, "Constitutive Equations for Fibrous Connective Tissues,"*Journal of Biomechanics*, **16**, pp.1-12, 1983.
2. M.A.N. Hendriks, *Identification of the mechanical behaviour of solid materials.* PhD Thesis, Eindhoven University of Technology, The Netherlands, 1991.
3. M.A.N. Hendriks and C.W.J. Oomens, "Identification of inhomogeneous solids," In, *Inverse problems in engineering mechanics* (ed. M. Tanaka and H.D. Bui) IUTAM, 1992.
4. C.W.J. Oomens, M.R. van Ratingen, J.D. Janssen, J.J. Kok and M.A.N. Hendriks, "A Numerical-Experimental Method for a Mechanical Characterization of Biological Materials," *Journal of Biomechanics*, **26**, pp. 617-621, 1993.
5. M.R. van Ratingen, *Mechanical identification of inhomogeneous solids.* PhD Thesis, Eindhoven University of Technology, The Netherlands, 1994.
6. H. Sol and C.W.J. Oomens, *Material identification using mixed numerical mehods*, Kluwer Academic Publishers, The Netherlands, 1997.
7. B. Finlay, "Scanning Electron Microscopy of the Human Dermis under Uniaxial Strain,"*Biomechanical Engineering*, **4**, pp. 322-327, 1969.
8. I.A. Brown, "Scanning Electron Microscopy of Human Dermal Fibrous Tissue," *Journal of Anatomy*, **72**, pp. 159-168, 1972.
9. R.P.M.J Feron, *A 3-D structural skin model: development and implementation.* MSc Thesis, WFW report 93.132, Eindhoven University of Technology, The Netherlands, 1993.
10. MARC Analysis Research Corporation, *Volumes A-E of the MARC Reference Library Manuals.* version K.5. Palo Alto, USA, 1994.
11. Y. Lanir, O. Lichtenstein and O. Imanuel, "Optimal Design of Biaxial Tests for Structural Material Characterization of Flat Tissues," *Journal of Biomechanical Engineering*, **118**, pp. 41-47, 1996.
12. J.F.M. Manschot, *The mechanical properties of human skin in vivo.* PhD Thesis, Nijmegen University, The Netherlands, 1985.
13. J.F.M. Manschot and A.J.M. Brakkee, "The Measurement and Modelling of the Mechanical Properties of Human Skin In Vivo- II. Modelling," *Journal of Biomechanics*, **19**, pp. 517-521, 1986.
14. K. Langer, "Zur Anatomie und Physiology der Haut. I. Über die Spaltbarkeit der Cutis," Sitzungsbericht der Mathematisch-naturwissenschaftlichen Classe der Kaiserlichen Academie der Wissenschaften, Wien, **44**, pp. 19-46, 1861.
15. R. Reihsner, B. Balog and E.J. Menzel, "Two-dimensional Elastic Properties of Human Skin in Terms of an Incremental Model at the *In Vivo* Configuration,", *Med. Eng. Phys.*, **17**, pp. 304-313, 1995.
16. H.L. Stark, "Directional Variations in the Extensibility of Human Skin,"*British Journal of Plastic Surgery*, **30**, pp. 105-114, 1977.
17. H. Cox, "The Cleavage Lines of the Skin,"*British Journal of Surgery*, **29**, pp. 234-240, 1941.
18. W.K.L. van der Voorden, *Characterization of the in-plane mechanical behaviour of human skin - a mixed numerical-eperimental approach employing a structural skin model.* MSc Thesis, WFW report 96.073, Eindhoven University of Technology, The Netherlands, 1996.
19. W.K.L. van der Voorden and L.F.A. Douven, "Characterization of the in-plane mechanical behaviour of human skin in vivo," In, *Material identification using mixed numerical mehods* (ed. H. Sol and C.W.J. Oomens) Kluwer Academic Publishers, The Netherlands, 1997.
20. J. Serup, J. Keiding, A. Fullerton, M. Gniadecka and R. Gniadecki, "High frequency ultrasound examination of skin: introduction and guide," In *Handbook of non-invasive methods and the skin* (ed. J. Serup and G.B.E. Jemec), CRC Press Inc., Boca Raton, FL., USA, pp. 239-256, 1995.
21. A. Viidik, "Mechanical Properties of Parallel-Fibred Collagenous Tissue: Interdependence between Structures and Function in Collagenous Tissue," *Biology of Collagen* (Viidik and Vuust, Aarhus, 1980), Chap. 17, pp. 239-255, 1980.
22. NAG, Numerical Algorithms Group Ltd., *Version MARC 15 of the NAG FORTRAN Library Manual*, Oxford, UK, 1993.

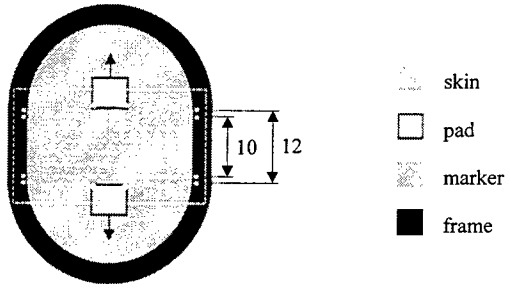


Figure 1: *In vivo* skin mechanically isolated from its surrounding area by a rigid plastic frame. The dash-dotted lines mark the camera view. The arrows point in the motion direction. Sizes in *mm*.

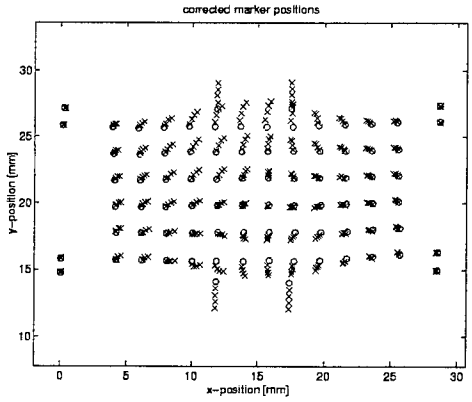


Figure 2: Corrected marker positions during the transverse experiment. The marker positions of the reference state are represented by 'o' and the displaced marker positions by ' × '.

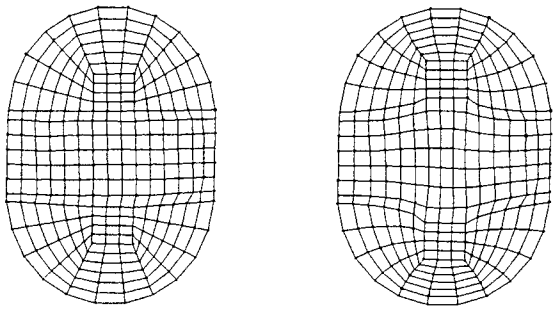

Figure 3: Finite element meshes of the undeformed state (a) and of deformed state 4 (b).

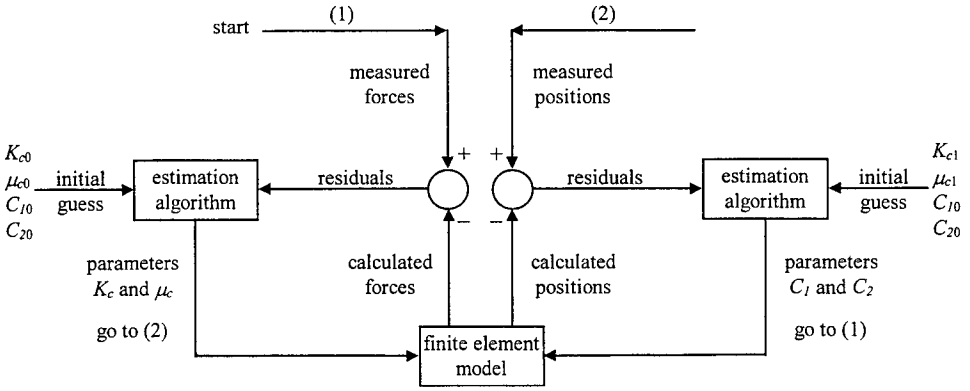


Figure 4: Flow diagram of the two-step estimation cycle.

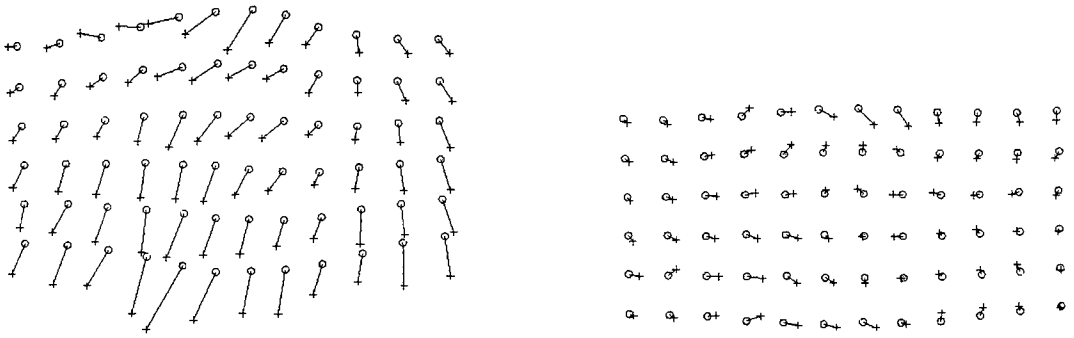

Figure 5: Residuals of the marker positions of deformation state 1 (a) and state 4 (b) for Case I of the transverse experiment. The measured markers positions are represented by 'o' and the calculated positions by '+'. The residuals are all multiplied by a factor 5, with the measured marker position fixed.

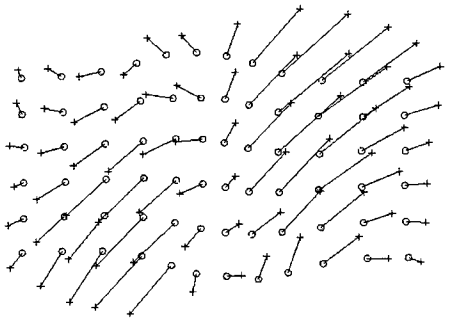

Figure 6: Residuals of the marker positions of deformation state 4 for Case II of the longitudinal experiment. The measured markers positions are represented by 'o' and the calculated positions by '+'. The residuals are all multiplied by a factor 5, with the measured position fixed.

Table I: Parameters of Lanir's Skin Model and their values as found in the literature. $S_c$, $S_e$, $K_e$, and $\sigma_c$ are fixed in the estimation process. For the non-fixed values, $K_c$, $\mu_c$, $C_1$, and $C_2$, the literature values are expected as results of the parameter estimation.

| Parameter | | Value | Dimension | Source |
|---|---|---|---|---|
| Fraction | $S_c$ | 0.30 | - | Manschot, |
| | $S_e$ | 0.02 | - | 1985 |
| Stiffness | $K_c$ | 100 | $N/mm^2$ | Viidik, |
| | $K_e$ | 1 | $N/mm^2$ | 1980 |
| Undulation of collagen | $\mu_c$ | 1.2-1.6$^{(*)}$ | - | Manschot, |
| | $\sigma_c$ | 0.2 | - | 1985 |
| Orientation distribution of collagen | $C_1$ | 0.4 - 0.8$^{(*)}$ | - | Langer, |
| | $C_2$ | 0.40$^{(*T)}$ | *rad* | 1861 |
| | | 1.96$^{(*L)}$ | *rad* | Reihsner *et al.*, 1994 |
| *c*: collagen | | * : expected | | |
| *e*: elastin | | $*^T$: expected for transverse experiment | | |
| | | $*^L$: expected for longitudinal experiment | | |

Table II: Estimation results of the transverse experiment.

| Parameter | Dimension | Case I Initial estimate | Case I Estimate 1st | Case I Estimate 2nd | Case I $\chi^2$ | Case II Initial estimate | Case II Estimate 1st | Case II Estimate 2nd | Case II $\chi^2$ |
|---|---|---|---|---|---|---|---|---|---|
| $K_c/100$ | $N/mm^2/100$ | 0.5 | 0.360 | 0.509 | $5.16 \cdot 10^6$ | 1.5 | 0.440 | 0.518 | $5.23 \cdot 10^6$ |
| $\mu_c$ | - | 1.5 | 1.418 | 1.433 | | 1.3 | 1.412 | 1.425 | |
| $C_1$ | - | 0.4 | 0.554 | 0.552 | $1.31 \cdot 10^9$ | 0.8 | 0.600 | 0.599 | $1.33 \cdot 10^9$ |
| $C_2$ | *rad* | 0.2 | 0.380 | 0.382 | | 0.6 | 0.277 | 0.279 | |

Table III: Arithmetic means and sample standard deviations of the residuals of the transverse experiment.

| State | Case I $\bar{r}_f$ [N] | Case I $\bar{r}_x$ [mm] | Case I $s_x$ [mm] | Case I $\bar{r}_y$ [mm] | Case I $s_y$ [mm] | Case II $\bar{r}_f$ [N] | Case II $\bar{r}_x$ [mm] | Case II $s_x$ [mm] | Case II $\bar{r}_y$ [mm] | Case II $s_y$ [mm] |
|---|---|---|---|---|---|---|---|---|---|---|
| 1 | 0.041 | 0.036 | 0.064 | -0.014 | 0.054 | 0.045 | 0.036 | 0.058 | -0.014 | 0.052 |
| 2 | 0.111 | 0.001 | 0.070 | -0.093 | 0.067 | 0.119 | 0.001 | 0.056 | -0.093 | 0.064 |
| 3 | 0.048 | -0.021 | 0.060 | -0.215 | 0.074 | 0.054 | -0.021 | 0.056 | -0.214 | 0.078 |
| 4 | -0.062 | -0.096 | 0.107 | -0.248 | 0.135 | -0.069 | -0.096 | 0.121 | -0.247 | 0.147 |

Table IV: Estimation results of the longitudinal experiment.

| Parameter | Dimension | Case I Initial estimate | Case I Estimate 1st | Case I Estimate 2nd | Case I $\chi^2$ | Case II Initial estimate | Case II Estimate 1st | Case II Estimate 2nd | Case II $\chi^2$ |
|---|---|---|---|---|---|---|---|---|---|
| $K_c/100$ | $N/mm^2/100$ | 0.5 | 0.794 | 0.774 | $3.97 \cdot 10^6$ | 1.5 | 0.888 | 0.857 | $3.36 \cdot 10^6$ |
| $\mu_c$ | - | 1.5 | 1.422 | 1.418 | | 1.3 | 1.434 | 1.429 | |

Table V: Arithmetic means and sample standard deviations of the residuals of the longitudinal experiment.

| State | Case I $\bar{r}_f$ [N] | Case I $\bar{r}_x$ [mm] | Case I $s_x$ [mm] | Case I $\bar{r}_y$ [mm] | Case I $s_y$ [mm] | Case II $\bar{r}_f$ [N] | Case II $\bar{r}_x$ [mm] | Case II $s_x$ [mm] | Case II $\bar{r}_y$ [mm] | Case II $s_y$ [mm] |
|---|---|---|---|---|---|---|---|---|---|---|
| 1 | -0.022 | 0.009 | 0.052 | 0.019 | 0.094 | -0.028 | 0.009 | 0.052 | 0.019 | 0.094 |
| 2 | -0.013 | 0.064 | 0.192 | -0.057 | 0.163 | -0.023 | 0.062 | 0.191 | -0.057 | 0.162 |
| 3 | -0.063 | -0.041 | 0.346 | 0.137 | 0.281 | -0.068 | -0.041 | 0.345 | 0.137 | 0.280 |
| 4 | 0.056 | 0.058 | 0.383 | 0.070 | 0.339 | 0.062 | 0.058 | 0.382 | 0.070 | 0.339 |

# Direct Measurement of Strain Rates in Biological Tissues

Sean J. Kirkpatrick[1] and Donald D. Duncan[2]

[1] Department of Biomaterials and Biomechanics, Oregon Health Sciences University, Portland OR, 97201, USA

[2] The Johns Hopkins University, Applied Physics Laboratory, Laurel, MD 20723, USA

**Abstract**

A novel, imaged laser speckle strain gauge is described for directly measuring strain rates in biological tissues. Cortical bone samples were tested in tension in a custom-designed microtensile testing machine. Strain rates were evaluated simultaneously with both the laser speckle strain gauge and contact strain gauges and extensometers. Young's modulus values of the bone samples were estimated using the strain data acquired by all methods. The strain rates and modulus estimates determined through all the methods compared favorably with each other, with the modulus estimates calculated using the speckle data slightly higher than by the other methods (mean of 16.88GPa for the speckle data *vs* 13.4 GPa for the contacting methods). The speckle strain gauge has a strain resolution at least on the order of single microstrain and should prove to be useful in the mechanical evaluation of both native and engineered tissues.

Keywords: Laser speckle, strain rate, biological tissues, tissue engineering

## 1. Introduction

Proper physiological functioning of biological tissue is inexorably linked to the mechanical behavior of the tissue. For example, the elastic properties of vascular tissue are essential in damping the pulsatile flow of blood through the body. The strength and stiffness of bone is essential for providing structural integrity to the body, yet bone has a high toughness, and therefore is not subject to brittle fracture. In the field of tissue engineering, particularly for tissues which must sustain dynamic loads, understanding the mechanics of the neotissue may provide insight into the ontogenetic evolution of the mechanical properties of tissues and may also provide clinically relevant data. For example, in the growth of new bone, it may be of value to track the development of the strength and stiffness of the tissue in order to determine the appropriate time for allowing the new tissue to be physiologically loaded, or to develop a model that correlates the rate of resorption of the tissue scaffold with the development of mature tissue. A further example lies in tissue engineering for the repair of cartilage which is designed to bear compressive loads. Immature cartilage does not respond to compressive loads in the same way as mature cartilage. This is believed to be largely due to the presence of undersulfated glycosaminoglycan side chains in the immature cartilage which are not present in mature cartilage. In more mature cartilage, the glycosaminoglycan side chains become sulfated and are linked to the proteoglycan aggregate of the extracelluar matrix of the cartilage. These links provide stability to the tissue by organizing the fluid phase of the cartilage and thereby help to control the hydrodynamic pressures experienced by the cartilage forming cells (chondrocytes). Because of this differential response to compressive loading between mature and neocartilage, premature loading of the immature tissue may lead to failure of the developing tissue.[1] Furthermore, it has been established that the mechanical properties of the scaffold upon which the engineered cartilage is grown and the mechanical environment in which the cartilage is grown have direct influences on the mechanics of the resultant cartilage. Thus, it is of use to be able to quantitatively evaluate these variables.[2]

Biological tissues are viscoelastic and, in many instances, pseudoelastic. There is a distinct dependence on time in the manner in which tissues will respond to an applied load. That is, the relationship between the applied strain and the resulting stress is not constant and linear elasticity theory does not apply in any simple manner. However, after a period of conditioning, i.e., after a period of sequential loadings and unloadings, a more-or-less steady state is arrived at in which the stress-strain relationship is not very sensitive to strain rate. This is the concept of pseudoelasticity[3] . Even here, though, the relationship between stress and strain is highly nonlinear and there is a distinct hysteresis loop



In *Laser-Tissue Interaction XI: Photochemical, Photothermal, and Photomechanical*, Donald D. Duncan, Jeffrey O. Hollinger, Steven L. Jacques, Editors, Proceedings of SPIE Vol. 3914 (2000) 1605-7422/00/$15.00

observable in the dynamic stress-strain curve. Once the steady-state has been arrived at, however, the size and shape of this hysteresis loop remains fairly constant. Thus, there is a need for methods that directly and noninvasively assess the time rate of the mechanical response of native and engineered tissues to an imposed load and the frequency dependent response on tissue to a dynamic loading situation. Contacting methods such as extensometers or resistance strain gauges are not appropriate for evaluating strains in developing soft or hard tissue because attachment of theses devices is difficult at best. Optical methods, which we will generally refer to as optical elastography, provide an avenue for evaluating tissue mechanics. Laser speckle techniques in particular show promise in this field of study. Herein, we will present one such method for evaluating the strain response of cortical bone to an imposed load using a novel, imaged laser speckle strain gauge.

## 2. Materials and Methods

### 2.1 Theory of the laser speckle strain gauge

Yamaguchi[4] has shown that the speckle motion for an object undergoing strain, observed at angle $\theta_o$ and illuminated from angle $\theta_s$ is given by

$$\delta x(\theta_o,\theta_s) = a_x\left(\frac{L_o\cos^2\theta_s}{L_s\cos\theta_o}+\cos\theta_o\right)-a_z\left(\frac{L_o\cos\theta_s\sin\theta_s}{L_s\cos\theta_o}+\sin\theta_o\right) -L_o\left[\epsilon_{xx}\left(\frac{\sin\theta_s}{\cos\theta_o}+\tan\theta_o\right)-\Omega_y\left(\frac{\cos\theta_s}{\cos\theta_o}+1\right)\right] \quad (1)$$

where $L_o$ is the observation distance (distance to the primary principal plane of the lens, see below), $L_s$ is the radius of curvature of the incident wavefront, $\theta_s$ is the illumination angle with respect to the specimen normal, $\theta_o$ is the observation angle, $\epsilon_{xx}$ is the in-plane strain in the plane of the laser beam and detector, the $a_x$ and $a_z$ terms are in-plane and out-of-plane rigid body motions, respectively, and $\Omega_y$ is a rotation about the axis perpendicular to the measurement plane. By observing normally ($\theta_o = 0°$), using collimated beams ($L_s \to \infty$), and subtracting the speckle motion as observed for two equal, but opposite illumination angles, a relation describing the differential speckle motion, $\delta A$, can be arrived at:

$$\delta A \equiv \delta x(0,+\theta_s)-\delta x(0,-\theta_s) = -2L_o\epsilon_{xx}\sin\theta_s \quad . \quad (2)$$

This equation suggests that by measuring the differential speckle motion, in-plane strains can be inferred.

The crux of the proposed method is to determine a shift in the speckle patterns resulting from an applied load to the object. Towards this end, the system generates what we have termed a 'stacked speckle history', which is a time series of one-dimensional views of the speckle pattern as recorded by a linear array camera combined into a spatio-temporal array such that the spatial dimension (camera pixel in microns) is along the abscissa and the temporal axis is the ordinate. Figure 1 is a grey-scale display of an imaged stacked speckle history taken from a stainless steel orthodontic

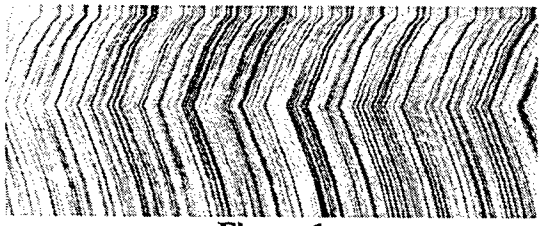

**Figure 1**

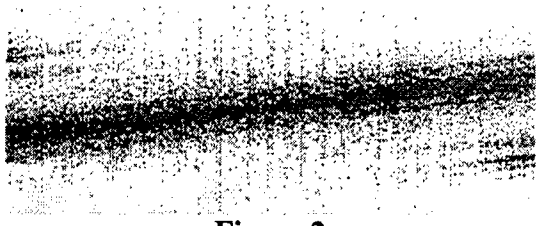

**Figure 2**

wire undergoing a slow sawtooth strain. The desired information, that is the time rate of speckle pattern shift is given by the tilt of the corrugated structure. To extract this information, a 2-dimensional frequency transform, such as a 2-dimensional Fourier Transform implemented with a fast-Fourier (FFT) algorithm suggests itself. Indeed, this approach has proven to be successful.[5,6] However, we have had better results using an FFT in the spatial dimension and a parametric estimator[7] in the temporal one. Specifically, we use an autoregressive (AR) estimator (modified covariance

method) on 10-20 records with 3-5 poles. Fig. 2 illustrates the transformed speckle history of the unloading (lower ½) portion of Fig. 1. The horizontal axis is now spatial frequency ($f_s$) in cycles per micron and the vertical axis is now temporal frequency (Hz). The DC point, or zero frequency, is in the center of the figure. The dark line passing through DC is perpendicular to the tilt of the corrugated structure. Inspection of the units of each axis reveals that the slope, $m$, of the dark line is the time rate of speckle shift in $\mu m \cdot sec^{-1}$. By taking the difference of these slopes as seen for the two illumination angles, the time rate of strain, $\dot{\epsilon}_{xx}$, can be inferred from Eq. (2). Specifically, we take the time derivative of Eq. (2):

$$\delta\dot{A} \equiv \delta\dot{x}(0,+\theta_s) - \delta\dot{x}(0,-\theta_s) = -2L_o\dot{\epsilon}_{xx}\sin\theta_s \quad . \tag{3}$$

Inversion of this equation yields

$$\dot{\epsilon}_{xx} = \frac{\delta\dot{A}_x}{-2L_o\sin\theta_s} = \frac{m_2 - m_1}{-2L_o\sin\theta_s} \tag{4}$$

where $m_1$ and $m_2$ represent the slopes as calculated for the two illumination angles. The gauge length over which the strain is estimated is the length of the uniformly illuminated spot. The total in-plane strain at any given time, $\epsilon(t)_{xx}$, can be calculated as

$$\epsilon(t)_{xx} = \int_0^t \frac{m_2 - m_1}{-2L_o\sin\theta_s}\, dt \tag{5}$$

where $t$ is the time length of the experiment. Confidence intervals about the strain rate estimate are given by

$$\dot{\epsilon}_{xx} = \frac{m_2 - m_1}{-2L_o\sin\theta_s} \pm \frac{\sqrt{(\sigma_2)^2 + (\sigma_1)^2}}{2L_o\sin\theta_s}\, t(\nu,\alpha) \quad , \tag{6}$$

where $\sigma$ is the standard deviation about each slope, respectively, and $t$ is now the critical value of the Student's $t$-distribution with $\nu$ degrees of freedom ($n$-2, where $n$ is the number of records transformed) at a probability level of $\alpha$.

### 2.2 Optical arrangement

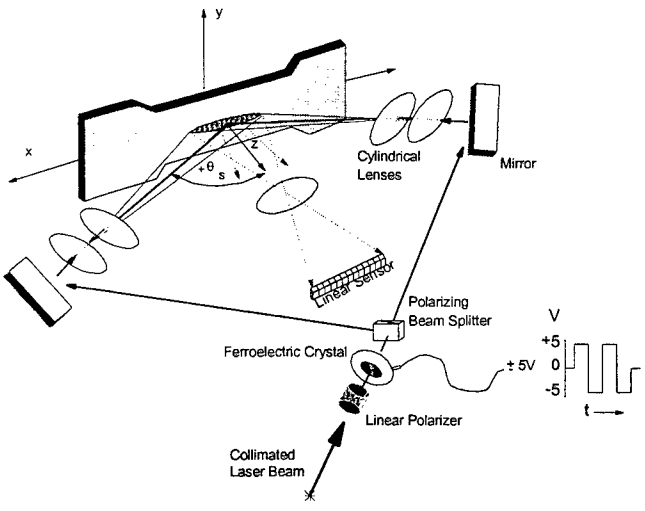


**Figure 3**

A 2-laser beam, 1-camera configuration was used to measure tensile strains in a non-contacting manner (Fig. 3). The laser was a thermoelectrically cooled, single-mode 150mW diode laser (Spectra Diode Labs, SDL-5422-H1). We have demonstrated that this laser is suitable for biomaterials testing[8-11] and is of sufficiently low power so as not to produce thermally induced speckle motion in cortical bone.[11] The beam was collimated, linearly polarized, passed through a ferroelectric crystal and split by a polarizing beam splitter (Fig. 3). The effect of this was to sequentially allow the beam to either transmit through or be reflected at the beamsplitter, depending upon the polarization of the beam exiting the ferroelectric crystal. A ferroelectric crystal is a binary device which, depending upon the voltage applied to it (typically ±5V), polarizes the light exiting the crystal in one of two orthogonal directions. Depending upon which polarization is passed, the polarizing beam splitter then either allows the beam to pass through it, or it reflects the beam 90°. The collimation restricts the sensitivity of the speckle system to in-plane strains only (Eqs. 1-4). Following the beamsplitter,

the beam was reflected off of front surface mirrors to sequentially illuminate the object through two equal, but opposite, illumination angles. A 1:1 magnification ratio telecentric lens system imaged the back-scattered speckle onto a linear array CCD camera. The linear array CCD camera (i2S, iDC181BC-8, 7.0 μm pitch) recorded the backscatter off of the bone samples for each illumination angle and placed the records into respective files. Serial views for each illumination angle were stacked into stacked speckle histories. The camera was triggered by the same FORTRAN code that controlled the data collection from the load cell, and the contact strain gauges and extensometer, which were used to evaluate strains in a more conventional manner so that comparisons between the speckle data and the contact strain gauge and extensometer data could be made. In addition, this same FORTRAN code controled the camera integration time, sample interval, and the switching of the ferroelectric crystal.

A perfectly focused imaging system would not result in a shift in the speckle pattern as the samples were strained.[12] Therefore, the system was misfocused by moving the camera and lens away from the sample. The further the misfocus distance, the greater the apparent speckle motion. That is, the misfocus distance can be thought of as a moment arm which multiplies the speckle motion as seen by the CCD array. This misfocus distance, that is the distance that the primary principal plane of the lens system was moved away from focus is the observation distance, $L_o$. In order to make the speckle motion more apparent, a substantial misfocus of 28.6cm was incorporated into the system.

### 2.3 Experiments

Cortical bone samples were machined from the body of a bovine mandible. The long axis of the samples (the direction in which the samples were ultimately loaded) was parallel to the occlusal plane (i.e. along the long axis of the mandible body). The samples were kept wet throughout the machining process and stored in a buffered physiological salt (HEPES) solution until tested. During testing the samples were kept wet through ad-lib spraying with the HEPES solution. Typical sample dimensions were 57cm (l) X 5cm (w) X 0.2cm (t).

For mechanical testing, the samples were mounted in a custom tensile testing machine.[8] The tensile testing machine was fitted with a 50N maximum load cell (Entran Devices, MLGLE-50) and a piezoelectric actuator (PZT) (Physik Instrument, model P-841.40) with a 60μm maximum expansion served to move the crosshead. The laser speckle strain gauge was arranged as described above, with the collimated beam striking the sample with a spot length of about 2.5cm. The parameters for the speckle strain gauge are given in Table 1. On two of the samples, an extensometer (MTS model 632.31) was mounted to the side opposite the laser spot and on two of the other samples, a contact strain gauge was bonded to the surface opposite the beam spot. One sample was not instrumented in any way. The output from the extensometer and strain gauge was conditioned via a Wheatstone bridge and collected through an A/D board mounted on the computer bus. A preload of approximately 20N was applied to the samples and a dynamic triangular stress waveform was applied through the PZT at 0.01Hz. The applied dynamic load and the location of the PZT was recorded through the same A/D board. Thus for a single experiment, 5 different data files were collected: 2 stacked speckle histories (one from each illumination angle), the output from either the extensometer or the contact strain gauge, the load, and the position of the PZT. An estimate of the Young's modulus of each of the samples was made by dividing the applied stress rate by the strain rate estimates from both the speckle data and the contact strain gauges or extensometer.

**Table 1. Parameters for the Speckle Strain Gauge Tests**

| Parameter | Value |
|---|---|
| Wavelength (nm) | 809 |
| Illumination angle | 42° |
| Misfocus distance (cm) | 28.6 |
| Camera integration time (ms) | 10 |
| Sample interval (s) | 0.08 |

## 3. Results

For all of the samples, strain rate and Young's modulus estimates were made. The results are summarized in Table 2. Differences in the strain rates estimated for a given test run were as large as 35% and as small as 4%. The largest differences noted were between the contact strain gauge estimates and the speckle derived estimates of strain rate (samples 1 and 5). The strain rate estimates derived from the extensometer data and the speckle data were in closer agreement with each other. In all cases, the strain rate estimates obtained with the contacting methods were higher than that obtained using the speckle data. This resulted in lower modulus estimates when calculated using the strain rates measured by the contacting methods. Nevertheless, the modulus estimates acquired through either method are in agreement with values found in the literature.[13]

**Table 2. Summary of Results of Strain Measurements on Cortical Bone**

| Sample | $\dot{\epsilon}_{speckle}$ ($\mu\epsilon$/s)* | $\dot{\epsilon}_{contact}$ ($\mu\epsilon$/s) | $E_{speckle}$ (GPa) | $E_{contact}$ (GPa) |
|---|---|---|---|---|
| 1 | -1.25(±0.870) | -1.97[1] | 11.0 | 7.0 |
| 2 | 4.96(±1.31) | 5.18[2] | 20.0 | 19.0 |
| 3 | 6.27(±2.60) | 8.42[2] | 18.4 | 13.7 |
| 4 | 8.36 (±1.27) | -------- | 14.0 | -------- |
| 5 | 1.05(±1.74) | 1.61[1] | 21.0 | 13.9 |

[1]Measured with an extensometer
[2]Measured with a contact strain gauge
*±80% confidence intervals

Figures 4a and 4b display a typical stacked speckle history obtained in a single experiment for one of the samples (Sample #2). The 20 records that were analyzed for the strain rate analysis are demarcated by the horizontal lines.

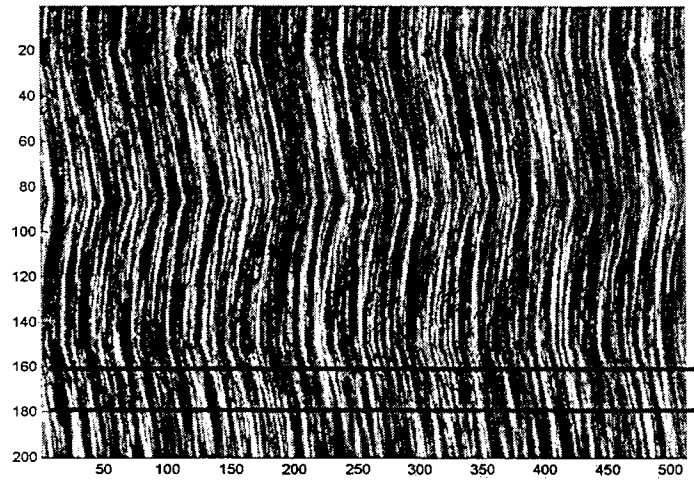


**Figure. 4a.** Stacked speckle history from the positive illumination angle for sample 2. The tilt in the history reflects the time rate of speckle pattern shift due to an imposed load. Time, as set by the sample interval, is along the ordinate and space (position on the CCD array) is along the abscissa.

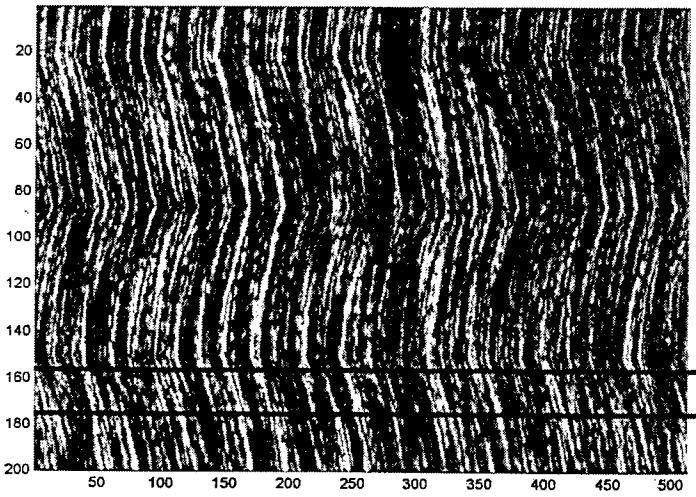


**Figure. 4b.** As in Fig. 4a, but from the equal, but opposite, illumination angle.

The tilts of the stacked speckle histories reflect the time rate of speckle motion and reflect the loading waveform applied to the bone specimen. Figure 5 is a display of the loading waveform applied during the test. Also shown is the position of the PZT actuator. The points where the loading changes from increasing to decreasing correspond to changes in the direction of tilt in the stacked speckle histories.

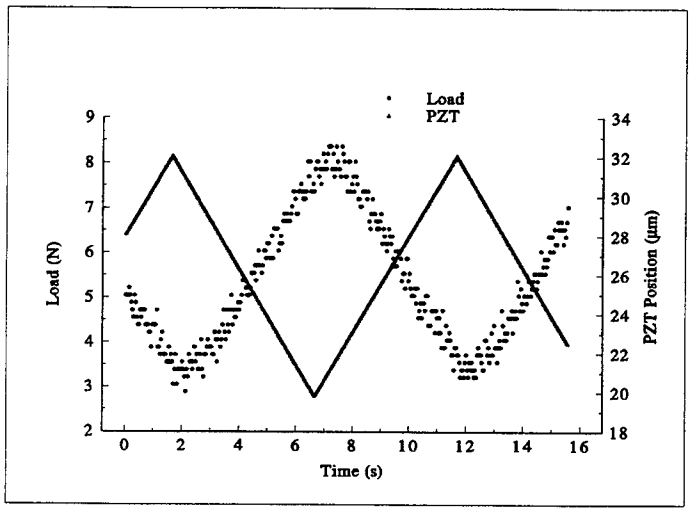


**Figure 5.** Loading waveform (left *y*-axis) and position of the PZT actuator (right *y*-axis) for the test that produced the stacked speckle histories of Figs. 4a and 4b.

The upper right quadrant of the 2-D frequency transforms of the selected data are shown in Figures 6a and 6b. The regression line is a weighted least squares fit where the weight is simply the value of the image at each peak. Both slopes ($m_1$ = 47.2μm/s; $m_2$ = 45.3μm/s) were highly significant ($p$ < 1e-15). This was the case for all tests.

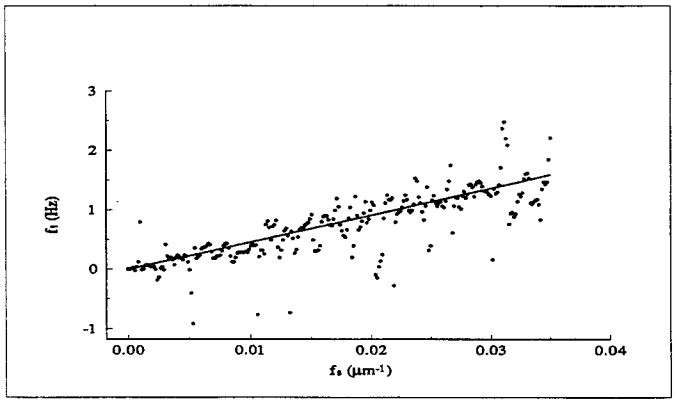


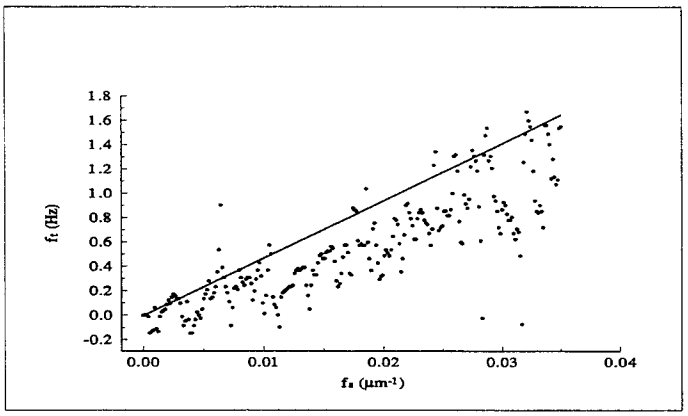


**Figures 6a & 6b.** 2-D frequency transforms of the data demarcated in Figs. 4a and 4b. The slopes of the weighted least squares fit to the data are significant ($p$ < 1e-15) and give the time rate of speckle shift in μm/s as observed when the sample is illuminated through the positive and negative illumination angles.

As a comparison, the data from the contact strain gauge is shown in Fig. 7. The strain gauge was configured in a 1/4 bridge configuration. This accounts for some of the noise in the data. Again, note that the change in the direction of the slope of the strain gauge data correspond to the change in the direction of tilt in the stacked speckle histories (Figs. 4a and 4b.

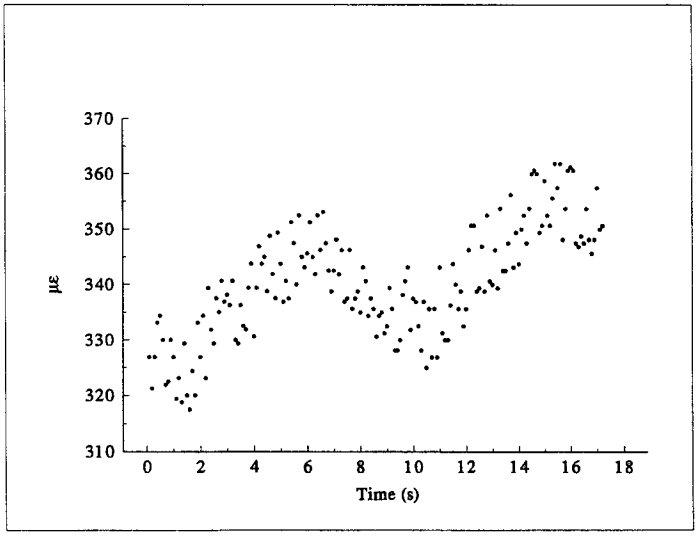


**Figure 7.** Contact strain gauge data for the same experiment that generated the stacked speckle histories of Fig. 4a and 4b.

## 4. Discussion

We have demonstrated a novel, imaged laser speckle strain gauge for evaluating the strain response in biological tissue. The gauge is sensitive only to in-plane strains (that is, strains in the plane of the laser and CCD array) and is highly sensitive. No effort was made to maximize the resolution of the system described here, yet we were able to record strain rates as low as 1.05$\mu\epsilon$/s. This corresponds to a total strain over the period in which the data were analyzed of 1.68$\mu\epsilon$. The strain resolution of the system described herein may be improved even further by employing a lens with a positive magnification. Total strains of this magnitude are very difficult to measure by conventional methods. For example, video dimensional analysis, a technique commonly employed in tissue mechanics research has a sensitivity on the order of a few thousand microstrain ($\mu\epsilon$). Contact strain gauges, while theoretically capable of measuring extremely small strains, are limited by the excitation and amplification electronics and typically give best results when the strains are on the order of at least 50$\mu\epsilon$. Figure 7 demonstrates this. The total peak to peak strains over the entire experiment as recorded by the contacting strain gauge were only on the order of 35$\mu\epsilon$ or so. Thus, the tests as run here were at the limits of the resolution of the contacting strain gauge. This likely accounts for much of the noise in the data of Figure 7, as we were forced to employ a high gain on the strain gauge amplifier.

A further modification to the speckle strain gauge would be to fiber couple the system so that a remote probe may be used to evaluate the mechanics of growing tissues in culture without disturbing them, or even *in vivo* through a skin flap in an animal model. Each of these experiments would require development of the measurement system and of an adequate means of loading the developing tissue. It should also be noted that the imaged speckle strain gauge is not limited to use on hard tissues. We have recently applied a very similar system to the evaluation of the strain response of healthy and diseased vascular tissue to a mechanical load.[14]

## 5. Acknowledgments

This study was funded through Research Grant #BES-9807497 from the National Science Foundation.

## 6. References

1. B.D. Boyer, C.H. Lohmann, J. Romero, and Z. Schwartz, "Bone and cartilage tissue engineering", *Clin Plast Surg* **26(4)**, 629-645, 1999.
2. G.C. Niederaurer, M.A. Slivka, N.C. Leatherbury, D.L. Korvick, and K. Kieswetter, "Multiphase implants with varying stiffness affect osteochondral cartilage repair", [abs] *Trans Soc Biomat.* **22**, 261, 1999.
3. Y.C. Fung, *Biomechanics, Springer-Verlag*, New York, 1981.
4. I. Yamaguchi, "Speckle displacement and decorrelation in the diffraction and image fields for small object deformation," *Opt. Acta.*, **28**, 1359-1376, 1981.
5. D.D. Duncan, S.J. Kirkpatrick, F.F. Mark, and Hunter, L. W. "Transform method of processing for speckle strain rate measurements," *Appl. Optics*, **33**, 5177-5186, 1994.
6. D.D. Duncan, F.F. Mark, and Hunter, L. W. "A new speckle technique for noncontact measurement of small creep rates," *Opt. Eng.* **31**, 1583-1589, 1992.
7. J. G. Proakis, and D. G. Manolakis, *Introduction to Digital Signal Processing*, Macmillan Publishing Co., New York, 1988.
8. S. J. Kirkpatrick, and D. D. Duncan, "Noncontact microstrain measurements in orthodontic wires," *J Biomed Mater Res.* **29**, 1437-1442, 1995.
9. S. J. Kirkpatrick,. and D. A. Covey, "Laser based microstrain measurements in dental materials," Abstract # 2165, *Proc. International Association for Dental Research Spring Meeting*, San Francisco, CA , 1996.
10. S. J. Kirkpatrick, and B. W. Brooks, "Micromechanical behavior of cortical bone as inferred from laser speckle data," *J Biomed Mater Res.* **39**, 373-379, 1998.
11. S. J. Kirkpatrick, D. A. Covey, and B. B. Brooks, "Direct measurement of strain rate variation in the vicinity of a round hole in mandibular cortical bone", Abstract #5 in the *Proceedings of the Twenty-first Annual Meeting of the American Society of Biomechanics,* Clemson, SC, 1997.

12. J. W. Goodman, "Statistical properties of laser speckles," in J. C. Dainty (ed), *Topics in Applied Physics, Vol 9: Laser Speckle and Related Phenomena,* Springer Verlag, New York, 1975.
13. S. A. Wainwright, W. D. Biggs, J. D. Currey, and J. M. Gosline, *Mechanical Desing in Organisms*, Princeton University Press, Princeton, NJ, 1982.
14. S. J. Kirkpatrick and M. J. Cipolla, "High resolution imaged laser speckle strain gauge for vascular applications" *J Biomed. Opt.* **5(1)**, 62-71, 2000.

# Processing techniques for laser speckle derived from biological tissues

Donald D. Duncan*[a], Sean J. Kirkpatrick[b]

[a]Johns Hopkins Applied Physics Laboratory, Laurel, MD 20723-6099

[b]Oregon Health Sciences University, Dept of Biomaterials & Biomechanics, Portland, OR 97201

## ABSTRACT

Laser speckle techniques are well known in the non-destructive evaluation community[1-4]. One particular application is to infer strain by monitoring the motion of the speckle pattern that results from coherently illuminating the object. Typically a reference image of the speckle pattern is acquired before deformation of the object. Motion (with respect to this reference image) of subsequent speckle patterns, which occurs when the object is stressed, are used to infer the resulting strain. A problem experienced in using this technique for measurements of hydrated tissues is the rapid decorrelation of the speckle patterns[5]. Thus, application of speckle techniques to assessment of strain in biological tissues relies on rapid sampling of the speckle patterns and the use of processing algorithms that are aimed at inferring strain rates rather than absolute strains. We discuss a number of approaches to estimating strain rates based on sequential speckle patterns. Maximum likelihood methods are shown to be especially useful.

Keywords: laser speckle, strain, biological tissues, processing algorithms

## 1. INTRODUCTION

Our objective is to use the laser speckle phenomenon to infer strains in biological materials. The approach adopted is basically that of Yamaguchi[6]. As depicted in Fig. 1, the specimen to be stressed is illuminated sequentially from two different directions and the objective or subjective speckle pattern is recorded by a single linescan camera. Alternatively, a single illumination beam and two cameras can be used. The data thus acquired appear as illustrated in Fig.2. Strain in the specimen is inferred according to the formula

$$\varepsilon_{xx} = \frac{\delta(\theta_s) - \delta(-\theta_s)}{-2L_o \sin\theta_s} , \qquad (1)$$

where $L_o$ is the observation distance, $\theta_s$ is the angle between the subject normal and illumination direction, and $\delta(\pm\theta_s)$ are the measured shifts in the speckle patterns for the respective illumination directions. This form assumes that the illumination beams are collimated.

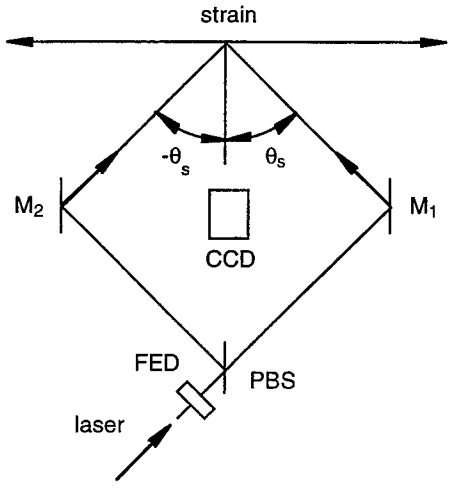


Fig. 1 Illustration of measurement configuration. Subject is illuminated sequentially through the use of FED: ferroelectric device; $M_{1,2}$: turning mirrors; and PBS: polarizing beamsplitter. CCD: charge coupled device camera.

* Correspondence: Email: donald.duncan@jhuapl.edu; Telephone: 240 228 6568; Fax: 240 228 6779

In *Laser-Tissue Interaction XI: Photochemical, Photothermal, and Photomechanical*, Donald D. Duncan, Jeffrey O. Hollinger, Steven L. Jacques, Editors, Proceedings of SPIE Vol. 3914 (2000)
1605-7422/00/$15.00

The crux of the problem then is to estimate the speckle motion in order to determine the strain or strain rate. The speckle patterns shown in Fig. 2 illustrate the problem; there is obvious speckle motion between records one and six, but there is also

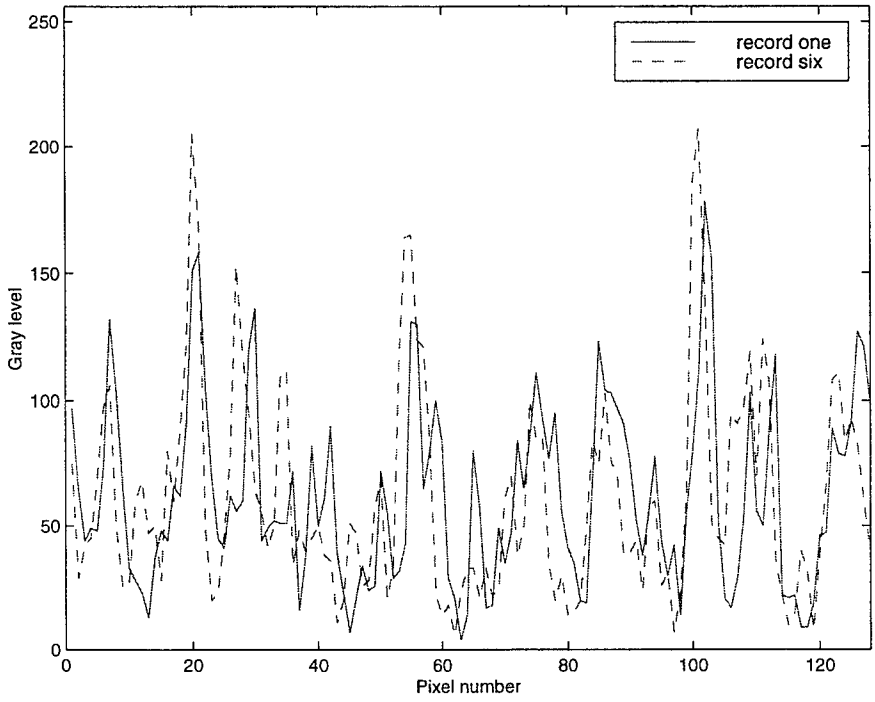


Fig. 2 Typical one-dimensional speckle pattern

a fair amount of decorrelation. In the material that follows, we discuss a number of different approaches to estimating speckle motion. As will be shown, some are better suited than others for coping with this decorrelation.

## 2. THEORY

There are a number of different approaches to determining speckle movement. One can categorize these as either parametric or non-parametric. An example of the latter is the correlation approach[7]. The cross-correlation of sequential records is calculated and the shift of the correlation peak determines the amount of speckle pattern shift. The basic resolution of this technique is determined by the pixel size of the camera. Another non-parametric approach is the transform method[8] in which a sequence of records is simply Fourier transformed. The result is a line passing through DC whose slope is equal to the time rate of the speckle pattern shift (see Fig. 3). Each of these techniques is non-parametric in that no a priori assumptions are made as to the properties of the speckle motion.

We contrast these techniques with a parametric approach to calculating speckle motion. We assume that, over a time on the order of a couple sequential exposures of the camera, the speckle pattern is fixed (see Fig. 4). Thus the speckle motion can be modeled as

$$g_{j+1}(x_i) = g_j(x_i - \beta) \quad , \tag{2}$$

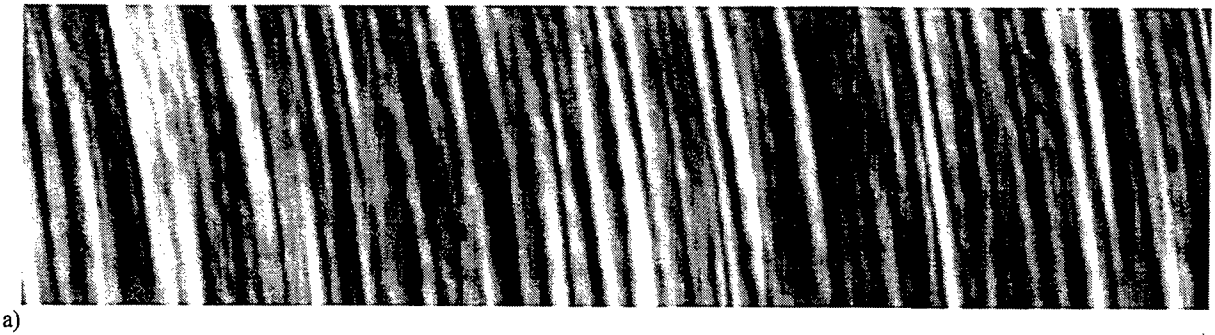

a)

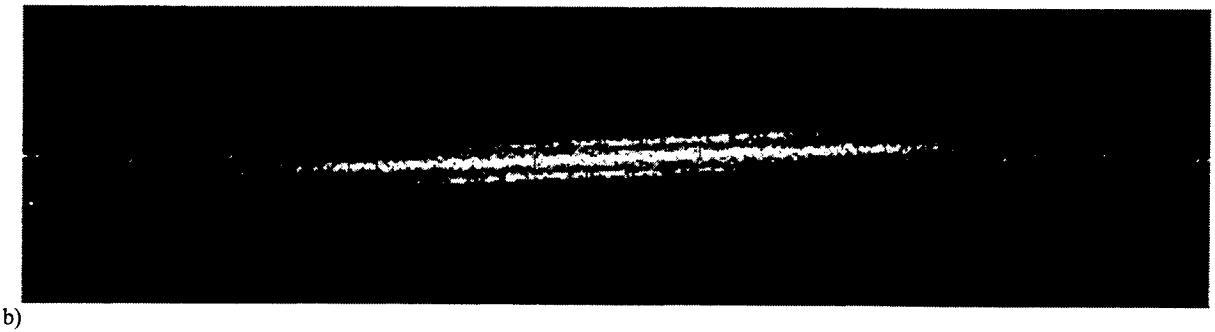

b)

Fig. 3 Illustration of transform approach to estimating speckle shift. a) Speckle history; b) Transform of speckle history. Units on the abscissa are spatial frequency (rad/m). Units on the ordinate are temporal frequency (rad/sec). Thus the units of the slope of the bright line are m/s, i.e., the speckle time rate of shift.

where the subscript $i$ denotes the pixel (spatial dimension) and the subscript $j$ represents the record (temporal dimension). We assume that the shift, $\beta$ is small compared to a pixel so that Eq. 2 can be approximated as

$$g_{j+1}(x_i) \approx g_j(x_i) + \beta\, g_j'(x_i) \quad . \qquad (3)$$

This is simply the first two terms of the Taylor series expansion for $g$. To introduce a degree of symmetry into the problem, we inspect the difference between the two speckle records on either side of the record of interest;

$$g_{j+1}(x_i + \beta) - g_{j-1}(x_i - \beta) \quad . \qquad (4)$$

We then seek the $\beta$ that minimizes the error,

$$\varepsilon_j^2 = \sum_{i=1}^{N}\left[g_{j+1}(x_i + \beta) - g_{j-1}(x_i - \beta)\right]^2 \quad , \qquad (5)$$

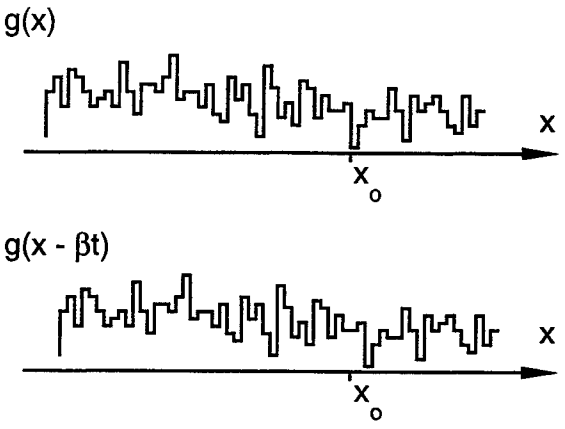


Fig. 4 Illustration of small-shift concept

where the sum is over all pixels in the array. If we make use of the approximation in Eq. 4, then differentiation with respect to $\beta$ and rearranging yields the formula

$$\beta_j = \frac{\sum_{i=1}^{N}\left[g_{j+1}(x_i) - g_{j-1}(x_i)\right]\left[g_{j+1}'(x_i) + g_{j-1}'(x_i)\right]}{\sum_{i=1}^{N}\left[g_{j+1}'(x_i) + g_{j-1}'(x_i)\right]^2} \quad . \qquad (6)$$

The first term in the denominator looks like a derivative with respect to time at a fixed location, $x_i$. In fact, the 1st central difference (as an estimate of the temporal derivative) is given by

$$\frac{d}{dt}g_j(x_i) \approx \frac{g_{j+1}(x_i) - g_{j-1}(x_i)}{2} \quad . \tag{7}$$

The remaining terms in Eq. 6 are spatial derivatives that can be estimated similarly:

$$\begin{aligned} g'_{j+1}(x_i) &\approx \frac{g_{j+1}(x_{i+1}) - g_{j+1}(x_{i-1})}{2} \quad ; \\ g'_{j-1}(x_i) &\approx \frac{g_{j-1}(x_{i+1}) - g_{j-1}(x_{i-1})}{2} \quad . \end{aligned} \tag{8}$$

Note that the shift parameter, $\beta$, is the time rate at which the speckle pattern shifts; units are pixels/record.

Up to this point, we have made no specific assumptions about the statistics of the speckle pattern or associated noise. The only a priori knowledge that we have introduced is that the speckle shift is small with respect to the pixel size. If we now make the assumption that the measured speckle signal comprises a deterministic speckle signal(!) plus noise, the measured signal looks like

$$d_j(x_i) = g_j(x_i) + n_j(x_i) \quad , \tag{9}$$

where $n$ is a zero-mean noise signal. If we calculate the central difference about the j[th] record, we get

$$\begin{aligned} d_{j+1}(x_i + \beta) - d_{j-1}(x_i - \beta) &= g_{j+1}(x_i + \beta) - g_{j-1}(x_i - \beta) \\ &\quad + n_{j+1}(x_i + \beta) - n_{j-1}(x_i - \beta) \quad . \end{aligned} \tag{10}$$

We assume that the sequential speckle patterns are constant mean. Further we assume that the noise is statistically independent Gaussian with zero mean and constant variance. As a result the noise probability density function can be written as

$$p(d_j \mid g_j) = p(n_j) = C\exp\left\{\frac{-1}{2\sigma^2}\sum_{i=1}^{N}\left[g_{j+1}(x_i + \beta) - g_{j-1}(x_i - \beta)\right]^2\right\} \quad , \tag{11}$$

where $C$ is a constant. Equation 11 is commonly referred to as the likelihood function. To choose the $\beta$ that maximizes this likelihood we set

$$\frac{\partial}{\partial\beta}\ln p(d_j \mid g_j) = 0 \quad . \tag{12}$$

Carrying out this calculation leads to the formula in Eq. 6. It is straightforward to show that this is an unbiased estimate of the speckle pattern shift and that the variance of the estimate attains the Cramér-Rao lower bound[9].

## 3. METHODS

For these measurements, a 2-laser beam, 1-camera configuration was used (Fig. 1). The laser was a thermoelectrically cooled, single-mode diode (Spectra Diode Labs, SDL-5422-H1). The beam was linearly polarized, passed through a ferroelectric crystal and then through a polarizing beam splitter. Depending on the polarization produced by the ferroelectric device, the beam was caused to take either of two paths to sequentially illuminate the sample from two equal but opposite angles. A 1:1 magnification ratio telecentric lens system imaged the speckle onto a linear array CCD camera (i2S, iDC181BC-8, 7.0μm pitch). A perfectly focused imaging system would not result in a shift in the speckle pattern as the samples were

strained. Therefore, the system was misfocused by moving the camera and lens away from the sample. The amount of misfocus constituted the effective observation distance, $L_o$.

Triggering of the camera, adjustment of integration time, and acquisition of the speckle patterns were under computer control. The same program was also used to switch the ferroelectric device and control an A/D board that was used to acquire various auxiliary data associated with conduct of the experiment.

Cortical bone samples were machined from the body of a bovine mandible. The long axis of the samples (the direction in which the samples were ultimately loaded) was parallel to the occlusal plane (i.e. along the long axis of the mandible body). Samples were kept wet throughout the machining process and stored in a buffered physiological salt (HEPES) solution until tested. During testing the samples were kept wet through ad-lib spraying with the HEPES solution.

Samples were mounted in a custom tensile testing machine[10] fitted with a 50N maximum load cell (Entran Devices, MLGLE-50) and a piezoelectric transducer (PZT) (Physik Instrument, model P-841.40, 60μm maximum expansion) that served to move the crosshead. The laser speckle strain gauge was arranged as described above, with a collimated beam (to restrict sensitivity to in-plane strains only) striking the sample over a spot length of about 2.5cm. A contact strain gauge was bonded to the surface opposite the beam spot. Output from the strain gauge was conditioned via a Wheatstone bridge and collected through the A/D board mounted on the computer bus. A preload of approximately 20N was applied to the sample and a dynamic triangular stress waveform was applied through the PZT. Applied dynamic load and location of the PZT were recorded through the A/D board. Pertinent parameters of the experiment are summarized in Table I.

Table I
Experimental parameters

| | |
|---|---|
| bone sample dimensions | 57.06 x 5.29 x 1.83mm |
| grip-to-grip distance | 42.2mm |
| illumination angle | ±42° |
| laser wavelength | 809nm |
| laser power | 150mW |
| effective observation distance | 28.6mm |
| camera integration time | 10ms |
| sample interval | 0.08s |
| loading waveform | triangular @ 0.1Hz |
| load variation | 5.5 ± 2.5N |

## 4. RESULTS

Figure 5 shows the speckle histories for this experiment. The resulting strain as calculated using the ML estimator is plotted in Fig.6. The stress-strain relationship for this result and that from the strain gauge are shown respectively in Figs. 7 and 8. Least-squares fits to these data sets yielded estimates of the modulus of elasticity of respectively 7.1 and 2.7GPa.

## 5. DISCUSSION

The stress-strain relationship displayed in Fig. 8 is quite noisy. As such, the modulus estimate using these data is suspect. The corresponding results (Fig. 7) using the speckle data is better behaved. Even so, the local slope of the stress-strain curve is quite variable. Estimation of the modulus through the formula

$$E = mean\left\{\frac{\Delta\sigma}{\Delta\varepsilon}\right\}, \tag{13}$$

yields the value of 18.9GPa. This is more in line with accepted values for cortical bone[11]. Note the obvious hysteresis displayed in Fig 7 of the stress-strain relationship using the speckle data.

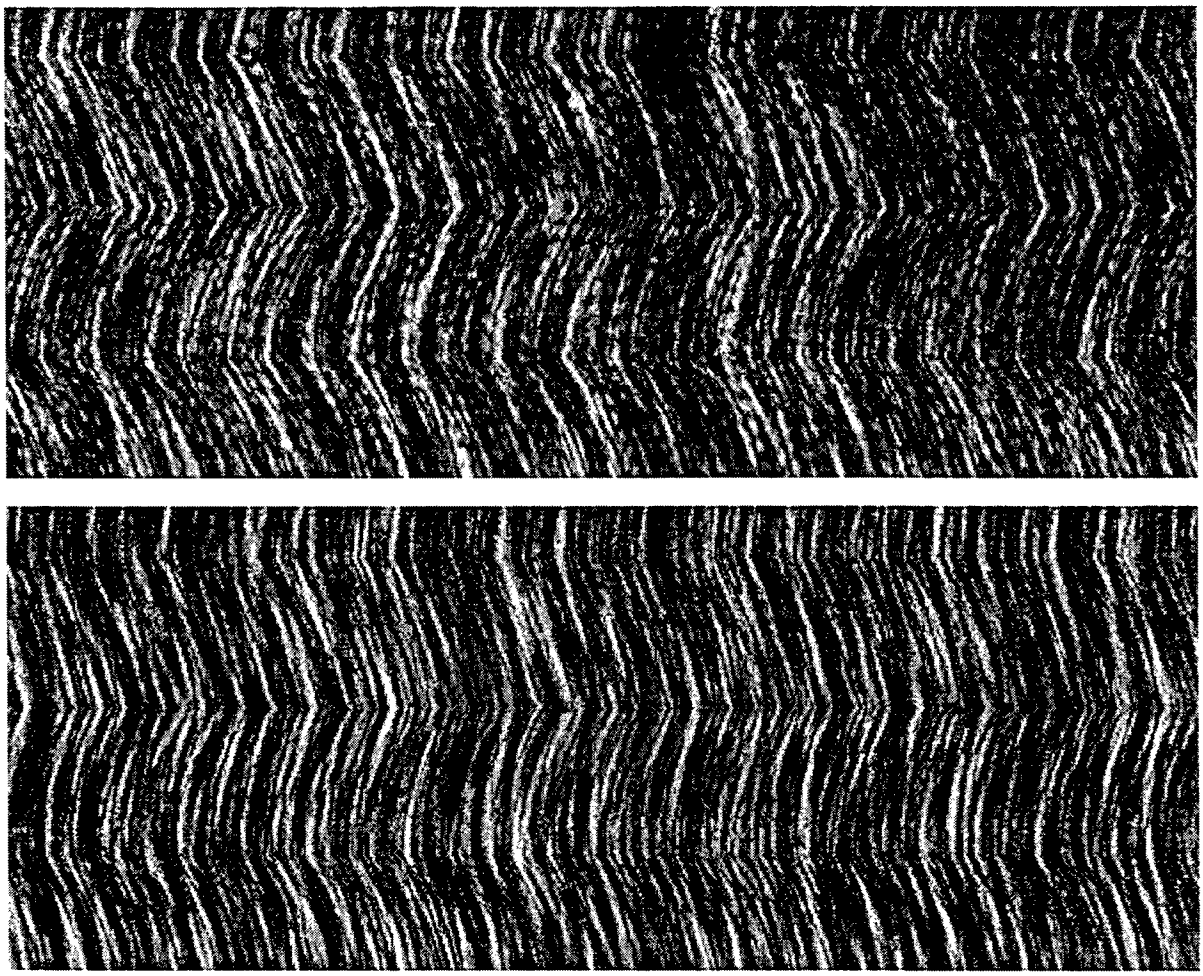

Fig. 5 Speckle histories for the experiment

The parametric approach taken in this algorithm makes use of the a priori knowledge that the speckle motions are small with respect to a pixel. Apart from this restriction, the resolution is not dictated by the size of the pixel. This is important in applications where rapid decorrelation of the speckle patterns is due to motion of various bodies within the hydrated tissues. In formulating the temporal shift in terms of the records on either side of the record of interest, the estimator took the form of the first central difference (Eq. 7). Alternatively, we could have chosen the $r$ records on either side. As an example, somewhat better noise characteristics are obtained with a derivative filter optimized with the Taylor series method[12], for example with the filter coefficients

$$\frac{1}{840}[-3, +32, -168, +672, 0, -672, +168, -32, +3] \quad . \tag{14}$$

In other words, the temporal derivative of Eq. (7) is calculated as

$$\begin{aligned} \frac{d}{dt} g_j(x_i) \approx \frac{1}{840}\big[&-3g_{j-4}(x_i) + 32g_{j-3}(x_i) - 168g_{j-2}(x_i) + 672g_{j-1}(x_i) \\ &-672g_{j+1}(x_i) + 168g_{j+2}(x_i) - 32g_{j+3}(x_i) + 3g_{j+4}(x_i)\big] \quad . \end{aligned} \tag{15}$$

Additionally, these higher order operators for the derivative can be used to estimate the spatial derivatives as in Eqs. (8). By making use of these higher order approximations to the first derivative, the processing can be tailored to the characteristics of the experiment.

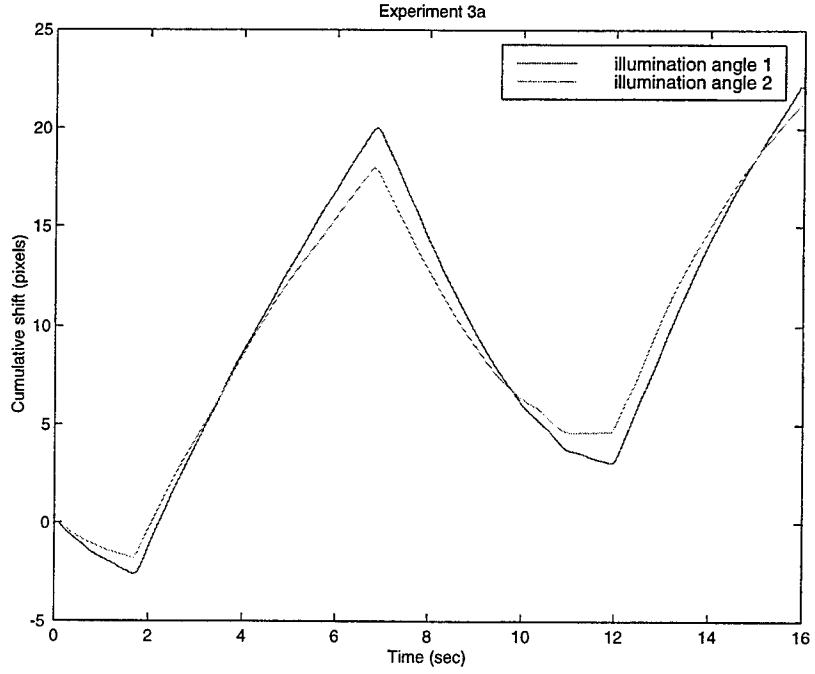


Fig. 6 ML estimates of speckle pattern shift

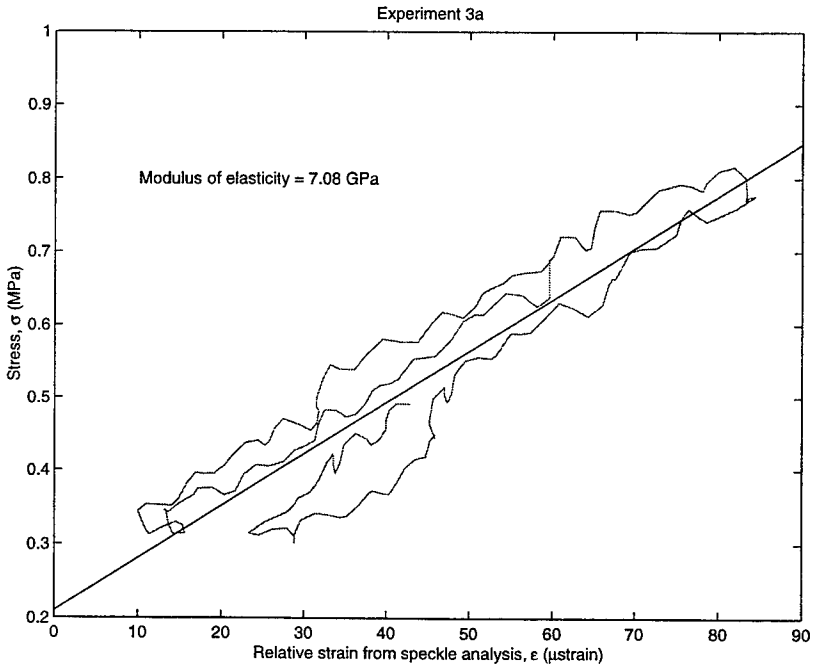


Fig. 7 Stress-strain relationship using speckle data

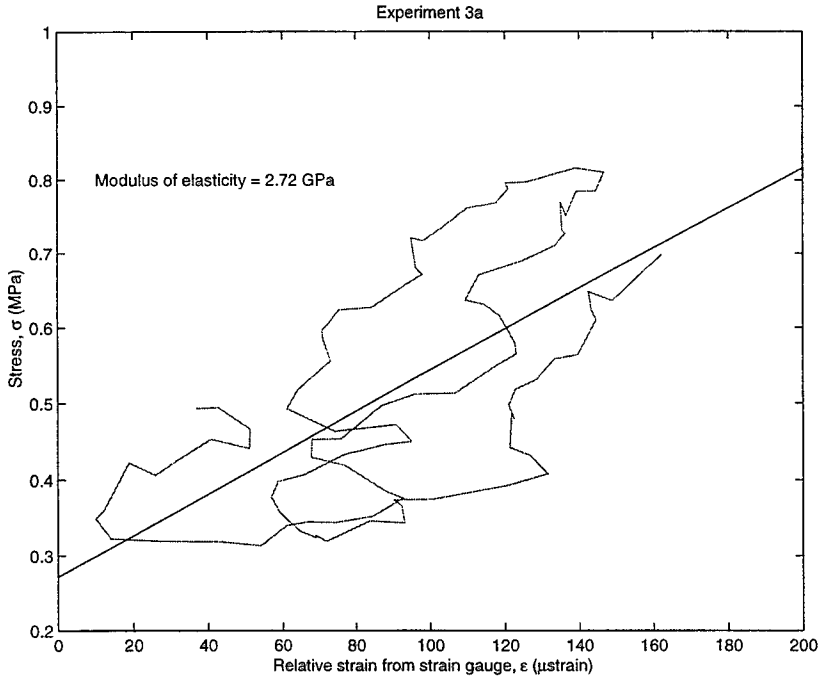


Fig. 8 Stress-strain relationship using strain gauge

The purpose in this paper was not to show that one method of estimating speckle motion was superior to another. Rather, the intent was to demonstrate that experimental concerns dictate the preferred processing technique. Correlation techniques are straightforward and computationally expedient, but are limited by the detector pixel size. The transform technique is very robust; it effectively disassociates the low frequency (speckle) behavior from that of the higher frequency noise. In fact, the bright line in "frequency space" produced by the transform is actually the autocorrelation of the illumination pattern[13]. Due to this property, the transform technique can cope with high noise levels. Ultimately, however, the resolution of the transform approach, like that of the correlation method, is related to the pixel size. Further, the transform approach depends upon the length of the data acquisition time through the uncertainty principle. The longer the data acquisition time, the better focused is the bright line in frequency space. On the other hand, very short data records in which speckle motions are small are where the ML estimator excels. Although this approach is more sensitive to noise in the data, this behavior can be mitigated somewhat by choice of the order of the first derivative calculation. Generally, the parametric approach as exemplified by the ML estimator, suggests other approaches that may be of interest, such as maximum entropy.[14, 15]

## ACKNOWLEGMENTS

We gratefully acknowledge the support for this research from NSF Grant BES-9807497.

## REFERENCES

1. R. Jones and C. Wykes, *Holographic and Speckle Interferometry. A discussion of the theory, practice and applications of the techniques*, Cambridge University Press, Cambridge, 1983.
2. K. J. Gåsvik, *Optical Metrology Second Edition*, John Wiley & Sons, Chichester, 1995.
3. G. Cloud, *Optical Methods of Engineering Analysis*, Cambridge University Press, Cambridge, 1995.
4. *Optical Measurement Techniques and Applications*, P. K. Rastogi, editor, Artech House, Inc., Boston, 1997.
5. A. Oulamara, G. Tribillon, and J. Duvernoy, "Biological activity measurement on botanical specimen surfaces using a temporal decorrelation effect of laser speckle," *J. Mod. Opt.*, **36**, pp. 165-179, 1989.
6. I. Yamaguchi, "Speckle displacement and decorrelation in the diffraction and image fields for small object deformation," *Opt. Acta.*, **28**, pp. 1359-1376, 1981.

7. T. Takemori, K. Fujita, I. Yamaguchi, "Resolution improvement in speckle displacement and strain sensor by correlation interpolation," *Computer Aided Interferometry, Proc. SPIE*, **1445**, pp. 137-148, 1991.
8. D. D. Duncan, S. J. Kirkpatrick, F. F. Mark, and L. W. Hunter, "Transform method of processing for speckle strain rate measurements," *Appl. Opt.*, **33**, pp. 5177-5186, 1994.
9. H. L. Van Trees, *Detection, Estimation, and Modulation Theory, Part I*, John Wiley and Sons, New York, 1868.
10. S. J. Kirkpatrick, and D. D. Duncan, "Noncontact microstrain measurements in orthodontic wires," *J. Biomed Mater Res.* **29**, pp. 1437-1442, 1995.
11. S. A. Wainwright, W. D. Biggs, J. D. Curey, and J. M. Gosline, *Mechanical Design in Organisms*, Princeton University Press, Princeton, 1982.
12. B. Jähne, CRC Press, Boca Raton, *Practical Handbook on Image Processing for Scientific Applications*, 1997.
13. J. W. Goodman, "Statistical properties of laser speckles," in J. C. Dainty (ed.), Topics in Applied Physics, Vol. 9*: Laser Speckle and Related Phenomena, Second Enlarged Edition*, Springer Verlag, New York, 1984.
14. A. Papoulis, *Probability, Random Variables, and Stochastic Processes, Third Edition*, McGraw-Hill, Boston, 1991.
15. B. R. Frieden, *Probability, Statistical Optics, and Data Testing: A Problem Solving Approach, Second Edition*, Springer-Verlag, Berlin, 1991.

# Addendum

The following papers were announced for publication in this proceedings but have been withdrawn or are unavailable.

[3914-03] **In-vivo release of tumor-associated antigens following photodynamic therapy (PDT)**
S. O. Gollnick, B. R. Lee, B. Owczarczak, L. A. Vaughan, B. W. Henderson, Roswell Park Cancer Institute (USA)

[3914-05] **Laser immunotherapy treatment on rats with prostatic tumors and lung metastases**
W. R. Chen, Univ. of Oklahoma (USA) and Oklahoma School of Science and Math (USA); H. Liu, Univ. of Virginia (USA); K. E. Bartels, J. W. Ritchey, Oklahoma State Univ. (USA); J. A. Nordquist, Wound Healing of Oklahoma, Inc. (USA); R. E. Nordquist, Univ. of Oklahoma (USA) and Wound Healing of Oklahoma, Inc. (USA)

[3914-06] **Possible immune response following interstitial laser thermotherapy of an adenocarcinoma transplanted into rat liver**
K. Tranberg, K. Ivarsson, A. Bruun, U. Stenram, Lund Univ. (Sweden)

[3914-09] **Thermal effects of cryogen spray cooling during laser treatment of port-wine stains**
T. Pfefer, T. E. Milner, A. J. Welch, Univ. of Texas/Austin (USA); D. J. Smithies, Beckman Laser Institute and Medical Clinic (USA); M. J. van Gemert, Beckman Laser Institute and Medical Clinic (USA) and Academic Medical Ctr. (Netherlands); J. S. Nelson, Beckman Laser Institute and Medical Clinic (USA)

[3914-14] **Laser-mediated nasal septal cartilage reshaping: optical, thermal, and quasi-elastic light scattering studies**
J. -I. Youn, K. F. Chan, E. H. Kim, N. C. Bhavaraj, D. P. Dave, S. A. Telenkov, Univ. of Texas/Austin (USA); B. J. F. Wong, Univ. of California/Irvine (USA); T. E. Milner, Univ. of Texas/Austin (USA)

[3914-24] **Heat accumulation under IR laser ablation: effects of the repetition rate**
D. Meyer, H. Fercher, H. Foth, Univ. Kaiserslautern (Germany)

[3914-53] **Polarization changes of back-reflected light in human skin**
J. F. de Boer, C. E. Saxer, B. H. Park, Z. Chen, J. S. Nelson, Beckman Laser Institute and Medical Clinic (USA)

[3914-54] **Dynamic light scattering in turbid media**
C. Cheung, A. G. Yodh, Univ. of Pennsylvania (USA)

[3914-62] **Molecular mechanisms of laser action on hemoglobin at the conditions of acute carbon monoxide poisoning**
E. Y. Stavitskaya, V. V. Salmin, A. B. Egorova, Krasnoyarsk State Medical Academy (Russia)

[3914-66] **Molecular basis for engineering craniofacial tissues**
C. Sfeir, Oregon Health Sciences Univ. (USA)

[3914-76] **Instrumental effects on in-vivo spectra of skin tissue using near-infrared diffuse reflectance spectroscopy**
P. Lampen, H. M. Heise, Institut für Spektrochemie und Angewandte Spektroskopie (Germany)

[3914-79] **Use of fluorescent dyes to assess chondrocyte viability**
A. Rasouli, Univ. of California/Irvine (USA)

# Author Index

ISSN 1605-7422
ISBN 0-8194-3530-9